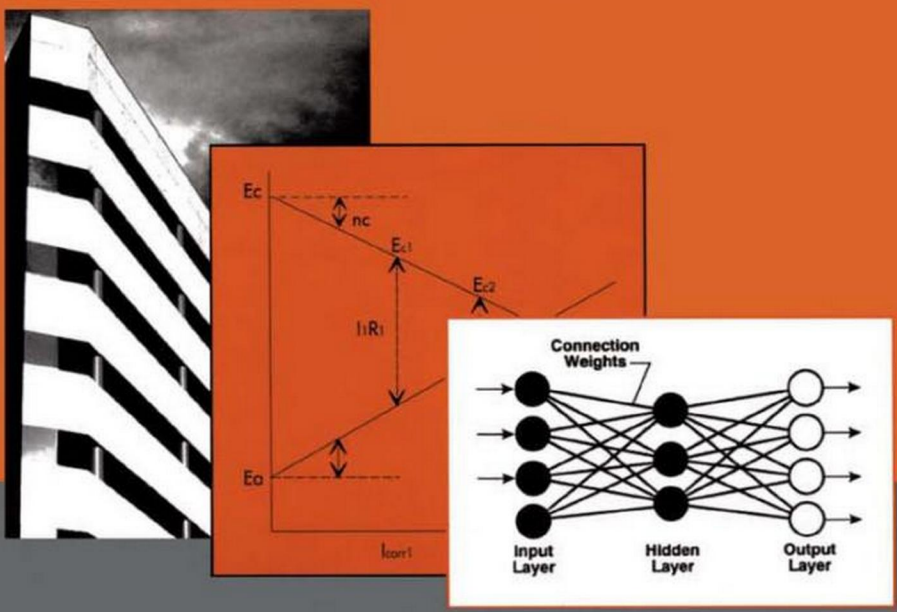
Handbook of Analytical Techniques in Concrete Science and Technology

Principles, Techniques and Applications



Edited by
V.S. Ramachandran
James J. Beaudoin

Building Materials Series

@Seismicisolation

HANDBOOK OF ANALYTICAL TECHNIQUES IN CONCRETE SCIENCE AND TECHNOLOGY

Principles, Techniques, and Applications

Edited by

V. S. Ramachandran

and

James J. Beaudoin

Institute for Research in Construction
National Research Council Canada
Ottawa, Ontario, Canada

NOYES PUBLICATIONS
Park Ridge, New Jersey, U.S.A.

WILLIAM ANDREW PUBLISHING, LLC
Norwich, New York, U.S.A.

@Seismicisolation

@Seismicisolation

Copyright © 2001 by William Andrew Publishing/Noyes Publications
No part of this book may be reproduced or utilized in any form or by any means, electronic or mechanical, including photocopying, recording or by any information storage and retrieval system, without permission in writing from the Publisher.
Library of Congress Catalog Card Number: 99-29616
ISBN: 0-8155-1437-9
Printed in the United States

Published in the United States of America by
Noyes Publications / William Andrew Publishing, LLC
Norwich, New York, U.S.A.

10 9 8 7 6 5 4 3 2 1

Library of Congress Cataloging-in-Publication Data

Ramachandran, V. S.
Handbook of analytical techniques in concrete science and technology / by V.S. Ramachandran and J.J. Beaudoin.
p. cm.
Includes bibliographical references.
ISBN 0-8155-1437-9
1. Concrete--Testing. 2. Concrete--Analysis. I. Beaudoin, J. J. II. Title.
TA440.R26 1999
624.1'83--dc21 99-29616
CIP

@Seismicisolation

@Seismicisolation

BUILDING MATERIALS SCIENCE SERIES

Editor

V. S. Ramachandran, National Research Council Canada

CONCRETE ADMIXTURES HANDBOOK; Properties, Science and Technology, *Second Edition:* edited by V. S. Ramachandran

CONCRETE ALKALI-AGGREGATE REACTIONS: edited by P. E. Grattan-Bellew

CONCRETE MATERIALS; Properties, Specifications and Testing, *Second Edition:* by Sandor Popovics

HANDBOOK OF ANALYTICAL TECHNIQUES IN CONCRETE SCIENCE AND TECHNOLOGY; Principles, Techniques, and Applications: edited by V. S. Ramachandran and James J. Beaudoin

HANDBOOK OF CONCRETE AGGREGATES; A Petrographic and Technological Evaluation: by Ludmila Dolar-Mantuani

HANDBOOK OF FIBER-REINFORCED CONCRETE; Principles, Properties, Developments, and Applications: by James J. Beaudoin

HANDBOOK OF POLYMER MODIFIED CONCRETE AND MORTARS; Properties and Process Technology: by Yoshihiko Ohama

WASTE MATERIALS USED IN CONCRETE MANUFACTURING: edited by Satish Chandra

Related Titles

CORROSION AND CHEMICAL RESISTANT MASONRY MATERIALS HANDBOOK: by W. L. Sheppard, Jr.

@Seismicisolation

NOTICE

To the best of our knowledge the information in this publication is accurate; however the Publisher does not assume any responsibility or liability for the accuracy or completeness of, or consequences arising from, such information. This book is intended for informational purposes only. Mention of trade names or commercial products does not constitute endorsement or recommendation for use by the Publisher. Final determination of the suitability of any information or product for use contemplated by any user, and the manner of that use, is the sole responsibility of the user. We recommend that anyone intending to rely on any recommendation of materials or procedures mentioned in this publication should satisfy himself as to such suitability, and that he can meet all applicable safety and health standards.

@Seismicisolation

Foreword

Material sciences have always been a leading driver in construction innovation. This is still true today with new technologies producing new materials and advancing the performance and applications of old ones. Many issues have to be addressed and resolved before such materials are confidently accepted in practice. Issues such as durability and long-term performance, design methods to allow their integration in construction, and new or modified standards to facilitate acceptance in the marketplace are often mentioned. This book on analytical techniques in concrete science and technology is a valuable addition to the literature addressing these subjects.

Over the past three decades, material scientists at IRC have contributed extensively to the advances on construction research through the development of experimental techniques. Their work is based on innovations in many areas including differential thermal methods, x-ray diffractometry, electron microscopy, petrography and design of special miniature techniques for determining mechanical behavior of cement systems. It is, therefore, natural to see that seven of the book's chapters are written by IRC scientists. To add to this strength, the other thirteen chapters are written by world-class experts in their respective fields.

The book is the first of its kind addressing technologies associated with the use of both organic and inorganic products and composite materials. The principles of the techniques are explained and applications clearly described. In addition, a wide selection of references are provided to give the reader ready access to more detailed information should it be required.

@Seismicisolation

The techniques described in the book are useful for analysis and prediction of many material-related issues such as: (*i*) resolving durability issues related to the mechanisms of reaction, (*ii*) determining parameters that influence reaction kinetics of processes that affect material properties and service life of building elements, (*iii*) developing and characterizing new materials for durable structures, (*iv*) establishing reasons for structural failures and conducting related forensic investigations, (*v*) providing a basis for the development of relevant standards and methods for advancing aspects of objective based codes, and (*vi*) validating numerical methods for predicting long-term performance of construction materials.

The result is a handbook that presents up-to-date information in the form that makes it valuable to read and come back to frequently. It should become a valuable reference source for students and practitioners as well as professionals engaged in standards writing.

Sherif Barakat
Director General
Institute for Research in Construction
National Research Council Canada
Ottawa, Canada

@Seismicisolation

Preface

Concrete is a composite material formed by mixing and curing ingredients such as cement, fine and coarse aggregates, and water. Most concretes, however, contain additional ingredients such as chemical admixtures including air-entraining admixtures, fly ash, fibers, slag, and other products.

The physical, chemical and durability characteristics of concrete depend on many factors such as the type and amount of the components, temperature, pore and pore size distribution, surface area, interfacial features, exposure conditions, etc. Consequently, a good understanding of various processes occurring in cementitious systems necessitates the application of diverse techniques.

Several physical, chemical, and mechanical techniques are applied in concrete research and practice. They provide important information, including characterization of raw materials and cured concrete, quality control, quantitative estimation of products, prediction of performance, development of accelerated test methods, study of interrelationships amongst physical, chemical, mechanical, and durability characteristics, development of new materials, etc. In most instances, no single technique provides all the needed information and hence application of several techniques becomes necessary. Information on the application of various techniques in concrete is dispersed in literature, and few books are available that serve as a source or reference. Hence a handbook incorporating the latest knowledge on the application of various investigative techniques in concrete science and

@Seismicisolation

technology has been prepared. Standard test methods are not covered in this book as they are well described in publications of national and international standards organizations.

The book is divided into twenty chapters. Each chapter describes the technique and its application and limitations for the study of concrete,. Each chapter also contains a list of important references that should serve as a useful guide for further information.

The first chapter on concrete science describes the essential concepts so that information presented in subsequent chapters can be easily followed. The chapter deals with the formation of cement, its hydration behavior, physicochemical processes related to the cement paste, and several important properties of concrete and durability aspects.

Chapter 2 deals with the description of a number of specialized techniques used in conjunction with petrography for the evaluation and analysis of aggregates of concrete.

Chemical analysis methods have been applied extensively to analyze the components of concrete, chemical and mineral admixtures, raw materials for making cement and also to estimate cement contents. Modern analytical tools enable much faster analysis than the wet chemical methods. In Chapter 3, chemical analysis techniques reviewed include atomic absorption, x-ray emission and plasma spectroscopy. The chapter also contains information on chemical (wet) methods of analysis.

Thermal analysis techniques based on the determination of physical, chemical, and mechanical changes in a material as a function of temperature, have been routinely used in concrete science and technology. Identification, estimation of compounds, kinetics of reactions , mechanisms of the action of admixtures, synthesis of compounds, quality control and causes leading to the deterioration of cementitious materials are investigated by these techniques. Various types of thermal techniques and their applications and limitations are included in Chapter 4.

Although comparatively recent, IR spectroscopy is gaining importance, especially with the development of user-friendly equipment as described in the fifth chapter. This technique has been applied for identification of new products and characterization of raw materials, hydrated materials, and deteriorated products., Discussion on Raman spectroscopy, a complementary technique to IR, also forms a part of this chapter.

Nuclear Magnetic Resonance spectroscopy (NMR) is a effective tool to probe atomic scale structure and dynamic behavior of cementing materials. The application of NMR for determining the pore structure and

@Seismicisolation

transport properties of cement and concrete via relaxation and imaging methods and its application to anhydrous cement and hydrated cement phases form some of the contents of Chapter 6.

Scanning Electron Microscopy and its adjunct, microanalytical unit, known as Energy Dispersive X-ray Analyzer, have been accepted as important investigative techniques in concrete technology. Chapter 7 comprises discussion on the microstructure of hydrated cement paste, C-S-H phase, calcium hydroxide, aluminate hydrate phases, paste-aggregate interface, admixtures, slags, and fly ashes. Also included are studies on the correlation of microstructure with durability.

The eighth chapter on the application of x-ray diffraction focuses on some of the fundamental aspects of the technique, the hardware and software developments, and its applications to cement and concrete.

An understanding of the rheology of fresh cement paste and concrete is essential for following the behavior of concrete in the fresh state. Additions and admixtures in concrete alter its rheological behavior. Chapter 9 deals with rheological techniques and their application to fresh cement paste and concrete.

Dimensional changes occur in cement paste and concrete due to physical, chemical, and electrochemical processes. A discussion of energetics of surface adsorption and volume changes forms the scope of Chapter 10. Relevance of length changes to concrete deterioration is also highlighted in this chapter.

The use of miniature specimens in cement science investigations has proven to be very valuable because it assures a greater homogeneity of the sample and increased sensitivity to the dimensional changes resulting from physical and chemical processes. Chapter 11 provides results on compacted powder used as a model system and includes discussion on creep and shrinkage, volume stability, workability, and surface chemical changes.

Corrosion of reinforced concrete is a major destructive process. Many electrochemical techniques have been developed to study corrosion. Chapter 12 presents a comprehensive treatment of the principles of corrosion, factors responsible for corrosion, and corrosion assessment techniques relevant to concrete.

Surface area has an important influence on the rate of reaction of cement to water and other chemicals. Many physical and mechanical characteristics of cement and concrete are modified by changes in the surface area. In Chapter 13, the techniques that are used for measuring surface area are given with respect to their application to systems such as

@Seismicisolation

raw materials for cement, hydrated cement, concrete mix, and also to durability studies.

The pore structure of hydrated cement systems influences significantly the physicomechanical and chemical behavior of concrete. Several experimental techniques have been employed to evaluate the microstructure of the cement paste. Chapter 14 presents a description of six techniques that have been developed for the determination of pore structure. The relationship between pore structure and strength/permeability is also included.

The application of silica polymerization analysis for an understanding of the hydration process and structure of calcium silicate hydrates is detailed in Chapter 15. Three major techniques used for polymerization studies are described.

In concrete, the physical structure and the state of water in the matrix influences the permeation process. In Chapter 16, test methods that are employed to measure various transport characteristics of concrete are evaluated. The applicability and limitations of these techniques is also reviewed.

Inspection and testing of placed concrete may be carried out by nondestructive testing methods. Sonic and pulse velocity techniques are commonly used. Nondestructive methods are also applied to estimate strength, surface hardness, pullout strength, etc. Details of various nondestructive techniques and their applications are included in Chapter 17.

There is evidence of a significant impact of computer and information technologies on concrete science and technology. General development of these technologies in recent years is reviewed in Chapter 18. The treatment includes computer models, databases, artificial knowledge-based and computer-integrated systems.

In Chapter 19, entitled "Image Analysis," steps needed to identify reactions of interest and extract quantitative information from digital images are reviewed. In image analysis, multiple images are acquired and analyzed. The principle steps required for image analysis of cementitious materials are described in this chapter.

Some of the more commonly used techniques in concrete studies are presented in Chapters 2 to 19. There has been continued interest in developing new techniques for the investigation of cement and concrete. Chapter 20 comprises the description and application of fourteen of these specialized techniques. They include such techniques as Auger Electron Microscopy, Chromatography, Mass Spectrometry, X-Ray Absorption Fine

@Seismicisolation

Structure Analysis, Synchrotron Orbital Radiation Analysis, Mössbauer Spectrometry, Radio Tracer Technique, and Photoacoustic Spectroscopy.

Although every attempt has been made to cover the important investigative techniques used in concrete technology, it is quite possible that some information has been excluded or is missing. In addition, some duplication of information occurs in some chapters. This was intentional because some specific chapters may only be of interest to specialized groups, and they provide enough self-contained information so that gleaning through other chapters will not be needed.

This comprehensive handbook should serve as a reference material to concrete technologists, materials scientists, analytical chemists, engineers, architects, researchers, manufacturers of cement and concrete, standards writing bodies, and users of concrete.

Ottawa, Canada
May 12, 2000

V. S. Ramachandran
James J. Beaudoin

@Seismicisolation

@Seismicisolation

Contributors

Xu Aimin
Sarkar and Associates
Houston, Texas

P. A. Muhammed Basheer
The Queen's University of Belfast
Belfast, Northern Ireland

James J. Beaudoin
National Research Council of Canada
Ottawa, Canada

A. K. Chatterjee
Cement House
Mumbai, India

James R. Clifton
National Institute of Standards and Technology
Gaithersburg, Maryland

David Darwin
University of Kansas
Lawrence, Kansas

Geoffrey Frohnsdorff
National Institute of Standards and Technology
Gaithersburg, Maryland

S. N. Ghosh
Structural Waterproofing Co.
P.O. – Shibpur, Howrah
West Bengal, India

P. E. Grattan-Bellew
National Research Council of Canada
Ottawa, Canada

@Seismicisolation

Gordon Ping Gu
National Research Council of Canada
Ottawa, Canada

Nataliya Hearn
Consultant
Timonium, Maryland

William G. Hime
Erlin, Hime and Associates
Northbrook, Illinois

Dipayan Jana
Sarkar and Associates
Houston, Texas

Xihuang Ji
University of Illinois at Urbana-Champaign
Urbana, Illinois

R. James Kirkpatrick
University of Illinois
Urbana, Illinois

V. M. Malhotra
Canada Centre for Mineral and Energy Technology
Ottawa, Canada

Jacques Marchand
Laval University
Quebec, Canada

Vangi S. Ramachandran
National Research Council of Canada
Ottawa, Canada

Shondeep L. Sarkar
Sarkar and Associates
Houston, Texas

Jan Skalny
Consultant
Timonium, Maryland

Leslie J. Struble
University of Illinois
Urbana-Champaign, Illinois

Guokuang Sun
University of Illinois
Urbana, Illinois

Hiroshi Uchikawa
Kanazawa Institute of Technology
Nonlchi, Ishikawa, Japan

J. Francis Young
University of Illinois
Urbana, Illinois

@Seismicisolation

Contents

1 Concrete Science 1

Vangi S. Ramachandran

1.0 INTRODUCTION 1
2.0 FORMATION OF PORTLAND CEMENT 2
3.0 INDIVIDUAL CEMENT COMPOUNDS 4
4.0 PORTLAND CEMENT 14
5.0 CEMENT PASTE 17
6.0 MODELS OF HYDRATED CEMENT 34
7.0 CONCRETE PROPERTIES 37
8.0 DURABILITY OF CONCRETE 42
REFERENCES 55

2 Petrographic and Technological Methods for Evaluation of Concrete Aggregates 63

P. E. Grattan-Bellew

1.0 INTRODUCTION 63
2.0 CHEMICAL TESTS 65
2.1 Chemical Tests for Alkali-Silica Reactivity 65
2.2 Chemical Analysis 66
2.3 Test Method ASTM C 289 69
3.0 AGGREGATES THAT RELEASE ALKALIS INTO THE PORE SOLUTION IN CONCRETE 73
4.0 DETERMINATION OF POROSITY AND WATER ABSORPTION OF AGGREGATES 75

@Seismicisolation

5.0 INSTRUMENTAL TECHNIQUES FOR DETERMINING THE POTENTIAL REACTIVITY OF SILICEOUS AGGREGATES . 78
5.1 X-Ray Diffraction Analysis in the Evaluation of Aggregates . 78
5.2 Infrared Spectroscopy 84
5.3 Differential Scanning Calorimetry (DSC) 87
6.0 STAINING TECHNIQUES FOR AGGREGATES 88
6.1 Copper Nitrate Staining Method 88
6.2 Methylene Blue Test 89
6.3 Measurement of Undulatory Extinction Angles 91
7.0 SHAPE AND SURFACE TEXTURE OF AGGREGATES 93
REFERENCES 98

3 Chemical Methods of Analysis of Concrete 105

William G. Hime

1.0 INTRODUCTION 105
1.1 The Analytical Problems for the Analyses of Hardened Concrete 105
1.2 The Components of Concrete 106
2.0 HARDENED CONCRETE ANALYSIS PROCEDURES 109
2.1 General 109
2.2 Cement Content Analysis 110
2.3 Sample Requirements and Procedure Choice 111
2.4 Calcium Oxide Content Procedure 112
2.5 Soluble Silica Content 112
2.6 Sulfate Content 113
2.7 Maleic Acid 113
2.8 Other Procedures 113
2.9 Chloride Analyses 113
2.10 Chloride Procedures 114
2.11 Sulfate and Sulfide Analyses 115
2.12 Water Analysis 115
2.13 Nitrate and Nitrite Analyses 117
2.14 Organic Components 118
2.15 Procedures 119
2.16 Elemental Concentrations 121
2.17 Compound and Mineral Compositions 122
3.0 MORTARS, GROUTS AND PLASTERS 124
3.1 Discussion 124
REFERENCES 125

4 Thermal Analysis 127

Vangi S. Ramachandran

1.0 INTRODUCTION 127
2.0 CEMENT CLINKER 130
3.0 SYNTHESIS OF CEMENT PHASES 133

@Seismicisolation

4.0 POLYMORPHISM IN SILICATES 136
5.0 HYDRATION OF CALCIUM SILICATES 138
6.0 HYDRATION OF C_3A AND C_4AF 146
7.0 HYDRATION OF CEMENT 151
8.0 DURABILITY 159
REFERENCES 169

5 IR Spectroscopy 174

S. N. Ghosh

1.0 INTRODUCTION 174
2.0 THEORY 174
2.1 Experimental Methods 176
3.0 THE SPECTRA OF ROCKS, MINERALS, CLAYS, ETC. 176
3.1 Calcite, Aragonite, and Magnesite 177
3.2 Estimation of Dolomite Content in Limestone 177
3.3 Argillaceous and Siliceous Limestones 183
3.4 Feldspar, Orthoclase, Quartz, and Jaspar 183
3.5 Tourmaline, Kyanite, Topaz, and Talc 184
3.6 Rhyolite, Granite, and Basalt 184
3.7 Kaolin, Red Clay, Black Cotton Soil, and White Clay 184
3.8 Chrysotile, Tremolite, and Asbestos 185
3.9 Biotite, Muscovite, Mica Schist, and Phlogophite Mica 186
3.10 Apatite, Phosphatic Rocks, and Gypsum 186
4.0 SPECTRA OF FLY ASH AND SLAG 187
5.0 ANHYDROUS CEMENT AND ITS PHASES 187
6.0 SOLID SOLUTION 192
7.0 HYDRATION STUDIES 193
7.1 C-S-H and Other Hydrates 194
7.2 Ettringite and Other Compounds 197
7.3 Hydration Studies under Different Conditions 198
8.0 STUDIES ON CONCRETE 199
9.0 MISCELLANEOUS STUDIES 199
ACKNOWLEDGMENT 200
REFERENCES 200

6 Nuclear Magnetic Resonance Spectroscopy 205

R. James Kirkpatrick

1.0 INTRODUCTION 205
1.1 Theory 205
1.2 Experimental Methods 215
2.0 STRUCTURAL INVESTIGATIONS OF ANHYDROUS CEMENT PHASES 216
2.1 Silicates 216
2.2 Aluminates 217
2.3 Glasses and Melts 217

@Seismicisolation

3.0 STRUCTURAL INVESTIGATIONS OF CALCIUM SILICATE HYDRATE (C-S-H) AND RELATED CRYSTALLINE PHASES .. 218
3.1 Tobermorite, Jennite, and Other Ca-Silicates 218
3.2 C-S-H 220
4.0 INVESTIGATIONS OF PORTLAND CEMENT HYDRATION . 221
5.0 INVESTIGATIONS OF ALUMINATE CEMENT HYDRATION .. 223
6.0 WASTE SOLIDIFICATION AND STABILIZATION 224
7.0 ALKALI SILICA GEL 224
8.0 STRUCTURAL INVESTIGATIONS OF RAW MATERIALS 224
9.0 NOTE ADDED IN PROOF 224
REFERENCES 225

7 Scanning Electron Microscopy, X-Ray Microanalysis of Concretes 231

Shondeep L. Sarkar, Xu Aimin, Dipayan Jana

1.0 INTRODUCTION 231
2.0 SCANNING ELECTRON MICROSCOPY, X-RAY MICROANALYSIS 232
2.1 Optical Microscopy-Electron Microscopy Transition 232
2.2 Scanning Electron Microscope 233
2.3 X-Ray Microanalysis 236
3.0 CONCRETE UNDER THE SEM 241
3.1 Basic Microstructure of Concrete 241
3.2 Admixtures in Concrete 248
4.0 INTERPRETATION OF CONCRETE DETERIORATION FROM SEM/EDXA 256
4.1 Types of Attack 256
4.2 Chemical Deterioration from External Agents 256
4.3 Chemical Deterioration from Internal Agents 265
4.4 Concrete Exposed to Marine Environment 266
5.0 SUMMARY 266
REFERENCES 272

8 X-Ray Diffraction 275

A. K. Chatterjee

1.0 INTRODUCTION 275
2.0 BASIC PRINCIPLE 276
2.1 Qualitative Analysis 276
2.2 Quantitative Analysis 279
3.0 DEVELOPMENTS IN INSTRUMENTATION 282
3.1 Microfocus X-Ray Diffractometer 284
3.2 Integrated XRD-XRF System 285
3.3 Time Resolved X-Ray Diffraction 285
3.4 Energy-Dispersive X-Ray Diffractometry 286

@Seismicisolation

4.0 COMPUTERS IN X-RAY DIFFRACTOMETRY AND SOFTWARE APPLICATIONS 286
4.1 Ab Initio Structure Determination from Powder Diffraction Data 288
4.2 Full Trace Diffraction Match and Files 288
4.3 Quantitative Phase Analysis Using Whole Powder Pattern Fitting 289
5.0 X-RAY DIFFRACTOMETRY OF CLINKER AND CEMENT 290
5.1 Methodological Aspects 291
5.2 Identification of Major Phases Present in Cement/Clinker 292
5.3 Semi-Quantitative and Quantitative Estimation of Phases 299
5.4 Quantitative Phase Analysis for Quality Control 305
5.5 Cement Substitute Materials 308
5.6 Standardization of X-Ray Diffractometry for Quantitative Phase Analysis 312
6.0 X-RAY DIFFRACTOMETRY OF HYDRATED CEMENT 313
6.1 Sample Preparation and XRD Study of Hydrated Specimens 314
6.2 Small Angle X-Ray Scattering 316
6.3 Application of Certain Quantitative Methods to Cement Substitute Materials 317
7.0 X-RAY DIFFRACTOMETRY IN CONCRETE CHEMISTRY 318
7.1 Cement Paste Aggregate Interface 319
7.2 Alkali-Silica Reaction 319
7.3 Sulfate Minerals 321
7.4 Other Studies of Concrete Damages 323
8.0 XRD IN MISCELLANEOUS CEMENTITIOUS SYSTEMS 323
9.0 CONCLUSIONS 326
ACKNOWLEDGMENTS 327
REFERENCES 327

9 Rheology 333

Leslie J. Struble and Xihuang Ji

1.0 INTRODUCTION 333
2.0 BACKGROUND 334
3.0 SUSPENSIONS 334
4.0 RHEOLOGICAL BEHAVIOR OF CEMENT PASTE 338
4.1 Static Flow Behavior 338
4.2 Dynamic Flow Behavior 344
5.0 CONCRETE 351
5.1 Flow Behavior 351
5.2 Effects of Composition 353
6.0 RHEOMETERS 357
6.1 Cement Paste 357
6.2 Concrete 359
ACKNOWLEDGMENTS 365
REFERENCES 365

@Seismicisolation

10 Dimensional Changes 368

James J. Beaudoin

1.0 INTRODUCTION 368
2.0 ENERGETICS OF ADSORPTION 369
2.1 Length Change Isotherms 369
2.2 The Theory of Flood and Heyding 373
3.0 CHEMICAL INTERACTIONS IN POROUS MEDIA 378
3.1 Volume Instability 378
3.2 Expansion of Impregnated Systems 380
3.3 Dimensional Change and Alkali-Aggregate Reactivity (AAR) 383
3.4 Sulfate Resistance 386
3.5 Dimensional Stability of Cement-Calcium Carbonate Systems 389
3.6 Dimensional Stability of Blended Cement Systems Exposed to Chloride Solutions 392
4.0 PHYSICOCHEMICAL INTERACTIONS IN POROUS MEDIA . 394
4.1 Low Temperature Length Change Isosteres 394
4.2 Dimensional Change—Shrinkage and Creep of Cement Systems 397
REFERENCES 401

11 Miniaturized Techniques 403

James J. Beaudoin

1.0 INTRODUCTION 403
2.0 COMPACTED POWDERS AND HYDRATED CEMENT PASTES AS MODEL POROUS SYSTEMS 404
2.1 Technique for Preparation of Compacts 405
2.2 Sorption Studies 406
2.3 Elastic Behavior of Compacted and Paste Hydrated Cement Systems 411
2.4 Compressive Strength of Individual Cement Minerals Determined Using Miniature Specimens 414
2.5 Evidence for a Model of C-S-H Structure Based on the Application of Miniature Tests 418
2.6 Remarks 421
3.0 CREEP AND DRYING SHRINKAGE MEASUREMENTS 422
3.1 Creep 422
3.2 Drying Shrinkage 427
4.0 VOLUME INSTABILITY OF POROUS SOLIDS 428
4.1 Accelerated Test Methods 428
4.2 Unsoundness of Lime 429
4.3 Failure of White Coat Plasters 430
4.4 Unsoundness of Portland Cement Containing MgO and CaO 430

@Seismicisolation

4.5 Durability of Cement Mortars Exposed to Chloride Solution .. 432
4.6 Miniature Rock Prism Test 435
5.0 THE MINI-SLUMP TEST 436
REFERENCES 438

12 Techniques for Corrosion Investigation in Reinforced Concrete 441

Gordon Ping Gu, James J. Beaudoin, and Vangi S. Ramachandran

1.0 INTRODUCTION 441
2.0 BASIC PRINCIPLES OF CORROSION 444
2.1 Half-Cell Potential 444
2.2 Butler-Volmer Equation 446
2.3 The Evans Diagram 447
2.4 Mixed Potential Theory 448
2.5 Corrosion Rate Controlling Mechanisms 452
2.6 The Evans Diagram and Polarization Curve 454
3.0 REINFORCING STEEL CORROSION IN CONCRETE 455
3.1 Concrete Properties 455
3.2 Mechanisms of Steel Corrosion in Concrete 457
3.3 General Steel Corrosion Process in Concrete 459
3.4 Carbonation Induced Corrosion 460
3.5 Chloride Ion Induced Corrosion 462
4.0 CORROSION ASSESSMENT TECHNIQUES 465
4.1 Mass Loss 467
4.2 Half-Cell Potential Measurement 468
4.3 Linear Polarization Measurement 472
4.4 The Transmission Line Model Approach 477
4.5 Tafel Extrapolation (Anodic/Cathodic Polarization) Technique 480
4.6 The Potential Step and Current Step Techniques 481
4.7 The Coulostatic Method 483
4.8 Cyclic Voltammetry 485
4.9 Alternating Current (ac) Impedance Spectroscopy (ACIS) 487
4.10 Macro-Cell Monitoring Techniques 493
4.11 Electrochemical Noise Monitoring 496
5.0 Concluding Remarks 496
REFERENCES 497

13 Surface Area Measurements 505

Jan Skalny and Nataliya Hearn

1.0 INTRODUCTION 505
1.1 The Importance of Surface Area in Cement/Concrete Science and Technology 507

@Seismicisolation

2.0 TECHNIQUES OF SURFACE AREA MEASUREMENT 508
2.1 Gas Sorption Techniques 510
2.2 Mercury Intrusion Porosimetry (MIP) 515
2.3 Wagner Turbidimeter 516
2.4 Permeability Methods 517
2.5 Small Angle X-Ray Scattering (SAXS) and Small Angle Neutron Scattering (SANS) 519
2.6 Nuclear Magnetic Resonance (NMR) 520
2.7 Image Analysis 521
3.0 APPLICATIONS 521
REFERENCES 524

14 Pore Structure 528

James J. Beaudoin and Jacques Marchand

1.0 INTRODUCTION 528
2.0 THE HELIUM INFLOW TECHNIQUE 529
2.1 The Concept 529
2.2 The Helium Comparison Pycnometer 529
2.3 General Procedure 530
2.4 Helium Inflow as a Function of Time 531
2.5 Mass Loss and the Volume of Helium Inflow 531
2.6 Space Vacated by Water Versus Degree of Drying 534
2.7 Pore Structure Models 534
2.8 Surface Area and Hydraulic Radius Calculations 536
2.9 Volume and Length Change Measurements on Rewetting to 11% RH 537
2.10 The Hydraulic Radius of the Internal Space of Hydrated Cement Paste 539
3.0 GAS ADSORPTION METHODS 540
3.1 Introduction 540
3.2 BET Adsorption Theory 541
3.3 The Kelvin Equation 543
3.4 Pore Size Distribution 544
3.5 Micropore Filling and V-t Plots 547
3.6 The Modelless Pore Method 548
3.7 The Micropore Analysis or MP Method 552
4.0 ALTERNATING CURRENT IMPEDANCE SPECTROSCOPY (ACIS) FOR PORE STRUCTURE CHARACTERIZATION 555
4.1 Basic Principles 555
4.2 Experimental Procedures 557
4.3 Equivalent Circuit Models 558
4.4 Electrical Circuit Models for Cement Paste 560
4.5 The High Frequency Arc 560
4.6 The High-Frequency Arc Diameter, R_2 564
4.7 Microstructural Parameter, ß 567

@Seismicisolation

5.0 THE SOLVENT REPLACEMENT TECHNIQUE 569
5.1 Introduction 569
5.2 Suitability of Organic Solvents for Microstructural Characterization 570
5.3 Diffusion Experiments 576
5.4 Investigation of Drying-Induced Pore Structure Alterations 582
6.0 MERCURY-INTRUSION POROSIMETRY 584
6.1 Introduction 584
6.2 The Concept 584
6.3 Operating Principle 586
6.4 Sample Preparation 587
6.5 Mercury Intrusion Experiment 588
6.6 Typical Mercury Intrusion Porosimetry Results 589
6.7 Problems Associated with Mercury Intrusion Porosimetry 591
6.8 Effect of Various Parameters on Mercury Intrusion Porosimetry Experiments 595
7.0 NUCLEAR MAGNETIC RESONANCE 600
7.1 Introduction 600
7.2 Basic Principles 601
7.3 Pore Structure Determinations 603
7.4 Typical Results 606
8.0 PHYSICO-MECHANICAL BEHAVIOR OF CEMENT SYSTEMS —PORE STRUCTURE RELATIONSHIPS 608
8.1 Strength-Porosity Relationships 608
8.2 High Performance Cement Systems 611
8.3 Relationships Between Pore Structure, Permeability and Diffusivity 613
8.4 Relationship Between Porosity and Degree of Hydration 617
REFERENCES 619

15 Silicate Polymerization Analysis 629

J. Francis Young and Guokuang Sun

1.0 Introduction 629
1.1 Analytical Methods 629
1.2 Silicate Structure of C-S-H 630
2.0 COMPLEXOMETRIC ANALYSIS 631
2.1 Basic Chemistry 631
2.2 Study of Cement Hydration 633
2.3 Analytical Procedure 633
3.0 TRIMETHYLSILYLATION 635
3.1 Basic Chemistry 635
3.2 Anhydrous Silicates 636
3.3 Application to Cements 637
3.4 Current TMS Method 639
3.5 Studies of Cement Hydration 641
3.6 Analytical Procedure 645

@Seismicisolation

4.0 SOLID STATE ^{29}Si NMR SPECTROSCOPY 645
4.1 Introduction to NMR Spectroscopy 645
4.2 Chemical Shifts 646
4.3 Acquisition of ^{29}Si Solid-State NMR Spectra 647
4.4 Application of ^{29}Si Solid-State NMR to the Study of Cements 651
5.0 CONCLUSIONS 653
REFERENCES 654

16 Permeation Analysis 658

P. A. Muhammed Basheer

1.0 DEFINITIONS AND TRANSPORT MECHANISMS 658
1.1 Physical Structure of Concrete 659
1.2 Forms of Water in Concrete 660
1.3 Definitions 661
1.4 Transport Mechanisms 662
2.0 ADSORPTION TESTS 666
3.0 DIFFUSION TESTS 667
3.1 Gas Diffusion Tests 667
3.2 Water Vapor Diffusion Tests 670
3.3 Ionic Diffusion Tests 672
4.0 ABSORPTION TESTS 685
4.1 Principle of Absorption Tests 685
4.2 Tests for Water Absorption Capacity 687
4.3 Sorptivity Tests 687
4.4 Absorptivity Tests 692
5.0 PERMEABILITY TESTS 699
5.1 Liquid Permeability Tests 700
5.2 Gas Permeability Tests 710
6.0 FACTORS INFLUENCING PERMEATION TESTS 718
6.1 Test Pressure and Duration of Test 718
6.2 Ambient Conditions at the Time of Test 719
6.3 Moisture Content of Concrete 719
7.0 RELATIONSHIP BETWEEN PERMEATION PROPERTIES AND DURABILITY OF CONCRETE 720
8.0 REMARKS ABOUT PERMEATION TESTS 726
REFERENCES 727

17 NDT Techniques 738

V. M. Malhotra

1.0 INTRODUCTION 738
2.0 RESONANT AND PULSE VELOCITY METHODS 739
2.1 Resonant Frequency Methods 739
2.2 Pulse Velocity Method 742
2.3 Stress Wave Propagation Methods 745

@Seismicisolation

3.0 SURFACE HARDNESS METHODS 745
3.1 Rebound Method 745
3.2 Probe Penetration Test 747
3.3 Pin Penetration Test 750
4.0 PULLOUT TEST 751
5.0 BREAK-OFF METHOD 753
6.0 MATURITY METHOD 754
7.0 PULL-OFF TESTS 756
8.0 COMBINED METHODS 757
9.0 CONCLUDING REMARKS 757
ACKNOWLEDGMENT 757
REFERENCES 758

18 Applications of Computers and Information Technology .. 765

James R. Clifton and Geoffrey Frohnsdorff

1.0 INTRODUCTION 765
1.1 Computer Applications in Material Science and Engineering 766
2.0 COMPUTER MODELS 767
2.1 Types of Models 767
2.2 Mathematical Language of Models 768
2.3 Material Science Models of Cement-Based Materials 768
3.0 DATABASE SYSTEMS 776
3.1 Applications of Databases in Concrete Technology 776
3.2 Existing Databases for Concrete and Concrete Materials 777
3.3 Standards for Databases, Database Formats, Quality of Data 779
3.4 Future Advances in Databases 782
4.0 ARTIFICIAL INTELLIGENCE AND KNOWLEDGE-BASED SYSTEMS 783
4.1 Expert Systems 783
4.2 Application Domains 784
4.3 Neural Networks 786
4.4 Case-Based Reasoning 788
5.0 COMPUTER-INTEGRATED KNOWLEDGE SYSTEMS (CIKS) FOR CONCRETE 788
5.1 Features and Development of a CIKS 788
5.2 Application of CIKS to Concrete Technology 789
6.0 SUMMARY 793
ACKNOWLEDGEMENTS 794
REFERENCES 794

19 Image Analysis 800

David Darwin

1.0 INTRODUCTION 800

@Seismicisolation

2.0 IMAGE ACQUISITION 801
2.1 Nature of the Signal and Contrast Mechanisms 802
2.2 Sample Preparation, Standards, and Imaging 805
2.3 Statistical Considerations 807
3.0 IMAGE PROCESSING 808
3.1 Contrast and Brightness 808
3.2 Thresholding 810
3.3 Image Modification 812
4.0 FEATURE RECOGNITION AND DATA ANALYSIS 813
4.1 Feature Recognition 813
4.2 Data Analysis 814
REFERENCES 818

20 Specialized Techniques 820

Hiroshi Uchikawa

INTRODUCTION 820
1.0 AUGER ELECTRON SPECTROSCOPY 821
2.0 SCANNING TUNNEL MICROSCOPY AND ATOMIC FORCE MICROSCOPY 829
2.1 Principle and Special Features 829
2.2 Application 833
3.0 CHROMATOGRAPHY 840
3.1 Principle and Special Feature 840
3.2 Apparatus 842
3.3 Applications 845
4.0 MASS SPECTROMETRY 847
4.1 Principle and Special Features 847
4.2 Apparatus 849
4.3 Applications 854
5.0 SECONDARY ION MASS SPECTROSCOPY 856
5.1 Principle and Special Features 856
6.0 CHROMATOGRAPHY-MASS SPECTROMETRY 860
6.1 Principle and Special Features 860
6.2 Apparatus 860
6.3 Applications 862
7.0 NUCLEAR QUADRUPOLE RESONANCE ANALYSIS 866
7.1 Principle and Special Features 866
7.2 Apparatus 870
7.3 Applications 871
8.0 X-RAY ABSORPTION FINE STRUCTURE ANALYSIS 872
8.1 Principle and Special Features 872
8.2 Apparatus 874
8.3 Applications 875

@Seismicisolation

9.0 SYNCHROTRON ORBITAL RADIATION ANALYSIS 878
9.1 Principle and Special Features 878
9.2 Apparatus 880
9.3 Applications 882
10.0 MÖSSBAUER SPECTROMETRY 885
10.1 Principle and Special Features 885
10.2 Apparatus 891
10.3 Applications 893
11.0 QUASI-ELASTIC NEUTRON SCATTERING ANALYSIS 896
11.1 Principle and Special Features 896
11.2 Apparatus 899
11.3 Applications 901
12.0 THERMOLUMINESCENCE ANALYSIS 907
12.1 Principle and Special Features 907
12.2 Apparatus 909
12.3 Applications 909
13.0 PHOTO-ACOUSTIC SPECTROSCOPY 914
13.1 Principle and Special Features 914
13.2 Apparatus 916
13.3 Applications 918
14.0 RADIO TRACER TECHNIQUE 920
14.1 Principle and Special Features 920
14.2 Apparatus 925
14.3 Applications 925
REFERENCES 927

Index 935

@Seismicisolation

1

Concrete Science

Vangi S. Ramachandran

1.0 INTRODUCTION

Concrete, made from cement, aggregates, chemical admixtures, mineral admixtures, and water, comprises in quantity the largest of all man-made materials. The active constituent of concrete is cement paste and the performance of concrete is largely determined by the cement paste. Admixtures in concrete confer some beneficial effects such as acceleration, retardation, air entrainment, water reduction, plasticity, etc., and they are related to the cement-admixture interaction. Mineral admixtures such as blast furnace slag, fly ash, silica fume, and others, also improve the quality of concrete.

The performance of concrete depends on the quality of the ingredients, their proportions, placement, and exposure conditions. For example, the quality of the raw materials used for the manufacture of clinker, the calcining conditions, the fineness and particle size of the cement, the relative proportions of the phases, and the amount of the mixing water, influence the physicochemical behavior of the hardened cement paste. In the fabrication of concrete, amount and the type of cement, fine and coarse aggregate, water, temperature of mixing, admixture, and the environment to which it is exposed will determine its physical, chemical, and durability behavior. Various analytical techniques are applied to study the effect of

@Seismicisolation

these parameters and for quality control purposes. The development of standards and specifications are, in many instances, directly the result of the work involving the use of analytical techniques. Discussion of the methods employed in standard specifications is beyond the scope of this chapter.

In this chapter, basic aspects of the physical, chemical, durability, and mechanical characteristics of cement paste and concrete are presented because of their relevance to the application of various analytical techniques discussed in other chapters.

2.0 FORMATION OF PORTLAND CEMENT

According to ASTM C-150, *portland cement* is a hydraulic cement produced by pulverizing clinker consisting essentially of hydraulic calcium silicates, usually containing one or more types of calcium sulfate, as an interground addition.

The raw materials for the manufacture of portland cement contain, in suitable proportions, silica, aluminum oxide, calcium oxide, and ferric oxide. The source of lime is provided by calcareous ingredients such as limestone or chalk and the source of silica and aluminum oxide are shales, clays or slates. The iron bearing materials are iron and pyrites. Ferric oxide not only serves as a flux, but also forms compounds with lime and alumina. The raw materials also contain small amounts of other compounds such as magnesia, alkalis, phosphates, fluorine compounds, zinc oxide, and sulfides. The cement clinker is produced by feeding the crushed, ground, and screened raw mix into a rotary kiln and heating to a temperature of about 1300–1450°C. Approximately 1100–1400 kcal/g of energy is consumed in the formation of clinker. The sequence of reactions is as follows: At a temperature of about 100°C (drying zone) free water is expelled. In the preheating zone (750°C) firmly bound water from the clay is lost. In the calcining zone (750–1000°C) calcium carbonate is dissociated. In the burning zone (1000–1450°C) partial fusion of the mix occurs, with the formation of C_3S, C_2S and clinker. In the cooling zone (1450–1300°C) crystallization of melt occurs with the formation of calcium aluminate and calcium aluminoferrite. After firing the raw materials for the required period, the resultant clinker is cooled and ground with about 4–5% gypsum to a specified degree of fineness. Grinding aids, generally polar compounds, are added to facilitate grinding.

@Seismicisolation

2.1 Composition of Portland Cement

The major phases of portland cement are tricalcium silicate ($3CaO•SiO_2$), dicalcium silicate ($2CaO•SiO_2$), tricalcium aluminate ($3CaO•Al_2O_3$), and a ferrite phase of average composition $4CaO•Al_2O_3•Fe_2O_3$. In a commercial clinker they do not exist in a pure form. The $3CaO•SiO_2$ phase is a solid solution containing Mg and Al and is called *alite*. In the clinker, it consists of monoclinic or trigonal forms whereas synthesized $3CaO•SiO_2$ is triclinic. The $2CaO•SiO_2$ phase occurs in the β form, termed belite, and contains, in addition to Al and Mg, some K_2O. Four forms, α, α', β and γ, of C_2S are known although in clinker only the β form with a monoclinic unit cell exists. The ferrite phase, designated C_4AF, is a solid solution of variable composition from C_2F to C_6A_2F. Potential components of this compound are C_2F, C_6AF_2, C_4AF, and C_6A_2F. In some clinkers small amounts of calcium aluminate of formula NC_8A_3 may also form.

ASTM C-150 describes five major types of portland cement. They are: Normal Type I—when special properties specified for any other type are not required; Type II—moderate sulfate resistant or moderate heat of hydration; Type III—high early strength; Type IV—low heat; and Type V—sulfate resisting. The general composition, fineness, and compressive strength characteristics of these cements are shown in Table 1.[1]

Portland cement may be blended with other ingredients to form blended hydraulic cements. ASTM C-595 covers five kinds of blended hydraulic cements. The portland blast furnace slag cement consists of an intimately ground mixture of portland cement clinker and granulated blast furnace slag or an intimate and uniform blend of portland cement and fine granulated blast furnace slag in which the slag constituent is within specified limits. The portland-pozzolan cement consists of an intimate and uniform blend of portland cement or portland blast furnace slag cement and fine pozzolan. The slag cement consists mostly of granulated blast furnace slag and hydrated lime. The others are pozzolan-modified portland cement (pozzolan < 15%) and slag-modified portland cement (slag < 25%).

@Seismicisolation

Table 1. Compound Composition, Fineness and Compressive Strength Characteristics of Some Commercial U.S. Cements

ASTM Type	ASTM Designation	Composition				Fineness cm^2/g	Compressive Strength % of Type I Cement*		
		C_3S	C_2S	C_3A	C_4AF		1 day	2 days	28 days
I	General purpose	50	24	11	8	1800	100	100	100
II	Moderate sulfate resistant-moderate heat of hydration	42	33	5	13	1800	75	85	90
III	High early strength	60	13	9	8	2600	190	120	110
IV	Low heat	26	50	5	12	1900	55	55	75
V	Sulfate resisting	40	40	4	9	1900	65	75	85

**All cements attain almost the same strength at 90 days.*

3.0 INDIVIDUAL CEMENT COMPOUNDS

3.1 Tricalcium Silicate

Hydration. A knowledge of the hydration behavior of individual cement compounds and their mixtures forms a basis for interpreting the complex reactions that occur when portland cement is hydrated under various conditions.

Tricalcium silicate and dicalcium silicate together make up 75–80% of portland cement (Table 1). In the presence of a limited amount of water, the reaction of C_3S with water is represented as follows:

$$3CaO{\bullet}SiO_2 + xH_2O \rightarrow yCaO{\bullet}SiO_2{\bullet}(x+y-3)H_2O + (3-y)Ca(OH)_2$$

or typically

$$2[3CaO{\bullet}SiO_2] + 7H_2O \rightarrow 3CaO{\bullet}2SiO_2{\bullet}4H_2O + 3Ca(OH)_2$$

The above chemical equation is somewhat approximate because it is not easy to estimate the composition of C-S-H (the C/S and S/H ratio) and there are also problems associated with the determination of $Ca(OH)_2$. In a fully hydrated cement or C_3S paste, about 60–70% of the solid comprises C-S-H. The C-S-H phase is poorly crystallized containing particles of

@Seismicisolation

colloidal size and gives only two very weak, diffuse peaks in XRD. The degree of hydration of C_3S can be measured by determining C_3S or $Ca(OH)_2$ by XRD, the non-evaporable water by ignition, or $Ca(OH)_2$ by thermal or chemical methods. Each of these methods has limitations. The $Ca(OH)_2$ estimated by XRD differs from that determined by chemical analysis. For example, Pressler, et al.,[2] found a value of 22% $Ca(OH)_2$ by XRD for portland cement pastes. The chemical extraction method gave values 3–4% higher and this difference was attributed to the presence of amorphous $Ca(OH)_2$. Lehmann, et al.,[3] on the other hand, reported that the extraction method yielded 30–90% $Ca(OH)_2$ higher than that by XRD. Thermogravimetric analysis gave identical values to those obtained by x-ray. Recently the technique of differential thermal analysis was applied by Ramachandran[4] and Midgley[5] for estimating $Ca(OH)_2$ in hydrating C_3S.

The direct methods of determining C/S ratios are based on electron optical methods such as electron microprobe or other attachments, or by electron spectroscopy (ESCA). Although several values are reported, the usual value for C/S ratio after a few hours of hydration of C_3S is about 1.4–1.6.[6] The C/S ratio of the C-S-H phase may be influenced by admixtures.

There are problems associated with the determination of H_2O chemically associated with C-S-H. It is difficult to differentiate this water from that present in pores. The stoichiometry of C-S-H is determined by assuming that little or no absorbed water remains in the sample at the d-dry condition (the vapor pressure of water at the sublimation temperature of solid CO_2, i.e., -78°C). In a recent investigation it has been shown that higher hydrates may exist at humidities above the d-dry state.[7] It has been proposed that drying to 11% RH is a good base for studying the stoichiometry of calcium silicate hydrate. At this condition, the estimate of adsorbed water can be made with some confidence. This does not mean that higher hydrates do not exist above 11% RH. Feldman and Ramachandran[8] estimated that the bottled hydrated C-S-H equilibrated to 11% RH (approached from 100% RH) had a composition 3.28 $CaO{:}2SiO_2{:}3.92\ H_2O$.

Hydration Mechanism. The mechanism of hydration of individual cement components and that of cement itself has been a subject of much discussion and disagreement. In the earliest theory, Le Chatelier explained the cementing action by dissolution of anhydrous compounds followed by the precipitation of interlocking crystalline hydrated compounds. Michaelis considered that cohesion resulted from the formation and subsequent desiccation of the gel.[9] In recent years, the topochemical or solid state mechanism has been proposed.

@Seismicisolation

In spite of a large amount of work, even the mechanism of hydration of C_3S, the major phase of cement, is not clear. Any mechanism proposed to explain the hydrating behavior of C_3S should take into account the following steps through which the hydration proceeds. Five steps can be discerned from the isothermal conduction calorimetric studies (Fig. 1). In the first stage, as soon as C_3S comes into contact with water there is a rapid evolution of heat and this ceases within 15–20 mins. This stage is called the *preinduction period.* In the second stage, the reaction rate is very slow. It is known as the *dormant* or *induction period* and may extend for a few hours. At this stage, the cement remains plastic and is workable. In the third stage, the reaction occurs actively and accelerates with time, reaching a maximum rate at the end of this *accelerating period*. *Initial set* occurs at about the time when the rate of reaction becomes vigorous. The *final set* occurs before the end of the third stage. In the fourth stage, there is slow deceleration. An understanding of the first two stages of the reaction has a very important bearing on the subsequent hydration behavior of the sample. The admixtures can influence these steps. The retarders, such as sucrose, phosphonic acids, calcium gluconate, and sodium heptonate, extend the induction period and also decrease the amplitude of the acceleration peak.

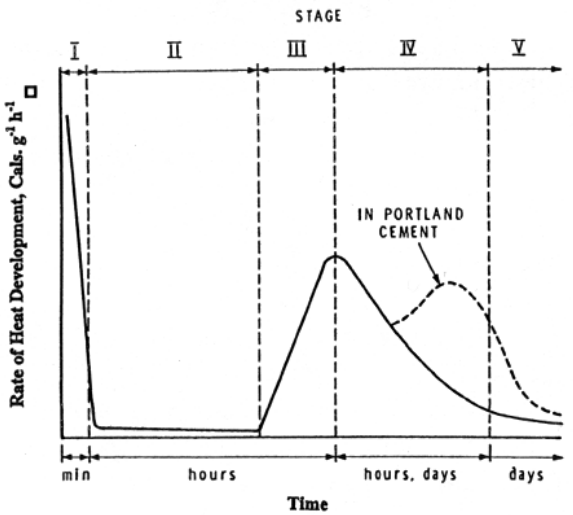


Figure 1. Rate of heat development during the hydration of tricalcium silicate and portland cement.[69] *(Reproduced with permission, Noyes Publications from* Concrete Admixtures Handbook, *2nd. Ed., 1995.)*

@Seismicisolation

The processes that occur during the five stages are as follows. In the first stage, as soon as C_3S comes into contact with water it releases calcium and hydroxyl ions into the solution. In the second stage, the dissolution continues and pH reaches a high value of 12.5. Not much silica dissolution occurs at this stage. After a certain critical value of calcium and hydroxide ions is reached, there is a rapid crystallization of CH and C-S-H followed by a rapid reaction. In the fourth stage, there is a continuous formation of hydration products. At the final stage, there is only a slow formation of products and at this stage the reaction is diffusion controlled.

It is generally thought that initially a reaction product forms on the C_3S surface that slows down the reaction. The renewed reaction is caused by the disruption of the surface layer. According to Stein and Stevels,[10] the first hydrate has a high C/S ratio of about 3 and it transforms into a lower C/S ratio of about 0.8–1.5 through loss of calcium ions into solution. The second product has the property of allowing ionic species to pass through it thus enabling a rapid reaction. The conversion of the first to the second hydrate is thought to be a nucleation and growth process. Although this theory is consistent with many observations, there are others which do not conform to this theory. They are: the C/S ratio of the product is lower than what has been reported, the protective layer may not be continuous, the product is a delicate film that easily peels away from the surface, and the early dissolution may or may not be congruent.

The end of the induction period has been explained by the delayed nucleation of CH. It is generally observed that the rapid growth of crystalline CH and the fall of calcium ions in solution occur at the end of the induction period. This suggests that the precipitation of CH is related to the start of the acceleratory stage. If precipitation of CH triggers the reaction, then additional Ca ions should accelerate the reaction unless it is *poisoned*. Addition of saturated lime is known to retard the reaction. Also, it does not explain the accelerated formation of C-S-H. Tadros, et al.,[11] found the zeta potential of the hydrating C_3S to be positive, indicating the possibility of the chemisorption of Ca ions on the surface resulting in a layer that could serve as a barrier between C_3S and water. During the precipitation of $Ca(OH)_2$ it is thought that Ca^{2+} from the solution is removed (which will in turn trigger the removal of Ca^{2+} from the barrier) and the reaction is accelerated.

@Seismicisolation

There are other mechanisms, based on the delayed nucleation of C-S-H, to explain the end of this induction period. One of them suggests that the stabilization action of the C_3S surface by a thin layer of water is removed when a high Ca^{2+} concentration in the solution causes the precipitation of C-S-H nuclei. According to Maycock, et al.,[12] the solid state diffusion within the C_3S grain controls the length of the induction period. The defects enhance diffusion and thereby promote the C-S-H nucleation. According to Fierens and Verhaegen,[13] the chemisorption of H_2O and dissolution of some C_3S occur in the induction period. The end of the induction period, according to them, corresponds to the growth of a critical size of C-S-H nuclei.

There are other theories which have been proposed to fit most of the observations. Although they appear to be separate theories, they have many common features. They have been discussed by Pratt and Jennings.[14] A detailed discussion of the mechanisms of hydration of cement and C_3S has been presented by Gartner and Gaidis.[15]

The hydration of C_2S proceeds in a similar way to that of C_3S, but is much slower. As the amount of heat liberated by C_2S is very low compared to that of C_3S, the conduction calorimetric curve will not show the well defined peaks as in Fig. 1. Accelerators will enhance the reaction rate of C_2S. The reaction of C_2S and water has been studied much less than that involving C_3S.

3.2 Dicalcium Silicate

Just as in the hydration process of C_3S, there are uncertainties involved in determining the stoichiometry of the C-S-H phase found in the hydration of C_2S. The hydration of dicalcium silicate phase can be represented by the equation.

$$2\,[2CaO{\bullet}SiO_2] + 5H_2O \rightarrow 3CaO{\bullet}2SiO_2{\bullet}4H_2O + Ca(OH)_2$$

The amount of $Ca(OH)_2$ formed in this reaction is less than that produced in the hydration of C_3S. The dicalcium silicate phase hydrates much more slowly than the tricalcium silicate phase.

Figure 2 compares the rates of hydration of C_3S and C_2S. The absolute rates differ from one sample to the other; for example, C_3S is much more reactive than C_2S. Several explanations have been offered to interpret the increased reactivity of C_3S. Proposed explanations include: the coordination number of Ca is higher than 6, coordination of Ca is

@Seismicisolation

irregular, holes exist in the crystal lattice, and differences occur in the position of the Fermi level. Some preliminary work has been done to test the relative reactivities of Ca^{2+} in CaO, $Ca(OH)_2$, C_3S, and C_2S by mixing each of them with known amounts of $AgNO_3$.[16] By heating them, it was found that the reaction of $AgNO_3$ with CaO, $Ca(OH)_2$, and hydrated C_3S, was stoichiometric with respect to Ca. Only 27% Ca present in C_3S and 6% Ca from C_2S reacted with $AgNO_3$. Possibly C_3S and C_2S structures are such that some Ca^{2+} ions are relatively more reactive owing to structural imperfections. There is evidence that if one mol of labeled Ca is reacted with C_2S to form C_3S, the hydration of C_3S would show that the initial reaction product contains mainly the labeled Ca ions. Further work would be necessary before definite conclusions can be drawn.

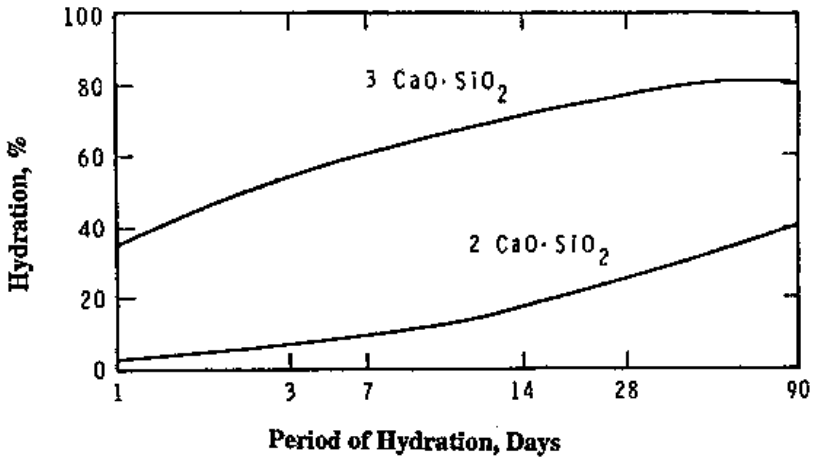


Figure 2. The relative rates of hydration of 3 CaO•SiO_2, and 2 CaO•SiO_2.[69] *(With permission, Noyes Publications,* Concrete Admixtures Handbook, 2nd Ed., *1995.)*

The rate of strength development of individual cement compounds was determined by Bogue and Lerch in 1934.[17] The comparison of reactivities and strength development of these compounds was not based on adequate control of certain parameters, such as particle size distribution, water:solid ratio, specimen geometry, method of estimation of the degree of hydration, etc. Beaudoin and Ramachandran[18] have reassessed the strength development in cement mineral pastes, both in terms of time and degree of hydration. Figure 3 compares the results of Bogue and Lerch

@Seismicisolation

with those of Beaudoin and Ramachandran.[18] Significant differences in the relative values of strengths developed by various phases were found. At ten days of hydration the strength values were ranked as follows by Beaudoin and Ramachandran: $C_4AF > C_3S > C_2S > C_3A$. At fourteen days the relative values were in the order $C_3S > C_4AF > C_2S > C_3A$. The Bogue-Lerch strength values both at ten and fourteen days were: $C_3S > C_2S > C_3A > C_4AF$. At one year, the corresponding values were $C_3S > C_2S > C_4AF > C_3A$ (Beaudoin-Ramachandran) and $C_3S = C_2S > C_3A > C_4AF$ (Bogue-Lerch). Beaudoin and Ramachandran found that compressive strength vs. porosity curves on a semilog plot showed a linear relationship for all pastes (Fig. 4). The lines seem to merge to the same value of a strength of 500 MPa at zero porosity. This would indicate that all the pastes have the same inherent strength. Comparison of strengths as a function of the degree of hydration revealed that at a hydration degree of 70–100%, the strength was in the decreasing order $C_3S > C_4AF > C_3A$.

3.3 Tricalcium Aluminate

Although the average C_3A content in portland cement is about 4–11%, it significantly influences the early reactions. The phenomenon of *flash set*, the formation of various calcium aluminate hydrates and calcium carbo- and sulfo-aluminates, involves the reactions of C_3A. Higher amounts of C_3A in portland cement may pose durability problems. For example, a cement which is exposed to sulfate solutions should not contain more than 5% C_3A.

Tricalcium aluminate reacts with water to form C_2AH_8 and C_4AH_{13} (hexagonal phases). These products are thermodynamically unstable so that without stabilizers or admixtures they convert to the C_3AH_6 phase (cubic phase). The relevant equations for these reactions are:

$$2C_3A + 21H \rightarrow C_4AH_{13} + C_2AH_8$$

$$C_4AH_{13} + C_2AH_8 \rightarrow 2C_3AH_6 + 9H$$

In saturated $Ca(OH)_2$ solutions, C_2AH_8 reacts with $Ca(OH)_2$ to form C_4AH_{13} or C_3AH_6, depending on the condition of formation. The cubic form (C_3AH_6) can also form directly by hydrating C_3A at temperatures of 80°C or above.[19][20]

$$C_3A + 6H \rightarrow C_3AH_6$$

@Seismicisolation

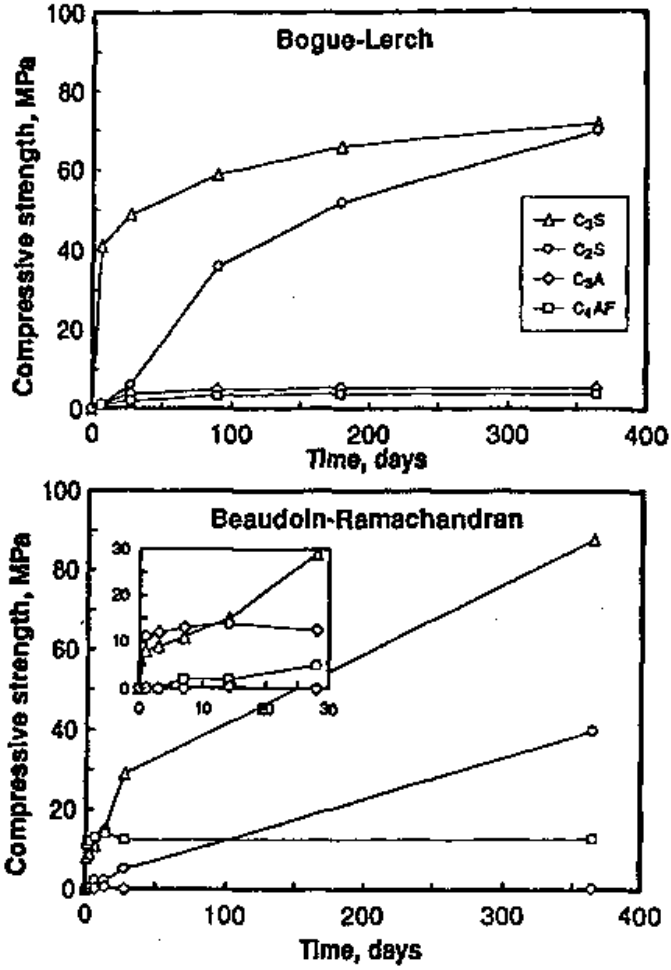


Figure 3. Compressive strength of hydrated cement compounds. *(With permission, Noyes Publications,* Concrete Admixtures Handbook, 2nd Ed., *1995.)*

@Seismicisolation

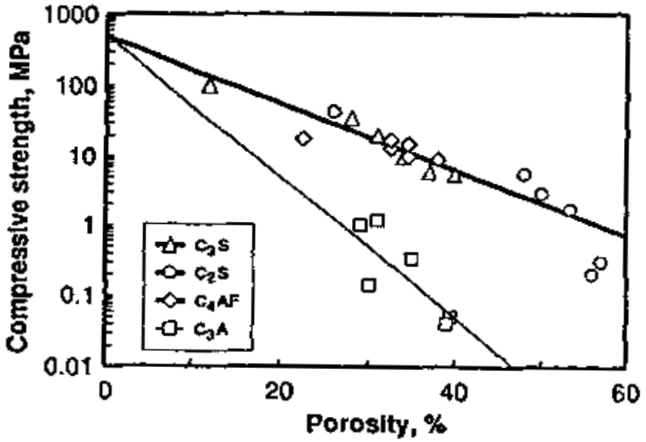


Figure 4. Porosity vs. strength relationships for cement compounds.[18]

The C_3A pastes exhibit lower strengths than do the silicate phases under normal conditions of hydration. This is attributed to the formation of the cubic phase. Under certain conditions of hydration of C_3A, i.e., at lower water/solid ratios and high temperatures, the direct formation of C_3AH_6 (resulting in the direct bond formation between the particles) can improve the strength of the body substantially.

In portland cement, the hydration of the C_3A phase is controlled by the addition of gypsum. The flash set is thus avoided. The C_3A phase reacts with gypsum in a few minutes to form ettringite as follows:

$$C_3A + 3CSH_2 + 26H \rightarrow C_3A{\bullet}3CSH_{32}$$

After all gypsum is converted to ettringite, the excess C_3A will react with ettringite to form the low sulfo-aluminate hydrate.

$$C_3A{\bullet}3CSH_{32} + 2C_3A + 4H \rightarrow 3[C_3A{\bullet}CSH_{12}]$$

Gypsum is a more effective retarder than lime for C_3A hydration and together they are even more effective than either of them. The common view for the explanation of the retardation of C_3A hydration by gypsum is that a fine grained ettringite forming on C_3A retards the hydration. This layer thickens, bursts, and reforms during the induction period. When all sulfate is consumed, the ettringite reacts with C_3A with the formation of monosulfo-aluminate hydrate. This conversion will occur in cements within

@Seismicisolation

12–36 hrs with an exothermic peak. Addition of some admixtures may accelerate or delay this conversion. It has also been suggested that ettringite may not, per se, influence the induction period[21][22] and that adsorption of sulfate ions on the positively charged C_3A retards the hydration. It has also been suggested that osmotic pressure may be involved in the rupture of ettringite needles. This theory is based on the observation of hollow needles in the C_3A-gypsum-H_2O system. Rupture of ettringite allows transfer of Al ions into the aqueous phase with the quick formation of hollow needles through which more Al^{3+} can travel.[14]

3.4 The Ferrite Phase

The ferrite phase constitutes about 8–13% of an average portland cement. In portland cement the ferrite phase may have a variable composition that can be expressed as $C_2 (A_nF_{1-n})$ where $O < n < 0.7$.

Of the cement minerals, the ferrite phase has received much less attention than others with regard to its hydration and physico-mechanical characteristics. This may partly be ascribed to the assumption that the ferrite phase and the C_3A phase behave in a similar manner. There is evidence, however, that significant differences exist.

The C_4AF phase is known to yield the same sequence of products as C_3A, however, the reactions are slower. In the presence of water, C_4AF reacts as follows:

$$C_4AF + 16H \rightarrow 2C_2(A,F)H_8$$

$$C_4AF + 16H \rightarrow C_4(A,F)H_{13} + (A,F)H_3$$

Amorphous hydroxides of Fe and Al form in the reaction of C_4AF. The thermodynamically stable product is $C_3(A,F)H_6$ and this is the conversion product of the hexagonal hydrates. Seldom does the formation of these hydrates cause flash set in cements.

Hydration of C_4AF at low water:solid ratios and high temperatures may enhance the direct formation of the cubic phase.[23] Microhardness measurement results show that at a w/s = 0.13, the samples hydrated at 23 and 80°C exhibit microhardness values of 87.4 and 177 kg/mm^2 respectively. The higher strengths at higher temperatures may be attributed to the direct formation of the cubic phase on the original sites of C_4AF. This results in a closely welded, continuous network with enhanced mechanical strength.

@Seismicisolation

In cements, C_4AF reacts much slower than C_3A in the presence of gypsum. In other words, gypsum retards the hydration of C_4AF more efficiently than it does C_3A. The rate of hydration depends on the composition of the ferrite phase; that containing higher amounts of Fe exhibits lower rates of hydration. The reaction of C_4AF with gypsum proceeds as follows:[24]

$$3C_4AF + 12CSH_2 + 110H \rightarrow 4[C_6(A,F)SH_{32}] + 2(A,F)H_3$$

The low sulfo-aluminate phase can form by the reaction of excess C_4AF with the high sulfo-aluminate phase.

$$3C_4AF + 2[C_6(A,F)SH_{32}] \rightarrow 6[C_4A,F)SH_{12}] + 2(A,F)H_3$$

At low water/solid ratios and high temperatures the low sulfo-aluminate may form directly.[25]

The above equations involve formation of hydroxides of Al and Fe because of insufficient lime in C_4AF. In these products, F can substitute for A. The ratio of A to F need not be the same as in the starting material. Although cements high in C_3A are prone to sulfate attack, those with high C_4AF are not. In high C_4AF cements, ettringite may not form from the low sulfo-aluminate, possibly because of the substitution of iron in the monosulfate. It is also possible that amorphous $(A, F)_3$ prevents such a reaction. Another possibility is that the sulfo-aluminate phase that forms is produced in such a way that it does not create crystalline growth pressures.

4.0 PORTLAND CEMENT

Although hydration studies of the pure cement compounds are very useful in following the hydration processes of portland cement itself, they cannot be directly applied to cements, because of complex interactions. In portland cement, the compounds do not exist in a pure form, but are solid solutions containing Al, Mg, Na, etc. The rate of hydration of alites containing different amounts of Al, Mg, or Fe, has shown that, at the same degree of hydration, Fe-alite shows the greatest strength. There is evidence the C-S-H formed in different alites is not the same.[26] The hydration of C_3A, C_4AF, and C_2S in cement are affected because of changes in the amounts of Ca^{2+} and OH^- in the hydrating solution. The reactivity of C_4AF can be influenced by the amount of SO_4^{2-} ions consumed by C_3A. Some SO_4^{2-} ions may be depleted by being absorbed by the C-S-H phase. Gypsum is also known to affect the rate of hydration of

@Seismicisolation

calcium silicates. Significant amounts of Al and Fe are incorporated into the C-S-H structure. The presence of alkalis in portland cement also has an influence on the hydration of the individual phases.

As a general rule, the rate of hydration in the first few days of cement compounds in cements proceeds in the order $C_3A > C_3S > C_4AF > C_2S$. The rate of hydration of the compounds depends on the crystal size, imperfections, particle size, particle size distribution, the rate of cooling, surface area, the presence of admixtures, the temperature, etc.

In a mature hydrated portland cement, the products formed are C-S-H gel, $Ca(OH)_2$, ettringite (AFt phases), monosulfate (AFm phases), hydrogarnet phases, and possibly amorphous phases high in Al^{3+} and SO_4 ions.[6]

The C-S-H phase in cement paste is amorphous or semicrystalline calcium silicate hydrate and the hyphens denote that the gel does not necessarily consist of 1:1 molar $CaO:SiO_2$. The C-S-H of cement pastes gives powder patterns very similar to that of C_3S pastes. The composition of C-S-H (in terms of C/S ratio) is variable depending on the time of hydration. At one day, the C/S ratio is about 2.0 and becomes 1.4–1.6 after several years. The C-S-H can take up substantial amounts of Al^{3+}, Fe^{3+}, and SO_4^{2-} ions.

Recent investigations have shown that in both C_3S and portland cement pastes, the monomer present in the C_3S and C_2S compounds (SiO_4^{4-} tetrahedra) polymerizes to form dimers and larger silicate ions as hydration progresses. The gas liquid chromatographic analysis of the trimethyl silylation derivatives has shown that anions with three or four Si atoms are absent. The polymer content with five or more Si atoms increases as the hydration proceeds and the amount of dimer decreases. In C_3S pastes, the disappearance of monomer results in the formation of polymers. In cement pastes, even after the disappearance of all C_3S and C_2S, some monomer is detected possibly because of the modification of the anion structure of C-S-H through replacement of some Si atoms by Al, Fe, or S.[6] Admixtures can influence the rate at which the polymerization proceeds in portland cement and C_3S pastes.

The minimum water:cement ratio for attaining complete hydration of cement has been variously given from 0.35 to 0.40, although complete hydration has been reported to have been achieved at a water:cement ratio of 0.22.[27]

In a fully hydrated portland cement, $Ca(OH)_2$ constitutes about 20–25% of the solid content. The crystals are platy or prismatic and cleave readily. They may be intimately intergrown with C-S-H. The density of $Ca(OH)_2$ is 2.24 g/cm^3. The crystalline $Ca(OH)_2$ gives sharp XRD

@Seismicisolation

patterns, shows endothermal peaks in DTA, and weight losses in TGA. The morphology of $Ca(OH)_2$ may vary and form as equidimensional crystals, large flat platy crystals, large thin elongated crystals, or a combination of them. Some admixtures, and temperature of hydration can modify the morphology of $Ca(OH)_2$. According to some investigators both crystalline and amorphous $Ca(OH)_2$ are formed in portland cement pastes.

The ettringite group, also called *AFt phase* in cement paste, stands for Al-Fe-tri (tri = three moles of CS) of the formula $C_3A•3CS•H_{32}$ in which Al can be replaced by Fe to some extent. The AFt phase forms in the first few hours (from C_3A and C_4AF) and plays a role in setting. After a few days of hydration only a little amount of it may remain in cement pastes. It appears as stumpy rods in SEM and the length does not normally exceed a few micrometers. The principle substitutions that exist in AFt phase are Fe^{3+} and Si^{4+} for Al^{3+} and various anions such as OH^-, CO_3^{2-}, and silicates for SO_4^{2-}.

The monosulfate group, also known as the *AFm phase*, is represented by the formula C_4ASH_{12} or $C_3A•CS•H_{12}$. AFm stands for Al-Fe-mono, in which one mole of C is present. In portland cement, this phase forms after the AFt phase disappears. This phase may constitute about 10% of the solid phase in a mature cement paste. In SEM, this phase has a hexagonal morphology resembling that of $Ca(OH)_2$ and the crystals are of submicrometer thickness. The principle ionic substitutions in the AFm phase are Fe^{3+} for Al^{3+} and OH^-, CO_3^{2-}, Cl^-, etc., for SO_4^{2-}. The density of this phase is 2.02 g/ml. The amount of crystalline hydrogarnet present in cement paste is less than 3%.[28] It is of type $Ca_3Al_2(OH)_{12}$ in which part of Al^{3+} is replaced by Fe^{3+} and $4OH^-$ by SiO_4^{4-} [e.g., $C_3(A_{0.5}F_{0.5})SH_4$]. It may be present in small amounts in mature cement pastes and is also formed at higher temperatures. The crystal structure of this phase is related to C_3AS_3 (garnet). The density of $C_6AFS_2H_8$ is 3.042 g/ml. Hydrogarnet is decomposed by CO_2 forming $CaCO_3$ as a product.[29]

It is the opinion of some workers that the lowest sulfate form of calcium sulfohydroxy aluminate hydrate, a crystalline solid solution phase in the system $CaO-Al_2O_3-CaSO_4-H_2O$, is also formed in cement pastes.[30]

The mechanisms that have already been described for pure cement compounds form a basis for a study of the hydration mechanism of portland cement. The conduction calorimetric curves of C_3S and portland cement are similar except portland cement may yield a third peak for the formation of monosulfate hydrate (Fig. 1). The detailed influence of C_3A and C_4AF on the hydration of C_3S and C_2S in cement is yet to be worked

@Seismicisolation

out. The delayed nucleation models and the protective layer models, taking into account the possible interactions, have been reviewed.[14] Although the initial process is not clear for C_3S (in cements), it appears that C_3A hydration products form through solution and topochemical processes.

5.0 CEMENT PASTE

5.1 Setting

The stiffening times of cement paste or mortar fraction are determined by setting times. The setting characteristics are assessed by *initial set* and *final set*. When the concrete attains the stage of initial set, it can no longer be properly handled and placed. The final set corresponds to the stage at which hardening begins. At the time of the initial set the concrete will have exhibited a measurable loss of slump. Admixtures may influence the setting times. The *retarders* increase the setting times and *accelerators* decrease them.

At the time of initial set of cement paste, the hydration of C_3S will have just started. According to some investigators, the recrystallization of ettringite is the major contributing factor to the initial set. The final set generally occurs before the paste shows the maximum rate of heat development, i.e., before the end of the 3rd stage in conduction calorimetry.

Concrete also exhibits *false* or *flash set*. When stiffening occurs due to the presence of partially dehydrated gypsum, false set is noticed. Workability is restored by remixing. False set may also be caused by excessive formation of ettringite especially in the presence of some retarders and an admixture such as triethanolamine. The formation of syngenite (KCS_2H) is reported to cause false set in come instances.

The setting time of cement can be determined by Gillmore (ASTM C 266) or the Vicat apparatus (ASTM 191). In the Gillmore method, a pat of cement paste 3 inches in diameter and 1/2 inch thickness is formed on a glass plate and is subjected to indentation by the needle. For the initial set the needle weighing 1/4 lb with 1/12 inch diameter is used while for the final set the corresponding figures are 1 lb and 1/24 inch. The initial set occurs when the pat will bear without appreciable indentation, the initial Gillmore needle. Similarly, the final set is determined by the final Gillmore

@Seismicisolation

needle. All standard ASTM cements should conform to an initial setting time not less than 60 mins and final setting time of not more than 10 hrs. The corresponding times using the Vicat needle are 45 mins and 8 hrs.

The Vicat apparatus is similar to the test method described above except that there are slight differences in the needle weight and diameter and the dimensions of the cement paste. In this method, the initial setting time occurs when a penetration of 25 mm is obtained. At the time of final set the needle should not sink visibly into the paste. The Canadian Standard method, CSA CAN 3-A5, specifies only the initial setting times. The Vicat apparatus is also specified by British Standard BS12.

5.2 Microstructure

Many of the properties of the cement paste are determined by its chemical nature and microstructure. *Microstructure* constitutes the nature of the solid body and that of the non-solid portion, viz., porous structure. Microstructural features depend on many factors, such as the physical and chemical nature of the cement, type, and the amount of admixture added to it, temperature and period of hydration, and the initial w/c ratio. The solid phase study includes examination of the morphology (shape and size), bonding of the surfaces, surface area and density. Porosity, pore shape, and pore size distribution analysis is necessary for investigating the non-solid phase. Many of the properties are interdependent and no one property can adequately explain the physico-mechanical characteristics of cement paste.

A study of the morphology of the cement paste involves observation of the form and size of the individual particles, particularly through high resolution electron-microscopes. The most powerful techniques that have been used for this purpose are Transmission Electron Microscopy, Scanning Electron Microscopy, High Voltage Transmission Electron Microscope using environmental cells, Scanning Transmission Electron Microscope (STEM) of ion-beam thinned sections, and High Resolution SEM using STEM instruments in reflection mode.

Attempts have been made to explain the strengths of pastes by a morphological examination, but several exceptions have been found.[31] It is beginning to be recognized that comparison of micromorphological results by different workers has an inherent limitation because of the small number of micrographs usually published and the correspondingly small

@Seismicisolation

area of these micrographs, which might not be representative of the structure. Sometimes, micrographs are selected for inclusion primarily because they show a well-defined morphology. In addition, what may be selected by one researcher as the representative structure may differ from that selected by another. Even the description of the apparently similar features becomes subjective. Another problem is the misinterpretation of a particular morphology. This could sometimes be obviated by microanalysis such as energy-dispersive x-rays. Sometimes misinterpretation of morphology may be due to the sample geometry and its relationship to incidental angle of the electron beam and takeoff angle of the detector. The hexagonal etch pits, for example, may appear to be cubic.[32]

Some attempts have been made to estimate the phases quantitatively. There are inherent limitations in these estimates because the fracture passes preferentially through the weaker phase and thus this phase may be overestimated. The visual estimate tends to be unreliable compared to point count estimates. In view of the above, it has been recognized that speculations on the origin of strength and other properties, when based on these observations, have limited validity, especially since many properties of cement paste are influenced at a much lower microlevel than can be observed by an ordinary Scanning Electron Microscope (see also Sec. 6.0).

The Calcium Silicate Hydrate Phase. The C-S-H phase is a major phase present both in the hydrated portland cement and tricalcium silicate. The principal products of hydration in portland cement or C_3S (other than CH) may be described as follows.[24] The early products in the hydration of C_3S consist of foils and flakes, whereas in portland cement a gelatinous coating or membrane of AFt composition is often observed. The products of C_3S which is a few days old will consist of C-S-H fibers and partly crumpled sheets, whereas in portland cement partly crumpled sheets, reticular network, rods and tubes of AFt are seen. At later stages of hydration, a dense, mottled C-S-H structure (inner product) is observed in hydrated C_3S and, in portland cement, a compact structure of equant grains and some plates of AFm phase.

The morphology of C-S-H gel particles has been divided into four types and described by Diamond.[33] Type I C-S-H, forming elongated or fibrous particles, occurs at early ages. The particles are also described as spines, acicular, aciculae, prismatic, rod-shaped, rolled sheet, or by other descriptions. They are a few micrometers long. Type II C-S-H is described as a reticular or honeycombed structure and forms in conjunction with Type I. It does not normally occur in a C_3S or C_2S paste unless it is

@Seismicisolation

formed in the presence of admixtures. In addition, in hardened cement pastes the microstructure can be nondescript and consist of equant or flattened particles (under 1000 Å in largest dimension) and such a morphological feature is described as Type III. Type IV, a late hydration product, is compact, has a dimpled appearance, and is believed to form in spaces originally occupied by cement grains. This feature is also found in C_3S pastes. The above list is not exclusive because other forms have also been described.

5.3 Bond Formation

Cementitious materials such as gypsum, portland cement, magnesium oxychloride, and alumina cement form porous bodies and explanation for their mechanical properties should take into account the nature of the void spaces and the solid portion. If the solid part determines strength, then several factors should be considered including the rate of dissolution and solubility of the cement, the role of nuclei and their growth, chemical and physical nature of the products, energetics of the surface and interfacial bonds.

The C-S-H phase is the main binding agent in portland cement pastes. The exact structure of C-S-H is not easily determined. Considering the several possibilities by which the atoms and ions are bonded to each other in this phase, a model may be constructed. Figure 5 shows a number of possible ways in which siloxane groups, water molecules, and calcium ions, may contribute to bonds across surfaces or in the inter-layer position of poorly crystallized C-S-H material.[31] In this structure, vacant corners of silica tetrahedra will be associated with cations such as Ca^{++}.

The technique of cold compaction and recompaction of hydrated cement at several hundred MPa pressure has shown that similar bonds can be formed in this process as by the normal hydration process.[34][35] In certain instances wetting seems to enhance the modulus of elasticity of the body. This is explained by water entering the inter-layer position and compensating for any decrease in Young's modulus when layers of C-S-H move apart. This emphasizes the bridging role of water. This type of bond implies that bonds between particles originating from separate nuclei during hydration can be similar to bonds within the particles.[36] The cement paste made at lower w/c ratios can be considered as a continuous mass around pores. Thus, the area of contact may be the critical factor determining mechanical properties.

@Seismicisolation

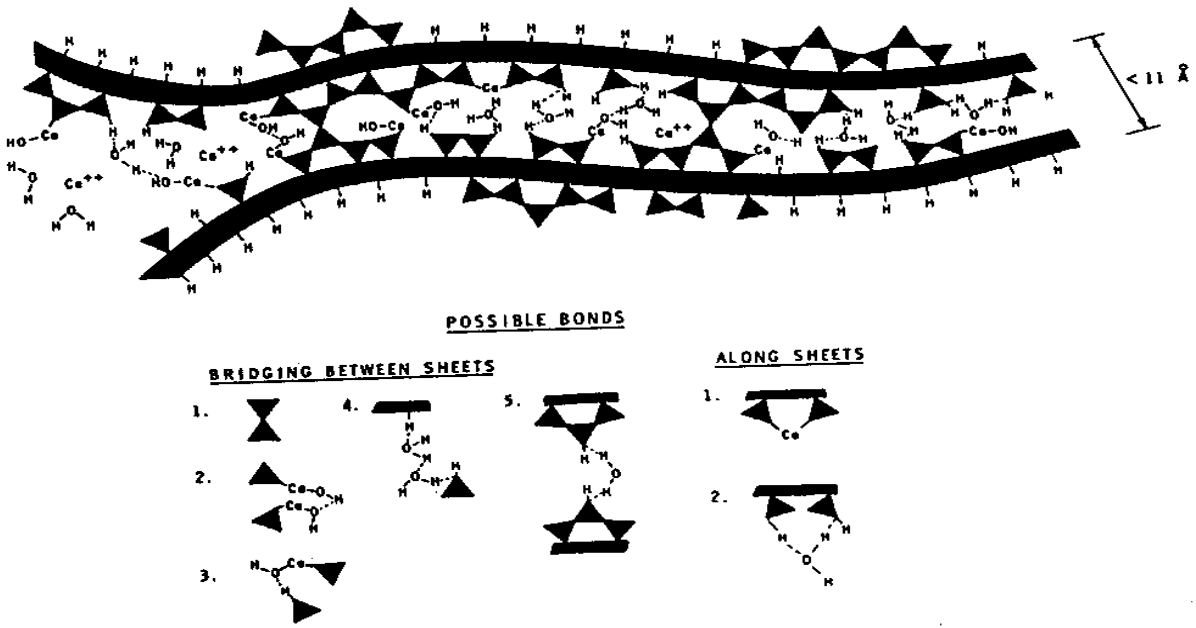


Figure 5. Suggested C-S-H structure illustrating bonds between and long sheets and polymerization of silicate ions.

@Seismicisolation

5.4 Density

The density value quoted in the literature for a given material is accepted without much question because it depends simply on mass and volume at a given temperature; that for hydrated portland cement is no exception. An accurate assessment of density, however, is one of the most important factors in determining porosity, assessing durability and strength, and estimating lattice constants for the C-S-H phase in hydrated portland cement.

Traditionally, density of hydrated portland cement was measured in the d-dried state by pycnometric methods, using a saturated solution of calcium hydroxide as a fluid. Since the d-dried hydrated portland cement rehydrates on exposure to water, this method is of questionable value. More realistic values can be obtained by proper conditioning of the sample and using fluids that do not affect the structure of the paste.

Table 2 shows the density values obtained using three methods, viz., helium pycnometry, dried methanol, and saturated aqueous $Ca(OH)_2$ solution.[37] The density values were obtained for the bottle-hydrated cement dried to 11% RH or at the d-dried state. Values are given for each fluid and four different sets of values are shown for the 11% RH condition. These values are different because of different types of corrections needed. It may be observed that drying to 11% RH and measuring with a saturated solution of $Ca(OH)_2$ gives an uncorrected value of 2.38 g/cc as compared to a corrected value (type d) of 2.35 g/cc and 2.34 g/cc by helium. At the d-dried state the exceptionally high value obtained by the $Ca(OH)_2$ solution technique is due to the penetration of water into the inter-layer positions of the layered structure of the crystallite.

5.5 Pore Structure

Porosity and pore size distribution are usually determined using mercury porosimetry and nitrogen or water adsorption isotherms. Total porosity may be obtained by using organic fluids or water as a medium. Water cannot be used as it may interact with the body. The d-dried hydrated portland cement, on exposure to water, rehydrates. This is illustrated in Table 3, in which pore volume and density of d-dried hydrated cement are determined with helium, $Ca(OH)_2$ solution or methanol.[37] The difference

@Seismicisolation

Table 2. Density of Bottle-Hydrated Portland Cement

Condition , 11% RH	Helium (g/cm^3)	Methanol (g/cm^3)	Saturated Aqueous $Ca(OH)_2$ Solution (g/cm^3)
(a) No correction	2.30 ± 0.015	2.25 ± 0.02	2.38 ± 0.01
(b) Monolayer adsorbed water correction	2.31 ± 0.015	2.26 ± 0.02	2.39 ± 0.01
(c) Helium flow taken into account	2.37 ± 0.015	2.32 ± 0.02	2.38 ± 0.01
(d) The interlayer space completely filled with water	2.34 ± 0.015	2.29 ± 0.02	2.35 ± 0.01
d-dry state	2.28 ± 0.01	2.285 ± 0.02	2.61 ± 0.01
(b) d-dry calculation for layers themselves (uncorrected for free $Ca(OH)_2$	2.51 ± 0.01 of paste (w/c ratio 0.8)		2.51 ± 0.01

Table 3. Pore Volume and Density of d-Dried Hydrated Cement Pastes Determined with Different Fluids

	Pore Volume Percentage (By Volume)			Density (g/ml)			
W/C ratio	Helium	$Ca(OH)_2$ Solution	Methanol	Helium	$Ca(OH)_2$ Solution	Methanol	Surface Area (N_2)
0.4	23.3	37.8	19.8	(i) 2.19±0.015 (ii) 2.19±0.015			30 m^2/g
0.5	34.5	44.8	36.6		2.64±0.06	2.27±0.06	55 m^2/g
0.6	42.1	51.0		(i) 2.28±0.015 (ii) 2.26±0.015			51 m^2/g
0.8	53.4	59.5		(i) 2.30±0.015 (ii) 2.27±0.015	2.66±0.06		57 m^2/g
0.8	51.4	58.7	51.6		2.61±0.06	2.27	
1.0				(i) 2.29 (ii) 2.26			57 m^2/g

@Seismicisolation

in porosity values obtained with $Ca(OH)_2$ solution or methanol at a w/c ratio of 0.4 on a volume/weight basis is equivalent to 8.6 cm^2/100 g of d-dried cement. Methanol has been used with the water-saturated hydrated cement by continually maintaining the methanol in the anhydrous state. Under this condition, methanol replaces all the water, including some bound water.[38] There is also evidence that under these conditions some chemical interaction occurs between methanol and cement.[39]

The quasi-elastic neutron scattering technique has the ability to distinguish between free and bound water.[40] Using this technique, the volume fraction of free water in saturated pastes is found to be approximately equal to the porosity determined for pre-dried pastes by fluids such as methanol, helium, and nitrogen.

Pore-Size Distribution. Mercury porosimetry involves forcing mercury into the vacated pores of a body by the application of pressure. The technique measures a range of pore diameters down to about 3 nm. Auskern and Horn[41] used 117° as the value of contact angle. It has also been reported that the porosity measured by carbon tetrachloride saturation is slightly higher than the porosity measured by Hg porosimetry. Beaudoin[42] measured total porosity by Hg porosimetry using pressures up to 408 MPa and concluded that the porosimetry and He pycnometry methods could be used interchangeably to determine porosity of cement paste formed at a w/c ratio equal to or greater than 0.40. In a study of the development of pore structure during the hydration of C_3S, Young[42] found that on measuring the Hg intrusion the pastes showed a threshold diameter that decreased with the amount of hydration. It was suggested that the large intrusion immediately below the threshold diameter of 100 nm results from the filling of void spaces between C-S-H gel needles and the filling of larger pores accessible only through inter-growth of needles.

Pore size distribution can be determined by applying the Kelvin equation to either adsorption or desorption isotherm. They are applicable to determination of pore diameters of about 3–50 nm.

5.6 Surface Area and Hydraulic Radius

Surface Area. This is the area available to gases or liquids by way of pores and the external area. Hydrated portland cement is very complex and there is controversy over the significance of H_2O as an adsorbate in

@Seismicisolation

determining surface area. With water as adsorbate, the surface area is about 200 m^2/g and remains constant for different w/c ratio pastes. The surface area varies with w/c ratio when using nitrogen, methanol, isopropanol, and cyclohexane as adsorbates.[43] With nitrogen, it varies from 3 to 147 m^2/g. Solvent replacement techniques, used in place of d-drying technique, yield different surface areas. Using this technique, Litvan found that one of the samples registered a surface area of 249 m^2/g with nitrogen as an adsorbate.[44] There is evidence to show that during the extended methanol soaking, interaction with the cement paste may occur.[39][45] This may be responsible for the increased surface area. Drying to various humidities, followed by solvent replacement, shows that the exposure to capillary tension between 80 and 40% RH results in large decreases in surface area.[35] High surface areas have been found with fast drying.[46]

The method of drying seems to determine the extent to which further layering and agglomeration of C-S-H sheets occurs during the removal of water and this manifests itself in surface area decreases and shrinkage. Subsequent treatment, such as wetting and drying and application of stress, also affects these properties. The low angle x-ray scattering data of Winslow, et al., have provided a value at 670 m^2/g for the hydrated cement in a wet state.[47]

Hydraulic Radius. The average characteristic of a pore structure can be represented by the *hydraulic radius,* which is obtained by dividing the total pore volume by the total surface area. The pore volume of d-dried paste, determined by nitrogen, helium, or methanol, is due to capillary porosity and hydraulic radius is known to vary from 30 to 10.7 nm for w/c ratios from 0.4 to 0.8. Calculation of the hydraulic radius of the inter-layer space can be done by knowing the surface area of the inter-layer space (total surface area less surface area of capillary space) and the volume of the inter-layer space. This varies with the degree of penetration of water molecules, but can be computed from pore volumes obtained by comparing values for water and nitrogen. An average value of 0.123 nm is obtained. A value for the hydraulic radius of partially water-occupied inter-layer space is found to be 0.1 nm. For a w/c ratio paste of 0.2, the value is about 0.15 nm. These results are consistent with the idea that most of the water in the inter-layer space is held as a single layer.[48]

@Seismicisolation

5.7 Mechanical Properties

Hydrated portland cement contains several types of solid phases and the theoretical treatment of such a material is complex.

Many observations have led to the conclusion that the strength development of hydrated portland cement depends on the total porosity, *P*. Most data can be fitted to an exponential dependence term, e^{-bP}, with *b* values associated with different types of pores. Porosity and grain size effects on strength become clearly separable as pores approach or become smaller than the grain size. Uniform distributions of different types of pores will have similar exponential strength-porosity trends, but the *b* values will change. They will depend on the pore location, size, and shape. The latter two are important only when the pore causing failure is large in comparison with the grain size or with the specimen size. For small pores, its location is important. Pores at grain boundaries are more critical than pores within grains.

The fracture mechanism at a region of stress concentration is often affected by the environment. Measurements of strength of hydrated cement paste in flexure as a function of relative humidity[49] have shown significant decreases in strength as the humidity is increased from 0 to 20%. Under high stress conditions, as at a tip of crack, the presence of H_2O vapor promotes rupture of the siloxane groups in the cement paste to form silanol groups as follows:

```
          |    |
From:  (-Si-O-Si-)
          |    |

          |          |
To:    (-Si-OH HO-Si-)
          |          |
```

Correlation of porosity with mechanical property values has led to several types of semi-empirical equations, the most common being that due to Ryshkewitch;[50]

$$M = M_o \exp(-bP)$$

where *M* is the mechanical strength property at porosity, *P*, M_o the value at zero porosity, and *b* is a constant. As stated previously, *b* is related to pore shape and orientation. This equation shows good agreement with experimental values at lower porosities. Another equation, due to Schiller,[51]

@Seismicisolation

$$M = D \ln \frac{P_{CR}}{P}$$

where D is a constant and P_{CR} is the porosity at zero strength, shows good agreement at high porosities.

Feldman and Beaudoin[52] correlated strength and modulus of elasticity for several systems over a wide range of porosities. The systems included pastes hydrated at room temperature, autoclaved cement paste with and without additions of fly-ash, and those obtained by other workers. Porosity was obtained by measurement of solid volume by a helium pycnometric technique and apparent volume through the application of Archimedes' principle. Correlation, based on the Ryshkewitch equation is shown in Fig. 6.

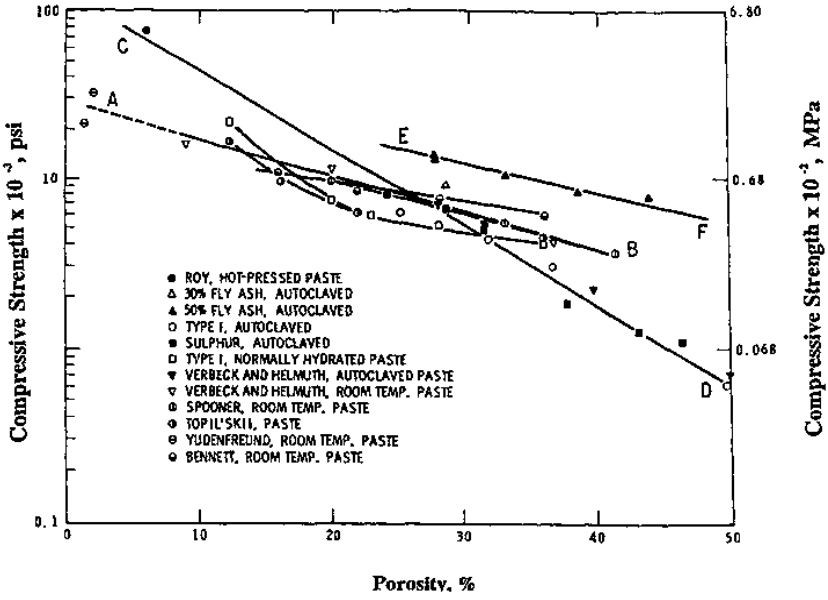


Figure 6. Strength vs. porosity for autoclaved and room temperature cured preparations. *(With permission, Noyes Publications,* Concrete Admixtures Handbook, 2nd Ed, *1995.)*

@Seismicisolation

There are essentially three lines of different slopes. Line AB represents the pastes cured at room temperature covering porosities from 1.4 to 41.5% and having a value of about 290 MPa at zero porosity. The second line, CD, represents the best fit for most of the autoclaved specimens, excluding those made with fly-ash. This line intersects AB at 27% porosity (corresponding w/c ratio = 0.45). On the basis of the same porosity, at porosities about 27%, the room temperature pastes are stronger than those made by autoclaving. When the line CD is extrapolated towards low porosities, it meets the point for hot-pressed cement paste.[53] At zero porosity, a strength of over 800 MPa would be obtained for this series. The third line, EF, for the autoclaved fly-ash-cement mixtures [containing 11 Å tobermorite, C-S-H (I) and C-S-H (II)] is parallel to the room-temperature paste line, shows higher strengths, and is composed of higher density material. Further work by Beaudoin and Feldman[54] on autoclaved ground silica-normal Type I cement showed that the results conformed to Ryshkewitch's equation. It was also found that the greater the density of the product, the greater was M_o and the slope, b, of the log M-porosity plot. Examination revealed that autoclaved mixtures made with low silica content contain largely well-crystallized, high density a-C_2S-hydrate, while those with 20–40% silica contain predominately C-S-H (I), C-S-H (II), and tobermorite. The mixtures with higher silica (50–65%) contain unreacted silica, tobermorite, C-S-H (I) and C-S-H (II).

These results indicated that an optimum amount of poorly crystallized hydrosilicate and well-crystallized dense material provides maximum values of strength and modulus of elasticity at a particular porosity. At higher porosity, not only porosity, but also bonding of individual crystallites, plays a role in controlling strengths.

It is apparent that disorganized, poorly crystallized units tend to form bonds of higher contact area, resulting in smaller pores. As porosity decreases, better bonding will develop between high density, well-crystallized, and poorly crystallized material and consequently, higher strengths will result. The potential strength of the high density and high strength material is thus manifested. This explains how very high strengths are obtained by hot-pressing. In this method, a small, but adequate quantity of poorly crystallized material at low porosities provides the bonding for the high-density clinker material. Work by Ramachandran and Feldman with C_3A and CA systems has shown that, at low porosities, high strength could be obtained from the C_3AH_6 product because a greater area of contact forms between crystallites than is possible at higher porosities.[20]

@Seismicisolation

Several attempts have been made to relate the strength of cement paste to the clinker composition. A series of equations was proposed by Blaine, et al., in 1968[55] to predict strength against a number of clinker compositions, ignition loss, insoluble fraction, air, and alkali contents. Other investigators have also proposed equations expressing the relationship between the clinker composition and the 28 day strength.[56]

The data on the effect of clinker composition on strength are rather conflicting although it is recognized that multiple regression equations reflect reasonably well the relationship for narrow ranges of cement composition. It is recognized that other effects, such as the texture, presence of minor components, particle size distribution, and amount of gypsum, will have a significant influence on the potential strength of cement.

5.8 Permeability of Cement Paste

The rate of movement of water through concrete under a pressure gradient, termed *permeability*, has an important bearing upon the durability of concrete. The measure of the rate of fluid flow is sometimes regarded as a direct measure of durability.

It is known that the permeability of hardened cement paste is mainly dependent on the pore volume. However, pore volume resulting at different water/cement ratios and degrees of hydration, does not uniquely define the pore system and thus is not uniquely related to the permeability.

Nyame and Illston[57] have used mercury intrusion data to define a parameter, termed the *maximum continuous pore size (r_α)*, and related it to the permeability. The relationship was found by linear regression to be

$$K = 1.684\, r_\alpha\, 3.284 \times 10^{-22}$$

with a correlation coefficient of 0.9576 where K = permeability (m/s) and r_α = maximum continuous pore radius (Å).

It was found that below w/c ratios of 0.7, the values of permeability and the maximum continuous pore radius did not change significantly after 28 days of hydration.

Permeability can be related to pore structure using the hydraulic radius theory, which relates flow rates to the viscous forces opposing flow. Permeability is related to hydraulic radius as follows:

$$\log K = 38.45 + 4.08 \log (\varepsilon\, r_h^2)$$

where r_h is the hydraulic radius and ε is the porosity.

@Seismicisolation

5.9 Aging Phenomena

Aging, within the context of surface chemical considerations, refers to a decrease in surface area with time. For hydrated portland cement this definition can be extended to include changes in solid volume, apparent volume, porosity, and some chemical changes (excluding hydration) which occur over extended periods of time.

Shrinkage and Swelling. The volume of cement paste varies with its water content, shrinking when dried and swelling when rewetted. It has been found that the first drying shrinkage (starting from 100% RH) for a paste is unique in that a large portion of it is irreversible. By drying to intermediate relative humidities (47% RH) it has been observed that the irreversible component is strongly dependent on the porosity of the paste, being less at lower porosities and w/c ratios.[58]

The irreversible component of first drying shrinkage is strongly dependent on the time the specimen is held in the 80–40% RH region. It is due to the capillary forces that exist in this humidity region and gradual movement of the surfaces of C-S-H sheets closer to each other during this process, with time permanent bonds form. This illustrates the similarity of first drying shrinkage to the creep phenomenon. Also, the shrinkage-water content relationship during first drying and redrying appears to depend significantly upon the length of time the specimen is held in the "dried" condition (47% RH) (Fig. 7).[58] Each of four specimens shown in Fig. 7 was held at 47% RH for different periods of time during first drying. Very little irreversible shrinkage or irreversible water loss resulted from drying for one day; however, with increased drying time, considerable irreversible shrinkage and water loss occurred.

First drying shrinkage can also be affected greatly by incorporation of some admixtures. A large, irreversible shrinkage of paste relative to that without admixture on drying to 47% RH, suggests that the admixture promotes dispersion in terms of the alignment of sheets of C-S-H. In addition, drying from 15% RH to the d-dry condition results in the same shrinkage at the same w/c ratio, regardless of the admixture content.[59]

Creep. Concrete exhibits the phenomenon of creep, involving deformation at a constant stress that increases with time. Creep of concrete (basic creep) may be measured in compression using the ASTM C512 method. There are two types of creep; *basic creep,* in which the specimen is under constant humidity conditions, and *drying creep,* when the specimen is dried during the period, under load.

@Seismicisolation

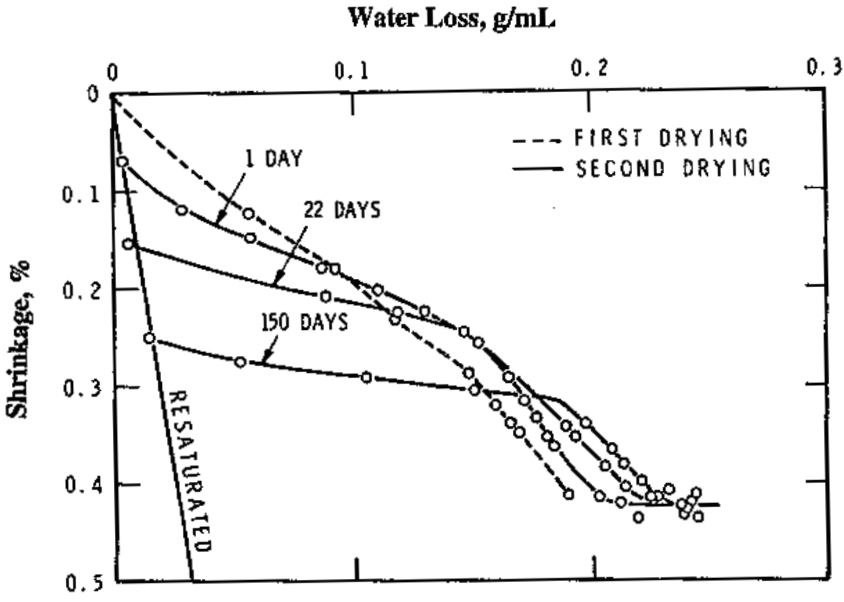


Figure 7. Effect of drying at 47% RH for periods indicated on length recovery, on saturation, and on shrinkage vs. water loss relationship of second drying.

Creep of a cement paste increases at a gradually decreasing rate, approaching a value several times larger than the elastic deformation. Creep is, in part, irrecoverable, as in drying shrinkage. On unloading, deformation decreases immediately due to elastic recovery. This instantaneous recovery is followed by a more gradual decrease in deformation due to creep recovery. The remaining residual deformation, under equilibrium conditions, is called the *irreversible creep*. Creep increases with w/c ratio and is very sensitive to relative humidity and water content. It may also be affected by admixtures.

Many theories have been proposed over the years to account for creep mechanisms in cement paste and each is capable of accounting for some of the observed facts. The descriptions and mechanisms are based on seepage,[61][62] change of solid structure,[63]–[65] and inter-layer space.[60][68]

@Seismicisolation

5.10 Role of Admixtures and Supplementary Cementing Materials

Admixtures are ingredients that are added to the concrete batch immediately before or during mixing. They confer certain beneficial effects to concrete, including frost resistance, sulfate resistance, controlled setting and hardening, improved workability, increased strength, etc. Special concretes are made with coloring pigments, polymer latexes, expansion producing admixtures, flocculating agents, antifreezing chemicals, corrosion inhibiting formulations, etc. Admixtures influence the physical, chemical, surface-chemical, and mechanical properties of concrete and its durability. Accelerating admixtures reduce the time of setting and increase the rate at which the strength is developed. They are used in cold weather concreting. Examples of accelerators include calcium chloride, formates, carbonates, nitrites, amines, etc. Water reducing admixtures reduce the amount of water (about 8–10%) required for concrete mixing at a given workability. These admixtures improve the strength and durability of concrete. Refined lignosulfonates, gluconates, hydroxycarboxylic acids, sugar acids, etc., act as water reducers. Retarders lengthen the setting times of concrete. They are particularly useful for hot weather concrete operations. Phosphonates, sugars, unrefined lignosulfonates, carbohydrate derivatives, and borates are some examples of retarders. Superplasticizing admixtures are capable of reducing water requirement by about 30%. The most popular formulations are based on sulfonated naphthalene formaldehyde and sulfonated melamine formaldehyde. Figure 8 shows the effect of dosage of superplasticizer on the slump increase of concrete. Air entraining agents incorporate minute bubbles in concrete. Such a concrete exhibits good frost resistance. Salts of wood resins, synthetic detergents, salts of sulfonated lignin, salts of proteinaceous materials, fatty and resinous acids and their salts, and organic salts of sulfonated hydrocarbons, are air entraining agents. There are many other admixtures used for special purposes. They include polymers, antifreezing admixtures, alkali-aggregate expansion reducing admixtures, corrosion inhibitors, expansion reducing admixtures, pigments, fungicidal admixtures, flocculators, permeability reducers, shotcreting admixtures, and damproofing admixtures. The application of these admixtures are discussed in a handbook.[69]

@Seismicisolation

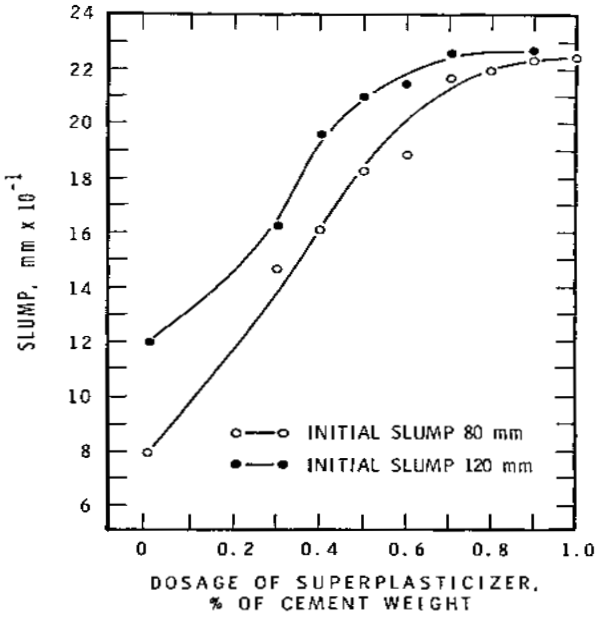


Figure 8. Effect of dosage of superplasticizer on slump of concrete.

Supplementary cementing materials are finely divided and are added to concrete in relatively large amounts (20–100%) by weight of cement. Granulated blast furnace slag and high calcium fly ash are cementitous and pozzolanic whereas condensed silica fume and rice husk ash are highly active pozzolans. Low calcium fly ash and naturally occurring materials (derived mainly from volcanic eruptions and calcined clays) are normal pozzolans. Weak pozzolanic materials include slowly cooled slag, bottom ash, boiler slag, and field burnt rice husk ash. Low Ca fly ash contains mainly aluminosilicate glass, sillimanite, and mullite. The glass content may be as high as 80%. Hematite, quartz, and magnetite are also found in low Ca fly ashes. The glassy phase in the high Ca fly ash is different from that in the low Ca fly ash. The principal phase in the high Ca fly ash is tricalcium aluminate. The crystalline phases in high calcium fly ash are much more reactive than those in low Ca fly ash. In general, in both fly ashes the spherical sizes of the glassy phase vary between 1 μm and 100 μm, most of the material being under 20 μm. Granulated blast furnace slag is essentially glassy, having a chemical composition corresponding to

@Seismicisolation

melilite, a solid solution phase between gehlenite (C_2AS) and akermanite (C_2MS_2). In slag-cement mixtures, hydration of cement provides alkali and sulfate for activating the glass. Slags cooled from a high temperature at a faster rate are likely to contain more reactive glass than those cooled slowly. Silica fume and rice husk ash, produced by controlled combustion contain essentially silica in a noncrystalline form. They have a high surface area (20–25 m^2/g for condensed silica fume and 50–60 m^2/g for rice husk ash). Addition of mineral admixtures (supplementary materials) can influence concrete mix proportions, rheological behavior of plastic concrete, degree of hydration of cement, strength and permeability of concrete, resistance to thermal cracking, alkali-silica expansion, and sulfate attack. These aspects are discussed in many books and notably in proceedings of the conferences organized by CANMET/American Concrete Institute, in 1983, 1986, 1989, 1992, and 1995, under the title "Fly Ash, Silica Fume, Slag, and Other Pozzolans in Concrete." A bibliography of references to many publications related to supplementary materials is to be found in the book edited by Malhotra.[70]

6.0 MODELS OF HYDRATED CEMENT

In order to predict the performance of concrete, it is important to have a model of cement paste that incorporates its important properties and explains its behavior. There are two main models. In the Powers-Brunauer model, the cement paste is considered a poorly crystalline gel and layered. The gel has a specific surface area of 180 m^2/g with a minimum porosity of 28%. The gel pores are assumed to be accessible only to water molecules because the entrance to these pores is less than 0.4 nm in diameter. Any space not filled with cement gel is called *capillary space.*

The mechanical properties of the gel are described using this model. The particles are held together mainly by van der Waal's forces (Fig. 9).[71] Swelling on exposure to water is explained by the individual particles separating due to layers of water molecules existing between them. Creep is the result of water being squeezed out from between the particles during the application of stress (Fig. 9c). This model recognizes the existence of some chemical bonds between the particles (Fig. 9b) and the existence of layers (Fig. 9d).

@Seismicisolation

In the Feldman-Sereda model, the gel is considered as a poorly crystallized layered silicate and that the role of water is much more complex (Fig. 10) than is recognized by the Powers-Brunauer model.[71]

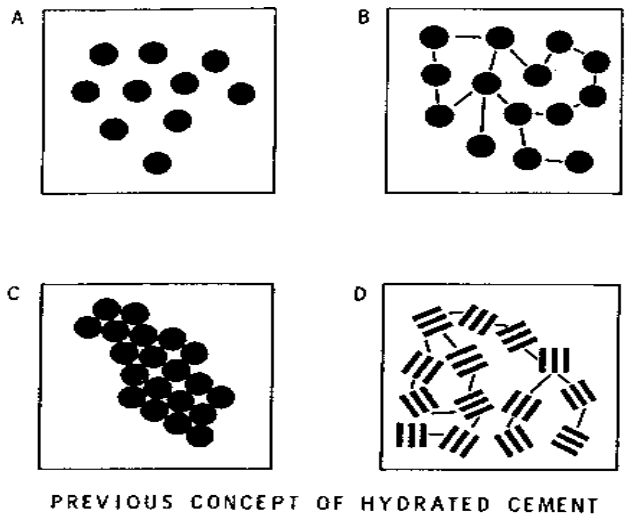


Figure 9. Development of Powers-Brunauer model.[71]

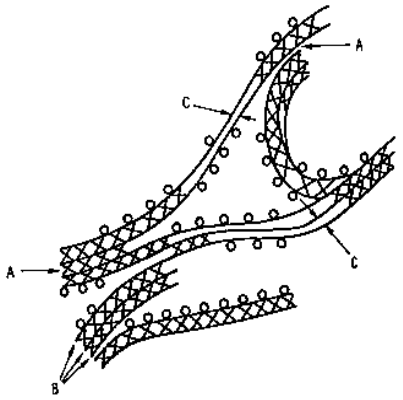


Figure 10. Structure of C-S-H gel according to Feldman-Sereda model.

@Seismicisolation

Water in contact with the d-dried gel acts in several ways: *(a)* it interacts with the free surface, forming hydrogen bonds; *(b)* it is physically adsorbed on the surface; *(c)* it enters the collapsed layered structure of the material even at humidities below 10% RH; *(d)* it fills large pores by capillary condensation at higher humidities.

Water that enters the inter-layer spaces acts as part of the solid structure and is more organized than normal water; it contributes to the rigidity of the system. Most of the water is removed from the structure below 10% RH, but some structural water is removed at higher humidities. Thus, the structural water is not considered as pore water, and gel pores in the Powers-Brunauer model should be considered as a manifestation of inter-layer spaces. According to the Feldman-Sereda model, gel pores, as such, do not exist; therefore, the total porosity can only be obtained by fluids that do not penetrate the inter-layer space; if they do, it should be taken into calculation. These fluids include methanol, nitrogen at liquid nitrogen temperatures, or helium gas at room temperature, and are used on cement at the d-dried state. Under conditions (saturated state) other than the d-dried state, some fluids, including methanol, do penetrate the inter-layer structure. The surface area of the gel, measured by nitrogen or methanol, varies approximately between 1 and 150 m^2/g, depending on the method of preparation and subsequent drying procedure.

Further modifications have been made to this model to explain the unstable nature of the material and its effect on the mechanical properties. It recognizes that this material derives its strength from a combination of van der Waal's forces, siloxane (-Si-O-Si-), hydrogen and calcium-silica (-Si-O-Ca-O-Si-) bonds. Swelling or wetting is not due just to separation of the primary aggregations or breaking of these bonds, but to the net effect of several factors: *(a)* reduction of the solid surface energy due to physical interaction of the surfaces with water molecules, known as Bangham effect; *(b)* penetration of water molecules between the layers and their limited separation as the H_2O molecules take up a more rigid configuration between the sheets; *(c)* menisci effects due to capillary condensation; *(d)* aging effects, generally considered to be a further agglomeration of sheets forming layers of the malformed crystallites. This last effect should result in decreased surface area, an increase in solid volume, and a net shrinkage.

Interlayer penetration occurs on wetting throughout the 0–100% RH range while the aging effect appears to be more dominant at humidities above 20% RH, especially in the zone where menisci forces exist (between 80 and 35% RH). The loss of compressive strength of the hydrated cement

@Seismicisolation

gel exposed to increasing RH is explained by a lowering of the stress of rupture of siloxane bonds in the presence of higher concentrations of water molecules.

Creep is a manifestation of aging, i.e., the material moves towards a lower total energy by aggregation of sheets due to the formation of more layers. Surface area is reduced by this process. Aggregation is accelerated by stress and facilitated by the presence of interlayer water.

There has been a significant interest in the development of computer-based models for the microstructure, hydration, and structural development in cement-based materials. Garboczi and Bentz[72] describe the computer based model of microstructure and properties as "a theoretical construct which is made using valid scientific principles expressed in mathematical language, that can be used to make quantitative predictions about a material's structure and/or properties." The computer-based model is thus used to numerically represent the amount and spatial distribution of different phases of the material being studied and thus predict, from the numerical representation of microstructure, properties that can be derived from actual experiments. Simulation of interfacial zone models have also been carried out. Details of the application of the models have been reviewed recently.[73][74] These models have also to consider that the properties of concrete depend on the fine structure of C-S-H as well as that of coarse aggregate. It is also important to determine the microstructural characteristics of the material as it deforms due to rheology, creep, shrinkage, and fracture.

7.0 CONCRETE PROPERTIES

7.1 Introduction

The role of pore structure and cement paste has already been described. Aggregates, occupying 60–80% of the volume influence the unit weight, elastic modulus, and dimensional stability of concrete and also its durability. Generally, aggregates are stronger than the matrix. Coarse aggregates are larger than 4.75 mm and fine aggregates are smaller than 4.75 mm. Typically, fine aggregates comprise particles in the range of 75 μm to 4.75 mm whereas coarse aggregates are from 4.75 mm to 50 mm. In mass concrete the coarse aggregates are much larger. Natural aggregates generally composed of sand, gravel, and crushed rock. The synthetic aggregates, such as expanded clay/shale, slag, and fly ash, are thermally

@Seismicisolation

processed materials and used in concrete. The crushed aggregates are of sandstone, granite, diorite, gabbro, and basalt. Natural silica is used extensively as a fine aggregate. ASTM-294 provides a descriptive nomenclature of the commonly occurring minerals in rocks.

Some minor constituents of fine or coarse aggregates such as clay lumps, friable particles, coal, lignite, chert, etc., may adversely affect the workability, setting, handling, and durability characteristics of concrete. A list of harmful substances and permissible limits is given in ASTM C-33.

The role of the *transition zone*, i.e., the interfacial region between the particles of coarse aggregate and cement paste and expansion due to alkali-aggregate reaction, is treated separately.

7.2 Workability

The quality of fresh concrete is determined by the ease and homogeneity with which it can be mixed, transported, compacted, and finished. It has also been defined as the amount of internal work necessary to produce full compaction.[75] The rheological behavior of concrete is related to the rheological terms such as *plasticity* and *viscoelasticity* of cement paste. As the workability depends on the conditions of placement, the intended use will determine whether the concrete has the required workability. A good workable concrete should not exhibit excessive bleeding or segregation. Thus, workability includes properties such as flowability, moldability, cohesiveness, and compactibility. One of the main factors affecting workability is the water content in the concrete mix. A harsh concrete becomes workable by the addition of water. Workability may also be improved by the addition of plasticizers and air entraining agents. The factors that affect workability include quantities of paste and aggregates, plasticity of the cement paste, maximum size and grading of the aggregates, and shape and surface characteristics of the aggregate.

Another term that has been used to describe the state of fresh concrete is *consistency* or *fluidity*. It describes the ease with which a substance flows. It is loosely related to and an important component of workability. The term *consistency* is sometimes used to describe the degree of wetness of concrete. Wet concrete is more workable than the dry concrete. A concrete having the same consistency may, however, have different workability characteristics. The ASTM C-187 and Canadian Standard CSA CAN 3-A5 measure the consistency of cement paste by a

@Seismicisolation

Vicat apparatus consisting of a needle with a diameter of 1 mm with a plunger 10 mm in diameter. The paste is considered to have a normal consistency when the rod settles to a point to 10 ± 1 mm below the original surface in 30 secs after it is released. In the determination of setting and soundness of cement paste, the material should be made to normal consistency requirements.

Although several methods have been suggested to determine workability, none is capable of measuring this property directly. It is therefore usual to measure some type of consistency as an index of workability. The most extensively used test is the *slump test.* This method is described by ASTM C143. The slump test uses a frustum of a cone 30 mm (12 in.) high. This cone is filled with concrete, the cone lifted slowly and the decrease in the height of the center of the slumped concrete is measured. For structural concrete, a slump of 75–100 mm (3–4 inches) is sufficient for placement in forms. Another method, called the *Compacting Factor Test*, is based on the measurement of the density ratio (the ratio of the density actually achieved in the test to the density of the fully compacted concrete). This method is described in the BS1881 and by AC1 211. Another method, called the *Ball Penetration Test*, is described in ASTM-C360. This method is based on measuring the penetration of a 150 mm (6 in) diameter steel cylinder with a hemispherically shaped bottom, weighing 13.6 kg (30 lbs). The ratio of slump to the penetration of the ball is about 1.5–2. In the *Remolding Test* developed by Powers, workability is assessed on the basis of the effort required in changing the shape of the concrete.[75] The *Vebe Test* is similar to the remolding test except that the inner ring is omitted and compaction is achieved by vibration instead of rolling. In addition to the above, other methods have been used. They include Vebe consistometer, German Flow Table, Nasser's K-probe, and Tattersall's two point test. The details of these methods are described in Refs. 27 and 28. All these tests attempt to measure workability and they are not comparable. No ideal test for workability has been developed as yet.

7.3 Setting

The setting of concrete is determined by the mortar contained in it. A penetrometer is used for determining the initial and final setting times of mortar. A needle of appropriate size has to be used. The force required to

@Seismicisolation

penetrate 1 inch in depth is noted. The force divided by the area of the bearing surface of the needle yields the penetration resistance. The *initial setting time* is the elapsed time, after the initial contact of cement and water, required for the mortar sieved from the concrete to reach a penetration resistance of 500 lbs/sq.in. (3.5 MPa). The corresponding resistance for the final setting time is 4000 lbs/sq.in. (27.6 MPa).

Concrete may exhibit flash set due to the reaction of C_3A, forming calcium aluminate hydrates and monosulfate hydrate. Workability will not be restored by remixing when flash set occurs.

7.4 Bleeding and Segregation

In a freshly placed concrete which is still plastic, settlement of solids is followed by the formation of a layer of water on the surface. This is known as *bleeding* or *water gain*. In lean mixes, localized channels develop and the seepage of water transports some particles to the surface. Bleeding may thus give rise to *laitance*, a layer of weak, nondurable material containing diluted cement paste and fines from the aggregate. If bleeding occurs by uniform seepage of water, no undesirable effects result and such a bleeding is known as "normal bleeding." Bleeding is not necessarily harmful. If undisturbed, the water evaporates so that the effective water:cement ratio is lowered with a resultant increase in strength.

The amount of bleeding can be reduced by using proper amounts of fines, high alkali or C_3A contents, increasing cement content, and admixtures such as pozzolans, calcium chloride, or air entraining admixtures. Bleeding characteristics are measured by bleeding rate or bleeding capacity, applying the ASTM C232 standard. In this method, the relative amount of mix water that appears on the surface of concrete placed in a cylindrical container is measured. At specified intervals, the water accumulating on the surface is determined until bleeding ceases. The top surface of concrete subsides during bleeding causing what is known as *plastic shrinkage.*

During the handling of a concrete mixture, there may be some separation of coarse aggregates from the mixture, resulting in a nonuniform concrete mass. This is known as *segregation.* Segregation may lead to flaws in the final product and honeycombing may occur in some instances. Segregation may result during handling, placing, vibrating, or finishing operations. The primary cause of segregation is the differences in the size of the particles and specific gravity of the mix. The tendency to segregate increases with slump, reduction in cement content, or increase in

@Seismicisolation

the maximum size and amount of aggregate. By proper grading of the constituents and handling, this problem can be controlled.

There is no standard procedure developed for measuring segregation. For over-vibrated concrete, proneness to segregation can be assessed by vibrating a concrete cube for about 10 mins., stripping it and observing the distribution of coarse aggregate.[75]

7.5 Mechanical Properties

The hardened concrete has to conform to certain requirements for mechanical properties. They include compressive strength, splitting tensile strength, flexural strength, static modulus of elasticity, Poisson's ratio, mechanical properties under triaxial loads, creep under compression, abrasion resistance, bond development with steel, penetration resistance, pull out strength, etc.

The mechanical behavior of concrete should be viewed from the point of view of a *composite material*. A composite material is a three-dimensional combination of at least two chemically and mechanically distinct materials with a definite interface separating the components. This multiphase material will have different properties from the original components. Concrete qualifies as such a multiphase material.[76] Concrete is composed of hydrated cement paste (C-S-H, CH, aluminate, and ferrite-based compounds) and unhydrated cement, containing a network of a mixture of different materials. In dealing with cement paste behavior, basically it is considered that the paste consists of C-S-H and CH with a capillary system. The model of concrete is simplified by treating it as a matrix containing aggregate embedded in a matrix of cement paste. This model provides information on the mechanical properties of concrete.

The factors that influence the mechanical behavior of concrete are: shape of particles, size and distribution of particles, concentration, their orientation, topology, composition of the disperse and continuous phases, and that between the continuous and disperse phase and the pore structure.

The important role played by cement paste and aggregate is already described. An important factor that determines the strength of concrete is the water:cement ratio. The relationship between the w/c ratio and strength was formulated by Abrams in 1918. The strength of concrete (S) is related to w (water/cement ratio) by the equation $S = A/B^w$, called Abram's law. The constants A and B depend on the age, curing regime, type of cement,

@Seismicisolation

and the testing method. This law is valid provided the concrete is fully compacted. This is the reason why, below a certain minimum, further reduction in the w/c ratio does not result in the expected strength gain. At such low w/c ratios, concrete is not workable enough to allow full compaction. Air entrainment reduces concrete strength and this effect should be considered while applying the law.[77]

The strength of concrete depends on the strength of the paste, coarse aggregate, and the paste-aggregate interface. This interface is the weakest region of concrete and is where the failure occurs before its occurrence on the aggregate or the paste. The weakness of this interface is due to weak bonding and the development of cracks which may develop due to bleeding and segregation and volume changes of the cement paste during setting and hydration. The transition zone extends about 50 μm from the surface of the aggregate. The transition zone has a higher porosity and permeability. This space is occupied by oriented, well developed crystals of calcium hydroxide and, in some cases, C-S-H and ettringite. The transition zonal effects are particularly significant with pastes or concrete made at w/c ratios greater than 0.4. The presence of silica fume, however, may modify or even eliminate the transition zone. This is generally attributed to the changes in the viscosity or cohesiveness imparted by silica fume to concrete. The altered transition zone, improved matrix-aggregate bond, and optimal particle packing in the presence of silica fume, result in enhanced strength.

8.0 DURABILITY OF CONCRETE

One of the most important requirements of concrete is that it should be durable under certain conditions of exposure. Deterioration can occur in various forms, such as alkali-aggregate expansion reaction, freeze-thaw expansion, salt scaling by deicing salts, shrinkage and enhanced attack on the reinforcement of steel due to carbonation, sulfate attack on exposure to ground waters containing sulfate ions, sea water attack, and corrosion caused by salts. Addition of admixtures may control these deleterious effects. Air entrainment results in increased protection against freeze-thaw action, corrosion inhibiting admixtures increase the resistance to corrosion, inclusion of silica fume in concrete decreases the permeability

@Seismicisolation

and consequently the rate of ingress of salts, and the addition of slags in concrete increases the resistance to sulfate attack.

8.1 Alkali-Aggregate Expansion

Although all aggregates can be considered reactive, only those that actually cause damage to concrete are cause for concern. Experience has shown that the presence of excessive amount of alkalis enhances the attack on concrete by an expansion reaction. Use of marginal quality aggregate and the production of high strength concrete may also produce this effect.

The alkali-aggregate reaction in concrete may manifest itself as map cracking on the exposed surface, although other reactions may also produce such failures. The alkali-aggregate reaction known as *alkali-silica* type may promote exudation of a water gel which dries to a white deposit. These effects may appear after only a few months or even years.

Three types of alkali-aggregate reactions are mentioned in the literature, viz., alkali-silica reaction,[78]-[80] alkali-carbonate reaction, and alkali-silicate reaction. The alkali-silicate reaction has not received general recognition as a separate entity. Alkali-silica reactions are caused by the presence of opal, vitreous volcanic rocks, and those containing more than 90% silica. The alkali-carbonate reaction is different from the alkali-silica reaction in forming different products.[81]–[83] Expansive dolomite contains more calcium carbonate than the ideal 50% (mole) proportion and frequently also contains illite and chlorite clay minerals. The alkali-silicate reaction was proposed by Gillott.[84] The rocks that produced this reaction were graywackes, argillites, and phyllites containing vermiculites.

The preventive methods to counteract alkali-aggregate expansion include replacement of cement with pozzolans or blast-furnace slag and addition of some chemicals, such as lithium compounds.[85]-[89]

In Fig. 11, the effect of LiOH on the expansion in mortar containing opal, is shown. Mix five, containing opal and high alkali cement, shows the maximum amount of expansion. Mixes one, two, three, and four do not have opal. Mixes six and seven are similar except that mix six has 0.5% LiOH and mix seven 1% LiOH.

@Seismicisolation

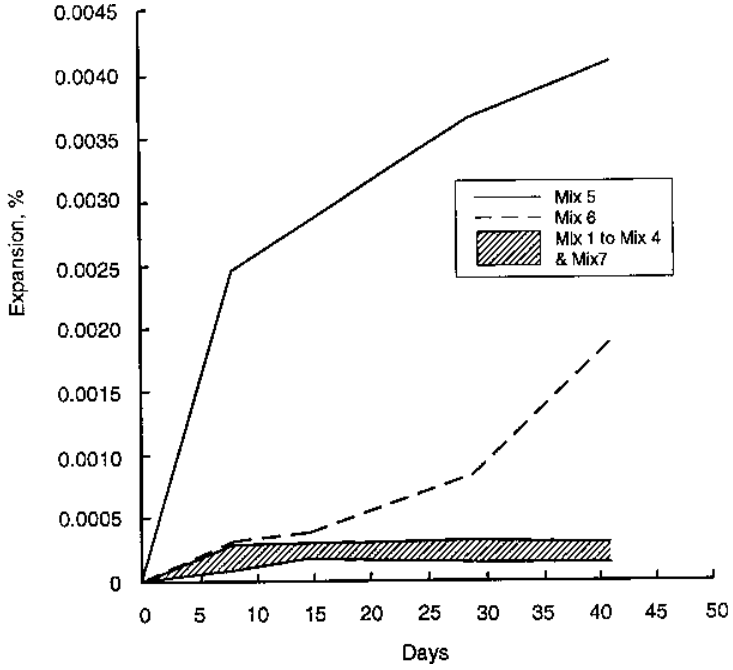


Figure 11. Expansion of mortar containing LiOH.

8.2 Frost Action

This is defined as the freezing and thawing of the moisture in materials and the resultant effects on these materials. Essentially three kinds of defects are recognized, viz., spalling, scaling, and cracking. Scaling occurs to a depth of an inch from the surface resulting in local peeling or flaking. Spalling occurs as a definite depression caused by the separation of surface concrete, while cracking occurs as D- or map-cracking and is sometimes related to the aggregate performance. Good resistance to frost expansion can be obtained by proper design and choice of materials and thus durability to frost action is only partly a material behavior. In addition to w/c ratio, quality of aggregate, and proper air entrainment, the frost resistance depends on the exposure conditions. Dry concrete will withstand freezing-thawing whereas highly saturated concrete may be severely damaged by a few cycles of freezing and thawing.

@Seismicisolation

According to many workers, frost damage is not necessarily connected with the expansion of water during freezing although it can contribute to damage. Although many organic compounds, such as benzene and chloroform, contract during freezing, they can cause damage during the freezing transition. When a water-saturated porous material freezes, macroscopic ice crystals form in the coarser pores and water which is unfrozen in the finer pores and migrates to the coarser pores or the surfaces.[90] The large ice crystals can feed on the small ice crystals, even when the larger ones are under constraint.

Length Changes During Freezing of Hydrated Portland Cement. The pore structure of hardened cement paste determines freezing of water contained in the pores. The pore structure depends largely on the initial w/c ratio and the degree of hydration. In general, the pore structure is composed of pores having diameters ranging from 1,000 to 5 nm for non-matured pastes and 100 to 5 nm for mature pastes. The higher the w/c ratio, the greater will be the volume fraction of larger pores. When these pores are saturated with water, a large amount of water will be able to freeze during cooling. A saturated concrete prepared at a higher w/c ratio and with a lower degree of hydration contains a greater amount of water.

Fully saturated samples on cooling at 0.33°C/min show dilations during freezing and residual expansion on thawing. These values are increased in samples made at higher w/c ratios. Thicker samples also exhibit larger expansions. Cooling rates also influence length change values. It has been found that during the slow cooling 30–40% of the evaporable water is lost from the samples. It is apparent that the large dilation is not only due to water freezing in larger pores, but also to water migrating from smaller pores, freezing in limited spaces, and generating stresses. When the rate of cooling is slow, there is enough time for water to vacate the small pores of the sample, causing contraction due to drying shrinkage. Powers and Helmuth[91] added an air-entraining admixture to the paste, producing various amounts of air bubbles of uniform size. With a knowledge of the total volume and average size of the bubbles, the average distance between them (air-void spacing) was calculated. Length change measurements on cooling (0.25°C/min) relatively thick specimens of different air-void spacings, but having similar porosity, are shown in Fig. 12. Shrinkage occurred in specimens with bubble spacings of 0.30 mm or lower. These specimens were saturated (except for the entrained space) and, therefore, the existence of closely-spaced air bubbles provided sites for water to migrate and for ice crystals to grow without the imposition of stress.

@Seismicisolation

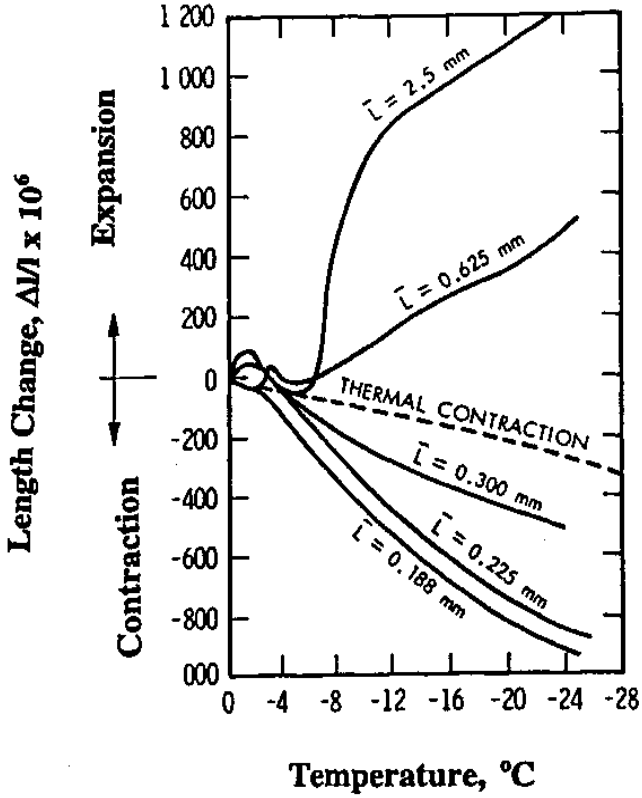


Figure 12. Length changes due to freezing of cement pastes of different air contents. (*L* is the spacing factor.)

De-Icing Salts—Deterioration of plain concrete due to deicing agents may generally be termed *salt scaling;* it is similar in appearance to frost action, but more severe. Any theory on salt scaling should account for this increased damage.

Length change measurements on freezing and thawing specimens saturated with different concentrations of brine solutions have been conducted by Litvan.[92] Typical results are shown in Fig. 13. The curves are qualitatively similar to those samples containing NaCl, but the magnitude of length changes is different. Maximum dilation effects are observed in solutions containing 5–9% NaCl. The explanation is that the vapor

@Seismicisolation

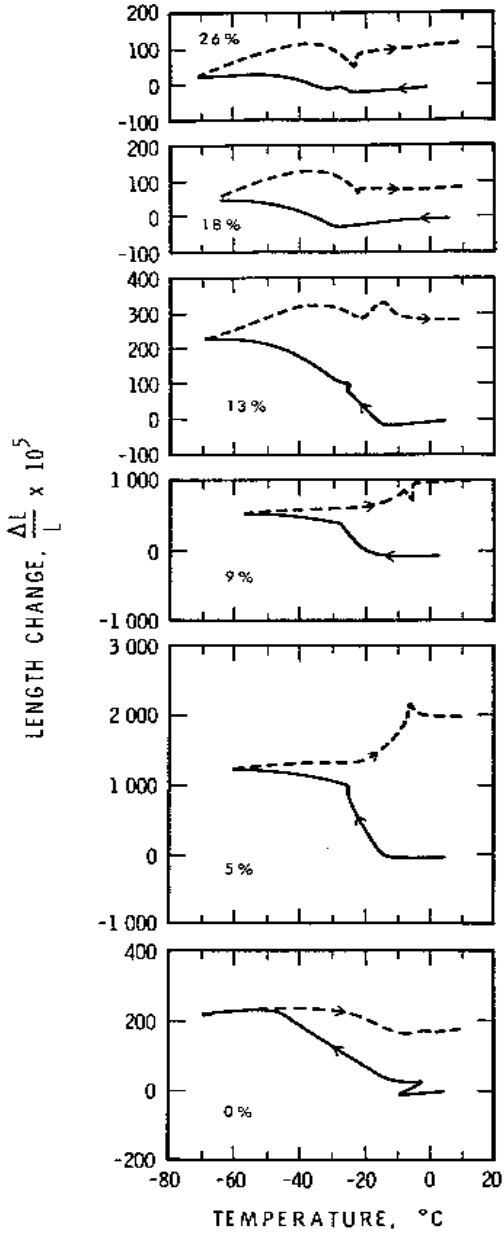


Figure 13. Length changes for air-entrained 0.5 w/c cement paste saturated with brine of various concentrations.

@Seismicisolation

pressure of the saline solution is decreased (with respect to water) and the tendency for the water to migrate from the smaller pores will be lower for the saline solution in comparison with that for pure water. The relative humidity created when bulk ice, $P_{o(Bs)}$, formed in larger pores will be $P_{0(Bs)}/P_{sol}$, which will be larger than $P_{0(Bs)}/P_{0(SL)}$ at any temperature. Consequently, on freezing, greater dilation will occur in the salt-containing specimen than in the salt-free specimen. At high salt concentrations other phenomena, such as a change in the range of freezing temperatures or the effect of high viscosity of the saline solution on the mechanical properties of the body, have to be considered.

In concrete, the pores of the aggregate may be such that the pore water may readily freeze. Larger pores, equivalent to air-entrained bubbles (diameter > 10 nm) may not exist in the aggregates. Thus, the tendency to expand due to freezing of water will either be taken up by elastic expansion of the aggregate or by water flowing out from the aggregate under pressure. For saturated aggregates, there may be a critical size below which no frost action occurs because, during freezing, water will flow out of the specimen.[93]

Tests for Frost Resistance. The most widely used test for assessing the resistance of concrete to freezing and thawing is the ASTM test on "Resistance of Concrete to Rapid Freezing and Thawing" (ASTM C 666). In procedure A, both freezing and thawing occur with the specimens surrounded by water and, in procedure B, the specimens are frozen in air and thawed in water. Procedure A is somewhat more reproducible than Procedure B.

Control of Frost Resistance. The general approach to preventing frost attack in concrete is to use an air-entraining agent. Tiny bubbles of air are entrapped in concrete due to the foaming action developed by the admixture during mixing. Many factors, such as the variability in the materials, impurities, mixing and placing methods, make it difficult to adjust the required amount of air containing the right bubble spacing and size. Trial mixes are often carried out for this purpose.

These problems could largely be avoided if the preformed bubble reservoirs could be added in the form of particles. Two inventions have used this principle; the plastic microspheres[94] and porous particles,[95] which have required air are added to concrete. It has been shown that addition of particles which correspond to less than 2% equivalent air is similar to conventional air-entrained concrete containing 5% air. Control of the right size and spacing of air pockets in these particles can add to the effectiveness to frost action.

@Seismicisolation

8.3 Sea Water Attack

Construction activity has been extending into the oceans and coastal areas because of the increasing number of oil and seabed mining operations. A large portion of these installations will be made from portland cement concrete and great demands will be made on it for increased safety and long term durability.

The deterioration of concrete due to sea water attack is the result of several simultaneous reactions; however, sea water is less severe on concrete than can be predicted from the possible reactions associated with the salts contained in it. Sea water contains 3.5% salts by weight. They include NaCl, $MgCl_2$, $MgSO_4$, $CaSO_4$, and possibly $KHCO_3$.

The deterioration of concrete depends on the exposure conditions. Concrete not immersed, but exposed to marine atmosphere will be subjected to corrosion of reinforcement and frost action. Concrete in the tidal zone, however, will be exposed to the additional problems of chemical decomposition of hydrated products, mechanical erosion, and wetting and drying. Parts of the structure permanently immersed are less vulnerable to frost action and corrosion of the reinforcing steel.

The aggressive components of sea water are CO_2, $MgCl_2$, and $MgSO_4$. Carbon dioxide reacts with $Ca(OH)_2$, finally producing calcium bicarbonate that leads to the removal of $Ca(OH)_2$. Carbon dioxide may also react with calcium aluminate monosulfate and break down the main strength-giving C-S-H component to form aragonite and silica. Even though $MgCl_2$ and sulfate are present only in small amounts they can cause deleterious reactions. These compounds react with $Ca(OH)_2$ to form soluble $CaCl_2$ or gypsum. Sodium chloride in sea water has a strong influence on the solubility of several compounds. Leaching of them makes the concrete weak. Magnesium sulfate may also react with calcium monosulfate aluminate in the presence of $Ca(OH)_2$ to form ettringite; this reaction is slowed down in the presence of NaCl[96] and may not occur if $Ca(OH)_2$ is converted by CO_2 to carbonate.

Calcium chloroaluminate seldom forms in sea water because, in the presence of sulfate, ettringite is the preferred phase. Ettringite formation affects the durability of concrete in seawater in the presence of cements containing $C_3A > 3\%$.[97] Tricalcium aluminate, in combination with high C_3S content, shows an even lower resistance to seawater than C_3A alone (Fig. 14). This is probably also due to the large amount of $Ca(OH)_2$ liberated by the hydration of C_3S. This explains why the addition of blast

@Seismicisolation

furnace slag or fly ash to cement improves the performance in sea water. This is due to the reaction of $Ca(OH)_2$ with the reactive SiO_2 and Al_2O_3 from the fly ash and the low level of $Ca(OH)_2$ that is generally present in good blast furnace slags after the hydration reaction.

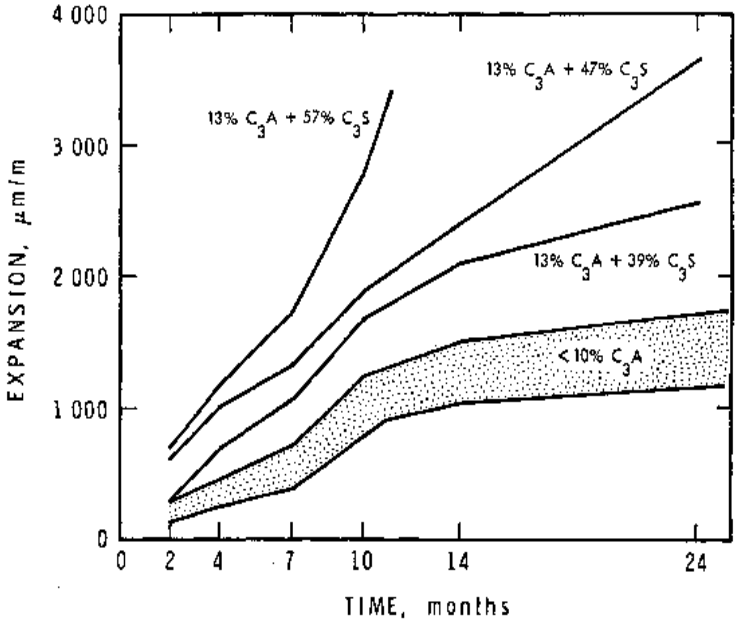


Figure 14. Linear expansion of mortar samples stored in sea water.

8.4 Corrosion of Reinforcement

Corrosion of steel in concrete is probably the most serious durability problem of reinforced concrete in modern times and, therefore, a clear understanding of the phenomenon is of crucial importance. The phenomenon itself is an electrochemical reaction. In its simplest form, corrosion may be described as current flow from anodic to cathodic sites in the presence of oxygen and water. This is represented by the following equations:

@Seismicisolation

AT ANODE $Fe \rightarrow Fe^{2+} + 2e^-$

AT CATHODE $\frac{1}{2}O_2 + H_2O + 2e^- \rightarrow 2(OH)^-$

These reactions would result in the formation of oxide at cathodic sites. The high alkalinity of cement paste, however, provides protection for the steel reinforcement. Although it is understandable that the likelihood of corrosion depends on the pH of the solution and the electrical redox potential of the metal, initial observations of diagrams, known as *Pourbaix plots* (showing equilibrium regions where the metal is in a state of immunity or passivity, or where corrosion will occur) for carbon steel or iron show that the redox potential for the hydrogen electrode lies above the region of immunity for iron in both acid and alkaline solutions, suggesting that iron will dissolve with evolution of hydrogen in solutions of all pH values. However, in the pH interval 9.5 to 12.5, a layer of ferrous oxide or hydroxide forms on the metal surface thus conferring immunity from corrosion in these solutions in this range. Some authors[98] refer to this layer, or film, as γ-Fe_2O_3. This protective film is believed to form quite rapidly during the early stages of cement hydration and may grow to a thickness of the order of 10^{-3} to 10^{-1} µm. Only indirect evidence of an oxide film exists and is mainly based on anodic polarization measurements. Much is not known about the conditions of formation, or chemical or mineralogical composition of these passivating layers and it is feasible that the film may consist of several phases.[99]

Chloride depassivation of steel is perhaps better understood than the passivation process and there are several mechanisms proposed.[100][101] One of the mechanisms involves the formation of a complex ion between chloride ion and the ferrous ion in the passive film. It is possible that low Cl ion concentrations enhance Fe solubility[102] even at pHs as high as 12–13 as a result of a chloride complex containing both Fe^{2+} and Fe^{3+}. Migration of this complex destabilizes the passive layer and by this mechanism chloride can rejuvenate the corrosion process. Chloride ions are also responsible for other deleterious effects. They contribute, together with CO_2 ingress, to the depression of the pH of the pore fluid and increase the electrical conductance of the concrete, allowing the corrosion current to increase.

Currently, a limit of 0.2 percent of chloride ion concentration by weight of cement in the concrete is proposed; however, there is no theoretical basis to this value, and it appears possible that this amount of

@Seismicisolation

hydroxyl ion in the cement paste modifies this value. Thus, some researchers have placed a limit on the ratio of chloride to hydroxyl ion[102][103] such that corrosion will occur if the ratio of Cl^- to OH^- is as follows:

$$\frac{Cl^-}{OH^-} > 0.6$$

Consequently the chloride ion threshold must also depend upon the alkalis in the cement. The effect of alkalis in aggregates and the removal of chloride ions by aluminate phases further complicate this picture, and it has been pointed out[101] that the fixation of chloride by the latter should not be considered permanent as the chloroaluminate may be unstable in the presence of sulfate or carbon dioxide.

Although the corrosion of the reinforcing steel in concrete is detrimental for the simple fact that the composite will lose strength, the main cause for concern is that this phenomenon causes cracking of the surrounding concrete. Estimates are that as little as 0.1 mil of rust thickness can cause cracking.

Early detection of the corrosion can allow remedial action to be made successfully. One of the more widely used tests is the measurement of the half-cell potential of the reinforcing steel embedded in the concrete (ASTM C876). It is usually understood that corrosion is taking place when half-cell potential values are more negative than -0.35 volts. However, frequently this rule does not strictly apply and it is recommended that corrosion rate values be obtained in questionable areas by measuring polarization resistance.

Generally, it is felt that the rate of corrosion of steel is primarily controlled by the diffusion of oxygen through the concrete cover, followed by the cathodic reaction involving reduction of oxygen.[104] However, there are situations where chloride contents are high and corrosion rates are much higher than would be expected from possible diffusion rates of oxygen. It has been postulated[104] that in these cases there are strong localized reductions in pH in crevices where iron is converted to $Fe(OH)_2$ through the prior conversion to chloride. These reactions involve hydrogen evolution.

Several methods of corrosion prevention have been tried over the years. These include protective coatings, placement of impermeable concrete overlays, cathodic protection, or the use of corrosion resistant steels and galvanized or epoxy coated bars. Recent work has shown[105] that

@Seismicisolation

galvanized steel may be of benefit if used in low chloride bearing concrete (0.3 percent by weight of cement). Epoxy-coated bars have performed well where the concrete contained up to 1.2% chloride, but a breakdown of the coating was detected at a chloride level of 4.8%, indicating finite tolerance limit for chloride. The best durability was exhibited by the stainless clad reinforcing bars.

8.5 Carbonation of Concrete

The corrosion of depassivated steel in reinforced concrete has focused attention to the reactions of acidic gases such as carbon dioxide with hydrated cement and concrete. As a result of the reaction of carbon dioxide, the alkalinity of concrete can be progressively reduced, resulting in a pH value below 10.

The process of carbonation of concrete may be considered to take place in stages. Initially, CO_2 diffusion into the pores takes place, followed by dissolution in the pore solution. Reaction with the very soluble alkali metal hydroxide probably takes place first, reducing the pH and allowing more $Ca(OH)_2$ into the solution. The reaction of $Ca(OH)_2$ with CO_2 takes place by first forming $Ca(HCO_3)_2$ and finally, $CaCO_3$. The product precipitates on the walls and in crevices of the pores. This reduction in pH also leads to the eventual breakdown of the other hydration products, such as the aluminates, CSH gel, and sulfo-aluminates.

The relative humidity at which the pore solution is in equilibrium will greatly affect the rate of carbonation. The relative humidity controls the shape and area of the menisci at the air-water interfaces of the pores; at relative humidities greater than 80 percent, the area of the menisci contacting the air becomes quite small, resulting in a low rate of absorption of CO_2. At relative humidities below 40 percent, no menisci exist and the pore water is predominantly adsorbed water and does not effectively dissolve the CO_2. Consequently, carbonation occurs at a maximum rate between 50 and 70 percent relative humidity. In addition to atmospheric conditions, carbonation rate is also influenced by the permeability of the concrete and the cement content of the concrete. Cement content of approximately 15% produces a concrete relatively resistant to carbonation. An increase over this level produces marginal increases, while below this, results in a precipitous drop in resistance. Generally, it is found that good compaction and curing cause larger improvements in concrete permeability and resistance to carbonation than minor alterations in mix design.

@Seismicisolation

Several workers[106]–[109] have concluded that carbonation depth is proportional to the square root of time. The proportionality constant is a coefficient related to the permeability of the concrete. Factors such as cement content in concrete, CO_2 concentration in the atmosphere, and the relative humidity, in addition to normal factors such as concrete density, affect the value of this coefficient. If the depth of carbonation is measured in mm and the time in years, the average coefficient for precast, prestressed quality concrete is < 1; for high strength concrete used in bridges, an average value of 1 is found, while normal in situ reinforced concrete an average value of 4–5 has been recorded. If the value of 1 is used and reinforced concrete is designed with a cover of 25 mm, predicted time for the carbonated layer to reach the steel would be 625 years. Some doubt may exist with regard to this prediction since some authors[109] have stated that the actual relationship between depth of carbonation and time may be between linear and square root of the time, making the above prediction optimistic. In addition, higher levels of carbonation can lead to densification and blocking of pores, which is beneficial, but carbonation can also lead to carbonation shrinkage and cracking, especially when carbonation occurs at relative humidities between 50 and 75%.

It has been clearly shown[107] that concretes with higher levels of fly ash (≅50%) have increased carbonation, especially when poorly cured. However, the carbonation of concretes containing lower levels of fly ash (15–30%) is generally similar to, or slightly higher than, that of the control concretes. This increased carbonation observed for the 50% fly ash concrete cannot be explained by increased permeability since it has been shown[107] that the permeabilities of these concretes are lower than those of the control. However, the lower permeabilities of these blended cement concretes is due to a discontinuous pore structure. Carbonation and shrinkage cracking may lead to an opening up of the structure, yielding continuous pores and an increase in permeability.

8.6 Delayed/Secondary Ettringite Formation

The potential for concrete deterioration as a consequence of the delayed ettringite formation in the precast industry has recently been recognized. One of the important factors required for this type of reaction is high temperature curing of concrete such as that occurring in the

@Seismicisolation

precast industry.[110] The delayed formation of ettringite is attributed to the transformation of monosulfo-aluminate to ettringite when steam curing is followed by normal curing at later ages. In recent work it was indicated that sulfate may be bound by the C-S-H gel that is released at later ages.[111] Increased temperature is expected to accelerate the absorption of sulfate by the silicate hydrate. It has also been confirmed that the ettringite crystals are usually present in cracks, voids, and transition zone at the aggregate-binder interface, causing expansion and cracking. It has also been observed that ASTM Type III cement is more vulnerable to deterioration due to the delayed ettringite formation than Type I or Type V cement. Thermal drying after high temperature curing intensifies the deterioration. In the secondary ettringite formation, calcium sulfate formed from the decomposition of AFt or AFm phase as a consequence of severe drying, dissolves upon rewetting and migrates into cracks to react with the local Al-bearing materials to cause expansion.[112]

REFERENCES

1. Bresler, B., *Reinforced Concrete Engineering*, Wiley-Interscience, New York (1974)
2. Pressler, E. E., Brunauer, S., Kantro, D. L., and Weise, C. H., Determination of the Free Calcium Hydroxide Contents of Hydrated Portland Cements and Calcium Silicates, *Anal. Chem.*, 33:877–882 (1961)
3. Lehmann, H., Locher, F. W., and Prussog, D., Quantitative Bestimmung des Calcium Hydroxide in Hydratisierten Zementen, *Ton-Ztg.*, 94:230–235 (1970)
4. Ramachandran, V. S., Differential Thermal Method of Estimating Calcium Hydroxide in Calcium Silicate and Cement Pastes, *Cem. Concr. Res.*, 9:677–684 (1979)
5. Midgley, H. G., The Determination of Calcium Hydroxide in Set Portland Cements, *Cem. Concr. Res.*, 9:77–83 (1979)
6. Taylor, H. F. W., Portland Cement: Hydration Products, *J. Edn. Mod. Materials, Sci. & Eng.*, 3:429–449 (1981)
7. Feldman, R. F., and Ramachandran, V. S., Differentiation of Interlayer and absorbed Water in Hydrated Portland Cement of Thermal Analysis, *Cem. Concr. Res.*, 1:607–620 (1971)

@Seismicisolation

8. Feldman, R. F., and Ramachandran, V. S., A Study of the State of Water and Stoichiometry of Bottle Hydrated Ca_3SiO_5, *Chem. Concr. Res.*, 4:155–166 (1974)
9. Taylor, H. F. W., The Chemistry of Cements, *Royal Inst. Chem., Series 2*, p. 27 (1966)
10. Stein, H. N., and Stevels, J., Influence of Silica on Hydration of $3CaO•SiO_2$, *J. App. Chem.*, 14:338–346 (1964)
11. Tadros, M. E., Skalny, J., and Kalyoncu, R., Early Hydration of C_3S, *J. Amer. Cer. Soc.*, 59:344–347 (1976)
12. Maycock, J. N., Skalny, J., and Kalyoncu, R., Crystal Defects and Hydration: I Influence of Lattice Defects, *Cem. Concr. Res.*, 4:835–847 (1974)
13. Fierens, P., and Verhaegen, J. P., The Effect of Water on Pure and Doped Tricalcium Silicate Using the Techniques of Absorboluminescence, *Cem. Concr. Res.*, 5:233–238 (1975)
14. Pratt, P. L., and Jennings, H. M., The Microchemistry and Microstructure of Portland Cement, *Ann, Rev. Mat. Sci.*, 11:123–149 (1981)
15. Gartner, E. M., and Gaidis, W. R., Hydration Mechanisms in Materials Science of Concrete I, (J. Skalny, ed.), *American Ceramic Society*, pp. 95–125 (1989)
16. Ramachandran, V. S., and Sereda, P. J., Application of Hedvall Effect in Cement Chemistry, *Nature*, 233:134–135 (1971)
17. Bogue, R. H., and Lerch, W., Hydration of Portland Cement Compounds, *Ind. Eng. Chem.*, 26:837–847 (1934)
18. Beaudoin, J. J., and Ramachandran, V. S., A New Perspective on the Hydration Characteristics of Cement Pastes, *Cem. Concr. Res.*, 22:689–694 (1992)
19. Feldman, R. F., and Ramachandran, V. S., Character of Hydration of $3CaO•Al_2O_3$, *J. Amer. Cer. Soc.*, 49:268–273 (1966)
20. Ramachandran, V. S., and Feldman, R. F., Significance of Low Water/Solid Ratio and Temperature on the Physico-Mechanical Characteristics of Hydrates of Tricalcium Aluminate, *J. App. Chem. Biotechnol.*, 23:625–633 (1973)
21. Tadros, M. E., Jackson, W. Y., and Skalny, J., Study of Dissolution and Electro-Kinetic Behavior of Tricalcium Aluminate, *Colld. Interface, Sci.*, 4:211–223 (1976)
22. Feldman, R. F., and Ramachandran, V. S., The Influence of $CaSO_4•2H_2O$ Upon the Hydration Character of $3CaO•Al_2O_3$, *Mag. Concr. Res.*, 18:185–196 (1967)

@Seismicisolation

23. Ramachandran, V. S., and Beaudoin, J. J., Significance of Water/Solid Ratio and Temperature on the Physico-Mechanical Characteristics of Hydrating $4CaO \cdot Al_2O_3 \cdot Fe_2O_3$, *J. Mat. Sci.*, 11:1893–1910 (1976)
24. Young, J. F., Hydration of Portland Cement, *J. Edn. Mod. Mat. Sci. Eng.*, 3:404–428 (1981)
25. Ramachandran, V. S., and Beaudoin, J. J., Hydration of C_4AF + Gypsum: Study of Various Factors, *Proc. VII Intern. Cong. Cements*, pp. 25–30, Paris (1980)
26. Mascolo, G., and Ramachandran, V. S., Hydration and Strength Characteristics of Synthetic Al-, Mg-, and Fe-Alites, *Mats. & Constr.* 8:373–376 (1975)
27. Beaudoin, J. J., and Ramachandran, V. S., Physico-Chemical Characteristics of Low Porosity Cement Systems, Chap. 8, *Materials Science of Concrete*, Vol. III, p. 362, (J. Skalny, ed.), American Ceramic Society (1992)
28. Raffle, J. F., The Physics and Chemistry of Cements and Concretes, *Sci, Prog.*, 64:593–616, Oxford (1977)
29. Ramachandran, V. S., *Applications of Differential Thermal Analysis in Cement Chemistry*, Chemical Publishing Co., New York (1969)
30. Hansen, T. C., Radjy, F., and Sellevold, E. J., Cement Paste and Concrete, *Annual Rev. Mat. Sci.*, 3:233–268 (1973)
31. Ramachandran, V. S., Feldman, R. F., and Beaudoin, J. J., *Concrete Science, A Treatise on Current Research*, p. 427, Heyden & Son, Ltd., UK (1981)
32. Grattan-Bellew, P. E., Quinn, E. G., and Sereda, P. J., Reliability of Scanning Electron Microscopy Information, *Cem. Concr. Res.*, 8:333–342 (1978)
33. Diamond, S., *Cement Paste Microstructure—An Overview at Several Levels in Hydraulic Cement Pastes—Their Structure and Properties*, p. 334, Conference, University of Sheffield (April, 1976)
34. Feldman, R. F., Sereda, P. J., and Ramachandran, V. S., A Study of Length Changes of Compacts Exposed to H_2O, *Highway Res. Rec.*, 62:106–118 (1964)
35. Soroka, I., and Sereda, P. J., The Structure of Cement Stone and the Use of Compacts as Structural Models, *Proc. Fifth Int. Symp. Chem. of Cement*, Part III, Vol. III, 67–73, Tokyo (1968)
36. Feldman, R. F., Factors Affecting the Young's Modulus-Porosity Relation of Hydrated Portland Cement Compacts, *Cem. Concr. Res.*, 2:375–386 (1972)

@Seismicisolation

37. Feldman, R. F., Density and Porosity Studies of Hydrated Portland Cement, *Cement Technology*, 3:3–11 (1972)
38. Parrott, L. J., Hansen, W., and Berger, R. L., Effect of First Drying Upon the Pore Structure of Hydrated Alite Paste, *Cem. Concr. Res.*, 10:647–655 (1980)
39. Day, R. L., Reactions Between Methanol and Portland Cement Paste, *Cem. Concr. Res.*, 11:341–349 (1981)
40. Harris, D. H. C., Windsor, C. G., and Lawrence, C. D., Free and Bound Water in Cement Pastes, *Mag. Concr. Res.*, 26:65–72 (1974)
41. Auskern, A., and Horn, W., Capillary Porosity in Hardened Cement Paste, *ASTM J. Test. Eval.*, 1:74–79 (1973)
42. Beaudoin, J. J., Porosity Measurements of Some Hydrated Cementitious Systems by High Pressure Mercury Intrusion - Microstructural Limitations, *Cem. Concr. Res.*, 9:771–781 (1979)
43. Mikhail, R. Sh., and Selun, S. A., Adsorption of Organic Vapors in Relation to the Pore Structure of Hardened Portland Cement Pastes, *Symposium on Structure of Portland Cement Paste and Concrete, Special Report 90*, HRB:123–134 (1966)
44. Litvan, G. G., Variability of the Nitrogen Surface Area of Hydrated Cement Paste, *Cem. Concr. Res.*, 6:139–144 (1976)
45. Beaudoin, J. J., Interaction of Aliphatic Alcohols with Cement, *Il Cemento*, 83:199–210 (1986)
46. Tomes, L. A., Hunt, C. M., and Blaine, R. L., Some Factors Affecting the Surface Area of Hydrated Portland Cement as Determined by Water-Vapor and Nitrogen Adsorption. *J. of Res., Nat. Bur. Stand*, 59:357–364 (1957)
47. Winslow, D. N., and Diamond, S., Specific Surface of Hardened Portland Cement Paste as Determined by Small-Angle X-Ray Scattering, *J. Am. Ceram. Soc.*, 57:193–197 (1974)
48. Feldman, R. F., Application of Helium Inflow Technique for Measuring Surface Area and Hydraulic Radius of Hydrated Portland Cement, *Cem. Concr. Res.*, 10:657–664 (1980)
49. Sereda, P. J., Feldman, R. F., and Swenson, E. G., Effect of Sorbed Water on Some Mechanical Properties of Hydrated Portland Cement Pastes and Compacts, *HRB Special Report 90*, pp. 58–73, Washington (1966)
50. Ryshkewitch, E., Compression Strength of Porous Sintered Alumina and Zirconia, *J. Amer. Ceram. Soc.*, 36:65–68 (1953)
51. Schiller, K. K., Strength of Porous Materials, *Cem. Concr. Res.*, 1:419–422 (1971)

@Seismicisolation

52. Feldman, R. F., and Beaudoin, J. J., Microstructure and Strength of Hydrated Cement, *Proc. VI Int. Congr. Chem. of Cement,* Vol. II, Book 1, pp. 288–293 Moscow (1974)
53. Roy, D. M., Gouda, G. R., and Bobrowsky, A., Very High Strength Cement Pastes Prepared by Hot Pressing and Other High Pressure Techniques, *Cem. Concr. Res.,* 2:349–366 (1972)
54. Beaudoin, J. J., and Feldman, R. F., A Study of Mechanical Properties of Autoclaved Calcium Silicate Systems, *Cem. Concr. Res.*, 5:103–118 (1975)
55. Blaine, R. L., Arni, H. T., and Defore, M. R., Interaction Between Cement and Concrete Properties, *Building Science Series 8,* Nat. Bur. Std. (1968)
56. Odler, I., Strength of Cement, *Materials & Structures,* 24:143–157 (1991)
57. Nyame, B. K., and Illston, J. M., Relationships Between Permeability and Pore Structure of Hardened Cement Paste, *Magazine of Concr. Res.*, 33:139–146 (1981)
58. Verbeck, G., and Helmuth, R. A., Structures and Physical Properties of Cement Pastes, *Proc. V Int. Symp. Chem. of Cement,* Vol. III, pp. 1–31, Tokyo (1968)
59. Feldman, R. F., and Swenson, E. G., Volume Change on First Drying of Hydrated Portland Cement With and Without Admixtures, *Cem. Concr. Res.*, 5:25–35 (1975)
60. Powers, T. C., Mechanism of Shrinkage and Reversible Creep of Hardened Cement Paste, *Intern. Conf. on the Structure of Concrete,* pp. 319–344, London (1965), Imperial College Cem. and Concr. Assoc. (1965)
61. Bazant, Z. P., Constitutive Equation for Concrete Creep and Shrinkage Based on Thermodynamics of Multiphase Systems, *Materiaux et Constructions,* 3:3–36 (1970)
62. Hannant, D. J., The Mechanism of Creep in Concrete, *Materials and Structures,* 1:403–410 (1968)
63. Wittmann, F., Einfluss des Feuchtigkeitgelialtes auf des Kriechen des Zement-Steines, *Rheologica Acta,* 9:282–287 (1970)
64. Gamble, B. R., and Illston, J. M., Rate Deformation of Cement Paste and Concrete During Regimes of Variable Stress, Moisture Content and Temperature, *Hydraulic Cement Pastes, Their Structure and Properties,* 297–311, Proc. Conf. held at Tapton Hall (1976)
65. Day, R. L., Ph.D. Thesis, Univ. of Calgary, Basic Rate Theory of Creep as Applied to Cement Paste and Concrete (1979)
66. Feldman, R. F., Mechanism of Creep of Hydrated Portland Cement Paste, *Cem. Concr. Res.,* 2:521–540 (1972)

@Seismicisolation

67. Hope, B. B., and Brown, N. H., A Model for Creep of Concrete, *Cem. Concr. Res.*, 5:577–586 (1975)

68. Feldman, R. F., and Beaudoin, J. J., Effect of Applied Stress on the Helium Inflow Characteristics of Hydrated Portland Cement, *Cem. Concr. Res.*, 13:470–477 (1983)

69. Ramachandran, V. S., (ed.), *Concrete Admixtures Handbook*, 2nd. Ed., Noyes Publications (1995)

70. Malhotra, V. M., *Supplementary Cementing Materials for Concrete*, CANMET, Canadian Government Publishing Center, Ottawa (1987)

71. Feldman, R. F., and Sereda, P. J., The New Model for Hydrated Portland Cement and Its Practical Implications, *Eng. J.*, 53:53–57 (1970)

72. Garboczi, E. J., and Bentz, D. P., Fundamental Computer-Based Models of Cement-Based Materials; *Materials Science of Concrete*, (J. Skalny, and S. Mindess, ed.), USA, Amer. Ceram. Soc., Westerville, Ohio (1991)

73. Garboczi, E. J., and Bentz, D. P., Computer-Based Models of the Microstructure and Properties of Cement-Based Materials, *9th International Congress on Cement Chemistry*, Vol. VI, pp. 3–15, New Delhi (1992)

74. Coverdale, R. T., and Jennings, H. M., Computer Modelling of Microstructure of Cement Based Materials, *Proc. 9th International Congress on Chemistry of Cement*, pp. 16–21, New Delhi, India (1992)

75. Neville, A. M., *Properties of Concrete*, Pitman Publishing Co, London (1981)

76. Mindess, S., and Young, J. F., *Concrete*, p. 671, Prentice Hall, New Jersey (1981)

77. Abrams, D. A., Design of Concrete Mixtures, Bulletin 1, *Structure of Materials Res. Lab.*, Lewis Inst., Chicago (1918); Published as *A Selection of Historic American Papers on Concrete, 1876–1926*, by ACI-SP-52, (H. Newlon, ed.), pp. 309–330, Detroit (1976)

78. Vivian, H. E., An Epilogue, *Symp. Alkali-Aggregate Reaction-Preventive Measures*, pp. 269–270, Reykjavik (1975)

79. Diamond, S., Chemical Reactions Other than Carbonate Reactions, Chapter 40, Significance of Tests and Properties of Concrete and Concrete-Making Materials, *ASTM Special Tech. Publn.*, 169B:708–721 (1978)

80. Hansen, W. C., Studies Relating to the Mechanism by which Alkali-Aggregate Reaction Produces Expansion in Concrete, *Proc. Amer. Concr. Inst.*, 40:213–227 (1944)

81. Swenson, E. G., A Reactive Aggregate Undetected by ASTM Tests, *Bull. No. 57, Amer. Soc. Testing Mat.*, 48–51 (1957)

@Seismicisolation

82. Swenson, E. G., and, Gillott, J. E., Alkali Carbonate Rock Reaction, Cement Aggregate Reactions, *Trans. Res. Board, Rec.* No. 525:21–40 (1974)

83. Swenson, E. G., and Gillott, J. E., Alkali Reactivity of Dolomitic Limestone Aggregate, *Mag. Concr. Res.*, 19:95–104 (1967)

84. Gillott, J. E., Practical Implications of the Mechanisms of Alkali-Aggregate Reactions, *Symp. Alkali-Aggregate Reaction*, pp. 213–230, Reykjavik (1975)

85. Powers, T. C., and Steinour, H. H., An Interpretation of Published Researches on the Alkali-Aggregate Reaction, *Amer. Concr. Inst. J. Procl.*, 51:497–516; 785–812 (1955)

86. McCoy, W. J., and Caldwell, A. G., New Approach to Inhibiting Alkali-Aggregate Reaction, *J. Amer. Concr. Inst.*, 47:693–706 (1951)

87. Luginina, I., and Mikhalev, Y., Phosphorous Additions Reduce the Negative Alkali Effect on the Cement Stone Strength, *Tsement,* 12:12–14 (1978)

88. Mehta, P. K., Effect of Chemical Additions on the Alkali-Silica Expansion, *Proc. 4th Cong. on Effects of Alkali in Cement and Concrete*, pp. 229–234, Perdue Univ., USA (1979)

89. Hansen, W. C., Inhibiting Alkali-Aggregate Reaction with Barium Salts, *J. Amer. Conc. Inst.*, 56:881–883 (1960)

90. Everett, D. H., The Thermodynamics of Frost Damage to Porous Solids, *Trans. Faraday Soc.*, 57:1541–1551 (1961)

91. Powers, T. C., and Helmuth, R. A., Theory of Volume Changes in Hardened Portland Cement Paste During Freezing, *Proc. of the Highway Res. Board*, 32:285–297 (1953)

92. Litvan, G. G., Phase Transition of Adsorbates: VI. Effect of Deicing Agents on the Freezing of Cement Paste, *J. Amer. Cer. Soc.*, 58:26–30 (1975)

93. MacInnes, C., and Lau, E. C., Maximum Aggregate Size Effect on Frost Resistance of Concrete, *Amer. Concr. Inst. J. Proc.* 68:144–149 (1971)

94. Sommer, H., A New Method of Making Concrete Resistant to Frost and De-Icing Salts, *Zement und Beton*, 4:124–129 (1977)

95. Litvan, G. G., Particulate Admixture for Enhanced Freeze-Thaw Resistance of Concrete, *Cem. Concr. Res.*, 8:53–60 (1978)

96. Biczok, I., Concrete Corrosion-Concrete Protection, 8th Ed., p. 545, *Akadamiai Kiado*, Budapest (1972)

97. Regourd, M., Physico-Chemical Studies of Cement Pastes, Mortars and Concretes Exposed to Sea Water, *ACI SP-65*, pp. 63–82 (1980)

98. ACI Committee 222, Corrosion of Metals in Concrete, *ACI Journal* 82:3–32 (1985)

@Seismicisolation

99. Sagou-Crentsil, K. K., and Glasser, F. P., Steel in Concrete, Part I, A Review of the Electrochemical and Thermodynamic Aspects, *Magazine of Concrete Research* 41:205–212 (1989)
100. Hoar, T. P., and Jacob, W. R., Breakdown of Passivity of Stainless Steel by Halide Ions, *Nature*, 216:1299–1301 (1967)
101. Hime, W. G., The Corrosion of Steel—Random Thoughts and Wishful Thinking, *Concrete Intern.*, 15:54–57 (1993)
102. Hausmann, H. D. A., Steel Corrosion in Concrete, *Materials Protection*, 6:19–22 (1967)
103. Gouda, V. K., Corrosion and Corrosion Inhibition of Reinforcing Steel, *Br. Corros. J.*, 5:198–203 (1970)
104. Gonzalez, J. A., Molina, A., Otero, E., and Lopez, W., On the Mechanism of Steel Corrosion in Concrete: The Role of Oxygen Diffusion, *Magazine of Concrete Research*, 42:23–27 (1990)
105. Rasheeduzzafar, Dakhil, F. H., Bader, M. A., and Khan, M. M., Performance of Corrosion Resisting Steels in Chloride-Bearing Concrete, *ACI Materials Journal*, 89:439–448 (1992)
106. Currie, R. J., Carbonation Depths in Structural Quality Concrete: An Assessment of Evidence from Investigations of Structures and from Other Sources, *B. R. E. Report*, p. 19, ISBN 0851251854 (1986)
107. Thomas, M. D. A., and Matthews, J. D., Carbonation of Fly-Ash Concrete, *Mag. Con. Res.*, 44:217–228 (1992)
108. McArthur, H., D'Arcy, S., and Barker, J., Cathodic Protection by Impressed DC Currents for Construction, Maintenance and Refurbishment in Reinforced Concrete, *Construction and Building Materials*, 7:86–93 (1993)
109. Vaysbard, A. M., Sabris, G. M., and Emmons, P. H., Concrete Carbonation—A Fresh Look, *The Indian Concrete Journal*, 67:215–221 (1993)
110. Heinz, D., and Ludwig, U., Mechanism of Secondary Ettringite Formation in Mortars and Concretes Subjected to Heat Treatment, ACI-SP 100, 2:2059–2071 (1987)
111. Grusczscinski, E., Brown, P. W., and Bothe, J. V., The Formation of Ettringite at Elevated Temperatures, *Cem. Concr. Res.*, 23:981–987 (1993)
112. Fu, Y., Grattan-Bellew, P. E., and Beaudoin, J. J., (Personal Communication)

@Seismicisolation

2

Petrographic and Technological Methods for Evaluation of Concrete Aggregates

P. E. Grattan-Bellew

1.0 INTRODUCTION

Aggregates are defined as "gravel, sand, slag, crushed rock or similar inert materials."[1] However, this description is not entirely accurate for concrete aggregates because, in the highly alkaline medium of the pore solution in concrete (pH >13), most minerals are at least partly unstable.[2] Minerals such as microcrystalline, cryptocrystalline quartz, other phases of SiO_2 such as tridymite and cristobalite, or amorphous silica (opal), are unstable in alkaline solution and give rise to the alkali-silica reaction in concrete.[3] Furthermore, the physical properties of some aggregates may make them unsuitable for use in concrete. For example, rocks which have an elongate shape, when crushed, adversely affect the workability and finishability of concrete. Other aggregates, such as some shales, disintegrate under cycles of freezing and thawing and cause rapid deterioration of concrete exposed to such conditions. Porous aggregates are also undesirable because they may be frost susceptible or may cause excessive

@Seismicisolation

shrinkage or D-cracking in concrete.[4] In reality, there is probably no such thing as a completely inert, natural, mineral aggregate.

Petrography is defined as the description of the composition and mode of formation of rocks. In petrographic studies of rocks for use as aggregates in concrete, the investigator is interested mainly in the composition of the rocks rather than in their mode of formation. The importance of petrographic evaluation of aggregates was recognized many years ago.[5] The basic practice for petrographic examination of aggregates for concrete is outlined in ASTM C-295.[6] Today, there are many technological tests for evaluating the suitability of aggregates for use in concrete, however, all have limitations and should not be used except in parallel with a petrographic examination. The current Canadian Standard, CSA A23.1-94,[7] specifies making a petrographic examination before running the technological tests such as the concrete prism test CSA A23.2-14A.[8] Most, if not all of the technological tests, are affected, to some extent, by the mineralogy of the aggregates and, hence, selection of an "appropriate test method" is dependent on the composition of the aggregate, which can only be determined by petrographic examination.

Petrographic examination of thin sections, which is familiar to all petrographers, is essential in the evaluation of concrete aggregates. However, some specialized training is required because the emphasis is on detecting the presence of materials (that may be deleterious even in very small quantities) rather than determining the mineralogical composition and the mode of formation of the rock, which is often the aim of petrographers in geological investigations. With some rocks, examination of thin sections alone is insufficient to identify the presence of potentially reactive minerals. In such cases, ancillary techniques, such as x-ray diffraction analysis, thermal analyses, infrared spectroscopy, or examination in the scanning electron microscope (SEM) is required.

In this chapter, rather than provide a list of standard petrographic and mineralogical techniques such as the examination of thin sections, the stock-in-trade of all petrographers, which are described in standard texts on petrography,[9]–[12] emphasis will be placed on a number of specialized techniques used in conjunction with petrographic evaluation in the analyses of aggregates for concrete. Many of these specialized techniques are described in a *Handbook of Concrete Aggregates* by Dolar-Mantuani.[13] In this chapter it is only possible to give an outline of the technological tests used to supplement the results of petrographic evaluation of aggregates.

@Seismicisolation

2.0 CHEMICAL TESTS

A wide variety of chemical tests may be used to supplement information obtained from examination of thin sections. Many of these tests are used to determine the potential alkali-silica reactivity of aggregates. Chemical tests include standard chemical whole rock analyses and a variety of specialized chemical tests developed specifically to evaluate the suitability of aggregates for use in concrete. The methodology for whole rock analysis is well adapted by laboratories specializing in this field. The use of whole rock analyses in evaluating rocks for concrete aggregate is discussed below.

2.1 Chemical Tests for Alkali-Silica Reactivity

Petrographic examination, although an essential step in the evaluation of the potential reactivity of aggregates, may not alone be sufficient to identify all aggregates susceptible to alkali-silica reaction. A petrographer frequently needs ancillary tests, such as x-ray diffraction, chemical analysis, or other analytical techniques to confirm the results of examination of thin sections of aggregates under investigation. The process of identifying potentially alkali-silica reactive components in aggregates is complicated by what is known as the *pessimum effect*, described by W. J. French.[14] Many reactive minerals cause maximum expansion in the mortar bar expansion test, ASTM C 227,[15] when present in very small amounts, sometimes as low as 1 to 5%. This is known as the pessimum effect. Such low percentages in an aggregate are easily overlooked in a thin section examination.

The mortar bar test is a good technique for confirming the potential reactivity of an aggregate, but it takes up to 6 months or longer to obtain the results and the test also has other problems. A rapid chemical test for alkali-silica reactivity was developed during the early years of research by Mielenz, et al., in 1947.[16] This test method was subsequently standardized as ASTM C 289 in 1952 and has undergone several minor revisions until the current version in 1987.[17] The need for chemical tests has been much reduced in recent years by the development of ultra accelerated mortar bar tests such as ASTM C 1260-94[18] and various autoclave tests.[19]–[21] The chemical tests are more suited to research than to the field evaluation of aggregates for use in concrete.

@Seismicisolation

2.2 Chemical Analysis

Bulk whole rock chemical analysis generally does not give a good indication of the potential reactivity of an aggregate because the amount of silica shown in the analysis does not provide sufficient information on the amount of potentially reactive silica minerals, micro crystalline quartz, opal, tridymite or cristobalite in the rock. The exceptions are glassy volcanic rocks which, because of their very fine texture, do not readily lend themselves for examination by a petrographic microscope. Volcanic rocks which are supersaturated in SiO_2 relative to the other elements will contain quartz, or, if the rock had been rapidly cooled, the high temperature polymorphs tridymite or cristobalite. Generally, glassy volcanic rocks containing over ~65% SiO_2 will contain quartz or one of its high temperature polymorphs (Fig. 1).[22][23]

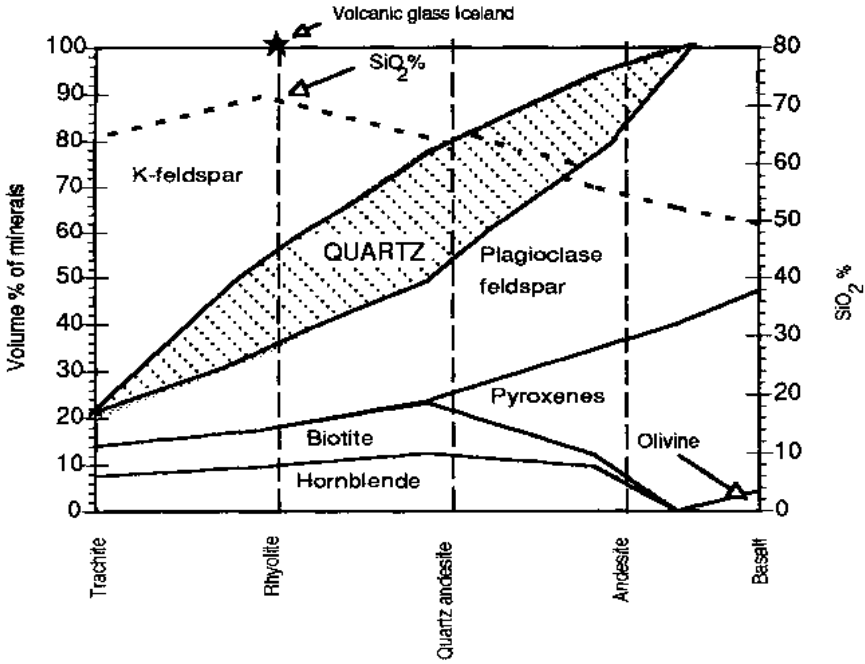


Figure 1. Diagram of SiO_2 content of volcanic rocks superimposed on their mineralogical composition. The (★) on the line representing rhyolite is the plot of the SiO_2 content of volcanic glass from Iceland.[23] *(Diagram modified from Klein & Hurlbut.[11])*

@Seismicisolation

In glassy volcanic rocks containing excess silica, x-ray diffraction analysis (XRD) may be used to confirm if potentially reactive silica minerals are present. However, if the reactive silica is present in very small quantities, special techniques such as phosphoric acid extraction may be necessary to concentrate the silica minerals so that they can be detected by XRD.[24]

Phosphoric Acid Extraction Technique. The phosphoric acid extraction technique is used to preferentially dissolve silicate minerals in rocks leaving the silica minerals, e.g., quartz, tridymite, or cristobalite, behind. The phase or phases of silica, in the rock can then be determined by x-ray diffraction of the residue.[22] This method may be used to determine the amount of silica minerals in fine grained rocks, such as diabase, graywackes, shales and tuffs. The principle of this method is that silicate minerals or metal oxides dissolve when heated in phosphoric acid, while quartz and other silica minerals are largely unaffected. The phosphoric acid method has, so far, only been published in Japanese,[24] however, a translation was made by Sumitomo Cement Company.[25] Due to the lack of an assessable English translation, an outline of the method is given here.

The entire sample is ground to pass a 74 μm sieve in such a way as to minimize the amount of dust fraction produced. The dissolution in phosphoric acid is carried out in a 300 ml conical flask with a flat bottom. A condenser, for the flask, is made by taking a filter funnel having an inside diameter of 60 mm at the top and bending the glass stem at the bottom of the funnel so, that when placed on top of the conical flask, it is in contact with the side. The heater for the flask consists of a 200 watt electric hot plate connected to a voltmeter and a variable transformer. An asbestos plate, with a hole just large enough to accommodate the bottom of the conical flask, is placed on top of the hot plate. The bottom of the flask must be in contact with the surface of the hot plate.

Procedure. Place 0.3 g of the ground rock in the bottom of the dry conical flask with care, to prevent any adhering to the wall of the flask. Add 25 ml of phosphoric acid and vibrate the flask to disperse the rock in the acid without getting it on the wall. Preheat the hot plate by setting the transformer to 80 volts until the temperature has stabilized. When the flask with the sample is placed on the heater, start a stop watch. When the heater is set correctly, the phosphoric acid should boil in one minute and thirty seconds. Continue boiling, but after three minutes shake flask lightly for three seconds to avoid local overheating. Repeat the shaking at intervals of one minute. After twelve minutes remove the flask and shake well for one minute to dissolve the gelatinous silicic acid on the wall of the flask.

@Seismicisolation

Remove the condenser so that the liquid in it runs down the wall of the flask. Allow the beaker to stand until it reaches room temperature. Pour 125 ml of hot water (60–70°C) into the flask so as to wash the inside wall. Shake the flask vigorously to dissolve the viscous phosphoric acid completely. Add 10 ml of fluoboric acid and shake. Add 10 ml of the filter paper slurry (Table 1) to the solution in the flask and wash the walls with 25 ml of water and allow to stand for one hour. Filter the solution from the flask through a funnel lined with filter paper to which a small amount of filter paper slurry was first added. Wash the wall of the flask, using a glass rod with a rubber end to remove any precipitate. Wash the filter paper several times with warm (1 + 9) hydrochloric acid, followed by eight to ten washings with hot water. Dry the filter paper containing the precipitate in a platinum crucible. Reduce the filter paper by low temperature ashing (without flame). Ignite the resulting ash in an electric furnace at 1000 ± 50°C for thirty minutes. Cool and weigh ash. Add 1–2 drops of sulfuric acid and 5–10 ml of hydrofluoric acid to the precipitate in the crucible. Heat to volatilize silicon and evaporate to dryness. Ignite in an electric furnace at 1000 ± 50°C for twenty minutes, cool and weigh.

Table 1. Reagents Used in the Phosphoric Acid Extraction Technique

Hydrochloric acid	Hydrofluoric acid
Sulfuric acid	Phosphoric acid
Fluoboric acid	Suspension of filter paper slurry*

*A slurry of filter paper is made by taking 1 g of finely chopped filter paper and shaking it with 100 ml water.

The amount of quartz remaining after heating the rock in phosphoric acid for twelve minutes is calculated from Eq. 1.

$$\text{Eq. (1)} \qquad Q_{12} = \frac{W_1 - W_2}{S} \times 100$$

Q_{12} - amount of insoluble quartz after twelve minutes

S - weight of sample

W_1 - weight of precipitate remaining after treatment in phosphoric acid.

W_2 - weight of precipitate remaining after treatment with hydrofluoric acid.

@Seismicisolation

If the residue W_2 is > ~5% of S, a considerable amount of silicate remains undissolved. In this case, repeat the dissolution with a new 0.3 g sample, but maintain the heating of the flask for fourteen minutes instead of the original twelve.

The amount of quartz in the rock is calculated from Eq. 2.

Eq. (2) $$Q = Q_{14} + k(Q_{12} - Q_{14})$$

Q_{14} - amount of insoluble quartz after fourteen minutes

k - compensation coefficient (normally 2)

A minimum of two analyses should be conducted and the results averaged.

2.3 Test Method ASTM C 289

Briefly, the chemical test ASTM C 289[17] consists of crushing a sample of aggregate to between 150 and 300 µm. A representative 25 g of the sized aggregate is sealed in a container with 25 ml 1 N NaOH and maintained at 80°C for 24 hours. After cooling, the solution is filtered, the amount of silica dissolved is determined, and the reduction in the normality of the sodium hydroxide is measured by titration with HCl using phenolphthalein as an indicator. Although this test method has been widely used over the years in many countries, the results obtained are not always satisfactory. The amount of dissolved silica (*Sc*) and the reduction in alkalinity (*Rc*) are affected by a number of mineralogical factors. The solubility of quartz increases with decreasing grain size, hence, inadequate screening out of material finer than 300 µm can increase the measured amount of dissolved silica. The measured *Sc* may be reduced by precipitation of silica in the presence of calcium as C-S-H which consumes OH^- ions and decreases the pH of the solution. Gypsum, zeolites, clay minerals, hydrated magnesium silicates, and iron oxides, or organic matter, all effect the results of the chemical test. The end point in titrating, using phenolphthalein as an indicator, is affected by the presence of carbonate ions and also by the amount of silica in solution, Dent Glasser and Kataoka.[26] The reduction in alkalinity can also be underestimated due to reactions involving sodium and potassium ions and some of the above minerals.[27]–[29]

Modified Chemical Methods for Potential Reactivity of Aggregates. A number of modifications to the Chemical Method ASTM C 289 have been proposed in an attempt to address some of the problems and make the test better suited to certain aggregates.[27]–[31] These include a modified chemical method for evaluating the potential reactivity of siliceous carbonate aggregates, and a kinetic version of the chemical test.

@Seismicisolation

The kinetic test, in addition to differentiating between reactive and non-reactive aggregates, also purports to permit identification of siliceous aggregates exhibiting the pessimum effect.

Proposed Chemical Method for Siliceous Carbonate Rocks. A modified chemical method has been proposed to determine the potential alkali-reactivity of siliceous carbonate aggregates.[27] In the proposed test for carbonate aggregates, the aggregate is crushed to yield 2 kg sized to between 150 and 300 μm. The sized aggregate is immersed in 12 N HCl to dissolve the carbonate phases, leaving the insoluble silica/silicate residue which is then filtered off and washed with distilled water. The percentage insoluble residue in the aggregate is determined and this value is used to correct the amount of silica dissolved, *Sc*, to allow for the very small proportion of the total aggregate used in the determination. The standard chemical test is then run on 12.5 g samples of the acid insoluble residue instead of the 25 g specified in ASTM C 289. When compared to the results obtained by running this test on the whole rock, the removal of the carbonate phases usually results in moving the points to the right of the diagram suggested in ASTM C289 for evaluating the results of the test, i.e., towards the deleterious or potentially deleterious area, Fig. 2.

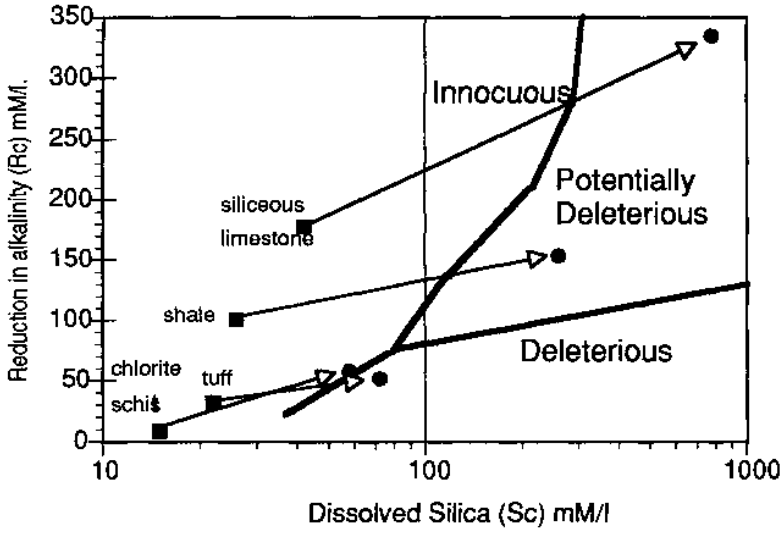


Figure 2. Plot of *Sc* versus *Rc* showing the increase in *Sc* values obtained using the modified chemical test, comparing the results obtained using ASTM C 289. The arrows show the increase in *Sc* obtained with the modified test procedure. *(Graph plotted with data from Bérubé & Fournier.)*[27]

@Seismicisolation

There is only moderate correlation between the results of the modified chemical test and the expansion of concrete prisms made with the aggregates and containing 350 kg cement with the alkali content adjusted to 1.25%, Fig. 3.

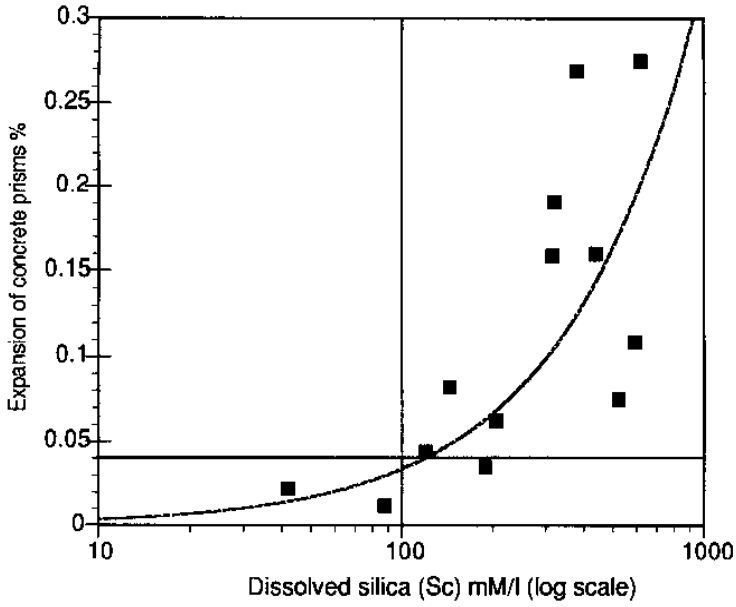


Figure 3. Expansion of aggregates in the concrete prism test plotted against the dissolved silica, *Sc*, determined in the modified chemical test. *(Graph plotted with data from Bérubé & Fournier.)*[7]

The lack of correlation may in part be due to the use of only 350 kg cement in the concrete prism test rather than the 420 kg specified in the Canadian Standard, CSA A23.2-14A,[8] which would probably result in the expansions being somewhat lower than they should be. However, other factors, such as those discussed above for the ASTM test C 289, undoubtedly also affect the results. Taking expansions greater than the CSA 0.04% expansion limit as the criterion for potential reactivity, it would appear that *Sc* values for carbonate rocks, in the modified chemical test, greater than about 100 mm/l are indicative of potentially deleteriously expansive aggregates. This is about the same limit of dissolved silica that is usually considered indicative of potentially reactive aggregates in ASTM C 289.

@Seismicisolation

Kinetic Test—Chemical Method. A modified version of the chemical test called the *Kinetic Test* was developed by Sorrentino, 1992.[31] This test was subsequently proposed as a French Standard, P18-589, in 1992. The test procedure is, in general, similar to that of ASTM C289 except that the sample is crushed and sieved to yield a sample with a grading between 40 and 315 µm. Twenty-five gram aliquots of the sized material are sealed, with 25 ml of 1 N NaOH in a number of containers. The subsequent heat treatment follows the procedure specified in C289. Containers with the samples are removed from the 80°C storage after 24, 48, and 72 hours, cooled and filtered. The SiO_2 and Na_2O contents of the filtrates are determined, the results are plotted on a diagram of storage time, in days, against (SiO_2 /Na_2O), Fig. 4.

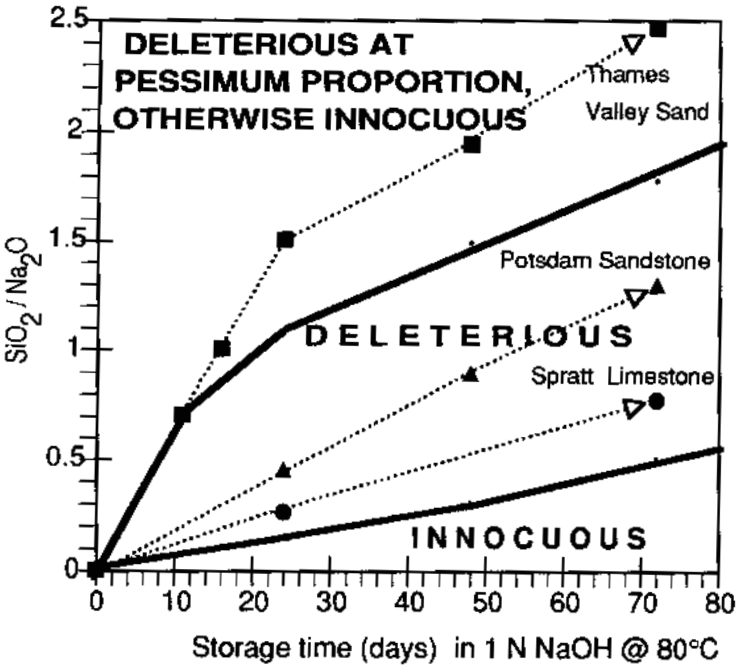


Figure 4. Graph showing change in SiO_2/Na_2O ratio with storage time in 1 N NaOH @ 80°C in the kinetic chemical test, for three aggregates, Spratt siliceous limestone (reactive), Potsdam sandstone (reactive), and Thames Valley flint (reactive, but showing pessimum). *(Graph redrawn after Sorrentino, et al.)*[31]

@Seismicisolation

The results of this test are interesting, as it would appear that it enables the investigator to determine which aggregates exhibit the pessimum effect. However, the results reported by Sorrentino, et al.,[31] were not reproduced by another researcher,[32] therefore, more investigation of this potential test method is required. Part of the difficulty with this test may be due to the various factors which affect ASTM C 289, which were discussed previously, and which would also effect the results of this test.

3.0 AGGREGATES THAT RELEASE ALKALIS INTO THE PORE SOLUTION IN CONCRETE

It has been observed that certain glassy volcanic rocks which are alkali-silica reactive, caused expansion in mortar bars even when a low alkali cement was used.[33] It is assumed that the unexpectedly high expansion was caused by alkalis leaching from the glassy volcanic rocks into the concrete pore solution. A similar effect was noted when phlogopite mica was added to concrete.[34] The authors showed that potassium in the phlogopite could exchange for calcium or sodium in a solution of calcium hydroxide containing NaOH. Clay minerals in siliceous limestone have also been shown to contribute alkalis to the pore solution in concrete made with a potentially reactive aggregate.[35]

Enhancement of the alkalis in the pore solution of concrete, over time, is particularly important in large hydraulic structures which typically have very long life expectancies.[36] The added alkalis from the aggregates can result in a marginally reactive aggregate, causing expansion and cracking of the concrete.[35]

A number of methods may be used to estimate the alkali contribution from aggregates to concrete. If the alkali content of the cement, and the cement content of old concrete are known, it is possible to calculate the alkali contribution to the pore solution by measuring the current alkali content and subtracting the original alkali content from it. A number of methods have been used to determine the alkali content of concrete. The most direct is to squeeze out the pore solution using a high pressure cell,[37] and analyzing it. An alternative is the hot water extraction method,[35] In this method, the concrete is ground to pass a 75 µm sieve. A representative 10 g of the <75 µm concrete is boiled in deionized water for five minutes and left to soak overnight. The sample is then filtered and the solution is

@Seismicisolation

made up to 1 liter. The sodium and potassium content are determined by atomic absorption spectroscopy. The results obtained should be corrected for the amount of alkalis which would be leached from the aggregates during the extraction process.[36] Alkali release from aggregates to the cement paste in old concrete can also be determined by selective leaching techniques using alkaline EDTA-TEA solutions that dissolve the paste while leaving the aggregates largely unaffected (see Goguel, Ref. 38). This method can also be used to estimate the alkali contribution of new concrete to the pore solution by making up mortar bars and testing them after six and twelve months moist storage.

Outline of EDTA-TEA dissolution method according to Goguel:[38]

Two dissolution solutions may be used:

1. A "MET" (mixed cation EDTA-TEA) solution.
2. A "TET" (TMA-EDTA-TEA) solution.

EDTA - ethylene-diamine-tetra-acetic acid
TEA - triethanolamine
TMA - trimethylamine

The amount of aggregate dissolved depends on the size fractions used:

1. Size range 500–1000 µm, 160 g.
2. Size range 63–125 µm, 160 g.

The MET and TET solutions are prepared at 40°C. Twenty-five milliliters of either solution are added to the sized aggregate. The solutions are shaken at 40°C for 2 hours for the 500–1000 µm size fraction, and for 1 hour for the 63–125 µm size fraction. At the end of the shaking period, the solids are separated by centrifugation and the solution analyzed for Ca, Sr, Si, Al, Fe, Mg, K, and Na. All samples are doped with Cs at a level of 1 ppm as a check on the recovery rate of the analysis. The results reported by Goguel are rather surprising in that, contrary to the results obtained in leaching experiments in calcium hydroxide and alkali hydroxide solutions[39] which indicated that most silicates, e.g., feldspars, were readily dissolved and would thus release alkalies to the pore solution, significant alkali release from feldspars only occurred with one albite feldspar that was poorly crystalline with a strained crystal lattice. Basalts containing nepheline and zeolites also released significant amounts of alkali into the TET or MET solutions. Results of extractions on the aggregates alone were

@Seismicisolation

used to compensate the amounts obtained from the mortar samples for alkalis dissolved directly from the aggregates.

Estimates of the potential of leaching of alkalis from aggregates to the pore solution in concrete have also been made by mixing the finely pulverized aggregate in a paste of calcium hydroxide and sealing the containers. Ten g of <75 μm aggregate is mixed with 3 g calcium hydroxide and 8 ml of water. After 1, 7, 28, and 90 days, the pastes were analyzed for sodium and potassium by the hot water extraction technique and atomic absorption spectroscopy. About 66 % of the alkalis extracted after ninety days were extracted after three days. This suggests that a three day test might be adequate. This would be more practical than some of the alternatives which have been suggested by Bérubé, et al.[36] However, the results reported by Goguel[38] cast some doubt on the validity of this method and that used by Bérubé, et al.[36] Further investigation is required.

4.0 DETERMINATION OF POROSITY AND WATER ABSORPTION OF AGGREGATES

Determination of the porosity of aggregates is more of a technological rather than a petrographic test, however, the porosity of rocks is related to their composition and should be considered along with other petrographic features. The properties of concrete are dependent on, among other parameters, the water to cement ratio (w/c). The porosity of an aggregate determines its water absorption capacity which in turn affects the w/c of the concrete. Porosity is also related to drying shrinkage of aggregates, which can lead to excessive shrinkage and damage to concrete.[40][41] The porosity of an aggregate, as it relates to surface roughness, may also effect the performance of the aggregate in a high strength concrete.

Water absorption of aggregate is particularly important in high performance concrete which is formed at a low w/c. The porosity of an aggregate can be measured indirectly by measuring its water absorption, ASTM C 127-88,[42] however, measurement of water absorption does not provide any information on the size distribution of the pores. In the past, mercury porosimetry was used to measure the pore size distribution; however, Diamond[43] showed that the mercury porosimeter does not in fact measure the pore size distribution. The reason for this is that, although the pore entry diameter is proportional to the pressure necessary to get the mercury to enter that pore, if the small diameter pore is connected to a

@Seismicisolation

larger diameter pore the mercury will continue to flow through the small pore until the large pore is also filled, giving the impression that the volume of the small diameter pore is much larger than it is.

Diamond[43] used backscattered imaging in a scanning electron microscope (SEM) to determine the porosity of the aggregate. Recently, Martinez and Rubiera[44] reported a method to measure the porosity of granitic aggregates using optical microscopy of thin sections combined with image analysis. In this procedure, a number of images are captured with the polarizers set to varying angles from parallel to fully crossed. The images are combined and analyzed. A new algorithm was developed to detect the small pores in the middle of the minerals in the aggregate particle. This yielded a histogram of the pore size distribution.

Polivka and Mehta[45] showed that water absorption by some aggregates is related to drying shrinkage in concrete made with these aggregates. A graph of shrinkage of concretes against water absorption of the aggregates is shown in Fig. 5.

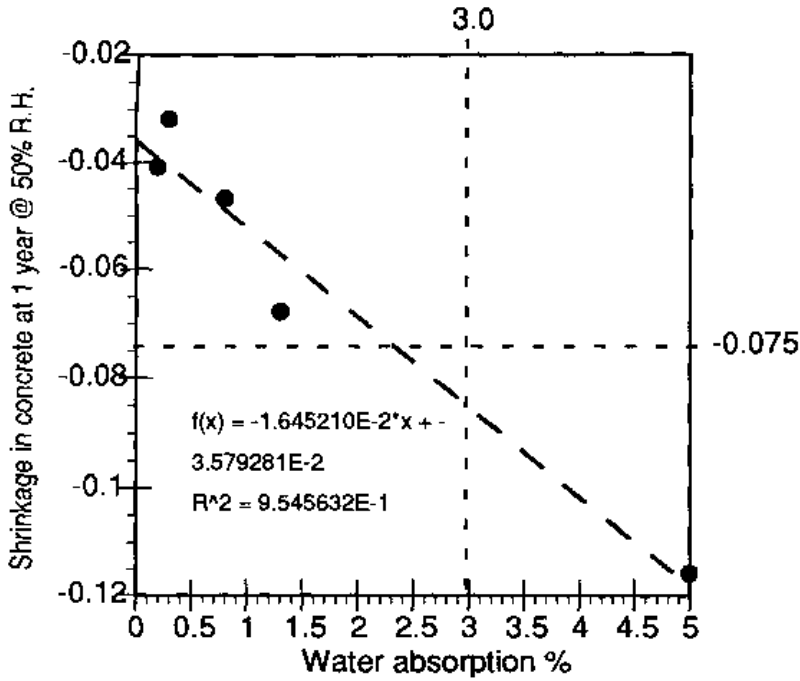


Figure 5. Shrinkage of concrete versus water adsorption of aggregates used in the concrete. The proposed U.K. shrinkage limit of -0.075% and the suggested 3% absorption limit for sandstones are shown superimposed on the diagram. *(Graph plotted with data from Polivka and Mehta.)*[45]

@Seismicisolation

Superimposed on the graph is the shrinkage limit (-0.075%) proposed by the Building Research Establishment (BRE)[41] to separate concretes suitable for all applications from those for which there are service limitations and the 3% absorption limit proposed by Collins[46] as the upper absorption limit for sandstone aggregates for use in high strength concrete. It is concluded from these results that aggregates with water absorptions of greater than 2.5 to 3% have a potential for causing excessive drying shrinkage in concrete.

The weathering of rocks also effects their water absorption. Weathering of granitic rocks is particularly significant in tropical climates where the humidity is high and where weathering extends to considerable depths. The effect of weathering on rock can be observed in thin sections in a petrographic microscope, but generally, x-ray diffraction is required to identify the weathering products, e.g., kaolin or illite. Water absorption usually increases with weathering because the weathering products are usually more porous. Moore and Gribble[47] investigated the effect of weathering on the water absorption of granites. They showed that as the feldspars altered to kaolinite, absorption increased and compressive strength of concrete containing the weathered aggregate decreased, Fig. 6.

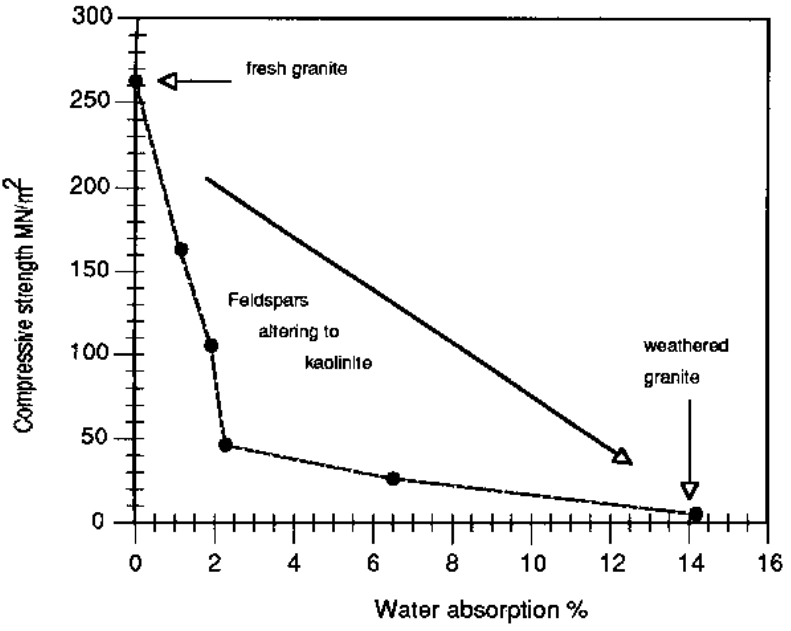


Figure 6. Plot of compressive strength of concrete versus water absorption of granite aggregates with varying degrees of weathering. *(Plotted with data from Moore and Gribble.)*[47]

@Seismicisolation

5.0 INSTRUMENTAL TECHNIQUES FOR DETERMINING THE POTENTIAL REACTIVITY OF SILICEOUS AGGREGATES

A number of methods have been suggested for evaluating the potential reactivity of siliceous aggregates by measuring the degree of crystallinity or the number of defects in the quartz lattice. These methods are all based on the concept that the free energy of quartz, which determines its solubility and hence potential alkali-reactivity, is related to the amount of defects in the lattice and/or its degree of crystallinity. It has been demonstrated that the proposed methods work in principle, however, due to a number of problems these methods, although useful for research, are not satisfactory techniques for determining the potential expansiveness of siliceous aggregates in concrete. Furthermore, the equipment for some of these methods, e.g., positron annihilation, would not be readily available to those investigating the potential reactivity of aggregates.

5.1 X-RAY DIFFRACTION ANALYSIS IN THE EVALUATION OF AGGREGATES

X-ray diffraction can be used in the normal way to identify potentially alkali-silica reactive minerals that may not readily be identifiable in thin sections viewed under a petrographic microscope, either because the particles are too fine (Schrimer),[48] or because they are present in too small a quantity, or a combination of the two. An example of a rock for which examination of thin sections proved inadequate is an altered diabase. Chemical analyses of diabase usually show about 50% SiO_2, enough to combine with the other elements to make the feldspars and mafic minerals which comprise the rock, but leaving no extra amount to form quartz,[10] hence, diabase should not contain any microcrystalline reactive quartz. No quartz was observed in the thin section, but the results of an ultra-accelerated mortar bar test for alkali-silica reactivity, ASTM C 1260-94,[18] showed the rock to be reactive.[48] Subsequently, an x-ray diffractogram showed that the rock contained very fine grained quartz, a secondary mineral formed after the rock had hardened. The quartz was too fine to be observed under a petrographic microscope. Another example of this is an obsidian containing finely divided cristobalite, the reactive high temperature polymorph of quartz, which could not be identified positively

@Seismicisolation

in a petrographic microscope. An x-ray diffractogram taking using copper radiation of the thin section of obsidian is shown in Fig. 7. Small peaks for cristobalite at ~21.9°2θ and for a feldspar at ~27.7°θ are seen superimposed on a broad maximum, centered at ~22.5°θ due to the silicate glass phase.

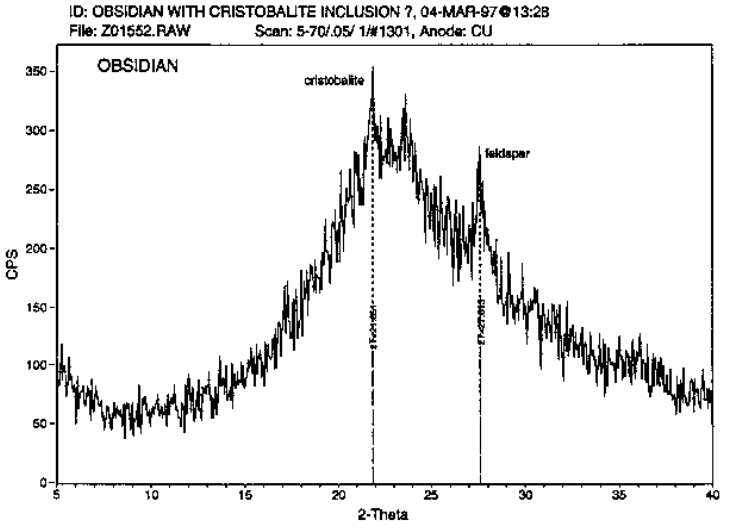


Figure 7. X-ray diffractogram taken of obsidian using CuKα radiation, showing sharp peaks due to cristobalite and feldspar superimposed on a broad maximum due to the glass phase.

Measurement of Crystallinity of Quartz. X-ray diffraction has also been used to measure the degree of crystallinity of quartz (QCI) which gives a measure of its crystallite size and, hence, potential alkali-silica reactivity.[49]–[51] The index of crystallinity, QCI, of quartz is determined by measuring the intensities of the quintuplet peak of quartz which occurs between 67° and 69°2θ with CuKα radiation. The procedure for determining the QCI is shown in Fig. 8. The QCI is determined by measuring the height from the top of the $21\bar{3}2$ peak at ~67.74°2θ(CuKα) to the base of the adjacent peak on the high angle side which is designated *(a)* in Fig. 8.

@Seismicisolation

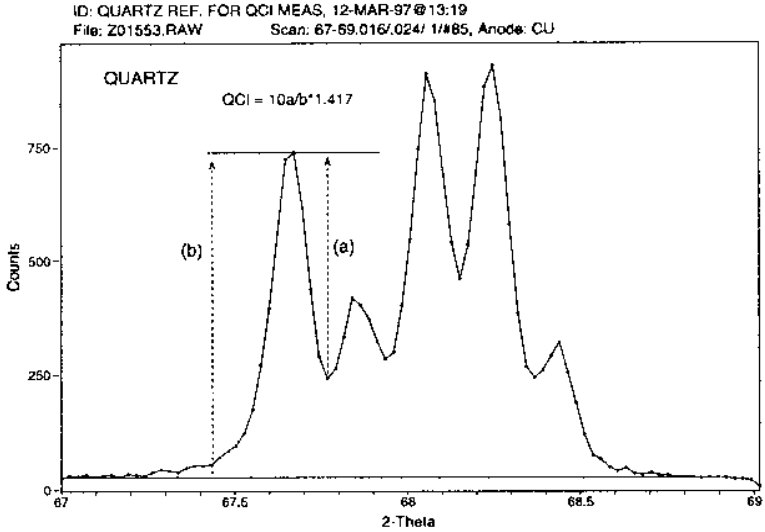


Figure 8. X-ray diffractogram (67 to 69°2θ) of crystal quartz taken using CuKα radiation, used in calculating the degree of crystallinity, QCI, of the quartz. The relative peak heights *(a)* and *(b)* are used in calculating QCI in Eq. 3.

The height of the $21\bar{3}2$ peak above the base line on the low angle side is designated *(b)*. The QCI is calculated from Eq. 3.

Eq. (3) $\quad QCI = 10\ a/b*F$

The factor F is determined for each diffractometer so that QCI for highly crystalline quartz = 10. (Using a Regaku Wide Angle Goniometer, F was found to be 1.417.)

The QCI values run from 10 for well crystalline quartz, to 1 for poorly crystalline material.

The shapes of the quintuplet peaks for crystal quartz, novaculite, and chert, are shown in Fig. 9.

The relatively high QCI of 8.6 for novaculite highlights a problem with this method. The novaculite is highly reactive and causes large expansions in mortar bars, but appears to be reasonably well crystalline. This may be due to the presence of a percentage of larger, well crystalline quartz in the dominantly finer micro crystalline novaculite. The high intensity of the diffraction pattern of the well crystalline material swamps

@Seismicisolation

the diffraction pattern of the poorly crystalline material. This problem can be overcome by careful selection of microcrystalline quartz grains containing no macrocrystalline quartz under a stereobinocular microscope. The diffraction pattern can also be obtained from a single chip, using a micro-diffractometer or a Gandolfi film camera.

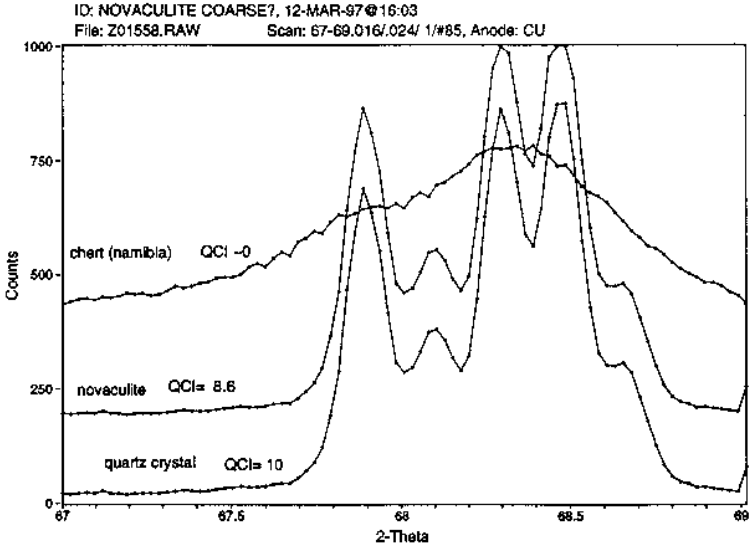


Figure 9. X-ray diffractogram (67 to 69°2θ) for quartz crystal, novaculite, and chert, showing varying degrees of crystallinity, QCI, from 10 for quartz crystal, to zero for chert.

Recently, Liang et al.,[52] used a different method for determining the degree of crystallinity of quartz, by curve fitting of the five peaks in the quintuplet occurring between 67° and 69°2θ. They used a profile fitting technique to deconvolute the five peaks and then measured the *full width at half maximum* (FWHM) which is related to the crystallinity of quartz. They obtained excellent correlation between the FWHM values for quartz in a series of cherts and the expansion of mortar bars made with these cherts, in the Chinese miniature autoclave test. However, the authors caution that aggregates with the same FWHM may give different expansions due to other factors, such as porosity, the size of the aggregates, and the distribution of reactive components in them.

@Seismicisolation

XRD Techniques for Identification of Swelling Clay Minerals. Clay minerals are undesirable in concrete aggregates and most standards have limits on the amount of clay in sands and provide test methods, e.g., CSA A23.1-94.[7] However, coatings of clay on the surfaces of other fine aggregates may also be detrimental to the properties of concrete and may not be detected by normal technological tests. Some sands derived from weathered volcanic rocks, common in many parts of the world, may contain montmorillonite [$(AlMg)_8(Si_4O_{10})(OH)_8 \cdot 12H_2O$)], a swelling clay mineral.[53] The structure of montmorillonite consists of an octahedral layer sandwiched between two tetrahedral layers. The layers are only held together by ionic bonds and, hence, water molecules can be readily adsorbed between the sheets, causing the structure to swell in the direction of the c-axis. There are a number of minerals in the smectite group, such as dioctahedral smectites, montmorillonite, beidellite, nontrolite, and trioctahedral smectites, saponite, and hectorite.

It is not the swelling of the clay that causes problems in concrete, rather, it is the absorption of water that occurs when the clay expands and water goes between the layers, which uses up part of the mixing water in concrete and, hence, increases its water demand.

It is not possible to differentiate between swelling and non swelling clays by simple x-ray diffraction of the material. However, the swelling clays can be identified by making successive diffractograms before and after treatment of the clay.[54]

Clay Sample Preparation. The procedure for the preparation of clay minerals for x-ray diffraction investigation consists of separation of the clay minerals from other silicates and carbonates by dispersing the clay in water and allowing the particles to settle out. The coarse particles settle first and are removed by centrifuging. The process is repeated until the <1 μm particles containing dominantly clay minerals are recovered.[55] Next, the clays must be cleaned by removal of iron oxides and organic matter. The iron oxides are removed by a solution of sodium dithionite buffered to a pH of 7 by sodium bicarbonate, $NaHCO_2$. The iron may be complexed to keep it in solution by the addition of sodium citrate. Organic material is removed by heating the clay in hydrogen peroxide, H_2O_2.

Because of the variable basal spacings found in the smectites, it is desirable to saturate the interlayer cation positions with a selected cation, e.g., Na^+, so that reproducible basal spacings are obtained. This is achieved by soaking the clay in a chloride solution of the selected cation. Finally, the clay is washed with de-ionized water to remove excess chloride.

@Seismicisolation

Optimum results from x-ray diffraction analyses are obtained from clay specimens with strong orientation of the (001) basal reflections parallel to the surface of the sample holder of the diffractometer. Such a specimen will show little or no (hkl) reflections in the diffractogram. This preferred orientation may be achieved either by sedimenting the clay on to a flat plate of suitable size to fit into the sample holder of the x-ray diffractometer or by sucking the water containing the clay through a porous plate which acts as the support for the sample.[56]

XRD Investigation of Clay. Clay samples are usually scanned in the diffractometer from 2° to about 70°2θ. However, the important range for differentiating the clay minerals is from 2° to ~30°2θ. After recording the initial diffractogram, the basal spacing of the clays is expanded to a constant value, near 17 Å, by glycolation. This is achieved by spraying the surface of the clay on the sample holder with ethylene glycol, using an atomizer. A second diffractogram is then run of the glycolated clay. Finally the oriented clay specimen is heated in an electric oven to a temperature in the range of 250° to 600°C. The selection of the heating temperature depends on the mineralogy of the clay.[54] Using a 12 Å montmorillonite as an example, the basal reflections occur at d-spacings 12 Å, 5 Å, and 3.3 Å, which occur with CuKα radiation at 7.36°2θ, 17.74°2θ, and 27°2θ, respectively. The shifts in the peaks after glycolation and heat treatment are shown in Table 2.

Table 2. Shifts in the d-Spacings of the Basal Planes After Treatment of the Clay With Glycol and Heat Treatment. *(After Thorez)*[54]

Untreated clay		Glycolated		Heated to 490°C
12 Å (S[1])	→	18 Å (S) 8.6Å (M[2])	→ →	9.6 Å (S)
5 Å (M)	→	5.6 Å (W[3])	→	5 Å (W)
3.3 Å (MS[4])	→	3.4 Å (W)	→	3.3 Å (S)

1. S = a strong peak
2. M = a medium strength peak
3. W = a weak peak
4. MS = a moderately strong peak.

@Seismicisolation

5.2 Infrared Spectroscopy

Infrared (IR) spectroscopy may be used as an analytical tool to identify the minerals in an aggregate; however, in general, it does not yield results as definitive as can be obtained by x-ray diffraction. An IR method was proposed to measure the degree of disorder (*Cd*) of the quartz crystal (see Baronio, et al.[57]).

The determination of *Cd* is made by recording the IR spectrum from about 2,000 cms^{-1} to 600 cms^{-1} (Fig. 10a). The heights of the ν_3 and ν_1 SiO_4 bands at about 1,100 and 800 cm^{-1}, respectively, are measured along with the width of the ν_1 peak at $^1/_3$ of its height. These measurements are put into Eqs. (4) and (5).

Eq. (4) $$A_b = I_g \frac{P+Z}{Z}$$

Eq. (5) $$Cd = \frac{\Delta\nu}{A_b}$$

The *Cd* is the ratio of the relative optical density (A_b) to the broadening at $^1/_3$ the height of the ν_1 band at about 780 cm^{-1}. The procedure for calculating *Cd* is illustrated in Fig. 10a.

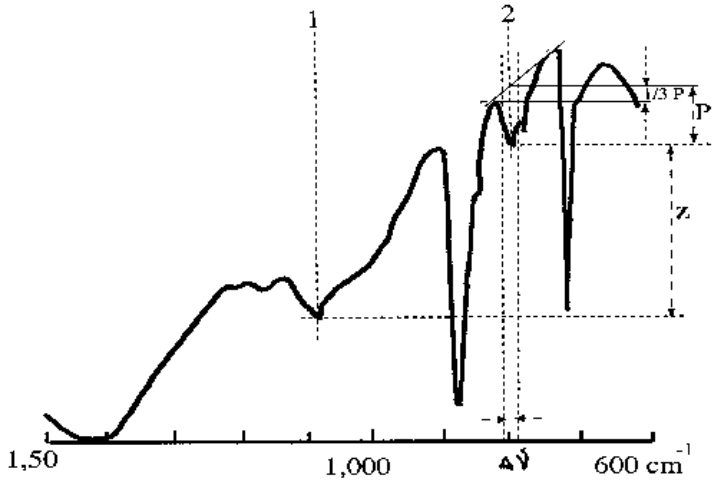
There are a number of problems with this method. The measurements can only be made on pure quartz as other silicate minerals have peaks which may interfere with the two peaks being measured.

In the procedure used by Baronio, et al.,[57] the sample is prepared by intergrinding quartz with potassium bromide which is then pressed into a pellet. The quartz is ground to <45 μm size. The solubility and, hence, alkali-reactivity of quartz increases asymptotically with decreasing grain size below 100 μm and, hence, there is a danger that in the sample preparation the disorder of the crystal lattice that is being evaluated is being created.[58] This author has observed that the shape of the peaks in the IR spectrum changed as the quartz was ground to successively finer size ranges. It is therefore highly unlikely that a reproducible spectrum could be obtained in different laboratories.

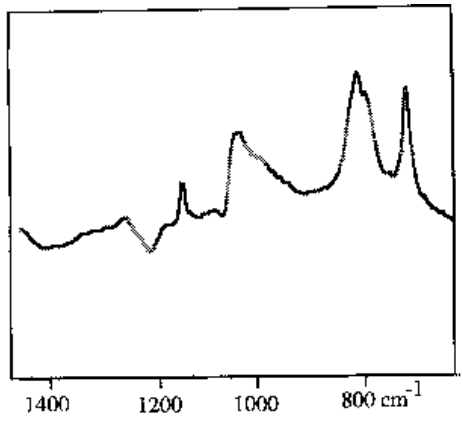
Furthermore, the shape of the spectrum varies considerably depending on the spectrometer used. The author tried a number of sample preparation techniques using two spectrometers, but was unable to reproduce the spectrum shown in Fig. 10a. A spectrum obtained using an 800

@Seismicisolation

Nicolet infrared spectrometer equipped with a MTRC photo acoustic cell for the analysis is shown in Fig. 10b.



(a)



(b)

Figure 10. *(a)* IR spectrum from well crystalline quartz, illustrating the measurements taken for use in calculating the degree of crystallinity *Cd*, from Eqs. 4 and 5. *(Modified after Baronio, et al.)*[57] Symbols: 1 = υ_3; 2 = υ_1. *(b)* IR spectrum of crystal quartz obtained with an 800 Nicolet spectrometer equipped with a photo acoustic cell. Note the different appearance of this spectrum compared to that in figure *(a)*.

@Seismicisolation

To minimize the creation of defects caused by grinding, the quartz was pulverized only to pass an 0.5 mm screen. It was then lightly interground with 39% KBr. The sample was scanned in a photo acoustic cell and the spectrum was ratioed against a background produced by pure KBr.

Although it may be possible, using one infrared spectrometer, to distinguish pure quartz samples of varying crystallinity, it seems very unlikely that this method could be used to compare results obtained with different spectrometers in different laboratories. For this reason the infrared method of measuring the degree of crystallinity of quartz *(Cd)* does not appear to be practical.

Positron Annihilation. Tang Mingshu, et al.,[59] proposed the measurement of positron annihilation as another method of evaluating the alkali reactivity of silica minerals. This method gives a measure of the defects in the crystal lattice. It is these defects which contribute to the increased solubility of silica in alkaline medium and, hence, reactivity in concrete. The correlation between expansion and the intensity of capture I_2 is relatively poor, Fig. 11. This is most likely due to several factors.

Firstly, the expansion of concretes containing chert, flint, chalcedony, and opal, depends on the proportion of the mineral in the aggregate (pessimum effect). This makes it difficult to obtain an absolute maximum expansion.

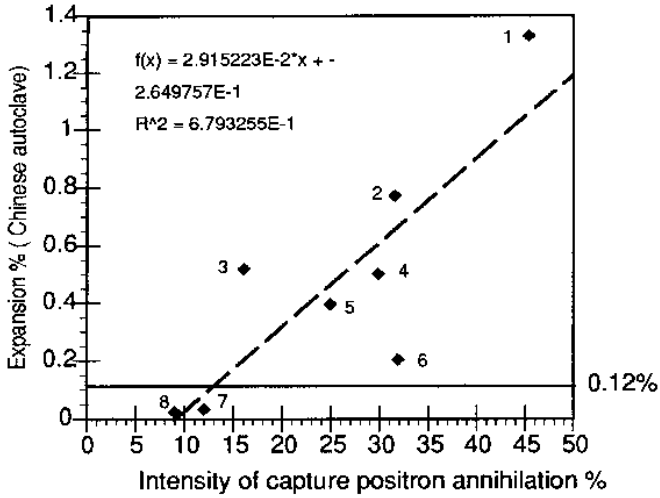


Figure 11. Intensity of capture of positron annihilation I_2 versus expansion in the Chinese autoclave test for a number of reactive and non reactive aggregates. *(1)* opal; *(2)* fused silica; *(3)* silica brick; *(4)* chalcedony; *(5)* perlite (with chalcedony); *(6)* chert; *(7)* chert; and *(8)* quartz sand. A line at an expansion of 0.12% indicates the proposed expansion limit corresponding to an I_2 value of ~13. *(Plotted from data from Mingshu, et al.)*[5]

@SeismicIsolation

Secondly, in these minerals it is rare that all the quartz is in the same size range. A few larger grains of well crystalline quartz can reduce the average number of defects in the material under evaluation resulting in a lower I_2 than would be measured if the microcrystalline quartz alone was measured. For these reasons, this method, although giving some indication of the potential reactivity of siliceous aggregates, can probably not accurately predict their potential expansiveness in concrete.

5.3 Differential Scanning Calorimetry (DSC)

The temperature of the high-low inversion point in quartz, which occurs at 573°C in well crystalline material, may be expected to change if the free energy of the quartz changes due to an increased number of lattice defects and/or a lower degree of crystallinity. This would result in a lowering of the inversion point if the free energy is higher. This is what was observed by Tang, et al.[59] If the silica is poorly crystalline, e.g., as in chert, and if, as is common, it contains a range of crystallite sizes, the high/low inversion would be expected to be smeared out, rather than occurring at a particular temperature, exactly what is observed, Fig. 12.

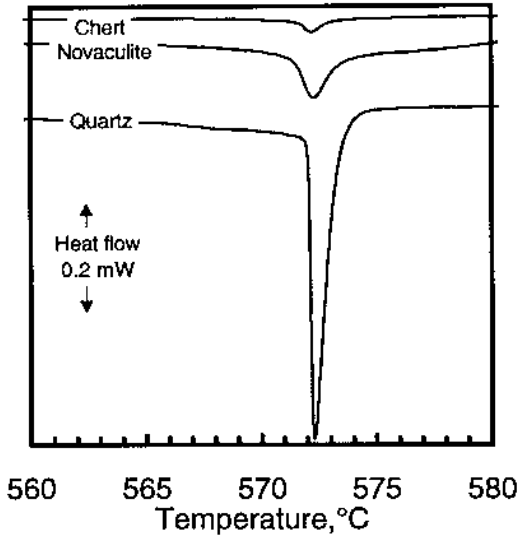


Figure 12. DSC trace for quartz crystal, novaculite, and chert between 560° and 580°C. The traces show that the free energy of the defective microcrystalline quartz in novaculite and chert reduces the high/low quartz transition temperature and also the amount of energy in the transition.

@Seismicisolation

It is interesting to note that in contrast to the x-ray diffractogram for novaculite, which yielded a *Cd* of 8.2, indicative of a relatively well crystalline quartz, the weak, broad peak in the DSC spectrum in Fig. 12 is indicative of highly disordered quartz. The high reactivity of novaculite was confirmed by an autoclave expansion test. This result would appear to indicate that the DSC method is a better indicator of potential reactivity of siliceous aggregates than the XRD method. However, Tang, et al., ibid., found poor correlation between DSC results and expansion in the autoclave test. The reasons for this are likely similar to those described for Positron Annihilation and IR analyses. It is concluded that although this method may give some estimate of the potential reactivity of a siliceous aggregate, it cannot be used to accurately predict the expansiveness of an aggregate in concrete.

6.0 STAINING TECHNIQUES FOR AGGREGATES

A variety of staining techniques have been used by petrographers to aid in the identification of minerals, both in hand specimens and in thin sections.[60] Staining is typically used to distinguish between potassium feldspars and plagioclase, which is of importance for petrographers. The rock surface is etched with hydrofluoric acid, rinsed, and stained with sodium cobaltinitrite solution.[60] Calcite stains bright yellow, plagioclase a chalky white. Staining is also used to differentiate calcite from dolomite. The rock is first etched with dilute hydrochloric acid (HCl) and then stained with a mixture of Alizarin Red S and potassium ferricyanide dissolved in HCl. Calcite stains pale pink to red, dolomite is unstained, and ferroan dolomite is stained deep turquoise. These staining procedures are not very practical for large scale testing of aggregates and, in addition, use potentially hazardous chemicals. For these reasons they are generally not used for this purpose. However two staining procedures have been developed which are suitable for use with aggregates.

6.1 Copper Nitrate Staining Method

The copper nitrate staining method[13] may be used to differentiate between calcite and dolomite and to identify shaly material in an aggregate which may give rise to durability problems in concrete. The aggregate to

@Seismicisolation

be tested is separated into a number of size fractions. The aggregates should be washed, to remove dust, after they have been separated into the size fractions. Two hundred particles of each size fraction are tested by immersion for sixteen hours in a solution of 250 g copper nitrate $Cu(NO_3)_2 \cdot 3H_2O$ in 1 litre of distilled water. Splits develop along shaly layers in the aggregate and friable weathered dolostones crumble. The number of split particles are counted and removed. The remaining aggregate particles are immersed in strong ammonium solution for a few minutes, washed in water until the water is colorless, and dried in air. This converts the stain on the calcite particles to a deep blue color. Pure limestones also stain a deep blue color. Dolomite stains a light blue, as do dolostones. Silicate minerals are not colored. The percentages of each rock type identified in each size fraction are recorded and summed to yield the overall composition of the aggregate.

The copper nitrate staining method[13] is a rapid, convenient procedure which may be used on large samples by a laboratory technician at a relatively low cost. This method, although useful for differentiating between limestones and dolostones and for identifying shaly particles, does not differentiate potentially reactive siliceous limestones or alkali carbonate dolomitic limestones[61] from innocuous carbonate aggregates, and is, therefore, of limited use.

6.2 Methylene Blue Test

The principle behind the methylene blue test is that the exchangeable inorganic cations, Ca^{+2}, Mg^{+2}, K^{+}, and Na^{+}, on the surface and interlayer positions in some clays, may be exchanged by methylene blue molecules.[62] The methylene blue molecule ($C_{16}H_{18}N_3SCl.3H_2O$) is comprised of an organic base in combination with an acid. In dilute solution in water, methylene blue is present mostly as a monomer. The approximate dimensions of the monomer molecule are 1.25 to 1.60 NM long by 0.57 to 0.84 NM wide with a thickness of about 0.5 NM. Due to its relatively large molecular size, methylene blue is not an ideal cation exchange reagent; however it has been successfully used for aggregate evaluation.[62][63]

The methylene blue test has also been adopted in France as a standard method of determining the presence of clays in aggregates.[64] The principle of the test method is that when an aggregate to be evaluated is immersed in a methylene blue solution, some of the methylene blue dye

@Seismicisolation

is adsorbed by clay minerals in the aggregate, thus reducing its concentration in the solution. The swelling clay minerals with larger basal d-spacings adsorb more methylene blue than the non-swelling minerals such as kaolinite and illite. It is evident from Fig. 13 that although there is a moderate correlation between interplanar spacing and methylene blue adsorption, there is considerable scatter.

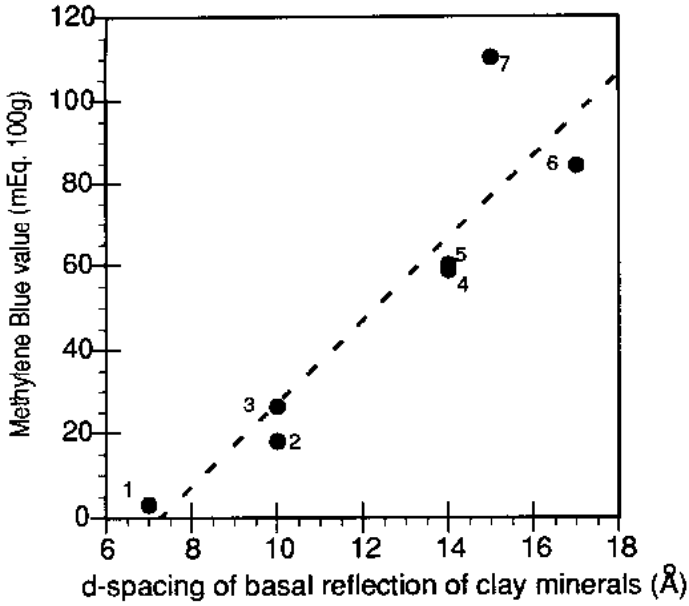


Figure 13. Amount of dye adsorbed versus basal interplanar spacing of selected clay minerals. Plotted from data by Taylor.[62] *(1)* Kaolinite (Cornwall); *(2)* illite (Fvon Fuzerradvany); *(3)* illite (Fithian); and *(4)* nontronite; *(5)* montmorillonite; *(6)* bentonite (Wyoming); *(7)* bentonite (Bischofszell).

Several minor modifications to the French test method have been proposed.[63][64] The simplest test protocol is probably that of Hosking and Pike.[63] The standard dye solution is made by dissolving 80 mg methylene blue in 1 liter of deionized water which is then made up to 2 liters. The solution must be stored in a light tight container and used within 48 hours of mixing. The aggregate is ground to pass a 1.18 mm sieve and be retained

@Seismicisolation

on a 600 μm sieve. Two, one gram portions, used for duplicate tests, are stored in glass vials. Twenty-five milliliters of the standard dye solution are added to each vial of the sub-sample which is then shaken for 30 seconds and stored in a lighttight box for 24 hours. It is then shaken again for 30 seconds. The dye concentration is determined by comparison of the color of the solution in the test samples with a set of calibrated solutions previously prepared. The calibrated solutions are prepared by taking the standard dye solution and diluting it incrementally in 2% steps so as to make a set of dilutions ranging from 2% to 98%.

In addition to being used to detect the presence of swelling clays in aggregates, the methylene blue test has also been used to identify aggregates susceptible to excessive drying shrinkage.[63] However, it is uncertain if this test could be used to identify all types of aggregates causing high shrinkage in concrete, e.g., the sandstone with a shrinkage of 0.116% in one year in concrete.[44] However, the concrete shrinkage test requires a minimum of several months to complete, in comparison to the two days needed for the methylene blue test. Further evaluation of the methylene blue test is evidently required to determine its suitability for use with all types of aggregates.

6.3 Measurement of Undulatory Extinction Angles

DeHills and Corvelan[66] correlated the intensity of geological stresses in Chilean granites to the undulatory extinction (UE) angles in the quartz grains in the granites. *Undulatory extinction* is the name given to the phenomenon, observed in thin sections of deformed quartz viewed in a petrographic microscope between crossed polarizers as the stage of the microscope is rotated. When a non-basal section of an undeformed quartz crystal is observed between crossed polarizers, as the stage is rotated by a few degrees the color of the crystal goes from bright to dark (extinction). When deformed quartz is observed between crossed polarizers, as the stage is rotated from the bright position a dark extinction band begins to form which moves across the crystal as the stage is rotated. The rotation angle between the first and last appearance of the extinction band as it moves across the crystal is called the UE angle. UE angles can range up to about 40°. The procedure for measurement of UE angles is detailed by Dolar-Mantuani.[13]

@Seismicisolation

White[67] showed that as stress built up in a quartz crystal, dislocations formed throughout it, but did not produce any optical effect. As the stress increases, as may happen under tectonic conditions within the earth's crust, the dislocations migrate to form sub-grain boundary walls within the crystal. In a highly deformed crystal, numerous dislocation boundary walls are produced and it is the successive misalignments across the sub-grain boundaries that produce the phenomenon of undulatory extinction. The migration of the dislocations to form the dislocation boundary walls is essentially a recovery process as the crystal adjusts to the applied stress and, hence, such a crystal would have a somewhat lower free energy and, hence, less potential alkali-silica reactivity than a crystal containing numerous random dislocations which would not give rise to optical effects.[68]

A number of authors have related high UE angles to the potential expansiveness of quartz aggregates in concrete;[13][51][69]–[71] however, when actual correlations have been attempted, the correlation has been poor.[72] There are several reasons for this. The measured UE angles are affected by two factors other than the stress level in the crystal lattice:

1. The orientation of the grain being measured relative to its optical axes, affects the angle measured.
2. The size of the crystal also has an effect on the measured angle, as small crystals yield smaller angles.

These two factors make it difficult to obtain reproducible UE angles. Although it is generally observed that quartz showing high UE angles is often alkali-reactive, it is shown that the reactivity is likely due to the presence of microcrystalline quartz, which is invariably present in rock containing quartz showing high UE angles rather than stress in large quartz grains.[73] It is concluded that although observation of high UE angles is a sign of potential reactivity, it is doubtful if any additional information concerning the potential reactivity can be obtained by measurement of the UE angles.

@Seismicisolation

7.0 SHAPE AND SURFACE TEXTURE OF AGGREGATES

There has been little concern for the shape and texture of aggregates apart from eliminating elongate particles when making ordinary portland cement concrete; however, that has changed since high strength, or high performance concrete came into use. The selection of aggregate particles with optimum shape and other properties, such as surface roughness and compressive strength, became important in obtaining the required strength of the concrete. The shape and surface properties of aggregates are still not covered in the ASTM specification for concrete aggregates, C 33, yet, as early as 1943 tests were carried out on the effects of shape and surface texture of aggregates on the properties of concrete.[74] Mather[75] reported on the effect of shape, surface texture, and coatings, on the properties of aggregates. Accurate descriptions of the shape and surface texture, or roughness, of aggregate particles need to be determined before the effects of these parameters on the properties of concrete can be evaluated.

The shape of particles is defined in ASTM C 125[76] by the three major axes of the particle, length, width, and thickness (*L*, *W*, and *T*, respectively). Zingg[77] developed a similar "sphericity" classification using the same three axes, which he designated *a*, *b*, and *c*. Particles are divided into four classes: *(i)* disks, *(ii)* spherical particles, *(iii)* blades, and *(iv)* rods. The two systems of classification of particle shape are illustrated in Fig. 14.

These two methods of classification of particle shape do not, however, address the surface roughness of the particles, which may have a significant effect on the bond to the cement paste in concrete. Mather[75] evaluated the effect of smooth particles on the flexural strength of concrete by mixing various proportions of smooth with rough particles; his results are shown in Fig. 15. However, he did not attempt to measure the roughness of the particles.

It is evident from Fig. 15 that there is a small, but not insignificant increase in flexural strength of concrete when smooth particles are replaced by rough ones. This difference would probably be of no significance for the production of normal portland cement concrete in the 20 to 30 MPa range, but could be important in the production of high strength concrete.

@Seismicisolation

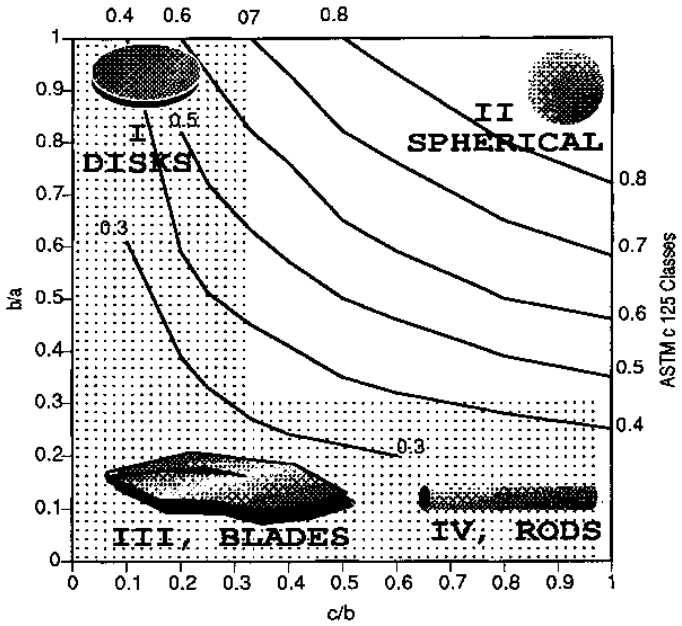


Figure 14. Plot of axial rations b/a versus c/b for variously shaped particles. The four Zingg classes are also shown on the diagram. Flat or elongated particles occur in the stippled areas of the diagram. The sphericity curves (ASTM C 125 classes) were plotted from the equation: $(\text{sphericity})^3 = bc/a^2$, where *a*, *b*, and *c*, are the length, width and thickness of the particle. *(Modified after Mather.)*[75]

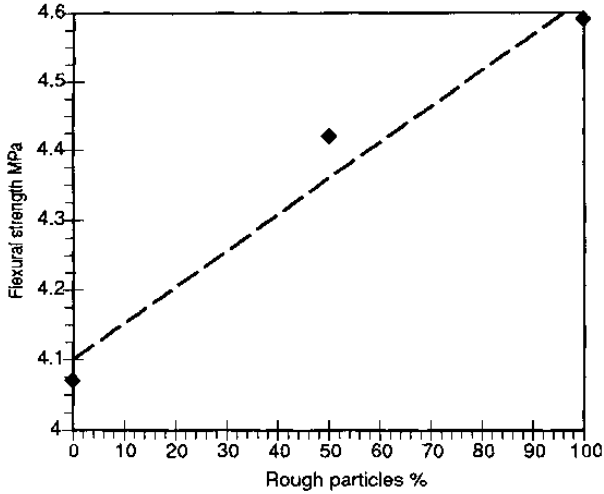


Figure 15. The effect of the percentage of rough particles on the flexural strength of concrete made with a mixture of smooth and rough aggregate particles. *(Drawn from data from Mather.)*[75]

@Seismicisolation

Before the advent of image analysis, measurement of surface roughness was difficult. A measure of surface roughness can be obtained using a profilometer, however, it is difficult on small, irregular shaped particles such as aggregates. Czarnecka and Gillott[78] analyzed the 2-D image of the particles using a modified Fourier Transform method. They calculated a number of coefficients: P_n, the gross shape coefficient, which is similar to the Zingg shape classes, and P_{ij}, which characterizes the surface texture (roughness). The term P_n represents the average squared deviation of the grain profile from a circle of equal area. The term P_{ij} is calculated based on a previously selected set of amplitude harmonics in the Fourier transform and represents the fine structure or surface roughness. A new term (T), for total roughness, was introduced, which combines P_n and P_{ij}. Czarnecka and Gillott[78] calculated P_n, P_{ij}, and T for a number of different shapes, a few of which are illustrated in Fig. 16.

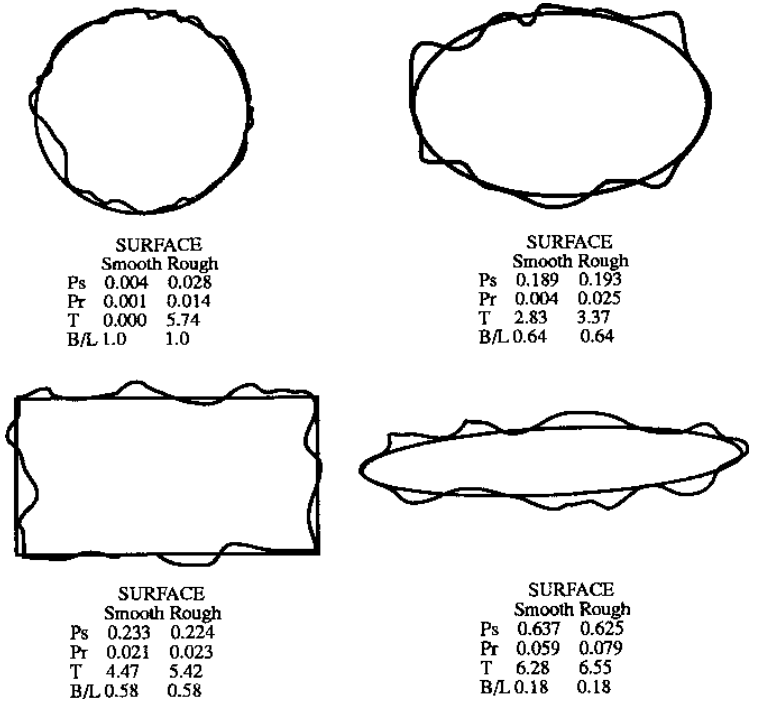


Figure 16. Results of Fourier computations of selected shaped particle profiles. *(Redrawn from Czarbecka and Gillott)*,[78] (Fig. 2). Symbols: *Ps*—modified coefficient representing particle shape; *Pr*—modified coefficient representing particle texture; *T*—coefficient of total roughness; *B/L*—width/length of particle.

@Seismicisolation

Two additional coefficients were used in calculating the shape factors from Fig. 16: $P_S = P_{ij}$ (based on the first few harmonics representing the shape factor) and $P_R = P_{ij}$ (based on the higher harmonics representing surface roughness). The coefficient varies from 0 for a particle with a smooth circular outline, to ~8 for an angular elongate particle, P_S varies from ~0 to ~0.6 and P_R varies from ~0 to ~0.1 for the same shaped particles. The new term P_{ij} was introduced because the gross shape factor dominated the term P_n, resulting in the surface texture being under represented. It was found that the total roughness coefficient, T, gave a better overall representation of the grain morphology than P_n or P_{ij}.

A somewhat different approach to the measurement of shape and surface texture of aggregate particles was taken by Hagermanm, Balck, and Lillieskold.[79] They used an automated image analyzer to measure length, L, width, B, and surface area, A, of aggregate particles. The factor B/L provides a measure of the elongation of the particles similar to that of Zingg, ibid. The factor A/BL measures the roundness or angularity of the particles. The calculated factors B/L and A/BL of a few shapes are shown in Fig. 17 and Table 3.

It is evident from Table 3 that using the factor A/BL provides significantly more information on the shape of the particle than does B/L. Using an image analyzer, these calculations can be made rapidly by placing the aggregate particles on a scanner and scanning in the profiles. This procedure assesses the overall surface roughness of the particles, but does not evaluate the effect of small holes or cracks in the surface (porosity), or the surface roughness. This latter factor could be of significance for aggregates for use in high strength concrete.

An image analytical method, which addresses both the overall shape and the surface porosity, was recently proposed by Martínez and Rubiera.[44] They used thin sections and obtained images under varied lighting conditions: normal light, polarized light between crossed polarizers, and light obtained with varying degrees of crossing of polars to obtain images with adequate resolution of the surface porosity. They calculated the total porosity of the sample from the images obtained. They also introduced an improved method for measuring the shape parameters, length and width. This procedure is illustrated in Fig. 18.

@Seismicisolation

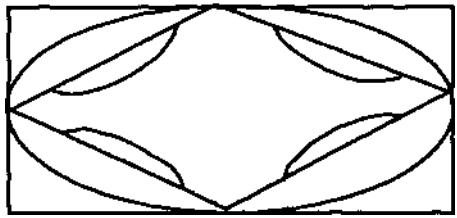


Figure 17. Diagram showing variation in *A/BL* for a variety of geometric figures. *(Redrawn from Hagerman, et al.)*,[78] Fig. 13. Rectangle—*A/BL* = 1.0; ellipse—*A/BL* = 0.79; diamond—*A/BL* = 0.50; scalloped diamond—*A/BL* = 0.38.

Table 3. Roundness of Particles Calculated Using *B/L* and *A/BL*

Particle Shape	*A/BL*	*B/L*
Rectangle	1.0	0.5
Ellipse	0.79	0.5
Diamond	0.50	0.5
Scalloped Diamond	0.39	0.5

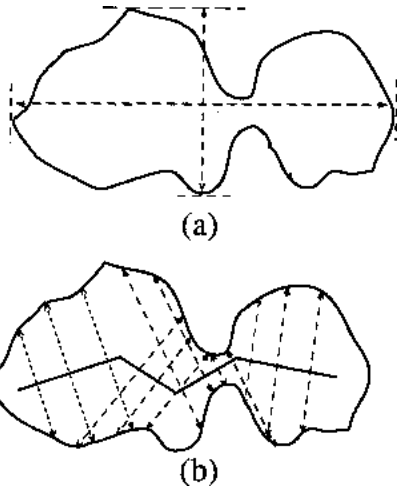


Figure 18. Particle with irregular profile comparing Feret's Window method for determining *B/L* with the new technique. *(After Martínez and Rubiera)*,[44] (Fig. 1).

@Seismicisolation

The method for calculating *B/L* using Feret's Window is shown graphically in Figure 18a. Calculated in this way, *B/L* yields a value of 0.50. In the proposed new method, *L* is segmented and a series of lines (*B*) normal to the segments of *L*, are generated. The shortest line is used for *B*. This yields a value of 0.10.

Another technique which may be used to characterize the surface topography of aggregate particles is confocal microscopy.[80] It is possible by use of a confocal laser-scanning microscope to capture a series of digital images at different focal distances. These are combined to form what is essentially a topographic map of the surface. The surface roughness (*RN*) is calculated by dividing the estimated surface area by the nominal geometric surface area, assuming a flat surface. A horizontal plane would have an *RN* of 1.0.

REFERENCES

1. Scott, J. S., *Dictionary of Civil Engineering, 4th Ed.*, p. 534, Chapman Hall, New York, London (1993)
2. Choquette, M., Bérubé, M. A., and Locat, J., Behavior of Common Rock-Forming Minerals in a Strongly Basic NaOH Solution, *Canadian Mineralogist*, 29**:**163–173 (1991)
3. Swamy, R. N. (ed.) *The Alkali-Silica Reaction on Concrete*, p. 336, Blackie, Glasgow and London, Van Nostrand Reinhold, New York (1992)
4. Stark, D., Characteristics and Utilization of Coarse Aggregates Associated with D-Cracking, *ASTM STP 597, Living with Marginal Aggregates*, pp. 45–58, ASTM, Philadelphia (1975)
5. Davis, R. E., Nielenz, R. C., and Polivka, M., Importance of Petrographic Analysis and Special Tests Not Usually Required in Judging Quality of Concrete Sand, *J. of Mats.*, 2:461–486 (1967)
6 ASTM C-295-90, Standard Guide of Petrographic Examination of Aggregates for Concrete, p. 1994, *Annual ASTM Standards in Building Codes*, 2:641–648, ASTM, Pennsylvania (1997)
7. CSA A23.l-94, Appendix B, A23.l-94, A23.2-94, *Concrete Materials and Methods of Concrete Construction, Methods of Test for Concrete*, Canadian Standards Association, Canada, pp. 112–135 (1994)
8. CSA A23.2-14A, A23.l-94, A23-2-94, *Concrete Materials and Methods of Concrete Construction, Methods of Test for Concrete*, Canadian Standards Association, pp. 205–214 (1994)

@Seismicisolation

9. Hutchison, C. S., *Laboratory Handbook of Petrographic Techniques,* p. 527, Wiley-Interscience Publication, John Wiley and Sons, New York (1974)
10. Turner, F. J., Verhoogen, J., *Igneous and Metamorphic Petrology, 2nd. Ed.*, p. 694, McGraw-Hill, New York (1960)
11. Klein, C., and Hurlbut, C. S., Jr., *Manual of Mineralogy,* (after James D. Dana), 21st Ed., p. 681, John Wiley & Sons, New York (1993)
12. Deer, W. A., Howie, R. A., Zussman, J., *Rock Forming Minerals*, Vols. 1–5, John Wiley and Sons, New York (1963)
13. Dolar-Mantuani, L., *Handbook of Concrete Aggregates,* p. 345, Noyes Publications, Park Ridge, New Jersey (1983)
14. French, W. J., Reactions Between Aggregates and Cement Paste—An Interpretation of the Pessimum, *Q. J. Eng. Geol.*, 13:231–247 (1980)
15. ASTM C 227-90, Standard Test Method for Potential Alkali Reactivity of Cement-Aggregate Combinations (Mortar Bar Method), *ASTM Standards in Building Codes,* Vol. 2, B429-D266, pp. 612–616, ASTM, Philadelphia (1995)
16. Mielenz, R. C., Greene, K. T., and Benton, E. J., Chemical Test for Reactivity of Aggregates with Cement Alkalies; Chemical Processes Cement-Aggregate Reactions, *J. American Concrete Inst.*, 19:193–221 (1947)
17. ASTM C 289-94, Standard Test Method for Potential Reactivity of Aggregates (Chemical Method), *Annual Book of ASTM Standards*, 4.02:156–162, ASTM, Philadelphia (1995)
18. ASTM C 1260-94, Standard Test Method for Potential Alkali Reactivity of Aggregates (Mortar Bar Method), *Annual Book of ASTM Standards*, 4.02:648–651, ASTM, Philadelphia (1994)
19. Tamura, H., A Test Method on Rapid Identification of Alkali-Reactivity Aggregate, (GBRC Method), *Concrete Alkali-Aggregate Reactions,* (P. E. Grattan-Bellew, ed.), pp. 304–308, Noyes Publications, Park Ridge, New Jersey (1987)
20. Fournier, B., Bérubé, M. A., and Bergeron, G., A Rapid Autoclave Mortar Bar Method to Determine the Potential Alkali-Silica Reactivity of St. Lawrence Lowlands Carbonate Aggregates (Quebec, Canada), *Cement Concrete and Aggregates,* 13:58–71 (1991)
21. Tang, M. S., Su-fen, and Shi-hua, A Rapid Method for Identification of Alkali-Silica Reactivity of Aggregate, *Cement and Concrete Research*, 13:417–422 (1983)

@Seismicisolation

22. Katayama, T, St. John, D. A., and Futagawa, T., The Petrographic Comparison of Some Volcanic Rocks from Japan and New Zealand - Potential Reactivity Related to Interstitial Glass and Silica Minerals, (A. Shayan, ed.), *Proc 10th Int. Conference on Alkali-Aggregate Reaction in Concrete*, pp. 537–542, Melbourne (1996)
23. Katayama, T., Helgason, T. S., and Olafsson, H., Petrography and Alkali-Reactivity of Some Volcanic Aggregates from Iceland, (A. Shayan, ed.), pp. 377–384, *Proc. 10th International Conference on Alkali-Aggregate Reaction in Concrete*, Melbourne (1996)
24. Quantitative Analysis of Quartz by Phosphoric Acid Method, The Cement Association of Japan, *Report of Committee on Chemical Analysis*, I-5, I-16 (In Japanese), (1959)
25. Katayama, T., Personal Communication of English Translation of Quartz Determination, (Phosphoric Acid Method) (1997)
26. Dent Glasser, L. S., and Kataoka, N., Some Observations on the Rapid Chemical Test for Potential Reactive Aggregate, *Cement and Concrete Research*, 11:191–196 (1981)
27. Fournier, B., and Bérubé, M. A., Evaluation of Modified Chemical Method to Determine the Alkali-Reactivity Potential of Siliceous Carbonate Aggregates, *Canadian Developments in Testing Concrete Aggregates for Alkali-Aggregate Reactivity*, Ministry of Transport of Ontario, Report E-M-92, pp. 118–135 (1990)
28. Bérubé, M. A., and Fournier, B., Accelerated Test Methods of Alkali-Aggregate Reactivity, CANMET/EMR, Ottawa, Canada, *Proceedings of Int. Symposium on Advances in Concrete Technology*, Athens, Greece, pp. 583–627 (1992)
29. Mielenz, R. C., and Benton, E. J., Evaluation of the Quick Chemical Test for Alkali-Reactivity of Concrete Aggregates, *Highway Research Bulletin*, 171:1–15 (1958)
30. Bérard, J., and Roux, R., La Viabilite des Betons due Québéc: le Role des Granulats, *Can. Journal of Civil Engineering*, 13:12–24 (1966)
31. Sorentino, D., Clément, Y. J., and Goldberg, J. M., New Approach to Characterize the Chemical Reactivity of Aggregates, *Proc. 9th Internat. Conference on Alkali Aggregate Reaction in Concrete*, pp. 1009–1016, London (1992)
32. Nixon, P. J., Personal Communication (1996)
33. Stark, D., Alkali-Silica Reactivity: Some Reconsiderations, *Cement Concrete and Aggregates*, 2:92–94 (1980)
34. Grattan-Bellew, P. E., and Beaudoin, J. J., Effect of Phlogopite Mica on Alkali-Aggregate Expansion in Concrete, *Cement and Concrete Research*, 10:789–797 (1980)

@Seismicisolation

35. Grattan-Bellew, P. E., Alkali Contribution from Limestone Aggregate to Pore Solution of Old Concrete, *ACI Materials J.*, 9l:173–177 (1994)

36. Bérubé, M. A., Duchesne, J., and Rivest, M., Alkali Contribution by Aggregates to Concrete, *Proc. 10th. International Conference on Alkali-Aggregate Reaction in Concrete*, (A. Shayan, ed.), pp. 899–906, Melbourne, (1996)

37. Barneyback, R. S., and Diamond, S., Expression and Analysis of Pore Fluids from Hardened Cement Pastes and Mortars, *Cement and Concrete Research*, 11:279–285 (1981)

38. Goguel, R., Alkali Release by Volcanic Aggregates in Concrete, *Cement and Concrete Research*, 25:841–852 (1995)

39. van Aardt, J. H. P., and Visser, S., Reactions between Rocks and the Hydroxides of Calcium, Sodium, and Potassium, Progress Report No. 1, National Building Research Institute, CSIR, Pretoria S. Africa, BRR 574, p. 14 (1982)

40. Sutterheim, N., Excessive Shrinkage of Aggregates as a Cause of Deterioration of Concrete Structures in South Africa, *Trans. S.A. Institution of Civil Engineers*, 4:17 (1954)

41. Shrinkage of Natural Aggregates in Concrete, *BRE Digest 357*, p. 4, BRE Building Research Establishment, Garston, Watford, U.K. (Jan., 1991)

42. ASTM C 127-88, Standard Test Method for Specific Gravity and Absorption of Coarse Aggregate, 1997 *ASTM Standards in Building Codes*, 2:433–437, ASTM, 100 Barr Harbor Drive, W. Conshohocken, Pa., 19428-2959, USA.

43. Diamond, S., and Leeman, M. E., Estimating Capillary Porosity of Cement Paste by Fluorescence Microscopy and Image Analysis, *Materials Research Society (MRS)*, 370:217–226 (1995)

44. Martínez, C. Á., and Rubiera, N. P., Análisis Microstructural de Granitos, por Técncas de Proceso Digital de Imágenes, para su Utilizacion como Áridos en Hormignones, *Ingeriería Civil*, 99:5–13 (1995)

45. Polivka, M., and Mehta, P. K., Use of Aggregates Producing High Shrinkage with Shrinkage-Compensating Cements, *Living with Marginal Aggregates*, ASTM STP 597, pp. 36–583 (1975)

46. Collins, R. J., Concrete Using Porous Sandstone Aggregate, *Quarry Management*, 13:33–42 (1986)

47. Moore, I. C., and Gribble, C. D., The Suitability of Aggregates from Weathered Peterhead Granites, *The Quarterly Journal of Engineering Geology*, 13:305–314 (1980)

48. Schrimer, F. H., Evaluation of an Alkali-Reactive Aggregate Unidentified by Petrographic Methods, *Proc. 10th. International Conference on Alkali-Aggregate Reaction in Concrete*, pp. 734–741 (A. Shayan, ed.), Melbourne, Australia (1996)

@Seismicisolation

49. Murata, K. J., and Norman, M. B., An Index of Crystallinity for Quartz, *American Journal of Science*, 276:1120–1130, (1976)
50. Strogen, P., Study of Cherts in Fine and Coarse Aggregates in Ireland, *Concrete*, 27:26–29 (1993)
51. Coretelezzi, C. R., Maiza, P., and Pavlicevic, E., Strained Quartz in Relation to Alkali-Silica Reaction, ASTM STP 1061, (B. Erlin and D. Stark, eds.), pp. 145–158, ASTM, Philadelphia, Pa., 19103 (1990)
52. Liang, T., Meihua, W., Sufen, H., Mingshu, T., Method to Evaluate the Reactivity of Microcrystalline Quartz in Carbonate Rocks, *Advances in Cement Research*, 9:55–63 (1997)
53. Higgs, N. B., Montmorillonite in Concrete Aggregate Sands, *Bull. Association of Engineering Geologists*, XII:57–71, (1975)
54. Thorez, J., *Phyllosilicates and Clay Minerals, A Laboratory Handbook for Their X-Ray Diffraction Analysis*, Editions G. Lelotte, B 4820 DISON, Belgique, p. 579 (1975)
55. Brindley, G. W., Brown, G., *Crystal Structures of Clay Minerals and Their X-Ray Identification*, Mineralogical Society, Great Britain, pp. 495, Reprinted (1984)
56. Kintner, E. B., and Diamond, S., A New Method for Preparation and Treatment of Oriented Aggregate Samples of Soil Clays for X-Ray Diffraction Analysis, *Soil Science*, 81:111–120 (1956)
57. Baronio, G., Berra, M., Bachorrini, A., Delmastro, A., Montanaro, L., and Negro, A., Infrared Spectroscopy in the Evaluation of Aggregates in A.S.R. Deteriorated Concretes from Many Parts of the World: Comparison with Other Methods, *Concrete Alkali-Aggregate Reactions*, (P. E. Grattan-Bellew, ed.), Noyes Publications, Park Ridge, New Jersey (1987)
58. Grattan-Bellew, P. E., Evaluation of Test Methods for Alkali-Aggregate Reactivity, *Proc. of 6th. International Conference on Alkalis in Concrete*, (G. M. Idorn, and R. Steen, eds.), pp. 303–314 Copenhagen (1983)
59. Tang, Mingshu, Meihua, W., and Sulfen, H., Microstructure and Alkali Reactivity of Siliceous Aggregates, *Proc. 8th International Conference on Alkali-Aggregate Reaction*, (K. Okada, S. Nishibayashi, and M. Kawamura, eds.), Kyoto, pp. 457–462 (1989)
60. Reid, W. P., Mineral Staining Tests, *Mineral Ind. Bull.*, 12(3):1–20 (1969)
61. Swenson, E. G., and Gillott, J. E., Characteristics of Kingston Carbonate Rock Reaction, *Highway Research Board, Bull.*, 275:18–31 (1960)
62. Taylor, R. K., Cation Exchange in Clays and Mudrocks by Methylene Blue, *J. Chem. Tech. Biotechnol.*, 35A:195–207 (1985)

@Seismicisolation

63. Hosking, J. R., and Pike, D. C., The Methylene Blue Dye Adsorption Test in Relation to Aggregate Drying Shrinkage, *J. Chem. Tech. Biotechnol.*, 35A:185–194 (1985)

64. Stewart, E. T., and McCullough, L. M., The Use of the Methylene Blue Test to Indicate the Soundness of Road Aggregates, *J. Chem. Tech. Biotechnol.*, 35A:161–167 (1985)

65. Tran Ngoc Lan, L'essai an Bleu de Methylene. Un Progres Dans le Mesure et le Control de la Propreté des Granulats, *Bull. Liason Laboratoire des Ponts et Chaussées*, 107:130–135, LPCP, France (1980)

66. DeHills, S. N., and Corvalan, J., Undulatory Extinction in Quartz Grains of Some Chilean Granitic Rocks of Different Ages, *Geol. Soc. America Bull.*, 75:363–366 (1964)

67. White, S., The Dislocation Structures Responsible for the Optical Effects in Some Naturally-Deformed Quartzes, *J. Mat. Sci.*, 8:490–499 (1973)

68. Grattan-Bellew, P. E., Is High Undulatory Extinction in Quartz Indicative of Alkali-Expansivity of Granitic Aggregates? *Alkali-Aggregate Reactions* (P. E. Grattan-Bellew, ed.), pp. 434–439, Noyes Publications, Park Ridge, New Jersey (1987)

69. Buck, A. D., and Mather, K., Reactivity of Quartz at Normal Temperatures, *U.S. Army Corps of Engineers, Technical Report SL-84-12*, p. 15, Department of the Army, Waterways Experiment Station, Corps of Engineers, Vicksburg, Ms. 39180 (1984)

70. Gogte, B. S., An Evaluation of Some Common Indian Rocks with Special Reference to Alkali-Aggregate Reactions, *Eng. Geology*, 7:135–153 (1973)

71. Buck, A. D., Alkali-Reactivity of Strained Quartz as a Constituent of Concrete Aggregate, U.S. Army Corps of Engineers Technical Report SL-83-13, p. 9, Department of the Army, Waterways, Experiment Station, Corps of Engineers, Vicksburg, Ms, USA (1983)

72. Mullick, A. K., Evaluation of ASR Potential of Concrete Aggregates Containing Strained Quartz, *NCB Quest*, pp. 35–46 (Aug., 1987)

73. Grattan-Bellew, P. E., Micro-Crystalline Quartz, Undulatory Extinction and the Alkali-Silica Reaction, *Proc. of 9th International Conf. on Alkali-Aggregate Reaction in Concrete*, l:383–394, The Concrete Society (1992)

74. Gilkey, H. J., Size, Shape, Surface Texture, and Gradings of Aggregates, *ASTM STP 22A*, p. 92, ASTM, Philadelphia (1943)

75. Mather, B., Concrete Aggregates, Shape, Surface Texture, and Coatings, Concrete & Concrete Making Materials, *ASTM STP 169*, pp. 415–431, ASTM, Philadelphia (1966)

@Seismicisolation

76. ASTM C 125-88, Standard Terminology Relating to Concrete and Concrete Aggregates, *1990 Annual Book of ASTM Standards*, 4.02:61–62, ASTM, Philadelphia (1990)
77. Zingg, Th., Beitrag zur Schotteranlyze, *Schweizerische Mineralogische und Petrographische Mitteilungen*, 115:39–140 (1935)
78. Czarnecka, E. T., and Gillott, J. E., A Modified Fournier Method of Shape and Surface Texture Analysis of Planar Sections of Particles, *Journal of Testing and Evaluation JTEVA*, 5:292–298 (1977)
79. Hagerman, T. H., Balck, K., and Lillieskold, M., Shape and Surface of Mineral Grains Automatically Determined for Mortar and Concrete Purposes Through Image Analysis, Report D26, p. 49, Swedish Council of Building Research, Stockholm (1980)
80. Abell, A. B., and Lange, D. A., Image-Based Characterization of Fracture Surface Roughness, *Mat. Res. Soc. Symp. Proc.*, 370:107–113 (1995)

@Seismicisolation

3

Chemical Methods of Analysis of Concrete

William G. Hime

1.0 INTRODUCTION

1.1 The Analytical Problems for the Analyses of Hardened Concrete

Portland cement is made using many of the same rocks, ores, or minerals that are used as aggregates in concrete. Thus, chemical (elemental) differentiation between the cement and the aggregates is often difficult. Further, no component of portland cement is reasonably constant in concentration from one cement manufacturer to another.

Complicating this problem of analyzing concrete is the present-day practice of including other mineral admixtures in the mix. As contrasted with industry practices forty years ago when most of the analytical techniques for concrete were developed, much of the concrete produced in the U.S. now contains fly ash, which itself presents an even greater analytical challenge: its composition is almost completely uncontrolled by its power plant producers. Ground granulated blast-furnace slag and silica fume are also used in increasing amounts in concrete.

The use of organic additives in cement and admixtures in concrete is now common, and analysis for them is enormously complicated for three reasons: they may be effective for their purpose at concentrations as low as

@Seismicisolation

one-hundredth of 1% by weight of the concrete; their life in their original form may be short because they degrade in the alkaline (pH values above 13) portland cement concrete; and, if proprietary, their composition may not be known to the analyst.

Although modern analytical instruments allow much faster analyses for the components of concrete, they require a large capital outlay. For instance, complete analyses of portland cement can now be performed by atomic absorption, x-ray emission (fluorescence), or plasma spectroscopy, in a half-hour instead of several days for the classical wet methods, but at a cost of tens of thousands of dollars for the instrumentation. Further, instrumentation has resulted in the replacement of chemists by instrumental technicians who often cannot provide the chemical insight that was the stock and trade of the wet analytical chemist. Indeed, there has been almost a complete dearth of published methods of analysis during the last three decades.

It is the aim of this chapter to outline both the classical (wet) and the instrumental methods of analysis for usual components of concrete and to provide some insight into their applicability, limitations, and advantages. The methods may also be applicable to grouts, mortars, and cement plasters, since these materials may differ from concrete primarily in the absence of coarse aggregate. Methods of analysis for cement and other materials in concrete are also detailed by Figg and Bowden,[1] the Society of Chemical Industry,[2] and Hime.[3]

1.2 The Components of Concrete

Portland cement concrete is made with, as a minimum, portland cement, fine aggregate (sand), coarse aggregate (stone or gravel), and water. The portland cement, in turn, may contain organic components such as pack-set inhibitors or air-entraining agents. Frequently the concrete may contain fly ash, slag, silica fume, set-accelerators or retarders, air-entraining agents, workability aids, and corrosion inhibitors, to name only the more common ones.

The analytical problem is thus enormous. Further, a definitive analysis usually requires the expertise of a microscopist or petrographer. For example, the presence of fly ash can seldom be determined by a chemist, but can quickly be found by a petrographer. Silica fume may not be identifiable by any technique, chemical or instrumental, although it may be detected by scanning electron microscopy if it is not completely dispersed.[4]

@Seismicisolation

Portland Cement. Portland cement is generally produced at a plant having a readily accessible limestone quarry. Limestone constitutes about 80% of the weight of the raw materials used in cement production. The remaining components are mainly clays or shales, as chosen to provide the required amount of silicates. If these materials, in turn, contain an aluminate concentration that is too high, then iron ore or other high-iron minerals or by-products must be incorporated in the mix to combine with a portion of the aluminates to prevent a concentration of tricalcium aluminate (the major aluminum-containing portland cement mineral) that is too great.

A blend of the raw materials is ground to face-powder fineness and burned in a rotating kiln having an exit temperature of about 2700°F (1500°C). The resulting clinker is then mixed with about 5 to 8% gypsum (or occasionally a mixture of gypsum and anhydrite) and the mix is again ground so that most particles are less than 20 microns in maximum dimension. In Canada and elsewhere and as proposed in the United States, limestone may replace some of the gypsum.

The properties of the raw components and the fineness of the resulting cement are varied in order to produce the required type of cement, as designated in the United States by ASTM C150 or AASHTO M85. Due to the temperature of the kiln and the burning process that uses an excess of oxygen, the elements of the raw materials are assumed to be present in their highest valence and as an oxide.

Cement chemists use a shorthand system to report how these oxides are combined. In this system, calcium oxide is denoted as C, silicon dioxide as S, aluminum oxide as A, iron oxide (ferric oxide) as F, sodium oxide as N, potassium oxide as K, H for water, and, since S is used for SiO_2, $\overline{S}$ is used for sulfur trioxide.

Using this system, portland cement is normally considered to contain the following major components: tricalcium silicate (C_3S), dicalcium silicate (C_2S), tricalcium aluminate (C_3A), an aluminoferrite complex having a formula approximating C_4AF, and gypsum ($C\overline{S}H_2$) or a blend of gypsum and anhydrite ($C\overline{S}$). Impurities usually include 0.2 to 1.2% K, 0.1 to 0.5% N, and small amounts of manganese, titanium, barium, strontium, and phosphorus, all present in their oxide forms.

Table 1 provides the approximate compositions of the various types of cement as produced in 1993 and 1994, based on a survey by Gebhardt.[5]

Portland cement may also contain additives such as air-entraining agents or processing chemicals such as pack-set inhibitors and grinding aids.

@Seismicisolation

Table 1. Average Compositions of U.S. Portland Cements, 1994*

Oxide or Compound	Type 1	Type 2	Type 3	Type 4	Type 5
SiO_2	20.55	21.19	20.03	22.16	21.34
Al_2O_3	5.41	4.60	5.34	4.56	3.60
Fe_2O_3	2.59	3.50	3.52	4.96	3.98
CaO	63.89	63.81	63.04	62.53	62.78
MgO	2.09	2.15	2.52	1.85	3.19
SO_3	3.03	2.69	4.08	2.16	2.42
Na_2O	0.21	0.19	0.26	—	0.26
K_2O	0.61	0.57	0.87	—	0.68
Loss on ignition	1.37	1.15	1.35	1.18	0.79
C_3S	54.46	54.67	52.63	42.2	55.7
C_2S	17.79	19.48	17.86	31.7	19.2
C_3A	10.29	6.48	10.49	3.7	3.4
C_4AF	7.88	10.64	7.00	15.1	12.1

*Not including specialty and low-alkali cements

Aggregates. In most areas of the world, the fine aggregate is siliceous and is often a relatively pure form of quartz. It is usually a natural sand although "manufactured" sands made by crushing the coarse aggregate are also common. The coarse aggregate is also often siliceous, but may instead be a crushed limestone or dolomite.

Mineral Admixtures. Some siliceous materials can react with hydrating portland cement to produce additional strength-producing compounds. This reaction is primarily with the calcium hydroxide product of portland cement hydration and the material is termed a *pozzolan.* Fly ash is now a frequent component of concrete and is sometimes present in amounts to 30 or 40%, by weight, of the portland cement. This by-product of the power industry consists of the unburned residue of the coal. It is usually a "Type F," consisting primarily of the oxides of aluminum, iron and silicon, or "Type C," containing up to 40% calcium oxide. Definitions and specifications for these types and of natural pozzolans are given in ASTM C618 and methods of analyses for these materials in ASTM C311.

Silica fume is used in amounts to 10% or more, by weight of cement, to provide higher strength and lower permeability. Ground granulated blast-furnace slag used widely in Europe is becoming more popular in the U.S., either as an admixture to concrete or, as mixed with portland cement, as a "blended" cement.

@Seismicisolation

Chemical Admixtures. Admixtures are now in sharp contrast to 50 years ago, components of much, if not most, of the concrete delivered in the U.S. Admixture components most frequently used include:

- Air-entraining agents such as tall oil soaps, wood resins, and synthetic surface-active agents.
- Set and strength accelerators, such as calcium chloride, calcium nitrate, or triethanolamine.
- Set retarders, such as sugars, corn syrups, and salts of hydroxycarboxylic acid.
- Workability aids, such as lignosulfonates.
- Corrosion inhibitors, such as calcium nitrite.
- Water-repelling or retarding agents, such as stearates.

Admixture types, components and uses are extensively detailed by Ramachandran.[6]

2.0 HARDENED CONCRETE ANALYSIS PROCEDURES

2.1 General

The analysis of concrete requires a skilled chemist having a good knowledge of cement and concrete components and properties. Further, many analyses require the services of a petrographer to ascertain the components of the sample and thus allow the analyst to determine how to avoid or make allowance for interferences to a particular analysis. Sometimes avoidance or allowance is impossible and the analyst must then report not only the result of his analysis, but also the likely direction and magnitude of the error associated with the result. A statement "portland cement at 8% or less" may be a quite sufficient answer to a problem relating to low strength.

It is not the intent of this chapter to present detailed descriptions of all the procedures for analysis; however, where the analyses require an extensive procedure, reference will be made to published methods. In most cases these will be the detailed procedures published by the American Society for Testing and Materials (ASTM). A list of these procedures is given in Table 2. British Standard 1881 presents similar procedures. The following sections will provide, where appropriate, both simplified methods and discussions of the accuracy and usefulness of the analyses.

@Seismicisolation

Table 2. ASTM Methods of Analysis of Concrete and Mortar*

Material Analyzed	ASTM Procedure	ASTM Volume
Concrete		
Cement content	C1084	4.02
Chloride, acid soluble	C1152	4.02
Chloride, water soluble	C1218	4.02
Sulfate (cement procedure)	C114	4.01
Sulfide (cement procedure)	C114	4.01
Mortar (applicable to plasters)	C1324	4.05

*Available from ASTM, 100 Barr Harbor Drive, West Conshohocken, PA, 19428, USA.

2.2 Cement Content Analysis

The cement content of concrete is usually determined by assuming that all of the acid-soluble calcium or silica in a concrete sample is due to those components in the portland cement. Although calcium oxide and silicon dioxide concentrations in portland cement vary from type to type, and from one cement producer to another, an assumption of 63.5% CaO and 21% soluble silica (SiO_2) in the cement usually will, in itself, not lead to an error greater than about 5% in the portland cement calculation.

Obviously, an analysis for portland cement by determination of calcium content will be erroneously high if the aggregate contains limestone or dolomite, or if fly ash, especially Type C, is present. Because siliceous components of most aggregates are not soluble, soluble silica is often perceived as an accurate method for cement content analysis. What is not usually recognized is that many aggregates, such as those containing feldspars, react with alkaline portland cement hydration products to produce, during service in the concrete, calcium or alkali silicates that are acid soluble. Overestimations can be almost as great by the soluble silica method when feldspars are present as they can be by the calcium oxide method when calcareous aggregates are present. Further, silica fume and fly ash react with the alkaline cement paste and produce silicates that cause high results. Portland cement contents determined by either the calcium or soluble silica procedures are seldom underestimations.

@Seismicisolation

Aggregate interferences can often be avoided by either of two methods: sulfate analysis, and maleic acid dissolution. Sulfate analysis appears at first glance to be attractive because all cements contain sulfate and very few aggregates do. However, the concentration of sulfate in portland cement can vary from less than 2% to over 4%, as SO_3 ($\bar{S}$). If the SO_3 content of the cement is not known and SO_3 is assumed at 3%, errors as high as 40% are possible.

Because all fly ashes contain sulfate, the sulfate procedure should not be used if fly ash is present. Further, many slags contain sulfates and the sulfate procedure is generally not applicable for concrete made with slag cement or slag aggregates. If analyses are made for total sulfur rather than sulfate then aggregates containing sulfides (e.g., pyrite) will cause overestimations of cement content.

Maleic acid dissolves hydrated portland cement, but not calcium carbonate (as calcite or dolomite). Thus it can be used with calcareous aggregates as well as with most siliceous aggregates. However, because calcium hydroxide is about a 20 to 25% component of hydrated portland cement and will react with carbon dioxide in the air to produce calcium carbonate, the concrete sample must be carefully chosen to eliminate carbonated portions. The maleic acid procedure also suffers in that there has not been an exhaustive study to determine the solubility of siliceous aggregates that have been exposed to the alkaline cement paste for extended periods of time. Because carbonation gives an erroneously low result and aggregate solubility gives a high result, the analyst may not be able to evaluate the direction or potential magnitude of the error.

2.3 Sample Requirements and Procedure Choice

The concrete sample must be representative of the structure in question. A concrete core having a diameter of three times the maximum size of the aggregate, and full depth, is usually representative for a particular concrete truck load or mix.

For maximum information, the concrete core should be weighed in air and in water after immersion for one minute and for twenty-four hours, then dried for twenty-four hours at 110°C. Unit weights, *as is* and *as placed*, and the cement content in bags per cubic yard or pounds per cubic yard, can then be calculated. Alternatively, the core can be used directly and reported on an *as-received* basis as a percentage of cement by weight. Ignition of the sample at 550°C will drive off free water and water of hydration

@Seismicisolation

(e.g., converting calcium hydroxide to calcium oxide) thus allowing comparison to the mix design before water addition.

It is useful to cut the core lengthwise, perpendicular to the diameter, at about a third point. The smaller portion is used for the petrographic study. The remainder is crushed andground to pass a No. 50 sieve, avoiding the loss of airborne fines. Very large samples may be ground to pass a No. 4 sieve, quartered, and a representative portion further ground to pass the No. 50 sieve. The pulverized samples should be well-mixed and duplicate two-gram samples analyzed for calcium or soluble silica or five-gram samples for sulfate. For the maleic acid procedure, 20 grams of material are used.

To help calibrate the procedure used, analysis of standard cements (available from the National Institute of Standards, NIST) at the same time as the concrete analysis is useful. The weight of the cement sample should be about 15% of the weight of the concrete sample used.

2.4 Calcium Oxide Content Procedure

Determine calcium oxide by ASTM C114, C1084, or other analytical procedure (e.g., atomic absorption or plasma spectroscopy), on a 1:4 (acid:water) hydrochloric acid extract of the representative sample. The filtrate from the soluble silica procedure may be used. The use of ice-cold hydrochloric acid to dissolve the calcium (and silica) from the concrete minimizes siliceous and dolomitic aggregate interference. Cement percentage by weight is % CaO divided by 0.635.

2.5 Soluble Silica Content

Determine soluble silica by ASTM C 1084 or as follows: digest the sample in 1:4 ice cold hydrochloric acid solution for 5 minutes, filter through a retentive paper (e.g., Whatman No. 40), then evaporate the filtrate to dryness, bake for 1 hour at 110°C, wet with concentrated hydrochloric acid and again evaporate and bake. Pour in 75 ml of 1:4 HCl, bring to a boil, then filter through retentive paper, washing with 1:10 HCl. Ignite the paper and contents carefully in a platinum crucible over a flame, charring the paper and not inflaming it. Place in a furnace at 1000°C for 1 hour, cool and weigh, add 3 drops of 1:1 sulfuric acid and 10 ml hydrofluoric acid. Evaporate without boiling to dryness, heat at 1000°C for 15 minutes, cool and weigh. The difference represents soluble silica. The percent soluble silica divided by 0.21 represents percentage of portland cement.

@Seismicisolation

2.6 Sulfate Content

A cement content determination based on sulfate analysis is appropriate only if the sulfate content of the cement used in the concrete is known or can be determined. Analysis can be made in accordance with the procedure of ASTM C 114 or by virtually any sulfate procedure employing hydrochloric acid dissolution of the sample. Analytical procedures for total sulfur (e.g., by LECO evolution/titration) are also generally applicable unless the concrete contains sulfides. If the odor of hydrogen sulfide is not noticed when acidifying the sample, sulfides are absent. A method is provided in Sec. 2.11, "Sulfate Procedure."

2.7 Maleic Acid

The method of ASTM C 1084-97 is appropriate as are the procedures of Tabikh,[7] Clemena,[8] Pistilli,[9] and Marusin.[10] Before pulverizing the concrete, spray a freshly broken surface with phenolphthalein. Cut off and discard any portion (e.g., top or bottom of a core) not turning red or purple.

2.8 Other Procedures

The only other procedure for cement content that has found general acceptance is petrographic examination and estimation by an experienced petrographer. A petrographic estimate is useful in any case to compare results with the chemical procedure and to allow the petrographer and chemist to ascertain probable reasons for discrepancies.

2.9 Chloride Analyses

A chloride analysis of portland cement is often necessary to determine if a chloride addition was made to the fresh concrete or if the concrete had been exposed to chloride salts. The former may explain unusually fast setting of the concrete and both the former and latter could explain why metals were corroding when embedded in the usually passivating portland cement system.

Two types of chloride analysis are most often requested: water-soluble, for chloride that is immediately capable of promoting corrosion, and acid-soluble, which includes both water-soluble chloride and that tied up in the aluminate phase of the concrete. The latter may become water-soluble if the concrete becomes carbonated or is exposed to sulfate.

@Seismicisolation

Acid-soluble chloride is usually, but not always, total chloride. Some organic compounds may contain chloride that is "bound" to the organic molecule and does not initially promote corrosion. However, continued exposure to the alkaline concrete may cause it to become water-soluble. Polyvinylidene chloride latex is an example.

Further complicating a "chloride analysis" request is the fact that some aggregates may contain chloride that will not be liberated during service in the concrete, but will be detected in the sample that has been pulverized for analysis. A recent method employing Soxhlet extraction of concrete, crushed to about 1/2 to 5/8 in pieces, has been proposed to determine water-soluble, available chloride.

2.10 Chloride Procedures

Sample. The sample may be chosen to represent the concrete as a whole or areas of a concrete core (e.g., the top inch). A ½" thick sample having a diameter three times the maximum aggregate size usually provides data sufficiently accurate for the purpose. The sample is pulverized to pass a No. 20 screen.

Quantitative Step. By far the most used, quickest, most accurate procedure, involves potentiometric titration of an acid solution employing a glass (pH) reference electrode and silver billet or other silver specific ion indicating electrode. Titration is with 0.1 M silver nitrate solution, using 0.2 ml increments. Alternatively, the titration can employ a colorimetric end point.

Water-Soluble Chloride. Immerse 10 grams of sample in 50 ml of water and allow to stand for 24 hours. Filter through a coarse paper, acidify with nitric acid, and titrate. The method of ASTM C1218 is applicable.

Acid-Soluble Chloride. Mix 10 grams of sample with 50 ml of 1:4 nitric acid solution. Filter through a coarse paper and titrate. The method of ASTM C1152 is applicable.

Total Chloride. Fuse 2 grams of sample, covered with a layer of calcium oxide, in a covered crucible. Transfer the melt to a beaker, add 25 ml of water, acidify with 50 ml of 1:4 nitric acid, filter through a coarse textured paper, and titrate.

Available Chloride. Crush the concrete sample to provide pieces about 1/2" to 5/8" in maximum size. Fill an extraction vial of 25 × 80 mm size or larger with a weighed amount of the crushed concrete and place in a Soxhlet extractor. Extract for 24 hours, acidify the extract and titrate. The method of the American Concrete Institute, ACI 222.1-96, is applicable.

@Seismicisolation

2.11 Sulfate and Sulfide Analyses

A sulfate analysis may be required to determine if sulfate has entered the concrete from the environment, if sulfate compounds (e.g., calcium sulfate hemihydrate-plaster) have been added to the concrete as an admixture, to determine cement content, or to determine reasons for unusual setting times.

Because most cements and aggregates do not contain sulfide sulfur, analyses for total sulfur are often an accurate measure of sulfate sulfur. Instrumental methods for sulfur, such as x-ray fluorescence or evolution-titration, are thus generally acceptable. However, if the result appears too high for the estimated cement contribution, sulfate analyses should be performed. The difference between total sulfur and acid-soluble sulfate determinations, each calculated as SO_3, is usually a measure of sulfide sulfur. Sulfide sulfur minerals may cause popouts or rust discoloration if they are close to the surface of a concrete member.

Sulfate Procedure. Digest 5 grams of concrete, pulverized to pass a No. 30 screen, in 20 ml of 1:4 hydrochloric acid solution. Filter through a coarse-textured paper inside or over a fine-textured paper into a 400 ml beaker. Determine sulfate by the procedures of ASTM C114 or as follows: place a small piece of filter paper in the beaker and hold down with a glass rod. Bring the solution to boiling and add drop-wise, through a pipet, 20 ml of barium chloride solution (10 g per 100 ml water). Boil until the white precipitate settles, then digest below boiling in the glass-covered beaker. Filter through a retentive filter paper, wash the paper 10 times with hot distilled water, place in a tared porcelain crucible, ignite over a flame without inflaming, then in a muffle furnace at 820°C. Weigh. Calculate SO_3 as 0.343 × weight of precipitate.

Sulfide Procedures. Sulfide may be determined by evolution of hydrogen sulfide using the procedure of ASTM C114. Alternatively, total sulfur may be determined by evolution/titration (e.g., LECO furnace) and sulfate sulfur by Sulfate Procedure. The difference between these values, both calculated as SO_3, multiplied by 0.4, is sulfide sulfur.

2.12 Water Analysis

Discussion. Analyses of hardened concrete for the original water content of the fresh concrete, in order to calculate water-cement ratio (w/c), are often requested because w/c is the best single measure of potential concrete strength. However, there has not been any chemical method

@Seismicisolation

developed that provides reasonable accuracy unless the original concrete components are available as standards. If one considers what water is present originally and what becomes of it, the difficulty of the analysis becomes clear:

The concrete mix contains sufficient water to render the aggregate "saturated surface-dry," plus "free water." Only the latter is the "w" of the w/c term. After casting:

- For most mixes, about half of the water evaporates, leaving holes of various sizes and shapes, some of which are connected to each other.
- Some of the water becomes loosely bound to the calcium silicates produced by the cement hydration.
- Some of the water becomes a component of crystalline compounds such as gypsum, ettringite, and calcium hydroxide.
- The crystalline water will not be driven off until the concrete is sufficiently heated, for example, to over 500°C (calcium hydroxide).
- Voids will also be present in the concrete due to incomplete compaction and to air-entrainment. Even in very good quality concrete, at least 1% entrapped voids is assumed in mix design. Concrete having 2 to 5% entrapped voids and 3 to 6% entrained air voids is not unusual. Free water did not occupy such voids when the concrete was placed.
- Some of the hydrate compounds, especially near surfaces, but to substantial depths in an old concrete structure, react with carbon dioxide in the air to convert the hydrates to carbonates. Thus calcium hydroxide converts to calcium carbonate within a few minutes at the concrete surface and even completely so over years or decades, depending upon the porosity of the concrete. The water liberated may evaporate from the concrete. No significant voids are produced (the reaction may involve a small volume change of the solids).

@Seismicisolation

Therefore, published methods that determine original water content by resaturating the concrete with water or other liquid and by heating to drive off free and combined water, do not properly account for aggregate water, carbonation, and compaction voids, among the major sources of error.

Experienced petrographers can estimate original water-cement ratio, at least between w/c values of about 0.35 to 0.75, using such optical and physical features as color, crystal size, hardness, and porosity. Such values are usually significantly more accurate than those determined chemically. Exceptions may occur if the original aggregate is available to determine the amount of water required to produce a saturated surface-dry condition and, if correction is made for compaction voids as estimated from petrographic measurements, such as by using the linear traverse procedure of ASTM C457.

Procedure for Water Content of the As-Is Hardened Concrete. The free water content of hardened concrete may be determined by drying in a vacuum, by desiccation, or by heating to 110°C.

The total water content is usually determined by heating to 600°C, which dehydrates most calcium silicate hydrates and calcium hydroxide, the major crystalline hydration product of portland cement. Some calcium silicate hydrates may not be dehydrated at this temperature. Ignition to 950°C will cause loss of carbon dioxide from carbonates and must be corrected for by determining carbon dioxide.

Sulfide sulfur will interfere by decreasing the ignition loss due to oxidation to sulfate. Sulfate determinations before and after ignition will provide a correction. Calculate sulfate in each determination as SO_3 and add the difference to the loss percentage.

Procedure for Water Content of Original Concrete Mix. As discussed in 2.12, a determination of the free water content of the original concrete mix, as based on analyses of the hardened concrete, is generally unadvisable. A petrographic estimate is often useful, especially because it is recognized as an estimate whereas a chemically determined value is often assumed, falsely in most cases, to be accurate. Accordingly, a detailed method will not be given here. If an analysis is decided upon, it should recognize all of the admonitions given in Sec. 2.12, and will be best made by trials with the concrete components used in the analytical sample.

2.13 Nitrate and Nitrite Analyses

Calcium nitrate is used as a set accelerator and its determination is frequently required. Nitrites are used as corrosion inhibitors. Both are best

@Seismicisolation

determined by water extraction and colorimetric methods, but anion exchange chromatography may also be used.

Nitrite Analysis. Water soluble nitrite in concrete usually represents total nitrite. A 2 gram sample is ground to 50 mesh and extracted three times with water, first with 200 ml for 30 minutes, then 200 ml for 10 minutes, and finally 100 ml for 10 minutes, filtering the decanted liquid through a fine filter paper into a 500 ml volumetric flask between extractions. An appropriate aliquot is taken and diluted to 50 ml in a 100 ml volumetric flask with water. The solution is pH-adjusted to between 6 and 7 using 1 N hydrochloric acid with phenolphthalein as an indicator. Sulfanilic acid solution and N-(1-naphthyl) ethylenediamine dihydrochloride reagent are added to develop the color. The absorbance of the solution is measured between 520 and 530 nm using visible spectroscopy.

Nitrate Analyses. Water soluble nitrate is determined using a 10 g sample of concrete and usually represents total nitrate. Extract the sample for 30 minutes with 75 ml of deionized water. Decant the liquid and filter through a medium filter paper. Extract the sample a second time with 50 ml of deionized water for 10 minutes. Filter through the same filter paper. Dilute to 200 ml. Adjust the pH of a 40 ml aliquot to between pH 6 and 7 using 5.25 N sulfuric acid. Determine nitrate concentration using a cadmium reduction method like Hach Nitrate HR or Nitrate MR methods. If nitrite is present, it will be determined as nitrate by this procedure and its concentration should be determined by 2.13 and subtracted out.

2.14 Organic Components

Discussion. In contrast to a few decades ago, concrete now usually contains one or more organic components. The cement may contain grinding aids, pack-set inhibitors, or air-entraining agents; however, the latter are now usually added to concrete by the ready-mix producer. Other admixtures added by the concrete producer now include water-repellents (e.g., stearic acid and stearate salts), set-retarding agents (usually carbohydrates), set-accelerators (e.g., triethanolamine), and workability aids (e.g., lignosulfonates). Recently, workability aids that allow large reductions in mix water content have been developed. This class of high-range-water-reducers or superplasticizers includes naphthalene and melamine sulfonate condensates.

Analyses for organic components are complicated by several factors including their low concentrations (stearates may be effective at concentrations of 0.01%), their breakdown or conversion to salts during exposure to

@Seismicisolation

the alkaline components of the portland cement paste, and their adherence to the silicate structure of the hydrated cement.

Further, the identities of the components of admixture may be a trade secret, although Material Safety Data Sheets (MSDS) may disclose some or all of their active components.

To determine these organic components, it is first necessary to extract them from the concrete. This may be done simply with water (e.g., carbohydrates), with sodium carbonate solutions (e.g., lignosulfonates), with organic solvents (e.g., stearates by chloroform) or, after acid-dissolution (e.g., conversion of stearate salts to stearic acid by digestion in hydrochloric acid), by extraction with a suitable solvent.

Recovery of the organic matter may be so complete that the analysis determines the concentration used in the mix. In many other cases, recovery is not 100% and, therefore, concrete standards must be made, preferably with the aggregates comparable to those used in the concrete. The concrete should be cured for a period approximating the life of the unknown concrete sample to be analyzed. After a period of about a month, recovery is often relatively constant, however, some admixtures may continue to degrade in a wet environment. Recognition of possible low recovery must be made.

Analytical procedures (e.g., infrared spectroscopy) may directly identify the organic components or may simply denote the presence or probable presence of an identifying characteristic or chemical component of the admixture (e.g., colorimetric analyses for sugars, or ultraviolet light spectroscopy for lignosulfonates).

2.15 Procedures

Procedures for determining several organic components in concrete have been detailed by Connolly, Hime, and Erlin.[11] That publication also reviews the literature. A summary of the methods is given below to allow the reader to determine the complexity of the analysis.

Several organic additives and admixtures for which methods have been developed are listed in Table 3, with literature references. The indicated methods for these components are given below.

Method 1, Acid-Chloroform Extraction. Dissolve at least 100 grams of the sample in dilute hydrochloric acid and extract with chloroform, using a separator funnel.

A further extraction of this extraction residue with hexane allows separation of plasticizers and oils.

@Seismicisolation

Table 3. Admixture Component Analysis Procedures and References

Component	Procedure	Ref.*
Acetate	Boiling Water Extraction (ethanol soluble)	
Acrylate	Acid-Chloroform Extraction and Acid Digestion/Thermogravimetric	
Alkyl aryl polyether	Acid-Chloroform Extraction	
Alkyl aryl sulfonate	Acid-Chloroform Extraction	
Fatty acid	Acid-Chloroform Extraction	
Fatty acid salts	Acid-Chloroform Extraction	
Formates	Boiling Water Extraction (ethanol soluble)	
Glycols	Boiling Water Extraction (ethanol and chloroform)	
Hydrocarbon oils	Acid-Chloroform Extraction (hexane soluble)	
Hydroxycarboxylic acids	Boiling Water Extraction	12
Hydroxycarboxylic salts	Boiling Water Extraction	
Lignosulfonates	Sodium or Potassium Carbonate Extraction at 340 nm	12, 13, 14, 16
Phthalate esters	Acid-Chloroform Extraction	
Resin acids and soaps	Acid-Chloroform Extraction	
Saccharides and sugars	Boiling Water Extraction	12, 15
Stearates		12, 14
Sulfonated melamine condensates	Sodium or Potassium Carbonate Extraction at 220 nm	
Sulfonated naphthalene formaldehyde condensate	Sodium or Potassium Carbonate Extraction at 230 nm	
Styrene butadiene	Acid-Chloroform Extraction and Acid Digestion/Thermogravimetric	
Triethanolamine	Boiling Water Extraction (ethanol & HCl)	10, 12
Vinyl compounds	Acid-Chloroform Extraction and Acid Digestion/Thermogravimetric	

*Methods for all listed components are given in the text and are detailed in Ref. 11.

The remaining residue may contain polymer modifiers, air-entraining agents and water-repellents. It can be analyzed by infrared spectroscopic methods for solids.

Method 2, Boiling Water Extraction. Extract with boiling water, evaporate to dryness and extract with ethanol.

@Seismicisolation

Treat the ethanol-insoluble portion with sulfuric acid and β-naphthol and digest in a boiling water bath. Measure the absorbance at 595 mm. This method is effective for some carbohydrate-based materials such as hydroxy carboxylic acids, corn syrups, and simple sugars.

Dry the ethanol-soluble portion and analyze the solids by infrared spectroscopy. This technique will detect acetates, formates, and glycols.

Extract a portion of the ethanol-insoluble portion with chloroform. Evaporate and analyze the residue by infrared spectroscopy.

Dry a portion of the ethanol extract and react with hydrochloric acid vapor. Analyze the acid-exposed portion by infrared spectroscopy.

Acid Digestion/Thermogravimetric Analysis. React a pulverized concrete sample with dilute hydrochloric acid. Filter off the solids, wash with water, and dry at 110°C. Weigh and ignite to 500°C for one hour. Determine loss on ignition. This technique is useful for polymer (latex solids) content.

Sodium or Potassium Carbonate Extraction. Extract the concrete or paste fraction with a 10% solution of sodium or potassium carbonate. Filter or centrifuge. Determine absorbances by ultraviolet spectroscopy.

Qualitative analyses for the extracted substances may be made by chromatographic separation with adsorption resins such as Amberlite XAD-2 or with an anion exchange resin such as DEAE Sephadex A-25. The chromatographed components are identified by infrared spectroscopy. This is an effective technique for qualitative analyses of lignosulfonates and naphthalene sulfonates.

2.16 Elemental Concentrations

The concentrations of most of the elements present in concrete can be determined by instrumental techniques. X-ray emission (fluorescence) provides accurate determinations of elements of atomic number above about 10, depending on the instrument, if good standards are available. Plasma and arc-spark spectrography generally provide lower accuracy for major components, but often very acceptable data for minor components.

For these instrumental methods use of NIST (National Institute for Standards Technology, formerly National Bureau of Standards (NBS)), standards is necessary for greatest accuracy. The present cement standards, Nos. 1880–1889, may be mixed with NIST mineral standards such as limestone (1c or 886), quartz (1413), or feldspar (70a or 99a), to as closely as possible match the matrix of the sample as estimated by x-ray diffraction or petrographic procedures.

@Seismicisolation

2.17 Compound and Mineral Compositions

The compound composition of concrete is best revealed by the use of x-ray diffractometry. Table 4 provides the d-spacings of most of the common components of portland cement concrete and the equivalent 2-theta angles for instruments using copper K-alpha radiation.

Table 4. Common Concrete Components and Their X-Ray Diffraction Spacing

Component	d-Spacings[1]	2-theta Angle[2]
Calcite (calcium carbonate)	3.04, 2.28, 2.10	29.40, 39.40, 43.14
Dolomite (calcium magnesium carbonate)	2.88, 2.19, 1.79	30.94, 41.13, 51.07
Ettringite (calcium sulfoaluminate hydrate)	9.72, 5.61, 3.87	9.09, 15.78, 22.94
Feldspars[3]	3.33, 3.20, 3.22, 3.26	26.70, 27.86, 27.68, 27.33
Gypsum (calcium sulfate dihydrate)	2.87, 4.28, 2.68	31.13, 20.74, 33.36
Portland cement[4]	2.78, 2.75, 2.61, 2.19	32.2, 32.6, 34.3, 41.2
Portlandite (calcium hydroxide)	2.63, 4.90, 1.93	34.09, 18.09, 47.12
Quartz	3.34, 2.56, 1.82	26.65, 20.85, 50.14

[1]*Three spacings of highest intensity*

[2]*Copper K-alpha radiation*

[3]*Approximate positions for major spacings of most feldspars*

[4]*Major spacing regions for unhydrated portland cement in concrete*

The use of x-ray diffractometry to determine the concentration of compounds or minerals in concrete is often unadvisable because of the lack of suitable standards, the impurity of minerals, crystal dislocations, and embedment of materials in other phases or in gels. The best examples of such effects are plaster or gypsum in portland cement or ettringite in concrete. In each of these examples, x-ray diffraction has been found to often underestimate or even not detect the substances, although they are shown to be present by other techniques.

For further information, see Ch. 9 on XRD.

@Seismicisolation

Differential thermal analysis (DTA) has been found to provide reasonable accuracy for the determinations of hydrated substances such as plaster and gypsum in cement and gypsum, monosulfoaluminate and ettringite in concrete. A standard addition technique provides the greatest accuracy.

Although each DTA instrument provides particular advantages such as ease of use, qualitative ability, accuracy, and cost, instruments that use several tenths of a gram of sample usually provide the best results.

Each instrument also provides exotherms and endotherms at different temperatures, however, the order of their appearance is the same for each instrument. Table 5 provides the more important thermal events for cement and concrete, as determined in the author's laboratory.

For further information, see Ch. 4, and the detailed book by Ramachandran.[17]

Table 5. DTA Peak Positions for Usual Concrete Components

Component	Peak Position[1] (°C)
Tobermorite (calcium silicate hydrate)[2]	130
Ettringite (calcium sulfoaluminate hydrate)	140
Gypsum (calcium sulfate dehydrate)	160
Amorphous hydrates	200–300
Syngenite (potassium calcium sulfate hydrate)	290
Brucite (magnesium hydroxide)	420
Portlandite (calcium hydroxide)	560

[1]*At 10°C per minute by DTA instrumentation used by author.*

[2]*Tobermorite (calcium silicate hydrate) - peak appears at about 120 to 130°C, or as a shoulder on the leading edge of an ettringite peak. Washing the sample with acetone and drying at 50°C maximum usually eliminates this peak, which may interfere in qualitative and quantitative analysis of ettringite.*

@Seismicisolation

Petrographic techniques are also useful in qualitative and semi-quantitative analyses for concrete components. Petrography can determine the presence of crystalline components (such as calcium hydroxide and ettringite) and of minerals such as limestone, as contrasted to calcium carbonate as produced by carbonation of calcium hydroxide. Petrography is the only technique that can readily identify such noncrystalline components as fly ash, and can provide a reasonable estimate of its concentration.

Petrographic methods must be supplemented by other techniques in some cases. For example, identifications of amorphous materials and of gels may require scanning electron microscopy (SEM) with its associated energy-dispersive x-ray analysis accessory. SEM can often allow identifications not possible by other procedures.

For further information, see chapter on "Petrography," and chapter on "Electron Microscopy."

3.0 MORTARS, GROUTS AND PLASTERS

3.1 Discussion

Analyses of mortars, grouts and plasters are generally made by the procedures detailed above for portland cement concrete. Although the absence of coarse aggregate simplifies the determination, component concentrations or proportions are complicated by the use in these materials of specialty cements and of additional components such as hydrated lime. For example, instead of portland cement, mortars are often made with masonry cements, and plasters with "plastic" cements. The former is often a mixture of portland cement, finely ground limestone, and an air-entraining agent, with 50 to 75% by weight being portland cement. The latter may also contain these components, but less limestone. Plasticizing substances may be present in either.

Unless cementitious materials are available for analysis or their components and concentrations known, an acceptable analysis is often not possible. Components may be identified and estimations of their concentrations may be made by an experienced petrographer and supplemented by XRD and DTA analyses.

Detailed procedures have been given by Hime and Erlin[18] and are presented in ASTM C 1324.

@Seismicisolation

REFERENCES

1. Figg, J. W., and Bowden, S. R., *The Analysis of Concretes*, Her Majesty's Stationery Office, London (1971)
2. SCI Monograph No. 18, *Analysis of Calcareous Materials*, London (1964)
3. Hime, W. G., Analyses for Cement and Other Materials in Hardened Concrete, Chapter 29 in ASTM STP 169C, *Significance of Tests and Properties of Concrete and Concrete-Making Materials*, (Paul Klieger and Joseph F. Lamard, eds.), ASTM, Philadelphia (1994)
4. Marusin, S. L., and Shotwell, L. B., Alkali-Silica Reaction in Concrete Caused by Densified Silica Fume Lumps, A Case Study, Supplementary Paper, *Fifth Canmet/ACI International Conference on Fly Ash, Silica Fume and Natural Pozzolans in Concrete*, pp. 45–49 (1995)
5. Gebhardt, R. F., Survey of North American Portland Cements: 1994, *Cement, Concrete and Aggregates*, 17:145–189 (1995)
6. *Concrete Admixtures Handbook, Properties, Science and Technology*, 2nd Edition, (V. S. Ramachandran, ed.), Noyes Publications, Park Ridge, New Jersey (1995)
7. Tabikh, A. A., Balchunas, M. J., and Schaefer, D. M., A Method for the Determination of Cement Content in Concrete, *Highway Research Board 370*, 1–7, Highway Research Board, Washington, D.C. (1971)
8. Clemena, G. G., Determination of the Cement Content of Hardened Concrete by Selective Solution, VHRC 72-R7, Virginia Highway Research Council, Charlottesville, Virginia (1972)
9. Pistilli, M. F., *Cement Content of Hardened Concrete*, presented at Cement Chemists Seminar, Portland Cement Association, Skokie, Illinois (1976)
10. Marusin, S. L., Use of Maleic Acid Method for the Determination of the Cement Content of Concrete, *Cement, Concrete and Aggregates*, pp. 89–92, (Winter, 1981)
11. Connolly, J. D., Hime, W. G., and Erlin, B., Analysis for Admixtures in Hardened Concrete, *Admixtures*, Concrete International 1980, Construction Press (1980)
12. Rixon, R. R., *Chemical Admixtures for Concrete*, E. and F. N. Span, London (1978)
13. Reul, H., Detection of Admixtures in Hardened Concrete, *Zement-Kalk-Gips*, 33 (3) (1980)
14. Shima, I., and Nishi, T., Determination of Saccharose in Hydrated Cement, *Semento Gijutusu Nempo*, 17:106–109 (1963); *Chemist Abstract* 61, 5344b (1964)

@Seismicisolation

15. Frederick, W. L., and Ellis, J. T., Determination of a Polyhydroxy Carboxylic Acid Retarder in Hardened Concrete, *Materials Research and Standards*, 8:14–18 (March, 1968)

16. Sanders, C. J., Jr., Sadeghi, S. S., and Nelson, N. C., Limitations of the Carbonated Extraction/UV Spectrophotometric Method for Determining Lignosulfonate-Based Admixtures in Hardened Concrete, *Cement, Concrete and Aggregates*, 17:37–47 (June, 1995)

17. Ramachandran, V. S., *Applications of Differential Thermal Analysis in Cement Chemistry*, Chemical Publishing Company, Inc., New York (1969)

18. Erlin, B., and Hime, W. G., Methods for Analyzing Mortar, *Proceedings, Third North American Masonry Conference*, Paper 63, The Masonry Society (1985)

@Seismicisolation

4

Thermal Analysis

Vangi S. Ramachandran

1.0 INTRODUCTION

An understanding of the complex physicochemical phenomena associated with the formation and behavior of cementitious compounds is facilitated through the application of many different types of investigative techniques. Techniques such as NMR, XRD, neutron activation analysis, atomic absorption spectroscopy, IR/UV spectroscopy, electron microscopy, surface area techniques, pore characterization, zeta potential, viscometry, thermal analysis, etc., have been used with some success. Of the thermal analysis techniques, the Differential Thermal Analysis (DTA) and to some extent, Thermogravimetric Analysis (TG) methods are more popularly used than others. They are more adaptable, easier to use, and yield important results in a short span of time. In this chapter the application of DTA will be highlighted and some work reported utilizing TG, conduction calorimetry, and other related methods will also be mentioned, with typical examples.

A substance subjected to thermal treatment may undergo physical or chemical changes as in dimension, magnetic susceptibility, weight, crystalline transition, mechanical property, acoustic property, heat effects, etc. In thermal analysis, these changes are followed as a function of temperature. It has been suggested that thermal analysis should also be extended to allow for rapid heating of the sample to some temperature followed by a measurement of the property with time under an isothermal condition.[1] In the quasi-static thermal analysis method, a substance is heated at known intervals of

@Seismicisolation

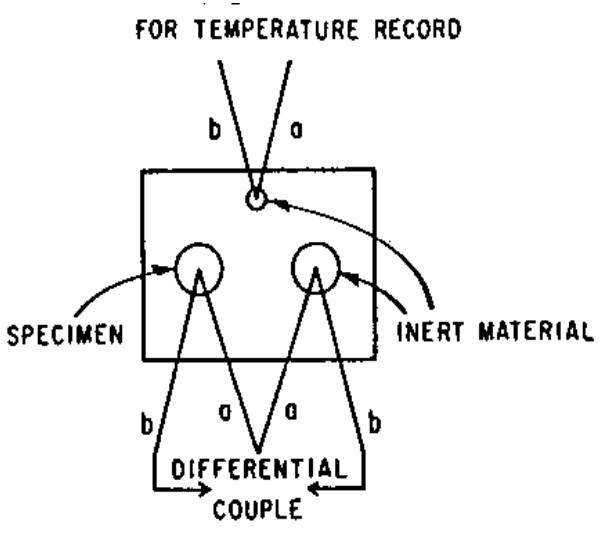
temperature for a few hours and a particular property is measured. In the dynamic method, such as DTA or TG, the property of a material is followed by continuous heating at a uniform rate.

In DTA the difference in temperature, ΔT, between the sample and a reference material such as αAl_2O_3 is recorded while both are subjected to the same heating program. In an endothermal reaction such as the decomposition of calcite or melting of a material, the temperature of the sample, T_s, will lag behind the temperature of the reference, T_r. The output, $\Delta T = T_s - T_r$ is recorded as a function of T_r. Figure 1 shows the blocks containing the specimen, the inert material, and how the thermocouples are connected. Thermocouples are so connected as to obtain both the temperature T_r of the inert material and the differential temperature ΔT, which is actually the difference in temperature between the sample and the inert material.

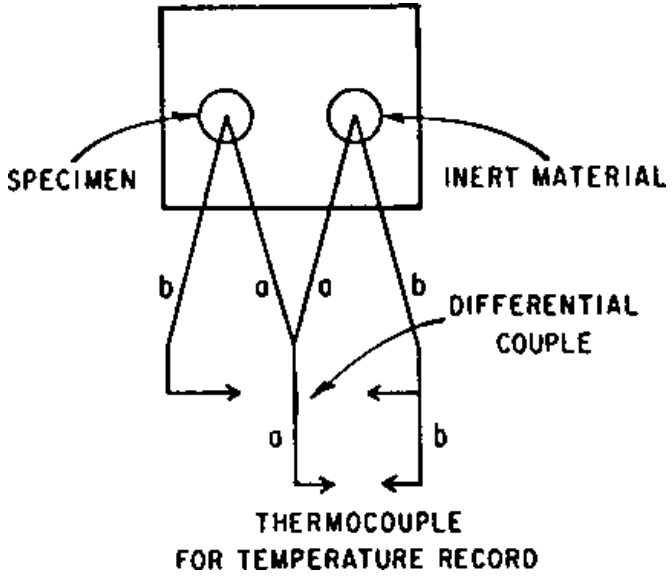
Generally, the temperature (x-axis) is plotted against the ΔT on the y-axis. The exothermal effects are shown upward and the endothermal effects downward with respect to the base line. In the DTA literature, thermal effects are reported in terms of the characteristic temperature, peak temperature, temperature range of the peak, peak width, peak amplitude or height, and peak area. By determining the nature of the peak (endothermic or exothermic), the temperature of the characteristic peak, and other general characteristics, it is possible to utilize DTA for both qualitative and quantitative purposes. By heating the binary or ternary mixtures in the DTA apparatus, the sequence of reactions during heating may also be followed. Many factors, such as the type and size of sample holder, furnace, thermocouple, rate of heating, sensitivity of the recording system, degree of dryness of the sample, the amount of sample, particle size and crystallinity, packing density, thermal conductivity, and shrinkage or swelling of the sample, will affect the results. The usefulness of DTA is further enhanced with the development of multipurpose types of equipment which incorporate one or more types of adjunct techniques to DTA. Examples are: DTA-Effluent Gas Analyzer, DTA-Mass Spectrometer, DTA-DTG-TG, DTA-TG-Radioactive Emission, DTA-TG-Dilatometer, DTA-XRD, etc.

Differential Scanning Calorimetry (DSC) has also been used in cement science investigations to some extent. It is based on a power compensated system. In this technique, the reference and the sample under investigation are maintained at a constant temperature throughout the heating schedule. The heat energy required to maintain the isothermal condition is recorded as a function of time or temperature. There are some similarities between DTA and DSC, including the appearance of thermal curves. DSC can be used to measure the heat capacities of materials. DSC measures directly the heat effects involved in a reaction.

@Seismicisolation



(a)



(b)

Figure 1. The specimen holder and connections in DTA.

@Seismicisolation

In Thermogravimetric Analysis (TG) the weight changes are determined as the sample is heated at a uniform rate. It differs from the semi-static or static method in which the sample is held at a constant temperature for a required period of time. In concrete investigations, TG is commonly used with DTA to follow the hydration reactions. The first derivative of change of mass (DTG) can also be used for identification purposes as it yields sharp peaks. TG cannot detect crystalline transitions as they do not involve weight losses.

Conduction calorimetry is another technique that is extensively used for following the hydration reactions of cement and cement compounds. In this method, heat evolved during the hydration reactions is followed as a function of time from the moment water comes into contact with the cement. The curves are obtained under isothermal conditions. This technique can also be used to study the rate of hydration at different temperatures. Conduction calorimetry has been used to determine kinetics of hydration and for studying the role of admixtures, relative setting times of cement, and for identification purposes.

A few other thermal techniques, such as thermochemical analysis, dilatometry, emanation analysis, etc., are only used to a limited extent in concrete investigations.

2.0 CEMENT CLINKER

The raw mix for the production of cement clinker comprises calcareous and siliceous materials. The siliceous clay raw material may contain one or more types of clay minerals. The clay mineral kaolinite, containing mainly alumina and silica, is a desirable material for the production of white cement. The montmorillonitic clay may be used provided it satisfies the chemical requirements. Illitic clays are suitable if they do not have excessive amounts of alkalis. Nontronitic clays are not suitable because they contain excessive amounts of iron. DTA can be applied to identify and estimate various types of clays and calcareous minerals (Fig. 2). These minerals can be differentiated by determining the temperature at which the endothermic and exothermic peaks occur. For example, kaolinites exhibit an endothermic peak at 550°–600°C due to the dehydration effect, followed by an exothermic peak at about 980°C associated with the formation of γAl_2O_3 or nucleation of mullite. Illites exhibit endothermal effects at 100–200°C, 500–650°C, and at about 900°C, and an exothermic peak immediately following the third endothermal peak. The first endothermal peak corresponds to the loss of interlayer, the second and the third to expulsion of water

@Seismicisolation

from the lattice and destruction of illite lattice, respectively. The exothermic peak is probably associated with the formation of a spinel. Illite differs from kaolinite in showing additional endothermal peaks at 100°–200° and 900°C.

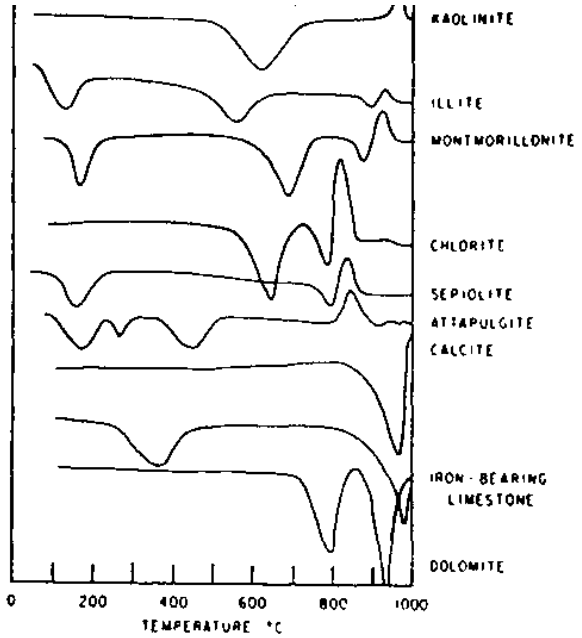


Figure 2. DTA of some raw materials for the manufacure of cement clinker.

DTA has been used to study the mechanism of the clinkering reaction and to establish the burnability of the raw mix. High temperature DTA is a useful tool for comparing the burnability of different raw materials. Figure 3 shows a typical DTA curve of an industrial raw meal.[2]

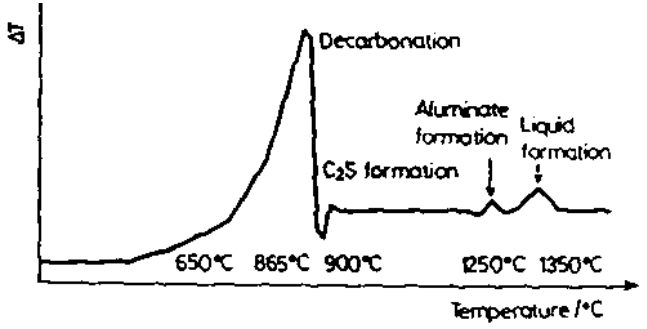


Figure 3. Typical DTA curve of an industrial portland cement raw mix.

@Seismicisolation

Four thermal peaks are evident in the curve. The first endothermal effect below 900°C can be attributed to the decarbonation of calcium carbonate. A small exothermal peak following this endothermal effect is ascribed to the formation of C_2S. The formation of aluminate and calcium aluminate ferrite phases is indicated by small heat effects and the liquid formation is indicated by a high temperature endothermal effect. The position and the intensity of the peaks are good indicators of the burnablity of the raw materials. By applying the thermodilatometry, the temperature of liquid formation and its quantity can be determined. The following clinkerization processes may be delineated through the application of DTA/TG: *(a)* calcination kinetics of raw mixes by calculation of rate constants and activation energies; *(b)* quantification of the raw materials in the mix: *(c)* determination of the practical heat of clinker formation; and *(d)* prediction of material temperature profile in a dolomite kiln.[3]

In the production of sulfo-aluminate cement from raw materials such as limestone, bauxite, and anhydrite, DTA has been used to monitor the reactions that take place when these mixes are heated to a temperature of 1025°C. By applying DTA and XRD it was found that the dehydration and decomposition of bauxite occurs at 530°C. At about 900°C, calcium carbonate is decomposed to CaO and it reacts with αSiO_2 to form C_2AS. At a higher temperature, C_2AS reacts with $CaSO_4$ to form calcium sulfo-aluminate and αC_2S[4]. Thermal analysis has also been applied to investigate the reactions occurring in the formation of a clinker from calcium carbonate mixed with CMS_2, C_3AS_3, and NAS_6[5].

There has been a continued interest in producing cement clinker at lower temperatures than what has been the normal practice. A study of binary and ternary systems containing limestone, alkaline basalt, and fluorite has been conducted to investigate the possibility of obtaining belite and alite at lower temperatures.[6] The reaction was followed by DTA, DTG, and TG. Several endothermal and exothermal peaks were obtained. Decarbonation occurred at about 650°C, a peak at 1145°C was linked to the formation of $C_{12}A_7$ and gehlenite, and the peak at 1170°C was attributed to the formation of belite, and that at 1235°C to the formation of alite.

Fluxes are compounds that are added to the raw mix to promote formation of certain products at lower temperatures. The effect of different amounts of a mineralizer fluorspar (CaF_2) on the temperature of formation of silicates in the manufacture of white cement has been investigated utilizing DTA and XRD. Increasing the amount of fluorspar reduced the temperature of formation of the melt and cement mineral formation. For

@Seismicisolation

example, the C_3S exotherm occurring at 1206°C was decreased to 1150°C by the addition of 0.25% fluorspar.[7]

Extensive work has been carried out on the utilization of waste and by-products in concrete industry. The utilization of cement kiln dust is an example of a waste material that is also a large source of pollution at the cement plant. In an investigation, a mix of kiln dust and kaolin were fired up to 1250°C and the resulting phases were studied by DTA and XRD.[8] Several peaks (two exothermal and five endothermal) were obtained in DTA. The DTA examination revealed that the dust consists of dolomitic limestones with some alkalis and quartz. At 1000°C, βC_2S formed as the main phase with some $C_{12}A_7$ and C_4AF and at 1100°C spurrite decomposition occurred. At 1250°C gehlenite was formed. This study was useful in assessing the temperature to which the dust should be calcined so that the resultant product could be utilized for making porcelain.

Although most cement clinkers are manufactured utilizing the rotary kilns, in some countries vertical kilns have been used. In addition to the mechanism of clinkering, the heating and cooling schedules in these two types of kilns are different. A study was undertaken to determine the difference in reactivities of the clinkers produced by these two methods by applying the DTA technique.[9] By conducting DTA of clinkers hydrated for various periods, it was concluded that the rate of hydration, as determined from the peak intensities of $Ca(OH)_2$, was lower for clinkers made in the rotary kiln.

Portland cement clinker takes up sulfate from the raw materials and fuel to form solid solutions. The setting properties of the cement are affected by the amount of substitution and the type of sulfate that reacts with the clinker minerals. Koo, et al.,[10] prepared clinkers containing 1–6% SO_3 by using sulfates such as ammonium sulfate, potassium sulfate, calcium sulfate, and sodium sulfate. The resultant clinkers were subjected to hydration studies involving conduction calorimetry and DTA. The hydration of alite was accelerated in substituted clinkers made with calcium and ammonium sulfates, but the hydration of the aluminate phase was unaffected. Potassium sulfate addition increased the rate of hydration of alite, but decreased the rate of hydration of the aluminate.

3.0 SYNTHESIS OF CEMENT PHASES

DTA of binary, ternary, and quarternary systems of relevance to clinkers has been examined. Mixtures containing various proportions of oxides such as calcium oxide, aluminum oxide, ferric oxide, and silica, are

@Seismicisolation

heated to high temperatures in the DTA apparatus and the endothermal and exothermal effects that develop are analyzed. In the heating of kaolin-lime mixtures, gehlenite (C_2AS) and a small amount of βC_2S were detected at 900°C. At 1050°C, formation of $C_{12}A_7$ was reported. At the temperatures of 1100°C and 1400°C, C_3A and C_3S were formed, respectively.[11] In the thermograms of $Ca(OH)_2$-SiO_2 mixtures, several endothermal and exothermal effects result and that can be attributed to the formation of βC_2S, γC_2S, $Ca(OH)_2$, etc.

DTA has been applied to investigate the efficiency of silicate materials to form C_3S when they are heated with CaO. In Fig. 4, thermograms of mixtures of CaO and siliceous materials such as silica gel, quartz, silica glass, αCS or βCS (synthetic glass), C_3S_2 and γC_2S are given.[12] The weak endotherms at about 1175K and 1225K may be attributed to C_3S transition. The endothermal inflection at about 1700K corresponds to the α' to αC_2S transition. By determining the peak intensities of the endothermal effects due to C_3S transitions, it is possible to assess the relative amounts of C_3S formed in various mixes. The results show that the largest amount of C_3S is formed in the mixture γC_2S+CaO and the lowest in the silica gel+CaO mixture.

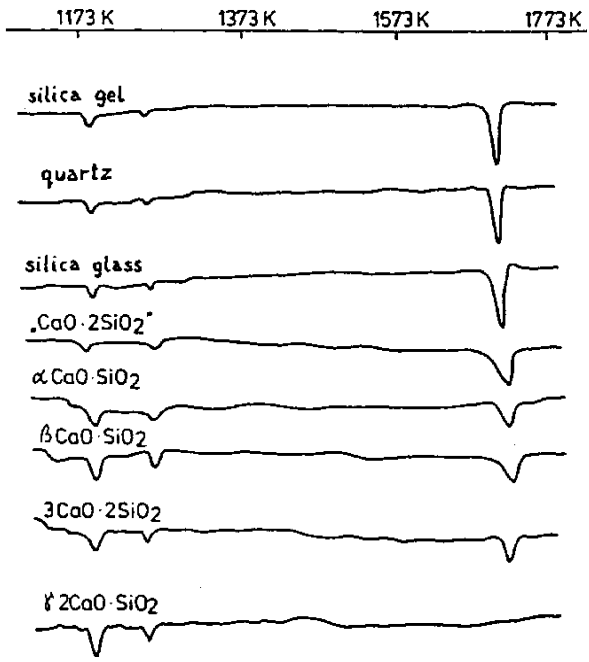


Figure 4. DTA curves of CaO heated with various siliceous materials.

@Seismicisolation

Another application of DTA is the assessment of the influence of mineralizers such as ZnO, CuO and MnO_2 on the formation of alite from a mixture of calcium carbonate and a silica-bearing material such as the rice husk ash.[13] Lithium carbonate is used to lower the decomposition temperature of calcium carbonate in the reaction of $CaCO_3$ with quartz. DTA-DTG of mixtures of $CaCO_3$ and quartz containing different amounts of lithium carbonate (equivalent to 0.1–5% Li_2O) was examined up to a temperature of 1450°C.[14] The decomposition temperature of calcium carbonate was lowered as the amount of lithium carbonate was increased. The CaO formed from the decomposition of the carbonate combined with SiO_2 to form C_2S. At 1% Li_2O, βC_2S formed, even at a temperature of 750°C, but the reaction was completed only at 1350°C. At an additional level of 5%, the final reaction temperature decreased to 1250°C. In terms of the decomposition of $CaCO_3$, at Li_2CO_3 contents of 0.5, 1, and 5%, approximately 2, 6, and 80% $CaCO_3$ decomposed at about 600°C.

In the system $CaCO_3$-Al_2O_3, exothermal effects due to the formation of CA and $C_{12}A_7$ have been detected. In the system containing CaO and Fe_2O_3, independent of the proportion of CaO and Fe_2O_3, CF forms at about 950°C. Melting occurs at 1150°C, which is reflected as an endothermal effect. An endothermal effect at 1300°C signifies incongruent melting of the mix. Some work has also been carried out by Barta on the ternary system containing calcium oxide-aluminum oxide-ferric oxide mixtures (Fig. 5).[11] Formation of C_4AF with an exothermal peak around 980°–1000°C and of C_2F with an endothermal peak at 1160°C is evident. At higher temperatures, $C_{12}A_7$ is formed.

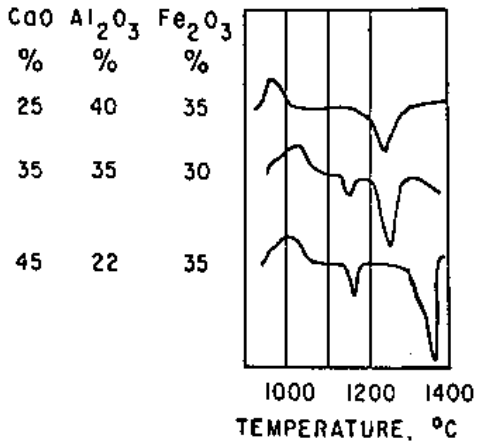


Figure 5. Thermograms of ternary mixture containing CaO, Al_2O_3, and Fe_2O_3.

@Seismicisolation

4.0 POLYMORPHISM IN SILICATES

Tricalcium silicate exists in several polymorphic forms. It can be triclinic, monoclinic, or trigonal. The stability of polymorphs and their transitions are temperature dependent and not easy to determine because many forms have small transition enthalpies. The triclinic form, T_I, can be stabilized with chromium oxide, the triclinic form, T_{II}, by ferric oxide, the monoclinic form, M_I, by MgO and monoclinic, M_{II}, form by zinc oxide.[15] The monoclinic form is present in commercial clinkers and only rarely has the rhombohedral form been detected.

The earliest studies on the thermograms of tricalcium silicate preparation and alites were carried out by Jeffery.[11][11a] Figure 6 compares the DTA curves of alite and a synthetically prepared tricalcium silicate. The C_3S preparation exhibits as many as six endotherms at 464, 622, 750, 923, 980, and 1465°C. The peak at 464°C is caused by the calcium hydroxide formed from the hydration of free lime present in the preparation. Dicalcium silicate, present as an impurity, exhibits three peaks at 622, 750, and 1465°C. The peaks at 923°C and 980°C are attributed to triclinic-to-monoclinic, and monoclinic-to-trigonal, or triclinic-to-trigonal and trigonal-to-trigonal transition plus rotation of ions, respectively. The thermogram of alite differs from that of the synthetic silicate by having only two endotherms at 825 and 1427°C. The effect at 825°C is ascribed to monoclinic to trigonal transition and corresponds to a similar effect in synthesized tricalcium silicate. This effect occurs at a lower temperature owing to the solid solution effect. In the cooling cycle, the endothermal effects show up as exothermal effects, indicating reversibility. More recently other investigations have been carried out on calcium silicates by applying different techniques and the temperatures of transitions may be at some variance from other published data. The variation in such effects is expected because the behavior of the silicate depends on the type of stabilizer used.

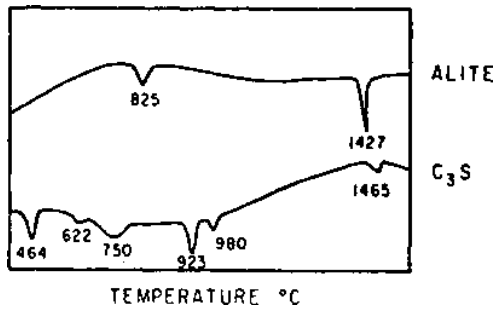


Figure 6. Thermograms of alite and synthesized tricalcium silicate.

@SeismicIsolation

Several polymorphic forms of dicalcium silicate are reported. Except γC_2S, all other forms are stable at high temperature. Basically the forms are α, α', β, and γ, and typically, compounds such as calcium phosphate, strontium oxide, boron oxide, and alkalis are capable of stabilizing them, respectively. Thermal behavior of dicalcium silicate has been studied both during heating and cooling cycles[11][11b](Fig. 7). Curve *A* shows the thermogram of γC_2S. The endothermal hump between 780 and 830°C indicates a sluggish transition of γ to $\alpha' C_2S$. At 1447°C the sharp endothermal effect can be correlated with the conversion of α' to αC_2S. The thermal effects are reversible, as indicated by the cooling curve, *B*. The exothermic peak at 1425°C indicates conversion of α to α' form and that at 670°C is due to α' to β transition. In addition, there is an irregular exothermal dent starting at 525°C for the β to γ inversion and this effect is accompanied by a sudden increase in volume of the mass. Curve *C* shows the behavior of βC_2S stabilized by CaO. The endotherms at 705° and 1447°C are, respectively, due to β to α' and α' to α transitions. The transition data of different forms of C_2S reported in the literature show some variation.

Not much work has been carried out on the thermal behavior of polymorphic forms of other phases in cement utilizing thermal techniques.

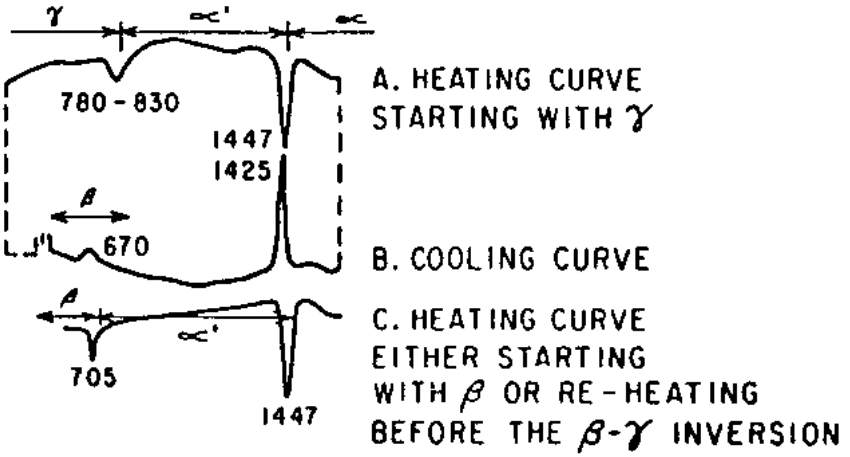


Figure 7. Inversions in dicalcium silicate.

@Seismicisolation

5.0 HYDRATION OF CALCIUM SILICATES

A knowledge of the hydration of individual cement compounds and their mixtures forms a basis of interpreting the complex reactions that occur when portland cement is hydrated under various conditions. Tricalcium silicate and dicalcium silicate together make up 75–80% of portland cement. In the presence of water the reaction products are calcium silicate hydrate (endothermal effects below 200°C) and calcium hydroxide, with an endothermal effect in the range 450–550°C. Some calcium carbonate may also be detected in the range 750–900°C by an endotherm. Under normal conditions of hydration it is difficult to prevent some carbonation of lime that is formed. At higher temperatures, some peaks may occur due to crystalline transformations. The calcium silicate hydrate is poorly crystallized and gives only weak diffusion lines in XRD. During the course of hydration, the degree of hydration may be estimated by determining the amount of lime formed, or non-evaporable water content, or by the amount of tricalcium silicate that has reacted. Several types of methods have been adopted to determine the degree of hydration, but each has its limitations. Thermal analysis techniques such as DTA, DSC, TG, and conduction calorimetry are found to be convenient, fast, and accurate, and yield results that are not easily obtainable by some other methods. Thermal techniques have been used to study kinetics of hydration, mechanism of hydration, the influence of admixtures, identification of new compounds formed, estimation of products, etc.

Conduction calorimetry of C_3S and cement shows five steps during the hydration process (Fig. 8). In the first stage, as soon as C_3S or cement comes into contact with water Ca and OH ions are released into the solution phase. This is followed by a rapid release of heat that ceases within 10–12 mins. This is called a *preinduction period.* In the second stage, the reaction rate is slow and it is known as the *dormant* or *induction period.* This may be extended or shortened by a few hours by the use of admixtures. In the third stage, the reaction proceeds rapidly and accelerates with time, releasing a maximum amount of heat at the end of the *acceleratory period.* At this stage, a rapid crystallization of CH and C-S-H occurs. In the fourth stage, there is a slow deceleration. At the final stage there is only limited formation of products and, at this stage, the reaction is diffusion-controlled. Conduction calorimetry permits determination of the rate of hydration as a function, temperature, water:cement ratio, type of admixture, particle size, pH, etc.

@Seismicisolation

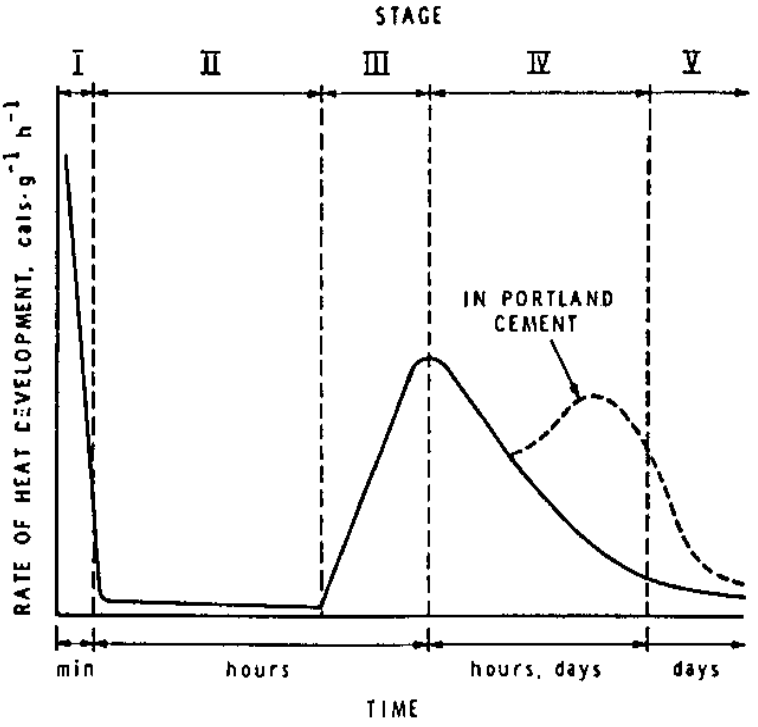


Figure 8. Conduction calorimetric curves of hydrating tricalcium silicate and cement.

Admixtures are added in small amounts to concrete to derive various beneficial effects. When assessing a number of potential chemicals as admixtures, it is convenient to apply thermal techniques to investigate the effect of various concentrations of admixtures and other parameters on the hydration of silicates and cement. In an example, the relative effects of various chemicals on the hydration of tricalcium silicate phase were studied by conduction calorimetry (Fig. 9).[16] The organic compounds, such as para, meta, and ortho nitrobenzoic acids affect the hydration of C_3S differently. The reference C_3S containing no additive (curve a) indicates a peak effect at about 7½ hrs. By the addition of acids, the peak occurs either earlier or later, depending on whether the hydration is accelerated or retarded. Of the additives p-nitrobenzoic acid (curve e)behaves as the best accelerator because not only does the peak occur earlier, but also its intensity is greater than that produced by the reference material.

@Seismicisolation

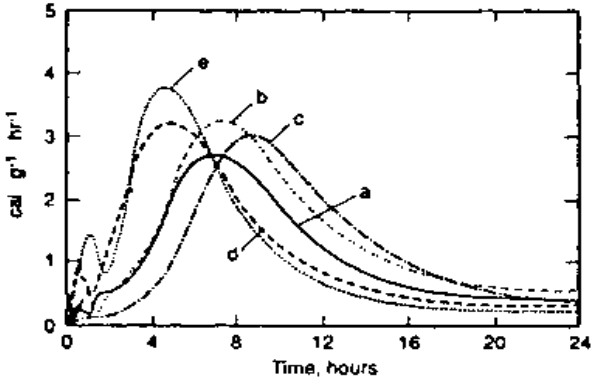


Figure 9. Conduction calorimetric curves of tricalcium silicate hydated in the presence of nitrobenzoic acids.

One of the methods of following the degree of hydration as a function of time is by the determination of the calcium hydroxide content. Figure 10 compares the relative amounts of calcium hydroxide formed at different times of hydration, using DTA and chemical methods. Although the general trend of the curves is similar, the values derived from the chemical analysis are somewhat higher than those from the thermal method. This may be due to attack of the C-S-H phase by the solvents used in the extraction of lime that is adopted in the chemical method.[17]

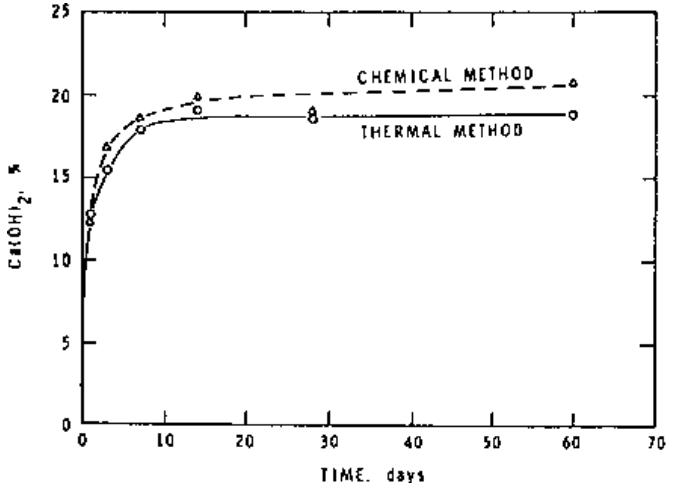


Figure 10. Amounts of $Ca(OH)_2$ formed in the hydration of C_3S.

@Seismicisolation

DTA is a convenient method to follow the hydration of C_3S as a function of time. In Fig. 11, the onset of hydration is evident from the small endothermal effect below 200°C.[18] This effect is caused by the removal of loosely bound water as well as firmly held water from the C-S-H gel. The increase in the intensity of this effect with time is indicative of increased formation of the C-S-H product with time. A very small endothermal effect at about 480°C appears within a few minutes, becomes more evident at 1 hr and is attributed to the dehydration of $Ca(OH)_2$. In the first eight hours, the amount of $Ca(OH)_2$ produced is about 25% of that formed in 30 days.

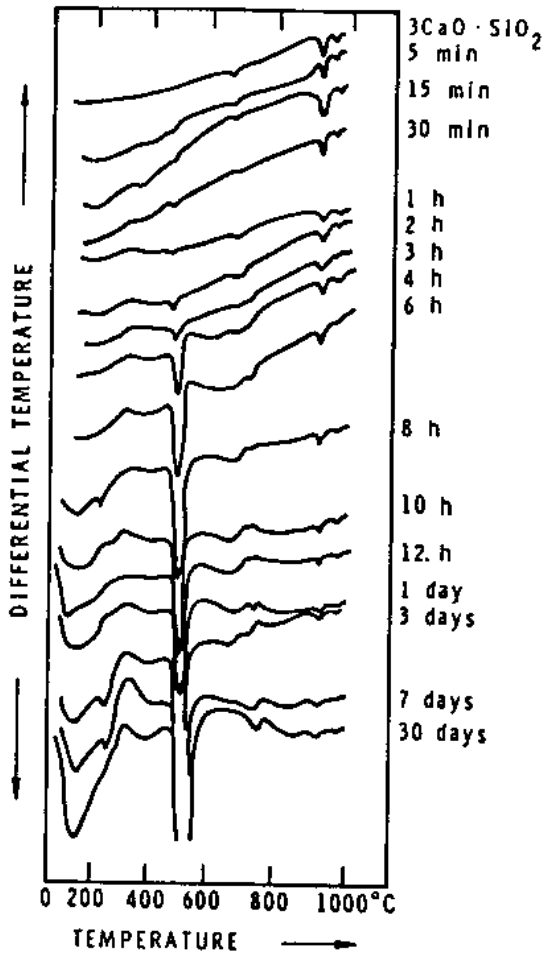


Figure 11. DTA curves of $3CaO{\cdot}SiO_2$ hydrated in water.

@Seismicisolation

A direct method of determining the degree of hydration of C_3S is to estimate its amount during the progress of hydration. Ramachandran[19] has provided a method to estimate tricalcium silicate using the DTA method. In this method, tricalcium silicate is heated to a temperature of 1000°C, cooled to 800°C, and reheated. This permits determining the intensity of the reversible transition of C_3S occurring at 915°C and this represents the amount of C_3S present in an unhydrated form. Applying this method, Mascolo and Ramachandran[20] compared the strength development in C_3S, containing Al, Mg, or Fe substitutes at different degrees of hydration (Fig. 12). At the same degree of hydration Fe-alite shows the greatest strength.

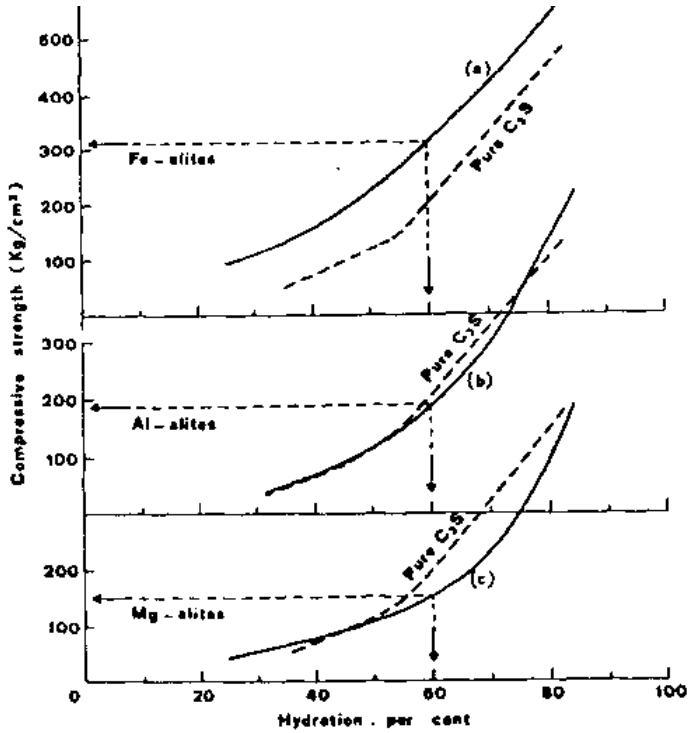


Figure 12. Kinetics of hydration of alites.

In the determination of the constitutional water associated with the C-S-H phase, it is important to differentiate the unreacted water from that which is bound by the gel. Feldman and Ramachandran[21] carried out

@Seismicisolation

TG/DTA of a bottle-hydrated C_3S that was conditioned at several humidities for lengthy periods, starting from the D-dry, 100%RH, and 11%RH. It was determined that the stoichiometry of the bottle-hydrated C-S-H gel at 11%RH (approached from 100%RH) is $3.28CaO{\bullet}2SiO_2{\bullet}3.92H_2O$.

The DTA technique is convenient for studying the effect of admixtures on the hydration of C_3S. This can be illustrated by comparing Figs. 11 and 13.[18] Figure 11 pertains to the DTA curves of the reference silicate and Fig. 13 to the silicate containing 1% $CaCl_2$. In the presence of chloride, the thermograms show significant differences. The endothermal peaks below 200°C in the presence of chloride are much larger than those obtained in the hydration of C_3S without any addition (Fig. 11). An endotherm appearing at 550°C up to 2 hrs in the presence of the chloride is absent in the reference material. There is also evidence that the endothermal effect due to $Ca(OH)_2$ is more intense in samples containing calcium chloride than without it. The onset of an intense exothermal effect at 690°C is always followed by a large endothermal dip at about 800–840°C. There is suggestion that it may be related to the chemisorbed chloride on the C-S-H phase and by presence of the chloride ions in the interlayer positions. The detailed mechanism is not clear. Many other studies have been reported on the application of DTA to cement-admixture systems, including two reviews.[22][23]

The DTG method can also be applied with success to estimate calcium hydroxide in a hydrated silicate system as the dehydration of calcium hydroxide is attended by a loss of water. DTG technique is also well suited to study the influence of admixtures on the hydration of cement components. Lignosulfonates are good retarders for the hydration of silicates. The lignosulfonates invariably contain some sugars. Since sugars are good retarders, it is proposed that the main retardation action of lignosulfonates is caused by the sugars contained in them. In Fig. 14, the DTG of C_3S hydrated with and without sugar-free lignosulfonate (NLS) is given. The curves show that the sugar-free lignosulfonate almost completely stops hydration up to 14 days, whereas the sample without the admixture exhibits endothermal effects caused by normal hydration.[25][25a] Ramachandran[24] applied the DTA technique and found that the sugar-free lignosulfonate is an efficient retarder.

Some work has been carried out using DTA/TG for identifying the admixtures directly. Khorami and Aitcin[26] have used these techniques to classify superplasticizers. They could successfully differentiate six industrial superplasticizers because the thermal stability and behavior of these superplasticizers showed differences.

@Seismicisolation

A combination of DTA and TG has been used to determine the CaO/SiO_2 ratio of the C-S-H product obtained in the hydration of tricalcium silicate in the presence of calcium carbonate.[27] TG was used to determine the ignited weight and percentage of $Ca(OH)_2$ formed at different periods of hydration. DTA estimated the amount of unhydrated C_3S remaining in the sample. The CaO/SiO_2 ratio was obtained by the applying the equation: $3–3.081\ m_3/m_2\text{-}m_4$, where m_2 is the ignited weight, m_3 is the percent calcium hydroxide, and m_4 is the percent unhydrated C_3S. The C/S ratios are shown as a function of time in Fig. 15. The ratio increases more significantly between 1 and 3 days than at later periods. There is evidence that the paste containing calcium carbonate has a slightly higher C/S ratio than that without it.

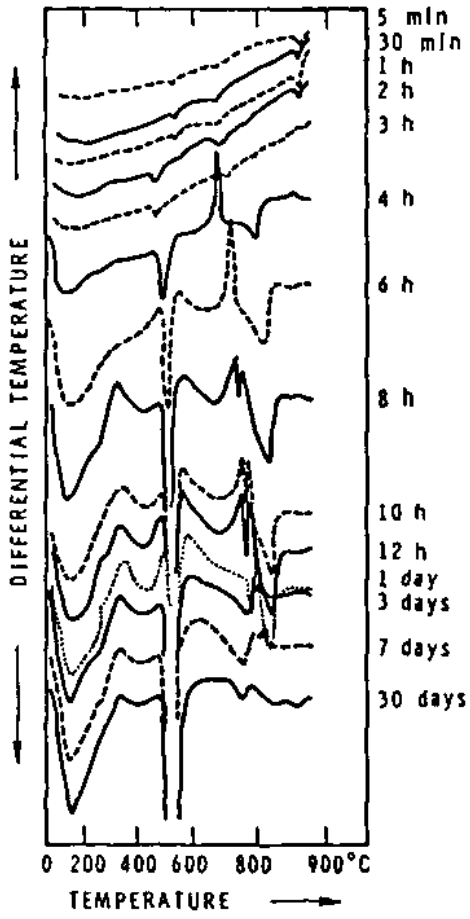


Figure 13. Hydration of $3CaO{\cdot}SiO_2$ in the presence of 1% calcium chloride.

@Seismicisolation

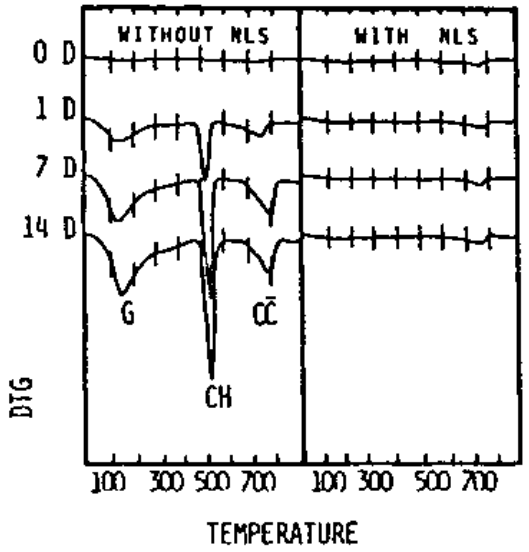


Figure 14. DTG curves for anhydrous and hydrated C_3S with and without 0.3% sugar-free sodium lignosulfonate.

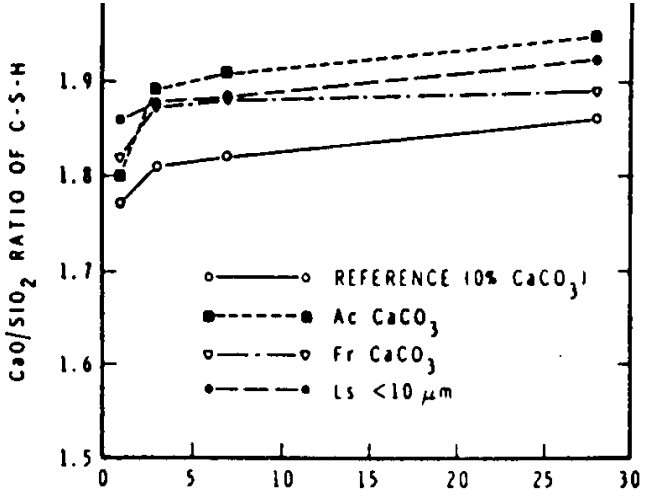


Figure 15. CaO/SiO_2 ratios of C-S-H formed during the hydration of C_3S.

The DTA/TG may also be used to derive kinetic parameters during the hydration processes. Chen and Dollimore[28] for example, found that the activation energy value of CH formation during the hydration of C_3S was increased by the addition of $Ca(NO_3)_2$. Calcium nitrite is known to be an accelerator for the hydration of silicates.

@Seismicisolation

A mature hydrated silicate paste contains both the C-S-H and CH phases. Any characterization study of the C-S-H phase is not easy because of the possible interference due to the presence of calcium hydroxide. A procedure has been developed by Ramachandran and Polomark for extracting calcium hydroxide from the C_3S paste without affecting the C-S-H phase.[29] It involves exposing a thin disc of the paste to an aqueous solution of calcium hydroxide in such a way that the concentration of the solution remains in the range 9–12 m·mol CaO/dm^{-3} throughout the extraction period. Calcium hydroxide remaining in the solid is monitored by DSC and further extraction is stopped when the amount of free lime remaining in the solid is almost nil.

Thermal analysis data on dicalcium silicate is sparse because it is time-consuming to follow the reaction of this phase, which is very slow. The characteristic products obtained during its hydration are not much different from those formed in C_3S hydration. Also, the major strength development that occurs in cement in the first 28 days (a period of practical significance) is mainly due to the tricalcium silicate phase. In Fig. 16, the influence of triethanolamine on the hydration of C_2S is given. In the absence of the admixture, even at 1 day the development of calcium hydroxide is evident by an endothermal peak just below 500°C. At any stage of hydration, the intensity of the endothermal peak is much lower in samples containing the amine, indicating a retardation effect. Thermograms also reveal a secondary endothermic effect in samples containing the amine. This indicates the possibility of formation of a microcrystalline or amorphous form of calcium hydroxide in samples with the amine.[22]

6.0 HYDRATION OF C_3A AND C_4AF

The aluminate phases, although present in small amounts, exert a significant effect on the setting and early strength development in cement pastes. In the hydration of tricalcium aluminate, the initial formation of hexagonal phases is identifiable by the endothermal effects at 150–200°C and 200–280°C. These are converted to a cubic phase of formula C_3AH_6. The cubic phase shows characteristic endothermal effects at 300–350°C and 450–500°C. Addition of admixtures influences the rate of formation of these phases and their interconversion. For example, in the presence of lignosulfonate, retardation of hydration as well as retardation of the

@Seismicisolation

conversion of the hexagonal phases to the cubic results. The hexagonal phases may be stabilized at least up to 14 days with lignosulfonate, whereas in that hydrated without the admixture, the cubic form appears even at 6 hours (a peak in the thermogram at 300°C) (Fig. 17).[22]

The alkali in the clinker is combined as a solid solution with the C_3A phase. The crystalline structure changes from cubic to orthorhombic or monoclinic structure, depending on the content of Na in the C_3A phase. Shin and Han[29a] studied the effect of different forms of tricalcium aluminate on the hydration of tricalcium silicate by applying DTA, TG, and conduction calorimetry. It was concluded that the hydration of tricalcium silicate is accelerated when orthorhombic, monoclinic, or melt C_3A was present in the mixture. The cubic form of tricalcium aluminate was least effective for accelerating the hydration of the silicate phase.

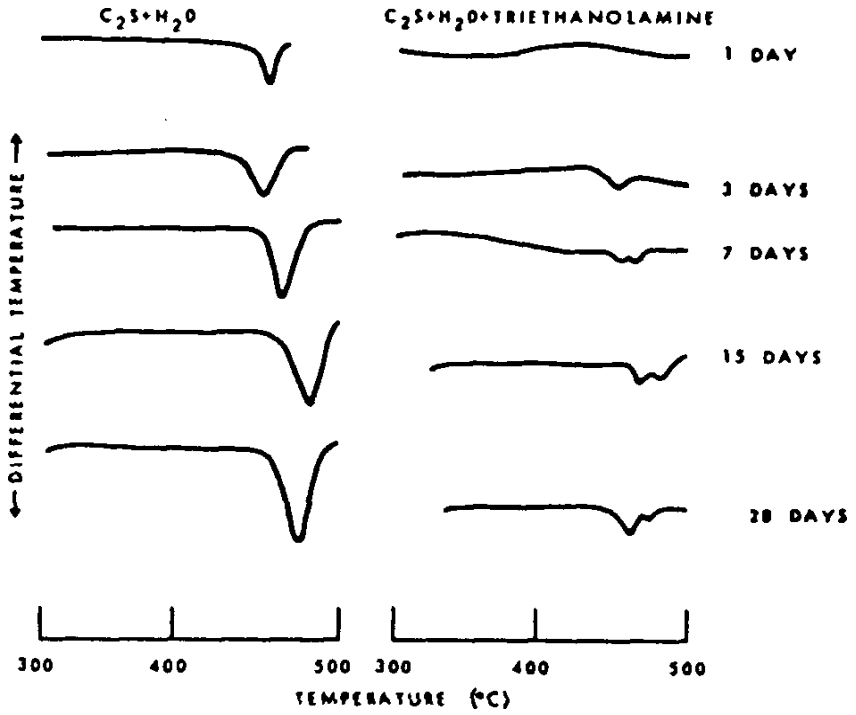


Figure 16. Thermograms of C_2S hydrated in the presence of triethanolamine.

@Seismicisolation

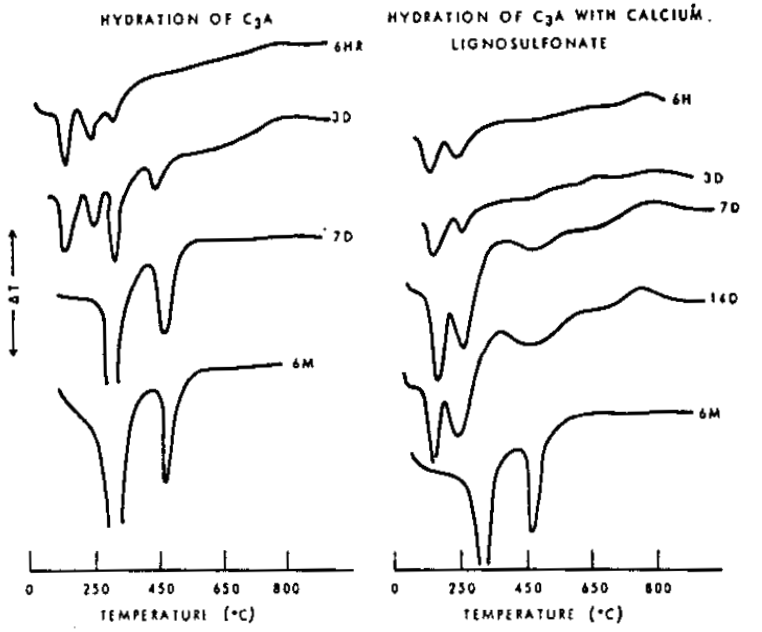


Figure 17. Influence of calcium lignosulfonate on the hydration of C_3A.

Many cements contain finely divided calcium carbonate as an additive and it is important to know its influence on the hydration of cement components. DTA and DTG have been applied to investigate the reactions occurring between C_3A and calcium carbonate.[30] In Fig.18, DTG of the products formed in C_3A samples hydrated with 12.5% calcium carbonate is shown. At 10 minutes, two peaks below 300°C signify the formation of carboaluminate. The hump at about 700–750°C and another at about 850–900°C are caused by the decomposition of calcium carbonate and calcium carboaluminate, respectively. As the length of hydration increases, cubic aluminate hydrate seems to form at 7 hours and 2 days with a peak effect at about 300–315°C. The combined $CaCO_3$ in the carboaluminates is indicated by the peak areas at 850–900°C. Calculations show that the combined carbonate amounts are 1.5, 6.0, and 8.2%, respectively, at 10 minutes, 7 hours, and 2 days.

@Seismicisolation

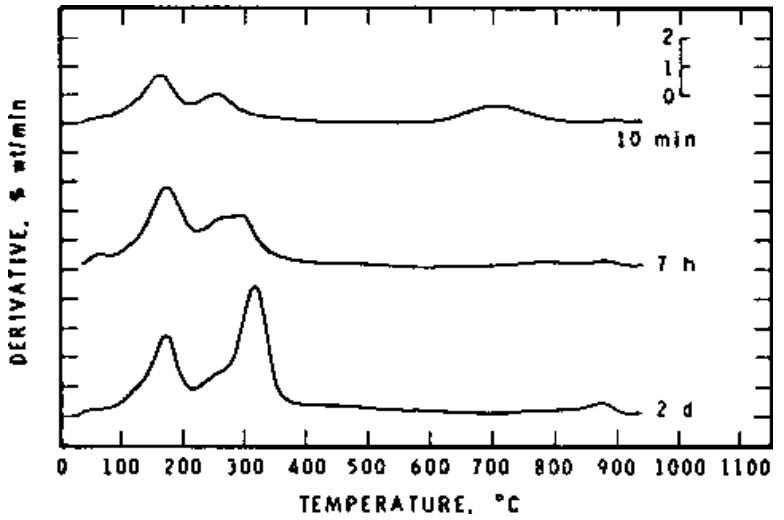


Figure 18. Differential thermogravimetric curves of tricalcium aluminate hydrated in the presence of 12.5% calcium carbonate.

When a mixture of C_3A and gypsum is hydrated, peaks occur due to the formation of ettringite and monosulfo-aluminate hydrate. Ettringite gives an endothermal peak in the vicinity of 100–150°C. The peak temperature, however, varies depending on the drying and heating conditions of the mixture. The effect of triethanolamine admixture on the hydration process of C_3A + gypsum mixture as illustrated in Fig. 19.[31] At 5 minutes, a larger amount of gypsum has disappeared from the sample containing triethanolamine. Comparison of the curves with and without gypsum indicates differences. Ettringite peak is more intense between 5 and 10 minutes in the triethanolamine treated samples. In the untreated sample, it occurs between 10 and 30 minutes. In other words, ettringite formation is accelerated by the amine. These results have been confirmed by applying conduction calorimetry.

In the hydration of C_4AF, similar thermal peaks to those of C_3A are indicated, but the rate of reaction of the ferrite phase is slower. Hexagonal and the cubic phases formed from the hydration of the ferrite phase contain Fe. Ramachandran and Beaudoin,[32] used DSC to investigate the amounts of the reaction products formed when C_4AF was hydrated with different amounts of gypsum (Fig. 20). Gypsum was estimated by the endothermal effect at 150–200°C, ettringite by the endothermal effect at 110–125°C, and

@Seismicisolation

the low sulfo-aluminate by the endothermal effect at 200–210°C. Figure 20 indicates that most of the gypsum has reacted within about 2 days. Its disappearance gives rise to the formation of ettringite and low sulfo-aluminate (Fig. 20). All samples in general have decreased amounts of ettringite after 3–7 hours. This decrease was found to result in the formation of increased amounts of the low sulfo-aluminate hydrate form.

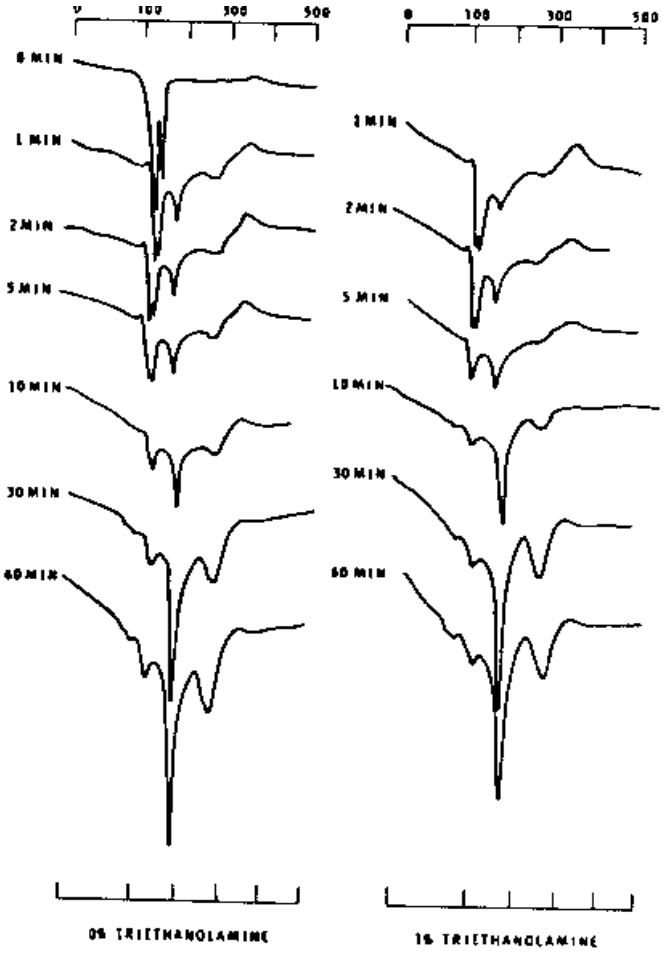


Figure 19. DTA curves of the hydration of C_3A + 25% gypsum in the presence of triethanolamine.

@Seismicisolation

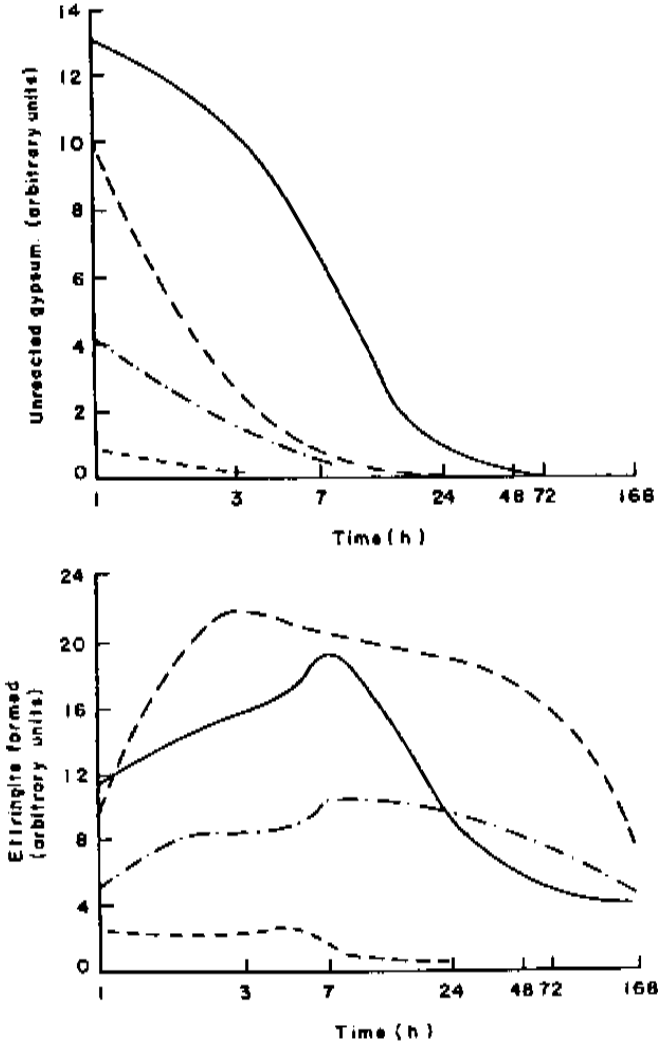


Figure 20. Relative amounts of gypsum and ettringite present in the system C_4AF-$CaSO_4 \cdot 2H_2O$.

7.0 HYDRATION OF CEMENT

In the hydration of Portland cement, several products can be detected by applying DTA and TG techniques. Unreacted gypsum may be identified by endothermal peaks in the temperature range 140–170°C, the C-S-H gel

@Seismicisolation

at temperatures below 150°C, ettringite at temperatures 120–130°C, calcium hydroxide by an endotherm in the range 450–550°C, and calcium carbonate at 750–850°C. It has to be recognized there are interference effects at low temperatures, depending on the drying procedures and the state of the material. In some instances, a small additional endotherm appears before the onset of the calcium hydroxide endotherm and this is attributed to the dehydration effect of the chemisorbed water on lime or to the finely divided form of lime. The amount of lime formed may be estimated by determining the endothermal area of the lime peak or weight loss.[33] The amount of lime is nearly proportional the degree of hydration of cement.

The sequence of hydration products formed in the hydration of cement at different periods has been followed by DTA (Fig. 21).[11][34] The endothermal effects at 140 and 170°C characterize gypsum and the endothermal peaks below 500°C and 800°C are due, respectively, to the decomposition of $Ca(OH)_2$ and $CaCO_3$. Within 5 minutes, an endothermic effect at 130°C is caused by the dehydration of ettringite. Gypsum is partly consumed at this period as evident from the reduced intensity of the peaks at 140°C and 170°C. At 1 hour, there is an increase in the intensity of the ettringite peak at the expense of the gypsum peak. The onset of an endotherm at about 500°C after 4 hours of hydration is due to the $Ca(OH)_2$ formed from the hydration of the C_3S phase. A small endotherm registered below 500°C may be due to the chemisorbed water on free lime or to the finely divided $Ca(OH)_2$. The endothermal effect at 800°C is caused by the decomposition of calcium carbonate.

The rate of hydration of cements can be determined through the heat development characteristics using a conduction calorimeter. In Fig. 8, the heat effect in the first few minutes is attributable to the heat of wetting and ettringite formation. Within a few hours another strong exotherm appears due to the hydration of C_3S. In some cases, depending on the composition of the cement, an additional peak is observed after the C_3S peak. This is related to the reaction of C_3A to form the low sulfo-aluminate hydrate.

The isothermal conduction calorimetry offers a method to follow the rate of hydration of cement at different temperatures of curing. Calorimetric curves of cement hydrated at 25, 30, 40, 50, and 60°C have been analyzed.[35] It was found that as the temperature increased the C_3S hydration peak appeared at earlier times. The shape of the curves also underwent changes. The apparent activation energy of hydration could be calculated.

In cement pastes the calcium silicate hydrate phase contains adsorbed as well as interlayer water. In order to differentiate and estimate these two types of water, Feldman and Ramachandran[36] carried out DTA/TG of

@Seismicisolation

cement pastes under controlled humidity conditions. Two endothermal peaks emerged in samples exposed to different humidities, one due to the adsorbed water at 90–110°C and the other, at 120–150°C, caused by the interlayer water.

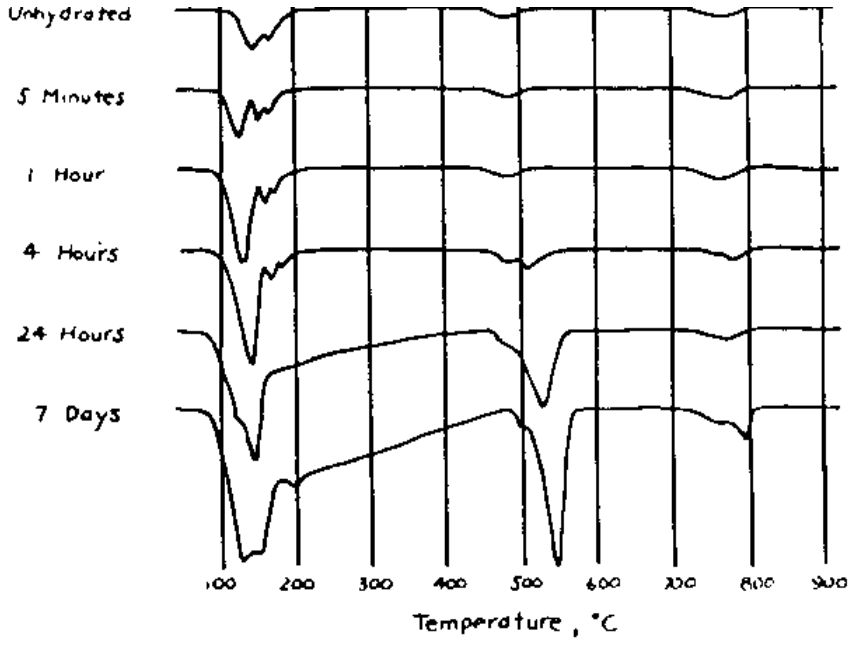


Figure 21. DTA of cement hydrated at different peaks.

The mechanism of setting of cement pastes is of considerable interest. It is generally thought the ettringite formation is a prerequisite for the setting of the paste. Some studies have suggested that some hydration of C_3S should take place before setting can occur. The evidence is based on the existence of an endothermal peak due to the dehydration of calcium hydroxide present at the time of setting. This was observed for several cement pastes containing various types of admixtures.[37]

The techniques of DTA, DSC, conduction calorimetry, and TG, are increasingly applied to evaluate the role of concrete admixtures in cement hydration. Studies have included determination of kinetics of hydration, identification of compounds, relative effects of newly developed admixtures, estimation of products, mechanism of the effect of admixtures, crystallinity of compounds, etc.

@Seismicisolation

The conduction calorimeter is capable of following the hydration of six cement samples simultaneously. Ramachandran and Lowery[38] followed the effect of eleven retarders on the induction periods during cement hydration. Several dosages of retarders were included in the study. Some typical results are summarized in Table 1. The results indicate the minimum concentration of a retarder that is needed to achieve different induction periods. The most efficient retarders were found to be Ca gluconate, Na heptonate, and sucrose, which need about 0.15% or less to extend the induction period to 40 hours. The least effective retarders that require more than 0.5% for an induction period of 40 hours are sugar-free lignosulfonate, Na pyrophosphate, Na hexametaphosphate, Na borate, and glycolic acid.

Table 1. Minimum Concentration of Various Retarders (%) Required to Achieve Desired Induction Period

	Induction Period (Hrs.)			
Retarding Agent	10	20	30	40
Ca Gluconate	0.10	0.12	0.13	0.14
Glucose	<0.10	0.15	0.23	>0.30
Glycolic Acid	<0.50	0.55	0.64	0.79
Na Borate	0.51	0.63	>0.70	<1.00
Na Citrate	0.21	0.32	0.39	<0.50
Ne Heptonate	<0.10	0.12	0.14	~0.15
Sucrose	0.04	0.06	0.07	>0.075
Na Pyrophosphate	<0.20	0.38	1.00	>1.20

Superplasticizers influence the rate of hydration of cement and the relative effect depends on the type of cement. In Type I cement, the exothermal peak occurring at about 5.5 hours in the reference sample is progressively decreased in intensity as the dosage of sulfonated melamine formaldehyde superplasticizer (SMF) is increased from 0 to 2%. At a 4% level, the rate of heat development at 5 hours for the sample containing the admixture is 25% of what is observed for the reference, indicating a retardation effect. Superplasticizers retard the hydration of Type V cement even more efficiently. The conduction calorimetric curves of Type I and Type V cement hydrated in the presence of 0.6% superplasticizer are shown in Fig. 22.[25] A more efficient retardation occurs with Type V cement, as can be judged by comparing the differences in the time of appearance of peaks between the reference and that containing the superplasticizer.

@Seismicisolation

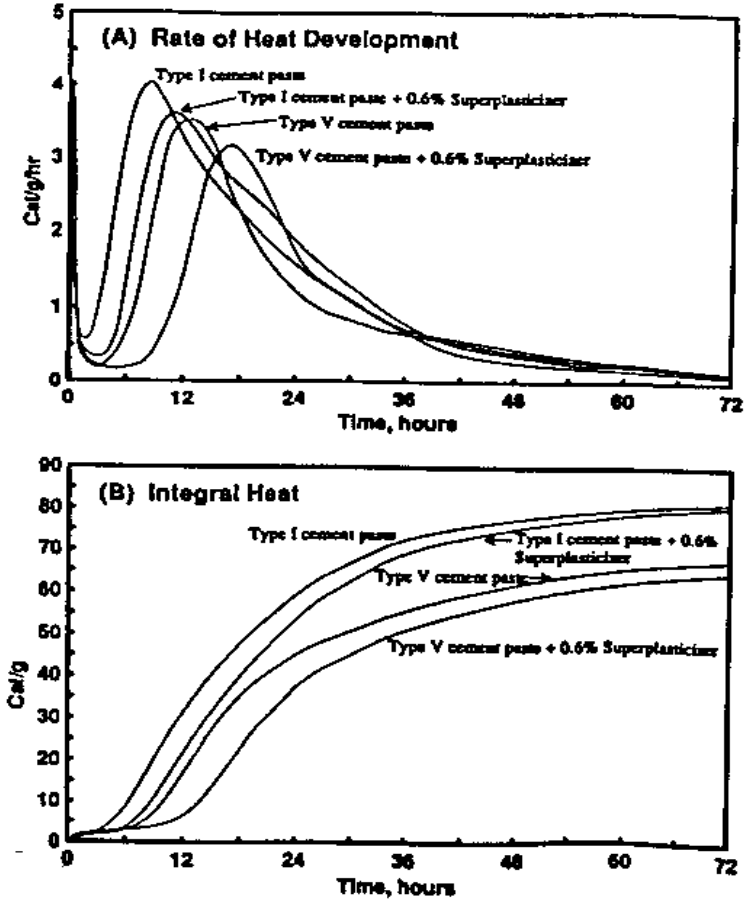


Figure 22. Conduction calorimetric curves for cements containing an SMF superplasticizer.

The relative effects of admixtures on the hydration of cements can be obtained by estimating lime through the application of DTA or TG. In conduction calorimetry the total heat generated at different times forms the basis for comparison of the degree of hydration. The relative acceleration effects of Ca chloride, Ca nitrite, and Ca formate, can be compared on the basis of heat evolution (Fig. 23).[25] The results show that calcium chloride is the best accelerator of the three admixtures studied.

Many of the mechanisms involving accelerators, water reducers, retarders, and superplasticizers, are related to surface chemical interactions occurring between the hydrating cement and the admixtures. Thermal methods have been applied with success to study these interactions.[39]

@Seismicisolation

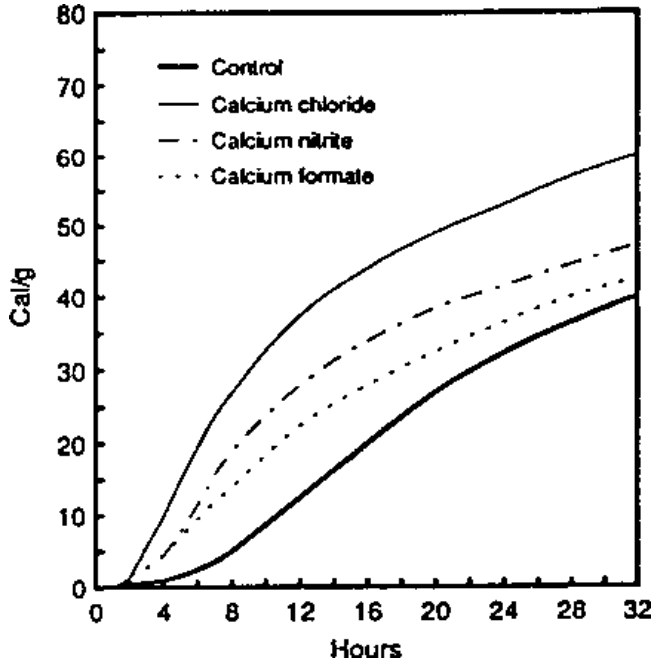


Figure 23. Effect of some accelerators on the hydration of type V cement.

In cold weather concreting, the rate of hydration of cement is very slow. Attempts have been made to develop the so-called "antifreezing admixtures" in which an accelerator and a freezing point depressant are used. Thiocyanates are potential accelerators that may be used in these formulations. A systematic work has been carried out to determine the effect of various thiocyanates such as Na, K, NH_4, Ca, and Li thiocyanates, at dosages of 1.5 and 3%, on the hydration of cement cured at 20, 0, and -5°C. Both conduction calorimetry and TG techniques were used.[40] All the thiocyanates increased the rate of hydration of cement at all temperatures. The most efficient early acceleration as well as strength development occurs with 3% Ca thiocyanate. A linear relationship exists between the amount of lime formed and strength, within a range of values (Fig. 24). The lines for the paste cured at -5°C can be broadly divided into three groups. Pastes containing 1.5% Na, Li, and K thiocyanate exhibit better strengths than the reference material at lime contents greater than 3%. Best strengths are obtained with 1.5–3.0% Ca thiocyanate and 3% Na,K, or Li thiocyanates. These data imply that the differences in the microstructure are responsible for the variation in the intrinsic strengths of the pastes, when compared at

@Seismicisolation

equal degrees of hydration. Similar studies have been carried out to compare the strengths of pastes at equal degrees of hydration by hydrating cement with calcium chloride. In Fig. 25 the compressive strengths of cement pastes (containing 0, 1, 2, and 3.5% calcium chloride) are plotted as a function of the degree of hydration.[40a] The non-evaporable water content (an indicator of the degree of hydration) was obtained by applying the TG technique. At any particular degree of hydration, samples with 3.5% calcium chloride have the lowest strength. At lower degrees of hydration the sample with 1–2% chloride forms stronger bodies than others. These studies not only indicate how the addition of calcium chloride affects the rate of hydration, but also demonstrates the changes in the intrinsic nature of the hydration products.

The possibility of using evolved gas analysis to identify commercial superplasticizers was considered by Gal, et al.[41] The total area under the curve was used to estimate the amount of the admixture in a mix.

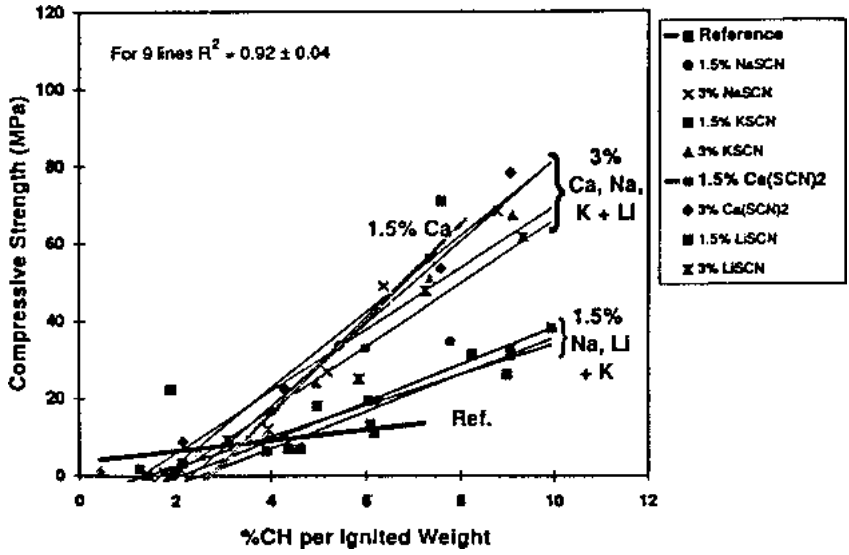


Figure 24. Relationship between strength and calcium hydroxide content in cement paste hydrated at -5°C.

@Seismicisolation

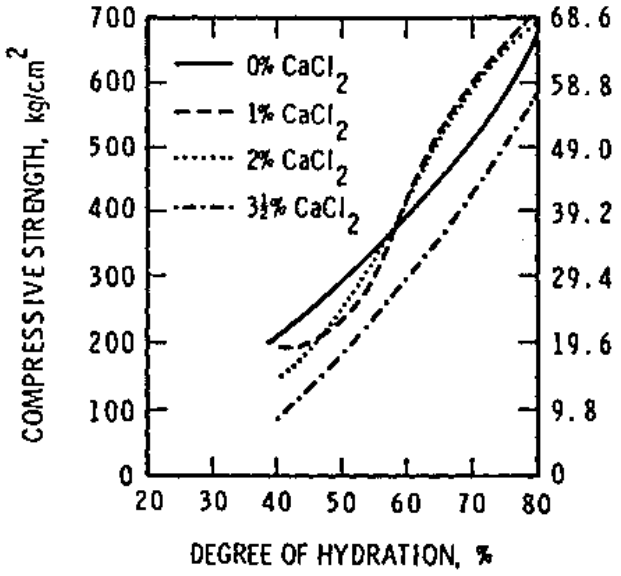


Figure 25. Strength vs. non-evaporable water relationship for cement paste containing calcium chloride.

Autoclaving of cements is employed to produce products of high early strength or reduced shrinkage. Many additives are mixed with cement for this purpose. DTA has been employed to identify the products that are formed under autoclaving conditions. The possible compounds formed are: CSH gel, αC_2SH hydrate, tricalcium silicate hydrate, calcium hydroxide, γC_2SH hydrate, etc. Kalousek pioneered the application of DTA to autoclaved cement systems.[11] By using DTA, the results of Menzel, showing variation of strength of cement-quartz mixes as a function of quartz, were explained. It was also demonstrated that the highest strengths were associated with the formation of 1.13 nm tobermorite/CSH, and the lowest with the formation of αC_2SH.

Several other applications of thermal techniques that pertain to concrete science are briefly described below. The effect of silica fume on the hydration of Portland cement has been investigated by DTA, TG, and conduction calorimetry.[42] Conduction calorimetry generated two peaks attributable to the hydration of C_3S and $Ca(OH)_2$–silica-fume interaction, respectively. In a DTA investigation of phospho-gypsum–fly-ash–cement–water system, the increased formation of ettringite and tobermorite with time could be monitored.[43] The DTA method was also used with success to

@Seismicisolation

determine the relative activation effects of slag by additives such as CaO, phospho-gypsum and $CaCl_2$.[44] The nature of the transition zone is an important factor that determines the strength of concrete. TG has been applied to identify products such as AFt and AH_3 phases in the transitional zone of a sulfo-aluminate cement.[45] The estimation of glass content in slags has been carried out by DTA. The exothermic devitrification peak effect at a temperature of about 800–900°C is used for this estimation. The interconversion effects of the hexagonal aluminates to the cubic aluminate form in the alumina cement are conveniently studied by DTA. Hydration reactions occurring in pozzolanic cements, oil well cement, hydraulic limes, expanding cements, acid-proof cement, magnesium oxychloride and oxysulfate cements, gypsum plaster, and calcium silicate products, have also been investigated by thermal analysis.

8.0 DURABILITY

Concrete may deteriorate if adequate precautions are not exercised to protect it from adverse effects that could result from exposure to natural or artificial conditions. Several physical, chemical, and electrochemical processes are known to induce cracking of concrete. Concrete can have durability problems as a consequence of its exposure to sea water, sulfates, chlorides, freeze-thaw action, carbon dioxide, etc., or when it is attacked by artificially induced processes such as exposure to acids and salts in chemical plants. If the raw materials in concrete are not carefully controlled, there may be an eventual failure of concrete elements. One typical example is the presence of excess alkali in concrete that promotes alkali-aggregate expansion reaction. Thermal techniques, in combination with others, have been employed with success to examine the raw materials as well as the failed concrete. The knowledge gained from such work has been applied to produce more durable concrete.

Some organic and inorganic compounds present in small amounts in aggregates may affect concrete strength and durability. Figure 26 gives the thermograms of some of the harmful impurities that may be present in concrete.[11] Pyrite exhibits two exothermic peaks between 400 and 500°C caused by oxidation. Gypsum shows two characteristic effects at 180 and 220°C for dehydration effects. Montmorillonitic clay mineral is characterized by three endothermal effects at 160, 660, and 900°C, due respectively, to the release of interlayer, dehydroxylation, and destruction of lattice. An

@Seismicisolation

exothermal effect at about 950°C is attributed to the formation of a spinel. Humus gives strong exothermal peaks over a wide range of temperature (200–600°C) and lignite exhibits three exothermal peaks caused by oxidation. Opal shows an endothermic peak at 80°C for the loss of water and another at 170°C due to a structural transformation. Marcasite manifests three exothermal peaks at 450, 470, and 520°C.

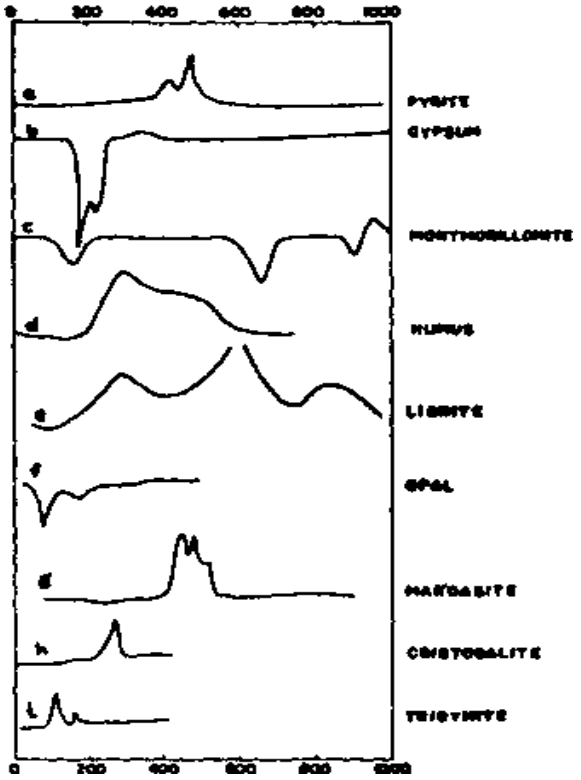


Figure 26. DTA of harmful constituents in aggregates.

The causes leading to the failure of concrete near the construction joints have been evaluated by TG.[46] The concrete sample exhibited peaks at 705–745°C and 905–940°C caused by the decomposition of calcite and dolomite, respectively. The slopes of the weight loss plot prior to the dolomite and calcite decompositions correlated with the field performance. In general, it was found that in durable dolomite aggregate, carbon dioxide loss occurs at 570°C and continues up to 705°C when the magnesium carbonate decomposes. Carbon dioxide from calcium carbonate is driven off at

@Seismicisolation

temperatures greater than 905°C. Poor durability dolomite showed very little weight loss until 700°C at which temperature CO_2 was expelled.

Magnesium oxide in cement exists mainly in a free state and its content does not exceed 6%. At the clinkering temperature of 1400–1500°C, free MgO is in a dead burnt state in the form of periclase. Under normal conditions of exposure it may take years for periclase to hydrate. The conversion of MgO to $Mg(OH)_2$ is attended by an expansion volume and, hence, there is a possibility of concrete to crack. Most specifications place a limit on the amount of MgO in cements and also a limit on the volume expansion of cements exposed to an autoclave treatment. Ramachandran[47] examined by thermal techniques the effect of curing conditions, viz., 50°C, boiling in water and autoclaving, on expansion and degree of hydration in cements containing different amounts of dead burnt MgO. It was found that at MgO contents <2% the expansion was lower and then there was steep increase at higher concentrations (Fig. 27). At any particular concentration of MgO, cement B showed higher expansion than cement A. Cement A contained higher amounts of C_3S, had better strength and, hence, was able to resist expansive forces.[47]

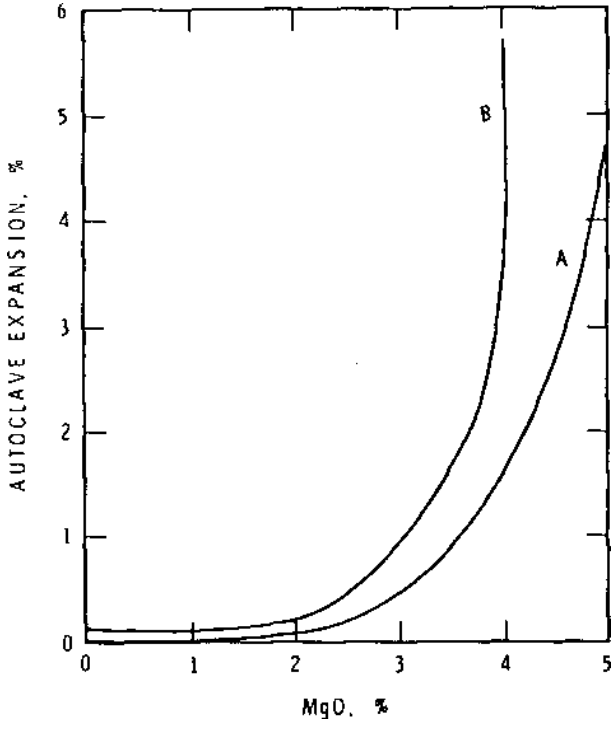


Figure 27. Effect of different amounts of MgO on the autoclave expansion of cements.

@Seismicisolation

Under exceptional situations the aggregates may be contaminated with MgO. A contaminated coarse aggregate containing dead burnt CaO and MgO was inadvertently added to concrete. After a few years the concrete exhibited large pop outs. DTA could be used to estimate the amount of $Mg(OH)_2$ present in the samples.[48] In another example, DTA[49] was applied to estimate the amount of unhydrated MgO present in a 15 year old concrete. The amount of $Mg(OH)_2$ was determined by the endothermic peak at 400°C. By estimating the amount of $Mg(OH)_2$ before and after autoclave treatment, the amount of unhydrated MgO present in the sample could be computed.

In field concrete, quick setting problems result in the production of concrete with poor durability. Thermal analysis has been used to explain certain abnormal phenomena occurring in cementitious materials. One example pertains to a flash set in an oil cement slurry containing lignosulfonate admixture.[50] Conduction calorimetry was one of the techniques used to study the hydration reactions of the systems such as Portland cement, C_3A-gypsum-lime, and C_4AF-lime-gypsum systems containing refined or unrefined lignosulfonate. The results showed that unrefined lignosulfonate destabilizes the hydration process of C_4AF-gypsum-lime mixture causing a flash set. In conduction calorimetry the C_4AF-10%gypsum-5%lime with 1–2% unrefined lignosulfonate (UL) dramatically increases the intensity of the very early ettringite peak and reduces the peak intensity (C_3S hydration peak) at about 9–10 hrs. (Fig. 28). Induction period is practically absent. It was concluded that xylose present in lignosulfonate was responsible for the flash set. Greene[51] investigated a quick setting problem involving a white cement that was used with a particular type of water reducing agent. Several combinations of cements were subjected to DTA examination. DTA peaks indicated the rate of formation of gypsum, ettringite, calcium monosulfate hydrate, and calcium hydroxide. Based on XRD and DTA, it was concluded that in the presence of the water reducer, consumption of SO_3 was accelerated with problem cements, and also insufficient amount of SO_3 remained in the solution in the period immediately following mixing.

Concrete undergoes expansion when exposed to higher temperatures, pressures, and humidities, and this may cause it to exhibit cracks. A new equipment has been devised to monitor thermal expansion of cementitious materials as a function of temperature.[52] Higher temperatures also chemically alter the concrete performance. Accidental fire causes damage to structural concrete elements. Assessment of the condition after a fire is important for recommendations for rehabilitation of concrete. DTA/TG techniques are useful to assess the temperature ranges to which the elements

@Seismicisolation

could have been exposed.[53] Damaged concrete (at different depths) has been analyzed by DTA/TG. The damaged concrete did not exhibit dehydroxylation peak of $Ca(OH)_2$, indicating that such concrete was exposed to temperatures above 500°C. The undamaged concrete contained $Ca(OH)_2$, as evidenced by the endothermal peak.

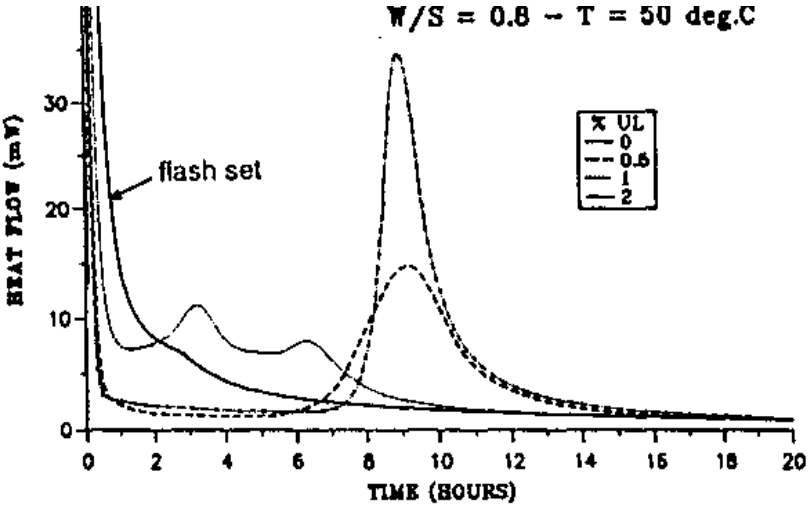


Figure 28. Effect of unrefined lignosulfonate on the hydration of C_4AF-10% gypsum-5% lime system.

Concrete is vulnerable to cracking when subjected to increasing numbers of freezing-thawing cycles. The influence of low temperatures (freeze-thaw cycles) on the rate of formation of AFm and AFt phases in cements containing low C_3A (1.7%) or high C_3A (10.7%) has been examined by DTG.[54] At 150 freeze-thaw cycles, cement with a low C_3A content was found to contain 53% AFm phase and 17% AFt phase and the corresponding figures for the C_3A rich cement was 34% and 38%, respectively. The increased damage that occurs when concrete is exposed to the freeze-thaw cycles and salts has been investigated by many workers.[55][56] Experiments involving measurements of length changes and heat changes that occur when the cement paste is exposed to temperatures between 15 and -70°C have yielded information on the mechanism of salt scaling.[55][56] Figures 29 and 30 present results of length changes and DTA of cement pastes saturated with NaCl (brine) of different concentrations (0, 5, 9, 13, 18, and 26%).

@Seismicisolation

During cooling cycles (Fig. 29), especially at lower concentrations, there is an expansion of 0.5% at 5% concentration compared to 0.08% in water and 0.01% at 26% concentration. On warming, a significant contraction occurs with highly concentrated salts at about -21°C, the melting point of the eutectic. In the cooling cycle (Fig. 30) the first exothermic peak is attributed to the commencement of formation of ice on the external surface. According to Litvan[55][56] this represents a freezing of the disordered liquid from the pores of the cement paste. The second exothermal effect at -22°C is ascribed to the freezing of the solution of eutectic composition. On warming, two processes occur; one at about -21°C and another a at higher temperature increasing in magnitude with increasing salt concentration. The peak at lower temperature represents melting of eutectic mixture and that at higher temperature the melting of pure ice. In addition to the physical mechanism of increased volume at low temperatures due to the presence of salts, chemical reactions may also occur, especially at higher temperatures. For example, at a calcium chloride concentration of above 22% the strength of concrete is reduced and salt scaling is increased.[57] The DTA method has been used to determine the reduction in $Ca(OH)_2$ content and increase in the content of complex $C_3A{\bullet}CaCl_2{\bullet}10H_2O$, depending on the exposure conditions and severity of attack. The existence of a complex salt $CaCl_2{\bullet}Ca(OH)_2{\bullet}10H_2O$ with a characteristic peak at 580°C was also confirmed.

Carbonation involves the reaction of CO_2 with the hydrated cement components, which will result in shrinkage. In addition, carbonation also decreases the pH of the system making the reinforcing bars more prone to corrosion. It is not easy to assess the extent to which the C-S-H phase undergoes carbonation and shrinkage on exposure to CO_2. In a method involving continuous leaching and monitoring of the lime remaining in a hydrated tricalcium silicate paste by DTA, the time to terminate extraction was determined. Ramachandran[58] was thus able to prepare lime-free C-S-H. The resultant C-S-H exhibited a much higher shrinkage than calcium hydroxide (Fig. 31). The carbonation effect of synthesized tobermorite has been examined by XRD/DTA.[59] An endothermal effect at about 180°C indicated the dehydration of tobermorite and an exothermal effect at about 800°C was caused by the formation of wollastonite. The carbonated samples exhibited a broad endothermal effect in the range 450–600°C and a sharp peak at about 600–650°C. The former indicated the presence of vaterite and the latter, calcite. The carbonation decreased the peak due to wollastonite. Thermal methods can also be used toestimate the amount of carbonation that

@Seismicisolation

has occurred at different depths in concrete. These techniques estimate the amount of calcium carbonate formed and also the amount of calcium hydroxide remaining in an uncarbonated form.

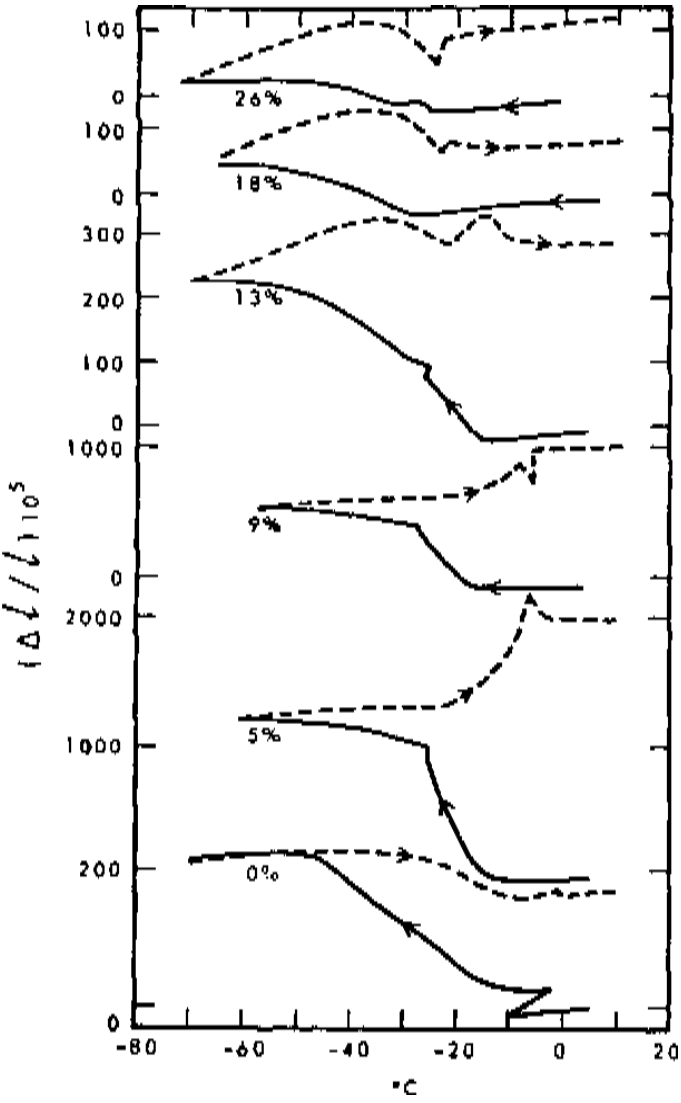


Figure 29. Length changes of air-entrained cement paste saturated with brine of various concentrations.

@Seismicisolation

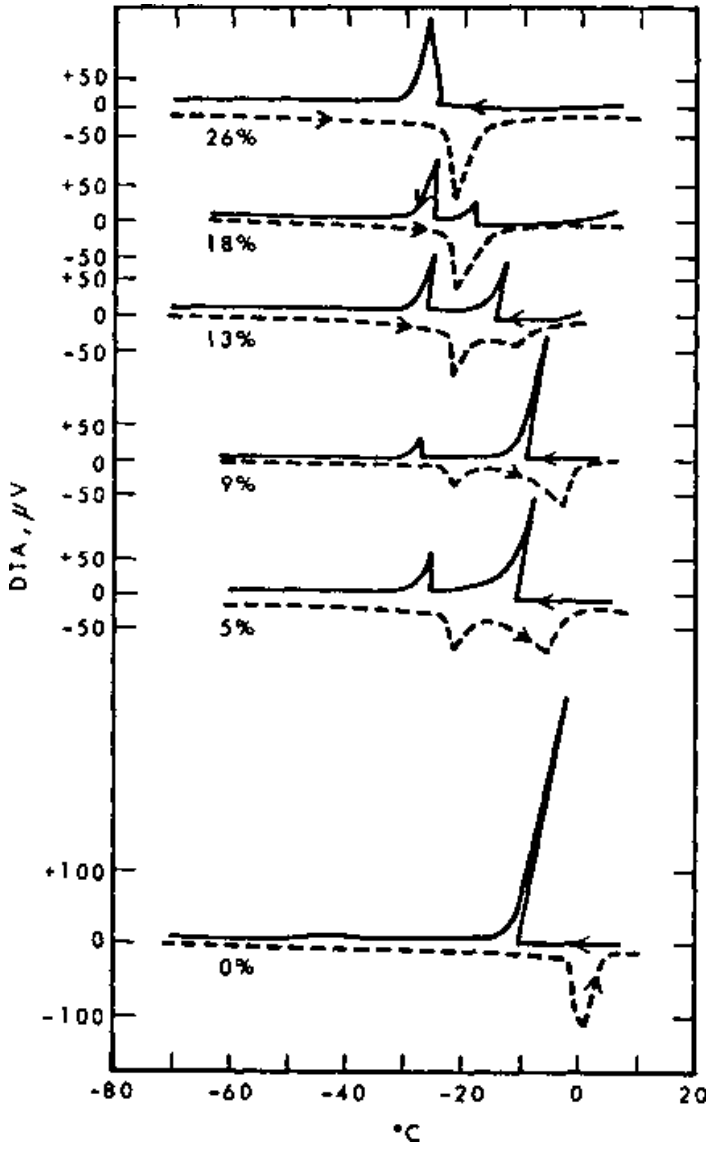


Figure 30. DTA of air-entrained 0.5 w/c cement paste saturated with brine of various concentrations.

@Seismicisolation

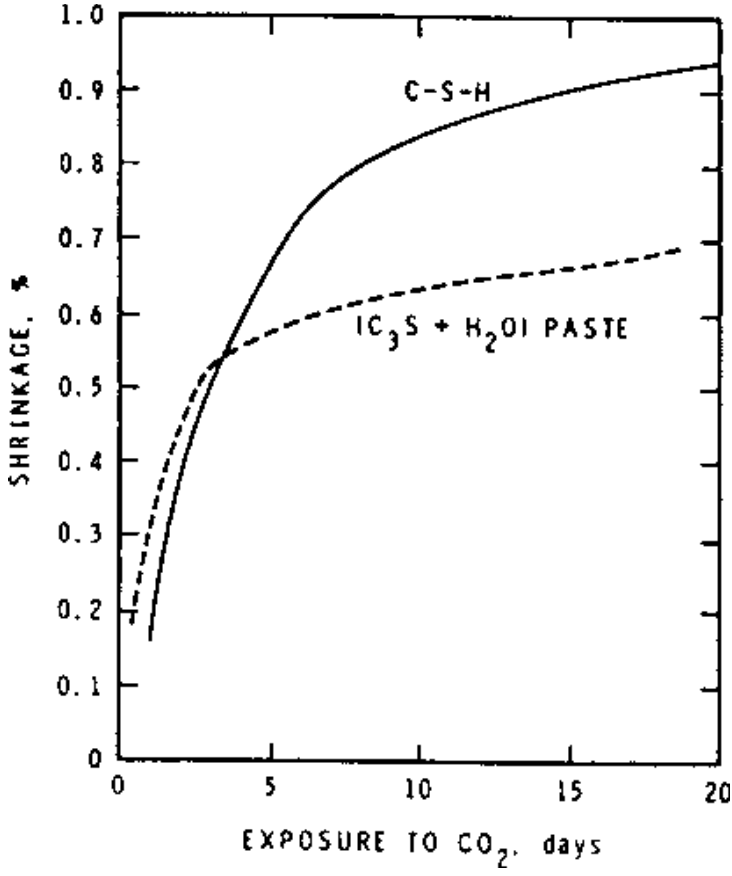


Figure 31. Carbonation shrinkage of C-S-H and hydrated C_3S paste.

@Seismicisolation

Several complex reactions occur when concrete is exposed to sea water. Compounds such aragonite, calcium bicarbonate, calcium monosulfate hydrate, ettringite, Ca-Mg silicate hydrates, magnesium silicate, thaumasite, etc., have been identified by the application of thermal analysis in conjunction with other techniques. Thus, the factors leading to the deterioration of concrete can be established.

In many chemical industries, the chemicals produced may react with concrete that is used as a construction material. In an example, the influence of formic acid on concrete was studied.[60] DTA curves of samples showed that as the exposure of concrete to the acid is increased, the peaks due to lime and calcium carbonate are decreased. This gave an indication of the severity of attack by acids. Another example pertains to a fertilizer plant. Ammonium nitrate fertilizer contained 75% NH_4NO_3 and 25% $CaCO_3$ as a filler. Concrete used in this plant was attacked by nitrate. The lime was found converted to calcium nitrate. Also, there was a reaction between calcium aluminate hydrate and ammonium nitrate resulting in the formation of calcium nitrate and calcium aluminate nitrate complex. These compounds could be identified by endothermal effects appearing in DTA.[61]

Many studies have been carried out on old concretes to determine the reactions that are responsible for deterioration. Sarkar, et al.,[62] examined a 75 year old stone building containing mortar that had shown signs of distress. The presence of gypsum (endothermic effect at 133°C), quartz (endothermal peak 578°C), and calcium carbonate (endothermal effect at 900°C), and tharndite (endotherm at 880°C), could be identified. It was concluded that one of the main causes of deterioration was the interaction of SO_2 from the atmosphere with mortar and sandstone. In another study,[63] a 50 year old concrete was subjected to examination by DTA, TG, SEM(EDX), porosimetry, and chemical analysis. TG showed a loss in weight at 60°C for the loss of adsorbed water, and other losses occurred due to the dissociation of C-S-H, $Mg(OH)_2$, $Ca(OH)_2$, and $CaCO_3$. The w/c ratio that was used to make concrete did not influence the total amount of combined water. Higher amounts of carbonate were found in concretes made at lower w/c ratios. It was also concluded that the transition zone contained C-S-H and $Ca(OH)_2$, the relative ratios depending on the type of cement and cement:aggregate:water ratio.

Thermal techniques have also been used to examine the properties and durability phenomena in non-Portland cements. In an investigation, structural concrete made from high alumina cement had shown failure after twenty-seven years of service.[64] The deteriorated samples were investigated by DTA and XRD. The compounds that were identified included AH_3, C_3AH_6, CAH_{10}, and $CaCO_3$. The failure was attributed to the conversion of

@Seismicisolation

CAH_{10} to the cubic form of C_3AH_6 and to the carbonation of the hydrated products that produced gibbsite and calcite of low binding properties. Thermal techniques are applicable to examine failed white coat plasters. Application of DTA and TG techniques permitted determination of the quantities of various ingredients such as gypsum, magnesium hydroxide, calcium hydroxide, magnesium oxide, and calcium carbonate, in such plasters.[65]

REFERENCES

1. Brown, M. E., *Introduction to Thermal Analysis*, p. 211, Chapman and Hall, UK (1988)
2. Sorrentino, F., and Castanel, R., Application of Thermal Analysis to the Cement Industry, *J. Thermal Analysis*, 38:2137–2146 (1992)
3. Bhattacharya, A., Simulating Minerals Pyroprocessing by Thermal Analysis, *J. Thermal Analysis*, 40:141–149 (1993)
4. Su, M., Deng, J, Wu, Z., and Liu, X., Research on the Chemical Composition and Microstructures of Sulfo-Aluminate Cement Clinker, *Proc. 9th Intern. Cong. Chem. Cements*, 2:94–100, New Delhi, India (1992)
5. Akhmetov, I. S., and Miryuk, O. A., Phase Transformations when Synthesizing Clinkers Produced of Technologeous Raw materials, *9th Intern. Cong. Chem. Cement.*, 2:74–80, New Delhi, India (1992)
6. Radnaassediin, S., Formation of Low Temperature Portland Cement Clinker by Using Non-Traditional Aluminosilicate Rock and Mineralizer, *9th Intern. Cong. Chem. Cements*, 2:315–321, New Delhi, India (1992)
7. Shah, H. U. and Iqbal, Z, Evaluation of Optimum Percentage Addition of Fluorspar in White Cement Raw Mix Containing 4% SO_3, *9th Intern. Cong. Chem. Cement*, 2:351–357 New Delhi, India (1992)
8. Abdel-Fattah, W. I. and El-Didamony, H., Thermal Investigation on Electrostatic Precipitator Kiln Dust, *Thermochimica Acta*, 51:297–306 (1981)
9. Raina, K., and Bhargava, R., Effect of Thermal Treatment on the Reactivity of Clinker Minerals Produced from Vertical Kiln, *9th Intern. Cong. Chem. Cement*, 2:132–138 New Delhi, India (1992)
10. Koo, J. S., Han, K. S., Jaung, J. D., and Choi, S. H., Hydration Characteristics of Sulfate Solid Solution in the Clinker, *9th Intern. Cong. Chem. Cements*, 4:97–103, New Delhi, India (1992)
11. Ramachandran, V. S., *Application of DTA in Cement Chemistry*, p 308, (1969); Chemical Publishing Co., New York; 11(a): Jeffery, J. W., The Tricalcium Silicate Phase, p. 30–48, *Proc. 3rd Intern Symposium. Chem Cements*, London, (1952); 11(b): Nurse, R. W., *The Dicalcium Silicate Phase*, p. 56–77, ibid (1952)

@Seismicisolation

12. Kurdowski, W., and Deja, J., Formation of C_3S in the Mixtures Containing Different Silicate Raw Materials,*Proc. 9th Inter. Congr. Chem. Cements*, 2:255–260, New Delhi, India (1992)

13. Misra, K. C., and Borthakur, P. C., Role of Mineralizers in Alite Formation in Rice Husk Ash-$CaCO_3$ Raw Mix,*Proc 9th Inter. Cong. Chem. Cements*, 2:301–307, New Delhi, India (1992)

14. Mathur, V. K., Gupta, R. S., and Ahluwalia, S. L., Lithium as Intensifier in the Formation of Dicalcium Silicate Phase.,*Proc. 9th Intern. Cong. Chem. Cements*, 2:406–412, New Delhi, India (1992)

15. Ghosh, S. N., *Advances in Cement Technology*, p. 804, Pergamon Press, Oxford (1983)

16. Ramachandran, V. S., Beaudon, J. J., and Paroli, R. M., The Effect of Nitrobenzoic and Aminobenzoic Acids on the Hydration of Tricalcium silicate: A Conduction Calorimetric Study, *Thermochimica Acta*, 190:325–333 (1991)

17. Ramachandran, V. S., Differential Thermal Method of Estimating Calcium Hydroxide in Calcium Silicate and Cement Phases, *Cem. Concr. Res.*, 9:677–684 (1979)

18. Ramachandran, V. S., Kinetics of Hydration of Tricalcium Silicate in the Presence of Calcium Chloride by Thermal Methods, *Thermochimica Acta*, 2:41–55 (1971)

19. Ramachandran, V. S., Estimation of Tricalcium Silicate Through Polymorphic Transition, *J. Thermal Analysis*, 3:181-190 (1971)

20. Mascolo, G., and Ramachandran, V. S., Hydration and Strength Characteristics of Synthetic Al, Mg and Fe Alites, *Mater. & Structures*, 8:373–376 (1975)

21. Feldman, R. F., and Ramachandran, V. S., A Study of the State of Waterand Stoichiometry of Bottle Hydrated Ca_3SiO_5, *Cem. Concr. Res.*, 4:155–166 (1974)

22. Ramachandran, V. S., Elucidation of the Role of Chemical Admixtures in Hydrating Cements by DTA Technique, *Thermochimica Acta*, 3:343–366 (1972).

23. Bhatty, J. I., A Review of the Application of Thermal Analysis to Cement-Admixture Systems, *Thermochimica Acta*, 189:313–350 (1991)

24. Ramachandran, V. S., Effect of Sugar Free Lignosulfonates on Cement Hydration, *Zement-Kalk-Gips*, 31:206–210 (1978)

25. Ramachandran, V. S., *Handbook of Concrete Admixtures*, 2nd Edition, Noyes Publications, Park Ridge, New Jersey, p. 1153 (1995). 25(a): Monosi, S., Moriconi, G., and Collepardi, M., Combined Effect of Lignosulfonate and Carbonate on Pure Portland Clinker Compounds Hydration, III. Hydration of Tricalcium Silicate Alone and in the Presence of Tricalcium Aluminate, *Cem. Concr. Res.*, 12:415–424 (1982)

@Seismicisolation

26. Khorami, J., and Aitcin, P. C., Physico-Chemical Characterization of Superplasticizers, *Proc. 3rd Conf. on Superplasticizers and Other Admixtures,* Amer. Conc. Inst., SP-119, p. 664 (1989)

27. Ramachandran, V. S., and Zhang, C. M., Dependence of Fineness of Calcium Carbonate on the Hydration Behavior of Tricalcium Silicate, *J. Durability of Building Materials,* 4:45–66 (1986)

28. Chen, D., and Dollimore, D., Kinetic Analysis of the Hydrates formed in the Hydration of Pure C_3S and With the Addition of $Ca(NO_3)_2$, *J. Therm. Anal.*, 44:1001–1011 (1995)

29. Ramachandran, V. S., and Polomark, G. M., Extraction of Portland Cement and $3CaO{\cdot}SiO_2$ Pastes, *J. Chem & Biotech.*, 32:946–952 (1982); 29(a): Shin, G. Y., and Han, K. S., The Effect of C_3A Polymorphs on the Hydration of C_3S, *9th Intern. Congr. Chem. Cements,* 4:90–96, New Delhi, India (1992)

30. Ramachandran, V. S., and Zhang, C. M., Thermal Analysis of the $CaO{\cdot}Al_2O_3$-$CaSO_4{\cdot}2H_2O$-$CaCO_3$-H_2O System, *Thermochimica Acta,* 106:273–282 (1986)

31. Ramachandran, V. S., Action of Triethanolamine on the Hydration of Tricalcium Aluminate, *Cem. Concr. Res.*, 3:41–54 (1973)

32. Ramachandran, V. S., and Beaudoin, J. J., Physico-Mechanical Characteristics of Hydrating Tetracalcium Aluminoferrite System at Low Water:Solid Ratios, *J. Chem Tech and Biotech.*, 34A:54–160 (1984)

33. Ramachandran, V. S., Differential Thermal Method of Estimating Calcium Hydroxide in Calcium Silicate and Cement Pastes, *Cem. Concr. Res.*, 9:677–684 (1979)

34. Greene, K. T., Early Hydration Reactions of Portland Cement, *4th Intern. Symp. Chem Cements,* Washington, p 359 (1960)

35. Scrivener, K. L., and Wieker, W., Advances in Hydration at Low, Ambient and Elevated Temperatures, *9th Intern Congr. Chem. Cements,* 1:449–482, New Delhi, India (1992)

36. Feldman, R. F., and Ramachandran, V. S., Modified Thermal Analysis Equipment and Technique for Study Under Controlled Humidity Conditions, *Thermochimica Acta,* 2:393–403 (1971)

37. Ramachandran, V. S., Evaluation of Concrete Admixtures Using Differential Thermal Technique, ACI/RLEM Symp., Monterray, Mexico, p. 35–52 (1985)

38. Ramachandran, V. S., and Lowery, M. S., Conduction Calorimetric Investigation of the Effect of Retarders on the Hydration of Portland Cement, *Thermochimica Acta,* 195:373–387 (1992)

39. Ramachandran, V. S., Admixture and Addition Interactions in the Cement-Water System, *Il. Cemento,* 83:13–38 (1986)

@Seismicisolation

40. Wise, T., Ramachandran, V. S., and Polomark, G. M., The Effect of Thiocyanates on the Hydration of Portland Cement at Low Temperatures, *Thermochimica Acta*, 264:157–171 (1995); 40(a): Ramachandran, V. S., and Feldman, R. F., Time Dependent and Intrinsic Characteristics of Portland Cement Hydrated in the Presence of Calcium Chloride, Il. *Cemento*, 3:311–322 (1978)

41. Gal, T, Pokol, G., Leisztner, L., and Gal, S., Investigation of Concrete by Evolved Gas Analysis, *J. Therm. Anal.*, 33:1147–1151 (1988)

42. Ramachandran, V. S., Hydration Reactions in Cement Containing Condensed Silica Fume, *Intern. Workshop on Condensed Silica Fume in Concrete*, 7, Montreal, Canada, (1987)

43. Singh, M., and Garg, M., Development of Cementitious Properties in Phospho-gypsum-Fly Ash System, *9th Intern. Congr. Chem. Cements*, 4:489–494, New Delhi, India (1992)

44. Vulkov, V. V., Delchev, N. A., and Nikonova, N. S., Chemical Activating of Metallurgical Slag in the Conditions of Granulating, *9th Intern. Congr. Chem. Cements*, 3:115–119, New Delhi, India (1992)

45. Wang, Y., Li, S., Lu, Y., and Su, M., Microstructure of the Interfacial Zones Between Hardened Sulfoaluminate Cement Pastes and Aggregates, *9th Intern. Congr. Chem. Cements*, 5:184–190, New Delhi, India (1992)

46. Dubborke, W., and Marks, V. J., Thermogravimetric Analysis of Carbonate Aggregates, *Trans. Res. Rec.*, 1362:38–43 (1982)

47. Ramachandran, V. S., A Test for Unsoundness of Cement Containing MgO. *3rd Intern. Conf. Durability of Bldg. Mater. and Comp., Espoo, Finland*, 3:46–54 (1984)

48. Scanlon, J. M., and Connolly, J. D., Laboratory Studies and Evaluation of Concrete Containing Dead-Burnt Dolomite, *Amer. Concr. Inst.*, SP-145, p. 1224, Durability of Concrete (1994)

49. Ramachandran, V. S., Estimation of $Ca(OH)_2$ and $Mg(OH)_2$ - Implications in Cement Chemistry, *Israel J. Chem.*, 22:240–246 (1982)

50. Michaux, M., and Nelson, E. B., Flash Set Behavior Oil Well Cement Slurries Containing Lignosulfonates, *9th Intern. Cong. Chem. Cements*, 4:584–590, New Delhi, India (1992)

51. Greene, K. T., A Setting Problem Involving White Cement and Admixture, *TRB 564*, p 21-26, Washington (1976)

52. Malek, R. I., Equipment to Measure Thermal Expansion of Cementitious Materials as a Function of Temperature, *9th Inter. Cong. Chem. Cements*, 5:427–430, New Delhi, India (1992)

@Seismicisolation

53. Handoo, S. K., Agarwal, S., and Maiti, S. C., Application of DTA/TGA for the Assessment of Fire damaged Concrete Structures, *Proc. Symp. Thermal. Anal.*, pp. 19–21, Bhubaneswar, India (1991)

54. Ludwig, H. M., and Stark, J., Effects of Low Temperature and Freeze Thaw Cycles on the Stability of Hydrated Products, *9th Intern. Cong. Chem Cements*, 5:3–9, New Delhi, India (1992)

55. Ramachandran, V. S., Calcium Chloride in Concrete, *Applied Sci. Publishers*, p. 216, London (1976)

56. Litvan, G. G., Phase Transitions of Adsorbates: Effect of Deicing Agents on The Freezing of Cement Paste, *J. Amer. Ceram. Soc.*, 58:26–30 (1975)

57. Yang, Q. B., Wu, X. L., and Huang, S. Y., Mechanisms of De-Icer Scaling of Concrete, *9th Intern. Cong. Chem. Cements*, 5:282–288, New Delhi, India (1992)

58. Ramachandran, V. S., Feldman, R. F., and Beaudoin, J. J., *Concrete Science*, p. 427, Heyden, London (1981)

59. Goto, S., and Ikeda, S., Effects of Carbonation on the Thermal Properties of Tobermorite, *9th Inter. Cong. Chem. Cements*, 6:304–309, New Delhi, India (1992)

60. Bajza, A., Corrosion of Hardened Cement Pastes by Formic Acid Solutions, *9th Intern. Cong. Chem. Cements*, 5:402–408, New Delhi, India (1992)

61. Mullick, A. K., and Chandra, S., Biological and Thermal Degradation Including Environmental Effects, *9th Intern Cong. Chem Cements*, 5:402–408, New Delhi, India (1992)

62. Sarkar, S. L. Bhadra, A. K., and Mandal, P. K., Investigation of Mortar and Stone Deterioration in the Victoria Memorial, Calcutta, *Mats. & Structures*, 27:548–556 (1994)

63. Concotto, M. A., and John, V. M., Some Characteristics of a 50-Year Old Concrete, *9th Intern. Cong. Chem. Cements*, 5:452–458, New Delhi, India (1992)

64. Lach, V., The Deterioration of Alumina Cement Concrete, *Concrete Durability Conference*, Amer. Conc. Inst., SP-100, 2:1903–1914 (1987)

65. Ramachandran, V. S., Sereda, P. J., and Feldman, R. F., Delayed Hydration in White Coat Plasters: Comparison of Different Methods of Analysis, *Mater. Res. & Standards*, 8:24–28 (1967)

@Seismicisolation

5

IR Spectroscopy

S. N. Ghosh

1.0 INTRODUCTION

Infrared spectroscopy (IR) is used in the areas of determination of molecular structure, identification of chemical species, quantitative/qualitative determination of chemical species, and in a host of other applications. This technique is used in the investigation of matter in the solid, liquid, and gaseous states. The application of IR is well known in the fields of chemistry, physics, materials science, etc. The application of this technique in the field of cement and concrete dates back to the Tokyo Symposium (1968). Though comparatively new in cement and concrete, IR study is gaining much importance with the advent of user-friendly equipment and continuing research on identification and characterization of reaction products, new materials, etc. Raman spectroscopy, a complementary to IR technique, is briefly described in this chapter.

2.0 THEORY

If a molecule is placed in an electromagnetic field (e.g., light), a transfer of energy from the field to the molecule will occur only when Bohr's frequency condition is satisfied.

@Seismicisolation

$$E = h\nu$$

where h = Planck's constant
ν = frequency of light

In the case of a diatomic molecule, it can be proven from mechanical considerations that the vibrations of the two nuclei in a diatomic molecule are equivalent to the motion of a single particle of mass, μ, whose displacement from its equilibrium position is equal to the change of the internuclear distance. The term μ is called the *reduced mass* and is given by:

$$1/\mu = 1/m_1 + 1/m_2$$

where m_1 and m_2 are masses of the two nuclei.

The kinetic energy, T, is then:

$$T = \tfrac{1}{2}\mu\dot{q}^2 = \tfrac{1}{2}\mu P^2$$

where P is the conjugate momentum $\mu\dot{q}^2$.

In the case of a harmonic oscillator, the potential energy ϕ is given by: $\phi = \tfrac{1}{2}kq^2$, where k is the force constant for the vibration. The Schrodinger wave equation becomes:

$$\frac{d^2\Psi}{dq^2} + \frac{8\pi^2\mu}{h^2}(E - \tfrac{1}{2}kq^2)\psi = 0$$

If this equation is solved with the condition that ψ is a well-behaved function, the eigen values are:

$$E_v = h\nu\,(\phi + \tfrac{1}{2}) = hc\,\nu\,(\phi + \tfrac{1}{2})$$

$$\nu = \tfrac{1}{2}\pi\sqrt{(k/\mu)} \quad \text{or} \quad \nu = \tfrac{1}{2}\pi\, c\sqrt{(k/\mu)}$$

where values of ϕ are vibrational quantum numbers, k is the force constant and c is the velocity of light.

According to the above equation, the frequency of the vibration in a diatomic molecule is proportional to the square root of k/μ If k is taken to be constant for a series of diatomic molecules, the frequency is inversely proportional to the square root of the reduced mass. In the case of a poly-atomic molecule, the situation is more complicated because all the nuclei perform their own harmonic oscillation. Generally these complicated vibrations of the poly-atomic molecule are represented as the superposition of a number of normal vibrations. Poly-atomic molecules have 3N-6 or, if

@Seismicisolation

linear, 3N-5 normal vibrations. For any given molecule, however, only those vibrations which are permitted by the selection rules for that molecule appear in the infrared and Raman spectra. The selection rules are determined by the symmetry of the molecule.

The infrared vibrational spectrum of a molecule consists of a series of bands, each of which results from a transition between pairs of vibrational levels associated with the ground electronic state.

With the help of quantum mechanics, the probability of a vibrational transition of a molecule can be obtained. The variation of the dipole moment vector can be expanded in a series in terms of the normal coordinates. Herzberg's treatise on this subject is a good reference.[1]

2.1 Experimental Methods

An analyst has to carefully go through IR instrument manuals for obtaining information about the capability of equipment which is commercially available. Proper precaution has to be taken for sample preparation and when KBr/Nujol mull techniques are to be used. For gas phase/liquid phase analysis of any sample, a similar approach has to be adopted so that one can get a good spectrum of a sample. One major problem to solve for routine operation of IR analysis is the avoidance of water and CO_2 absorption from the atmosphere in the range of a normal study. With the help of a double-beam instrument and humidity controlled room conditions, this problem is somewhat avoided, but the absorption of the water/CO_2 from atmosphere during sample preparation sometimes leads to erroneous conclusions. Standard analytical textbooks are available for further guidance.

3.0 THE SPECTRA OF ROCKS, MINERALS, CLAYS, ETC.

The major raw materials used for cement manufacture are limestone, shale and siliceous materials, laterite, bauxite, sandstone, etc. These materials contain a variety of minerals in different forms. IR spectroscopy has been found to be very useful in identifying most of these minerals. The fundamental modes of vibration which lead to absorption bands in the region 400–4000 cm^{-1} are, in general, the stretching and bending modes.

@Seismicisolation

The vibrational frequencies of these modes for the species under study vary considerably, depending on parameters such as molecular structure, chemical bonds, crystal forms, impurities in solid solution, etc. The presence of several phases of nearly similar absorption characteristics makes the study more complex. The salient features of each set of minerals are discussed.

3.1 Calcite, Aragonite, and Magnesite

The carbonate rocks have three to four intense bands in the IR region (Figs. 1–3).[2] The 1420 and 876 cm^{-1} region bands are more or less unaltered in the spectra of these materials. The 700 cm^{-1} region band is characteristic for identification even in a mixture of these rocks because magnesite, calcite, and aragonite absorb at 748, 711, and 700 cm^{-1}, respectively. The aragonite sample is not pure and contains calcite. Further, aragonite has an extra band at 1083 cm^{-1}.

3.2 Estimation of Dolomite Content in Limestone

The spectrum of dolomite is similar to that of calcite except for the 700 cm^{-1} region band which appears at 727 cm^{-1} in dolomite. This band has been used for the estimation of dolomite in limestone.[2][3] The spectrum of kankar (limestone in the form of nodules used as a raw material for the manufacture of cement in India) shows characteristic calcite and clay (1020 cm^{-1}) bands. Dolomite, $CaMg(CO_3)_2$, occurring as an impurity in limestone mineral, is observed to be the major contributor to the ultimate MgO content in cement clinker. Further, the investigation[2] on the high magnesia clinker, up to at least 10% MgO, makes it necessary to assess the mineral forms in which MgO occurs in limestone. The detection and estimation of dolomite in limestone is very important in cement manufacture. An infrared spectral technique for rapid estimation of dolomite has been developed and the results of the analysis have been compared with other existing data.

The infrared spectra of calcite and dolomite are characterized by bands at 711 and 727 cm^{-1}, respectively. These bands appear unperturbed and sharp, with varying intensity, depending on the concentration of these minerals (Fig. 4).

The carbonate rocks (a dolomite stone and a pure limestone) chosen for preparing the standard mixes are given in Table 1.

@Seismicisolation

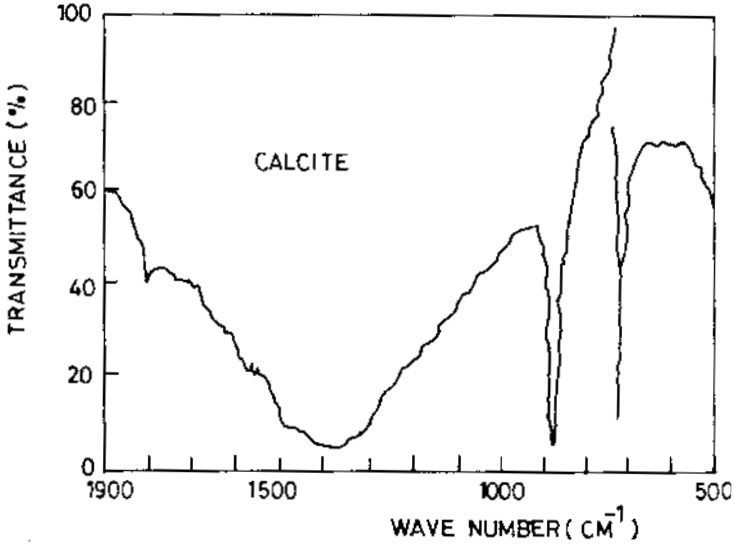


Figure 1. IR spectrum of calcite.

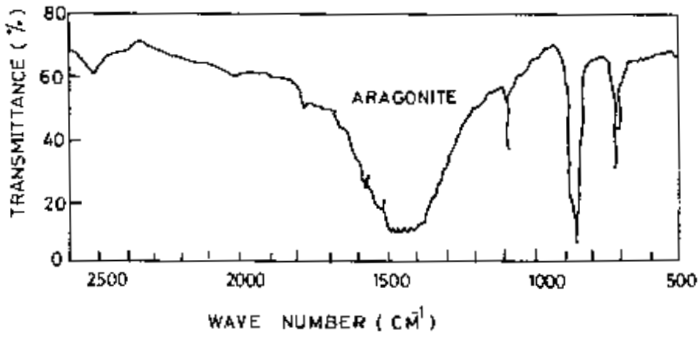


Figure 2. IR spectrum of aragonite.

@Seismicisolation

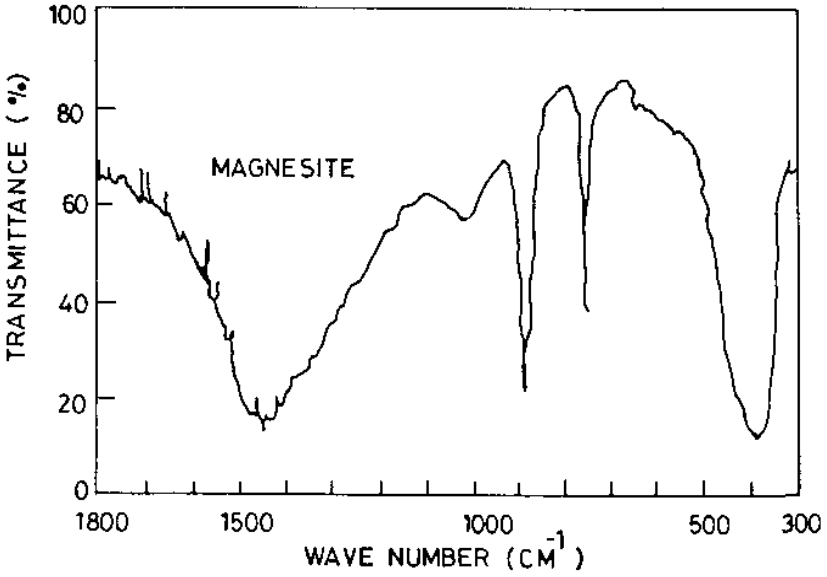


Figure 3. IR spectrum of magnesite.

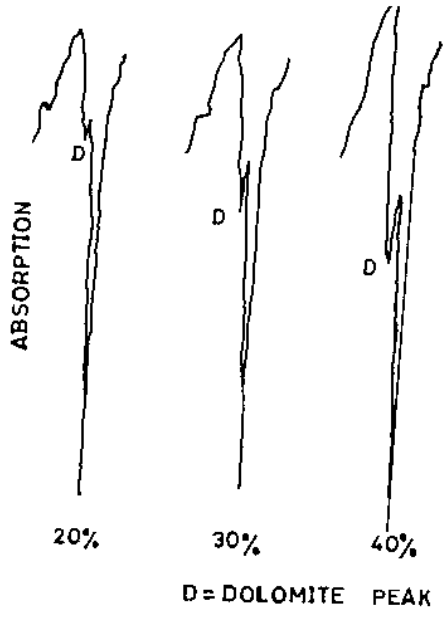


Figure 4. Infrared spectra of standard mixes.

@Seismicisolation

Table 1. Chemical Analysis of Standard Mix Components

Constituents	% Limestone	Dolomitic rock
SiO_2	4.92	1.20
Fe_2O_3	0.75	0.28
Al_2O_3	1.12	0.19
TiO_2	0.046	0.02
MnO	0.20	0.03
CaO	50.90	30.10
SrO	0.14	0.01
MgO	0.36	21.30
Na_2O	0.04	0.01
K_2O	0.25	0.12
P_2O_3	0.08	0.01
CO_2	40.40	46.60
LOI	41.10	46.70

The standards were found to be free from each other (from x-ray diffraction study), i.e., no dolomite in the limestone and no calcite in the dolomite stone. The actual dolomite content was 97.46% (recalculated from the chemical analysis). A satisfactory homogeneous mixing of the standards was carried out in a Perkin-Elmer vertical tube vibrator. Three milligrams of the standard mix or unknown sample were mixed with 250 mg of spectral grade KBr for making pellets for infrared studies. Both the absolute intensity (dolomite peak intensity at 727 cm^{-1}) and relative intensities (ratio of the intensities, dolomite/calcite, bands) of the standard mixes were plotted against concentration of dolomite. The regression line obtained is shown in Fig. 5.

The results of the analysis of two limestone samples (L1 = 43.9% CaO and 16.79% SiO_2; L2 = 54.15% CaO and 1.60% SiO_2; to each of which 30%, by weight, of the dolomite standard sample was added) are presented in Table 2.

The absolute intensity method gives one kind of measure of impurities (here SiO_2 in L1). The higher value of dolomite content (33.50%) in L1 is caused by the lower calcite content as evident from the high percentage of compensating SiO_2. The results of three unknown samples are presented in Table 3 and are verified by DTA and chemical analysis.

@Seismicisolation

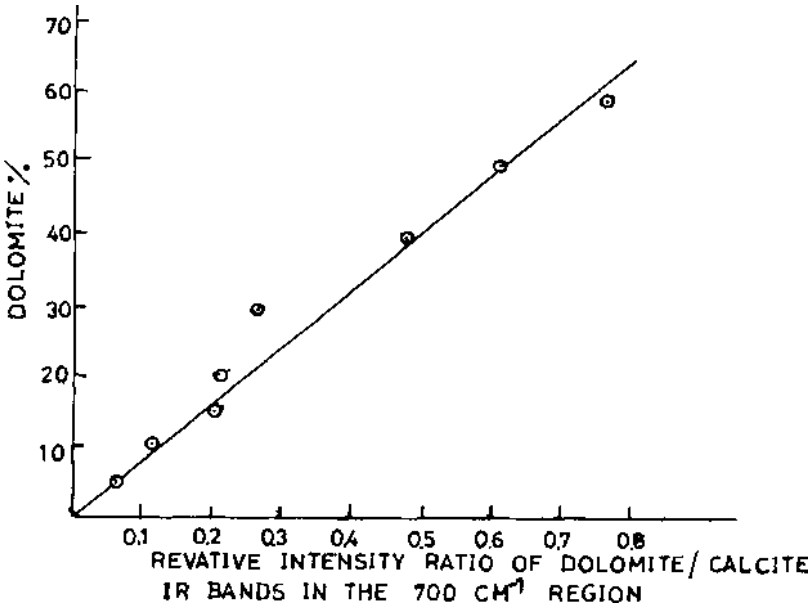


Figure 5. Infrared calibration curve based on the absolute intensity of dolomite band.

Table 2. Comparative Analysis of Limestones by Absolute and Relative Intensity Methods

The absolute intensity method

Samples	Infrared absorption intensity at 727 cm^{-1}	Actual dolomite content (%)	Determined dolomite content (%)	Difference obtained in dolomite
Mix L1	8.4	29.25	27.25	2.00
Mix L2	9.2	29.25	28.50	0.75

The relative intensity method

Samples	Relative intensity ratio of 727 & 711 cm^{-1} bands	Actual dolomite content (%)	Determined dolomite content (%)	Difference obtained (%)
Mix L1	0.41	29.25	33.50	4.25
Mix L2	0.34	29.25	28.25	1.00

** Measured in arbitrary units.*

@Seismicisolation

Table 3. Analysis of Unknown Limestones

Sample No.	Chemically determined		Dolomite percentage recalculated	Dolomite content determined by:	
	CaO	MgO		Infrared spectra	Thermal Method
RS 727	41.10	10.17	46.43	42.5	41.4
BMLS 8	34.63	5.0	22.88	20.5	17.5
RM 353	49.65	3.43	15.78	14.8	15.8

**Absolute intensity method*

It is noted that the results obtained by the infrared spectrometric method are the mean values of those obtained by DTA and chemical analysis. The experimental error of the method has been calculated by running three separate mixes of two samples (70% L1 + 30% reference dolomite stone) and is presented in Table 4.

Table 4. Reproducibility of Results by the Absolute Intensity Method

Sample No.	Absolute intensity of 717cm^{-1}	Mean	Standard deviation	Coeff. of variation	Standard deviation for the mean	Coeff. of variation for the mean values
L1-1	8.5	8.43	0.16	1.9%		
	8.2					
	8.6					
L1-2	8.0	8.20	0.17	2.1%	0.011	1.33%
	8.2					
	8.4					
L1-3	8.3	8.23	0.05	0.61%		
	8.2					
	8.6					

**Measured in arbitrary units*

@Seismicisolation

Based on the above investigation the following conclusions can be drawn:

1. The infrared spectroscopic method of quantitative estimation of dolomite-containing limestone is direct and dependable. It takes about 30 minutes to analyze a sample, the results of which compare favorably with thermal and x-ray methods.
2. The relative intensity method is useful for a check of other impurities (SiO_2, etc.) besides being complementary to the absolute intensity method.
3. Only a conventional infrared spectrometer is required for this analysis and the range studied (400 to 700 cm^{-1}) is free from atmospheric interference.
4. The estimation of calcite can also be carried out simultaneously.

3.3 Argillaceous and Siliceous Limestones

The spectrum of argillaceous limestone has the usual calcite bands besides the bands at 1000, 799, 510 and 462 cm^{-1}. The presence of clay is indicated. The spectrum of coral limestone indicates very little clay or silica. The spectra of siliceous limestone and limestone with jasper show a high percentage of quartz, as is evident from the strong bands at 1165, 1090, 798, 775, 692, 515 and 465 cm^{-1}. The quartz bands in the spectrum of jaspar are broader, especially at 1090 cm^{-1}, indicating the cryptocrystalline nature of jasper.

3.4 Feldspar, Orthoclase, Quartz, and Jaspar

The spectrum of orthoclase is characterized by several bands at 1138, 1050, 1010, 772, 725, 645, 603, 584, 538, 468 and 425 cm^{-1}. The spectrum of feldspar is quite similar to that of orthoclase except that the 1000 cm^{-1} band is unresolved and the main peak head in this region shifts down to 980 cm^{-1} with slight shifting of other bands. The spectra of quartz and jaspar are almost identical except for some differences in band positions; for example, jaspar has a band at 1165 cm^{-1} while quartz has this band at 1175 cm^{-1}.

@Seismicisolation

3.5 Tourmaline, Kyanite, Topaz, and Talc

The spectra of topaz and talc consist of a few absorption bands. The spectrum of topaz has a characteristic medium intensity band at 1162 cm^{-1}, a shoulder at 1000 cm^{-1}, and the main band head in this region is at 865 cm^{-1}, while the spectrum of talc has a weak shoulder at 1050 cm^{-1}. The other characteristic bands are at 670 and 615 cm^{-1}. The hydroxyl stretching band appears at 3636 cm^{-1} in the spectrum of topaz. Kyanite, being a nesosilicate (same as topaz), has a complex spectrum below 750 cm^{-1}, unlike that of topaz. The spectrum of tourmaline (cyclosilicate) has a characteristic doublet at 1300 and 1000 cm^{-1}. The spectrum has some similarity with that of kaolinite below 800 cm^{-1}.

3.6 Rhyolite, Granite, and Basalt

The spectrum of granite indicates the presence of quartz (sharp band at 697 cm^{-1}) and orthoclase (at 650 cm^{-1}). The other regions are overlapped. The spectrum of basalt is simple since the principal constituents, albite and anorthite, have Si_3O_8 units and overlap in the same region. The spectrum of rhyolite shows the presence of quartz (bands at 800 and 780 cm^{-1}), but the presence of feldspar cannot be detected in its spectrum because of the amorphous nature of feldspar.

3.7 Kaolin, Red Clay, Black Cotton Soil, and White Clay

The spectrum of kaolin is characterized by bands in the 3600 cm^{-1} region (hydroxyl stretching), at 1150 to 960 cm^{-1} (Si-O stretching region), and below 960 cm^{-1} (bending and lattice modes) (Fig. 6). The spectrum of white clay shows a broad and unresolved band in the Si-O, stretching band appears at 1025 cm^{-1} (red clay) and at 1070 cm^{-1} (white clay). The spectrum of black cotton soil is diffused and the soil sample is very poorly crystalline. Neyveli clay and fire clay are principally kaolinitic. The spectrum of bentonite indicates the presence of the montmorillonite mineral, with bands at 1102, 1030, 915, 521, and 467 cm^{-1}. The spectrum of laterite closely resembles that of kaolinite, goethite, gibbsite, etc., which are the constituents of laterite.

@Seismicisolation

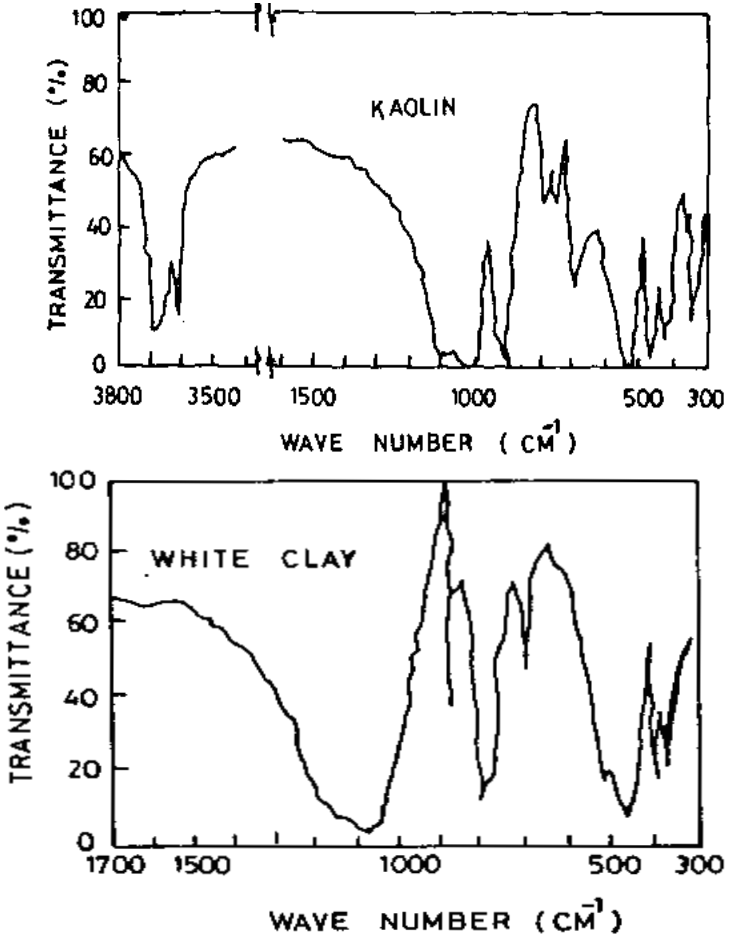


Figure 6. Spectra of kaolin and white clay.

3.8 Chrysotile, Tremolite, and Asbestos

The spectra of chrysotile and tremolite are different. The former consists of Si_2O_5 double-layer while the latter has Si_4O_{11} units in the structure. The 1000 cm^{-1} Si-O stretching region has multiple bands in the spectrum of tremolite. The presence of carbonate in tremolite is shown by the weak band at 1400 cm^{-1}. The spectrum of asbestos shows some bands (800 to 600 cm^{-1}) common to tremolite, but the bands near 900 cm^{-1} are not present in chrysotile or tremolite.

@Seismicisolation

3.9 Biotite, Muscovite, Mica Schist, and Phlogophite Mica

The mica group belongs to phyllosilicate. Each SiO_4 unit is linked to three other SiO_4 groups, similar to that in talc. The spectrum of biotite mica is characterized by strong bands at 1018 and 465 cm^{-1} and two weak bands at 728 and 685 cm^{-1}. The spectra of mica schist and muscovite are similar; the band in the 1000 cm^{-1} region is fairly broad. The spectrum of phlogophite is different to that of muscovite in the 800 to 600 cm^{-1} region.

3.10 Apatite, Phosphatic Rocks, and Gypsum

The spectrum of apatite rock is characterized by strong bands at 1040, 610, and 570 cm^{-1}, while that of gypsum (Fig. 7) is identified by the bands at 1140, 668, and 602 cm^{-1}.

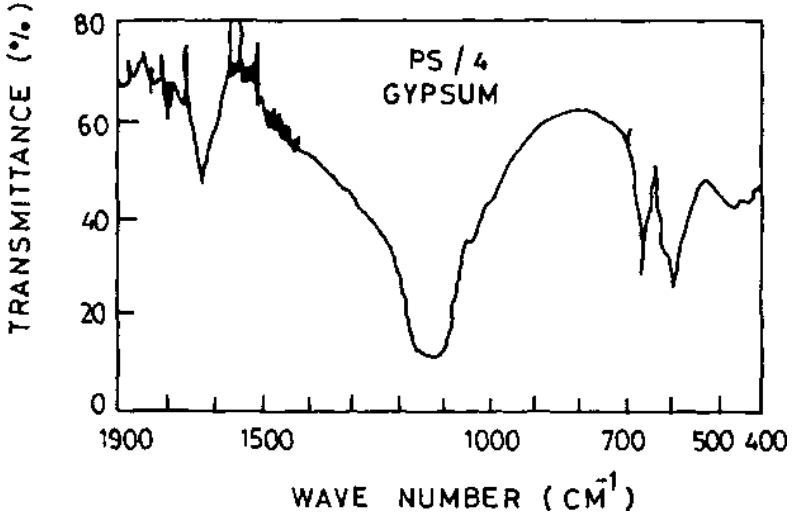


Figure 7. IR spectrum of gypsum.

@Seismicisolation

4.0 SPECTRA OF FLY ASH AND SLAG

The spectrum of the fly ash sample is not well defined (Fig. 8). The presence of bands in the region 800 to 600 cm^{-1} can arise from the presence of sillimanite and mullite. Recent study by Vempati, et al.,[5] on Texas lignite Class-F fly ash is more elaborate in respect of IR band assignments. The bands at 1137, 625 and 476 cm^{-1} are assigned to mullite and the strong band at 800 cm^{-1} is related to an amorphous aluminosilicate phase. The occurrence of ν_3 band at 1080 cm^{-1} is explained by a high degree of polymerization.

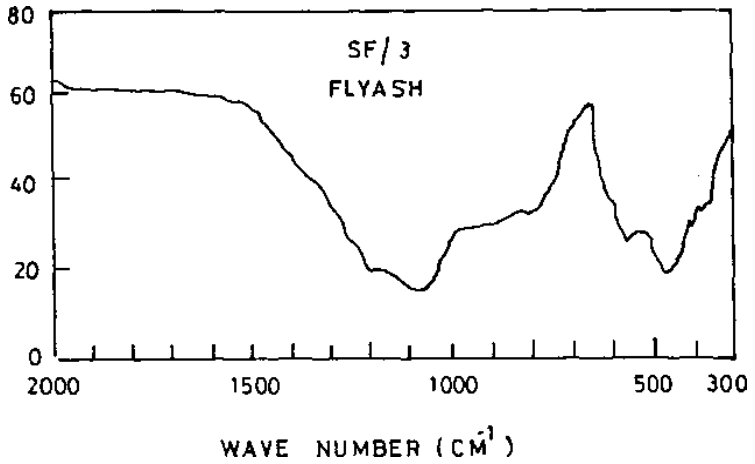


Figure 8. IR spectrum of fly ash.

The spectrum (Fig. 9) of blast furnace slag indicates the amorphous nature of the material (broad bands), while the same slag, crystallized in the laboratory, shows the presence of melilite.[6] The bands in the spectrum closely resemble those of melilite. The spectrum of the ferrochrome slag is reported to have the presence of β-Ca_2SiO_4.[7][8]

5.0 ANHYDROUS CEMENT AND ITS PHASES

Earlier studies on IR spectra of portland cement and its phases were reported by Launer,[9] Roy,[10] Hunt,[11] and Midgley.[12] The spectrum of β-C_2S from 620–1500 cm^{-1} has been measured by Launer. Roy reported spectra of C_3S and β-C_2S and found C_2S to give an altered spectrum of KBr

@Seismicisolation

pellets. Hunt presented IR absorption spectra of C_2S (α and β), C_3S and other compounds. Apparently, the attempts were directed towards the identification of all minerals, individually and in combination, in order to make use of this technique in quantitative estimation of phases in portland cement. Ghosh and Chatterjee[13] presented absorption and reflectance spectra (ATR) of portland cement and its phases (Fig. 10) and of a number of NBS cement samples. The spectral regions of interest are the 500 cm^{-1} and 900 cm^{-1} regions. The spectrum of portland cement is the resultant of all the phases. An attempt has been made to correlate the band intensity ratio (bands around 925 and 805 cm^{-1}) for quantitative estimation of the silicate phases in cement. It appears that a semi-quantitative estimation of the silicate phases is possible in certain cement samples. Butt, et al.,[14] have observed that IR absorption spectra of cements are basically similar, consisting of the absorption bands of alite at 925, 895–885, 520, and 465 cm^{-1}.

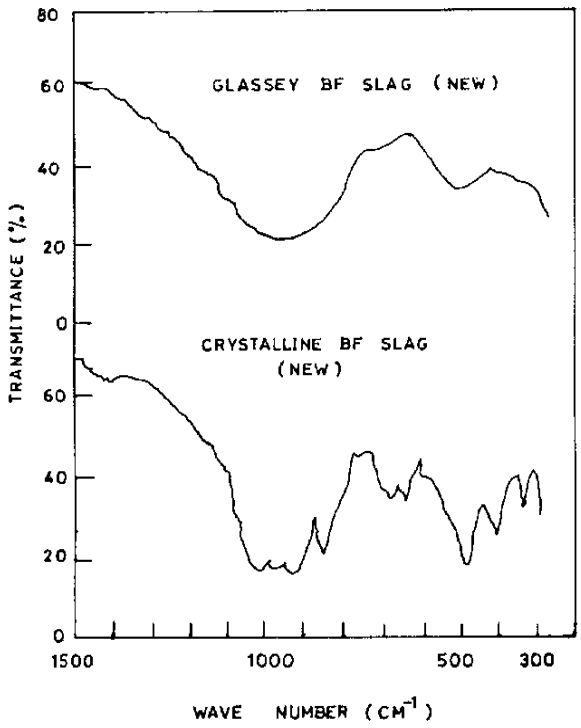


Figure 9. IR spectra of blast furnace slags.

@Seismicisolation

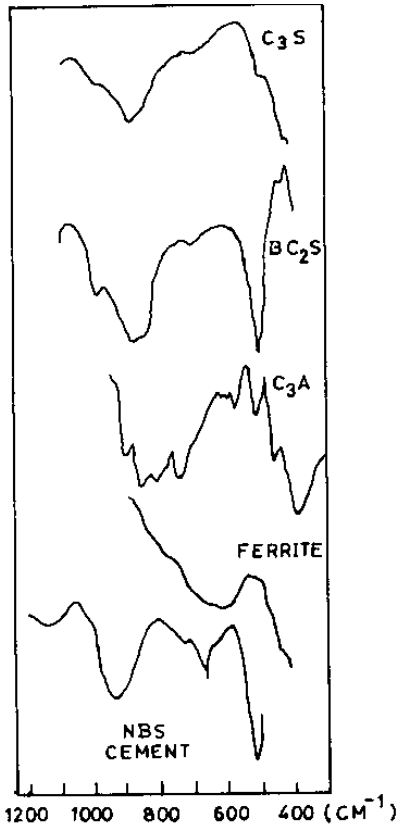


Figure 10. IR reflection spectra of cement minerals and cement.

The IR bands of belite at 965–985 cm^{-1} and 845–850 cm^{-1} are also present in the spectra of cement. The band at 1080–1100 cm^{-1} in the spectra of clinker is due to the presence of sulfate. The band at 770 cm^{-1} in the spectrum of high alumina cement could be assigned to (A1-O) vibrations of aluminate mineral components. Ghosh and Hando[15] observed that with the help of IR spectroscopy the presence of a particular mineral component or an individual compound, even if present in very small amounts in portland cement, can be determined.

Spectra of pure phases are still a matter of much interest for identification, structure determination (coordination number, etc.), polymorphism, etc. The spectral investigations on C_3A for obtaining structural information were reported by several investigators.[14][16]–[18] Qualitative interpretations of the spectra of C_3A have also been made. Bensted and

@Seismicisolation

Varma,[19] in their studies, tabulated the spectral data of the cement phases with tentative assignments. Substitution of various ions in the C_3S lattice reduces the sharpness or even causes disappearance of some silicate bands and broadening of bands. Alite contains discrete SiO_4^{4-} tetrahedra which are very much affected by the proximity of other ions present in the lattice; however, such effects are weaker in belite. C_3A shows discrete bands in its spectrum, in contrast to that of the ferrite phase (C_4AF), which is somewhat glass-like.

Boikova, et al.,[20] reported IR spectra of the different crystal forms of C_3A. The band positions are given in Table 5.

Considerable differences in band position and in band number have been observed for different crystal forms of C_3A. Factor group analysis was performed to explain the spectra of the different crystal forms of C_3A. The spectral data of C_3A had earlier been reported by Bensted and Varma,[19] and others.[14][17][18]

Bensted and Varma[21] also studied the polymorphs of C_2S. The spectral data are listed in Table 6. The spectra (Fig. 11) are characteristic. The spectra of the high temperature polymorphs are quite similar.

Table 5. IR Bands of Different Crystal Forms of C_3A

	Chemical Composition (%)				
C_3A	CaO	Al_2O	Na_2O	900-700 cm^{-1}	Below 700 cm^{-1}
Cubic	60.57	37.40	2.42	894, 862, 842, 816 804, 788, 742, 710	626, 593, 525, 512 460, 431, 415
Orthor-hombic	59.04	37.50	3.80	904, 861, 824, 801 745, 716	592, 540, 510 473, 431, 417
Tetra-gonal	57.52	37.22	4.83	879, 862, 790, 732 723	597, 537, 523, 494 430, 416
Mono-clinic	56.30	37.38	5.70	870, 794, 733, 724 493, 432, 416	610, 596, 537, 523
C_3A (Cubic)	62.50	37.23	—	922, 874, 794, 735 724	609, 598, 537 522, 492, 432, 416

The IR study of all polymorphs of C_3S appears to be not reported so far. Conjeand and Boyer[22] observed an extra band at 832 cm^{-1} in the Raman spectra of monoclinic alite, but this band was found to be absent in the IR spectrum of synthetic monoclinic alite.

@Seismicisolation

Table 6. IR Spectral Data of C_2S

			440 m
			455 sh
510 s	500 sh	500 sh	495 s
550 sh	515 s	520 s	515 s
	550 m	540 sh	565 s
			815 w
840 sh	850 sh	845 vs	855 vs
		870 sh	
930 vs, b	935 vs, b	890 vs	920 w
		920 sh	930 sh
1000 sh	980 s	1000 s	950 s
1150 w	1150 w	1170 vw	1150 vw

s = strong sh = shoulder vs = very strong
b = broad w = weak vw = very weak

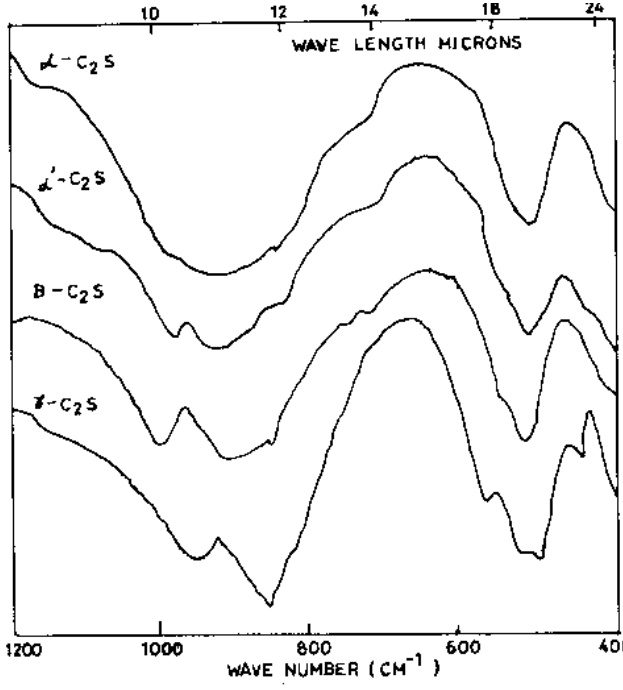


Figure 11. IR spectra of C_2S polymorphs in KBr discs.

@Seismicisolation

Bonen, et al.,[23] published FT Raman spectra of commercial and synthetic C_3S, C_2S and synthetic C_3A and C_4AF phases. According to these authors, the main band of the synthetic C_3S polymorph corresponds to the out-of-plane Si-O bending ν_4 and it is shifted to higher frequency for the commercial C_3S. The main band for the C_3S mineral, however, corresponds to the asymmetric Si-O stretching ν_3. The analysis for synthetic C_3A polymorphs and C_4AF conforms with the earlier published data (Table 7).

Table 7. Main FT Raman Bands of Commercial and Synthetic Cement Phases

Phase		Wave numbers cm^{-1}						
C_3S	Triclinic	541	714	798	925	1340		
	Monoclinic	593	—	—	938	1361		
	Oxidizing	663			1040	1464		
		(657–668)			(101 1–1058)	(1456–1471)		
C_2S	β-C_2S		722	799	1016	1116		1389
	Oxidizing	671		1013	1112	1459		
		(659-682)			(1019-1040)	(1442-1470)		
	Reducing	679			980	1125		1462
		(670-688)			(951-1020)			
C_3A	Cubic	504	753		1083	1525		
	Ortho	493	521	763	1078			
	C_4AF	581			1064			
	Quartz	128	206	265	355	465	809	1081

6.0 SOLID SOLUTION

Tarte,[24][25] while studying IR spectra of solid solution ($C_2A_pF_{1-p}$), observed an increase in wave number, but above $C_2A_{0.7}F_{0.3}$ no change in spectra until at higher alumina contents up to $C_2A_{8.85}F_{0.15}$. The position of certain lines changes, due, apparently, to the appearance of new phases such as C_3A and $C_{12}A_7$. An interesting comparison of spectral absorption characteristics was made for the C_2F solid solution (vitreous and crystalline phases) and of the C_4AF phase. The isomorphous replacement of Al-Fe was also studied by Tarte[26] and this was accompanied by a change of position

@Seismicisolation

of bands and the appearance of a new band which was assigned to the tetrahedral FeO_4 group. Sakurai, et al.,[27] reported IR spectra of Cr substituted ferrite phase in the C_2F-C_2Cr system and observed that the absorption peaks at 1160, 950, and 710 cm^{-1} became stronger with increasing substitution while the bands in the 640–580 cm^{-1} region became weaker. A similar phenomenon was observed in the C_4AF-C_2Cr system, i.e., the 1160 and 720 cm^{-1} became stronger with increasing substitution of Cr_2O_3 whereas the strong absorption spectra at 780 and 430 cm^{-1} became weaker. The bands in 720–780 cm^{-1} and at 430 cm^{-1} belong to AlO_4 tetrahedra and the 610–660 cm^{-1} to FeO_4 tetrahedra.

Toropov[28] reported the IR spectra of solid solution of Ca_3SiO_5-Ca_3GeO_5 in the range 700–1200 cm^{-1} and observed differences in intensity and positions of 930 and 780 cm^{-1} bands. Singh[29] observed no change of C_3S spectrum when C_3S was doped with NiO and concluded that Ni might not replace Si. Also, the liberation of free lime was found to increase with the addition of NiO, which could indicate that Ni substitutes for Ca. Shchetkina, et al.,[30] also failed to notice any change in the band position in the IR spectra of C_3S doped with Cr_2O_3 (0.8%); however, they observed a drop in intensity of the absorption bands at 825, 450, and 410 cm^{-1}.

Between the IR spectra of the cubic C_3A (pure) and cubic C_3A (2.4% Na_2O), some shifts of frequencies and redistribution of intensities in the 460 cm^{-1} region occur, which have been assigned to the structural disordering as a result of Ca-Na substitution.[20]

7.0 HYDRATION STUDIES

Studies on hydrated products of cement phases reveal[11] that spectral details in the 700 to 1200 cm^{-1} are lost when C_3S is hydrated. Lehman & Dutz[31] discussed the IR spectral characteristics during the progress of hydration, fixation of water and absorption of carbon dioxide, and nature of the hydration products of cement minerals. They also reported the spectra of hydrated γ-C_2S and β-C_2S and observed spectral changes in 1000–800 cm^{-1}. They referred to the rapid changes in spectral lines (lowering of intensity, etc.) for C_3S (one day hydrated) and $C_{12}A_7$ (one hour hydrated). The spectral changes for hydrated CA, C_3A, etc., were also noted. Midgley[12] reported the spectrum of C_4AH_{13} and ettringite. An attempt was made to assign bands in the spectrum of portland cement. Bensted[32] studied the IR spectra of hydrated α-, α'-, β-, and γ-C_2S samples. It was observed that the 930 cm^{-1} band in the spectrum of the anhydrous

@Seismicisolation

phase shifted to higher frequency. Slow hydraulic behavior of the phases was also observed in the IR study.

7.1 C-S-H and Other Hydrates

A number of researchers have reported the spectra of C-S-H.[10]–[13] The IR spectra of plombierite, C-S-H (I), techaranite, and tobermorite are all similar to one another, but different from those of fairly closely related phases, such as xonotlite.[33] It has been inferred that a fair degree of structural similarity exists in these four phases, though the x-ray diffraction evidence indicates that techaranite and plombierite differ from tobermorite and C-S-H (I) in more than the relative degree of crystalline order. Spectra of okinite, gyrolite, lock enort, tobermorite, afwillite, hillebrandite, and a synthetic xontlite have been obtained.[11] Midgley[12] reported spectra of C_3SH_2, tobermorite and afwillite as well as those of flints, CSH(A), $\gamma C_2S\ H_2$, βC_2SH and αC_2SH. These spectra, in general, can be used for identification purposes.

Raman studies of C-S-H and other hydrated products were reported by Bensted.[32] For identification of C-S-H in a hydrating cement material, the band at 970 cm^{-1} is designated as ν_3 SiO_4. Conjeand and Boyer[22] reported the Raman spectra of C-S-H (I) and found only one characteristic broad line, at 670 cm^{-1} in the spectrum. The main products of hydration, calcium hydroxysilicate of the C_2SH_2 and CSH (β) types were detected in the IR spectra from the ν_3 (Si-O) absorption band at 965–975 cm^{-1} and calcium hydroxide from the ν_{OH} absorption band at 3640 cm^{-1}. Progressive hydration of portland cement is accompanied by the increase of the intensities of these absorption bands and simultaneous decrease of the intensities of the absorption bands of the constituent mineral phases in portland cement. In the case of amorphous hydration products (especially formed at lower temperatures), an IR spectrum is useful for identification. Butt, et al.,[14] conducted IR studies of forms in which water is bound in hydrated binders. They discussed the possibility of using IR spectroscopy in determining the presence of water in absorbed and capillary liquid form as well as bound H_2O in the hydrated clinker minerals as water of crystallization or bound OH.

Puertas, et al.,[34] reported the use of IR spectroscopy in studying hydration of $4CaO{\cdot}Al_2O_3{\cdot}Mn_2O_3$ and $4CaO{\cdot}Al_2O_3{\cdot}Fe_2O_3$ in the presence and absence of gypsum. In the high frequency region, i.e., 4000–2600 cm^{-1}, the bands at 3695, 3555, and 3490 cm^{-1} of one day hydrated sample of C_4AF were assigned to the OH^- groups of the metallic hydroxide and also water

@Seismicisolation

molecules. The band at 2990 cm^{-1} was assigned to a hydrate of the hexagonal type and a monocarbonate phase. In the low frequency region, the IR bands at 600, 530, 420, 350, and 250 cm^{-1} were assigned to hexagonal hydrate and that at 375 cm^{-1} to cubic hydrate. The IR spectra of the seven day and 28 day samples indicated the presence of cubic hydrate (sharp bands near 3670–75 cm^{-1} and at 524, 400, and 375 cm^{-1}). These latter bands were assigned to Al-O and Ca-O vibrations.

In the case of C_4AMn hydration, the IR spectra confirmed the mineralogical composition as determined by XRD. The IR spectra of the one day and seven day pastes are practically identical with absorptions assignable to hexagonal hydrates and carbo-aluminates. The bands at 3685–90 and 3540–45 cm^{-1} were assigned to the CH-group vibration of a tetracalcium aluminate hydrate of the type C_4AH_9. The absorption band at 2990–3000 cm^{-1} is characteristic of highly hydrated carbo-aluminates. The bands at 780, 600, 530, 425, 420, 305 and 250 cm^{-1} confirmed the presence of a hydrate of the hexagonal type. The IR spectrum of the 28 day sample differs notably from the previous ones. The sharp band at 3645 cm^{-1} can be taken as characteristic of OH-group vibrations in hydrated calcium aluminates of the cubic type. Another band at 3540 cm^{-1} indicates the presence of hexagonal hydrates. The presence of cubic hydrates (bands at 527, 400, and 325 cm^{-1}) and hexagonal hydrates (bands at 420 and 300 cm^{-1}) has been indicated. The ettringite bands in the spectra of paste hydrated (in presence of gypsum) (up to 28d) C_4AF and C_4AMn indicate that the formation of this compound is continuous in C_4AF while it is completed in early age (~7 days) in C_4AMn.

The effects of sodium lignosulfonate superplasticizer on the hydration of portland Type-V cement were investigated by XRD and FTIR techniques.[35] A comparison of IR bands between dry cement clinker, hydrated OPC (V), and superplasticizer-added OPC (V), was carried out. The data are given in Table 8.

The explanation given for the shifting to higher frequency of Si-O vibration bands in hydrated cement is due to polymerization; however, the effect is less in superplasticized cement paste. Stevula, et al.,[36] studied the hydration product at the interface between blast furnace slag aggregate and hydrated cement paste using IR, SEM, and XRD Methods. The hydrated OPC paste showed a band at 970 cm^{-1} (Si-O stretching) and the bands at 1426, 873, and 712 cm^{-1} were assigned to carbonate bands. The IR spectrum of BFS was found to change after one year of hydration. The Si-O stretching vibration at 1015 cm^{-1} shifted to 985 cm^{-1} and acquired higher intensity. The absorption band of hydrated cement paste from the interface appeared

@Seismicisolation

at 974 cm^{-1}; the band due to melilite slag being at 1000 cm^{-1}). A broad shoulder near 1110 cm^{-1} was assigned to SO_4 vibration of ettringite and the 3636 cm^{-1} band to $Ca(OH)_2$ vibration.

Table 8. IR Spectral Data of Hydrated OPC with a Superplasticizer

Band Assignment	Dry Clinker	OPC paste W/C = 0.35	SP/OPC 1.0% W/C = 0.35	SP/OPC 1.5 W/C = 0.35	SP/OPC 1.0 W/C = 0.25
ν_3)	925	980	947	936	937
ν_4)SiO_4	525	536	530	521	522
ν_2)	455	467			
ν_3)	1100	–	1112	1114	1115
)SO_4^{2-}	1160				
ν_4)	667	667	665	664	665
ν_1+ ν_2/H_2O		3325	3340	3330	3330
		3450	3420	3425	3425
ν_2 H_2O		1630	1666	1673	1673
ν_{OH^-}		3645	3640	3640	3640
ν_3)		1425	1425	1430	1425
ν_2) CO_3^{2-}		1497	1483	1485	1490
ν_4)		876	877	876	878
		732	732	730	730

Hanna, et al.,[37] reported the use of IR spectroscopy in cement hydration of cement-based solidification of hazardous wastes. They observed a cyanide peak at 2108 cm^{-1} in the spectrum of the solidified material. Sodium cyanide is known to retard the normal hydration of cement. The ν_3 SO_4^{4-} band shifted to a lower frequency and it was interpreted by a lower degree of polymerization.

Sakai and Sugita[38] studied the IR spectra of the material at the surface and interface of cement or aggregate in a polymer modified cement (PMC). A copolymer of ethylene vinyl acetate (EVA) was used in this study. The spectra indicated the presence of EVA in a polymeric form. The films formed on the surface of the PMC and in the interface, improved the adhesive property of PMC.

@Seismicisolation

Kurbus and Marin Kovic[39] studied hydrothermal metastability and structural disorder of the 0.301 nm phase. The IR spectra of scawtite and 0.301 nm phase are closely related, especially in the region of the deformation vibration of carbonate group, ν_2 and ν_4, while in the ν_3 region, there is some difference in the splitting pattern. The 0.301 nm phase spectrum is more diffuse. The authors concluded that the 0.30 nm phase has a structure that is basically that of scawtite, but somewhat disordered, and probably with some replacement of CO_3 by OH ions.

7.2 Ettringite and Other Compounds

The study of ettringite and monosulfate by IR has received much attention.[19][40] Raman study of ettringite is reported by Bensted.[32] There is little difference among the spectra of substituted ettringites (T1, Cr, Mn, or Fe) as reported by Bensted and Varma;[41] however, there is considerable difference between the spectra (Fig. 12) of monosulfate and ettringite (Table 9).[42]

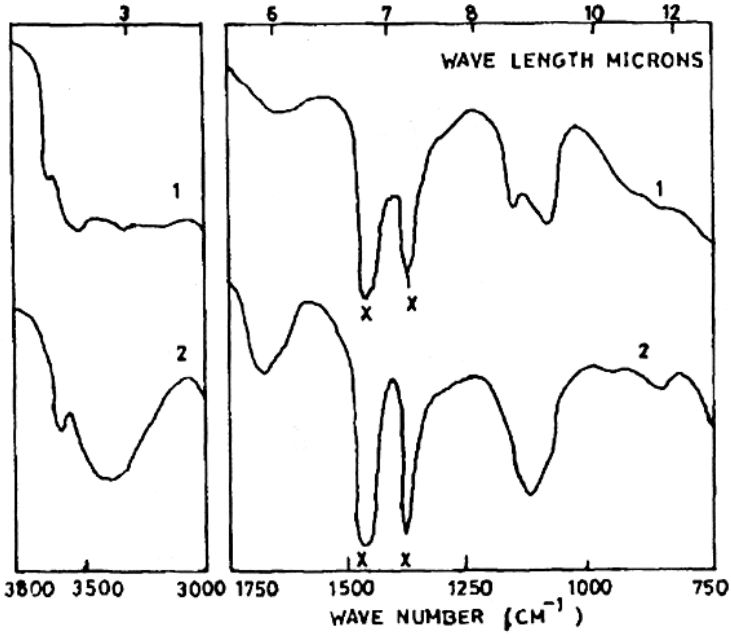


Figure 12. IR spectra of *(1)* monosulfate and *(2)* ettringite in nujol mull; X = bands due to nujol.

@Seismicisolation

Table 9. IR spectral Data of Monosulfate and Ettringite

Monosulfate	Ettringite
850 vw	855 vw
1100 vs	1120 vs
1170 s.sh	1640 b, m
1600 w	1675 b, s
3100–3500 vs, b	2190 vw
3540 vs	3420 b, vs
3675 s	3635 m

s = strong sh = shoulder vs = very strong
b = broad w = weak vw = very weak

The various forms of calcium sulfate can be clearly identified by IR spectroscopy.[43] The useful IR range for their characterization is 1000–1300, 1550–1750, and 3100–700 cm^{-1}. This qualitative demonstration of different forms of calcium sulfate has been used for characterization of oil well cements. The quantitative estimation is not possible due to extensive overlap of bands. While IR spectroscopy may not be a substitute for other usual quality evaluation techniques, it can be indicated whether a detailed examination of a sample is necessary or not.

7.3 Hydration Studies under Different Conditions

Gouda and Roy[44] used IR spectroscopy for studying hot-pressed cement materials. They observed that anhydrous C_2S is present in the hot-pressed compound. It was also observed that the bands due to A1-O and Fe-O show stretching shift. An absorption peak at 3500 cm^{-1}, due to free hydroxyl stretch, was found in all hot-pressed and water cured materials. The presence of CO_2 (1440 cm^{-1}) was observed in some of the compounds. It was also noted that all the standard and hot-pressed Ca-silicate or cement paste studied had absorption maximum more similar to one another (in the 1025 to 775 cm^{-1} region). Arizumi[45] reported the spectral characteristics of gehlenite (C_2ASH_8) at different temperatures (200–1000°C and room temperature). Baird, et al.,[46] studied the effect of carbonation on C-S-H produced by refluxing slurries of $Ca(OH)_2$ and silica gel.

The influence of alkali carbonates on the hydration of cement by using IR spectroscopic method was reported by Neil[47] and extinction values were used for obtaining a quantitative result. IR spectroscopy was

@Seismicisolation

applied for studying hydration of OPC in the presence of $CaCl_2$ and Ca-formate and it was observed[48] that more C-S-H gel was formed with the $CaCl_2$ additive. Turriziani and Rio[49] used IR spectroscopy in high chemical resistance pozzolanic cements. The effect of various gypsum set-retarders (by-product gypsum, ferrogypsum and phosphogypsum) on the hydration of cement was also studied.[50] McCall and Mannone[51] used IR spectroscopy to determine the concentration of triethanolamine in cement hydration. The bands at 1030 and 900 cm^{-1} were used for this purpose. Connally and Hime[52] confirmed this observation. Singh, et al.,[53] concluded, from IR study of the mixes of C_3A and sulfanilic acid, that strong bonding exists between them. Ben-Dor and Rubinstein[54] observed a lowering of the intensity of the OH band with increasing amount of P_2O_5 in a hydrated C_3S sample.

8.0 STUDIES ON CONCRETE

Sugama and Kukacka[55] studied the effect of C_2S and C_3S on the thermal stability of vinyl-type polymer concrete. The most significant changes in the spectra are in the absorption band of the CH_2 group vibration in the region 3020 to 2900 cm^{-1} of PMMA containing the C-S system and cement. These absorption bands were found to be much weaker in intensity than that of the bulk PMMA. It was inferred that the reaction occurs between the calcium oxide in the filler and the CH_2 groups in the polymer. Berry, et al.,[56] made use of Raman spectroscopy in their study of a sulfur infiltrated concrete sample and postulated the presence of Sr^{2+} species from the band positions of its spectrum with that of Na_2SO_4 in aqueous solution. Hirche[57] observed from the studies of reactive aggregates that cement aggregates with high infrared absorption bands in 3800 and 2800 cm^{-1} regions are alkali reactive. It was suggested that all alkali aggregates with total absorption greater than 8×10.5 cm/mol would be detrimental to the durability of concrete.

9.0 MISCELLANEOUS STUDIES

Iob, et al.,[58] used IR for the identification of constituents in a commercial concrete waterproofing material. The constituents identified are cement, carbonates, (Na/NH_4) fumarate, and melamine formaldehyde polymer.

Way and Shayan[59] presented spectra of crystalline analogues of alkali-aggregate reaction products.

@Seismicisolation

Studies[60] have been carried out on the ancient gypsum mortars from St. Engracia, with the help of IR spectroscopy. Three broad groups of repair materials were identified. Spectral lines corresponding to gypsum, carbonates (dolomite), silicate, and nitrates (in some samples) were observed. The presence of wax with oil or resin, or egg yolk, was also identified.

Sugama and Carciello[61] studied the sodium phosphate-derived calcium phosphate cements. In the IR spectrum, the appearance of a new peak at 1110 cm^{-1} and the disappearance of peaks due to P-O and P-O-H have been accounted for by the formation of sodium calcium phosphate. Similarly, the formation of orthophosphate hydrate salt was identified by a peak at 3430 cm^{-1}. They were able to correlate the higher strength of sodium polybasic (Na-P) salt-derived calcium phosphate cements.

ACKNOWLEDGMENT

The author thanks Messrs. Gujarat Ambuja, Cements, Ltd., for providing assistance in preparing this chapter. The author thanks ABI, New Delhi, for permission to use materials published in *Cement and Concrete - Science & Technology*, Vol. 1, Part-II, edited by S. N. Ghosh (1992), and the Palladian Publications, Ltd., England, for permission to reproduce Figs. 11 and 12.

REFERENCES

1. Herzberg, G., *Infrared and Raman Spectra*, and other volumes, D. Van Nostrand, New York (1945)
2. Handoo, S. K., and Ghosh, S. N., Infrared Spectroscopic Study of Cement and Raw Materials, *Cement and Concrete Science & Technology*, Vol. I, Part II, pp. 222–252, ABI, New Delhi (1992)
3. Ghosh, S. N., Viswanathan, V. N., and Chatterjee, A. K., Estimation of Dolomite Mineral in Limestone by Infrared Spectroscopy, *J. Mater. Sci.*, 11:1167 (1976)
4. Farmer, V. C., and Russell, J. D., The Infrared Spectra of Layer Silicates, *Spectrochim Acta.*, 20:1149 (1964)
5. Vempati, R. K., Rio, A., Hess, T. R., Cocke, D. L., and Lawer, H. V., Jr., Fractionation and Characterization of Texas Lignite Class F Fly Ash by XRD, TGA, FTIR and SEM, *Cem. & Concr.*, 24:1153–1164 (1994)

@Seismicisolation

6. Hariya, Y., Pollase, W. A., and Kennedy, G. C., An Experimental Investigation of the Relationship of Mullite to Sillimanite, *Am. Miner.*, 54:1419 (1969)
7. Keller, W. D., Sootts, J. H., and Biggs, D. L., Infrared Spectra of Some Rock Forming Minerals, *J. Am. Sci.*, 250:453 (1962)
8. Ghosh, S. N., and Chatterjee, A. K., Absorption and Reflection Infrared Spectra of Major Cement Minerals, Clinker and Cements, *J. Mater. Sci.*, 9:1577 (1974)
9. Launer, P. J., Regularities in the Infrared Absorption Spectra of Silica Minerals, *Am. Miner.*, 37:764 (1952)
10. Roy, D. M., Subsolidus Data for the Join Ca_2SiO_4-$CaMgSiO_4$ and the Stability of Merwinite, *Miner. Mag.*, 31:187 (1956)
11. Hunt, C. M., Nitrogen Sorption Measurement and Surface Area of Hardened Cement Pastes, *Sym. On Structure of Portland Cement Paste and Concrete, Highway Research Board*, pp. 112–122 (1996)
12. Midgley, H. G., The Formation and Phase Composition of Portland Cement Clinker, *5th Sym. Chem. Cem.*, 1:479, Tokyo (1968)
13. Ghosh, S. N., and Chatterjee, A. K., Attenuated Total Reflectance Infrared Spectra of Portland Cement, *J. Mater. Sci.*, 9:1454 (1974)
14. Butt, Yu. M., Application of Infrared Spectroscopy to Study of Portland Cement and Its Hydrate Phases, *J. Appl. Chem .*, 48:1046, USSR (1975)
15. Ghosh, S. N., and Handoo, S. K., Infrared and Raman Applications in Cement and Concrete, *Cem. and Concr. Res.*, 10:771 (1980)
16. Tarte, P., Infrared Spectra of Inorganic Aluminates and Characteristic Vibrational Frequencies of $A1O_4$ Tetrahedra and $A1O_6$ Octahedra, *Spectrochem Acta.*, 23A:2127 (1967)
17. Bardick, V. L., and Day, D. E., Coordination of Aluminum Ions in Tricalcium Aluminate, *J. Am. Ceram. Soc.*, 50:97 (1967)
18. Schroeder, R. A., and Lyons, L. L., Infrared Spectra of the Crystalline Inorganic Aluminates, *J. Inorg. Nucl. Chem.*, 28:1155 (1966)
19. Bensted, J., and Varma, S. P., Some Applications of Infrared and Raman Spectroscopy in Cement Chemistry, Part I, Examination of Dicalcium Silicate, *Cem. Tech.*, 5:256 (1974)
20. Boikova, A. I., Domansky, A. I., Paramonova, V. A., Stavitskaja, G. P., and Nikoshehanko, V. M., The Influence of Na_2O on the Structure and Properties of C_3A, *Cem. and Concr. Res.*, 7:483 (1977)
21. Bensted, J., and Varma, S. P., Some Applications of Infrared and Raman Spectroscopy in Cement Chemistry, Part I, Examination of Dicalcium Silicate, *Cem. Tech.*, 5:256 (1974)
22. Conjeand, M., and Boyer, H., Some Possibilities of Raman Microprobe in Cement Chemistry, *Cem. Concr. Res.*, 10:61 (1980)

@Seismicisolation

23. Bonen, D., Johnson, T. J., and Sarkar, S. L., Characterization of Principal Clinker Minerals by FT-Raman Microscopy, *Cem. and Concr. Res.*, 24(5):959 (1994)
24. Tarte, P., Al-Fe Isomorphic Substitution in $CaO{\cdot}Al_2O_3$ and 2 $CaO{\cdot}Fe_2O_3$ and Interactions between the so called C_3A and C_4AF Phases,*Nature 207, No.* 500, p. 973 (1965)
25. Tarte, P., Structural Researches on the Constituents of Cements—Study of Interactions Between Tricalcium Aluminate and Dicalcium Aluminate, *Silic. Ind.*, 31:343 (1952)
26. Tarte, P., Infrared Study of Dicalcium Ferrite $2CaO{\cdot}Fe_2O_3$ and Solid Solutions of $2CaO(Al, Fe)2O_3$, *Rev. Chem. Miner.*, 1:425 (1964)
27. Sakurai, T., Sato, T., and Yoshinage, A., The Effect of Minor Components on the Early Hydraulic Activity of the Major Phases of Portland Cement Clinker, *5th Symp. Chem. Cem.*, 1:300 Tokyo, (1968)
28. Toropov, N. A., Cation and Anion Replacements in the Structure of Tricalcium Silicate, *5th Sym. Chem. Cem.*, 1:49 (1968)
29. Singh, N. B., Effect of Nickel Doping on the Solid State Properties of C_3S, *Cem. and Concr. Res.*, 6:409 (1976)
30. Shchetkina, T. Y., Skrynnik, L. N., and Strarominskaya, P. A., Results of Studies in Some Clinker Minerals by X-ray Diffractometry and Spectroscopy, *6th Symp. Chem. Cem.*, Moscow (1974)
31. Lehman, H., and Dutz, H., Infrared Spectroscopy Studies on the Hydration of Clinker Minerals and Cements, *4th Symp. Chem. Cem.*, 1:297–305, Washington (1960)
32. Bensted, J., The Hydraulicity of β-Dicalcium Silicate, *Cem. and Concr. Res.*, 9:97 (1979)
33. Taylor, H. F. W., Crystal Chemistry of Portland Cement Hydration Products, *6th Int. Symp. Chem. Cem.*, Moscow (1974)
34. Puertas, F., Blanco Vareta, M. I., and Dominguez, R., Hydration of $4CaO{\cdot}Al_2O_3{\cdot}Mn_2O_3$ in the Absence and the Presence of Gypsum. A Comparative Study with the Hydration of $4CaO{\cdot}Al_2O_3{\cdot}Fe_2O_3$, *Cem. Concr. Res.*, 23:20 (1993)
35. Mollah, M. Yousuf, Palta, Padmavathy, Hess, T. R., Vempati, R. K., and Cocke, D. L., Chemical and Physical Effects of Sodium Lignosulfonate Superplasticizer on the Hydration of Portland Cement and Solidification/Stabilization Consequences, *Cem. Concr. Res.*, 25:671 (1995)
36. Stevula, L., Madej, J., Kozankova, J., and Madejova, J., Hydration Products at the Blast Furnace Slag Aggregate-Cement Paste Interface, *Cem. Concr. Res.*, 24:413 (1994)

@Seismicisolation

37. Hanna, R. A., Barrie, P. J., Cheeseman, C. R., Hills, C. D., Buchler, P. M., and Perry, R., Solid State 29Si and 17Al NMR and FTIR Study of Cement Pastes Containing Industrial Wastes and Organics, *Cem. and Concr. Res.*, 25:1435 (1995)

38. Sakai, K., and Sugita, J., Composite Mechanism of Polymer Modified Cement, *Cem. and Concr. Res.*, 25:127 (1995)

39. Kurbus, B., and Marinkovic, V., Hydrothermal Metastability and Structural Disorder of 0.301 nm Phase, *Cem. and Concr. Res.*, 16:733 (1986)

40. Schwiete, H. E., and Ludwig, U., Crystal Structure and Properties of Cement Products (Hydrated Calcium Aluminate and Ferrites), *5th Symp. Chem. Cem.*, 2:37, Tokyo (1968)

41. Bensted, J., and Varma, S. P., Studies of Ettringite and its Derivatives, *Cem. Tech.*, 2:73 (1971)

42. Bensted, J., and Varma, S. P., Application of Infrared and Raman Spectroscopy in Cement Chemistry, Part 2, Portland Cement and its Constituents, *Cem. Tech.*, 4:112 (1973)

43. Benstead, J., Application of Infrared and Raman Spectroscopy in Cement Chemistry, *8th Int. Cong. Chem. Cem.*, 3.3.331, Brazil (1986)

44. Gouda, G. R., and Roy, D. M., Characterization of Hot-Pressed Cement Pastes, *J. Am. Ceram. Soc.*, 59:412 (1976)

45. Arizumi, A., Formation of Hydrated Gehlinite Through the Reaction of Clay Minerals of Lime, *5th Symp. on Chem. Cem.*, 2:38, Tokyo (1968)

46. Baird, T., Cairnes-Smith, A. G., and Snell, D. S., Morphology and CO_2 Uptake in Tobermorite Gel, *J. Coll. Interface, Sci.*, 50:387 (1975)

47. Nie, E. M. M. G., The Influence of Alkali-Carbonate on the Hydration of Cement, *5th Symp. Chem. Cem.*, 2:1067, Tokyo (1968)

48. Bensted, J., Early Hydration Behavior of Portland Cement in Water, Calcium Chloride and Calcium Formate Solutions, *Sil. Ind.*, 43:117 (1978)

49. Turriziani, R., and Rio, A., High Chemical Resistance Pozzolanic Cements, *4th Symp. Chem. Cem.*, 2:1067, Washington (1960)

50. Bensted, J., Early Hydration Behavior of Portland Cement Containing Chemical By-Product Gypsum, *W. Cem. Tech.*, 10:404 (1979)

51. McCall, M. T., and Mannone, J., Analysis of Cement Pastes for Triethanolamine, *Cem. and Concr. Res.*, 5:489 (1975)

52. Connally, J. D., and Hime, W. G., Analysis of Concrete for Triethanolamine, *Cem. and Concr. Res.*, 6:741 (1976)

53. Singh, V. K., Ali, M. M., and Narang, K. K., Infrared Spectral Study of Tricalcium Aluminate and Sulfanilic Acid Compounds, *Ind. Ceram.*, 20:305 (1977)

@Seismicisolation

54. Ben-dor, L., and Rubinstein, Y., The Microstructure and Infrared Spectra of Hydrated Tricalcium Silicate Containing Phosphate, *J. Mater. Sci.*, 14:365 (1979)

55. Sugama, T., and Kukaoka, L. E., Studies on Dicalcium Silicate (C_3S) on the Thermal Stability in Vinyl Type Polymer Concrete, *Cem. Concr. Res.*, 9:69 (1979)

56. Berry, E. E., Soales, J. A., and Malhotra, V. M., Leaching of Sulphur and Calcium From Infiltrated Concrete by Alkali and Neutral Aqueous Media, *Cem. Concr. Res.*, 7:185 (1977)

57. Hirche, D., Infrared Spectroscopic Method to Test the Alkali Reactivity, *Symp. Alkali Aggreg. React.,* p. 205, Reykjavik (1975)

58. Iob, A., Saricimen, H., Narasimhan, S., and Abbas, N. H., Spectroscopic and Microscopic Studies of a Commercial Concrete Water Proofing Material, *Cem. and Concr. Res.*, 23:1085 (1993)

59. Way, S. J., and Shayan, A., Synthesis and Characterization of Crystalline Analogues of Alkali-Aggregate Reaction Products, *Cem. and Concr. Res.*, 23:471 (1993)

60. Luxan, M. P., Dorrego, F., and Laborde, A., Ancient Gypsum Mortars from St. Engracia (Zaragosa, Spain): Characterization, Identification of Additives and Treatments, *Cem. and Concr. Res.*, 25:1755 (1995)

61. Sugama, T., and Carciello, N. R., Sodium Phosphate Derived Calcium Phosphate Cements, *Cem. and Concr. Res.*, 25:91 (1995)

@Seismicisolation

6

Nuclear Magnetic Resonance Spectroscopy

R. James Kirkpatrick

1.0 INTRODUCTION

Nuclear magnetic resonance (NMR) spectroscopy is one of the most effective probes of the atomic-scale structure and dynamical behavior available for many materials, and during the past twenty years it has found wide application in cement science. This chapter reviews the basic theory of NMR and briefly describes examples of applications to atomic-scale structural and dynamical studies of cement materials. Space limitations prevent detailed review of the now-large literature. Despite this large and growing literature, the range of potential applications has only barely been touched, and future work is likely to be even more varied. NMR methods are also useful for probing pore structure and transport properties in cement and concrete via relaxation and imaging methods. These applications are discussed in the appropriate chapters in this volume. General introductions and specific applications of NMR to cement science are available in the proceedings of the 1992 and 1996 conferences on this subject.[1][2]

1.1 Theory

NMR observes radio frequency signals from atomic nuclei occupying excited spin states, and understanding the observations is best accomplished though a combination of the quantum mechanical and classical

@Seismicisolation

descriptions of the phenomena. There are a number of effective introductory descriptions of the theory[3]–[7] as well as standard advanced texts.[8][9] This chapter presents without support only a simple introduction adequate to understand spectral interpretation and experimental operation.

Quantum Description. In the quantum description, NMR active nuclei are considered to have a quantized property called *spin*, which can usefully be thought of as being caused by physical spinning of the nucleus. The angular momentum, *J*, of such a nucleus is given by

Eq. (1) $$J = \hbar [I(I + 1)]^{1/2}$$

where $\hbar$ is Planck's constant/2π and I is the spin quantum number which can be either an integer or half-integer. Nuclei with even mass number and even charge (e.g., ^{12}C, ^{16}O) have zero spin and are of no interest to NMR spectroscopy. Nuclei with odd mass numbers (e.g., ^{17}O, ^{27}Al, ^{29}Si) have half-integer spins and are of most interest here. Nuclei with even mass numbers and odd charge (e.g., ^{2}H, ^{14}N) have integer spins and can be more difficult to examine, but can also be of considerable importance. Most nuclei have spins between 0 and 9/2. The magnetic moment, $\vec{\mu}$, of a nucleus is a fundamental property and is given by:

Eq. (2) $$\vec{\mu} = \gamma \vec{J}$$

where γ is the gyromagnetic ratio which is defined by Eq. 2 and is a constant for each nucleus.

Each nucleus has $2I + 1$ spin energy levels which take on the values I, $I - 1$, $I - 2$, ..., $-I$. In the absence of a magnetic field, these energy levels are degenerate (have the same energy), but when a magnetic field is present this degeneracy is lifted (Fig. 1). The energy difference between these states, ΔE, is given by:

Eq. (3) $$\Delta E = \left| \gamma \hbar H \right|$$

where H is the magnitude of the magnetic field at the nucleus. The relative populations of the higher and lower energy levels, N_a and N_b, respectively, is given by the Boltzmann distribution (Eq. 4).

Eq. (4) $$\frac{N_a}{N_b} = \exp\left(\frac{\Delta E}{kT}\right)$$

@Seismicisolation

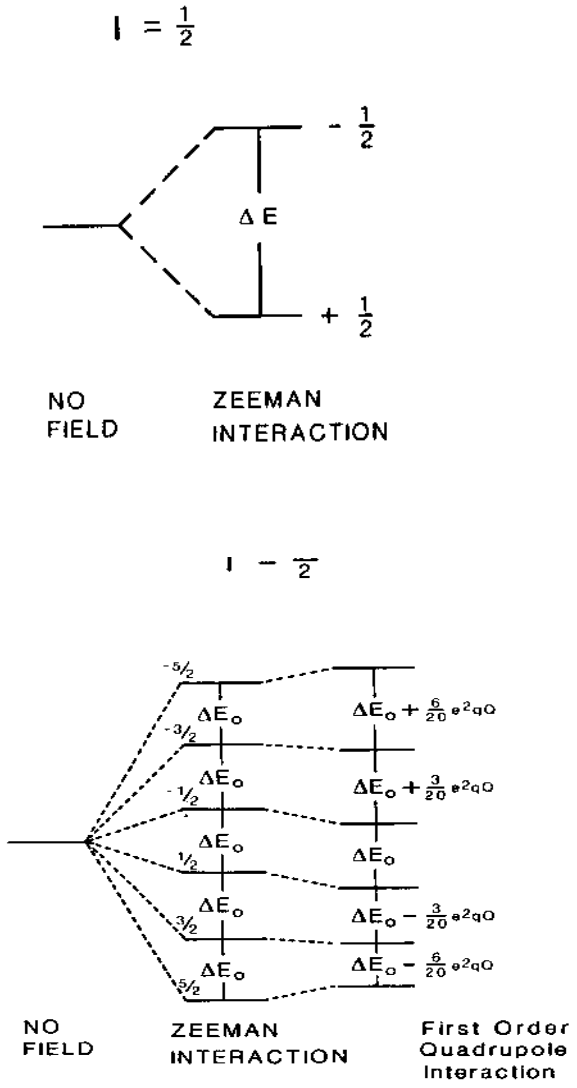


Figure 1. Nuclear spin energy level diagrams for: *(A)* a spin $I = ½$ nucleus such as ^{29}Si and ^{1}H, and *(B)* a spin $I = 5/2$ nucleus such as ^{27}Al and ^{17}O. For an $I = ½$ nucleus the only nuclear spin transition is between the ½ and -½ energy states. For nuclei with a quadrupole moment the presence of an electric field gradient at the nucleus causes additional changes in the energy levels. In many cases when the central (½, -½) transition is observed, the line shape is modified by unaveraged second-order quadrupole effects.

@Seismicisolation

An individual nucleus can increase or decrease its energy only by absorbing or emitting a photon with a frequency given by

Eq. (5) $$\nu = \gamma \frac{H_0}{2\pi} H$$

It is the frequency of this radiation which is measured in the NMR experiment and, because ΔE is quite small, these are in the radio frequency range.

One of the most useful aspects of the NMR phenomenon is that the electrons in the vicinity of the observed nucleus shield it from the applied magnetic field, H_0, a small amount. Nuclei in different structural environments, then, have slightly different frequencies. This shielding is commonly anisotropic and is described by the tensor, σ_{ij}. The isotropic shielding, σ_{ij}, is $^1/_3 Tr\sigma_{ij}$ and the chemical shift anisotropy (CSA, $\Delta\sigma$) is

Eq. (6) $$\Delta\sigma = \sigma_{33} - {}^1/_2(\sigma_{11} + \sigma_{22})$$

Due to this shielding the magnetic field at the nucleus is given by

Eq. (7) $$H = H_0 (1-\sigma)$$

Similarly,

Eq. (8) $$\nu = \gamma \frac{H_0}{2\pi}(1-\sigma)$$

The absolute values of H_0 and thus the NMR frequencies are difficult to measure accurately and the frequencies are normally reported as chemical shifts, δ, relative to an experimentally useful standard.

Eq. (9) $$\delta = \left(\frac{\nu_{sample} - \nu_{std}}{\nu_{std}} \right) \times 10^6$$

The chemical shift corresponding to the isotropic shielding is called the isotropic chemical shift, δ_i, and has units of ppm. More negative or lesspositive chemical shifts correspond to larger shieldings. In many cases, the isotropic chemical shift is the most useful NMR parameter for structural investigations and many NMR investigations of cement materials are based on it.

@Seismicisolation

Classical Description. Understanding the signal observed in an NMR experiment is often easier in the context of either the classical description or a combination of the quantum and classical descriptions. In the classical description (Fig. 2) the spin of the nucleus causes the magnetic moment of the nucleus to precess about the magnetic field, taken to be the Z-axis, in the same way a spinning gyroscope precesses about a gravitational field. The frequency of this precision, the Larmor frequency, is identical to the frequency of the quantum description. The magnetic moments of all the individual nuclei in the sample, called the *spin system*, can be viewed as forming a cone about the Z-axis yielding a net magnetization, M, parallel to H_0

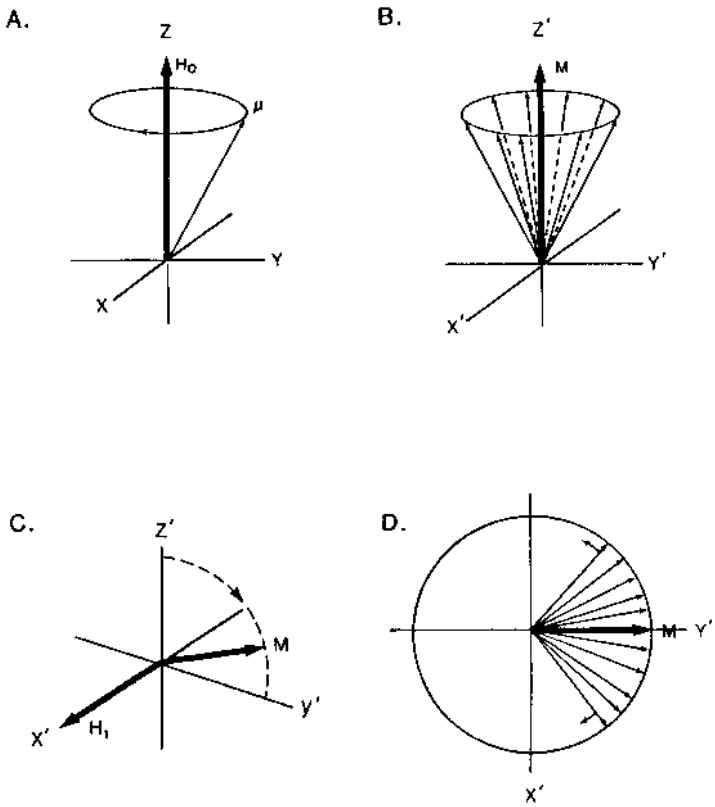


Figure 2. Diagrams illustrating the classical description of NMR. *(A)* A precessing nuclear moment, *m*, and the net magnetization (thick arrow) parallel to a static applied magnetic field. *(B)* A system of individual magnetic moments and the net magnetization, *M*, in the rotating frame of reference. *(C)* The rotation of the net magnetization in the Z´-Y´ plane due to the small H_1 field caused by irradiating the sample at the Larmor frequency. *(D)* Dephasing of the spin system in the X´- Y´ plane of the rotating frame with a time constant, T_2.

@Seismicisolation

The simplest NMR experiment (a 1-pulse experiment) is done by irradiating the sample with plane-polarized radio frequency radiation such that a small magnetic field, H_1, is generated parallel to the X-axis of a reference frame. This H_1 field rotates with the magnetization and causes the spin system to tip with respect to the H_o field in the Y-direction of a reference frame which rotates about H_0 at the Larmor frequency (the rotating frame). In the simplest experiment, the tip angle is 90° (corresponding to equal populations of the two spin energy levels involved). The net magnetization is now in the X-Y plane, but is still precessing about H_o at the Larmor frequency (the resonance frequency). It is this fluctuating field in the X-Y plane that is actually detected by the spectrometer. For the signal to be detected, the H_1 field is turned off and at this point two things happen to the spin system. The number of nuclei in the excited state begins to decrease causing the orientation of M to return to its equilibrium orientation parallel to Z. Ideally, this relaxation is exponential and the time constant describing it is called T_1. In addition, the individual nuclei have slightly different Larmor frequencies or, through various processes, lose phase coherence. Thus, with time, the individual spins become out of phase with each other. The time constant for this process is called T_2. For many solids at room temperature, T_2 is much less than T_1 and the net magnetization in the X-Y plane decreases to 0 before the spin system relaxes to its equilibrium energy. The T_1 and T_2 relaxation times can both be useful parameters in studying the atomic-scale dynamical behavior in materials.

In modern spectrometers, the signal emitted by the sample as the spin system precesses is detected as a function of time (the time domain) to yield a free induction decay (FID, Fig. 3). The signals resulting from many H_1 pulses are added together to increase the signal/noise ratio [proportional to (number of pulses)$^{1/2}$]. The total FID is then Fourier-transformed into the frequency domain to give the usual NMR spectrum. These spectra contain one or more peaks, each corresponding to structural sites for the observed nucleus, with different chemical shifts.

Quadrupolar Interaction. Nuclei with spin $I > 0$ can be classified into two types, those with $I = ½$ and those with $I \geq 1$. The spin ½ nuclei (e.g., ^{1}H, ^{29}Si) have only two spin energy levels (Fig. 1) and a spherical distribution of charge. Those with spin ≥ 1 (quadrupolar nuclei; e.g., ^{17}O, ^{27}Al) have three or more spin energy levels and a non-spherical distribution of charge. Thus, their magnetic fields are more complicated and have, in addition to a magnetic dipole moment, a magnetic quadrupole moment. Interaction of this quadrupole moment with an electric field gradient (EFG)

@Seismicisolation

at the nucleus causes changes in the differences between the spin energy levels (e.g., Fig. 1), giving rise to different resonance frequencies for the $2I + 1$ different transitions. If the EFG is large (often the case in solids), only the central (½, -½) transition is excited and observed. To first order, ΔE for this transition is not affected by the EFG, but to second order it is. The result of this effect is that the observed peaks are often broad and not symmetrical. The quadrupole interaction is described by its magnitude (the quadrupole coupling constant, QCC, proportional to the magnitude of the EFG) and its deviation from axial symmetry (the asymmetry parameter, η). Both of these parameters can sometimes be useful structural parameters because they are related to the symmetry of the electronic environment at the nucleus, which is a property of the material.

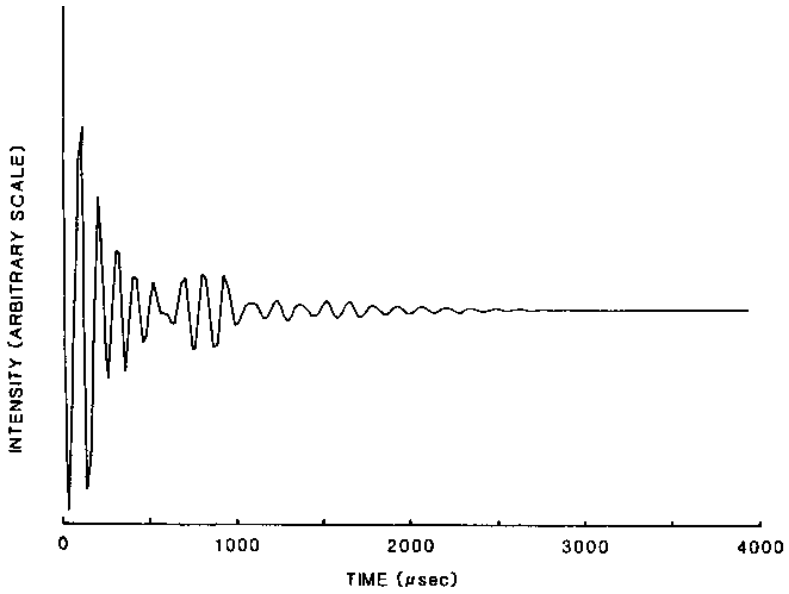


Figure 3. A typical NMR free induction decay.

Magic-Angle Spinning (MAS) NMR. MAS is an experimental technique commonly used for solids to overcome peak broadening caused by a number of important nuclear interactions. These interactions cause either a range of magnetic fields at individual nuclei or anisotropic effects

@Seismicisolation

which cause nuclei in sites oriented differently with respect to H_0 to have different resonance frequencies. The most important interactions for solids include *(1)* the interactions of the dipole moment of the observed nuclei with the dipole moments of other individual nuclei of the same or other species (homonuclear and heteronuclear *dipole interaction*), *(2)* the anisotropy of the shielding (CSA) described above, and *(3)* the anisotropy of the electrical field gradient causing the quadrupole interaction. Other interactions, such as the indirect nuclear interaction (J-coupling) are usually less significant for solids, but can be important for liquids.

In low viscosity liquids and gases, rapid isotropic molecular tumbling causes time averaging of these interactions resulting in a narrow range of resonance frequencies and thus very sharp peaks. This effect is the origin of the very high resolution routinely available in spectra of, for example, organic molecules in solution. In solids, however, such motion rarely occurs. Magic angle spinning reduces the peak broadening caused by these interactions by spinning the sample at frequencies of from ~1 – 35 kHz around an axis oriented 54.7° to H_0. This rotation mimics the effect of rapid molecular tumbling for the dipolar and CSA interactions by making the time-averaged orientation of the observed sites = 54.7°. At this orientation, these interactions have a value of 0. The effect of MAS for $I = ½$ (non-quadrupolar) nuclei is dramatic and often makes the difference between a useful spectrum and an unresolved hump (e.g., Fig. 4). Unfortunately, for quadrupolar nuclei under simple MAS, the line narrowing is only a factor of about 3 and the peaks often remain broad and have non-symmetrical shapes.

Decoupling and CPMAS. In many cases, the simple MAS experiment just described is adequate to provide the information required; in other cases peak overlap or unaveraged nuclear interactions prevent optimal resolution and other more complicated experiments are needed. Indeed, the ability of modern spectrometers to accurately control the number, timing, phase, and amplitude of the RF pulses has lead to an extraordinary array of NMR experiments (pulse sequences) that involve complex manipulation of spin systems. In many cases these experiments provide information, such as bond connectivities, not contained in simple MAS experiments.

@Seismicisolation

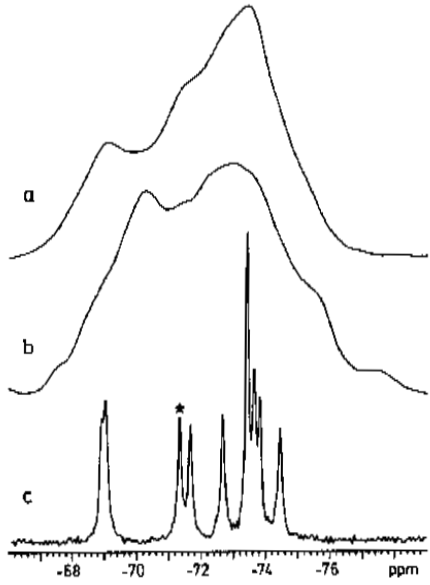


Figure 4. ^{29}Si MAS NMR spectra of *(a)* monoclinic M_I alite, *(b)* monoclinic M_{III} alite, *(c)* triclinic C_3S. The alite samples contain substitutional impurities. The ★ peak for C_3S is due to minor impurity C_2S. (From Ref. 14.)

Because many cement materials are hydrous, one often desires to either eliminate the strong dipolar interaction between protons (^{1}H) and an observed nucleus (e.g., ^{29}Si) or use this interaction to enhance observed signal or understand the structural relationships between hydrogen atoms and atoms of the observed nucleus. Elimination of the heteronuclear dipolar interaction which is often so strong that it is not completely eliminated by MAS and causes unwanted peak broadening, requires strong continuous or pulsed RF at the ^{1}H resonance frequency arranged in such a way that the ^{1}H and observed spin systems do not interact (are decoupled). For some cement materials, decoupling appears to be useful, but for others rapid motion of the ^{1}H-containing species causes self-decoupling and there is no peak-width decrease in the MAS spectra due to decoupling. The ^{1}H coupling to an observed nucleus can be used to enhance the observed signal (at the loss normally of quantitative signal intensity) via cross polarization with MAS (CPMAS). This experiment

@Seismicisolation

works by bringing the ^1H and observed spin systems into the Hartmann-Hahn condition

Eq. (10) $$\gamma^H H^H = \gamma^i H^i,$$

where the H's are the H_1 fields for ^1H (H^H) and the observed nucleus (H^i). Under these conditions the two spin systems precess about their respective H_1 fields (but not H_o) at the same frequency, allowing magnetization transfer from the ^1H spin system to the observed spin system. If the hydrogens are within a few Å of the observed nucleus, these conditions can increase the signal/noise (S/N) ratio of the spectrum and reduce the acquisition time. Perhaps most importantly, the spectrum contains essentially only signals from observed nuclei located near the hydrogens, effectively discriminating hydrous from anhydrous materials. As for decoupling, if the ^1H-containing species are in rapid motion independently of the observed nucleus, the two spin systems are self-decoupled and CP is ineffective. Many spectra of cement materials are taken under CPMAS conditions.

Two-Dimensional (2-D) Experiments. The spectra obtained using the techniques described above (e.g., Fig. 4) can be thought of as 1-dimensional spectra in the sense that signal intensity is presented as a function of only one parameter (resonance frequency/chemical shift). Two-dimensional (2-D) NMR spectroscopy takes advantage of the large number of nuclear interactions to correlate nuclei of atoms related to each other in some way (e.g., in space, via chemical exchange, or with similar NMR parameters). The spectra consist of two frequency axes with intensity plotted in the third dimension. Two-dimensional techniques have proliferated in the past two decades[4] and a complete compilation is beyond the scope of this chapter. Briefly, they work by use of multiple-pulse sequences which include a time period between pulses that is varied. Multiple spectra are collected with different values of this time period and Fourier transformation is done over both this time period and the usual acquisition time. Among the various 2-D methods, dynamic-angle spinning (DAS)[10] and multiple quantum (MQ)[11][12] methods are potentially the most important for cement science. Both significantly increase the resolution and information available for quadrupolar nuclei. MQ may become the most useful of these techniques because it requires no special equipment beyond an MAS NMR spectrometer and can provide independent chemical shift,

@Seismicisolation

quadrupole coupling constant, and asymmetry parameter data for multiple sites in the same sample. At the time of writing (late 1996) there have been no published applications of MQ NMR to cement materials, and, indeed, the methods are still under development. (See note added in proof at the end of this chapter.)

1.2 Experimental Methods

The Spectrometer. NMR spectrometers consist of electronics for generating and receiving radio frequency pulses, a computer to control the system and collect and process data, a magnet to generate the H_0 field, and a sample probe to place the sample in the magnet, spin it as desired, irradiate it with the RF radiation, and allow precise tuning. Most modern spectrometers are based on powerful superconducting magnets and are categorized by their H_0 field strength, typically from ~ 2.3 to 17.5 tesla (T), corresponding to ^{1}H resonance frequencies of from 100 to 750 MHz.

The Sample. Samples used for solid state NMR range in size from a few mg to more than a gram, but are typically 50 to 300 mg. For static spectra, the sample can be held in a wide variety of closed or open capsules that are chemically compatible with the sample and that have a low background for the observed element. For MAS, the sample container is typically a hollow cylinder (a rotor) made of a material of adequate strength, typically plastic for low spinning speeds or a ceramic for higher spinning speeds. There are flutes either cut into the cylinder or onto end caps on which compressed air blows to drive the spinning. Samples can be powders, large pieces, or mixtures of solid and liquid, but if sample spinning is desired the sample must be mechanically stable in the rotor.

Capabilities and Limitations. For situations to which it can be applied, NMR often provides the greatest resolution of any spectroscopic structural probe (e.g., IR, Raman, and x-ray absorption spectroscopies). It is also element-specific, an important advantage over vibrational spectroscopy. Unfortunately, the presence of paramagnetic impurities (primarily Fe, but also other transition metals) can destroy the signal, significantly limiting applications. In addition, not every potentially interesting element has an abundant NMR-active nuclide. For cement and concrete science, the absence of a naturally occurring Ca isotope is especially limiting. Nonetheless, there are many issues to which NMR is readily applicable.

@Seismicisolation

2.0 STRUCTURAL INVESTIGATIONS OF ANHYDROUS CEMENT PHASES

2.1 Silicates

NMR investigation of the structure of silicate phases of interest to cement science has been undertaken using primarily ^{29}Si, and crystalline Ca-silicates, which were among the first phases to be examined after the experimental methods were developed. The data for them provide a reference from which to interpret the data for materials with less well understood structures. The following are the major points. The ^{29}Si NMR chemical shifts for all silicates become more negative (more shielded) with increasing polymerization.[13]–[16] The polymerization is characterized by the Q^n nomenclature where Q indicates an Si atom on a tetrahedrally coordinated site and n indicates the number of bridging oxygens per tetrahedron. Thus, the Si sites of the primary cement phases alite and belite have Q^0 polymerization, and quartz has Q^4 polymerization.The nine crystallographically distinct Si sites of high-purity C_3S resonate between about -68.9 and -74.5 ppm (Fig. 4),[14] and the Q^0 sites of the various C_2S phases resonate between -70.1 and -73.5 ppm, well within the range for such sites. Pure silica phases, on the other hand, resonate between about -107 and -114 ppm.

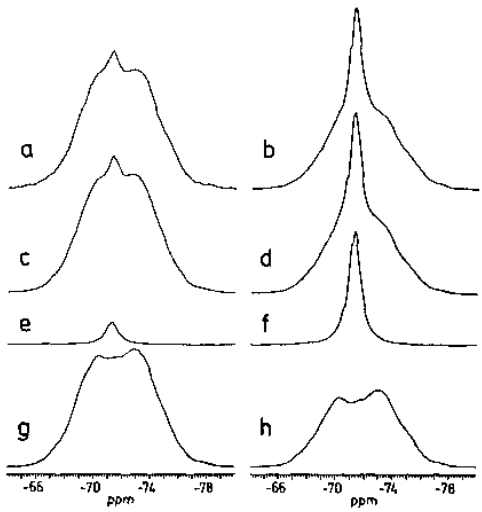


Figure 5. ^{29}Si MAS NMR spectra of *(a)* and *(b)* two Portland cements; *(c)* and *(d)* are optimized simulations of the line shapes with the components of *(e)* and *(f)* belite, and *(g)* and *(h)* M_{III} alite. (From Ref. 14.)

@Seismicisolation

The ^{29}Si peaks for the high-purity phases are quite narrow (<1 ppm) if they are well crystallized (e.g., C_3S, Fig. 4), and the spectra are well resolved. The alite and belite of real portland cement, however, are quite impure and, because of distortion of the electronic environments of the Si due to these impurities, their spectra are quite broad and poorly resolved (Figs. 4 and 5). A significant amount of the ^{29}Si signal is probably lost due to paramagnetic interactions.

Despite the possibility of such signal loss, recent work has shown that quantitative spectral deconvolution of the ^{29}Si MAS NMR spectra of production portland cements with a wide range of compositions provide quite accurate alite/belite ratios (Fig. 5).[14] Thus, this method has the potential to be an accurate, partial measure of the phase composition of production cements.

2.2 Aluminates

The most useful nucleus for aluminates has been ^{27}Al , but because it is quadrupolar, its spectra are less well resolved than those of ^{29}Si. It effectively distinguishes Al with different nearest neighbor coordination by oxygen, tetrahedral Al,[4] octahedral Al,[6] and the rare pentahedral Al.[5][14]–[17] The chemical shifts for $Al^{[4]}$ distinguish Al in aluminates (isotropic chemical shifts from ~ 75 to 85 ppm) from that in aluminosilicates (isotropic chemical shifts from ~ 50 to 70 ppm). For structurally well ordered materials, it also provides information about the Al site symmetry via the quadrupole coupling constant and asymmetry parameter. The very high field magnets now available (H_o > 17.5 T) yield significantly increased resolution for ^{27}Al.

2.3 Glasses and Melts

There is a large body of literature describing NMR investigations of aluminosilicate glasses potentially relevant to cement manufacture. Depending on the spectral resolution, it is sometimes possible to determine Si polymerization and often Al coordination. There has been no comprehensive review of this literature.[16]

In addition to studies of glasses at room temperature, it is possible to use in-situ high-temperature NMR methods to study silicate and aluminate melt structure and dynamics.[18][19] These techniques are difficult and still evolving, but in-situ ^{27}Al results for laser heated $CaAl_2O_4$ melt samples

@Seismicisolation

show that the Al is essentially all $Al^{[4]}$ near the glass transition temperature, but that some Al enters 5- and/ or 6-coordination at high temperature. The data also show that the NMR correlation times for Al reorientation correlate reasonably well with those for shear viscosity.[19] Such in-situ experiments have significant potential for studying the processes occurring in the melt phase during cement production and laser heating is likely to be necessary to achieve the required temperatures of ~ 1500°C.

3.0 STRUCTURAL INVESTIGATIONS OF CALCIUM SILICATE HYDRATE (C-S-H) AND RELATED CRYSTALLINE PHASES

NMR methods have found their widest application to cement and concrete science in structural studies of Ca-silicate hydration products (C-S-H) and their hydrous crystalline model compounds, and in studies of portland cement hydration. This section first describes the results for relevant hydrous model compounds, then calcium silicate hydrate (C-S-H), and finally hydration studies.

3.1 Tobermorite, Jennite, and Other Ca-Silicates

Tobermorite and jennite have long been considered relevant model compounds for the C-S-H structure,[20] and ^{29}Si MAS NMR provides a direct probe of their structures and reference chemical shifts for Si-sites of different polymerizations for comparison to C-S-H. Ideal tobermorite has a layer structure with a sheet of Ca-polyhedra sandwiched between two sheets of chains of silicate tetrahedra (Q^2) polymerization.[21] Several published ^{29}Si MAS NMR spectra show the situation to be more complicated than this.[22]–[26] Many samples of 1.1 nm tobermorite show a dominant peak for Q^2 (chain) tetrahedra at ~ -85 to -86 ppm with a smaller peak for Q^1 tetrahedra (broken chain ends) near -79 to -80 ppm, and Q^3 tetrahedra (tetrahedra which cross-link chains) near -96 ppm (Fig. 6). A few samples yield primarily signal for Q^2 tetrahedra. Clearly, different samples have significantly different states of structural order. Studies of Al-substituted tobermorites using ^{27}Al MAS NMR show that Al occurs in tetrahedral coordination in a number of different configurations.[27][28]

The structure of jennite has not been solved by diffraction methods, but the ^{29}Si MAS NMR spectrum of a reasonably well crystallized sample contains a single peak near -86 ppm for Q^2 tetrahedra, confirming a proposal based on powder x-ray diffraction data (Fig. 6).[20][25]

@Seismicisolation

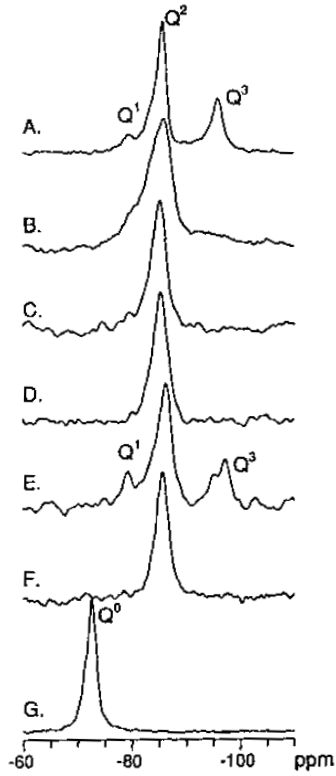


Figure 6. ^{29}Si MAS NMR spectra of the following crystalline Ca-silicate hydrates. *(A)* 1.1 nm tobermorite; *(B)* 1.4 nm tobermorite; *(C)* 1.1 nm tobermorite made from the 1.4 nm tobermorite by dehydration at 105°C; *(D)* jennite; *(E)*xonotlite; *(F)* hillebrandite; and *(G)* calciochondrodite. (From Ref. 25.)

There have been many ^{29}Si MAS NMR studies of hydrous crystalline Ca-silicates, including, e.g., xonotlite, hillebrandite, tricalcium silicate hydrate and others.[24][25][29]–[31] These studies confirm the chemical shift assignments for tobermorite and jennite and provide important new structural information concerning these phases.

Important structural information concerning hydrous Ca-silicates can also be provided by ^{1}H NMR. In some cases, it is possible to distinguish hydrogens in CaOH linkages, water molecules, and SiOH linkages.[32][33] The ^{1}H chemical shift becomes less shielded (more positive) with increasing hydrogen bond strength of the hydrogen.

@Seismicisolation

3.2 C-S-H

C-S-H is the dominant strength-forming phase in portland cement paste, and determination of its structure and behavior has been a central topic in cement science for many decades. NMR spectroscopy has contributed significantly to this effort in recent years. Most importantly, it has provided both a confirmation of the long-standing idea[34]–[41] that the C-S-H structure is similar to those of tobermorite and jennite and information about how the compositional variation of C-S-H is accommodated structurally. The ^{29}Si MAS NMR spectra of most C-S-H samples contain peaks for only Q^1 and Q^2 sites, with the Q^1/Q^2 ratio increasing with increasing C/S ratio up to ~ 1.2 (e.g., Fig. 7). At C/S ratios less than ~ 0.9, some samples yield a peak for Q^3 sites, but significant intensity for Q^0 peaks are never observed for single phase samples. At C/S ratios greater than ~ 1.2, the Q^1/Q^2 ratio does not change systematically with C/S ratio.

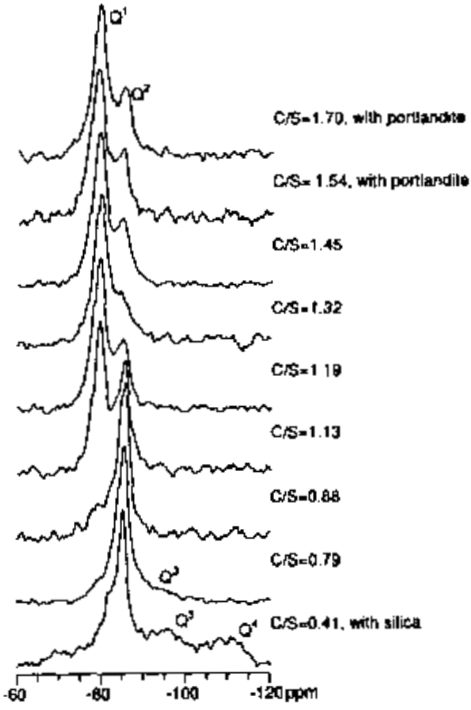


Figure 7. ^{29}Si MAS NMR spectra of synthetic C-S-H samples with the indicated bulk C/S ratios determined by x-ray fluorescence analysis. Samples with C/S ratios from 0.79 to 1.45 are single phase, as determined by x-ray diffraction. (From Ref. 38)

@Seismicisolation

These observations can be explained by a structural model based on tobermorite in which compositional variation at C/S less than ~ 0.9 is accommodated by cross-linking of tetrahedral chains (as in many tobermorites), compositional variation between C/S = 0.9 to 1.2 is accommodated primarily by omission of bridging tetrahedra, and compositional variation at C/S greater than ~ 1.2 is accommodated primarily by omission of silicate chains or chain segments (giving jennite-like regions). The results of ^{17}O MAS NMR support this model, with the compositional variation of the relative abundance of non-bridging oxygens (NBOs) being in accord with the model.[39] NMR is a local structural probe, however, and does not address well the spatial distribution of these different structural components.

Recent high-resolution TEM observation of C-S-H from hydrated cement paste shows the presence of crystalline mesoscale regions 5 to 10 nm across surrounded by amorphous appearing regions.[42] The crystalline regions have lattice spacings varying between those of tobermorite and jennite, confirming the presence of structural elements of these types. These results are also consistent with solid solution of tobermorite, jennite, and Ca-hydroxide. There is continuing controversy about the number of thermodynamically distinct C-S-H phases (1, 2, or 3)[(36][37][38] and a quantitative and comprehensive structural model for C-S-H and its variation with composition and mode of formation awaits development.

A study of C-S-H using ^{27}Al MAS NMR shows that, as for tobermorite, Al enters the structure as Al[4] and Al[6].[43][44] (See note added in proof at end of this chapter.)

4.0 INVESTIGATIONS OF PORTLAND CEMENT HYDRATION

Over the past decade, ^{29}Si MAS NMR has developed into an important probe of the hydration of portland cement complimentary to thermal, microscopic and x-ray diffraction methods. Because the ^{29}Si peaks for the C-S-H reaction product are well separated from those of the anhydrous reactants, as described above, the data provide a well resolved and quantitative probe of both the extent of reaction and the structure of the products. There have been a large number of published NMR studies of the hydration of various portland cements and individual phases such as C_3S

@Seismicisolation

and C_2S.[45]–[50] In many cases, the initial hydrous product contains many Q^o sites which are perhaps not in C-S-H, but in a surface-product on the anhydrous grains. The Q^o sites are sometimes detectable above noise only in CPMAS spectra. The abundance of Q^0 sites usually decreases with reaction time while the abundance of Q^1 and Q^2 sites increases. The Q^1/Q^2 ratio decreases with time and reaches a constant value. The Q^1/Q^2 ratio of well aged samples often decreases with increasing temperature.

NMR spectroscopy (^{29}Si NMR) also effectively characterizes the extent of reaction and C-S-H structure in cement formulations containing pozzolans, including DSP and RCP cements.[51]–[55] In general, the C-S-H in these materials is more polymerized than C-S-H in OPC and may contain significant concentrations of Q^3 sites. The reaction rate increases with increasing temperature and is greater in the presence of pozzolans. Studies using samples containing ^{29}Si-enriched SiO_2 show that the silicon of the pozzolan first enters the C-S-H primarily in Q^1 sites and later moves into Q^2 and Q^3 sites.[52]

The molecular scale processes occurring during portland cement hydration can also be effectively studied using ^{1}H relaxation rate measurements with both the spin-spin relaxation time, T_2, and the spin-lattice relaxation time, T_1, providing useful information.[56]–[59] After the dormant period, five different groups of protons with different T_1 values can be identified and some of these can be further subdivided into two components with different T_2 values. These components include the following: *(i)* Protons in structural water and OH in crystalline phases such as ettringite and Ca-monosulfate ($T_1 \approx 50$ ms). *(ii)* Protons in adsorbed water molecules in pores ($T_1 \approx 10$ ms). *(iii)* Protons in the C-S-H gel ($T_1 \approx 1$ ms). *(iv)* Protons in portlandite ($T_1 \approx 1$ s). *(v)* Undifferentiated protons near paramagnetic impurities ($T_1 \approx 2$ ms). Based on slightly different T_2 values, the first three groups include liquid-like and solid-like components which are in homonuclear dipolar contact. The abundances of these various components can be readily followed with hydration time, and the changes are typically as expected, with the relative abundance of protons in C-S-H and portlandite increasing with time. The total amount of water uptake into hydrated phases can also be monitored. The advent of very high field magnets and MAS spinning frequencies of > 20 kHz open the possibility of combining high-resolution spectra and relaxation measurements to better understand the molecular level roles of protons in hydrating cements.

@Seismicisolation

5.0 INVESTIGATIONS OF ALUMINATE CEMENT HYDRATION

NMR study of Ca-aluminate-based cement similar to those just described for portland cement systems have been undertaken using ^{27}Al and ^{1}H methods, although the work has been less extensive.[60]–[64] ^{27}Al MAS NMR shows the conversion of the $Al^{[4]}$ of the Ca and CA_2 reactants to the $Al^{[6]}$ of the product phases (CAH_{10}, C_2AH_8, C_3AH_6, and gibbsite, depending on temperature (Fig. 8).[60]–[63] It also shows the presence of $Al^{[4]}$ and $Al^{[6]}$ in an amorphous initial reaction product and at least $Al^{[4]}$ in a reaction intermediate.[63] ^{1}H T_1 measurements can be used to characterize the phases present during hydration at room temperature and elevated temperatures (Fig. 8).

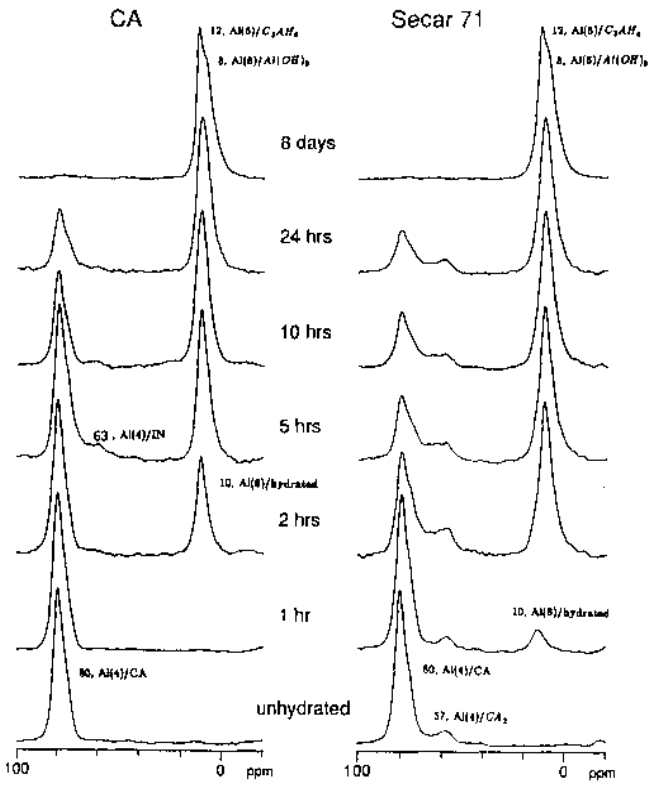


Figure 8. ^{27}Al MAS NMR spectra of $CaA1_2O_4$ and commercial Secar 71 aluminate cement hydrated at 50°C for the indicated times. (From Ref. 63.)

@Seismicisolation

6.0 WASTE SOLIDIFICATION AND STABILIZATION

The use of cement-based waste forms to solidify and stabilize chemical and nuclear hazardous waste has become a significant topic in recent years, but there has been little direct NMR investigation related to it. Janusa, et al.,[65] have used deuterium (^{2}H) NMR methods to study the behavior of phenol in white portland cement and showed that the minimum bond strength is of the order of 5.5 kcal/mol. Other studies have found ^{29}Si and ^{27}Al MAS NMR useful in studying the effects of organic and inorganic waste components on the rate and extent of hydration.[66][67] The wide range of NMR methods now available for studying solids and solid/solution composites are likely to find significant application in this regard.

7.0 ALKALI SILICA GEL

NMR methods have the potential to usefully probe the structure and formation of alkali silica reaction gels, but there have been few studies. Cong, et al.,[68] have shown that in hydration experiments containing reactive silica and portlandite, Si-sites identical to those in C-S-H were formed as well as more polymerized sites associated with K.

8.0 STRUCTURAL INVESTIGATIONS OF RAW MATERIALS

There is an extensive literature describing NMR studies of rocks and minerals, but there are no studies specifically directed at cement feed stocks. Review of this literature is beyond the scope of this chapter.

9.0 NOTE ADDED IN PROOF

Since this chapter was written in 1996, there has been significant advance in the use of multiple quantum methods and very high H_0 field strengths to study ^{27}Al NMR of Al in C-S-H. Faucon et al.[69] used ^{27}Al multiple quantum methods to characterize several Al[4] and Al[6] sites, and Sun et al.[70] used ^{27}Al MAS at H_o = 17.5 T to characterize three Al[4] sites, Al[5] sites and Al[6] sites. They assigned the Al[4] sites to the tetrahedral chains and the Al[5] and Al[6] to the interlayer space. Faucon et al.[69] provide recent references to the multiple quantum technique.

@Seismicisolation

REFERENCES

1. Colombet, P., and Grimmer, A. R., (eds.), *Application of NMR Spectroscopy to Cement Science*, p. 484, Gordon and Breach, Paris (1994)
2. Colombet, P., Grimmer, A. R., and Zanni, H., (eds.), *Proceedings of the 2nd International Conference on NMR Spectroscopy of Cement-Based Materials*, Springer-Verlag (1998)
3. Sanders, J. K. M., and Hunter, B. K., *Modern NMR Spectroscopy*, 2nd Edition, p. 314, Oxford University Press, Oxford (1993)
4. Friebolin, H., *Basic One and Two-Dimensional NMR Spectroscopy*, p. 368, VCH, New York (1993)
5. Engelhardt, G., and Michel, D., *High-Resolution Solid-State NMR of Silicates and Zeolites*, p. 485, Wiley, New York (1987)
6. Fukushima, E., and Roeder, S. B. W., *Experimental Pulse NMR, a Nuts and Bolts Approach*, p. 539, Addison-Wesley, New York (1981)
7. Harris, R. K., *Nuclear Magnetic Resonance Spectroscopy, a Physicochemical View*, p. 378, Longmanns, London (1986)
8. Abragam, A., *The Principals of Nuclear Magnetism*, p. 599, Oxford, Clarendon (1961)
9. Schlicter, C. P., *Principals of Magnetic Resonance*, 2nd Ed., p. 542, Springer, Berlin (1978)
10. Mueller, K. T., Sun, B. Q., Chingas, G. C., Zwanziger, J. W., Terao, T., and Pines, A., Dynamic-Angle Spinning of Quadrupolar Nuclei, *J. Mag. Reson.*, 86:470–487 (1990)
11. Medek, A., Harwood, J. S., and Frydman, L., Multiple-Quantum Magic-Angle Spinning NMR: A New Method for the Study of Quadrupolar Nuclei in Solids, *J. Am. Chem. Soc.*, 117:12779–12787 (1995)
12. Massiot, D., Touzo, B., Trumeau, D., Coutures, J. P., Virlet, J., Florian, P., and Grandinetti, P. J., Two-Dimensional Magic-Angle Spinning Isotropic Reconstruction Sequences for Quadrupolar Nuclei, *Solid State Nucl. Mag. Reson.*, 6:73–83 (1996)
13. Grimmer, A. R., Structural Investigation of Calcium Silicates from ^{29}Si Chemical Shift Measurements, in *Application of NMR Spectroscopy to Cement Science*, p. 484, Gordon and Breach, Paris (1994)
14. Skipsted, J., and Jakobsen, H. J., Characterization of the Calcium Silicate and Aluminate Phases of Portland Cements by ^{27}Al and ^{29}Si MAS NMR Spectroscopy, in *Proceedings of the 2nd International Conference on NMR Spectroscopy of Cement-Based Materials*, (P. Colombet, A. R. Grimmer, and H. Zanni, eds.), Springer-Verlag (1998)

@Seismicisolation

15. Kirkpatrick, R. J., MAS NMR Spectroscopy of Minerals and Glasses, in *Spectroscopic Methods in Mineralogy and Geology*, (F. C. Hawthorne, ed.), p. 698, Mineral Soc. Am., Washington, D. C. (1988)

16. Stebbins, J. F., Nuclear Magnetic Resonance Spectroscopy of Silicates and Oxides in Geochemistry and Geophysics, in *Handbook of Physical Constants, Volume 2, Mineral Physics and Crystallography*, (T. J. Ahrens, ed.), p. 354, Am. Geophys. Union, Washington, D. C. (1995)

17. Massiot, D., Cote, B., Taulelle, F., and Coutures, J. P., ^{27}Al MAS NMR of Crystalline and Amorphous Materials, in *Application of NMR Spectroscopy to Cement Science*, (P. Colombet and A. R. Grimmer, eds.), Gordon and Breach, Paris (1994)

18. Cote, B., Massiot, D., Coutures, J. P., Poe, B. T., and McMillan, P., ^{27}Al NMR of CaO-Al_2O_3-SiO_2 and CaO-Al_2O_3 Liquids and Glasses, in *Application of NMR Spectroscopy to Cement Science*, (P. Colombet and A. R. Grimmer, eds.), Gordon and Breach, Paris (1994)

19. Massiot, D., Trumeau, D., Touzo, B., Farnan, I., Rifflet, J. C., Douy, A., and Coutures, J. P., Structure and Dynamics of $CaAl_2O_4$ from Liquid to Glass: a High Temperature ^{27}Al NMR Time Resolved Study, *J. Phys. Chem.* 99:16455–16459 (1995)

20. Taylor, H. F. W., *Cement Chemistry*, Academic Press, London (1990)

21. Hamid, S. A., The Crystal Structure of the 11Å Natural Tobermorite,*Zeit. Kristall.*, 154:189–198 (1981)

22. Weiker, W., Grimmer, A. R., Winkler, A., Magi, M., Tarmak, M., and Lippmaa, E., Solid-State High-Resolution ^{29}Si NMR Spectroscopy of Synthetic 14Å, 11Å, and 9Å Tobermorites, *Cem. Concrete Res.*, 12:333–339 (1982)

23. Komarneni, S., Roy, R., Fyfe, C. A., and Kennedy, G. J., Naturally Occurring 1.4 nm Tobermorite and Synthetic Jennite: Characterization by ^{27}Al and ^{29}Si MAS NMR Spectroscopy and Cation Exchange Properties, *Cem. Concrete Res*., 17:891–895 (1987)

24. Bell, G. M. M., Bensted, J., Glasser, F. P., Lachowski, E. E., Roberts, D. R., and Taylor, M. J., Study of Calcium Silicate Hydrates by Solid State High Resolution ^{29}Si Nuclear Magnetic Resonance, *Adv. Cem. Res.*, 3:23–37 (1990)

25. Cong, X., and Kirkpatrick, R. J., ^{29}Si and ^{17}O NMR Investigation of the Structure of Some Crystalline Calcium Silicate Hydrates, *Adv. Cem. Based Mat.*, 3:133–143 (1996)

26. Mitsuda, T., Toraya, H., Okada, Y., and Shimoda, M., Synthesis of Tobermorite: NMR Spectroscopy and Analytical Electron Microscopy, *Ceram. Trans.*, 5:206–313 (1989)

@Seismicisolation

27. Komarneni, S., Roy, R., Roy, D. M., Fyfe, C. A., Kennedy, G. J., Bothner-By, A. A., Dadok, J., and Chesnick, A. S., ^{27}Al and ^{29}Si Magic-Angle Spinning Nuclear Magnetic Resonance Spectroscopy of Al-Substituted Tobermorites, *J. Mat. Sci*., 20:4209–4214 (1985)

28. Tsuji, M., Komarneni, S., and Malla, P., Substituted Tobermorites: ^{27}Al and ^{29}Si MAS NMR, Cation Exchange, and Water Sorption Studies, *J. Am. Cer. Soc*., 74:274–279 (1991)

29. Ishida, H., Yamazaki, S., Sasaki, S., Okada, Y., and Mitsuda, T., α-Dicalcium Silicate: Preparation, Decomposed Phase and its Hydration, *J. Am. Cer. Soc*., 76:1707–1712 (1993)

30. Okada, Y., Sasaki, K., Ishida. H., and Mitsuda, T., ^{29}Si NMR Study of the Thermal Decomposition of Hydrothermally Formed Hillebrandite and Xonotlite, *Ceram. Trans*., 37:11–20 (1993)

31. Skipsted, J., Hjorth, L., and Jakobsen, H. J., Quantification of Thaumasite in Cementitious Materials by ^{29}Si{^{1}H} Cross-Polarization Magic-Angle Spinning NMR Spectroscopy. *Adv. Cem. Res*., 7:69–83 (1995)

32. Heidemann, D., Proton High-Resolution Solid-State NMR Spectroscopy Using CRAMPS Techniques for Studies in Silicate and Cement Sciences, in *Application of NMR Spectroscopy to Cement Science*, (P. Colombet and A. R. Grimmer, eds.), Gordon and Breach, Paris (1994)

33. Rassem, R., Zanni-Theveneau, H., Heidemann, D., and Grimmer, A. R., Proton High Resolution Solid State NMR Study of C_3S Hydration, *Cem. Concrete Res*., 23:169–176 (1993)

34. Taylor, H. F. W., Tobermorite, Jennite, and Cement Gel, *Zeit. Kristall*., 202:41–50 (1992)

35. Young, J. F., Investigations of Calcium Silicate Hydrate Structure Using Silicon-29 Nuclear Magnetic Resonance Spectroscopy, *J. Am. Cer. Soc*., 71:C118–C120 (1988)

36. Grutzeck, M., Benesi, A., and Fanning, B., Silicon-29 Magic-Angle Spinning Nuclear Magnetic Resonance Study of Calcium Silicate Hydrates, *J. Am. Cer. Soc*., 72:665–668 (1989)

37. Damidot, D., Nonat, A., Barret, P., Bertrandie, D., Zanni, H., and Rassem, R., C_3S Hydration in Diluted and Stirred Suspensions: (III) NMR Study of C-S-H Precipitated During the Two Kinetic Steps, *Adv. Cem. Res*., 7:1–8 (1995)

38. Cong, X., and Kirkpatrick, R. J., ^{29}Si MAS NMR Study of the Structure of Calcium Silicate Hydrate, *Adv. Cem. Based Mat*., 3:144–156 (1996)

39. Cong, X., and Kirkpatrick, R. J., ^{17}O MAS NMR Investigation of the Structure of Calcium Silicate Hydrate Gel, *J. Am. Cer. Soc*., 79:1585–1592 (1996)

@Seismicisolation

40. Cong, X., and Kirkpatrick, R. J., Effects of Temperature and Relative Humidity on the Structure of C-S-H Gel, *Cem. Concrete Res.*, 25:1237–1245 (1995)

41. Cong, X., and Kirkpatrick, R. J., ^{1}H-^{29}Si CPMAS NMR Study of the Structure of Calcium Silicate Hydrate,*Adv. Cem. Res.*, 7:103–111 (1995)

42. Viehland, D., Li, J. F., Yuan, L. J., and Xu, Z., Mesostructure of Calcium Silicate Hydrate (C-S-H) Gels in Portland Cement Paste: Short-Range Ordering, Nanocrystallinity, and Local Compositional Ordering, *J. Am. Cer. Soc.*, 79:1731–1744 (1996)

43. Richardson, I. G., Brough, A. R., Byrdson, R., Groves, G. W., and Dobson, C. M., Location of Aluminum in Substituted Calcium Silicate Hydrate (C-S-H) Gels as Determined by ^{29}Si and ^{27}Al NMR and EELS, *J. Am. Cer. Soc.*, 76:2285–2288 (1993)

44. Richardson, I. G., Brough, A. R., Groves, G. W., and Dobson, C. M., The Characterization of Hardened Alkali-Activated Blast-Furnace Slag Pastes and the Nature of the Calcium Silicate Hydrate (C-S-H) Phase, *Cem. Concrete Res.*, 24:813–829 (1994)

45. Lippmaa, E., Magi, M., Tarmak, M., Wieker, W., and Grimmer, A. R., A High Resolution^{29}Si NMR Study of the Hydration of Tricalcium Silicate, *Cem. Concrete Res.*, 12:597–602 (1982)

46. Rodger, S. A., Groves, G. W., Clayden, N. J., and Dobson, C. M., Hydration of Tricalcium Silicate followed by ^{29}Si NMR with Cross-Polarization, *J. Am. Cer. Soc.*, 71:91–96 (1988)

47. Parry-Jones, G., Al-Tayyib, A. J., Al-Dulaijan, S. U., Al-Mana, A. I., ^{29}Si MAS-NMR Hydration and Compressive Strength Study in Cement Paste, *Cem. Concrete Res.*, 19:228–234 (1989)

48. Ishida, H., Sasaki, K., and Mitsuda, T., Highly Reactive β-Dicalcium Silicate, I: Hydration Behavior at Room Temperature, *J. Am. Cer. Soc.*, 75:353–358 (1992)

49. Masse, S., Zanni, H., Lecourtier, J., Roussel, J. C, and Rivereau, A., ^{29}Si Solid State NMR Study of Tricalcium Silicate and Cement Hydration at High Temperature, *Cem. Concrete Res.*, 23:1169–117 (1993)

50. Brough, A. R., Groves, W., Richardson, I. G., Rodger, S. A., and Dobson, C. M., Kinetics of Hydration and Other Reactions of Calcium Silicates and Cements, in*Application of NMR Spectroscopy to Cement Science*, (P. Colombet and A. R. Grimmer, eds.), Gordon and Breach, Paris (1994)

51. Hjorth, J., Skipsted, J., and Jakobsen,^{29}Si MAS NMR Studies of Portland Cement Components and Effects of Microsilica on the Hydration Reaction, *Cem. Concrete Res.*, 18:789–798 (1988)

52. Brough, A. R., Dobson, C. M., Richardson, I. G., and Groves, G. W., Application of Selective ^{29}Si Isotopic Enrichment to Studies of the Structure of Calcium Silicate Hydrate (C-S-H) Gels, *J. Am. Cer. Soc.*, 77:593–596 (1994)

@Seismicisolation

53. Justnes, H., Meland, I., Bjorgum, and Krane, J., The Mechanism of Silica Fume Action in Concrete Studied by Solid State ^{29}MAS NMR, in *Application of NMR Spectroscopy to Cement Science*, (P. Colombet and A. R. Grimmer, eds.), Gordon and Breach, Paris (1994)

54. Zanni, H., Cheyrezy, M., Maret, V., Philippot, S., and Nieto, P., Investigation of Hydration and Pozzolanic Reaction in Reactive Powder Concrete (RPC) Using ^{29}Si NMR, *Cem. Concrete Res*., 26:93–100 (1996)

55. Sun, G. K., and Young, J. F., Quantitative Determination of Residual Silica Fume in DSP Cement Pastes by ^{29}Si NMR, *Cem. Concrete Res*., 23:480–483 (1993)

56. Lahajnar, G., Blinc, R., Rutar, V., Smolej, V., Zupncic, I., Kocuvan, I., and Ursic, J., On the Use of Pulse NMR Techniques for the Study of Cement Hydration, *Cem. Concrete Res*., 7:385–394 (1977)

57. Schreiner, L. J., MacTavish, J. C., Miljkovic, L., Pintar, M. M., Blinc, R., Lahajnar, G., Lasic, D., and Reeves, L. W., NMR Line Shape-Spin-Lattice Relaxation Correlation Study of Portland Cement Hydration, *J. Am. Cer. Soc*., 68:30–36 (1985)

58. Lasic, D. D., Corbett, J. M., Jian, J., MacTavish, J. C., and Pintar, M. M., NMR Spin Grouping in Hydrating Cement at 200 MHz, *Cem. Concrete Res*., 18:649–653 (1988)

59. Rumm, R., Haranczyk, H., Peemoeller, H., and Pintar, M. M., Proton Free Induction Decay Evolution During Hydration of White Synthetic Cement, *Cem. Concrete Res*., 21:391–393 (1991)

60. Müller, D., Rettel, A., Gessner, W., and Scheler, G., An Application of Solid-State Magic-Angle Spinning ^{27}Al NMR to the Study of Cement Hydration, *J. Magn., Reson*., 57:152–156 (1984)

61. Rettel A., Gessner, W., Müller, D., and Scheler, G., On the Hydration of $CaAl_2O_4$ at Various Temperatures, *Br. Ceran. Trans. J*., 84:25–28 (1985)

62. Müller, D., Rettel, A., Gessner, W., Bayoux, J. P., and Capmas, A., Progress in the ^{27}Al MAS NMR Spectroscopic Monitoring the Hydration of Calcium Aluminate Cements, in *Application of NMR Spectroscopy to Cement Science*, (P. Colombet and A. R. Grimmer, eds.), Gordon and Breach, Paris (1994)

63. Cong, X., and Kirkpatrick, R. J., Hydration of Calcium Aluminate Cements: A Solid-State ^{27}Al NMR Study, *J. Am. Cer. Soc*., 76:409–416 (1993)

64. Kosmac, T., Lahajnar, G., and Sepe, A., Proton NMR Relaxation Study of Calcium Aluminate Hydration Reactions, *Cem. Concrete Res.*, 23:1–16 (1993)

65. Janusa, M. A., Wu, X., Cartledge F. K., and Butler, L. G., Solid-State Deuterium NMR Spectroscopy of d_5-Phenol in White Portland Cement: A New Method for Assessing Solidification/Stabilization, *Environ. Sci. Technol*., 27:1426–1433 (1993)

@Seismicisolation

66. Hanna, R. A., Barrie, P. J., Cheeseman, C. R., Hills, C. D., Buchler, P. M., and Perry, R., Solid State ^{29}Si and ^{27}Al NMR and FTIR Study of Cement Pastes Containing Industrial Wastes and Organics, *Cem. Concrete Res*., 25:1435–1444 (1995)

67. Chen, J. H., Wang, Y. Y., Wan, C. C., and Liou, D. C., MAS/NMR Studies of the Hydration Process of β-C_2S in the Presence of Chromium, *Cem. Concrete Res*., 24:319–324 (1994)

68. Cong, X., Kirkpatrick, R. J., and Diamond, S., ^{29}Si MAS NMR Spectroscopic Investigation of Alkali Silica Reaction Product Gels, *Cem. Concrete Res*., 23:811–823 (1993)

69. Faucon, P., Carpentier, T., Nonat, A., and Petit, J. C. Triple-Quantum Two Dimentional ^{27}Al Magic Angle Magnetic Resonance Study of the Aluminum Incorporation in Calcium Silicate Hydrates, *J. Am. Chem Soc*., 120:12075–12082 (1998)

70. Sun, G.-K., Young, J. F., and Kirkpatrick, R. J., The Role of Al in C-S-H:Results for Precipitated Samples and a Hydrated White Cement, *J. Am. Ceram. Soc*., (submitted)

@Seismicisolation

7

Scanning Electron Microscopy, X-Ray Microanalysis of Concretes

Shondeep L. Sarkar, Xu Aimin, and Dipayan Jana

1.0 INTRODUCTION

Not many methods of "visual" evaluation of concrete are available to the concrete technologist except possibly optical microscopy. Most of the properties of concrete are evaluated, that is, tested and analyzed, according to standard procedures. For example, the ASTM C 856 method is used for petrographic analysis of hardened concrete, the ASTM C 39 method for testing compressive strength of concrete, the AASTHO T 227 for chloride ion permeability, and the ASTM C 133 method for chemical analysis. In this respect, scanning electron microscopy (SEM) and its adjunct microanalytical unit, commonly known as the energy dispersive x-ray analyzer (EDXA), do not fall under the realm of any standard procedure. It is a relatively new technique which is yet to be universally accepted by the concrete technologist as an investigative tool. One of the first applications of SEM in cement hydration study was by Gupta, Chatterji, and Jeffery, in the early 1970s.[1] Following the development of EDXA, Diamond[2] brought to our attention

@Seismicisolation

the advantages of this SEM attachment in the microanalysis of concrete. Since then several researchers have practiced, and even improved the technique of concrete evaluation using SEM-EDXA.[2]–[4]

It appears that transmission electron microscopy (TEM) had been in use before the potential of scanning electron microscopy in the study of concrete began to be recognized. Despite its higher resolution, the TEM suffers from an inherent drawback in that in-situ samples cannot be observed. In fact, the sample must be reduced to a very thin film so that the beam can transmit through it before it can be examined under the TEM. This thinning process, which is either done by ion-thinning or grinding, is known to destroy some very important integral characteristics such as the paste-aggregate interface, interparticle bonding, etc. Though it is not possible to examine massive samples under the SEM, in the TEM the sample size must be reduced still further, to only about 1–2 mm. Nonetheless, the TEM still remains a powerful electron-optical instrument for studying early hydration products and ultra fine particles such as silica fume.[6]

To appreciate the functional utility of SEM-EDXA, it is necessary to understand the important principles governing this combined visual and microanalytical technique.

2.0 SCANNING ELECTRON MICROSCOPY, X-RAY MICROANALYSIS

2.1 Optical Microscopy-Electron Microscopy Transition

A microscope is a device that reveals details of an object finer than what can be seen by the naked eye. Certainly the development of the optical microscope, ever since its discovery in the late 16th century, brought a new era in scientific instrumental examination. The performance of a microscope, and, therefore, the quality of examination, depends on the resolution of the microscope and its ability to provide an image which has sufficient contrast to distinguish the observed phases against the background.

The resolution or the resolving power of a microscope to reproduce the object is defined as the smallest separation of two points in the object that can be distinctly shown by the image. A resolution of 210 nm was already achieved by optical microscopes built 100 years ago.

@Seismicisolation

Two discoveries in the 1920s, namely, the wave nature of particle streams by L. de Broglie, and that electrons can be focused by a magnetic field, demonstrated by H. Busch, heralded the development of electron microscopes.[7] Owing to the much shorter wavelength of the incident electron beam, the electron microscope is capable of producing distinctly higher resolution images compared to optical microscopes. The first commercial SEMs became available in the 1960s and today's SEM has achieved a resolution better than 10 nm, that is an improvement by a factor about 10^3 relative to light microscope.

2.2 Scanning Electron Microscope

When a beam of primary electrons strikes a bulk solid, the electrons are either reflected (scattered) or absorbed, producing various signals, Fig. 1. The incident electrons disperse into a "pear shaped" volume in the solid. Besides secondary electrons, backscattered electrons (BSE), x-rays, Auger electrons, and other responses, are also produced. Different modes of observation and/or microanalysis can thus be employed on the object under examination. The most frequent modes in the SEM involve the capture of secondary and backscattered electrons, while the most commonly used microanalytical techniques, based on the detection of x-rays, are energy dispersive x-ray analysis and wavelength dispersive (WD) analysis. Modern SEMs are usually equipped with the EDX detector while the WD analyzer unit remains an option for the expensive models.

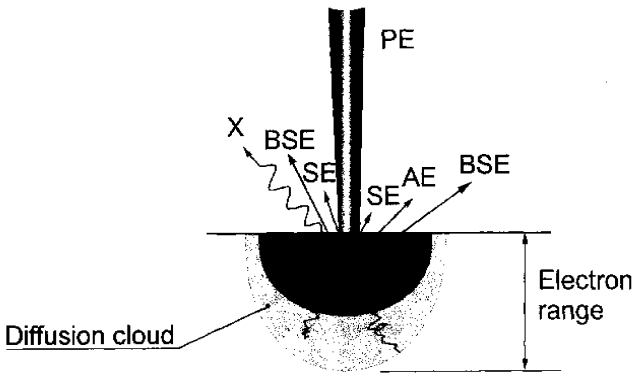


Figure 1. Different interactions of an electron beam *(PE)* with a solid target. *BSE* = backscattered electron, *SE* = secondary electron, *X* = x-ray, *AE* = auger electron.

@Seismicisolation

The intensity of the reflected electrons is proportional to the atomic number of the substances in the object and the density of the material. The energy level of primary electrons (PE) is up to about 50 eV and so are the scattered electrons. One distinctive feature of the BSE is its relatively high energy. It is important to note that all these responses are produced in a shallow zone of the target.

The principle of SEM can be explained with the help of the illustration shown in Fig. 2. The electron beam is formed by the electron gun which is successively condensed by the projecting lens and the objective (magnetic) lens to a spot about 5–100 nm in diameter at the specimen plane. The entire system is tightly sealed so that when it is in an operational state the microscope column can be evacuated to about 10^6 torr (1.33×10^{-4} Pa). A scan generator simultaneously drives the X- and Y-scan coils in the microscope column and in the cathode ray tube (CRT). Among the different types of responses produced, the secondary electrons (SE) and x-rays are collected by the photomultiplier to form an image and provide chemical compositional data.

A conventional collector is illustrated in Fig. 3. The secondary electrons at the specimen surface are accelerated under a potential difference of 10 kV towards the scintillator where light is created and passed down a light pipe to a photomultiplier. The function of the photomultiplier is to convert light into an electric current ready for further amplification by an amplifier and eventual display on a CRT screen.

Any object can be microscopically examined as long as it is electrically conductive. The contrast formed by the collected signals originate from the difference in surface topography and composition. Both SE and BSE modes provide imaging facility; the SE mode, however, is dominated by topographic contrast, whereas the BSE mode is much more oriented to detecting atomic density which can be related to the atomic number and density of the grains forming the object.

Acceleration Voltage. An appropriate voltage must be chosen subject to the composition of the specimen. With most modern SEMs it is possible to select a voltage from as low as 0.2 kV to as high as 30 kV. While a higher voltage provides a stronger contrast it may lead to increased surface charging and, thus, deterioration in the quality of the image. Typically, 15 to 20 kV is suitable for studying ordinary concrete specimens, but 15 kV is desirable for specimens containing a high volume of fly ash. For materials more vulnerable under the electron beam, e.g., polymers, a lower voltage of about 5 kV is preferred.

@Seismicisolation

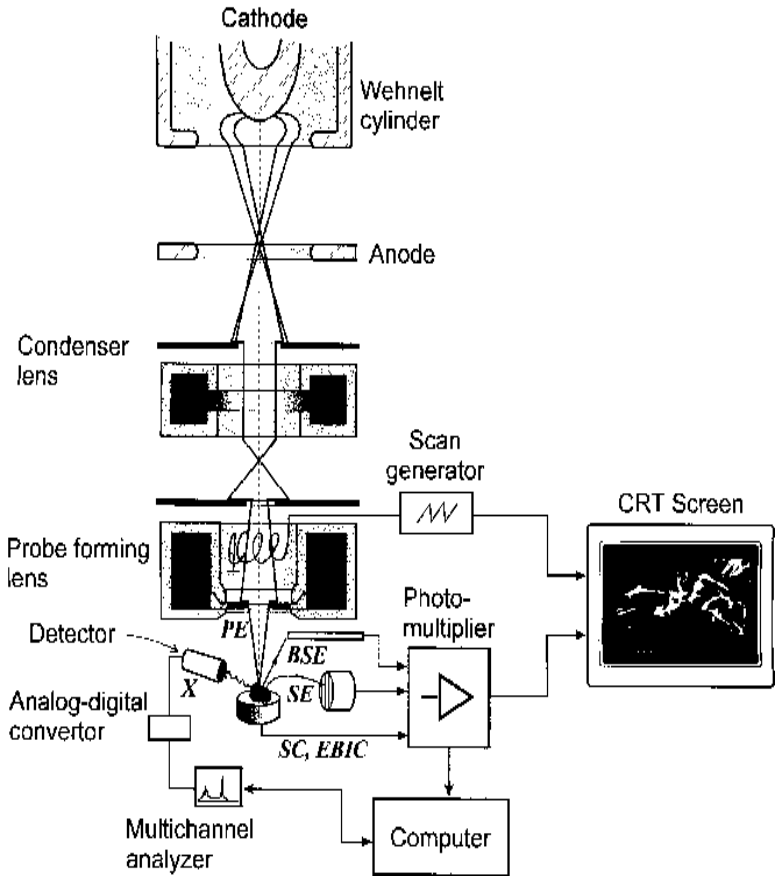


Figure 2. Schematic of a scanning electron microscope.

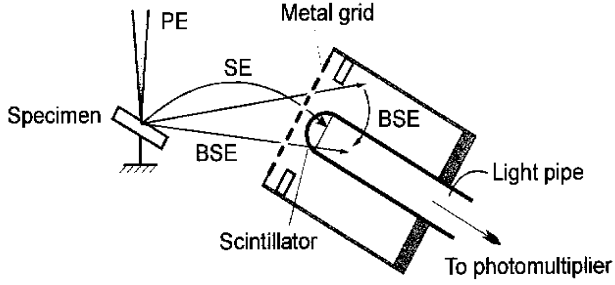


Figure 3. A conventional collector for secondary electrons *(SE)* and backscattered electrons *(BSE)*. *PE* = primary electron beam.

@Seismicisolation

Depth of Focus. The small aperture(s) defining the electron beam (the same as in the case of an ordinary camera) results in a large depth of focus, which is much higher than that of the optical microscope. For example, a rough surface will remain in focus and usually one area can be clearly examined by SEM in a single view without changing the focus, though the depth of focus reduces at very high magnifications. Surface irregularities, however, do influence SE emission and signal collection. The signal yield is poor from flat areas while it is much stronger from inclined areas; areas with a rough surface may hinder some signals, leading to a better morphological image at the cost of details.

Backscattered Electron Imaging. Reflection of primary electrons by the specimen is higher when the atomic density of the specimen is higher, i.e., a material having a high atomic number results in more efficient reflection. Cement provides some good examples in this respect. The aluminoferrite phase (C_4AF) in cement appears brighter than tricalcium aluminate (C_3A) due to the presence of iron whose atomic number, Z = 26, is higher than that of calcium[20] or aluminum,[13] and unhydrated cement grains are brighter while the C-S-H is darker in the BSE mode (Fig. 4).

Contrary to the SE mode, the specimen for BSE examination, preferably, should be flat in order to reduce the noise produced by an uneven surface. Compared to SE, BSE has a much higher energy, thus, only those features that are in direct line of sight of the collector are detected and the resultant micrograph does not show much detail for deeper layers, e.g., in a hole.

2.3 X-Ray Microanalysis

The process of using the scanning electron microscope and energy dispersive x-ray analyzer to simultaneously examine the morphology of an object and analyze its elemental composition is called SEM/EDXA. The x-ray microanalysis can be done *(a)* in the spot mode, i.e., for analyzing a small spot in a constituent for its elemental composition; *(b)* in the area mode, to analyze the bulk composition of an area; *(c)* in dot mapping mode, to scan a particular area of interest for elemental mapping to study the distribution density of different elements in a particular phase or region; or, *(d)* in linear traverse mode, to determine variation in concentration of one or several elements along a line.

@Seismicisolation

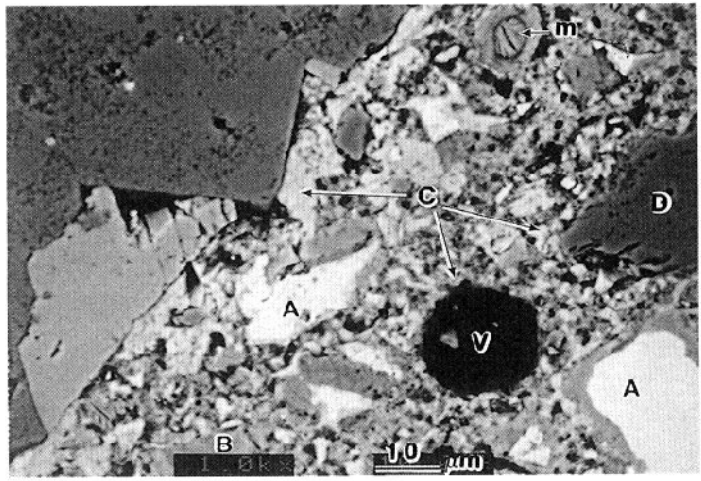


Figure 4. Backscattered electron image of interficial transition zone along dolomite aggregate *(D)* and noncontinuous calcium hydroxide deposit *(C)* along aggregate boundaries and air voids *(V)*. *A* = partly hydrated cement grains, *B* = C-S-H, and *m* = calcium monosulfate. *(Courtesy of Dr. David Bonen, US Gypsum Corporation.)*

EDXA is based on the detection of x-rays emitted by the specimen under investigation and that every element has a characteristic emission. Conventional EDX detector which is maintained under cryogenic conditions, is made of lithium (Li) drifted silicon (Si); a beryllium (Be) window often separates the spectrometer and the microscope. The x-ray photons that originate from the specimen are collected by the Si-Li detector. After undergoing a conversion process to voltage pulse output, it is then transformed into counts/channel. These counts are displayed on the cathode ray tube screen. Since each element has its characteristic energy position, different elements can be readily identified by means of a cursor. For example, aluminum Kα is at 1.5 keV, silicon Kα at 1.74 keV, sulfur Kα at 2.34 keV, and calcium Kα at 3.7 keV. In practice, the accelerating voltage exceeds the critical excitation potential of the characteristic x-rays, e.g. for K radiation of atoms up to Z = 40, a 30 kV voltage is commonly used. The high voltage used for microanalysis indicates that the sampled volume is comparatively large. The total number of counts for a particular element is proportional to the amount of that element present in the object. An example of EDXA applied to concrete is shown in Fig. 5.

@Seismicisolation

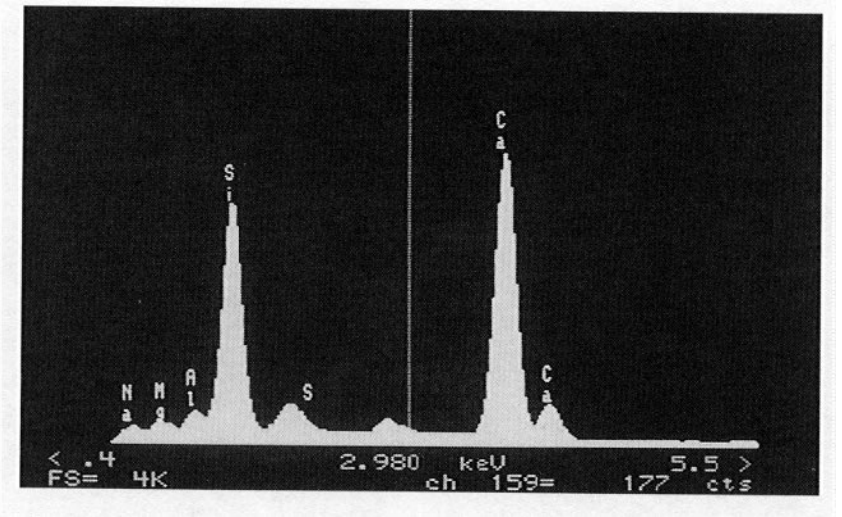


Figure 5. EDX spectrum of C-S-H in the hydrated paste of a concrete. Calcium and Si are the principal peaks. Trace amounts of Na, Mg, Al, and S, are present as impurities.

Most EDX systems are equipped with software for quantitative analysis, also known as ZAF for the three major corrections that are applied, namely atomic number *(Z)*, absorption *(A)*, and fluorescence *(F)*. Quantitative analysis, however, must be carried out on flat polished surfaces, or errors are bound to occur. Phase delineation of concrete specimens can be a major problem which is overcome by using the backscattered electron imaging technique. For practical purposes, however, the concrete technologist is rarely interested in phase quantification. To study the effects of deterioration of concrete or its performance characteristics, qualitative phase identification, grain morphology, distribution pattern, and association with other phases, are some of the chief interests one has in studying concrete under the SEM.

The EDX system can simultaneously detect elements with energy higher than 1 keV (elements with $Z = 11$, i.e., sodium); lower-energy elements are absorbed by the Be window. Modern EDX detectors are windowless, therefore it is possible to detect lower atomic number elements such as carbon (C) and oxygen (O). The advantage is that discrete differences between certain minerals that may be present in concrete can be readily made despite very similar morphologies. This is well demonstrated in the analysis of ettringite and thaumasite, Figs. 6a and 6b.

@Seismicisolation

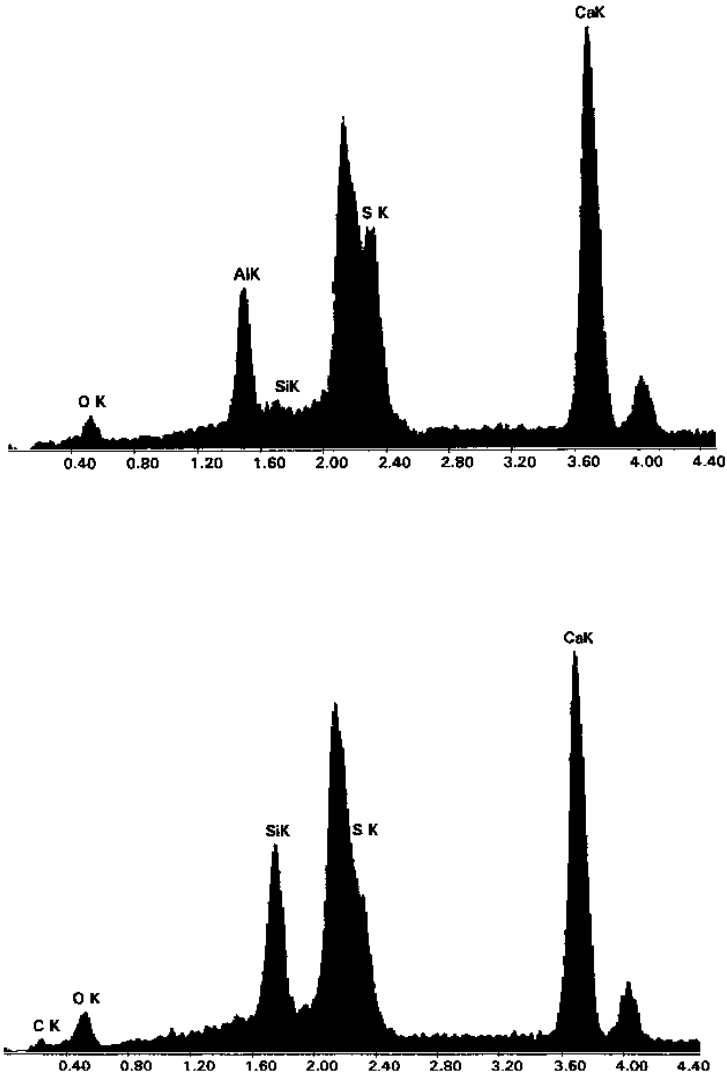


Figure 6. EDX spectrum of *(a)* ettringite, showing Ca, Al, S, and O peaks; *(b)* thaumasite, showing Ca, Si, S, O, and C peaks.

Caution. Since EDXA is not restricted to a small volume, contributions from the surrounding regions and from below the object being analyzed may jeopardize the analysis results. It is possible for the electron beam to

@Seismicisolation

pass through the object if it is either a fine fibrous or a thin platy type. Additional elemental peaks may appear during analysis; for example, silicon from neighboring or underlying C-S-H is a very common occurrence in ettringite analysis because of ettringite's fibrous morphology which permits beam penetration through the crystals. This, however, does not imply that the fibrous crystals are composed of thaumasite and ettringite. To positively distinguish one from the other, the presence or absence of carbon must be verified using a windowless detector.

Specimen Preparation. One of SEMs great advantages lies in the possibility of examining a fractured concrete specimen which is first mounted either on a metal or a graphite stub using a rapid drying glue. A powder sample can be mounted by spraying the powder on the stub topped with glue or a double sided tape. Pressing the sample with a piece of clean Al-film helps to reduce the number of loose grains. Since cement paste and concrete tend to be nonconductive they need to be coated with a thin layer of electrically conductive material.

The commonly used methods of coating are high voltage sputtering and evaporation. For cold sputtering, a range of coating materials such as gold (Au), gold-palladium (Au-Pd), chromium (Cr), silver (Ag), etc., may be used, while carbon is used for evaporation. The selection of coating material depends on the requirement of the compositional analysis. For example, to analyze concrete which has undergone sulfate attack, Au coating is not appropriate, because the L-line of Au interferes with the K line of sulfur (S). Similarly, the interference of the M-line of Pd with the K-line of chloride (Cl) must be taken into consideration when the presence of additional Cl in concrete is to be evaluated, such as reinforced concrete in a marine environment. Silver or chromium sputtering or carbon evaporation can be used in these cases. Once a coating of suitable material and thickness has been applied on the specimen surface it is ready to be inserted in the SEMs specimen chamber for examination. Actually, concrete specimen preparation for SEM and qualitative EDXA requires minimal effort.

Specimen Size. The size of the specimen that can be accommodated inside the microscope depends on the model of the SEM being used. In some SEMs, it is possible to insert specimens that are several square inches in size, while others are capable of accepting relatively small-size specimens. It must be remembered that the larger the size of the specimen, the longer it takes for the SEM to pump down. Compared to the TEM and optical microscope, the thickness of the specimen for SEM is much larger. A regular criticism addressed towards this type of microanalysis is that the results are based on examination of much too small areas. Thus, it is

@Seismicisolation

preferable to examine a relatively large area in a specimen for the study to be representative.

Specimen Pre-Conditioning. Examination of a freshly exposed concrete surface is desirable in order to avoid carbonation and other spurious surfacial effects. Specimens for BSE imaging should be flat and smooth, which helps to provide more reproducible results.

The sample must be sufficiently dry otherwise moisture in the sample begins to evaporate under the high vacuum in the microscope, thus deteriorating the vacuum in the SEM column and affecting the efficiency of the electron beam.

It has been noted that drying of the concrete specimen at a high temperature results in additional cracks. If the drying time is long, some water-sensitive crystals exhibit a tendency to change form. For example, gypsum ($CaSO_4 \cdot 2H_2O$) can transform to hemihydrate ($CaSO_4 \cdot 0.5H_2O$) at a fairly low temperature, around 100°C, though in a dynamic condition this normally occurs at about 150°C. Even a relatively short drying time can decompose ettringite crystals.

Recent progress in SEM enables us to use an "environmental cell," which allows the examination to be performed under a weak vacuum, e.g., 5×10^{-3} torr (0.67 Pa). This permits retention of moisture in the specimen and wet specimen imagery at the same high level of resolution as the conventional SEM. Thus, cement hydration can be recorded in real-time and for routine examination the specimen does not suffer from the micro-shrinkage or crystallization due to the moisture evaporation.[8]

3.0 CONCRETE UNDER THE SEM

Having described the principle and instrumentation of scanning electron microscopy-x-ray microanalysis at some length sets the stage for examining the applications of SEM/EDXA in concrete science and technology. The very first item that one needs to become familiar with is the basic microstructure of concrete.

3.1 Basic Microstructure of Concrete

The term *basic microstructure* indicates the structure which develops in concrete at a micro-level when water is added to cement and aggregates.

@Seismicisolation

Whether it is to understand the cause, extent and mechanism of deterioration, or how to improve some of the properties of concrete, a thorough awareness of the basic microstructure of hardened concrete is required. Mechanical properties of concrete more than often depend on its intrinsic microstructure. The high resolution capability of SEM coupled with the possibility of instantaneous microanalysis using EDXA has opened a world of opportunities in the field of concrete technology which otherwise would have been impossible by the standard petrographic technique using an optical microscope.

The microstructure of concrete is described as an integrated system consisting of *(i)* hydrated cement paste (HCP); *(ii)* coarse and fine aggregates; and *(iii)* the interface between aggregate and hydrated cement paste (HCP), also known as the interfacial transition zone (ITZ) or paste-aggregate interface.

Hydrated Cement Paste (HCP). The hydrated cement paste in a normal concrete with a water/cement ratio (W/C) in the range of 0.50 to 0.55 consists of cement hydration products that include *(i)* calcium silicate hydrate (C-S-H) which forms 50–60% of the solid volume in HCP; *(ii)* calcium hydroxide (CH) crystals contributing another 20–25% to the solid volume; and *(iii)* the remainder is occupied by calcium sulfoaluminate hydrates AFt (ettringite) and AFm (monosulfate), incompletely hydrated cement particles (IHCP), and paste porosity, (small 5–20 mm gel pores accounting for the porosity in solid C-S-H and large capillary pores in the paste matrix) Fig. 7. The amount of IHCP in a concrete depends on cement fineness, water/cement ratio, and the degree of cement hydration.

C-S-H Phase. The C-S-H phase is the most important component in concrete since it provides the necessary cementitious or binding property to the final product (by Van der Waals force of attraction) and, hence, contributes to the strength of concrete. Scanning electron microscopy has been extremely useful in characterizing the morphology and chemical composition of the C-S-H phase which can vary somewhat within limits. The C-S-H phase in concrete produced at normal temperature is represented by gel structure whereas, at elevated temperatures, it can range from poorly-crystalline to crystalline. Under the SEM, the overall morphology of normal temperature C-S-H can actually vary from the common fibrous type to irregular grains forming a reticular network, Figs. 8a and 8b. Microanalysis of C-S-H phase has shown that the Ca/Si molar ratio can vary depending on the water/cement ratio or the presence of mineral admixtures in concrete.

@Seismicisolation

Calcium Hydroxide (CH) Crystals. Calcium hydroxide crystals appear in many different shapes and sizes, starting from massive, platy crystals often tens of microns across with distinctive hexagonal prism morphology, large thin elongated crystals, blocky masses to finely disseminated crystals. Calcium hydroxide crystals tend to develop a preferred orientation along the paste-aggregate interface with their c-crystallographic axis parallel to the interface (Fig. 9).

Calcium Sulfoaluminate Hydrates (AFt and AFm Phases). The scanning electron microscope identifies the two distinct morphologies of calcium sulfoaluminate hydrates, that is, ettringite phase (AFt) and monosulfate (AFm) in concrete. Usually ettringite forms needlelike crystals in vacant spaces during early hydration (Fig. 10). Those formed later are known to cause disruption; agglomerates of these crystals formed in a confined space absorb water and expand. Monosulfate appears as hexagonal platy crystals. Early-formed monosulfate tends to crystallize in clusters, rosettes of irregular plates, whereas those formed later grow into well-developed, but very thin hexagonal plates.

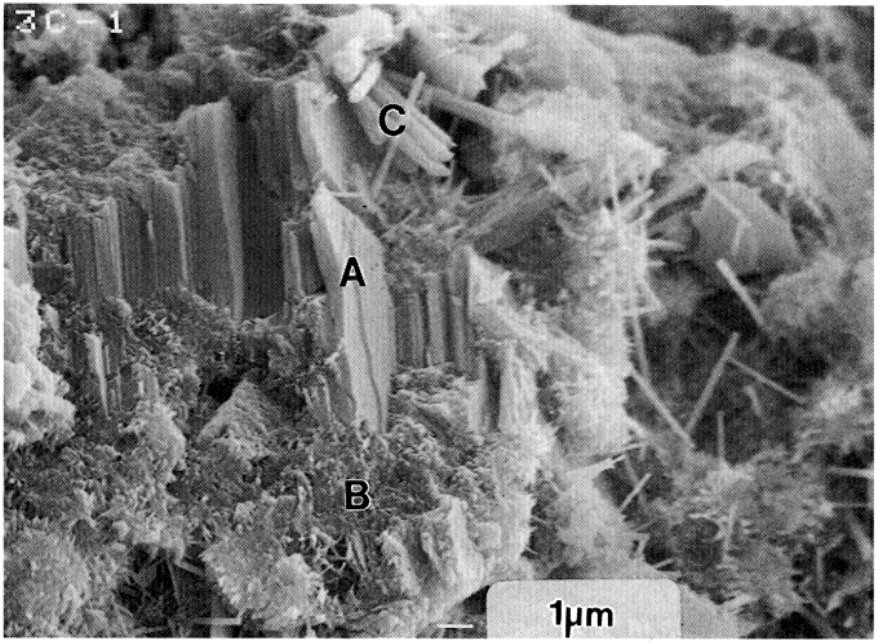
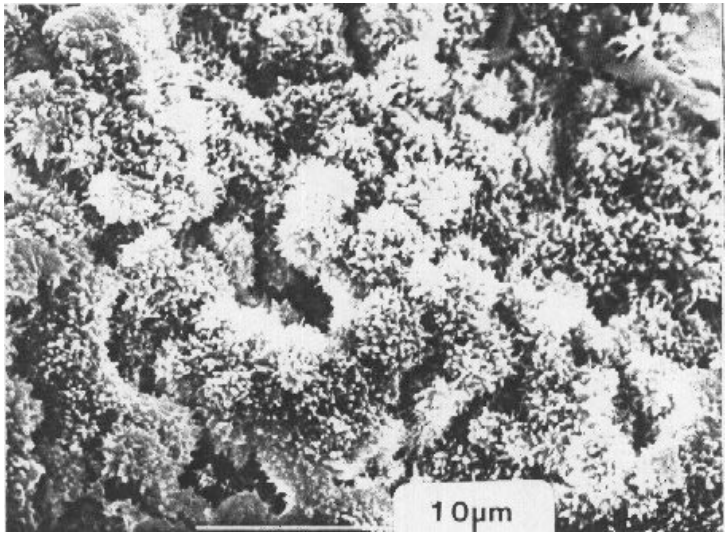
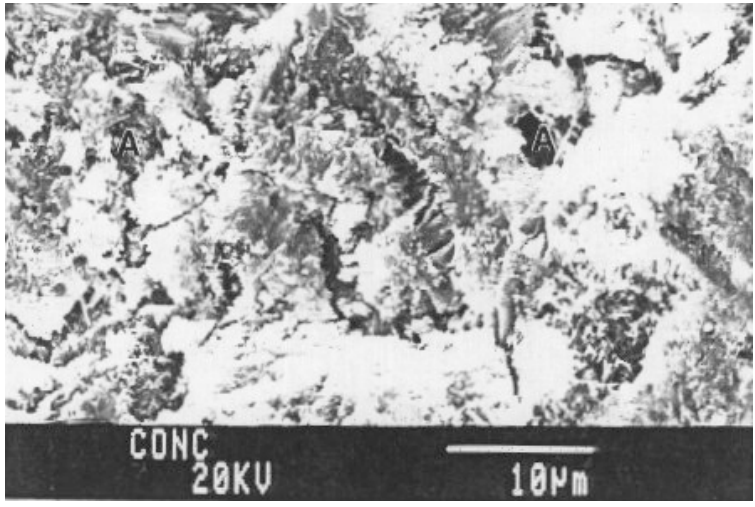


Figure 7. Hydrated cement paste of 0.55 W/C concrete, where *A* = CH, *B* = C-S-H, and *C* = ettringite needles.

@Seismicisolation



(a)



(b)

Figure 8. *(a)* Fibrous C-S-H forming a porous and permeable HCP in a high W/C concrete. *(b)* Denser HCP in a low W/C (0.40) concrete. Pores (*A*) are small and permeability is low.

@Seismicisolation

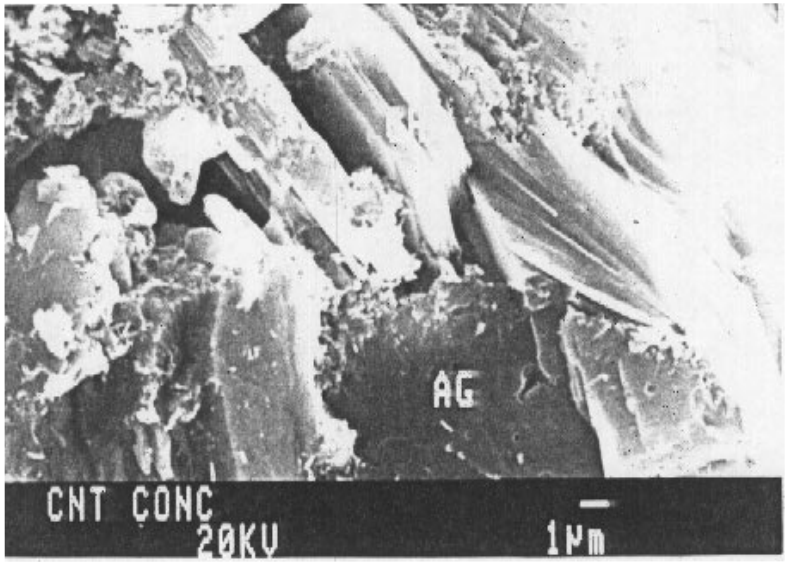


Figure 9. Paste-aggregate interface showing increased paste porosity and oriented growth of CH crystals (*CH*) on the aggregate face. *AG* = aggregate.

Incompletely Hydrated Cement Particles (IHCP). These can be very easily identified by their characteristic brightness in the BSE image (see Fig. 4) and from their morphology in the secondary electron mode (Fig. 11). These particles have a tendency to attract each other and form flocs which can entrap a large amount of mixing water. The undesirable variation in local water/cement ratio thus created results in a heterogeneous pore structure. Scanning electron microscopy can be extremely helpful in studying the ultimate distribution of pores in the HCP.

Porosity of Hydrated Cement Paste. The hydrated cement paste contains two types of pores, *(a)* large "capillary pores" representing areas which were originally occupied by water in between the unhydrated cement grains, but now appear as vacant spaces between the hydrated C-S-H gel. These are distinctly visible, both in the secondary and backscattered electron imaging mode of the SEM, and *(b)* smaller "gel pores" inside the C-S-H gel itself. Gel pores, however, are too small to be resolved by SEM.

@Seismicisolation

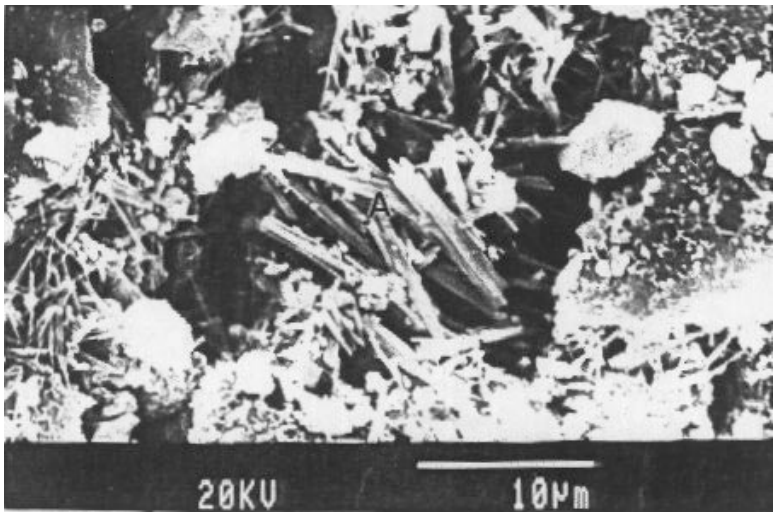


Figure 10. Ettringite needles *(A)* growing in a vacant area in the HCP of a concrete.

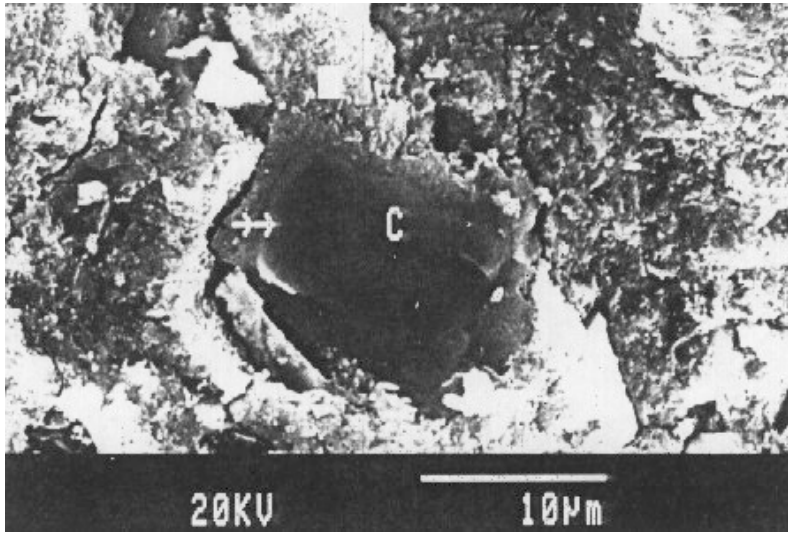


Figure 11. An incompletely hydrated cement grain *(c)* in the HCP. (→→) shows the hydration rim.

@Seismicisolation

Aggregates. Although petrography still remains an invaluable tool for mineralogical identification of constituents, their shape, size, surface texture, and potential alkali reactivity, SEM usually serves as a useful companion to *(a)* determine the nature and chemical composition of deleterious constituents in aggregates (fine particles, clay lumps, organic matter, iron sulfides, sulfate contaminants, etc.); *(b)* identify the products of deleterious reaction of aggregates with cement (like alkali-aggregate reaction gel precipitated along cracks or rims around aggregates); and *(c)* the porosity and pore connectivity (permeability) of aggregates.

Paste-Aggregate (P-A) Interface. The paste-aggregate interface is claimed to be the weakest microstructural component in concrete.[9] An important application of SEM in concrete microstructure has been the numerous studies on the properties of interfacial transition zone.[10][11] Micromorphological investigations have demonstrated the presence of a thin layer of hydration product on the aggregate surface. Barnes, et al.,[12] identified this layer as a "duplex film" consisting of calcium hydroxide crystals with their c-axis oriented perpendicular to the aggregate surface, surrounded by a layer of C-S-H. Beyond this thin film of hydration is the main transition zone, about 50 mm thick with pronounced high porosity, which makes the interface the weakest zone in concrete. Important microstructural features observed in this zone are *(a)* preferred orientation of large platy CH crystals (with the c-axis parallel to the aggregate surface); *(b)* lack of anhydrous cement particles; *(c)* higher porosity than the bulk paste; and *(d)* increased concentration of ettringite. The complete hydration of cement in this zone indicates that the water/cement ratio at the interface is higher than elsewhere.

The paste-aggregate interface in lightweight aggregate concrete represents a different type of bonding easily distinguishable under the SEM. Lightweight aggregates usually have a porous outer layer which encourages the migration of mobile ions towards the periphery, leading to the formation of a more dense interfacial zone. Additionally, the rough surface texture also improves mechanical interlocking of the aggregate with HCP, as illustrated in Fig. 12.[13][14]

The strength and durability of concrete can be greatly enhanced by refining the P-A interface. One way to achieve this improvement is by reducing the W/C of the concrete, so that the amount of CH along the interface diminishes. Examination of the interface under the SEM can readily determine the effect of W/C reduction on the increase in P-A bonding. Since CH also forms in vacant spaces in the paste, its formation is directly related to availability of space and higher water content; thus,

@Seismicisolation

reducing the W/C results in a corresponding decrease in CH crystallization. The other alternative is to incorporate mineral admixtures such as silica fume, fly ash or slag, in the concrete; consumption of CH by pozzolanic reaction helps to refine the P-A interface.

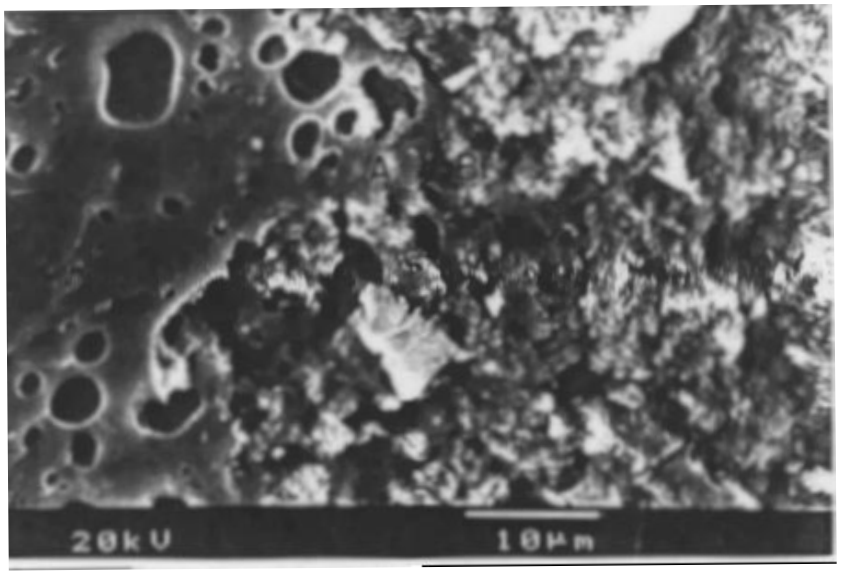


Figure 12. Mechanical bonding at the paste-aggregate interface of a lightweight aggregate concrete, where *A* = aggregate, *B* = HCP.

3.2 Admixtures in Concrete

Traditionally, and actually since historical times, the purpose of adding mineral and/or chemical admixtures in concrete has been to improve its properties, either in the fresh state, hardened state, or both. The combined use of these admixtures has resulted in a new generation of concrete called *high-performance concrete* (HPC). These admixtures change the basic microstructure of concrete; for example, whereas silica fume and fly ash are pozzolanic, slag is strictly cementitious. Enhancing our understanding on the role of admixtures depends on in-depth microstructural investigation using SEM as a function of hydration time and in terms of the final product.[15]

@Seismicisolation

Mineral Admixtures. Mineral admixtures bring about two important modifications in the concrete microstructure. First, its addition creates a dense, highly impermeable HCP (Fig. 13) and a strong P-A interface with a distinctly lower amount of CH crystals forming in this zone (Fig. 14). The resultant concrete acquires greater resistance to penetration of external aggressive chemicals. Microanalysis of the principal hydration product, C-S-H, shows a close compositional resemblance to the C-S-H produced in normal concrete, but with lower Ca/Si ratio. Second, the size and volume of CH crystals is lower.[16] All these features, such as matrix densification, refined paste-aggregate interface, increased impermeability, and reduced porosity, can be recognized under the SEM.

Furthermore, SEM/EDXA can be very useful in studying the reaction kinetics of different mineral admixtures which are quite different. It is in this light that a description of the hydration products of the common mineral admixtures and the corresponding microstructures under the SEM are presented below.

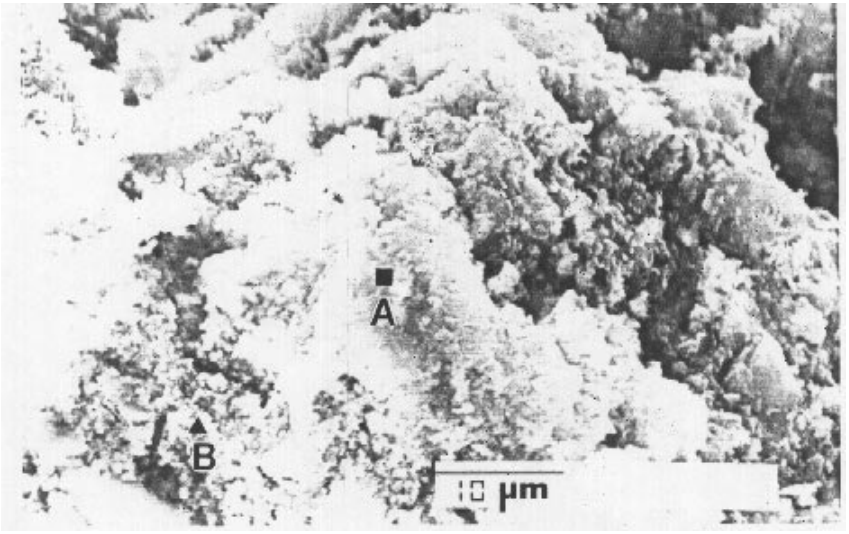


Figure 13. Dense HCP in a low W/C silica flume concrete. *A* = C-S-H, *B* = tiny crystals of CH.

@Seismicisolation

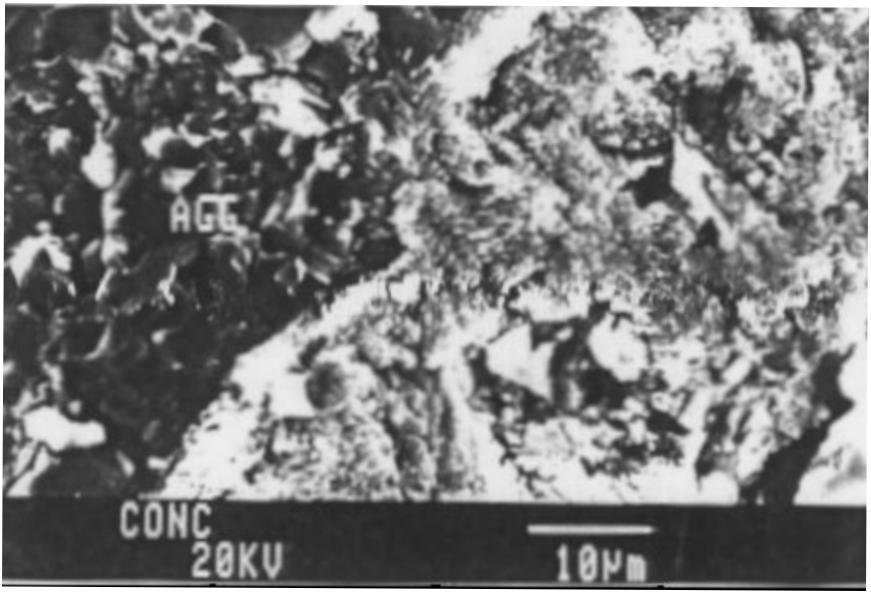


Figure 14. Paste-aggregate interface of a low W/C silica fume concrete. Note the absence of CH crystals at the interface. *AGG* = aggregate, *P* = HCP.

Fly Ash in Concrete. *Fly ash particles* mostly occur as solid glassy spheres (Fig. 15), but hollow spheres, called *cenospheres* (completely empty), and *plerospheres* (packed with several small spheres), may sometimes be present. Usually the surface of low-Ca (Class F) ash particles appear cleaner than their counterpart, high-Ca (Class C) particles. Deposits of alkali-sulfates on the particle surface can be identified from EDX analysis just as the hydration product of fly ash, which closely resembles C-S-H produced from normal hydration of portland cement, with the exception of higher aluminum in the fly ash hydrate (C-A-S-H, Fig. 16). Precipitation of a similar gel as C-S-H results in a reduction in the capillary porosity and, consequently, a denser paste with finer pore structure is produced in fly ash concrete (Fig. 17).[17]

@Seismicisolation

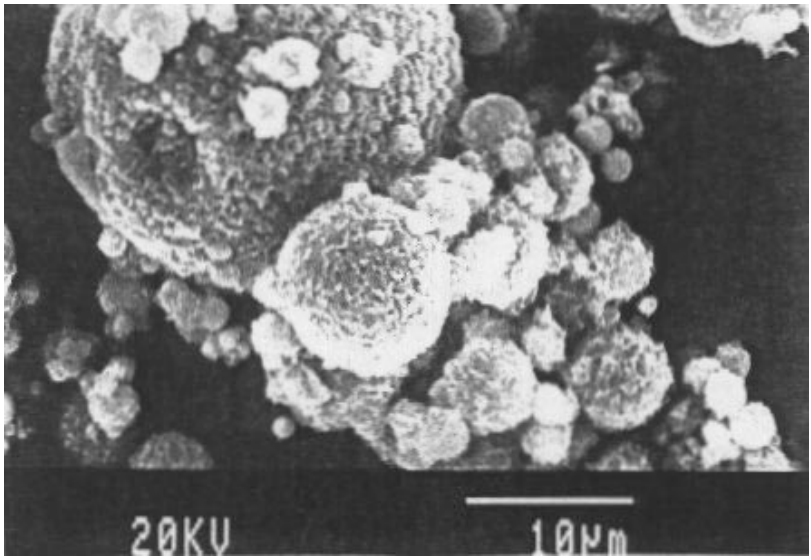


Figure 15. Spherical fly ash particles under the SEM.

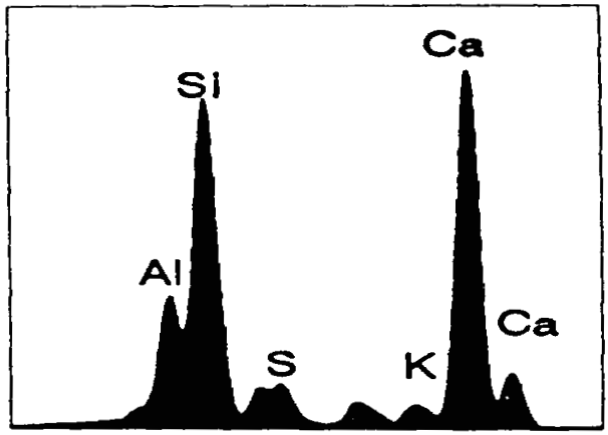


Figure 16. EDX analysis of a fly ash particle showing CA, Al, and Si as the principal elements.

@Seismicisolation

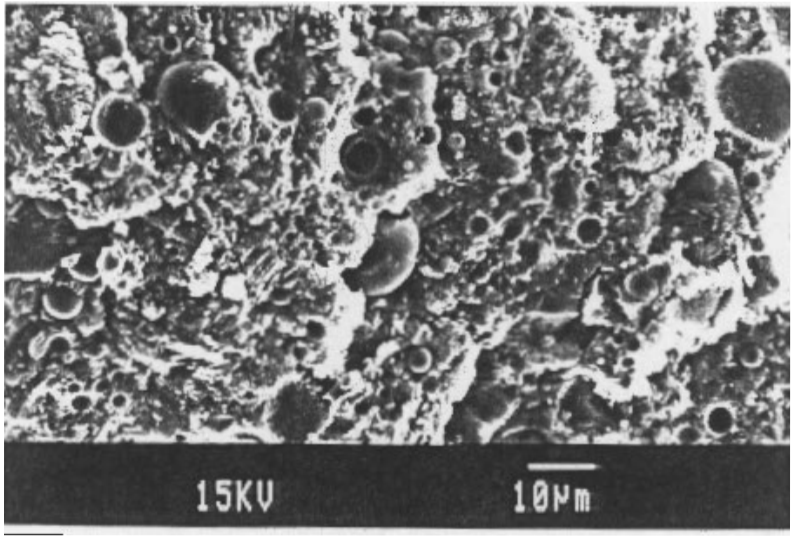


Figure 17. Dense HCP in a low W/C fly ash concrete. The pores are distinctly smaller and the permeability is extremely low.

Ground Granulated Blast-Furnace Slag (GGBS) in Concrete. GGBS is a finely ground, nonmetallic, rapidly chilled, blast-furnace slag consisting essentially of silicates and aluminosilicates of calcium and other bases that are developed in a molten condition simultaneously with iron in the blast furnace. Slag forms shard-like particles, that are usually larger than cement grains. Rapid chilling results in a preponderance of amorphous or glassy phase in slag (Fig. 18). The total glass content (which determines its reactivity) can be estimated from SEM examination. SEM or BSE imaging can be applied to estimate the amount and distribution of slag in a hardened cement paste of any age. A distinct reaction rim begins to appear around slag particles as they hydrate (Fig. 19). These become more vivid as hydration progresses. Hydration of GGBS produces a higher amount of C-S-H gel and lower amount of CH than normal concrete at any given hydration age, together with a significant densification of the microstructure.[18] Like fly ash, the initial hydration of GGBS is very slow and depends on the alkali-concentration of pore water.

@Seismicisolation

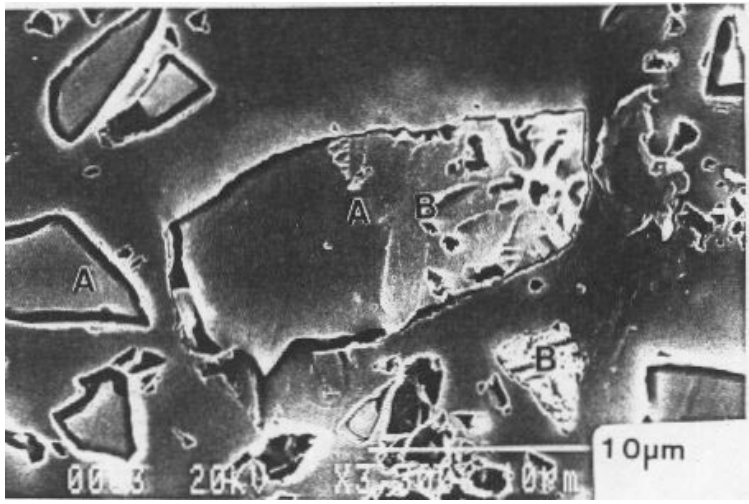


Figure 18. Slag particles where *A* = glass component and *B* = crystalline component.



Figure 19. A slag particle undergoing hydration in a concrete. It is covered with hydration product.

@Seismicisolation

Silica Fume (SF) in Concrete. Ultra-fine silica fume, shown in Fig. 20 (0.1μm), being almost an order of magnitude finer in grain size than that of portland cement or fly ash, makes it impossible to identify silica fume particles under the optical microscope. In this respect, SEM proves a better tool, although TEM with its still higher resolution power is ideal for studying hydration characteristics of silica fume (Fig. 21). Silica fume in concrete, either as a replacement of cement or as an addition, promptly reduces the amount of CH generation, and helps to fill the pores. Additional C-S-H is formed due to the pozzolanic reaction of silica fume. The overall microstructure becomes much more dense and compact than a normal concrete (Fig. 13). Numerous studies of silica fume concrete have also shown significant improvement in P-A bonding (see Fig. 14) which is said to occur fairly early and is directly responsible for high early strength of silica fume concrete.[19]

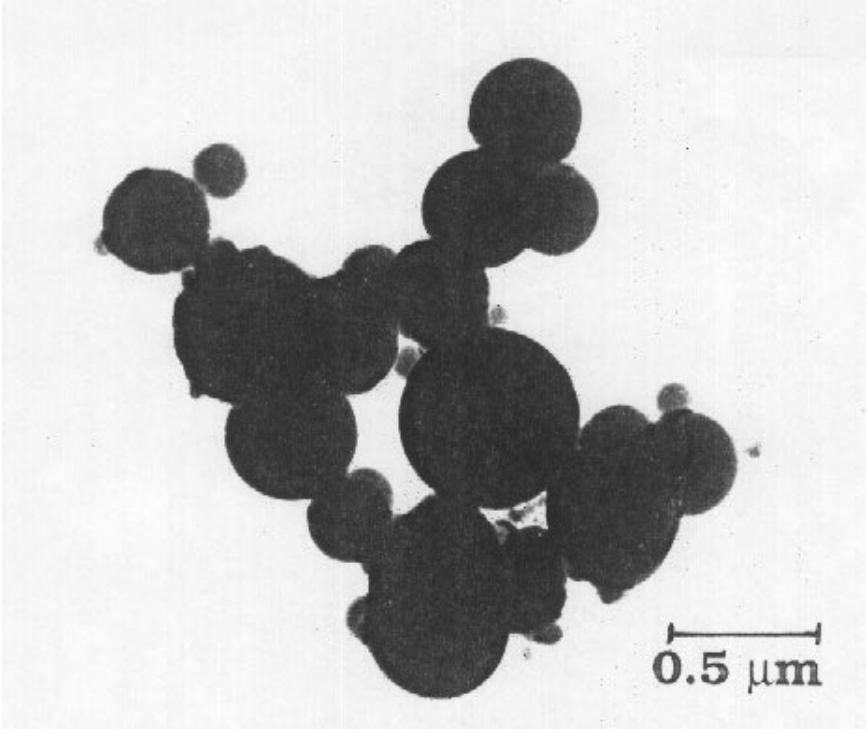


Figure 20. Ultra-fine silica fume particles under the TEM. Majority of the particles are less than 0.5 μm.

@Seismicisolation

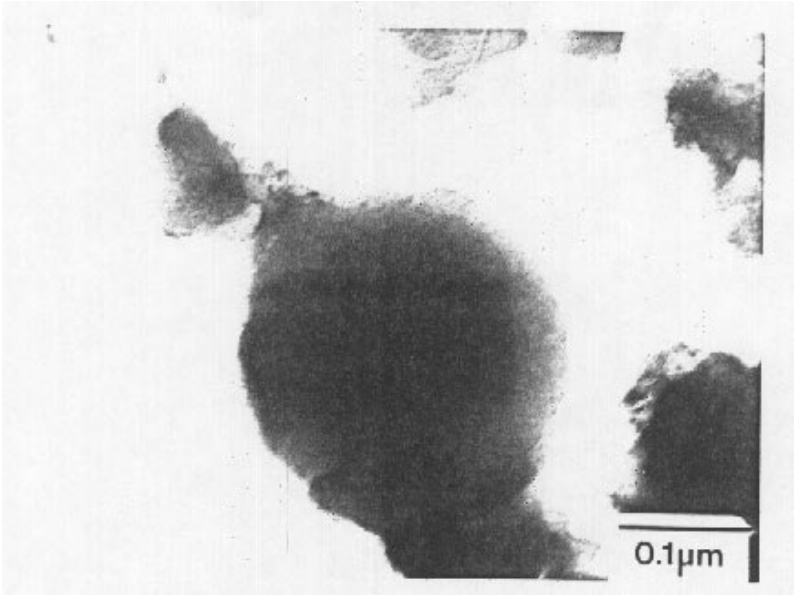


Figure 21. A silica fume particle in a state of dissolution, as seen under the TEM.

Chemical Admixtures. Although SEM is mostly used to examine the microstructural changes in concrete containing mineral admixtures, it has also been utilized to study the effects of addition of chemical admixtures on the microstructure of concrete. A large overdose of set-retarding chemical admixture can be determined from the unusual abundance of incompletely hydrated cement particles. The scanning electron microscope can be very helpful in determining the action of the two most commonly used corrosion inhibiting admixtures, *(a)* the calcium nitrite-based admixture which inhibits corrosion by reacting with ferrous ions to form a protective ferric oxide film; and *(b)* the water-based organic admixtures (amines and esters) which function by reducing chloride ion ingress into concrete and by forming a coating on the surface of the embedded steel.

@Seismicisolation

4.0 INTERPRETATION OF CONCRETE DETERIORATION FROM SEM/EDXA

Correlation of concrete microstructure and durability has received rather scant attention because concrete technologists continue to rely on engineering tests to determine concrete deterioration. Though these methods will remain valuable tools for investigating the soundness of concrete, SEM has been very productively used to ascertain the cause and extent of deterioration in concrete due to different internal and external deleterious agents.

4.1 Types of Attack

Types of chemical attack that involve external agents include efflorescence, paste carbonation, sulfate attack, and corrosion of reinforcing steel, while alkali-aggregate reactions and delayed ettringite formation are classified as chemical deterioration by internal agents. Freeze-thaw, salt weathering, fire damage, and cracking due to structural loading or thermal shock are commonly described as physical deteriorations. Concrete exposed to a marine environment experiences both chemical and physical deterioration.

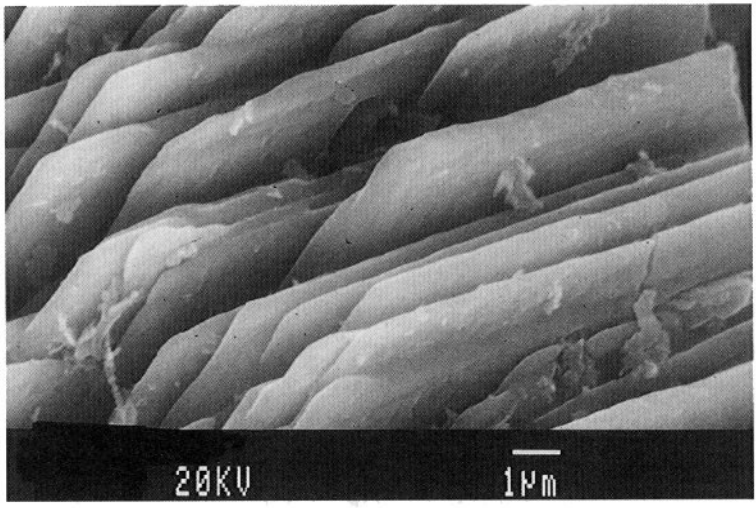
4.2 Chemical Deterioration from External Agents

Efflorescence. The term *efflorescence* or *salification*, in general, refers to salt crystallization on the exposed surface of building materials. The salt-laden solution from the interior rises to the drier exterior part where it evaporates, leaving the salt to precipitate. The pore characteristics determine the passage of such solutions and efflorescence obviously is associated not only with availability of salts, but also with moisture. Seasonal variations, from drier to wetter atmospheric condition and vice versa, extend the process still further.[20]21]

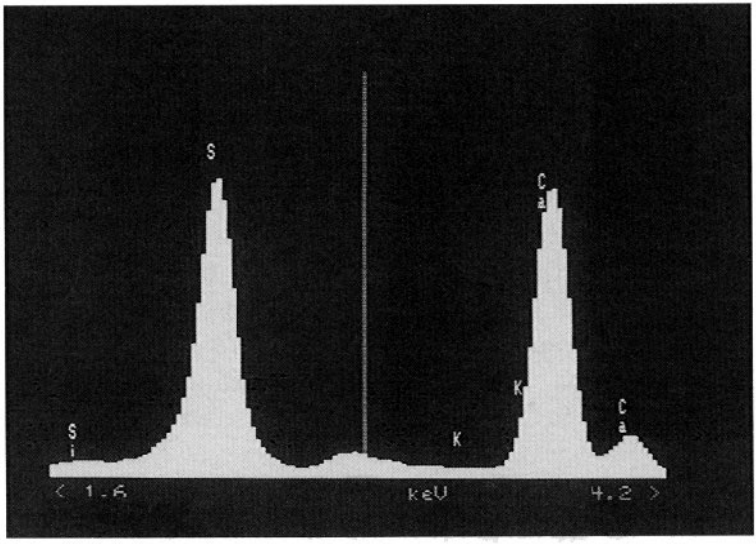
The most commonly occurring salts are different types of sulfates, such as gypsum ($CaSO_4 \cdot 2H_2O$, Fig. 22), thenardite (Na_2SO_4), mirabelite ($Na_2SO_4 \cdot 10H_2O$, Fig. 23), hydroglauberite ($CaO \cdot Na_2SO_4 \cdot 6H_2O$), and apthitalite ($(Na,K)2SO_4$). The efflorescent mechanism appears to be related to the saturation level of the solution and dissolution capacity of these salts. In any case, disintegration due to salt crystallization arises from a pressure differential. Under thermodynamic equilibrium conditions,

@Seismicisolation

pressure builds up in the saturated salt solution due to crystal growth. The volume change associated with crystallization exerts pressure against the pore wall, which eventually collapses.



(*a*)



(*b*)

Figure 22. *(a)* Gypsum crystals formed due to efflorescence and *(b)* EDX spectrum showing the principal peaks, Ca and S.

@Seismicisolation

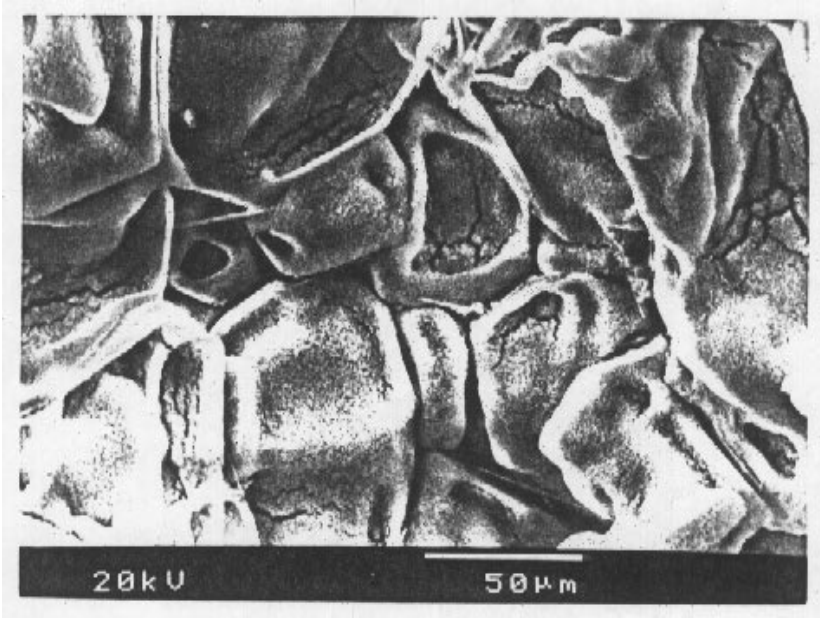
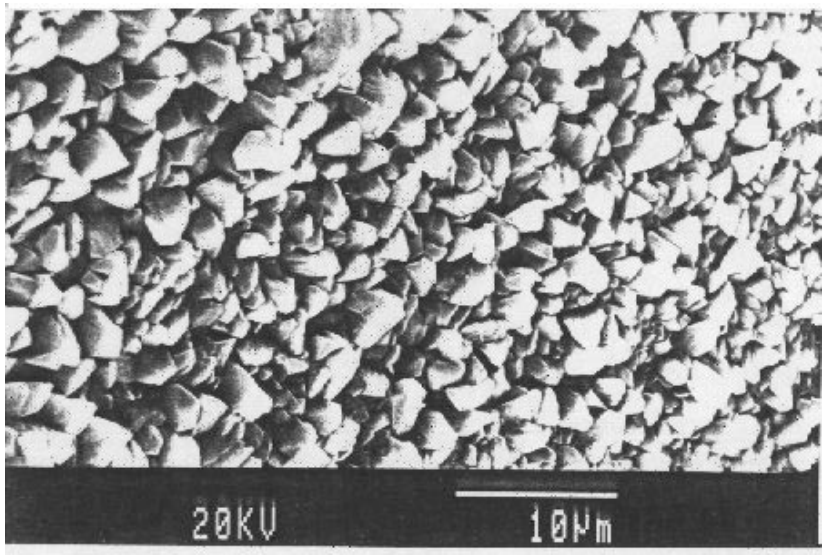


Figure 23. Dehydrated mirabelite crystals.

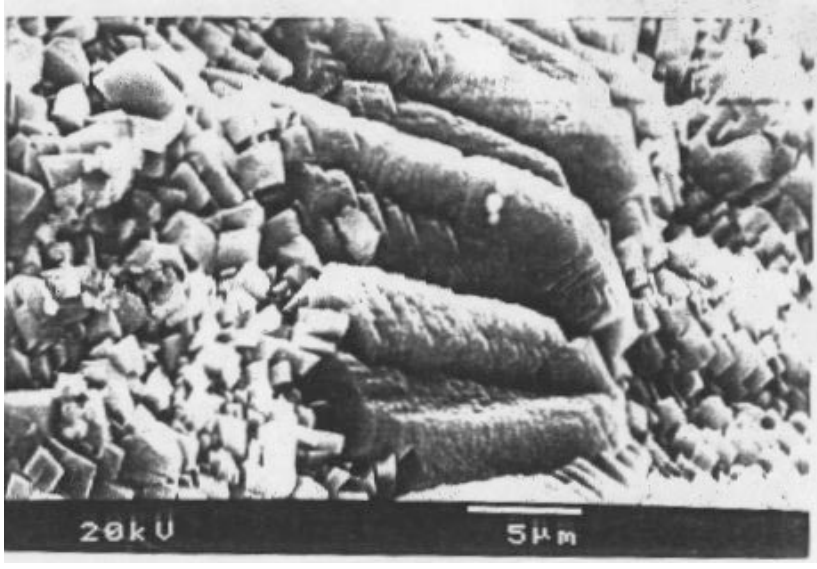
Paste Carbonation. A very common reaction is the cation exchange between the calcium-bearing constituents of concrete and CO_2 in the moist atmosphere to form calcium carbonate ($CaCO_3$). In fact, CO_2 attack is possibly the most common form of attack.[22] Carbonation can start instantaneously when the cement is mixed with water in which atmospheric CO_2 has dissolved, but a well cured concrete may show only a thin (5–10 mm) carbonated layer at the top. Formation of insoluble calcite crystals on this latent layer effectively blocks the pore spaces, reduces the permeability, and provides a protective capping against penetration of aggressive chemicals from outside. In a poorly cured concrete with high W/C, the depth of carbonation, however, can proceed significantly deeper with abundant prismatic or framboid $CaCO_3$ crystals (see Figs. 24a–24d for different morphologies). Concrete exposed to excessive dissolved CO_2 develops a porous microstructure which is distinguishable under the SEM; CO_2 not only converts CH crystals into calcite, decalcification of C-S-H also occurs at a later stage:

$$\text{C-S-H} + HCO_3 \rightarrow CaCO_3 + SiO_2 + H_2O$$

@Seismicisolation



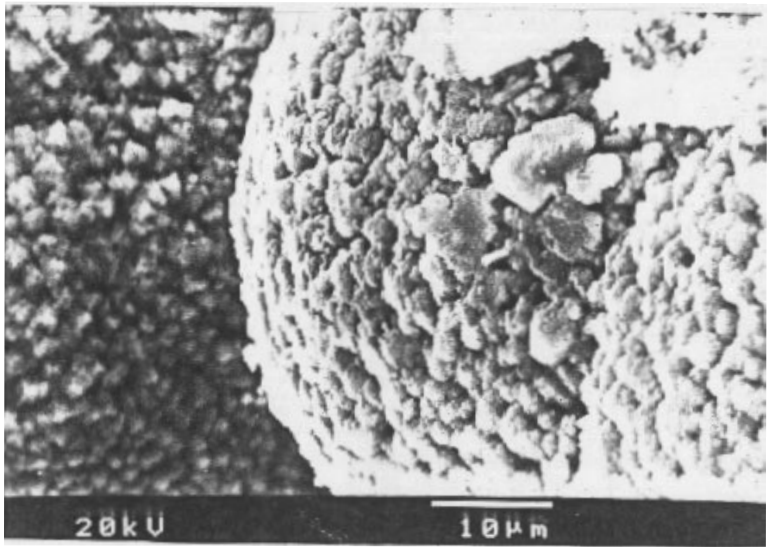
(a)



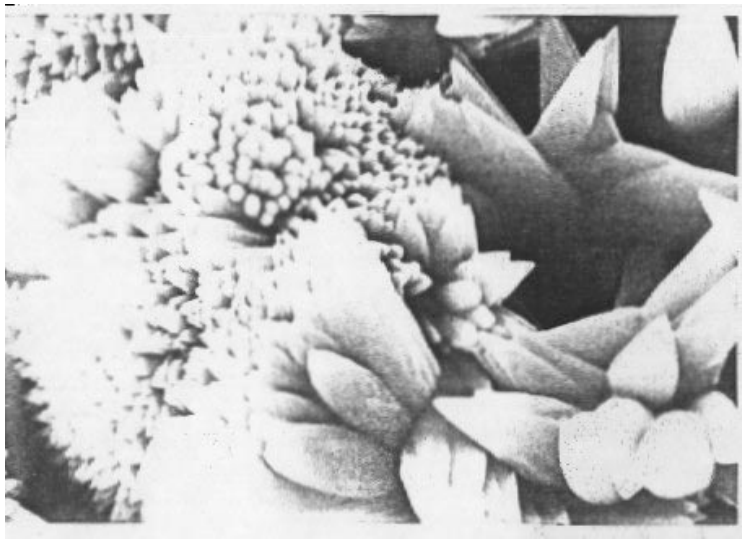
(b)

Figure 24. $CaCO_3$ morphologies, *(a)* granular crystals, *(b)* stacked, prismatic crystals, *(c)* globular crystals, and *(d)* dogtooth crystals.

@Seismicisolation



(c)



(d)

Figure 24. *(Cont'd.)*

@Seismicisolation

Sulfate Attack. Sulfates of sodium, calcium, and magnesium ions in soil or groundwater can react with almost all hydrated cement phases, starting from CH to calcium aluminate hydrate and eventually attacking the C-S-H gel at a more advanced stage. The reaction products usually are gypsum (Fig. 25), secondary ettringite (Fig. 26), and sodium or magnesium hydroxides. Formation of these mineral phases results in a significant increase in volume which may lead to disruptive expansion and cracking in the concrete.[23][24]

A calcium silicosulfate-carbonate mineral known as *thaumasite* closely resembles the ettringite needle structure. It is an analog of ettringite. Although it can form by itself, carbonation of ettringite also results in the formation of thaumasite which is more pernicious than secondary ettringite because it affects the C-S-H phase. As a consequence, besides expansion and cracking, softening, and eventual disintegration of paste is known to occur (Fig. 27).[25] Thaumasite, however, crystallizes only at low temperatures in the presence of continuous moisture and where sources of sulfate and carbonate ions are available. Though thaumasite closely resembles the ettringite needle structure it can be distinguished from EDX analysis by its characteristic Ca, Si, C, and S peaks (see EDX spectra of ettringite and thaumasite in Fig. 6a and 6b).

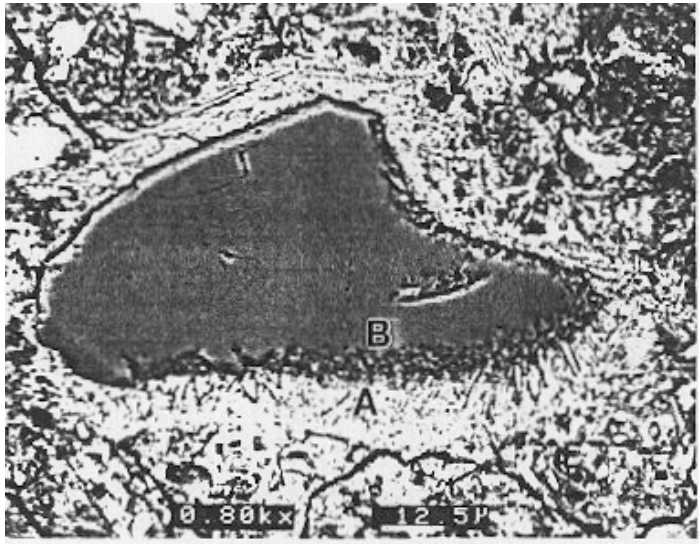


Figure 25. BEI micrograph of mortar which has undergone magnesium sulfate attack. A gypsum layer *(A)* 20 to 60 µm thick was deposited around a quartz grain, *(B)* resulting in expansion and cracking. *(Courtesy of Dr. David Bonen, US Gypsum Corp.)*

@Seismicisolation

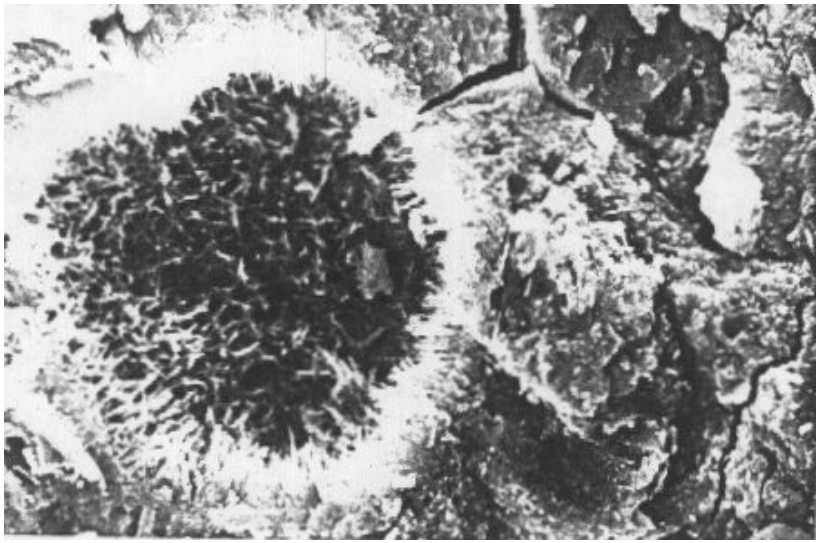


Figure 26. Secondary ettringite crystals causing the surrounding HCP to crack.

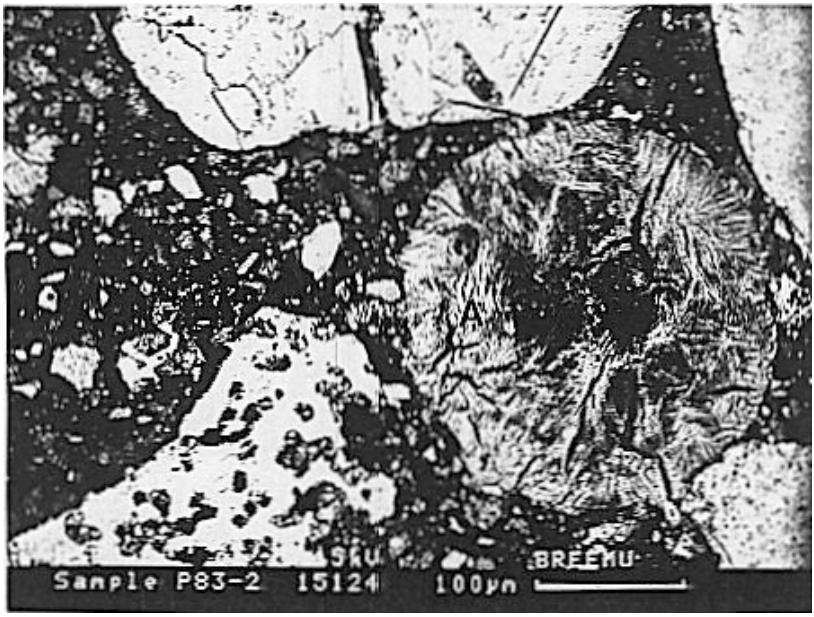


Figure 27. A spherical pore*(A)* completely filled with fibrous thaumasite.*(Courtesy of Dr. Norah Crammond, Bldg. Research Establ., England.)*

@Seismicisolation

Deicing Salt Attack. In addition to the common deicing salt-related deteriorations that affect concrete, like salt scaling and corrosion of reinforcing steel (discussed below), chloride-based deicing salts produce different types of deterioration products which require SEM examination for precise identification.[26] First, deicing salts react with aluminous phases and CH crystals in the HCP to form hexagonal tabular or platy crystals of calcium chloroaluminate, often 10–20 μm in size. It has still not been well established whether chloroaluminate has the potential to expand, or its formation in reinforced concrete is beneficial in the sense that it arrests migration of chloride ions to the rebar.[12] Simultaneous sulfate attack, however, converts chloroaluminate into ettringite. Reaction of sodium chloride deicing salt and sulfate ions (either from outside or sulfoaluminate phase in the HCP) deposits thenardite crystals in the HCP at the P-A interface or rebar-paste interface (Fig. 28). Breakdown of NaCl followed by reaction of Na ions with CO_2 often results in the formation of trona (Fig. 29). Additionally, chloride solution causes CH to leach from the HCP due to enhanced solubility of CH in saline solution.

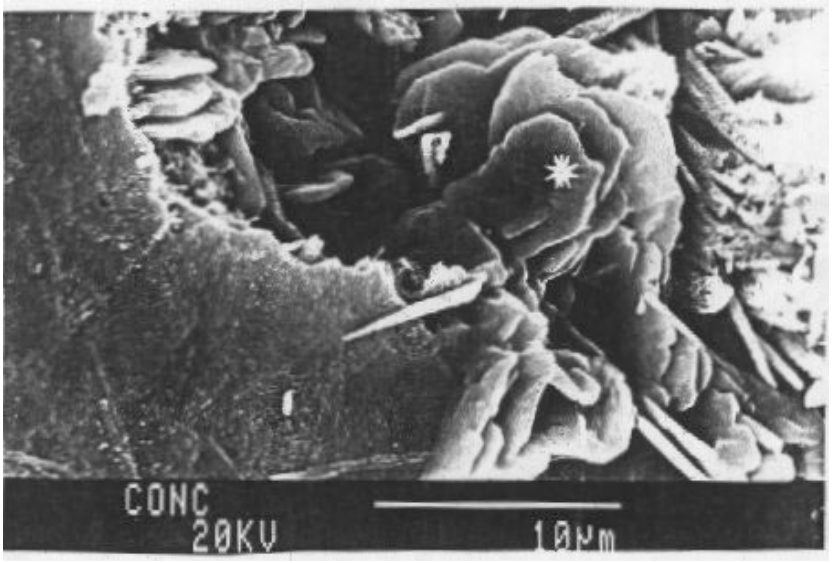


Figure 28. Thenardite (Na_2SO_4) crystallization (*) at a paste-aggregate interface due to deicer salt penetration.

@Seismicisolation

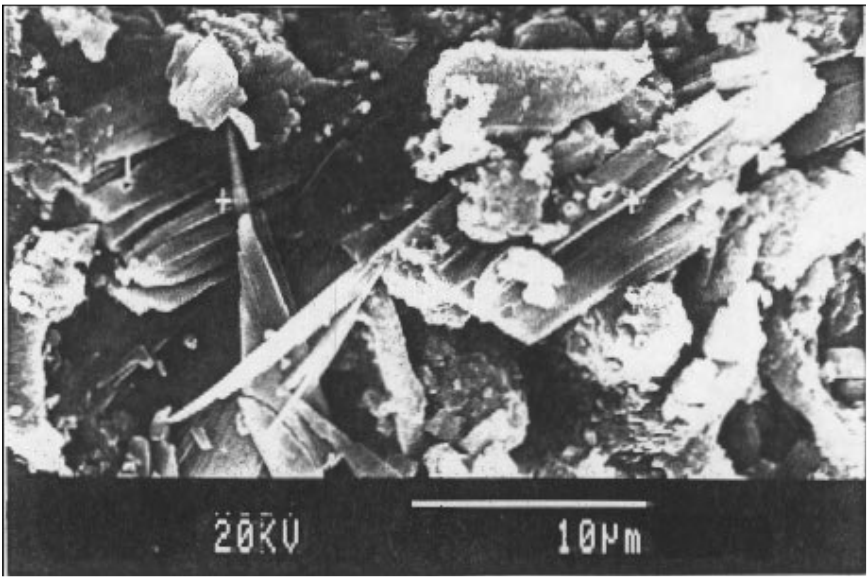


Figure 29. Crystals of trona (+) formed due to deicer salt penetration.

Corrosion of Reinforcing Steel. Penetration of chloride ions into reinforced concrete of relatively high permeability and absorptivity or severe carbonation of paste which reduces concrete's pH can destroy the protective ferric oxide film which is stable in the alkaline (high pH) environment around the steel rebar. This induces corrosion of steel, expansion in volume due to corrosion products and subsequent cracking and spalling of concrete from the reinforcement. Though not very many microstructural investigations on rebar corrosion have been reported, SEM studies on corroded paste-rebar interface have revealed that the reaction products consist of a host of iron oxides and oxychloride complexes.[27][28] Furthermore, the exfoliated lamellar crystals (Fig. 30) appear to be responsible for expansion rather than the delicate, globular, and whiskery minerals (Fig. 31).

@Seismicisolation

4.3 Chemical Deterioration from Internal Agents

Alkali-Aggregate Reactions (AAR). Reactive aggregates in the presence of high alkali and hydroxyl ion concentrations exude gels of varying compositions. Absorption of moisture by the gel causes expansion which is often the primary cause of cracking in concrete affected by AAR. SEM not only provides highly magnified image of the reaction gel, which can be both amorphous and crystalline (Figs. 32 and 33), its composition can also be reasonably accurately determined. In fact, instantaneous microanalytical capability of in-situ samples by EDX analyzer has been a major breakthrough in furthering our knowledge of alkali-aggregate reactions. Regourd and Hornain[29] presented some outstanding scanning electron micrographs of morphologically distinct varieties of AAR gel ranging from massive (dense) and isotropic gel to spongy, textured, grainy, or foliated gel. Ahmad Shayan's[30] contributions over the years underscore the importance of microstructure in the field of AAR.

Delayed Ettringite Formation (DEF). Contrary to external attack of concrete by sulfate ions from water or soil, which destroy the inherent cementitious properties of concrete by forming secondary and expansive gypsum and ettringite, another type of attack can occur from the internal sulfate ions. Very similar to external sulfate attack, it forms ettringite (Fig. 34), and causes expansion and cracking. Primary ettringite, formed at the early stages of cement hydration by reaction of gypsum or alkali sulfates in clinker with C_3A in the cement, can decompose at a higher temperature (for example, during heat curing), remain lodged in the C-S-H gel, and reappear much later (at high relative humidities) as ettringite needles, the process being known as *delayed ettringite formation (DEF)*. Controversy still rages as to whether the cracking observed in concrete is consequential to expansion associated with ettringite formation or due to some other unrelated mechanism (e.g., freeze-thaw, ASR, etc.) which opens up spaces for the ettringite to precipitate. Sufficient moisture, inadequate air voids, high sulfate content in cement, and high permeability of concrete, are known to enhance ettringite-related distress. Microstructural evaluation of a large number of deteriorated precast (heat cured) concrete members has revealed a propensity of delayed ettringite needles along the aggregate-paste interface and in cracks in the HCP.[31]

@Seismicisolation

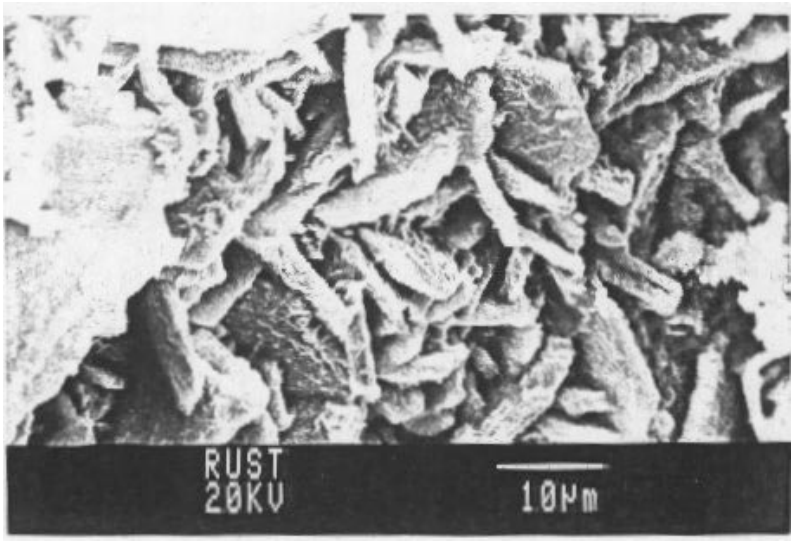
4.4 Concrete Exposed to Marine Environment

Concrete exposed to a marine environment shows several types of chemical as well as physical deterioration which can be readily observed under the SEM. Sea water contains dissolved ions, such as Cl^-, CO_3^{2-}, SO_4^{2-}, Mg^{2+}, that are deleterious for concrete. Brucite ($Mg(OH)_2$), aragonite, and calcite ($CaCO_3$), resulting from reaction of dissolved magnesium ion, or CO_2 in sea water and CH in paste, have been reported. Carbonation of CH crystals and C-S-H gel by dissolved carbonate in seawater (as carbonic acid) reduces the cementitious properties of paste and eventually creates a porous paste (Fig. 35). Concrete exposed to the splash zone shows a profusion of scalenohedral or dogtooth $CaCO_3$ crystals in the HCP (shown in Fig. 24d). Corrosion of reinforcing steel by penetration of seawater dissolved chloride has also been noted from SEM studies. SEM/EDXA investigation of marine concrete has also revealed chloroaluminate crystallization in HCP (Fig. 36).[32]–[34]

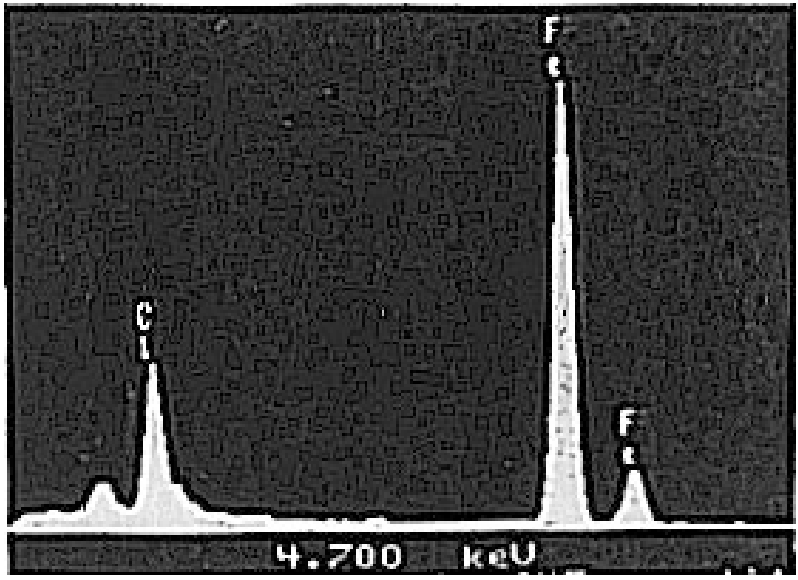
5.0 SUMMARY

A foreknowledge of the basic microstructure of concrete, which can be obtained from examination of a normal concrete under the SEM, is essential for understanding its mechanistic behavior and long-term performance. The introduction of SEM/EDXA into concrete research has provided much greater insight into the kinetics of cement hydration, the morphology and chemical composition of hydration products, the microstructure of hydrated cement paste, the importance of the paste-aggregate interface, matrix densification, and the reduced permeability of HCP resulting from additions of mineral and chemical admixtures. In other words, most of the factors that control the durability and mechanical properties of concrete can be ascertained by SEM/EDXA. This spectrum of applications of SEM/EDXA in the field of concrete technology emphasizes the need to expand its role from research-oriented equipment to a routine investigative tool. With its high resolution, SEM provides a much clearer delineation of ultra-fine phases and intricate details in the microstructure than the optical microscope. Additionally, the in-situ microanalytical capability of the ancillary EDX attachment enables rapid and accurate identification of individual phases and particles, ranging from inherent constituents of concrete to deterioration products generated by external agents.

@Seismicisolation



(a)



(b)

Figure 30. *(a)* Lamellar products of rebar corrosion; *(b)* the crystals are mainly composed of Fe and Cl.

@Seismicisolation

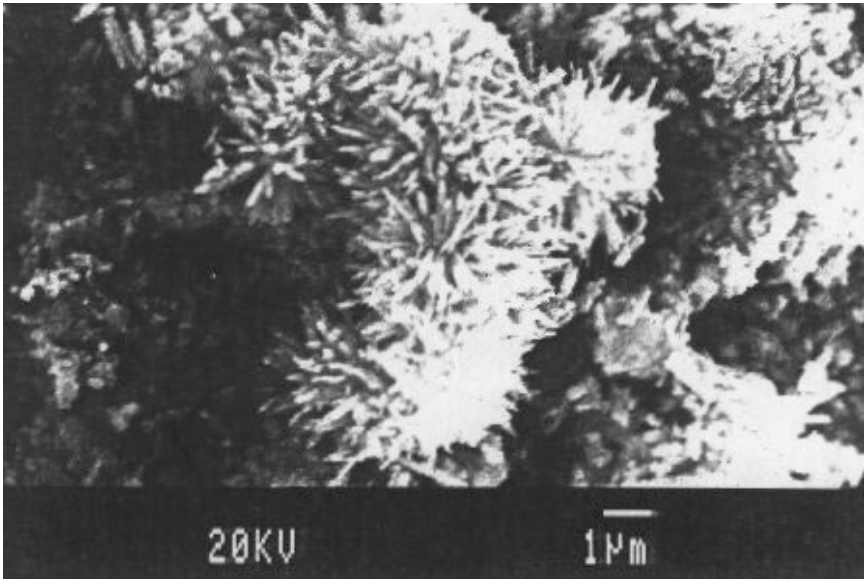


Figure 31. Delicate globular and whiskery mineral formed due to rebar corrosion.



Figure 32. Crystalline ASR gel showing rosette structure.

@Seismicisolation

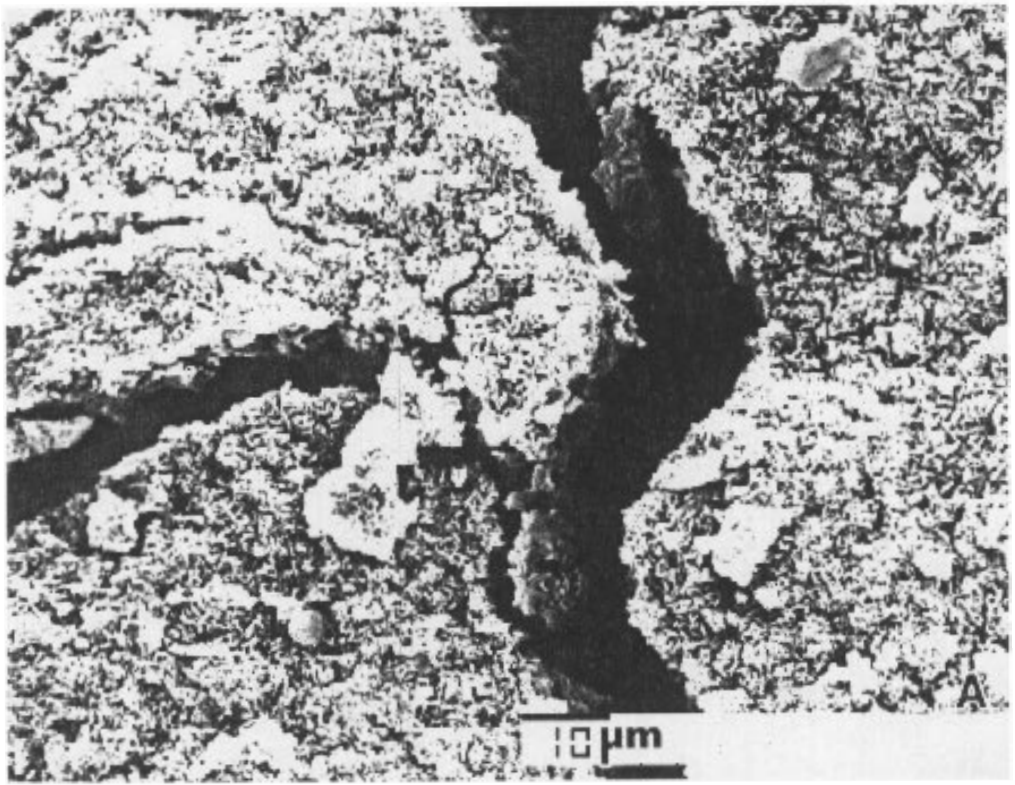
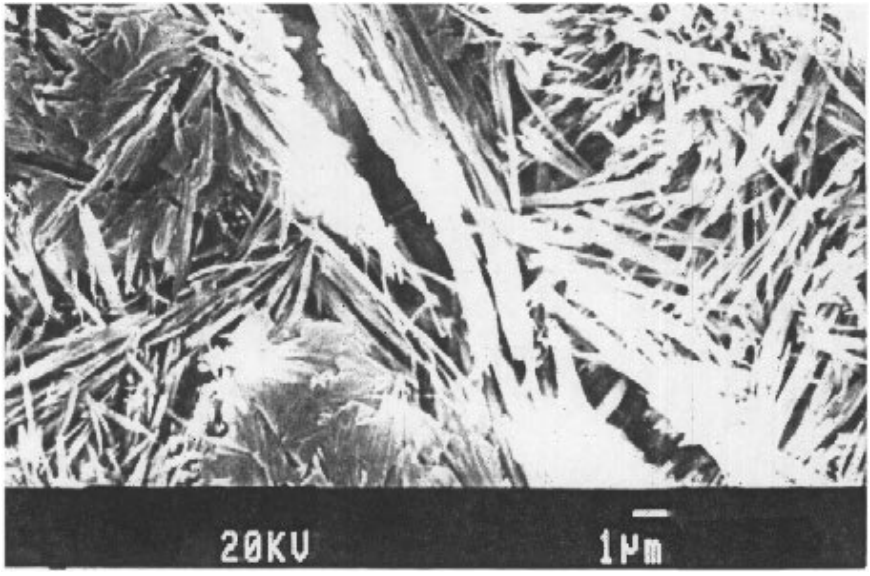
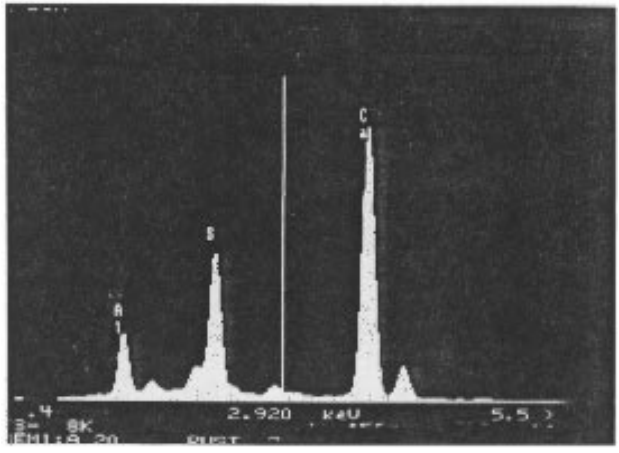


Figure 33. Amorphous ASR gel which has cracked due to expansion.

@Seismicisolation



(a)



(b)

Figure 34. *(a)* Delayed ettringite crystals formed in a heat-cured concrete block. Note the expansion being caused from crystallization. *(b)* EDX spectrum of ettringite needles.

@Seismicisolation

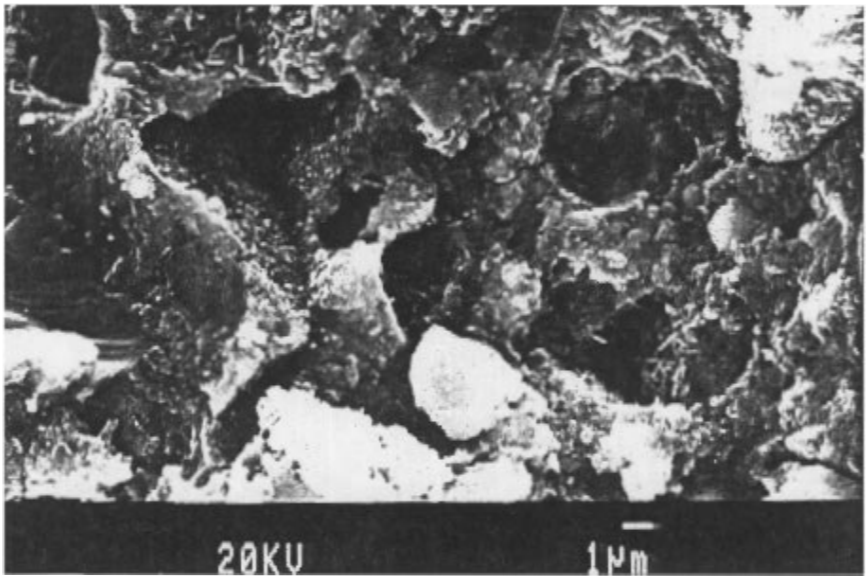


Figure 35. Leaching of constituents in a concrete exposed to marine conditions, creating vacant spaces in the HCP.

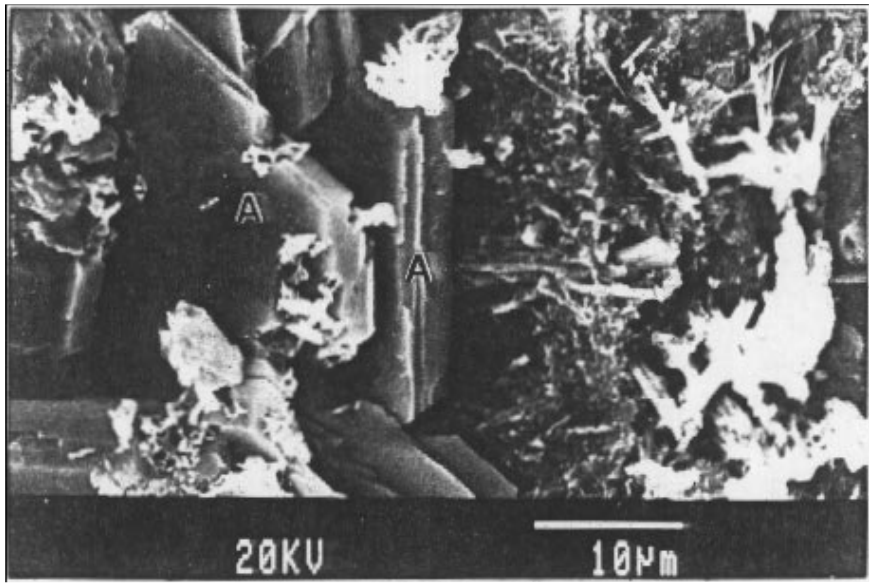


Figure 36. Tabular chloroaluminate crystals (+) in a marine concrete.

@Seismicisolation

Determining the nature, extent, and products of common chemical attack on concrete is another important application of SEM/EDXA. Dissolution and leaching of constituents of HCP rendering it porous and permeable, paste carbonation, sulfate attack resulting in the crystallization of expansive minerals, and corrosion of reinforcing steel, are a few of the aspects that can be adequately explained through SEM investigation. Furthermore, our knowledge of AAR in concrete has been greatly enriched by SEM observations and EDX analysis of AAR reaction products. Despite the relatively high cost of SEM/EDXA, it is undoubtedly emerging as the quintessential investigative tool for the concrete technologist because of its wide range of applications.

REFERENCES

1. Gupta, P., Chatterji, S., and Jeffery, J. W., Studies on the Effect of Various Additives on the Hydration Reaction of Tricalcium Aluminate, Part I, *Cem. Tech.*, 1:3–10 (1970)
2. Diamond, S., Cement Paste Microstructure—An Overview at Several Levels, *Proc. Conf. on Hydraulic Cement Pastes: Their Structure and Properties*, pp. 2–30, Sheffield, Cement and Concrete Association (1976)
3. Diamond, S., The Microstructure of Cement Paste in Concrete,*Proc. 8th. Int. Cong. Chem. of Cem.*, pp. 122–147, Rio de Janeiro (1986)
4. Scrivener, K. The Microstructure of Concrete, *Materials Science of Concrete,* (J. Skalny, ed.), l:127–162, American Ceramic Society, Westerville (1989)
5. Sarkar, S. L.,*The Importance of Microstructure in Evaluating Concrete, Advances in Concrete Technology*, 2nd. Ed., (V. M. Malhotra, ed.), pp. 125–160, CANMET, Ottawa (1994)
6. Sarkar, S. L., and Aitcin, P. C., Dissolution Rate of Silica Fume in Very High Strength Concrete, *Cem. Conc. Res.*, 17:591–601 (1987)
7. Marton, L., *Early History of the Electron Microscope*, San Francisco Press, Inc., San Francisco (1968)
8. Sarkar, S. L. and Aimin, X., Preliminary Study of Very Early Hydration of Superplasticized C_3A + Gypsum by Environmental SEM,*Cem. Conc. Res.*, 22:605–608 (1992)
9. Monteiro, P. J. M., and Mehta, P. K., Improvement of the Aggregate-Cement Paste Transition Zone by Grain Refinement of Hydration Products,*Proc. 8th. Int. Cong. Chem. of Cem.*,2:433–437, Rio de Janeiro (1986)

@Seismicisolation

10. *Proceedings of the Coloque International sur Liaisons Pates de Ciment Materiaux Associes,* p. 148, Toulouse, RILEM (1982)
11. Monteiro, P. J. M., Maso, J. C., and Ollivier, J. P., The Aggregate-Mortar Interface, *Cem. Conc. Res.*, 15:953–958 (1985)
12. Barnes, B. D., Diamond, S., and Dolch, W. L., Micromorphology of the Interfacial Zone Around Aggregates in Portland Cement Mortar, *J. Am. Ceram. Soc.*, 62:21–24 (1979)
13. Zhang, M. H., and Gjorv, O. E., Microstructure of the Interfacial Zone Between Lightweight Aggregate and Cement Paste, *Cem. Conc. Res.*, 20:610–618 (1990)
14. Sarkar, S. L., Chandra, S., and Berntsson, L., Interdependence of Microstructure and Strength of Structural Lightweight Aggregate Concrete, *Cem. & Conc. Comp.*, 14:239–248 (1992)
15. Sarkar, S. L., Roles of Silica Fume, Slag, and Fly Ash in the Development of High-Performance Concrete Microstructure, *Proc. ACI Int. Conf. High Performance Conc.*, pp. 449–460, Singapore (1994)
16. Mehta, P. K., Pozzolanic and Cementitious By-Products in Concrete, *Proc. 3rd Int. Conf. on FA, Slag, SF, and Natural Pozzolans in Conc.*, pp. 32–37, Trondheim (1990)
17. Berry, E. E., and Malhotra, V. M., *Fly Ash in Concrete,* CANMET SP 85-3, Ottawa 1986
18. Regourd, M., Structure and Behavior of Slag Portland Cement Hydrates, *Proc. 8th. Int. Cong. Chem. of Cem.,* Vol. 1, pp. III-2/10–2/26, Paris (1980)
19. Sarkar, S. L., Baalbaki, M., and Aitcin, P. C., Microstructural Development in a High-Strength Concrete Containing a Ternary Cementitious System, *Cem., Conc. and Aggr.*, 13:81–87 (1991)
20. Collepardi, M., Degradation and Restoration of Masonry Walls of Historical Buildings, *Mats. and Struc.*, 23:81–102, (1990)
21. Sarkar, S. L., Chandra, S., and Rhode, M., Microstructural Investigation of Natural Deterioration of Building Materials in Gothenburg, Sweden, *Mats. and Struc.*, 25:429–435 (1992)
22. Bonen, D., and Sarkar, S. L., Environmental Attack on Concrete, *Proc. 15th Int. Conf. on Cem. Micros*., pp. 11–23, Richmond (1994)
23. Mehta, P. K., Sulfate Attack on Concrete—A Critical Review, (J. Skalny, ed.), *Mat. Sci. of Conc.*, 3:105–130, American Ceramic Society (1993)
24. Roy, D. M., Mechanism of Cement Paste Degradation Due to Physical and Chemical Factors, *Proc. 8th Int. Cong. Chem. of Cem.*, pp. 362–380, Rio de Janeiro (1986)

@Seismicisolation

25. Crammond, N. J., and Halliwell, M. A., The Thaumasite Form of Sulfate Attack in Concretes Containing a Source of Carbonate Ions—A Microstructural Overview, *Proc. 2nd Int. Symp. on Advances in Conc. Tech.*, pp. 357–380, Las Vegas (1995)

26 Sarkar, S. L., and Beaulieu, J., Microstructural Evaluation of a Concrete Overpass System During Rehabilitation, *Cem. and Conc. Res.*, 23:874–884 (1993)

27. Marchese, B., Microstructural Alterations of Cement Paste-Steel Interface Exposed to Seawater, (J. M. Scanlon, ed.), *K&B Mather Int. Conf. on Conc. Durability*, pp. 362–380 (1987)

28. Sarkar, S. L., and Aitcin, P. C., Phenomenological Investigation of Concrete Deterioration in a Median Barrier, *Cem. and Conc. Res.*, 21:917–927 (1991)

29. Regourd, M., and Hornain, H., *Microstructure of Reaction Products, Concrete Alkali-Aggregate Reactions*, (P. E. Grattan-Bellew, ed.), pp. 375–380, Noyes Publications, New Jersey (1987)

30. Shayan, A., Re-Examination of AAR in an Old Concrete, *Cem. Conc. Res.*, 19:434–442 (1989)

31. Mielenz, R., Marusin, S. L., Hime, W. G., and Jugovic, Z. T., Investigation of Prestressed Concrete Railway Tie Distress, *Conc. Int.*, pp. 62–68 (Dec., 1995)

32. Conjeaud, M. L., Mechanism of Sea Water Attack on Cement Mortar, (V. M. Malhotra, ed.), *Performance of Concrete in Marine Environment*, ACI, pp. 39–61 (1980)

33. Sarkar, S. L., and Malhotra, V. M., Microstructure Durability of Concretes Exposed to Arctic Conditions, (K. Sakai, et al., ed.), *Concrete Under Severe Conditions*, 1:828–838, E & FN Spon (1995)

34. Regourd, M., Physico-Chemical Studies of Cement Pastes, Mortars and Concrete Exposed to Sea Water, (V. M. Malhotra, ed.), *Performance of Concrete in Marine Environment*, pp. 1–19, ACI (1980)

@Seismicisolation

8

X-Ray Diffraction

A. K. Chatterjee

1.0 INTRODUCTION

It is now over a century since the phenomenon of x-radiation was discovered by Wilhelm Conrad Roëntgen. It was soon realized that x-rays have wavelengths in the angstrom range, are sufficiently energetic to penetrate solids, and are well poised to probe their internal structure. Based on these findings quite a few useful tools and techniques for materials analysis and evaluation have been developed and perfected for application. Among them, there are two major systems that are well known and widely practised, one based on x-ray fluorescence for elemental analysis and another based on x-ray diffraction (XRD) for structural and phase composition studies. This chapter focuses on some of the fundamentals of the XRD technique, the hardware and software developments, and application to the cement and concrete materials.

@Seismicisolation

2.0 BASIC PRINCIPLE

2.1 Qualitative Analysis

X-ray diffraction is the elastic scattering of x-ray photons by atoms in a periodic lattice. The scattered monochromatic x-rays that are in phase give constructive interference. Figure 1 illustrates how diffraction of x-rays by crystal planes allows one to derive lattice spacings by using the Bragg's law.

Eq. (1) $$n\lambda = 2d \sin \theta$$

where n is an integer called the order of reflection, λ is the wavelength of x-rays, d is the characteristic spacing between the crystal planes of a given specimen and θ is the angle between the incident beam and the normal to the reflecting lattice plane. By measuring the angles, θ, under which the constructively interfering x-rays leave the crystal, the interplanar spacings, d, of every single crystallographic phase can be determined.

In order to identify an unknown substance, the powder diffraction pattern is recorded with the help of a camera or a diffractometer and a list of d-values and the relative intensities of the diffraction lines is prepared. These data are compared with the standard line patterns available for various compounds in the *Powder Diffraction File* (PDF) database. This file is released and annually updated by the International Centre for Diffraction Data (ICDD). It contains line patterns of more than 60,000 different crystallographic phases. In practice, for any unknown sample, the appearance of three most intense characteristic lines from the standard PDF line pattern is a sufficiently convincing evidence of the existence of a crystalline phase in either a homogeneous substance or even in a multicomponent mixture. In some cases a distinction between two or more possible phases can be done by comparing the other characteristic lines. Furthermore, a prior knowledge of the class of materials under investigation and the chemical analysis data can be of great value.

From such qualitative determination of the mineral or phase composition, attempts are often made to evaluate the suitability of raw materials for clinkerization, the quality of clinker formation, the attainment of targeted cement formulation, the nature of hydration reactions, the impact of various admixtures on such reactions, the state of phase transformation of concrete in performance, and so on. The characteristic XRD lines for some of the common minerals relevant to the area dealt with in this chapter are furnished in Table 1 for ready reference.

@Seismicisolation

It may be relevant to mention here that while the peak positions and intensities associated with an x-ray diffraction pattern enable qualitative analysis, as highlighted above, these parameters are also useful for lattice constant determination and stress determination of the sample. The peak angles and profiles may further be used to determine particle size and degree of crystallization as well as in conducting precise x-ray structural analysis.

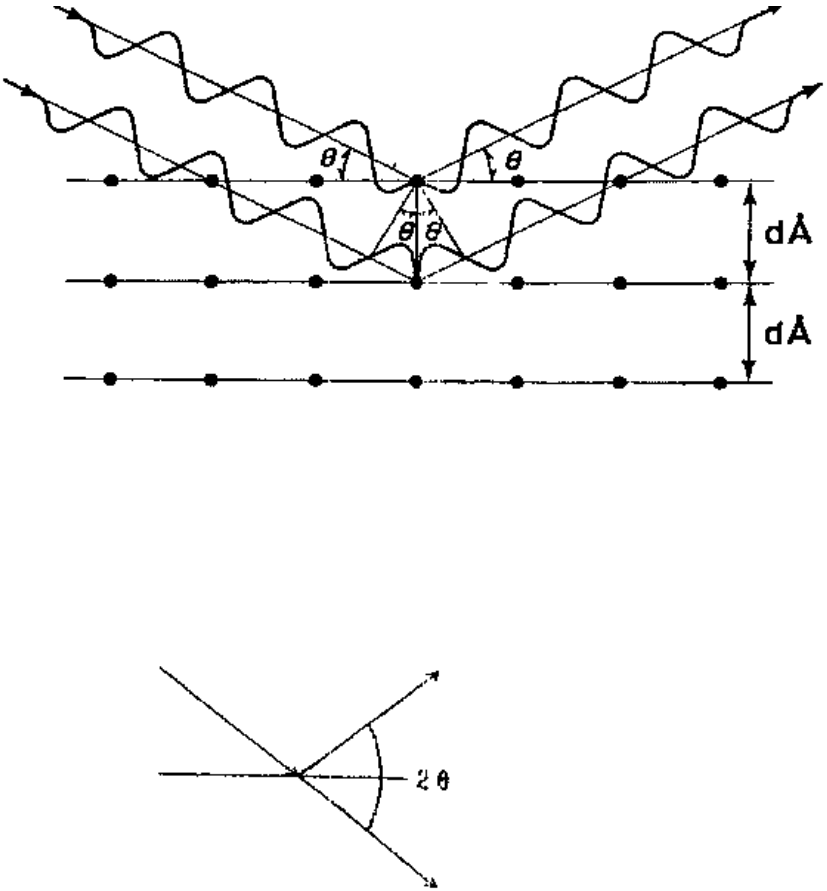


Figure 1. Schematic representation of Bragg's Law.

@Seismicisolation

Table 1. Characteristic XRD Lines of Some Relevant Minerals and Compounds

Minerals/Compounds	*d*Å/(I)		
Calcite $CaCO_3$	3.030 (100)	1.8726 (34)	3.8525 (29)
Calcium Oxide CaO	3.33 (100)	3.00 (100)	2.28 (60)
Calcium Hydroxide $Ca(OH)_2$	2.628 (100)	4.90 (74)	1.927 (42)
Magnesite $MgCO_3$	2.742 (100)	2.102 (45)	1.700 (35)
Dolomite $MgCO_3{\cdot}CaCO_3$	2.888 (100)	2.193 (19)	1.787 (13)
Periclase MgO	2.106 (100)	1.489 (52)	1.216 (12)
Brucite $Mg(OH)_2$	2.365 (100)	4.77 (90)	1.794 (55)
Quartz SiO_2	3.342 (100)	4.257 (22)	1.8179 (14)
Gibbsite $Al_2O_3.3H_2O$	4.8486(100)	4.3711(70)	2.3851(55)
Bayerite $Al_2O_3.3H_2O$	2.222 (100)	4.71 (90)	4.35 (70)
Diaspore β-$Al_2O(OH)$	3.99 (100)	2.317 (56)	2.131 (52)
Triclinic Alite C_3S	2.789 (100)	2.613 (90)	2.192 (75)
β-Belite C_2S	2.783 (100)	2.79 (97)	2.745 (83)
Cubic Aluminate C_3A	2.699 (100)	1.909 (45)	1.5587 (45)
Monoclinic Aluminate C_3A	2.698 (100)	2.694 (95)	1.5658 & 1.5636) (35)
Orthorhombic Aluminate C_3A	2.693 (100)	2.714 (65)	1.919 & 1.5636 (35)
Aluminoferrite C_4AF	2.644 (100)	7.25 (45)	1.8149 (45)
Gypsum $CaSO_4.2H_2O$	4.28 (100)	7.59 (80)	3.06 (60)
Anhydrite $CaSO_4$	3.49 (100)	2.849 (35)	2.328 & 2.208 (20)
Hematite Fe_2O_3	2.70 (100)	2.519 (70)	1.6941 (45)

@Seismicisolation

Crystal Size Effect. Clear diffraction peaks are only observed when the sample possesses adequate long range order. Diffraction lines from perfect crystals are very narrow. For crystallite sizes below 100 nm, line broadening occurs due to incomplete destructive interference in scattering directions where the x-rays are out of phase.

The Scherrer equation relates crystal size to line width

Eq. (2) $$<L>=\frac{K\lambda}{\beta \cos \theta}$$

where $<L>$ is a measure of the dimension of a particle in the direction perpendicular to the reflecting plane, λ is the x-ray wavelength, β is the peak width, θ is the angle between the beam and the normal on the reflection plane, and K is a constant which is often taken as unity. X-ray line broadening provides a quick, but not always reliable estimate of the particle size. It is desirable to understand the line profile analysis with Fourier transform method.

2.2 Quantitative Analysis

A fairly comprehensive coverage of the history of quantitative methods in diffraction analysis in general for the period 1936–1976 is available in Ref. 1. The author divided the span of four decades into three eras. The early era, from 1936 to 1950, was essentially the era of development of a photographic-microphotometric method[2] that was applied to samples prepared with an admixed internal standard. The basic approach was to microphotometer the Debye-Scherrer patterns of the samples under quantitative analysis and to determine the ratio of the heights of the phase to be quantified and the standard line from the photometer trace. The phase concentration was determined by reference to calibration curve prepared from known mixtures of the phase to be quantified and the internal standard. It was observed that the method yielded accuracies ranging from 5 to 10% of the amount present for higher concentrations of the analyte.

The middle era of 1950–1970 saw the invention of diffractometer in which a reflection intensity could be recorded digitally.[3] At the same time, a firmer theoretical basis for quantitative analysis of mixed polycrystalline phases was formulated.[4]

The third era, in the seventies (1970–1976), witnessed furtherance of the internal standard concept. A brief recapitulation of only the relevant aspects is attempted below.

@Seismicisolation

Internal Standard Method. The integrated intensity of reflection *i* of component *J* is given by:

Eq. (3)
$$I_{iJ} = \frac{K_{iJ} x_J}{\rho_J \left[X_J \left(\mu_j - \mu_M \right) + \mu_M \right]}$$

where, x_J and ρ_J are, respectively, the weight fraction and density of the analyte, μ_J and μ_M are the mass absorption coefficients of component *J* and the matrix, and K_{iJ} is a constant whose value depends on the diffracting power of component *J* and the geometry of the apparatus.

Equation (3) can be further simplified to:

Eq. (4)
$$I_{iJ} = K_{iJ} x_J / \rho_J \bar{\mu}$$

if we consider $x_J (\mu_J - \mu_M) + \mu_M$ in Eq. (3) as the mass absorption coefficient, $\bar{\mu}$, of the entire specimen. If a constant weight fraction, x_S, of an internal standard is added to the sample, the weight fraction of component *J* can now be given in terms of the direct proportionality of the intensities:

Eq. (5)
$$x_J = k^1 \times (I_{iJ} / I_{kS})$$

where, I_{kS} relates to intensity of the *k* line of the internal standard.

In this approach of quantitative analysis two important findings were made by various investigators over a period of time:

1. Integrated intensities are preferred to peak intensities to compensate for possible variations due to lattice distortions and variations in crystallite sizes.
2. Crystallites larger than 5 microns in mean diameter add to the fluctuations in intensities.

Diffraction Absorption Method. Since it is logical to represent Eq. (4) for pure component *J* as:

Eq. (6)
$$(I_{iJ})_o = K_{iJ} / \rho_J \mu_J$$

and since by dividing Eq. (4) by (6) we obtain

Eq. (7)
$$x_J = \bar{\mu} I_{ij} / \mu_J (I_{iJ})_o$$

a method of analysis involving direct measurement of $\bar{\mu}$ rather than an internal standard to compensate for x-ray absorption by the specimen was developed.[5]–[7]

While this method showed advantages of avoiding problems relating to the mixing of an internal standard and measuring its intensity, certain

@Seismicisolation

infirmities were observed. Those related to strongly x-ray absorbing specimens and were primarily due to errors in direct measurement of $\bar{\mu}$, particularly in cases of small-angle scattering, as well as due to appreciable deviations between theoretical and experimental diffraction-absorption curves of polychromatic and even monochromatic incident beams.

Dilution Method. Copeland and Bragg[8] suggested that, particularly for samples containing relatively small concentrations of analyte, one may probably dispense with an internal standard and add instead a known weight fraction y_J of the analyte, which is already present in an unknown weight fraction x_J. If the sample also contains some other constituent, L, having a strong line suitable for reference intensity measurement, i_J and k_L will be

Eq. (8)
$$\frac{I_{iJ}}{I_{KL}} = \frac{K_{iJ}\rho_L(x_J+y_J)}{K_{KL}\rho_J x_L} + \text{constant } x(x_J + y_J)$$

A typical plot of I_{iJ}/I_{kL} against y_J is shown in Fig. 2.[9] The concentration of component J in the original sample is obtained from the negative abscissa intercept of x_J.

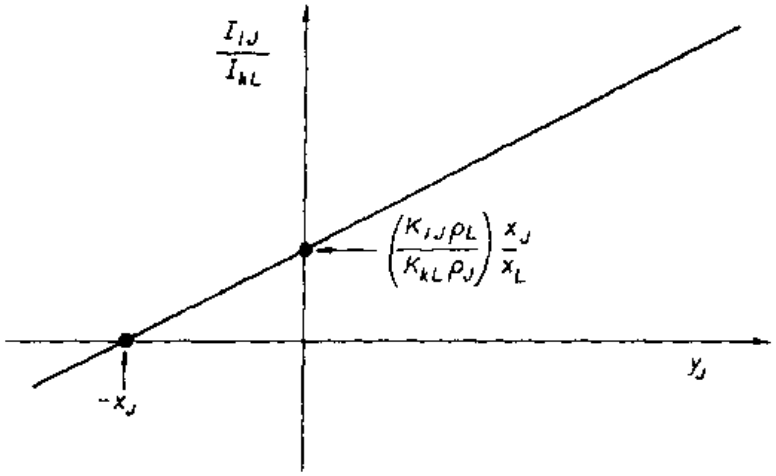


Figure 2. Analysis by dilution with a known weight fraction of the analyte.

@Seismicisolation

A similar treatment has also been made for N-component samples as well.[8]

Further Extension of Internal Standard Theory. In order to simplify the analytical procedure, an attempt was made to apply the internal standard concept[10][11] in the form:

Eq. (9)
$$x_J = x_S \frac{\left[I_{KS}\right]}{\left[I_{iJ}\right]_{50:50}} \times \frac{\left[I_{iJ}\right]}{\left[I_{KS}\right]}$$

where, $x_J = x_S = 0.5$ and $(I_{kS}/I_{iJ})_{50:50}$ is the intensity ratio of a 50:50 binary mix of components *S* and *J*. The above equation shows that for any multicomponent system a plot of I_{iJ}/I_{jS} versus x_J intersects the origin and is linear with the slope $x_S(I_{kS}/I_{iJ})_{50:50}$. This permits the slope of calibration curve to be precalculated, thus eliminating the preparation of a series of standard mixes.

3.0 DEVELOPMENTS IN INSTRUMENTATION

A schematic diagram of an x-ray diffractometer used for qualitative and quantitative analysis of materials is shown in Fig. 3. From the figure it is evident that a diffractometer is primarily made up of a compact x-ray protected housing, a goniometer, a high-voltage transformer for x-ray tubes, x-ray tubes with filters, a highly stable x-ray generator, a detector, and a data processing system.

The x-ray tubes may have different radiation targets like Mo, Cu, Co, Fe, Cr, and W, with different k_β filters like Zr for Mo, Ni for Cu, Fe for Co, Mn for Fe, and V for Cr. The tubes can be of normal, broad, or long fine focus type. Depending on the target and nature of focus the maximum load of x-ray tubes generally varies from 1 to 3 kW while the tube voltage and current are mostly in the range of 0–60 kV and 0–80 mA, respectively. Primary beam monochromators made of quartz to remove undesirable radiations and secondary monochromators made up of LiF flat crystals, or more extensively bent graphite crystal adjusted for Cr, Co, Fe, Cu or Mo-Kα radiation in order to eliminate fluorescent radiation from the samples are used in the incident and diffracted beam paths, respectively, along with different slits (fixed, variable, and soller types). Stepping motor-controlled slits can be coupled with the theta movements in order to keep the irradiated

@Seismicisolation

area of the sample surface constant, using computer controlled positions. In a sense this acts as a theta filter. Different types of sample holders are used, viz., general purpose ones made up of aluminum, special-purpose ones made up of glass for lattice constant measurement or for micro samples, non-reflective ones made up of silicon for ultramicrosamples. Depending on the applications, the system can be equipped with a scintillation counter, a proportional counter, a position-sensitive detector, or with a semiconductor detector.

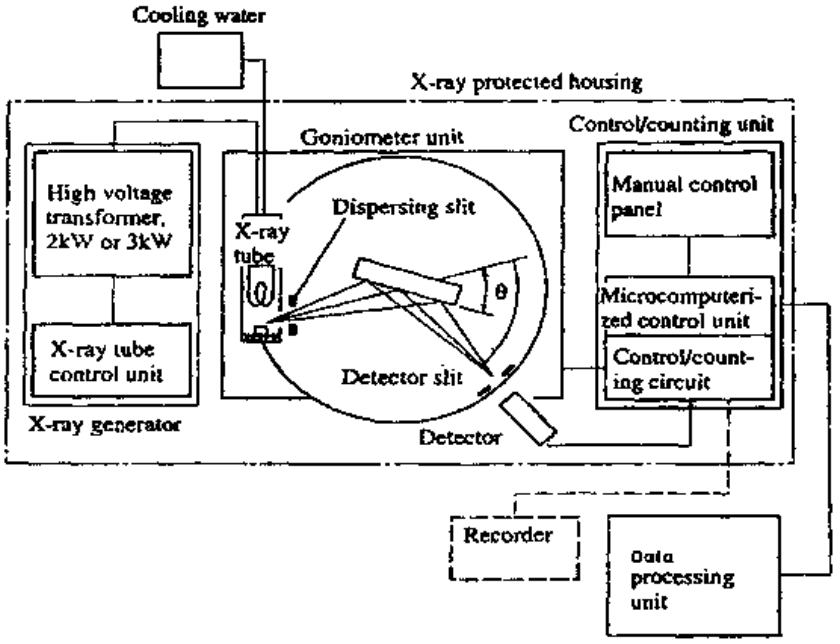


Figure 3. Block Diagram of a x-ray diffractometer.

In the actual operation of the setup as briefly narrated above, the intensities are recorded with a stationary incident beam and with synchronized rotation of the sample and the detector. In order to satisfy the geometry of diffraction the detector rotates at twice the speed of the sample.

@Seismicisolation

In recent times it has also been possible to have systems with θ/θ configuration in which the table and the detector are moved, keeping the sample fixed horizontally. Apart from liquid samples, this configuration is useful for large and bulk samples that cannot be moved with the diffractometer.

For studies of phase transformations or chemical reactions at different temperatures and in different atmospheres, different high and low temperature chambers are available for investigations in the temperature range of about -270° to + 2700°C.

Generally, a scintillation counter is adequate for intensity measurement purposes. For weak diffraction lines, a solid state detector is preferred. Use of a position sensitive detector for fast data acquisition has also been reported by equipment manufacturers.

In order to obtain clear resolution in the diffractograms, the fundamental requirements are the plane sample surface and precise location in the measurement position. For non-flat samples the adoption of parallel beam, x-ray optics with Göbel mirrors is also known to result in proper resolution and avoidance of line shifts. For high temperature experiments in which the heating process disturbs the constancy of the sample surface, this optic is more useful.

3.1 Microfocus X-Ray Diffractometer

The microfocus x-ray diffractometer (Fig. 4)[12] is regarded as an advanced tool to obtain structural information of a microscopic region of a sample by taking x-rays in a spot of 1 mm by 1 mm and converging the x-rays into a size of tens of microns in diameter with a collimator while the conventional x-ray diffractometer has a line x-ray source of hundreds of microns by 10 mm. Since the sample size is too small in a microfocus setup, there is a system of tri-axial rotation of the sample in order to prevent the Debye-Scherrer ring from discontinuity. A high-power x-ray source of 10–18 kW is used and a curved position-sensitive proportional counter (PSPC) of 80 mm in radius is used to detect and integrate the diffracted x-rays. Although the spatial resolving power is 0.2° (2θ), which is lower by two orders of magnitude than that of conventional x-ray diffractometer, the measuring range is as wide as 0 to 150° (2θ) so that even higher-angle diffracted lines can be measured.

With microbeams used as an x-ray probe, diffraction characteristics can be mapped as a function of sample position. The information can be plotted as a diffraction function map (DFM).

@Seismicisolation

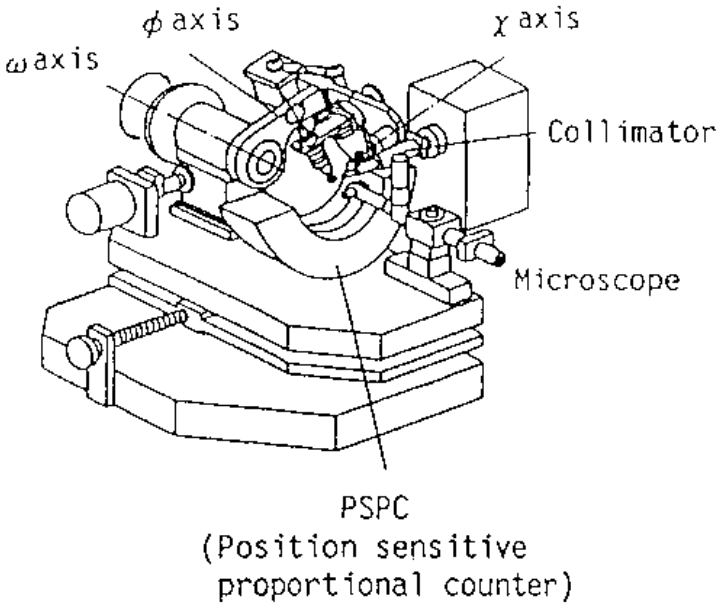


Figure 4. Microfocus x-ray diffractometer.

3.2 Integrated XRD-XRF System

With a view to serving the cement industry, an x-ray spectrometer which integrates both x-ray fluorescence for elemental analysis and x-ray diffraction for phase analysis has been designed.[13] The equipment is reportedly capable of being equipped with a maximum of eleven XRF fixed channels, one XRF goniometer, and one XRD system. The XRD system is said to possess high sensitivity owing to closely coupled diffraction optics, very high reliability of measurement due to gearless optical encoder technology and vacuum environment.

3.3 Time Resolved X-Ray Diffraction

In order to study transient structures that occur practically in every physical, chemical, and biological reaction, the time-resolved x-ray diffraction has received attention of many equipment developers. Nanosecond time resolution has been achieved by the employment of picosecond x-ray

@Seismicisolation

pulses from synchrotron sources while sub-nanosecond resolution x-ray diffraction experiments have been reported using laser produced plasma as the x-ray source.[14]

3.4 Energy-Dispersive X-Ray Diffractometry

For certain applications, attempts were made to try out the energy-dispersive x-ray diffractometry in place of conventional scanning diffractometry, with controversial results.[15] It was expected that with high-speed data acquisition facility the energy-dispersive technique would offer important advantages, but the practical application of this technique has so far been restricted by the slower response of detectors. It is believed that the wider adoption of EDD techniques may still happen with progress in the development of smaller detector lead times and sharper energy resolution.

4.0 COMPUTERS IN X-RAY DIFFRACTOMETRY AND SOFTWARE APPLICATIONS

The historical perspective of the impact of computers on x-ray analysis for the period 1960–1990 has been summarized in Ref. 16. It is reported that most of the early use of computers for the control of diffractometers came from the single crystal field rather than the powder community. The *Numerical Control Powder Diffractometer* was first described in the 1966 Denver Conference and in 1971 the first commercial automated powder diffractometer was introduced. Thereafter, the instrument development cycle closely followed the developments in computer hardware and peripherals. The movement from punch cards to CD-ROM also had a significant impact on software for x-ray analysis. Certain developments of software of significance to x-ray diffractometry have been dealt with in Ref. 17 and the basic programs required or in use for XRD are summarized below:

1. Programs for routine analysis that include, in general, hardware control: Pattern Processing (background and α_2 removal, automatic peak finding and characterization, peak editing, overlay, comparison, etc.), search and matching with the help of databases, access to materials database such as PDF, NIST-CDF, metals, etc., and finally, reporting codes such as spreadsheet, word processor, etc.

@Seismicisolation

2. The second category of programs that include profile codes for extracting overlapped peaks, for particle sizing, cell refinement, and cell indexing, etc.
3. The third category covers structure refinement, typically with the help of Rietveld method, residual stress, Laue simulations, synchrotron data processing, etc.
4. The fourth category relating to hardware control such as for low and high temperature stages, thin film devices, polymer attachments, small scale scattering devices, etc.

Some of the commonly used and commercially available softwares are shown in Table 2 and a few illustrations of complex use of multiple programs are given below.

Table 2. An Illustrative List of Softwares

NAME OF SOFTWARE	PURPOSE
INDEX	Indexing of powder pattern
DE-CONV	Line profile generation and fitting, deconvolution.
D-SEARCH	Search/Match for full or sub-file search from ICDD.
DIFFRAC^{PLUS} AND DIFFRA^{PLUS} BASIC DATA EVALUATION	Basic data acquisition with control of diffractometer, generation of *d/I* files, overlay of several files, quantitative analysis using Chung's or Regression methods.
DIFFRAC^{PLUS} SEARCH	Search/Match
DIFFRAC-AT V3.2, SOCABIM	Data acquisition and treatment Search/Match.
DICVOL	Indexing of XRD pattern
SHADOW	A-system for x-ray powder diffraction pattern analysis.
ORTEP	Crystal structure plot
"NBS-LATTICE"	A program for lattice relationship
MDAT AND MDATAUTO	Identification of minerals by use of analytical data such as qualitative and quantitative chemical analysis, physical and optical, crystallographic data, etc. Identification of solid solutions.

@Seismicisolation

4.1 Ab Initio Structure Determination from Powder Diffraction Data

The steps involved in an ab initio structure determination by the powder diffraction method, as reported in Ref. 18, are briefly reproduced below along with the programs used in those steps:

- Instrument control and data processing—DIFFRAC-AT (Socabim/Siemens)
- Identification—PDF data bases (ICDD), DIFFRAC-AT SEARCH, NIST-CDF(ICDD)
- Pattern decomposition—DIFFRAC-AT FIT
- Powder pattern indexing and space group information—DICVOL 91, TREOR, ITO, NBS AID83, REDUC, PRUM
- Extraction of integrated intensities—FULLPROOF
- Structure solution—SHELX, PATSEE, SIRPOW
- Structure refinement—FULLPROOF, DBWS, WYRIET
- Bond lengths and angle calculation—BONDPC
- Structure model display—CRYES, ATOMS, WYRIET

Since quite a few structure analyses for oxides have been successfully done by adopting this approach, it appears that the above chain of programs is necessary for an exercise of structure analysis. Most of these programs are listed in the Powder Diffraction Program Information 1990 Program List.

4.2 Full Trace Diffraction Match and Files

The advantages of using the full trace as input for search and match rather than the traditional list of *d/I* values are being increasingly appreciated and attempted.[19][20] There are quite a few commercially available softwares for qualitative phase analysis that take into account full information, such as peak widths, peak asymmetries, shoulders on the peaks, and peaks with very low intensity. This enables precise analysis of complicated multiphase mixtures. This approach makes it possible to reach better detection limits than usually expected. For instance, in favorable cases it is possible to identify phases contributing to only about 1/100th of the whole pattern net intensity. Cases like detection of trace impurities of zircon or

@Seismicisolation

kaolinite in pure quartz or minor solid solution replacement of Ca by Mg in calcite, have been reported through application of the above technique.[19]

Success of this technique has led to the development of a file of digitized full diffraction traces for clay minerals like kaolin, smectite, mica clay, and chlorite groups, under ICDD.[20]

It appears that in the materials field where the phases produce anomalous diffraction traces there is a potential for full-trace databases. Among many other industrial materials, cement and cement hydration products, corrosion compounds, blending materials, and cement substitute substances like fly ash suggest themselves for creation of such full-trace digitized databases.

4.3 Quantitative Phase Analysis Using Whole Powder Pattern Fitting

Some of the important methods practiced for the quantitative phase analysis (QPA) based on the intensity-concentration formula for single lines have been dealt with in the previous sections of this chapter. The use of whole-powder-pattern data for QPA is rather a new approach. The whole-powder-pattern fitting method can be classified into two categories, the Rietveld method for structure refinement[21] and the whole-powder-pattern decomposition (WPPD) method.[22] In both methods all peak positions are constrained by adjustable unit-cell parameters and the profile models over whole patterns are angle-and-energy dependent. However, the principle difference between the two methods is that the integrated intensities are the function of structural parameters in the Rietveld method while they are independent variables in the WPPD method. Although, historically the WPPD method has developed from the Rietveld method, the former can refine the unit-cell parameters and decompose the whole-powder-pattern into individual Bragg reflections in one step without reference to a structural method. Hence, in recent times an approach of QPA based on whole-powder-pattern decomposition (WPPD) method has been proposed extensively.[23][24] The WPPD method refines integrated intensity parameters together with unit cell and profile parameters by least squares or by iteration.

The WPPD-based QPA may be performed by the following two major steps. In the first step, whole-powder-pattern fitting (WPPF) refinements are performed for respective pure components and integrated intensity parameters are fitted, then the sets of integrated intensities obtained for

@Seismicisolation

respective phases are stored in data files as source data. In the second step, the WPPF refinement is carried out for the mixture sample and the scale factors for individual components are adjusted while individual integrated intensities are not varied. The refined scale factors are proportional to the volume fractions of respective phases and can be converted to their weight fractions. Sets of integrated intensities calculated from structure models or those from ICDD PDF can also be used as source intensity-data after appropriate correction for scaling. Testing of this method using two to five component mixes with known weight fractions gave the average deviations of desired weight fractions within the range of 1–1.5%. The detailed treatment of the steps followed in such studies has been given in Ref. 24.

It should, however, be borne in mind that intrinsically overlapping reflections at the same Bragg angle cannot be decomposed by the WPPD method. Severely overlapping reflections are also difficult to resolve. The effective separation limit in pattern decomposition (measured as the shortest 2θ distance between two adjacent peaks) ranges from 0.1 to 0.5 times the full-width at half-maximum (FWHM). Experience indicates that the complete decomposition of a powder pattern is not required for phase identification, quantitative phase analysis, measurement of unit-cell parameters, or crystallite size and strain. Complete decomposition, however, is quite important for ab initio structure determination and preparing Fourier maps.

5.0 X-RAY DIFFRACTOMETRY OF CLINKER AND CEMENT

As already elaborated in the previous section of this treatise, the x-ray diffractometry, being a direct method for qualitative and quantitative characterization of polyphase materials, has also turned out to be a virtually indispensable tool to analyze clinker and cement. Each phase of cement produces a unique diffraction pattern independent of others with the intensity of each pattern being proportional to the concentration of the phase in a mixture, however, the patterns are complex with many overlaps. In addition, compositional and structural variations of each phase influence peak positions and relative intensities. As a result, peak intensity measurements and selection of standard reference materials are quite problematic. Hence, the XRD studies have for several decades been more qualitative than quantitative in nature. In recent years, however, more emphasis is seen on applying newer quantitative techniques, which will be dealt with later.

@Seismicisolation

5.1 Methodological Aspects

For general purpose diffractometric studies of cement and clinker phases, the normal-focus x-ray tube with Cu target and Ni-filter combined with a monochromator system is widely used. Generally, an aluminium sample holder is made use of. In order to achieve an isotropic distribution of the crystals in the samples in all directions, the particle size is brought down to about five micron or less. The particle size is reduced to this level by wet grinding of the sample in an inert solvent such as benzene, isopropyl alcohol, or cyclohexane.

Accuracy in powder diffractometry or how close a measurement of peak position, intensity, or shape comes to the true value is often overlooked in experimental measurements, but can be attained with routine analysis. This primary method of assessing and attaining accuracy is through the use of representative standards and profile fitting. It is also important to recognize that sample preparation techniques that optimize accuracy for one measurement may not be appropriate for another. For example, the very fine crystallite size that is optimum for quantitative analysis is often unnecessary and sometimes can be detrimental in d-spacing and peak-shape measurements due to introduction of strain-related peak shifts and profile broadening. It is, thus, always desirable to take recourse to appropriate standards, systematic-error correction, and proper sample preparation.

Although, as already mentioned, the CuKα radiation is more widely used, it is also known that this radiation causes iron atoms to fluoresce and the fluorescent intensity is proportional to the iron content of the sample.[25] This fluorescent background intensity tends to submerge the low-intensity broad lines, particularly of the cement hydration products in the low angle range as reported for C_4AF.[26] It is preferable to use, in such situations, CoKα radiation or to adopt other means of counteracting the effect of fluorescence, such as pulse height analyzers.

The concept of theta filter, as explained in an earlier section, may also be a source of some confusion in the cement field. Most of the reported powder intensity data have been collected using diffractometers without a theta filter—a condition at which the surface area exposed to radiation during scanning underwent continuous change. However, in the instruments fitted with theta filters the area exposed is kept constant. The intensities recorded by the two sets of instruments are not identical, however, the ratio of two intensities vary smoothly with the angle of diffraction. The presence of any spike in the intensity ratio versus angle or d-spacing curve will indicate the occurrence of some other mechanisms on the line intensity generation.[27]

@Seismicisolation

5.2 Identification of Major Phases Present in Cement/Clinker

It is well known that the portland cement clinker contains four principal phases which are known as alite (C_3S), belite (C_2S), aluminate (C_3A), and aluminoferrite (C_4AF). Clinkers often show, in addition, the presence of free lime (CaO), periclase (MgO), alkali sulfates, and a glass that is virtually x-ray amorphous, but compositionally lying in between the aluminate and ferrite phases. Ordinary portland cement is produced by grinding this clinker with a permitted amount of gypsum. The crystallochemical characteristics of the major clinker phases are briefly summarized in Table 3.

Table 3. Salient Crystallochemical Characteristics of Major Clinker Phases

Name, Basic Composition and (Proportion in Clinker)	Foreign elements generally present	Approximate impurity level	Crystallographic modifications known
Alite C_3S (50–70%)	Al, Fe, Mg, Cr, Ti, S, P, Ba, Mn, Na, K	4%	3 triclinic + 3 monoclinic + 1 rhombohedral polymorphs in temperature range of 620–1070°C
Belite C_2S (15–30%)	Al, Fe, Mg, Cr Ti, Mn, V, Ba, S, P, Na, K	6%,	α (trigonal-hexagonal) α'_H & α'_L (orthorhombic) β (monoclinic) and γ (orthorhombic) polymorphs in temperature range of 500–1425°C.
Aluminate C_3A (5–10%)	Fe, Mg, Si, Ti, Na, K	10%	No polymorphs. Foreign elements as solid solutions. Only alkalis cause change in symmetry, viz., cubic, orthorhombic and monoclinic.
Aluminoferrite C_2 (A,F) (5-15%) more commonly expressed as C_4AF	Mg, Si, Ti, Mn, Cr	13%	C_2F orthorhombic (pseudo-tetragonal)

@Seismicisolation

The x-ray diffraction measurements of the majority of these phases started almost five decades back.[28]–[30] Earlier diffraction studies essentially related to the synthesis of pure phases, solid solubility of different elements in different phases, polymorphic transformations, and comparison with industrial clinkers and cements. Status reports on these kinds of studies are available in the literature.[31][32] Certain practical observations of XRD patterns of individual clinker phases occurring in industrially produced clinkers are briefly dealt with in the following sections.

Alite (C_3S). From available knowledge it is apparent that the XRD patterns of alite polymorphs, particularly in industrial clinkers, are closely alike and the interpretation becomes complicated due to peak overlaps and peak shifts due to foreign ions present. Monoclinic and triclinic forms are predominant in clinkers and the rhombohedral form is rare. The latter, whenever observed, causes a peak at 51.7° 2θ (CuKα radiation) to be a singlet. It breaks with a shoulder in the case of M_{II} polymorph, it transforms into a doublet when M_I polymorph is present, and results in a triplet in all three variants of the triclinic polymorphs, the triplet being the most distinctive in the T_I form. Some of these patterns as recorded for the plant-produced clinkers in the author's laboratory are reproduced in Fig. 5.

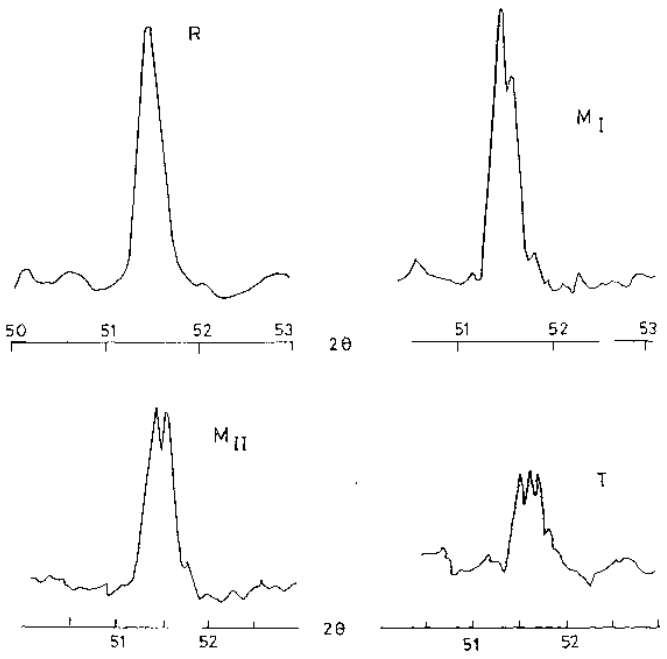


Figure 5. Different polymorphs of alite in some industrial clinkers (CuKα radiation).

@Seismicisolation

One of the rare applications of microfocus diffractometry in clinker mineralogy has been to study the zonal structure of alite (Fig. 6). The figure shows the difference in the polymorphic states of the core and periphery.[12]

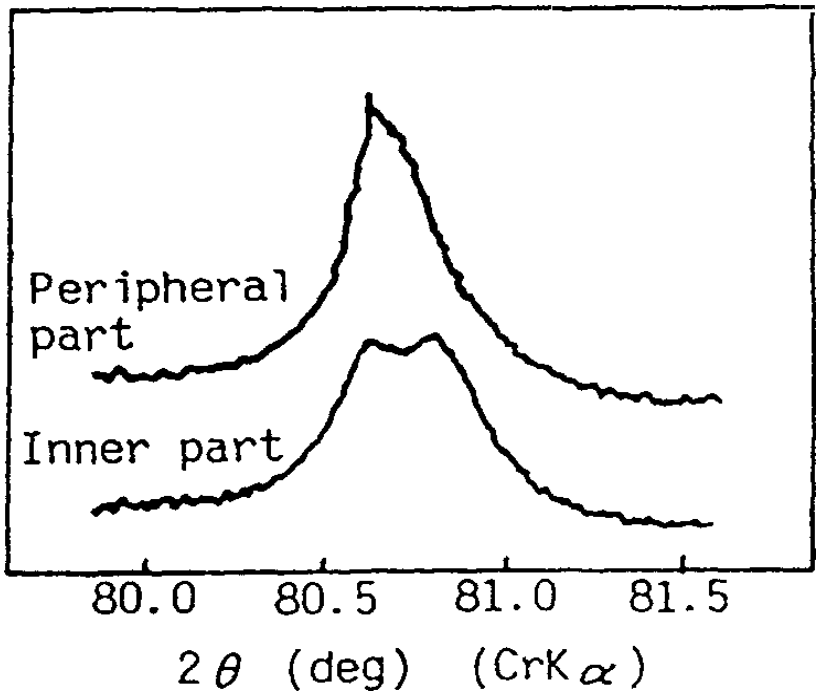


Figure 6. Alite with zonal structure determined by microfocus diffractometer.[12]

Belite (C_2S). It is widely known that in the majority of clinkers the belite phase is predominantly or entirely in the β-polymorphic state. The simultaneous presence of α and α′ along with the β-form is also known. Characterization of the polymorphs is rendered difficult by the similarities between the powder patterns (Fig. 7) and also by overlaps with alite peaks.

The Aluminate Phase. It has already been shown in Table 3 that pure C_3A does not exhibit polymorphism and it is of cubic symmetry. This phase can incorporate Fe, Mg, Si, Na, and K, in the lattice up to about 10%, but only the alkalis produce a change in symmetry.

@Seismicisolation

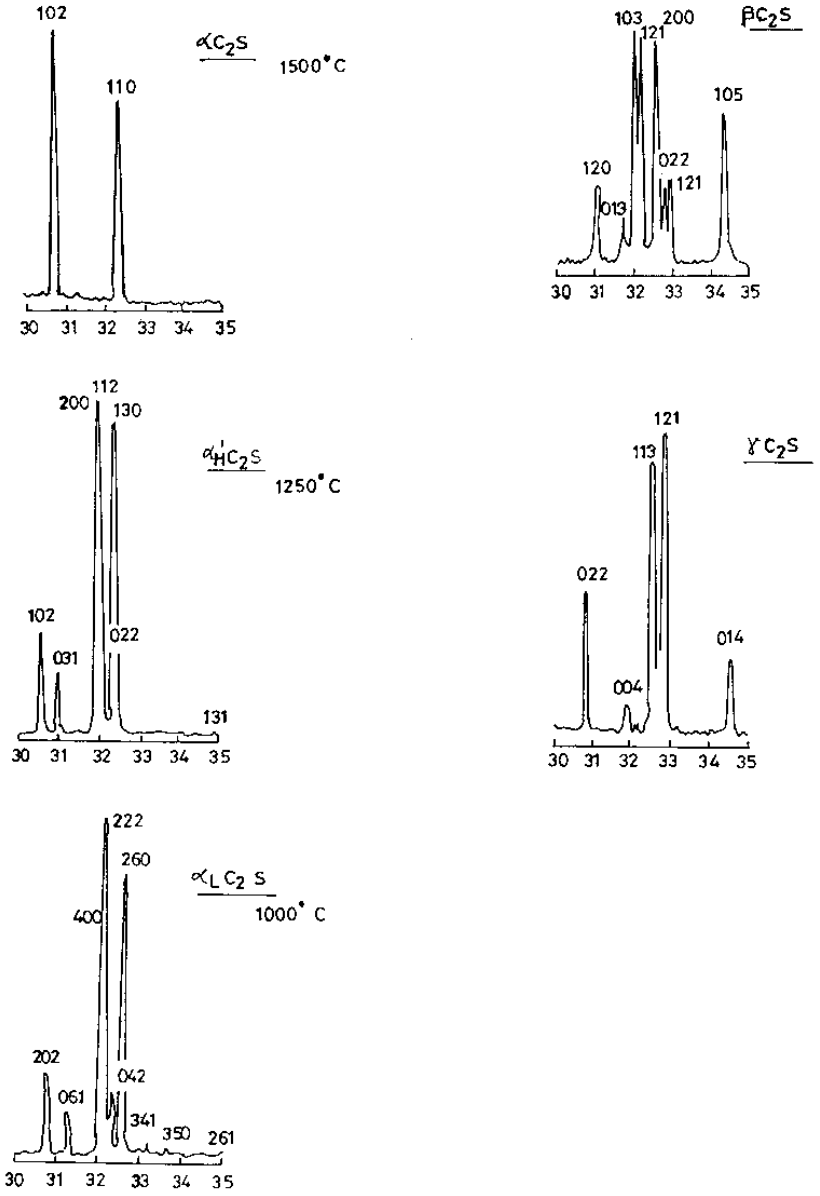


Figure 7. Different polymorphs of belite.[31]

The limit of substitution of Ca^{2+} by two ions of Na^{+} is 5.7%. This range of substitution leads to a series of variants of the structure of the aluminate phase (Table 4).

@Seismicisolation

Table 4. Relation of Alkali Content in C_3A with its Crystal Systems[32]

Approximate Range of Na_2O%	Crystal System	Designation
0.0–1.0	Cubic	C_1
1.0–2.4	Cubic	C_{11}
2.4–3.7	—	C_{11} + O
3.7–4.6	Orthorhombic	O
4.6–5.7	Monoclinic	M

Industrially produced clinkers are known to contain cubic or orthorhombic forms alone or in combination. The monoclinic form has not been reported. The XRD powder pattern of the cubic form is characterized by strong singlet peaks at about 33.3°, 47.7°, and 59.4° 2θ (CuKα radiation). The orthorhombic phase, on the other hand, shows a splitting of the peak at 33.3° 2θ with a strong singlet at 33.2° and a weak doublet at 32.9°–33.0° (Fig. 8).

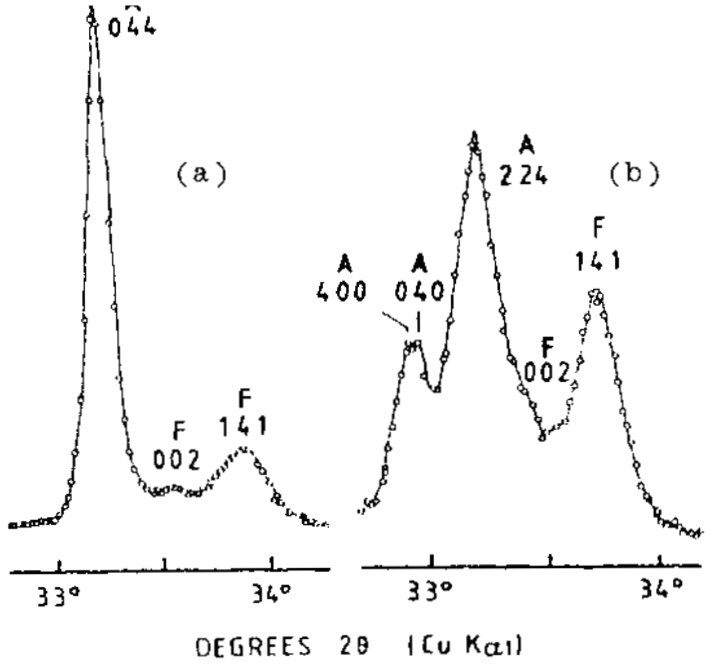


Figure 8. Cubic *(a)* and orthorhombic *(b)* aluminate phase in clinker. (*A*: aluminate peaks, *F*: ferrite peaks).[31]

@Seismicisolation

The Aluminoferrite Phase. This phase in industrially produced clinkers is orthorhombic. Taking into account the substitutions due to SiO_2, MgO, TiO_2, Mn_2O_3, and Cr_2O_3, the aluminoferrite composition is very close to C_4AF, although the pure phase composition is given by the solid solution series $Ca_2 (Al_x Fe_{1-x})_2 O_5$, where $O < x < 0.7$ and C_4AF is only a point in this series with $x = 0.5$.

The XRD patterns of clinker ferrites are affected by the cooling rate of clinker. Disappearance of many peaks other than the three most intense reflections (200, 141, and 202) and broadening of the peaks are primarily caused by the poor crystallinity due to rapid cooling. The XRD traces of the aluminoferrite phase in different plant-produced clinkers as scanned around 47° two-theta are shown in Fig. 9.

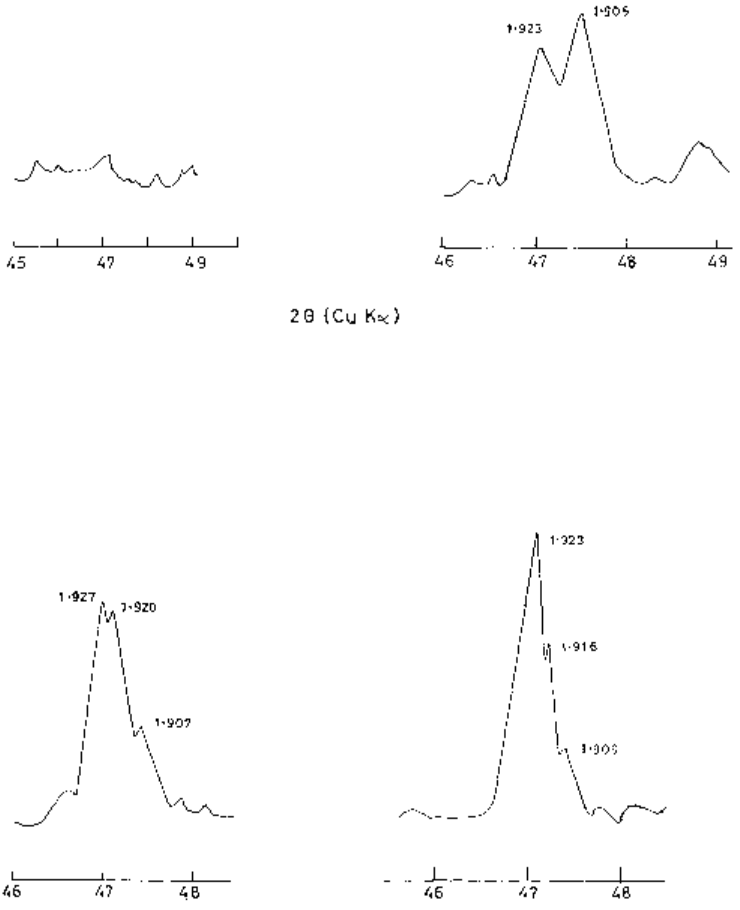


Figure 9. Various XRD traces of the aluminoferrite phase in industrial clinkers.

@Seismicisolation

It may be relevant to mention here that the calculated patterns for the individual clinker phases based on the results of x-ray structure determinations have been furnished in Ref. 32, which can be treated as one of the reliable databases for XRD studies on clinker mineralogy.

Selective Dissolution of Phases for XRD. Despite the availability of voluminous information and data on the XRD characteristics of pure synthesized clinker phases over the last several decades, the in-depth crystallochemical understanding of industrially produced clinkers remains unattained in the scientific world to the extent desired because of complexities of patterns, as mentioned earlier. Hence, right from the '70s, extensive attempts were made to achieve selective separation of clinker phases through dissolution with the help of specific solvents.[33] A solution containing 30 g of potassium hydroxide and 30 g of sucrose in 300 ml of water (referred to as a KOSH solution) is heated to 95°C, 9 g of cement are added to this solution and stirred for a minute, after which time the solution is filtered and the residue washed in 50 ml of water followed by 100 ml of methanol and dried at 60°C. This allows the removal of interstitial phases, leading to the concentration of the silicates.[34] Further, in the same study it was seen that by using a salicylic acid-methanol solution it was possible to dissolve preferentially the alite phase contained in the residue obtained from a KOSH solution treatment.

Solvents like maleic acid in methanol (1:5) or salicylic acid in methanol (1:5) or maleic acid and salicylic acid in methanol (1:1:10) are reported to be effective in separating the silicate phases, leaving C_3A and $C_2(A,F)$ in the residue. For the separation of the above two phases it has also been suggested that a 3% aqueous solution of sucrose can be employed.[35][36]

A large number of such separations were carried out in the author's laboratory for the qualitative identification of matrix phases in some plant-produced clinkers and a typical XRD pattern of the matrix and the isolated ferrite phase after separation of the silicate phases is shown in Fig. 10, which also shows the separation of the aluminate phase from the matrix.

Selective extraction of sulphate phases present in a clinker from its maleic acid residue treated in a 10% NH_4Cl solution has also been successfully attempted.[37] In this study the concept of selective extraction of silicate and sulfate phases was adopted in order to identify and distinguish the cubic and orthorhombic forms of C_3A on one hand and to perform profile fitting on the other, for measuring the aluminate and aluminoferrite phases quantitatively through their integrated peak area by using a computer program.

@Seismicisolation

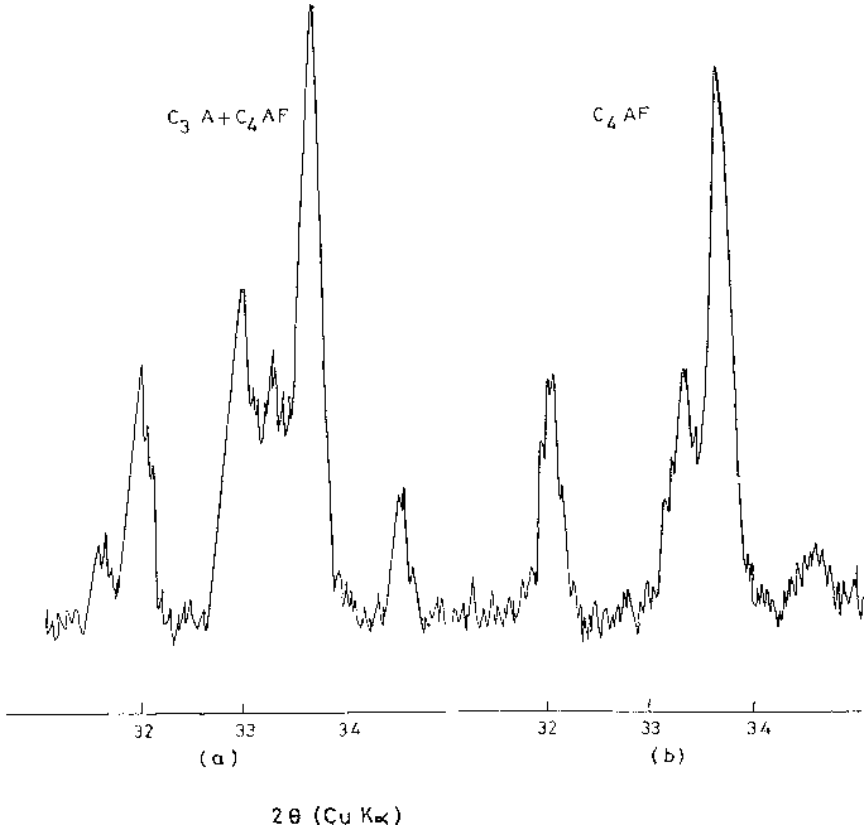


Figure 10. XRD pattern of the matrix *(a)* after separation of the silicates and *(b)* after further removal of the aluminate phase.

5.3 Semi-Quantitative and Quantitative Estimation of Phases

As an alternative to Bogue's calculation for quantification of phases on one hand and optical microscopy on the other, numerous attempts have been made to apply and perfect a technique based on x-ray diffractometry since the late fifties.[38]–[41] A majority of the attempts have been based on mixed internal standards although a few other procedural variants have also been tried. The common practices and emerging trends are briefly dealt with here.

@Seismicisolation

Routine Analysis by the Mixed Internal Standard Method. The basic principles of this method have already been discussed earlier in this chapter. For routine semi-quantitative phase estimates by this method, first, mechanical mixtures of known concentrations of synthetically prepared four pure phases are prepared along with an internal standard (rutile, silicon, KBr, CaF_2, or corundum), interground, and blended thoroughly. The characteristic diffraction lines selected for measurement of clinker phases are:

Alite	3.04 Å or 1.76 Å
Belite	2.87 Å
Aluminate	2.699 Å
Aluminoferrite	2.67 Å

After measuring the intensities in all the mixtures with the various phases in known concentrations, a plot of I_c/I_s vs. C is obtained for each phase.

C is the concentration of the phase

I_c is the intensity of the line corresponding to the phase concerned

I_s is the intensity of the line corresponding to the internal standard

Thereafter, a known weight of the same internal standard is also ground with the sample under investigation and the corresponding values of I_c/I_s are determined for each phase. Interpolation of these values in the calibration curves gives the concentrations of each phase under investigation. A typical calibration line is shown in Fig. 11.

Although for routine work this method is widely practiced, it suffers from three major shortcomings:

1. Deviation in the composition of the phases actually present in the sample under investigation and those used in calibration.
2. Long preparation time for the calibration curves.
3. Achieving homogeneity in the blending of the internal standard.

Unmixed Internal Standard Method. In view of the above shortcomings and volume of work involved in the mixed internal standard method, the author introduced a simplified version for routine assignments, which is reported in Ref. 42.

@Seismicisolation

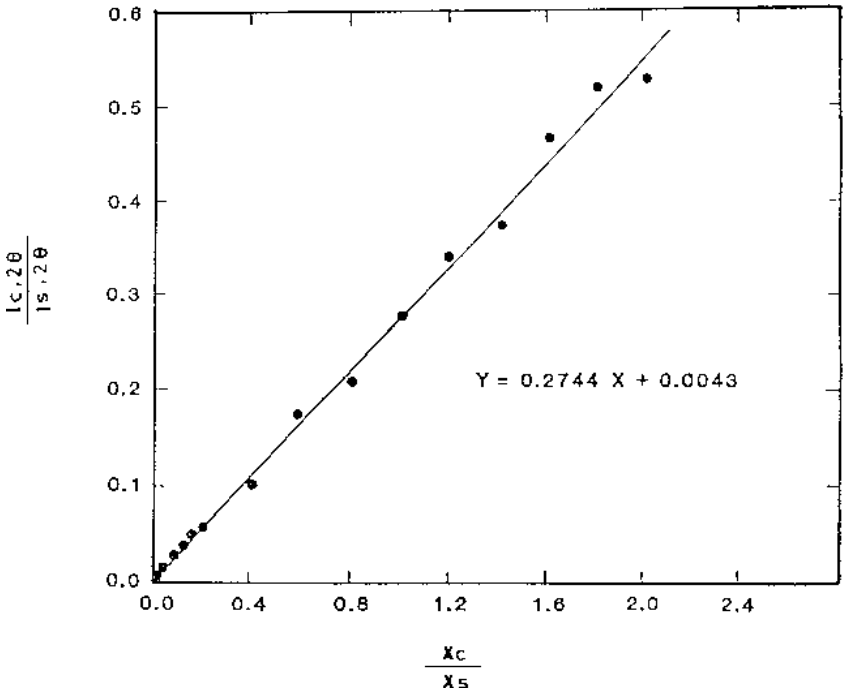


Figure 11. An illustrative calibration curve.

In this method a standard cement or clinker of predetermined composition is used as a reference sample. A platinum foil of 99.99% purity with essentially flat surface measuring 1 mm × 1 mm and weighing 0.49 g is used as an unmixed internal standard with its characteristic line at 2.27 Å.

For rapid estimation, samples ground to less than 44 μ are used with a carefully flattened surface in an aluminium holder in which the internal Pt standard is lightly placed at a predetermined position, generally in line with the curvature of the goniometer circle, for reproducibility. A typical trace is shown in Fig. 12.

For any given phase, the concentration, C_s of the phase in the test sample is given by:

Eq. (10) $$C_s = C_r \frac{I_s}{I_r} \times \frac{I_{rp}}{I_{sp}}$$

@Seismicisolation

where, C_r is the concentration of the same phase in the reference sample, I_s and I_r are the intensities of the line due to the phase in the test sample and reference sample, respectively, and I_{sp} and I_{rp} are the intensities of the platinum line in the test samples and reference sample, respectively.

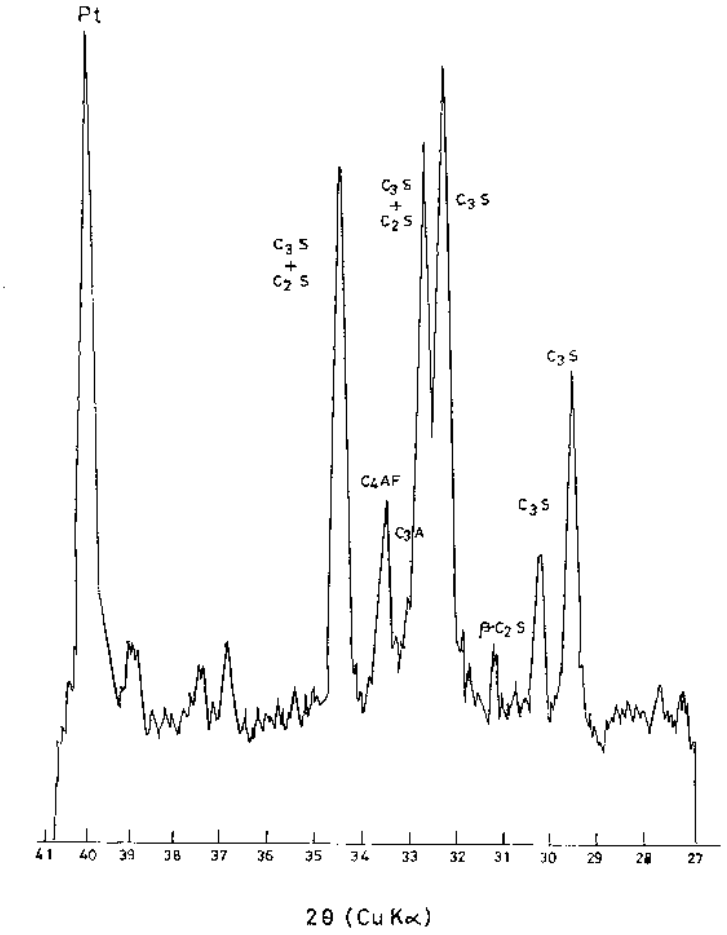


Figure 12. XRD pattern of a clinker sample with Pt as an internal standard.

Pattern Fitting for Quantitative XRD of Cement and Clinker. The semi-quantitative methods described above relied on intensity measurements of single resolvable diffraction peaks. As an improvement over this approach, the alternative techniques of whole-pattern fitting, the principles of which have been described earlier, have been applied to the cement field.

@Seismicisolation

These methods primarily rely on the measurement of the reference intensity ratio (RIR),[43] which is adapted from the internal standard method, in which the slope, RIR, of the calibration plot is given by:

Eq. (11) $$\frac{I_\alpha}{I_s} \times \frac{X_s}{X_\alpha} = \text{RIR}_\alpha$$

where: I_s = pattern intensity of internal standard S

I_a = pattern intensity of phase α

X_a = mass fraction of phase α

X_s = mass fraction of internal standard S

The calibration using the RIR method involves the following steps.

1. Collection of diffraction patterns of individual phases for reference profiles.
2. Collection of diffraction patterns of multiphase mixture of known composition with a known mass of intermixed standard.
3. Calculation of pattern intensities and of the RIR constant relating peak intensity ratio with mass fraction ratio using Eq. (11).

An unknown sample, then, is treated for analysis in the following manner.[46]

1. Addition and homogenization of a known mass of internal standard.
2. Three replicate diffraction scans, repacking for each.
3. Measurement of the background subtracted intensities.
4. Calculation of the mass fraction of each phase using:

Eq. (12) $$\frac{I_\alpha}{I_s} \cdot \frac{I_s}{\text{RIR}_{\alpha,s}} = X_\alpha$$

The mass fractions of the unknown phases are a mixture including the internal standard and, therefore, a correction is introduced using:

Eq. (13) $$X'_\alpha = \frac{X_\alpha}{1 - X_s}$$

@Seismicisolation

Studies on the application of whole-pattern fitting for the quantitative phase analysis of clinker and cement are limited, but seem to be gaining ground in recent times.

One of the attempts made in the eighties[44] was based on a least squares fit between diffractometer trace of the sample with internal standard and a simulated trace summing the contributions from the component phases. The trace was obtained over the range of 24°–39° by step counting at 0.05° intervals using $CuK\alpha_1$ radiation and stored in a computer. Auxiliary procedures were devised for dealing with background levels, adjusting the peak widths, and to some extent, peak positions in the reference patterns to match those in clinker, and matching the observed and computed patterns.

In another study,[45] spacings and integrated intensities of XRD patterns were calculated from the published crystal structures for the major phases of clinkers and for corundum. The reference intensity ratios were calculated. Based on such ratios, methods were evolved for the approximate determination of the quantitative phase composition from a diffractometer trace without using reference standard by normalizing the total to an assumed value.

In a recent study[46] the application of whole-pattern fitting was attempted using Dataplot, a graphics and data analysis language developed at NIST. Trials using known mixture of clinker interstitial phases indicated a very good agreement with the known phase abundance values with absolute errors, based on the whole cement, of less than 1 percent.

Rietveld Techniques. With some variance to the above approaches, the possibility of quantifying the phase composition of a clinker by theRietveld method was shown by many investigations.[47]–[50] In a more recent study,[51] the alite, belite, aluminate, and ferrite phases were synthesized in the laboratory to match the compositions of the main phases of an industrially produced clinker. All structures were refined by the Rietveld PC software. In the next step the synthesized phases were mixed in different proportions and quantified by the same software. Three different mixtures showed a deviation from the input data by less than one percent (Table 5).[51]

In this direction, another interesting study has been carried out to generate reliable standard x-ray powder diffraction patterns for C_3A, gypsum and ettringite and to test if the application of the Rietveld method to the hydration reactions of C_3A is possible. It was observed that the quantitative results of the standard mixes were within 0.5% of the true values. Finally, it was shown that the concentrations of C_3A, gypsum, and ettringite, in hydrating mixtures of C_3A and gypsum could be calculated with standard deviations of about ± 1% using powder patterns taken with the "wet cell" of the diffractometer.[52]

@SeismicIsolation

Table 5. The Rietveld Analysis Results (wt.%)

Phases	Proportions Actually Mixed	Calculated Properties	Standard Deviation
Alite	65	64.8	0.9
Belite	20	20.8	0.8
C_3A	10	9.6	0.6
C_4AF	5	4.8	0.6
Alite	55	55.3	1.1
Belite	25	25.4	1.2
C_3A	10	9.7	0.6
C_4AF	10	9.6	0.6
Alite	70	69.9	0.7
Belite	15	15.7	0.8
C_3A	5	5.0	0.6
C_4AF	10	9.4	0.9

5.4 Quantitative Phase Analysis for Quality Control

With a view to exploiting the potential of XRD, some of the investigators have attempted to adopt certain quality control measures based on various other approaches for quantitative phase analysis. A few illustrations are furnished here.

1. On-line and reliable analysis of free lime in clinkers is one of the most important process control requirements in any cement plant. Free lime in clinkers as opposed to the total CaO can be quantitatively determined in less than 60 seconds using the integrated XRF-XRD system mentioned earlier.[13] As reported, typical accuracy of 0.1–0.15 is achieved in addition to excellent reproducibility.
2. It is known that there is a close connection between NO values in kiln exhaust gases and the operating conditions of a rotary kiln. Since the operating conditions of a kiln are also reflected in the final quantitative phase composition of the clinker that is produced, an attempt has been made to correlate the NO values with the varying sum-total of the quantitative phase analysis of clinker during the kiln

@Seismicisolation

operation, for effective process control.[53] According to this study, it was observed that for well crystallized C_3S the quantities determined by XRD were of the same order as calculated by the Bogue equation. However, large differences between the experimental and calculated values were found for C_2S, C_3A, and C_4AF, primarily due to substantial variations in crystallinity of these phases caused by the fluctuations in the process control of kiln and cooler. The author reported that for consistent kiln operation the sum of clinker phases as determined by QXRD based on prior calibration plus liquid phase as computed by the Lea equation fluctuates between 98% and 102%. Disruptions in the kiln operation can cause quite large fluctuations as shown in Fig. 13. The figure also shows the corresponding time profile of NO values in kiln exhaust gas for comparison. It apparently indicates that the degree of crystallinity of the C_2S, C_3A, and C_4AF, as determined by XRD may be used as a measure of the burning and cooling conditions of a kiln system and may serve, on perfection as a tool, as an additional instrument for kiln control.

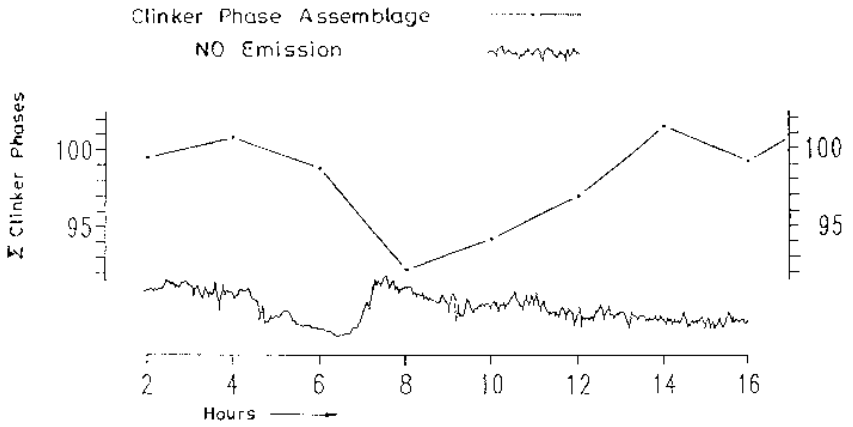


Figure 13. Real-time relationship between NO values and clinker phase assemblage.

@Seismicisolation

3. It is a common knowledge that there is a correlation between the alite (C_3S) content in clinker and the expected strength of the corresponding cement under a given set of grinding conditions. Due to this fairly well-established relation, the on-line determination of clinker phases is becoming more and more important. In a particular investigation[54] toward this objective it was observed that the XRD calibration was dependent on the presence of minor constituents in the phase, sample preparation including grinding conditions and peak position and shape as influenced by solid solubility of elements such as magnesia in C_3S. The strong possibility of predicting the 28-day strength of cement from the clinker alite content through adoption of such precise calibration in an on-line system has been indicated.
4. In another investigation[55] a more comprehensive attempt was made to develop a quality control scheme. It was considered that the determination of burning conditions in a kiln system as well as the prediction of 3-day and 28-day cement strengths can ensure a reliable QC system. With this in view, the following three indices were reported based on a statistical correlation of selected peak intensities.

   (*a*) C_n as the ratio of pulse counts (Cukα radiation) corresponding to d = 2.78 Å (32.2° 2θ) and d = 2.74 Å (32.7° 2θ) to be used as an index of burning conditions. C_n should generally be below 1.5 for normal operating conditions, higher values indicating abnormal situations.

   (*b*) X_n as the ratio of pulse counts (CuKα radiation) corresponding to d = 2.959 Å (30.2° 2θ) and d = 2.874 Å (31.1° 2θ) as an index to predict the 3-day cement strength by the following relations in kg/cm^2.

Eq. (14) $$CCS_{3\text{-}d} = 240\, x_n \qquad \text{when } x_n < 1$$

Eq. (15) $$CCS_{3\text{-}d} = 240 + 26(x_n - 1) \qquad \text{when, } 1 < x_n < 5.5$$

   (c) $I_n = 90 - 10\, X_n$, where $X_n < 5.5$ as the index to arrive at the predicted 28-day cement strength in a given situation by the following relation in kg/cm^2.

@Seismicisolation

Eq. (16) $$CCS_{28-d} = CCS_{3-d} + \frac{CCS_{3-d} \times I_n}{100}$$

where CCS_{3-d} is derived from X_n.

The concept has also been extended to strength prediction of portland slag cement.[56] It is, however, not very clear at this stage how universal the applicability of the relations based on the above indicies is and how much further validation under diverse plant conditions is necessary.

5. The influence of material and process parameters on the microstructure of clinker have been investigated statistically with the help of XRD.[57] The XRD patterns were taken in the 2θ ranges: 32.4°–32.8° (profile A) and 32.9°–34.1° (profile B). Profile A covered the alite and belite peaks while profile B related to the aluminate and ferrite peaks. The statistical method applied was the partial least square regression (PLSR). Parameters like alite size and bulk chemical composition were correlated with the XRD profiles. The height of the overlap of alite and belite peaks and the position of the peaks changed with the variation of CaO, SiO_2, MgO and K_2O contents in clinker (Fig. 14). Significant influence of the above elements, in addition to that of Al_2O_3 and Fe_2O_3, was seen for profile B (Fig. 15).

5.5 Cement Substitute Materials

With ever increasing importance of blended cements such as portland pozzolana or slag cement (Fig. 16) and use of a variety of blending materials, the assessment of quality and estimation of quantity present in a cement have turned out to be an essential process control step. It appears that XRD as a technique may fulfill this requirement quite adequately.

Another typical example could be the estimation of limestone used as a filler in masonry cement (Fig. 17). From the figure it is evident that the diffraction peak due to $CaCO_3$, around 2.49 Å, is distinctly identifiable from the clinker phases and the scans further demonstrate that the higher the limestone peak intensity the lower is the intensity of clinker phases.

@Seismicisolation

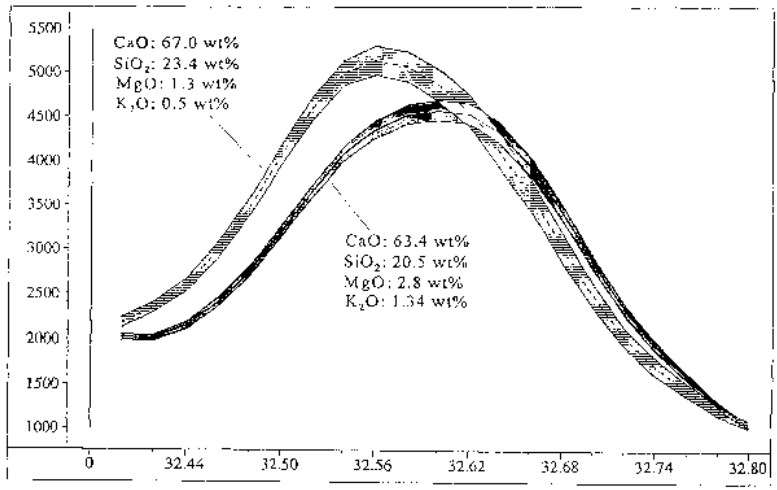


Figure 14. Changes in the profile A counts at $d = 2.74$ Å with changes in oxides variables.

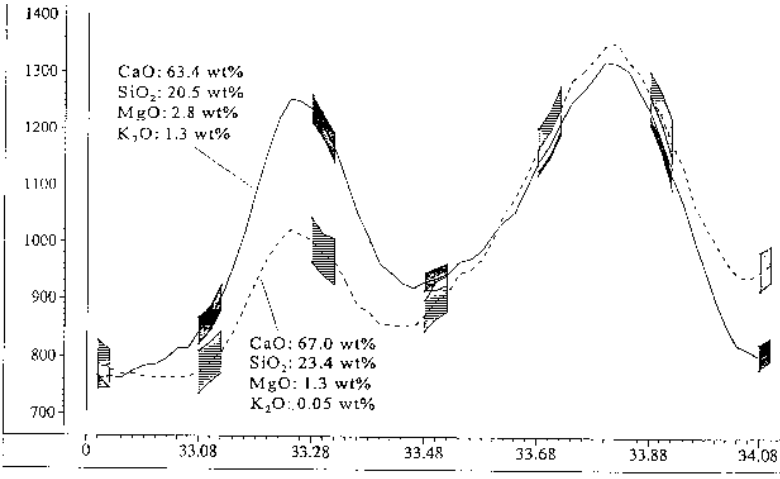


Figure 15. Changes in the profile B counts with simultaneous increases in CaO and SiO_2 and decreases in MgO and K_2O.

@Seismicisolation

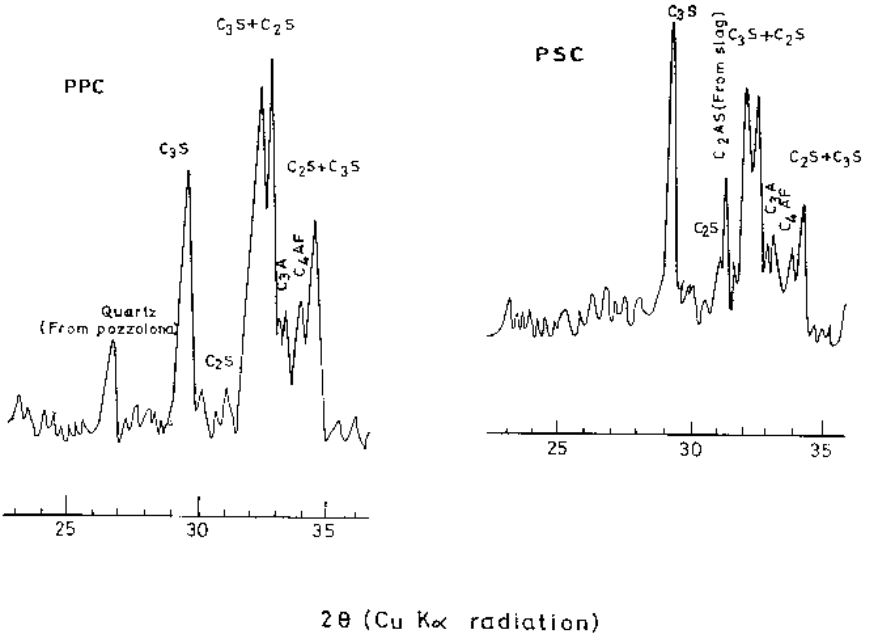


Figure 16. Typical XRD traces of commercially produced blended cements (16% pozzolana in PPC and 42% slag in PSC).

@Seismicisolation

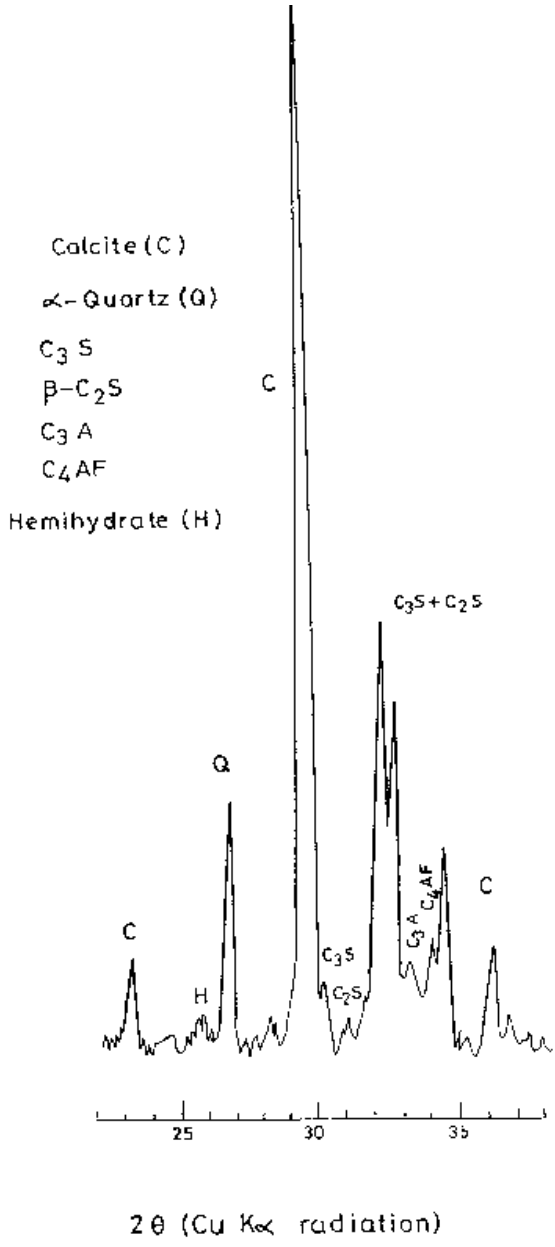


Figure 17. An illustrative XRD trace of a masonry cement.

@Seismicisolation

Another interesting study has recently been reported regarding the diffractometric estimation of granulated blast furnace slag content in the portland slag cement.[58] It has been claimed that the ratio of the pulse counts of slag cement samples at 2θ angles, 30.6° and 22.5°, has an almost linear relationship with the proportion of slag in the cement. Based on a set of reference samples containing slag from the same source as in the cement and ensuring that the glass content in the slag varies within a range of ± 5%, it is claimed that the slag content in a cement can be estimated in the range of 10–70% with an accuracy of ±1%.

5.6 Standardization of X-Ray Diffractometry for Quantitative Phase Analysis

A large number of studies have been carried out to evaluate the relative accuracy of quantitative XRD. Comparison has particularly been attempted to compare phase composition determined by microscopy, chemical analysis, and Bogue's method.[30][38][39][41] The results obtained by different methods showed substantial deviations from each other. Even in the '80s it was felt that x-ray diffraction analyses were not quite accurate for quantitative phase estimation.[59][60] Despite these findings, there was a progressive buildup of confidence that with the adoption of proper XRD methodology the major clinker phases can be determined with an absolute accuracy of 2–5% for alite and belite and 1–2% for aluminate and ferrite.

Since the achievement of this level of accuracy is not universal, the need for a standard procedure for quantitative phase analysis by XRD is being increasingly felt. In fact, an ASTM task force was formed in 1980 to investigate the state-of-the-art and to recommend a standardized method to the extent possible.[61] The preliminary efforts of the task force indicate the following.

1. The proportions of cubic C_3A (d = 0.4236 nm and d = 0.4083 nm), orthorhombic C_3A (d = 0.4210 nm), C_4AF (d = 0.3654 nm) and MgO (d = 0.2106 nm) in clinkers may be determined with reasonable precision (1.7%) by using the technique referred to in the above article.
2. A single synthesized phase may reasonably be used to represent the XRD pattern of that phase in a range of clinkers.

@Seismicisolation

3. The application of quantitative XRD methods to the silicate phases is likely to be more difficult due to the overlapping peaks and multiplicity of polymorphs.

The study still remains to be completed and the XRD method still continues to vary from one laboratory to another, depending on the material to be analyzed and the instrument to be used.

6.0 X-RAY DIFFRACTOMETRY OF HYDRATED CEMENT

In the hydration of cement, the chemical reactions that take place between anhydrous cement and water are generally complex in nature because of their multiphase nature and also for simultaneous effects of many variables. Without going into the details of these reactions, it may be relevant in the context of XRD studies to mention the following features of the reaction sequence and products, the understanding of which has come through studies spanning several decades.[62]–[67]

1 Since the clinker phases have different reaction sequences and rates, unreacted phases in different proportions coexist along with various reactants at different ages.

2. The silicate phases lead to the formation of CH and C-S-H, the latter being a generic name for amorphous or poorly crystalline calcium silicate hydrates.

3. The reactions of the aluminate and ferrite phases in the presence of gypsum lead to the early formation of AF_t (Al_2O_3-Fe_2O_3-tri) phases and later conversion to AF_m (Al_2O_3-Fe_2O_3-mono) phases. The most important AF_t phase is ettringite ($C_3A{\cdot}3C\bar{S}{\cdot}32H$) that forms during the early hydration of cement and later converts to monosulfate ($C_3A{\cdot}C\bar{S}{\cdot}12H$) belonging to AF_m family. Among other common phases mention may be made of C_2AH_8, C_4AH_{13} and C_3AH_6.

4. A large number of analytical techniques have been applied to study the above reaction products. More commonly applied techniques are quantitative XRD, measurement of non-evaporable matter, chemical

@Seismicisolation

shrinkage, heat of hydration, infrared spectroscopy, dielectric capacity measurement, etc. Despite certain limitations of the extensive applicability of XRD to the study of gel-like hydration products, this technique continues to be widely relied upon for a host of other potentials and advantages that are not available from the other investigation tools. Some of these features will be touched upon in the following sections.

6.1 Sample Preparation and XRD Study of Hydrated Specimens

The XRD studies of hydration products demand a very careful preparation of samples as the studies are related to discrete ages of hydration and the specimens may often interact with various other reactants in the atmosphere. The procedure generally followed in the author's laboratory comprises the following steps:

- To fill the hydrated blends in small plastic vials or bottles with tight lids and to store these vials under lime solution in order to protect the sample from carbonation.
- To remove the sample from the vial at a desired age and to submerge in isopropyl alcohol to stop hydration for at least 25 min.
- To wet grind the sample thereafter, in alcohol medium to a fineness level of about minus 200 mesh without allowing the sample to dry up, in order to avoid carbonation.
- To filter the slurry and to wash first with alcohol and then with diethyl ether.
- To load the dry sample into the metallic sample holder ensuring that there is no preferred orientation of crystal and that there is a smooth surface.
- To run the diffractogram at slow speed and to scan at lower angles because of the presence of the distinguishing peaks in that range.

Typical XRD patterns of neat cement paste on early age hydration are shown in Fig. 18. From such studies on pastes with w/c ratio in the range of 0.45–0.65 and hydration reactions occurring at temperature of 15–25°C, the ettringite phase appears at d-values of 9.73 Å and 5.61 Å and peaks intensify

@Seismicisolation

in a day's time. The peaks sometimes disappear, but mostly remain virtually unchanged up to 28 days. In case there is appearance of AF_m phase at the expense of ettringite or AF_t phase, new peaks are observed at 2.88 Å and 1.66 Å. Generally, the CH phase starts to show up within a day or so and progressively intensifies at *d*-values such as 4.90 Å, 2.63 Å, 2.28 Å, and dominates within a few days. The appearance of CH crystals is accompanied by a decrease in the amount of anhydrous clinker phase between 3.02 and 2.60 Å *d*-values. Sometimes, in exposed samples, the carbonation process is observed in the samples hydrated for, say, 3 days, with the appearance of monocarboaluminate hydrate and calcite which may increase with time.

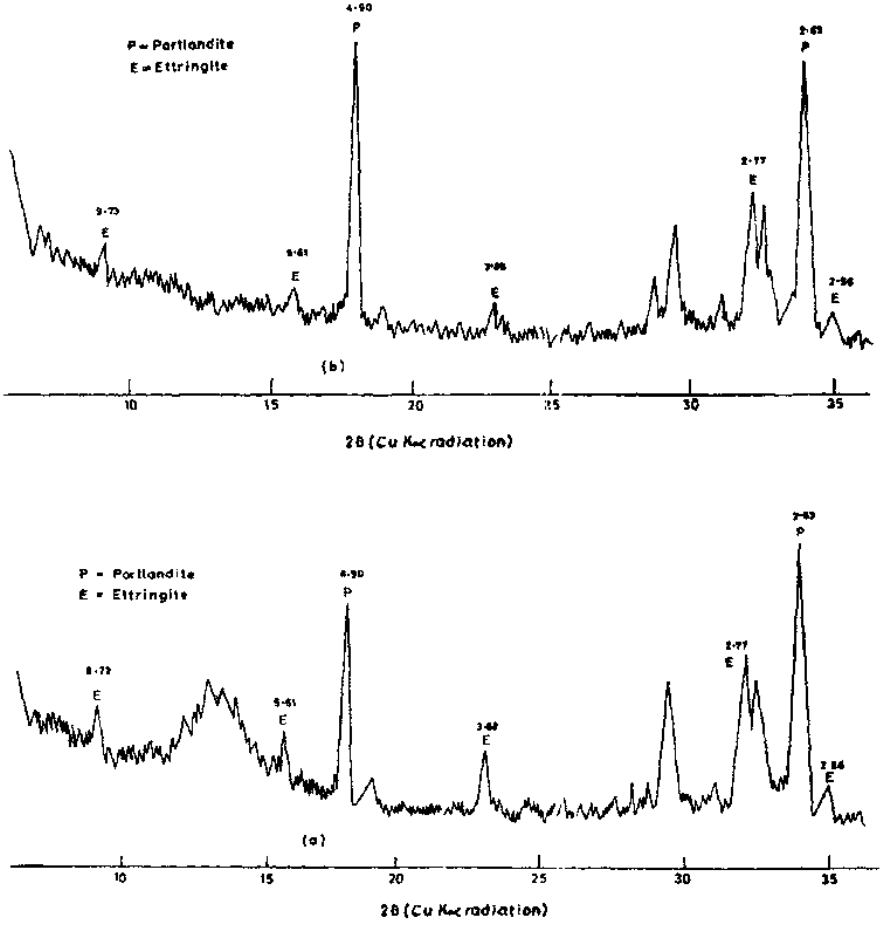


Figure 18. XRD pattern of hydrated OPC paste, *(a)* 1-day hydration, *(b)* 7-day hydration.

@Seismicisolation

It is assumed that, after a certain part of the Ca ions liberated in the first stages of paste reaction have crystallized out as stacks of ordinary CH layers in the capillary spaces, the rest of Ca ions lead to the formation of C-S-H hydration products of Ca/Si ratio between 1.5–2.0, which form ill-crystallized structure elements around the disappearing anhydrous nuclei in ionic arrangements strongly resembling that of CH.[67] The C-S-H cryptocrystalline phase shows a diffuse band at 2.7–3.1 Å coupled with a sharp band at 1.82 Å.

Many crystalline calcium silicate hydrates are known, but most of them are formed under hydrothermal conditions. The x-ray diffractometric characteristics of these phases, which include such calcium silicate hydrates as 1.4-nm tobermorite ($C_5S_6H_9$ approximately), 1.1-nm tobermorite, jennite ($C_9S_6H_{11}$), C-S-H (I) and C-S-H (II) have not been covered in the present discussions. However, one may refer to Ref. 32 for a reasonable compilation of the available x-ray data.

6.2 Small Angle X-Ray Scattering

The physical phenomena of small angle x-ray scattering reveals information on the areas of surfaces between regions of markedly different electron density. This approach of investigation has been adopted by some investigators to study the layered structure of the calcium silicate hydrates in the cement system.

In a hydration study of the C_3S paste[68] it was shown that the scattering intensity could be represented by:

Eq. (17) $$j(s)s^3 = a + bs^2$$

where $j(s)$ is the scattered density, s is a function of the scattering angle and the x-ray wavelength, a, is related to the interface surface, and b is related to the interlayer distance.

The results showed that at the initial stages both a and b increase synchronously. After about 50 hours of hydration, a continued to increase slowly whereas b remained nearly constant up to 250 hours. The results had been interpreted as a continued increase of the hydration products with a constant interlayer separation. The authors attributed the near-constant value of b to a gradual unsaturation of the pastes probably due to the autogenous shrinkage.

Further information of the interlayer characteristics came from the small-angle x-ray scattering results presented in Ref. 69. Some relevant data are shown in Table 6.

@Seismicisolation

Table 6. Surface Areas of Portland Cement, 86% Hydrated at w/c = 0.4

Treatment of sample	Surface area in m^2/g ignited sample	
	After preliminary treatment	After re-saturation
Saturated	708	708
Equilibrated at 52% H	330	—
P-dried	272	697
D-dried	224	707
Oven dried at 105°C	180	651

P-drying means drying to 8×10^{-4} mm pressure
D-drying means drying to 5×10^{-4} mm pressure

From Table 6 it is evident that drying causes a reversible loss of surface. The higher the degree of drying, the greater is the loss. D-drying reduced the surface area to one-third of the saturated sample. On re-saturation the surface area is regained. This reversible loss of surface could be interpreted as due to a collapse and regeneration of the interlayer separation.

However, no attention seems to have been paid on the loss of surface associated with the equilibration to 52% RH. A sample at this stage is expected to have its interlayer water as well as surface adsorbed water.[70] From the actual measurement of scattered intensity one may find that nearly half of the measured x-ray intensity is lost due to the removal of free water. This loss of scattered intensity will mean that either there is an electron density difference between surface adsorbed water and free water or the collapsing of interlayer separation starts at about 52% RH. Although at present it is not clear how this loss of x-ray intensity at 52% RH may affect the interpretation of earlier results it is not expected to alter the inference that C-S-H is a layer structured material.

6.3 Application of Certain Quantitative Methods to Cement Substitute Materials

The utilization of fly ash, silica fume, and ground granulated blast furnace slag as replacement materials for cement has received quite a wide acceptance all over the world. Therefore, it is often necessary to understand

@Seismicisolation

the behavior of such cement substitute materials in hydrated systems and the factors that control such behavior. X-ray diffractometry has provided reliable avenues to quantify such properties and behavior.

A selective dissolution method using a picric acid-methanol-water solution coupled with x-ray diffraction and energy-dispersive x-ray analysis has been reported to be effective in removing reacted cementitious products, leaving a residue of unhydrated pozzolanas in cement-fly ash or cement-silica fume systems.[71]

Since the glass content in slags and fly ashes is an index of their reactivity, the quantitative determination of the glass content in these materials has received the attention of the scientific community.

In a sample containing glassy and crystalline phases, the weight fraction of each crystalline phase can be determined by the internal standard method. If the major crystalline phases are known, the glass content can be found out by difference after estimating the sum-total of the crystalline phases. Following this approach, with CaF_2 as the internal standard and after identifying the presence of quartz, mullite, magnetite, and hematite in fly ashes, the glass contents of eight different fly ashes were determined in the range of 53.4% to 94.5%. Similarly, for two slags with melilite as the only crystalline phase, the slag contents were determined to be 88.1 and 88.3%.[72] The method was found to be time consuming, particularly when the samples contained multiple crystalline phases. Further, the errors in quantitative determination of those multiple phases were also likely to add to the final errors in the determination of glass content. Notwithstanding this limitation, this procedure for glass determination in cement substitute materials appears adequate for all practical purposes.

7.0 X-RAY DIFFRACTOMETRY IN CONCRETE CHEMISTRY

It is well known that the major use of cement is through the route of concrete which, as a composite product, has a more complex character than what is normally realized. The microstructural differences observed in the cement paste-aggregate interface as distinct from the bulk cement paste, formation of new compounds on account of exposure of concrete to different aggressive environments, characteristic patterns in the natural deterioration of concrete, etc., have compelled the extension of XRD to

@Seismicisolation

investigations relating to the production, service, and durability of concrete. A few applications of XRD to concrete chemistry are described here in an illustrative manner.

7.1 Cement Paste Aggregate Interface

Although the cement paste-aggregate interface has continued to be a subject of extensive studies by the concrete technologists for several decades, recently an investigation has been reported[73] comparing the interface characteristics obtained through conventional concrete mixing on one hand, and through a modified system of concrete mixing involving addition of water in two stages into the mixer, on the other. In the preparation of concrete by both the mixing methods, glass slides were used as pseudo-aggregates in order to obtain standardized surfaces for both the techniques which can be easily examined by XRD to reveal the differences between them. The glass slides with cement paste on either side were picked and removed from the mixes and were laid in small airtight plastic tanks for twenty-four hours before being transferred to curing tanks for retention up to the required age of examination. The glass slides were cut into small pieces (2 cm^2) by diamond saw. The flat bond surface was removed from these small samples onto aluminum holders (1.5 cm^2) for XRD analysis. The hydration products were determined for both the surfaces—one bonded with the glass and the other on the reverse side. The determinations were for 1 and 28 days. Repetitive measurements were made. Quantitative phase analysis was also attempted. The XRD patterns of 28 day old samples revealed the high concentration of well crystallized CH layer at the interface in the two stage mixing, demonstrated by the higher peak intensity around 21° two-theta, virtual disappearance of anhydrous silicate phases, and higher proportion of C-S-H phase as seen from 33° and 59° two-theta positions.

7.2 Alkali-Silica Reaction

The occurrence of reactive aggregate in concrete leading to its deterioration due to alkali-silica reaction (ASR) is quite well known. Although many attempts have been made to understand the factors leading to the occurrence of ASR, its prediction is still very imprecise due to lack of appreciation of the factors that contribute to the completeness of silica

@Seismicisolation

dissolution and resultant expansion of concrete. Crystal deformation, grain size, nature of grain boundaries, presence of fluid inclusions, etc., are known to contribute to a reasonable estimate of probability of ASR in a pH medium of 12–14. Since these are reflections of the intrinsic crystallinity of the silica form, a study has been carried out to determine the Crystallinity Index (CI) of silica by the XRD technique.[74] The method is based on the measurement of the relative heights of the (2132)α1 peak and (2132)α2 peak occurring between the 2θ angles of 67° to 68° (Fig. 19).

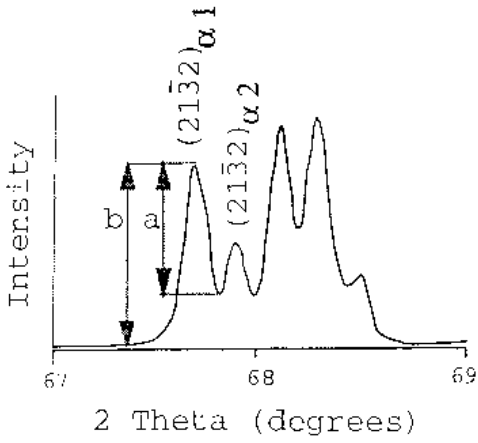


Figure 19. XRD peaks used to calculate crystallinity index.

A value of zero is assigned when the diffractogram is a rounded hump representing amorphous or weakly crystalline character of the aggregate. The relationship of mortar bar expansion with CI of various forms of silica is illustrated in Fig. 20. The regression line shows a moderate correlation between decreasing expansion and increasing crystallinity ($R^2 = 0.77$) as determined by XRD.

@Seismicisolation

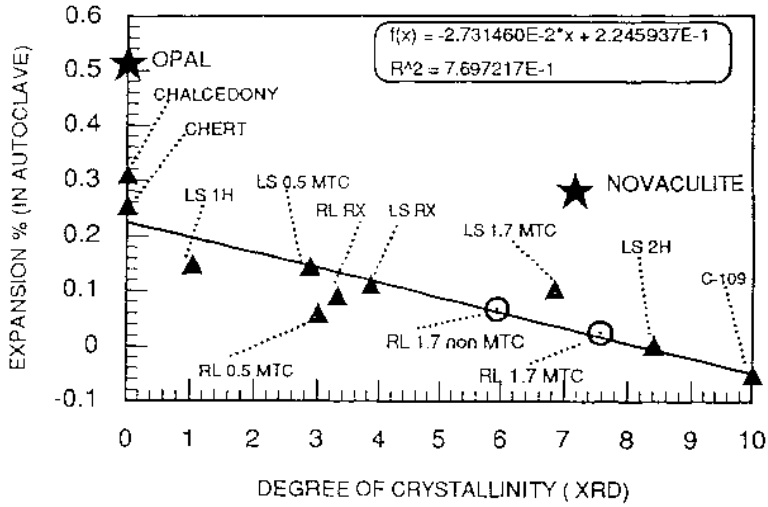


Figure 20. Relationship between average percent expansion of autoclaved motor bars and XRD crystallinity index.

7.3 Sulfate Minerals

There are three important sulfate minerals that form within concretes and mortars, viz., ettringite ($C_3A{\cdot}3C\bar{S}{\cdot}31H$), thaumasite ($CS{\cdot}CaCO_3{\cdot}C\bar{S}15H$), and gypsum ($C\bar{S}2H$). The quantitative assessment of the above potentially expansive sulfate minerals in concrete has been attempted and reported in Ref. 75. The method adopted was based on the use of Boehmite as the internal standard at 14.48° two-theta, which is sufficiently close to and does not overlap with the main sulfate peaks. The average peak positions for each of the 100% intensity lines were 9.08° for ettringite, 9.14° for thaumasite, and 11.69° for gypsum. Two additional peaks, one for ettringite at 15.78° and one for thaumasite at 16.00°, were also included in the data set. This was to overcome the problem of poor resolution of peaks at 9.08° and 9.14° two-theta positions (Fig. 21).

The calibration method was found to be acceptable for all of the three sulfate minerals as the results obtained from the standard samples comprising mixtures of known composition fell within the standard deviation limits calculated from the calibration curves (Table 7).

This quantitative phase analysis method was applied to the study of laboratory prepared concrete cubes undergoing sulfate attack.

@Seismicisolation

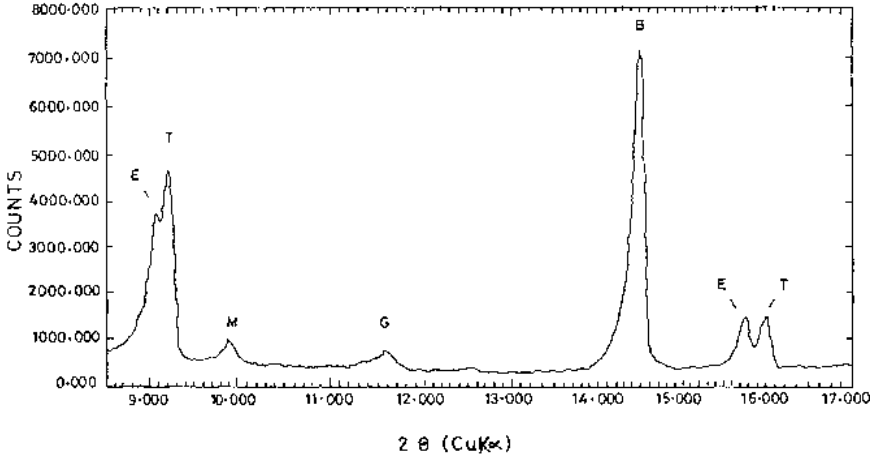


Figure 21. XRD trace of a mix of sulfate phases with an internal standard. (*E* = ettringite, *T* = thaumasite, *M* = calcium monosulfate hydrate, *G* = gypsum, *B* = Boehmite.)

Table 7. Comparison of Actual and Calculated Proportions of Sulfate Phases[75]

Standard samples	Ettringite		Thaumasite	
	Actual	Calculated	Actual	Calculated
1	1	1.3	1	1.1
2	2	2.1	2	2.2
3	5	5.1	5	5.0
4	5	5.7	10	11.4
5	10	10.9	5	5.9
6	10	11.9	10	10.5

It may be relevant to mention here another attempt made to quantify the formation of ettringite during the process of setting and hardening of cements.[76] In this method α-CaSO4·1/2H_2O was taken as the internal standard and XRD peaks of 0.601 and 0.5614 nm for the internal standard and ettringite, respectively, were considered. The closeness of peaks made it possible to use a small two-theta range of 14°–16°. It was revealed that different calibration lines were needed for different matrices, but they were all linear and showed a high degree of correlation. Even low quantities of ettringite (>0.63%) could be detected.

@Seismicisolation

7.4 Other Studies of Concrete Damages

In concrete chemistry it is quite well established that apart from sulfate attack and occurrence of ASR, the formation of chloroaluminate hydrate phase or the occurrence of alkali carbonate reaction due to environmental conditions often lead to concrete damages. The diagnosis of such damages is considerably facilitated by the XRD technique. According to the study reported in Ref. 77, the cement pastes attacked by $CaCl_2$ and analyzed by the XRD technique show a line that can be ascribed to monochloroaluminate hydrate ($C_3A{\cdot}CaCl_2{\cdot}10H_2O$). When the samples are moist, other lines characteristic of the calcium oxychloride ($3CaO{\cdot}CaCl_2{\cdot}15H_2O$) are recorded, which disappear, when the samples are dried. It has also been shown that when $3CaO{\cdot}CaCl_2{\cdot}15H_2O$ is obtained from the reaction of $Ca(OH)_2$ and Cl_2 in aqueous solution the compound is transformed into another oxychloride $CaO{\cdot}CaCl_2{\cdot}2H_2O$ which is not obtained in the dried cement pastes.

In the context of alkali-carbonate reactions, a mention may be made of the investigations of several concrete and masonry structures in Sweden in which XRD was applied along with SEM and energy-dispersive x-ray analysis.[78] The occurrence of carbonation, appearance of alkali sulfate salts causing internal and external efflorescence, etc., were revealed through such studies.

8.0 XRD IN MISCELLANEOUS CEMENTITIOUS SYSTEMS

Due to the versatility of XRD as a tool of investigation and characterization its application extends much beyond the defined systems of portland cement pastes and concrete. Recent examples are the uses of XRD for the characterization of high alumina cements,[79] expansive cement paste based on high-alumina cement,[80] study of cement-solidified organic wastes,[81] etc.

In the course of a variety of investigations pertaining to the synthesis and application of different types of cement in the author's laboratory, XRD patterns have been obtained for calcium aluminate cement, calcium sulfoaluminate cement, calcium fluoroaluminate cement, expansive K-type clinker, etc. Some of these patterns are reproduced in Fig. 22 and the characteristic peaks for the important phases are listed in Table 8 for ready reference.

@Seismicisolation

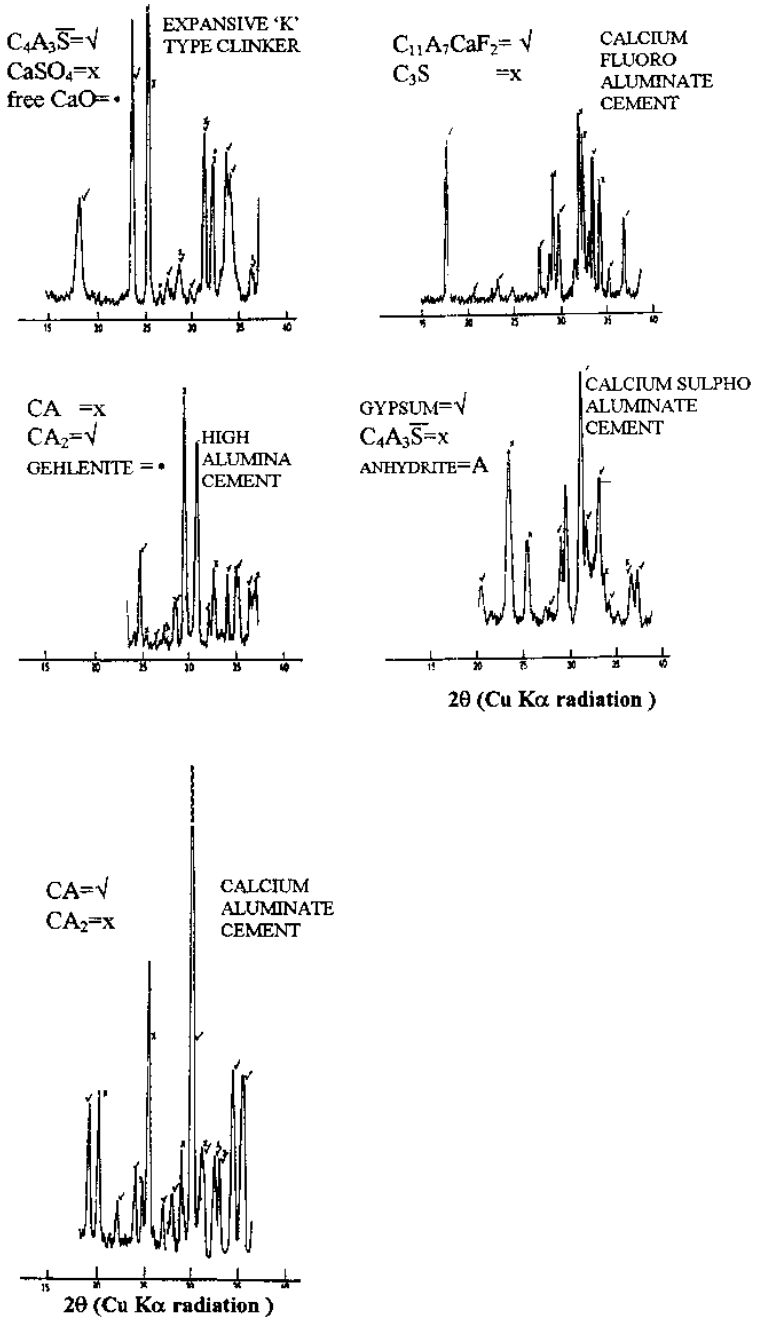


Figure 22. XRD patterns of miscellaneous cementitious systems.

@Seismicisolation

Table 8. Characteristic XRD Lines of Non-Silicate Phases Occurring in Cementitious Systems

Mineral/Phase	*d*Å	*hkl*	I/I_1
$CaO{\cdot}Al_2O_3$	4.67	112, $11\bar{2}$	25
	2.971	123, $12\bar{3}$	100
	2.966	220	100
	2.518	$30\bar{3}$	35
$CaO{\cdot}2Al_2O_3$	4.44	020	55
	3.60	220	20
	3.50	$31\bar{1}$	100
	2.599	$11\bar{2}$	60
$12CaO{\cdot}7Al_2O_3$	4.89	211	95
	2.988	400	45
	2.680	420	100
	2.447	422	50
	1.945	611	30
$11CaO{\cdot}7Al_2O_3{\cdot}CaF_2$	6.87	—	20
	3.24	321	100
	3.02	400	60
	2.33	510	40
	1.70	710	35
$3CaO{\cdot}3Al_2O_3{\cdot}CaSO_4$	4.92	321	6
	3.76	422	100
	2.65	444	25
	2.17	822, 644	20
$2CaO{\cdot}Al_2O_3{\cdot}SiO_2$	3.72	111	30
	2.857	211	100
	1.819	330	55
	1.7608	312	45

@Seismicisolation

9.0 CONCLUSIONS

Clinker, cement, hydrated pastes, mortar, and concrete, are multicomponent heterogenous systems with widely varying microstructure ranging from nanometer to centimeter scale. The characterization of these systems is indispensable for both the end objectives of manufacture and application. Further, the assessment of service performance and failure analysis of cement mortar pastes and concrete are also dependent on proper characterization. Among the various bulk and microscopic characterization techniques, the x-ray powder diffractometry has turned out to be universal and reliable. From simple qualitative identification of phases in such multicomponent systems, the technique has been extended to cover quantitative phase analysis, determination of crystallinity of phases, identification of reaction products, etc. Further, the techniques of quantitative phase analysis have been refined by introducing a major change from intensity-concentration relation of selected individual peaks to whole-pattern fitting. In the latter concept, further progress has been seen in applying the Rietveld technique as well as the WPPD method. All this has happened because of significant development of software devoted to x-ray diffractometry on one hand and the basic hardware on the other. The PC-based software developments have offered unexpected speed of operation without the sacrifice of accuracy. The hardware developments have resulted in high levels of flexibility and precision. The use of microfocus diffractometer has now opened up certain opportunities of characterization which could not be contemplated earlier. Attempts are being made to combine the techniques of photon-induced x-ray fluorescence and x-ray microdiffraction into one instrument to ensure the coincidence of the analyzed areas and to take full advantage of the smaller beam sizes. Similarly, the development of fast dynamic real-time diffraction analysis both for ambient and high temperature studies may facilitate the faster and real characterization of the reactions involved in cement and concrete chemistry. The future evolution of hardware and software in these directions will certainly expand the potential of XRD techniques much beyond what is considered feasible today.

@Seismicisolation

ACKNOWLEDGMENTS

The author gratefully acknowledges the help and encouragement received from Dr. S Chatterji of Denmark, Dr. W A Gutteridge of the UK, Building Research Establishment of the UK, British Cement Association and Portland Cement Association of the USA, apart from the colleagues of the Associated Cement Companies, Ltd., India, in the preparation of this chapter.

REFERENCES

1. Alexander, L. E., Forty Years of Quantitative Diffraction Analysis, *Advances in X-Ray Analysis*, (H. W. McMurdie, et al., eds.), 20:1–13, Plenum Press, New York (1977)
2. Clark, G. L., and Reynolds, D. H., Quantitative Analysis of Mine Dusts, *Ind. Eng. Chem., Anal. Ed.*, 8:36–40 (1936)
3. Friedman, H., Geiger Counter Spectrometer for Industrial Research, *Electronics*, 18:132–137 (1945)
4. Alexander, L. E., and Klug, H. P., Basic Aspects of X-Ray Absorption in Quantitative Diffraction Analysis of Powder Mixtures, *Anal. Chem.*, 20:886–889 (1948)
5. Leroux, J., Lennox, D. H., and Kay, K., Direct Quantitative X-Ray Analysis by Diffraction-Absorption Technique, *Anal. Chem.*, 25:740–743 (1953)
6. Lennox, D. H., Monochromatic Diffraction-Absorption Techniques for Direct Quantitative X-Ray Analysis, *Anal. Chem*., 29:766 (1957)
7. Ergun, S., and Tiensun, V. H., Determination of X-Ray Absorption Coefficients of Inhomogeneous Materials, *J. Appl. Phys*., 29:946–949 (1958)
8. Copeland, L. E., and Bragg, R. H., Quantitative X-Ray Diffraction Analysis, *Anal. Chem*. 30:196–208 (1958)
9. Klug, H. P., and Alexander, L. E., *X-Ray Diffraction Procedures*, 2nd Ed., p. 554, Wiley, New York (1974)
10. Chung, F. H., A New X-Ray Diffraction Method for Quantitative Multicomponent Analysis, *Advances in X-Ray Analysis*, (C. L. Grant, et al., eds.), 17:106–115, Plenum Press, New York (1974)

@Seismicisolation

11. Chung, F. H., Quantitative Interpretation of X-Ray Diffraction Patterns of Mixtures, I. Matrix-Flushing Methods for Quantitative Multicomponent Analysis, *J. Appl. Cryst*., 7:519–525 (1974)
12. Uchikawa, H., Advances in Physico-Chemical Characterization and Quality Control Techniques for Cement and Concrete, *General Report, 9th ICCC*, New Delhi (1992)
13. Yellepeddi, R., and Bonvin, D., Applications and Perspectives for the use of an Integrated XRF-XRD Spectrometer, *World Cement*, pp. 54–59, (Nov., 1995)
14. Warks, J. S., Riley, D., Woolsey, N. C., Keihn, G., and Whitlock, R. R., Direct Measurements of Compressive and Tensile Strain During Shock Breakout by Use of Subnanosecond X-Ray Diffraction, *J. Appl. Phys*., 68:4531–4534 (1990)
15. Ferrell, R. E., Jr., Applicability of Energy-Dispersive X-Ray Powder Diffractometry to Determinative Mineralogy, *Amer. Mineral*., 56:1822–1831 (1971)
16. Jenkins, R., Impact of the Personal Computer on X-Ray Analysis: Historical Perspective 1960–1990, *Advances in X-Ray Analysis*, (J. V. Gilfrich, et al., eds.), 37:1–6, Plenum Press, New York (1994)
17. Johnson, Q., Software for XRD, *Advances in X-Ray Analysis* (J. V. Gilfrich, et al., eds.), 37:7–12, Plenum Press, New York (1994)
18. Louër, M., and Louër, D., The Use of PCs for Ab Initio Structure Determination from Powder Diffraction Data, *Advances in X-Ray Analysis* (J. V. Gilfrich, et al., eds.), 37:21–25 (1994)
19. Nusinovici, J., and Winter, M. J., DIFFRACT-AT SEARCH: Search/Match Using Full Traces as Input, *Advances in X-Ray Analysis* (J. V. Gilfrich, et al., eds.), 37:59–66 (1994)
20. Smith, D. K., and Johnson, G. G., Jr., A Full Trace Database for the Analysis of Clay Minerals, *Advances in X-Ray Analysis* (P. Predecki, et al., eds.), 38:117–125 (1995)
21. Rietveld, H. M., A Profile Refinement Method for Nuclear and Magnetic Structures, J. *Appl. Cryst*., 2:65–71 (1969)
22. Pawley, G. S., Unit Cell Refinement from Powder Diffraction Scans, *J. Appl. Cryst*., 14:357–361 (1981)
23. Toraya, H., Applications of Whole-Powder-Pattern Fitting Technique in Materials Characterization, *Advances in X-Ray Analysis*, (J. V. Gilfrich, et al., eds.), 37:37–47 (1994)
24. Toraya, H., Quantitative Phase Analysis Using the Whole-Powder-Pattern Decomposition Method: II. Solution Using External Standard Materials, *Advances in X-Ray Analysis* (P. Predecki, et al., eds.), 38:69–73 (1995)

@Seismicisolation

25. Henry, N. F. M., Lipson, H., and Wooster, W. A., *The Interpretation of X-Ray Diffraction Photographs*, p. 32, Macmillan and Co. Ltd., London (1960)
26. Ramachandran, V. S., Beaudoin, J. J., and Feldman, R. F., Physico-Chemical Studies of $3CaO{\cdot}Al_2O_3$, $4CaO{\cdot}Al_2O_3{\cdot}Fe_2O_3$ and $CaO{\cdot}Al_2O_3$ Hydrated at Low Water: Solid Ratios, *Il Cemento*, 89:3–16 (1992)
27. Chatterjee, S., A Discussion of the Paper "The Kinetic of Ettringite Formation" by P. W. Brown and P. Lacroix, *Cem. Con. Res.*, 19:669–70 (1991)
28. Harrington, E. A., X-Ray Diffraction Measurements on Some of the Pure Components Concerned in the Study of Portland Cement, *Amer. J. Sci*., 13, p. 78 (1927)
29. Hansen, W. C., Further Studies on Portland Cement Compounds by the X-Ray Diffraction Method, *J. Amer. Ceram. Soc.*, 11(2):68–78 (1928)
30. Bronmiller, L. T., and Bogue, R. H., The X-Ray Method Applied to a Study of the Constitution of Portland Cement, Bureau of Standards, *J. Research*, Vol. 3, Research Paper No. 233 (1930)
31. Regourd, M., and Guinier, A., The Crystal Chemistry of the Constituents of Portland Cement Clinker, *Principal Paper, 6th ICCC*, Moscow (1974)
32. Taylor, H. F. W., *Cement Chemistry*, Academic Press, London (1990)
33. Klemm, W. A., and Skalny, J., Selective Dissolution of Clinker Minerals and Its Application, Martin Marietta Laboratories, *MML. TR 77–32*, pp. 1–30 (1977)
34. Gutteridge, W. A., On the Dissolution of the Interstitial Phases in Portland Cement, *Cem. Con. Res*., 9:319–324 (1979)
35. Odler, I., and Abdul-Marula, S., Possibilities for the Separation of the Individual Constituents of Portland Cement by Means of Selective Solvents, *ZKG*, 10:504–507 (1979)
36. Patino, G., Viceros, A., and Avila, M. I., Procedures for Quantitative X-Ray Diffraction Portland Cement Clinker Analysis, *Proc. 17th Inter. Conf. Cem. Micros*., pp. 71–82 (1995)
37. Saini, A., and Giuliani, N., XRD Analysis of Aluminate and Aluminoferrite Phases on the Selective Extraction Clinker Residue by Using a Profile Fitting Program, *Proc. 16th Inter. Conf. Cem. Micros*., pp. 24–43 (1994)
38. Brunauer, S., Copeland, L. E., Kantro, D. L., Weise, C. H., and Schultz, E. G., Quantitative Determination of the Four Major Phases in Portland Cement by X-Ray Analysis, *Proc. Am. Soc. Testing Materials*, 59:1091–1100 (1959)
39. Copeland, L. G., Brunauer, S., Kantro, D. L., Shulz, E. G., and Weise, G. H., Quantitative Determination of the Four Major Phases of Portland Cement by Combined X-Ray and Chemical Analysis, *Anal. Chem.*, 31:1521–1530 (1959)

@Seismicisolation

40. Copeland, L. E., and Bragg, R. H., Quantitative X-Ray Diffraction Analysis, *Anal. Chem*., 30:196–201 (1958)
41. Kantro, D. L., Copeland, L. E., Weisc, C. H., and Brunauer, S., Quantitative Determination of the Major Phases in Portland Cements by X-Ray Diffraction Methods, *J. PCA Res. Dev. Lab*., 6:20–40 (1964)
42. A Monograph on Routine Mineral Analysis of Portland Cement/Clinker by XRD Using an Unmixed Internal Standard, *Cement Research Institute of India*, New Delhi (1978)
43. Snyder, R. L., and Bish, D. L., Quantitative Analysis in Reviews in Mineralogy (D. L. Bish and J. E. Post, eds.), 20:101–149 (1989)
44. Gutteridge, W. A., Quantitative X-Ray Powder Diffraction in the Study of Some Cementive Materials, *Brit. Ceram. Proc.* No. 35:7–15 (1984)
45. Taylor, H. F. W., Use of Calculated X-Ray Powder Diffraction Patterns in the Quantitative Phase Analysis of Portland Cement or Clinker, *Ceram. Trans*., 16:185–98 (1991)
46. Stutzman, P. E., Pattern Fitting for Quantitative X-Ray Powder Diffraction Analysis of Portland Cement and Clinker, *Proc. 18th Inter. Conf. Cem. Micros*., pp. 10–20 (1996)
47. Mumme, W. G., Crystal Structure of Tricalcium Silicate from a Portland Cement Clinker and its Application to Quantitative XRD Analysis, *N. Jb. Miner. Mh*., 4:145–160 (1995)
48. Taylor, J. C., Zhu, Rui , and Aldridge, L. P., Simultaneous use of Observed and Standard Patterns in Quantitative XRD Analysis of Minerals by the Multiphase Rietveld Method: Application to Phase Quantitation of Mineral and Sands and Portland Cement, *Mater. Sci. Forum*, pp. 133–136 (1993)
49. Taylor, J. C., and Aldridge, L. P., Full Profile Rietveld Quantitative XRD Analysis of Portland Cement: Standard XRD Profiles for the Major Phase Tricalcium Silicate, *Powder Diffraction*, 3:138–144 (1993)
50. Moller, H., Standardless Quantitative Phase Analysis of Portland Cement Clinker, *World Cement*, 75–84 (Sept., 1995)
51. Neumauer, J., Kuzel, H. J., and Seiber, R., Rietveld Quantitative XRD Analysis of Portland Cement: II-Quantification of Synthetic and Technical Portland Cement Clinkers, *Proc. 18th Inter. Conf. Cem. Micros*., pp. 100–111 (1996)
52. Kuzel, H. J., Rietveld Quantitative XRD Analysis of Portland Cement: I-Theory and Application to the Hydration of C_3A in the Presence of Gypsum, *Proc. 18th Inter. Conf. Cem. Micros*., pp. 87–99 (1996)
53. Fröhlich, A., Quantitative Clinker Phase Analysis Using XRD, *Proc. VDZ Congress*, 212–215 (1993)
54. Beilmann, R., and Bruggemann, H., Quantitative XRD Clinker Analysis a Tool for Process Optimization and Cement Quality Control, *Ciments, Betons, Platres, Chaux*, 791:241–251 (1991)

@Seismicisolation

55. Goswami, G., Cement Quality Control System in the Coming Years - Application of XRD, *Cement Industry*, 89–94 (1992)
56. Goswami, G., Panigraphy, P. K., and Panda, J. D., Rapid Strength Prediction of Portland Slag Cement by X-Ray Diffractometry, *Proc. 16th Inter. Conf. Cem. Micros*., pp. 257–268 (1994)
57. Svinning, K., Bremseth, S. K., and Justnes, H., X-Ray Diffraction Studies on Variations in Microstructure in Portland Clinker Correlated to Variations in Production Conditions in the Kiln, *Proc. 18th Inter. Conf. Cem. Micros*., pp. 382–403 (1996)
58. Goswami, G., Panigraphy, P. K., and Panda, J. D., Estimation of Blast Furnace Slag in Blended Cement by X-Ray Diffractometry, *Adv. Cem. Res*., 8:67–71(1996)
59. Aldridge, L. P., Accuracy and Precision of Phase Analysis in Portland Cement by Bogue, Microscopic and X-Ray Diffraction Methods, *Cem. Conc. Res*., 12:381–398 (1982)
60. Aldridge, L. P., Accuracy and Precision of an X-Ray Diffraction Method for Analyzing Portland Cements, *Cem. Conc. Res*., 12:437–446 (1982)
61. Struble, L. J., Quantitative Phase Analysis of Clinker Using X-Ray Diffraction, *Cement, Concrete and Aggregates*, 13(2):97–102 (1991)
62. Kantro, D. L., Copeland, L. E., and Anderson, E. R., An X-Ray Diffraction Investigation of Hydrated Portland Cement Pastes, *Proc. Amer. Soc. Test. Matls*., 60:1020–1035 (1960)
63. Seligmann, P., and Greening, N. R., New Techniques for Temperature and Humidity Control in X-Ray Diffractometry, *J. PCA Res. Dev. Lab*., 4(2):2–9 (1962)
64. Seligmann, P., and Greening, N. R., Studies of the Early Hydration Reactions of Portland Cement by X-Ray Diffraction, *Highway Research Record*, No. 62:80–105 (1964)
65. Ludwig, U., Investigations on the Hydration Mechanism of Clinker Minerals, *Principal Paper, 6th ICC*, pp. 1–50, Moscow (1974)
66. Parrott, L. J., Geiker, M., Gutteridge, W. A., and Killoh, D., Monitoring Portland Cement Hydration: Comparison of Methods, *Cem. Conc. Res*., 20:919–926 (1990)
67. Grudemo, A., The Crypto-Crystalline Structure of C-S-H Gel in Cement Pastes Inferences from X-Ray Diffraction and Dielectric Capacitivity Data, *Cem. Con. Res*., 17:673–680 (1987)
68. Vollet, D., Craievich, A., and Regourd, M., Small-Angle X-Ray Scattering from Hydrating Tricalcium Silicate, J. *Amer. Ceram. Soc*., 67:315-318 (1984)
69. Winslow, D. N., and Diamond, S., Specific Surface and Hardened Portland Cement Paste as Determined by Small-Angle X-Ray Scattering, J. *Amer. Ceram. Soc*., 57:193–197 (1974)

@Seismicisolation

70. Ramachandran, V. S., Feldman, R. F., and Beaudoin, J. J., Concrete Science, pp. 1-89, Heydon, London (1981)

71. Shiqun Li, Roy, D. M., and Kumar, A., Quantitative Determination of Pozzolanas in Hydrated Systems of Cement or $Ca(OH)_2$ with Fly-Ash or Silica Fume, *Cem. Conc. Res*., 15:1079–1086 (1985)

72. Roode, M. V., Douglas, E., and Hemmings, R. T., X-Ray Diffraction Measurement of Glass Content in Fly Ashes and Slags, *Cem. Con. Res*., 17:183–197 (1987)

73. Tamimi, A. K., and Najeim, H. A., XRD and SEM Investigations of the Cement Paste-Aggregate Interface for Concrete Produced by Both the Conventional Mixing and a New Mixing, *Proc. 16th Inter. Conf. Cem. Micros*., pp. 354–368 (1994)

74. Thomson, M. L., Grattan-Bellew, P. E., and White J. C., Application of Microscopic and XRD Techniques to Investigate Alkali-Silica Reactivity Potential of Rocks and Minerals, *Proc. 16th Inter. Conf. Cem. Micros.*, pp. 174–192 (1994)

75. Crammond, N. J., Quantitative X-Ray Diffraction Analysis of Ettringite, Thaumasite and Gypsum in Concretes and Mortars, *Cem. Conc. Res*., 15:431–441 (1985)

76. Ludwig, U., and Rudiger, I, Quantitative Determination of Ettringite in Cement Pastes, Mortars and Concretes, *ZKG Int.*, Ed. B, 46:150–153 (1993)

77. Monosi, S., and Collepardi, M., Research on $3CaO.CaCl_2.15H_2O$ Identified in Concretes Damaged by $CaCl_2$ Attack, *IL Cemento*, 87:3–8 (1990)

78. Sarkar, S. L., and Chandra, M. R., Microstructural Investigations of Natural Deterioration of Building Materials in Gothenburg, Sweden, *Materials and Structures, Research and Testing*, 25(151):429–435, RILEM, Paris (1992)

79. Sawkow, J., Investigation of the Phase Constitutions and Service Properties of High-Alumina Refractory Cements, *ZKG*, 46:275–281 (1993)

80. Yan Fu, Sheikh, S. A., and Hooton, R. D., Microstructure of Highly Expansive Cement Pastes, *ACI Materials J*., 91:46–53 (1994)

81. Vipulanandan, C., and Krishnan, S., XRD Analysis and Leachability of Solidified Phenol-Cement Mixtures, *Cem. Con. Res*., 23:792–802 (1993)

@Seismicisolation

9

Rheology

Leslie J. Struble and Xihuang Ji

1.0 INTRODUCTION

The rheological behavior of fresh cement paste and concrete is a topic of considerable interest. Fresh concrete is a fluid material and its rheological behavior affects or even limits the ways it can be processed, therefore, measurement and control of rheological parameters are very important in the production of quality concrete. *Slump*, of course, is a rheological measurement, but slump only describes a part of the behavior. More importantly, slump is an empirical measure; it cannot be compared with other rheological measures. Other measures of concrete workability exist, but they are less common and share the same drawbacks. If concrete technology is going to advance, it is important to apply more basic principles of rheology. Much that is known about the flow behavior of concentrated suspensions can help us measure and understand the behavior of fresh concrete.

The objective of this chapter is to present recent developments in the application of rheological principles to fresh cement paste and concrete. It covers both *rheology* (the study and understanding of flow behavior) and *rheometry* (the measurement of flow behavior).

@Seismicisolation

2.0 BACKGROUND

Rheology is a well established area of study for a wide range of materials. It is often included in textbooks dealing with chemistry or with fluid mechanics. An excellent introductory treatment of rheology is given by Barnes, et al.[1] A more fundamental treatment of colloid chemistry, including rheology, is given by Hunter.[2] Finally, Tattersall, and Banfill provide a thorough review and discussion of concrete rheology, though now somewhat dated.[3] Much of the information in this chapter is based on these books.

Rheology is defined as the study of flow behavior. It is normally applied to fluid materials (or materials that exhibit a time-dependent response to stress). Flow is typically measured using shear and the shear parameters of stress (τ) and strain rate ($\dot{\gamma}$) are calculated from measurements of torque and flow rate. Viscosity (η) is defined as $\eta = \tau/\dot{\gamma}$. This is more precisely called apparent viscosity—there are other ways to define viscosity (e.g., plastic viscosity, the slope of stress versus strain rate for a plastic material, as discussed below, and differential viscosity, the slope of the curve relating stress and strain rate) so it is important to identify the specific type of viscosity when reporting results.

Several types of flow behavior are generally recognized (Fig. 1). The simplest is Newtonian behavior, with a linear relationship between stress and strain rate and zero stress at zero strain rate. This is the ideal fluid behavior, analogous to Hookean behavior in a solid. Many fluids show plastic behavior (also called Bingham), in which flow only initiates above some level of stress (called the *yield stress*), and once flow initiates the relationship between stress and strain rate is linear. Another common behavior is pseudoplastic (or *shear thinning*), in which viscosity decreases as strain rate increases. Occasionally materials show thickening behavior, but this is not common for suspensions.

3.0 SUSPENSIONS

Because suspensions of solid particles in a liquid generally behave as a fluid, it is often useful to characterize their rheological behavior. Two key factors affect this behavior, the volume fraction of solid particles in the suspension and the extent to which the particles are agglomerated or flocculated. Increasing the volume fraction of solids (ϕ) causes a considerable

@Seismicisolation

increase in viscosity. The effect of solids volume fraction on viscosity was recognized by Einstein, who proposed the relationship

Eq. (1) $$\eta = \eta_c(1 - 2.5\phi)$$

where η is the viscosity of the suspension and η_c is the viscosity of the fluid phase. However, it was later realized that this equation only applies at quite low volume fractions. As the volume fraction is increased above a few percent, viscosity increases progressively from that predicted by Eq. 1. Several equations have been proposed to better describe the full relationship between volume fraction and viscosity, and one used extensively in colloidal suspensions was proposed by Krieger and Dougherty:

Eq. (2) $$\eta = \eta_c\left(1 - \frac{\phi}{\phi_m}\right)^{-[\eta]\phi_m}$$

where ϕ_m is the maximum possible volume fraction for the particular assemblage of particles. The maximum volume fraction has a value of 65% for randomly close-packed spheres. The other parameter, $[\eta]$, is intrinsic viscosity, defined as:

Eq. (3) $$[\eta] = \lim_{\phi \to 0} \frac{\eta/\eta_c - 1}{\phi}$$

The intrinsic viscosity is 2.5 for spherical particles and higher for non-equant shapes. Eq. (2) correctly predicts the substantial increase in viscosity observed as $\phi \to \phi_m$.

The other factor affecting flow behavior is the extent to which particles are flocculated or dispersed. Flocculation is especially important for colloidal particles (i.e., particles smaller than 1 μm in diameter) which may flocculate spontaneously. Flocculated particles either form discrete aggregates or a gel (a continuous three-dimensional network), as shown in Fig. 2. The forces are often fairly weak and easily broken by shear, so enough stress can be applied to cause disruption of the flocculated network such that the suspension begins to flow. The stress at which such a breakdown occurs is called the yield stress. Thus, flocculation produces plastic behavior with the yield stress reflecting the forces holding particles together.

@Seismicisolation

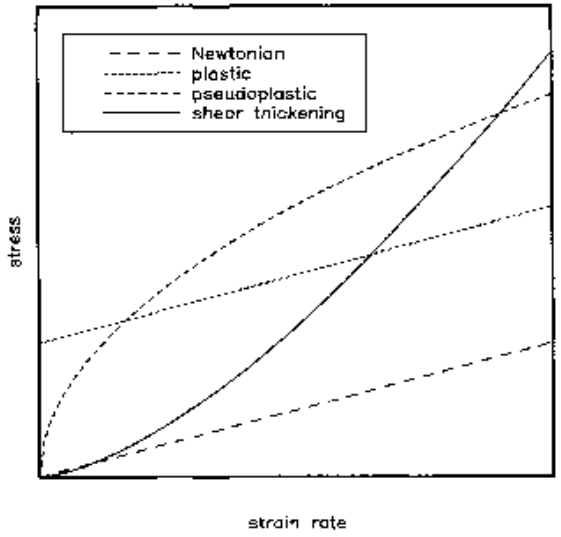


Figure 1. Types of rheological behavior.[26]

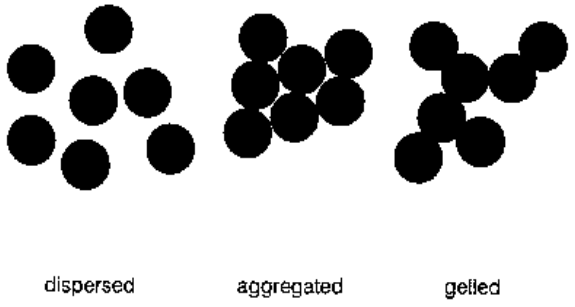


Figure 2. Suspension microstructures.(26)

Often this breakdown is not complete at the yield stress so the suspension is still somewhat flocculated even though it flows and this remaining flocculation is progressively disrupted as the strain rate is increased further. Such a situation produces pseudoplastic (shear thinning) behavior often accompanied by *thixotropy,* a progressive and reversible decrease in viscosity on application of a constant stress level. Even with

@Seismicisolation

pseudoplastic behavior it is common to refer to the *yield stress*, in this case determined by extrapolating back to zero from the more-or-less linear curve, high strain rates. Dispersed suspensions usually show Newtonian behavior, though at sufficiently high concentrations they develop pseudoplastic behavior with a modest yield stress. Thus, yield stress and viscosity depend on both concentration and degree of flocculation. In dispersed suspensions the yield stress increases with concentration; dispersed suspensions show plastic behavior at high concentrations because crowding restricts the ability of particles to flow. Because both high concentration and flocculation cause plastic or pseudoplastic behavior it can be difficult to differentiate between a flocculated suspension and a dispersed, but highly concentrated suspension, based solely on the flow curve.

Viscosity increases with concentration according to Eq. (2) (although the physical significance of the parameters exists only for a dispersed suspension). The yield stress also increases as concentration increases. This relationship can usually be described using a power law

Eq. (4) $$\tau_{ys} = \phi^{x}$$

with x lying between 2 and 4 (as reviewed in Ref. 9). The yield stress also depends in some general way on the force (interparticle potential) responsible for flocculation. For weakly flocculated suspensions, the effects of concentration and interparticle potential may be combined to give (Ref. 6, p. 485)

Eq. (5) $$\tau_{ys} = \frac{\phi^2}{a^2}\Phi'_{max}$$

where a is the particle radius and Φ'_{max} is the maximum interparticle force (maximum slope of the pair potential).

These are not the only factors that affect flow behavior. Fluids are sensitive to temperature. Barnes, et al., (Ref. 1, p. 13) note that liquids with higher viscosities generally have greater temperature sensitivity. Thus, water is not particularly sensitive to temperature though polymeric liquids can be quite sensitive. Viscosity generally increases with increasing pressure, but the changes are small at atmospheric pressures.

@Seismicisolation

4.0 RHEOLOGICAL BEHAVIOR OF CEMENT PASTE

4.1 Static Flow Behavior

The static flow technique measures the stress to achieve a given strain rate (or vice versa). This is usually done at a series of strain rates to provide a flow curve, a plot of stress as a function of strain rate. The rheological behavior may alternatively be presented as a plot of viscosity as a function of strain rate or stress.Examples are given in Fig. 3 for some of the constitutive models discussed below.

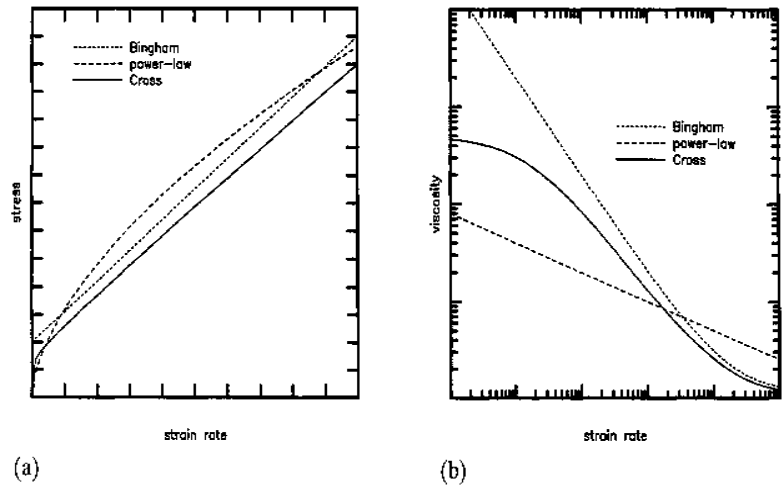


Figure 3. Constitutive behavior computed according to various models.

Typical static flow behavior of cement paste is shown in Fig. 4. When dispersed using a superplasticizer, cement paste shows Newtonian behavior at low concentrations and plastic behavior at high concentrations. The effect of water-to-cement ratio (w/c) on viscosity is well described by Eq. 2 (here in terms of concentration). The effect of w/c on yield stress is described by Eq. 4 (in terms of concentration).

Constitutive Models. A major thrust in rheological research has been the development of models that describe constitutive behavior (the relationship between stress and strain rate). With such models it may be possible to reduce flow behavior, especially the more complex non-Newtonian behaviors, to a few rheological parameters in order to more easily determine

@Seismicisolation

general relationships between flow behavior and materials aspects such as molecular structure, microstructure, and chemical composition. Several of these models have been applied to cement paste. Hunter[2] described these models in some detail, including their microscopic basis.

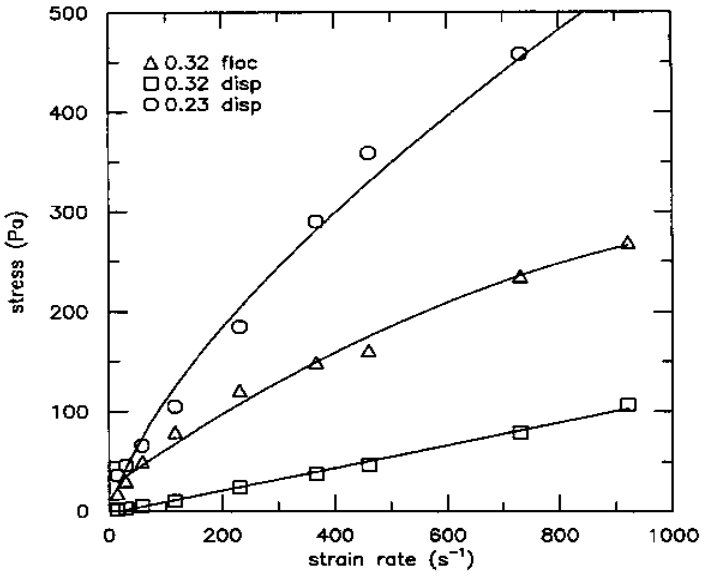


Figure 4. Flow behavior of cement paste showing changes due to high concentration and due to flocculation.[26]

The constitutive relationship for plastic behavior is the Bingham model:

Eq. (6) $$\tau = \tau_0 + \eta_{pl}\dot{\gamma}$$

A common model for pseudoplastic behavior is the power-law equation:

Eq. (7) $$\tau = K\dot{\gamma}^{n}$$

The Herschel-Bulkley model is a combination of the power-law equation with the Bingham model:

Eq. (8) $$\tau = \tau_o + K\dot{\gamma}^{n}$$

@Seismicisolation

where τ_o is the yield stress, K is the consistency, and n is the power index, which represents the deviation from Newtonian behavior. Note that n is less than unity for shear thinning systems.

The Cross equation provides a more general model for pseudoplastic materials:

Eq. (9) $$\frac{\eta_0 - \eta}{\eta_0 - \eta_\infty} = \frac{1}{1 + (K\dot{\gamma})^m}$$

where η_0 and η_∞ are the asymptotic values of viscosity at very low and very high strain rates, and K and m are constants. At intermediate values of strain rate ($\eta \gg \eta_0$ and $\eta \ll \eta_\infty$) the equation reduces to a power-law model often used to describe pseudoplastic liquids and if $m = 1$ and only the lower range of viscosity is considered ($\eta \gg \eta_0$), the equation reduces to the Bingham model. This model is equivalent to the Ellis and Meter models, which are presented in terms of stress rather than strain rate.

The Eyring model (with two adjustable parameters) is

Eq. (10) $$\tau = \alpha \sin h^{-1}(b\dot{\gamma})$$

where α and b are constants. This model does not include a yield value term. Development of this model was based on the concept of activated transport.

Three of these models are presented in Fig. 3. These are not actual data, but rather, computations using the equations discussed above. The power-law and Cross models both describe pseudoplastic behavior while the Bingham model describes plastic behavior. The differences between plastic and pseudoplastic behavior are readily apparent, both from the plot showing stress as a function of strain rate and from the plot showing viscosity as a function of strain rate. However, the differences between the power-law model and the Cross model may not be so obvious. When viscosity is plotted as a function of strain rate it can be seen that the Cross model shows a limiting viscosity at both the low and the high strain rate whereas the power-law model does not, but this difference in behavior may not be readily observed in the plot of stress versus strain rate.

It should also be noted that a yield stress may be estimated for a pseudoplastic material by extrapolation of the flow curve to zero strain rate from the high strain rate region. In the power-law model, the curve is not particularly linear, even at high strain rate, making this extrapolation subject to some uncertainty.

@Seismicisolation

Papo[4] evaluated these and other rheological models for cement pastes (w/c ranging from 0.34 to 0.42). He found that the Herschel-Bulkley model provided good fit with experimental data while the Bingham model fit only at very high w/c ratios, and the Eyring model always gave the worst fit. Atzeni, et al.,[5] also evaluated these models with cement pastes (w/c ranging from 0.30 to 0.45). He found that the Eyring model and the Herschel-Bulkley model gave satisfactorily agreement. Thus, it appears that the Herschel-Bulkley is a suitable constitutive model for cement paste.

Hysteresis. An important aspect of flow behavior is the extent to which hysteresis is observed between the stress as strain rate is increased from zero and the stress as strain rate is decreased from high values. This hysteresis reflects some lack of equilibrium between the microstructure and the strain rate, often because the material is undergoing some type of structural breakdown during shear. In that case, the stress on increasing strain rate is greater than the stress when strain rate is decreasing and the hysteresis takes the form shown in Fig. 5.

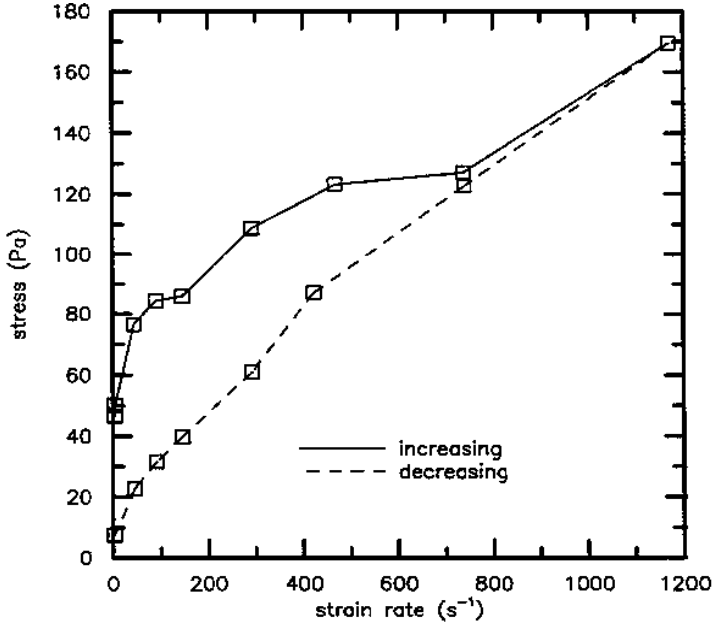


Figure 5. Flow curve for cement paste showing hysteresis when strain rate is increased and then decreased.

@Seismicisolation

If equilibrium measurements are desired, it is necessary to adjust the experimental procedure to minimize the hysteresis. The simplest way to do this is to measure stress while decreasing the strain rate from high to low. Another approach is to wait at each strain rate until equilibrium is attained, but at low strain rates a suspension may be very slow to reach equilibrium.

Thixotropy produces hysteresis of the general type shown in Fig. 5. Thixotropy is a time-dependent decrease in viscosity when tested at constant stress or strain rate. Thixotropy is recoverable: on removal of stress or strain rate the viscosity gradually returns to its initial level. Thixotropy often accompanies pseudoplastic behavior in flocculated suspensions. The flocculated microstructure breaks down during shear; if this breakdown is slow (compared to the duration of measurement) it produces thixotropy or shear thinning. Such breakdown is reversible so it is appropriate to speak of the time-dependent changes as thixotropy.

In cementitious materials, hydration also produces hysteresis. Unlike thixotropy, hydration produces a higher stress during the second measurement (whether at increasing strain rate or decreasing strain rate) than during the first measurement. The stress increases progressively with each subsequent measurement. These changes are not reversible.

Another feature observed with cementitious materials is an irreversible structural breakdown on first mixing. It also produces hysteresis of the type shown in Fig. 5.This is not thixotropy (it is not reversible), but it would be easily confused with thixotropy if the reversibility were not assessed. Tattersall and Banfill called this an *irreversible structural breakdown* (Ref. 3, pp. 50–52). Once the breakdown has occurred, the material shows reversible behavior. As Tattersall and Banfill noted, this behavior has critical implications to rheological techniques. When shear is first increased, the yield stress is high and quite variable. When shear is decreased (and on subsequent shearing) the yield stress is much lower and much more reproducible.

Depending on shear history, this breakdown may or may not occur during mixing. If not, then it will be observed during the rheological experiment. For this reason it is important to consider the shear history when designing the rheological experiment. One must decide whether to mix the cementitious material at high shear or low shear before measuring its flow behavior. We have opted for a high shear treatment in the rheometer (as discussed later in this chapter) so the breakdown occurs before any measurements of flow behavior. In this way we obtain a suspension with low yield stress, no hysteresis, and reproducible flow behavior. Others have

@Seismicisolation

mixed slowly, using gentle hand mixing, to minimize breakdown prior to the flow measurement. Mixing should reflect the objective of the study. If the objective is to study the initial structural breakdown, which is irreversible, then a gentle mixing is required. If the objective is to study the subsequent response to shear, then high shear mixing is required. If the objective is to predict performance in the field, then the mixing should match the field conditions.

Tattersall and Banfill suggested that the breakdown occurs because mixing causes the initial flocculated structure to break down. Before shear, the interparticle forces include both the force causing dry particles to flocculate and the additional force provided by the thin layer of hydration product (which they call a *membrane envelope*).With shear, the structure breaks down and the membrane bridge is ruptured. When shearing is stopped the particles reflocculate. Because shear has broken the membrane bridge, the reflocculate microstructure is weaker than before shearing causing the reduction in yield stress. This model explains the irreversible decrease in yield stress observed on first mixing.

We offer a slightly different model for this breakdown, as illustrated in Fig. 6. It is reasonable to presume that initial flocculation of cement particles prior to any hydration occurs (at least in part) due to heterocoagulation. This is an electrostatic attraction that occurs in polymineralic particles with charges of different signs at different sites on the surface. On shear, the flocculated particles break down and any remaining anhydrous surface becomes coated with hydration product. When the shearing is stopped, the particles reflocculate. However, the hydration product now shields the differences in surface charge and prevents reestablishment of the heterocoagulation. The reflocculation is, therefore, due to van der Waal's forces between hydration product surfaces, somewhat weaker than the initial electrostatic attraction. This model also explains the irreversible decrease in yield stress on first mixing.

Tattersall and Banfill (Ref. 3, pp. 262–268) reviewed the various types of hysteresis behavior and their interpretation. They advocated the use of hysteresis behavior only to provide a preliminary indication of thixotropy. If one is interested in investigating time-dependent flow behavior (such as thixotropy) it is wise to directly measure stress as a function of time at some strain rate rather than trying to infer it from hysteresis in measurements of stress as a function of strain rate.

@Seismicisolation

4.2 Dynamic Flow Behavior

A key development in recent years in rheology has been been the development of dynamic techniques for characterization of viscoelastic materials. Such techniques measure the behavior when there is a change in strain rate or shear stress. A flow curve, as shown in several of the preceding figures, is a static technique measuring the stress to achieve a particular strain rate (or vice versa). The key dynamic techniques used for suspensions are low-amplitude *oscillatory shear* and *creep/recovery*.*

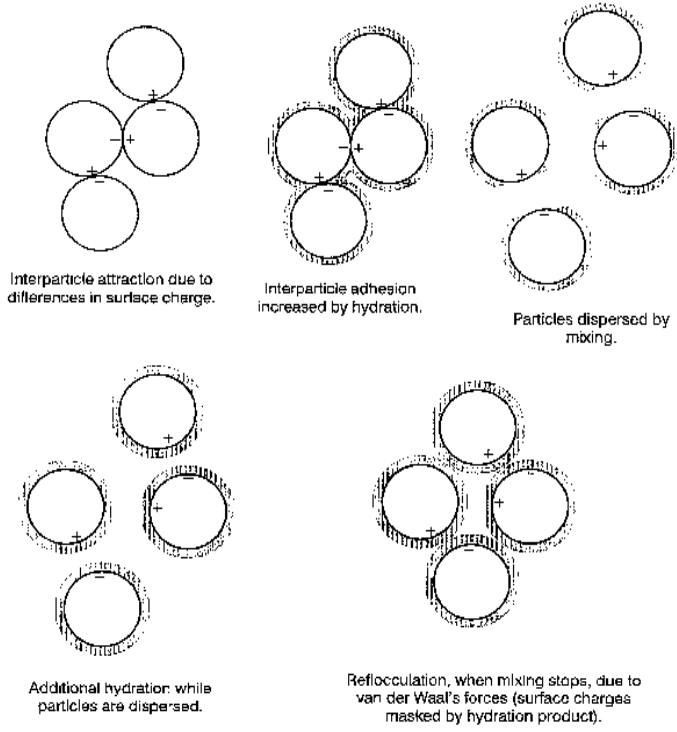


Figure 6. Schematic diagram showing microstructural changes proposed to cause irreversible structural breakdown on first mixing.

*This terminology is not entirely standard. In rheology literature, *oscillatory shear* is considered a dynamic technique, but *creep/recovery* is considered static. However, because creep measures the response to a change in stress, it seems more appropriate to call it a dynamic technique.

@Seismicisolation

These techniques are very useful when characterizing flocculated suspensions. Using static tests to measure yield stress of a flocculated suspension requires that the suspension be made to flow. This flow breaks down the flocculated microstructure whose characterization is often the primary objective of the measurement. Therefore, one perturbs the very feature one is attempting to measure and subsequent measurements are, therefore, altered unless the microstructural changes are reversible. That is not the case when using small-strain dynamic techniques.

Furthermore, the dynamic techniques provide information for the full range of material behavior (elastic solids, viscoelastic solids, viscoelastic liquids, and viscous liquids) whereas the static technique provides only limited information about elastic behavior (i.e., the yield stress) and only for viscoelastic liquids. Flocculated suspensions show viscoelastic behavior at low strains (below the yield stress) and dynamic techniques provide a more complete characterization of this behavior.Based on values of shear modulus, measured dynamically, it is often possible to derive or infer values of the interparticle forces responsible for flocculation. Such fundamental aspects of dynamic rheology and their application to colloidal suspensions are discussed in considerably more detail by Hunter[2] and by Russel, et al., (Ch. 14 in Ref. 6).

Both these dynamic techniques have recently been applied to cement paste in our laboratory, and the following discussion is taken largely from a series of papers on this topic.[7][11] What has motivated this work is the potential offered by these dynamic techniques for measuring changes in cement paste due to hydration. Static flow causes microstructural changes that are not recovered when flow is stopped, changes similar in general to the microstructural breakdown that takes place on first shearing (described previously). Because of these changes, the progressive increase in yield stress that one expects with hydration is disrupted (effectively the clock is reset each time flow occurs). Therefore, it has not been possible to use rheology to measure changes due to hydration. Because these dynamic techniques involve only very small strains in the range where the material responds elastically, there is no microstructural breakdown and the techniques can be used to measure progressive changes due to hydration.

Creep/Recovery. The creep/recovery technique measures strain when a stress is applied (creep) or removed (recovery); from this is determined the *compliance* (strain divided by stress). When a stress is abruptly imposed, held constant for some time interval and then abruptly released (Fig. 7a), solids and liquids behave as follows.

@Seismicisolation

1. An ideal elastic solid responds to the imposed stress with a characteristic instantaneous strain. This strain does not change for the duration of the stress. The strain is recovered as soon as the stress is released (Fig. 7b).
2. An ideal viscous liquid has no instantaneous strain in response to the imposed stress. It responds to the imposed stress with a characteristic and constant rate of strain, so strain increases at a constant rate throughout the duration of the stress. None of the strain is recovered when the stress is released (Fig. 7c).
3. A viscoelastic solid (Fig. 7d) responds to the imposed stress with a characteristic instantaneous strain, but superimposed on this instantaneous elastic response is a time-dependent, retarded elastic strain. At long times the strain approaches some limiting value. When the stress is released some of the strain is recovered instantaneously and the remainder is recovered through a time-dependent, retarded elastic recovery.
4. Likewise, the behavior of a viscoelastic liquid (Fig. 7e) is intermediate between that of an elastic solid and a viscous liquid. It responds to the imposed stress with an instantaneous strain and a retarded elastic strain. In addition, there is superimposed a time-dependent, viscous strain that continues as long as the stress is imposed. When the stress is removed there is an instantaneous and a retarded elastic strain recovery, but not all the strain is recovered.

For a viscoelastic material, creep experiments show the basic nature of its response, allowing one to determine whether it is a solid with some viscous component or a liquid with some elastic component to its behavior. Creep curves also show whether the material is linear in its behavior (i.e., whether the compliance or the viscosity is independent of applied stress).

As with any flocculated suspension, creep/recovery behavior for cement paste, shown in Fig. 8, depends on the stress level. At low stress (e.g., 8 Pa in Fig. 8), the creep/recovery behavior is typical of a viscoelastic solid with an instantaneous strain superimposed on a retarded (time-dependent) elastic strain. The equilibrium compliance value (after 30 s) is very low, approximately 0.01 Pa^{-1}. When stress is removed, the behavior is more

@Seismicisolation

typical of a viscoelastic liquid, with little or no instantaneous recovery and only a very slow time-dependent recovery and what appears to be a considerable non-recovered strain. At a slightly higher stress (e.g., 9 Pa in Fig. 8), the behavior is typical of a viscous liquid, with a steady and approximately linear increase in strain throughout the duration of stress. After 30 s the compliance value was quite high, approximately 9 Pa^{-1}. When the stress is removed there is no recovery. The transition from solid-like behavior to liquid-like behavior corresponds to the yield stress observed in static flow curves. This transition was observed across a remarkably narrow stress increment, 1 Pa or less.

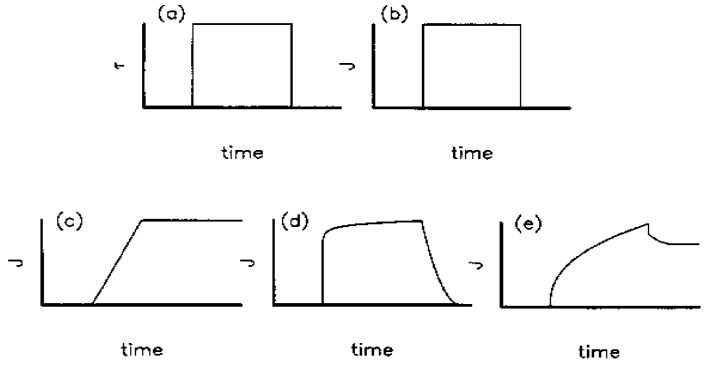


Figure 7. *(a)* Applied stress and *(b)–(e)* ideal response (creep and recovery) of various types of materials: *(b)* elastic solid, *(c)* viscous liquid, *(d)* viscoelastic solid, and *(e)* viscoelastic liquid.[8] The dependent variable, *J*, is compliance (strain divided by stress).

Through careful analysis of the creep/recovery behavior it is possible to estimate yield stress sequentially as a function of hydration time without exceeding yield stress (and thus disrupting the microstructure as discussed previously). When the applied stress is well below the yield stress, the paste shows elastic behavior (creep compliance is fully instantaneous and recovery is instantaneous and complete). As the applied stress approaches the yield stress, the behavior becomes increasingly viscoelastic (creep compliance increased with time and a considerable portion of the creep compliance was not recovered). The stress level at which the paste shows a modest degree of viscous response provides an approximate measurement of yield stress.

Figure 9 shows the time evolution of the yield stress measured sequentially on a single specimen. The yield stress development agrees well with more conventional measurement setting by penetration resistance. It

@Seismicisolation

also follows rather closely the kinetics of hydration as measured using isothermal calorimetry. During the induction period, the yield stress increases slowly and once the acceleratory period begins, the yield stress increases much more rapidly. Thus, the creep/recovery measurements provide an estimation of yield stress that can be used to characterize the setting behavior of cement paste. However, it must be remembered that setting is a microstructural phenomenon while hydration is a chemical phenomenon; in order for set to occur, it is necessary but not sufficient that hydration take place.

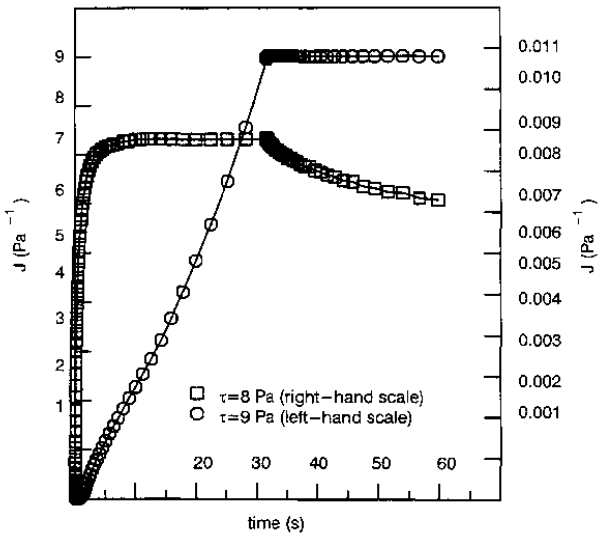


Figure 8. Creep/recovery curves for cement paste at w/c 0.40 and at stress levels below and above the solid-liquid transition.[8]

Oscillatory Shear. The oscillatory shear technique measures stress when the materials are subjected to an oscillating strain (or vice versa) from which is determined the modulus (G) or the viscosity (η). The strain is oscillated according to a sine function. In addition to the resulting stress, the technique measures the extent to which the stress is in phase with the applied strain. By limiting the strain to small amplitudes (i.e., <1%) the particles stay in close contact with one another and are able to recover elastically, so the microstructure is not disturbed and the paste behaves as a solid. At larger amplitudes the particles are separated and the paste

@Seismicisolation

becomes liquid in its behavior. Thus, oscillatory shear provides information concerning the viscoelastic properties of suspensions both below yield (at small amplitudes where behavior is essentially solid) and above yield (at large amplitudes where behavior is liquid).

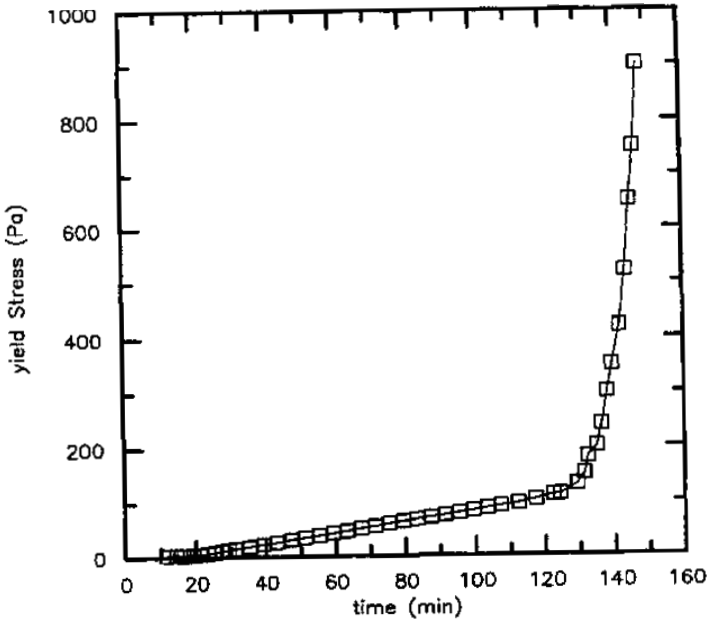


Figure 9. Yield stress as a function of hydration time for fresh cement paste (w/c 0.45).[26]

The dynamic modulus (G^*) can thus be shown to consist of a *storage modulus* (G'), in phase with the oscillating strain, and a *loss modulus* (G''), 90° out of phase with the oscillating strain. The storage modulus is a measure of the elastic response; an elastic solid has some storage modulus and a zero loss modulus. Likewise, a viscous liquid has some loss modulus (that corresponds to its viscosity) and a zero storage modulus. The dynamic viscosity (η^*) also consists of an inphase component (η') and an out-of-phase component (η''). Relationships between these components, often expressed using real and imaginary numbers, may be found in textbooks on rheology (e.g., Ref. 1 or 2).

It is common to plot G' and G'' as a function of γ, measured at a fixed frequency of oscillation. Such a plot for cement paste is shown in Fig. 10. The variation observed in storage and loss modulus is typical of a flocculated suspension. Storage modulus is independent of strain amplitude up to some

@Seismicisolation

critical strain, then at higher strain values the storage modulus decreases with increasing strain. The loss modulus increases from a very low value to a maximum at a strain somewhat greater than the critical strain, then decreases at higher strain levels. The loss modulus is smaller than the storage modulus below the critical strain, indicating a solid-like response.

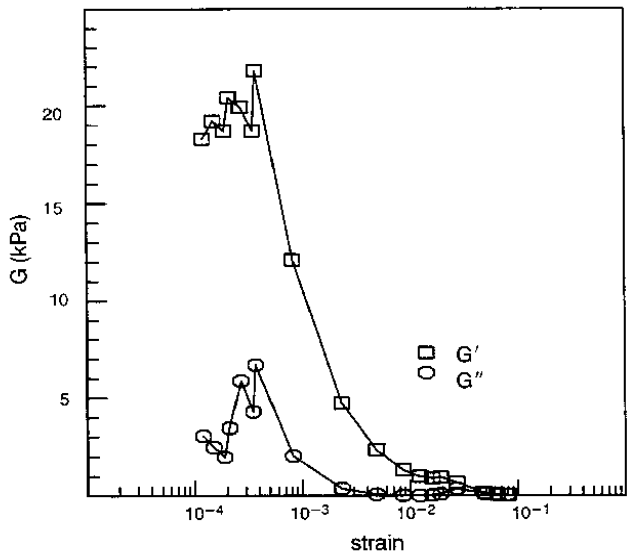


Figure 10. Strain sweep for cement paste at w/c 0.40.[7]

The critical strain values observed for ordinary cement pastes are quite low, about 10^{-4}, while the low-strain storage modulus is rather high, about 10 kPa, before much hydration has occurred and much higher after hydration. This combination makes the experimental measurements rather difficult. Accurate measurements require a torsion bar that is sensitive enough to measure such small strains while stiff enough to overcome the high modulus of the cement suspensions. Modulus values at strains above the critical strain reflect the nonlinear properties of the material and, therefore, must be used with caution.

Although they are not the same, the storage modulus and yield stress are closely linked. In a general sense the relationship between these parameters is similar to the relationship between modulus and strength in a solid material. The product of the critical strain and the low-strain modulus provide a useful estimate of the yield stress, although no fundamental basis has been proposed for this relationship.

@Seismicisolation

Storage modulus can also be measured as a function of time in order to follow changes due to hydration. If the strain is kept small (near or below critical strain) there is no structural breakdown such as observed during static flow. Results for cement paste are shown in Fig. 11. The development of storage modulus with time is fairly similar to the development of yield stress (compare Figs. 9 and 11). Both show a more-or-less exponential increase with time.

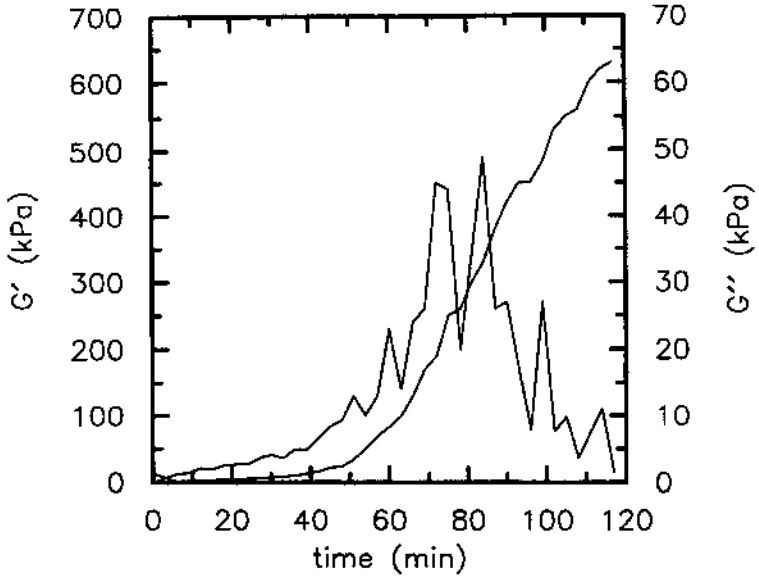


Figure 11. Storage and loss moduli as a function of hydration time (w/c 0.40 flocculated paste).

5.0 CONCRETE

5.1 Flow Behavior

Concrete is widely recognized to show plastic behavior. A typical flow curve is shown in Figure 12. This curve was measured using a rheometer similar in design to the BTRHEOM (discussed in Sec. 6, "Rheometers"). The yield stress of this concrete was 610 Pa and the plastic viscosity was 57 Pa.

@Seismicisolation

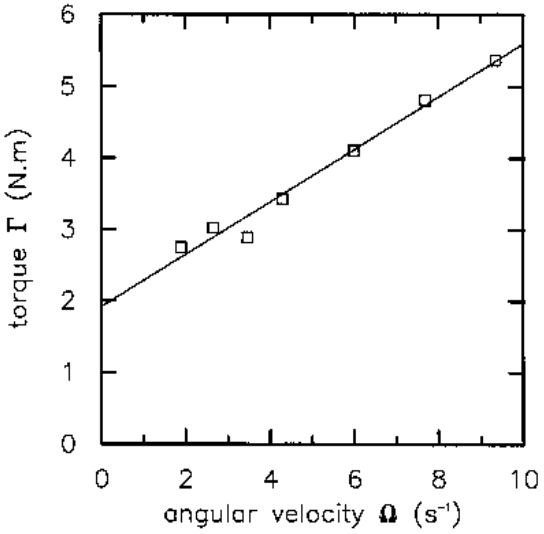


Figure 12. Concrete flow curve.

The flow behavior of fresh concrete follows the same general pattern as discussed previously for colloidal suspensions and for cement paste. The flow depends on concentration of particles and on the extent to which cement particles are flocculated. The particles cover a very broad size range, from submicron sized cement and silica fume particles to centimeter-sized aggregates. Flocculation is only important for the finer particles. One important difference is that the range of strain rates is usually rather low, only about 0–10 s^{-1} (the strain rate employed for cement paste and for colloidal suspensions often extends as high as 1000 s^{-1}). This low strain rate reflects the low rate experienced by concrete in actual applications (e.g., mixing, transporting, and finishing).

@Seismicisolation

5.2 Effects of Composition

Many of the results discussed in this section are unpublished data from work in our laboratory. We have two concrete rheometers, one similar in design to the BTRHEOM and the other a Tattersall apparatus (both are discussed in Sec. 6, "Rheometers"). Data given in rheological units of stress and strain rate were measured with the BTRHEOM and data in units of torque and velocity were measured with the Tattersall.

The flow behavior of concrete, like that of cement paste, is influenced by w/c. An example is shown in Fig. 13. Increasing the w/c results in lower yield stress and lower plastic viscosity. Similar results have been reported by other researchers. The total aggregate content also affects flow, especially plastic viscosity. Increasing the concentration of aggregate results in an increased plastic viscosity. The aggregate type also affects flow. Concrete with river gravel, due to its much rounder and smoother surface, usually has lower viscosity and yield stress.

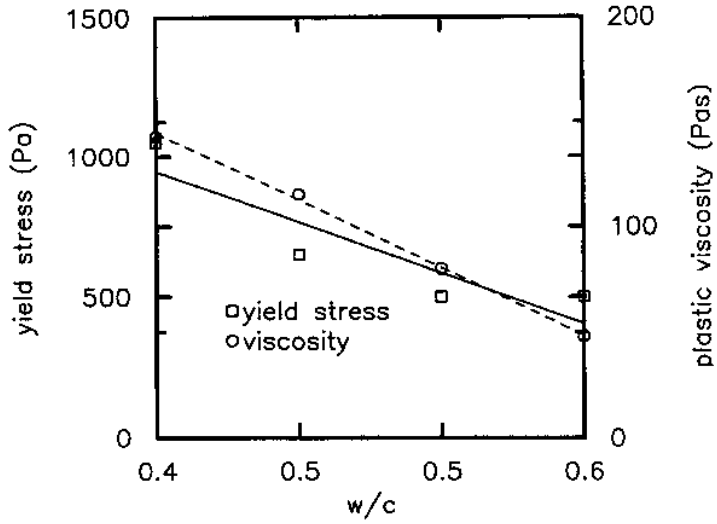


Figure 13. Effect of w/c on yield stress (gravel, 60% total aggregate, 40% sand).[13]

Figure 14 shows the relationship between flow behavior and sand content. The sand ratio has a great influence on the yield stress. For both types of coarse aggregate, the lowest yield stress occurred when the sand

@Seismicisolation

ratio was about 38%. This sand ratio coincided approximately with the sand content that provided for the highest packing density for these same coarse aggregates. Similar behavior was observed for plastic viscosity.

Admixtures also affect concrete flow. The replacement of cement by fly ash was reported by Banfill to reduce both yield stress and plastic viscosity.[12] Studies in our laboratory, however, gave somewhat different results; we found that yield stress increased at low fly ash contents and decreased only at higher values (Fig. 15).[13] The effects of superplasticizer dosage on rheology are shown in Fig. 16. The addition of superplasticizer significantly reduced the yield value of concrete. The superplasticizer initially reduced the plastic viscosity, but beyond a certain dosage level the viscosity increased slightly. Hu and colleagues[14][15] found similar behavior and suggested that plastic viscosity increases when it reaches its saturation concentration. Effects of silica fume on the development of yield stress and viscosity are shown in Fig. 17. It is interesting to note that silica fume also reduced the initial plastic viscosity though it considerably increased the yield stress.[16]

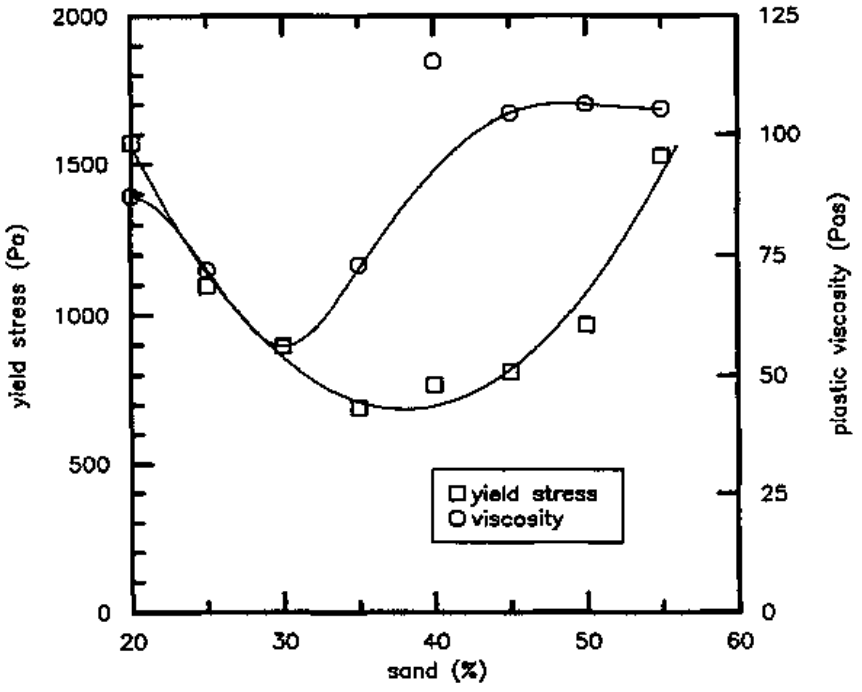


Figure 14. Yield stress and plastic viscosity versus sand content (gravel, w/c 0.45).[13]

@Seismicisolation

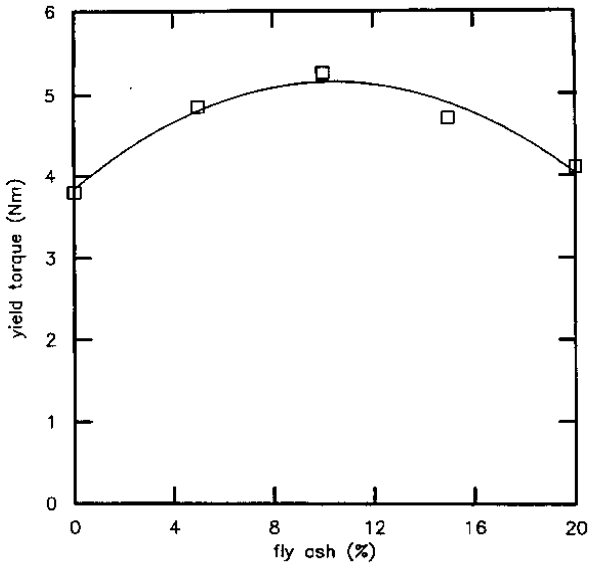


Figure 15. Yield torque versus fly ash content (river gravel, w/c 0.45, 40% sand).[13]

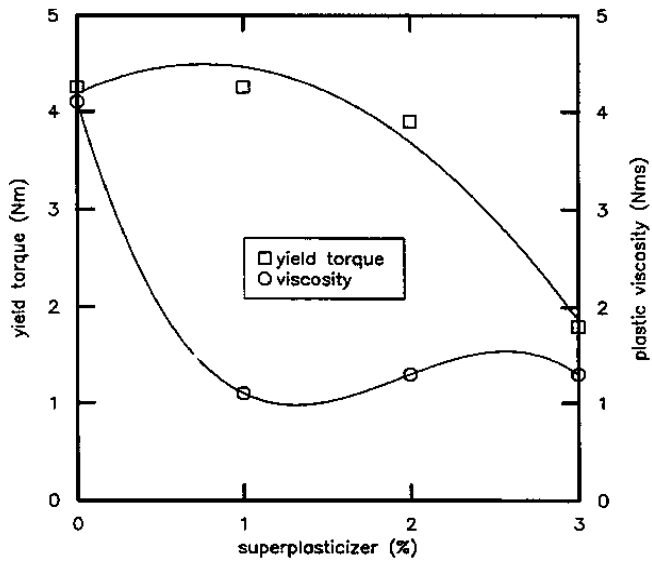


Figure 16. Yield torque versus superplasticizer dosage (river gravel, w/c 0.45, 40% sand).[13]

@Seismicisolation

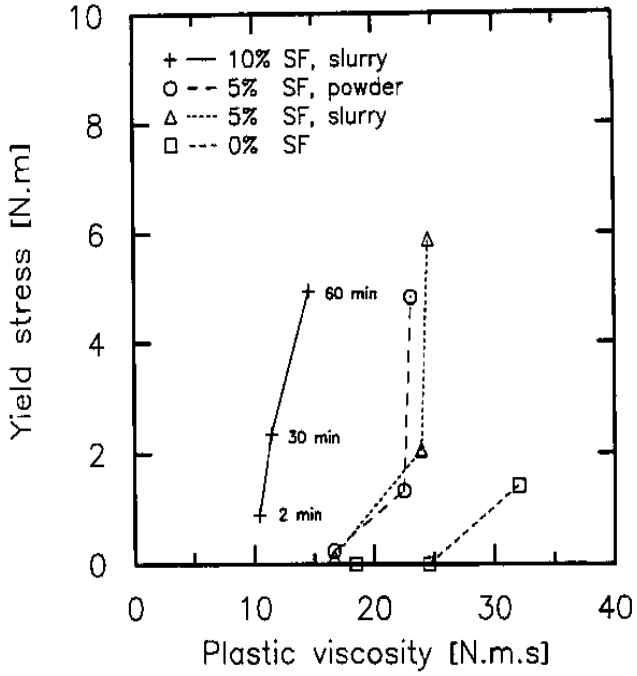


Figure 17. Effect of silica fume content on yield stress and plastic viscosity (2, 30, and 60 minutes after mixing).[16]

The effects of elapsed time on the rheology were studied by Hu and de Larrard.[17] Figure 18 shows that yield stress increased considerably with elapsed time while plastic viscosity was changed only slightly. It should be noted, however, that these measurements were made on a single batch of concrete whose flow curve was measured sequentially after various hydration times. Our own experience suggests that the hydrating cement was probably altered in microstructure due to the flow, as discussed previously (in the section on dynamic techniques in paste rheology), although in a subsequent paper from the same research group[18] it was shown that repeated shear did not alter the microstructural evolution in concrete.

Punkki, et al.,[16] studied the effects of different mixing procedures (delayed addition of portion of water and delayed addition of superplasticizer) and elapsed time on the yield stress and plastic viscosity. Both yield stress and plastic viscosity increased with the elapsed time after mixing. When the superplasticizer was added simultaneously with water the increase in yield stress was very high while the increase in the viscosity was insignificant. The

@Seismicisolation

rapid increase in yield stress resulted in a dramatic loss of slump. When the superplasticizer was added after the water, in two increments, the increase in yield stress was the lowest and the increase in plastic viscosity was also the lowest. In general, longer delay in the addition time of superplasticizer resulted in a lower increase in yield stress.

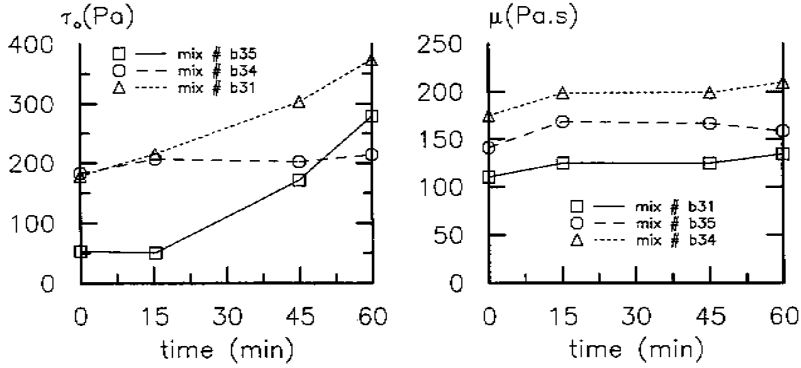


Figure 18. Evolution of the yield stress and plastic viscosity of high performance concrete.[17]

6.0 RHEOMETERS

6.1 Cement Paste

Shear rheometers, instruments for measuring flow behavior, usually operate in rotation and measure torque and rotational speed and the rheological parameters of stress and strain rate are computed from these measurements. It is important that the rheometer provide simple shear flow and a simple stress field so that stress and strain rate can be computed.

Often the rheometer employs coaxial cylinders or parallel plates (shown in Fig. 19). Sample sits between, and one of the cylinders or plates rotates. In this geometry it is necessary that the gap be considerably wider than the diameter of the largest particles. It is necessary with coaxial cylinders that the gap be narrow compared to the cylinder diameter in order to provide a uniform strain rate. Wide-gap coaxial-cylinder rheometers

@Seismicisolation

exist,* but calculation of stress and strain rate require assumptions concerning these parameters over the range of shear across the gap. Thus, narrow-gap rheometers are preferable because they do not require such assumptions. Our own experiments on cement paste utilize a coaxial cylinder rheometer with a gap of 0.7 mm.

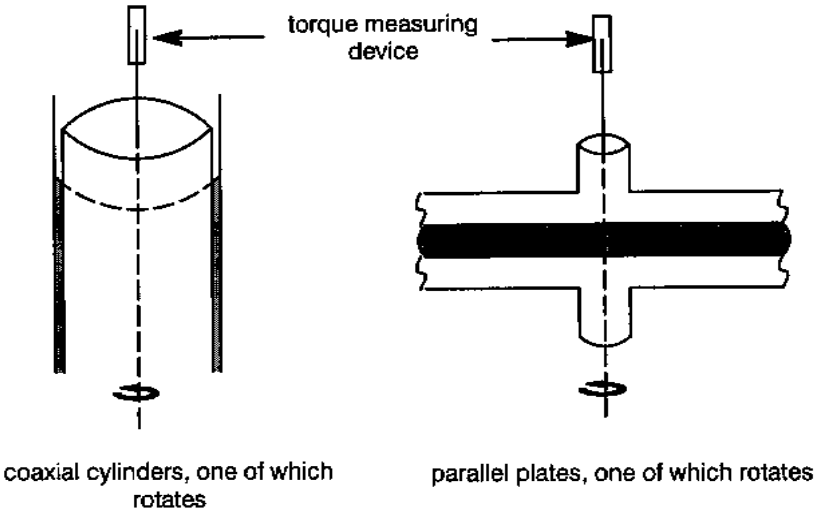


Figure 19. Two common geometries for rotational rheometry.[26]

Rheometers either control the stress and measure strain rate or control the strain rate and measure stress. Either mode is suitable for measurement of static flow curves and for measurement of oscillatory shear. The controlled stress rheometer provides more precise control and more sensitive measure at very low stress levels. Creep/recovery measurements can only be made using a controlled stress rheometer.

Several experimental difficulties are recognized when making rheological measurements. One common problem with suspensions is *segregation*, in which particles fall to the bottom during the experiment. Large particles are especially prone to segregation. It is more likely in a plastic or pseudoplastic suspension at higher strain rates because viscosity is lower.

*The Brookfield rheometer is an example.

@Seismicisolation

Specialized rheometers have been designed to reduce or prevent segregation, usually using a helical impeller or similar shape that lifts particles as it rotates. Of course, with such a shape the flow is no longer simple and it is probably not possible to calculate stress and strain rate. Segregation is less likely in flocculated suspensions and at very high concentrations. In our own studies of dispersed cement paste, segregation limited the range of concentration we could explore at high w/c. Segregation is also a common problem in measurements of concrete rheology (discussed below).

The other common source of error is *slip* at the wall. If the suspension is more fluid at the wall of the rheometer then it may flow only at the wall producing slip and causing an erroneously low stress. If the suspension flows only at both walls of a coaxial cylinder rheometer, *plug flow* occurs. These are especially common problems when studying plastic or pseudoplastic suspensions whose stress is very sensitive to strain rate.

Slip probably results from the wall effect in which particles are constrained to have a lower density at the wall. Barnes, et al., (Ref. 1, p. 128) have hypothesized that slip also results from migration of particles from regions of high shear rate to regions of low shear. Slip is generally assessed by varying the separation between cylinders or plates. If there is slip, the viscosity changes when the separation is altered.

There are several ways to reduce or minimize slip and plug flow. The most common is to use vanes or a rough texture on the surface of the rheometer. Of course, a rough or vaned surface may introduce complex flow (e.g., turbulent flow), complicating the computation of stress and strain rate. For this reason vaned cylinders are often used only to measure yield stress not to measure viscosity. Another approach used increasingly in colloidal suspensions is to use a very narrow gap. With coaxial cylinders the gap must be sufficiently narrow that the ratio of the inner cylinder radius to the outer cylinder radius is greater than 0.97. Finally, slip is unlikely when using dynamic shear techniques at low strain levels.

6.2 Concrete

Designing a rheometer for testing fresh concrete presents considerable challenges. Because the flow of concrete is generally found to be plastic (Bingham) its flow behavior must be described using the two characteristic values of yield stress and plastic viscosity. The suspension contains particles with a wide range of sizes, from submicron-sized cement to centimeter-sized coarse aggregate. The larger particles tend to settle due to gravity. It is somewhat thixotropic, making segregation even more likely

@Seismicisolation

during shear. Slip is a common problem aggravated by the plastic flow behavior and by the large size of the coarse aggregate which necessitates a rather large gap. Concrete rheometers are typically designed with vanes to reduce slip or with a helical impeller to reduce segregation. These designs may not provide simple flow, making computation of stress and strain rate difficult or impossible.

There are several rheometers available for testing fresh concrete and mortar. Much progress in measuring the flow curve (torque versus angular velocity) has been made since the development of the two-point workability apparatus by Tattersall.[6] Tattersall's apparatus was further modified and improved by Beaupre (UBC Rheometer)[22] and by Wallevik and Gjørv (BML Viscometer).[23] Some problems still exist with this type of apparatus. The flow field of concrete in the cylinder is quite complicated and flow turbulence is likely so it is very difficult calculate the yield stress and shear rate. Hence, it is not possible to determine the rheological constants (yield value and plastic viscosity) in fundamental rheological units. Further progress was made by Hu, et al.,[3] with a rheometer (BTRHEOM) that gives rheological parameters in fundamental rheological units. These various rheometers are discussed in more detail below.

Coaxial Cylinder Rheometer. Perhaps the simplest design is the coaxial cylinder rheometer, which has been used with both mortar[19][20] and concrete;[21][22] but there are some problems encountered with this type of rheometer for concrete because the particle sizes of concrete aggregates are significantly larger than those of cement particles. Slip between the concrete and the rotating surface of cylinder, plug flow (in which some portion of the concrete in the gap between the inner cylinder and outer cylinder is not sheared) occurs and end effects (in which torque is absorbed at the lower end of the inner cylinder).

As discussed previously, the gap between the inner and outer cylinder in a coaxial cylinder rheometer must be large compared to the maximum particle size and small compared to the diameter of the inner cylinder. To satisfy these requirements, the dimensions of the rheometer for concrete would be impractically huge, requiring a truckload of concrete for one rheological test.

Apart from the problem of huge size, the coaxial cylinder rheometer still has some other problems: *(i)* tendency of segregation (especially for low viscosity concrete) during the test,*(ii)* slip between the cylinder surface and the concrete, a problem that cannot be eliminated in a coaxial cylinder concrete rheometer, and *(iii)* plug flow when the angular velocity of the rheometer is low.

@Seismicisolation

The rheometer used by Murata and colleagues[21][22] had an inner cylinder 150 mm in radius and 200 mm long. The flow behavior they observed with this rheometer was plastic, well described with the Bingham model. They used a multi-point method to measure the flow velocity distribution of concrete, sprinkling foamed polystyrene powder on the top surface of the concrete to serve as gauge marks for this measurement and recording the movement of these gauge marks by video camera. Based on the flowing velocity of the outer flowing part of the sample in the gap and the flowing velocity of the sample in contact with the inner-cylinder surface as well as the torque, they plotted a flow curve and computed plastic viscosity. They noticed slippage between the concrete and the rotatinginner cylinder. Even with concrete of a relatively wet consistency the sample at the outer periphery was not flowing (the angular velocity was zero). Increasing the angular velocity increased the sheared portion of the concrete, and they observed that when velocity exceeded at least 60 rpm, the range of flow of the sample became roughly constant irrespective of the velocity.

A discontinuity has been observed in the flow curve at shear rates of 30 to 40 s^{-1}. Some authors have attributed this to the development of both slip and plug flow at low shear rates.[23][24]

Tattersall Apparatus. Tattersall and Banfill designed the two-point concrete rheometer to overcome the problem of segregation[3] and based on their experimental observation that fresh concrete can be well described using the Bingham model (with two intrinsic rheological constants, yield stress and plastic viscosity). The current version of the Tattersall Apparatus is shown schematically in Fig. 20. The helical impeller has a vertical axis and rotates in a cylindrical container of fresh concrete (having the same axis). The blades reduce any tendency to segregation.[15]

The test consists of measuring the relation between the torque (Γ) exerted on the helical impeller and its angular velocity (Ω). Due to the complex flow field it is difficult to calculate stress and strain rate (and hence, yield stress and plastic viscosity in absolute rheological units). From the flow curve two parameters are obtained by linear regression, G ($N \times m$) and H($N \times m \times s$), which are analogous to yield value and viscosity, respectively:

Eq. (11) $$\Gamma = G + H\Omega$$

This resembles the rheological equation for Bingham flow. The rheological properties of different concretes can be compared quantitatively using the G and H values.

@Seismicisolation

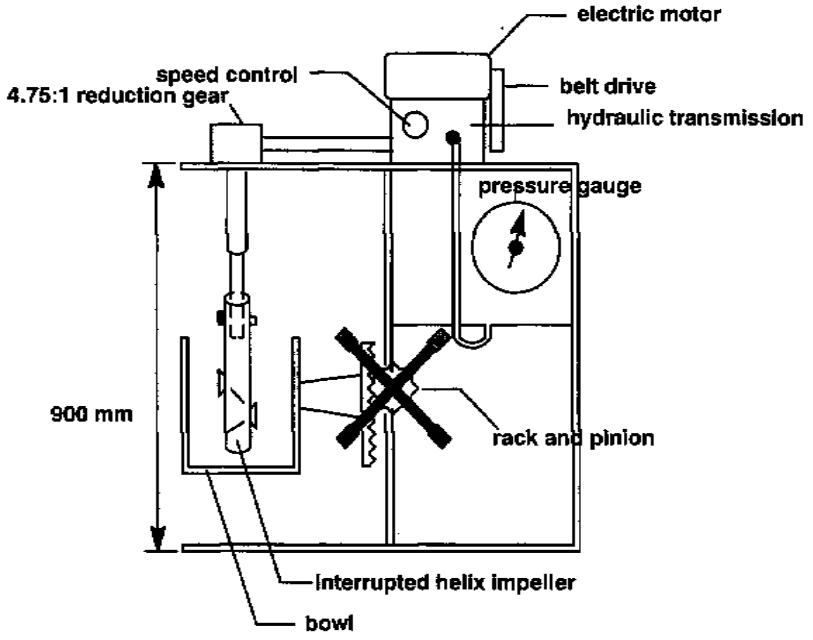


Figure 20. The Tattersall apparatus (Ref. 3, p. 83).

BML Viscometer. More recently, Wallevik and Gjørv[25] developed a fully automated and computerized rheometer, called the BML viscometer, for measuring the rheological properties of fresh concrete and mortar. During rheological tests with the Tattersall apparatus, they had encountered problems with segregation and they found the operation to be somewhat difficult and unreliable. They designed the new rheometer to alleviate these problems.

The BML viscometer is a coaxial cylinder with vanes on the inner and outer cylinders (Fig. 21). The equipment measures the torque (Γ) produced on the stationary inner cylinder while the outer cylinder is rotating at various speeds (Ω). In order to eliminate slip between the inner cylinder surface and the concrete, the inner cylinder has ribs. One of the characteristics of the equipment is that changing measuring speed and measuring torque are fully computerized and automated. The equipment measures the torque from high speed to low speed. By comparing the torque at a given speed in the first registration sequence and the torque at the same speed, but in another registration sequence, the computer assesses whether the concrete is prone to segregation.

@Seismicisolation

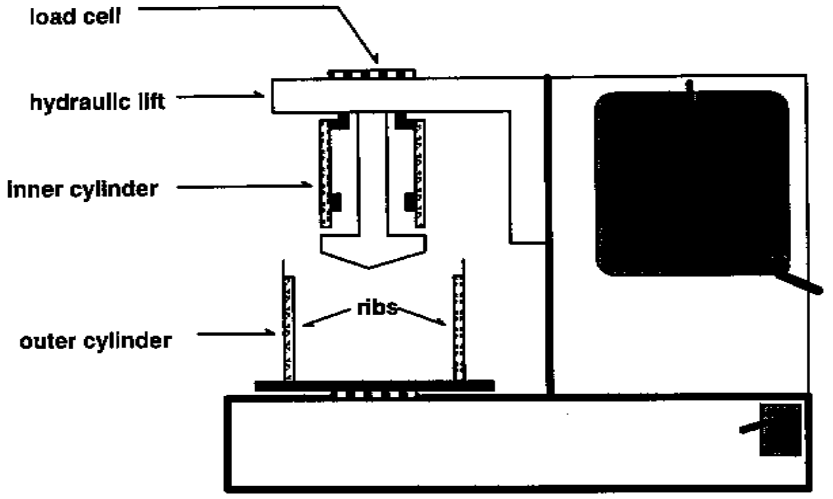
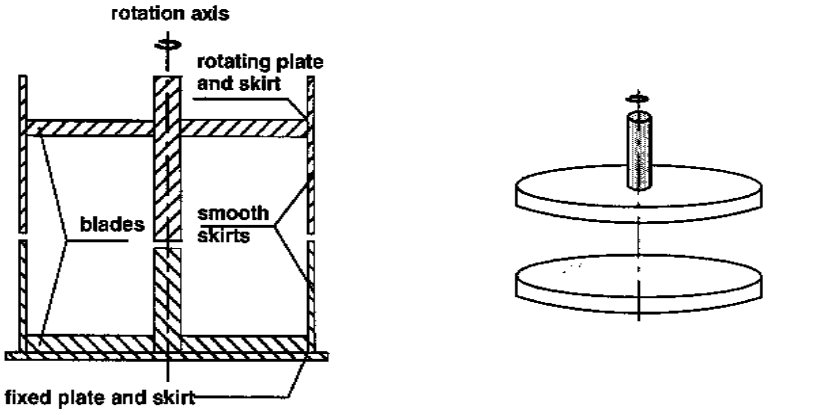


Figure 21. BML viscometer.[25]

A comparison between the BML viscometer and the Tattersall apparatus showed that the Tattersall apparatus created a small additional stress to the test results. This additional stress was probably related to the under pressure that was created under the blades of the impeller. The evaluation of this equipment also indicated that the equipment had good reproducibility. A recent study of high-strength concrete (w/c >0.29) showed plug flow for all mixes with slump < 20 cm and concluded that the rheometer is not suitable for mixes with slump <10 cm.[14]

BTRHEOM Rheometer. Hu, et al.,[15] developed a rotational rheometer called the BTRHEOM, shown schematically in Fig, 22. The rheometer utilizes a parallel plate geometry in which each plate is vaned. This rheometer allows the calculation of the absolute rheological parameters, yield stress, and viscosity. The problem of plug flow, which was often encountered with the coaxial-cylinder viscometers, is claimed not to occur in this rheometer; slip and plug flow are prevented by the vanes in both the upper and lower plate. The horizontal shear in the fresh concrete serves to offset the effect of segregation by gravity. The BTRHEOM is unique not only because it allows calculation of rheological parameters in fundamental units of stress and strain rate, but also because it is small enough to be easily transported to a construction site.

@Seismicisolation



(a) 2–D diagram of the container (b) Schematic diagram illustrating the principle

Figure 22. BTRHEOM rheometer.[15]

From measurements of torque (Γ) and angular velocity (Ω) at different applied loadings, the behavior of the concrete under shear can be determined by the following equations:

Eq. (12) $$\tau(\dot{\gamma}) = \frac{h\dot{\gamma}}{2\pi R_2^4} \sum_{i=0}^{\infty} \left[\left(\frac{R_1}{R_2} \right)^{4i} F\left(\frac{R_1}{R_2} \right)^{i} \frac{h\dot{\gamma}}{R_2} \right]$$

with

Eq. (13) $$F(\Omega) = (3/\Omega)\Gamma(\Omega) + \partial\Gamma(\Omega)/\partial\Omega$$

and

Eq. (14) $$\dot{\gamma} = \Omega R_2/h$$

where τ is the shear stress, γ the shear rate, R_1 and R_2 the inside and outside radii of the sample (or container), the effective height of the sample, Γ is the torque applied to the sample, and Ω is the angular velocity of the rotating part. The two characteristics of Bingham materials, the shear yield stress, τ_o, and plastic viscosity, η_{pl}, can then be calculated with the following equations:

@Seismicisolation

Eq. (15) $$\tau_0 = \frac{3\Gamma_0}{2\pi\left(R_2^3 - R_1^3\right)}$$

and

Eq.(16) $$\eta_{pl} = \frac{2h\left(\partial\Gamma/\partial\Omega\right)}{\pi\left(R_2^4 - R_1^4\right)}$$

where Γ_0 is the torque at zero velocity and $\partial\Gamma/\partial\Omega$ is its slope.

ACKNOWLEDGMENTS

Funding for this research was provided by the National Science Foundation (through a Young Investigator Award to the first-named author) and the portland Cement Association. Several colleagues at the University of Illinois have contributed to our understanding of cement and concrete rheology. In particular we wish to acknowledge contributions of Prof. Charles Zukoski, Mark Schultz, Wei-Guo Lei, Wei Shi, Guo-Kuang Sun, Richard Szecsy, and Guy Salinas. Unpublished data on paste rheology were provided by both Wei-Guo Lei and Guo-Kuang Sun.

REFERENCES

1. Barnes, H. A., Hutton, J. F., and Walters, K.,*An Introduction to Rheology*, Elsevier, New York (1989)
2. Hunter, R. J., *Foundations of Colloid Science,* Vols. I and II, Oxford Science Publications, London (1987 and 1989)
3. Tattersall, G. H., and Banfill, P. F. G., *The Rheology of Fresh Concrete*, Pitman Advanced Publishing, Boston (1983)
4. Papo, A., Rheological Models for Cement Paste, *Mater. Struct.*, 21:41–46 (1988)
5. Atzeni, C., Massidda, L., and Sanna, U., Comparison Between Rheological Models for Portland Cement Pastes, *Cem. Concr. Res.*, 15:511 (1985)

@Seismicisolation

6. Russel, W. B., Saville, D. A., and Schowalter, W. R., *Colloidal Dispersions*, Cambridge University Press, Cambridge (1989)
7. Schultz, M. A., and Struble, L. J., Use of Oscillatory Shear to Study Flow Behavior of Fresh Cement Paste, *Cem. Concr. Res.*, 23:273–282 (1993)
8. Struble, L. J., and Schultz, M. A., Using Creep and Recovery to Study Flow Behavior of Fresh Cement Paste, *Cem. Concr. Res.*, 23:1369–1379 (1993)
9. Zukoski, C. F., and Struble, L. J., Rheology of Cementitious Systems, *Mater. Res. Soc. Bul.*, 18:39–42 (1993)
10. Struble, L. J., and Lei, W. G., Rheological Changes Associated with Setting of Cement Paste, *J. Adv. Cem. Based Mater.*, 2:224–230 (1995)
11. Lei, W. G., and Struble, L. J., Changes in Oscillatory Shear Behavior Associated with Setting of Portland Cement, submitted to *J. Adv. Cem.-Based Mater.* (1996)
12. Banfill, P. F. G., The Rheology of Fresh Mortar, *Mag. Concr. Res.*, 43:13–21 (1991)
13. Szecy, R. S., Concrete Rheology, Ph.D. Thesis, University of Illinois at Champagne-Urbana (1997)
14. Hu, C., de Larrard, F., and Gjørv, O. E., Rheological Testing and Modelling of High Performance Concrete, *Mater. Struct.*, 28:1–7 (1995)
15. Hu, C., de Larrard, F., Sedran, T., Boulay, C., Bosc, F., and Deflorenne, F., Validation of BTRHEOM, The New Rheometer For Soft-to-Fluid Concrete, *Mater. Struct.*, 29:620–631 (1996)
16. Punkki, J., Golaszewski, J., and Gjørv, O. E., Workability Loss of High Strength Concrete, *ACI Mater. J.*, 93:427–431 (1996)
17. Hu, C., and de Larrard, F., The Rheology of Fresh High-Performance Concrete, *Cem. Concr. Res.*, 26:283–294 (1996)
18. de Larrard, F., Hu, C., Szitkar, J. C., Jolu, M., Claux, F., and Sedran, T., A New Rheometer for Soft-to-Fluid Fresh Concrete, submitted for publication in *ACI Mater. J.*, (1995)
19. Banfill, P. F. G., and Saunders, D. C., On the Viscometric Examination of Cement Pastes, *Cem. Concr. Res.*, 11:363–370 (1981)
20. P. F. G. Banfill, Feasibility Study of a Co-Axial Cylinders Viscometer for Mortar, *Cem. Concr. Res.*, 17:329–339, (1987)
21. Murata, J., and Kikukawa, H., Viscosity Equation for Fresh Concrete, *ACI Mater. J.*, 89:230–237 (1992)
22. Murata, J., Flow and Deformation of Fresh Concrete, *Mater. Constr.*, 17:117–129 (1994)
23. Banfill, P. F. G., A Viscometric Study of Cement Pastes Containing Superplasticizers with a Note on Experimental Techniques, *Mag. Concr. Res.*, 33:37–47 (1981)

@Seismicisolation

24. Lapasin, R., Papo, A., and Rajgelj, S., Flow Behavior of Fresh Cement Paste. A Comparison of Different Rheological Instruments and Techniques, *Cem. Concr. Res.*, 13:349–356 (1983)

25 Wallevik, O. H., and Gjørv, O. E., Development of a Coaxial Cylinders Viscometer for Fresh Concrete, in: *Properties of Fresh Concrete*, pp. 213–224, Chapman and Hall, Cambridge (1990)

26. Struble, L. J., Lei, W. G., Sun, G. K., and Szecsy, R. S., Rheology of Cement Paste and Concrete, submitted to *Cem. Concr. Aggregates* (1996)

@Seismicisolation

10

Dimensional Changes

James J. Beaudoin

1.0 INTRODUCTION

Dimensional changes occurring in concretes are extensively studied and reported in books and standards. Dimensional change of cement systems (compacts, pastes, mortars, concretes) can result from chemical interaction (solution/precipitation in micropores; solution/solid topochemical reactions) or physical processes associated with adsorption phenomena and other stress generating internal mechanisms. The monitoring of length or volume-change is relatively simple. The magnitude, rate and character of the length-change time response can provide insight on the nature of destructive mechanisms associated with the durability of cement and concrete products. In addition, the engineering characteristics of the microstructure itself can be determined from length-change adsorption isotherms. The volume instability of porous solids is dependent on the interaction of aggressive media with the host material or other solids/impregnates resident in the micropores. The associated dimensional changes can often be considered descriptors of distress.

The fundamentals of the energetics of surface adsorption relating to volume change in cement pastes form the scope of this chapter. Studies specifically chosen to highlight the relevance of length-change measurements with respect to concrete deterioration will also be described in this chapter.

@Seismicisolation

2.0 ENERGETICS OF ADSORPTION

2.1 Length Change Isotherms

Length change of thin cement paste samples can be measured using modified Tuckerman optical extensometers placed in individual cells equipped with optical windows.[1] The sensitivity of these devices is about 2×10^{-6} mm/mm. A schematic diagram of the extensometer is provided in Fig. 1. The sample (1) is held against the knife edges (2 and 3) by a light spring (4), the sample resting on a holder (5). The optical system consists of a fixed mirror (6) and a tilting mirror (7) which is one face of the rocking lozenge. The whole assembly is supported by a stand (8). The assembly can be placed in a hydration cell or other closed vessel for length change measurements in a variety of closed environments.

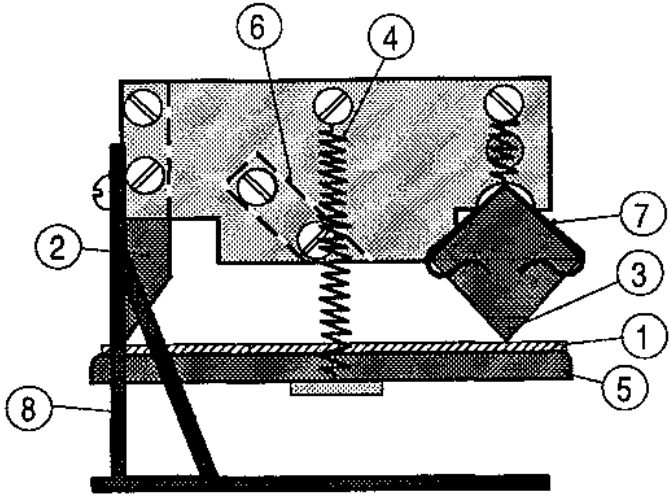


Figure 1. Schematic of a modified Tuckerman Optical Extensometer. The number designated parts of the apparatus are defined in the text.[1]

A typical length change isotherm for hydrated cement paste is illustrated in Fig. 2.[2] It is essentially the length change response at various partial pressures (water vapor as the adsorbate). Measurements utilizing the extensometers described above are taken in a high vacuum system with the facility to admit water vapor at various intermediate vapor pressures below

@Seismicisolation

saturation. The isotherm exhibits large primary and secondary hysteresis over the entire range of partial pressures. It is apparent that non-adsorption processes are operative. The presence of scanning loops provides a means of separating the isotherm into reversible and irreversible components, Fig. 3.[3] The scanning loop is graphically separated into the "adsorbed" component and "interlayer" component in steps and a reversible isotherm reconstructed accordingly, Fig. 4.[2]

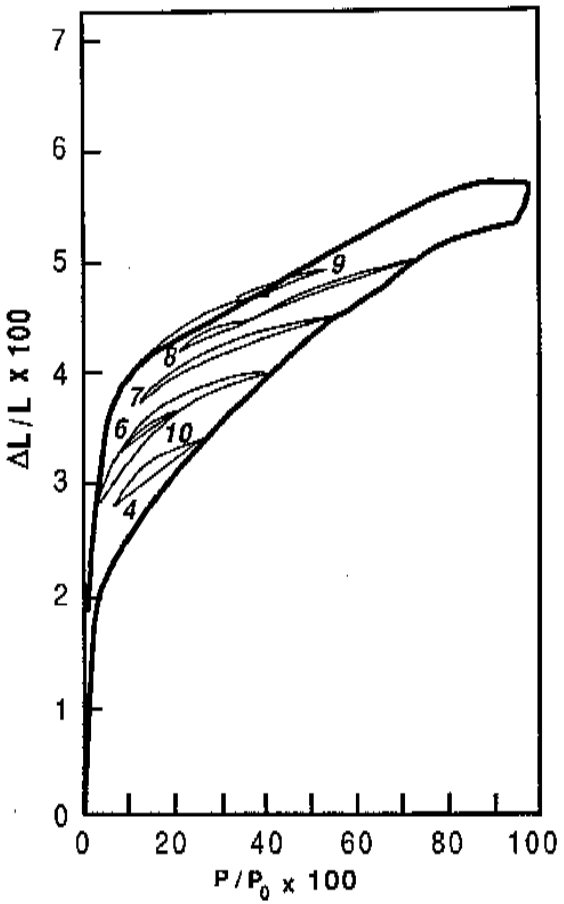


Figure 2. A typical length-change isotherm of hydrated portland cement paste (water-cement ratio, 0.50). Scanning loops are marked.[2]

@Seismicisolation

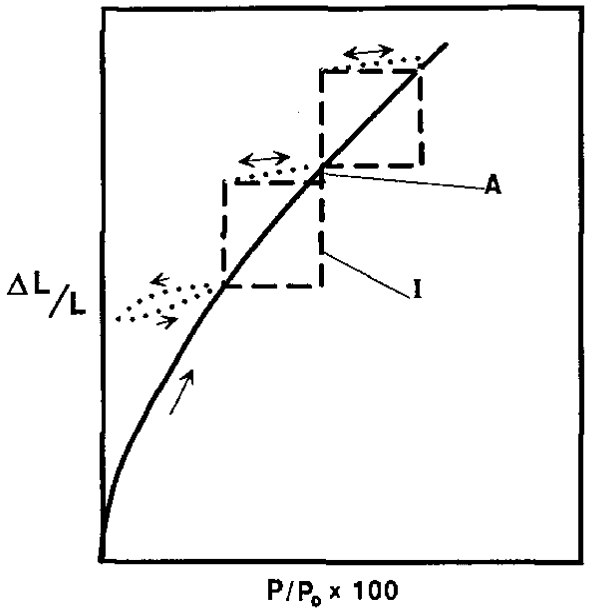


Figure 3. A schematic of a length-change isotherm illustrating a method of separation of interlayer and adsorbed water.[3]

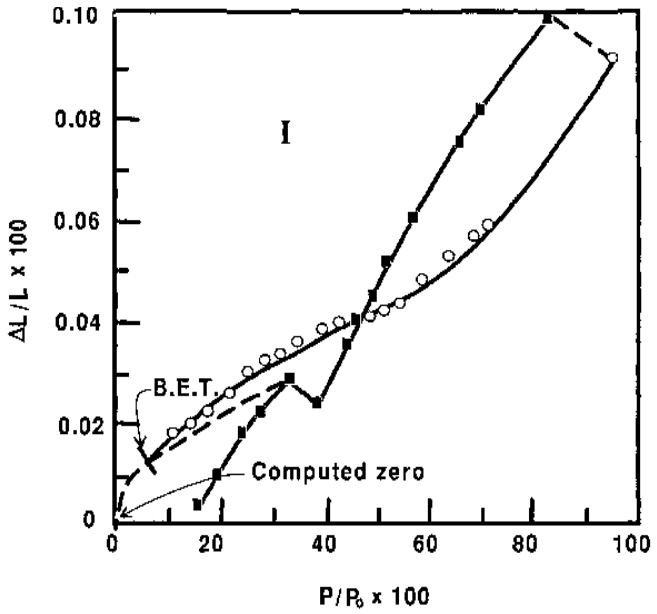


Figure 4. A reconstructed reversible water isotherm using the method illustrated in Fig. 3.[2]

@Seismicisolation

The change in surface free energy, $\Delta\gamma$, can be expressed by the following equation:

Eq. (1) $$\Delta\gamma = \frac{RT}{\sigma} \cdot n \int_{P1}^{P2} \frac{dP}{P}$$

where, n is the number of moles of adsorbate on a fixed mass of adsorbent; σ is the solid surface area; R is the gas constant; T is the temperature and P the vapor pressure.

Length change, $\Delta L/L$, can then be estimated from the following relationship:

Eq. (2) $$\frac{\Delta L}{L} = K\Delta\gamma$$

A plot of $\Delta L/L$ versus $\Delta\gamma$ is given in Fig. 5.

The elastic modulus of the solid material can be calculated from

Eq. (3) $$E = \rho \frac{\sigma}{K}$$

where E is the elastic modulus, ρ is the density and K the proportionality constant in Eq. (2). A value of K determined from the slope of the line in Fig. 5 is 3.90×10^{-6} cm/dyne. A value of E for the C-S-H solids is about 2.99×10^4 dyne/cm^2 or 4.35×10^6 psi assuming the solid density is 2.86 g/cm^3 and the surface area is 40.8 m^2/g (estimated from the reversible weight change isotherm).

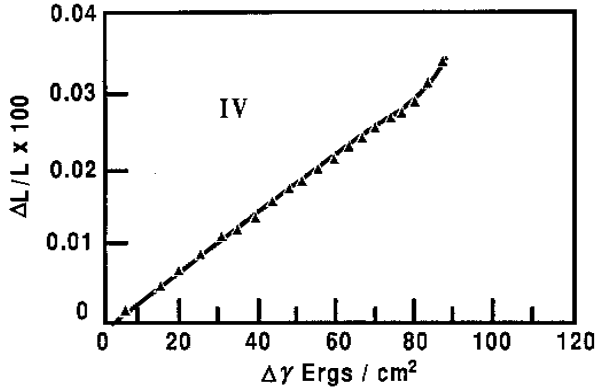


Figure 5. Length change versus change in surface free energy determined from a constructed reversible water isotherm as illustrated in Fig. 4.[2]

@Seismicisolation

2.2 The Theory of Flood and Heyding

A length-change theory developed by Flood and Heyding (F-H) for microporous solids can be applied to cement paste in order to determine the effect of porosity and compressibility on the solid phase.[4]

Briefly, the F-H theory assumes that assemblies of volumes of pure adsorbable gas and assemblies of volumes of pure adsorbent can exist separately in equilibrium with externally applied forces in states thermodynamically identical to those in the adsorbent-adsorbate system. The conditions of reversibility and equilibrium lead to the following expression for the pressure of the pure adsorbate, p_a, in the pore volume V_a

Eq. (4) $$p_a = \int_o^{p_1} \frac{\rho_a}{\rho_1} dp_1 = \overline{(\rho_a/\rho_1)} \cdot p_1 = \alpha\, p_1$$

where ρ_a is the mean density of the substance in V_a, and p_1 and ρ_1 are the gas pressure and density of the gas surrounding the sample. The term, α, is the mean value of ρ_a/ρ_1 averaged over the pressure interval dp_1.

If $\phi = V_a/V_s$, where V_s is the nonporous solid volume, it may be shown that $p_s = (1 + \phi - \alpha\phi)p_1$, which is the pressure on the solid adsorbent in equilibrium with the surrounding gas at pressure p_1.

If the pressure on the solid adsorbent is uniform, the length change isotherm can be obtained from the equation

Eq. (5) $$\frac{\delta \ell}{\ell} = \frac{1}{3}\beta(1 + \phi - \phi\alpha)dp_1$$

where β is the compressibility of the porous body.

Where solid pressures are not constant, κ, a small numerical factor dependent upon the structure of the porous solid, is introduced into Eq. (5), i.e., the term in brackets becomes $(1 + \phi\kappa - \phi\kappa\alpha)$. The term κ, the ratio of the linear average pressures to volumetric average pressures, is generally independent of the nature of the adsorbate, but is a characteristic of the structure of the adsorbent. Flood and Heyding determined values of κ for various ideal models of pore structure, e.g., $\kappa = 1.0$ for a system of continuous non-intersecting straight capillaries, and $\kappa = 5.6$ for a system of continuous intersecting straight capillaries. If the shape of the average pore

@Seismicisolation

is not statistically independent of the surface free energy of the solid enclosing the average micropore, then κ will become a function of p_1. For large adsorptions $\alpha >> 1$ and

Eq. (6) $$\frac{\delta \ell}{\ell} = \frac{1}{3} \beta \phi \kappa dp_a$$

i.e., $\frac{\delta \ell}{\ell}$ becomes proportional to $\int_o^{p_1} \frac{\rho_a}{\rho_1} dp_1$

A brief comment on the assumptions made in using isotherm data to apply the F-H procedure follows. Along the adsorption branch of the cement paste-water isotherm several reversible and irreversible effects occur. If relative humidity is reduced from a particular value on the adsorption curve, a scanning curve is obtained, for example, curves 1, 2, 3, Fig. 6. It has been argued that (to a first approximation) mainly reversible processes occur over a large part of the scanning curve. A "reversible" isotherm can be constructed by appropriate summation of reversible portions of the scanning curves, as described previously. It is assumed that irreversible effects can thus be separated from reversible ones. In addition, it is recognized that the reversible adsorption processes operative along each scanning curve are acting on a material that has changed since the previous scanning curve, i.e., the material is different for each of curves 1, 2, 3, Fig. 6. Thus, in transferring from curves 1 to 2 to 3, irreversible processes are operative.

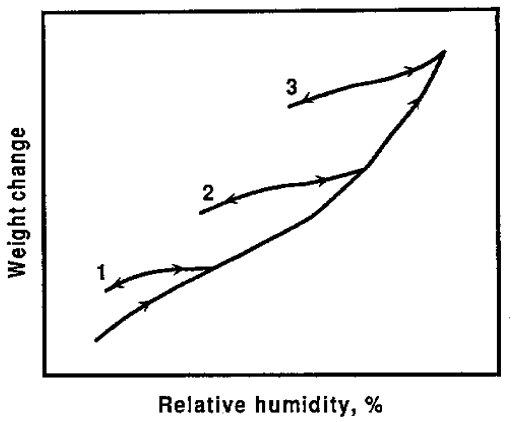


Figure 6. A schematic of a primary adsorption curve with scanning curves.[4]

@Seismicisolation

Application of the F-H procedure to the reversible isotherm assumes, however, that the irreversible changes in the solid material (interlayer penetration, etc.) do not affect the nature of the reversible adsorption processes occurring on the surface of the layers and that surface energy changes are acting on a different material with different properties when positions are changed on the isotherm. It is assumed then, that a step-by-step application of the F-H procedure along the reversible adsorption path is valid, even where intercalation of the layered silicate hydrate occurs; i.e., since the scanning isotherm is reversible, the F-H procedure is applicable. If scanning isotherms are irreversible, then changes have occurred in the porous system and the F-H procedure cannot be applied. Thus, the procedure may not be applicable when major changes in pore structure occur.

Figure 7 is a plot of length change versus vapor pressure, giving curves for Eq. (6) and experimental values. A single average value of $\beta\kappa = 1.76 \times 10^{-4}$ MPa^{-1} was chosen to give a close fit between the experimental length change data and Eq. (6).

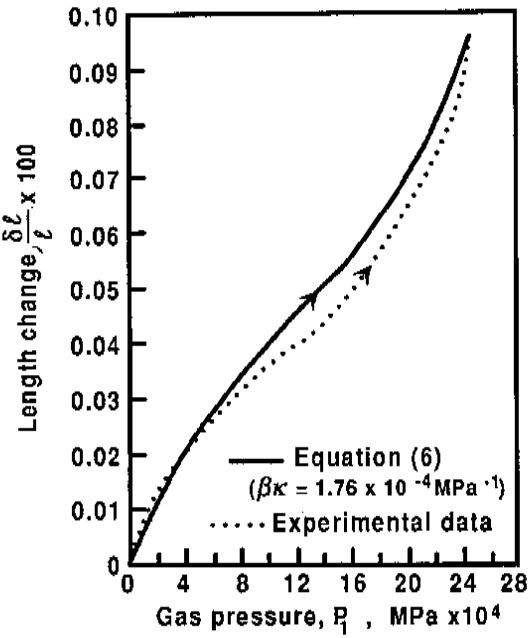


Figure 7. Reversible length change isotherm for portland cement paste (water-cement ratio 0.50) showing experimental and theoretical (Flood and Heyding) results.[4]

@Seismicisolation

Although this value of $\beta\kappa$ gives an approximation of the experimental data, $\beta\kappa$ varies with p_1 and a more exact fit can be obtained by calculating $\beta\kappa$ at each data point. Values of $\beta\kappa$ at different humidities along the adsorption curve were calculated from Eq. (6) using experimental values of $\delta\ell/\ell$.

Values of $\beta\kappa$ were also calculated for a cement paste-water isotherm scanning curve over the range 56 to 11% RH. The $\beta\kappa$ was approximately constant over that portion of the scanning curve (56–40% RH) used to construct the reversible isotherm. This supports the assumption that material properties are constant on the segment of each scanning curve used to construct the reversible isotherm.

Values of β are calculated from $\beta\kappa$ values, assuming κ = 1.91. Choice of this κ value gives an initial value of β comparable to β calculated from the relation

$$\beta = \frac{3}{E}(1 - 2\nu)$$

where ν is Poisson's ratio of 0.20, as well as β determined by other methods.

Figure 8 is a plot of $\beta\kappa$ versus relative humidity for cement paste showing that $\beta\kappa$ is dependent on RH. The dependence of $\beta\kappa$ on RH is expected for cement paste since the hydrated calcium silicates are unstable, i.e., C-S-H solids change as RH increases.

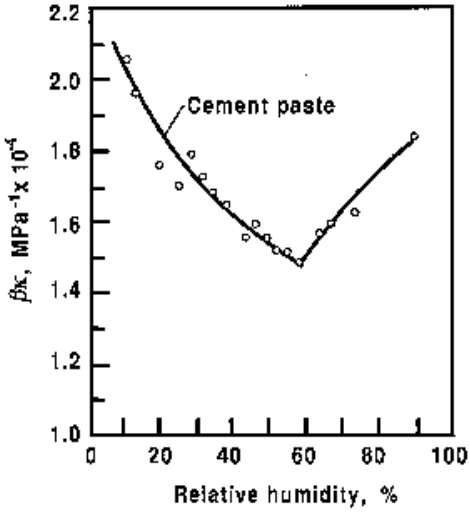


Figure 8. Dependence of the compressibility term $\beta\kappa$ on relative humidity for portland cement paste.[4]

@Seismicisolation

Figure 9 is a plot of modulus of elasticity, E, versus RH for paste. One of the curves is a plot of the calculated E (determined by F-H procedure using $\kappa = 1.91$).

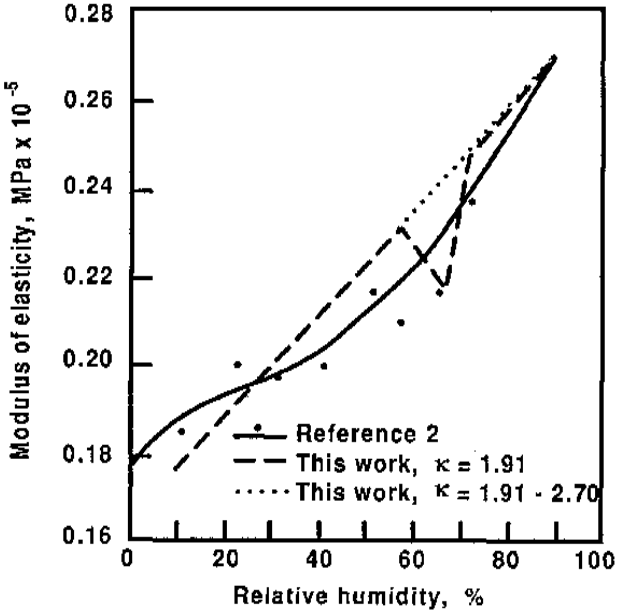


Figure 9. Modulus of elasticity versus relative humidity for cement paste determined using Flood and Heyding approach (water-cement ratio, 0.50).[4]

On adsorption up to 56% RH, the two curves have a maximum difference in E (at any RH) of only 0.01×10^5 MPa, and E increases with RH. At higher humidities, use of the structure factor $\kappa = 1.91$ gives decreasing values of E to 68% RH, followed by another increase in E as RH increases further. By adjusting κ at each humidity above 56% RH, however, (and determining a new value of β from $\beta\kappa$), the calculated value of E increases monotonically as the dashed curve (Fig. 9) is extended from 56 to 88% RH. The extended curve also gives values of E close to those determined by experiment.

@Seismicisolation

3.0 CHEMICAL INTERACTIONS IN POROUS MEDIA

3.1 Volume Instability

Volume change of porous solids, e.g., cement paste due to chemical attack, has been reported in numerous studies.[5][6] The length change of porous glass due to dissolution in 0.2N NaOH solution (Fig. 10) and cement paste immersed in 1.0N aqueous HC1, Figs. 10 and 11, and leaching of porous glass in acid and cement paste in ethylene glycol are remarkably similar.

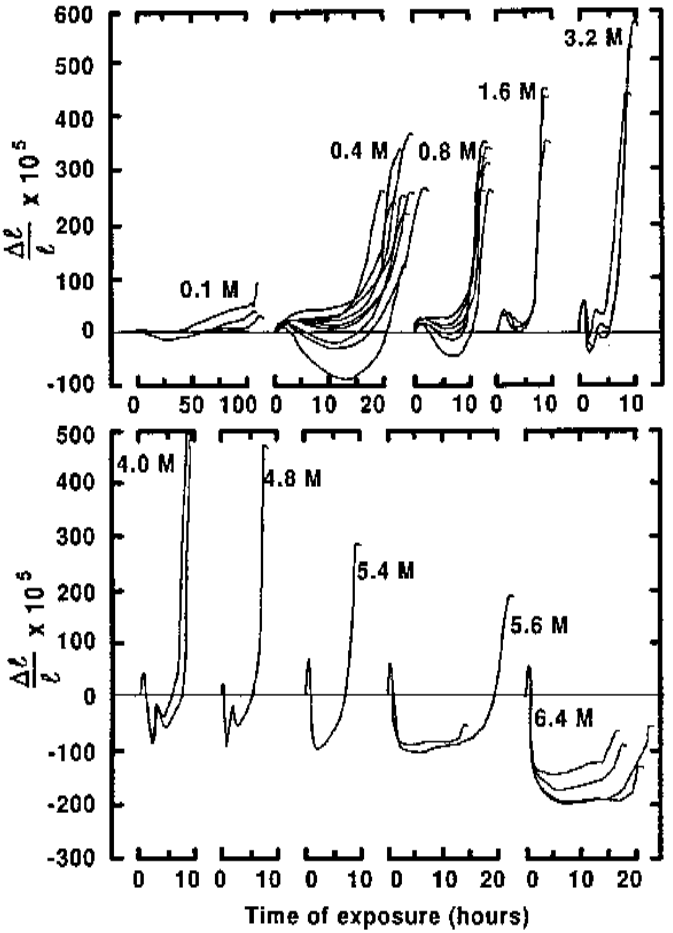


Figure 10. Length-changes of 3 mm thick porous glass specimens on exposure to NaOH solutions of various concentrations.[5]

@Seismicisolation

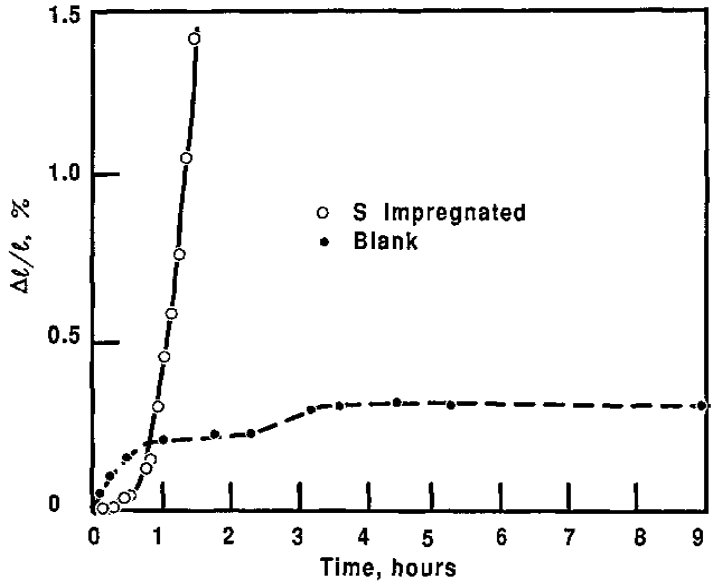


Figure 11. Length-change of porous glass impregnated with sulfur and exposed to water vapor.[7]

Osmotic pressure, crystallization pressure, and mechanical pressure, exerted by the volume requirement of the reaction product which is greater than the space available, plus gel formation followed by water adsorption have all been suggested as causes of volume expansion of cement paste on chemical attack. None of these theories is universally accepted.

The solid matrix itself has not generally been considered responsible for volume change, but was assumed to expand passively in response to an internal pressure generated in the void space (e.q., crystallization or osmotic pressure). Changes occurring on the surface, whether sorption of inert ions or dissolution of either a constituent of a non-homogeneous matrix or a portion of the entire solid, result in expansion of a magnitude that induces cracking. It appears that such alteration of the surface energy is sufficient for the disjoining pressure to become dominant. This assumption offers a simple and unified explanation of a number of deterioration processes leading to excessive volume instability and cracking.

The character of the length-change curves of porous glass in NaOH solution is dependent on the concentration of the alkali and thickness of the specimen. The results (e.g., Fig. 10) suggest that dissolution of glass leads

@Seismicisolation

to expansion and that surface reaction and chemisorption lead to contraction. The presence of calcium cations in solution (e.g., 1 M $CaCl_2$) significantly retard dissolution and expansion. The saddle effect (6.4 M NaOH solution, Fig. 10) can be attributed to opposing actions, i.e., dissolution, causing expansion, and adsorption, causing contraction. The largest expansions occur just before collapse because the unaffected core of the glass restricts expansion of the specimen. Thus, when the core is reduced to a minimum or zero, the restraint is removed. The adsorption induced contraction depends on the silicate concentration of the solution (i.e., the amount of glass already dissolved), the time available for the species to diffuse to the interior of the specimen, and the size of the undissolved glass volume in which adsorption takes place. Thus, expansion is dominant in the last phase of dissolution while adsorption and the resulting contraction increases during the course of dissolution, reaching a maximum value at an intermediate phase.

There are several causes of the expansion that occurs during dissolution of the porous glass: changes in surface-free energy of the glass, osmotic pressure due to regional differences in concentration of dissolved species, and disjoining pressure due to overlapping electric fields of two surfaces. The double layer outside the surface contains mainly cations adjacent to the SiO^- groups and anions in the outer regions; release of internal compressive stresses occurs through leaching of B_2O_3.

It is suggested that the contraction observed during dissolution experiments is due to adsorption of the reaction products on the undissolved glass. Pronounced shrinkage occurs in the thicker specimens which favor conditions for enhanced adsorption. This is because adsorption of the reaction products depends on the final silicate concentration of the solution, which is determined by specimen thickness. Further support for the hypothesis of contraction-surface reaction is provided by dissolution experiments in presence of $CaCl_2$. The time dissolution is much longer than in the reference calcium-free solution and shrinkage is promoted.

3.2 Expansion of Impregnated Systems

The durability of impregnated porous bodies can be assessed by measurements of dimensional change in various environments. The length change results of sulfur impregnated porous glass exposed to vapors of methanol, carbon tetrachloride, and water, are similar.[7] The large expansions within the first hour of exposure to water vapor are shown in Fig. 11.

@Seismicisolation

Length change of impregnated, autoclaved portland cement and cement-silica mixtures exposed to water vapor are illustrated in Fig. 12.

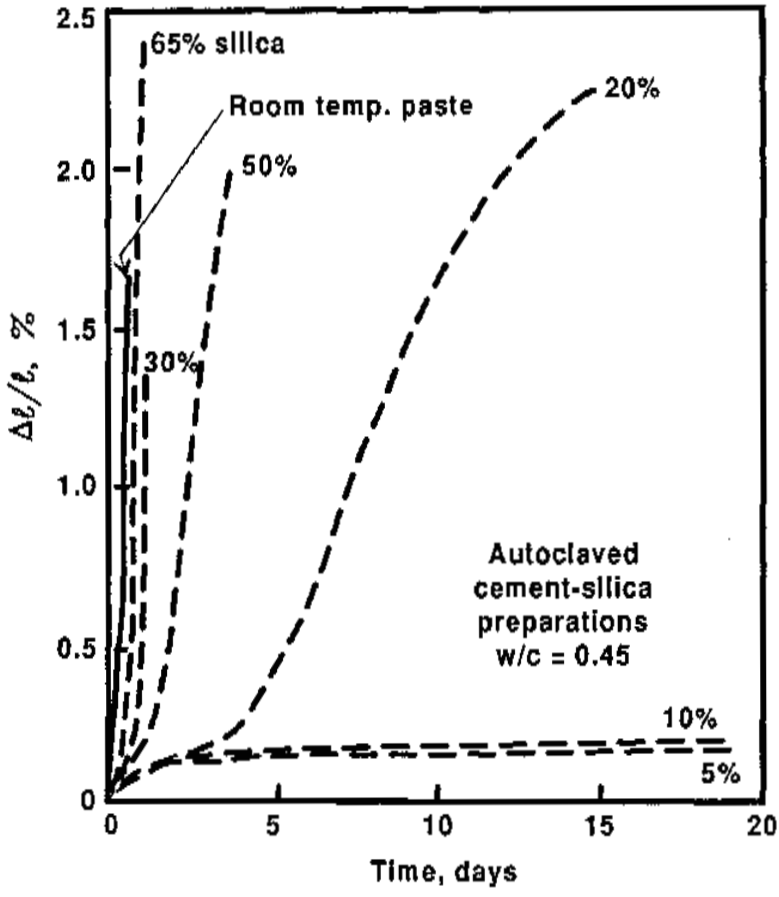


Figure 12. Length-change of impregnated, autoclaved, cement-silica preparations on exposure to water vapor versus time.[7]

Preparations containing greater than 20% silica undergo large rapid expansions similar to that for room temperature paste. All specimens conformed to the observation that the greater the specific surface area of the matrix material, the greater the expansion on exposure to water vapor.

@Seismicisolation

The sulfur impregnant in very small pores is in a very finely divided state. It may be calculated that the surface of the glass containing sulfur is in excess of 500 m^2/g due to space available between pore walls and sulfur surfaces. The potential swelling stresses due to the Bangham effect are enormous. Scanning microscopy reveals that the impregnant leaves the pores and the glass matrix ruptures.

The use of polymethyl methacrylate (PMMA) impregnant in cement systems and other porous bodies has been extensively studied. The length changes of porous glass impregnated with PMMA on exposure to water and chloroform vapors are shown in Fig. 13.[8] Length changes in the order of 0.5% are more than twice the expansion that occurs on complete saturation of dry unimpregnated glass. The length increase per unit length on adsorption of 0.0154 g water per gram glass is 50×10^{-5}. An equivalent expansion for unimpregnated glass occurs only when 0.050 g water per gram of glass is adsorbed. The moisture expansion is not totally recoverable on drying in vacuum for several months. Only 62% proved to be reversible. Considering its nonpolar nature, expansion caused by adsorption of chloroform is surprisingly large. The specimen continued to expand beyond 498 days.

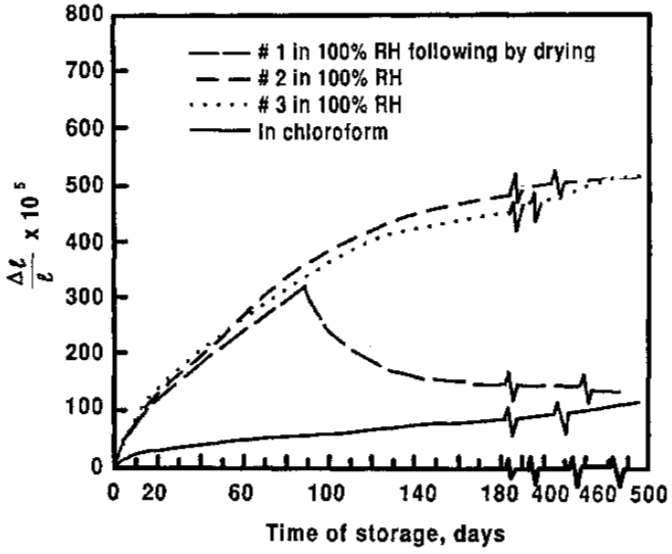


Figure 13. Dimensional changes of porous glass impregnated with PMMA on exposure to water and chloroform vapors.[8]

@Seismicisolation

An important practical difference between sulfur and polymers as impregnant is the size and shape of the molecules. PMMA, for example, is a very long polymer that can easily become entangled and, therefore, has a very high flow resistance. Although PMMA as an impregnant is perhaps inherently unstable, no migration or exudation takes place because of the hindered flow and apparently strong interaction with the siliceous surfaces. The difference in behavior of the two systems must be ascribed to better bonding of PMMA to glass. The low nitrogen surface area of 0.22 m^2/g compared to about 1.60 m^2/g for the sulfur-glass system indicates relatively good sealing of the pores and good contact between the impregnant and the substrate.

PMMA can absorb vapors and the associated swelling could generate pressure against the walls. Swelling of PMMA-impregnated glass and the increase of elastic modulus measured in flexure is possibly due to vapor adsorption. The continuing expansion after 498 days of exposure to water vapor with no associated water uptake may be explained by the static fatigue concept that is a common occurrence in glass under a sustained load. It is apparent that if vapor can penetrate a fairly impervious system, a highly uneven distribution of stress will be created that can easily lead to failure.

The above discussion is applicable, in general, to impregnated solids having small pores. However, in some cases, such as PMMA-impregnated glass, apparent stability can exist owing to good interaction between the polymer and glass, the cross-linking in the polymer, and the spatial hindrance to flow.

3.3 Dimensional Change and Alkali-Aggregate Reactivity (AAR)

Expansion of concrete due to interaction between alkali in cement and reactive aggregate has been studied extensively and various hypotheses have been proposed to explain the operative mechanisms. Alkali-silica and alkali-carbonate reaction mechanisms have been described.

Length-change isotherms of reactive aggregate have been used to explore expansion mechanisms.[9] Comparison with results for porous glass obtained for similar conditions suggests that the mechanism of expansion is similar to the alkali-silica complex formed in the pores of Vycor glass.

Sorption isotherms of alkali-treated limestone are characteristically different from untreated limestone, Fig. 14. There is an increase in sorbed water along the isotherm, an increase in porosity, distortion of the normal

@Seismicisolation

hysteresis loop observed in untreated samples, and large secondary hysteresis. The sorption isotherm for the treated porous glass has similar characteristics to that for treated limestone. Typical length change isotherms for treated and untreated limestone are shown in Fig. 15. The expansion of the treated sample is 0.12% compared to 0.04% for the untreated sample.

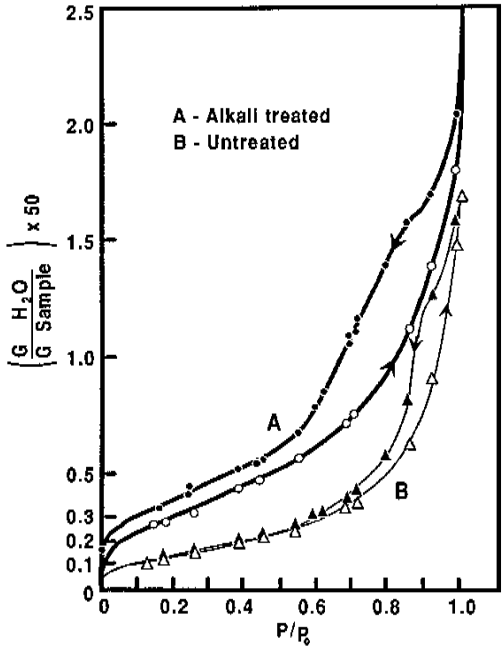


Figure 14. Sorption isotherms of alkali treated and untreated Kingston limestone (24–30 ft. bed) green.[9]

If expansion is due to a formation of a gel or a hydrate, a degree of reversibility is expected on dehydration. This seems to be the case. The secondary hysteresis is typical of a sorption system which swells. This can be explained by intercrystal penetration of water during sorption. Removal is irreversible. There is considerable evidence that the material causing expansion and identified by the characteristics in the isotherms of the treated limestone, whether it be a gel or a hydrate, is produced either as the result of or in association with the dedolomitization reaction. The sorption and length change isotherms of the alkali-treated limestone establish the presence within the pores of trace amounts of a material that caused expansion when water is made available to it. The mechanism of expansion

@Seismicisolation

is similar to that attributed to the alkali-silica complex formed in the pores of porous glass although the composition of the material may be different. It is apparent that techniques involving dimensional change can establish the presence and character of expansive agents in porous materials.

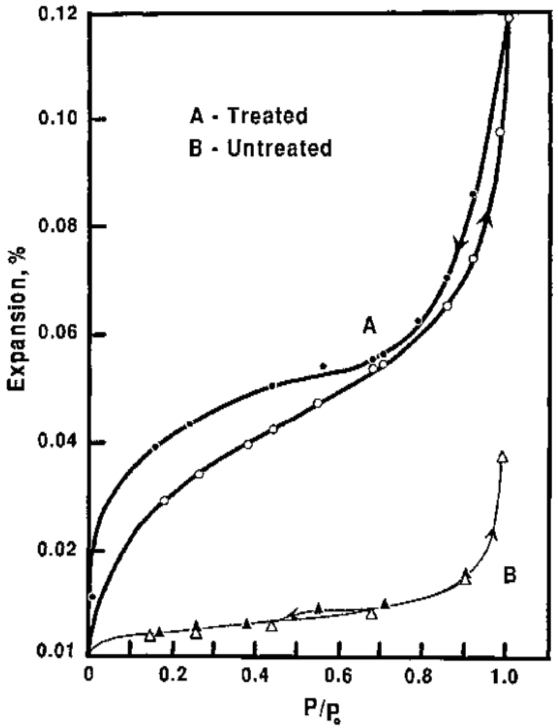


Figure 15. Length-change isotherms for alkali treated and untreated Kingston limestone (24–30 ft, bed) green.[9]

Several test methods for alkali expansivity rely on dimensional change measurements as an indicator of performance. These include: ASTM C289 (Quick Chemical Test); ASTM C227 (Mortar Bar Test); Modified ASTM C227 (Concrete Prism Test); Modified ASTM C586 (Rock Cylinder Test). An accelerated rock prism test was suggested as being useful for preliminary screening of potential aggregates to determine which would need further testing by the more protracted mortar bar or concrete prism methods.[10]

@Seismicisolation

The test is used to illustrate the utility of dimensional changes for distinguishing the expansive potential of different rock types. Small rock prisms, 20 × 6.35 × 3.18 mm thick, are employed. The prisms are vacuum saturated with 2N NaOH solution at the start of the experiment. Length change is continually monitored. Typical expansion curves for three pairs of rock prisms are shown in Fig. 16. The two feldspathic quartzites are known from concrete prism tests to be expansive; the amphibolite is non-expansive. The problem is how to designate rocks that have curves lying between the quartzites and the amphibolite. Nevertheless, the rock prism test shows promise of providing a relatively rapid method of screening aggregate which may be potentially alkali-silicate reactive.

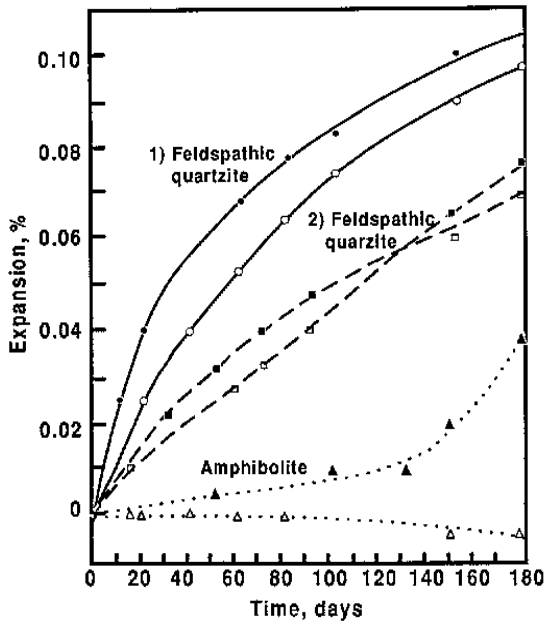


Figure 16. Expansion results from the rock prism test on duplicate samples of aggregate immersed in 2N NaOH solution.[10]

3.4 Sulfate Resistance

The literature on the sulfate resistance of portland cement concrete is extensive.[11] The cement chemistry relating to the interaction of sulfates with cement minerals is well documented and will not be covered in this chapter.

@Seismicisolation

The mortar bar tests with added sulfate (bringing the SO_3 content to 7% by mass of cement) conducted by the U.S. Corps of Engineers serve to illustrate the utility of dimensional change as a descriptor of chemical resistance.[12] Expansion versus C_3A content of the cement is plotted in Fig. 17. The data in the figure describe the relationship between the 28 day and 1 year expansion and calculated C_3A content. An anomaly in one of the cements (No. 15 indicated on the figure) was observed. It had an unusually low expansion ranging from 0.132 to 0.143%.

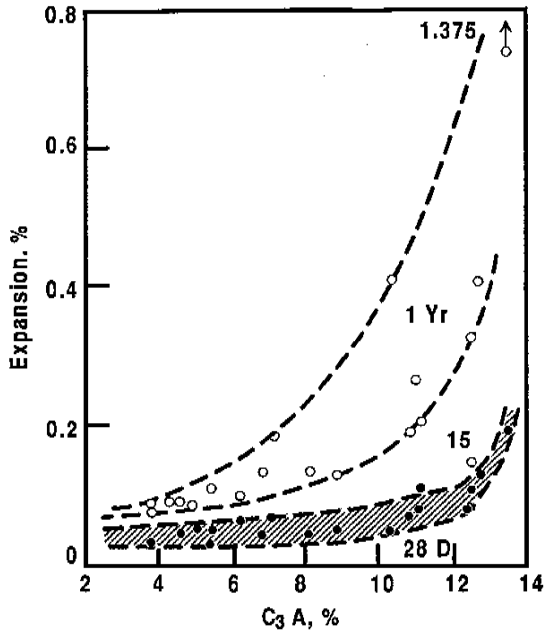


Figure 17. The relationship between expansion and tricalcium aluminate content in the sulfate resistance test.[12] The results for Cement 15 are identified and discussed in the text.

Significant differences in the shapes of the curves for expansion versus time were also noted, Fig. 18. The numbers in the figure refer to the original cement designations. The expansion levels at which the plateaus were observed did not conform to the expected levels based on amounts of C_3A and sulfate. Cement 15 (Fig. 17) had only one third as much expansion as Cement 13 although it contained 2.5% more C_3A. The cements had similar fineness values, but Cement 15 had a significantly greater amount of C_3A, larger heat of hydration, and nearly double the compressive

@Seismicisolation

strength. It is apparent that the low expansion of Cement 15 was contributed to by its rapid rate of strength development. Conversely, the higher expansion of Cement 13 was contributed to by its slow rate of strength development.

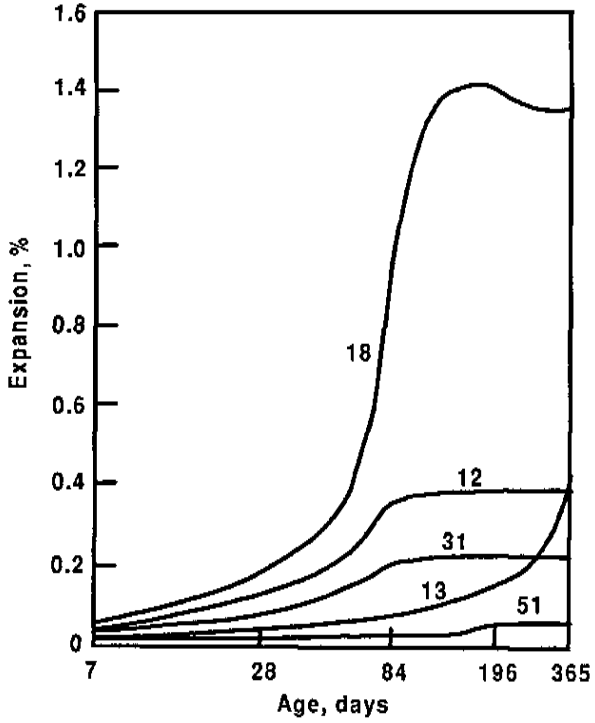


Figure 18. Sulfate-resistance test results for selected cements (see text).[12]

The expansion results described above were similar to those found for portland blast-furnace slag cements, i.e., the indicated sulfate resistance appeared to be primarily influenced by the calculated C_3A content of the portland cement clinker constituent of the blended cement.

The ASTM C1038-89 is a test which determines the expansion of mortar made from portland cement of which sulfate is an integral part. It should be noted that the above discussion is essentially a precursor of this test. Excess sulfate content is identified, the effects of which are related, but independent in any absolute sense to attack by external sulfates.

@Seismicisolation

The immersion of well-hydrated mortar in a sulfate solution forms the basis for the ASTM C1012-89 test method. Excessive expansion is used as a failure criterion. It should be noted that specimen geometry may affect inferences drawn from test methods that rely on dimensional change. This is particularly true in a test method that relies on the ingress of aggressive media into a concrete sample. Layering of mortar or concrete due to deleterious reactions within a few millimeters of the sample surface may occur while the core of the specimen remains unaffected. The use of thin samples, where possible, may be more effective, as described in Ch. 11.

The deterioration of concrete due to delayed ettringite formation (DEF) in high temperature cured cement products has been reported extensively.[13] Damage of concrete due to DEF (as distinct from secondary ettringite formation (SEF) which does not necessarily require initial high temperature curing) has been investigated primarily in concrete members subjected to high temperature curing followed by open-air weathering and hence drying/re-wetting cycles, e.g., precast front panels and railway sleepers.[14] Cases have been observed in Germany, Finland, Australia, South Africa, and the USA. These concretes were mostly made with high early strength portland cement and accelerated steam curing was employed. The products underwent drying/wetting, freezing/thawing, and fatigue cycles, year around. Heat-drying is possibly experienced during summer.

Dimensional change was shown to be a useful tool for establishing the relative importance of microcrack formation following high temperature curing on subsequent deterioration of concrete due to DEF.[15]

Expansion measurements indicated that only certain concretes subjected to high temperature curing followed by severe heat-drying suffered large expansion due to delayed ettringite formation. Other treatments, such as loading/unloading cycles, freezing/thawing cycles, and room temperature drying, did not show DEF-induced expansion. The expansion of the heat-dried concrete (made with cement having surface area greater than 5000 cm^2/g and total SO_3 content greater than 4.0%) increased to about 0.2% after 110 days curing and reached about 0.5% at 250 days.

3.5 Dimensional Stability of Cement-Calcium Carbonate Systems

The practice of producing portland cement containing finely ground limestone has increased in North America during the 1990s. Despite the well

@Seismicisolation

documented benefits of carbonate addition there appears to be considerable uncertainty concerning the durability of concrete products containing these cements. Dimensional change assessment of these materials in aggressive environments provides a means of determining performance.

Addition of calcium carbonate to portland cement influences not only the kinetics of hydration of the individual phases, but also the setting and mechanical properties.[16][17] Few studies have been directed at the long-term durability aspects of cement-carbonate systems. It has been found that mortar containing calcium carbonate, after exposure to sea water, exhibits higher expansion than the reference mortar containing no carbonate.[18] Length change measurements were also used to assess the effect of sodium and magnesium chloride solutions on mortar containing up to 15% calcium carbonate.[19]

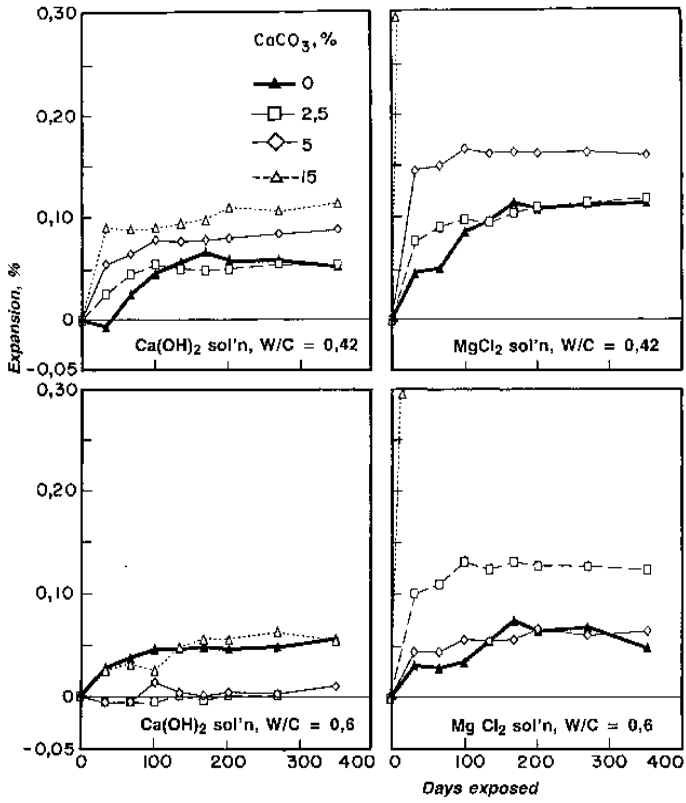


Figure 19. The effect of precipitated calcium carbonate on expansion of mortars exposed to magnesium chloride.[18]

@Seismicisolation

The effect of precipitated calcium carbonate on expansion of mortars (cement-sand ratio, 1:2.75; water-cement ratio, 0.42 and 0.60) exposed to magnesium chloride solution is illustrated in Fig. 19.

Generally, expansions observed for samples exposed to $MgCl_2$ solutions (40 g/l) are greater than those exposed to seawater.[19] Samples with precipitated calcium carbonate in amounts greater than 2.5% and prepared at water-cement ratio 0.42 show increased expansion on exposure to $Ca(OH)_2$ solution. The expansion relative to ground (coarser) $CaCO_3$ is also higher.

Exposure to $MgCl_2$ solution causes major increases in expansion both with respect to the reference and the sample containing the ground carbonate addition and exposed to $Ca(OH)_2$ solution. The expansion is also greater than that observed for the same samples exposed to NaCl solution and in some instances to seawater.

A brief description of the cement chemistry associated with chloride interactions is helpful to understand the length change phenomena described above. The major compounds that may be formed at 14 days in the cement paste before exposure to chloride solution are as follows: calcium silicate hydrate (some carbonate may be associated with it); calcium hydroxide; high/low calcium sulfoaluminate hydrate (some replacement of Al by Fe); and low/high calcium carboaluminate hydrate. After exposure to chloride solutions, additional compounds may form such as: low/high chloroaluminate hydrates, C-S-H containing bound or chemisorbed chloride and thaumasite.

The dimensional behavior of cement-carbonate systems is significantly different than that occurring in the absence of carbonate. The higher expansion values in pastes containing carbonate occurring on exposure to chloride solutions are related not only to the initial values at 14 days, but also to subsequent interactions. Some of the possibilities include: a weakened structure due to the formation of chloroaluminates at the expense of carboaluminates,[20][21] replacement of Ca in the C-S-H phase with Mg from $MgCl_2$ resulting in increased porosity,[22] formation of a solid solution series by substitution of Ca by Mg in $C_3A{\cdot}CaCO_3{\cdot}11\ H_2O$; formation of a modified ettringite-like complex containing SiO_2 and Cl^-; decrease in density of the chloroaluminate phase compared to the carboaluminate phase from which it may form,[23] formation of taumasite; interaction of chloride with the C-S-H phase, substituted carboaluminate formation, and increased solubility of products due to lower pH conditions.

It was concluded that expansion of cement systems containing both ground (surface area, 2.25 m^2/g) and precipitated (surface area, 6.88 m^2/g) calcium carbonate increased upon exposure to NaCl or MgCl solutions relative to values obtained on exposure to $Ca(OH)_2$ solution.[19] Deleterious

@Seismicisolation

effects were dependent on the water-cement ratio, carbonate fineness, and its concentration. The greater deleterious effects for the precipitated carbonate can be explained by the increased rate of the relevant reactions and an increase in the amounts of the products formed at a particular period. It appears that continuous monitoring of length change is a reasonably good nondestructive technique to assess the durability of mortars exposed to various aggressive solutions.

3.6 Dimensional Stability of Blended Cement Systems Exposed to Chloride Solutions

Substantial work in the 1990s has demonstrated the benefit of using supplementary cementing materials to improve the durability of concrete structures. The performance of blended cement binders has been shown to be effective in extending the service-life of concrete exposed to aggressive environments, e.g., chloride solutions adjacent to potash mine shafts.[24]

Condensed silica fume has been found to react relatively rapidly with hydrating cement to produce a dense impermeable material. The dimensional stability of blended cement systems can be determined by continuous monitoring of length change during exposure to concentrated solutions of salts containing chlorides. This is illustrated by the results of experiments where mortars containing 0, 10, and 30% silica fume (water-cementitious solids ratio, 0.45 and 0.60) were exposed to a solution containing 27.5% $CaCl_2$, 3.9% $MgCl_2$, 1.8% NaCl, 0.1% $NaHCO_3$ - pH = 6.3. The salt solution simulated that of groundwater from a potash mine. Resistance to the salt solution (as determined by the length change response) improved greatly after 7 days moist curing for the specimens containing 30% silica fume and having the water-solids ratio 0.45. Specimens containing 10% silica fume and prepared at water-solids ratio 0.45 were also resistant after 28 days moist curing.

The freezing-thawing resistance results (expansion versus number of freezing-thawing cycles) for mortars cured for 28 days are presented in Fig. 20. None of these samples was air-entrained. The expansion results for cement-silica fume systems are indicative of some apparent anomalies with respect to the effect of water-cement ratio and strength on frost resistance.

The sample designations in Fig. 20 are explained as follows: B-blended cement mortar; C-plain cement mortar. The subscripts refer to the amount (mass %) of silica fume. The superscripts (H or ℓ) refer to high or low water-solid ratio. Specimens C^{ℓ} and B_{10}^{ℓ} showed no sign of deterioration

@Seismicisolation

and insignificant expansion after 600 cycles of freezing and thawing. Specimen B_{30}^{ℓ} failed, however, after 190 cycles although it had the highest compressive strength at 28 days. Previous work indicated that concrete prepared at a water-cement ratio 0.40 and silica fume content of 20–30% can undergo excessive expansion.[25] The samples prepared at water-solids ratio 0.60 displayed different behavior. Specimen C^{H} broke after 128 cycles, however, specimen B_{10}^{H} showed little sign of deterioration after 600 cycles. Specimen B_{30}^{H}, while showing 0.02% expansion at 250 cycles was still intact after 580 cycles. These results indicate a significant improvement in durability with addition of moderate amounts of silica fume to portland cement binders.

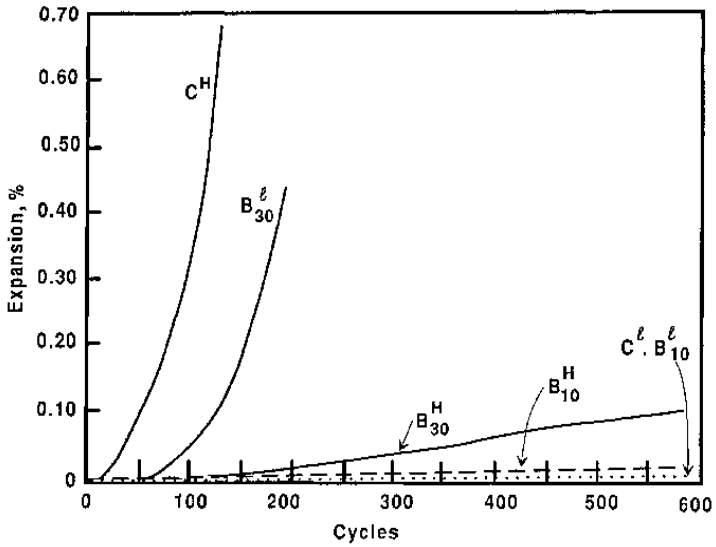


Figure 20. Linear expansion versus the number of cycles of freezing and thawing for mortars containing silica fume. The notation is explained in the text.[25]

The rapid deterioration of mortar specimen B_{30}^{ℓ} with freezing-thawing cycles is probably related to its low *permeability* and high silica fume content, i.e., 30%. The amount of silica fume is in excess of that needed for complete reaction of $Ca(OH)_2$. A relatively large amount of evaporable water was also present. The greater permeability of specimen B_{30}^{H} ensures greater frost resistance.

Specimen B_{10}^{H}, with less silica fume, displayed very little sign of deterioration. The large pores with narrow necks, simulating air-entrainment, may be responsible for the better frost resistance observed for some

@Seismicisolation

of the preparations. It was concluded that the frost resistance of mortars, even those cured at water-solid ratio 0.60 (without air-entrainment), can be improved with appropriate amounts of silica fume addition.

4.0 PHYSICOCHEMICAL INTERACTIONS IN POROUS MEDIA

4.1 Low Temperature Length Change Isosteres

Adsorption of vapors on solids at temperatures below the bulk triple-point of the substance and the anomalous behavior exhibited by porous solid-adsorbate systems on cooling are phenomena relevant to the low temperature performance of building materials.[26] Equilibrium among the three phases of a single component substance can be achieved at temperatures other than the triple point if the radii of curvature of the interfaces assume the appropriate values.

Length change isosteres for vacuum saturated cement paste specimens are shown in Fig. 21. It is apparent the curves are water-cement ratio dependent. High water-cement ratio pastes contain substantially greater amounts of capillary porosity and the dilation following initial freezing is significantly larger as is the residual length change on warming.

The length change curves are very similar to those obtained for the porous glass-water system. The anomaly in the vicinity of -8°C is associated with an exothermic heat effect and is caused by the freezing of water driven to the external surface or large pores by the vapor pressure difference that exists between the liquid-like water in micropores and ice in the macropores or on external solid surfaces.

It has been suggested that expansion occurs if the water concentration is higher than the equilibrium value at the prevailing relative humidity. This is supported by the observation that, on freezing, the length of thicker specimens increases more than the corresponding length of thinner specimens. An increase in migration path to sites of ice crystallization reduces the amount of water leaving the specimen and dilation occurs. The quantity of water exuded is dependent on the cooling rate, the shape of the desorption isotherm, and the initial degree of saturation at 0°C.

The mechanism by which air-entrained bubbles protect cement paste is one in which the bubbles serve as reservoirs into which expelled water

@Seismicisolation

escapes on cooling. The migration of water is assisted by the short distances between the bubbles.

Deicing agents can aggravate the freezing behavior of cementitious materials. Length change isosteres for air-entrained cement paste (water-cement ratio = 0.50) saturated with NaCl solutions of varying concentration are shown in Fig. 22.

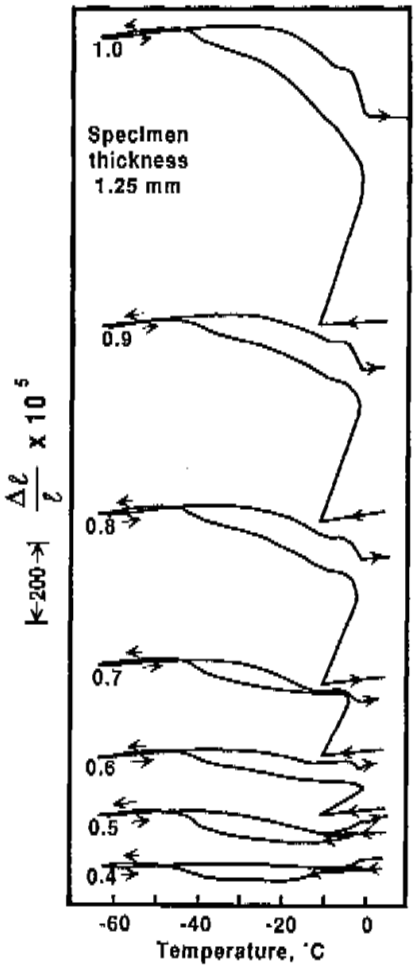


Figure 21. Length-changes of vacuum saturated plain cement specimens in temperature cycles (0.33°C/min.). Water-cement ratios vary from 0.4 to 1.0.[16]

@Seismicisolation

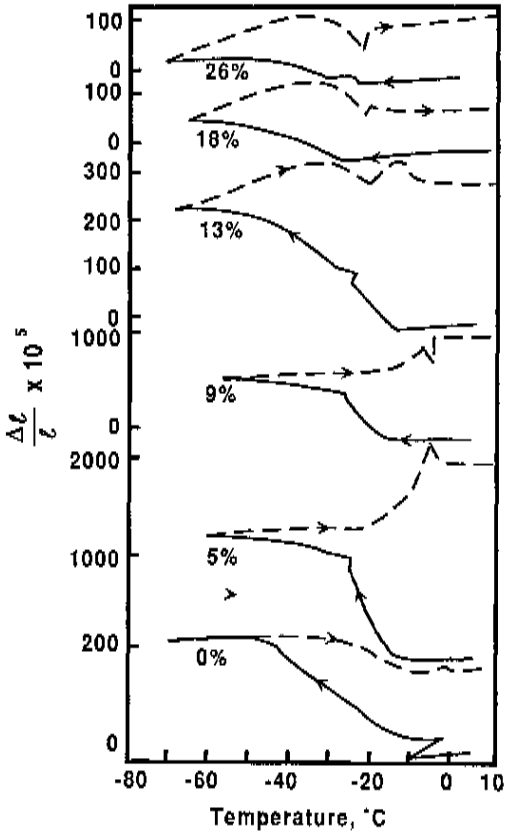


Figure 22. Length-changes of 0.5 water-cement ratio cement paste, air entrained and saturated with NaCl solutions of concentrations indicated during temperature cycles (0.33°C/min.). Specimens 1.27 mm thick.[16]

The general features of the curves are similar to those described previously. The aggravating effect in presence of salt is explained as follows. Freezing-thawing action results due to a difference between the vapor pressure of the pore liquid and external (macropores, cracks, free surfaces) ice. This difference is reduced by the lowering of the adsorbate content that normally occurs on cooling when a portion of the warm adsorbate distills to the cold surroundings. When a salt solution is adsorbed in the porous body no distillation takes place because the vapor pressure of the solution is usually less than the vapor pressure of the external ice or water. This excess not only results in complete saturation, but prevents desorption even if a moderate temperature gradient exists on cooling. The alleviating effect of desiccation does not occur in most cases when salts are present.

@Seismicisolation

4.2 Dimensional Change—Shrinkage and Creep of Cement Systems

Shrinkage and creep of cement systems are moisture related volume changes of interest to engineers and scientists engaged in the art and science of concrete making.

The physical changes that occur in the micro-units of the solid and the solid body itself as a result of changes in exposure conditions impact the magnitude and nature of the dimensional changes due to mass transfer of adsorbate or applied mechanical load.[27] An example of the instability of hydrated cement paste is provided by the length change-weight change curves plotted in Fig. 23. The initial starting condition is equivalent to the d-dried state (drying to the vapor pressure of dry-ice at -78°C). Results for the first drying are not shown. For subsequent cycles the samples were heated for several hours at 97°C to achieve the same weight loss. The consecutive cycles measured on the one sample are plotted so that the final value for $\Delta\ell / \ell$ on every cycle represents the net shrinkage with respect to zero at the commencement of that cycle and an increase in overall net irreversible shrinkage commencing with cycles I and II. Curve II shows a total length change of 0.528% compared with 0.768% for curve VIII. The extra weight gain (curve VIII vs. curve II) does not cause much length change and is probably due to a greater degree of condensation in the large pores at 100% RH. The additional expansion only partially reflects the irreversible shrinkage accumulated between curves II and VII. This amounts to 1.026% while the increase in expansion is only 0.24%. The total irreversible shrinkage for the eight cycles, including first d-drying, is 1.906%.

The irreversible shrinkage is plotted as a function of the maximum relative humidity of re-exposure in Fig. 24. The subscripts on the points at 100% RH represent cycles II and VIII. Irreversible shrinkage increases abruptly beyond 50% relative humidity after a relatively constant low value between 10 and 50% relative humidity. This is analogous to the results of Wittmann of the creep rate versus relative humidity of exposure. It is concluded that each time the solid is exposed to more than 50% RH it is altered in some way so that it possesses the potential for irreversible shrinkage when d-dried. This is consistent with Wittmann's observations.[28] It would appear that change in the potential for creep and the potential for irreversible shrinkage are manifestations of the same change that has occurred in the solid. It is inferred that the creep process is

@Seismicisolation

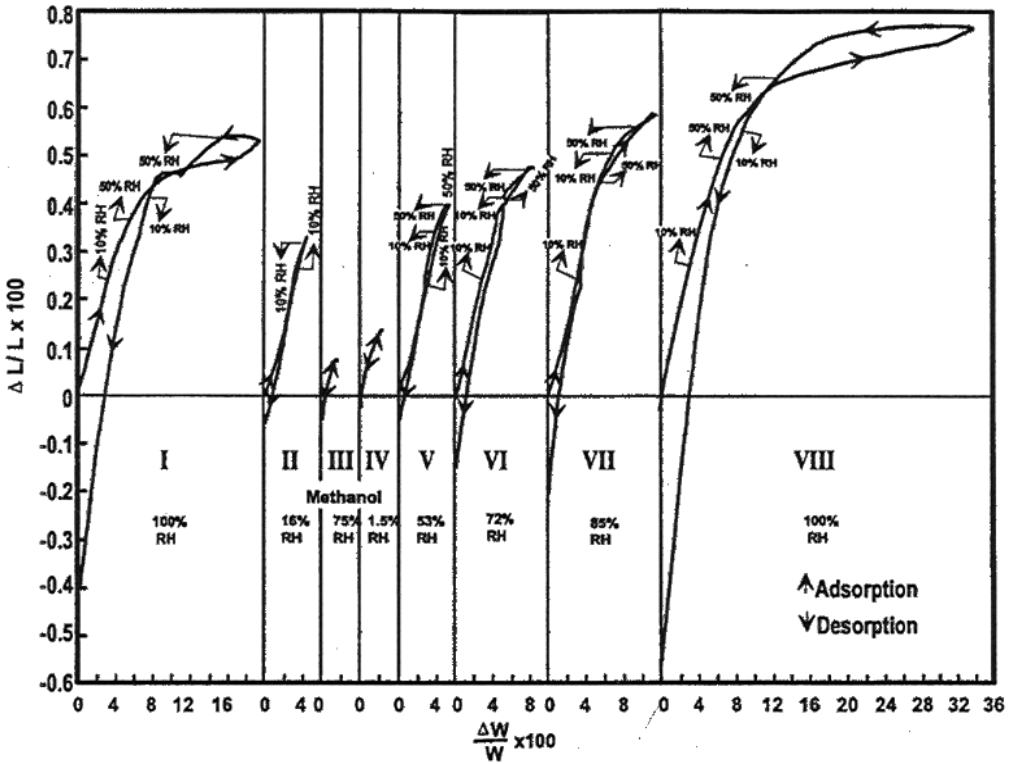


Figure 23. Length-change versus weight change for hydrated cement compacts subjected to successive cycles of wetting at higher humidities and drying (cycles II to VIII).[17]

@Seismicisolation

associated with a moving together of layers of silicate to form new interlayer space. The solid material is unstable and will move towards a lower free-energy position and surface area. This process may be partly reversible, depending on how close the layers have moved towards each other.

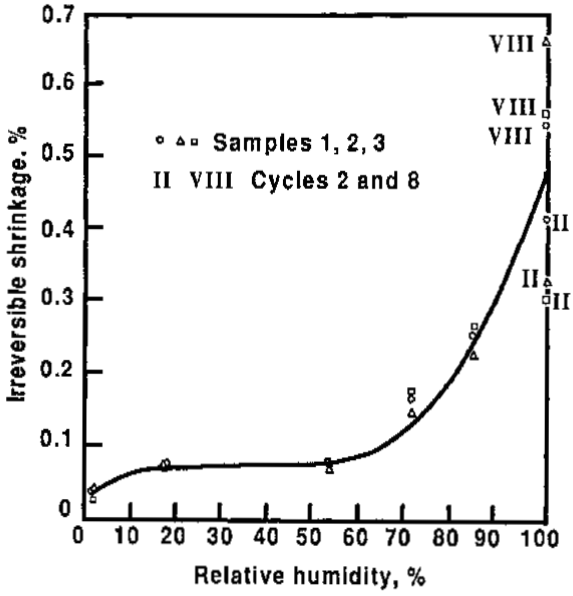


Figure 24. Irreversible shrinkage versus re-exposure to relative humidity for hydrated cement compacts.[17]

The creep rate is generally low upon re-exposure to humidities below 50% although the length change is about 70% of the total expansion. This suggests that the strongly held interlayer water is not responsible for creep. Pores up to about 14 Å diameter have been filled at this point suggesting that *disjoining pressure* related to physically adsorbed water does not play a role. This argument would appear to be supported by the shrinkage data where on desorption little of the potential irreversible shrinkage has yet occurred at 10% RH. It appears that the water beyond the surface layer is not largely load-bearing. This and the conclusion that the water involved is to be found at the entrances to layers indicate that adsorbed water movement does not contribute very much to the long-term time dependent feature of creep. It is, therefore, suggested that creep is a manifestation

@Seismicisolation

of gradual crystallization or aging in a poorly crystallized material, accelerated by drying or stress. Water transport from entrances to interlayer spaces occurs and probably controls creep rate at early stages. The process may activate the rate determining processes at later stages, including crystal slippage, microcracking, and bond breaking and reforming.

Carbonation can significantly affect the properties of hydrated cement systems because free $Ca(OH)_2$ may constitute more than 20% of the volume of the material. Dimensional change studies of compacted and normally hydrated pastes have been useful in developing concepts on the effects of carbonation.[29]

Dimensional changes of hydrated cement compacts preconditioned at various relative humidities are shown in Fig. 25. Maximum carbonation shrinkage occurred when samples had been preconditioned at 50% relative humidity. Much lower values were attained at high and low relative humidities. Degree of carbonation was limited well below 100% of the theoretical value. For compacts of hydrated cement it was found that the degree of carbonation and carbonation shrinkage increased as the amount of free lime decreased. It is apparent that carbonation of combined lime results in shrinkage to an even greater extent than for the free lime because the former is finer.

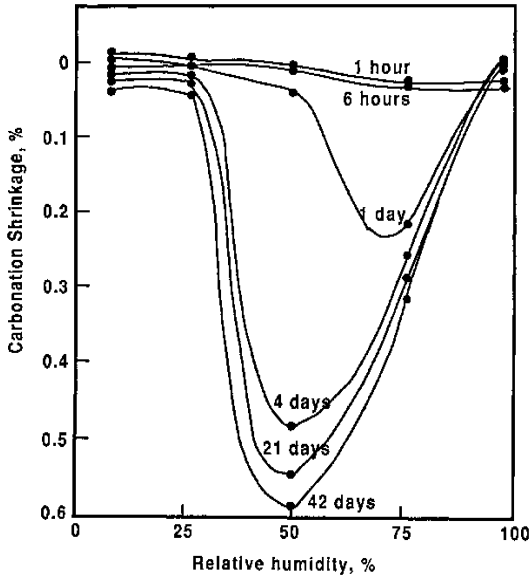


Figure 25. Carbonation shrinkage of bottle-hydrated cement compacts preconditioned at various relative humidities. Compaction pressure 60,000 psi; 100% CO_2.[19]

@Seismicisolation

Carbonation reactions of the cement compacts involving the combined lime are complex as decomposition of the silicate hydrate takes place. Carbonation shrinkage of these systems may be considered to be connected with the dehydration and polymerization of the hydrous silica product of carbonation.

REFERENCES

1. Feldman, R. F., Sereda, P. J., and Ramachandran, V. S., A Study of Length Changes of Compacts of Portland Cement on Exposure to H_2O, *Highway Res. Rec. No. 62,* 106–118 (1964)
2. Feldman, R. F., Sorption and Length-Change Scanning Isotherms of Methanol and Water on Hydrated Portland Cement, *Proc. Fifth Int. Symp. Chem. Cem.,* Part III, 3:53–66, Tokyo (1968)
3. Feldman, R. F., and Sereda, P. J., A New Model for Hydrated Portland Cement and Its Practical Implications, *Engineering J.,* 53:53–59 (1970)
4. Beaudoin, J. J., and Feldman, R. F., Stresses and Strains in the Hardened Cement Paste-Water System, *Cem. Concr. Res.,* 14:231–237 (1984)
5. Litvan, G. G., Volume Instability of Porous Solids: Part 1, *Proc. Seventh Int. Congr. Chem. Cement,* Vol. III, VII-46–VII-50, Paris (1980)
6. Litvan, G. G., Volume Instability of Porous Solids: Part 2, Dissolution of Porous Silica Glass in Sodium Hydroxide, *J. Matls. Sci.,* 19:2473–2480 (1984)
7. Feldman, R. F., and Beaudoin, J. J., Some Factors Affecting Durability of Sulphur-Impregnated Porous Bodies, *Cem. Concr. Res.,* 8:273–282 (1978)
8. Litvan, G. G., Feldman, R. F., and Grattan-Bellew, P. E., Durability of Cement and Glass Impregnated with Sulfur and Polymethyl Methacrylate, *Cem. Concr. Res.,* 12:649–659 (1982)
9. Feldman, R. F., and Sereda, P. J., Characteristics of Sorption and Expansion Isotherms of Reactive Limestone Aggregate, *J. Amer. Concr. Inst.,* 58:203–214 (1961)
10. Grattan-Bellew, P. E. and Litvan, G. G., Testing Canadian Aggregates for Alkali Expansivity, *Proc. Alkali Symp.,* 227–245, London, U.K. (1976)
11. Performance of Concrete - A Symposium in Honour of Thorbergur Thorvaldson, (E. G. Swenson, ed.), U. of Toronto Press, p. 243 (1968)
12. Mather, B., Field and Laboratory Studies of the Sulphate Resistance of Concrete, in Performance of Concrete, (E. G. Swenson, ed.), U. of Toronto Press, 66–76 (1968)

@Seismicisolation

13. Taylor, H. F. W., Delayed Ettringite Formation, Advances in Cement Concr., *Proc. Eng. Foundation Conf.*, p. 122, Durham, NH, USA (1993)
14. Heinz, D., and Ludwig, U., Mechanism of Subsequent Ettringite Formation in Mortars and Concretes after Heat Treatment, *Proc. Eighth Int. Congr. Chem. Cem.*, 5:190, Brazil (1986)
15. Fu, Y., and Beaudoin, J. J., Microcracking as a Precursor to Delayed Ettringite Formation in Cement Systems, *Cem. Concr. Res.*, 26:1493–1498 (1996)
16. Mayfield, L. L., Limestone Additions to Portland Cement: An Old Controversy Revisited, *Cem. Concr. Aggreg.*, 10:3–8 (1988)
17. Soroka, I., and Setter, N., The Effect of Fillers on Strength of Cement Mortars, *Cem. Concr. Res.*, 7:449–456 (1977)
18. Ramachandran, V. S., Feldman, R. F., and Beaudoin, J. J., Influence of Seawater Solution on Mortar Containing Calcium Carbonate, *Mat. and Struct.*, 23:712–717 (1990)
19. Feldman, R. F., Ramachandran, V. S., and Beaudoin, J. J., Influence of Magnesium and Sodium Chloride Solutions on Durability of Mortar Containing Calcium Carbonate, *Il Cemento*, 89:195–208 (1992)
20. Zhang, F., Zhou, Z., and Zonghan, Z., Solubility Product of Ettringite, *Proc. Seventh Int. Congr. Chem. Cem.*, 2:88–93, Paris, France (1980)
21. Arya, C., Buenfeld, N. R., and Newman, J. B., Factors Influencing Chloride-Binding in Concrete, *Cem. Concr. Res.*, 20:291–300 (1990)
22. Cole, W. F., A Crystalline Hydrated Magnesium Silicate Formed in the Breakdown of a Concrete Sea Wall, *Nature*, 171:354–355 (1953)
23. Taylor, H. F. W., *Cement Chemistry*, p. 475, Academic Press, London, U.K. (1990)
24. Feldman, R. F., and Cheng-yi, H., Microstructural Properties of Blended Cement Mortars and Their Relation to Durability, *Proc. RILEM Seminar on Durability of Concrete Structures under Normal Outdoor Exposure*, pp. 133–140, Hannover (1984)
25. Carette, G. G., and Malhotra, V. M., The Frost Resistance of Silica Fume Concrete, *CANMET Report M-38-82-1E*, pp. 1–5, Ottawa, Canada (1982)
26. Litvan, G. G., Adsorption Systems at Temperatures Below the Freezing Point of the Adsorptive, *Adv. in Coll. Int. Sci.*, 9:253–302 (1978)
27. Feldman, R. F., Mechanism of Creep of Hydrated Portland Cement Paste, *Cem. Concr. Res.*, 2:521–540 (1972)
28. Wittmann, F., Einfluss des Feuchtigkeitgehaltes auf des Kriechen des Zementsteines, Rheologica Acta, 9:282–287 (1970)
29. Swenson, E. G., and Sereda, P. J., Mechanism of the Carbonation Shrinkage of Lime and Hydrated Cement, *J. Appl. Chem.*, 18:111–117 (1968)

@Seismicisolation

11

Miniaturized Techniques

James J. Beaudoin

1.0 INTRODUCTION

Laboratory investigations of the behavior of cement-based systems under a variety of loading and environmental conditions often require protracted periods before the information generated can be used to predict performance or provide design of guidelines for durability. This disadvantage can sometimes be overcome through the use of experimental techniques employing miniature samples. The requirements for rigorous control of experimental parameters or application of classical theories can be facilitated through test design that minimizes thermal and moisture gradients and enhances homogeneity. The attainment of true hydral equilibrium conditions, for example, can only be achieved in a reasonable period if the least dimensions of a specimen are limited to values less than about one millimeter. This is an important consideration for the development of structural models of C-S-H and those experiments (e.g., creep measurements) intended to reveal mechanistic information as many of these involve mass transport of chemical species in solution.

Deleterious reactions, kinetics, and associated phenomena that influence the durability of porous construction materials are affected by pore structure, pore continuity, and the path length for the transport of aggressive chemical species. The use of miniature specimens in tests not only minimizes this path (providing greater homogeneity within the sample), but can

@Seismicisolation

increase the sensitivity of a response to dimensional changes that are a direct result of destructive processes.

The effects of moisture diffusion in interfacial regions of impregnated porous solids can be catastrophic. Detection of incipient damage can be accelerated through the use of very thin samples exposed to saturated vapor.

Other areas in cement science that can benefit from the use of miniaturized techniques or processes include admixture technology, soundness testing of cement, microstructural investigations, and certain studies of mechanical behavior.

The National Research Council of Canada has been involved in the development of miniature techniques for physicochemical and physicomechanical studies of cement systems for three decades. Hence, many of the references are related to work emanating from this laboratory.

This chapter will be necessarily selective and focus on the following areas: compacted powders as model porous systems; miniature specimens for creep and drying shrinkage measurements; volume instability of porous solids; miniature workability tests; surface chemical-based microstructural probes.

2.0 COMPACTED POWDERS AND HYDRATED CEMENT PASTES AS MODEL POROUS SYSTEMS

The fabrication of rigid porous bodies by powder compaction was used to study the various phenomena, especially dimensional changes, associated with the sorption of water on internal surfaces of materials. Naturally occurring materials are usually non-homogeneous, non-isotropic and non-reproducible from sample to sample, and contain impurities in varying amounts. To avoid some of the limitations of natural rigid porous materials, a technique was developed by Sereda and Feldman[1][2] to produce porous bodies with a wide range of properties by compressing fine powders of different materials into compacts, as was done by Dollimore and coworkers[3][4] and others in powder metallurgy and catalyst technology.

Powders of different materials including portland cement were compressed in a mold at pressures up to 200,000 psi (1361 MPa). Each powdered material has optimum conditions of moisture content and pressure at which satisfactory compacts are made. Although all finely powdered material will produce a rigid body when compressed at a suitable

@Seismicisolation

pressure, not all such compacts can withstand immersion in water without disintegration nor do all have sufficient mechanical strength when dry.

The formation of a rigid body by compression of a fine powder must involve, in the first place, the bringing together of enough of the surface at distances where the van der Waals' attractive forces come into play. Much of the strength of the compact can be derived from primary bonds resulting from bridging between particles in contact where the surfaces are under pressure or are deformed and will recrystallize, hydrate, or react more readily than other surfaces. Solid-state reactions can be postulated for the formation of bridges.[5]

For portland cement, only traces of water may be required to cause bridging by the formation of minute quantities of the hydrate.

2.1 Technique for Preparation of Compacts

Compacts measuring 3.12 cm (1.23 in.) in diameter and about 1.50 mm (0.06 in.) thick can be made in a steel mold consisting of a cylinder and two closely fitting pistons. The cylinder is first mounted vertically with the bottom piston located in the cylinder about 1.2 cm below the top (this spacing varied for different powders and different compacting pressures in order to make the samples the same thickness). The powder is placed in the mold by tamping with the edge of a spatula against the top edge of the cylinder while excess powder remained heaped over the mold. Tamping with equally spaced strokes in two directions, at right angles to each other, is concluded by striking off the excess powder level with the top edge of the cylinder. The bottom piston is lowered with the sample and the top piston placed in the cylinder; the assembly is then mounted in a testing machine. While the first increment of load is applied, the cylinder is rotated slightly and held up to allow both pistons to float and to ensure that the compression of the sample is equal from both sides.

Pressures up to 200,000 psi (1361 MPa) have been used in compressing samples; when inert materials were used a small amount of water was added to improve compression. All powders in the particle sizes 10 μm (0.39×10^{-3} inch) and smaller have to be agglomerated by working them in a mortar with pestle (with or without the addition of water) until the powder formed coarse agglomerates, which could be packed more uniformly into the mold. This step proved important when compacting very fine powders such as silica (Cab-O-Sil), although in the case of plaster of Paris it was not necessary because the fine particles were already in a state of agglomeration.

@Seismicisolation

While some materials will form satisfactory compacts over a very wide range of pressures, others require a specific pressure. The forming of a satisfactory compact above a certain pressure may be impossible if, after compression, the material tends to rebound or relax as if in a high state of strain. Any density variation will result in cracking along lines of maximum density gradient representing different magnitudes of recovery or relaxation between two adjacent sections of the compact.

2.2 Sorption Studies

Samples for determining both the sorption and expansion isotherms can be obtained from the same compact. Feldman and Sereda used compacts made in the form of a disc 1.5 mm (0.06 in.) thick cut to give two rectangular prisms 7 × 28 mm (0.28 × 1.10 in.) to be mounted on extensometers, and two segments weighing about 1 g to be mounted on the quartz spirals.

Before determining the sorption and expansion isotherm, all samples were outgassed at 150–200°C to a vacuum of less than 10^{-6} mm Hg until negligible mass loss had been recorded for 15 h. For equilibrium to be attained between points along the isotherm, different periods were required for different samples. In all cases a period of about 15 h of negligible mass change and negligible dimensional change was allowed before the system was considered to be in equilibrium.

One of the most important properties of a compact used for studies such as those described here is the void fraction or porosity. It can be changed as much as twofold by varying the pressure of forming for such materials as plaster of Paris (see Fig. 1).

The void fraction can be determined from measurements of the dimensions of the compact, the dry mass, and the absolute density of the materials.

It is considered important to determine the uniformity of the apparent density or porosity throughout the compact. To examine this property, compacts of different thicknesses were made at a series of constant pressures. Even though the thicknesses were varied tenfold there was no significant difference in the void fraction for plaster of Paris at several pressures and similar results were indicated for other materials (see Fig. 2).

In the use of compacts for the study of the dimensional changes of materials during sorption of water, the important question to be answered is whether any strain remains in the compact as the result of compression

@Seismicisolation

of particles that may be relaxed during wetting, thus exhibiting a dimensional change in no way related to sorption of water on the surfaces. Compacts of some materials, such as plaster of Paris and calcium carbonate, will disintegrate when immersed in water although they will not do so in kerosene or carbon tetrachloride. In fact, the dimensional change of these compacts during saturation from the dry state with these solvents is negligible. This would indicate that there is no residual strain in the compact.

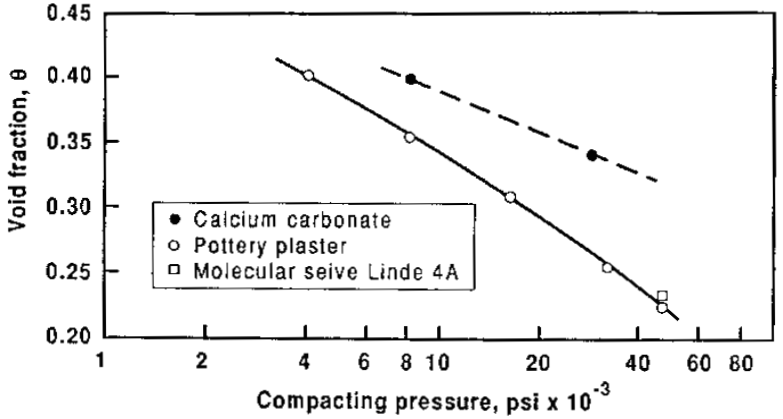


Figure 1. The effect of pressure on the void fraction of compacted materials.[1]

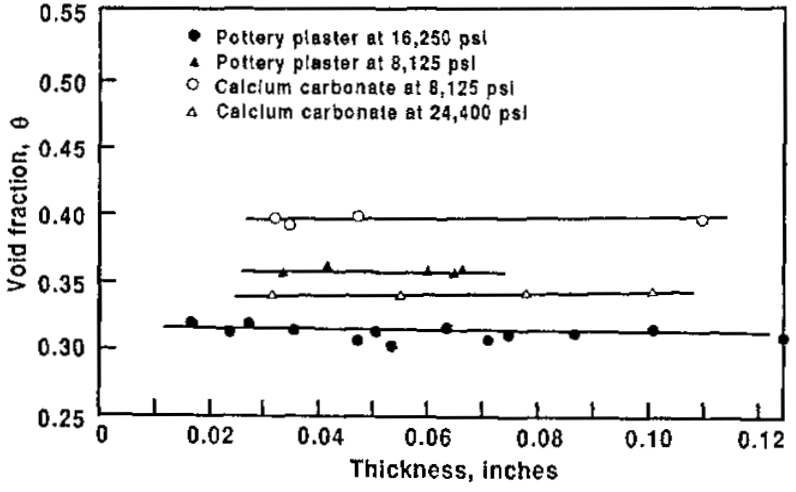


Figure 2. The effect of thickness on the void fraction of compacts made at constant pressure.[1]

@Seismicisolation

That residual strain is absent is further supported by the results obtained by an application of the Gibbs adsorption equation. This equation relates lowering of the surface-free energy, ΔF, as sorption occurs on a surface to the pressure, p dynes/cm^2, of the absorbate and the surface concentration s of the adsorbate on the adsorbent in g-mol/cm^2.

Eq. (1) $$\Delta F = RT\int_0^p s/p\,dp$$

When ΔF (ergs/cm^2), commonly called ϕ, the spreading pressure, is calculated, a plot of $\Delta\ell/\ell$ vs. ϕ should, according to the Bangham relation, $\Delta\ell/\ell = \lambda\Delta F$, yield a straight line through the origin (Fig. 3). The quantity, $\Delta\ell/\ell$, is the expansion due to sorption and λ is a constant related to the elastic coefficient of the material.

This plot does, in fact, produce acceptable straight lines through the origin for the Cab-O-Sil, bottle hydrated portland cement and $CaCO_3$ samples in the region where adsorption without capillary condensation occurred.

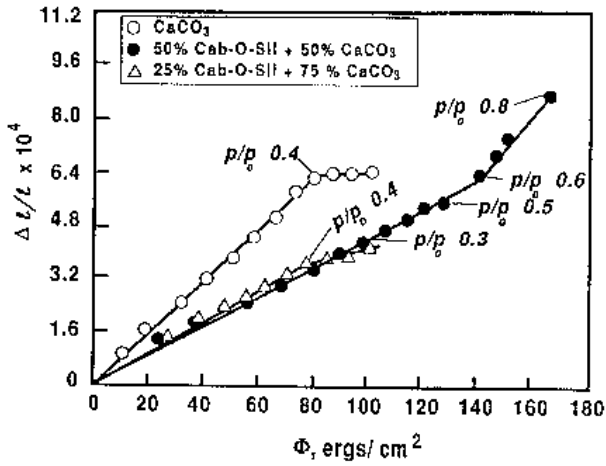


Figure 3. The expansion of compacts as a function of the calculated spreading force.[1]

The Young's or elastic modulus E for the material can be calculated from the Bangham relation using the $\Delta\ell/\ell$ vs ϕ plot

Eq. (2) $$E = \rho A/\lambda$$

where, ρ is the absolute density of the material (g/cc) and A the area (cm^2/g). A value for E of 6.97×10^{10} dynes/cm^2 was obtained using a value of

@Seismicisolation

2.93 g/cc for ρ. This value is within the same order of magnitude as published values for materials of this nature.

Compacts of bottle hydrated portland cement paste produce similar results. When hydrated in this way the cement paste remains as a powder of less than 1 μm particle size. These can be made reproducible (void fraction) and, as they are no more than 1.5 mm thick they attain equilibrium quickly. Results obtained with compacts of other materials also confirm that compacts of hydrated cement will be reasonably representative of normal hydrated paste having the same void fraction and similar pore sizes. Sorption and length change scanning isotherms for bottle hydrated compacts, Figs. 4 and 5, provide a means of constructing "reversible" isotherms isolating adsorption from intercalation phenomena.[6] These along with a plot of $\Delta\ell/\ell$ versus ϕ are shown in Fig. 6.

An integration over the adsorption branch of the reversible isotherm is made between P/P_o values of 0.05 (to avoid the extrapolated area and errors in integration as the pressure approaches zero) and 0.60, according to Gibbs' equation. The change in state of stress of the solid ΔF is plotted against $\Delta\ell/\ell$. As shown on Fig. 6, this plot yields a very good straight line and it appears that the whole procedure in constructing the reversible isotherm is justified. The slope of this line, λ, is 3.90×10^{-6} cm/dyne.

Using a value of $\rho = 2.86$ g/cc for $Ca_3Si_2O_2{\cdot}2H_2O$[7] since at a P/P_o of 0.30 only about 40 percent of the irreversible water has reentered the C-S-H and since most of the adsorption is taking place on this "crystal" which constitutes most of the area and using 40.8 m^2/g for the surface area, the value of E from Eq. (2) is 2.99×10^{11} dyne/cm^2 or 4.35×10^6 lb/in^2. This value is about eight times as large as that measured for the equivalent compact[8] or of the equivalent water to cement ratio paste.[9] This calculated value, however, represents E for the solid material not the porous body. Helmuth and Turk[9] extrapolated from porosity E-plots to get E of "gel phase" as 4.5 and of "solid phase" 10.8×10^6 (lb/in^2). This latter value was similar to the extrapolation of Soroka and Sereda.[8] Both these values suffer from the difficulty of measuring the correct porosity. However, a large part of the water removed during *d-drying* (drying to the vapor pressure of dry-ice at 78°C) is interlayer water which returns on sorption. Thus, the porosity (determined by water) would be much lower than anticipated making the extrapolated value much too high. Considering these assumptions, the value found for the modulus of elasticity of the solid phases is very good and is considered as further evidence of the validity of this approach.

@Seismicisolation

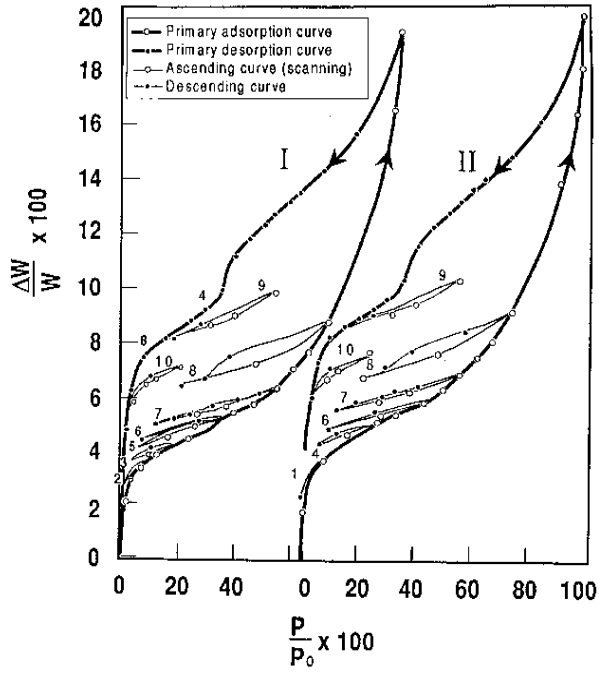


Figure 4. Weight change isotherms for bottle-hydrated portland cement compacts: *I* - degassed at 80°C; *II* - degassed at 96°C (scanning loops marked 1 to 10).[6]

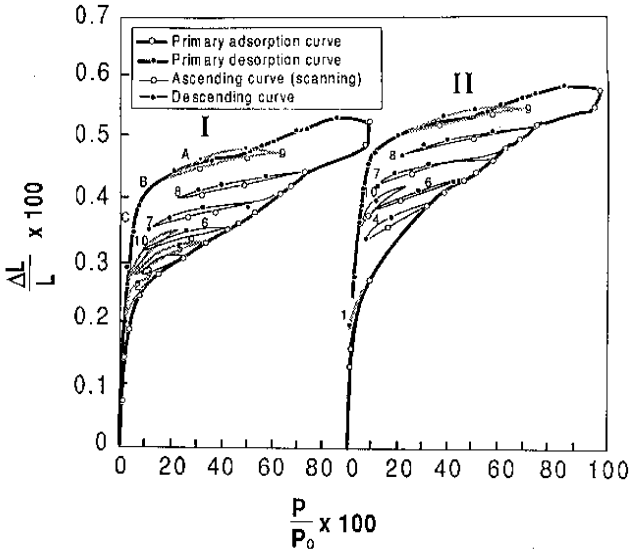


Figure 5. Length change isotherms for bottle-hydrated portland cement compacts: *I* - degassed at 80°C, *II* - degassed at 96°C (scanning loops marked 1 to 10).[6]

@Seismicisolation

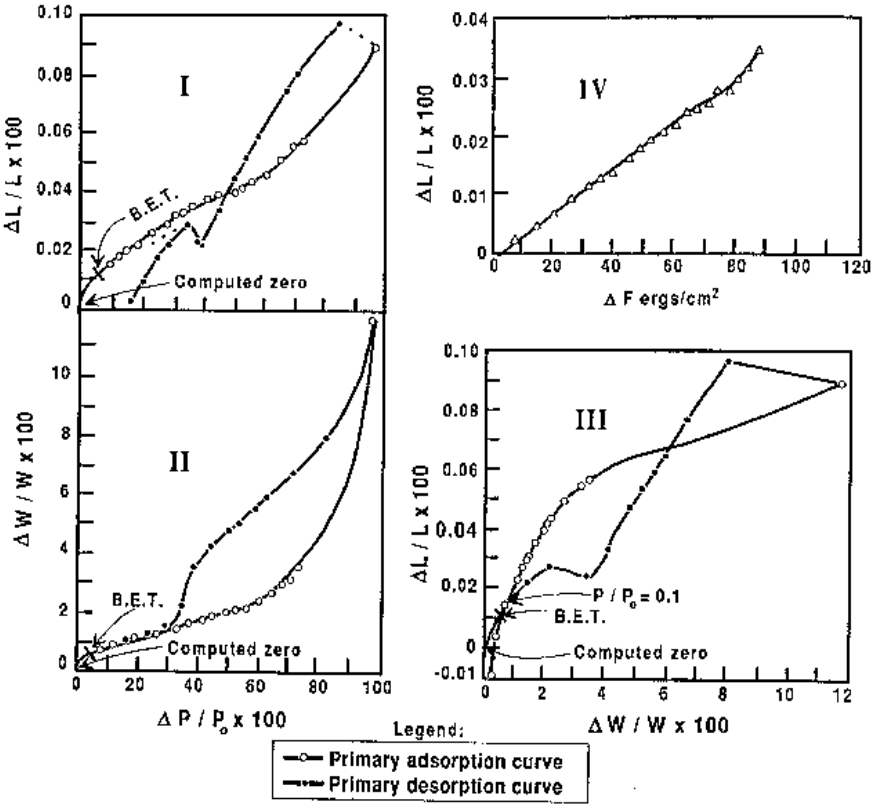


Figure 6. Constructed reversible water isotherm and computations.[6]

2.3 Elastic Behavior of Compacted and Paste Hydrated Cement Systems

Miniature testing machines can be constructed to provide a means of loading compacted disks or disk-shaped cement paste specimens.[10]

Timoshenko[11] deals with the deflection (*Def*) of a circular disk loaded at the center and supported at three equally spaced edge supports. The equation given is

Eq. (3) $$Def = \frac{0.754 Pr^2}{Et^3} \text{in}$$

@Seismicisolation

where,

P = load, lb
r = radius of the circle of support, inches
E = Young's modulus
t = thickness

This formula assumes a Poisson's ratio of 0.25.

Figure 7 shows Young's modulus as a function of relative humidity for hydrated cement compacts fabricated at three different pressures.

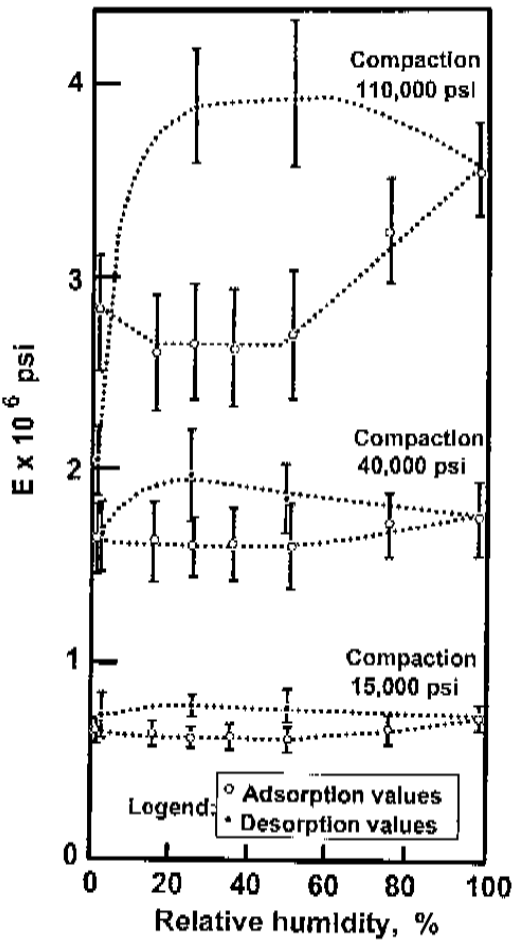


Figure 7. Young's modulus as a function of relative humidity for compacts.[10]

@Seismicisolation

Approximately 25 samples at each conditioning humidity for each fabrication pressure were used in the measurements. In this plot the confidence interval of results from the arithmetic mean is shown at the 95% limit. This indicates that the results at a particular compaction pressure vary by approximately ± 10%.

From these results it is clear that within the confidence value of the points there is no variation from 0 to 50% RH. Beyond 50% RH for the 110,000 psi compacts, there is a significant increase in *E*. Although there is a suggestion of the same result for the 40,000 psi compacts, it is not in itself significant. For the compact fabricated at 40,000 psi there is a significant increase in *E* for 98% RH over the 50% RH value and this trend appears to start after 50% RH. Thus, on the basis of the three different series of compacts within the stated significance of the results, *E* shows no change from 0 to 50% RH, but there is a definite trend to an increase in *E* beyond this. At 0% RH for the 110,000 psi compacts, the value of *E* is 2.9 × 106 psi; at 97% RH it is 3.6 × 106 psi.

On desorption there is a further increase in *E* down to 26% RH. On drying to nearly the starting condition of dryness, the *E* decreased to the starting value for the 15,000 (102 MPa) and 40,000 psi (272 MPa) compacts and below it for the 110,000 psi (748 MPa) compacts.

The same experimental procedure was repeated for paste samples hydrated at w/c ratios of 0.3, 0.4, 0.5, 0.6, and 0.7; qualitatively the results agreed in all details with results obtained for the compacts.

The paste samples were measured in the wet condition after hydration and before drying prior to conditioning. This gave values of Young's modulus for the first drying cycle. This could not be obtained for the compacts. It is evident that the value of *E* is unchanged during adsorption in the region 0 to 50% RH and that at higher humidities *E* increases, being highest near saturation. On desorption the high value of *E* persists to a condition approaching the dry state. Final measurements were made before complete equilibrium was reached with magnesium perchlorate.

In order to make a more statistically significant comparison of the fracture-strength results between compacts and pastes, all fracture values between 15 and 97.5% RH (for each porosity or w/c ratio) were used to obtain an arithmetic mean value representing each point. The validity of this was based on the previous conclusion that no significant reduction in strength occurred in this region. The results of fracture-strength against porosity for the compacts and pastes fall together and show that the character of the relationship is similar to that of the plot of *E* vs. porosity, Fig. 8. The chapter

@Seismicisolation

on pore structure provides additional detail related to mechanical property-porosity relationships.

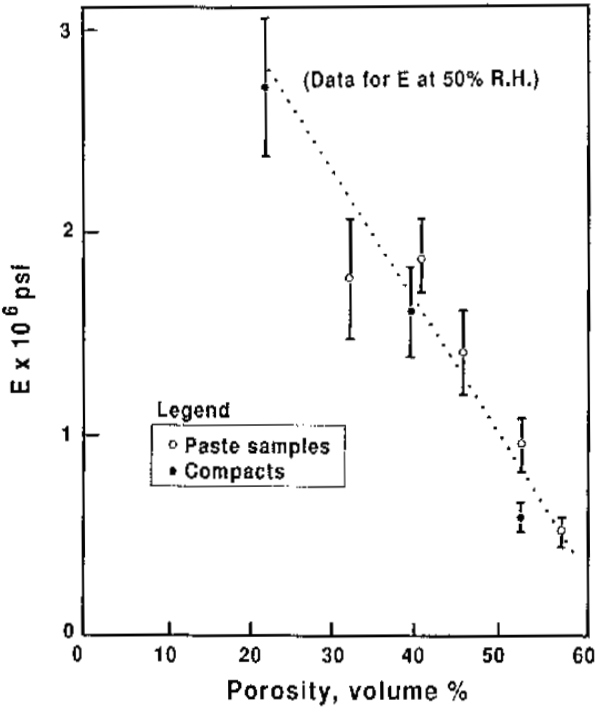


Figure 8. Young's modulus as a function of computer porosity.[10]

2.4 Compressive Strength of Individual Cement Minerals Determined Using Miniature Specimens

Miniature specimens, e.g., cylinders for compression strength determination, are convenient and permit effective study of mechanical properties of cement systems when large or sufficient quantities of material are not readily available. Results correlate well with other microtechniques such as methods for determining microhardness.[12] This section will focus on the application of miniaturization for the determination of the mechanical properties of individual cement phases and the use of mini-techniques in the development of a model for hydrated cement paste.

@Seismicisolation

Portland cement, the most extensively used of all cements, contains four principal mineral components: tricalcium silicate (C_3S), dicalcium silicate (C_2S), tricalcium aluminate (C_3A), and calcium aluminoferrite, of average composition C_4AF. Hydration and other chemical aspects of these compounds have been studied extensively.[13][14] A pioneering contribution in 1934 by Bogue and Lerch has been viewed worldwide as "prima facie" evidence of the relative rates of strength development of the cement minerals.[15] However, inconsistencies such as inadequate control of the particle size distribution of the minerals, variable amounts of water (i.e., water/solid ratio from 0.30 to 0.60), inappropriate specimen geometry (cylinder with length/diameter ≤ 2) and inaccurate methods of estimating the degree of hydration have led to questionable conclusions. In addition, the strength differences were attributed mainly to changes in structure and nature of hydrated material and amount of so-called "fixed water" was used to explain strength differences. The role of porosity and pore structure was not considered. Many of the shortcomings mentioned above were circumvented or minimized by the following procedure that utilizes mini-cylinders.

Experiments were conducted with well-characterized starting materials and pastes were prepared by uniform procedure. The particle size distribution based on the percentage number of particles rather than on mass percentage was the same for all samples so that variation in the reaction kinetics due to this factor could be avoided. The mixes were prepared at a water/solid ratio of 0.45. Strength measurements were carried out on 1.27 cm diameter × 2.54 cm cylinders of the pastes to realize a length to diameter ratio of 2, thus minimizing the end effects occurring due to shear in the compression test. Microhardness values were also determined by Vicker's Microhardness Indentor as they reflect the nature of the interparticle bonds at a microlevel.[17] The degree of hydration was obtained by XRD and calculated on the basis of the residual amount of anhydrous phase, a more realistic indicator of the degree of hydration. Porosity and pore size distribution values obtained by mercury porosimetry provided a means to measure the intrinsic characteristics of the paste samples.

Significant differences from Bogue-Lerch data were observed for relative strengths (Fig. 9). The strength values at 10 days were in the order $C_4AF > C_3S > C_2S > C_3A$, whereas those of Bogue-Lerch were in the order $C_3S > C_2S > C_4AF > C_3A$. At 1 year the values were $C_3S > C_2S > C_4AF > C_3A$, but those of Bogue-Lerch were $C_3S = C_2S > C_3A > C_4AF$. On a semilog plot of strength vs. porosity (Fig. 10a), the data points for the phases C_3S, C_2S, and C_4AF showed linearity and fell on the same line. The points for

@Seismicisolation

the C_3A phase showed linearity, but had a different slope from other phases. The "intrinsic strength," defined as the strength extrapolated to zero porosity, was the same for all the pastes, the value being 500 MPa.

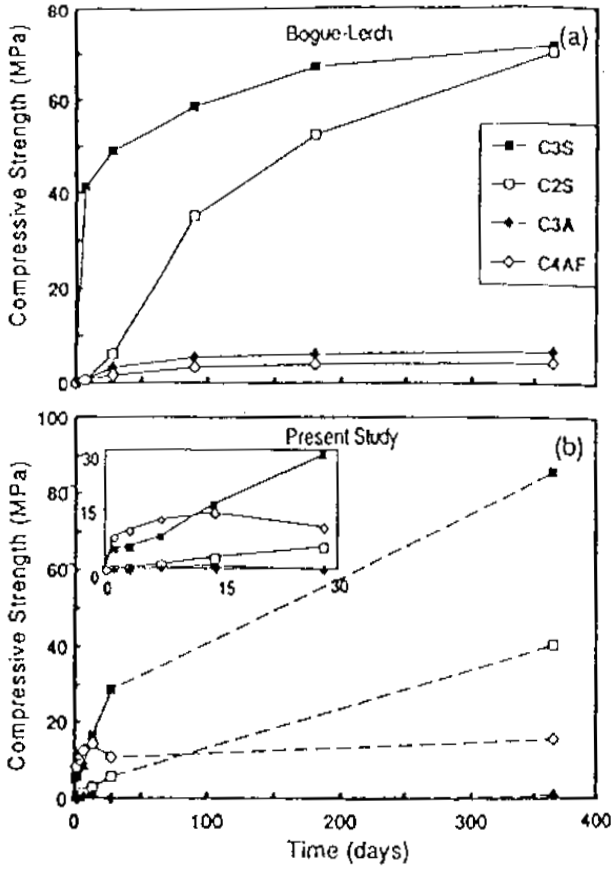


Figure 9. *(a)* Compressive strength of hydrated C_3S, C_2S, C_3A, and C_4AF paste versus time after Bogue-Lerch.[15] *(b)* Compressive strength of hydrated C_3S, C_2S, C_3A, and C_4AF paste versus time.[16]

Microhardness-porosity data (Fig. 10b) can be considered to describe a single curve for all the samples. Microhardness is apparently not as sensitive to microcracking as compressive strength.

@Seismicisolation

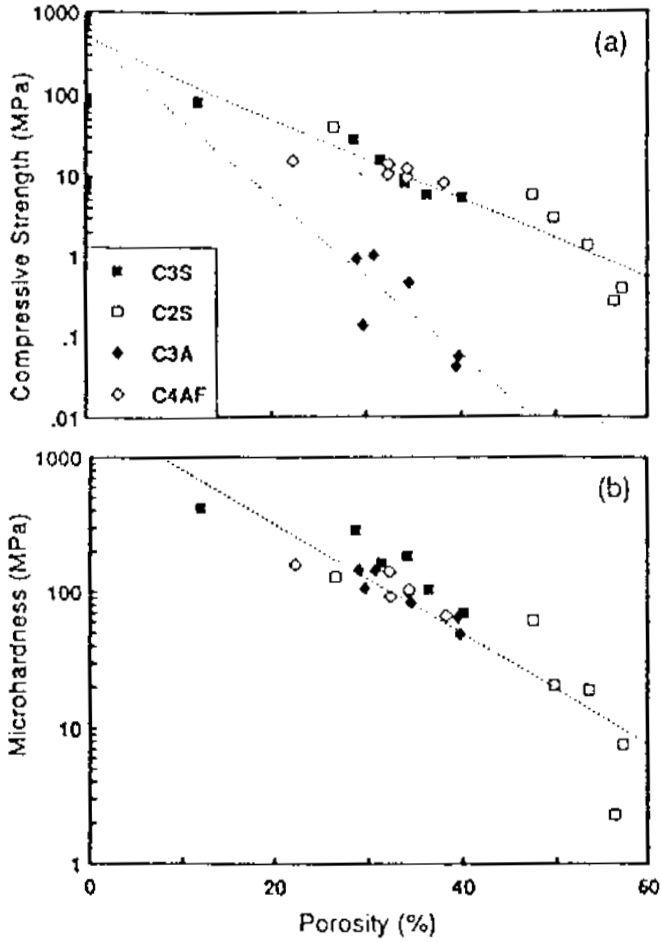


Figure 10. *(a)* Compressive strength of hydrated C_3S, C_2S, C_3A, and C_4AF paste versus porosity. *(b)* Microhardness of hydrated C_3S, C_2S, C_3A, and C_4AF paste versus porosity.[16]

The zero porosity (intrinsic) value of microhardness is about 3000 MPa for all the mineral systems. Coincidence of the strength, microhardness-porosity curves suggests that the inherent or intrinsic "cementing" characteristics of the pastes of four principal cement minerals are similar. The strength values, however, are particularly lower for C_3A paste with respect to others in porous pastes. The results of this work reveal that pore size

@Seismicisolation

distribution plays a less significant role (with the exception of C_3A) in strength development as the data lie on a single curve. Porosity is apparently a more suitable descriptor of strength than time or degree of hydration. Important parameters influencing strength development include mineral particle size and water-solid ratio insofar as they influence the resultant porosity of the hydrating system. Intrinsic strength of hardness appears to be independent of mineral type. Although normally only very low strengths are obtained with C_4AF and C_3A at normal temperatures and w/s ratios, very high strengths may be obtained when the pastes are prepared at very low w/s ratios and high temperatures.[18][19] The compressive strength-time curves presented by Bogue-Lerch cannot be considered as universal descriptors of strength development of C_3S, C_2S, C_3A, and C_4AF and should be interpreted with caution. It is apparent that there is no unique strength-time relation for hydrated cement systems. The relative values depend on the particle size distribution, water-solid ratio, method of mixing, temperature, time, and other parameters. The results also have revealed that by manipulating the right conditions same strengths can be obtained with all the cement compounds.

2.5 Evidence for a Model of C-S-H Structure Based on the Application of Miniature Tests

Miniature specimens of hydrated cement paste have been particularly useful in obtaining physicomechanical and physicochemical data, enabling inferences about the structure of C-S-H to be made.[14] Very few measurements, for example, have been made of the variation of the modulus of elasticity of cement pastes containing water or other sorbate, due largely to difficulties in conditioning the samples. In order to achieve equilibrium at any vapor pressure within a reasonable time and without the imposition of large stress gradients, the specimens have to be very thin, drying should be carefully controlled, and measuring techniques should be accurate. These conditions can be met with miniature specimens in the form of thin disks (for flexural tests) or T-shaped specimens with 1 mm thick walls (for compression tests).

A simple model of C-S-H showing the entry and exit of interlayer water corresponding to equilibrium positions on the modulus of elasticity isotherm is shown in Fig. 11.

@Seismicisolation

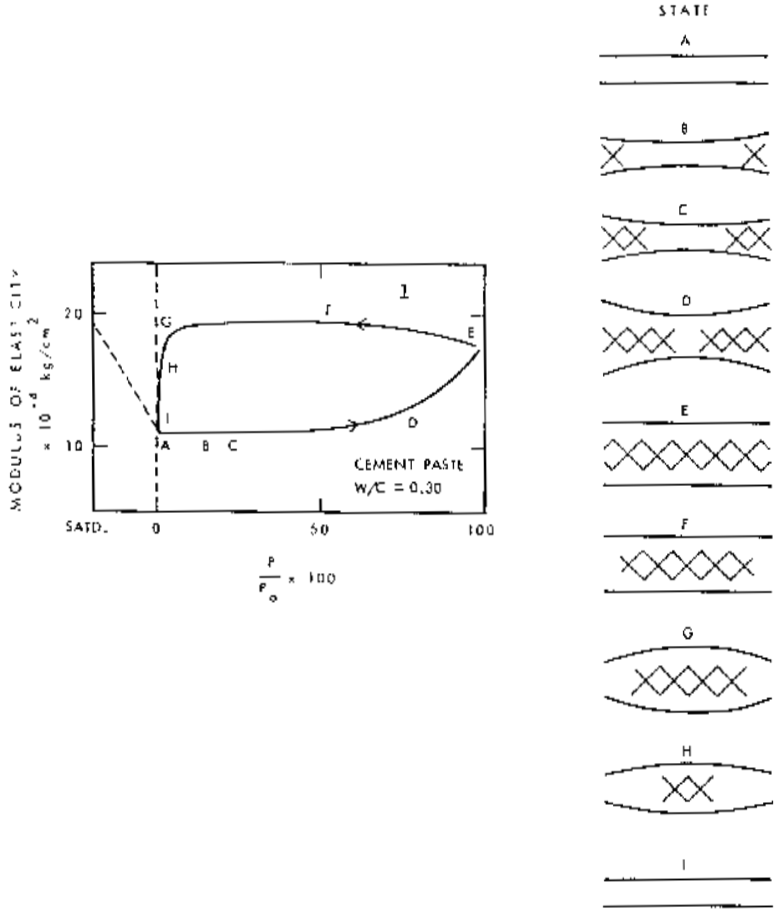


Figure 11. Simple model showing entry and exit of interlayer water with change in modulus of elasticity.[14]

Water that enters the interlayer region contributes to the stiffness of the structure and is more effective in the central locations of the layers. Hence, enhanced stiffening occurs at humidities greater than 50% as water penetrates deeper into the structure. This was briefly discussed in Sec. 2.3. The increased stiffness remains on desorption until drying at very low

@Seismicisolation

humidities occurs (i.e., < 11% RH). It is at these low humidities that the water in the central portion of the layers is finally removed.

The change in microhardness or strength of cement paste as a function of relative humidity is illustrated in Fig. 12. The results for cement paste, porous glass, and fused quartz, show a similar trend.

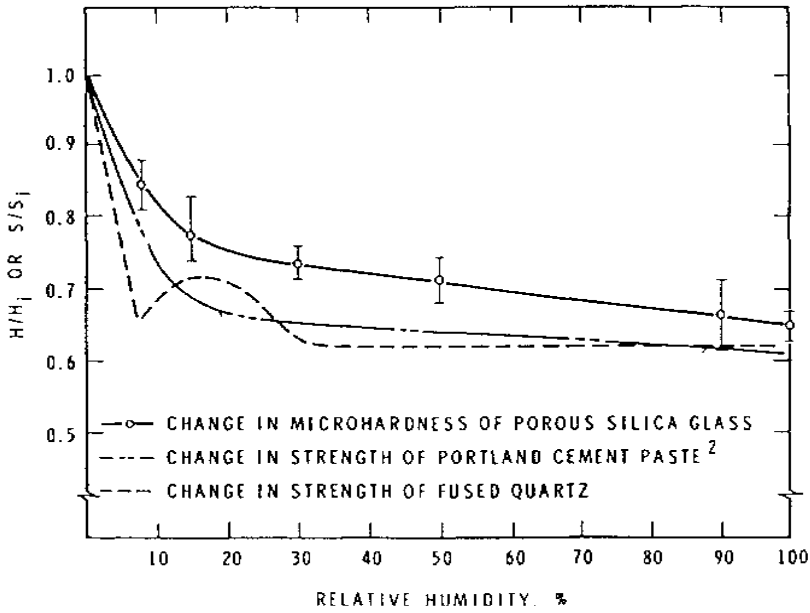
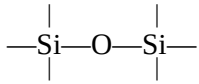


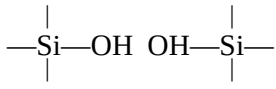
Figure 12. Effect of humidity on microhardness and strength.[14]

The microhardness or strength decreases with humidity and is more pronounced in the low humidity region. This suggests that the mechanism controlling strength is different from that influencing the modulus of elasticity. This behavior is consistent with a layered model of C-S-H structure, but cannot be explained by colloidal gel models such as the structure advanced by Powers.[20] It is assumed that the fracture mechanism at a region of stress concentration is affected by the environment. Under high stress conditions the presence of moisture promotes the rupture of the siloxane groups:



@Seismicisolation

in the cement paste to form silanol groups



Application of the Griffith equation

$$\sigma = \sqrt{2E\gamma/\pi c}$$

where, σ is the applied stress, E is the modulus of elasticity, γ is the specific surface energy, and c is half the length of the crack, is questionable. A lower value of γ is expected when the material is wet; however, when an existing crack propagates, the energy involved would be that of the free surface. In addition, measurements with other adsorbates on other materials, such as glass, have shown no correlation of strength decrease with surface energy decrease.

2.6 Remarks

The effect of sorbed water on the mechanical properties of hydrated cement compacts or paste samples is similar. Young's modulus remains constant within the accuracy of the results (± 10%) in the region of 0 to 50% RH. This conclusion supports the hypothesis for length change based on the idea that crystallites are in a state of stress and that they themselves expand when adsorption occurs. This also supports the assumption of Flood[21] who considered that the change in the thermodynamic state of an adsorbent arising from physical adsorption is wholly equivalent to a change in its volumetric mean state of stress.

Mere compaction of hydrated cement powder attains high values of fracture-strength and Young's modulus. Porosity is the basic parameter determining the strength and Young's modulus. An increase in Young's modulus in the region 50 to 100% RH is likely due to the re-entry of water into the lattice of the tobermorite-like C-S-H.

Highest strength for samples of a given porosity is attained at 0% RH and the largest reduction of strength is experienced in going from 0 to 15% RH. In going to any humidity above 15% RH there is only a slight further reduction in strength.

The results discussed above (for thin disks) are based on equilibrium data, avoiding gradients (use of thin samples). and all extraneous processes such as carbonation by the use of special procedures.

@Seismicisolation

3.0 CREEP AND DRYING SHRINKAGE MEASUREMENTS

The factors that affect time dependent strain of cement paste under sustained load, i.e., creep, include specimen geometry and thickness. Miniature thin-walled cement paste cylinders have been found to be effective in minimizing the time required for equilibrium moisture distribution. This is important for investigations of the mechanisms responsible for deformation.

3.1 Creep

Bazant and coworkers developed a thin-walled cement paste cylinder for creep tests at variable humidity or temperature.[22][23] The specimen manufacture is described in their publication. The mold for casting the specimens is made of teflon reinforced by aluminum. Cement paste is mixed under vacuum and spread on the lower part of the open mold. The teflon model is then pressed lightly into the paste. Paste is then spread on top of the mandrel and the top half of the mold is closed. A delicate procedure involving cooling in ice-water is used to unmold the specimen. The thermal coefficient of teflon exceeds that of aluminum by about 15 times. This difference allows for the displacement of the mandrel during the unmolding procedure. The wall thickness of the specimen produced was 0.71 mm (0.028 in.). This permitted the achievement of uniform humidity distribution in less than one day. Specimen ends are ground to achieve a flat surface. The test specimens were hollow, cylindrical tubes of wall thickness 0.71 mm, external diameter 15 mm (0.590 in.), and length 92 ± 3 mm (3.62 ± 0.12 in.). The axial compressive strength (wet) at 28 days was 37.9 MPa and the initial tangent modulus was 19.0 GPa. Axial strain in creep tests was measured using mechanical dial gauges. This of course introduces a certain error caused by the fact that the gauges are not attached to the specimen itself, but to the loading platens.

An apparatus for testing the response of small specimens to controlled environmental changes was also constructed by Day.[24] The design provided for controlled changes of temperature and humidity concurrently with deformations. A hydraulic system was used for rapid load application. Rapid environmental change was achieved by keeping the specimen chamber as small as possible. The geometry of the specimens was chosen to facilitate attainment of hydral equilibrium and was essentially a grooved

@Seismicisolation

prism (Fig. 13). Three millimeters (0.12 in.) diameter quartz glass rods were attached to the specimen ends. The miniature creep rig and specimens are shown in Fig. 14.

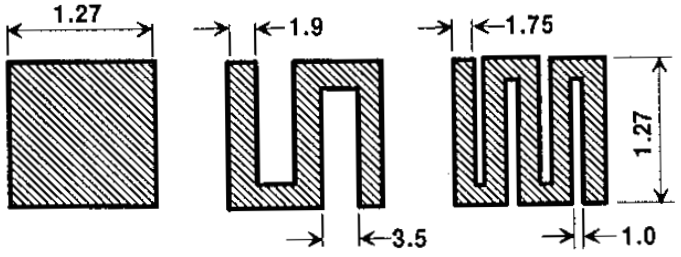


Figure 13. Geometry of miniature creep specimens after Day.[15]

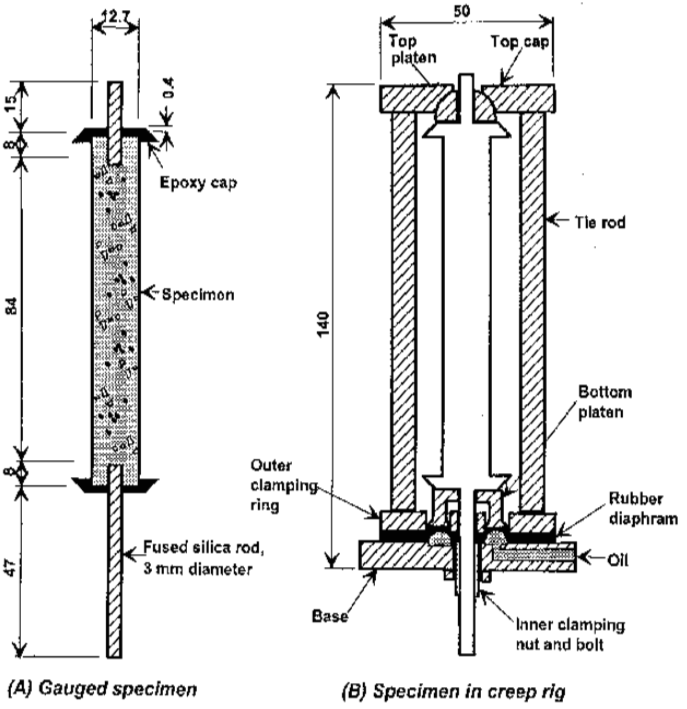


Figure 14. Miniature creep rig after Day.[15]

@Seismicisolation

A copper sleeve with a cavity wall passed tightly around the creep rig. The cavity wall allowed the use of circulating fluid for a controlled temperature environment. Strains were measured using displacement transducers. Drying creep results for slotted specimens of hydrated cement paste have been obtained. Data are illustrated in Fig. 15.

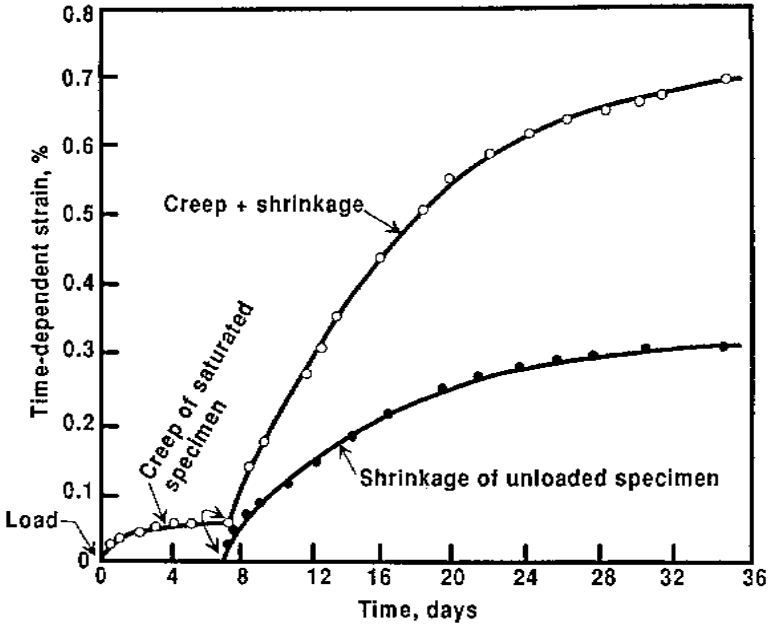


Figure 15. Creep data obtained by Day using miniature creep rig.[15]

Creep measurements on cylindrical thin-walled specimens similar to those produced by Bazant were carried out by Mindess and co-workers.[25] A schematic of the creep and shrinkage cells is shown in Fig. 16. Typical results for hydrated C_3S (water/solid = 0.40; degree of hydration = 85%) are presented in Fig. 17.

Drying creep is at 53% RH with a stress strength ratio of 0.1. It was found that creep and drying shrinkage of calcium silicate pastes were less than that of portland cement paste. No significant drying creep was observed with pastes of a low degree of hydration. The percentage of irreversible strain was greater for specimens with a low degree of hydration even though no drying creep was observed.

@Seismicisolation

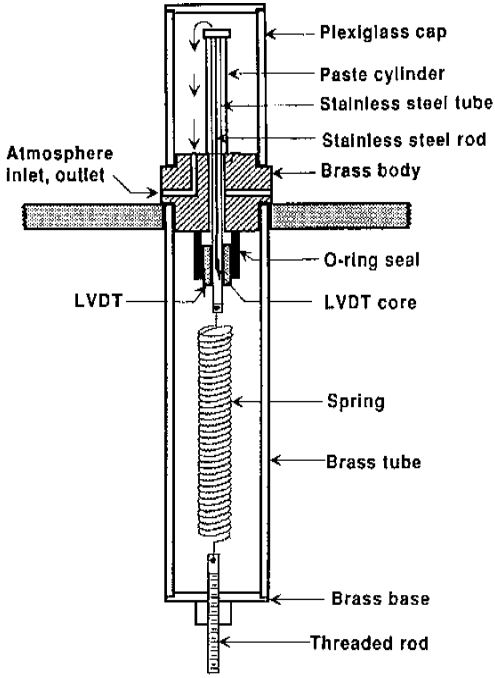


Figure 16. Schematic of miniature creep apparatus after Mindess, et al.[16]

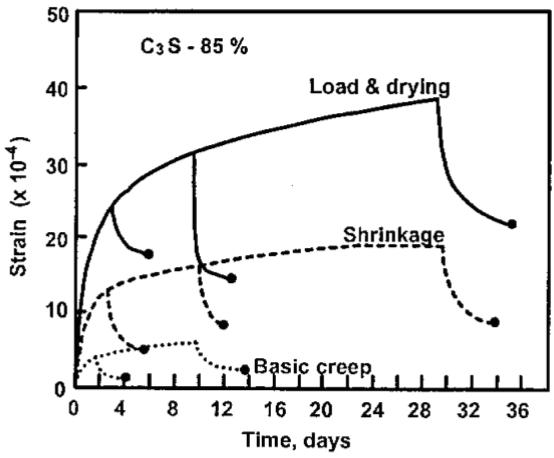


Figure 17. Creep results for hydrated C_3S paste.[16]

@Seismicisolation

An alternate type of miniature specimen for creep measurements was developed by Feldman.[26] The specimen was designed in the form of a stubby column with a "tee" shaped cross-section. The web thickness of the tee was approximately 1.25 mm. The flange was about 12 mm wide and the column height 30 mm. The load was applied through a spring loading device using specially designed miniature frames (Fig. 18).

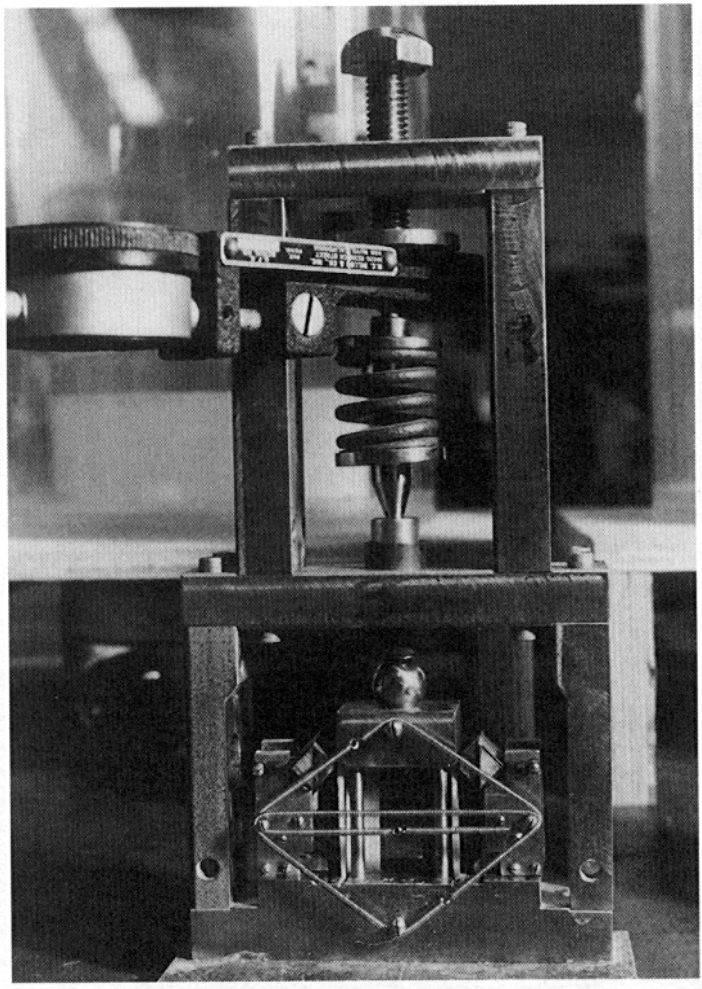


Figure 18. Miniature creep apparatus after Feldman.

@Seismicisolation

Load was centrally applied and distributed to two specimens on either side of the frame. Strain (sensitive to 1 μ strain) was measured using modified Tuckerman extensometers attached to the flange of the column specimens. The entire assembly was placed in a perspex cylinder over a salt solution for humidity control. A significant amount of creep in the dry-state was observed for cement paste specimens subjected to solvent replacement with methanol prior to drying to 0% relative humidity. Specimens dried under normal conditions exhibit very low values of creep. It is suggested that processes other than those based on diffusion mechanisms (e.g., interparticle shear, sliding) contribute to creep.

3.2 Drying Shrinkage

Drying shrinkage is one of the least understood phenomena in concrete technology. It has not been possible to correlate the drying shrinkage with any one of the many factors affecting it. Shrinkage itself imposes severe stress gradients on the material and affects measurements and in large specimens it is virtually impossible to reach a state of equilibrium. However, this could be obviated to a large extent by the use of miniature specimens. An investigation was carried out to study the effect of admixtures and other factors on the drying shrinkage of such specimens.

Specimens were cut in thin wafers, 1.2 mm (0.05 in.) thick, 10 mm (0.38 in.) wide, and 30 mm (1.18 in.) long, from two cement pastes made from Type I cements containing total alkali contents of 0.8 and 1.3%. They were made with w/c ratios of 0.5 and 0.8 with two different amounts of admixtures and cured for over a year. Two methods of drying were used. In the so-called slow method, each sample was exposed to eleven different humidities from 100 to 15% RH for a total period of 6 months. The fast method involved exposing the samples directly to 40% relative humidity.

Shrinkage values for an admixture-free sample and one containing three times the normal dosage of calcium lignosulfonate are shown in Fig. 19. Shrinkage on drying from 100 to 40% relative humidity is 0.44% for the standard and 0.94 for the sample containing calcium lignosulfonate. The residual shrinkage values (nonrecoverable shrinkage after re-wetting to 100% relative humidity) for the corresponding samples are 0.16 and 0.60%. Shrinkage values for these samples following drying from 15 to 0% RH are 0.94 and 0.92%, respectively. Extensive data, using samples with different mixtures and w/c ratios lead to the following conclusions.[27] Depending on the type of admixture, varying amounts of first drying shrinkage may be

@Seismicisolation

obtained, these values increasing with extra admixture dosages. On first drying, large shrinkage occurs down to 50% relative humidity, the value of which depends on the type and amount of admixture. All samples behave similarly when dried from 50 to 15% relative humidity, re-wetted to 100% RH, or dried from 15 to 0% RH. It was also found that the higher the w/c ratio, the larger the shrinkage.

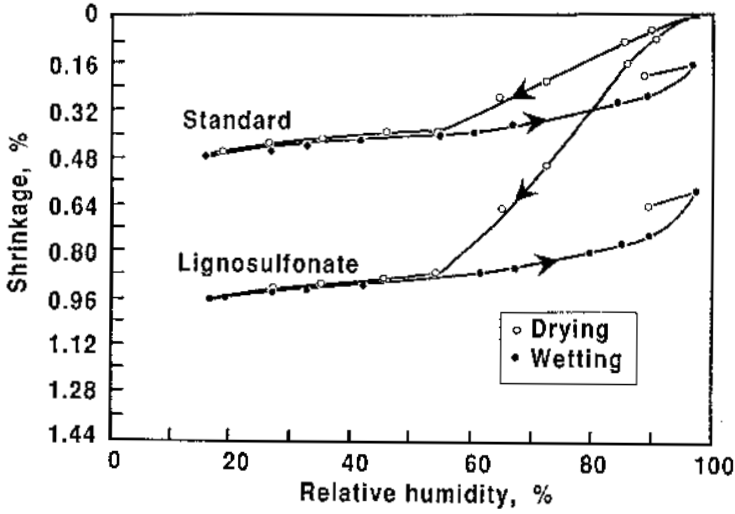


Figure 19. Shrinkage and expansion of cement pastes with and without water-reducing admixtures.[18]

The fact that large differences in drying shrinkage occur between 50 and 100% relative humidity suggests that admixtures mainly influence the degree of dispersion of the hydrated cement in terms of the alignment of sheets and displacement of ends of sheets. This technique provides a definitive and rapid method of determining the effect of admixtures on drying shrinkage of hydrated cements.

4.0 VOLUME INSTABILITY OF POROUS SOLIDS

4.1 Accelerated Test Methods

Typical examples of tests designed to predict the long-term performance of portland cement systems are the ASTM Test for Potential Expansion of

@Seismicisolation

Portland Cement Mortars Exposed to Sulfate (C452-75) and the ASTM Test for Compressive Strength of Hydraulic Cement Mortars (C109-77).

The smallest specimens used in tests at present are 25 by 25 mm (1 by 1 in.) in cross-section of which at least 12.5 mm (0.50 in.) must be penetrated by elements of the environment before a full response in terms of the reaction of the whole specimen is recorded by the measurement of length.

Mechanical properties are measured with 50 mm (2 in.) cubes or 75 mm (3 in.) diameter cylinders where changes in response to the environment may take longer. Miniature specimens are well adapted to measuring properties of individual constituents of cement paste or aggregates[28][29] and permit study of the mechanisms of deterioration.[30] A sample having one dimension of about 1.5 mm (0.06 in.) will attain equilibrium with the environment earlier than larger specimens and will give an indication of the intrinsic response of the material. In cases where failures involve critical stress gradients, specimens of larger dimensions may be needed. Depending on the material and conditions of test, several other advantages can result from the use of miniature specimens. The use of pressed disks, for example, eliminates mixing with a binder. Also, the expansion values in such specimens are much greater than those formed by normal methods, thus enabling better sensitivity in measurements. In a single test more miniature specimens can be accommodated than would be possible otherwise, because of their small size. This results in the saving of space, material, and total time required to obtain the results. They are especially valuable when only small amounts of samples are available. Miniature specimens are particularly adaptable to nondestructive test methods because they can be made with uniform properties and can be exposed more easily to controlled conditions of exposure.

This section presents examples of some possible applications of techniques involving miniature specimens in testing the durability of building materials. The studies include unsoundness of lime, failure of white coat plasters, unsoundness of cement containing magnesium oxide (MgO) and calcium oxide (CaO), durability of cement mortars exposed to chloride solutions, and the resistance of sulfur-impregnated cements subjected to high humidities.

4.2 Unsoundness of Lime

Failure in plaster finish coat or mortar can occur due to the expansion resulting from the conversion reaction $MgO \rightarrow Mg(OH)_2$. Disks of lime with a nominal diameter of 31.25 mm (1.25 in.) and thickness 2 mm

@Seismicisolation

(0.08 in.) were made by pressure compaction at 110 MPa (16,200 psi).[31][32] The disks were autoclaved at 2 MPa (295 psi) for 3 h. The linear expansion of the compacts containing varying amounts of a dolomitic lime and calcium hydroxide was measured and found to vary linearly with the amount of unhydrated MgO. Compounds such as calcium carbonate, magnesium hydroxide, and calcium hydroxide, normally present in dolomitic limes, show negligible autoclave expansion and, hence, do not influence the test results.

4.3 Failure of White Coat Plasters

The pressed disk technique was used to investigate the potential soundness of a plaster that failed on one wall and not the others of a particular building.[33] The autoclave expansion values of disks for the sound plaster and the failed plaster were 15.4 and 5.4 percent, respectively. The difference was due to differences in the unhydrated MgO content. It was concluded that this expansion was responsible for the failure of white coat plaster on the wall in question. The technique appears to have considerable potential for establishing limits of the amount of permissible MgO in white coat plasters provided the dependence of percent of expansion on the amount of hydration of dolomitic lime can be established.

4.4 Unsoundness of Portland Cement Containing MgO and CaO

Dead burnt MgO and CaO if present in portland cement in the free form can promote volume expansion. A study was undertaken to evaluate the potentiality of thin disks as a replacement for the 25 by 25 by 282 mm (1 by 1 by 11¼ in.) prisms normally recommended in standard specifications for the autoclave test and also to compare the relative expansive nature of CaO and MgO.

A normal portland cement containing 1.28% MgO and 0.48% CaO was mixed with dead burnt MgO or CaO (0.5 to 4.5 percent by weight) and made into disks 12.5 mm (1.2 in.) in diameter by a compaction load of 27.8 MPa (800 psi) or 31.25 mm (1.25 in.) in diameter at a load of 8.25 MPa (1200 psi). These disks, and the prisms made according to the ASTM Test for Autoclave Expansion of Portland Cement (C151-74a), were subjected to autoclave treatment at 2 MPa (295 psi).

Figure 20 shows the relative autoclave expansion values for portland cement disks 12.5 mm (0.5 in.) pressed at 27.8 MPa (800 psi) containing MgO or CaO.

@Seismicisolation

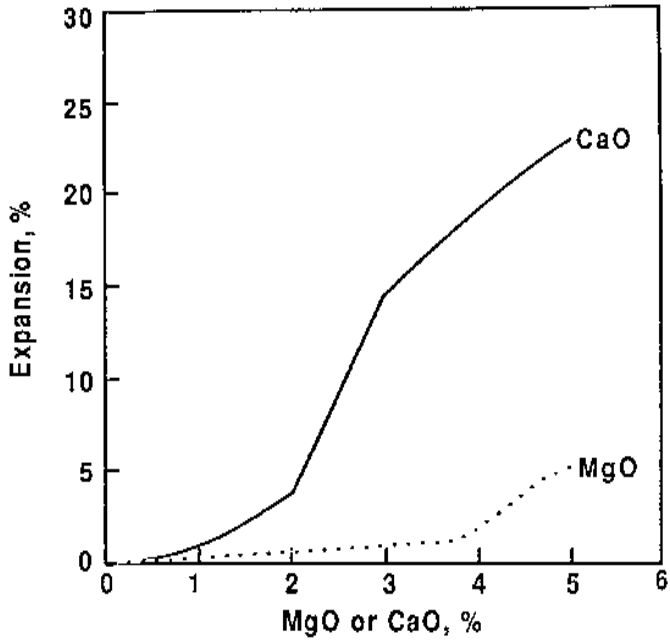


Figure 20. Autoclave expansion of portland cement compacts containing MgO or CaO.[20]

In the cement containing MgO the expansion is low up to about 4% addition, after which a steep increase occurs. The expansion values are much higher in disks containing CaO. A molar expansion of 90% for the reaction $CaO \rightarrow Ca(OH)_2$ compared with 117% for the $MgO \rightarrow Mg(OH)_2$ reaction cannot explain these differences. If expansions are compared on equivalent molar basis (1 g CaO = 0.018 mol and l g MgO = 0.0248 mol), MgO would be expected to show more expansion. It appears that the particle size of the oxides, the crystalline dimensions, and crystalline growth pressures, may be important factors influencing the overall expansion. These results also reveal that in specifications for unsoundness of cement the limitations should be based on the potential expansive nature of CaO and MgO and not just on MgO.

Figure 21 compares the autoclave expansion of disks 31.25 mm (1.25 in.) in diameter pressed at 8.25 MPa (1200 psi) with that of prisms containing different amounts of MgO. This work is also relevant to that discussed in the chapter on dimensional changes.

@Seismicisolation

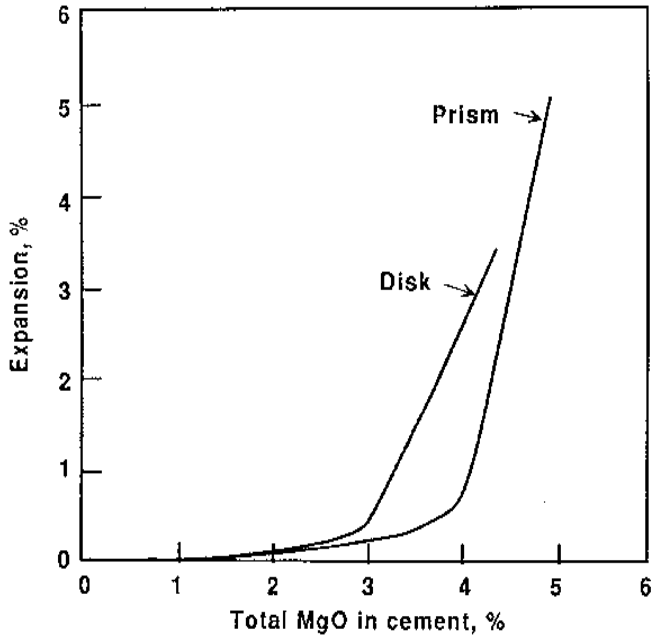


Figure 21. Comparison of autoclave expansion of portland cement compacts and prisms containing different amounts of MgO.[20]

At 4% MgO, the prism expands by about 0.75%, close to the limit specified by ASTM. At this concentration, the expansion in the disk is much higher, being 2.4%. The results demonstrate that disks are much more sensitive to autoclave treatment than the prisms, providing an alternate technique for the determination of unsoundness in cements.

4.5 Durability of Cement Mortars Exposed to Chloride Solution

The period for detection of the onset of deterioration due to ingress and attack from strong solutions of sodium, potassium, calcium, and magnesium chlorides, can be considerably shortened through the use of thin samples in the form of disks.[29] Hence, studies were made using mortar disks 75 mm (3 in.) in diameter and 6.4 mm (0.25 in.) thick sliced from 75 by 254 mm (3 by 10 in.) cylinders. The mortars were cured for 15 or 240 days before exposure to a salt solution. The salt solution contained 27.5% $CaCl_2$, 3.9% magnesium chloride ($MgCl_2$), 1.8% sodium chloride

@Seismicisolation

(NaCl) and 0.1% sodium bicarbonate ($NaHCO_3$). A nondestructive test involving the measurement of deflection in flexure under constant load as a function of time of exposure to salt solution was adopted to investigate the durability of the mortar; this test is similar to one previously described for disks, but on a larger scale. Because deflection in this mode of testing is inversely proportional to the cube of the thickness, a small effect at the surface can be detected quickly.

Two sulfate-resisting cements and one Type I normal portland cement were used. Two samples of fly ash containing 47.6 and 55.6% SiO_2 were used as replacements of cement at 20 and 35% forming a blend with the sulfate-resisting cement. The blended cements made by mixing Type I portland cement with 37.5, 50, and 70% blast furnace slag also were examined.

The results are recorded as the difference between the deflection of the samples stored in the salt solution and those stored in water. Results for some of the samples are presented in Figs. 22 and 23. Figure 22 for the 15-day cured samples shows that the slag-containing cement sample has a relatively high resistance to the salt solution even at 700 days.

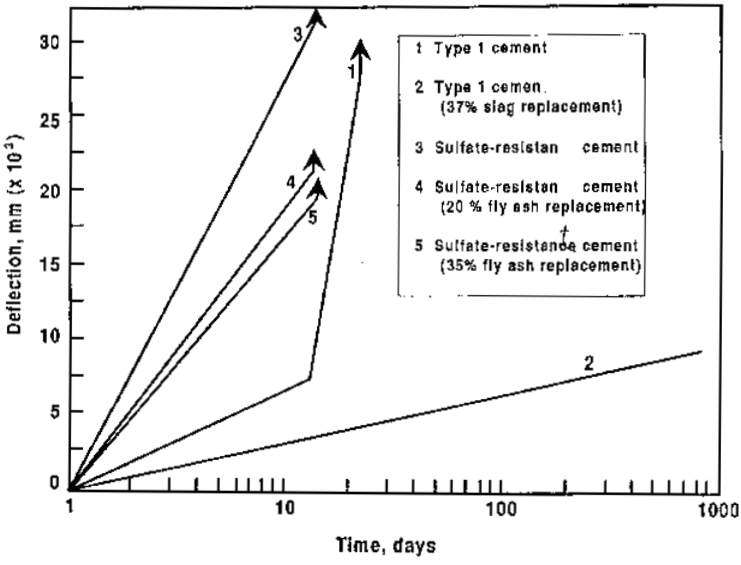


Figure 22. Deflection of mortar disks cured 15 days and exposed to chloride solutions (see text).[20]

@Seismicisolation

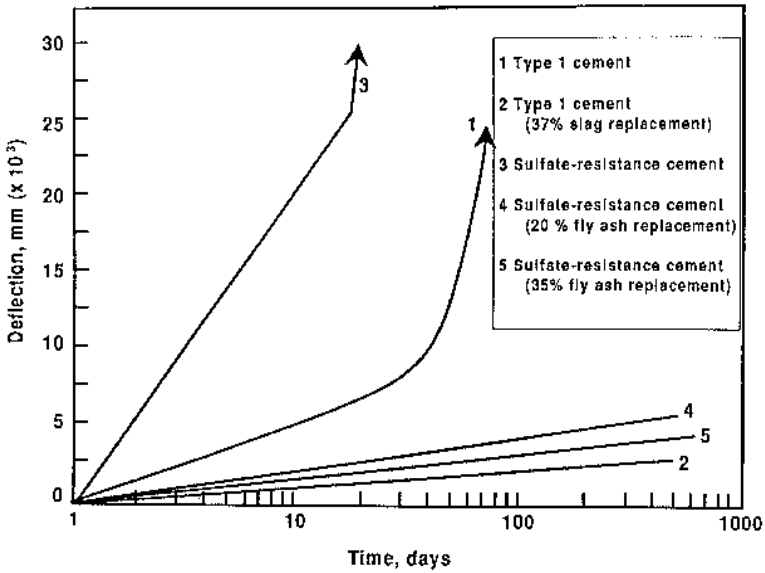


Figure 23. Deflection of mortar disks cured 240 days and exposed to chloride solution (see text).[20]

Of the remaining samples, the sulfate-resisting cement mortar failed first, followed by the two fly ash-replaced cement mortars, and then the Type I cement mortar. The results for the 240-day cured samples in Fig. 23 show a similar sequence as before except that the fly ash-replaced cement mortars are now much more durable and rank in the same order as the slag cement mortar. All the specimens cured for 240 days are more durable than those cured for only 15 days.

These results are, in general, consistent with the observation that the greater the amount of free $Ca(OH)_2$ in the specimen, the more susceptible it is to attack. This is also true for the sulfate-resisting cements which have a higher tricalcium silicate content.

Additional information on the volume stability of cement systems in aggressive media is presented in the chapter on dimensional changes.

@Seismicisolation

4.6 Miniature Rock Prism Test

A miniature rock prism test was designed to accelerate the determination of potential expansivity of carbonate rocks.[34] Expansion of miniature rock prisms sawn normal to the layering of the rock (to avoid the effects of anisotropy) and stored in 2N NaOH commences within the first week compared with the long initiation period typical of the rock cylinder method ASTM C586. Miniature rock prisms 3 × 6 × 30 mm (0.12 × 0.24 × 1.18 in.) can be sawn from a slab or rock or even cut from a large gravel pebble. Length change measurements (to 0.1μm) can be made with a linear variable differential transformer (LVDT). The rock prism is clamped in an invar frame. A nut at the lower end is provided so that the LVDT can be adjusted to read zero with the sample in place. The length of the dry prism is first measured, then placed in water and its length monitored until a constant value is obtained. This is taken as the zero value for expansion in alkali. The frame containing the prism is then placed in 2N NaOH and left undisturbed for the duration of the experiment. This normality was selected to maximize the rate of expansion. Several prisms should be measured from each sample.

Results of expansion for an alkali-expansive carbonate aggregate (from the Pittsburg Quarry in Kingston) determined by ASTM C586 correlate well with those determined by the miniature rock prism test. The advantage of the miniature test is that a given expansion is obtained in a shorter time. Excellent correlation was also found between the expansion of miniature rock prisms in 2N NaOH and expansion of concrete prisms in a modified form of CSA 23.2-14A in which samples are stored at 30°C and 100% RH.

The miniature rocks prism test avoids gel-like deposits that occur on specimen surfaces when the rock cylinder method is employed.

The expansion of concrete containing either opal or agate is due to the formation and swelling of a gel-like phase not to the direct expansion of the aggregate as is the case with the alkali-carbonate reactive aggregates. A correlation between the rates of expansion or contraction of miniature rock prisms of classical alkali-silica reactive aggregates and expansion of concrete made with these aggregates cannot, therefore, be expected.

The miniature rock prism test may be particularly useful for evaluating the potential expansivity of the horizons in a quarry containing thinly bedded carbonate rocks. For slowly expanding siliceous aggregates, quartzites, argillites, quartz-biotite gneiss, and graywackes, the miniature rock prism test results are not as promising. The miniature rock prisms first

@Seismicisolation

expanded then contracted and disintegrated. Although the rates of expansion or contraction do not give a measure of the potential expansivity of concrete prisms made with these aggregates they do indicate that the rock is potentially deleteriously expansive in concrete.

5.0 THE MINI-SLUMP TEST

A miniature slump test was developed by Kantro for neat portland cement paste.[35] The new procedure was designed to compare the performance of water-reducing admixtures and follow the loss in workability with time. Pat areas rather than heights are measured and the results are expressed as a percentage of water reduction.

A miniature slump cone was fabricated of lucite. Its dimensions were: top diameter, 19 mm (¾ in.); bottom diameter, 38 mm (1½ in.); and height, 57 mm (2¼ in.). The dimensions are in the same proportions as the slump cone described by ASTM C143. The cone (1 minute after filling) is lifted with a motion rapid enough to remain clear of the flowing paste, but slow enough to avoid imparting a significant upward momentum to the paste. Rapid area determinations can be made from the fresh pats with callipers. The area of a circle can be calculated from the average diameter. The areas show large differences with different workabilities.

Plots of pat area versus water-cement ratio are linear, in the range 0.36 to 0.45 for most cements. The influence of different sugar derivatives on mini-slump area is shown in Fig. 24. Sodium gluconate produces significant water reduction with relatively small quantities. Larger quantities of other derivatives are required to produce similar effects.

Collepardi, et al.,[36] and Chiocchio, et al.,[37] employed mini-slump measurements in investigations of cement pastes containing admixtures. It was observed that trends in results obtained from the mini-slump test corresponded to those from the standard concrete slump test. Ramachandran, et al.,[38] extended the use of the miniature slump tests to concrete containing binary admixture systems. Slump values of cement paste, mortar, and concrete, were assessed not only on the basis of height, but also in terms of base area measurement. Mini-slump tests for cement paste were carried out according to the procedure of Kantro, described above. The mortar tests were carried out with a slump cone having the following dimensions: top diameter 37.5 mm (1.5 in.); bottom diameter 75 mm (3.0 in.) and height 112.5 mm (4.4 in.). Mix proportions were cement:natural sand = 1:2.75

@Seismicisolation

with water-cement ratio = 0.50. The method for measuring slump of concrete conformed to ASTM C192-81 and ASTM C143-78. The concrete mix proportions were cement:sand:coarse aggregate = 1:2:3.2 with water-cement ratio = 0.50.

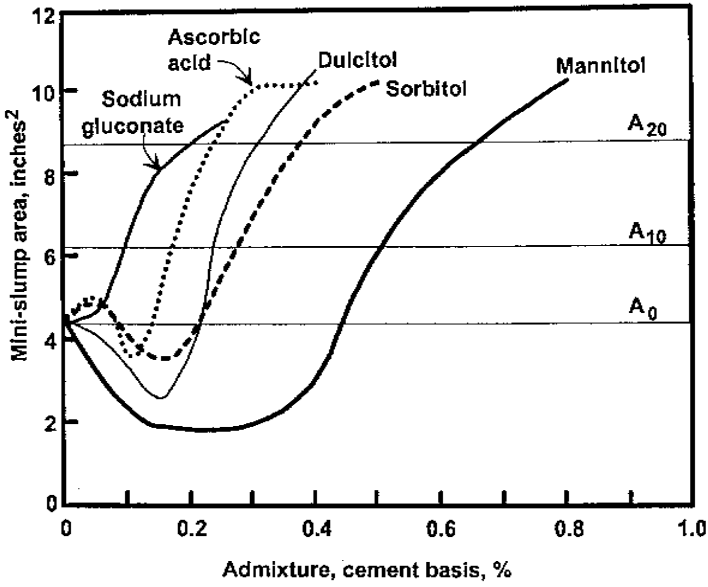


Figure 24. The influence of different sugar derivatives on minislump area.[26]

Mini-slump values of cement paste and mortars containing different amounts of superplasticizer and a water dispersible polymer show a similar trend to concrete slump values using standard methods. Mini-slump values of superplasticized cement paste and mortar show a linear relationship with concrete slump values determined on the basis of area measurement. The relationship between slump measured by area and height for superplasticized concrete is given in Fig. 25. Preliminary slump experiments based on area should be carried out to establish interrelationships between cement paste, mortar, and concrete containing binary and ternary admixture systems. It appears that for superplasticized concrete, slump measurements based on area are a good indicator of workability.

@Seismicisolation

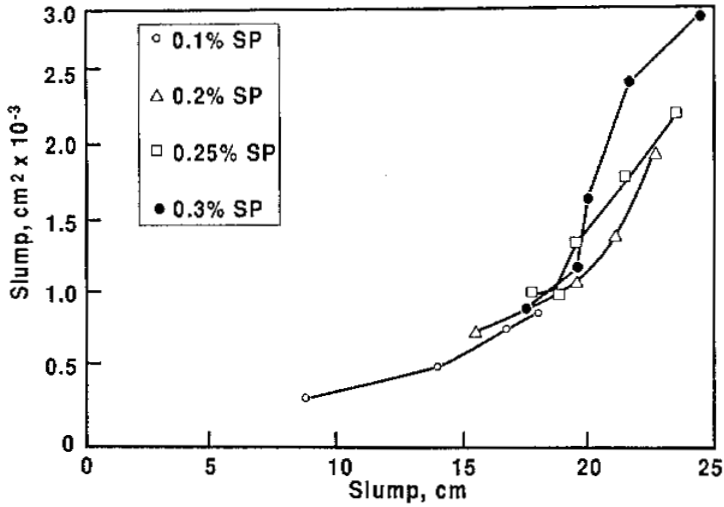


Figure 25. Slump of superplasticized concrete measured by height and area.[29]

REFERENCES

1. Sereda, P. J., and Feldman, R. F., Compacts of Powdered Material as Porous Bodies for Use in Sorption Studies, *J. Appl. Chem.*, 13:150–158 (1963)
2. Sereda, P. J., and Feldman, R. F., Sorption of Water on Compacts of Bottle-Hydrated Cement, I. The Sorption and Length Change Isotherms; II. Thermodynamic Considerations and Theory of Volume Change, *J. Appl. Chem.*, 14:87–104 (1964)
3. Dollimore, D., and Gregg, S. J., Some Observations on the Interaction of Kaolin and Water, II. The Effect of Water Adsorption on the Strength of Kaolinite Compacts, *Trans. Brit. Ceram. Soc.*, 54:262–271 (1955)
4. Dollimore, D., and Heal, G. R., The Effect of Various Vapors on the Strength of Compacted Silica, *J. Appl. Chem.*, 11:459–463 (1961)
5. Kingery, W. D., *Introduction to Ceramics*, p. 781, Wiley, New York (1960)
6. Feldman, R. F., Sorption and Length-Change Scanning Isotherms of Methanol and Water on Hydrated Portland Cement, *5th Int. Symp. Chem. Cements*, Part III, III:54–66, Tokyo, Japan (1968)
7. Brunauer, S., Kantro, D. L., and Copeland, L. E., The Stoichiometry of the Hydration of β-Dicalcium Silicate and Tricalcium Silicate at Room Temperature, *J. Phys. Chem.*, 80:761–767 (1958)

@Seismicisolation

8. Soroka, I., and Sereda, P. J., The Structure of Cement-Stone and the Use of Compacts as Structural Models, *5th Int. Symp. Chem. Cements*, Part III, III:67–73, Tokyo, Japan (1968)
9. Helmuth, R. H., and Turk, D. H., Elastic Moduli of Hardened Portland Cement and Tricalcium Silicate Paste, *Highway Res. Board, Special Report 90*, pp. 135–144 (1966)
10. Sereda, P. J., Feldman, R. F., and Swenson, E. G., Effect of Sorbed Water on Some Mechanical Properties of Hydrated Cement Pastes and Compacts, *Highway Res. Board, Special Report 90*, pp. 58–73 (1966)
11. Timoshenko, S., *Theory of Plates and Shells*, p. 479, McGraw-Hill, New York (1940)
12. Sereda, P. J., Significance of Microhardness of Porous Inorganic Materials, *Cem. Concr. Res.*, 2:717–729 (1972)
13. Taylor, H. F. W., *Cement Chemistry*, p. 475, Academic Press, New York (1990)
14. Ramachandran, V. S., Feldman, R. F., and Beaudoin, J. J., *Concrete Science*, p. 328, Heyden and Sons, London (1981)
15. Bogue, R. H., and Lerch, W., Hydration of Portland Cement Compounds, *Ind. and Eng. Chem.*, 26:837–847 (1934)
16. Beaudoin, J. J., and Ramachandran, V. S., A New Perspective on the Hydration Characteristics of Cement Phases, *Cem. Concr. Res.*, 22:689–694 (1992)
17. Beaudoin, J. J., and Feldman, R. F., A Study of Mechanical Properties of Autoclaved Calcium Silicate Systems, *Cem. Concr. Res.*, 5:103–118 (1975)
18. Ramachandran, V. S., and Feldman, R. F. Significance of Low Water-Solid Ratio and Temperature on the Physico-Mechanical Characteristics of Tricalcium Aluminates, *Appl. Chem. Bitechnol*, 23:625–633 (1973)
19. Ramachandran, V. S., and Beaudoin, J. J., Significance of Water-Solid and Temperature on the Physico-Mechanical Characteristics of Hydrating 4 $CaO{\cdot}Al_2O_3{\cdot}Fe_2O_3$, *J. Matls. Sci.*, 11:1893–1910 (1976)
20. Powers, T. C., Properties of Cement Paste and Concrete, *Proc. Fourth Int. Symp. on the Chem. of Cem.*, p. 590, Washington (1960)
21. Flood, E. A., and Heyding, R. P., Stresses and Strains in Adsorbent-Adsorbate Systems, *Can. J. Chem.*, 32:660–682 (1954)
22. Bazant, Z. P., Hemann, J. H., Koller, H., and Najjar, L. J., A Thin-Wall Cement Paste Cylinder for Creep Tests at Variable Humidity or Temperature, *Materiaux et Constr.*, 6:277–281 (1973)
23. Bazant, Z. P., Asghari, A. A., and Schmidt, J., Experimental Study of Creep of Hardened Portland Cement Paste at Variable Water Content, *Materiaux et Constr.*, 9:279–290 (1976)
24. Day, R. L., An Apparatus for Testing the Response of Small Specimens to Controlled Environmental Changes, *Mag. Concr. Res.*, 34:146–154 (1982)

@Seismicisolation

25. Mindess, S., Young, J. F., Lawrence, F. V., Creep and Drying Shrinkage of Calcium Silicate Pastes, I. Specimen Preparation and Mechanical Properties, *Cem. Concr. Res.*, 8:591–600 (1978)
26. Feldman, R. F., Unpublished work.
27. Feldman, R. F., and Swenson, E. G., Volume Change on First Drying of Hydrated Portland Cement With and Without Admixtures, *Cem. Concr. Res.*, 5:25–35 (1975)
28. Grattan-Bellew, P. E., and Litvan, G. G., Testing Canadian Aggregates for Alkali Expansivity, *Proc. Alkali Symp.*, pp. 227–245, London (1976)
29. Feldman, R. F., and Ramachandran, V. S., New Accelerated Methods for Predicting Durability of Cementitious Materials, Durability of Building Materials and Components, Amer. Soc. Testing and Mat., Spec. Tech. Pub. 691, pp. 313–325 (1980)
30. Mehta, P. K., and Gjorv, O. E., A New Test for Sulfate Resistance of Cements, *J. Test. Eval.*, 2:510–514 (1974)
31. Ramachandran, V. S., Feldman, R. F., and Sereda, P. J., An Unsoundness Test for Limes without Cement, *Matls. Res. and Stds.*, 5:510–515 (1965)
32. Ramachandran, V. S., and Sereda, P. J., The Role of Cement in Autoclave Expansion of Cement-Lime-Limestone Mixtures, *World Cement Technology*, 9:3,6–8 (1978)
33. Ramachandran, V. S., Sereda, P. J., and Feldman, R. F., Delayed Hydration in White-Coat Plaster, *Matls. Res. Stds.*, 4:663–666 (1965)
34. Grattan-Bellew, P. E., Evaluation of Miniature Rock Prism Test for Determining the Potential Alkali-Expansivity of Aggregates, *Cem. Concr. Res.*, 11:699–711 (1981)
35. Kantro, D. L., Influence of Water-Reducing Admixtures on Properties of Cement Paste - A Miniature Slump Test, *Cem. Concr. Agg.*, 2:95–102 (1980)
36. Collepardi, M., Corradi, M., Baldini, G., and Pauri, M., Influence of Sulfonated Napthalene on the Fluidity of Cement Pastes, *7th Int. Congr. Chem. Cement*, Vol. III, VI 20-VI 25, Paris (1980)
37. Chiocchio, G., Mangialardi, T., and Paolini, A. E., Effects of Addition Time of Superplasticizers on Workability of Portland Cement Pastes with Different Mineralogical Composition, *Il Cemento*, 82:69–80 (1986)
38. Ramachandran, V. S., Shihua, Z., and Beaudoin, J. J., Application of Miniature Tests for Workability of Superplasticized Cement Systems, *Il Cemento*, 85:83–88 (1988)

@Seismicisolation

12

Techniques for Corrosion Investigation in Reinforced Concrete

Gordon Ping Gu, James J. Beaudoin, and Vangi S. Ramachandran

1.0 INTRODUCTION

The reinforced concrete corrosion damage is a multibillion dollar problem in the United States and other countries[1]–[4] and the major contributing factor to the deterioration of the nation's highway infrastructure. A report by the United States Secretary of Transportation estimated that there were more than 200,000 deteriorating bridge structures the repair cost of which exceeded $40 billion in 1982 and $50 billion in 1986.[5] The annual expenditure for repair and rehabilitation of concrete structures in the 90s has exceeded fifty percent of the total construction costs[6] and it is expected that this trend will continue to the year 2000. Early diagnosis of corrosion, therefore, has become a very important task to the construction engineers, repair practitioners, and owners of buildings and bridges, since it allows preventive action and avoids expensive repair.

@Seismicisolation

Many electrochemical techniques have been used in reinforced concrete corrosion studies. Most of the electrochemical techniques are rapid, nondestructive, and easy to perform. They are used to determine the polarization resistance (R_p) from which the corrosion rate is obtained. Electrochemical techniques for corrosion rate measurement can be categorized into two groups: steady-state and transient. Tafel slope extrapolation, linear polarization measurement, and cyclic polarization are examples of steady-state methods. The term steady-state implies that measurement is made at the equilibrium condition of the test system. In the steady-state technique, potential is normally varied and the current is allowed to reach the steady state before it is recorded. The second group comprises the transient method. It includes potential or current steps, small and large amplitude cyclic voltammetry, and ac impedance spectroscopy. These methods involve the application of a rapid potential or current change and the corresponding current or potential response is recorded. The corrosion resistance is obtained along with interface double layer capacitance.

Corrosion monitoring techniques have also played an important role in concrete corrosion studies. For example, the macro-cell, electrochemical noise and open circuit potential measurement techniques are often used in field monitoring of reinforced concrete structures. These techniques are particularly useful since they provide in-situ corrosion evaluation.

Theoretically, the diagnosis of reinforced concrete corrosion should be relatively easy since one can apply any electrochemical technique to the reinforced concrete to determine the corrosion resistance and rate. In reality, however, determining the corrosion rate of steel in reinforced concrete is far more difficult than that in the solution phase. This is because many factors, as indicated below, make the corrosion rate measurement in reinforced concrete unique and difficult.

- *Non destructive requirement:* To maintain the integrity of the steel/concrete interface, the electrochemical technique used to measure the rebar corrosion rate must be nondestructive. If there is any distortion it should be small. The measurement should not result in the decrease of the steel/concrete bond strength.
- *Microenvironment:* The location and the rate of corrosion of the rebar depend mainly on the microenvironmental conditions at the concrete/steel interface, e.g., the pH value, chloride content, moisture content, oxygen availability, etc.

@Seismicisolation

- *Concrete resistivity:* The high resistivity of the concrete electrolyte requires a so-called IR drop correction (the voltage drop through the electrolyte) even in the linear polarization measurement. The latter is not normally required when carried out in the solution.
- *Mass transport:*The corrosion deterioration process of reinforced concrete is influenced decisively by the transport mechanism of the reactants (such as oxygen, carbon dioxide, and chloride ions) and/or products (iron oxides) within the pore structure of the concrete.
- *Undefined testing area:* It is always a problem to define the rebar area that is polarized when a counter-electrode is at the surface of the concrete along with the reference electrode. This is especially the case if the rebar is some meters in length and is closely spaced with other adjacent rebars.

Moreover, reinforced concrete in the field undergoes large changes in temperature and moisture content. These changes can occur within hours, and lead to changes of corrosion rate even at the same location. Sometimes, corrosion rates can vary by orders of magnitude over a period of time.

It is difficult to obtain meaningful and reliable data from the reinforced concrete field structures. Data analysis and interpretation require the operator to have a good corrosion knowledge and field experience. The objectives of this chapter are to describe the phenomena of ordinary steel corrosion in concrete, to outline different techniques that are commonly used for corrosion research and assessment of reinforced concrete in the laboratory and field, and to discuss the principles, applications, and limitations of these techniques. It is not the purpose of this chapter to include all testing methods used in the field and laboratory investigations, but those that assist field practitioners in the following:

1. Comprehension of the electrochemical principles of each test method involved so that proper test procedures and precautions can be taken to ensure the accuracy of measurements.
2. Acquisition of knowledge of the application conditions and limitations of each test method. This helps to properly select a test method in accordance with the survey conditions.

@Seismicisolation

3. Identification of the cause of corrosion to facilitate a cost-effective repair. A clear understanding of the relevant deterioration processes and reproducible measurement techniques are essential for improving durability and effective design procedures as well as for monitoring and developing repair techniques.

2.0 BASIC PRINCIPLES OF CORROSION

2.1 Half-Cell Potential[7]

A potential difference arises at the liquid/solid interface when a piece of metal is immersed in a solution. This is because of the uneven charge distribution in both solid and liquid phases. It is impossible to determine either the absolute value or a single interface potential difference; therefore, a second electrode must be introduced to complete an electrical circuit, as illustrated in Fig. 1. The potential measured across the two electrodes is called the cell potential, which is the sum of two half-cell potentials. Considering iron dissolution in a dilute acid solution, the cell reaction is written as:

Eq. (1) $Fe + 2H^{+} \rightarrow Fe^{++} + H_2$

The above reaction represents summation of the following two half-cell reactions

Eq. (1a) $2H^{+} + 2e^{-} \rightarrow H_2$

Eq. (1b) $Fe \rightarrow Fe^{++} + 2e^{-}$

Eq. (1) $Fe + 2H^{+} \rightarrow Fe^{++} + H_2$

A fixed potential difference can always be obtained with reference to a common electrode or so-called reference electrode that has a half-cell potential defined as zero. Any half-cell reaction can be chosen for this standard reference point. It is, however, universally accepted that a hydrogen-hydrogen ion half-cell potential is zero when the hydrogen ion activity is unity. All other half-cell potentials are calculated with respect to the standard hydrogen reference electrode. As an example, the iron half-cell potential of -0.44 V is observed if a high resistance voltmeter is connected with the two electrodes (Fig. 1).

@Seismicisolation

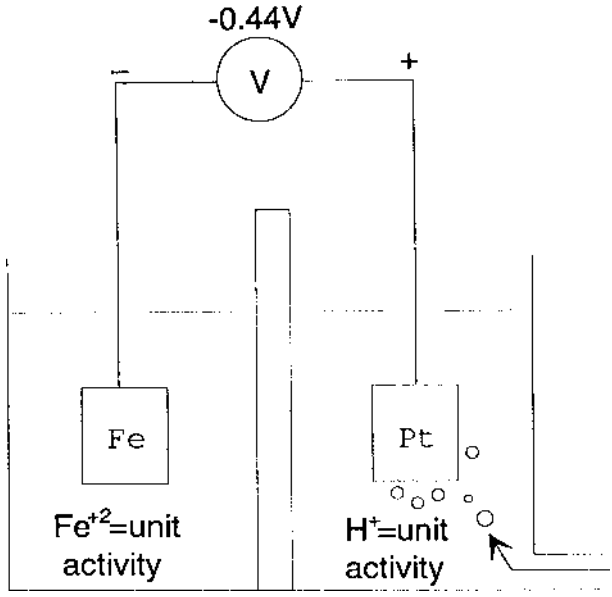


Figure 1. A electrochemical cell containing hydrogen and iron in equilibrium with their ions.

The half-cell potential of a system in which the reactant is not at unit activity can be easily calculated from the Nernst equation[8] as follows:

Eq. (2)
$$\Phi^0 = \Phi_0 + \frac{2.3RT}{nF} \log \frac{a_{oxid}}{a_{red}}$$

where Φ^0 is the half-cell potential (Φ^0 is also called reversible potential if the half-cell reaction is reversible), Φ_0 the standard half-cell potential, R is the gas constant, T is absolute temperature, n is the number of electrons transferred, F is the Faraday constant, a_{oxid} and a_{red} are activities of oxidized and reduced species.

@Seismicisolation

2.2 Butler-Volmer Equation[8]

Considering an iron half-cell, e.g., an iron electrode in ferrous solution, two reactions will likely happen: the Fe atoms dissolve into the solution by giving up two electrons and ferrous ions in the solution deposit back to the solid phase by accepting the electrons as described:

Eq. (3a) $Fe \rightarrow Fe^{++} + 2e^-$

Eq. (3b) $Fe^{++} + 2e^- \rightarrow Fe$ or

Eq. (3) $Fe \leftrightarrows Fe^{++} + 2e^-$

The reaction (3a) is named *anodic* reaction since it represents an oxidation process, and the reaction (3b) is called *cathodic* reaction since it is a reduction reaction. If no external potential is applied, the iron electrode/ ferrous solution system will reach equilibrium when the anodic reaction rate is equal to the cathodic reaction or:

Eq. (4) $i_o = i_{(anodic)} = i_{(cathodic)}$

where the i_o is so-called exchange current density. The corresponding potential is called reversible (or half-cell) potential, To describe how the reaction rate across a metal-solution interface depends on the potential difference between the actual non-equilibrium and equilibrium potentials, we need to introduce the Butler-Volmer equation, one of the most fundamental equations in electrode kinetics.[8]

Eq. (5) $$i = i_o \exp\left(\frac{(1-\beta)\eta F}{RT}\right) - \exp\left(\frac{-\beta\eta F}{RT}\right)$$

The first exponential term in the Butler-Volmer equation describes the anodic reaction and the second term the cathodic reaction. The $1-\beta$ and $-\beta$ are the energy fractions of the reaction in the anodic and cathodic direction, respectively; the term η, called the *overpotential*, measures how far the electrode potential is shifted away from the equilibrium potential. Depending on which direction the shift is, it can be an anodic or cathodic overpotential, e.g.:

Eq. (6a) $\eta_a = \Phi - \Phi^0$

Eq. (6b) $\eta_c = \Phi^0 - \Phi$

If an external potential is large enough, the Butler-Volmer equation can be simplified according to either anodic or cathodic polarization. For example, for anodic polarization the current density is given as:

@Seismicisolation

Eq. (7a) $$i = i_a = i_o \exp\left(\frac{(1-\beta)\eta F}{RT}\right)$$

or it can be rearranged to equation (7(*b*)) for convenience in plotting,

Eq. (7b) $$\eta_a = \frac{-2.3RT}{(1-\beta)F}\log i_o + \frac{2.3RT}{(1-\beta)F}\log i$$

Equation (7b) can be expressed in the general form, $\eta = a + b \log i$, which is the so-called Tafel equation where, b is the Tafel slope for anodic or cathodic reaction and its value is given by the following expressions:

$$b_a = \frac{2.3RT}{(1-\beta)F} \text{ for anodic reaction, or}$$

Eq. (7c) $$b_c = \frac{2.3RT}{-\beta F} \text{ for cathodic reactions}$$

2.3 The Evans Diagram

The Butler-Volmer equation can be used to produce a plot of potential as a function of current density. The symbols Φ and E are sometimes used interchangeably to denote potential. Figure 2 is an example plot for the iron/ferrous solution half-cell. The plot (dotted line) contains two branches, the iron anodic reaction (top branch) and the iron cathodic reaction (bottom branch).

The potential-logarithmic current density curves can be simplified by showing only the solid lines. Such a simplified plot is referred to as an Evans diagram, after U. R. Evans who first proposed this type of simplification.[9] The solid lines are the extrapolation of the linear portions of the anodic and cathodic branches of the potential-logarithmic current density plot. The intercept is the point where the anodic current density is equal to the cathodic current density. The corresponding potential is the reversible potential, and current density is the exchange current density. The Evans diagram is a very useful tool in understanding not only the electrode kinetics, but also the corrosion theory. It will be used frequently in this chapter.

@Seismicisolation

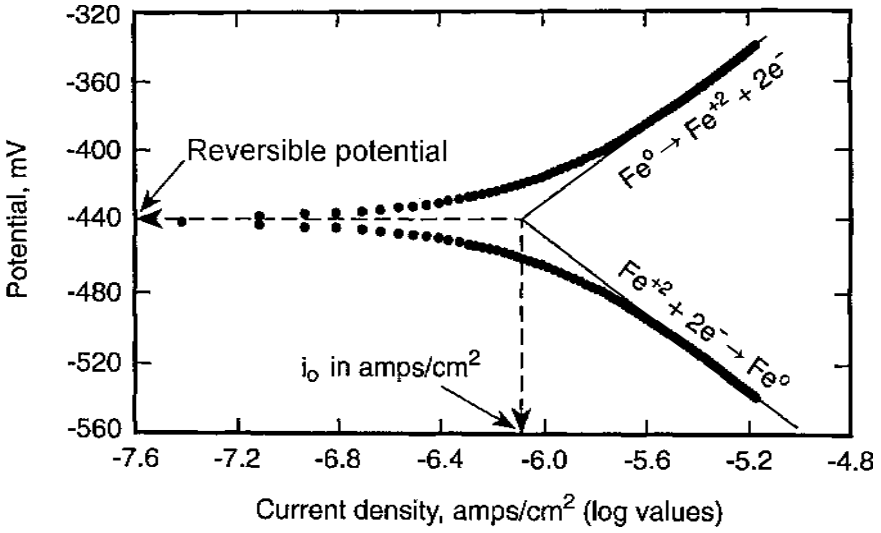


Figure 2. A plot of potential as a function of current density.

2.4 Mixed Potential Theory

Considering the Fe/Fe^{++} half-cell reaction ($Fe = Fe^{++} + 2e^{-}$), if iron dissolution and re-deposition are the only pair of reversible reactions that take place on the surface of the iron electrode, there will be no corrosion of the iron electrode because the system is reversible and the loss of iron is redeposited back to the electrode at the same rate. However, if other half-cell reactions exist and consume the electrons generated by the iron dissolution reaction, for example, the hydrogen evolution reaction ($2H^{+} + 2e^{-} = H_2$) in the case of the iron electrode in hydrochloric acid containing ferrous ions, the iron electrode corrodes, accompanied by the generation of hydrogen gas. The hydrogen evolution reaction prevents the iron re-deposition reaction and the corrosion of iron electrode becomes irreversible. The electrode will fail to remain at reversible potentials of either Fe/Fe^{++} or H_2/H^{+}, but must lie at a potential in between the two. This potential is achieved when the hypothesis of the mixed-potential theory is satisfied: the total rate of oxidation must equal the total rate of reduction.

@Seismicisolation

The mixed-potential theory can be illustrated graphically by an Evans diagram. An example is given in Fig. 3 for iron corrosion in acid, which contains two reversible reactions, the Fe/Fe^{++} or H_2/H^+. Both reversible reactions have anodic and cathodic branches, as indicated by the subscripts *a* and *c* in the figure. Their corresponding reversible potentials are $\Phi^o_{Fe/Fe^{++}}$ and $\Phi^o_{H_2/H^+}$, respectively. The intersect between the iron dissolution curve (the anodic branch of the Fe/Fe^{++} reversible reaction) and the hydrogen evolution curve (the cathodic branch of the H_2/H^+ reversible reaction) represents the condition at which the anodic (oxidation) and cathodic (reduction) currents are equal and no net external current flows. The current value at such a point is defined as the *corrosion current* and the corresponding potential is the "mixed-potential" or corrosion potential, Φ_{corr}. The value of the corrosion potential must lie between the reversible potentials of the individual reactions (Fig. 3), e.g.:[10]

Eq. (8) $$\Phi^o_1 < \Phi_{corr} < \Phi^o_2$$

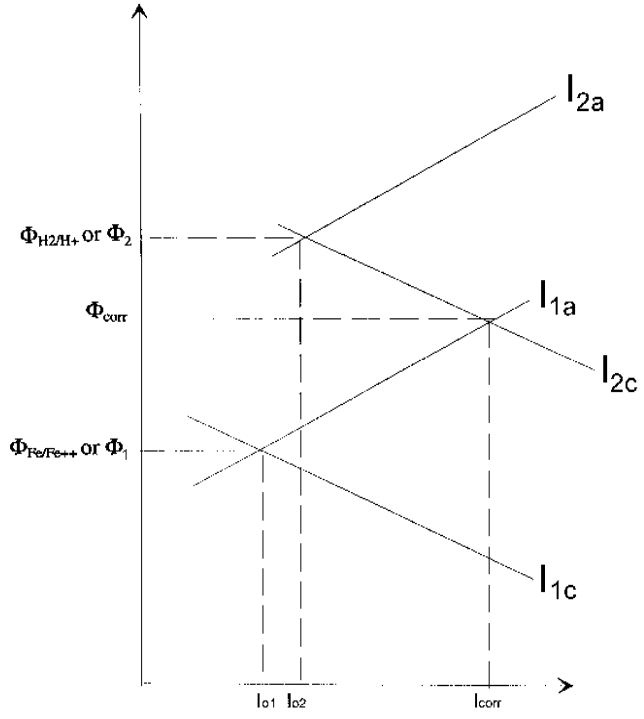


Figure 3. An Evans diagram illustrating the mixed-potential theory for iron corrosion in an acid system.

@Seismicisolation

According to the mixed potential theory, the current, I, at any potential, Φ, is the sum of all partial currents for the reactions, e.g.:

Eq. (9) $$I = I_{1a} + I_{1c} + I_{2a} + I_{2c}$$

where the reactions 1 and 2 are the Fe/Fe^{++} and the H_2/H^+ reversible reactions, respectively. The subscripts a and c are the abbreviations of the anodic and cathodic branches of the reversible reaction. Assuming a potential, Φ, is in between the two reversible potentials $\Phi^o_{Fe/Fe^{++}}$ and $\Phi^o_{H_2H^+}$, the iron reduction (cathodic branch) and the hydrogen oxidation (anodic branch) reactions can be simply neglected. According to the equations (7a) and (7c), the current at such a potential, Φ, is expressed as:

Eq. (10) $$I = I_{1a} + I_{2c} = I_{o1}\exp\left(\frac{\Phi - \Phi_1^o}{b_{1a}}\right) - I_{o2}\exp\left(\frac{\Phi - \Phi_2^o}{-b_{2c}}\right)$$

At the corrosion potential, Φ_{corr}, the external current is zero and the corrosion current is equal to either anodic or cathodic reaction current.

Eq. (11) $$I_{corr} = I_{1a} = I_{2c}, \text{ or}$$

Eq. (12) $$I_{corr} = I_{o1}\exp\left(\frac{\Phi_{corr} - \Phi_1^o}{b_{1a}}\right) = I_{o2}\exp\left(\frac{\Phi_{corr} - \Phi_2^o}{b_{2c}}\right)$$

Combining equations (10) and (12), leads to

Eq. (13) $$I = I_{corr} = \exp\left(\frac{\Phi - \Phi_{corr}}{b_{1a}}\right) - \exp\left(-\frac{\Phi - \Phi_{corr}}{b_{2c}}\right)$$

We define

Eq. (14a) $$\eta'_a = \Phi - \Phi_{corr}$$

Eq. (14b) $$\eta'_c = \Phi_{corr} - \Phi$$

@Seismicisolation

Now, Eq. (13) can be rewritten as:

Eq. (15) $$I = I_{corr} = \exp\left(\frac{\eta'_a}{b_{1a}}\right) - \exp\left(-\frac{\eta'_c}{b_{2c}}\right)$$

It should be noted that the Butler-Volmer, Eq. (5), and Eq. (15) are very similar; but the physical meanings of the parameters are very different, as indicated in Table1.

Table 1. Comparison of Butler-Volmer Eq. (5) and Corrosion Eq. (15)

Eq. (5): Butler-Volmer Equation	**Eq. (15): Corrosion Equation**
I_o; exchange current density	I_{corr}; corrosion current density
η_a, η_c; overpotentials for a half-cell reaction	η'_a, η'_c; overpotentials for corrosion cell reactions
b_a, b_c; Tafel slopes for anodic and cathodic branches of a half-cell reaction	b_{1a}, b_{2c}; Tafel slopes for anodic and cathodic reactions of a corrosion cell reaction

Equation (13) is the theoretical foundation of many electrochemical techniques of corrosion rate measurement; therefore, it is important to understand the assumptions made in the derivation of the equation and its limitations. Some of the major assumptions are indicated below:[11]

- The electrochemical kinetics of the corrosion system can be described by the Butler-Volmer equation
- The ohmic resistance of the electrolyte and surface films are negligible
- The mass transport or concentration polarization process is not the rate controlling step of the corrosion system
- The corrosion potential does not lie close to the reversible potential of either of the two half reactions occurring, e.g., the reverse reactions can be neglected
- The whole metal functions simultaneously as a cathode and an anode rather than separated areas of cathodes and anodes

@Seismicisolation

- There are no secondary electrochemical reactions occurring

Unfortunately, none of the above assumptions are clearly satisfied in reinforced concrete systems due to the complexity of the concrete environment. The mass transport and ohmic resistance are two of the major factors that control the corrosion rate of reinforcing steel in concrete.

2.5 Corrosion Rate Controlling Mechanisms[12]

There are three types of corrosion rate controlling processes that are operative, depending on the controlling step of the corrosion kinetics: activation energy, mass transport, and ohmic resistance.

Activation energy control occurs when the electrode kinetics or corrosion rate is controlled by a slow electrochemical step. This slow step has a very high activation energy. The larger the activation energy is, the smaller the corrosion rate would be, as shown in Fig. 4, for an anodic control corrosion system.

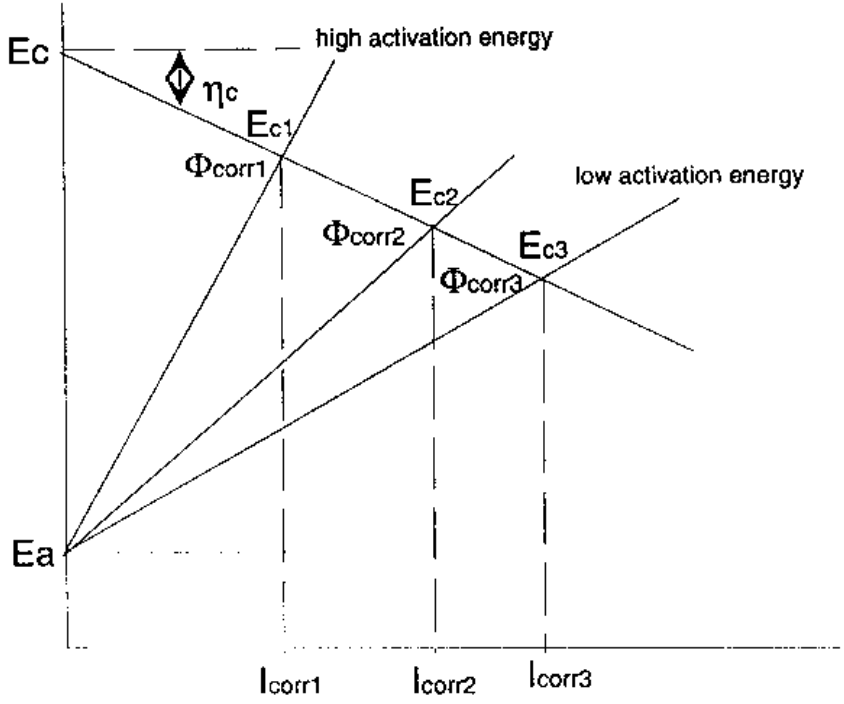


Figure 4. An anodic control corrosion system.

@Seismicisolation

Mass transport control occurs when the corrosion rate is limited by a diffusion or mass transport process involving the reactant at the electrode surface. This often occurs in the high density reinforced concrete corrosion where the rate of oxygen diffusion through the concrete to the reinforcement fails to keep up with the rate of steel corrosion; therefore, the reinforcing steel corrosion process is mass transport or diffusion controlled (Fig. 5).

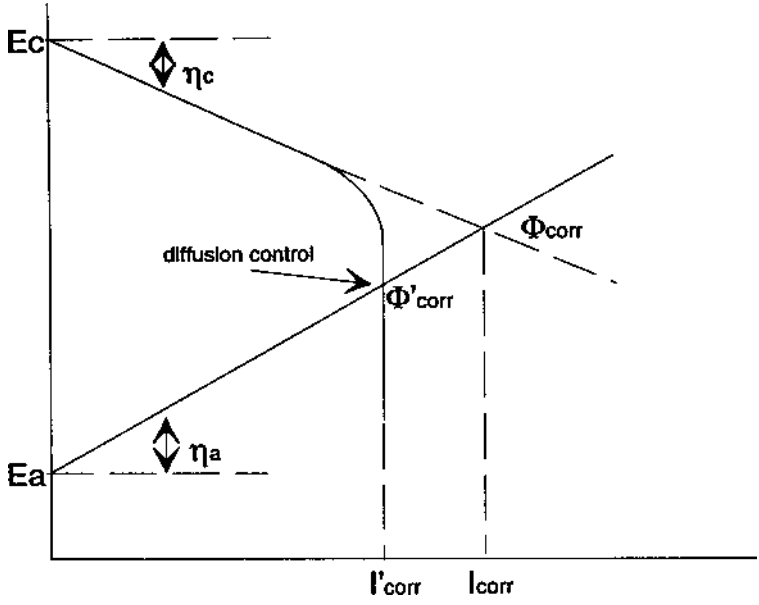


Figure 5. The effect of a diffusion control process on an electrochemical reaction.

Ohmic resistance control occurs when the corrosion rate is controlled by the ohmic resistance of the electrolyte or oxide films on the electrode surface. In reinforced concrete corrosion the electrolyte is the concrete pore solution. The resistance can be very large depending on the environmental humidity and moisture content in concrete. Figure 6 illustrates two cases of ohmic resistance control where the potential available for corrosion reactions is the difference in potentials between the anode and cathode minus the relevant potential loss due to the concrete resistance. The corrosion current decreases as the concrete resistance increases.

@Seismicisolation

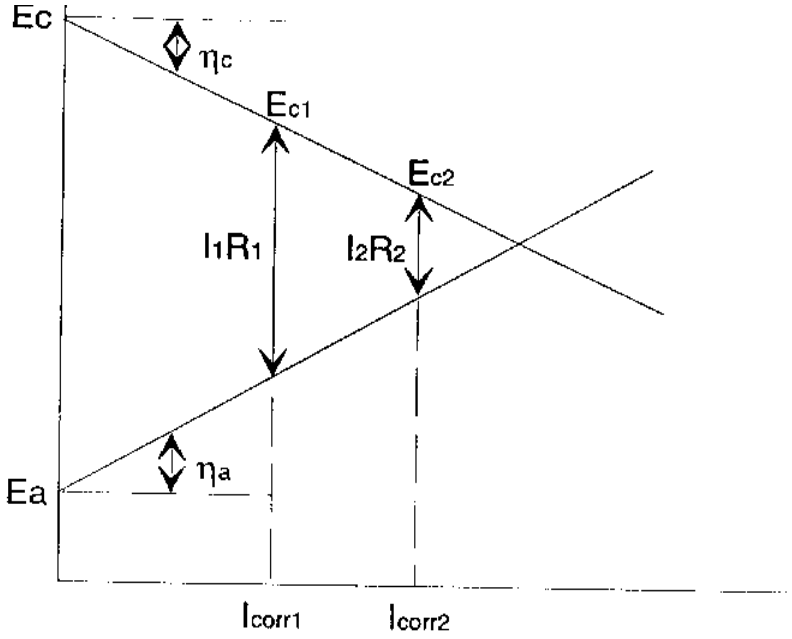


Figure 6. A plot of potential versus current illustrating the resistance polarization effect.

2.6 The Evans Diagram and Polarization Curve

Both the Evans diagram and polarization curves can be used to describe a metal corrosion system. They are related, but different. The Evans diagrams are simplified plots of anodic and cathodic reaction curves of an electrochemical system, while the polarization curves describe the potential current density behavior obtained experimentally by applying an external potential or current. Figure 7 illustrates the difference between an Evans diagram (dashed lines) and a polarization curve (solid lines). The latter curve is the combination of both cathodic and anodic reaction curves and it can be obtained experimentally.

@Seismicisolation

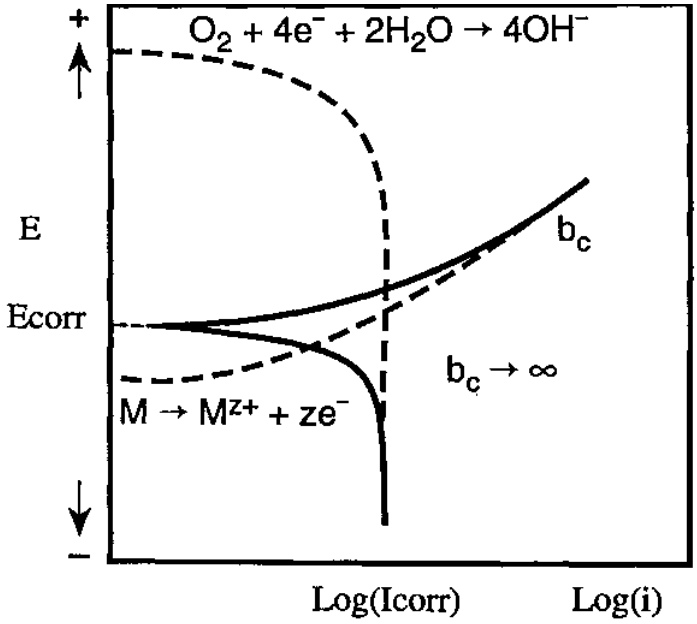


Figure 7. An illustration of the difference between an Evans diagram (dashed lines) and a polarization curve (solid lines).

3.0 REINFORCING STEEL CORROSION IN CONCRETE

3.1 Concrete Properties

Concrete is a heterogeneous material with many special characteristics, including high alkalinity of the pore solution, high electrical resistivity, structure that acts as a physical barrier for mass transport and crack behavior. These characteristics determine the extent of reinforcing steel corrosion.

High Alkalinity. Concrete is a composite material made with cement, sand, aggregates, water, and chemical admixtures. Portland cement hydration involves initial dissolution of CaO, $CaSO_4$ hemihydrate or dihydrate, alkalis, and aluminate phases, etc. This is followed by reactions between the main components, C_3S* and C_2S, and free water resulting in

*C = CaO; S = SiO_2; H = H_2O

@Seismicisolation

the formation of C-S-H, calcium hydroxide (CH), ettringite, and other minor compounds. These reactions bridge the individual particles, fill up the capillary pores, bind aggregates together, and promote formation of a rigid microstructure and strength development.[13][14] The pore solution of concrete has a pH value between 12–14 because of the presence of calcium hydroxide along with small amounts of Na_2O and K_2O. A well-hydrated portland cement may contain from 15 to 30% calcium hydroxide by mass of the original cement.[15] This is usually sufficient to maintain the pore solution pH at about 13 in the concrete, independent of moisture content. The alkalinity of the concrete may be reduced in a number of ways; leaching of soluble alkaline salts with water and reaction with carbon dioxide are common processes leading to a reduction of the pH value of concrete.

High Electrical Resistivity. The conduction in concrete is principally through the motion of ions, such as $Na^{,+}$, K^+, OH^-, SO_4^{2-}, and Ca^{++}, in the pore solution. A typical value of the electrical resistivity of pore solution in cement paste is about 25–35 Ωcm[16]. The conventional aggregates used in concrete, however, are relatively good insulators with electrical resistivity values ranging from 10^5 to 10^{14} Ωcm.[17] For air-dried portland cement paste and concrete, the resistivity is in the region 0.6–1.2 MΩcm.[17] The moisture content of concrete significantly affects its electrical resistivity. Moist concrete and cement paste have values of 2.5–4.5 kΩcm and 1.0–1.3 kΩcm, respectively. The progressive drying of initially weather-saturated concrete results in a rapid increase of the electrical resistivity.[18] The chemical admixtures and chloride ions may further reduce the resistivity of wet concrete.

Mass Transport. Corrosion of reinforcing steel in concrete is determined by three mass transport processes: oxygen diffusion, carbonation, and chloride ion diffusion. Good quality concrete provides a physical barrier to prevent reinforcing steel from carbonation and chloride induced corrosion. It also limits the availability of oxygen, a reactant of the steel corrosion process, at the steel surface. The moisture content in the concrete affects the rate of diffusion processes of the above corrosion reactants. For example, the oxygen diffusion rate is slower in the water-saturated concrete than that of a half dry concrete.[19][20] Moreover, concrete cracking accelerates the rebar corrosion since it provides easier access for chloride ions, carbon dioxide, moisture, and oxygen, to the reinforcing steel. Cracks can be formed due to many physical and chemical phenomena that may not be related to steel corrosion, such as shrinkage, applied stress, alkaline aggregate or sulfate reaction, and freezing-thawing cycles.

@Seismicisolation

3.2 Mechanisms of Steel Corrosion in Concrete

Pourbaix Diagrams. The half-cell potentials can be used to determine criteria for the onset of corrosion. The most negative or least noble half-cell tends to be oxidized and the most positive or noble half-cell tends to be reduced. One of the best demonstrations of the application of thermodynamics to corrosion phenomena is provided by the potential-pH plots or Pourbaix diagrams.[21] An example of a pH-potential diagram for iron is shown in Fig. 8. Each line in the diagram describes the conditions of equilibrium between two species, e.g., Fe and $Fe(OH)_2$, or Fe^{++} and $Fe(OH)_3$. The main applications of this diagram are *(i)* prediction of the spontaneous direction of the corrosion reactions; *(ii)* estimation of the composition of corrosion products; and *(iii)* prediction of the occurrence of corrosion as the environment changes. Reinforcing steel is oxidized to form a passive oxide film, $Fe(OH)_2$, in a concrete environment (pH = 10–13) (Fig. 8). This oxide film converts to Fe^{++} when the pH value drops below 9. However, a potential-pH diagram represents equilibrium conditions of electrochemical systems. It does not indicate the velocity of the reactions or corrosion rate of metal dissolution.

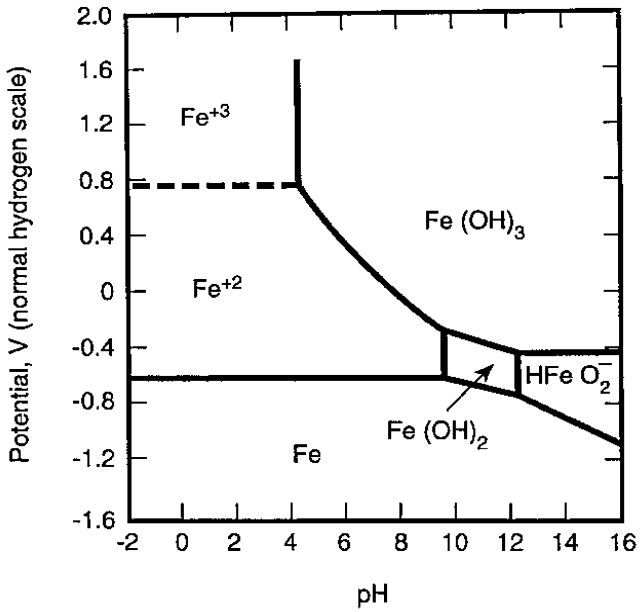


Figure 8. A simplified potential-pH diagram for the Fe-H_2O system.

@Seismicisolation

Steel Passivation. Passivity can be simply defined as a loss of chemical reactivity due to the presence of a strong oxidizer resulting in formation of an ultrathin protective film on the surface of the metal. The corrosion rate of a metal is significantly reduced in the passive state. The reduction in corrosion rate could be of the order of magnitude of 4–6.[8] The passive state is, however, often relatively unstable and subject to damage. Although passivity offers a unique possibility for reducing corrosion, it must be used with caution. Figure 9 schematically illustrates the passivation behavior of iron in an alkaline environment. The diagram can be conveniently divided into three regions: active, passive, and transpassive. Reinforcing steel in a concrete environment lies in the passive region due to the high alkalinity (the passivity is also indicated in the Pourbaix diagram, Fig. 8). This passivating film appears to be a mixed oxide composed of γ-Fe_2O_3 and magnetite, Fe_3O_4, with a thickness of 10–100 Å.[22] It protects metallic iron from further corrosion. The steel corrosion rate in this region is about 0.1 µm/year[23] which is insignificant for most concrete structures.

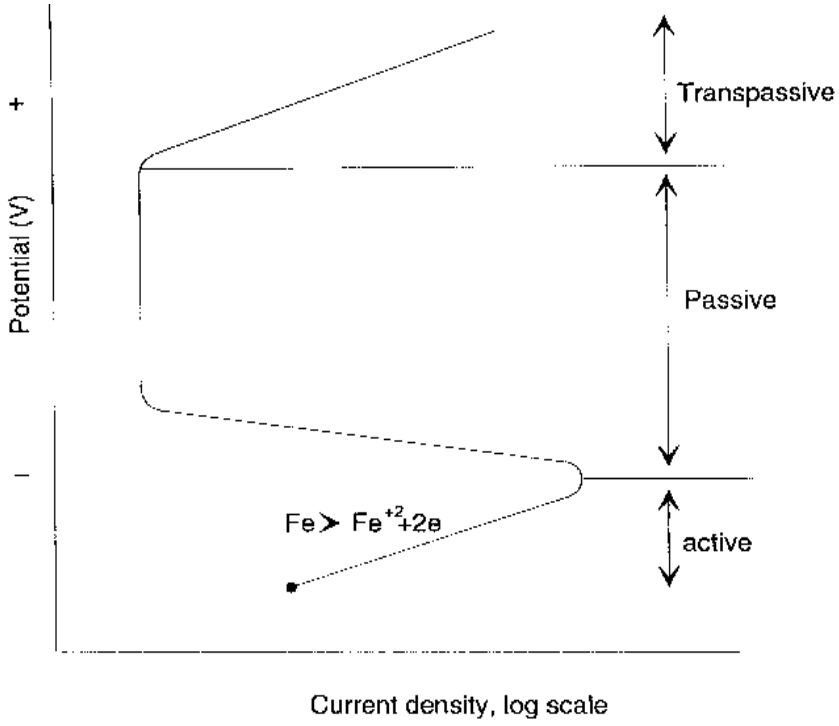


Figure 9. A schematic of the passivation behavior of iron in an alkaline environment.

@Seismicisolation

Passivity of steel embedded in concrete will break down if chloride ions are incorporated in the concrete mix or penetrate from an external source into the concrete. A decrease of the pH value in concrete caused by reactions between the concrete and carbon dioxide in the atmosphere can also affect the passivity. Corrosion of the steel reinforcement decreases the integrity of the steel/concrete interface causing concrete delamination. Decrease of the rebar diameter weakens the mechanical properties of the concrete and cracking and spalling of the concrete cover occur.

3.3 General Steel Corrosion Process in Concrete

A corrosion system consists of four basic elements. These are: an anode, where electrochemical oxidation takes place; a cathode, where electrochemical reduction occurs; an electrical conductor; and an electrolyte. The anode and cathode in reinforced concrete can be in the same rebar or in different rebars. Moisture in concrete provides an electrolytic path for electron transfer from anode to cathode. The rebar is the electrical conductor that completes the corrosion cell. The corrosion of reinforcing steel in an alkaline concrete environment generally involves the following anodic and cathodic reactions.[24]–[28]

Anodic Reaction:

Eq. (16) $$Fe \rightarrow Fe^{++} + 2e^{-}$$

$$Fe^{++} + OH^{-},\ O_2 \text{ and } H_2O \rightarrow Fe(OH)_2,\ \alpha - FeOOH,\ \gamma - FeOOH,\ Fe_3O_4,\ \alpha - Fe_2O_3$$

Cathodic Reaction:

Eq. (17) $$\tfrac{1}{2}O_2 + H_2O + 2e^{-} \rightarrow 2OH^{-}$$

The anodic reaction involves the oxidation of iron to ferrous or ferric oxides and the cathodic reaction normally is the reduction of oxygen to hydroxide ions (Eqs. 16 and 17). A hydrogen evolution reaction occurs instead of oxygen reduction in the absence of oxygen and at a pH value less than 9, as described below:[24]

Eq. (18) $$2H_2O + 2e^{-} \rightarrow H_2 + 2OH^{-}$$

@Seismicisolation

Hydrogen evolution (Eq. 18) rarely happens as oxygen is always available in the atmosphere.

3.4 Carbonation Induced Corrosion

The maintenance of the passivity of steel in concrete requires a high pH environment. Concrete can, however, lose its high alkalinity if significant carbonation occurs. Carbonation refers to the reaction of carbon dioxide gas in the air (0.03%) with ions in the pore solution of hydrated portland cement paste. These reactions include the following:

Eq. (19) $CO_2 + 2NaOH \rightarrow Na_2CO_3 + H_2O$

Eq. (20) $CO_2 + Ca(OH)_2 \rightarrow CaCO_3 + H_2O$

The moisture condition and permeability of the concrete affect the carbonation. The dependence of the amount of carbonation of concrete on the ambient relative humidity is shown in Fig. 10. In dry concrete, $Ca(OH)_2$ reacts very slowly with CO_2, but the reaction is much faster when a surface film of water (50% RH) is present on the grains of $Ca(OH)_2$. The CO_2 gas must first diffuse through the water. If the humidity is high in the pores of the paste (>75% RH), the diffusion rate is considerably lower than through the air.[29]

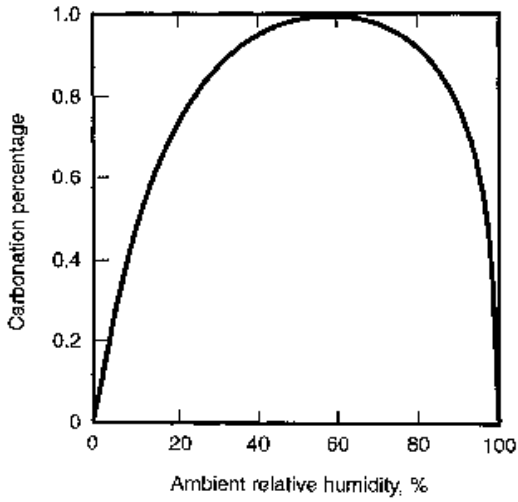


Figure 10. A plot of concrete carbonation percentage versus ambient relative humidity.

@Seismicisolation

A simplified "square root of time" equation from Tuutti's model is often used to describe the carbonation diffusion process:[30]

Eq. (21) $$x = k\sqrt{t}$$

where, x is the carbonation depth (mm), t is time (s), and k is a constant depending on concrete characteristics and ambient conditions.

The change of pH in concrete due to carbonation is very steep with a very narrow zone referred to as the "carbonation front" separating two sides. One side towards the surface has pH values below 8, the other into the concrete core has pH values above 12. When the carbonation front reaches the reinforcement, the passive film is no longer stable and corrosion rate, therefore, increases. Figure 11 is an Evans diagram that shows the effect of carbonation on steel corrosion. Curve "C" is the cathodic reaction (oxygen reduction) and the "A" curves are anodic reaction curves for the steel oxidation. As the steel/concrete interface pH value decreases, there is a reduction in the passive region and the anodic reaction curves shift to the right from A1 to A2.[31] The corrosion potential decreases from E_{corr} to E'_{corr} and the corrosion rate increases from I_{corr} to I'_{corr}.

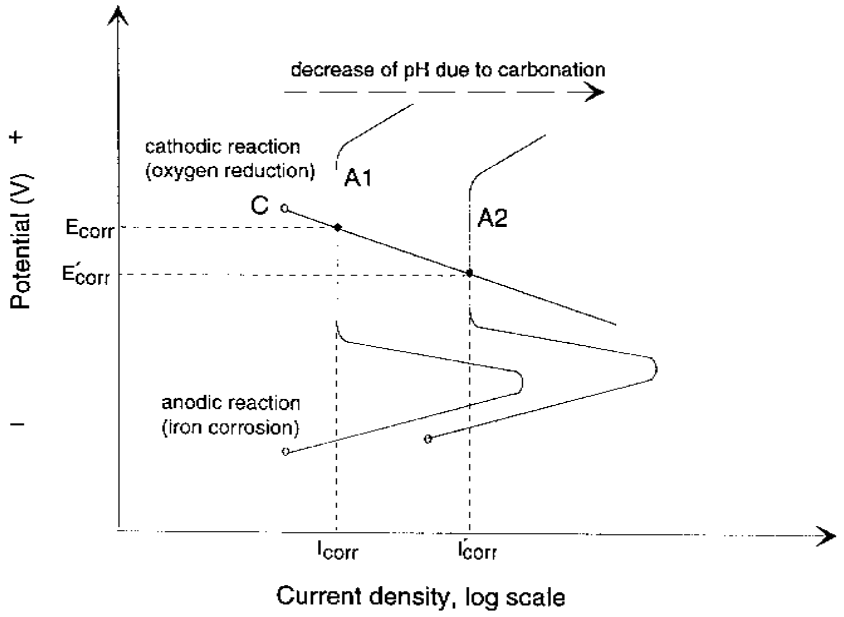


Figure 11. An Evans Diagram illustrating the effect of carbonation on steel corrosion.

@Seismicisolation

The reinforcing steel corrosion process due to carbonation is normally homogeneous, producing over the long term a reduction in the cross-sectional area of the steel and a significant amount of oxides which may crack the concrete cover or diffuse through the pores to the surface of the concrete.

Groundwater or drain water can also cause a reduction of pH value by leaching out the alkaline ions associated with K_2O and Na_2O in hydrated cement paste. Subsequently, CH is leached. The leaching mechanism for CH relies on the reaction with carbonic acid and bicarbonate ions.[32] Carbonic acid neutralizes CH directly. Steel corrosion rate can be accelerated when the pH value is less than 8. This may occur when significant carbonation or decalcification (leaching of CH) takes place. Both processes produce a loss of lime (calcium hydroxide); however, carbonation is a very slow process especially in concrete with low permeability.

3.5 Chloride Ion Induced Corrosion

Source of Chloride Ion. Chlorides can be introduced into concrete through two main routes, *(i)* as a contaminant or an additive in the original mix, and *(ii)* as a result of "post-setting" exposure to the environment. The common sources of chloride are listed below:

- Construction error involving the use of excessive calcium chloride as an accelerating agent for the hydration of portland cement
- Use of admixtures (e.g.,. some water-reducing agents) containing small amounts of calcium chloride to offset the set-retarding effect of the water reducer
- Use of chloride contaminated aggregates and water in the concrete mix
- Use of NaCl as a deicing salt for winter traffic control
- Exposure to seawater or chloride-bearing air in marine areas

Introduction of chloride through the first source initiates corrosion reactions immediately; however, the most common source of chloride (the second route) is from an external source and involves penetration into the concrete. The chloride builds up with time, possibly leading to a condition where the concrete is no longer able to protect the reinforcement from corrosion. Chlorides can penetrate through the cracks and capillary pores.

@Seismicisolation

The suction of salt water into a dry concrete can also result in several millimeters of penetration in a few hours. In contrast, the penetration is much slower by diffusion of the chloride ions through the cement paste pore solution when driven by the concentration gradient in a wet or highly moist concrete. The typical diffusion rate for fully saturated cement paste is in the order of 10^{-12} m^2/s.[33]–[35]

Chloride Binding.[36]–[37] Concrete can immobilize chloride ions. Chloride ions can be incorporated in the lattice of crystalline hydration products in the form of $3CaO{\cdot}Al_2O_3{\cdot}CaCl_2{\cdot}1OH_2O$ (Friedels salt) and $3CaO{\cdot}Al_2O_3{\cdot}3CaCl_2{\cdot}32H_2O$. The C_3A content of the cement has a significant influence on the amount of chloride remaining in solution. Chloride ions are also chemisorbed at the surface or intercalated into the structure of the C-S-H hydration product. The amount of immobilized chloride is dependent on the presence of other anions, e.g., sulfates, carbonates, and cations, e.g., Ca^{++}, K^+ or Na^+. Temperature and pH are also contributing factors.

The major sources of chloride ions are marine water and deicing salts. It is assumed by many authors that the ingress of chloride ions within concrete follows diffusion mechanisms described by a simplification of Fick's second law of diffusion.[38]–[40]

Eq. (22) $$C_x = C_s\left(1 - erf\frac{x}{2\sqrt{Dt}}\right)$$

where C_x and C_s are the chloride ion concentration at a certain depth x and the surface, respectively. The parameter D is the chloride diffusion coefficient (m^2/s) and t is the time. Using this model it is possible to calculate the time required for the critical chloride corrosion initiation threshold to be reached at the level of the reinforcing steel. The time taken to obtain the critical chloride concentration is dependent on the diffusion properties of the concrete, the surface concentration of chloride, and the depth of the concrete cover above the reinforcing steel; however, such a prediction model has been questioned since it neither considers the effect of chloride adsorption nor the concrete cracking.

Chloride attack is a major cause of reinforced concrete deterioration.[24]–[28][41][42] Figure 12 is an Evans diagram that illustrates the effect of chloride ion contamination on steel corrosion.[31] Curve "C" is the cathodic reaction and the "A" curves are anodic reaction curves in the presence of various chloride ion concentrations. As chloride ion concentration increases there is a reduction in the passive region and the anodic reaction curves shift from "A1" to "A3." In the extreme case ("A4"), the

@Seismicisolation

passive region disappears. The corrosion potentials decrease toward more negative values ($E_{corr4} < E_{corr3} < E_{corr2} < E_{corr1}$) and the corrosion rate, I_{corr}, increases ($I_{corr4} > I_{corr3} > I_{corr2} > I_{corr1}$).

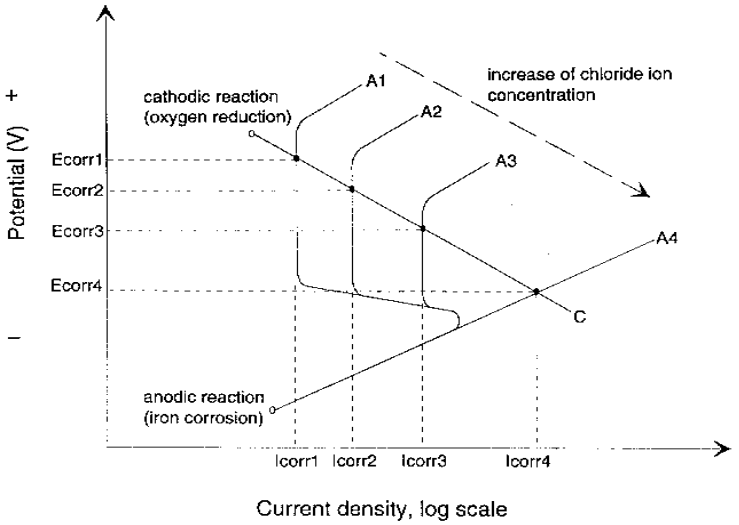


Figure 12. An Evans diagram illustrating the effect of chloride ion contamination on steel corrosion.

Mechanism of Chloride Attack on Reinforcing Steel. There are three modern theories to explain the effects of chloride ions on steel corrosion:[43]

1. The Oxide Film Theory—It is believed that the oxide film is responsible for passivity and protection of the rebar against corrosion. This theory postulates that chloride ions penetrate the film easier than other ions (e.g., $SO_4^{=}$). Alternatively, the chloride ions may colloidally disperse the oxide film, thereby making it easier to penetrate.
2. The Adsorption Theory—Chloride ions are adsorbed on the rebar surface in competition with dissolved O_2 or hydroxyl ions. The chloride ion promotes the hydration of the iron ions and thus facilitates the corrosion of steel.

@Seismicisolation

3. The Transitory Complex Theory—According to this theory, the chloride ions become incorporated in the passive film replacing some of the hydroxides increasing both its conductivity and its solubility. The film, therefore, loses its protective character. The reactions may be expressed as follows:

Eq. (23) $$Fe(OH)_x + xCl^- \rightarrow FeCl_x + xOH^-$$

followed by

Eq. (24) $$FeCl_x + xOH^- \rightarrow Fe(OH)_x + xCl^-$$

where x can be 2 or 3, depending on the oxidation state of iron. It should be noted that the consumption of chloride ions in the reaction described by Eq. (23) is balanced by the release of chloride ions in Eq. (24). The presence of chloride ions promotes the disruption of the iron oxide layer through the looping reaction process. The product of Eq. (23), $FeCl_x$, also accelerates the disruption of the protective oxide film due to its high solubility. The non-homogeneous distribution of chloride ions over the steel surface and the imperfections of the passive iron oxide film allow easy incorporation of the chloride ions and breakdown of the passive film locally. This local phenomenon results in the creation of macro-cells. The local active areas will act as anodes where the iron will easily dissolve at a relatively low potential. The remaining passive areas will act as cathodes where oxygen reduction takes place at a higher potential. The rate of dissolution of iron in the macro-cells will depend, in addition to the normal controlling factors for corrosion, on *(i)* the cathode:anode area ratio and *(ii)* the electrical resistivity of the concrete between the cells.

The expansion of the iron oxides as they are transformed to higher oxidation states is the major cause of concrete failure. The specific volume of the hydrated iron oxides can be up to nearly seven times that of the iron from which it is formed.[24] The resulting stresses generated in the concrete are considerably greater than its fracture strength and lead to cracking and spalling of the concrete cover.

4.0 CORROSION ASSESSMENT TECHNIQUES

Many electrochemical techniques are applied in reinforcing steel corrosion research. Most of them are still limited to laboratory scale

@Seismicisolation

investigation and a few can be used in the field. The commonly used electrochemical techniques are either steady-state or transient types. If the interface double layer capacitance effect is taken into account, Eq. (13) can be rewritten as:[44]

Eq. (25) $$I = I_{corr}\ \exp\left(\frac{\Phi - \Phi_{corr}}{b_{1a}}\right) - \exp\left(-\frac{\Phi - \Phi_{corr}}{b_{2c}}\right) + C\left(\frac{\partial \Phi}{\partial t}\right)$$

where C is the interfacial capacitance associated with the electrochemical double layer and $(\partial\Phi/\partial t)$ is the potential scan rate. The steady-state techniques focus on the first term of Eq. (25), which describes the steady-state behavior of the electrode kinetics. In order to reduce the errors induced by the second term, the potential scan should be as slow as possible, e.g., the term $C(\partial\Phi/\partial t)$ approaches zero. ASTM standard G-59[45] recommends a potential scan rate of 0.167 mV/s, which is desirable to obtain the corrosion rate at steady state, especially in the polarization method. The steady state techniques require a slow potential scan rate so that the effect of the interfacial double layer capacitance, the second term of Eq. (25), can be minimized. In contrast, the transient techniques require rapid potential scan rates to measure the interfacial effect. The interface is modeled using a Randles equivalent circuit that consists of a solution resistance (R_s) in series with a parallel circuit of a double layer capacitance (C_{dl}) and a charge polarization resistance (R_p) (Fig. 13). The circuit parameters (R_s, C_{dl} and R_p) can be determined by applying a transient potential (or current) signal such as pulse, triangle wave or sinusoidal wave, to the interface. Long term monitoring techniques are also often applied to the reinforced concrete corrosion studies. Parameters such as corrosion potential and macro-cell corrosion current are commonly measured for a long period of time to monitor the progress of rebar corrosion. The ASTM G109-92[46] procedure and the electrochemical noise technique are examples of these methods.

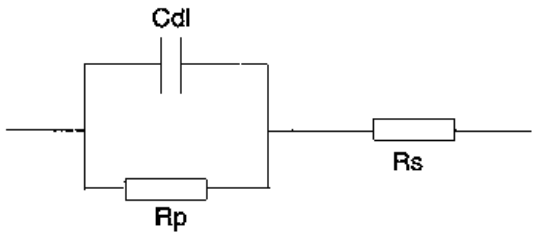


Figure 13. The Randles equivalent circuit.

@Seismicisolation

In this section the techniques discussed are mass loss, half-cell potential, linear polarization, Tafel extrapolation, macro-cell corrosion monitoring, electrochemical noise monitoring, coulostatic, potential and current steps, and the ac impedance methods. It is difficult to address all the techniques that are used in electrochemical corrosion studies; therefore, only those techniques that have been used in reinforced concrete corrosion work will be discussed. Techniques including half-cell potential, linear polarization, and ac impedance spectroscopy, are particularly suitable for field assessment of corrosion in concrete structures. They are, therefore, described in greater detail.

4.1 Mass Loss

The mass loss technique is one of the oldest and most reliable methods of determining the corrosion rate of steel. The corrosion current or rate can be calculated from the mass loss over a known period of time using Faraday's Law:[44]

Eq. (26) $$W = \frac{I_{corr}\, tM}{nF}$$

or

Eq. (27) $$I_{corr} = \frac{WnF}{tM}$$

where W is the mass loss (g), t is time (s), n is the number of electrons involved in the corrosion reaction, F is Faraday's constant (96487 C/g-eq.) and M is the molecular weight of the iron.

Corrosion rate can be expressed as the penetration rate assuming that I_{corr} ($\mu A/cm^2$) is uniformly distributed over the entire wetted surface area or known actively corroding area:

Eq. (28) $$CR = \frac{3.27\times10^{-3}\, I_{corr}\, E.W.}{d}$$

Where CR is the corrosion rate (mm/per year), $E.W.$ is the equivalent weight (dimensionless), and d = metal or alloy density, g/cm^3. The constant, 3.27×10^{-3}, has units of mm-g/μA·cm·year.

The mass loss method is often used in atmosphere and immersion corrosion studies. It is also used as a tool to validate other electrochemical

@Seismicisolation

methods such as linear polarization and ac impedance techniques. It is, however, not as commonly used as the latter two in reinforced concrete corrosion studies because of the following disadvantages:

- It is a destructive method. It requires destruction of the reinforced concrete specimens and careful cleaning work to obtain the mass loss of the reinforcing steel.
- It is a time consuming and tedious process since there is not any electrochemical acceleration of the corrosion process.
- It may not be applied in the field corrosion assessment due to the nature of the method.

4.2 Half-Cell Potential Measurement

The half-cell potential measurement is the most common method used in the bridge deck corrosion surveys.[41]–[42][47]–[54] An indication of the relative probability of corrosion activity can be empirically obtained through measurement of the potential difference between a standard portable half-cell placed on the surface of the concrete and the steel rebar underneath. The copper-copper sulfate ($Cu/CuSO_4$) and silver-silver chloride (Ag/AgC1) standard reference electrodes are normally used. The data analysis guideline described in ASTM C876-91 provides general principles for evaluation of reinforcing steel corrosion in concrete.[55] These are outlined in the table below.

Table 2. General Principles for Evaluation of Reinforcing Steel Corrosion in Concrete

Half-cell potential reading, vs. $Cu/CuSO_4$	Corrosion Activity
less negative than -0.200V	90% probability of no corrosion
between -0.200 V and -0.350V	an increasing probability of corrosion
more negative than -0.350V	90% probability of corrosion

Figure 14 is a schematic of a half-cell potential measurement in a reinforced concrete system where the concrete (containing a certain amount

@Seismicisolation

of moisture) acts as the electrolyte. A high input resistance (at least 10 MΩ) voltmeter is required for the actual measurement. The measured voltage is the sum of steel/concrete potential, $V_{steel/conc}$, the concrete/reference potential, $V_{conc/ref}$, the potential drop across the concrete, IR_{conc} and the contact resistance, $V_{contact}$, as expressed below:

Eq. (29) $$\Delta V_{measured} = V_{steel/conc} + VC_{conc/ref} + IR_{conc} + V_{contact}$$

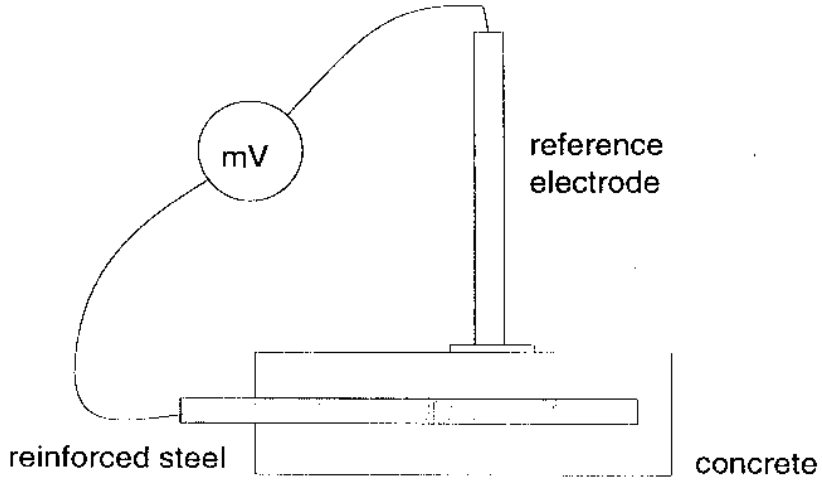


Figure 14. A schematic illustration of the half-cell potential measurement procedures in a reinforced concrete system.

Half-cell potential measurement is more sensitive to active corrosion areas of the rebar than the passive areas. The potential may only represent the corroding bar when actually two rebars are crossing. This point can be further demonstrated by considering a hypothetical situation of a single corroding area on a passivated rebar. The resultant half-cell potential readings of three different locations are shown in Fig. 15. It is clear that cell placement location is critical in the actual measurement of the corroding potential. Readings should be taken at close spaces to correctly evaluate the corrosion activity.[56]

@Seismicisolation

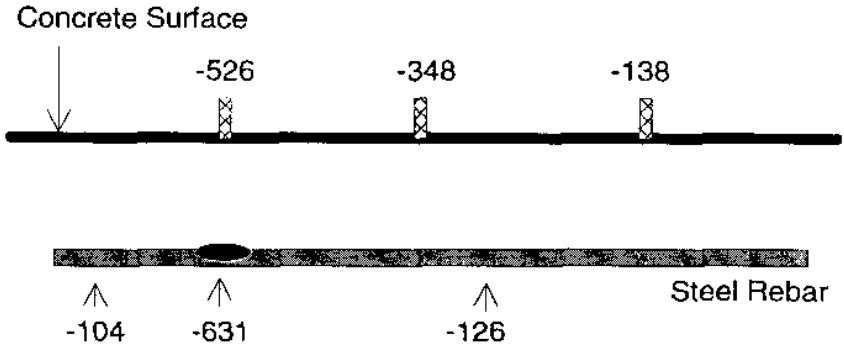


Figure 15. The effect of position of a reference electrode on the half-cell potential reading.

Half-cell potential measurement is one the most commonly used electrochemical techniques in field corrosion assessment. It has many advantages including:

- Rapid estimation of the extent of corrosion; nondestructive character
- Cost-effectiveness
- Ease of operation
- Use of data to guide corrosion measurements
- Application of data to confirm surveys obtained by other techniques

Unfortunately, data analysis and interpretation of half-cell potential measurement have become more complicated due to advances in concrete technologies. Factors such as chloride and moisture content, cell placement, electrical continuity, and temperature, are known to have a significant influence on half-cell potential readings. Steel fiber reinforcement, dense material overlays, and concrete sealers, tend to make the potential measurement more difficult and sometimes impossible. Cathodic protection systems, stray currents, and previous repair patches, etc., can also cause interference. Confirmation with other nondestructive corrosion rate determination methods is, therefore, necessary in evaluating half-cell potential results. A simple comparison of potential data with the ASTM guideline could prove meaningless.

@Seismicisolation

As an example, oxygen concentration at the rebar interface affects the half-cell potential readings as well. A low oxygen concentration at the rebar surface may result in a more negative potential reading as illustrated in Fig. 16.[31] Curve "A" represents the anodic reaction and curves "C1"–"C3" cathodic reactions representing various initial oxygen concentrations available at the reinforcing steel surface. The corrosion potential, Φ_{corr}, shifts toward more negative potential values(Φ'_{corr} and Φ''_{corr}) as the initial oxygen concentration decreases. However, I_{corr} remains small when the intercept falls in the passive region.

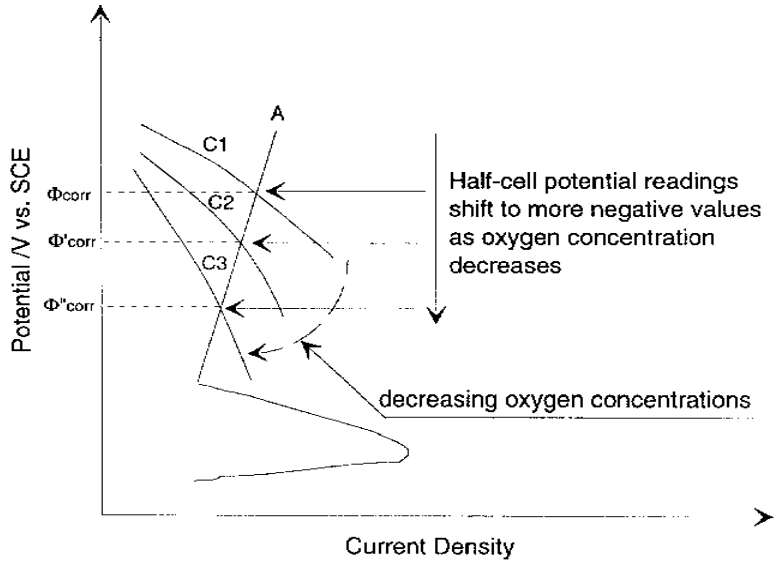


Figure 16. The effect of oxygen concentration on the electrochemical behavior of iron corroding with a diffusion-controlled cathodic process.

A more negative reading of potential in general is considered to indicate a higher probability of corrosion. This general "rule" may not be valid all the time. Comparison of the differences in the half-cell potential across a structure is more indicative of the level of corrosion activity than absolute values.[56] For example, a variation of 100 mV (from -150 mV to -250 mV) in half-cell potential reading may indicate more active rebar

@Seismicisolation

corrosion at a given section than a similar section with a 30 mV variation (from -250 mV to -280 mV). Evaluation of rebar corrosion only from the "absolute" half-cell potential values may be misleading and cause errors in judgment if other factors are not taken into account.

4.3 Linear Polarization Measurement

Basic Principle. The electrochemical principle behind the linear polarization technique is expressed by the Stern-Geary equation:[57]

Eq. (30) $$I_{corr} = \frac{b_a b_c}{2.303(b_a + b_c)} \left(\frac{\partial I}{\partial \Phi} \right)_{\Phi corr} = \frac{B}{R_p}$$

The polarization resistance, R_p, of the corroding electrode is defined as the slope of a potential-current density plot at the corrosion potential, Φ_{corr}.

Eq. (31) $$R_p = \left(\frac{\partial \Phi}{\partial I} \right)_{\Phi corr}$$

and

Eq. (32) $$B = \frac{b_a b_c}{2.303(b_a + b_c)}$$

Equation (30) can be derived from Eqs. (12) and (13). References 11 and 13 provide mathematical detail. The Stern-Geary constant B is a function of the anodic and cathodic Tafel slopes (b_a and b_c, the subscript numbers are omitted for simplification) of the corrosion cell reactions and their values should be determined using the weight loss method. However, a B value of 26 or 52 mV has been utilized in the calculation for the bare steel in the active and passive stages, respectively, for the rebar corrosion.[58]

The linear polarization technique involves application of a slow potential scan (usually 0.167 mv/s) close to the corrosion potential, Φ_{corr}, (ranging from -20 mV to +20 mV). The response, polarization current density, I, is recorded. The measurement can also be made in a galvanostat mode in which the current is monitored in order to obtain a small polarization potential. Figure 17 is a schematic potential-current density plot in which the slope is R_p. The corrosion rate, *C.R.*, can be computed using Faraday's Law (Eq. 28),[44] and the reduction of rebar diameter in the steel cross section can be calculated according to the following equation:[59]

@Seismicisolation

Eq . (33) $\phi(t) = \phi_i - 0.023\, I_{corr}\, t$

where $\phi(t)$ = remaining diameter (mm) at time, t, (years), ϕ_i = initial diameter and 0.023 is a factor to convert $\mu A/cm^2$ to μm/year.

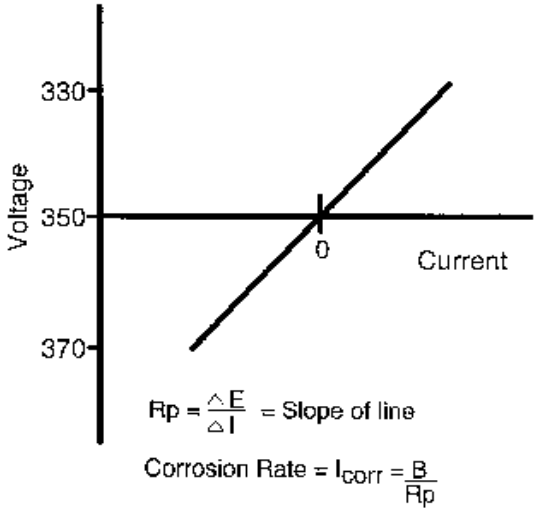


Figure 17. A schematic of a linear polarization plot (potential versus current density).

Experimental Set-Up. A normal setup for linear polarization measurement consists of three electrodes, as shown in Fig. 18. A working electrode connects to the rebar and auxiliary (or counter) and reference electrodes are placed on the concrete surface over the reinforcing steel. A direct application of a laboratory instrument to reinforced concrete corrosion studies has proved to be difficult. The area of the working electrode, e.g., the reinforcing steel bars, is normally much larger than that of the counter electrode. Thus, the current distribution between the working and counter electrodes is not defined precisely. Neither the area of the working electrode that is polarized nor the contribution of the signal received from

@Seismicisolation

the defined working electrode area is known. Two approaches have been taken to solve this difficulty. The first uses a "guard ring," i.e., a second, concentric counter electrode surrounding the first counter electrode. The same potential is applied at the guard electrode to confine the current paths between the central counter electrode and the working electrode ensuring that they are essentially straight. Only the current passing through the center counter is recorded. Thus, the area of the working electrode polarized by the central counter electrode is, in theory, equal to the area of the central counter electrode (Fig. 19).[5][60] Preferably, the "guard ring" should be placed symmetrically on concrete over the rebar. The reference electrodes should be in contact with the concrete, aligned over the rebar. Displacement of the probe from the center of the rebar will increase the polarization area resulting in a smaller R_p value (Fig. 20). The second approach, involving tedious mathematical calculation, is to model the steel/concrete system using electrical transmission line theory to determine the effective polarization range of the counter electrode.[28][61][62]

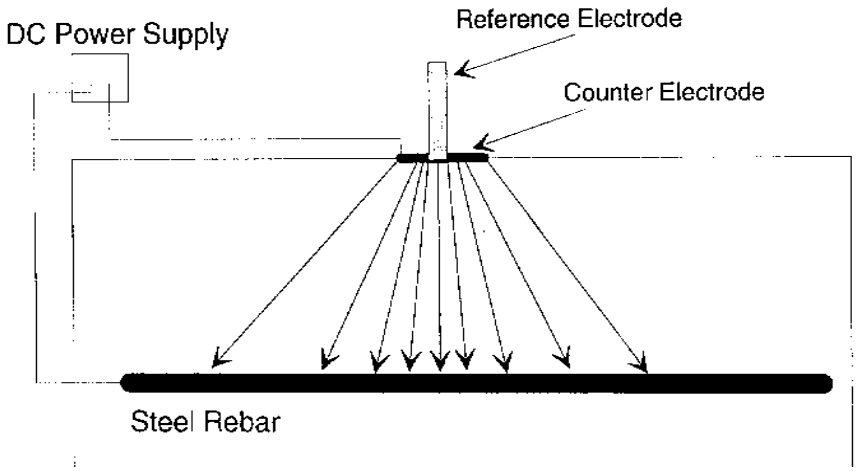


Figure 18. A schematic of a normal three electrode linear polarization measurement.

@Seismicisolation

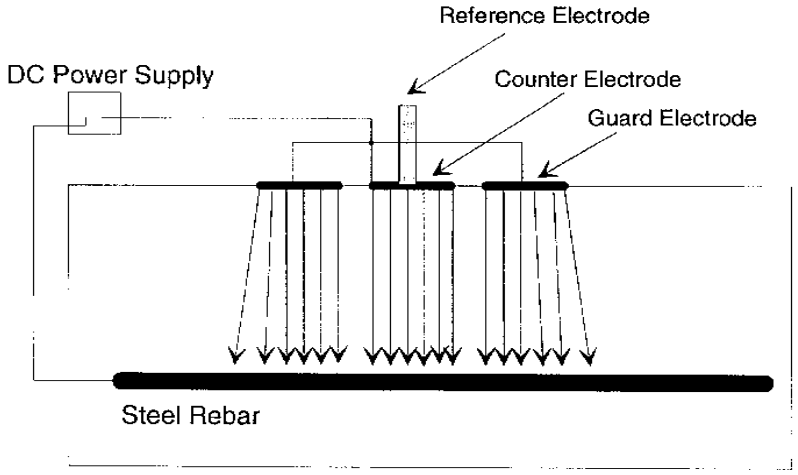


Figure 19. A schematic of an experimental setup for the linear polarization measurement with a guard electrode.

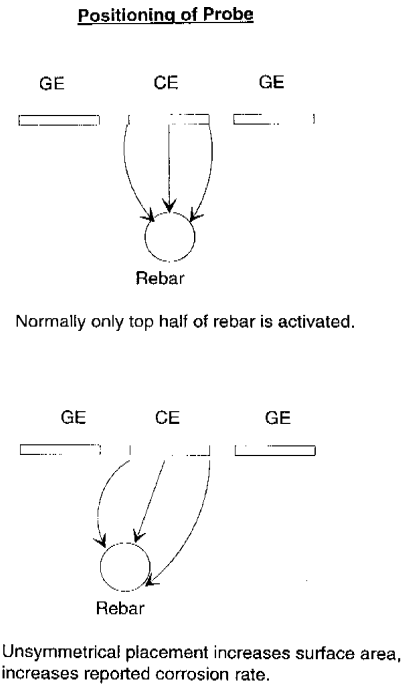


Figure 20. The effect of positioning of the linear polarization probe (from the center of the rebar) on the R_p value.

@Seismicisolation

Guidelines for Data Interpretation. Three types of linear polarization devices with the guard ring feature are commercially available for corrosion evaluation of reinforced concrete: PR Monitor (Cortest Columbus Tech., Inc.), Gecor (GEOCISA), and NSC (Nippon Steel Corp.). The basis of operation for the first is linear polarization theory. However, the latter two devices are slightly different; they operate using a galvanostatic pulse. The measured R_p will vary due to the differences in the type of equipment. It has been reported that the corrosion current density values obtained from NSC and 3LP equipment are much larger than those obtained from the Gecor. The relative magnitude of I_{corr} values is Gecor < NSC < 3LP.[60] The high variation of data from the 3LP device is attributed to the absence of current distribution confinement. Data analysis requires caution because of the inconsistency of the R_p values obtained from different devices. Different devices may have their own data analysis guidelines. Guidelines for the estimation of corrosion extent using I_{corr}, and *C.R.* in reinforced concrete practice for the 3LP and Gecor, respectively, are given in the following table.[49][63]

Table 3. Guidelines for Estimation of Corrosion Extent for 3LP and Gecor

Corrosion current Density (μA/cm^2)	Corrosion Rate (μm/year)	Extent of corrosion
Applied to devices without guard ring		
$I_{corr} < 0.22$	< 2.57	No corrosion damage
$0.22 < I_{corr} < 1.08$	2.57 < C.R. < 12.6	Corrosion damage is possible in the range of 10 to 15 years
$1.08 < I_{corr} < 10.8$	12.6 < C.R. < 126	Corrosion damage is possible in the range of 2 to 10 years
$I_{corr} > 10.8$	> 126	Corrosion damage is expected in 2 years or less
Applied to devices with guard ring (mainly Gecor)		
$I_{corr} < 0.1$	< 1.17	Passive condition
$0.1 < I_{corr} < 0.5$	1.17 < *C.R.* < 5.85	Low to moderate corrosion
$0.5 < I_{corr} < 1$	5.85 < *C.R.* < 11.7	Moderate to high corrosion
$I_{corr} > 1$	> 11.7	High corrosion rate

@Seismicisolation

Corrosion rate can be reported in units of mils per year (mpy), milliamps per square foot (mA/ft^2), or microamps per square centimeter ($\mu A/cm^2$). The conversion factors are $mA/ft^2/0.96 = \mu A/cm^2$ and $\mu A/cm^2 \times 0.4615 = mpy$.

The linear polarization technique is the most successful nondestructive, relatively fast, cost-effective, and a quantitative approach in reinforced concrete corrosion assessment to date. It allows the corrosion rate of rebar to be determined and the remaining diameter to be estimated. It is a very useful technique in the field assessment of the remaining service life of the reinforced concrete structure.

4.4 The Transmission Line Model Approach

An alternative approach to overcome the nonuniform current distribution during the linear polarization measurement is to determine the effective polarization range of the counter electrode using the electrical transmission line model. This approach involves a tedious analytical solution of the Laplace equation or numerical calculations, and it is often found difficult to apply in the field. However, a simplified method based on a unidirectional transmission line model has been developed by Andrade, et al.[61][62]

A reinforced concrete beam can be represented by a unidirectional transmission line model (Fig. 21a, b) which consists of the unit length electrolytic resistance of concrete, R_e, and unit length polarization resistance, R_t, of the rebar. Taking an infinitesimally small beam, dx, in the lengthwise direction and considering du as the change in potential and di the variation of current (Fig. 21c), the following equations are obtained:[61][62]

Eq. (34) $$du = -iR_e dx$$

Eq. (35) $$di = -\left(\frac{u}{R_t}\right)dx$$

Take the second derivative of these equations.

Eq. (36) $$\frac{d^2u}{dx^2} - \left(\frac{R_e}{R_t}\right)u = 0$$

Eq. (37) $$\frac{d^2i}{dx^2} - \left(\frac{R_e}{R_t}\right)i = 0$$

@Seismicisolation

The general solution of Eqs. (36) and (37) is given below.

Eq. (38) $u(x) = Ae^{-\alpha' x} + Be^{\alpha' x}$

Eq. (39) $u(x) = A'e^{-\alpha' x} + B'e^{\alpha' x}$

where

Eq. (40) $\alpha' = \sqrt{R_e / R_t}$

and A, A', B and B' are constants. Based on this model, three methods were proposed by Andrade, et al.,[61][62] to determine the corrosion polarization resistance of the reinforcing steel. They are critical length, signal attenuation, and double-counter, as briefly discussed below.

Critical length. It is assumed in this method that the potential signal reaches a limiting length beyond which point the current (the response variation) is equal to zero (Figure 21(*d*)). Such a length is defined as the *critical length*:

Eq. (41) $L_{crit} \approx 1.5\sqrt{R_t / R_e}$

and the unit length polarization resistance, R_t, can be expressed as:

Eq. (42) $R_t = 4(R_p') 2/R_e$

where the R_p' is the apparent polarization resistance which can be directly obtained in the measurement.

Signal Attention. The α' term can be determined from the following equation by taking readings of potential $u(x)$ at two different distances from the counter electrode, say, x_1 and x_2,

Eq. (43) $$\alpha' = \frac{1}{x_2 - x_1} \ln \frac{u(x_1)}{u(x_2)}$$

and the R_1 is calculated using Eq. (27), i.e.:

Eq. (44) $R_1 = R_e / \alpha'^2$

@Seismicisolation

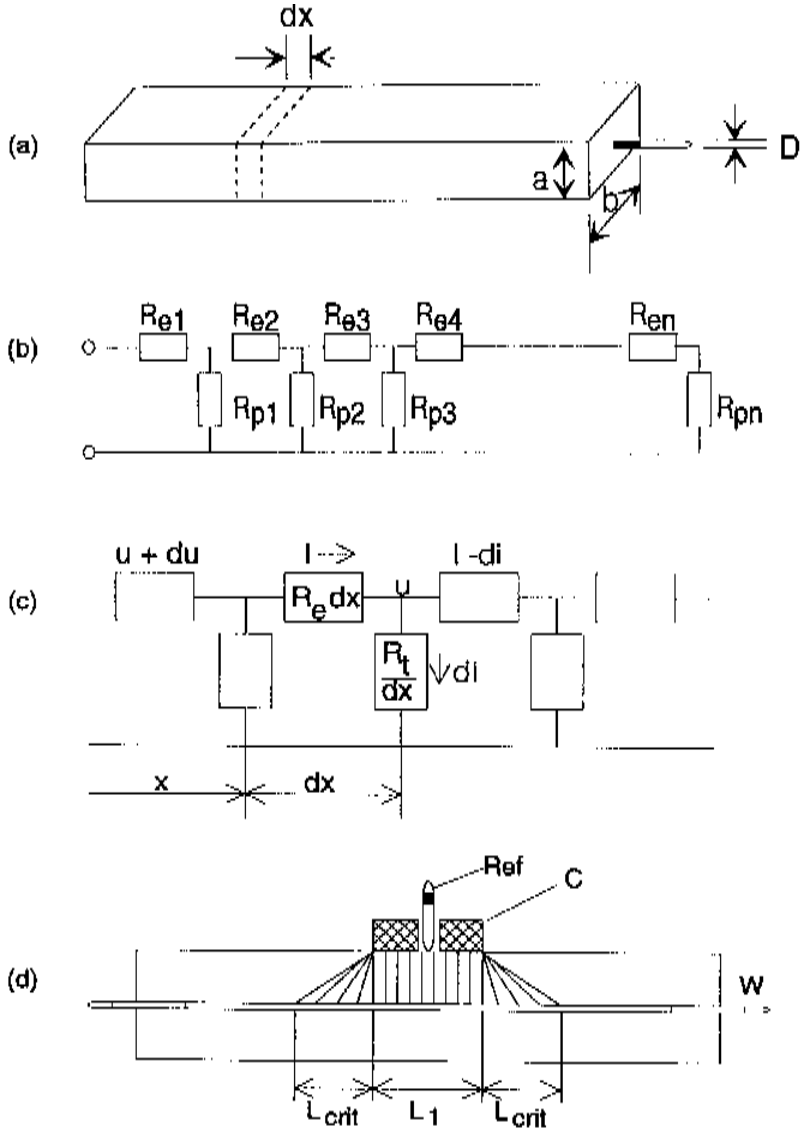


Figure 21. *(a)* A reinforced concrete beam; *(b)* a unidirectional transmission line model; *(c)* an infinitesimally small beam of length, *dx*; and *(d)* the critical length.

@Seismicisolation

Double-Counter. This method is also based on the existence of critical length, L_{crit}, beyond which the applied signal has little effect on the distribution of the current on the rebar. By using two different sizes of counter electrodes, say L_2 and L_1, the measured current difference between L_2 and L_1 is considered to be equal to the current measured by using a counter electrode with the size of L_2 - L_1 and the corrosion resistance, R_p, is determined by:

Eq. (45) $$R_p = p\left(L_2 - L_1\right)\frac{R'_{p(L1)}R'_{p(L2)}}{R'_{p(L1)} - R'_{p(L2)}}$$

where p is the perimeter of the rebar (or the sum of the perimeters if more than one rebar is considered), $R'_{p(L1)}$ and $R'_{p(L2)}$ are the apparent corrosion resistance values measured using the two counter electrodes with a size of L_2 and L_1, respectively. It is noted that the double counter method measures the R_p directly; however, both the critical length and signal attenuation methods require knowledge of the unit length electrolytic resistance of concrete, R_e, in order to calculate the R_t and R_p. Normally, the R_e can be approximated as

Eq. (46) $$R_e = 2R_wD/S$$

Eq. (47) $$R_p = pR_t$$

where D is the diameter of the small disk electrode and S is the section area of the reinforced beam. The R_w is the ohmic resistance between the disk electrode and a very large electrode located at a distance at least higher than 1.5 D.

The accuracy of the electrical transmission line model approach in determination of the corrosion resistance of reinforced concrete has been studied mainly in the laboratory. A relatively good agreement appears to exist between the data obtained from nonuniform current distribution measurements, analyzed using of the transmission line model equations, and the data obtained using uniform current distribution measurements.[62]

4.5 Tafel Extrapolation (Anodic/Cathodic Polarization) Technique

This method involves a large range of anodic and cathodic potential polarization that is applied to the working electrode. The polarization curve is normally presented in a potential versus log (current density) plot (or so-called *Tafel plot*) as shown in Fig. 22. The linear portion of the curve

@Seismicisolation

describing a relatively high polarization potential follows the Tafel relationship ($\eta = a + b \log i$); the slope is referred to as the Tafel slope. I_{corr} is determined from extrapolation of the current curve from either the anodic or the cathodic Tafel region to the open-circuit potential (corrosion potential). This method is commonly used in corrosion studies and also used by reinforced concrete corrosion pioneers in the 1950s.[65][66] However, there are some complications associated with this method when it is applied to the corrosion of reinforced concrete:

- This method may damage the reinforcing steel/concrete interface since a large overpotential must be applied. This is particularly true in the case of anodic polarization, in which the steel surface is changing because of corrosion and/or passivation. This may weaken the steel/concrete interface bond strength.
- The ohmic resistance arising from the resistivity of the concrete, location of the reference electrode, and magnitude of the current, can contribute a large error to the measured potential (Fig. 22).
- The concentration polarization complication is significant. The Tafel relationship depends on pure activation control. In the reinforced concrete system, the oxygen reduction rate is fast enough that the mass transport of the oxygen process becomes the kinetic limitation. Therefore, cathodic reaction may be under mixed charged transfer-mass transport or mass transport control. The cathodic polarization behavior associated with mixed control makes the Tafel extrapolation difficult because the Tafel region is not extensive.

Considering the above problems, this method may not be suitable for field corrosion assessment of reinforced concrete structures.

4.6 The Potential Step and Current Step Techniques

The potential and current step are among the simplest methods for R_p determination.[67][68] Basically, a small amplitude of potential or current is applied to the steel/concrete interface and the current or potential response is recorded. Figures 23 and 24 show the current and potential response in the determination of R_p by applying a potential step of 10 mV and current step of 10 μA, respectively.[69] The decay of the current response (Fig. 23) and

@Seismicisolation

the slow increase of potential response (Fig. 24) are due to the presence of the double-layer interface capacitance; therefore, a certain time is required to reach a constant ΔI and $\Delta\Phi$ to ensure the R_p accuracy.

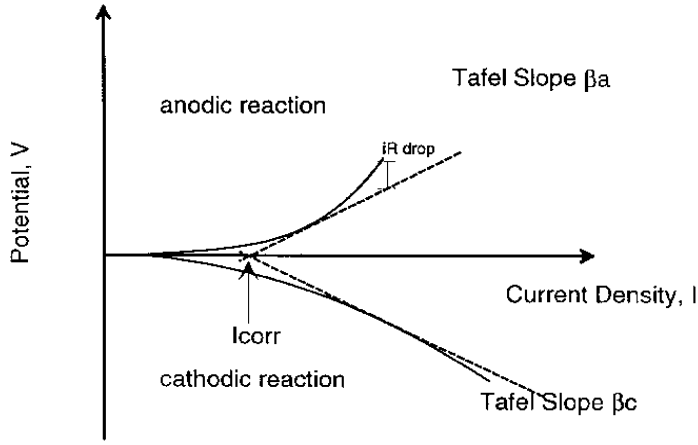


Figure 22. A potential versus log (current density) plot (or Tafel plot).

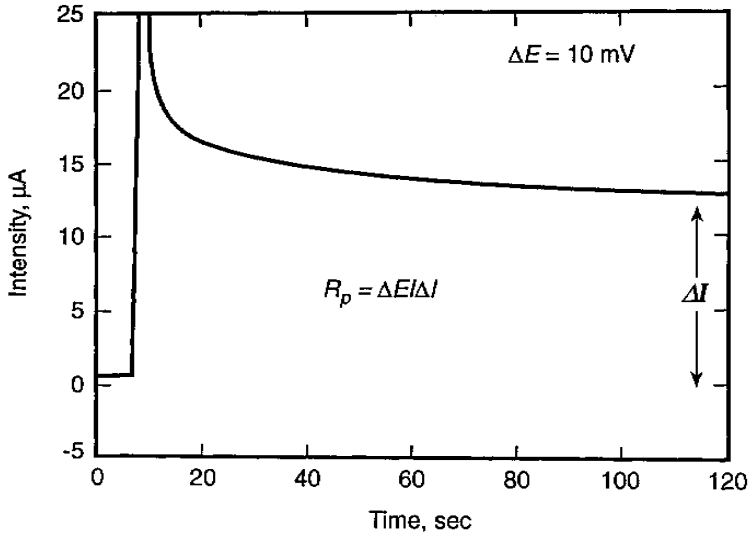


Figure 23. A plot of the current response in the determination of R_p by applying a potential step of 10 mV.

@Seismicisolation

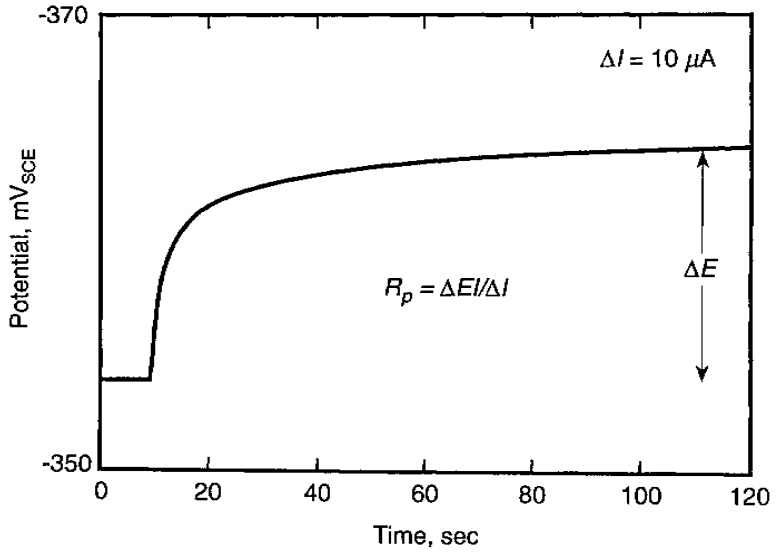


Figure 24. A plot of the potential response in the determination of R_p by applying a current step of 10 mA.

Although these two methods are simple they require a small amplitude of either potential or current, e.g., small polarization within the linear potential-current behavior near the corrosion potential. This may lead to a small signal/noise ratio that makes the measurement difficult and, in the extreme case, impossible.

4.7 The Coulostatic Method[70]

The theory behind this method is that when a small amount of charge, ΔQ, is applied to an interface, the potential across the interface will instantaneously shift to a value, η_o. This potential value is expressed as:

Eq. (48) $$\eta_o = \frac{\Delta Q}{C_{d1} A}$$

where C_{d1} is the steel/concrete interface double-layer capacitance, A is its surface area of the rebar, and η_o is the initial polarization. As soon as the

@Seismicisolation

charging is over, the potential of the rebar will decay back to the corrosion potential Φ_{corr}. Assuming the Randles equivalent circuit model is applicable (Fig. 13), the decay process at a time, *t*, is described by the equation below:

Eq. (49) $$\frac{\eta_t\, dt}{R_p} + C_{d1}\, d\eta_t = 0$$

Integration leads to

(Eq. (50) $$\eta_t = \eta_o \exp(-t/C_{d1}R_p)$$

Taking the logarithm of both sides of the equation gives rise to

Eq. (51) $$\ln(\eta_t) = \ln(\eta_o) - \frac{t}{C_{d1}R_p}$$

A plot of $\ln(\eta_t)$ versus *t* yields a straight line the slope of which allows the time constant, $C_{dl}R_p$, to be calculated (Fig. 25). The R_p value can also be determined since C_{d1} is known through Eq. (48). This method is potentially applicable for field corrosion investigations because the current pulse results in a small perturbation of the system and provides a simultaneous rapid response.

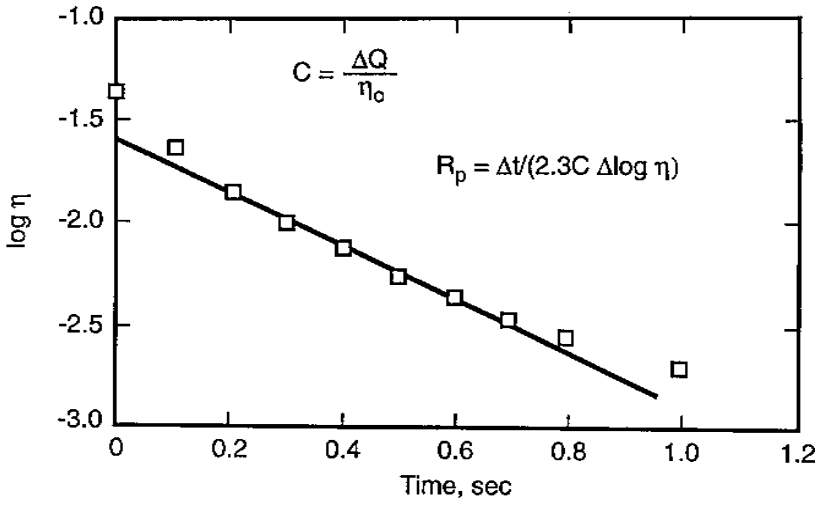


Figure 25. A plot of log (η_t) versus time; the slope allows the time constant, $C_{d1}R_p$, to be calculated.

@Seismicisolation

4.8 Cyclic Voltammetry

Depending on the amplitude of the potential signal, small or large amplitude cyclic voltammetry techniques have been applied to study reinforced concrete corrosion. The small potential amplitude is normally within tens of mV, and it can be used to determined the polarization resistance, R_p. Figure 26 is an example that shows results of a test of a steel reinforcement embedded in mortar containing 2% Cl^-. The interface capacitance, C_{d1}, and polarization resistance, R_p, are calculated using the equations below:

Eq. (52) $C_{d1} = \Delta I(2d\Phi/dt)$

Eq. (53) $R_p = \Delta\Phi/\Delta I$

where $d\phi/dt$ is potential scan rate, $\Delta\Phi$ is the potential amplitude and ΔI is current difference of the forward and backward scan.

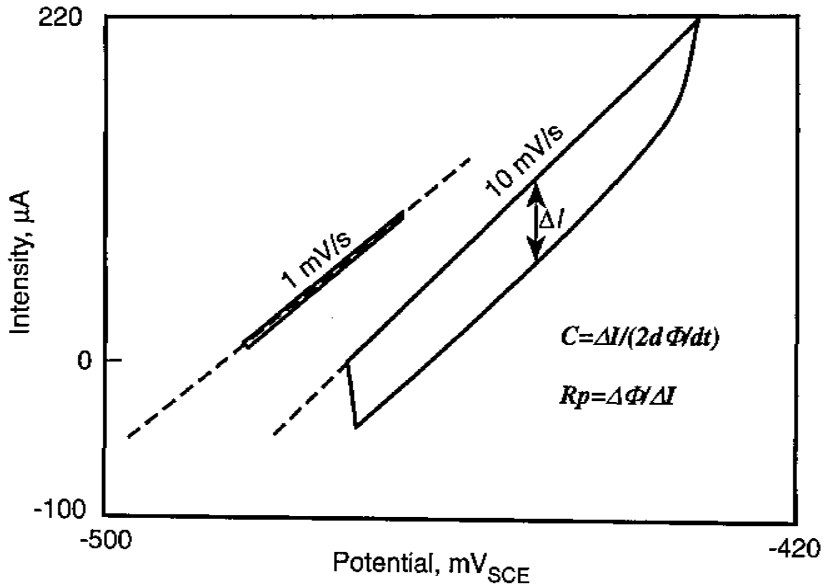


Figure 26. An example of the small potential amplitude cyclic-voltammetry in the determination of the polarization resistance, R_p.

@Seismicisolation

The large amplitude cyclic voltammetry involves polarizing the test specimen anodically from the corrosion potential and recording the current needed for this polarization. The potential is then returned to the original corrosion potential using a constant sweep rate of the potential (usually 10–100 mV/s). The peaks in the current versus potential plot can be analyzed to provide useful information regarding the electrochemical corrosion processes occurring at the steel/concrete interface. This allows one to make predictions about the mechanism of the corrosion process and analyze the passivation behavior to determine the reactions which went into making the passive film. A voltammogram of iron obtained at a sweep rate of 50 mv/s in a fresh cement slurry solution (pH = 12.7), after 80 cycles of potential sweeping between -1.35 V to 0.85 V (vs. SHE), is shown in Fig. 27. Two anodic peaks *(B)* and *(C)* and two corresponding cathodic peaks *(H)* and *(I)* are distinguished. These anodic/cathodic peaks correspond to the iron dissolution reactions including formation of a ferrous hydroxide film and ferrous-ferric transformations, etc.[71] Analysis of the voltammogram provides useful information regarding the electrochemical corrosion processes occurring at the steel/concrete interface.[72]–[75] However, this method requires polarization of several hundred mV for the corrosion potential which may reduce the steel/concrete bond strength.

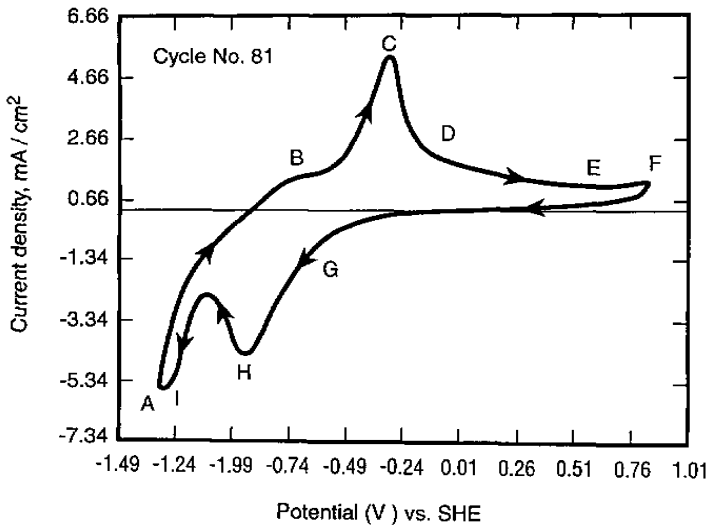


Figure 27. A voltammogram of iron obtained at a scan rate of 50 mv/s in a fresh cement slurry solution (pH = 12.7), after 80 cycles of potential sweeping between -1.35 V to 0.85 V (vs. SHE).

@Seismicisolation

4.9 Alternating Current (ac) Impedance Spectroscopy (ACIS)

Alternating Current (ac) Impedance Spectroscopy (ACIS) is a powerful method of characterizing many of the electrical properties of materials and their interfaces. It is widely used in both fundamental and applied electrochemical studies including aspects of electrode kinetics, battery performance, corrosion, and high temperature electrochemistry. This technique has been used extensively in determining the corrosion rate of reinforcing steel in concrete.[76]–[87] However, due to the sophistication of the measurement and relatively high cost of the equipment, this technique is more frequently used in laboratory studies rather than in field surveys. Nevertheless, ACIS was validated as a useful tool in field corrosion assessment of reinforced concrete structures in a SHRP report.[28] It allows the corrosion rate of rebar to be measured quantitatively, provides rebar corrosion kinetics information, and insight into corrosion mechanisms vital to repair and protection decision making.

Basic Principles. The ac impedance spectroscopy technique involves application of a small amplitude sinusoidal voltage or current signal to a system. A response current or potential signal is generated and recorded. The impedance of the system is easily evaluated through the analysis of the ratio of the amplitudes and phase shift between the voltage and current. The impedance is defined as a vector:

Eq. (54) $$Z(\omega) = \frac{V}{I}$$

A plot of real and imaginary components is the so-called "complex plane" plot. This leads to definitions of impedance in terms of the complex quantities.

Eq. (55) $$Z(\omega) = Z'(\omega) - jZ''(\omega)$$

Eq. (56) $$Z'(\omega) = |Z| \cos(\theta)$$

Eq. (57) $$Z''(\omega) = |Z| \sin(\theta)$$

@Seismicisolation

where $|Z|$ is the modulus and (θ) the phase angle, $Z'(\omega)$ is the real component and $Z''(\omega)$ is the imaginary component of the impedance. The complex plane type of plot was first introduced by Cole and Cole[88] and plots of log $|Z|$ and phase angle vs. log frequency are referred to as *Bode plots*.[89].

Equivalent Circuit Models for Reinforcing Steel and the Steel/ Concrete Interface. A simple parallel combination of a pure resistor and capacitor along with the corresponding impedance plots in the complex plane (Cole-Cole plot) and log $|Z|$ and phase angle vs. log frequency (Bode plots) are illustrated in Figs. 28 (a–d). The impedance of the circuit can be described by the following equation:

Eq. (58)
$$Z(\omega) = \frac{R}{1+(\omega CR)^2} - \mathbf{j}\frac{\omega CR^2}{1+(\omega CR)^2}$$

where $\omega = 2\pi f$, and $\mathbf{j} = \sqrt{-1}$. A plot of Eq. (58) in the complex plane (Fig. (28b) gives rise to a perfect semicircle characterized by a single conductivity relaxation time ($\tau = RC$); the maximum value of the imaginary impedance occurs at the characteristic frequency $f_o = \frac{1}{2}\pi RC$. An ideal semicircle is generally not observed in practice for most materials. It is normally an inclined semicircle with its center depressed below the real axis by an angle α_i, Fig. (29a). This behavior normally associated with a spread of relaxation times that cannot be described by the classical Debye equation employing a single relaxation time. A dispersive, frequency-dependent element or so called constant phase element (CPE)[89]–[90] as depicted in Fig. (29b) is used to account for the shape of the depressed complex plot. The corresponding impedance is expressed as follows:

Eq. (59)
$$Z(CPE) = \frac{R}{\left[1 + RC(j\omega)^{\alpha_i}\right]}$$

where α_i ($0 < \alpha_i < 1$) can be used to represent the degree of perfection of the capacitor and represents a measure of how far the arc is depressed below the real impedance axis.

@Seismicisolation

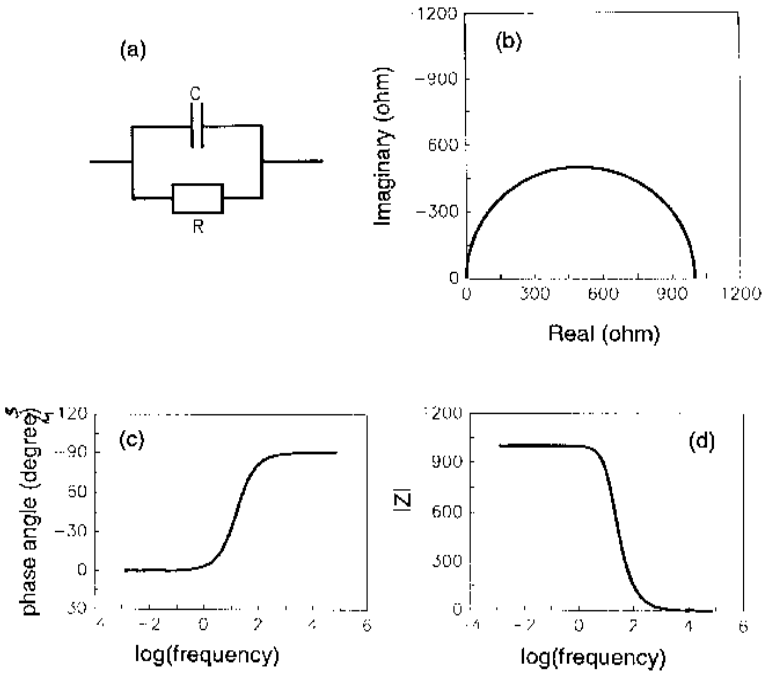


Figure 28. *(a)* A simple parallel equivalent *RC* circuit consisting of a pure resistor and capacitor; *(b)* corresponding impedance plot in the complex plane (Cole-Cole plot); *(c) p*hase angle vs. log (frequency); and *(d)* $|Z|$ vs. log (frequency).

Sagoe-Crentsil, et al.,[82] have proposed a physical model to describe the steel/concrete interface as shown in Fig. 30. The model consists of a layer of compact iron oxide film and interfacial film adjoined by the concrete matrix. It was suggested that the interfacial film consisted of $Ca(OH)_2$ and other cement hydration products deposited onto the surface of steel. Interpretation of an impedance spectrum requires modeling with a selected equivalent circuit until the electrical response of the elemental microstructure of the cement paste is well simulated. The usefulness of the analyses is strongly dependent on how the electrical components are selected and the extent to which they represent the structure of the steel/concrete interface. Many equivalent circuits have been proposed to describe the different stages of the steel/concrete corrosion process including active and passive corrosion processes, diffusion control, and passivated film, etc.[81][84][87] A more complicated model such as the one dimension transmission line analysis was also used to describe corrosion in a large reinforced concrete slab.[28]

@Seismicisolation

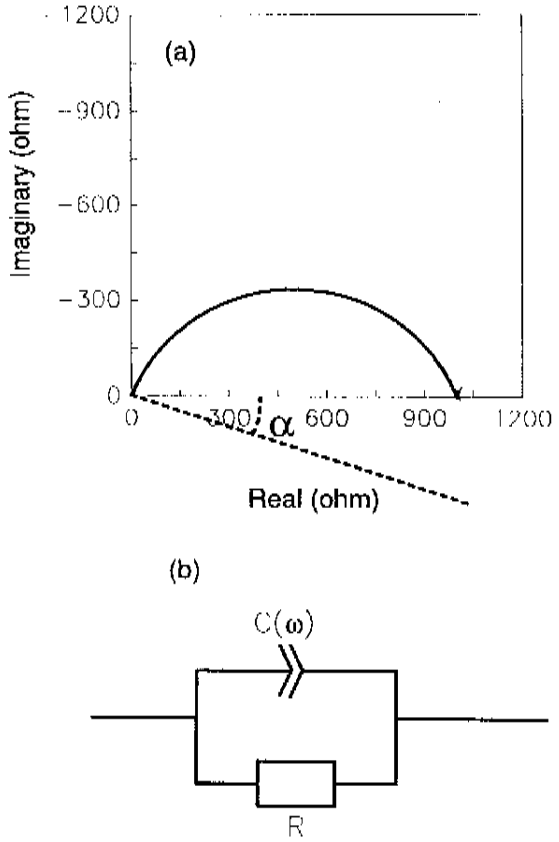


Figure 29. *(a)* An impedance plot containing an inclined semicircle with its center depressed below the real axis by an angle α; and *(b)* an equivalent circuit containing a constant phase element (CPE).

Corrosion Rate Measurement and R_p Determination. *RC* parameters can easily be determined through a computer simulation of the experimental spectra using the electrical equivalent analysis method. This applies especially at very low frequencies when data is difficult to obtain experimentally due to time or equipment limitations. The corrosion rate determination involves acquisition of impedance spectra and data processing using electrical equivalent circuit fitting. As an example, Fig. 31 shows an impedance spectrum in both Cole-Cole and Bode plots for a mild steel reinforced concrete specimen.[91] The circles represent the experimental data and the solid line is a computer simulation curve. There are three regions in the frequency domain, as indicated in the figure. Only a tail of

@Seismicisolation

a semicircle is depicted in the high frequency range. This is attributed to concrete matrix microstructure. A depressed semicircle at frequencies ranging from kHz to Hz represents the interfacial film. The large and incomplete semicircle in the very low frequency region is due to double layer and polarization resistance contributions. Corrosion rate is estimated from R_p obtained from the impedance spectra simulation process using the Stern-Geary equation (Eq. 30).

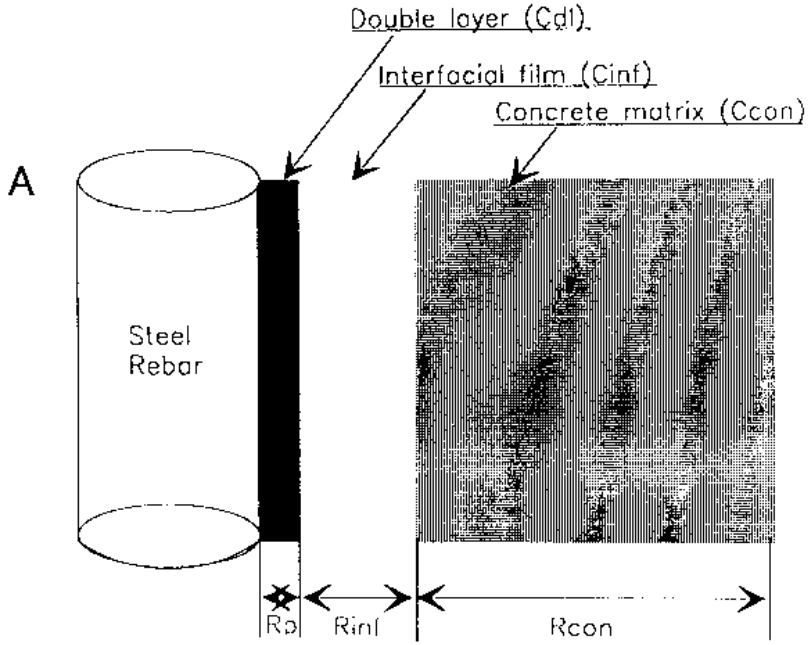


Figure 30. A physical model to describe the steel/concrete (or cement paste) interface.

The problem of extracting the polarization resistance, R_p, from impedance data has essentially been solved. This development is important for the engineers in the field since a practical technique (based on sound theory) is available for nondestructive evaluation of rebar corrosion rate. However, similar to the linear polarization technique, this method also encounters the same difficulties as experienced by the former in the field, i.e., nonuniform current distribution and non-defined polarized area. Lemoine, et al.,[82] have attempted the application of a guard ring counter electrode (same principle as the linear polarization) and it appears that such an approach enables the operator to distinguish the active and passive areas in a reinforcing steel bar in the concrete slab. It is reasonable to expect that an

@Seismicisolation

impedance field instrument package might consist of the following components:

- A test probe which consists of guard ring, counter and reference electrodes
- Frequency generator and analyzer
- Data acquisition hardware/software driven by micro-computer
- Data analysis software based on electrical equivalent circuit fitting or simulation

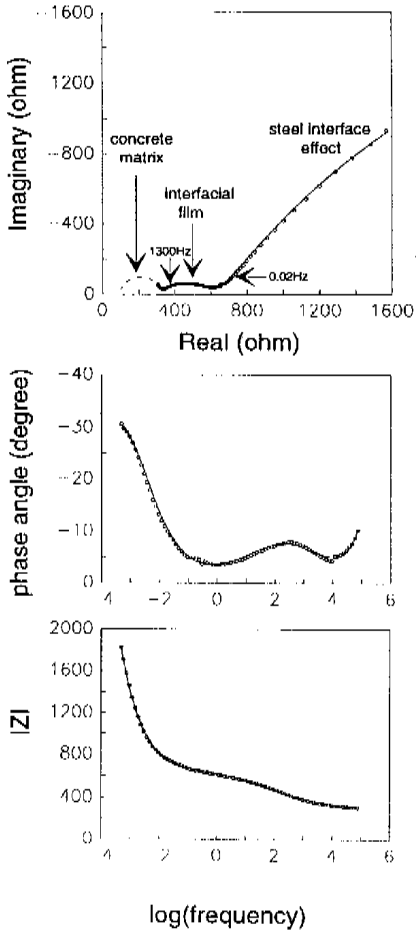


Figure 31. An impedance spectrum for a mild steel reinforced concrete specimen*(a)* Cole-Cole; *(b)* and *(c)* Bode plots. The circles represent the experimental data and the solid line is a computer simulation curve.

@Seismicisolation

The ac impedance technique is one of most powerful electrochemical methods used in steel or reinforced steel corrosion investigation. It provides information on corrosion mechanism and kinetic process. The information is important in understanding the nature of corrosion. In addition to the determination of R_p and corrosion rate of rebar, ac impedance measurement provides information relating to steel/concrete interface structure and capacitive constants that other techniques do not. The impedance technique is also a relatively fast and nondestructive, quantitative technique.

This method requires substantial knowledge and working experience in order to interpret the spectra correctly. The extraction of corrosion polarization resistance is tedious since the curve fitting has been proven to be time consuming. It is an electrochemical technique. It will, therefore, have similar difficulties in actual field performance as the half-cell potential and linear polarization methods. The cost of an impedance instrument could be much higher than a linear polarization field instrument.

4.10 Macro-Cell Monitoring Techniques

The embedment of macro-cell devices in reinforced concrete has been used frequently for long term corrosion monitoring. The electrochemical principle behind the technique is to deliberately set up a macro-cell using dissimilar metals (stainless steel is often used)[92] or embedding steel in concrete containing a large amount of chloride to create a corrosion chloride concentration cell. ASTM G109-92[46] is a typical example of the latter method for evaluation of the chemical admixtures on the corrosion of embedded steel reinforcement in concrete. Concrete specimens are made with a single top rebar and two bottom rebars. The top rebar is located in concrete contaminated by chloride solution ponding on the concrete surface. The two bottom rebars are in a chloride free concrete environment (Fig. 32). The current flow between the top and bottom is measured through a precision resistor.

The chloride that permeates through the concrete reaches the top rebar causing the corrosion potential to change and a potential difference occurs between the upper and the bottom bars (Fig. 33). As a result, a macro-cell forms. The top bar becomes the anode where it begins to corrode while the bottom bars act as cathodes. The macro-cell potential of the system is determined by the sums of all the individual anodic and cathodic currents obtained for each material at each potential when the following condition is met

Eq. (60) $$I_a A_a = I_c A_c$$

@Seismicisolation

where I_a and I_c are the anodic and cathodic current densities, and A_a, A_c are the anodic and cathodic areas. The macro-cell potential can be determined by direct measurement with a reference electrode. The macro-cell corrosion rate may be estimated by measuring the potential between the resistor or using a zero-resistance ammeter with direct connection between the two layers of bars.

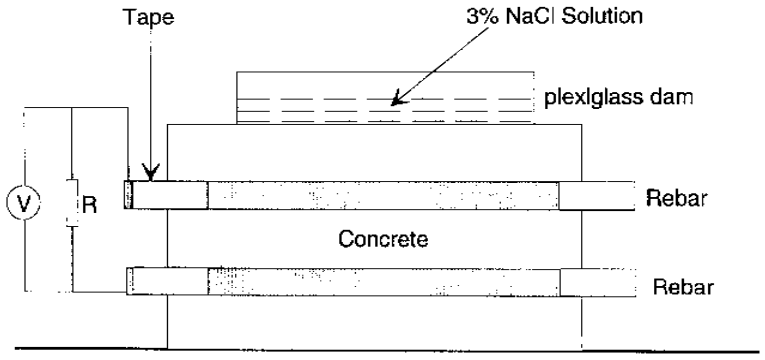


Figure 32. A schematic of concrete specimen for macro-cell study.

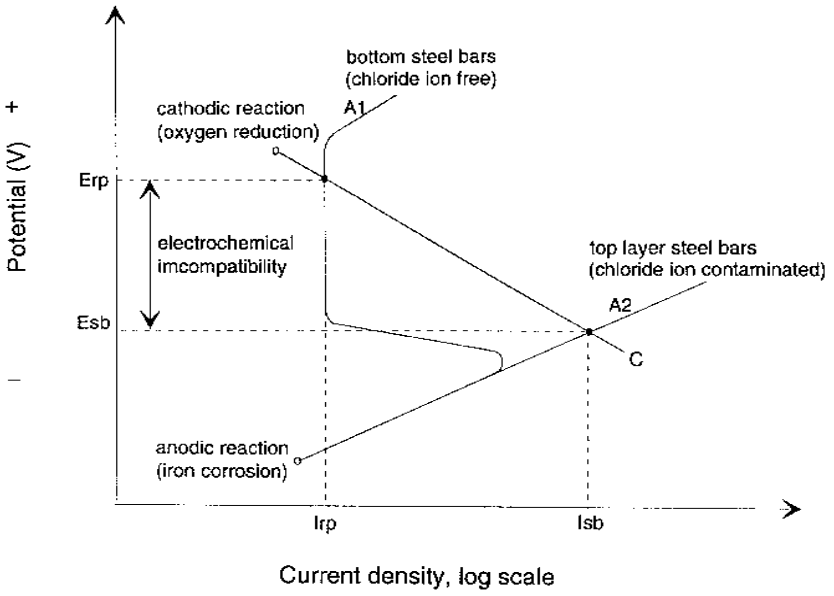


Figure 33. A potential difference occurs between the upper and the bottom bars due to the chloride that permeates through the concrete and reaches the top rebar.

@Seismicisolation

One of the advantages is that this technique can be permanently set up for a long-term monitoring of the reinforced concrete corrosion process. In this method the macro-cell current is directly determined as a function of time. However, what actually is measured and how representative the macro-cell current is to the true corrosion current in the reinforcing steel is moot.[31][93] This is because the measured macro-cell corrosion rate is affected by the coupling of additional cathodic reactions and is not equal to the true corrosion rate measured by the linear polarization method. This is illustrated in Fig. 34, where point "a" is the intercept of anodic and cathodic reactions without a macro-cell and I_{corr} is the corresponding corrosion rate (which can be measured with LPM). The intercept with macro-cell is at point "t" and its corresponding corrosion rate (measured by ASTM C-109) is $I_{corr'}$ which is larger than I_{corr}.

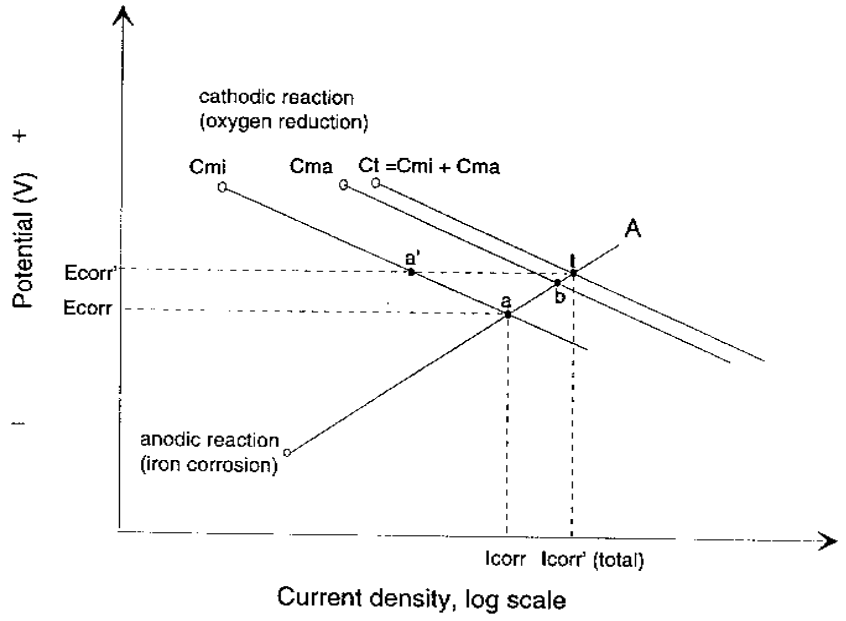


Figure 34. The coupling of additional cathodic reactions leading to a large macro-cell corrosion rate.

@Seismicisolation

4.11 Electrochemical Noise Monitoring

This technique involves the measurement and analysis of the random events occurring naturally during a corrosion process. The events are observed as fluctuations in corrosion potential at μV-mV level) and corrosion current (at nA-μA level). A correlation between potential noise and corrosion rate has been reported in laboratory investigations.[94][95] Several data interpretation methods including electrochemical,[96] statistical,[97][98] and spectral,[99][100] have been proposed to determine pit sizes and current density.

It is apparent that the noise monitoring technique could be used as an indicator in the field application of corrosion monitoring since it does not perturb the system during measurements. This method is also sensitive to the destruction of the protective film on steel. However, more research is required since this method is still not often used in reinforced concrete corrosion studies. Individual measurements may also take a long time and substantial experience is required to interpret the results correctly. The reinforced concrete structures can act as antennae to capture non-corrosion noise that may mask the actual effects of corrosion.

5.0 CONCLUDING REMARKS

Corrosion has been identified as a major cause of the deterioration of the built infrastructure. Considerable research and numerous field surveys have been performed both in Canada and the United States to resolve the problem and seek possible solutions. It is believed that an understanding of the factors causing the reinforcing steel corrosion, the basic principles of corrosion, and the advantages and limitations of the techniques to assess it, will facilitate the process. It will also reduce the chance of introducing errors during data acquisition and analysis. This is essential to decision making regarding repair and maintenance of reinforced concrete structures.

A decision as to what technique should be applied in a field survey or for a laboratory investigation may depend on the actual situation and availability of the equipment and budget. Comparison of these techniques is difficult as every single technique has its advantages and limitations. Table 4[69] provides a comparison of various electrochemical techniques.

@Seismicisolation

Table 4. Comparison of Various Electrochemical Techniques for Corrosion Assessment of Reinforced Concrete[69]

	measurement speed	quantitative information	non-destructive	cost-effectiveness	corrosion mechanism	corrosion rate determination	accuracy
Weight loss	slow	yes	no	labor costly	no	yes	excellent
Half-cell potential	rapid	no, only qualitative	yes	very cheap	no	probability of corrosion	good
Linear polarization 3LP	fast	yes	yes	relatively expensive	no	Rp and Icorr	very good
Linear polarization Clecor	rapid	yes	yes	relatively expensive	no	Rp and Icorr	excellent
Linear polarization Transmission line model	fast	yes	yes	relatively expensive	no	Rp	excellent
Anodic/ cathodic polarization	fast	yes	may be	relatively expensive	yes	Icorr, Tafel slope	very good
Noise monitoring	very slow (monitoring)	maybe	yes	relatively expensive	no	indication of corrosion	relatively poor
Macro-cell	slow (monitoring)	yes	yes	inexpensive	may be	Icorr	questionable
Coulostatic method	rapid	yes	yes	inexpensive	yes	Icorr, Rp, Cdl	excellent
Small amplitude cyclic-voltammetry	fast	yes	yes	relatively expensive	no	Rp, Cdl	very good
Large amplitude cyclic-voltammetry	relatively slow	yes	may be	relatively expensive	yes	B-I plot	good
Potential step	fast	yes	yes	cheap	no	Rp , Cdl	fair
Current step	relative fast	yes	yes	cheap	no	Rp, Cdl	fair
A.c. impedance	fast	yes	yes	expensive	yes	Icorr, Rp, Cdl, and more	excellent

REFERENCES

1. Slater, J., Corrosion of Metals in Association with Concrete, ASTM STP 818, p. 83, ASTM, Philadelphia, PA (1983)
2. Borgard, B., Warren, C., Somayaji, S., and Heidersbach, R., Corrosion Rates of Steel in Concrete, (N. S. Berke, V. Chaker, and D. Whiting, eds.), ASTM STP 1065, pp. 174–188, ASTM, Philadelphia, PA (1990)
3. Litvan, G., and Bickley, J., Concrete Durability, (J. Scanlon, ed.), ACI SP 100, pp. 1503–1515, Detroit, MI (1987)

@Seismicisolation

4. Cady, P. D., Corrosion of Reinforcing Steel in Concrete - A General Overview of the Problem, *Chloride Corrosion of Steel in Concrete*, ASTM 629, pp. 3–11, Philadelphia (1977)
5. Flis, J., Sehgal, A., Li, D., Kho, Y. T., Sabotl, S., Pickering, H., Osseo-Asare, K., and Cady, P. D., Condition Evaluation of Concrete Bridges Relative to Reinforcement Corrosion, Volume 2: Method for Measuring the Corrosion Rate of Reinforcing Steel, SHRP-S324, National Research Council, Washington DC. (1992)
6. Mailvaganam, N. P., and Alexander, T., Selection of Repair Materials with Expert Advice, *Concrete Repair Bulletin*, pp. 12–15 (1996)
7. O'M Bockris, J., and Reddy, A. K. N., Modern Electrochemistry, Vol. 2, Chapter 7, pp. 623–687, Plenum Press, New York (1970)
8. O'M Bockris, J., and Reddy, A. K. N., *Modern Electrochemistry*, Vol. 2, Chapter 8, pp. 845–908, Plenum Press, New York (1970)
9. Tait, W. S., *An Introduction to Electrochemical Corrosion Testing for Practicing Engineers and Scientists*, pp. 12–14, PairODocs Publications, (1994)
10. Fontana, M. G., *Corrosion Engineering*, Third Edition, Chap. 9, pp. 462–468, McGraw-Hill Book Company, USA (1986)
11. Mansfeld, F., The Polarization Resistance Technique for Measuring Corrosion Currents, in Advances in Corrosion Science and Technology, Vol. 6, (M. G. Fontana and R. W. Staehle, eds.), pp. 163–262, Plenum Press, New York and London (1970)
12. ACI Committee 222, *Corrosion Metals in Concrete*, ACI 222r-96, American Concrete Institute, Farmington Hills, MI (1996)
13. Ramachandran, V. S., and Feldman, R. F., *Concrete Admixtures Handbook: Properties, Science and Technology*, (V. S. Ramachandran, ed.), Chap. 1, pp. 10–16, Noyes Publications, New Jersey, USA (1984)
14. Mehta, P. K., *Concrete Structure, Properties and Materials*, Chap. 6, p. 170, Prentice-Hall, Inc., Englewood Cliffs, New Jersey (1984)
15. Weise, C. H., Determination of the Free Calcium Hydroxide Contents of Hydrated Portland Cements and Calcium Silicates, *Analytical Chemistry*, 33(7):877–822 (June, 1961)
16. Buenfeld, N. R., and Newman, J. B., The Permeability of Concrete in a Marine Environment, *Mag. Concr. Res.*, 36:67–80 (1984)
17. Whittington, H. W., McCarter, J., and Forde, M. C., The Conduction of Electricity Through Concrete, *Mag. Concr. Res.*, 33:48–60 (1984)
18. Gjørve, O. E., Vennesland, ∅., and El-Busaidy, A. H. S., Electrical Resistivity of Concrete in the Oceans, OTC Paper No. 2803, pp. 581–588, 9th Ann. Offshore Tech. Conf., Houston (May, 1977)

@Seismicisolation

19. Gjørve, O. E., Vennesland, Ø., and El-Busaidy, A. H. S., Diffusion of Dissolved Oxygen Though Concrete, Paper No. 17, NACE, Houston (March, 1976)

20. Shalon, R., and Raphael, M., Influence of Sea Water on Corrosion of Reinforcement,*ACI Journal, Proceedings,* 55(8):1251–1268 (Feb., 1959)

21. Pourbaix, M.,*Atlas of Electrochemical Equilibria in Aqueous Solutions*, p. 458, Pergamon Press, Oxford (1966).

22. Conway, B. E., Theory and Principles of Electrode Processes, pp. 170–272, The Ronald Press Company, New York (1965)

23. Hansson, C. M., The Corrosion of Steel and Zirconium in Anaerobic Concrete, *Mat. Res. Soc. Sym. Proc.*, 50:475–482 (1985)

24. Rosenberg, A., Hansson, C. H., and Andrade, C., Mechanisms of Corrosion of Steel in Concrete,*Materials Science of Concrete,* (J. Skalny, ed.), pp. 285–313, The American Ceramic Society, Inc. (1989)

25. Currie, R. J., and Robery, P. C., Repair and Maintenance of Reinforced Concrete, Building Research Establishment Report (1994)

26. Perenchio, W. F., Corrosion of Reinforcing Steel, in Concrete and Concrete Making Materials, ASTM STP 169C, (Paul Klieger and J. F. Lamond, eds.), ASTM, Philadelphia, pp. 164–172 (1994)

27. Sagoe-Crentsil, K. K., and Glasser, F. P., Steel in Concrete, Part I: A Review of the Electrochemical and Thermodynamic Aspects, *Mag. Conc. Res.*, 41:205–212 (1989)

28. MacDonald, D. D., El-Tantawy, Y. A., Rocha-Filho, R. C., Urquidi-MacDonald, M., Evaluation of Electrochemical Impedance Techniques for Detecting Corrosion on Rebar in Reinforced Concrete, SHRP-ID/UFR-91-524, National Research Council, Washington, DC (1994)

29. Venuat, M., Relationship between Concrete Carbonation and Corrosion of Reinforcement, Recentres CEFRACOR-77, JTBTP (October, 1977)

30. Tuutti, K.,*Corrosion of Steel in Concrete,* Swedish Cement and Concrete Instituto (CIB), No. 4-82, Stockholm (1982)

31. Gu, P., Beaudoin, J. J., Tumidajski, P. J., and Mailvaganam, N. P., Electrochemical Incompatibility of Patches Used in Reinforced Concrete Repair, *Concrete International*, pp. 68–72 (August, 1997)

32. Taylor, H. F. W., *Cement Chemistry*, pp. 403–405, Academic Press, Toronto (1990)

33. Page, C. L., Page, N. R., and El-Tarras, A., Diffusion of Chloride Ions in Hardened Cement Paste, 11:395, *Cem. Concr. Res.*, (1981)

34. Preece, C. M., Grønvold, F. O., and Frølund, T., The Influence of Cement Type on the Electrochemical Behavior of Steel in Concrete, *Corrosion of Reinforcement in Concrete Construction*, (A. P. Crane, ed.), pp. 393–406, Ellis Horwood, Ltd., Chichester, UK (1983)

@Seismicisolation

35. Hansson, C. M., Strunge, H., Markussen, J. B., and Frølund, T., The Effect of Cement Type on the Diffusion of Chloride, Nordic Concrete Research Publication No.4, Paper No. 6 (1985)

36. Foley, R. T., Complex Ions and Corrosion, *J. Electrochem. Soc.*, 122(11):1493–1549 (1975)

37. Byfors, K., Chloride Binding in Cement Pastes, Nordic Concrete Research Publication No.5, Paper No.1 (1986)

38. Andrade, C., Calculation of Chloride Diffusion Coefficients in Concrete From Ionic Migration Measurements, *Cement Concrete Research*, 23:724–742 (1993)

39. Andrade, C., Sanjuan, M. A., Recuero, A., and Rio, O., Calculation of Chloride Diffusivity in Concrete from Migration Experiments in Ion Steady-State Conditions, *Cement Concrete Research*, 24:1214–1228 (1994)

40. Tang, L. P., and Nilsson, L. O., Rapid Determination of the Chloride Duffsivity in Concrete by Applying an Electrical Field, *ACI Materials Journal*, pp. 49–52, (Jan.–Feb., 1992)

41. Herald, S. E., Henry, M., Al-Qadi, I., Weyers, R. E., Feeney, M. A., Howlum, S. F., and Cady, P. D., Condition Evaluation of Concrete Bridges Relative to Reinforcement Corrosion, Volume 6: Method of Field Determination of Total Chloride Content, SHRP-S-328, National Research Council, Washington DC (1992)

42. Grantham, M. G., An Automated Method for the Determination of Chloride in Hardened Concrete, *Proceedings 5th International Conference on Structural Faults and Repair*, 2131–136 (1993)

43. *Corrosion Metals in Concrete*, ACI Committee, 222 ACI 222r-85, American Concrete Institute, Detroit, MI (1985)

44. Gileadi, E., *Electrode Kinetics for Chemists, Chemical Engineers and Materials Scientists*, VCH Publisher, New York (1993)

45. Wear and Erosion; Metal Corrosion, *Annual Book of Standards*, American Society for Testing and Materials, ASTM, Vol. 03.02, G59-91, Philadelphia (1993)

46. Wear and Erosion; Metal Corrosion, *Annual Book of Standards*, American Society for Testing and Materials, ASTM, Vol. 03.02, G109-92, Philadelphia (1993)

47. Cady, P. D., and Gannon, E. J., Condition Evaluation of Concrete Bridges Relative to Reinforcement Corrosion, Volume 1: State of the Art of Existing Methods, SHRP-S-330, National Research Council, Washington DC (1992)

48. Titman, D. J., Fault Detection in Civil Engineering Structures Using Infra-Red Thermography, *Proceedings 5th International Conference on Structural Faults and Repair*, 2:137–140 (1993)

@Seismicisolation

49. Broomfield, J. P., Assessing Corrosion Damage on Reinforced Concrete Structures, Corrosion and Corrosion Protection on Steel in Concrete, *Proceedings of International Conference,* (R.N. Swamy, ed.), University of Sheffield, U.K., 1:1–25 (1994)

50. Langford, P., and Broomfield, J. P., Monitoring the Corrosion of Reinforcing Steel, *Construction Repair,* 1:32–36 (1987)

51. Spellman, D. L., and Stratfull, R. F., Concrete Variables and Corrosion Testing, Highway Research Record 423 (1973)

52, Stratfull, R. F., Half-Cell Potentials and the Corrosion of Steel in Concrete, Highway Research Record 433 (1973)

53. Clear, K. C., and Hay, R. E., Time to Corrosion of Reinforcing Steel in Concrete Slabs, Vol. 1, Federal Highway Administration Report FHWA-RD-73-32, Washington DC (1973)

54. Virmani,. Y. P., Clear, K. C., and Pasko, T. J. Jr., Time to Corrosion of Reinforcing Steel in Concrete Slabs, Vol. 1, Federal Highway Administration Report FHWA-RD-83-012, Washington DC (1983)

55. Standard Test for Half-Cell Potentials of Uncoated Reinforcing Steel in Concrete, *Annual Book of ASTM Standard*s, C876-91, Vol. 04.02, Philadelphia (1992)

56. Corrosion Detection in Reinforced Concrete Bridge Structure, User Manual, U.S. Department of Transportation, Federal Highway Administration, Demonstration Project No. 84 (March, 1992)

57. Stern, M., and Geary, A. L., Electrochemical Polarization I. A Theoretical Analysis of the Shape of Polarization Curves, 104:56–63, *Journal of Electrochemical Society* (1957)

58. Andrade, C., and Gonzales, J. A., Quantitative Measurements of Corrosion Rate of Reinforcing Steels Embedded in Concrete Using Polarization Resistance Measurements, *Werkstoffe und Korrosion,* 29:515-519 (1978)

59. Andrade, C., *Quantification of Durability of Reinforcing Steel, Concrete Technology, New Trends, Industrial Applications,* (A. Aguado, R. Gettu, and S. P. Shah, eds.), E&FN SPON, pp. 157–175, an Imprint of Chapman & Hall, London (1994)

60. Feliu, S., Gonzalez, J. A., Escudero, M. L., Feliu, S. Jr., and Andrade, C., Possibilities of the Guard Ring for Electrical Signal Confinement in the Polarization Measurements of Reinforcements, *Corrosion,* 46:1015 (1990)

61. Andrade, C., Macias, A., Feliu, S., Escudero, M. L., and Gonzalez, J. A., Quantitative Measurement of the Corrosion Rate Using a Small Counter Electrode in the Boundary of Passive and Corroded Zones of a Long Concrete Beam, *Corrosion Rates of Steel in Concrete,* (N. S. Berke, V. Chaker, and D. Whiting, eds.), ASTM STP 1065., pp. 134–142, ASTM, Philadelphia, PA (1990)

@Seismicisolation

62. Feliu, S., Gonzalez, J. A., Andrade, C., and Feliu, V., On-Site Determination of the Polarization Resistance in a Reinforced Concrete Beam, *Corrosion Engineering*, 44:761–765 (1988)

63. Collins, W. D., Weyers, R. E., and Al-Qadi, I. L., Chemical Treatment of Corroding Steel Reinforcement after Removal of Chloride-Contaminated Concrete, *Corrosion*, 49:75 (1993)

64. Tafel, A., *Phys. Chem.*, 50:641 (1904)

65. Keasche, H., Testing of the Danger to Steel Reinforcement due to Admixture in Concrete, *Zement-Kalk-Gips*, 12:289–294 (1959)

66. Bäumel, A., The Effect of Admixtures on the Corrosion Behaviour of Steel in Concrete, *Zement-Kalk-Gips*, 12:204–305 (1959)

67. Kissinger, P. T., Small-Amplitude and Related Controlled-Potential Techniques, *Laboratory Techniques in Electroanalytical Chemistry*, (P. T. Kissinger, and W. R. Heineman, eds.), pp. 143–161, Marcel Dekker, Inc., New York (1984)

68. Bard, A. J., and Faulkner, L. R., *Electrochemical Methods: Fundamentals and Applications*, John Wiley & Sons, New York (1980)

69. Rodriguez, P., Ramirez, E., and Gonzalez, J. A., Methods for Studying Corrosion in Reinforced Concrete, *Mag. Concr. Res.*, 46:81–90 (1994)

70. Rodriguez, P., and Gonzalez, J. A., Use of the Coulostatic Method for Measuring Corrosion Rates of Embedded Metal in Concrete, *Mag. Concr. Res.*, 46:91–97 (1994)

71. Gu, Ping, Fu, Yan, Xie, Ping, Beaudoin, J. J., A Method for Evaluating the Corrosion Potential of a Cement Slurry to Reinforcing Steel, *Cement and Concrete Research*, 24:38–48 (1994)

72. Hinatsu, J. T., Graydon, W. F., and Foulkes, F. R., Voltammetric Behavior of Iron in Cement. I. Development of a Standard Procedure for Measuring Voltammograms, *J. of App. Electrochemistry*, 19:868–876 (1988)

73. Hinatsu, J. T., Graydon, W. F., and Foulkes, F. R., Voltammetric Behavior of Iron in Cement. II. Effect of Sodium Chloride and Corrosion Inhibitor Additions, *J. of App. Electrochemistry*, 20:841–847 (1990)

74. Hinatsu, J. T., Graydon, W. F., and Foulkes, F. R., Voltammetric Behavior of Iron in Cement. III. Comparison of Iron versus Reinforcing Steel, *J. of App. Electrochemistry*, 21:425–429 (1991)

75. Ushirode, W. M., Hinatsu, J. T., and Foulkes, F. R., Voltammetric Behavior of Iron in Cement. IV. Effect of Acetate and Urea Additions, *J. of App. Electrochemistry*, 22:224–229 (1992)

76. Wenger, F., and Galland, J., Analysis of Local Corrosion of Large Metallic Structures or Reinforced Concrete Structures by Electrochemical Impedance Spectroscopy, *Electrochimica Acta*, 35:1573–1578 (1990)

@Seismicisolation

77. John, D. G., Searson, P. C., and Dawson, J. L., Use of ac Impedance Technique in Studies on Steel in Concrete in Immersed Conditions, *Br. Corrosion J.*, 16:102–106 (1981)

78. Somuah, S. K., Boah, J. K., Leblanc, P., Al-Tayyib, A. H. J., and Al-Mana, A. I., Effect of Sulfate and Carbonate Ions on Reinforcing Steel Corrosion as Evaluated Using ac Impedance Spectroscopy, *ACI Materials Journal*, 88:49–55 (1991)

79. Matsuoka, K., Kihira, H., Ito, S., and Murata, T., Corrosion Monitoring for Reinforcing Bars in Concrete, *Corrosion Rates of Steel in Concrete*, ASTM STP 1065, (N. S. Berke, V. Chaker, and D. Whiting, eds.), pp. 103–117, ASTM, Philadelphia, PA (1990)

80. Lemoine, L., Wenger, F., and Galland, J., Study of the Corrosion of Concrete Reinforcement by Electrochemical Impedance Measurement, *Corrosion Rates of Steel in Concrete*, ASTM STP 1065, (N. S. Berke, V. Chaker, and D. Whiting, eds.), pp. 118–133, ASTM, Philadelphia, PA (1990)

81. Alonso, M. C., and Andrade, C., Corrosion of Steel Reinforcement in Carbonated Mortar Containing Chloride, *Advances in Cement Research 1*, pp. 155-163 (1988)

82 Crentsil, K. K. S., Glasser, F. P., and Irvine, J. T. S., Electrochemical Characteristics of Reinforced Concrete Corrosion as Determined by Impedance Spectroscopy, *British Corrosion Journal*, 27:113–318 (1992)

83. Crentsil, K. K. S., Yilmaz, V. T., and Glasser, F. P., Impedance Spectroscopy Analysis of the Influence of Superplasticizers on Steel Corrosion in OPC Mortar, *Journal of Materials Science*, 27:3400–3404 (1992)

84. Hachani, L., Carpio, J., Fiaud, C., Raharinaivo, A., and Triki, E., Steel Corrosion in Concrete Deteriorated by Chlorides and Sulfates: Electrochemical Study Using Impedance Spectrometry and Stepping Down the Current Method, *Cem. Concr. Res.*, 22:57–66 (1992)

85. Hachani, L., Fiaud, C., Triki, E., and Raharinaivo, A., Characteristics of Steel /Concrete Interface by Electrochemical Impedance Spectroscopy, *British Corrosion Journal*, 29:122–127 (1994)

86. Wheat, H. G., Corrosion Rate Determination on Repaired Reinforced Concrete Specimen, Corrosion Rates of Steel in Concrete, ASTM STP 1065, (N. S. Berke, V. Chaker, and D. Whiting, eds.), ASTM, pp. 52–65, Philadelphia, PA (1990)

87. Andrade, C., Merino, P., Novoa, X. R., Perez, M. C., and Soler, L., Passivation of Reinforcing Steel in Concrete, *Materials Science Forum*, 192–194:891–898 (1995)

88. Cole, K. S., and Cole, R. H., Dispersion and Absorption in Dielectrics I. Alternating Current Characteristics, *J. Chem. Phys.*, 9:341–351 (1941)

@Seismicisolation

89. Bonanos, N., Steele, B. C. H., Butler, E. P., Johnson, W. B., Worrell, W. L., MacDonald, D. D., and McKubre, M. C. H., *Application of Impedance Spectroscopy*, Ch. 4, (J. R. McDonald, ed.), Wiley & Sons, NY (1987)

90. Sluyters-Rehbach, M., and Sluyters, J. H., in *Electroanalytical Chemistry*, 4:1–125, (A. J. Bard, ed.), Marcel Dekker, New York (1970)

91. Gu, Ping, Hristova, R., Elliott, S., Beaudoin, J. J., Brousseau, R., and Gartner, J., Evaluation of Corrosion Inhibitors in Chloride Contaminated Concrete by A.C. Impedance Spectroscopy, *Journal of Material Science*, In Press (1997)

92. Ehrlich, S. G., and Rosenberg, A., Methods of Steel Corrosion Control and Measurement in Concrete, *Materials Science of Concrete II*, (J. Skalny, and S. Mindess, eds.), pp. 201–219, The American Ceramic Society, Inc. (1991)

93. Andrade, C., Maribona, I. R., Feliu, S., Gonzales, J. A., and Feliu, S. Jr, The Effect of Macro-Cells Between Active and Passive Areas of Steel Reinforcements, *Corrosion Science*, 33(2):237–249 (1992)

94. Dawson, J. L., et al., Electrochemical Methods for the Inspection and Monitoring of Corrosion of Reinforcing Steel in Concrete, *Corrosion of Reinforcement in Concrete Structures*, (C. L. Page, K. W. J. Treadaway, and P. B. Bamforth, eds.), pp. 358–371, Published for the Society of Chemical Industry by Elsevier, London (1990)

95. Hardon, R. G., et al., Relationship between Electrochemical Noise and Corrosion Rate of Steel in Salt Contaminated Concrete, *Br. Corrosion J.*, 23:225–228 (1988)

96. Williams, D. E., Stewart, J., and Balkwill, B. E., Proceedings of the Symposium on Critical Factors in Localized Corrosion, (G. S. Frankel, and R. C. Newman, eds.), *ECS*, 92-9:36 (1992)

97. Eden, D. A., and Rothwell, A. N., Electrochemical Noise Data: Analysis and Interpretation, Paper 92, Corrosion 92, NACE, Houston, TX (1992)

98. Searson, P. C., and Dawson, J. L., *Journal of the Electrochemical Society*, 135:1908–1915 (1988)

99. Hladky, K., and Dawson, J. L., *Corrosion Science*, 21:317–322 (1982)

100. Hladky, K., and Dawson, J. L., *Corrosion Science*, 22:231–237 (1982)

@Seismicisolation

13

Surface Area Measurements

Jan Skalny and Nataliya Hearn

1.0 INTRODUCTION

Surface size and surface quality are two of the most important parameters of organic and inorganic solid materials. Surfaces of most solids, in tandem with other basic materials properties and environmental conditions, control to a large degree the rate of the relevant chemical and/or physicochemical reactions, thus the behavior of the material in real-world applications. The degree of this control relates to the *surface area* of the reacting material(s), aided by their *reactivity*—a quality depending on the crystallographic and other basic physical and chemical properties of the reacting solid.

Specific surface area is defined as the surface area per unit of mass, typically expressed in square centimeters per gram (cm^2/g) or square meters per kilogram (m^2/kg). Specific surface area depends on the particle size, particle shape, and any imperfections or flaws present at the surface. Although not linearly related, knowledge of the surface area of a system of particles (and assuming that they are monosized, nonporous spheres) allows estimation of the average particle size of the powder and vice versa. The *particle size* of a solid body depends on the degree of natural or man-made growth or size-diminution. A larger particle will have a larger mass and volume per unit of surface area than a smaller particle. When a larger

@Seismicisolation

particle is subdivided into smaller particles by cutting, grinding, or other similar process, the total surface area will dramatically increase. For example, division of a 1 m^3 cube into one micrometer cubed particles would increase the surface area from 6 m^2 to 6×10^6 m^2, a millionfold increase.

The surface area of a solid also depends on the shape of the particle which, theoretically, can vary from a perfect sphere (minimum surface area-to-volume ratio) to a collection of atoms bonded along a one-dimensional chain (maximum surface area-to-volume ratio). The particle shape of real-world particles lies between these two extremes and so does the related surface area. Exact determination and classification of the three-dimensional shape of a particle is difficult; the best approximation is achieved by two-dimensional evaluation by means of computerized image analysis.

In addition to its size and shape, the surface area of a particle depends on the amount, size and shape of the flaws (surface imperfections), varying from visible flaws to flaws at the atomic or crystal lattice level. Porosity of a particle can be then defined as the volume of those surface flaws which have a depth greater than the width.[1] Depending on the size and shape of the flaws or pores, the surface area of a solid can vary widely and the influence of flaws/pores can often overwhelm other factors controlling the surface area. Because of the above phenomena, the technical literature often distinguishes between internal and external surface area and between surfaces (often expressed in terms of porosity) accessible or inaccessible to certain chemicals or measurable by a particular methodology.

Considering the above, it is clearly understandable that surface area is much more influential with respect to the properties of a material in highly divided or dispersed solids with higher concentrations of flaws and pores than in a coarse material with lesser concentration of flaws and pores. Thus, for example, the surface of a concrete aggregate is less important with respect to concrete properties than is the surface area, thus reactivity, of the cement. Another example: it is the grinding of the clinker granules to high surface area that enables production of a highly reactive portland cement.

It is important to realize that the value of the measured surface area will depend on the experimental technique used to measure it. For example, as discussed in Sec. 2.1, the surface area measured by gas adsorption techniques such as BET method[2] will vary with the quality (cross-sectional area and other properties of the molecule) of the gas used as the sorbate. In a similar manner, the surface area of a powder calculated from particle size distribution measurements will differ from the surface area of the same powder estimated on the basis of image analysis techniques. Other examples abound.

@Seismicisolation

Please note that some of the test methods described in this chapter overlap with the measurements of porosity and pore size distribution discussed elsewhere. This overlap is caused by the inherent relationship between porosity, pore size distribution, and surface area.

It is impossible to discuss all available techniques in detail. Each section, therefore, contains references to the original publications or a more detailed text for specifics in the derivation and application of each method.

1.1 The Importance of Surface Area in Cement/Concrete Science and Technology

Treval C. Powers and Stephen Brunauer were among the first who recognized the extraordinary importance of surfaces in explaining the complex phenomena leading to the development and degradation of physical properties of cement-based material. The rates of hydration reactions of individual components of portland and other cements are related to the surface area of the particular cement, thus controlling the rate of development and the quality of the desired physical properties. This is true in particular for the calcium silicate components of the portland cement clinker, tricalcium silicate (alite, Ca_3SiO_5) and dicalcium silicate (belite, beta-Ca_2SiO_4), both of which hydrate to form high-surface area calcium silicate hydrates (C-S-H, the "heart of concrete"),[3]] the most important component of the portland cement paste.[4] It is the semi-amorphous structure of the C-S-H and its complex porosity and high surface area that are mostly responsible for the time-dependent engineering properties of concrete, e.g., volume stability, strength, and modulus of elasticity.

It should be recognized, however, that surface area alone is not an adequate measure of the quality or reactivity of a material. For example, it is known that two cement clinkers made from the same raw material, but in two different kiln systems, may produce clinkers that when ground to the same surface area will have different rates of reaction with water. This is related, among other factors, to the differences in the flaws concentration, thus surface quality.[5][6] Presence of heat-induced crystal lattice defects in the clinker minerals such as C_3S and C_3A influences the reactivity of the clinker and the resulting cement. In a similar fashion, clinker quality may be modified by introduction of flaws due to rapid rate of cooling or the intensity of grinding.

@Seismicisolation

Conversely, it is the quality of the cement paste, primarily its porosity and permeability, that controls the rate of concrete deterioration. Whether the concrete deteriorates due to physical processes (e.g., freezing-thawing,) or chemical reasons (such as sulfate attack, acid attack, or alkali-silica reaction), the overall porosity and its distribution are crucial in controlling the time dependency of the damage. At a more technical level it is the increase in the liquid-accessible pore surface area as well as the rate of movement of moisture through the concrete rather than the porosity itself that cause a highly porous and permeable concrete to deteriorate at a rate higher than a less porous, less permeable concrete.

The importance of surface area as a measure of cement quality is widely recognized by the research and business communities and by ASTM, CSA, CEN, and other standardization organizations; for example, ASTM requires all cement types to pass certain minimum surface area (fineness) requirements, thus helping the cement producer and user to control the product quality.[7] On the other hand, the practical importance of the surface area of the hydration products formed as a consequence of the water-cement reactions is much less appreciated by the typical field engineer and some of the underlying details and principles are still not completely understood.

On the following pages a brief review of the most common techniques of surface area determination is presented. The review is not meant to be a comprehensive state-of-the-art compilation of the existing knowledge, just a brief introduction to the most important approaches used. The methodologies discussed include air permeability methods, methods based on particle size distribution, gas adsorption techniques, and scattering techniques.

2.0 TECHNIQUES OF SURFACE AREA MEASUREMENT

In the area of cement and concrete research, two main types of materials need to be characterized: powder materials such as cement, fly ash and silica fume (microsilica), and solid materials such as hardened cement paste and concrete.

The surface area of the powder material is of importance due to its effect on the reactivity. That is why the rapid-hardening portland cement (ASTM Type III) has a specific surface area of 450 to 600 m^2/kg as compared to 250 to 400 m^2/kg for ordinary portland cement (ASTM Type I). Measurement of the surface area of powders is dependent on the particle

@Seismicisolation

size, with coarser powders measured using sedimentation or elutriation (such as Wagner turbidimeter—ASTM C115-93). For cements, air permeability—Blaine method (ASTM C204-94), which is a modified Lea and Nurse method, is used to determine surface area. For powders finer than portland cement (silica fume or fly ash) nitrogen adsorption or mercury intrusion porosimetry are used to determine the surface area.

The hydration process increases the surface area as the fragile calcium silicate hydrate gel structure is formed. Figure 1 shows the increase in the surface area with the progress of hydration. The surface area of hydrated cement paste is a thousand times greater than that of the unhydrated cement with the reported values dependent on the measurement technique used and sample conditioning. For instance, the water adsorption results yield surface area of 200,000 m^2/kg,[8] while x-ray scattering gives 600,000 m^2/kg.[9]

Because concrete is by nature an inhomogeneous material, sample preparation often damages the finest portion of the pore structure and many test methods use only very small samples, it is very difficult to obtain statistically significant results. Also, to further complicate the situation, the pore sizes and surfaces to be measured span several orders of magnitude.

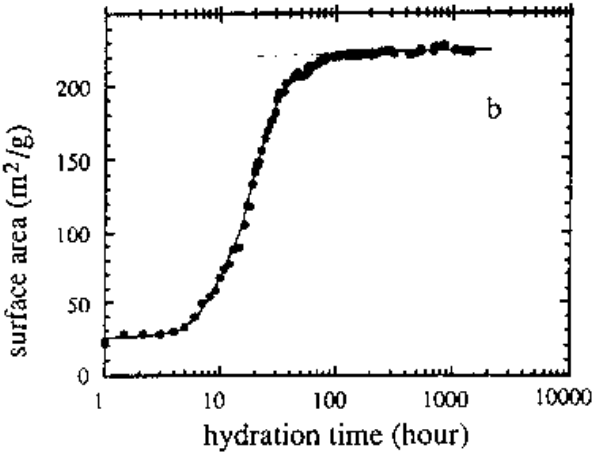


Figure 1. Total surface area as a function of hydration time.[10]

To overcome these difficulties, several techniques based on different principles were developed over the years. Some of these techniques measure the resistance of a material to flow of an inert gas/liquid or the adsorption of

@Seismicisolation

gases and vapors, some measure the porosity by monitoring the pore size filled with a liquid at an applied pressure, and others use the deflection of electron and neutron beams.

2.1 Gas Sorption Techniques

Gas sorption techniques are based on physical adsorption of gases or vapors on surfaces of solids. In contrast to chemical adsorption, also called chemisorption or irreversible adsorption, during physical adsorption the sorbed molecules are not restrained to specific sites on the surface of the measured solid and are free to cover the whole surface. For this reason, determination of surface areas is possible.

Physical adsorption is fully reversible and, with the exception of small pores, equilibrium can be easily achieved since no activation energy is involved. Because physical adsorption does not occur at elevated temperatures, sufficiently clean surfaces can be prepared prior to the actual low-temperature surface area measurements.

Although numerous methods for surface area measurements based on physical adsorption of gases were developed, the best known method for determination of surface areas of porous solids is the so-called BET method grounded on the work of Brunauer, Emmett, and Teller.[2][3] Since its development in the late 1930s, this method became the most universally used method for surface area determination of such diverse materials as catalysts, carbon blacks, finely divided silica, and hydrated cement pastes and components. The BET methodology gives surface areas two to three times higher than the Lea and Nurse and Blaine methods discussed above.

The term *sorption* is used to describe the interaction of a gas with a solid surface; this interaction may be in the forms of adsorption, absorption, or capillary condensation. When a gas is removed from a surface the process is called *desorption*. The gas interacting with the surface is usually referred to in the literature as a *sorbate*.

The BET method as well as some previous related work is based on the experimental establishment of the relationship between the pressure of a gas that is in equilibrium with a solid surface and the volume of the gas adsorbed at the particular pressure at the surface. The theoretical basis for this approach is the Langmuir theory based on the kinetic theory of gases.[11][12]

Gas sorption techniques are based on the assumption that gas molecules are strongly attracted and adsorbed on a virgin surface. The method assumes also that the sorbent molecules have access to the walls of the pores

@Seismicisolation

within the studied solid and that the distance between the walls of a pore is large when compared to the molecular dimensions of the sorbate. As a monolayer of the sorbent gas forms on the surface the repulsion of the previously adsorbed gas molecules makes the formation of a second and subsequent layers less likely. This process is gas pressure dependent, thus with increased relative pressure the degree of gas adsorption increases. Gas molecules may be adsorbed in subsequent layers before the underlying layer is completely covered.

The BET Method. To enable generalization of the Langmuir's approach to multilayer adsorption, the BET theory makes two basic assumptions regarding the heat of adsorption:

1. It is constant throughout the formation of the first layer of adsorbed gas.
2. In the second and higher layers it is equal to the heat of liquefaction.

More about the accuracy of these BET assumptions can be found in Refs. 2, 12, and 13.

A plot of the amount of gas adsorbed at a certain temperature against the relative pressure is called a *sorption isotherm*. It is usually presented as the volume of adsorbed gas versus the relative pressure, p/p_o, see Fig. 2.[12]

From such a plot the amount of gas needed to form a monolayer can be determined and, assuming the cross-sectional area of the sorbate molecule, the surface area of the measured solid can be calculated. The relative humidity at which a monolayer completely covers the solid surface depends both on the nature of the used sorptive gas and the nature of the solid. Table 1 gives the approximate cross-sectional areas of some commonly used sorbates.

Because the capillary condensation in a set of pores of certain size at adsorption does not occur exactly at the same relative pressure as capillary evaporation from the same pores at desorption, the combined adsorption-desorption isotherms may, and usually do, show a hysteresis. A schematic example is shown in Fig. 3.[15] Several types of adsorption-desorption isotherms were identified.[16]

The BET equation can be given as:

$$v/v_m = ckx/(1 - kx)\,[\,1 + (c - 1)\,kx]$$

or in its linear form as:

$$kx/v(1 - kx) = (1/v_m c) + [(c - 1)/v_m c]kx$$

@Seismicisolation

where: x is the relative pressure, p/p_o
k is a number smaller than 1 (see Ref. 11)
c is the BET ("adsorption coefficient") constant
v_m is the volume of the sorbate at monolayer coverage
v is the volume of the adsorbed sorbate

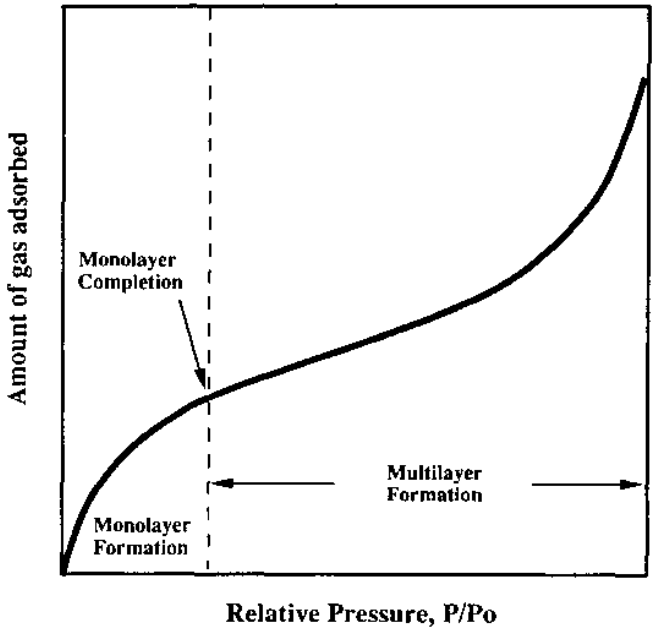


Figure 2. Sorption isotherm for a planar surface (adopted from Ref. 12, Fig. 2).

Table 1. Most Commonly Used Sorbates

Sorbate	Area in Å
Argon	14.2
Benzene	40.0
Nitrogen	16.2
Oxygen	14.1
Water vapor	10.8
Xenon	2.5

@Seismicisolation

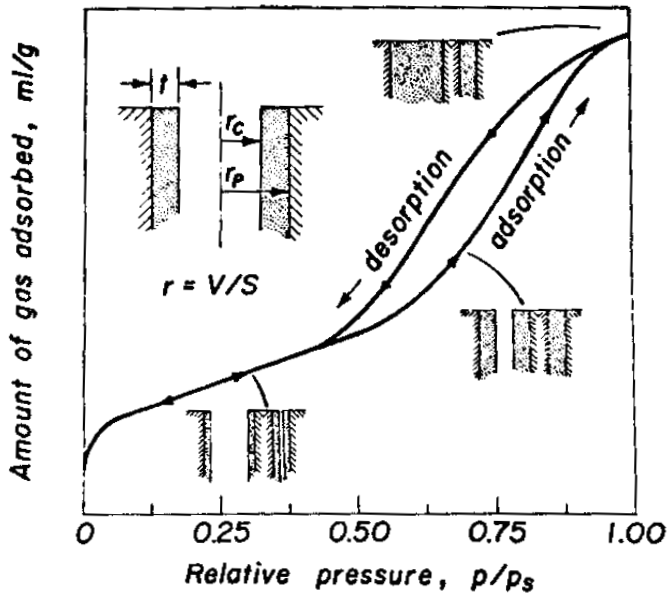


Figure 3. Adsorption isotherm showing capillary condensation (Fig. 1, Ref. 15).

The actual analysis is usually done by plotting $x/[v\,(1 - x)]$ against x for the linear (multilayer adsorption) region of the isotherm. This plot, referred to as the BET plot, is fitted with a least-square algorithm. The equations for the slope (S_{BET}) and intercept (I_{BET}) of the BET plot are given as:

$$S_{BET} = (c - 1)/v_m c$$

$$I_{BET} = 1/v_m c$$

The BET method is applicable for solids with pore diameters from above ~4 nm. Below 8 nm the calculations are believed to be inaccurate. It is accepted that BET gives the most accurate results for the mesopores (160 nm to about 10,000 nm). The range of relative humidities (p/p_o) at which the BET method applies is from about 0.05 to 0.35. For additional information see, for example, Refs. 12, 17, and 18.

@Seismicisolation

The BET method has been used in cement science for several decades now. Whereas the technique enabled better understanding of the nature of the hydration products and of the mechanisms of hydration, it also led to controversies regarding the best sorbate to be used in determination of the "true" surface area of the hydrates.

The sorbates used most often are water vapor and nitrogen, neither of which can measure accurately all the surface area located in the complex pore system. Water sorption may give erroneous results due to the possible adsorption of the polar water molecules within the vacated interlayer spaces of C-S-H. Nitrogen (N_2) and other nonpolar sorbents, on the other hand, may give much lower surface areas; this phenomenon is related, among other reasons, to the failure of these nonpolar sorbents to reach the surface of the pores of certain size or shape (e.g., so-called ink-bottle pores). For more information, see Refs. 12, 15, and 19. The differences can be quite substantial. BET surface areas computed from N_2 adsorption isotherms are between 13,000 and 84,000 m^2/kg, while calculations made from the water adsorption isotherms are about 200,000 m^2/kg. Oxygen, argon, and organic vapors (cyclohexane and isopropanol), give results similar to the N_2, and methanol, 50,000 to 114,00 m^2/kg.[20] The preparation of specimens for the adsorption methods requires drying. Techniques which do not require pre-drying of specimens, such as small angle x-ray scattering, small angle neutron scattering, and nuclear magnetic resonance, show that 200,000 m^2/kg obtained by water BET is up to three times lower than the surface area of saturated specimens (Table 3).

The primary advantage of the BET method is its capability of measuring disconnected microcracks and cracks that are open only at one end. The main disadvantage is its complexity—it requires skilled labor and is time consuming; however, automated BET equipment is now available for routine use. The method does not make any assumptions regarding the pore size or pore size distribution.

At relative pressures higher than about p/p_o above 0.35–0.40, capillary condensation can take place and pore size distribution can be obtained from Kelvin equation linking the vapor pressure of the sorbate with curvature of the meniscus formed by the liquid inside the pores. Several approaches to complete pore structure analysis were developed.[15][21] In most such calculations assumptions must be made about the shape of the pores.

@Seismicisolation

2.2 Mercury Intrusion Porosimetry (MIP)

One of the best known techniques used for determination of particle size or pore size distribution that can also be used to indirectly determine the surface area is the Mercury Intrusion Porosimetry. MIP is based on the relationship between pressure and the corresponding volume of pores filled with a non-wetting liquid. Due to the high pressure needed to infiltrate the pores, this method is applied mainly to hydrated cement paste and concrete both of which can withstand the applied pressure without much damage to the measured microstructure.

The liquid typically used is mercury. It is a non-wetting liquid having a contact angle with concrete of 130–140°. The applied pressure and the resulting volume of mercury entering the tested material can be related to the pore diameter and the amount of pores of the particular size:

$$\left|2 \cdot \gamma \cdot \cos \theta\right| = P \cdot r$$

where: γ is the surface tension of mercury
θ is the contact angle
P is pressure
r is the radius of pore

The method uses two major assumptions: *(i)* the surface tension and the wetting angle are constant throughout the tested specimen, and *(ii)* all pores have the shape of an ice cream cone. The first assumption may not be accurate because the contact angle changes with the changing pore solution in the tested material. The second assumption causes the space behind the neck of the ink-bottle to be treated as a cylinder with radius of the pore opening.

The pressures typically applied during testing ranges from 0.5 psi (~3,800 Pa) to about 60,000 psi (~45 MPa). These pressures allow the measurement of pores from about 2 nm to about 20 μm.[22]–[24] The upper limit on the pressure used for testing is set to limit the damage caused to the pore structure damage.

MIP is one of the more useful methods because it enables measurement of porosity over several orders of magnitudes; however, the range of pores present in hydrated portland cement or concrete is wider than what can be measured by MIP. Smaller pores are not detected due to the restraint on the applied pressure, whereas larger pores are misrepresented because it is

@Seismicisolation

difficult to define boundaries between the largely interconnected pores.[25] Furthermore, MIP does not measure the true pore distribution, but rather, indicates the accessibility to mercury of the overall porosity as a function of pore size. This is a form of invasion percolation.

The use of MIP requires complete drying of the pore structure. This process damages the microstructure and subsequent measurement of the surface area may yield erroneous results.

As with many other techniques used to measure surface area the tested sample is typically very small, on the order of a few grams. One has to, therefore, bear in mind the possible analytical errors, the heterogeneity of concrete and of the other measured solids, and the statistical significance of the obtained results.

Rootare and Prenzlow derived another method for surface area measurement using mercury.[26] This method is based on the amount of work (given by the area under the pressure vs. volume curve) needed to cover the surface of the examined solid with mercury. This method requires no assumptions regarding the pore shape distribution; however, it has been thirty years since its development and it has been hardly used.

2.3 Wagner Turbidimeter

The primary use of this technique is in measurement of surfaces of powders. The Wagner turbidimetry is based on measurement of the terminal free fall velocity governed by Stoke's law. By using a beam of light, the concentration of particles suspended in kerosene is measured by determining the percentage of light transmitted through the suspension to a photocell.[27] The method was adapted by ASTM as Standard Test Method C 115.

The technique usually gives consistent results, the main error being the assumption of uniform distribution of particles smaller than 7.5 μm. The use of the average particle size of 3.8 μm below the 7.5 μm is an overestimation resulting in the lower calculated surface area. The assumption that the average particle below 7.5 μm is 3.8 μm is overestimated; thus the calculated surface areas are too low. Because it is these finest pores that govern the specific surface area, their influence on the calculated results is overwhelming; a modification to reduce this error was proposed by Hime and LaBonde.[29]

Both MIP and Wagner Turbidimeter results have to be recalculated into specific surface area using the equation:

@Seismicisolation

$$S = 6 \cdot 10^6 \cdot F \cdot \frac{\sum f}{d \cdot \rho}$$

where: S is the specific surface area in $m^2\ kg^{-1}$

F is an empirical constant that takes into account the assumed pore shape distribution specific surface area

f the weight fraction of material consisting of grains assumed to have a diameter d, in μm

r is the density, given in $kg\ m^{-3}$

These techniques of surface area measurement do not always yield satisfactory results because, among other reasons, the specific surface area is highly dependent on the assumed particle or pore shape distribution. More about these techniques is given in Ch. 14.

2.4 Permeability Methods

Permeability measurements are applicable for situations when the flow through a material is caused mainly by pressure gradient. If this assumption is true, permeability is the property of a porous material which characterizes the ease with which a fluid may be made to flow through the material. The coefficient of permeability can thus be related to the surface area of the tested material.

The relationship that governs the flow through porous media was developed first by H. Darcy in the late 1800s.[30] Originally, it was meant to define the flow of water through sand.

The principal equation is given as:

$$Q = A \cdot \frac{k \cdot \Delta P}{\Delta L}$$

where: Q is the flow rate

A is the cross-sectional area

$\Delta P / \Delta L$ is the pressure gradient.

Lea and Nurse applied Darcy's law to describe the surface area of materials.[11] They developed an apparatus which measures steady state flow of air through a bed of material with known porosity. The surface is then calculated as:

@Seismicisolation

$$S_w = \frac{14}{\rho \cdot (1-\varepsilon)} \cdot \sqrt{\frac{\varepsilon^3 \cdot A \cdot h_{11}}{K \cdot L \cdot h_2}}$$

where:
- ρ is the density of cement
- ε is the porosity of cement bed (0.475 in the British Standard test)
- A is the cross-sectional area of the bed (5.066 cm^2)
- L is the height of the bed (1 cm)
- h_1 is the pressure drop across bed
- h_2 is the pressure drop across the flowmeter capillary (between 25 and 55 kerosene)
- K is the flow meter constant

Blaine modified the Lea and Nurse method; instead of measuring pressure drop during the steady state flow, the Blaine approach measures the pressure change as a specified volume of air passes through the tested material.[31]

The Lea and Nurse and Blaine methods yield similar results, but because both of them measure only the interconnected pores the surface areas are low compared to some other techniques. By leaving out the disconnected pores, especially the very small pores which are highly desirable in good quality concrete, they underestimate the magnitude of the surface area.

The Blaine method is used as the standard method to measure the fineness of cement in North America.[32] It has two main advantages: the method is simple and fast. The main disadvantage, not critical in determination of cement fineness, is its poor accuracy which becomes worse with increasing variability of the particle size, pore tortuously, and surface area. Due to these factors the Blaine method becomes extremely unreliable at surface areas exceeding 500 m^2/kg.

The use of permeability methods requires complete drying of the pore structure. This process damages the microstructure and subsequent measurement of the surface area yield erroneous results. This is one of the reasons that it is primarily used to measure fineness of cements and other dry powders, but not surfaces of hydrated materials or materials that have to be dried.

Table 2 shows the surface area of two types of cements measured using the above described methods.

@Seismicisolation

Table 2. Surface Area of Cements (m^2/kg) [Adapted from Ref. 33]

Cement	Wagner Method	Lea & Nurse Method	Nitrogen Adsorption
I	179	260	790
II	227	415	1000

2.5 Small Angle X-Ray Scattering (SAXS) and Small Angle Neutron Scattering (SANS)

The basic principle of SAXS and SANS is the scattering of the beam of radiation as it passes through a material. At low angles the scattering is particularly noticeable and can be monitored to describe the inhomogeneities or boundaries in a two phase system (e.g. solid and air, or solid and water). Figure 4 shows schematics of an x-ray scattering arrangement. The detailed explanation of the theory and treatment of SAXS and SANS data can be found in Refs. 34 and 35. In brief, the interpretation of the x-ray or neutron scattering for calculating specific surface area is based on the Porod's theory.[36] The theory is based on the scattering purely by the interfaces where a sharp boundary between phases exists. In cementitious systems other sources of scatter exist, such as pore fluid in the gel spaces, so that the data has to be corrected by subtracting the non-boundary scatter. Mathematical models for interpretation of the experimental data are needed[37] and work has been done relating SAXS data and fractal geometry.[38]

The main advantage of the scattering techniques for measurement of the specific surface area is that they do not require any drying or pretreatment of the samples, thus measuring unaltered microstructure of the cementitious systems.[39] The x-ray and neutrons can readily penetrate small size pores which are inaccessible to nitrogen and mercury with SAXS lower limit of detection of 30 nm and SANS of 0.1 nm.

Extensive work by Winslow and Diamond using SAXS to analyze the effect of pretreatment conditioning on the pore structure characterization of hydrated cement pastes has shown the effectiveness of the technique to assess the evolution and destruction of the surface area. Their results are shown in Table 3.

@Seismicisolation

Table 3. Surface Area of Cement Pastes of Different w/c Ratios and in Saturated and Dry Conditions[9]

w/c	Age (days)	Hydration (%)	Condition	Surface Area (m^2/g)
0.3	513	78	Saturated	527
0.3	513	78	D-dried	159
0.4	514	86	Saturated	708
0.4	514	86	D-dried	224
0.6	512	91	Saturated	782
0.6	512	91	D-dried	284

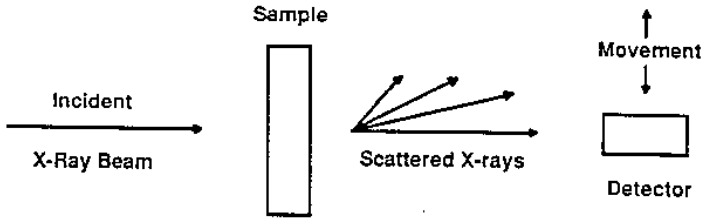


Figure 4. Schematic of scattering arrangement.[39]

2.6 Nuclear Magnetic Resonance (NMR)

One of the new techniques for determination of the total pore volume and surface areas is NMR, specifically the technique referred to as spin-spin relaxation.[10][40] The method is based on the relaxation of longitudinal or transverse magnetization at the interface between a solid and the liquid, in other words, on the dependence of the exact resonance frequency upon the local magnetic field.

Because the measured relaxation is surface dominated, the NMR experiments enable determination of the total surface area and of the distribution of the surface-to-volume ratio, in other words, of the pore volume distribution function. In theory, interconnected pore structure can be completely characterized by surface-to-volume ratio. The method may be used for saturated samples, does not require drying of the sample, thus damage to the pore structure is not an issue and the volume of the fine pores can be accurately measured.

@Seismicisolation

The NMR theory is quite complex. Its use for surface area determination is based on two principles:

- In the region containing evaporable water, the first molecular layer on the hydrated surface has a uniform, well-defined relaxation time
- All conditions for fast exchange of water present in the first surface layer and of the remaining evaporable water in the pore structure are met

The absorption spectrum of a material will depend on the environment of the protons in the sample, thus the technique allows estimation of the water mobility or its state in the sample. For more information, see Ref. 41.

2.7 Image Analysis

Image analyses of visible light (optical) or backscattered electron images of specially pretreated samples can be, in principle, used for determination of pore size distributions and surface areas. However, as discussed elsewhere in this book (Ch. 19), in addition to some advantages (e.g., no need for drying), the technique suffers from several disadvantages:

- Two-dimensional images have to be recalculated into three-dimensional pore distribution data
- The visible pore images do not represent reality because the measured cross-sections are smaller than the cross-section at the maximum pore diameter
- Inadequate resolution of the instrumentation at high magnifications
- Limitation on the number of displayable pixels

Because of these and some other reasons, at this stage of development, estimation of surface areas from pore size distributions based on image analysis is not practical and is not used routinely.[42][43]

3.0 APPLICATIONS

Knowledge of the surface area is of utmost importance in many concrete-related applications. Whereas some of the techniques discussed

@Seismicisolation

above are routinely used in the production and quality control/assurance others are of interest only at the scientific level and in the development of new products. The following paragraphs will give a few, very superficial examples of such applications; the list is certainly not complete and serves only as a reminder of the importance of surfaces in better understanding and control of materials properties.

Cement Raw Meal. The quality of a cement clinker and the productivity of its manufacturing depends among others, on the rate at which the components of the raw meal are transformed during its burning into the clinker of desired quality. Under otherwise constant conditions the raw meal-to-clinker transformation depends on the surface area of the kiln feed. Knowing the differences in the reactivity of the raw meal components—for example the relative reactivates of the carbonaceous versus siliceous versus iron-containing components—the fineness of the kiln feed can be adjusted to give a surface area that will guarantee a burning rate acceptable from both economic and technical points of view.

For the above reasons the surface area of the kiln feed is closely monitored, primarily by control of its particle size, a measure of the available reactive surface.

Concrete Mixture Components. The concrete mixture components for which surface area plays a crucial role are the cement and mineral admixtures, such as fly ash, condensed silica fume (microsilica), and granulated blast furnace slag. The quality and quantity of the fine and coarse aggregate surface are important, however, to a lesser degree than the above components. The reason for this is the fact that whereas the cementitious materials participate in chemical reactions of hydration (reactions between water and the components of cement, blending materials, and chemical admixtures), the aggregate surface can be under most conditions considered to be inert.

Based on this knowledge, the concrete manufactures expect to receive from the materials suppliers cement and mineral admixtures that conform to the codes and the standards requirements, and enable them to produce high quality concrete (primary requirement) within the essential time and budget (secondary consideration).

The most common techniques of mixture components surface area evaluation are particle size measurements and air permeability techniques.

Hydrated Portland Cement and Concrete. As implied above, surface area plays a most important role in chemical reactions that lead to development of concrete properties. Whereas the surface area of the anhydrous cement compounds does affect the rate at which a given cement

@Seismicisolation

contributes to the development of the concrete engineering properties, it is the surface area and other qualities of the newly formed hydration products that are responsible for the microstructural behavior and physical performance of concrete.

The cement paste component of most influence on concrete properties is calcium silicate hydrate, C-S-H. It constitutes about 50–60% of the volume of the solids in a fully hydrated cement paste and its surface area, depending on the conditions of its formation (temperature, humidity, water-to-cement ratio, etc.), and the type of measuring technique, is reported to vary between 10 and more than 250 square meters per gram. Most literature data agree today that the surface area of a fully hydrated, D-dried portland cement paste is about 200 $m^2 g^{-1}$.[31] However, values as high as 700 to 800 $m^2 g^{-1}$ per ignited weight were obtained using small angle x-ray scattering.[45]

The primary properties of concrete that are influenced by the surface area of the C-S-H are the dimensional changes, creep, strengths, and modulus of elasticity. This is related to the structure and composition of the C-S-H, in particular to the movement of water between and within the C-S-H particles.[4][31]

Because of this importance, the issue of the surface area of C-S-H and cement paste is an important topic of research for several decades, and many of the obtained results remain controversial.[25] Different experimental techniques give different results and some of the data interpretations are inconsistent and confusing. This is not only related to the differences in the measurement principles of the individual techniques, but also to the fact that the chemistry and fine internal structure of the C-S-H and thus, its "true" surface area, are unknown. Also unknown are the basic differences between the surface properties of the individual forms of C-S-H that can be observed by electron microscopic techniques (e.g., the so-called "inner" versus "outer" C-S-H product).

As mentioned earlier, the most common classical research technique for determination of surface areas of cement paste and hydration products is the BET technique.[2][3] Primarily water vapor and nitrogen, but also other gases are used as sorbents. In recent years, these gas adsorption techniques were supplemented by others, such as SANS, SAXS, and NMR, discussed in more detail above. Novel data are being obtained, but clear and experimentally proven interpretations are lacking.

Concrete Durability. In a sense, deterioration of concrete is the reverse process when compared to the hydration reactions. In the former case, discussed above, the chemical reactions lead to formation of a

@Seismicisolation

microstructure that controls or guarantees certain mechanical properties of the concrete. In the latter case the chemical reactions lead to destruction of the previously formed microstructure by transformation or decomposition of the matrix components from those possessing cementitious properties, primarily of C-S-H, to new compounds that do not possess them.

Because, as discussed earlier, the accessibility to liquids of the surface area in cement-based materials is closely dependent on the porosity and its structure (pore structure, spatial distribution, connectivity), the rate of concrete deterioration by most if not all of the possible mechanisms of chemical deterioration is porosity dependent (e.g., alkali-silica reaction, alkali-carbonate reaction, sulfate attack, acid attack). Thus, stated in a somewhat oversimplified form, the durability is controlled by the water-to-cement ratio.

The absolute size of the surface area exposed to chemical reactions of deterioration and its time dependency are difficult to measure or are not needed, thus the most common modes of evaluation of the deterioration rate are the changes in porosity, pore structure, water or certain ions permeability, and vapor transmission. These methods constitute an indirect measure of the effects of the reacting surfaces.

REFERENCES

1. Lowell, S., *Introduction to Powder Surface Area,* John Wiley & Sons, New York (1979)
2. Bruanuer, S., Emmett, P. H, and Teller, E., Adsorption of Gases in Multi-Molecular Layers, *J. Am. Chem. Soc.*, 60:309 (1938)
3. Brunauer, S., *The Adsorption of Gases and Vapors*, Oxford University Press, London (1943)
4. Skalny, J., and Young, J. F., Mechanisms of Portland Cement Hydration, Vol. I, *Proc.7th. Int. Symp. Chem. Cem.*, Paris, II-1/3 (1986)
5. Sakurai, T., Sato, T., and Yoshinago, A., The Effect of Minor Components on the Early Hydraulic Activity of Portland Cement Clinker, *Proc. 5th. Int. Symp. Chem. Cem.*, p. 300, Tokyo (1968)
6. Maycock, J. N., Skalny, J., and Kalyoncu, R., Crystal Defects and Hydration, I. Influence of Lattice Defects, *Cem. Concr. Res.*, 4:835 (1974), see also *ibid* 3:701 (1973)
7. ASTM, see for example the Standard Test Methods C 115-94, C 184-94, C 204-94a, C 430-94, and C 786-94.

@Seismicisolation

8. Powers, T. C., Structure and Physical Properties of Hardened Portland Cement Paste, *J. Amer. Ceramic Soc.*, 41:1–6 (Jan., 1958)
9. Winslow, D., and Diamond, S., Specific Surface of Hardened Portland Cement Paste as Determined by SAXS, *J. Amer. Ceramic Soc.*, 57:193–197 (May, 1974)
10. Halperin, W. P, .Jehng, Y-Y., Song, Y-Q, Application of Spin–Spin Relaxation to Measure of Surface Area and Pore Size Distribution in a Hydrating Cement Paste, *Magnetic Resonance Imaging*, 12(2):169–173 (1994)
11. Langmuir, I., The Adsorption of Gases on Plain Surfaces of Glass, Mica and Platinum, *J. Am. Chem. Soc.*, 40:1361–1403 (1918)
12. Rarick, R. L., Bhatty, J. I., and Jennings, H. M., Surface Area Measurement Using Gas Sorption: Application to Cement Paste, *Materials Science of Conc*, (J. Skalny, and S. Mindess, eds.), 4:1–40, The American Ceramic Society, Westerville, OH (1995)
13. Brunauer, S., Skalny, J., and Bodor, E. E., Adsorption on Nonporous Solids, *J. Coll. Interface Sci.*, 30:546–552 (1969)
14. Gregg, S. J., and Sing, K. S. W., *Adsorption, Surface Area, and Porosity* (2nd Ed.), Academic Press, New York (1982)
15. Brunauer, S., Skalny, J., and Odler, I., Complete Pore Structure Analysis, Pore Structure and Properties of Materials, *Proc. RILEM-IUPAC Int. Symp.*, Prague (1973)
16. Brunauer, S., Demming, L. S., Demming, W. S., and Teller, E., On a Theory of the Van der Waals Adsorption of Gases, *J. Am. Chem. Soc.*, 62:309–319 (1938)
17. DeBoer, J. H., *The BET Method International Symposium on the Surface Area Determination*,(D. H. Everett and R. H. Ottewill, eds.), Butterworths, London (1969)
18. Milburn, D. R., and Davis, B. H., Comparison of Surface Areas Calculated from Nitrogen Adsorption and Mercury Porosimetry, *Ceram. Eng. Proc.*, 14:130–134 (1993)
19. Taylor, H. F. W., *Cement Chemistry*, Academic Press, London (1990)
20. Mikhail, R. S., and Selim, S. A., Adsorption of Organic Vapors in Relation to the Pore Structure of Hardened Portland Cement Paste, Highway Res. Board, Spec. Rep. No. 90, p. 123 (1966)
21. Wheeler, A., *Advan.Catalysis*, 3:250 (1951)
22. Winslow, D., Some Experimental Possibilities with Mercury Intrusion Porosimetry, *Mat. Res. Soc. Symp. Proc.*, 137:93–103 (1989)
23. Milburn, D. R., and Davis, G. H., Comparison of Surface Areas Calculated from Nitrogen Adsorption and Mercury Porosimetry, *Ceram. Eng. Proc.*, 14:130–134 (1993)

@Seismicisolation

24. Diamond, S., Rapid Particle Size Analysis of Fly Ash with Commercial Laser Diffraction Instrumentation, *Mat. Res. Soc. Symp. Proc.*, 137:83 (1989)
25. Lange, D. A., Jennings, H. M., and Shah, S. P., The Influence of Pore Structure on the Properties of Cement Paste, *Mat. Res. Symp., Proc.*, 147:47–54 (1989)
26. Rootare, H. M., and Prenzlow, C. F., *J. Phys. Chem.*, 71:2733 (1967)
27. Wagner, L. A., A Rapid Method for Determination of Specific Surface Area of Portland Cement, Proceedings, *ASTM, ASTEA,* Vol. 33, Part II, p. 553, (1933)
28. Standard Test Method for Fineness of Portland Cement by the Turbidimeter, ASTM C 115-94, (1994)
29. Hime, W. G., LaBonde, E. G., Particle size Distribution of Portland Cement From Wagner Turbidimeter Data, *J. Protl. Cem.,* Assoc. Research and Development Laboratories, 7:66–75 (1965)
30. Darcy, H., *Determination of the Laws of the Flow of Water Through Sand,* Victor Dalmont Publisher, Paris (1856)
31. Blaine, R., Measurement of Specific Surface by Air Permeability, ASTM Bull. 108, pp. 17–20 (1943)
32. Standard Method for Fineness Of Hydraulic Cement by Air Permeability Apparatus, ASTM C 204-94a, (1994)
33. Sereda, P. J., and Ramachandran, V. S., Predictability Gap Between Science and Technology of Cements: 1. Characterization of Hydraulic Cements, *J. Am. Ceramic Soc.,* 58, 3–4, pp. 94–99 (1975)
34. *Neutron, X-Ray and Scanning: Introduction to an Investigation Tool for Colloidal and Polymeric Systems,* (P. Linder, and Th. Zemb, eds.), North Holland, Amsterdam (1991)
35. Kratky, O., and Laggner, P., X-Ray Small Angle Scattering, *Encyclopedia of Physical Science and Technology,* Academic Press, London, 17:727–781 (1992)
36. Porod, G., Die Rontgenkleinwinkelstreuung von Dichtgepackten Kolloiden Systemen, *Kolloid-Z.,* I. Teil, 124, pp. 83–113 (1951)
37. Haussler, F., Eichor,. F., Rohling, S., and Baumbach, H., Monitoring of the Hydration Process of Cement Pastes by Small Angle Neutron Scattering, *Cement and Concrete Research,* 20:644–654 (1990)
38. Kriechbaum, M., Degovics, G., Laggner, P., and Tritthart, J., Investigation on Cement Pastes by Small-Angle X-Ray Scattering and BET: The Relevance of Fractal Geometry, *Advances in Cement Research,* 6(23): 93–100 (1994)
39. Winslow, D. N., Bukowski, J. M., and Young, J. F., The Early Evolution of the Surface of Hydrating Cement, *Cement and Concrete Research,* 24:1025–1032 (1994)

@Seismicisolation

40. Bhattachrja, S., Moukwa, M., D'Orazio, F., and Jehng, J. Y., Microstructure Determination of Cement Pastes by MNR and Conventional Techniques, *Advn. Cem. Bas. Mat.*, 1:67–76 (1993)

41. Feldman, R. F., The Porosity and Pore Structure of Hydrated Portland Cement Paste, *Mat. Res. Soc. Symp. Proc.*, 137:59–73 (1989)

42. Eberly, D., Lancaster, J., and Alyassin, A., On Gray Scale Image Measurements, *Graphical Models and Image Processing*, 53:550–562 (1991)

43. Barnett, M. I., Optical Microscopy for Particle Size Analysis, *International Symposium on the Surface Area Determination*, (D. H. Everett and R. H. Ottewill, eds.), Butterworths, London (1969)

44. Winslow, D. N., and Diamond S., Specific Surface of Hydrated Portland Cement Paste as Measured by X-Ray Scattering, *Coll. Interface Sci.*, 45:425 (1973)

@Seismicisolation

14

Pore Structure

James J. Beaudoin and Jacques Marchand

1.0 INTRODUCTION

The development of the pore structure of hydrating portland cement systems is fundamental to the physico-mechanical and chemical behavior of concrete exposed to a variety of aggressive environments. It influences mass transport of ions into the material and their interaction with concrete constituents as well as the diffusion characteristics of concrete. Deleterious reactions with chlorides and sulfates and the corresponding kinetics are particularly affected by pore size and continuity and are of wide interest to the research community.

The characterization of the pore structure of portland cement paste is difficult due to the uncertainties associated with the lack of a universal definition of the primary structural elements, i.e., the calcium silicate hydrates. This complicates interpretation of data provided by individual techniques. Clarification of some of these points will be attempted for the techniques described in this chapter.

Numerous experimental techniques have been employed to describe the microstructure of cement paste. This chapter will focus on six techniques: helium inflow, gas adsorption, ac impedance spectroscopy, nuclear magnetic resonance, mercury porosimetry, and solvent replacement. These techniques represent a blend of more recent and traditional methods. Pore

@Seismicisolation

structure-property relations and their relevance to concrete durability issues will also be examined. An attempt is made to provide a critical analysis of the techniques in terms of their relevance to arguments for various pore structure models and the nature of the calcium silicate hydrate structures in the paste.

2.0 THE HELIUM INFLOW TECHNIQUE

2.1 The Concept

The helium inflow technique was originally developed by Feldman to follow changes to the solid phase in hydrated portland cement microporous systems that result from the removal of the interlayer and physically adsorbed water.[1]–[4] The volume of the space that was originally occupied by water can be penetrated by helium and determined using elementary gas laws. The penetration of helium is time dependent and generally nears completion after 48 hours. The density of the water removed can, therefore, be calculated using the mass difference and the volumes determined by helium gas that enters vacated space in the C-S-H structure. Changes to the solid envelope comprising C-S-H, adsorbed water and interlayer water can also be determined by measuring the differences in the instantaneous solid volume resulting from an incremental removal of water as detected by helium displacement prior to the onset of inflow into the structure. The technique can be used to study changes to the pore structure of hydrated portland cement on drying and rewetting.[2]–[4]

2.2 The Helium Comparison Pycnometer

The volumes of helium that enter the cement paste systems can be determined using a helium comparison pycnometer as shown in Fig. 1.

The sample is placed in a cylinder illustrated in Fig. 1 which is then evacuated. Helium is allowed to fill the two cylinders at approximately 1 atm. The cylinders are then isolated and compressed to 2 atm by moving the reference piston to the forward fixed position (Fig. 1); in doing this the volume is exactly halved and the pressure is doubled. The sample piston is moved simultaneously with the reference piston, and by reference to the differential pressure indicator, the pressure in the two cylinders is kept the same.

@Seismicisolation

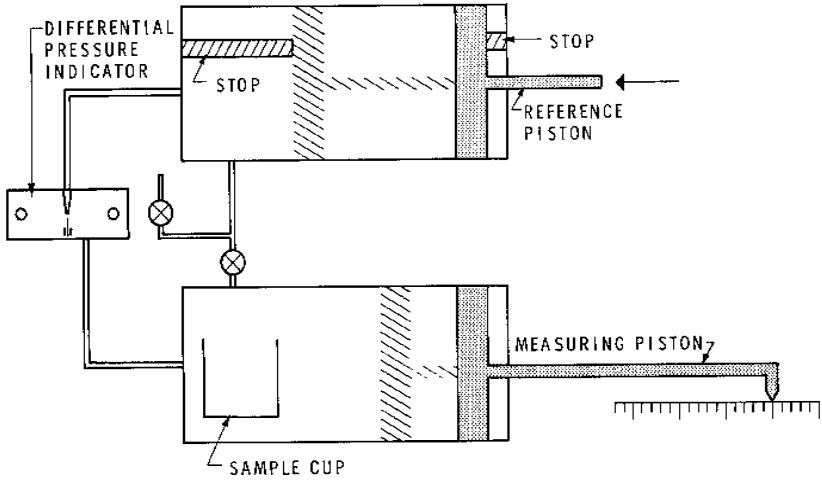


Figure 1. A simplified schematic diagram of a helium comparison pycnometer.[1]

In the actual experiment, the sample is evacuated for 10 min and helium is then admitted to the sample for 15 sec. Pressure equalization between the cylinders and compression takes a further 1 min 45 sec. Helium inflow readings begin as soon as compression to 2 atm is complete. The sample cylinder is always returned to 2 atm before a reading is taken by comparing with the reference cylinder through the differential manometer. Inflow is plotted as milliliters of helium at 2 atm per 100 g of sample versus time.

Density values and parameters associated with collapse of structure due to dehydration of other layered silicates, gypsum and other microporous hydrates can be determined using helium inflow methods.

2.3 General Procedure

Cement paste samples are conditioned at 11% RH prior to helium inflow measurements. The samples are heated under vacuum before a run, in a separate vacuum vessel to remove increments of water. After a prescribed period of time, dry air is allowed to enter the vessel and the sample is transferred to the pycnometer's samples cylinder in a glove-box dried with

@Seismicisolation

magnesium perchlorate. The sample is usually in the form of several disks (3.20 cm diameter × 1 mm thick), the total mass varying from 15 to 30 g. The runs on the hydrated cement samples are done at different moisture contents. At first, moisture is removed by evacuation alone and then by heating at increasing temperature for different periods of time. The samples are weighed after the helium inflow run, which extends over 40 hrs, so the change in flow characteristics can be plotted as a function of mass change. All runs are performed in a temperature-controlled laboratory at 22°C.

2.4 Helium Inflow as a Function of Time

The inflow of helium versus time curves for the paste with water-cement ratio 0.4 (mass loss up to 10.8%) are presented in Fig. 2. The curves in Fig. 2 can be divided into three types. The curve for the sample at 11% RH and the subsequent two curves up to a mass loss of 1.92% show a very rapid helium inflow for approximately the first 50 min. From about 8 to 10 hrs onward, the rate is no greater than that of the blank run and one can assume that helium is no longer flowing into the sample. This is the first type of curve, designated Type I. Further mass loss, up to 4 or 5%, yields curves which show even more rapid helium flow at the early periods and a less rapid decrease in rate. The rate at 10 hrs is still significant, but becomes insignificant at 40 hrs. This second type of curve (Type II) is observed up to a mass loss of 6 to 7%.

The rate in the first 50 min becomes less than for Type I curves, but the curves crossover at a later period, with more helium penetrating ultimately. The rate at 40 hrs at 6% mass loss now exceeds that of the blank run and it appears that at 40 hrs helium has not yet fully penetrated. The third type of curve (Type III) occurs beyond 6 to 7% mass loss. A decrease compared to Type II curves is observed before 1 hr and a net decrease in helium flow at 40 hrs. Mass loss beyond 7% shows the rate decreasing at both the early and late periods. The rate at 10.82% mass loss after 40 hrs is quite low even though little penetration has occurred.

2.5 Mass Loss and the Volume of Helium Inflow

Helium inflow varies with moisture content. The volume that flowed into the sample at 50 min and at 40 hrs was plotted as a function of moisture removed from the 11% relative humidity condition, Fig. 3.

@Seismicisolation

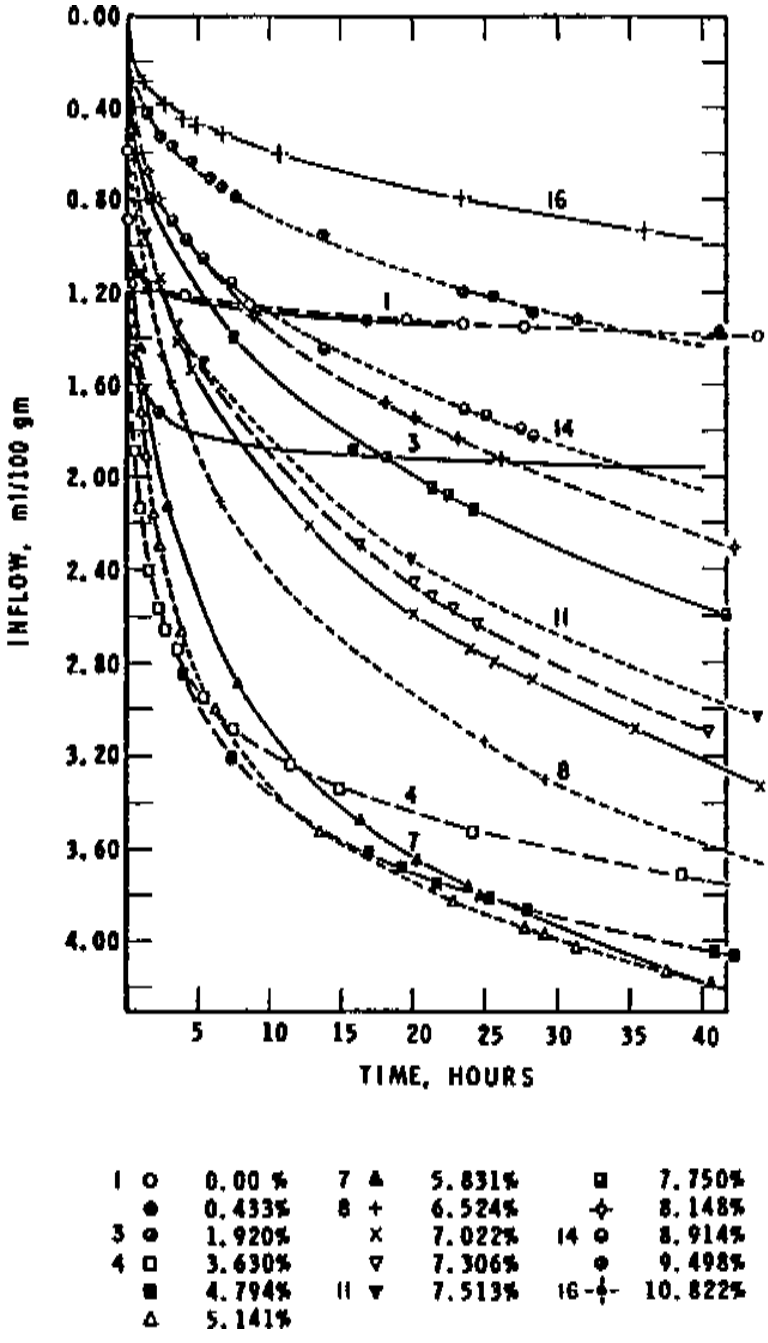


Figure 2. Typical helium inflow versus time curves for portland cement paste (water-cement ration 0.40). Changes in mass on drying from the 11% RH condition are indicated in the legend for each curve.[1]

@Seismicisolation

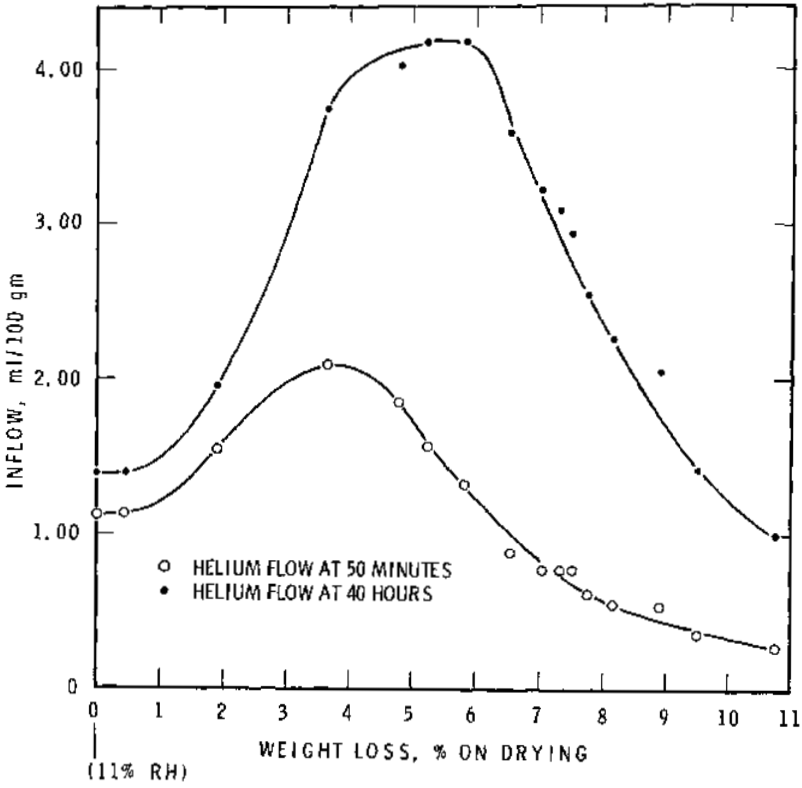


Figure 3. Helium inflow at 40 min and 40 hrs plotted as a function of weight loss for cement paste (water-cement ratio 0.40).[1]

The maximum inflow was approximately 4.2 ml/100 g for the water-cement ratio of 0.4. Helium inflow increased up to a mass loss of about 4%. The curves show a decreasing amount of helium inflow after 50 min at approximately 4 to 4.5% mass loss, while the amount that flowed in after 40 hrs decreased very steeply after 6 to 6.5% mass loss. There is little further decrease in helium flow after 8 to 9% mass loss.

@Seismicisolation

2.6 Space Vacated by Water Versus Degree of Drying

A term that represents the space occupied by water prior to its removal from the C-S-H can be calculated from the helium inflow data. It is the algebraic sum of the change in solid volume (ΔV) and the change in helium inflow (ΔD). Hence the parameter, $\Delta V - \Delta D$ is obtained, where the decrease in solid volume is negative and the increase in inflow is regarded as positive. Figure 4 is a plot of $\Delta V - \Delta D$ and ΔV versus mass loss on drying for 10 different cement pastes. The parameter $\Delta V - \Delta D$ is linear up to about 5.5% mass loss. The inverse of the slope is an estimate of the density of water from 0 to 5.5% mass loss. This value is 1.27 ± 0.08 g/cm^3. The data beyond 5.5% mass loss show considerable scatter. The removal of water in this region cannot be described as the simple removal of water from pores. The process corresponds to an increase in the rate of change of ΔV and a very abrupt decrease in the amount of helium inflow into the microspaces of the sample.

2.7 Pore Structure Models

Results of the helium inflow experiments can be used to examine the validity of pore structure models for cement paste. Models based on the existence of narrow-necked pores of fixed dimension or the presence of layered crystals with interlayer water between adjacent layers have been postulated.

An increase in inflow would be expected from both models as more water is removed from the sample. Volume change can be explained in the early stages for both models if it is assumed that the monolayer of adsorbed water on the external surface was being removed. In either model this can only be used to explain a small part of the volume change, however, because the complete monolayer would occupy less than 1 ml/100 g of a sample. The interlayer model can explain this since one would expect a diminution in "solid volume" as dehydration proceeds further into the layers due to a slight collapse of the layers. The rest of the volume vacated by water will result in increased inflow for the Type I flow curves.

At a mass loss of 5.2%, ΔV is too large to be explained by the fixed-dimension narrow-necked pore model. The flow curves and the value of density for the water would be consistent with both models up to about 4% mass loss. Beyond this loss, however, the flow curves show a decrease in initial rate although more helium has flowed in at 40 hrs. This cannot be explained by the fixed-pore model. There is no mechanism in this model to account for a decrease in flow rate or total inflow.

@Seismicisolation

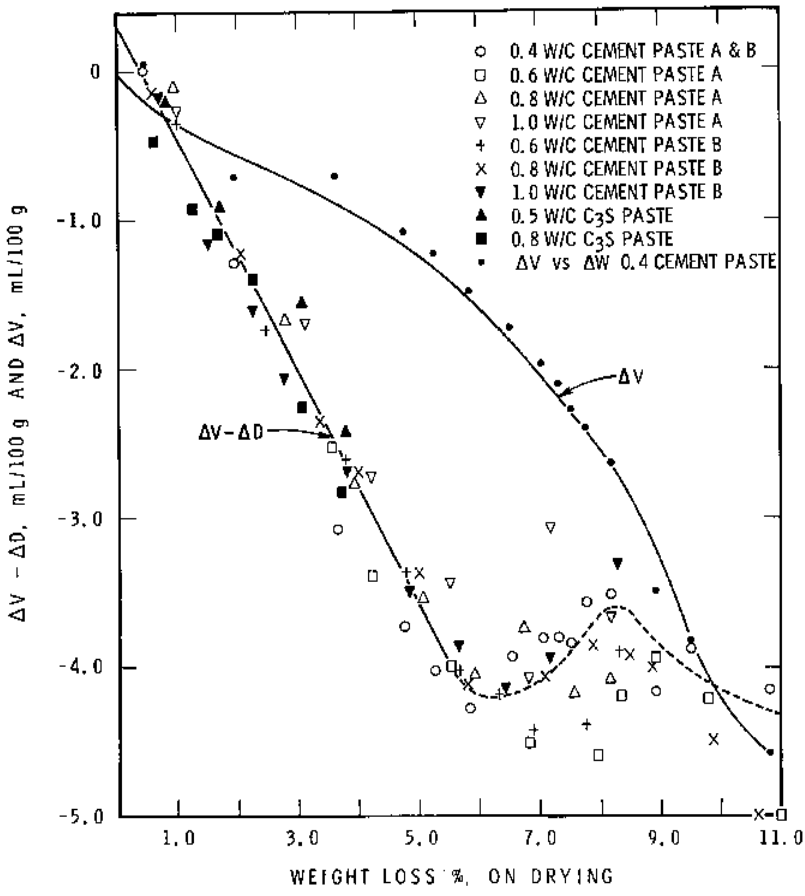


Figure 4. Plot of $\Delta V - \Delta D$ and ΔV as a function of weight loss for 10 different cement pastes. The terms are defined in the text.[1]

These results can be completely explained by the interlayer model. As water is removed from the interlayer spaces, more space is vacated and some collapse occurs. The rate of volume change with mass loss increases significantly where the mass loss is between 5 and 6%. This fits in well with the flow curves, Fig. 2. Figure 3 shows how rapidly the rate of flow decreases

@Seismicisolation

over a very small mass loss range. It is suggested that in this region the collapsing layers not only present "narrow necks" to the helium atoms, but also long narrow slits which greatly restrict inflow.

In effect, the collapse of the layers has trapped space vacated by water, and helium cannot enter this space even after 40 hrs of exposure. Thus, the interlayer model also explains the behavior of the ΔV - ΔD versus mass loss plot. The restricted-pore model would predict this plot to continue in essentially a linear fashion.

2.8 Surface Area and Hydraulic Radius Calculations

The helium inflow technique has been used to study changes to the C-S-H structure that occur during removal and reentry of water and of the pore structure as well. Interlayer spaces and other pores can also be distinguished.

The surface area and hydraulic radius of interlayer and capillary pore systems can also be calculated from helium inflow data.[5] Length change and the determination of the solid volume change by helium pycnometry as the sample is exposed to different relative humidity (RH) conditions can be used to calculate the surface area of the material. The total surface area of hydrated portland cement paste (determined by low-angle x-ray scattering) and the total volume of interlayer space (by the helium inflow technique) can be used to calculate the hydraulic radius of the interlayer space.

The instantaneous solid volume change measured by helium displacement is made up of four main components:

1. Volume change due to change in solid surface-free energy, depending on the quantity of adsorbed water.
2. Volume change due to the attachment or removal of interlayer or structural water.
3. Volume change due to aging effects, i.e., further alignment of sheets.
4. Volume change due to removal or attachment of adsorbed water on the solid surface.

Change in length should be due to components (1) and (2) if aging is not a factor. The difference between $\Delta V/V$ and $3\Delta\ell/\ell$ should then leave component (4), the adsorbed water. Thus,

@Seismicisolation

Eq. (1) $\Delta V/V - 3\Delta \ell/\ell = \Delta v/V$

where v is the volume of the adsorbed layer and V is the volume of the d-dried sample.

If the experiments are carried out by exposing specimens equilibrated at 0 to 11% RH, or vice-versa, assuming that an adsorbed monolayer exists at 11% RH, then Δv is the volume of an adsorbed water monolayer. Using the value of the density of the water as 1.20 g/ml the mass of the monolayer of adsorbed water per unit mass of d-dried sample, W, is $\Delta v \times 1.20/W$[3]. The surface area may thus be calculated, assuming that one water molecule covers 10.8 Å^2.

The hydraulic radius is calculated by dividing the total pore volume of a pore system by its bounding surface area. For definite shapes, the diameter is a fixed multiple of the radius and is useful for defining systems. For parallel plates, the distance separating the plates is twice the hydraulic radius.

2.9 Volume and Length Change Measurements on Rewetting to 11% RH

The helium inflow technique can be applied to hydrated cement systems re-wet from the dry conditions. The results for several hydrated cement, C_3S pastes, and autoclaved cement systems containing sulfur are presented in Table 1. Columns 2, 3, 4, present, respectively, the percent mass of water sorbed, the percent solid volume change, and the relative length change, on a d-dried basis following exposure of d-dried specimens to 11% RH. The actual values for the d-dried solid volume and its mass are tabulated in columns 5 and 6, respectively. Calculation of the term $(\Delta V/V - 3\Delta \ell/\ell) \times 1.2V/100$ gives the mass of the monolayer of adsorbed water for volume, V (column 5), on the basis of the d-dried sample. The monolayer of adsorbed water per 100 g of d-dried sample is tabulated in column 7 and the surface area calculated from this in column 8. Surface areas from nitrogen adsorption measurements are tabulated in column 9. A plot of the surface area determined by nitrogen adsorption versus surface area computed from Eq. (1) is presented in Fig. 5. The points vary somewhat from the line of equality, especially at low surface areas, but overall agreement is considered good. It is possible that some of the assumptions may not be strictly valid at low surface areas.

Using the same method of calculation, surface areas are computed from data for drying the material from 11% RH to the D-dry condition (i.e.,

@Seismicisolation

the vapor pressure of dry-ice at -78°C). These results are tabulated in column 10 and it is clear that the surface areas are much higher than those in columns 8 and 9. Previous results have shown that under this condition aging occurs in the sample, and Eq. (1) does not take this factor into account. In addition, it is probable that the porosity of the specimen decreases with drying and that $3\Delta\ell/\ell$ is not equal to the volume change of the solid phase transmitted through the body. Surface area may, however, decrease, but the process is difficult to quantify through the simple analysis of Eq. (1).

Table 1. Data for Calculation of Surface Area from Helium Pycnometry

	Rewetting Percent at 11% RH				Drying				
							M^2/g		M^2/g
Sample	ΔW/W × 100	ΔV/V × 100	$\Delta\ell/\ell$ × 100	V	W	w	SA_{He}	SA_{N2}	SA_{He}
					Percent				
1	2	3	4	5	6	7	8	9	10
Portland Cement									
w/c 0.25	3.78	1.706	0.332	40.16	91.30	0.38	13.6	5.2	236
w/c 0.40	4.74	2.827	0.362	41.98	91.83	0.96	34.8	30.1	65
w/c 0.60	4.96	3.567	0.342	40.59	91.71	1.35	49.0	52.0	110
w/c 0.80	5.36	3.420	0.359	38.72	89.38	1.22	44.4	52.0	188
C_3S									
w/c 0.50	4.81	4.033	0.304	41.31	92.82	1.67	60.4	56.5	83
w/c 0.80	5.01	4.137	0.278	40.95	92./87	1.74	63.5	67.3	138
Lignosol									
w/c 0.80	5.04	4.238	0.394	39.87	91.44	1.77	58.1	70.0	–
Sulphur Aut 0%									
w/c 0.35	1.23	1.197	0.057	37.17	98.45	0.47	16.9	8.9	–
Sulphur Aut 2%									
w/c 0.35	2.96	1.990	0.176	38.48	95.16	0.71	25.8	12.9	–
Sulphur Aut 10%									
w/c 0.35	3.30	2.54	0.306	35.46	91.87	0.75	27.3	24.0	179

Aut = Autoclaved

@Seismicisolation

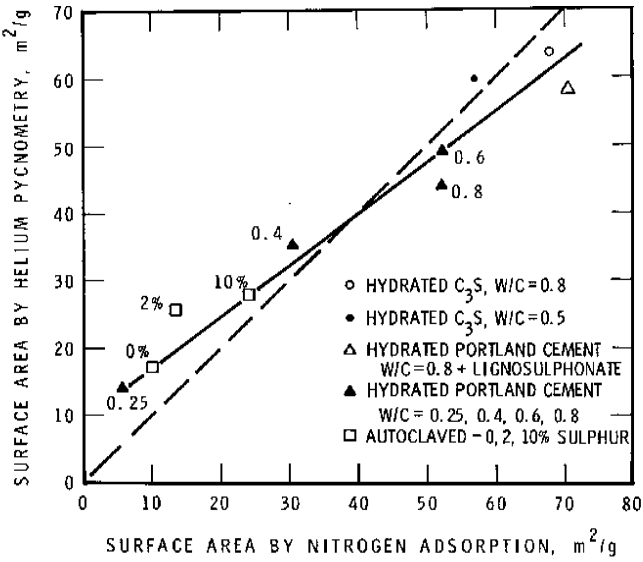


Figure 5. A relation between surface area of cement systems determined by helium pycnometry and by nitrogen adsorption.[5]

2.10 The Hydraulic Radius of the Internal Space of Hydrated Cement Paste

The hydraulic radius of the internal space, using the ratio of volume of the internal structure to internal surface area, can be estimated. Until recently this calculation could not be carried out without assuming a particular structure for the C-S-H gel. The low-angle x-ray scattering data of Winslow and Diamond, however, has provided the internal surface area.

Previous work has shown that the "internal structure" is reopened by exposure (of d-dried specimens) to over 42% RH when more water enters the structure.[3] Helium can, at this condition, fully enter the internal space within 40 hrs.

The volume of the internal structure (interlayer space) can thus be measured in the open or partially open state, depending on the relative humidity of exposure (using helium to measure the remaining internal volume).

Calculation of the surface area of the capillary pore structure shows that 1.35% of the water for the paste formed at 0.6 w/c is sorbed on the outer surface following exposure to 11% RH; after exposure to 100% RH and re-drying to 11% RH, 10.8% of the water is retained. This leaves 9.45% in the internal structure. In addition, 2.4 ml of space, unoccupied by water, is also

@Seismicisolation

measured in the structure by helium inflow. Using the density of water as 1.20 g/ml the volume of the internal space amounted to 10.28 ml and using the surface area of the internal space as 670 - 49 = 621 m^2/g, the hydraulic radius was equal to 1.65 Å (0.165 nm).

Assuming that the pores are bounded by two parallel plates, the average separation between the plates is 3.3 Å (0.33 nm) (twice the hydraulic radius). This model is consistent with the concept of the internal system being composed of layers separated, on the average, by one water molecule. The validity of this calculation is further supported by the following calculation. If 9.45% of water is held as a single layer between two sheets, it will cover twice the normal area per molecule, i.e., 10.8 × 2 $Å^2$ (0.216 nm^2). This will result in a surface area of 687.2 m^2/g, close to 621 m^2/g given by low-angle x-ray scattering. The calculation assumes, however, that all the water is held as a single layer. There may be "kinks" in the alignment of the sheets, leaving room for more than one layer of water. On the other hand, the value of 10.8 $Å^2$ (0.108 nm^2) for the coverage per molecule may be too high.

The hydraulic radius can also be calculated for the sample exposed to 42% RH, a state that corresponds to 5.15% water and 2 ml of space between the sheets. An average hydraulic radius of 1.0 Å (0.1 nm) is obtained because of a partial collapse of the interlayer space.

The evidence strongly suggests that the microstructure of the hydrated silicates is composed of two structures: one made up of relatively coarse pores whose size distribution can be measured by nitrogen adsorption and possibly by mercury porosimetry and whose total porosity can be measured by helium and other fluids such as methanol; the second, a layered structure composed of poorly aligned and poorly crystallized sheets separated by spaces approximately 3 Å wide. The material has the ability to stabilize itself further when subjected to various treatments like wetting, drying, and application of stress.

3.0 GAS ADSORPTION METHODS

3.1 Introduction

Gas adsorption techniques have been used extensively in cement science to characterize the pore structure of hardened cement systems.[6] Methods based on the interaction of water vapor or other adsorbates with the solid surfaces of microporous adsorbents such as hydrated portland cement are briefly described.

@Seismicisolation

The application of models employing capillary condensation theory (e.g., the Kelvin equation) and adsorption-desorption processes (the Brunauer-Emmett-Teller [BET] equation) is presented.[7] Procedures for determining pore size distribution, surface area, and the significance of sorption isotherms and related *V-t* curves, will be outlined. Surface area techniques are described in greater detail in the chapter dedicated to this topic. The 'modelless' method of pore structure analysis developed by Brunauer and co-workers[8] coupled with the Micropore Analysis or MP method[9] is presented as a means of obtaining a "complete" pore-size distribution, including micropores and capillary pores.

It is emphasized that the basis of much of the pore-size analysis for hardened cement systems is predicated on the assumption that the cement-paste is representative of an ideal adsorbent and the paste-water interaction is a reversible thermodynamic adsorption process. This has been challenged by Feldman and coworkers who account for intercalation of the adsorbate (into a layered silicate structure) in their analysis.[10]

3.2 BET Adsorption Theory

Brunauer, Emmett, and Teller (BET) developed a multilayer adsorption theory that is widely used.[7] Surface area values can be readily calculated from application of the BET equations to sorption isotherm data. Typical isotherms (nitrogen adsorbate) for hardened portland cement paste (water-solid ratio 0.20) are shown in Fig. 6.[11] The number of molecules of adsorbate required to form a monolayer on the surface of the adsorbent can be readily determined. This is in reality a fictitious quantity as adsorption takes place in several layers simultaneously. All sorption sites are assumed to be energetically similar. The heat of adsorption of the second and higher layers are assumed equal to the heat of liquefaction.

The BET equation was derived after equating the rate of condensation and the rate of evaporation for a given layer and summing over an infinite number of layers. It is expressed as follows:

Eq. (2)
$$V = \frac{V_m \cdot c \cdot p}{(p_o - p)\{1 + (c-1)p/p_o\}}$$

where: V = volume of gas adsorbed (cm^3)

V_m = monolayer capacity (cm^3)

c = constant, related to the average heat of adsorption of the monolayer

@Seismicisolation

p = vapor pressure (kPa)

p_o = saturation vapor pressure (kPa)

It is convenient to rearrange the BET equation in linear form as follows:

Eq. (3)
$$\frac{p}{V(p_o - p)} = \frac{1}{V_m \cdot c} + \frac{(c-1)\cdot p}{V_m \cdot c \cdot P_o}$$

A plot of $p/\{V(p_o - p)\}$ vs p/p_o generally gives a straight line in the adsorption (reversible) region of the isotherm (i.e., $0.05 < p/p_o < 0.35$).

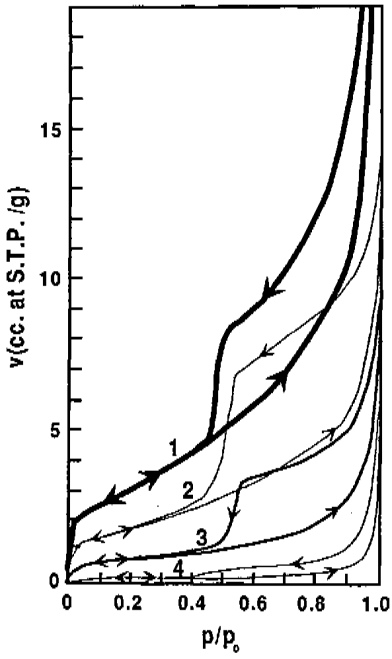


Figure 6. Nitrogen adsorption-desorption isotherms of four cement pastes (water-cement ration, 0.20). *Curve 1*, hydrated 1 d; *curve 2*, 3 d; *curve 3*, 7 d; *curve 4*, 28 d. A diethyl carbonate grinding aid was used.[11]

The monolayer capacity, V_m, and the BET constant c can be determined from the slope and the intercept of the linear plot. The total surface area can be calculated using the equation:

$$S_{BET} = \frac{V_m \overline{N} A}{\overline{M}} \cdot 10^{-20} \ (\mathrm{m^2/g})$$

@Seismicisolation

where A is the projected area of one adsorbate molecule on the surface (m^2/molecule), M is the molar volume (cm^3/g·mole) and N = Avogadro's number (6.023×10^{23} molecules/g·mole).

The BET theory underestimates the extent of adsorption at low pressures ($p/p_o < 0.05$) and overestimates it at high pressures ($p/p_o > 0.35$).

A single point BET method is described in ASTM D4567.

3.3 The Kelvin Equation

The theory for condensation effects in pores is attributed to Kelvin. The Kelvin equation relates the size of a pore to the partial pressure at which capillary condensation occurs for the fluid (adsorbate) within the pore. The thickness of the adsorbate film on the pore walls increases with relative pressure and condensation occurs first in small diameter pores and progresses into larger ones.

The accuracy of the Kelvin equation decreases with decreasing pore size. It is not applicable in the micro-pore filling region of the sorption isotherm, i.e., up to the partial pressure where the sorption and desorption branches join when nitrogen is the adsorbate.

The Kelvin equation for cylindrical pores is given by the following equation.

Eq. (4)
$$r_{cp} = \frac{-2\gamma V \cos\phi}{RT \ell n\, p/p_o}$$

where:

r_{cp} = radius of the pore in which condensation occurs

ϕ = contact angle with which the liquid meets the pore wall

V = molar volume of the adsorbate (for liquid nitrogen = 3.5×10^{-5} m^3/mol at 77°K)

γ = surface tension of the adsorbate (8.85×10^{-3} N/m for liquid nitrogen)

R = gas constant (8.31 J/K·mol)

T = temperature (°K)

p/p_o = relative pressure

p = equilibrium vapor pressure

p_o = saturation vapor pressure

@Seismicisolation

Adsorption within the pores includes layers of adsorbate attached to pore walls in addition to bulk condensate. The radius of the pore calculated from the Kelvin equation is smaller than the true pore radius by an amount equal to the thickness of the surface adsorbed layers. The thickness of the adsorbed layer, *t*, as a function of pressure may be estimated by adsorption measurements on nonporous solids.[12]

The thickness of the adsorbed layer can be estimated from the use of the Halsey equation.[13]

Eq. (5) $$t = \sigma\left[\frac{5}{2.303\log(p_o/p)}\right]^{1/3}$$

where, σ is the thickness of a monolayer of adsorbate molecules, i.e., 3.54 Å (nitrogen).

Wheeler employed the Halsey equation for pores having radii in the range of 20 Å to 300 Å.[14]

3.4 Pore Size Distribution

The equation governing the determination of a pore size distribution based on capillary condensation methods has the following form.[13]

Eq. (6) $$V_s - V_a = \int_r^{\infty} (r-t)^2 \cdot L(r)\, dr$$

where:
- V_s = volume of adsorbate at the saturation vapor pressure
- V_a = volume of adsorbate at an intermediate vapor pressure, *p*
- $L(r)dr$ = total length of pores whose radii fall between *r* and *r* + *dr*
- r = pore radius
- t = multilayer thickness at pressure *p*

The pore size distribution is obtained by constructing a plot of the derivative of the cumulative pore volume-pore radius curve versus pore radius.

The pore size distribution function is unknown in Eq. (6). Particular distribution functions and subsequent numerical integration methods have

@Seismicisolation

been adopted.[12] A simpler and reasonably accurate procedure using the Kelvin equation to characterize a porous alumina sample is briefly described. A spread sheet (Table 2) can be constructed to facilitate calculation using sorption isotherm data.[15] The distribution is given in Fig. 7.

Table 2. A Spread Sheet for Calculation of Pore Size Distribution in Porous Alumina (Nitrogen Adsorption)

p/p_o	r	r_k	r_p	Δt	Δv	Δv_f	Δv_k	Δv_p	Δs_p	$\sum(\Delta s_p)$
---	---	---	---	---	---	---	---	---	---	---
---	---	---	---	---	---	---	---	---	---	---

The terms in Table 2 are defined as follows:

t = thickness of the adsorbed layer

r_k = Kelvin radius at a particular value of p/p_o (Eq. (4); $\bar{r}_k$ = average value in the interval between two values of p/p_o

r_p = $r_k + t$; $\bar{r}_p$ = average value in desorption step

Δt = diminution of film thickness on desorption/adsorption from p_1 to p_2

Δv = element of volume desorbed in the pressure interval

Δv_f = element of volume desorbed from the adsorbed layer on the pore walls = $0.064\,\Delta t \sum(\Delta s_p)$

Δv_k = element of volume ascribed to the cylinder core derived from capillary condensation = $\Delta v - \Delta v_f$

Δv_p = element of actual pore volume = $\Delta v_k \left(\bar{r}_p / \bar{r}_k\right)^2$

Δs_p = surface of the pores associated with incremental desorption

$$2\,\Delta v_p / \bar{r}_p$$

A pore size distribution curve is obtained by plotting $\Delta v_p/\Delta r_p$ vs. r_p. The distribution is limited to pore radii exceeding about 16 Å as the Kelvin equation is not applicable to micropore filling.

The analysis is completed at a value of p/p_o of about 0.32, i.e., the point where the primary hysteresis collapses and the reversible adsorption region is reached. Micropore-filling occurs at lower values of partial pressure.

@Seismicisolation

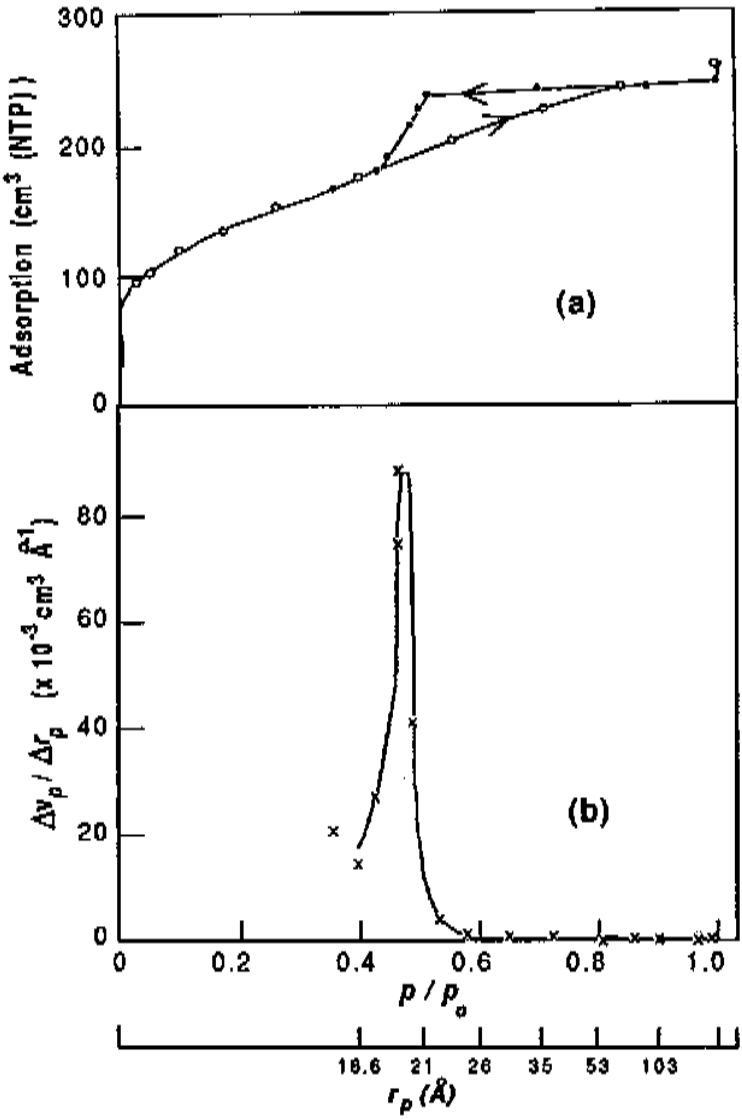


Figure 7. A pore-size distribution curve for alumina determined from a nitrogen sorption isotherm (*a*) isotherm: o, adsorption; • desorption (*b*) pore-size distribution curve.[15]

@Seismicisolation

3.5 Micropore Filling and *V-t* Plots

The use of the Kelvin equation is considered inappropriate for pores smaller than 15–20 Å. The Dubinin-Radushkevich equation[16] has been applied to determine values of micropore volume and pore width.

Eq. (7) $$V = V_o \exp\left\{-K\left(\frac{E}{\beta}\right)^2\right\}; \quad E = RT \ln \frac{p_o}{p}$$

V = micropore volume at a relative pressure of p/p_o (cm^3/g)

V_o = total micropore volume (cm^3/g)

E = adsorption potential (J/mole); the work required to compress a mole of gas from p to p_o

R = gas constant = 8.31 J/K · mol

T = temperature (°K)

K = shape constant for pore size distribution

β = solid dependent affinity coefficient; the ratio of characteristic adsorption energies of test and reference vapors

p = equilibrium vapor pressure

p_o = saturation vapor pressure

Equation 7 can be written in the form

$$\log V = \log V_o - D\left[\log\left(\frac{p_o}{p}\right)\right]^2; \quad D = 2.303K\left(\frac{RT}{\beta}\right)^2$$

The micropore volume V_o can be obtained graphically from the intercept of a plot of log V vs. $[\log (p_o/p)]^2$.

V-t plots can be constructed from sorption isotherm data and the corresponding t values for a given relative humidity. The slope of the linear *V-t* plot yields an estimate of surface area. A downward deviation from linearity indicates that micropores become filled by multilayer adsorption at low humidity reducing the surface available for continued adsorption. Combining

$$t = \frac{V_a}{V_m} t_m \quad \text{and} \quad S = \frac{V_m \overline{N} A}{\overline{M}} \cdot 10^{-20}$$

@Seismicisolation

for nitrogen, $S = 4.35 \cdot V_m$ where:

V_a = volume of adsorbate (cm^3/g)

V_m = monolayer capacity (cm^3/g)

t_m = monolayer thickness

S = surface area (m^2/g)

A = projected area of adsorbate molecule (m^2/molecule)

M = molecular volume ($cm^3/g \cdot mole$)

N = Avogadro's number (6.02×10^{23} molecules/g · mole)

A schematic illustrating the character of *V-t* plots for different mechanisms of pore filling is provided in Fig. 8.

3.6 The Modelless Pore Method

A method of pore structure analysis was developed by Brunauer and coworkers in which pore volume and surface distributions were obtained without assuming any shape for the pores.[8] The hydraulic radius, r_h, defined as V/S (V is the volume of a pore group and S is the surface area of the pore walls) was utilized instead of the Kelvin radius. Adsorption and desorption isotherms were used conventionally to determine pore volumes. The surface values were calculated using a different procedure which will be described in this section.

Mikhail, et al., found good agreement with BET areas and pore wall areas in most cases when the adsorption branch of the nitrogen isotherm for portland cement pastes was utilized.[9] They, therefore, used the adsorption branches of their isotherms for pore structure analysis.

The inference of the modelless method is only that no pore shapes are assumed. The hydraulic radius is, therefore, employed as a measure of the average width of a group of pores independent of pore shape. The Kiselev equation for capillary condensation is employed.

Eq. (8) $\gamma ds = \Delta\mu \, da$

where, γ is the surface tension of the adsorbate, ds is the surface area that disappears when a pore is filled by capillary condensation, $\Delta\mu$ is the chemical potential, and da is the number of moles of liquid taken up by the pore.[17] The term ds is not the surface of the walls of a pore, but the surface of the inner core.

@Seismicisolation

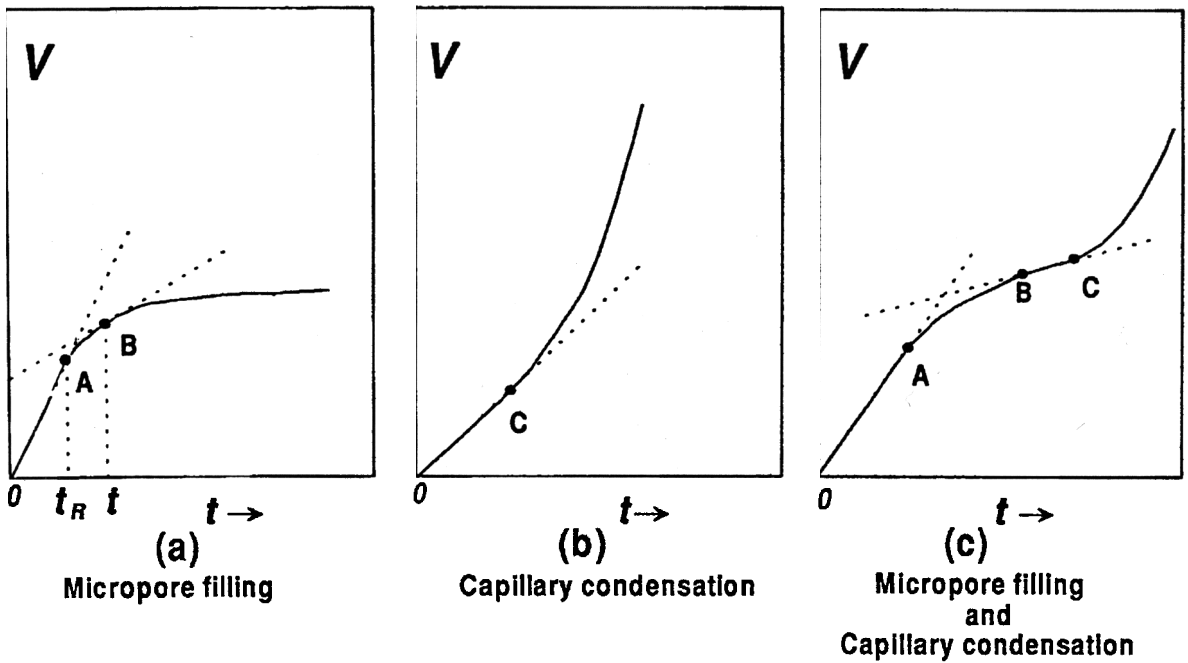


Figure 8. The *V-t* plot for different mechanisms of pore filling. (*a*) Micropore filling; 0A - adsorption proceeds on free surfaces and micropores begin to fill at 'A.' (*b*) Capillary condensation: 0C - adsorption proceeds on free surfaces and capillary condensation begins at 'C.' (*c*) Combined micropore filling and capillary condensation: 0A - adsorption proceeds on free surfaces; AB - micropore filling occurs; BC - free surface adsorption; C- capillary condensation begins.

@Seismicisolation

Integration of Eq. (8) results in the following expression for the *surface area* of the entire adsorbent

Eq. (9) $$s = \frac{1}{\gamma}\int_{a_H}^{a_s} X_a da$$

where, $X_a = -\Delta\mu = -RT \ln p/p_o$ is the differential free energy of adsorption, a_H is the number of moles adsorbed at the inception of the hysteresis loop and a_s is the number of moles adsorbed at saturation. The total surface area of the inner cores is estimated from the Kiselev integration. The core area is generally smaller than the BET area.

The computational steps for determining the surface areas on desorption are described as follows. The surface area of the first group of pores (e.g., desorption in the region $1 \geq p/p_o \geq 0.95$) can be determined by graphical integration of Eq. (9). The core volume divided by the core surface gives the hydraulic radius of the cores. The volume desorbed (v_2) in the second interval (e.g., $0.95 > p/p_o > 0.90$) is not the volume of the inner cores of the second group. The volume desorbed must be corrected for the amount desorbed from the pore walls of the first group (v_2'). The volume of the cores of the second group is then $v_2 - v_2'$. The core hydraulic radius of the second group is obtained by dividing the core volume by the core surface. The correction terms increase from core group to core group and eventually the volume correction becomes equal to the volume desorbed when the hysteresis loop closes.

The correction terms are calculated on the basis of a *t*-curve. The thickness of the adsorbed film is obtained by dividing the volume of nitrogen adsorbed by the BET surface area. The thickness is then plotted against p/p_o. A pore shape model must be assumed in order to make the corrections. The correction (parallel plate model) for the second group of pores ($0.95 \geq p/p_o \geq 0.90$) is given by $v_2' = 10^{-4}(t_1 - t_2) S_1$. The terms t_1 and t_2 are the statistical thicknesses of the adsorbed film at $p/p_s = 0.95$ and 0.90, respectively and S_1 is the core surface area of the first group of pores. The core surface area of the second group is calculated using this correction term. The correction term for the third group of pores is given by $v_3' = 10^{-4}(t_2 - t_3)(S_1 + S_2)$. The procedure continues in a similar manner for all subsequent groups.

It was demonstrated that the corrections add little significant information to that obtainable from the uncorrected values. The pore volume distribution curves, $\Delta v/\Delta r$ vs. r, calculated from the uncorrected and the corrected data are not significantly different.

@Seismicisolation

An example of a typical spread sheet is provided by Table 3.

Pore volume distribution curves for hardened cement paste having water-cement ratio = 0.50 are illustrated in Fig. 9. Curve 1 is the completely modelless structure curve without correction. Curve 2 was calculated from the corrected data. Curve 3 represents the structure curve obtained by the method of Cranston and Inkley (cylindrical model).[12]

Table 3. Analysis of a Nitrogen Desorption Isotherm[8]

p/p_o	V_{ads} (STP)	V_{deg} (STP)	V_{des} (ml)	V_{des} (ml)	S (m^2/g)	S (m^2/g)	r_h (Å)	r_h (Å)
			uncorr	corr	uncorr	corr	uncorr	corr
---	---	---	---	---	---	---	---	---

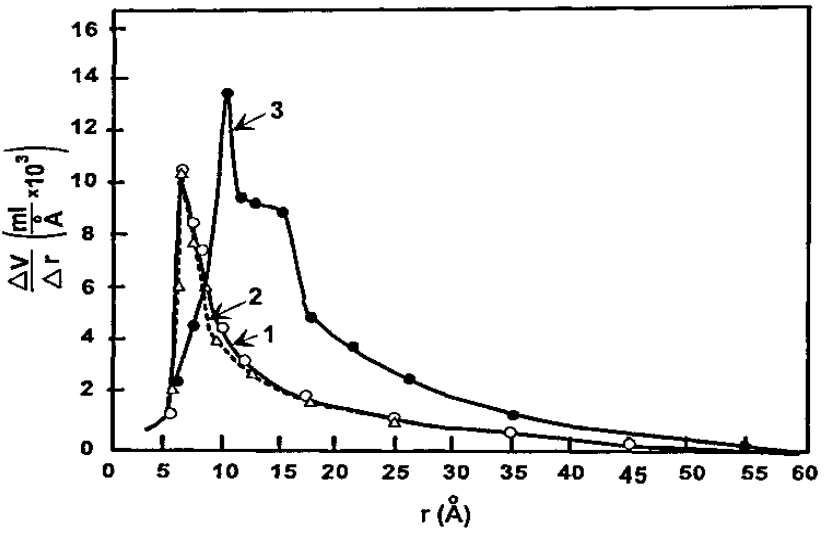


Figure 9. The pore volume distributions of cement paste (water-cement ratio, 0.5) determined from a nitrogen desorption isotherm. Curve 1: modelless method; curve 2: corrected cores; curve 3: method of Cranston and Inkley.[8]

@Seismicisolation

The maxima of the Cranston and Inkley curves appear at larger hydraulic radii than those of the other curves and the corresponding $\Delta V/\Delta r$ values are considerably higher. Curve 3 is based on cylindrical pore volumes and hydraulic radii and curves 1 and 2 on core volumes and hydraulic radii.

The modelless method can analyze pores up to $p/p_o = 1$ because the hydraulic radius is finite at saturation pressure. Comparison of adsorbents on the basis of core dimensions leads to larger differences than comparison based on pore dimensions.

3.7 The Micropore Analysis or MP Method

A complete pore structure analysis requires distribution data for the micropore system and the capillary pore system. *Micropores* are pores that have widths of the order of 16 Å or less.

Mikhail and coworkers developed a method of micropore analysis referred to as the *MP method*.[9] It is basically an extension of the "*t*-method" of de Boer and his coworkers.[18] The volumes, surfaces, and hydraulic radii of groups of pores are calculated from the downward deviations of the straight line in the de Boer *v*-*t* plot.

A combination of the MP method for narrow pores and the corrected modelless method for wide pores can give the complete pore volume and surface distribution of the silica gels.

The statistical thickness of the adsorbed film is obtained by dividing the volume of nitrogen adsorbed as liquid at a given relative pressure p/p_o by the BET surface

Eq. (10) $$t = 10^{-4}\, v/S_{BET}$$

The thickness, *t*, is obtained in angstroms when *v* is in ml and S_{BET} in m^2/g. The molal volume of liquid nitrogen is 34.65 ml at 77.3°K. The slope of the straight line in the *v*-*t* plot gives the surface area of the adsorbent designated S_t. S_t should be equivalent to S_{BET}. This will be true if the *t*-curve is based on adsorbents that have approximately the same heats of adsorption. The values of *c* in the BET equation indicate the relative magnitude of the heats of adsorption. It is imperative that a correct *t*-curve be employed in the micropore analysis. The first points on the *v*-*t* plot determine the slope of the straight line from which S_t is calculated.

The MP procedure is briefly described. The isotherm is converted into a *v*-*t* plot, e.g., Fig. 10. The downward deviations from a straight line (a part of the surface has become unavailable due to micropore filling) are used for

@Seismicisolation

determining the pore volume and pore surface distributions of micropores. The volume of the group of pores (between t_1 and t_2) is given by:

Eq. (11) $$v_1 = 10^4 \ (S_1 - S_2)\left(\frac{t_2 + t_1}{2}\right)$$

where, S_1 and S_2 are the surface areas obtained from the slopes of curves 1 and 2 and t_1 and t_2 are the thicknesses of the films in the narrowest and widest pores of the group.

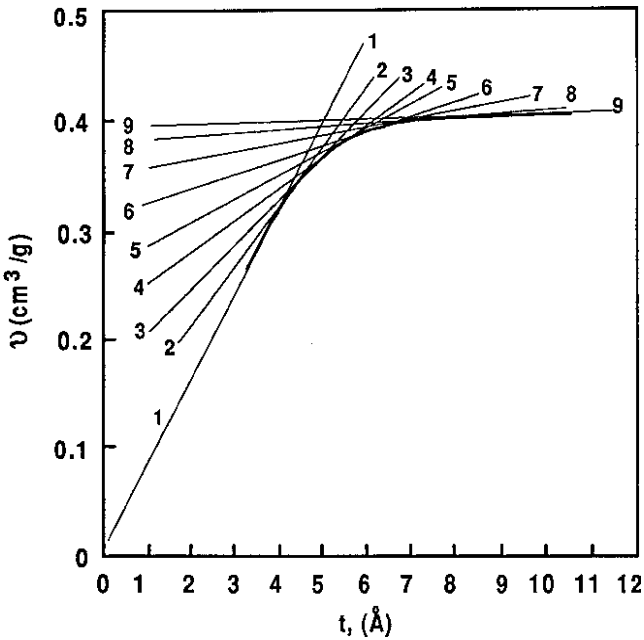


Figure 10. A de Boer *v-t* plot. The surface areas of the pore walls for the different pore groups are obtained from differences between the slopes of straight lines 1 to 9 and the pore widths are obtained from the abscissa values. The figure illustrates the MP method of analysis of micropores.[9]

The hydraulic radius of a group of pores is defined as V/S (volume of the pores/surface area of the pores). It is half the distance between the plates in a parallel plate pore model.

The slope of curve 3 gives the surface S_3. The surface, hydraulic radius, and volume of the second group of pores are calculated in a similar

@Seismicisolation

manner to that of the first group. The analysis is continued until there is no further decrease in the slope of the *v-t* plot and multilayer adsorption is essentially complete.

A micropore volume distribution curve for a silica gel is shown in Fig. 11. It was concluded that a combination of the MP method for micropores and the corrected modelless method makes possible a complete analysis of the pore system. A "complete" analysis of micropores and wider pores (using the methods of Brunauer and coworkers) for hardened cement paste of low porosity is illustrated in Fig. 12. The agreement between cumulative surface and BET surface as well as between cumulative volume and total pore volume would appear to be valid criteria for the correctness of the analysis.

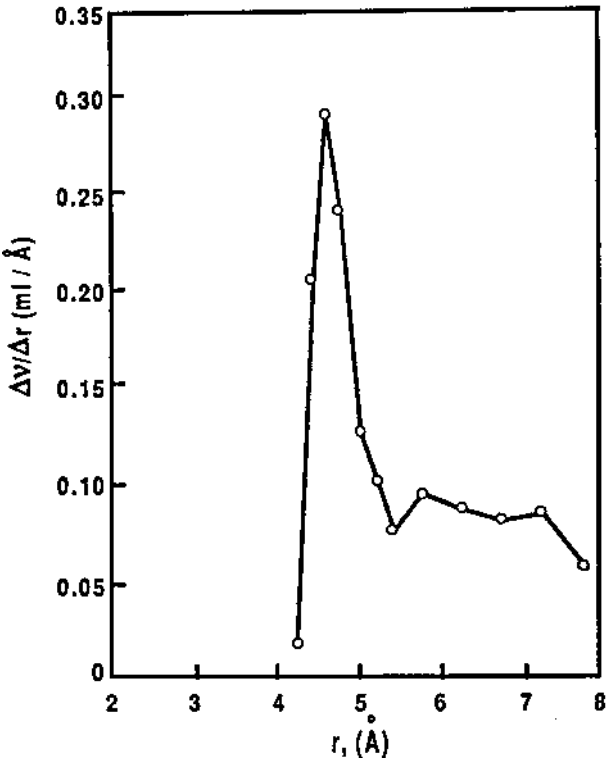


Figure 11. A pore-size distribution curve for silica gel.[9]

@Seismicisolation

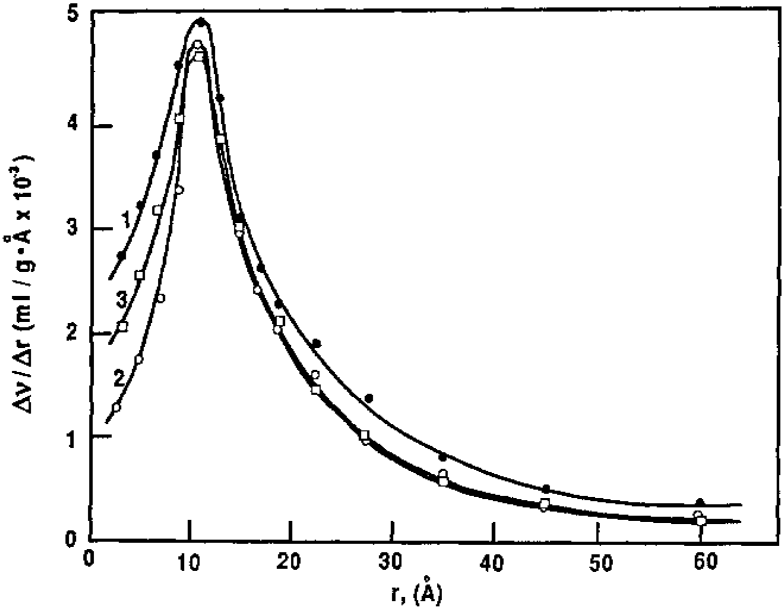


Figure 12. Pore-size distribution curves of type II cement pastes (water-cement ratio, 0.20). Curve 1: 5°C, 180d; curve 2: 25°C, 28d; curve 3: 50°C, 7d. All pastes were approximately 70% hydrated.[9]

4.0 ALTERNATING CURRENT IMPEDANCE SPECTROSCOPY (ACIS) FOR PORE STRUCTURE CHARACTERIZATION

Alternating current impedance spectroscopy (ACIS) is widely used in both fundamental and applied electrochemical studies.[19] The scope of applied ac impedance spectroscopy work is wide. A brief description of the relevant aspects of ACIS related to the pore structure of cement systems will be presented.

4.1 Basic Principles

The ac impedance spectroscopy technique involves application of a small amplitude sinusoidal voltage or current signal to a system; a response current or potential signal is generated and recorded. The impedance of the system is easily evaluated through analysis of the ratio of the amplitudes

@Seismicisolation

and phase shift between the voltage and current. The electrodynamics theory of sinusoidally alternating currents and voltages is based on relatively simple laws.

If the alternating voltage is given by $V = V_m \sin(\omega t)$, the resulting current for a resistance, R, would be:

Eq. (12) $$i = \frac{V_m}{R} \sin(\omega t)$$

The terms ω, t and V_m are angular frequency, time and maximum voltage, respectively.

The impedance Z is defined as a vector with modulus $|Z| = V_m/i_m$ and phase angle (θ). The following expressions are derived from the impedance plot (Fig. 13):

Eq. (13) $$Z'(\omega) = |Z| \cos(\theta) \text{ and } Z''(\omega) = |Z| \sin(\theta)$$

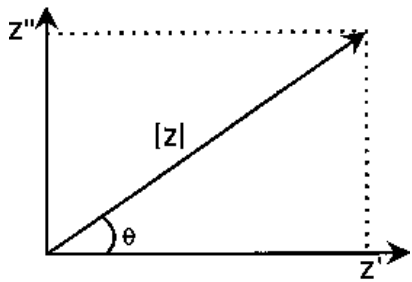


Figure 13. The impedance vector plotted in the complex plane.

The real component is plotted as the abscissa and the imaginary component as the ordinate in the so-called "complex plane" plot. This leads to definitions of impedance and admittance in terms of the complex quantities.

Eq. (14) $$Z(\omega) = Z'(\omega) - jZ''(\omega)$$

where, $Z'(\omega)$ is the real component and $Z''(\omega)$ is the imaginary component of the impedance. The complex plane type of plot was first applied by Cole and Cole[20] in their study of relaxation effects in the dielectric polarization

@Seismicisolation

of a polar medium. A similar expression was applied to the kinetic behavior of electrode processes by Rehbach and Sluyters[21] in 1961. The complex plane method of analysis has since become widely used in the treatment of surface kinetics and other processes at electrodes.[20][21] Plots of log $|Z|$ and phase angle vs. log frequency can also be employed to provide a description of the impedance behavior. These are referred to as *Bode plots*.[22]

4.2 Experimental Procedures

The most common ACIS procedure is to measure impedance directly in the frequency domain by applying a single-frequency voltage to the testing system and measuring the phase shift and amplitude, or the real and imaginary parts of the resulting current at that frequency. Commercial instruments are available, such as the HP-4192A impedance analyzer and Solatron 1260 frequency response analyzer that can be used to measure the impedance as a function of frequency automatically. The analyzer is usually interfaced to a microcomputer with real-time plotting capability. A signal amplitude of less than 0.5 V[23] is used throughout the sweep. The advantages of this technique include operationally simple instrumentation and the capability and possibility of controlling the frequency in the range of most interest.

Cement paste and concrete specimens are usually cast in rectangular or cylindrical shapes[24][25] with stainless steel used as electrical contacts. An example of typical impedance data plotted in the complex plane (real vs. imaginary) for hydrating cement paste at various hydration times is given in Fig. 14.[26] A single arc in the high-frequency range and part of a second arc in the relatively low-frequency region are observed at later hydration times. The high-frequency arc is attributed to the bulk paste impedance behavior and the second arc to the cement-electrode surface capacitance effect. The reliability of the data depends on:

- Maintenance of specimens at 100% relative humidity in an environmental chamber during the measurements. Since the frequency scanning may take more than a minute, the bulk resistance can increase due to the loss of water resulting in a highly disturbed high-frequency arc.
- Correction of conductive or lead effects in the MHz frequency range (since there is an impedance contribution from a conductor, $Z = 2\pi fL$). The electrical wiring should be kept as short as possible.

@SeismicIsolation

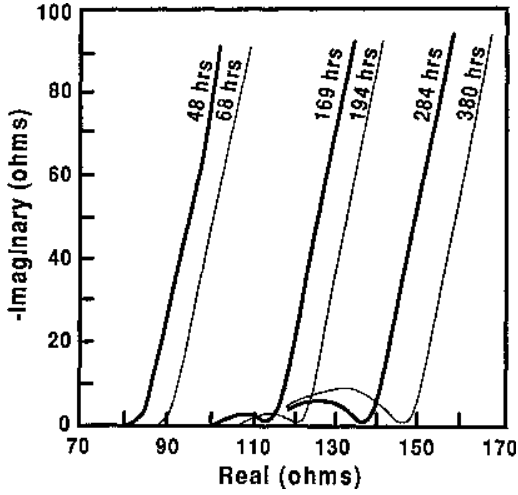


Figure 14. A plot of the imaginary versus real impedance for cement paste (water-cement ratio, 0.35) hydrated for various periods.[26]

4.3 Equivalent Circuit Models

Impedance spectra can be interpreted by an equivalent circuit model made up of ideal resistors, capacitors, and perhaps inductance and various disturbed circuit elements. In these circuits a resistance element represents a conductive path; capacitance and inductance elements are generally associated with space charge polarization regions and special adsorption effects at electrode interfaces. This approach is often applied in electrochemistry and solid-state studies because of the simplicity of simulation and good approximation of the results. It also provides a fundamental understanding of most impedance spectra. A simple parallel combination of a pure resistor and capacitor is illustrated in Fig. 15(a) and (b) along with the corresponding impedance plot in the complex plane. The impedance of the circuit can be described by the following equation:

Eq. (15) $$Z(\omega) = \frac{R}{1 + (\omega CR)^2} - j\frac{\omega CR^2}{1 + (\omega CR)^2}$$

where, $\omega = 2\pi f$, and $j = \sqrt{-1}$. A plot of Eq. (15) in the complex plane (Fig. 15b) gives rise to a perfect semicircle characterized by a single conductivity relaxation time ($r = RC$); the maximum value of the imaginary impedance

@Seismicisolation

occurs at the characteristic frequency $f_o = \frac{1}{2}\pi RC$. In practice, an ideal semicircle is generally not observed in most materials. It is normally an inclined semicircle with its center depressed below the real axis by an angle $\alpha_d \pi/2$ (Fig. 15c). This behavior, normally associated with a spread of relaxation times, cannot be described by the classical Debye equation employing a single relaxation time. A dispersive, frequency-dependent element or so-called constant phase element (CPE)[21][22] can be introduced to account for the shape of the depressed complex plot. The impedance contribution of this element can be expressed as follows:

Eq. (16) $$Z(\text{CPE}) = A_o^{-1}(j\omega)^{-n}$$

where $n = 1 - \alpha_d$ and $\alpha_d \pi/2$ is the depression angle. Therefore, n can be used to represent the degree of perfection of the capacitor and represents a measure of how far the arc is depressed below the real impedance axis.

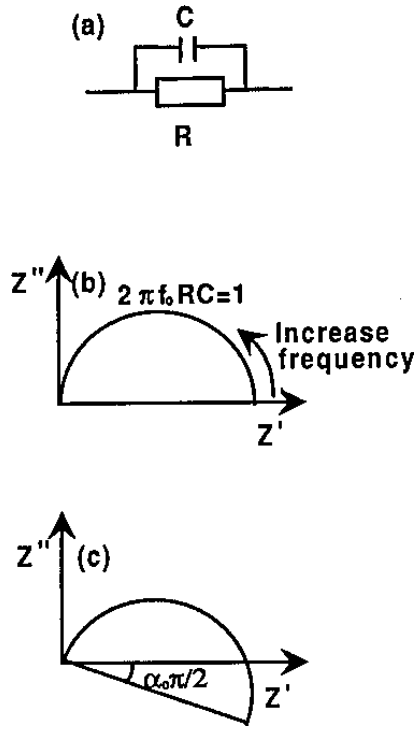


Figure 15. The impedance behavior of cement paste: (*a*) a simple parallel electrical circuit; (*b*) the corresponding impedance plotted in the complex plane; (*c*) the impedance plot showing a semicircle arc inclined at $\alpha_o \pi/2$.

@Seismicisolation

Disturbed circuit elements are associated with two types of physical interpretation. The first is associated directly with a non-local process, for example, diffusion. The other arises because microscopic material properties are themselves often distributed.

4.4 Electrical Circuit Models for Cement Paste

Numerous equivalent circuit models have been proposed for cement pastes.[23] A typical equivalent circuit model to investigate the mechanism of hydration of portland cement paste is briefly described. The electric circuit was chosen so that its *RC* parameters would physically represent microstructural elements of the cement paste. A layer model of hydrating portland cement paste was applied for equivalent circuit construction. The electric network of the cement paste was represented by many unit cells in series as shown in Fig. 16(a), in which the R_s, R_l, R_{int}, and C_{int} terms are the resistance of solid, liquid, and interface phases and the capacitance of the interface in the nth unit cell, respectively. The total impedance of the cement paste, taking the electrode effect into account can, therefore, be simulated by the circuit displayed in Fig. 16(b). A modified equivalent circuit containing a frequency-dependent resistance element, $R'_{int} = B/\omega$ (where B is a real constant) is applied to simulate the depression phenomenon.[26] This equivalent circuit indicates that the impedance behavior of hydrating cement paste depends on the existence of solid-liquid interfaces.

4.5 The High Frequency Arc

An understanding of the significance of the high frequency arc is relevant to interpretations of pore structure based on electrical measurements.

The total impedance for cement paste can be expressed as follows:

Eq. (17)
$$Z = R_1 + \frac{R_2}{1 + \left(\omega/C_d R_2\right)^2} - j\frac{\omega C_d R_2^{\,2}}{1 + \left(\omega/C_d R_2\right)^2}$$

where

Eq. (17′)
$$R_1 = \frac{L}{S}\frac{1}{(1-\psi_s)}\frac{1}{\sigma_\ell}$$

@Seismicisolation

Eq. (17′′) $R_2 = NR_f$ and $C_d = C_f/N$

L = thickness of the specimen in the direction of the electrical field

S = area of specimen normal to the electrical field

ψ_s = area fraction of the solid phase

σ_ℓ = electrical conductivity of the liquid phase

R_f and C_f are the electrical resistance and capacitance of the solid-liquid interfacial zone and N is the total number of solid-liquid interfaces within the specimen in the direction of the electric field.

The corresponding arc and electrical circuit are depicted in Fig. 17.

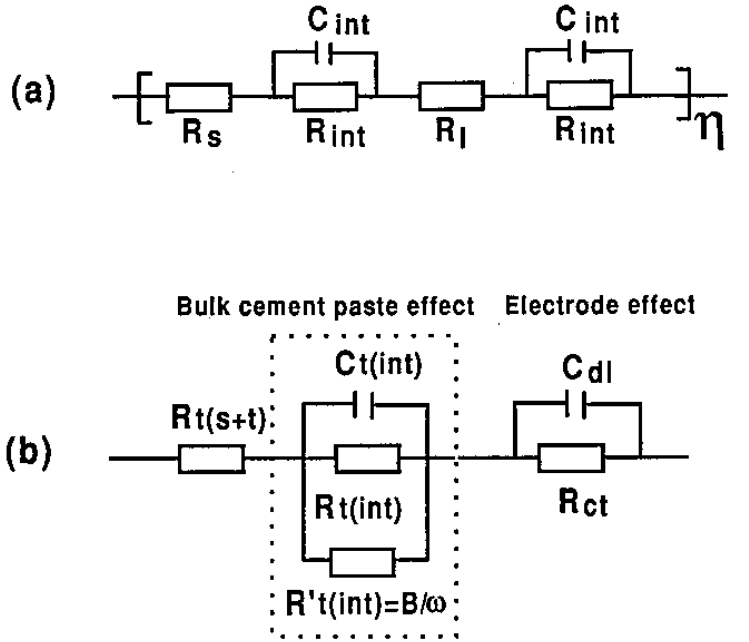


Figure 16. (*a*) An equivalent circuit for a single layer of cement paste based on a "solid-liquid interface unit cell" model; (*b*) a simplified equivalent circuit for one layer of cement paste including a frequency-dependent element.[26]

@Seismicisolation

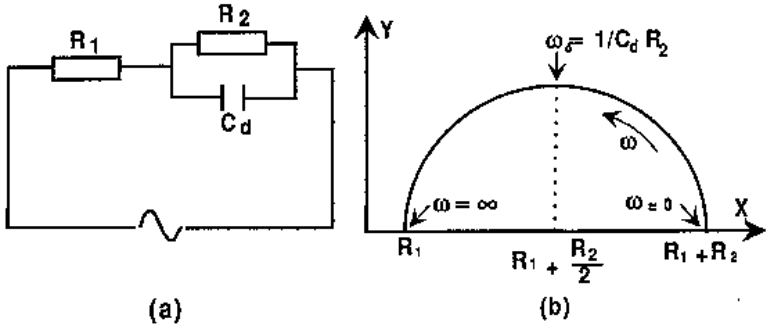


Figure 17. (*a*) The equivalent circuit for an ac impedance spectrum for hydrated cement paste and (*b*) the corresponding high-frequency semicircle.[28]

The value R_1 (expressed in Eq. 17) is a function of both microstructure of the solid phase and the ion concentration of the pore solution.

Consider the following two part (A and B) analysis of Eq. (17).

A. ψ_s is constant. In the case where ψ_s is constant, Eq. (17′) becomes $R_1 = \kappa' (1/\sigma_1)$ where $\kappa' = K/(1 - \psi_s)$. The pore solution conductivity is equal to $\sigma_1 = \lambda c/10^3$ with λ given by the *Kohlrausch's law*, that is, $\lambda = \lambda_o (1 - \beta' \sqrt{c})$. Equation (17′) then gives:

$$\text{Eq. (18)} \qquad R_1 = \kappa' \left(\frac{10^3}{\lambda_o \left(1 - \beta' \sqrt{c}\right) c} \right)$$

where, λ is the equivalent conductivity, λ_o is the equivalent conductivity at infinite dilution, and β' is the experimental constant related to ionic interactions and viscosity of the solution, etc.

B. σ_1 is constant. In the case where σ_1 is constant, Eq. (17′) can be expressed as $R_1 = K[\rho_\ell /(1 - \psi_s)]$ where ρ_ℓ is the resistivity of pore solution. Since the cement particles can be considered as small spheres, it is reasonable to assume that the area fraction of solid is proportional to its volume fraction, for example, $\psi_s = \alpha' \varphi_s$, and $\varphi_s = 1 - P$. Equation (17′) then becomes:

$$\text{Eq. (19)} \qquad R_1 = K \left(\frac{\rho_\ell}{1 - \alpha' (1 - P)} \right)$$

@Seismicisolation

Combining Eqs. (18) and (19), the HFR, R_1, can be expressed as:

$$\text{Eq. (20)} \quad R_1 = K\left(\frac{1}{1-\alpha'(1-P)}\right)\left(\frac{1}{\lambda_o\left(1-\beta'\sqrt{c}\right)c}\right)$$

A plot of $1/R_1$ vs. P gives a straight line if the pore solution resistivity can be obtained. Equation (19) is a very simple relation between the HFR and porosity. It is applicable to hydrated cement systems in which the conductivity of pore solution has reached a relatively constant value. Figure 18 contains experimental plots of $1/R_1$ versus porosity for hydrating cement paste systems with water/cement ratios varying from 0.25 to 0.55, respectively. Porosity values were determined at hydration times of 3–27 days. A linear relation was obtained for all cement systems as predicted by Eq. (19).[27]

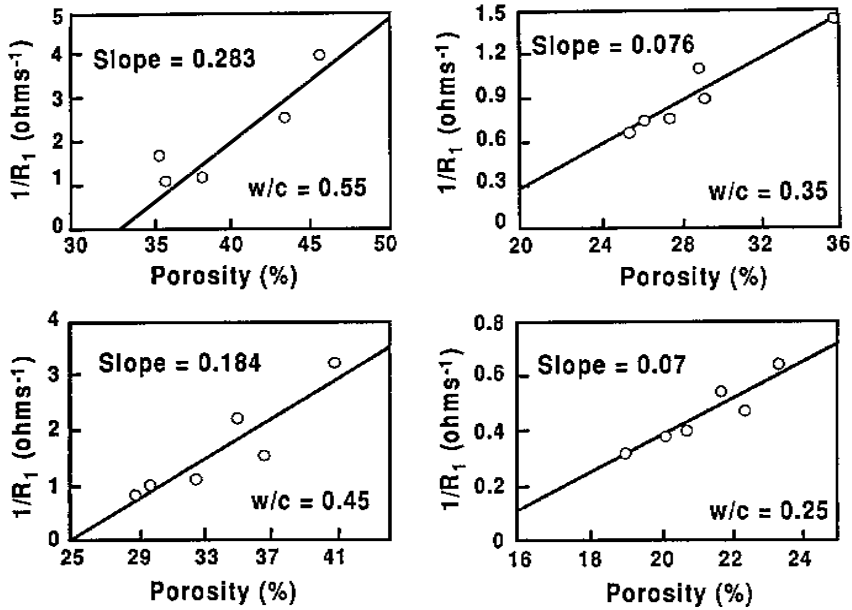


Figure 18. Plots of the inverse high-frequency resistance, *I/R*, versus porosity for cement paste systems at various hydration times (water-cement ratios 0.55 to 0.25.)[27]

@Seismicisolation

4.6 The High-Frequency Arc Diameter, R_2

The high frequency arc diameter appears to be a function of specific pore structure descriptors of cement paste. The arguments are developed below.

The ac impedance behavior of the hydrating cement paste system is controlled by the solid-liquid interfacial zone in the system.[28] The solid-liquid interfacial zone consists of two parts, the Stern layer and a diffuse layer.[29] The Stern layer is a layer of counter-ions strongly adsorbed to the solid surface. The ions in the Stern layer are difficult to move due to the attraction of the solid surface. A diffuse layer exists behind the Stern layer. The diffuse layer contains a net excess of counter-ions compared with the neutral bulk liquid. It is apparent that the interfacial zone has a different electrical conductivity than the bulk liquid.

Expressions for R_f, σ_f, and δ (conductivity and thickness of the interfacial zone) are given as follows, assuming Kohlrausch's law is valid in the double layer.[29][30]

Eq. (20´) $$R_f = \frac{\delta_f}{S_{s\ell}} \cdot \frac{1}{\sigma_f}$$

Eq. (21) $$\sigma_f = \lambda_o \left(1 - \beta' \sqrt{[C_f]}\right)[C_f]$$

Eq. (22) $$\delta_f = \delta_{st} + \delta_d = \delta_{st} + \frac{k_1}{\sqrt{c}}$$

where, δ_{st} and δ_d are the thickness of the Stern layer and diffuse layer and c and $[C_f]$ are the concentrations of ions in the bulk pore solution and diffuse layer, respectively. R_f is the interfacial resistance. The specific constant, k_1, varies with temperature and the valences of various ions in the pore solution.

Consider $[C_f]$ to be approximately constant for cement-based materials,[27] as σ_f is relatively constant. The R_2 - c relation can be obtained by combining Eqs. (20´), (21), and (22):

Eq. (23) $$R_2 = k_2 + \frac{k_3}{\sqrt{c}} \quad (k_2, k_3 \text{ are constants})$$

@Seismicisolation

This linear relation between HFA diameter, R_2, and the reciprocal of the square root of the concentration of ions in pore solution was examined experimentally in mature portland cement systems.[31] A plot of R_2 vs. $1/\sqrt{c}$ is given in Fig. 19.

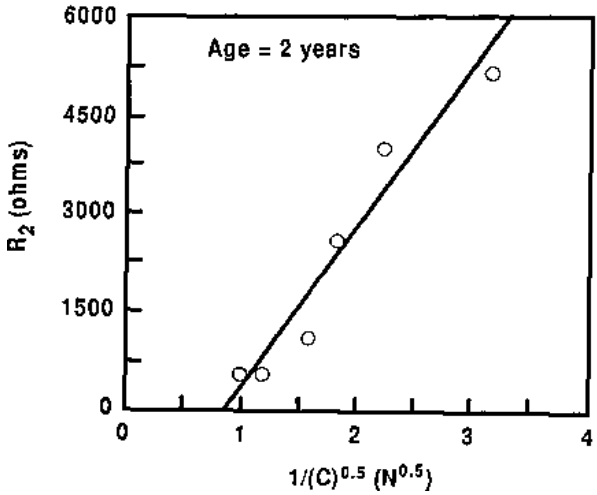


Figure 19. A plot of the high-frequency arc diameter, R_2, versus the ionic concentration term $1/\sqrt{c}$, for a mature cement paste system.[31]

The HFA diameter, R_2, is also dependent on porosity, P, and mean pore size, r_o. The following relationship was derived by Xu, et al.,[31] and validated by experiments.

Eq. (24) $$R_2 = \frac{k_4}{\sigma_f}\left(\delta_{st} + \frac{k_5}{\sqrt{c}}\right)\left(\frac{1}{P \cdot r_o}\right) \quad (k_4, k_5 \text{ are constants})$$

It is apparent from Eq. (24) that the occurrence of the high-frequency arc in porous materials depends on the product of porosity and mean pore size in addition to ionic concentration. High porosity, large pore size, and the increasing ionic concentration, result in a very small high-frequency semicircle. If the pore ion concentration is relatively constant, R_2 can be expressed as:

@Seismicisolation

Eq. (25) $$R_2 = \frac{k_6}{P \cdot r_0} \quad (k_6 \text{ is constant})$$

A plot of R_2 vs. $1/(P \cdot r_0)$ is illustrated in Fig. 20. Linear regression analysis resulted in a correlation coefficient of 0.99. The linear Eq. (25) is validated by the experimental results.[31]

The impedance behavior of hydrating cement paste systems in accordance with the above discussion is attributed to solid-liquid interface phenomena. Characteristics of the *RC* parameters can be summarized as below.

- The high-frequency resistance, R_1, is an inverse function of both porosity and ionic concentration in the pore solution
- The high-frequency arc diameter (or chord), R_2, is an inverse function of porosity, mean pore size, and ionic concentration of the pore solution.

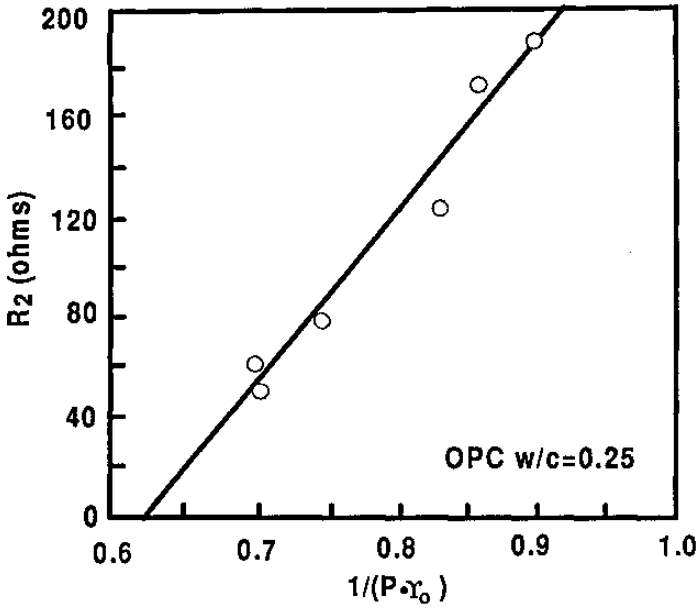


Figure 20. A plot of the high frequency arc diameter, R_2, versus the inverse of the product of porosity and mean pore size, $1/(P \cdot r_0)$, in a cement paste system.[31]

@Seismicisolation

4.7 Microstructural Parameter, β

Complementary work (based on electrical conductivity methods) at Northwestern University and the National Institute for Standards and Technology (NIST, USA) supports the view that ACIS techniques can reveal useful time-dependent microstructural information for hydrated cement systems.

Garboczi[32] has described the conductivity of cement paste using the following equation:

Eq. (26) $$\sigma = \sigma_o \beta V_f$$

where, σ is the composite conductivity, σ_o is the conductivity of the pore solution resident in the capillary pores, V_f is the volume fraction of capillary porosity and β is a microstructural parameter related mainly to the *tortuosity* and *connectivity*. The parameter β is an empirical constant related to the spatial distribution of conductive phases.

A plot of the normalized conductivity, σ/σ_o versus volume fraction of the dominant conductive phase, V_f, for portland cement paste is given in Fig. 21.[33] The upper and lower bounds for simple two phase models (parallel and series) are also plotted. It would appear that the cement paste microstructure changes character from parallel to predominantly series as capillary porosity decreases. It was concluded (despite suggestions of de-percolation) that the hydration reaction can be explained by an increase in tortuosity of the capillary pore structure without considerations of disconnected porosity on the basis of a description of two-arc behavior presumed related to the tortuosity of the capillary pore structure blended with a continuous C-S-H phase.

Christensen, et. al., obtained similar data to that presented in Fig. 21.[34] The relative conductivity is plotted versus porosity in Fig. 22 for white cement paste. Computer simulation results agree reasonably well over the entire range of capillary porosities. It is noted that the experimental conductivity values do not conform to a $\phi^{1.5}$ power law at porosities less than about 50%. The corresponding degree of hydration is approximately coincident with final set time and the departure from criteria applicable to suspensions. The separation of bulk conductivity into microstructural and pore solution components provided the basis for a rapid method of pore structure investigation.

@Seismicisolation

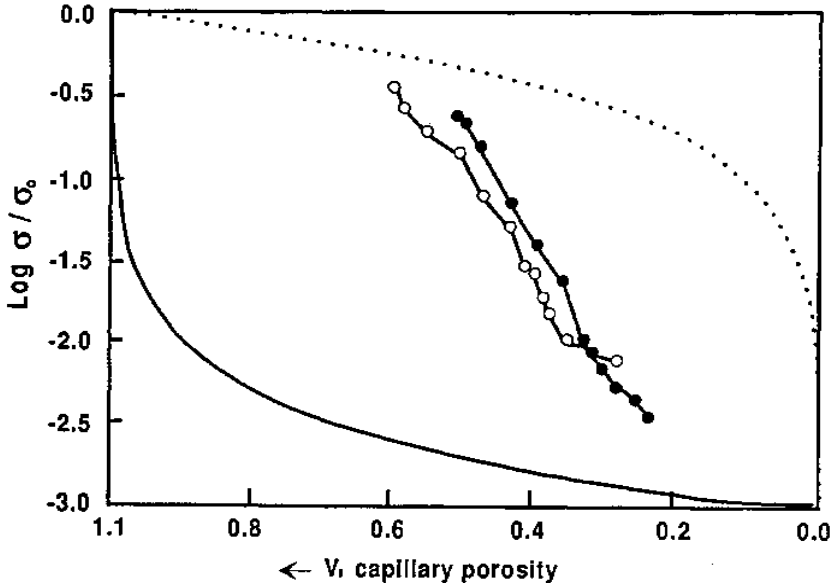


Figure 21. Normalized conductivity data for two ordinary portland cement pastes [w/c: (•) 0.50, (o) 0.35]. Parallel (·····) and series (—) bounds.[33]

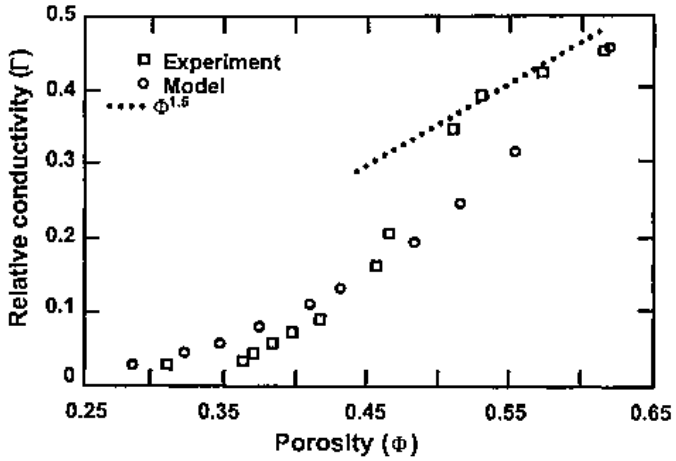


Figure 22. Simulation and experimental results for relative conductivity versus capillary porosity for white cement paste (water-cement ratio, 0.5).[34]

@Seismicisolation

5.0 THE SOLVENT REPLACEMENT TECHNIQUE

5.1 Introduction

The solvent replacement technique has been used by numerous researchers for various applications.[35] Some authors have relied on organic solvents to stop the hydration of cement.[36][37] Attempts have also been made to use some organic solvents as cement-hydration retarding admixtures [38]–[40] or to study the rheological properties of fresh cement paste mixtures.[40]

As can be seen in Table 4, organic solvents (such as benzene, acetone, ethanol, methanol, and isopropanol) have physical properties that present numerous advantages from the standpoint of pore structure characterization. For instance, solvents are characterized by a surface tension which is usually much lower than that of other liquids, such as water. The replacement of the cement paste pore water by a low surface-tension organic fluid has been extensively used by several authors as a precursor treatment to minimize pore structure damages upon drying.[35][41]–[43] It has been shown that the removal of the solvent after it has replaced the pore water attenuates the stresses induced in the system and preserves, at least to a certain degree, the fine pore structure of the materials.[41]–[43]

The specific gravity of most organic solvents is also significantly lower than that of water, see Table 4. Due to their reduced density, organic solvents tend to naturally replace the hydrated cement paste pore solution by a simple counter-diffusion process. In recent years many researchers have relied on organic solvents to assess the diffusion properties of various cement systems.[44]–[46] Organic solvent diffusion measurements have also been used to investigate the pore structure alterations induced to cement-based materials by drying-resaturation treatments.[46]–[48]

A brief overview of the suitability of organic solvent for microstructural characterization will be presented. The remaining discussion will focus on the use of the solvent replacement technique for the determination of the diffusion properties of cement-based materials. The application of the technique to the investigation of drying-induced pore structure alterations will also be discussed. The effects of solvent replacement as a precursor treatment on pore size distribution measurements by mercury intrusion porosity will be addressed in the following section.

@Seismicisolation

Table 4. Characteristics of Various Organic Solvents

Organic Solvent	Chemical Composition	Surface Tension (mN/m)	Specific Gravity	Cross-Molecular Area, Å^2	Diffusion Coefficient in Water ($\times 10^{-5}$ cm^2/s)
Water	H_2O	70.80	1.0000	11.4	—
Acetone	C_3H_6O	23.46	0.7899	—	1.28
Benzene	C_6H_6	25.00	0.8765	—	1.02
Ethanol	C_2H_6O	21.97	0.7893	—	1.24
Isopropanol	C_3H_8O	20.93	0.7855	-18.1	2.02
Methanol	CH_3OH	22.07	0.7914	27.7	1.28

5.2 Suitability of Organic Solvents for Microstructural Characterization

The primary assumption in the use of organic solvents is that these liquids do not physically or chemically interact with cement systems. The question is obviously of importance from the standpoint of microstructural characterization. The subject is also of interest for diffusion experiments since any interaction of the solvent with the solid will significantly influence the interpretation of the experimental data.

The hypothesis of minimal interaction of organic solvents with cement-based materials has been challenged by a number of investigators. Although opinions on the subject tend to differ, evidences of chemical reactions and strong physical interaction have been brought forward by many investigators.[35] For instance, in a comprehensive investigation of the interaction of organic liquids with tricalcium silicate pastes, Taylor and Turner found that acetone could react with the solid to form mesityl oxide, phorone, and isophorone.[49] In a recent investigation of the length change response of calcium hydroxide compacts immersed in various organic solvents Beaudoin, et al.,[50] observed a significant color change for the samples immersed in acetone. The change of color and the length change response were interpreted as signs of strong chemical interaction between acetone and calcium hydroxide; however, the nature of the chemical reaction products was not identified.

@Seismicisolation

Numerous reports have suggested that other solvents, such as ethanol, methanol, or isopropanol, were probably more suitable as replacement fluids. On the basis of DTA analyses, Dollimore[51] and Parrott[52][53] could not identify any signs of chemical interaction of cement pastes with organic liquids and specifically methanol. These observations were supported by Thomas[54] and Marchand[46] who concluded that methanol and isopropanol were suitable for the preparation of the samples for pore structure characterizations. Techniques employed in both studies included TGA, XRD, IRS, and mercury intrusion porosimetry. Thomas' investigation was carried out on $Ca(OH)_2$ compacts and hydrated OPC pastes while Marchand's study was conducted on four different blended cement pastes.

The conclusions of these various studies have been challenged by different authors. Methanol, for instance, has been found to react with portlandite to form "carbonate-like materials."[55] Similar observations were made by Beaudoin[56] who determined that the surface area of calcium hydroxide samples nearly tripled after twenty-four hours of immersion in methanol. Calcium methoxide or a methylated complex were identified by XRD, DTA, and IRS, as reaction products between methanol and $Ca(OH)_2$ (see Figs. 23 and 24).[56] More recently, length-change experiments reported by Beaudoin et al.,[50] suggest that other solvents, such as benzene and isopropanol, could also chemically react with calcium hydroxide. Strong interaction of methanol with hydrating and mature cement paste has also been reported in the literature.[38][57]

Although the nature and the extent of the chemical interaction between the various organic solvents and the hydrated cement paste is still a matter of discussion, several investigations suggest that methanol is not a suitable fluid for pore structure determinations. In addition to its potential chemical reaction with the cement paste hydration products, methanol has been found to alter the cement paste pore structure.[43][45][56][58] For instance, length-change measurements reported by Feldman[45] (see Fig. 25) clearly indicate that immersion of thin cement paste samples in methanol results in large expansions while samples immersed in isopropanol shrink. The increase of volume was associated with the penetration of the layered silicate structure by the relatively small methanol molecules (see Table 4). The separation of the sheets by methanol leaves a marked imprint on the sample pore structure. Evidence of pore structure alterations reported by Sellevold and Bager[58] indicate that methanol can also affect the coarser part of the distribution.

@Seismicisolation

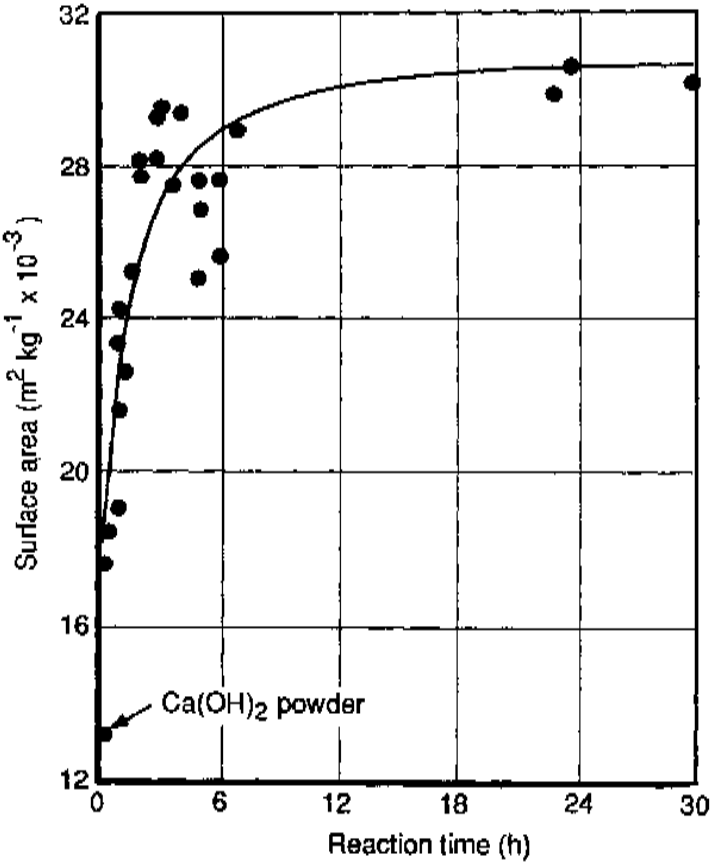


Figure 23. Nitrogen surface area of $Ca(OH)_2$ samples immersed in methanol.[56]

@Seismicisolation

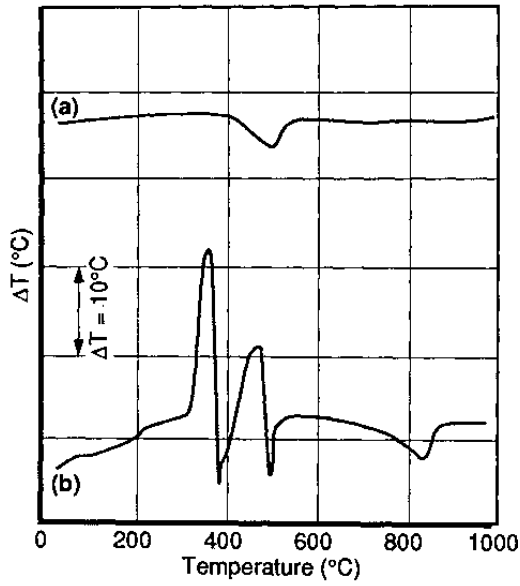


Figure 24. DTA curves in air for (*a*) $Ca(OH)_2$ and (*b*) $Ca(OH)_2$ immersed in methanol for three days.[56]

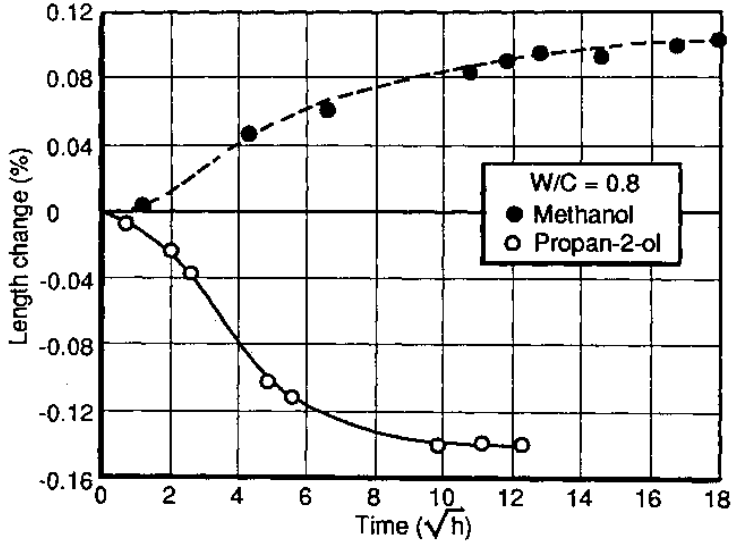


Figure 25. Length change of hydrated cement paste samples immersed in methanol and isopropanol as a function of the square root of time.[45]

@Seismicisolation

Numerous investigations also clearly demonstrate that most solvents tend to be strongly adsorbed on the pore walls and cannot be entirely removed by conventional drying techniques like vacuum or oven drying.[46][50][54] As can be seen in Fig. 26, isopropanol and methanol vapor isotherms reported by Mikhail and Selim[59] were characterized by a marked hysteresis at low relative pressures after several adsorption-desorption cycles. Similar hystereses were noted for samples which had been subjected to prolonged vacuum-drying at room temperature. For the authors, this was a clear indication of an incomplete removal of the adsorbate. It was concluded that drying temperatures exceeding 100°C were needed to remove the sorbed solvent molecules from the hydrated cement paste pore surface.

Unfortunately, such a severe drying treatment can hardly be used in practice. It is well established that drying at temperatures above 105°C tends to remove structural water and results in an irreversible decomposition of the cement paste itself.[60]

The conclusions drawn by Mikhail and Selim were recently supported by a series of gas chromatography data reported by Hazrati.[61] Results obtained for a solvent-exchanged mortar clearly support the view that temperatures up to 170°C are needed to completely desorb isopropanol from the hydrated cement paste pore surface (see Fig. 27). The gradual desorption of isopropanol over a 50°C temperature range (i.e., from 120°C to 170°C) was also seen as a good indication that isopropanol molecules were held with different degrees of binding energy. According to these data a significant amount of isopropanol was retained in the solid microporosity and/or covered more than one molecular layer at the surface of the material.

The strong adsorption of solvent molecules on the hydrated cement paste pore walls calls into question the use of solvent replacement techniques for the preconditioning of cement-based material samples. Such a phenomenon could be particularly important for surface area determinations which are usually made on the basis of gas sorption measurements. As emphasized in the previous section, most interpretations of gas sorption data are based on the fundamental assumption that the intensity of the acting adsorption forces varies with the distance separating the individual adsorbate molecules from the solid surface. Furthermore, most of these theories also assume that at any given vapor pressure the amount of molecules adsorbed on the surface is directly proportional to the surface area of the solid. The presence of residual solvent molecules on the surface of the solid clearly complicates the interpretation of gas sorption data on the basis of classical theories.[61]

@Seismicisolation

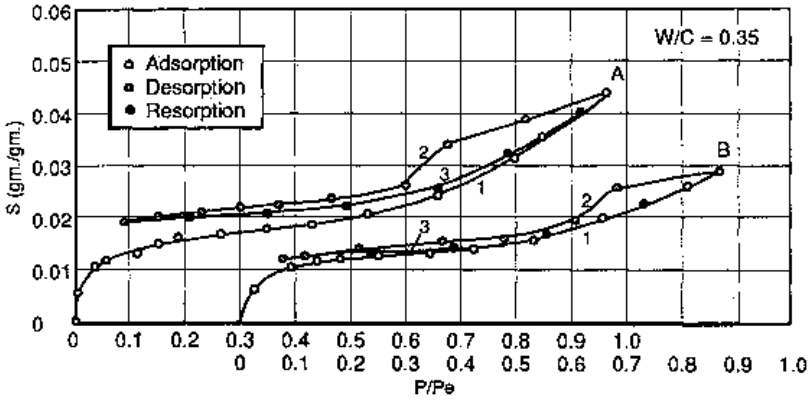


Figure 26. Adsorption/desorption isotherms of methanol for a 0.35 water/cement ratio hydrated cement paste.[59]

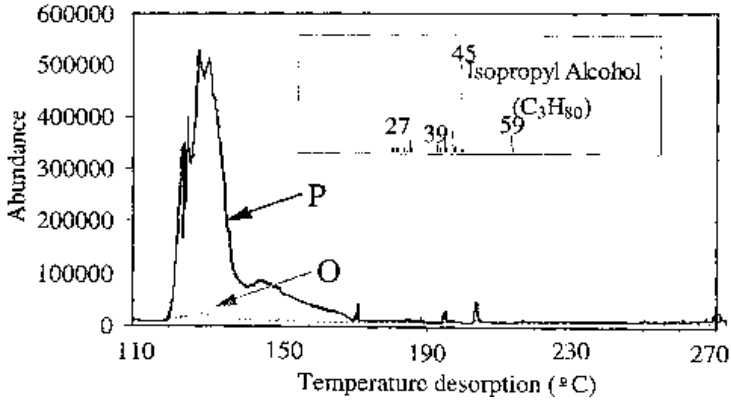


Figure 27. Gas chromatography spectra and mass spectrometry results *(inset)* for a 0.6 water/cement ratio paste immersed in isopropanol and oven-dried (P) and simply oven-dried (O).[61]

The adsorption of residual solvent molecules should also, at least from a theoretical point of view, affect the intrusion of mercury during a porosimetry experiment. The presence of sorbed molecules may significantly modify the contact angle of the solid and impede the penetration of mercury in small pores. This will be discussed further in the following section.

@Seismicisolation

5.3 Diffusion Experiments

The solvent replacement technique has been used by many authors to assess the diffusion properties of saturated cement-based materials. The method is relatively straightforward and can be performed in any laboratory. It consists of immersing saturated surface-dry specimens into a large volume of solvent. The solution to sample volume ratio is important (at around 100:1) since the point of saturation of water in most organic solvents is quite low. Furthermore, in order to keep the boundary conditions as stable as possible, the solvent should be renewed regularly (i.e., every hour during the first twenty-four hours of experiment and then less frequently).

Once the sample is immersed, the solvent immediately penetrates the material and replaces the pore solution. During the experiments the penetration of the solvent within the sample is simply monitored by weight measurements which are carried out at regular intervals. Work by Parrott[44] and by Feldman[45] have indicated that the replacement of the pore water by an organic solvent is a simple physical process of counter-diffusion. This assumption has recently been supported by carbon and H^1 NMR data obtained by Hansen and Gran who studied the exchange of ethanol with water in saturated cement pastes.[62]

Typical diffusion curves for methanol and isopropanol in saturated OPC paste disks (diameter = 38 mm, thickness ≈ 1.35 mm) are presented in Fig. 28. These results are expressed as W_t/W_∞ versus time (at a square root scale). The quantity of solvent diffused in the sample at a certain time is represented by W_t while W_∞ stands for the amount entered at equilibrium. The values of W_t can be calculated knowing the density of each solvent and assuming that the solvent exchanges pore water on a one-to-one volume basis. Methods to determine the value of W_∞ will be discussed in the following paragraphs.

The calculation of a diffusion coefficient on the basis of solvent replacement test data can be simply done by considering the law of mass conservation and resolving Fick's second law. The general form of Fick's equation is given by:

Eq. (27) $$\frac{\partial c_i}{\partial t} = \mathrm{div}\,(D_i \nabla \mathrm{c}_i) - \frac{\partial S}{\partial t}$$

where D is the diffusion coefficient (m^2/s) and t the time (s). The last term on the right-hand side of the equation accounts for any physical or chemical interaction of the solvent with the solid. Despite the numerous evidences

@Seismicisolation

that organic solvents tend to physically and chemically interact with cement systems, authors have generally neglected the interaction term. Such an omission can simply be explained by the fact that little is known of the mechanisms of interaction. Although it is highly probable that the interaction of organic solvents with the hydrated cement paste is a concentration-dependent process, more research is needed to develop a mathematical description of the phenomenon.

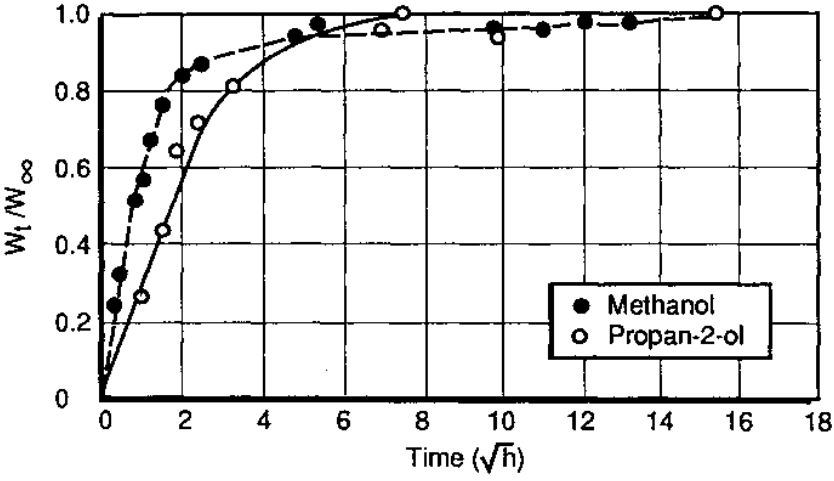


Figure 28. Typical diffusion curves for methanol and isopropanol in a saturated OPC sample.[45]

If the interaction term is neglected Eq. (27) is then reduced to:

Eq. (28) $$\frac{\partial c_i}{\partial t} = \text{div}\,(D_i \nabla c_i)$$

As emphasized by Day[63], various forms of the mass balance equation can be developed according to the type and the shape of the specimens under investigation. For a long circular cylinder of radius (r) in which the penetration of the solvent is everywhere radial, Eq. (28) becomes:

Eq. (29) $$\frac{\partial c_i}{\partial t} = \frac{1}{r}\frac{\partial}{\partial r}\left(r D_i \frac{\partial c_i}{\partial r}\right)$$

@Seismicisolation

The theory for a number of classical cases is outlined by Crank.[64] For each of these cases, the diffusion coefficient of the material can be calculated by simply integrating the mass balance equation. A general solution of the diffusion equation (more or less independent of the sample geometry) is given by Barrer:[63][64]

Eq. (30)
$$\frac{W_t}{W_\infty} = 1 - \left\{ \frac{6}{\pi^2} \sum_{n=1}^{\infty} \left[\frac{1}{n^2} \exp\left(\frac{Dn^2\pi^2 t}{r_0^2} \right) \right] \right\}$$

In this equation, r_0 stands for the "effective" radius of the sample. The effective radius is defined as the radius of a sphere which has the same surface/volume ratio as the sample under consideration. For a cylinder, r_0 is equal to 3 × volume/surface area ratio of the sample. It can also be shown that for small *t*, Eq. (30) can be simplified to become

Eq. (31)
$$\frac{W_t}{W_\infty} = \frac{6}{r_0}\sqrt{\frac{Dt}{\pi}}$$

It should be emphasized that Eqs. (30) and (31) were developed assuming that the diffusion coefficient (D) and the boundary conditions remain constant during the entire exchange process. There is no published evidence that the diffusion coefficients of organic solvents should be concentration-dependent parameters. The boundary conditions can be easily kept constant by regularly renewing the solvent during the diffusion experiment.

As underlined by Day[63], the value of W_∞ can be established in a number of ways. First, it can be calculated by assuming that all the evaporable water in the sample can be replaced by the solvent on the basis of the following equation

Eq. (32)
$$W_\infty = \left(\frac{\rho_s}{\rho_w} \right) (Q_0 - Q_{0d})$$

where Q_0 is the initial saturated-surface dry mass of the sample, Q_{0d} is its oven-dry mass, ρ_s the density of the solvent, ρ_w the density of water. The assumption that the solvent replaces all the evaporable water at equilibrium has been found to be valid for isopropanol and ethanol.[45][46][65][66] As can be seen in Fig. 29, test results indicate, however, that the amount of water

@Seismicisolation

replaced by methanol may be slightly greater than the volume of evaporable water contained in the sample. Methanol molecules may be able to penetrate the layered silicate structure of the material and replace some of the structural water.

The second method is to immerse the sample in the solvent for a very long period or use very small samples such that a negligible rate of weight loss and a well-defined asymptote can be established. As emphasized by Day,[63] for all but very small samples, this method is not suitable because a very long immersion time (up to several months in certain cases) is required.

Typical isopropanol replacement curves obtained by Feldman[45] for a series of hydrated cement paste samples prepared at various water/cement ratio (ranging from 0.3 to 1.0) are shown in Fig. 30. The samples tested by Feldman were thin (1.14 mm thick) disks of paste initially saturated with water. The diffusion coefficients calculated by the author on the basis of these experimental data are summarized in Table 5. The diffusion coefficients given in the table were calculated using the following equation which is a modified version of Eq. (31)

Eq. (33) $$\frac{W_i}{W_\infty} = 1.127\sqrt{\frac{Dt}{L^2}}$$

In this equation, L corresponds to the half thickness of the sample.

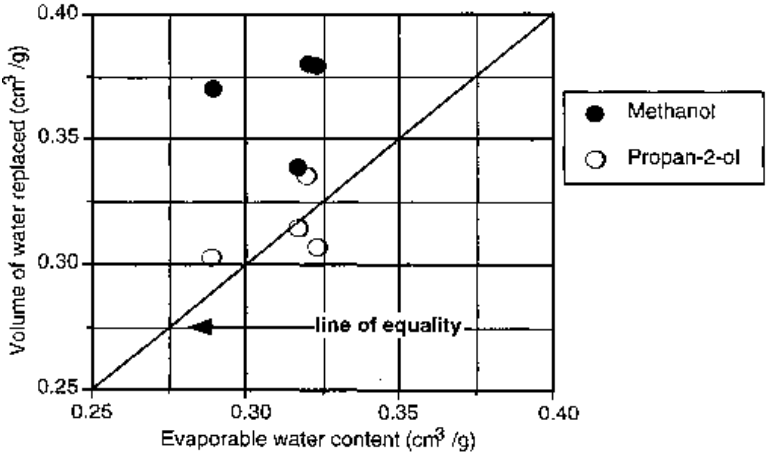


Figure 29. Volume of water replaced by isopropanol and methanol as a function of the evaporable water content of the samples.[46]

@Seismicisolation

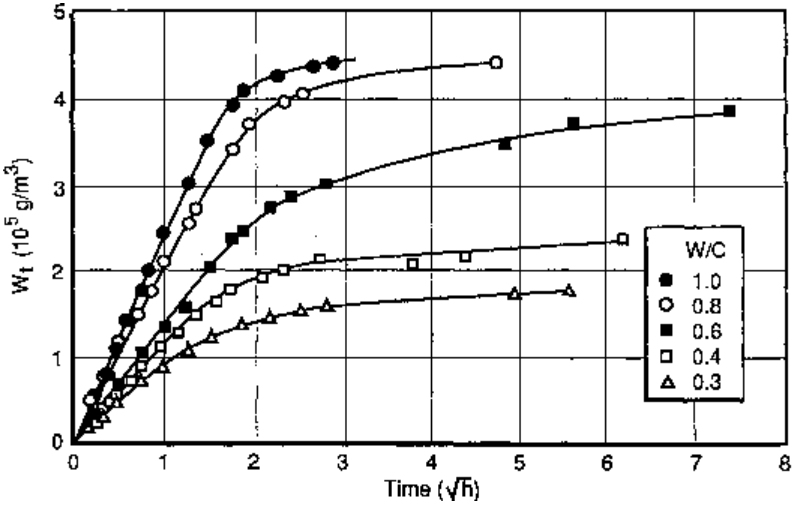


Figure 30. Diffusion of isopropanol in saturated cement paste samples.[45]

As can be seen, the values for the diffusion coefficient tabulated in Table 5 vary between approximately 5×10^{-12} to 2×10^{-11} m^2/s. As emphasized by Feldman,[45] this is in the same range as values obtained by other workers for ions such as Na^+ and Cl^- diffusing through water-saturated ordinary portland cement samples. The results obtained by Feldman[45] clearly demonstrate the potential of solvent diffusion experiments to rapidly determine the transport properties of cement-based systems. Recently the solvent replacement technique has been used by some authors to determine the formation factor of cement systems.[65]

The solvent replacement technique shows promise as a rapid method of assessing the transport properties of cement systems. More research is, however, needed to fully develop the method. For instance, the choice of the right solvent for the diffusion measurements appears problematic. Recent work by Hughes[66] and by Hughes and Crossley[67] suggests that the suitability of these fluids for diffusion coefficient measurements can be strongly related to the system considered. Results of Hughes' experiments indicate that, while the penetration of methanol in saturated silica fume pastes appears to be a standard counter-diffusion process, the immersion of similar specimens in ethanol and isopropanol yields unexpected results. Instead of continuously losing weight until equilibrium was achieved,

@Seismicisolation

samples were found to first lose weight then to partially regain it (see Fig. 31). Anomalous behaviors were also reported for slag and fly ash cement pastes immersed in both methanol and isopropanol.[46][67][68] This phenomenon most probably results from a bulk removal of water by the solvent where the rate of removal exceeds the rate of replacement. The anomalous penetration of the solvent appears particularly important for finely divided systems containing supplementary cementing materials. Additional research is needed to select a suitable solvent for which the interaction with the solid is minimal and that can easily penetrate the pore structure of dense cement systems.

Table 5. Isopropanol Diffusion Coefficient and Related Parameters for Pastes of Different Water/Cement Ratios[45]

Water/Cement Ratio	Diffusion Coefficient ($\times 10^{-11}$ m^2/s)	Correlation Coefficient	Diffusion Rate ($g/m^3h^{1/2}$)
0.3	0.753	0.9847	937.2
0.3	0.535	0.9820	862.4
0.3	0.895	0.9826	1179.7
0.4	1.025	0.9902	1307.7
0.4	0.880	0.9600	1494.6
0.4	0.672	0.9300	1257.0
0.5	0.467	0.9830	—
0.5	0.366	0.9704	883.6
0.5	0.440	0.9965	948.9
0.6	0.872	0.9986	1597.1
0.8	1.059	0.9671	—
0.8	1.382	0.9964	2323.0
1.0	2.289	0.9991	2910.0

@Seismicisolation

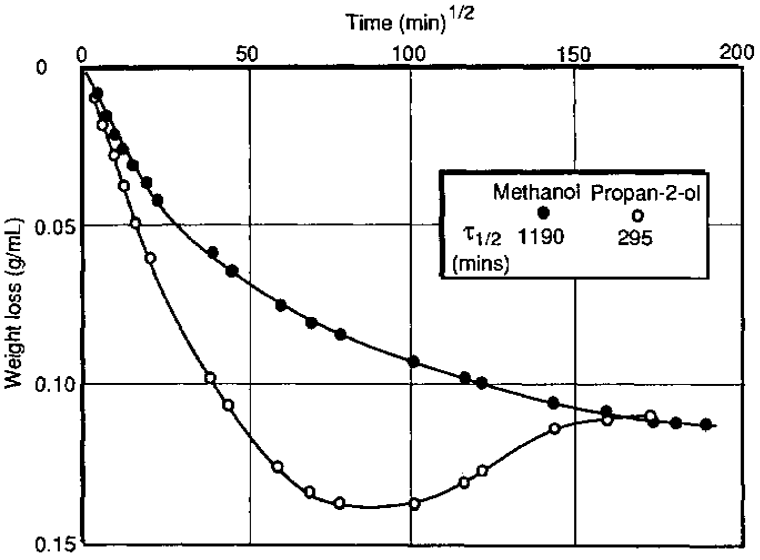


Figure 31. Diffusion of isopropanol and methanol in saturated blended silica fume cement paste samples.[66]

Additional information on the penetration mechanisms is also required to adequately interpret solvent replacement curves. Many authors have observed that the diffusion of solvent in well-cured cement pastes and mortars was not linear as a function of the square root of time even for the initial portion of the replacement process.[46][63][68] The non-linearity of the solvent replacement curves is probably related to the interaction of the solvent with the hydrated cement paste. More research is thus needed to fully understand the nature of these interactions in order to be able to correctly model them with a mathematical equation.

5.4 Investigation of Drying-Induced Pore Structure Alterations

The microstructure of hydrated cement paste is an intricate and unstable system that is very sensitive to changes in moisture and temperature. Drying, for instance, tends to induce severe internal stress gradients into the material. Besides cracking, several investigations have clearly established

@Seismicisolation

that drying can also significantly alter the hydrated cement paste pore structure.[3][4][46][69]–[73] According to these studies, pore structure modifications are to a large extent irreversible and affect the entire range of the pore size distribution. Such alterations can have considerable consequences on the engineering properties of cementitious materials.

Considering that many pore structure characterization techniques (like mercury intrusion porosimetry and gas adsorption-desorption analyses) can solely be performed on dried samples, researchers have been looking for various ways to investigate the drying-induced pore structure alterations. Along with low-temperature calorimetry and ac impedance, solvent replacement is among the few experimental techniques capable of investigating the pore structure characteristics of saturated specimens. Drying-induced microstructural alterations can, therefore, be studied with minimum perturbations from the procedure itself.

Feldman[48] was among the first researchers to rely on solvent diffusion experiments to evaluate the influence of drying on the microstructure of ordinary portland cement (OPC) pastes prepared at various water-cement ratios. Using isopropanol as a replacement fluid, he found that predrying at 42% relative humidity had the tendency to significantly increase the rate of diffusion of the solvent in thin (1.14 mm thick) cement paste disks. Parrott[47] also reported a substantial increase of the rate of replacement of pore water by methanol in predried alite pastes. The greater influence of drying (compared to the results reported by Feldman) can probably be attributed to the presence of microcracks in the specimens. Parrott worked with 3 mm thick specimens that were more likely to be microcracked during the drying procedure.

The increased diffusivity of the predried OPC paste is also in good agreement with the low-temperature calorimetry data reported by Bager and Sellevold.[73] Their results clearly indicate that drying increases the amount of large pores and decreases the amount of smaller pores. Due to the relatively fine pore structure of the hydrated cement paste, high capillary tensions can be induced during desorption. Such forces originate from the formation of curved menisci within the small capillaries and can reach appreciable values. The thin walls of hydrates separating some of the relatively small pores present in the structure collapse under these stresses to create a continuous network of larger pores.

@Seismicisolation

6.0 MERCURY-INTRUSION POROSIMETRY

6.1 Introduction

Mercury-intrusion porosimetry appears to be the most commonly used pore structure characterization technique. This method is regularly used to characterize the internal structure of various porous systems such as ceramics, stones, clays, and cement-based materials. The method is relatively straightforward and generally yields reproducible pore size distributions. Parameters such as the total porosity, the threshold diameter, the theoretical pore diameter, or the maximum continuous pore diameter and the mean pore diameter, can be deduced from these distributions.

Despite its numerous advantages, the method is not believed to give the "true" pore size distribution of complex systems such as hydrated cement paste and concrete. As will be discussed in the following paragraphs, the technique covers a large but incomplete portion of the whole range of possible pore sizes found in cement-based composites. In addition to the fact that the distributions obtained by this method are based on numerous simplistic assumptions,[74] the pore filling by mercury intrusion has been reported to significantly alter the pore structure of hydrated cement paste systems. Numerous studies have also clearly indicated that the results obtained are strongly influenced by the sample preparation procedure.

6.2 The Concept

The technique is based on the principle that non-wetting liquids (see Fig. 32) such as mercury, can only intrude a porous material if a certain pressure is applied on the system.[75] The pressure required to intrude mercury in a given porous material is a function of the contact angle, the surface energy of the liquid, and the geometry of the pores intruded. If one assumed that the pores filled with mercury have a cylindrical shape, the size of the intruded pores can be related to the mercury pressure according to the following equation:

Eq. (34) $$\Delta P = \frac{-2 \cdot \sigma_{l/v} \cdot \cos\theta}{r}$$

@Seismicisolation

where, ΔP is the pressure (in excess of the ambient pressure) required to cause the mercury intrusion, r is the radius of the cylindrical pore being intruded, $\sigma_{l/v}$ is the surface tension of mercury (usually 485 mN/m) and θ is the contact angle between the mercury and the cylindrical pore wall.

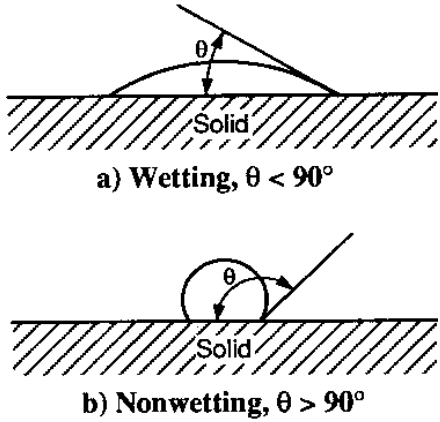


Figure 32. Wetting and non-wetting liquids on a surface.[75]

Equation (34) was derived by Washburn[76] and is valid for any liquid intrusion phenomenon in capillary porous systems. As can be seen in Fig. 33, for wetting angles less than 90°, cos θ is positive and P is negative, indicating that pressure greater than ambient must be applied to the top of a liquid column in a capillary to force the liquid out. When θ is greater than 90°, resulting in capillary depression, cos θ is negative and pressure greater than ambient must be applied to the liquid in the reservoir in which the capillary is immersed to force the liquid into the capillary. When $\theta = 0°$, Eq. (34) reduces to Eq. (35) where ΔP is identical to the pressure within a bubble in excess of ambient.

Eq. (35) $$\Delta P = \frac{2\sigma_{l/v}}{r}$$

According to the Washburn equation (34), a capillary of sufficiently small radius will require more than one atmosphere of pressure differential in order for a non-wetting liquid to enter the capillary. A cylindrical capillary with a radius of 18Å (18×10^{-10} m) would require nearly 415 MPa

@Seismicisolation

of pressure before mercury would enter, so great is the capillary depression.[75] The method of mercury porosimetry requires evacuation of the sample and subsequent pressurization to force mercury into the pores. Since the pressure difference across the mercury interface is then the pressure (P) applied on the system, Eq. (34) reduces to :

Eq. (36) $$P = \frac{-2 \cdot \sigma_{l/v} \cdot \cos\theta}{r}$$

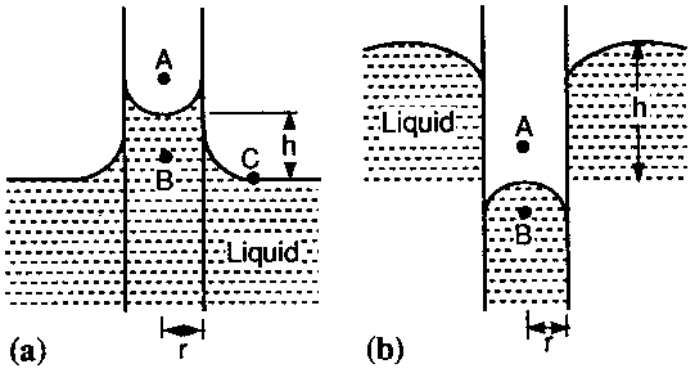


Figure 33. (*a*) Capillary rise (• < 90°) and (*b*) capillary depression (• > 90°).[75]

One of the major drawbacks of mercury intrusion porosimetry is that in order to calculate pore size distributions according to the Washburn equation one has to make a certain assumption concerning the morphology of the pores contained in the solid body. In most cases researchers have chosen to model the individual pores as cylinders.[74][77] As emphasized by Diamond,[74] the hydrated cement paste does not have cylindrical pores, but different classes of voids of various shapes, some being exceedingly complex.

6.3 Operating Principle

Mercury intrusion porosimetry can be performed using several different instruments commercially available. These instruments are commonly

@Seismicisolation

called mercury porosimeters. The first mercury porosimeter was constructed by Ritter and Drake nearly sixty-five years ago.[77] A large number of varying designs have been proposed since then; however, despite the variety of apparatuses built, the principle of the mercury intrusion technique remains the same. In fact, this technique involves two main stages: *(i)* the selection and the preparation of the samples and *(ii)* the mercury intrusion itself (at low and high pressures). In the next paragraphs the selection, the sample preparation, and the mercury intrusion technique, are briefly discussed.

6.4 Sample Preparation

The sample used for mercury intrusion porosimetry (realized with commercially available instruments) typically ranges in volume from a few cubic centimeters up to 15 cm^3 with a maximum mercury intrusion volume of 5 to 10% of the sample volume. It is advantageous to use large samples in order to reduce the effect of local heterogeneities and to obtain more representative results. However, the maximum volume of the sample that can be used during an experiment is mainly controlled by two parameters. One is the size of the sample chamber where the sample is housed during the mercury intrusion experiment. Indeed, the tested samples must fit into the sample chamber of the porosimeter. The other is that the intrudable pore volume must not exceed the range over which the mercury porosimeter can detect intrusion.[78] Recent data by Hearn and Hooton[79] indicate that porosity measurements by mercury intrusion are somewhat sensitive to the size of the samples. For a given series of measurements special care should be taken to use samples of similar dimensions in order to reduce as much as possible this effect.

Prior to initiating an intrusion experiment, the porous sample must be completely dried. In fact, the pores of the sample must be free from any bulk or adsorbate liquids. It is essential to remove all the bulk and adsorbate liquid in the porous system in order to prevent any unexpected changes in the contact angle between the mercury and the solid phase. According to Eq. (36) a modification of the contact angle can affect, for a given mercury pressure, the diameter of the pore intruded. Furthermore, adsorbate liquid (on the pore wall) can significantly reduce the effective diameter of numerous small pores.

Liquids (usually water for cementitious materials) can be removed by heating, desiccation, evacuation, or some combination of these techniques,

@Seismicisolation

however, the liquid removal will generate capillary pressure that can affect the pore structure of the material being tested. In fact, the capillary pressure can cause shrinkage.[78] As underlined in the previous section, it is possible to replace the pore water with an organic solvent of lesser surface tension and thus reduce the capillary tension that produces the alterations of the porous system. The effect of solvent replacement as a precursor treatment on mercury intrusion pore size distributions is further discussed in the following paragraphs.

6.5 Mercury Intrusion Experiment

The porous sample under test is placed in a capillary tube. This tube is called the sample cell, dilatometer, or, most frequently, the penetrometer. When the sample is ready to be tested, the air in the penetrometer (and in the porous sample) has to be evacuated. This evacuation has two main functions: removing the adsorbed water from the sample and removing the air out of the penetrometer. The removal of adsorbed water is important in order to obtain the right expected contact angle when the solid is in contact with mercury.[80]

Once evacuated, mercury is flooded into the penetrometer at low pressure. The minimum pressure at which the flooding of mercury takes place will determine the upper limit on the size of pores that can be included in the distribution being determined.[78] In theory, the upper limit on the size of pores that can be included in the distribution may be extended to approximately 1 mm.[81]

After the initial mercury filling, the penetrometer and the supply of mercury are separated. At this moment the pressure on the mercury is progressively raised. When the pressure is raised from mainly 0 to 0.1 MPa (i.e., approximately 1 atm) the pores with diameters ranging from several hundreds of microns down to several tens of microns are intruded by mercury.[78] The rate of pressure buildup must not be too high because a certain time is needed to allow the transport of mercury through the porous network of the material. This is particularly important at low pressures. When a sufficient pressure is reached, the mercury enters the pores with a given radius (see Eq. 36). The size of the intruded pores is related to the mercury pressure and the volume of the intruded pores is the volume of mercury forced into them.[78]

@Seismicisolation

Most commercial instruments have a pressure range reaching 400 MPa. At this pressure a pore diameter of approximately a few nanometers can be detected.[81] However, at such high pressures some problems may appear during the experiment. One problem is that the temperature of the pressured system may rise appreciably and then change the volume of mercury intruded. Consequently, the results of the mercury intrusion experiment (i.e., the volume occupied by the pore in the material) will be erroneous. The other problems concern the compression of the sample, the mercury, and the penetrometer.[78] When the mercury is highly compressed, its volume is decreased and then an apparent intrusion equal to the compressibility of mercury can be observed. However, the mercury compression and the loss of volume of the penetrometer tend to offset one another.

6.6 Typical Mercury Intrusion Porosimetry Results

The results of a mercury intrusion porosimetry experiment are usually expressed as a distribution of the pore volume of the material with respect to its pores sizes. Typically, the experimental pore size distribution of a given sample is presented in the form of a cumulative pore size distribution curve. For instance, Fig. 34 shows typical mercury intrusion pore size distributions obtained by Winslow and Lovell for a 0.6 water/cement ratio cement paste cured from 1 to 318 days.[82] In this figure the accumulated pore volumes include the largest diameter pore to the smallest. The pore volume axis is expressed in cubic centimeters of mercury intruded in the sample per gram of dry material. The pore diameter axis (in μm) presents the data on a logarithmic scale. This representation of the experimental data is often chosen in order to avoid crowding all of the smaller sizes against one end of the axis.

Early work by Diamond and Dolch[83] clearly showed that mercury intrusion test results could be well modeled by generalized lognormal distributions bounded by the existence of a maximum diameter, but not by a minimum diameter. Their analysis also indicated that mercury intrusion pore size distributions could be adequately described in terms of three empirical parameters: the limiting upper bound diameter (M_∞) and two parameters M^* and M´, describing the geometric mean and standard deviation, respectively, of the lognormal distribution. According to the authors, the cumulative pore-size distribution is given by the following empirical equation:

@Seismicisolation

Eq. (37)
$$P(M) = 50 - 50\,erf\left(\frac{\ln\frac{M'}{M^*}}{\sqrt{2}\cdot\ln\sigma}\right)$$

where, $P(M)$ is the percentage pore volume in diameters larger than M, M' is $(M \cdot M_\infty)/(M_\infty - M)$, and *erf* is the error function. Data obtained by the authors indicate that M_∞ and M^* vary with the water/cement ratio and the degree of hydration.

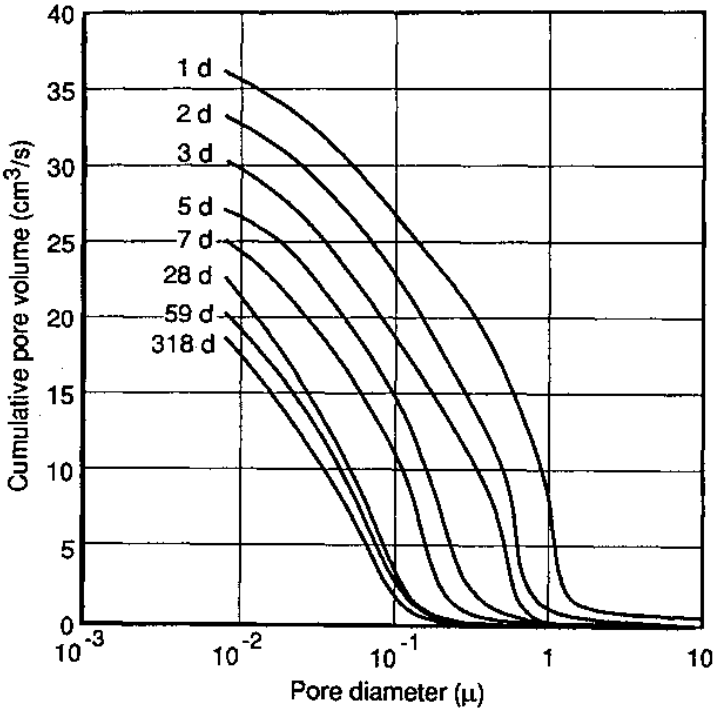


Figure 34. Pore size distribution of 0.6 water/cement ratio cement pastes.[82]

@Seismicisolation

6.7 Problems Associated with Mercury Intrusion Porosimetry

Despite the great deal of interest in the past decades, mercury intrusion porosimetry has always been subjected to various problems.[74][81] In addition to the required pore shape assumption, an important factor is that pore size distribution calculations are based on the tacit assumption that pores occur spatially in a graded array with the largest diameter pores presented to the outside of the sample and progressively smaller diameter pores occurring in successive layers towards its center.[74] For intricate porous materials the pore sizes measured by the mercury intrusion (at a given mercury pressure) are not necessarily the true pore diameters, but are rather the pore entry diameters. This phenomenon is schematically illustrated in Fig. 35. Indeed, at a mercury intrusion pressure equal to P_{Hg} this figure indicates that the large pore (on the right) cannot be intruded by mercury despite its relatively high radius. In fact, mercury will first fill the large pore (on the left) and then intrude the second large pore on the right only when the applied pressure will be sufficient to penetrate the connecting channel.

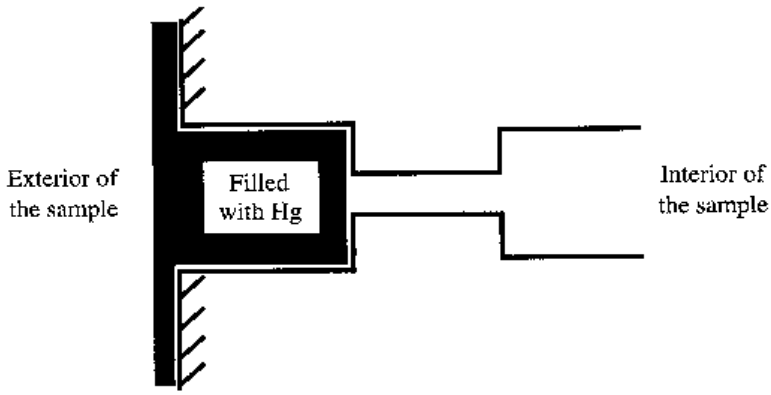


Figure 35. Influence of pore arrangement on the intrusion of mercury during an experiment.

The "neck-bottle" effect has been found to have a significant influence on the pore size distributions. As can be seen in Fig. 36, large discrepancies are usually observed between pore size distributions determined by mercury intrusion porosimetry and those derived from image analysis which are less affected by the morphological features of the pore structure.[84]

@Seismicisolation

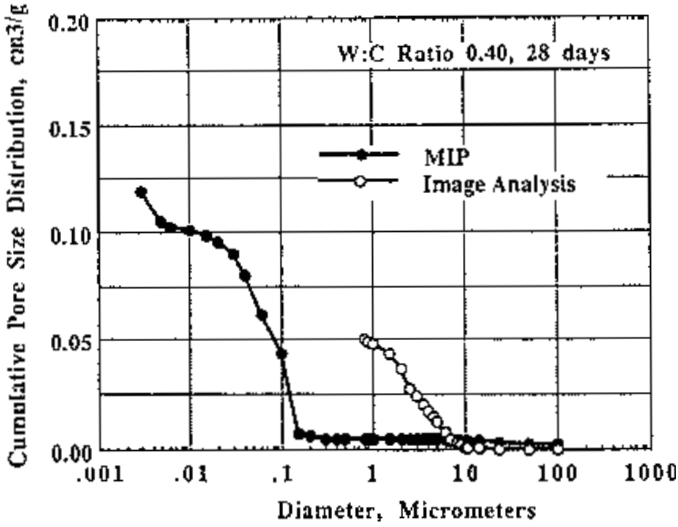


Figure 36. Comparison of image analysis and MIP pore size distributions for a 0.40 water/cement ratio paste cured for 28 days.[84]

Another problem associated with mercury intrusion porosimetry is usually called the *lost porosity*, i.e., the pores that mercury seems to be unable to reach at any pressure. In fact, numerous investigations have shown that mercury is unable to reach the total pore space of the sample. Table 6 presents a comparison of the total porosity measured by two different techniques. One is the mercury intrusion porosimetry and the other is the water porosimetry (i.e., the porosimetry measured by the differences of mass following an extensive drying at 105°C). Table 6 clearly indicates that the water porosity is substantially higher than the total mercury intruded. The data were obtained using cement paste samples prepared with two water/cement ratios (w/c = 0.6 and 0.8) and cured for 4 to 36 days at room temperature.

In another investigation, Winslow and Diamond[85] did report similar results. In fact, their results (obtained with an apparatus which could apply a maximum pressure of 102 MPa) indicated that the volume of pores intruded by mercury tends to vary significantly from one sample to another. In some cases it can reach approximately 35% of the total pore volume while in other cases it could be much less than 20%.

@Seismicisolation

Table 6. Pore Analysis Data[81]

Sample Identity	w/c Ratio	Age (days)	Hg Volume Intruded (cm^3/g)	Pore Volume* (cm^3/g)	Volume Intruded (cm^3/g)
1	0.3	5	0.133	0.188	70.8
	0.3	11	0.116	0.187	61.9
	0.3	34	0.104	0.187	57.0
2	0.6	4	0.335	0.440	76.2
	0.6	22	0.278	0.431	64.5
	0.6	36	0.251	0.412	60.9
3	0.8	4	0.489	0.565	86.5
	0.8	22	0.449	0.527	85.2
	0.8	36	0.425	0.521	81.6

**measured from water immersion experiments*

It should be emphasized that most commercial porosimeters are capable of working to pressures in excess of 400 MPa (i.e., as much as four times the maximum pressure level tested by Winslow and Diamond in their early study). The application of these high pressures largely contributes to expand the range of pores tallied by the method. However, recent studies clearly demonstrate that the technique is intrinsically limited and that even if high pressures are applied to the system mercury is unable to intrude the entire hydrated cement paste pore volume. According to Diamond[86] this phenomenon can be explained by presence of pore spaces too fine to be intruded by mercury or completely isolated from the exterior (e.g., encapsulated pockets of gel). Beaudoin[87] later suggested that the lost porosity could rather be explained by the existence of micro-space between aggregations of C-S-H sheets that are accessible to gas penetration (such as helium or nitrogen), but not to mercury. Results reported by Beaudoin[87] also indicated that the intrusion of mercury can be impeded by blocked pore space due to the presence of an interfering phase, e.g., polymer latex film.

Over the past decades numerous studies have also indicated that the application of high pressures could markedly alter the hydrated cement paste pore structure. If the problem did not seem to be particularly significant when the applied pressures were limited to 100 MPa[88] evidences of damage

@Seismicisolation

induced by the intrusion of mercury at high pressures were brought forward by Shi and Winslow[89] and by Feldman.[90] To investigate the effect of mercury intrusion on the pore structure of OPC and blended cement pastes, Feldman[90] developed a technique in which mercury could be removed by high-temperature distillation after the initial intrusion. Distilled samples were then subjected to a second intrusion. As can be seen in Fig. 37, pore size distributions for the OPC pastes were found to be marginally affected by mercury intrusion, but those of blended cement pastes were markedly affected, displaying a coarser pore size distributions. It was concluded that the latter samples were composed of relatively large, but discontinuous pores into which mercury enters by breaking through the pore structure.

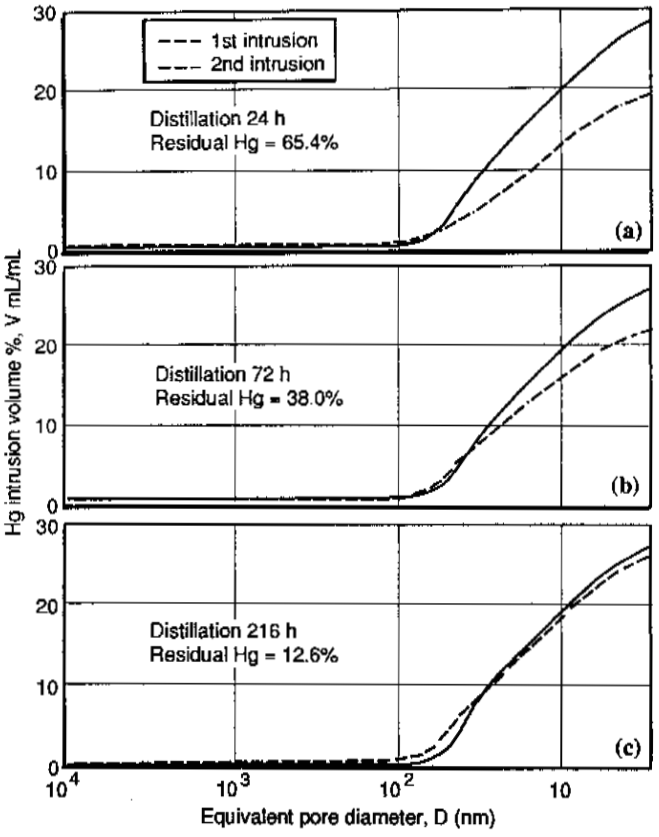


Figure 37. Influence of residual Hg content on the pore size distribution of OPC paste samples hydrated for one year at 55°C.[90]

@Seismicisolation

In a subsequent study, Shi and Winslow[89] demonstrated that the large discrepancies observed by Feldman[90] between the distributions obtained for a first and second intrusion could be explained by a combination of three factors: *(i)* the presence of residual mercury on the pore wall that could not be removed by distillation, *(ii)* the modification of the contact angle induced by the high-temperature distillation treatment, and *(iii)* the damage induced to the sample pore structure by the intruding mercury during the first intrusion. The effect of the first two factors on the mercury/hydrated cement paste contact angle is summarized in Table 7. According to Shi and Winslow[89] the intrusion of mercury at high pressures does not result in a coarser pore structure, but rather, contributes to collapse and crushing of some of the pores in the paste, the net effect being a reduced total porosity.

Table 7. Influence of Various Parameters on Contact Angle[89]

Sample	Contact Angles (°) Separate Measurements			Average Contact Angle (°)
1-day OPC	129	126	132	129
28-day OPC	123	121	132	129
28-day FA-1	132	130	133	132
28-day FA-2	134	137	132	134
28-day FA-3	128	130	131	130
28-day OPC (heated 1 month)	128	126	130	128
28-day OPC (Post-Intrusion)	135	138	132	135

6.8 Effect of Various Parameters on Mercury Intrusion Porosimetry Experiments

The pore size distribution obtained with the mercury intrusion technique can be affected by several variables. Using Eq. (36) one can easily see that the pore size distribution highly depends on the value of the contact angle (θ) assumed for a given mercury intrusion experiment. The pore size distribution also depends on the surface tension of mercury $(\sigma_{l/v})$ used for the test. This parameter can be related to the purity of mercury. Finally, two

@Seismicisolation

other variables can affect the mercury intrusion test results. One is the technique used to dry the samples. The other is the rate of mercury pressure buildup during the experiment. In the following paragraphs, the effect of all these parameters will be briefly discussed.

Contact Angle. As previously emphasized, the pore size distributions yielded by the technique are particularly sensitive to the contact angle between mercury and the pore wall. In fact, the accuracy of the measurement of pore radii into which mercury intrusion occurs is limited by the accuracy to which the contact angle is known.[75] In order to determine whether or not two samples have the same pore size distribution and pore volume, it is adequate to select a value for the contact angle between 130° to 140°. However, if absolute data are required, the value of the contact angle must be very accurately measured. Indeed, the value of the cosine function for materials exhibiting contact angles near 140° changes substantially with the angle. For instance, an error of only 1° at 140° would introduce an error of nearly 1.5% on the pore radius. The significant influence of the contact angle on the pore size distribution is illustrated in Fig. 38.[89]

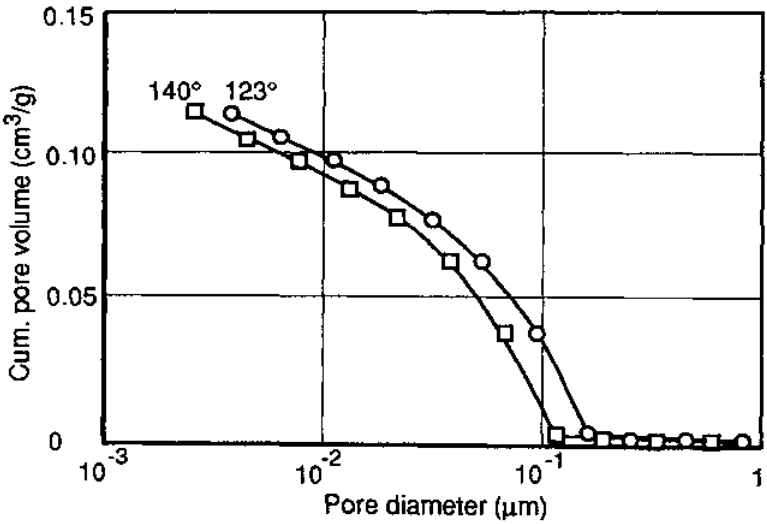


Figure 38. Comparison of pore structures plotted with correct (123°) and wrong (140°) contact angles.

@Seismicisolation

The determination of the contact angle can be done using a mercury contact anglometer.[75] This apparatus measures the contact angle of various materials under the same conditions that prevail in a mercury intrusion experiment. In order to measure the contact angle of a given material with this equipment the material must be crushed into a powder. The powder is then compacted and a cylindrical hole of known radius is made in the compacted material. A fixed volume of mercury is then placed above the powder at a known height (and pressure) in a sample holder. After placing the powder sample and the mercury into the anglometer, the apparatus is evacuated. Air is then slowly allowed into the anglometer and mercury pressure is constantly monitored. When the breakthrough pressure is reached, mercury is forced through the cylindrical hole and the pressure is then recorded. The corresponding value of $\cos(\theta)$ (which is proportional to the mercury pressure) can then be calculated (see Eq. 36). The complete procedure to measure the contact angle of various materials can be found in Lowell and Shields.[75]

A slightly different procedure was developed by Winslow and Diamond[85] to assess the contact angle of cement paste. The particularity of the method developed by Winslow and Diamond is that holes are drilled directly in a paste sample. The crushing operation is thus avoided.

It should be emphasized that the contact angle of cement-based materials can be influenced by various parameters such as the type of binder and the type of drying procedure. For instance, Winslow and Diamond[85] measured the contact angle of a thoroughly dried paste as 117° while for P-dried samples it was found to be 130°. The influence of solvent replacement on contact angle has never been systematically investigated.

The effect of fly ash (FA) and the extent of the curing period on the contact angle are shown in Table 7. Data appearing in the table were measured by Shi and Winslow[89] according to the procedure developed by Winslow and Diamond.[85] As can be seen, the contact angle tends to be slightly reduced as the degree of hydration of the hydrated cement paste increases. The addition of fly ash appears to increase the contact angle, however, different fly ashes do not greatly influence the contact angle.

Sample Drying. Mercury intrusion experiments have to be performed on dry samples. The samples can be dried using one of the following procedures: oven drying at 105°C, equilibrated over magnesium perchlorate hydrates (P-dry condition), evacuation over dry ice (D-dry condition), and solvent replacement followed by oven drying. The methods are given in order of reducing severity of water removal.

@Seismicisolation

Using the first three previous drying conditions, some mercury intrusion porosimetry experiments were conducted by Diamond[86] on cement paste samples prepared at a water/cement ratio of 0.4 and moist cured for nearly six months at room temperature. Figure 39 shows the pore size distribution obtained for each of the three drying procedures considered in the study. The results shown on this figure indicate that the coarse pore region roughly coincides whatever the drying treatment. However, for the pore space in diameter classes smaller than about 0.1 μm, the pore size distribution is markedly affected by the severity of the drying treatment.

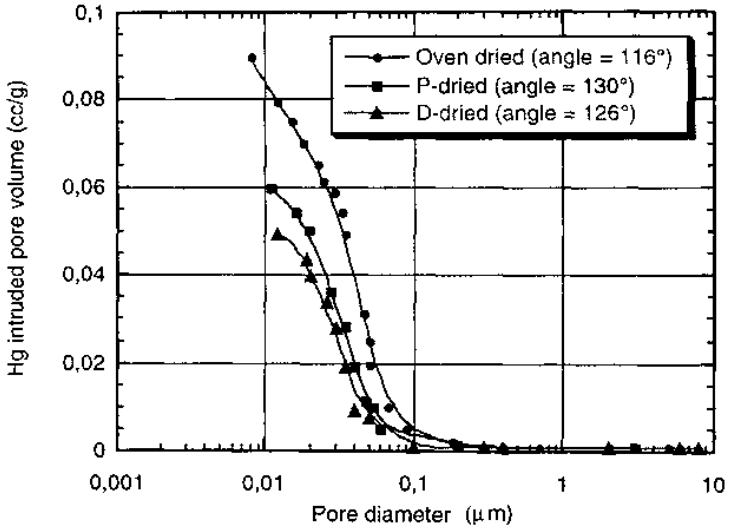


Figure 39. Influence of various procedures on mercury intrusion pore size distributions.[86]

According to Diamond,[86] the relatively large change in the apparent mercury pore size distribution in the fine pore region can be attributed to small differences in the amount of residual water retained at equilibrium with respect to the different drying treatments. In fact, the differences in the amount of residual water retained at equilibrium (from one drying technique to another one) can strongly affect the value of the contact angle. Furthermore, the thickness of the layer of adsorbed water remaining in the tested samples (for D-dry and P-dry conditions) can significantly reduce the effective diameter of the small pore measured by the mercury intrusion technique as compared to the oven dried samples. As pointed out by Diamond,[86] the changes in the apparent mercury pore size distribution in the

@Seismicisolation

fine pore region are not associated to microcracking or other reversible changes accompanying the more rigorous oven drying procedure.

Several studies[42][43][46][61][68]–[73] have clearly indicated that drying results in a generally coarser and more interconnected pore structure. Besides microcracking, the pore structure alterations are mainly induced by the local development of high tensile stresses exerted on the pore walls by the receding water menisci. Such tensile stresses tend to collapse some pore walls causing the fracture of some bonds and the creation of new contact points between the gel particles. The cohesive force between water molecules which produces the tensile stresses is surprisingly high and can reach values up to approximately 110 MPa.[91] In smaller pores, i.e., the interlayer gel pores (5 to 20 Å radius), no meniscus can be formed and the water is only adsorbed at the surface of the pore walls. Removal of the adsorbed water from the pore walls of interlayer gel pores may also have an effect equivalent to capillary tension which can draw some solid surfaces together to create new contact points between the dry surfaces of silicate particles.[3]

In practice, all drying procedures affect the microstructure. Several studies indicate that the use of solvent replacement as a precursor treatment prior to drying tends to attenuate the damages induced by drying (see Fig. 40).[42][43][92] The beneficial influence of the solvent replacement technique is generally attributed to the reduced surface tension of most organic solvents. When the solvent is removed from the pore structure, the solid material is stressed to a lesser degree than if water was removed directly. However, the influence of the residual solvent molecules that remain strongly adsorbed to the pore walls even after long drying periods in the oven has not been systematically investigated.

Mercury Purity. It is often recommended that distilled mercury has to be used to conduct mercury intrusion experiments. This recommendation is often made in order to eliminate any variation in the contact angle or surface tension of mercury. However, Moscou and Lub[80] did not see any significant influence of the mercury purity on intrusion test results. In their study, the authors compared the data obtained with chemically pure mercury to those yielded for the same type of mercury which had been used many atime for penetration analysis of hydrodesulfurization catalysts (consisting ofmolybdenum oxide and cobalt oxides supported by α-Al_2O_3). However, before each utilization the mercury was purified from solid particles by filtration.

Rate of Pressure Build-Up. The rate of mercury pressure buildup is another parameter that can be expected to influence the mercury intrusion porosimetry test results. In order to reduce the duration of the mercury intrusion experiment it is advantageous to increase the pressure applied to

@Seismicisolation

mercury at a relatively high rate. However, this rate must not be too high so as to allow sufficient time for mercury to be transported though the porous system of the sample. In commercial mercury porosimeters, a compromise between intrusion equilibrium and analysis speed is reached.[80] Usually the porosimeter pressure pump automatically stops when mercury intrusion occurs and when the mercury level in the penetrometer becomes constant again the pressure pump restarts. According to Moscou and Lub[80] real mercury intrusion equilibrium is reached with this procedure.

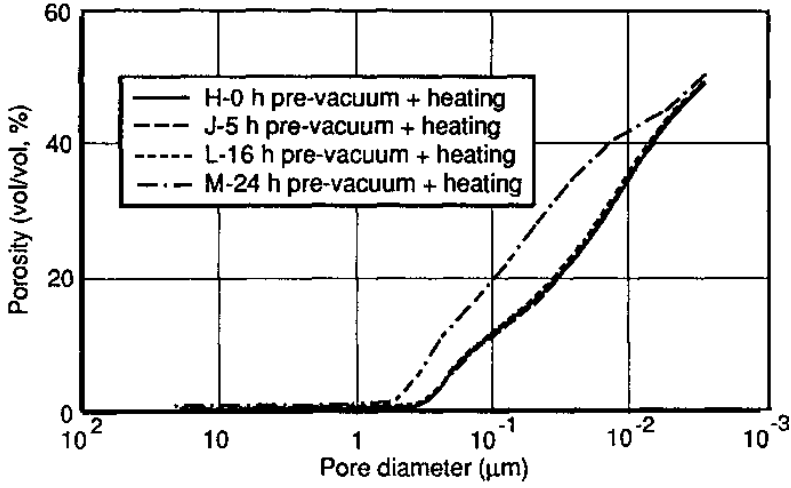


Figure 40. Pore size distributions of isopropanol-treated 0.8 water/cement OPC samples.[43]

7.0 NUCLEAR MAGNETIC RESONANCE

7.1 Introduction

As emphasized in the previous sections of this chapter the characterization of the pore size distribution of solids is of great interest in a wide range of applications. A few years ago investigators logging for petroleum formations found that the nuclear magnetic resonance (NMR) technique could provide a great deal of information on the state of liquids confined to restricted geometries.[93][94] Following this unexpected breakthrough, it was

@Seismicisolation

quickly established that NMR relaxation measurements could also be used to investigate the pore structure of various solids.[93][98] The application of NMR techniques to the characterization of the microscopic geometry of porous media has since received a great deal of theoretical and experimental attention.

As discussed in the following paragraphs, NMR relaxation techniques are particularly attractive from the standpoint of pore structure characterization. Contrary to more conventional methods, like mercury intrusion porosimetry, gas adsorption/condensation, and optical/electron microscopy, NMR techniques are both nondestructive and non-invasive. That represents a big advantage since NMR experiments can be made on saturated samples that can then be reutilized for other testing purposes. Furthermore, the cost of dedicated instruments for the measurement of relaxation behavior is relatively modest. Finally, the technique is sensitive to both the pore geometry and size and thus may potentially yield more useful information when related to the pore size distribution via an appropriate mathematical model.[94][95][98][99]

After a brief description of the basic principles of magnetic resonance techniques the relevant aspects of NMR relaxation methods related to pore structure characterization will be presented and discussed. It should be emphasized that NMR techniques are widely used in both fundamental and applied research. However, the application of NMR relaxation techniques to the investigation of the pore structure of cement-based materials is only recent. Particular problems related to the application of these techniques to cement systems will be discussed in detail.

7.2 Basic Principles

Excellent descriptions of the nuclear resonance theory and the basic concepts of NMR techniques can be found in various text books.[100]–[102] The basis of all nuclear magnetic resonance methods is that almost all nuclei have a magnetic dipole moment resulting from their spin-angular momentum.[103] A nucleus can be seen as a charged sphere spinning around its axis. The rotation generates a magnetic moment which differs from one nucleus to another.

In pulsed NMR experiments, the orientation of the moments of the spins in a static magnetic field is manipulated by short electromagnetic pulses at the resonance frequency. There exists a relationship between the frequency *(f)* of the applied RF field and the gyromagnetic ratio *(γ)* of the nucleus:

@Seismicisolation

Eq. (38) $$f = \frac{\gamma}{2\pi} B_0$$

where B_0 represents the externally applied static magnetic field. By selecting the proper frequency the spins of a particular atomic species can be excited, and the amplitude of the resulting spin-echo signal is directly proportional to the number of nuclei taking part in the experiment.[101] Unlike many nondestructive methods, NMR techniques have the marked advantage of being selective of a particular nucleus, e.g., the hydrogen nucleus for the study of water transport in concrete or the silicon nucleus for hydration studies.

More recently it has been demonstrated that the NMRI can provide additional information on the material physical properties. The method rests on the fact that after the pertubating radio-frequency pulses the system naturally returns to equilibrium and the signal decreases in intensity with time. The rate of decrease of the signal is called the relaxation rate. The basic principles underlying NMR relaxation phenomena were first introduced in a report by Bloembergen, Purcell, and Pound in 1948 very shortly after the discovery of NMR by Bloch and Purcell.[102] Two mechanisms will contribute to restore the magnetic equilibrium:

- Interactions between the nuclei themselves causing the so-called spin-spin (or transverse) relaxation
- Interactions between the nuclei and their environment, causing the so-called spin-lattice (longitudinal) relaxation

Assuming that both mechanisms result in a single exponential relaxation and that spin-lattice relaxation is much slower than the spin-spin relaxation, the magnitude of the NMR spin-echo signal is given by:[101]

Eq. (39) $$S \approx \rho \left[1 - \exp\left(\frac{-TR}{T_1} \right) \right] \exp\left(\frac{-TE}{T_2} \right)$$

where p is the density of the nucleus under study, T_1 the spin-lattice relaxation time, T_2 the spin-spin relaxation time, TR the frequency of the spin-echo experiment, and TE the so-called "spin-echo time." For "free" paramagnetic liquids, such as water, the ratio of T_1 and T_2 is equal to one ($T_1 = T_2 = 3$ s), but for liquids in a pore system, the values of both relaxation times decrease significantly because of surface interactions. It has been

@Seismicisolation

shown that T_1 and T_2 relaxation times are both a function of the saturation level of the material and the rate of molecular motion within the pore system. For fluids in isothermal porous media, the rate of molecular motion varies with the surface to volume ratio of the pore space.[97][98] Spin relaxation times T_1 and T_2 are shortened for larger specific surface areas.

The presence of paramagnetic and ferromagnetic impurities can also shorten relaxation times and make NMR experiments difficult or impossible. This is the case of ordinary portland cement which contains approximately 3% of Fe_2O_3 (by mass). The presence of paramagnetic ions markedly alters the magnetic field leading to a reduction of the NMR signal which subsequently limits the spatial resolution of the method. This is the main reason why most researchers have limited their work to the investigation of the pore structure of white cement systems.

7.3 Pore Structure Determinations

Over the past decade NMR techniques have been extensively used to monitor the transport of liquids in porous media and to investigate the mechanisms of hydration of cement systems. Excellent surveys of the application of NMR techniques for the study of these phenomena are listed in the Refs. 61, 103, and 105.

The application of NMR for the determination of pore structure characteristics relies on the fact that relaxation times are very sensitive to changes in the molecular environment and in the molecular mobility. For a paramagnetic liquid confined in a porous medium the presence of a surface results in the enhancement of the relaxation rate. Over the years it has been observed that the NMR relaxation decays of water in complex porous media (such as cement systems) could be well modeled by a multi-exponential function.[106][107] This behavior of the relaxation time results from the fact that water is present under various states (bound and free) or in different environments (small and big pores).

Most of the pore structure investigations have been carried out by measuring the T_1 relaxation behavior. Since spin-spin relaxation time (T_2) is always much shorter than the longitudinal relaxation time (T_1), Jehng[107] has recently recommended the use of T_2 measurements for a more detailed investigation of the pore structure of intricate materials (such as most cement-based materials) with a wide range of pore sizes. The transverse relaxation experiments have more spatial resolution than longitudinal relaxation studies.

In 1979, Brownstein and Tarr[108] established that the relaxation phenomenon could be characterized by two limiting regimes:

@Seismicisolation

(a) the fast diffusion regime, where

Eq. (40) $$\rho \frac{r}{D} \geq 1$$

(b) diffusion limited regime, where

(Eq. (41) $$\rho \frac{r}{D} \leq 1$$

In this equation, ρ is the pore surface relaxivity (in cm/s), r the pore radius (in Å), and D the diffusion coefficient of water (= 2.5×10^{-5} cm^2/s). The pore surface relaxivity is given by:

Eq. (42) $$\rho = \lambda / T_{2\,surf}$$

where λ is the thickness of a single layer of water molecules (= 3 Å) and T_{2surf} (in μs) is the characteristic surface relaxation of the water molecules in the monolayer adsorbed on the surface of the solid. The T_{2surf} can be obtained from the spin-spin relaxation time of the partially dry materials (i.e., equilibrated at a relative humidity low enough to limit the water adsorption process to a single monolayer).

According to the Brownstein and Tarr model, the exchange between the bound and free (or bulk) water within a pore occurs very quickly upon the fast diffusion regime. The observed relaxation rate is thus an average value between the free water and the bound water leading to a mean relaxation time depending on the pore size. The presence of different pore sizes should result in different relaxation times and thus in a multi-exponential behavior because of different relative amounts of bound and free water.

In the case of the diffusion limited regime, the bound and the free water exhibit completely different relaxation times resulting in a multi-exponential behavior in a single pore. In that case, the analysis of the relaxation curve provides information on the state of the water rather than generating data on the pore characteristics.

Very few values of T_{2surf} have been reported in the literature for cement-based materials. Jehng[107] found that T_{2surf} was approximately equal to 60 μs for white cement pastes. In a study of the pore size distributions of white cement mortars, Hazrati measured T_{2surf} values of 85 ±12 μs for mixtures prepared at various water/cement ratios (ranging from 0.25 to 0.60). According to these results it can be calculated on the basis of Eqs. 40

@Seismicisolation

and 42 that most pores contained in cement-based materials (i.e., all the pores ranging from a few angstroms to approximately 1 mm in diameter) are in the fast diffusion regime where pore-surface relaxation effects dominate the total NMR relaxation.

It has been established that, for a material containing a distribution of interconnected pores, the relaxation rate is influenced by the surface-to-volume ratio of each pore:[61][106][108]

Eq. (43) $$\frac{1}{T_{2i}} = \left(1 - \frac{\lambda S_i}{V_i}\right)\frac{1}{T_{2B}} + \rho\frac{S_i}{V_i}$$

where T_{2i} is the spin-spin relaxation rate in each individual pore, S_i/V_i is the surface-to-volume ratio of the pore and T_{2B} is the bulk spin-spin water relaxation rate which is independent of the pore size. For water, T_{2B} is long and approximately equal to 3 seconds.

For a single pore, Eq. (43) can be simplified to:

Eq. (44) $$\frac{1}{T_{2i}} = \rho\frac{S_i}{V_i}$$

Considering the case of cylindrical pores where $r = 2V/S$, Eq. (44) thus gives:

Eq. (45) $$r = 0.0706T_2$$

In a case of a single isolated pore, of volume V and surface area S, the NMR signal *(M)* is proportional to the total magnetization of the pore:

Eq. (46) $$M = \int_V m d\tau$$

where, m is the magnetic moment per unit volume of water.[101] The decay of the total magnetization as a function of time is given by:

Eq. (47) $$M(t) = M_0 e^{-i/T_2}$$

where M_0 is the initial total magnetization at $t = 0$.

The pore size distribution of a solid can be divided into a certain number of categories, each of them defined by a given pore range. Each category is thus characterized by its own surface-to-volume ratio and spin-spin relaxation time (Eq. 46). The relaxation results can therefore be averaged over each category which contributes additively to the NMR signal

@SeismicIsolation

Eq. (48) $$M(t) = M_0 \sum_{r=0}^{\infty} I_r e^{-i/T_2 r}$$

where I_r is the pore distribution.

7.4 Typical Results

So far, very few researchers have relied on NMR to investigate the pore structure of cement systems. Bhattacharya, et al.,[106] and Jehng[107] measured the spin-spin relaxation times (T_2) of saturated white cement pastes (W/C = 0.40) at different curing times. In general, a two-component pore size distribution was found regardless of the hydration stage, indicating pore diameters of 180 Å and 900 Å. These two components were identified by the authors as *capillary* and *open-gel* (outerlayer and interlayer) pores. During the hydration, these sizes remained fixed, but the volume fraction of open pore space was found to shift progressively from the larger to the smaller component.

Bhattacharya, et al.,[106] also compared the NMR pore size distribution results to mercury porosimetry and nitrogen sorption experiments. It was concluded that the mercury only intrudes the larger pores and that nitrogen experiments are only sensitive to some fraction of the smallest pores.

The two-component character of the pore size distributions of cement based materials has been later confirmed by Hazrati[61] who tested well-cured white cement mortars. On the basis of T_2 relaxation measurements, the author observed that the pore size distributions of the mortar mixtures (after two years of hydration) were characterized by two well-defined families of pores, small interlayer spaces with an average diameter of approximately 40 Å and capillary pores with a mean diameter of 400 Å. As can be seen, if the two series of data are in good agreement with respect to the two-component character of the distributions, the families of pores determined by Hazrati[61] appear to be much finer than those observed by Bhattacharya, et al.[106]

As can be seen in Figs. 41 and 42, a relatively good correlation was observed for the results obtained from the NMR and those obtained from more conventional methods like the MIP and the water vapor sorption tests. The NMR results were also compared to those obtained by water vapor sorption (BET) since, as previously emphasized, mercury cannot intrude small pores below 0.01 µm. The pore sizes obtained from the BET method were found to be finer than those obtained from NMR.

@Seismicisolation

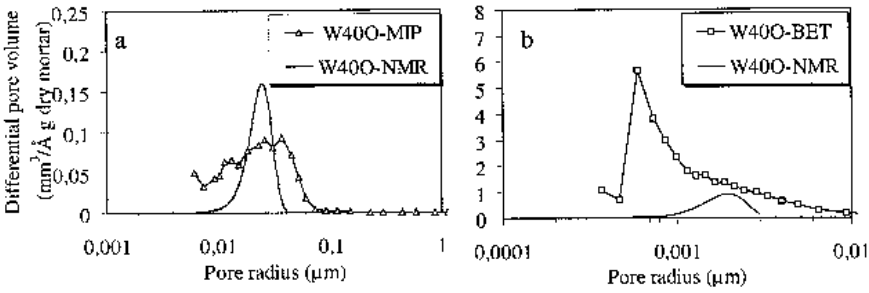


Figure 41. Pore structure of 0.40 water/cement ratio mortar sample (oven-dried), (*a*) comparison between MIP and NMR pore size distributions; (*b*) comparison between water adsorption (BET) and NMR pore size distributions.[61]

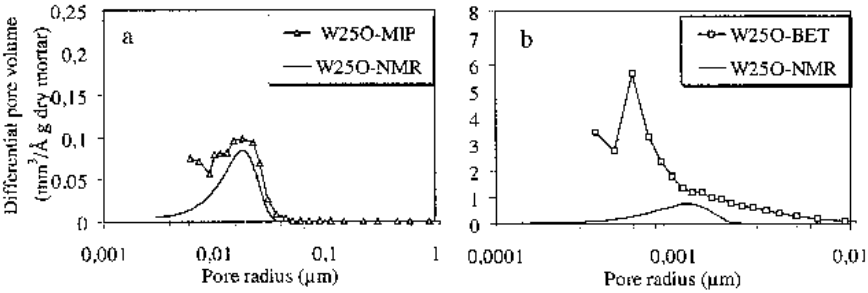


Figure 42. Pore structure of 0.25 water/cement ratio mortar sample (oven-dried), (*a*) comparison between MIP and NMR pore size distributions; (*b*) comparison between water adsorption (BET) and NMR pore size distributions.[61]

More recently, Best, et al.,[109] calculated the pore size distribution of a hardening white cement paste mixture on the basis of T_1 relaxation data. The cement paste was prepared at a water/cement ratio of 0.42 and its pore size distribution was measured after 100 hours of hydration. Results were consistent with a trimodal pore size distribution indicating pores with mean diameters of 20–120 nm, 120–2600 nm and 2.6–14 µm, respectively.

These three studies clearly emphasize the great potential of NMR for pore structure determinations. Contrary to most techniques, NMR is nondestructive and requires no pretreatment of the sample. However, more research is needed to apply the technique to real cement systems containing a certain amount of paramagnetic impurities. Furthermore, more work is also required to refine the interpretation of the results.

@Seismicisolation

8.0 PHYSICO-MECHANICAL BEHAVIOR OF CEMENT SYSTEMS — PORE STRUCTURE RELATIONSHIPS

The dependence of strength, modulus of elasticity and microhardness on porosity, pore size, and other microstructural descriptors, has been extensively studied. Techniques for measuring mechanical properties of small paste samples are described in detail in another chapter. The relationships that have been developed are examined in this section. Factors that influence strength-porosity functions and their relevance to durability issues are presented.

8.1 Strength-Porosity Relationships

Several expressions relating strength and porosity have been proposed.[110] Some relate strength to various pore size fractions. Odler and Rössler[111] developed the following expression for strength of pastes hydrated at 25°C and prepared with water-cement ratios in the range 0.25 to 0.31:

Eq. (49) $$S = S_0 - aP_{<10\ \text{nm}} - bP_{10\text{–}100\ \text{nm}} - cP_{>100\ \text{nm}}$$

where P is porosity; a, b, and c, are constants; and S_0 is strength at zero porosity. Porosity was measured by mercury intrusion. The inability of mercury to penetrate all the pore space in pastes prepared at $w{:}c < 0.40$ raises questions about the validity of this expression.

Atzeni, et al.,[112] obtained a linear correlation between compressive strength, S, and a parameter, $S_0\ (1 - \mathrm{P})\sqrt{r_m}$, where r_m is the radius value of the mean pore size, P is the pore volume fraction, and S_0 is as defined above. The term r_m is obtained from the following expression:

Eq. (50) $$\ln r_m = \frac{\sum V_i \ln r_i}{\sum V_i}$$

where V_i is the volume intruded at pore radius r_i. The relationship is tenuous due to the limitations of mercury porosimetry at low water:cement ratios.

Yiun-Yuan, et al.,[113] introduced the concept of specific surface area of the pores into the strength equation. They proposed the following expression:

@Seismicisolation

Eq. (51) $$S = K_1 \frac{1-P}{1+2P}\left[K_2(1-P)\right]^{K_3 W + K_4}$$

where K_i (i = 1 to 4) are experimentally determined constants, P is porosity, and W is the pore specific surface area.

Advances in ceramic science often provide insight into the mechanical behavior of cementitious systems. Tensile strength of porous ceramics has been related to porosity through estimates of the minimal solid contact area between sintered particles. Strength-porosity relations of ceramic bodies have often been described by the type of relationship represented by the equation $S = S_o e^{-BP}$ where S is strength and P is porosity and B, S_o are constants. Further understanding of the porosity-tensile strength relationship in porous systems was developed by Evans and Tappin.[114] They proposed the existence of pores that act as "failure causing flaws" in addition to pores that simply affect strength by concentrating stress. Pereira, et al.,[115] and Rice[116] proposed a more general pore-crack model relating tensile strength and porosity characteristics of ceramic materials:

Eq. (52) $$\sigma = \frac{\pi}{2}(\beta \tan \beta)^{1/2}\left(\frac{\sigma_p}{\sigma_c}\right)\cdot\frac{E\gamma}{d+1}$$

where β is $\pi d/(2d + h)$; d is the diameter of a spherical pore; h is the average pore spacing; l is the length of crack emanating from the pore (dependent on grain size); E is Young's modulus; γ is fracture energy; σ_p/σ_c is the ratio of the stress to propagate a single microcrack to the stress to propagate a pore-crack combination of dimension d + 1. It can be seen from this equation that tensile strength is heavily influenced by E and γ. This is the reason these three properties tend to have a similar porosity dependence. Direct relationships between porosity and fracture toughness of ceramics (K_{IC}) have not been well established. It is apparent, however, that K_{IC} is a function of the porosity-dependent Young's modulus and fracture energy terms as given by the following expression:

Eq. (53) $$K_{IC} = \sqrt{2E\gamma}$$

@Seismicisolation

Feldman and Beaudoin[117][118] reported results of an in-depth analysis of strength and modulus of elasticity data for several cement systems over a wide range of porosities. Compressive strength and Young's modulus of paste hydrated at room temperature and autoclaved cement paste with and without addition of fly ash were measured. Data of other workers[119][120] were also included. Correlations were based on the equation $S = S_o e^{-BP}$ and an analogous equation for modulus of elasticity:

Eq. (54) $$E = E_o e^{-BP}$$

where E_o is Young's modulus at zero porosity and B is a constant dependent on pore geometry and orientation of the pores with respect to the stress field. Distinct curves were obtained for each class of materials (Fig. 43).

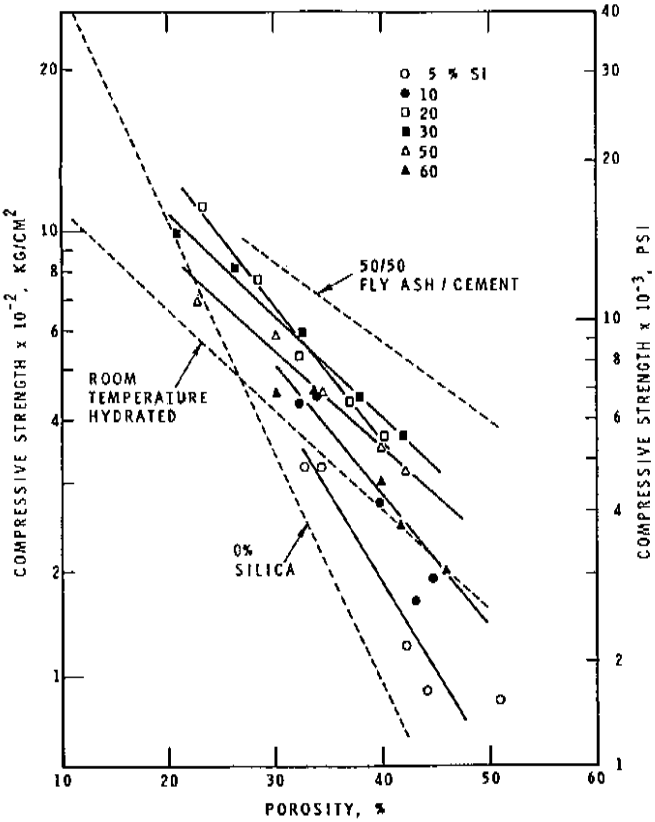


Figure 43. Compressive strength versus porosity for various autoclaved and room-temperature hydrated cement and cement-silica preparations.[118]

@Seismicisolation

The average values of density and pore size for these binders varied widely. This work confirmed the view that strength and modulus of elasticity are related to pore size distribution as well as porosity. In addition, it was apparent that it may also be related to the type of bonding within the bulk material or between crystallities. Further work by Beaudoin and Feldman[121][122] supported the view that an optimum amount of poorly crystallized hydrosilicate and well-crystallized dense hydrate products provides maximum values of strength and modulus of elasticity at a specified porosity.

It is apparent that the presence of disorganized, poorly crystallized material in cement pastes tends to favor formation of greater particle contact area and a larger number of bonds resulting in an increased population of small pores. Improved bonding develops between high-density, well-crystallized, and poorly crystallized material, as porosity decreases and thus higher strength results. The potential strength of the high-density, high-strength material is manifested. This provides an explanation of how very high strength can be obtained by hot-pressing.[123] A small quantity of poorly crystallized material at these low porosities is sufficient to provide the necessary bonding for the high-density clinker material. Work with a variety of fly ashes[122] of variable composition has confirmed these concepts. Work by Ramachandran and Feldman[124] with C_3A and CA systems has shown that at low porosities high strengths can be obtained from the C_3AH_6 product due to the increased area of contact between crystallites.

8.2 High Performance Cement Systems

Cements hydrated at low water:cement ratios yield pastes with very low porosities. It is difficult to quantitatively delineate low from high-porosity pastes. The minimum water:cement ratio (w:c) for attaining complete hydration has been variously given from 0.35 to 0.40 although a relatively high degree of hydration (70 to 80%) has been approached at 0.22 w:c with the use of special rheological aids.[125] This section of the review focuses on cement pastes formed at w:c ratios less than 0.25.

Low-porosity cement systems formed by pressure compaction techniques have been investigated by several workers.[126] The validity of using compacted samples in these studies is examined in the chapter on miniaturization. Salient features of this work are described as follows. Minimum porosity was achieved with a combination of coarse and fine powders. The strength of anhydrous clinker particles is manifested through hydrate bonds

@Seismicisolation

rather than ceramic bonds. Intimate bonding of C-S-H and closely packed cement or clinker particles results in very high strength. It was found that strength-porosity relationships could be represented by a general expression of the form $\log_{10}$(strength) = constant K (porosity).

Hot-pressing techniques were employed by Roy and Gouda[127] in attempts to produce materials with strengths approaching zero-porosity values in hydrated portland cement systems. Compressive strength values up to 408 MPa were achieved at pressures up to 344 MPa at temperatures of about 150°C. Hot-pressed, low-porosity systems (w:c = 0.10) have a typically dense, relatively homogeneous morphology. Fibrous growths and large CH crystals typical of normally hydrated pastes are characteristically absent. Reactions associated with hot-pressing take place in one hour, suggesting rapid crystal growth and formation of small amorphous intergrowths surrounding residual, unhydrated cement grains. High-pressure compaction without heat provides an environment where reactions continue over a longer period of time allowing growth of some larger crystals resulting in less overall homogeneity. Compressive-strength values of hot-pressed and high-pressure-pressed pastes fall on the same strength-porosity curve. Extrapolation to zero porosity yields a value of about 503 MPa for intrinsic strength. Work with hot-pressed C_6A_2F yielded the highest strength, 592 MPa at 0.5 hour. It was concluded that porosity is the dominant factor limiting strength. Porosity values as low as 1.8% were achieved. In work similar to the hot-pressing employed by Roy and Gouda,[127] strength values obtained by Lu and Young (>700 MPa)[128] suggest that the intrinsic strength may be higher. The strength-porosity relationship can be described by a Rhyschkewitch equation. A difference in product formation at higher temperatures may be partly responsible. These systems contained 5% silica fume and were compacted for two hours at 460 MPa and 200°C. Subsequent moist-curing for 28 days and drying at 200°C produced the very high strength values.

Principles of strength development relevant to low-porosity systems are further clarified by examination of the strength contours in a porosity versus content of crystalline material plot (Fig. 44).[129] The line *AB* represents a paste system with high strength at low porosity due to an increasing degree of crystallinity. The latter comes from the higher strengths of unhydrated cement. The line *CD* typifies hot-pressed systems where high strengths at lower porosities are obtained with little change in the degree of hydration and a relatively high proportion of crystalline material. The line *EF* corresponds to autoclaved cement-fly ash mixtures. Lines *P* through *T* are representative of cement systems containing quartz with different particle size.

@Seismicisolation

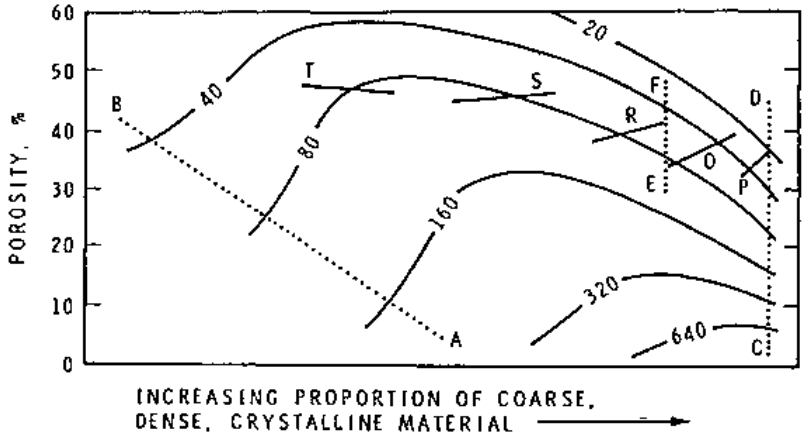


Figure 44. Compressive strength (MPa) of cement pastes as a function of porosity and particle crystallinity distribution.[129] The significance of lines *AB*, *CD*, and *EF* is described in the text.

8.3 Relationships Between Pore Structure, Permeability and Diffusivity

Permeability and diffusivity are often used as descriptors of concrete quality with respect to durability in aggressive environments. A discussion of the pore structure of cement pastes and its implication for durability follows. Methods of permeability measurement are described in detail in Ch. 16.

The basic factors relating pore models and permeability can be derived from the Hagen-Poiseville law.[130] A simplified description is given by:

Eq. (55) $$\frac{Q}{A} = K\frac{\Delta P}{\eta h}$$

where Q/A is the volume flux passing through the specimen area A, ΔP is the pressure difference between the two sides of the specimen, η is the viscosity, h is the thickness of the specimen, and K is the coefficient of permeability.

@Seismicisolation

The coefficient of permeability, K, can be related to the mean pore radius r_t by the following expression:

Eq. (56) $$K = w \varepsilon r_t^2$$

where w is a form factor (1/8 for cylindrical pores) and ε is the porosity.

A more rigorous estimate can be obtained by including pore size distribution in the analysis. Hence:

Eq. (57) $$K = C \int r^2 f(r)\, dR$$

where C is a constant.

Strict adherence to these equations is generally not observed due to the irregular shape of pores and their tortuosity. It is clear that flow through a series of parallel pores will be governed by the largest pores; flow through pores in series will be controlled by the smallest pores.

Graf and Setzer[130] identified the principle factors correlating pore size distribution with permeability. They calculated a mean pore radius from permeability data using an effective porosity of $\varepsilon/3$. A value r_m determined from mercury intrusion data was taken from the maximum of the differential curve. The ratio r_m/r_t increased greatly with the water:cement ratio, and r_t was always smaller than r_m. The authors ascribed this to phenomena associated with each of the two different measurements.[130]

Many authors[131][133] have used pore size distribution results obtained from mercury intrusion porosimetry to define a mean pore radius. One, derived from the dV/dP (P = mercury intrusion pressure) versus pore radius plot was termed the "critical pore radius" or the "maximum continuous pore radius."[131] These radii are similar, but not identical to the "threshold radius" coined by Diamond.[132] The median pore radius (the radius at the point where 50% of the pore volume is intruded by mercury) is also similar. A linear relationship between log (water permeability) and mean pore radius has been reported.[133] Materials included cement pastes of different water:cement ratios made with pure portland cement and slag, fly ash, and silica fume blends. Nyame and Illston[131] related pore structure and permeability using the radius obtained from the differential mercury intrusion curve

Eq. (58) $$K = 1.684 r_m^{3.284} \times 10^{-22}$$

@Seismicisolation

The value of the correlation coefficient was 0.96, but for values of r_m less than 100 nm the data scatter was large.

Bier, et al.,[134] measured permeability of water through oven-dried and non-oven-dried specimens. They found that oven drying created visible cracks and increased the permeability by about an order of magnitude. The high values, however, decreased during further exposure to water and reached the same values as observed for samples not dried in a short period. This result occurred despite the fact that the oven-dried samples had coarser pore structures as determined by mercury intrusion after the experiment. It was concluded that the deposition of particles into the cracks rapidly reduced permeability. This emphasizes the difficulty in making precise conclusions with regard to pore size distribution-permeability relations. The effective ionic diffusivity in a porous body can be determined from the results of a simple steady-state experiment and the use of Fick's first law. The simplified equation is:

Eq. (59) $$C_2 = \frac{DAC_1\left(t - t_0\right)}{V \cdot l}$$

A cement paste specimen of thickness l and cross-section area A is inserted between two solution-filled compartments. One contains an ionic species with concentration C_2, where $C_2 \ll C_1$. C_1 is effectively constant and C_2 increases linearly. V is the volume of compartment 2 and t_o is the time for steady-state conditions to occur. D (cm^2/s) is the effective diffusivity of the ion.

This diffusivity, also called the intrinsic diffusivity, is related to the diffusivity in free liquid as follows:

(Eq. (60) $$D_i = D_t \frac{\varepsilon\delta}{T^2}$$

where δ, the constrictivity, is dependent on both the porous medium and the diffusing species. T is tortuosity.

It is also known that ion-pore wall interaction leads to a substantial decrease in diffusion in free liquid.[135] In addition, it has been found that during leaching monovalent ions are released by a diffusion mechanism. The release of other ions is generally slower, controlled by a combination of mechanisms.[136]

@Seismicisolation

Much work[137]–[139] has been reported on the effect of mineral admixture additions to portland cement as it relates to pore structure and diffusivity of materials based on hydrated cement. In most cases there is a considerable decrease in the values of mean pore radius and diffusivity. Diffusivity values were measured over periods in excess of 200 days for mortars made with ordinary portland cement (OPC) and silica fume and slag mixtures.. Values for OPC pastes were as much as 25 times greater than for the blends. Electrical conductivity measurements show similar trends. A plot of electrical conductivity of mortars versus median pore size (Fig. 45) illustrates the effect of mineral addition on diffusivity. A linear relationship for the OPC pastes is apparent. The curves for the blend are significantly lower. It is apparent, however, that considerable damage occurs during mercury intrusion into blended cements.[140] This is probably a result of penetration through thin pore walls and into isolated or ink-bottle pores. This appears to reinforce arguments expressing doubt as to the validity of mercury intrusion results for these systems.

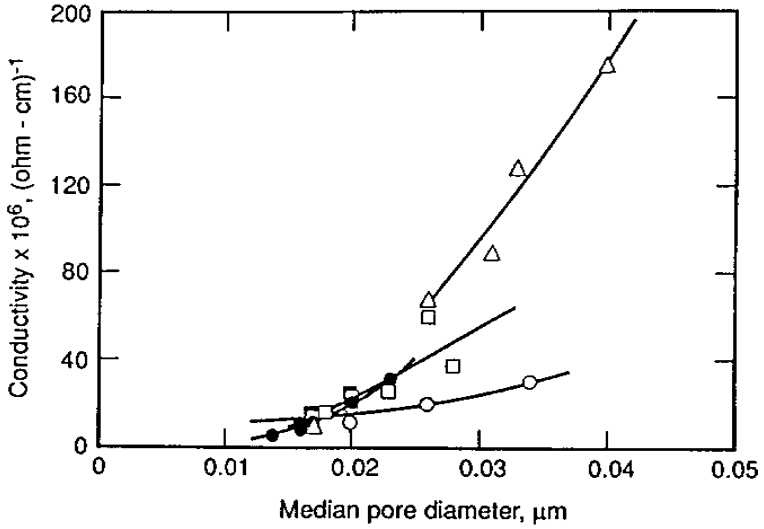


Figure 45. Electrical conductivity of mortars versus median pore diameter.[139] Cement systems: Δ, type 10 cement; O, type 50 cement, 10% silica fume; ■, type 50 cement, 3% silica fume, 65% blast furnace slag; , type 50 cement, 5% silica fume, 30% fly ash; ●, type 50 cement, 3% silica fume, 75% blast furnace slag.

@Seismicisolation

8.4 Relationship Between Porosity and Degree of Hydration

Porosity of hydrated cement systems decreases with an increase in degree of hydration as the original pore structure formed on setting is modified by the infilling of pores with hydration product.

The changes in the properties of concrete in the presence of admixtures, e.g., calcium chloride, may be due to both the degree of hydration and a change in the intrinsic structure of the cement paste. Monitoring these two parameters provides insight on the behavior of these systems. At common degrees of hydration (pastes containing 0–3.5% $CaCl_2$), the porosity surface area, strength, absolute density, and microstructural features reveal differences.[141]

The compressive strength and porosity values of cement pastes expressed as a function of the degree of hydration are shown in Fig. 46 and 47. The results indicate that the intrinsic characteristics of cement pastes are changed by the addition of $CaCl_2$. At constant degree of hydration the porosity of the pastes is in the order: 3.5% $CaCl_2$ > 1–2% $CaCl_2$ > 0% $CaCl_2$. The compressive strength at 28 days is in the order: 1–2% $CaCl_2$ > 0% $CaCl_2$ > 3.5% $CaCl_2$ and the absolute density is in the order: 3.5% $CaCl_2$ > > 1–2% $CaCl_2$ > 0% $CaCl_2$. The highest compressive strengths in the pastes containing 1–2% $CaCl_2$ may be due to a combination of a reasonably high density and low porosity, which would promote relatively better bonding between particles.

@Seismicisolation

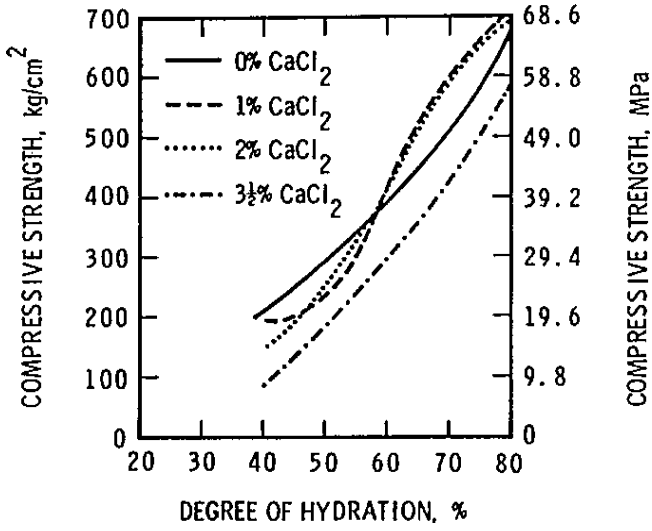


Figure 46. Strength versus degree of hydration relationship for cement paste containing calciuim chloride (w/c = 0.40).[141]

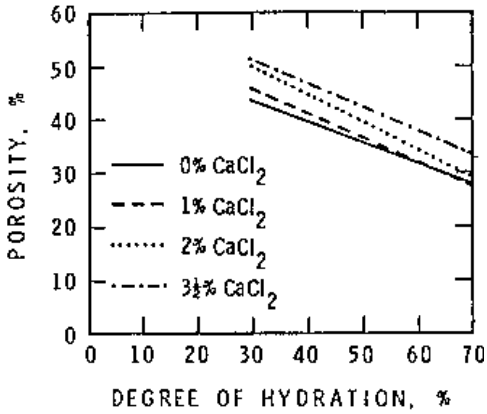


Figure 47. Porosity versus degree of hydration relationship for cement paste containing calcium chcloride (w/c = 0.40).[141]

@Seismicisolation

REFERENCES

1. Feldman, R. F., The Flow of Helium into the Interlayer Spaces of Hydrated Portland Cement Paste, *Cem. Concr. Res.*, 1:285–300 (1971)
2. Feldman, R. F., Helium Flow Characteristics of Rewetted Specimens of Dried Portland Cement Paste, *Cem. Concr. Res.*, 3:777–790 (1973)
3. Feldman, R. F., Changes to Structure of Hydrated Portland Cement on Drying and Rewetting Observed by Helium Flow Techniques, *Cem. Concr. Res.*, 4:1–11 (1974)
4. Feldman, R. F., Helium Flow and Density Measurement of the Hydrated Tricalcium Silicate-Water System, *Cem. Concr. Res.*, 2:123–136 (1972)
5. Feldman, R. F., Application of the Helium Inflow Technique for Measuring Surface Area and Hydraulic Radius of Hydrated Portland Cement, *Cem. Concr. Res.*, 10:657–664 (1980)
6. Powers, T. C., The Growth of Basic Research on the Properties of Concrete in the PCA Laboratories, *Proc. of Symp. on Structure of Portland Cement Paste and Concrete*, Washington, Highway Res. Board, Special Report, 90:3–8 (1966)
7. Kantro, D. L., Brunauer, S., and Copeland, L. E., *BET Surface Areas - Methods and Interpretations in the Solid Gas Interface*, (E. A. Flood, ed.), pp. 413–430, Marcel Dekker, NY (1967)
8. Brunauer, S., Mikhail, R. S. R., and Bodor, E. E., Pore Structure Analysis Without a Pore Shape Model, *J. Coll. Inter. Sci.*, 24:451–463 (1967)
9. Mikhail, R. S. R., Brunauer, S., and Bodor, E. E., Investigation of a Complete Pore Structure Analysis: 1. Analysis of Micropores, *J. Coll. Inter. Sci.*, 26:45–53 (1968)
10. Feldman, R. F., Sorption and Length-Change Scanning Isotherms of Methanol and Water on Hydrated Portland Cement, *Proc. 5th Int. Symp. Chem. Cement*, Part III, 3:53–66 (1968)
11. Bodor, E. E., Skalny, J., Brunauer, S., Hagymassy, J., and Yudenfreund, M., Pore Structures of Hydrated Calcium Silicates and Portland Cements by Nitrogen Adsorption, *J. Coll. Inter. Sci.*, 34:560–570 (1970)
12. Cranston, R. W., and Inkley, F. A., The Determination of Pore Structures from Nitrogen Adsorption Isotherms, Advances in Catalysis, 9:143–154 (1957)
13. Halsey, G. D., Physical Adsorption on Non-Uniform Surfaces, *J. Chem. Phys.*, 16:931–937 (1948)
14. Wheeler, A., *Catalysis*, Vol. II, p. 118, Reinhold, NY (1955)
15. Gregg, S. J., and Sing, K. S. W., *Adsorption, Surface Area and Porosity*, p. 164, Academic Press, NY (1967)

@Seismicisolation

16. Misna, D. N., Adsorption on Heterogeneous Surfaces. A Dubinin-Radushkevich Equation, *Surface Science,* 18:367–372 (1969)

17. Kiselev, A. V., *Usp. Khim (in Russian),* 14, p. 367 (1945)

18. de Boer, J. H., Linsen, B. G., van der Plas, Th., and Zondervan, G. J., Studies on Pore Systems in Catalysts VII. Description of the Pore Dimensions of Carbon Blacks by the t-Method, *J. Catalysis*, 4:649–653 (1965)

19. MacDonald, J. R., *Impedance Spectroscopy-Emphasizing Solid Materials and Systems,* p. 346, John Wiley & Sons, NY (1987)

20. Cole, K. S., and Cole, R. H., Dispersion and Absorption in Dielectrics I. Alternating Current Characteristics, *J. Chem. Phys.*, 9:341–351 (1941)

21. Sluyters-Rehback, M., and Sluyters, J. H., *Electroanalytical Chemistry*, 4:1–125, (A. J. Bard, ed.), Marcel Dekker, N.Y. (1970)

22. Bode, H. W., *Network Analysis and Feedback Amplifier Design,* p. 262, D. Van Nostrand Co. (1945)

23. McCarter, W. J., and Brousseau, R., The ac Response of Hardened Cement Paste, *Cem. Concr. Res.,* 20:891–900 (1990)

24. Scuderi, C. A., Mason, T. O., and Jennings, H. M., Impedance Spectra of Hydrating Cement Pastes, *J. Mater. Sci.,* 26:349–357 (1991)

25. Christensen, B. J., Mason, T. O., and Jennings, H. M., Influence of Silica Fume on the Early Hydration of Portland Cements Using Impedance Spectroscopy, *J. Amer. Cer. Soc.*, 75:939–945 (1992)

27. Gu, P., Xu, Z., Xie, P., and Beaudoin, J. J., Application of A.C. Impedance Techniques in Studies of Porous Cementitious Materials, (I). Influence of Solid Phase and Pore Solution on High-Frequency Resistance, *Cem. Concr.*, Res. 23:531–540 (1993)

28. Xie, P., Gu, P., Xu, Z., and Beaudoin, J. J., A Rationalized A.C. Impedance Model for Microstructural Characterization of Hydrating Cement Systems, *Cem. Concr. Res.*, 23:359–367 (1993)

29. Adamson, A. W., Physical Chemistry of Surfaces, Fourth Edition, pp. 185–195, John Wiley & Sons (1982)

30. Bockris, J., and Reddy, A. K. N., *Modern Electrochemistry,* 1:357–440, Plenum Pub. Co., NY (1970)

31. Xu, Z., Gu, P., Xie, P., and Beaudoin, J. J., Application of A.C. Impedance Techniques in Studies of Porous Cementitious Materials (II). Relationship Between ACIS Behavior and the Porous Microstructure, *Cem. Concr. Res.*, 23:853–862 (1993)

32. Garboczi, E. J., Permeability, Diffusivity and Microstructural Parameters: A Critical Review, *Cem. Concr. Res.*, 20:591–601 (1990)

@Seismicisolation

33. Coverdale, R. T., Christensen, B. J., Jennings, H. M., Mason, T. O., Bentz, D. P., and Garboczi, E. G., Interpretation of Impedance Spectroscopy of Cement Paste via Computer Modelling, *J. Matls. Sci.*, 30:712–719 (1995)

34. Christensen, B. J., Mason, T. O., Jennings, H. M., Bentz, D. P., and Garboczi, E. J., Experimental and Computer Simulation Results for the Electrical Conductivity of Portland Cement Paste, *Proc. Mat. Res. Soc. Symp.*, 245:259–264 (1992)

35. Beaudoin, J. J., and Brown, P. W., The Structure of Hardened Cement Paste, *Proceedings of the 9th International Congress on the Chemistry of Cement*, Vol. 1, Theme III, pp. 485–528, New Delhi, India (1992)

36. Häuβler, F., Eichorn, E., Rohling, S., and Baumbach, H., Monitoring of the Hydration Process of Hardening Cement Pastes by Small-Angle Neutron Scattering, *Cem. Concr. Res.*, 20:644–645 (1990)

37. Parrott, L. J., Patel, R. G., Killoh, D. C., Effect of Age on Diffusion of Hydrated Alite Cement, *J. Amer. Cer. Soc.*, 67:233–237 (1984)

38. Ramachandran, V. S., and Beaudoin, J. J., Use of Methanol as an Admixture for Portland Cement, *Il Cemento*, 2:165–172 (1987)

39. Collepardi, M., and Massidda, L., Hydration of Tricalcium Silicate, *J. Amer. Cer. Soc.*, 54:419–425 (1971)

40. Muhua, T., and Roy, D. M., An Investigation of the Effect of Organic Solvents on the Rheological Properties and Hydration of Cement Paste, *Cem. Concr. Res.*, 17:983–994 (1987)

41. Litvan, G. G., Variability of the Nitrogen Surface Area of Hydrated Cement Paste, *Cem. Concr. Res.* 6:139–144 (1976)

42. Marsh, B. K., Day, R. L., Bonner, D. G., and Illston, J. M., The Effect of Solvent Replacement Upon the Pore Structure Characterization of Portland Cement Paste, *Proceedings of the RILEM/CNR International Symposium on Principles and Applications of Pore Structural Characterization*, pp. 365–374, Milan, Italy (1985)

43. Feldman, R. F., and Beaudoin, J. J., Pretreatment of Hardened Cement Pastes for Mercury Intrusion Measurements, *Cem. Concr. Res.*, 21:297–308

44. Parrott, L. J., An Examination of Two Methods for Studying Diffusion Kinetics in Hydrated Cements, *Materials and Structures*, 17:131–137 (1981)

45. Feldman, R. F., Diffusion Measurements in Cement Paste by Water Replacement using Propan-2-ol, *Cem. Concr. Res.*, 17:602–612 (1987)

46. Marchand, J., Contribution to the Study of the Scaling Deterioration of Concrete in Presence of Deicing Salts, *Ph.D. Thesis, École Nationale des Ponts et Chaussées*, (in French), p. 326, Paris, France 1993

@Seismicisolation

47. Parrott, L. J., Effect of Drying History upon the Exchange of Pore Water with Methanol and upon Subsequent Sorption Behaviour in Hydrated Alite Paste, *Cem. Concr. Res.* 11:651–658 (1981)

48. Feldman, R. F., Effect of Pre-Drying on Rate of Water Replacement from Cement Paste by Propan-2-ol, *Il Cemento,* 3:193–201 (1988)

49. Taylor, H. F. W., and Turner, A. B., Reactions of Tricalcium Silicate Paste with Organic Liquids, *Cem. Concr. Res.,* 17:613–623 (1987)

50. Beaudoin, J. J., Gu, P., Marchand, J., Myers, R. E., and Liu, Z., Solvent Replacement Studies of Hydrated Portland Cement Systems- The Role of Calcium Hydroxide, *Adv. Cem.-Bas. Mtls.,* 8:56–65 (1998)

51. Dollimore, D., Gamlen, G. A., and Mangabhai, R. J., *Proc. 2nd Eur. Symp. Therm. Anal.,* pp. 485–488, Heyden, London, (1981)

52. Parrott, L. J., Novel Methods of Processing Cement Gel to Examine and Control Microstructure and Properties, *Royal Society of London Philos, Trans.,* A310:155–166 (1983)

53. Parrott, L. J., Thermogravimetric and Sorption Studies of Methanol Exchange in an Alite Paste, *Cem. Concr. Res.,* 13:18–22 (1983)

54. Thomas, M. D. A., The Suitability of Solvent Exchange Techniques for Studying the Pore Structure of Hardened Cement Paste, *Adv. Cem. Res.,* 2:29–34 (1989)

55. Day, R. L., Reactions Between Methanol and Portland Cement Paste, *Cem. Concr. Res.,* 11:341–349 (1981)

56. Beaudoin, J. J., Validity of Using Methanol for Studying the Microstructure of Cement Paste, *Materials and Structures,* 20:27–31 (1987)

57. Beaudoin, J. J., Interaction of Aliphatic Alcohols with Cement Systems, *Il Cemento,* 3:190–210 (1986)

58. Sellevold, E. J., and Bager, D. H., Some Implications of Calorimetric Ice Formation Results for Frost Resistance Testing of Cement Products, *Technical Report 86/80,* p. 28, The Technical University of Denmark, Building Materials Laboratory (1985)

59. Mikhail, R. Sh., and Selim, S. A., Adsorption of Organic Vapors in Relation to the Pore Structure of Hardened Portland Cement Pastes, *Highway Research Board, Special Report 90,* 123–134 (1966)

60. Abo-El-Enein, S. A., Hanafi, S., and Hekai, E. E., Thermal and Physicochemical Studies on Ettringite-Part II: Dehydration and Thermal Stability, *Il Cemento,* 2:121–131 (1988)

61. Hazrati, K., Mechanisms of Penetration of Chloride Ions in Unsaturated Cement Systems, *Ph.D. Thesis,* Dept. Of Civil Engineering, Laval University, Québec, Canada

@Seismicisolation

62. Hansen, E. W. and Gran, H. C., Carbon NMR used in Probing the Exchange of Ethanol with Water in Water-Saturated Cement Pastes, *Magn. Res. Imag.*, 14:903–904.

63. Day, R. L., Rate of Solvent Exchange as an Indicator of Permeability of Cement-Based Materials, *Proc. 3rd Can. Symp. Cem. Concr.*, 234–247, National Research Council, Ottawa, Canada (1993)

64. Barrer, R. M., *Zeolites and Clay Minerals as Sorbents and Molecular Sieves*, Academic Press (1978)

65. Tumidajski, P. J., and Schumacher, A S., On the Relationship Between the Formation Factor and Popan-2-ol Diffusivity in Mortars, *Cem. Concr. Res.*, 26:1301–1306 (1996)

66. Hughes, D. C., The Use of Solvent Exchange to Monitor Diffusion Characteristics of Cement Pastes Containing Silica Fume, *Cem. Concr. Res.*, 18:321–324 (1988)

67. Hughes, D. C., and Crossley, N. L., Pore Structure Characterization of GGBS/OPC Grouts using Solvent Techniques, *Cem. Concr. Res.*, 24: 1255–1266 (1994)

68. Gimblett, F. G. R., Mohd Amin, Z., and Sing, K. S. W., Influence of Pretreatment on the Microstructure of Calcium Silicate Hydrate Gels, *7th Int. Congr. Chem. Cem.*, II:225–231, Paris, France (1980)

69. Beaudoin, J. J., Gu, P., Tumidajski, P. J., and Perron, S., Microstructural Changes on Drying and Rewetting of Hydrated Cement Paste–An A.C. Impedance Spectroscopy Study, in: *Concrete, From Material to Structure*, pp. 32–42, RILEM, Paris, France

70. Sellevold, E. J., and Radjy, F., Drying and Resaturation Effects on Internal Friction in Hardened Cement Pastes, *J. Amer. Cer., Soc.*, 59:256–258 (1976)

71. Nadeau, J. S., Bennett, R., and Mindess, S., Acoustic Emission in the Drying of Hardened Cement Paste and Mortar, *J. Amer. Cer. Soc.*, 64:410–415 (1981)

72. Pearson, D., Allen, A., Windsor, C. G., Alford, N. McN., and Double, D. D., An Investigation on the Nature of Porosity in Hardened Cement Pastes using Small Angle Neutron Scattering, *J. Matls. Sci.*, 18:430–438 (1983)

73. Bager, D. H., and Sellevold, E. J., Ice Formation in Hardened Cement Paste - Part II: Drying and Resaturation of Room Temperature Cured Paste, *Cem. Concr. Res.*, 16:835–844 (1986)

74. Diamond, S., Methodologies of Pore Size Distribution Measurements in Hydrated Cement Pastes: Postulates, Pecularities, and Problems, Matls. Res. Soc., *Proc. Symp. on Pore Struct. and Perm. Cem. Mtls.*, 137:83–89 (1989)

75. Lowell, S., and Shields, J. E., *Powder Surface Area and Porosity*, Second Edition, pp. 205–216, Chapman and Hall, NY (1984)

@Seismicisolation

76. Washburn, E. W., Note on a Method of Determining the Distributions of Pore Sizes in Porous Materials, *Proc. Natl. Acad. Sci. USA*, 7:115–116 (1921)

77. Van Brakel, J. V., Modry, S., and Svata, M., Mercury Porosimetry: State of the Art, *Powder Technology*, 29:1–12 (1981)

78. Winslow, D. N., Advances in Experimental Techniques for Mercury Intrusion Porosimetry, *Surface and Colloid Science*, pp. 259–282, Egon Matijevic and Robert J. Good, NY (1984)

79. Hearn, N., and Hooton, R. D., Sample Mass and Dimension Effects on Mercury Intrusion Porosimetry Results, *Cem. Concr. Res.*, 22:970–980 (1992)

80. Moscou, L., and Lub, S., Practical use of Mercury Porosimetry in the Study of Porous Solids, *Powder Technology*, 29:45–52 (1981)

81. Alford, N. M., and Rahman, A. A., An Assesment of Porosity and Pore Sizes in Hardened Cement Pastes, *J. Mater. Sci.*, 16:3105–3114 (1981)

82. Winslow, D. N., and Lovell, C. W., Measurements of Pore Size Distributions in Cements, Aggregates and Soils, *Powder Technology*, 29:151–165 (1981)

83. Diamond, S., and Dolch, W. L., Generalized Log-Normal Distribution of Pore Sizes in Hydrated Cement Paste, *J. Colloid Interface Sci.*, 38:234–244 (1972)

84. Diamond, S., and Leeman, M. E., Pore Size Distributions in Hardened Cement Paste by SEM Image Analysis, *Matls. Res. Soc., Proc. Symp. On Microstructure Cem.-Bas. Sys./Bond. Int. Cemt. Matls*, 376:217–226 (1995)

85. Winslow, D. N., and Diamond, S., A Mercury Porosimetry Study of the Evolution of Porosity in Portland Cement, *J. Mater.*, 5:564–585 (1970)

86. Diamond, S., A Critical Comparison of Mercury Porosimetry and Capillary Condensation Pore Size Distributions of Portland Cement Pastes, *Cem. Concr., Res.* 1:531–545 (1971)

87. Beaudoin, J. J., Porosity Measurements of Some Hydrated Cementitious Systems by High-Pressure Mercury-Microstructural Limitations, *Cem. Concr. Res.*, 9:771–781 (1979)

88. Modry, S., and Hejduk, J., The Limitation of High Pressure Mercury Porosimetry to the Study of Hardened Cement Pastes, *7th Int. Congr. Chem. Cem.*, 6:387–389, Paris, France (1980)

89. Shi, D., and Winslow, D. N., Contact Angle and Damage During Mercury Intrusion into Cement Paste, *Cem. Concr. Res.*, 15:645–654 (1985)

90. Feldman, R. F., Pore Structure Damage in Blended Cements Caused by Mercury Intrusion, *J. Amer. Cer. Soc.*, 67:30–33 (1984)

91. Bazant, Z. P., Constitutive Equations for Concrete Creep and Shrinkage Based on Thermodynamics of Multiphase System, *Materials and Structures*, 3:3–36 (1970)

@Seismicisolation

92. Litvan, G. G., Variability of the Nitrogen Surface Area of Hydrated Cement Paste, *Cem. Concr. Res.*, 6:139–144 (1976)

93. Lipsicas, M., Banavar, J. R., and Willemsen, J., Surface Relaxation and Pore Sizes in Rocks—A Nuclear Magnetic Resonance Analysis, *Appl. Phys. Lett.*, 48:1544–1546 (1986)

94. Cohen, M. H., and Mendelson, K. S., Nuclear Magnetic Relaxation and the Internal Geometry of Sedimentary Rocks, *J. Appl. Phys.*, 53:1127–1135 (1982)

95. Mendelson, K. S., Nuclear Magnetic Relaxation in Fractal Pores, *Phys. Rev. B*, 34:6503–6505 (1986)

96. Munn, K., and Smith, D. M., A NMR Technique for the Analysis of Pore Structure: Numerical Inversion of Relaxation Measurements, *J. Colloid Interface Sci.*, 119:117–126 (1987)

97. Gallegos, D. P., Munn, K., Smith, D. M., and Stermer, D. L., A NMR Technique for the Analysis of Pore Structure: Application to Materials with well Defined Pore Structure, *J. Colloid Interface Sci.*, 119:127–140 (1987)

98. Gallegos, D. P., and Smith, D. M., A NMR Technique for the Analysis of Pore Structure: Determination of Continuous Pore Size Distributions, *J. Colloid. Interface Sci.*, 122:143–153 (1988)

99. Davies, S., and Parker, K. J., Pore-Size Distributions from Nuclear Magnetic Resonance Spin Lattice Relaxation Measurements in Fluid Saturated Porous Solids - I: Theory and Simulation, *J. Appl. Phys.*, 67:3163–3170.

100. Farrar, T., and Becker, E. D., *Pulse and Fourrier Transform NMR - Introduction to Theory and Methods*, Academic Press, New York (1971)

101. Abragam, A., *Principles of Nuclear Magnetism*, Oxford University Press, New York (1985)

102. Bloembergen, E. M., Purcell, E. M., and Pound, R. V., Relaxation Effects in Nuclear Magnetic Resonance Absorption, *Phys Rev.*, 73:679–712

103. Pel, L., Moisture Transport in Porous Building Materials, *Ph. D. Thesis*, p. 125, Eindhoven University of Technology, The Netherlands (1995)

104. Halperin, W. P., D'Orazio, F., Bhattacharya, S., and Tarczon, J. C., *Magnetic Resonance Relaxation Analysis of Porous Media, Molecular Dynamics in Restricted Geometries*, J. Klafter and J.M. Drake, John Wiley and Sons, New York (1989)

105. Faucon, P., Durability of Concrete : Physico-Chemical Analysis of the Degradation of Concrete upon Leaching, *Ph.D. Thesis*, Université de Cergy-Pontoise, France (1997)

106. Bhattacharya, S, Maoukwa, M., D'Orazio, F., Jehng, J. Y, and Halperin, W. P., Microstructure Determination of Cement Pastes by NMR and Conventional Techniques, *Advanced Cement Based Materials*, 1:67–76 (1993)

@Seismicisolation

107. Jehng, J. Y., Microstructure of Wet Cement Pastes: A Nuclear Magnetic Resonance Study, Ph. D. Thesis, p. 187, Northwestern University, U.S.A. (1995)

108. Brownstein, K. R., and Tarr, C. E., Importance of Classical Diffusion in NMR Studies of Water in Bilogical Cells, *Phys., Rev.* 19:2446–2453 (1979)

109. Best, G., Cross, A., Peemoeller, H., Pintar, M. M., and Blinc, R., Distribution of Pore Sizes in White Cement Paste from Proton NMR Spin-Lattice Relaxation, *Adv. Cem. Res.,* 8:163–166.

110. Beaudoin, J. J., Feldman, R. F., and Tumidajski, P. J., Pore Structure of Hardened Portland Cement Pastes and Its Influence on Properties, *Advn. Cem. Bas. Mat.,* 1:224-236, (1994)

111. Odler, I., and Röbler, M., Investigations on the Relationship Between Porosity, Structure and Strength of Hydrated Portland Cement Pastes II. Effect of Pore Structure and of Degree of Hydration, *Cem. Concr. Res.,* 15:401–410 (1985)

112. Atzeni, C., Massidda, L., and Sanna, U., Effect of Water/Cement Ratio on Pore Size Distribution in Hardened Cement Pastes Porosity-Strength Relationship, *Mater. Eng.,* 1:467–473 (1989)

113. Yiun-Yuan, H., Wei, D., and Ping, L., The Influence of Pore Structure on the Compressive Strength of Hardened Cement Paste, *Matls. Res. Soc., Proc. Symp. Very High Strength Cement-Based Materials,* 42:123–131 (1984)

114. Evans, A. G. and Tappin, G., Effects of Microstructure on the Stress to Propagate Inherent Flaws, *Proc. Brit. Ceram. Soc.,* 20:275–297 (1972)

115. Pereira, C. J., Rice, R. W., and Skalny J. P., Pore Structure and its Relationship to Properties of Materials, *Matls. Res. Soc., Proc. Symp. on Pore Structure and Perm. Cem. Matls.,* 137:3–21 (1988)

116. Rice, R. W., Pores as Fracture Origins in Ceramics, *J. Mat. Sci.,* 19:895–914 (1984)

117. Feldman, R. F., and Beaudoin, J. J., Microstructure and Strength of Hydrated Cement (in Russian), *Proc. 6th Int. Congr. Chem. Com.,* Moscow, 2:288–293 (1974)

118. Beaudoin, J. J., and Feldman, R. F., A Study of Mechanical Properties of Autoclaved Calcium Silicate Systems, *Cem. Concr. Res.,* 5:103–118 (1975)

119. Balshin, M. Y., Dependence of Mechanical Properties of Porous Materials Based on the Porosity Dependence of Porous Metal Ceramics (in Russian), *Dokl. Akad. Nauk. SSSR,* 67:831–834 (1949)

120. Yudenfreund, M., Hanna, K. M., Skalny, J. P., Odler, I., and Brunauer, S., Hardened Portland Cement Pastes of Low Porosity V. Compressive Strength, *Cem. Concr. Res.,* 2:731–743 (1972)

@Seismicisolation

121. Beaudoin, J. J., and Feldman, R. F., Microstructure and Strength of Hydrated Cement, *Cem. Concr. Res.*, 6:103–119 (1976)

122. Beaudoin, J. J., and Feldman, R. F., Partial Replacement of Cement by Fly Ash in Autoclaved Products: Theory and Practice, *J. Mat. Sci.*, 14:1681–1693 (1979)

123. Roy, D. M., Gouda, G. R., and Bobrowsky, A., Very High Strength Cement Pastes Prepared by Hot Pressing and Other High Pressure Techniques, *Cem. Concr. Res.*, 2:349–366 (1972)

124. Ramachandran, V. S., and Feldman, R. F., Significance of Low Water/Solid Ratio and Temperature on the Physico-Mechanical Characteristics of Hydrates of Tricalcium Aluminate, *J. Appl. Chem. and Bio. Tech.*, 23:625–633 (1973)

125. Odler, I., Yudenfreund, M., Skalny, J., and Brunauer S., Hardened Portland Cement Pastes of Low Porosity III. Degree of Hydration, Expansion of Paste, Total Porosity, *Cem. Concr. Res.*, 2:463–480 (1973)

126. L'hermite, R., and Valenta, M., Effect of Pressure on Setting Cements, *An. de l'Inst. Tech. du Bâtiment et des Trav. Pub.*, 2:23–27 (1937)

127. Roy, D. M., and Gouda, G. R., Optimization of Strength in Cement Pastes, *Cem. Concr. Res.*, 5:153–162 (1975)

128. Lu, R., and Young, J. F., Hot Pressed DSP Cement Paste, *Symposium on Adv. Cem. Systems*, 245:321–328 (1992)

129. Crennan, J. M., El-Hemaly, S. A. S., and Taylo, H. F. W., Autoclaved Lime-Quartz Materials I. Some Factors Influencing Strength, *Cem. Concr. Res.*, 7:493–502 (1977)

130. Graf, H., and Setzer, M., Influence of Water/Cement Ratio and Curing on the Permeability and Structure of Hardened Cement Paste and Concrete, *Matls. Res. Soc. Proc., Pore Structure and Permeability of Cementitious Materials*, 137:337–347 (1988)

131. Nyame, B. K., and Illston, J. M., Capillary Pore Structure and Permeability of Hardened Cement Paste, *Proc. 7th Intl. Congr. Cem. Chem.*, Vol. III:VI-181–VI-185 Paris, (1980)

132. Diamond, S., Pore Structure of Hardened Cement Paste as Influenced by Hydration Temperature, *Proc. RILEM Conf. Pore Struct. and Prop. Matls.*, 1:B73–B78, Prague (1973)

133. Li, S., and Roy, D. M., Investigation of Relations Between Porosity, Pore Structure and Diffusion of Fly Ash, and Blended Cement Pastes, *Cem. Concr. Res.*, 16:749–759 (1986)

134. Bier, T. A., Ludirdja, D., Young, J. F., and Berger, R. L., The Effect of Pore Structure and Cracking on the Permeability of Concrete, *Matls. Res. Soc., Proc. Symp. on Pore Struct. and Perm. Cem. Matls.*, 137:235–241 (1988)

@Seismicisolation

135. Anderson, K., Torstenfelt, B., and Allard, B., Diffusion of Cs and I in Concrete, Proc. Intl. Symp., *Scientific Basis for Nuclear Waste Management*, 3:235–242 (1981)

136. Roy, D. M., Relationships Between Permeability, Porosity, Diffusion and Microstructure of Cement Pastes, Mortar and Concrete at Different Temperatures, *Matls. Res. Soc., Proc. Symp. on Pore Structure and Perm. Cem. Matls.*, 137:179–189 (1988)

137. Malek, R. I. A., Roy, D. M., and Fang, Y., Pore Structure, Permeability and Chloride Diffusion in Fly Ash and Slag Containing Pastes and Mortars, *Matls. Res. Soc., Proc. Symp. Pore Struct. and Perm. of Cem. Matls.*, 137:403–410 (1988)

138. Hanson, C. M., and Berke, N. S., Chlorides in Concrete, *Matls. Res. Soc., Proc. Symp. Pore Struct. and Perm. of Cem. Matls.*, 137:253–270 (1988)

139. Feldman, R. F., Chan, G. W., and Brousseau, R. J., Chloride Ion Diffusivity of Blended Cement Mortars: A.C. Impedance, *Il Cemento*, 90:207–220 (1993)

140. Feldman, R. F., Pore Structure, Permeability and Diffusivity as Related to Durability, *Proc. 8th Intl. Congr. Chem. Cem.*, l:336–356 (1986)

141. Ramachandran V. S., and Feldman R. F., Time-Dependent and Intrinsic Characteristics of Portland Cement Hydrated in the Presence of Calcium Chloride, *Il Cemento*, 75:311-321 (1978)

@Seismicisolation

15

Silicate Polymerization Analysis

J. Francis Young and Guokuang Sun

1.0 INTRODUCTION

For many years, cement scientists have assumed that the amorphous calcium silicate hydrate (C-S-H) that forms during hydration of portland cement is a degenerate form of the tobermorite structure, but direct evidence was difficult to come by. In the late 1960s, two methods of determining the structure of the silicate ions in inorganic compounds were developed and applied to the analysis of hydrated portland cement. Later, a third method,solid state NMR spectroscopy became available in the late 1970s. In this chapter we describe the development of these three techniques and discuss the type of information they provide. The application of silicate polymerization analysis to understanding the hydration process and the structure of C-S-H is also considered.

1.1 Analytical Methods

All three analytical techniques rely on the fact that all silicate structures are derived from a combination of bonding oxygens which links the silicon atoms together with strong siloxane (Si-O-Si) bonds and non-bonding

@Seismicisolation

oxygens (Si-O) which carry either a negative charge or hydrogen atom (i.e., hydroxyl group).

Spectrophotometry. This relies on the rate of formation of a silicomolybdate complex that can be determined quantitatively by spectrophotometric analysis. The method is no longer used very often since it is limited in the information it can provide.

Trimethylsilylation. The silicate compound is reacted to form the trimethylsilyl derivative of the silicate ion that occurs in the compound. Mixtures of the silicate derivatives are separated by chromatography. The method suffers from side reactions, but derivation can occur quantitatively under the right experimental conditions and the amount of each silicate species present measured.

Solid State ^{29}Si NMR Spectroscopy. Solid state nuclear magnetic resonance (NMR) spectroscopy with magic angle spinning (MAS) provides a spectrum of well resolved resonance peaks whose position depends on the local chemical environment of the silicon atoms within the silicate structure. Peak areas can be used for quantitative analysis.

1.2 Silicate Structure of C-S-H

The structure of tobermorite is based on a layer structure in which infinite chains of silica tetrahedra are condensed onto both sides of a sheet of Ca-O octahedra through edge-sharing, as shown in Fig. 1. All of the oxygens in the central octahedral sheet are shared with silica tetrahedra, however, not all silica tetrahedra are linked to the sheet. The chains have a repeating array of three tetrahedra, called *dreierketten*, providing a kinked conformation. The central (bridging) tetrahedron of the chain unit has one hydroxyl group with the fourth oxygen bonded weakly to a calcium atom in the sheet. The composition of the dreierketten unit is $[Si_3O_8(OH)]^{5-}$ and the overall composition of the layer is $Ca_4[Si_3O_8(OH)]_2^{2-}$. The negative charge is balanced by a Ca^{2+} ion between the layers together with water molecules to give the overall composition of $Ca_5Si_6O_{16}(OH)_2 \cdot 8H_2O$. The CaO/SiO_2 (C/S) molar ratio is 0.83. Since C-S-H has a C/S ratio close to 1.7, it has been proposed[1] that random omission of silica tetrahedra from the dreierketten chains, and probably whole omission of chains, occurs. The structure may lie closer to jennite, $[Ca_9Si_6O_{16}(OH)_{10} \cdot 6H_2O]$ where every other silicate chain is omitted.

@Seismicisolation

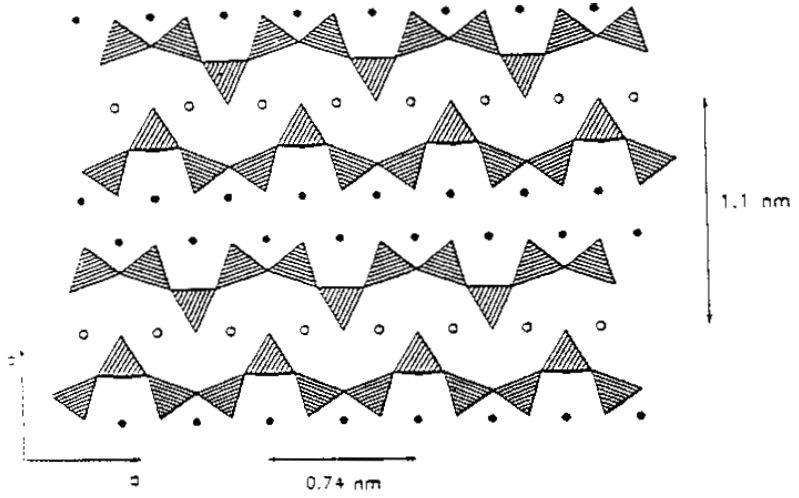


Figure 1. Schematic representation of the tobermorite structure.

2.0 COMPLEXOMETRIC ANALYSIS

2.1 Basic Chemistry

The first analyses of the degree of silicate polymerization by the complexometric method was reported by Funk and Frydrych[2] in 1964. The method is based on the colorimetric analysis for soluble silicate utilizing the formation of a colored silicomolybdic acid complex:

Eq. (1) $7H_4SiO_4 + 12H_6Mo_7O_{24} \rightarrow 7[H_4SiMo_{12}O_{40}] + 36H_2O$
(silicic acid) paramolybdic acid β-silicomolybdic acid

This study extended earlier work which showed that the rate of complexation is determined by the rate of depolymerization of condensed silicic acids as they are acid-leached from an inorganic silicate compound. Funk and Frydrych were able to follow the rate of complexation for up to five silicate structures (see Fig. 2 and Table 1). The first order kinetic curves were obtained by the quantitative precipitation and analysis of the quinoline salt of

@Seismicisolation

the silicomolybdate complex after different types of reaction. Later Weiker[3] developed a method to follow the rate of complexing spectrophotometricaIly using a strong adsorption peak in the near UV region. This is the basis of a well-known colorimetric method for analysis of dissolved silica.

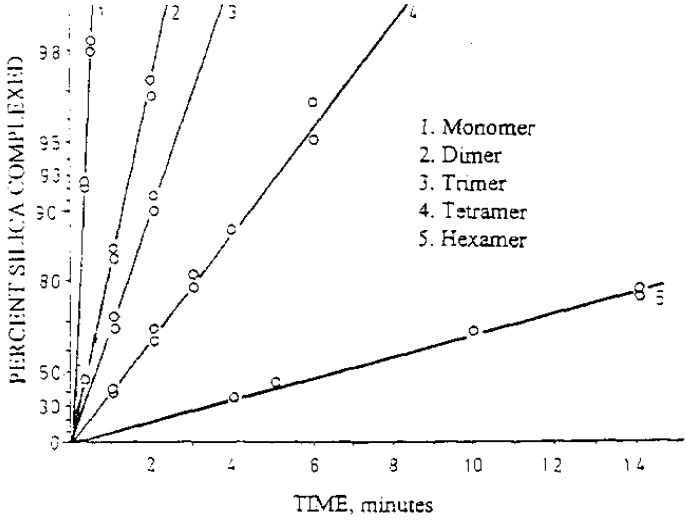


Figure 2. Kinetics of complexing for simple silicic acids (after Ref. 2).

Table 1. Complexing Rate of Single Silicic Acids[2]

Silicate Structure	Formula	Source	Half Life (sec)	Rate Constant (sec)
Mononomer	H_4SiO_4	β- or γ-Ca_2SiO_4	5.5	0.1
Dimer	$H_6Si_2O_7$	$Ca_2Na_2Si_2O_7$*	23.5	0.032
Cyclic trimer	$H_6Si_3O_9$	pseudo wollastonite	36	0.019
Cyclic tetramer	$H_8Si_4O_{12}$	$K_4H_4Si_4O_{12}$	83	0.0084
Bicylic trimer	$H_{12}Si_6O_{18}$	dioptase	360	0.0018

*Rankinite was also used.

@Seismicisolation

To ensure that the silicate structure is correctly represented, subsequent condensation of the leached silicic acid must be avoided. This is done by using methanolic HCl, complexing the acid immediately after the solid has dissolved. The solid needs to dissolve rapidly (<30 sec.) to avoid condensation. Fortunately, most calcium silicates dissolve rapidly in methanolic HCl.

2.2 Study of Cement Hydration

The method was shown to be applicable to the study of the hydration of portland cement and calcium silicates[3]–[6] as well as precipitated C-S-H.[5] Typical complexing curves for hydrating portland cement are shown in Fig. 3, however, it is difficult to quantitatively separate the contribution by individual silicic acids to an overall complexing curve. Parrot and Taylor[4] developed a method for hydrated cement paste that allowed for quantitative analysis of monomer, dimer, and polysilicate (more than four connected silicon atoms). The method assumed that only these species are present and that each silicate species has its own rate constant for complexation. The proportion of silica complexed (y) is given by:

Eq. (2) $$y = a_1 f_1(t) + a_2 f_2(t) + a_p f_p(t)$$

where a_1, a_2, and a_p are the proportions of each species present and $f(t)$ are exponential expressions describing the complexing curve for each species. Equation (2) is solved by an iterative least squares solution. This analysis confirmed earlier assumptions that the polysilicate content could be estimated from the amount of silica uncomplexed after 5 min.

Parrott[6][7] showed that strong dependance of curing temperature on silicate polymerization (see Table 2). His studies also suggested that polymerization is disconnected from hydration. Bentur, et a1.,[8] also confirmed the importance of the degree of silicate polymerization in determining shrinkage of calcium silicate pastes.

2.3 Analytical Procedure

Anhydrous HCl gas is dissolved in methanol to produce a 0.15N methanolic HCl solution at 250°C. To 100 ml of this solution is added 100–200 mg sample of the powdered cement paste (< 20 μm). The sample size should be such that it contains at least 100 mg as SiO_2 and the amount

@Seismicisolation

of HCl should be sufficient to make the silicic acid at least 0.1M with respect to HCl. Vigorous stirring is required to effect rapid and complete dissolution. Twenty ml of the silicic acid solution is added to a reaction vessel containing 170 ml of hydrochloric acid solution with a pH of 1.6 equilibrated at 25°C together with 10 ml of a paramolybdate solution. The formation of the yellow β-silicomolybdic acid complex was monitored using a flow-through cell in a spectrophotometer set at a wavelength of 400 nm. The concentration of dissolved silica can be calculated from a prepared calibration curve. Further details are given in Ref. 4.

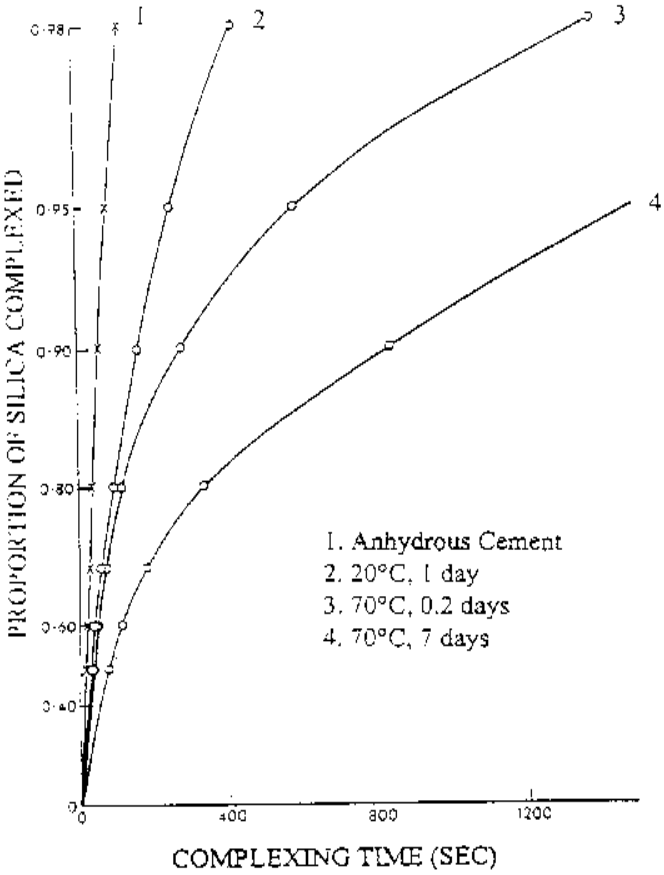


Figure 3. Complexometric curves for hydrated cement pastes (after Ref. 6).

@Seismicisolation

Table 2. Effect of Temperature on Silicate Polymerization in Hydrated Cement Paste

Temp °C	Time (days)	Percent Silicate Not Complex	Half-time of Complexing
20	1	3.7	153
70	0.2	9.6	380
	7	21.4	525
95	0.2	13.6	375
	3.2	20.7	565
	10	26.4	760

3.0 TRIMETHYLSILYLATION

3.1 Basic Chemistry

Trimethylsilylation (TMS) analysis has become a very popular method to probe the silicate structures of minerals and to follow the polymerization of silicate ions during hydration of portland cement. The method involves acid leaching of the solid to remove cations thereby forming silicic acids, as shown in Eq. (3):

Eq. (3) $Ca_2SiO_4 + 4HCl \rightarrow Si(OH)_4 + 2CaCl_2$

The silicic acids formed correspond to the original silicate ion structure, but will quickly polymerize to more highly condensed structures. To prevent this, the acids are immediately end-blocked with trimethylsilyl (TMS) groups:

Eq. (4) $Si(OH)_4 + 4(CH_3)_3SiCl \rightarrow (CH_3Si)4SiO_4 + 4HCl$

The net reaction is:

Eq. (5) $Ca_2SiO_4 + 4(CH_3)_3SiCl \rightarrow (CH_3Si)_4SiO_4 + 2CaCl_2$

The resulting TMS derivatives can be extracted into a hydrophobic organic solvent and separated using chromatographic techniques. Usually, gel permeation chromatography is used.

A wide variety of compounds have been analyzed using the TMS method, and those summarized in Table 3 have been used for calibration purposes. Table 3 also illustrates the various nomenclatures that have been

@Seismicisolation

used. The shorthand nomenclature Q_xM_y for the TMS derivatives is very useful. Q_x is the number of silicon atoms in the base structure, while M_y is the number of TMS groups. It can be seen that y equals the charge on the silicate ions since bridging oxygens do not react.

Table 3. TMS Derivatives of Various Silicate Species

Formula	Degree of Polymerization	TMS Derivatives		
		Nomenclature	MW	Source
SiO_4^{4-}	Monomer	QM_4	384	Ca_3SiO_5, Ca_2SiO_4 Olivine
$Si_2O_7^{6-}$	Dimer	Q_2M_6	606	Hemimorphite
$Si_3O_{10}^{8-}$	Linear Trimer	Q_3M_8	828	Natrolite
$Si_3O_9^{6-}$	Cyclic Trimer	Q_3M_6	666	Pseudowollastonite
$Si_4O_{13}^{10-}$	Linear Tetramer	Q_4M_{10}	1050	—
$Si_4O_{12}^{8-}$	Cyclic Tetramer	Q_4M_8	888	Laumontite
$Si_5O_{15}^{10-}$	Cyclic Pentamer	Q_5M_{10}	1110	—
$Si_6O_{17}^{10-}$	Bicyclic Trimer	Q_6M_{10}	1170	Dioptase
$Si_8O_{20}^{8-}$	Bicyclic Tetramer	Q_8M_8	1128	TMA salt#
$Si_{10}O_{25}^{10-}$	Bicyclic Pentamer	$Q_{10}M_{10}$	1410	TBA salt*

\# Trimethyl ammonium salt
* Tributyl ammonium salt

3.2 Anhydrous Silicates

Lentz[9] was the first to report trimethylsilylation of inorganic silicates. The mineral structures he analyzed were olivine (an orthosilicate), in which $(TMS)_4SiO_4$ was formed in 70% yield; hemimorphite (a pyrosilicate) forming $(TMS)_6Si_2O_7$ in 78% yield and natrolite (a trisilicate) which recovered $(TMS)_8Si_3O_{10}$ in 68% yield. The derivatization of natrolite shows the specificity of this method for silicate structures since the moiety Si_3O_{10} is part of an aluminosilicate framework. Al-O-Si bonds are cleaved as cations are leached from the structure, while Si-O-Si bonds are sufficiently stable to be unaffected. The reaction medium was an aqueous mixture of HCl, isopropyl alcohol and hexamethyldisiloxane (HMDSO) which is water immiscible. The HCl was used to leach cations from the solids and to generate silylating reagents from HMDSO:

@Seismicisolation

Eq. (6) $(CH_3Si)_2O + HCl \rightarrow CH_3SiC1 + CH_3SiOH$

The HMDSO also acts as a solvent for the TMS derivatives as they are formed. The role of the alcohol is less clear, but it was suggested that it might increase the solubility of HMDSO in water and stabilize the silicic acids prior to end-blocking. The relatively low yields are due to side reactions, the major ones being condensation, and acid cleavage of a siloxane (Si-O-Si) linkage. For example, 10% of the monomer species in olivine was recovered as the dimer derivative while 22% of monomer and dimer could be recovered from the more condensed structures.

Subsequently Milestone[10] modified Lentz' method by substituting t-butanol for isopropanol, adding water in the form of ice, and saturating the aqueous phase with sodium chloride. The modification of the original Lentz method by Milestone improves the derivatization of less soluble compounds. Apparently the t-butanol minimizes condensation of silicic acids prior to TMS end-blocking, due probably to steric effects. Earlier Gotz and Masson[11][12] had modified the process by eliminating the use of HCl and substituting trimethylchlorosilane (TMCS) as the silylating agent. Enough HCl for acid leaching was generated by hydrolysis of TMCS through the addition of water so that the cations can be fully leached from the mineral:

Eq. (7) $(CH_3)_3SiC1 + H_2O \rightarrow (CH_3)_3SiOH + HCl$

Although this method gives a better representation of the original silicate structure by reducing the side reactions, the results are extremely sensitive to the amount of water used and complete dissolution of the mineral does not occur.

3.3 Application to Cements

Lentz[13] applied his method to make the first silicate analyses of hydrated portland cement pastes. Samples of Ca_3SiO_5 and Ca_2SiO_4 and afwillite $Ca_3Si_2O_8(OH)_2$ were also analyzed as reference compounds (all are monomers), however, the yields of the known monomer structures were stillonly 65–75%, not high enough for an accurate quantitative analysis. Nevertheless, he was able to conclusively demonstrate the progressive decline of the monomer derivative as Ca_3SiO_5 and Ca_2SiO_4 are consumed by hydration and the progressive increase in a polysilicate fraction over time. These general conclusions were confirmed subsequently using TMS

@Seismicisolation

methods of greater accuracy. The formation of linear trimer and tetramer are probably due to side reactions.

In 1976 Tamas, Sarkar, and Roy,[14] reported a further modification for the TMS derivatization of silicate structures which has become the basis of all TMS methods currently used. The reaction mixture uses dimethylformamide (DMF) as the solvent together with HMDSO and TMCS. The yields of monomer from β-Ca_2SiO_4 and Ca_3SiO_4 were 91% and 94%, respectively, the side reactions being principally the formation of dimer (Fig. 4). The reaction mixture is a relatively mild silylating mixture. No water is required, a small amount of water dissolved in the DMF should provide sufficient HCl from Eq. (6) to leach the calcium silicates; however, this solvent should be freshly distilled to ensure reproducible results. In hydrated systems sufficient additional water is probably released as derivatization proceeds, however, the reaction mixture is not strong enough to derivatize other silicates. Thus, to calibrate the gas chromatograms other methods must be used to derivative minerals of known structure, as discussed in the previous section.

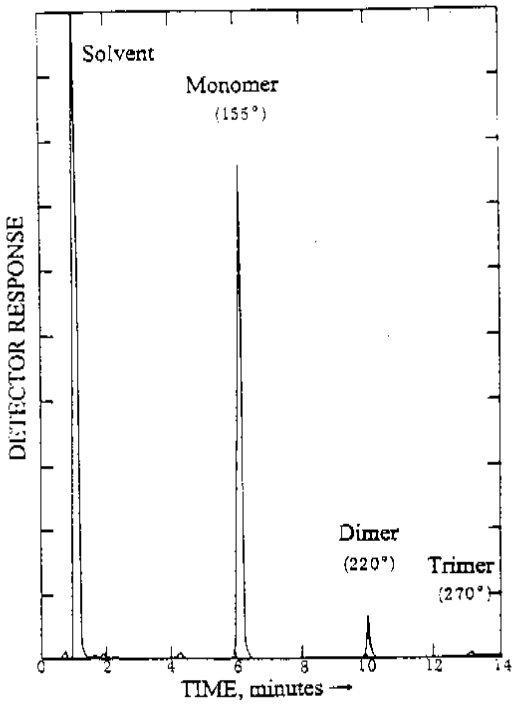


Figure 4. Gas chromatogram of silylated Ca_3SiO_5 (after Ref. 14).

@Seismicisolation

3.4 Current TMS Method

The use of gas-liquid chromatography (GLC) to separate the TMS derivatives provides good separation of low molecular weight (MW) species such as monomer and dimer, however, its detection range is limited because of decreasing volatility with molecular weight. Thus, the species larger than cyclic pentamer ($Si_5O_{15}^{10-}$) or linear tetramer ion ($Si_4O_{13}^{10-}$) (MW of TMS derivatives: 1110 and 1050, respectively) are not seen; because it was clear that higher MW species were formed during cement hydration, an alternate separation mode was needed.

Sarkar and Roy[15] demonstrated the applicability of liquid phase gel permeation chromatography (GPC), also known as *size-exclusion chromatography*. The technique involves passing a dissolved mixture of compounds through a column packed with a medium having a controlled pore structure of nanometer dimensions. Smaller molecules diffuse through the pore network and thus, take longer to pass through the column than larger molecules that are excluded from the pores on account of their size. Therefore, in the chromatogram the components of the mixture are eluted in order of decreasing molecular weight. A calibration curve can be constructed from the derivatization of known silicate structures (Fig. 5) to relate the eluted volume to molecular weight. Since GPC depends really on the effective hydrodynamic radius of the molecule in solution there will be small differences between molecular species that have a similar molecular weight, but different molecular conformations (e.g., a ring versus a linear chain). The use of high pressure liquid chromatography (HPLC) makes GPC a powerful separation technique.

The early work[15] used tetrahydrofuran as the solvent and the resolution was rather poor; however, using a slight variation in the reaction mixture (Table 4), switching to toluene as the solvent, and using columns with improved resolving power,[16] produced much better results (Fig. 6a). Further improvements in columns have allowed full separation of pentamers and octamers (Fig. 6b). Distinction between cyclic and linear species is also possible.

Lachowski[17] compared the quantitative accuracy of the methods of Lentz, Gotz, and Masson, and Tamas et al., for estimating Ca_3SiO_5 and $Ca_3Si_2O_7$ using gas chromatography. The method by Tamas et al., clearly gave the best results. Parallel work by Lachowski[18] and later by Hirljac et a1.,[16] developed quantitative analysis using GPC fractionation of the GPC derivatives. Bentur and Young[19] showed that it was possible to determine the amount of polysilicate without using GPC analysis by controlled heating to remove monomer and dimer.

@Seismicisolation

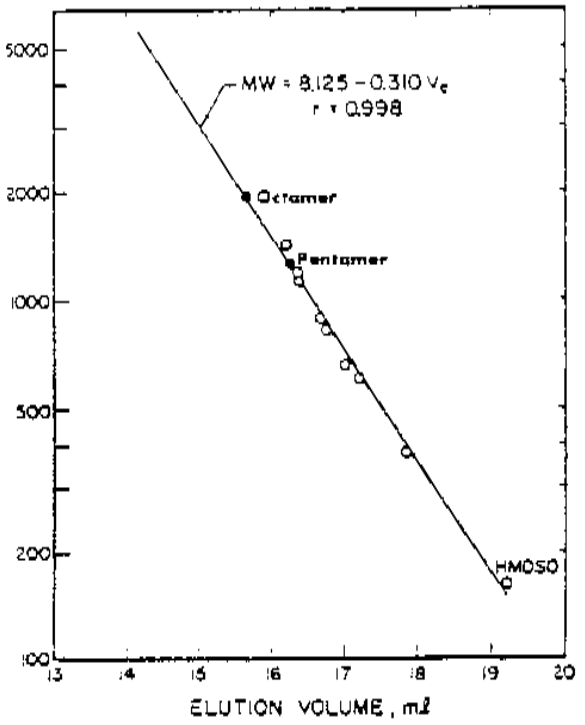


Figure 5. Calibration curve for GPC analysis of silicate species (after Ref. 16).

Table 4. Comparison of Some Trimethylsilylating Formulations*

Component	Lentz[9]	Milestone[10]	Gotz & Masson[11]	Tamas et al.[14]	Hrljac et al.[16]
HMDSO	10	10	9	5	5
I-Propanol	15	—	0.8	—	—
HCl	25	2	—	—	—
Water	6.3	2	0.2	—	—
TMCS	—	—	2	5	2
DMF	—	—	—	10	10

*Quantities given in mls.

@Seismicisolation

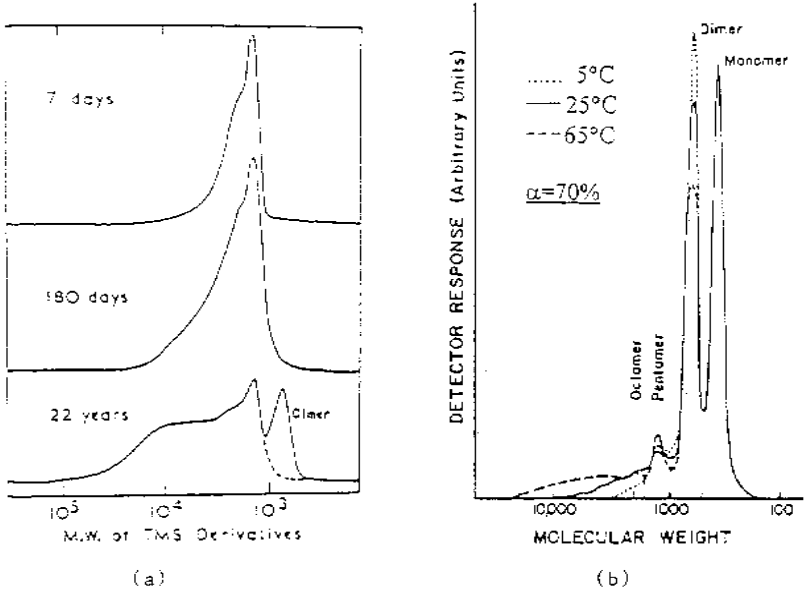


Figure 6. GPC chromatograms of hydrated Ca_3SiO_5 pastes; *(a)* ca. 1979; *(b)* ca. 1983.

3.5 Studies of Cement Hydration

The TMS method has been used extensively to follow the progress of polymerization so that an exhaustive literature review is not feasible. We briefly review selected publications that have established the value of this method. The first comprehensive studies that followed polymerization in hydrating Ca_3SO_5 pastes from the beginning of hydration were made by Taylor and coworkers,[20][21] and Hirljac, et a1.[16] Both studies confirm that in the very early stages only dimers are formed (Fig. 7). Later polysilicate (polymer) forms, but dimer is always a significant proportion of the hydrated paste. Plots of both dimer and polymer are linear with degree of hydration at least up to 50% hydration (Fig. 8) and polymerization is a function of temperature (Fig. 8b). The amount of monomer decreases monotonically with time. Assuming no monomer occurs in C-S-H (an assumption confirmed by ^{29}Si NMR spectroscopy) the monomer contact can be used to estimate degree of hydration.

@Seismicisolation

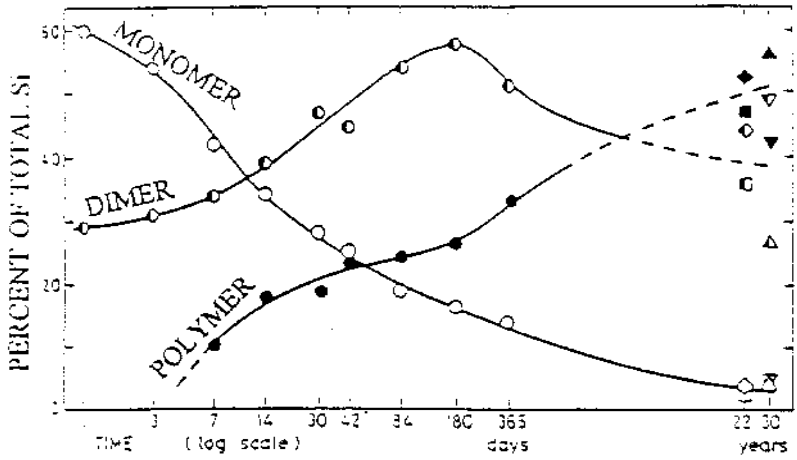


Figure 7. Profile of silicate species over time in hydration Ca_3SiO_5 pastes (after Ref. 21).

Polysilicate Fraction. Generally, polysilicate collectively refers to all silicate species higher than dimer, but it is clear that this fraction is polydisperse (Fig. 6). Estimates of the number[18][21] suggested averages of 7–10 for well-hydrated pastes (i.e., 7–10 silicon atoms in the basic silicate structure); improved GPC columns now make it possible to partially resolve the components of the polysilicate fraction. Initially, pentamer and octamer fractions could be separated,[10] as shown in Fig. 6b. Currently it is possible to also resolve peaks corresponding to 11-mer and 14-mer (Fig. 9). Also detectable are small quantities of trimer and cyclic tetramer species. These were earlier reported in gas-chromatographic analyses.

Polymerization Sequence. Based on extensive GPC analysis, it appears that the sequence of reactions during polymerization could occur as follows:

Eq (8) Monomer → Dimer

Eq. (9) Dimer → Pentamer → Octamer → etc.

@Seismicisolation

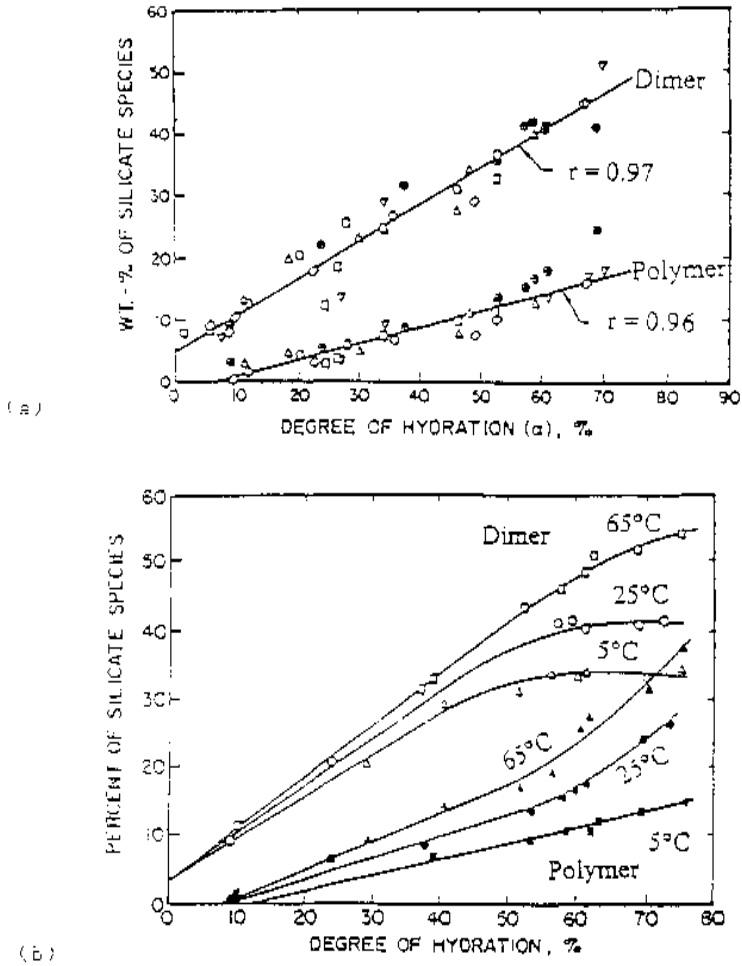


Figure 8. Plots of silicate species vs. degree of hydration. *(a)* Regression analysis at 20°C; *(b)* effect of hydration temperature.

@Seismicisolation

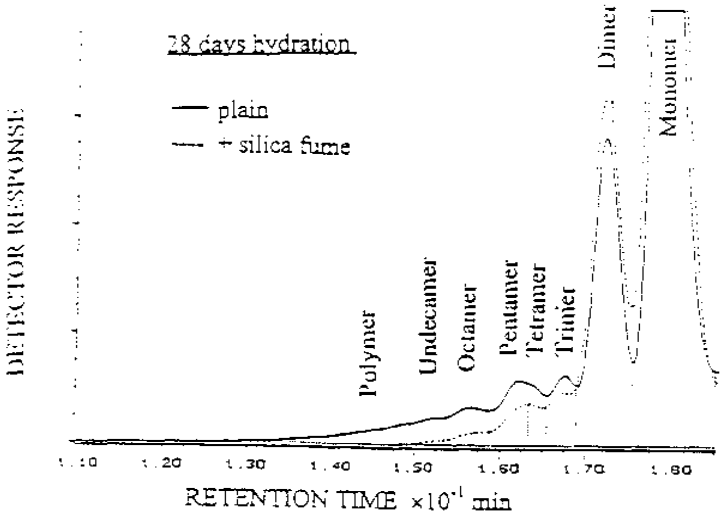


Figure 9. GPC chromatograms of hydrated Ca_3SiO_5 paste using current column technology.

The sequence of events described in Eqs. (8) and (9) suggest that C-S-H first forms with dimeric species. This would be consistent with the central Ca-O, sheets of the tobermorite structure provide a template for an arrangement of dimers that can subsequently be converted into dreierketten chains by the insertion of bridging tetrahedra. The intermediate species (pentamer, octamer, etc.) are present in relatively small quantities that quickly achieve steady-state levels. Thus, the sequence of converting dimers to short chains and then short chains to longer chains seems to be a scenario that is consistent with the concept of a gradual change towards the tobermorite structure over time.

Factors Affecting Polymerization. The strong effect of temperature on polymerization has already been noted (see Fig. 8b). An activation energy of 13 kcal/mole has been estimated,[16] however, the addition of chemical admixtures does not change polymerization when plotted against degree of hydration. The addition of mineral admixtures, such as silica fume[22][23] or fly ash,[24] tend to increase the degree of silicate polymerization, as does carbonation.[25] A recent study[27] on the hydration of highly reactive β-Ca_2SiO_4 is one of the few studies comparing TMS analysis with ^{29}Si NMR spectroscopy.

@Seismicisolation

3.6 Analytical Procedure

The derivatization begins with placing 10 ml of DMF, 5 ml HMDSO, and 2 ml TMCS, in a 50 ml Erlenmeyer flask and stirring gently for 15 minutes with a magnetic stirrer. Both DMF and HMDSO should have been distilled within one week and kept in well-stoppered containers. Then, 200 mg of the dry, powdered cement paste is added to the flask and stirred for 3–4 hours until the sample is dissolved. The sample is transferred to a separatory funnel and the flask rinsed with 1 ml HMDSO, which is added to the funnel. Add 25 ml deionized water to the funnel, shake well, and then drain off aqueous phase. Wash the organic solution with a further 10 ml of water and again remove and discard the aqueous phase (washing removes calcium chloride).

The organic phase is placed in a clean screw-top flask containing 3 g of molecular sieves as a drying agent. Wash funnel with 1 ml HMDSO and add it to the flask. The samples are stored overnight to remove all traces of water. Filter off molecular sieves through filter paper pre-wetted with HMDSO, catching the filtrate in a 10 ml volumetric flask, rinsing the storage flask and sieves with 1–2 ml HMDSO. Fill the volumetric flask to the line with HMDSO. Transfer the solution back to the screw top flask which now contains 2 g of ion exchange beads in the hydrogen form. Cap tightly and store overnight to allow complete conversion to fully trimethylsilylated derivatives.

Samples can be safely stored for subsequent GPC analysis. To avoid clogging the column, a 4 ml sample is extracted from the flask, using a syringe equipped with a two-micron filter, and stored in a vial tightly sealed with teflon lined screw caps.

4.0 SOLID STATE ^{29}SI NMR SPECTROSCOPY

4.1 Introduction to NMR Spectroscopy

Nuclei with fractional spin numbers ($I = n/2$) can give rise to nuclear magnetic resonance (NMR) spectra due to induced transitions between spin states when they are split in a strong magnetic field. The theory of NMR spectroscopy is summarized by Kirkpatrick[27] in this volume, so only information relevant to ^{29}Si spectroscopy is summarized here. Although ^{28}Si ($I = 1$) does not give rise to NMR spectra, the isotope ^{29}Si has $I = ½$ and is of sufficient natural abundance (4.7%) that NMR spectra of silicon containing compounds can be easily obtained. Lippmaa, et a1.,[28] were the first to apply ^{29}Si NMR spectroscopy to the study of cement-related compounds.

@Seismicisolation

In a strong magnetic field of 7.04 T, the resonance frequency for ^{29}Si nuclear spin transitions is 59.54 MHz.

Solid-state MAS NMR has the following advantages. It is a physical method that requires minimal sample preparation (normally powder samples are used) and there are no side reactions that will change the structure. The information that can be obtained depends only upon short range order. The details of the local chemical environment of a specific nucleus can be obtained from both crystalline and amorphous material. In this respect, it is most useful in studying the cement hydration products which are amorphous in nature.

4.2 Chemical Shifts

In different chemical environments, shifts in resonance frequency arise from partial shielding of the Si nuclei from the applied magnetic field by the electrons surrounding the nucleus. This gives rise to the *chemical shift*, (expressed in ppm of the applied field), the value of which is characteristic of a particular chemical environment. The chemical shift is determined with respect to a reference compound which is arbitrarily given zero chemical shift (δ = 0 ppm). Preferably, the reference compound should give rise to a single sharp peak somewhat apart from the other peaks of interest. A perfect candidate in the case of ^{29}Si is tetramethylsilane $(CH_3)_4Si$ (TMS). The use of TMS as an internal standard is so popular that its signal also defines the reference point in all ^{1}H and ^{13}C spectra. In addition, there are two references commonly used as secondary standards in ^{29}Si solid-state NMR spectroscopy: the trimethylsilyl ester of the double four-ring octameric silicate $[Si(CH_3)]_8Si_8O_{20}]$ (designated Q_8M_8) and tetrakis (trimethylsilyl) silane $[(CH_3)_3Si]_4Si$ or TTMS]. The chemical shift of the trimethylsilyl group M of Q_8M_8 is +11.5 ppm from TMS, while the chemical shift of the trimethylsilyl group in TTMS is -9.9 ppm from TMS.

Lippmaa, et al.,[28] studied a series of silicate compounds with known molecular structure by solid-state ^{29}Si NMR. They found that the total range of ^{29}Si chemical shifts in silicate is from -60 to -120 ppm with significant subdivision into well-separated ranges for isolated silicon-oxygen tetrahedra (Q^0), linked tetrahedra in pyrosilicates or as the end groups of linear chains (Q^1), middle tetrahedra in chains (Q^2), bridging tetrahedra linking two chains (Q^3), and the tetrahedra three-dimensional cross-linked framework (Q^4). The designations Q^0 to Q^4 refer to the connectivities of the Si-O tetrahedra. They are shown in Table 5.

@Seismicisolation

For example, quartz has a single Q^4 peak; xonotlite (linked dreierketten chains) has Q^3 and Q^2 peaks in a 1:2 intensity ratio; pseudowollastonite has a single Q^2 peak characteristic of the cyclic trimer silicate units; and β-Ca_2SiO_4 has a single Q^0 peak corresponding to SiO_4^{4-}. From the study of a large variety of zeolite structures, the ^{29}Si chemical shift ranges of aluminosilicates was also established. The SiO_4 tetrahedra are connected through shared oxygen atoms with $nA1O_4$ tetrahedra (n = 0–4) in the aluminosilicate framework. The more Al-O tetrahedra connected to the Si-O tetrahedron, the less negative will be the values for the chemical shift of the Si nuclei.

Table 5. Ranges of ^{29}Si Chemical Shifts for Different Structural Units of Silicate Species

Connectivity	Type	Chemical shift (δ, ppm)
Q^O	orthosilicate (monomer)	-66 to -74
Q^1	pyrosilicate (dimer)	-77 to -82
Q^2	linear chains or ring	-85 to -89
Q^3	cross-linked chains	-92 to -100
Q^4	3-D network	-103 to -115

4.3 Acquisition of ^{29}Si Solid-State NMR Spectra

All Fourier transform NMR experiments are combinations of pulses and delays. The two most commonly used methods in the study of silicon polymerization during cement hydration are the simple one pulse MAS NMR experiment and cross-polarization magic angle spinning (CPMAS) experiment.

One Pulse Experiment. This is called a "one pulse" (1PULS) experiment because one rf pulse is applied per cycle. The pulse excites the nuclei, which then reradiate during the acquisition time, giving an NMR signal. The pulse has a width which is measured in microseconds and is on the order of 10 μs. It is commonly described in terms of a flip angle in degrees. A 90° pulse is the power required to obtain a maximum response from the sample. For routine experiments, a pulse width less than 90° is used.

@Seismicisolation

The recycle delay allows time for the nuclei to relax toward thermal equilibrium so that the system can be pulsed for a second time. The pulse width and recycle delay are correlated and should be carefully selected by means of preliminary experiments to get the best result.

The Recycle Delay and Inversion-Recovery Measurement of T_1. To avoid saturation there should be enough time between pulses for the nuclei to reach (or nearly reach) their original equilibrium; therefore, this recycle time is a function of T_1 and for good quantitative results, the recycle delay should be five times the length of T_1. The T_1 values for nuclei in a sample are most commonly measured using a simple two-pulse sequence, given in Fig. 10. A single π(180°) pulse is used to invert the equilibrium populations of the energy levels of nuclei in the sample. Following the pulse, the populations begin to recover towards equilibrium during the delay τ. A $\pi/2$ pulse is used to convert the population difference between levels to a detectable NMR signal. When a τ is zero (or very small) the sample effectively receives a $3\pi/2$ pulse and the observed signal is negative. When τ is long, the sample relaxes fully between the π and $\pi/2$ pulses and maximum (positive) signal is observed. Between these extremes, the observed signal increases exponentially with τ. The most convenient way to obtain T_1 is from the slope of a graph.

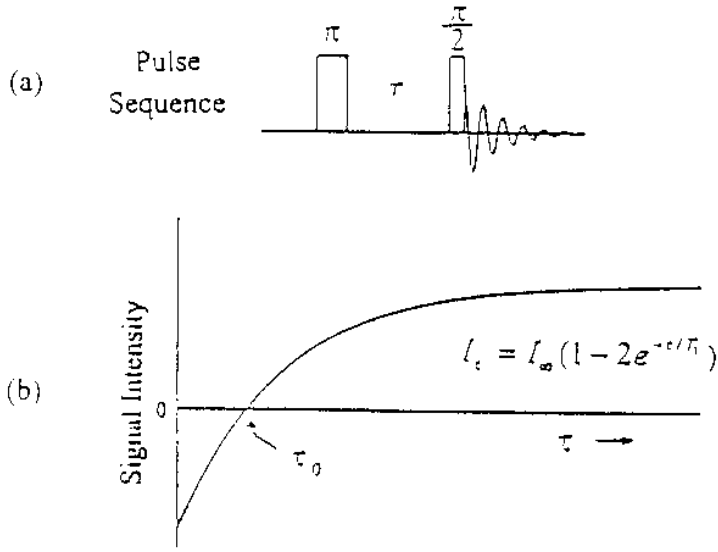


Figure 10. Representation of inversion-recovery measurement of T_1. *(a)* Pulse sequence. *(b)* Intensity of spectrum versus τ after several repetitions.

@Seismicisolation

Cross Polarization Sequence. Cross-polarization (CP) allows transfer of magnetization from an abundant species to a rare species. The cross polarization technique affects the rare species signal intensity in two ways. Firstly, there is a direct signal enhancement by a factor of $\gamma_{abundant}/\gamma_{rare}$ for the rare species; in the case of ^{1}H and ^{29}Si, a factor of 5. Secondly, there is a signal enhancement because the repeat cycle of experiment is determined by the proton relaxation times, which are generally much faster than silicon or carbon relaxation times and, therefore, S/N can be accumulated at a more rapid recycle rate (usually 2–3 seconds for ^{29}Si studies) than if they were observed without CP.

There is another benefit from CP studies and this depends on the fact that the effectiveness of the CP phenomenon is proportional to r^{-3}, where r is the distance between the abundant nucleus and the rare nucleus. The efficiency of transfer of magnetization falls off extremely rapidly as the distance between the two nuclei increases. For example, the use of cross-polarization ^{29}Si NMR enables one to examine Si nuclei that are close to the surface OH groups separately from those in the bulk material. In CPMAS experiments the so called "Hartmann-Hahn condition" should be met in which the ^{1}H and ^{29}Si nuclei precess with the same frequency with respect to the "spin-locking" field and during the spin-locked period (the "contact time") equilibration of the proton and the rare nuclei populations proceeds by population transfer from the ^{1}H spectrum to the rare nuclei spectrum. Since the contact time (typically several milliseconds in duration) may have an effect on the peak intensity ratios, care should be taken in interpretation.

Quantitative Analysis (for MAS NMR). Another important feature of the NMR method is that the intensity of a signal is directly proportional to the number of nuclei that generate the signal. This allows us to do quantitative analysis, provided that correct parameters are selected. Relaxation times of ^{29}Si nuclei can be very long. In quantitative analysis, the relaxation times of the nuclei must be determined carefully and recycle delay times should be set long enough to allow nuclei to relax sufficiently. The presence of paramagnetic ions such as Fe^{2+} may shorten the relaxation time of the ^{29}Si nucleus by as much as an order of magnitude. On the other hand, the presence of very large amounts of paramagnetic ions, such as fly ash/cement blends, may prevent the observation of some, or all, of the ^{29}Si nucleus signal.

A line shape simulation program is usually provided by the spectrometer for computer deconvolution of spectra with overlapping peaks. The program provides the position, intensities, widths, and relative areas, of the individual lines. The individual line parameters (position, height, and width) can be changed manually to obtain the optimum visual fit on the video display

@Seismicisolation

monitor. In some programs, a maximum of more than twenty overlapping lines can be handled one by one. The simulated line shape can vary from 100% Lorentzian to 100% Gaussian to get the best fit for the real curve. The program calculates the area percentage of the individual lines. Once the best fit is obtained, the real and synthesized spectra and the individual lines can be plotted.

The following is an example of the ^{29}Si NMR analysis for quantifying small amounts of β-C_2S impurity in γ-C_2S preparation.[29] It is difficult to accomplish the analysis by x-ray diffraction since there are so many overlapping peaks, however, in ^{29}Si NMR spectrum the chemical shift of γ–C_2S (-73.7 ppm) is 2.4 ppm away from that of β-C_2S (-71.3 ppm), as shown in Fig. 11. A spectrum was acquired for the synthetic γ-C_2S sample and, by applying the line simulation program, the two phases were successfully quantified.

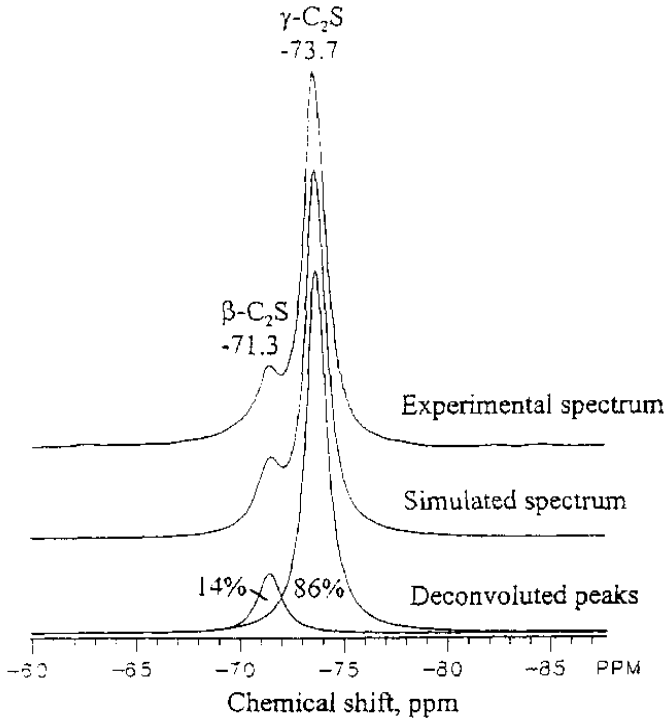


Figure 11. ^{29}Si MAS NMR quantitative analysis for small amounts of β-Ca_2SiO_4 in a γ-Ca_2SiO_4 preparation.

@Seismicisolation

4.4 Application of ^{29}Si Solid-State NMR to the Study of Cements

MAS NMR has become a commonly used technique to study the cement related materials and reactions. This section provides an overview of the kind of information that has been obtained. As an example, the MAS NMR and CPMAS spectra of Ca_3SiO_5 paste hydrated in the presence of reactive silica (silica fume) for nine months is shown in Fig. 12. Ca_3SiO_5 is mixed with silica fume in a starting $CaO/SiO_2 = 0.5$, water solid ratio being 0.2. MAS NMR shows the remaining Ca_3SiO_5 as the monomer (Q^0) at -71 ppm, the main hydration product (Q^2) at -85 ppm and the remaining silica fume (Q^4) centered at -110 ppm. The shoulder at -79 ppm represents Q^1 species in the hydration product (either dimer or the end group of a chain). A Q^3 peak is also seen as a hump at around -94 ppm. In the CP mode, the anhydrous Q^0 peak is not observed, but a hump at about -110 ppm, indicates that the silica fume surface is protonated after extended hydration.

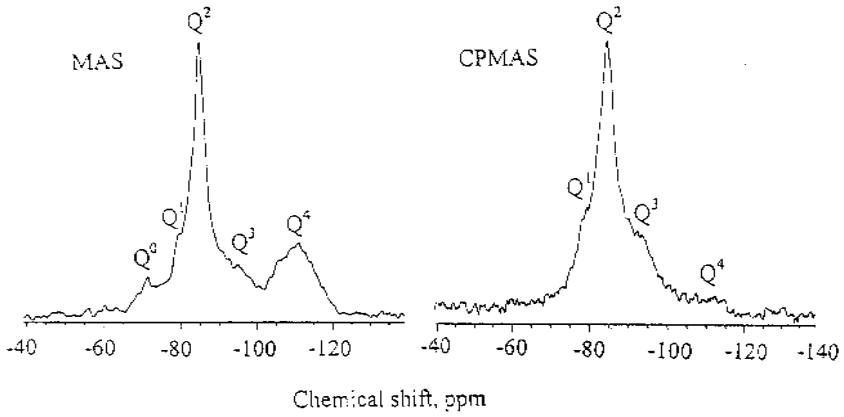


Figure 12. The MAs NMR and CPMAS spectra of Ca_3SiO_5 paste hydrated in the presence of reactive silica.

Crystalline Calcium Silicate Hydrates. Bell, et a1.,[30] hydrothermally synthesized a body of calcium silicate hydrates which were examined by ^{29}Si NMR spectroscopy. The results were compared with the crystal structures obtained by other methods. NMR spectra suggest some of the postulated structures are incorrect. By using ^{29}Si NMR, Wieker, et a1.,[31]

@Seismicisolation

were able to confirm that some hydrothermally prepared 11 Å tobermorites consisted of double chain silicate ions, contrary to the published structure.

Anhydrous Phases. Ca_3SiO_5 and Ca_2SiO_4 polymorphs all contain isolated SiO_4 tetrahedra, i.e., Q^0 units. ^{29}Si NMR spectra have shown that the Ca_3SiO_5 has at least nine peaks in the range of -69 to -75 ppm. The β-Ca_2SiO_4 has a single narrow peak at -71.3 ppm. These observations are consistent with the published crystal structures. Skibsted, et a1.,[32] tried to quantify these phases in cements by deconvolution of the spectra combined with the bulk SiO_2 content obtained from elemental analysis. They found that the conventional Bogue calculations overestimates the belite content and underestimates alite; NMR results have better correlation with the results from Taylor-Bogue calculations.[33]

Hydration Reactions. The hydration and hydration products of portland cement and calcium silicates have been studied extensively using ^{29}Si solid state MAS NMR and CPMAS NMR.[34]–[47] It is well established that the main hydration product C-S-H contains Q^1 and Q^2. In other words, they are either dimers and chains or rings. The area associated with each species can be calculated though it is not possible now to distinguish a dimer from the end group of a chain. The Q^2/Q^1 ratio gives an estimate of the *average* chain length which is equal to $[(Q^2/Q^1) + 1] \times 2$. It is shown that while Q^0 decreases with time during hydration the Q^2/Q^1 ratio increases and hence, the average chain length. It is possible, in principle, to estimate the amount of dimer by TMS-GPC analysis and deducting the contribution of dimers from the Q^1 signal to calculate, the average length of chains, however, no such analysis has been reported.

The influence of temperature on the composition of the hydration products also has been studied using ^{29}Si enrichment. Brough, et a1.,[37] found that the rate of reactions and also the degree of silicate polymerization at a given degree of hydration were both significantly increased at elevated temperatures. They found that at room temperature the early hydrates are essentially dimeric material. It was concluded that potential mechanism for polymerization is the linking of dimeric-silicate units by insertion of monomers, as proposed by Hirljac et a1.[16] from TMS studies.

Hydration with Reactive Silica. The use of reactive silicas as mineral admixtures in concrete has attracted much attention. Groves and Rodger[38] found that the chain length of the hydration products of C_3S increases in the presence of silica fume and chains of eight units were reported. Justnes, et a1.,[39] observed that silica fume accelerates the hydration of cement minerals at the early age, but retards the hydration at a

@Seismicisolation

late stage. They also came to the conclusion that the average chain length of the linear polysilicate anions in the C-S-H gel is longer in mixes with silica fume than without. In a more recent development, cross-linking Q^3 species has been positively identified in the system with a wide range of silica fume added into cement.[40] Moreover, after extended hydration the surface of silica fume has reacted with water and a Q^4 peak is found in the CP-NMR. Brough, et a1.,[41] studied the pozzolanic reaction using selective isotopic enrichment of ^{29}Si in the reactants (Ca_3SiO_5 and SiO_2). They compare the behavior of the silicon nuclei originating from either source. They showed that the silicon atoms from the two components are not equilibrated throughout the hydration products, but are preferentially located in distinct species.

A method was developed[42] to use a type of silicon carbide ($\delta = 22$ ppm) as a standard in ^{29}Si MAS NMR to determine the residue silica fume in a white cement-silica fume DSP paste. In combination with the determination of the degree of reaction of cement measured by TMS-analysis they were able to calculate by mass balance the CaO/SiO_2 ratio of the resulting C-S-H in the system with varying starting CaO/SiO_2 ratios hydrated for a range of ages up to 1.5 years.[22]

5.0 CONCLUSIONS

The analysis of silicate polymerization has proven to be a powerful tool in the study of cement hydration and the structure of hydrated silicates. TMS analysis and ^{29}Si NMR spectroscopy are the two most versatile and widely used techniques. If both techniques were used in combination they could provide complementary information, but this has not yet been done, to our knowledge. Both analytical approaches can provide useful quantitative information.

@Seismicisolation

REFERENCES

1. Taylor, H. F. W., Proposed Structure for Calcium Silicate Hydrate Gel, *J. Amer. Ceram. Soc.*, 69(6):464–467 (1986)
2. Funk, H., and Frydrych, R., The Degrees of Anion Condensation in Silicic Acids and Silicates, in *Structure of Portland Cement Paste and Concrete*, Spec. Rpt. 90, pp. 284–290, Highway Research Board, Washington, DC (1966)
3. Wieker, W., New Methods of Investigation of the Hydration Processes of Portland Cements, *Proc. 6th. Intern. Congr. Chem. Cement, Moscow 1974*, 2:165–185, Stoiizdat, Moscow (1976)
4. Parrott, L., and Taylor, M. G., A Development of the Molybdated Complexing Method for the Analysis of Silicate Mixtures, *Cem. Concr. Res.*, 9:483–488 (1979)
5. Funk, H., The Alteration of Silicate Anions in Tobermorite Gels, *Proc. 5th Intern. Conf. Chem. Cement*, VI:128–132, Cement Association of Japan, Tokyo (1968)
6. Parrott, L. J., Effect of a Heat Cycle During Moist Curing Upon the Deformation of Hardened Cement Paste, in *Hydraulic Cement Pastes: Their Structure and Properties*, pp. 189–203, Cement and Concrete Association, Slough, U.K. (1976)
7. Parrott, L. J., Basic Creep, Drying Creep, and Shrinkage of a Mature Cement Paste After a Heat Cycle, *Cem. Concr. Res.*, 7:597–604 (1977)
8. Bentur, A., Kung, J. H., Young, J. F., Berger, R. L., Milestone, N. B., Mindess, S., and Lawrence, F. V., Influence of Microstructure on Creep and Drying Shrinkage of Calcium Silicate Pastes, *Proc. 7th Intern. Congr. Chem. Cement*, III:VI.26–32, Editions Septima, Paris (1980)
9. Lentz, C. W., Silicate Minerals as Sources of Trimethylsilyl Silicates and Silicate Structure Analysis of Sodium Silicate Solutions, *Inorg. Chem.*, 3:574–579 (1964)
10. Milestone, N. B., A New Method for Qualitative Silylation of Silicates, *Cem. Concr. Res.*, 7:345–346 (1977)
11. Gotz, J., and Masson, C. R, Trimethylsilyl Derivatives for the Study of Silicate Structures, Part I. A Direct Method of Trimethylsilylation, *J. Chem. Soc.*, (A), pp. 2683–2690 (1970)
12. Gotz, J.,. and Masson, C. R., Trimethylsilyl Derivatives for the Study of Silicate Structures, Part II. Orthosilicate, Pyrosilicate and Ring Structures, *J. Chem. Soc.*, A, pp. 686–688 (1971)
13. Lentz, C. W., The Silicate Structure Analysis of Hydrated Portland Cement Paste, in *Structure and Properties of Portland Cement Paste and Concrete, Spec. Rpt. 90*, pp. 269–283, Highway Research Board, Washington DC (1966)

@Seismicisolation

14. Tamas, F. D., Sarkar, A. K., and Roy, D. M., Effect of Variables Upon the Silylation Products of Hydrated Cements, in *Hydraulic Cement Pastes: Their Structure and Properties,* pp. 55–72, Cement and Concrete Association, Slough, UK (1976)

15. Sarkar, A. K., and Roy, D. M., A New Characterization Technique for Trimethylsilylated Products of Old Cement Pastes, *Cem. Concr. Res.*, 9:343–352 (1979)

16. Hirljac, J., Wu, Z-Q., and Young, J. F., Silicate Polymerization During the Hydration of Alite, *Cem. Concr. Res.*, 13:877–886 (1983)

17. Lachowski, E. E., Trimethylsilylation as a Tool for the Study of Cement Pastes (I) Comparison of Methods of Derivatization, *Cem. Concr. Res.*, 9:111–114 (1979)

18. Sachowski, E. E., Trimethylsilyation as a Tool for the Study of Cement Pastes (2) Quantitative Analysis of the Silicate Fraction of Portland Cement Pastes, *Cem. Concr. Res.*, 9:337–342 (1979)

19. Bentur, A., and Young, J. F., Simplified Method for Determining the Polysilicate Content in Cementitious Pastes Using Trimethylsilyl Derivatives, *Cem. Concr. Res.*, 11:287–290 (1981)

20. Dent Classer, L. S., Lachowski, E. E., Mohan, K., and Taylor, H. F. W., A Multi-Method Study of C_3S Hydration, *Cem. Concr. Res.*, 8:733–740 (1978)

21. Mohan, K., and Taylor, H. F. W., A Trimethylsilylation Study of Tricalcium Silicate Pastes, *Cem. Concr. Res.*, 12:25–31 (1982)

22. Lu, P., Sun, G., and Young, J. F., Phase Composition of Hydrated DSP Cement Pastes, *J. Amer. Ceram. Soc.*, 76:1003–1007 (1993)

23. Lu, P., and Young, J. F., Slag-Portland Based DSP Paste, *J. Amer. Ceram. Soc.*, 76:1329–1334 (1993)

24. Mohan, K., and Taylor, H. F. W., Pastes of Tricalcium Silicate with Fly Ash - Analytical Electron Microscopy, Trimethylsilylation and Other Studies, *Effect of FIy Ash Incorporation in Cement and Concrete Products,* pp. 54–59, Materials Research Society, Pittsburgh, PA (1981)

25. Lentz, C. W., Effect of Carbon Dioxide on Silicate Structures in Portland Cement Paste, *Proc. XXVI Congr. Intern. Chim. Industr. BrusseIs Compte Rend,* II:174–175 (1966)

26. Okada, Y., Ishida, H., Sasaki, K., Young, J. F., and Mitsuda, T., Characterization of C-S-H from Highly Reactive β-Dicalcium Silicate Prepared from Hillebrandite, *J. Amer. Ceram. Soc.*, 77:1313–1318 (1994)

27. Kirkpatrick, R., NMR Spectroscopy, Ch. 6 in this book.

28. Lippmaa, E., Magi, M., Samoson, A., Engelhardt, G., and Grimmer, A. R, Structural Studies of Silicates by Solid-State High-Resolution ^{29}Si NMR, *J. Am. Chem. Soc.*, 102:4889–4893 (1980)

@Seismicisolation

29. Matkovic, B., Paljevic, M., Mikoc, M., Carin, V., Halle, R., Sun, G-K., and Young, J. F., The Effect of Combined Additions of Silica Fume, Calcium Sulpho-aluminate, and Gypsum on the Hydration and Strength Development of Ca_2SiO_4, *Adv. Cem. Res.*, 4:9–15 (1991/92)

30. Bell, C. M. M., Bensted, J., Glasser, F. P., Lachowski, E. E., Roberts, D. R., and Taylor, M. J., Study of Calcium Silicate Hydrates by Solid State High Resolution ^{29}Si Nuclear Magnetic Resonance, *Adv. Cem.Res.*, 3:23–37 (1990)

31. Wieker, W., Grimmer, A. R., Winkler, A., Mägi, M., Tarmak, M., and Lippmaa, E., Solid-State High-Resolution ^{29}Si NMR Spectroscopy of Synthetic 14 Å, 11 Å, and 9 Å, Tobermorites, *Cem. Concr. Res.*, 12:333–339 (1982)

32. Skibsted, J., Jakobson, H. J., and Hall, C., Quantification of Calcium Silicate Phases in Portland Cements by ^{29}Si MAS NMR Spectroscopy, *J. Chem. Soc. Faraday Trans.*, 91:4423–4430 (1995)

33. Taylor, H. F. W., *Cement Chemistry*, Wiley and Sons, London (1990)

34. Clayden, N. J., Dobson, C. M., Groves, G. W., Hayes, C. J., and Rodger, S. A., Solid State NMR Studies of Cement Hydration, *Brit. Ceram. Proc.*, 35:55 (1984)

35. Lippmaa, E., Magi, M., Tarmak, M., Wieker, W., and Grimmer, A. R, A High Resolution ^{29}Si NMR Study of the Hydration of Tricalciumsilicate, *Cem. Concr. Res.*, 12:597–602 (1982)

36. Barnes T. R., Clague, A. D. H., Clayden, N. J., Dobson, C. M., Hayes, C. J., Groves, G. W., and Rodger, S. A., Hydration of Portland Cement by ^{29}Si Solid State NMR Spectroscopy, *J. Mater. Sci. Letters*, (4)::1293–1295 (1985)

37. Brough, A. R., Dobson, C. M., Richardson, I. G., and Groves, G. W., In-Situ Solid-State NMR Studies of Ca_3SiO_5: Hydration at Room Temperature and at Elevated Temperatures Using ^{29}Si Enrichment, *J. Mat. Sci.*, 29:3926–3940 (1994)

38. Groves, G. W., and Rodger, S. A., The Hydration of C_3S and Ordinary Portland Cement with Relatively Large Additions of Microsilica, *Adv. Cem. Res.*, 2:135–140 (1989)

39. Justnes, H., Meland, I., Bjoergum, J. O., and Krane, T., A., ^{29}Si MAS NMR Study of the Pozzolanic Activity of Condensed Silica Fume and the Hydration of Di and Tricalcium Silicates, *Adv. Cem. Res.*, 3:111–116 (1990)

40. Sun, G. K., Brough, A. R., and Young, J. F., ^{29}Si NMR Study of the Hydration of Ca_3SiO_5 and β-Ca_2SiO_4 in the Presence of Silica Fume, *J. Amer. Ceram.* Soc., in press.

41. Brough, A. R., Dobson, C. M., Richardson, I. G., and Groves, G. W, A Study of the Pozzolanic Reaction by Solid-State ^{29}Si Nuclear Magnetic Resonance Using Selective Isotopic Enrichment, *J. Mater. Sci.*, 30:1671–1678 (1995)

@Seismicisolation

42. Sun, G-K., and Young, J. F., Quantitative Determination of Residual Silica Fume in DSP Cement Pastes by 29-NMR, *Cem. Concr. Res.*, 23:480–483 (1993)

43. Cong, X., Kirkpatrick, R. I., and Diamond, S., ^{29}Si MAS NMR Spectroscopic Investigation of Alkali Silica Reaction Product Gels,*Cem. Concr. Res.*, 23:811–823 (1993)

44. Richardson, I. G., Brough, A. R. Brydson, R., Groves, G. W., and Dobson, C. M., Location of Aluminium in Substituted Calcium Silicate Hydrate (C-S-H) Gels as Determined by ^{29}Si and ^{27}A1 NMR and EELS, *J. Am. Ceram. Soc.*, 76:2285–2288 (1993)

45. Stade, H., and Müller, D., On the Coordination of Al in Ill-Crystallized CSH Phases Formed by Hydration of Tricalcium Silicate and by Precipitation Reactions at Ambient Temperature, *Cem. Concr. Res.*, 17:553–561 (1987)

46. Skibsted, J., and Jakobson, H. T., Direct Observation of Aluminium Guest Ions in the Silicate Phases of Cement Mineral by 27A1 MAS NMR Spectroscopy, *J. Chem. Soc. Faraday Trans.*, 90:2095–2098 (1994)

47. Cong, X., and Kirkpatrick, R. J.,^{17}O and ^{29}Si MAS NMR Study of β-C_2S Hydration and the Structure of Calcium-Silicate Hydrates, *Cem. Concr Res.*, 23:1065–1077 (1993)

@Seismicisolation

16

Permeation Analysis

P. A. Muhammed Basheer

1.0 DEFINITIONS AND TRANSPORT MECHANISMS

Gradients of moisture content, hydrostatic pressure, stress, temperature, and concentration of chemicals, disturb the state of equilibrium of fluids in a porous material,[1] therefore, the transfer of fluid flux occurs in order to restore the equilibrium. This process of transport of fluid flux is generally described in terms of adsorption, diffusion, absorption, and permeability.[2]–[4] In concrete both the physical structure of concrete and the state of water in pores influence these processes. The hydrodynamics of porous materials, treating the porous body as a continuum could be used to obtain equations defining these transport processes;[5] however, empirical laws, such as Fick's law, Poiseuille's equation, and Darcy's equation, were found[6]–[14] to be widely used for concrete. The theoretical descriptions of the transport processes generally form the basis to measure the transport properties of concrete. This chapter provides details of test methods which can be used to measure the various transport characteristics of concrete. However, a knowledge of both the pore structure of concrete and various forms of water in it is beneficial in order to understand fully the various transport mechanisms.

@Seismicisolation

1.1 Physical Structure of Concrete

Concrete has a highly heterogeneous and complex structure, therefore, it is difficult to constitute exact models of the concrete structure from which the behavior of the material can be reliably predicted. At the macroscopic level (i.e., which can be identified with human eyes) concrete may be considered to be a two phase material consisting of aggregate particles dispersed in a matrix of the cement paste.[15][16] At the microscopic level (i.e., which can be identified with a microscope), a third phase—the transition zone—may be identified.[17] This represents the interfacial region between the particles of aggregate and the hydrated cement paste (hcp) existing as a thin shell, typically 10 to 50 μm thick, around aggregates. It may be recognized that each of the three phases is itself multi-phase in nature. The two components of the structure, the hcp and the transition zone, are subjected to changes with time and environmental conditions, and, therefore, concrete behaves like a living system. As the physical properties, such as absorption and permeability, primarily depend on the characteristics of these two phases, an understanding of the details of their structure is important.

Structure of Hydrated Cement Paste (hcp). At any stage of hydration of cement, the hcp consists of solid products of hydration collectively called gel, crystals of calcium hydroxide, unhydrated cement, and space originally occupied by the water which was added for the hydration of cement. The gel is composed of gel particles and interstitial voids, known as gel pores. In the context of permeation properties of concrete, the various types of pores in concrete are significant. There are three main types of pores in hardened cement paste:

1. Interlayer space in calcium silicate hydrate (previously termed as gel pores).
2. Capillary pores.
3. Air voids.

The features and significance of each type of pore in the permeation properties of concrete are given below.

Interlayer Space in Calcium Silicate Hydrate (C-S-H). Although the original work by Powers[16] assumed a width of 18 Å (1 Å = 10^{-10} m) within the C-S-H structure, relatively recent work by Feldman and Sereda[18] suggested that these spaces vary from 5 to 25 Å. Anyhow, these spaces do not play any significant role in the flow of water through concrete because

@Seismicisolation

it has been shown[19]–[22] that pores with a radius of less than 500 Å do not contribute to the water permeability.

Capillary Pores. Capillary pores represent the spaces not filled by solid components of the hcp; therefore, the volume and size of the capillary voids depend on the distance between unhydrated cement particles in the freshly mixed cement paste (i.e., water-cement ratio) and the degree of hydration.[23][24] In well hydrated and low water-cement ratio pastes, the capillary voids may range from 100 to 500 Å, whereas in high water-cement ratio pastes at early ages of hydration the capillary voids may be as large as 3000 to 5000 Å.[20]

Air Voids. Air voids in concrete are due to either entrapped air during casting or intentionally entrained by using an air-entraining agent. The entrapped air may be as large as 3 mm and the entrained air may range from 50 μm (500,000 Å) to 200 μm (2,000,000 Å). They are much larger than the capillary voids and have a significant role in the permeability of concrete.

Structure of the Transition Zone. It is reported[17] that a preferential orientation of large crystals of calcium hydroxide and calcium sulfoaluminate results around the aggregates due to local increase in water-cement ratio close to them. A water film formed around the aggregates in the fresh compacted concrete accounts for this variation in water-cement ratio. As a result, concrete becomes more porous close to the aggregates with larger size capillary voids closer to them. Therefore, the properties of the transition zone significantly affect the permeability of concrete.

1.2 Forms of Water in Concrete

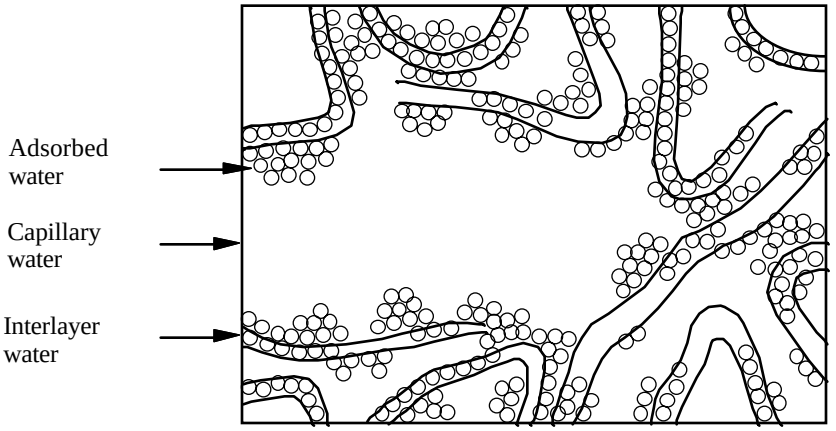
The different forms of water associated with the C-S-H structure are illustrated in Fig. 1.[18] *Chemically combined water* is the water that is an integral part of the structure of various cement hydration products. This water is not lost on drying, however, upon heating, at elevated temperatures the decomposition of hydrates releases it.

Interlayer water penetrates between layers of calcium silicate hydrates (C-S-H). Upon strong drying (i.e., below 11% relative humidity)[17] this water will be lost, resulting in the closure of space between the C-S-H layers and the shrinkage of the hardened cement paste (hcp).

Adsorbed water is the water that is close to the solid surface, which is held by physical forces of attraction. It has been suggested[17] that up to six molecular layers of water (15 Å) can be physically held on the surface, however, the force of attraction decreases with an increase in distance of the

@Seismicisolation

molecule from the solid surface. Therefore, a major portion of the adsorbed water can be lost by drying the hcp to 30% relative humidity. The loss of adsorbed water is mainly responsible for the shrinkage of the hcp in drying.



+ Chemically combined water in cement hydrates which is not shown

Figure 1. Different forms of water.[18]

Water which is free from the attractive forces exerted by the solid surface is free to move in capillaries. This water is generally present in voids larger in diameter than about 50 Å and is called *capillary water*. In concrete, this free water is known to be the cause of many types of physical processes of degradation (e.g., frost attack). As a vehicle for transport of aggressive ions, water can also be a source of chemical process of degradation. As a solvent, water is noted for its ability to dissolve more substances than any known liquid; therefore, the transport mechanisms associated with water in capillaries is very significant.

1.3 Definitions

Adsorption. *Adsorption* is a process in which molecules adhere to the solid surfaces in concrete (C-S-H sheets) either by physical forces of adhesion or as a result of chemical bonds.[3][18] Another term commonly

@Seismicisolation

used along with adsorption is *desorption*, which is the liberation of adsorbed molecules from the solid surfaces in concrete.

Diffusion. *Diffusion* is the process by which a liquid, gas, or ion, can pass through the concrete under the action of a concentration gradient.[2][3] The transfer of mass is as a result of random motion of free molecules or ions in solution.

Absorption. *Absorption* is the process by which concrete takes in a fluid due to capillary suction in pores in order to fill the space within the material.[2][3]

Permeability. *Permeability* of concrete may be defined as that property which characterizes the ease with which a fluid passes into and through the body of the concrete under a pressure differential.[2][3][25]

Although the term *permeability* is strictly related to a flow that occurs under a pressure differential, it is used most frequently to include other transport mechanisms such as absorption and diffusion.[26] However, the term *permeation properties* or *permeation characteristics* is used in this chapter where reference is made in a general sense. Quite often permeability is mistaken for porosity and vice versa; the latter is only concerned with the relationship of pores to the total volume. It is conceivable, though improbable, that a concrete could be porous, but impermeable if it contained a series of disconnected air pockets separated by impermeable material.

1.4 Transport Mechanisms

Rose[2] distinguished six stages in the transfer of fluid flux through a porous medium. These are presented in Fig. 2 from *(a)* to *(f)*. In addition to these stages, Report No. 31 of the Concrete Society[3] outlined two more stages *(g)* and *(h)* for the ionic diffusion through a partially saturated and fully saturated porous system. For the convenience of discussion, a single pore with a neck at each end only is presented in Fig. 2. A vapor flux is incident from the left in *(a)* to *(f)*, and an ionic flux is incident from the left in *(g)* and *(h)*. The various stages presented in Fig. 2 are explained below.

The first stage is one of adsorption (stage *a*) and, until this is complete, a vapor flux cannot be transmitted and "conductivity" has no meaning, even though flux will move to adsorption sites as vapor. This does not prevent surface diffusion in the adsorbed phase. After the initial adsorption, the second stage is one of unimpeded vapor movement (stage *b*) where the vapor behaves like an ideal gas. This is expressed by Fick's first law for diffusion:

@Seismicisolation

Eq. (1) $$J_x = -D_x \frac{\partial c}{\partial x}$$

where, J_x = flux of fluid at a position x in a direction x from the origin

D_x = diffusion coefficient at position x

$\partial c/\partial x$ = concentration gradient at position x.

(Fick's second law for diffusion relates the rate of change of concentration gradients by assuming that the diffusion coefficient is independent of position).

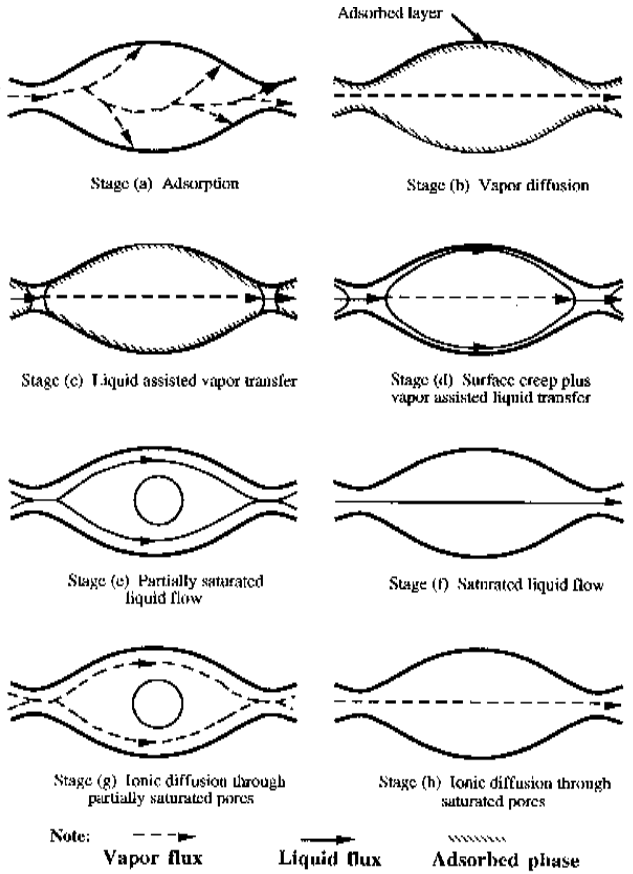


Figure 2. Idealized model of transfer liquids and ions within concrete.[2][3]

@Seismicisolation

The third and fourth stages occur when the necks contain liquid, either without or with a thin film, of significant thickness on the walls of the cavity, (stages *c* and *d*, respectively). In stage *c*, the system is impervious to an inert gas and pervious to liquid only by a process of distillation in which the necks act as short-circuits for vapor movement. The process is described as liquid assisted vapor transfer, the assistance arising because the liquids shorten the effective path length for vapor diffusion.

In stage*d*, the condition is one of surface creep, i.e., flow in thin liquid films, in which there is vapor assisted liquid transfer. Eventually there is a transition to the fifth and sixth stages where there is liquid flow, with stage *e* representing the unsaturated condition and stage *f* representing the saturated condition. There is an important difference between stages *d* and *e* best revealed by ignoring the arrows and treating the diagram as depicting a dynamic equilibrium. In stage *e*, the air-water boundary will have the same curvature everywhere, but in *d* the curvature away from the necks is largely determined by the shape of the solid surface.

As the flow occurs in the pore due to the pressure differential across the boundary (meniscus) in stage*e*, the rate of flow is given by Washburn's equation.[4]

Eq. (2) $$v = \frac{r\gamma}{4d\mu}\cos\theta$$

where,
- v = rate of flow
- r = capillary radius
- γ = surface tension
- d = depth of penetration of fluid
- μ = fluid viscosity
- θ = contact angle.

The flow in stage *f*, i.e., in the saturated condition, is due to a high pressure head existing across the pore, therefore, the rate of flow is governed by Darcy's law. For a non-compressible fluid and a saturated porous medium, Darcy's law states that the steady state rate of flow is directly proportional to the hydraulic gradient.

Eq. (3) $$v = Q/A = -Ki = -K\frac{\partial h}{\partial l}$$

where,
- v = apparent velocity of flow
- Q = flow rate
- A = cross sectional area

@Seismicisolation

i = hydraulic gradient
∂h = head loss over a flow path of length ∂l
K = coefficient of permeability or hydraulic conductivity

It must be emphasized that the application of Darcy's equation to the flow through porous media is based on the following assumptions:

1. Complete saturation has been achieved.
2. Flow is laminar and viscous.
3. Equilibrium flow conditions have been established.

A more rational concept of permeability which is independent of the fluid properties and dependent purely on the characteristics of the porous body is intrinsic permeability. This is expressed as:

Eq. (4) $$v = Q/A = \frac{k}{\mu}\frac{\partial p}{\partial l}$$

where,
v = velocity of flow
Q = volume rate of flow
A = area of cross section
∂p = pressure loss over the flow path of length ∂l
μ = viscosity of the fluid
k = intrinsic permeability of the porous medium

In addition to the stages *a–f,* ionic diffusion may take place in stages *e* and *f* as shown in stages *g* and *h*. This is superimposed over the other transport processes already explained with reference to these figures. The ionic diffusion also is governed by Fick's first law.

It can be seen in Fig. 2 that the moisture condition of the concrete influences various stages of the transfer of fluids through it. Various factors influencing permeation measurements are further discussed in subsequent sections.

Permeation tests can be described according to the above mechanisms which govern the transport of fluids in concrete. Therefore, the primary test methods are:

1. Adsorption tests
2. Diffusion tests
3. Absorption tests
4. Permeability tests

@Seismicisolation

2.0 ADSORPTION TESTS

The experimental observation most frequently made for the adsorption test is of the adsorption isotherm (Fig. 3); this is the measurement of the quantity of adsorbed material as a function of its vapor pressure at constant temperature. Both nitrogen and water vapor had been used in the past.[18][27] When the relative vapor pressure is between 0.05 and 0.40 the theory of multimolecular adsorption developed by Brunauer, Emmett, and Teller, known commonly as the BET theory, can be used to determine the specific surface area of hydrated portland cement.[28] At relative vapor pressures above 0.40 capillary condensation occurs along with the multimolecular adsorption.

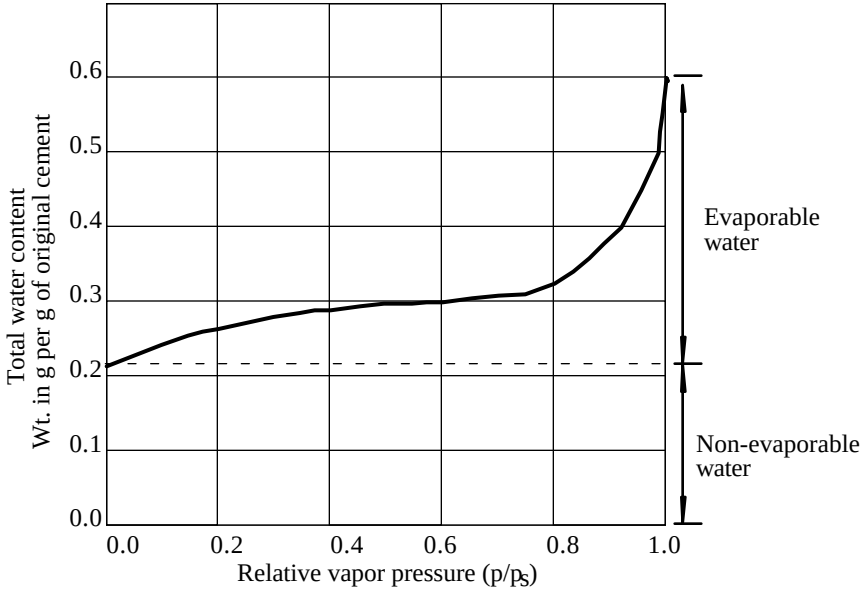


Figure 3. A typical adsorption isotherm for hardened cement paste.[28]

@Seismicisolation

In the context of testing concrete, the adsorption tests will not be practicable. This is because the increase in weight due to adsorption is normally very small and a very thin sample of concrete will have to be used if adsorption tests are to be carried out. From a practical point of view the transport of aggressive substances into concrete is primarily by other mechanisms and, hence, adsorption tests do not have much significance.

3.0 DIFFUSION TESTS

The transport of either gas, water vapor, or ion, due to a concentration gradient across concrete can be used to determine its diffusion characteristic. Therefore, diffusion tests can be classified as:

1. Gas diffusion tests
2. Water vapor diffusion tests
3. Ionic diffusion tests

As different procedures of testing are used for each one of these types, they are individually discussed below.

3.1 Gas Diffusion Tests

Principle of the Test. In this method, two streams of gas of equal pressure and temperature are passed through either side of the specimen, therefore, the transfer of gases by diffusion is stimulated by a difference in concentration. Traces of one gas are detected in the stream of the second gas (which is normally an inert gas) to measure the rate of gas diffusion through the specimen. For steady state conditions of the transfer of gases, Fick's first law of diffusion can be used to determine the gas diffusion coefficient. In non-steady state conditions the evaluation of the diffusion coefficient is based on Fick's second law of diffusion.

Fick's First Law of Diffusion. This is presented in Eq. (1). In the context of experimental procedures used to calculate the diffusion coefficient the various parameters in Eq. (1) can be redefined. Fick's first law of diffusion states that the rate of transfer of mass through unit area of a section, J, is proportional to the concentration gradient, $\partial c/\partial x$ and the diffusion coefficient, D.[29] Therefore:

@Seismicisolation

Eq. (5) $$J = -D\frac{\partial c}{\partial x}$$

where,
- J = mass flux ($g/m^2 \cdot s$)
- D = diffusion coefficient (m^2/s)
- c = concentration (g/m^3)
- x = distance (m)

The rate of transfer of mass through unit area of a section, J, can be defined as:

Eq. (6) $$J = \frac{\partial m}{\partial t}\frac{1}{A}$$

where
- m = mass of substance flowing (g)
- t = time (s)
- A = area (m^2)

Fick's Second Law of Diffusion. For non-steady state conditions (transient diffusion processes) the balance equation, generally referred to as Fick's second law of diffusion, describes the change in concentration in a unit volume with time.[29]

Eq. (7) $$\frac{\partial c}{\partial t} = \frac{\partial}{\partial x}\left(D\frac{\partial c}{\partial x}\right)$$

Here, D may be constant or a function of different variables, such as time, temperature, concentration, etc. The solution of Eq. (6) for the boundary condition of $c = c_0$ and the initial condition of $c = 0$ for $x > 0$ and $t = 0$ is given by:

Eq. (8) $$c = c_0\left[1 - \text{erf}\left(\frac{x}{2\sqrt{Dt}}\right)\right]$$

where erf is the error function. Values of erf $x/2\sqrt{Dt}$ versus $x/2\sqrt{Dt}$ are available either in mathematical tables or may be computed. Therefore, if the diffusion coefficient is assumed to be constant and experimental data of c versus x at time, t, are known, Eq. (8) can be used to calculate the diffusion coefficient.

@Seismicisolation

If the diffusing material becomes partially immobilized due to chemical interaction or physical adsorption with the progress of the transfer of mass, the balance equation (Eq. 7) will have to be modified to include a sink, *s*:[30]

Eq. (9) $$\frac{\partial c}{\partial t} = \frac{\partial}{\partial x}\left(D\frac{\partial c}{\partial x} \right) - s$$

However, it is quite likely that the pore structure characteristics of concrete change with this effect and, therefore, the diffusion coefficient changes with time. In such cases an apparent diffusion coefficient can be calculated by using Eq. (6), which then depends on time, *t*.

Test Procedure. Two types of gas diffusion cells have been used; one by Lawrence[31][32] and the other by Richardson.[33] In both the cells the basic principle of the test is the same (Fig. 4); the amount of oxygen in the stream of nitrogen is measured continually with a gas analyzer and, when a steady state of diffusion is achieved, a diffusion coefficient is calculated by means of Fick's first law of diffusion (Eq. 5).

The non-steady state flow has very rarely been used to calculate the gas diffusion coefficient. This test can be carried out either by a set-up similar to that in Fig. 4 or by exposing one face of the sample to open air and the other face to a stream of nitrogen. With time, oxygen diffuses through the test sample and from an analysis of the concentration of oxygen in the stream of nitrogen the diffusion coefficient can be calculated by using Fick's second law of diffusion (Eq. 7).

In gas diffusion tests, test specimens may be disk shaped with 100–150 mm diameter and 40–50 mm thickness. The thickness of the specimen is generally taken as 2–3 times the maximum size of aggregate in order to obtain the combined effect of cement mortar and the interfacial transition zone. If thin specimens are used the effect of the interfacial transition zone may become exaggerated. The test specimens are generally sealed on their curved surface and oxygen and nitrogen gas streams are passed on opposite parallel faces. The diffusion coefficients for different gases might be different due to different molecular sizes. As the moisture content of the specimen and the relative humidity at the time of test significantly affect the process, test specimens are preconditioned to a low level of humidity (typically 40% or so) prior to the test.

@Seismicisolation

Typical values of oxygen diffusion coefficient at 28 days for concrete conditioned at 55% relative humidity are:[3]

High permeability concrete: $> 50 \times 10^{-8}$ m^2/s

Average permeability concrete: 5×10^{-8} to 50×10^{-8} m^2/s

Low permeability concrete: $< 5 \times 10^{-8}$ m^2/s

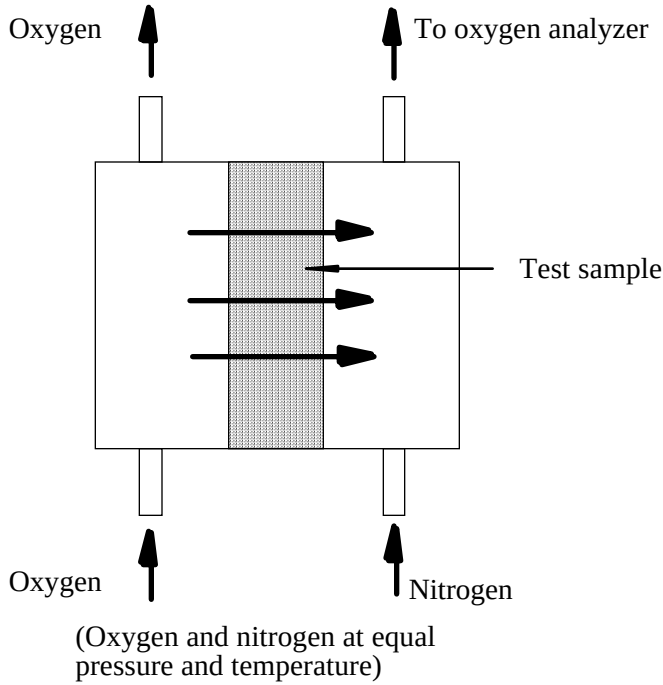


Figure 4. A typical gas diffusion test setup.

3.2 Water Vapor Diffusion Tests

The water vapor diffusion tests can be considered under *water vapor transmission tests* and *water vapor transpiration tests*. In water vapor transmission tests, the water vapor passing through the specimen is collected, either by condensing it or by absorbing with a desiccant. In water vapor transpiration tests, the loss of weight of a saturated specimen due to the breathing (evaporation of water from concrete) is measured.

@Seismicisolation

Water Vapor Transmission Tests. The most commonly used water vapor transmission test is the dry cup method.[3][34] In this test, a cup containing a desiccant (such as anhydrous calcium chloride) is sealed with the specimen and placed in a humidity controlled environment (Fig. 5). The water vapor passing through the specimen is absorbed by the desiccant at the ambient temperature and humidity. Therefore, the weight of the desiccant is taken periodically, which results in a graph like that shown in Fig. 6. The common practice is to weigh the cup and the specimen together to determine the increase in weight of the desiccant. The rate of increase in mass at the steady state is substituted in Fick's first law of diffusion (Eq. 5) and a diffusion coefficient calculated. This method is, however, restricted to small samples due to practical difficulties of weighing large specimens accurately for a small change in weight. Typical diffusion coefficients for cement mortar specimens at 39% RH are 0.6×10^{-12} m^2/s for 0.5 w/c and 2×10^{-12} m^2/s for 0.65 w/c.[35]

Water Vapor Transpiration Test. The general principle of water vapor transpiration test is to allow moisture to evaporate from a saturated specimen,[32][36] however, there is no standard test procedure and variations in the test can be found in literature.[36] One of the common practices is to make use of concrete containers of suitable size. These are filled with water and covered with a glass seal. The loss of weight with time is then measured and reported as the water vapor transpiration. The test may last for several days (typically 20–25 days), rather than several hours.

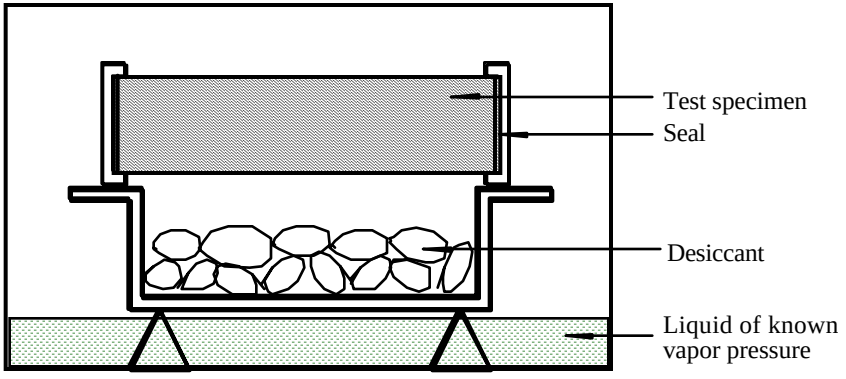


Figure 5. The dry cup method.[3][34]

@Seismicisolation

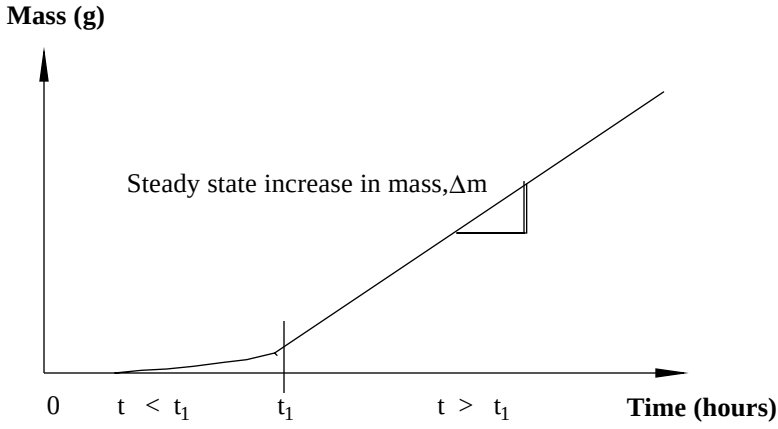


Figure 6. Water vapor transmission data from the dry cup method.

The main drawback of the water vapor diffusion test is that the value of diffusion coefficient obtained with both the water vapor transmission test and the water vapor transpiration test depends on the ambient conditions, i.e., both relative humidity and temperature. Therefore, test conditions need to be standardized as well as standardizing the procedure. If very dry samples are used (less than 40% RH), water vapor may diffuse like a gas; however, it may introduce extensive microcracking in the cement paste structure.

3.3 Ionic Diffusion Tests

Recently there has been an increased interest in ionic diffusion tests because the rate at which ions, particularly chloride ions, can diffuse through concrete is highly significant to the corrosion of reinforcement in structures. The transport of ions in concrete involves diffusion, capillary suction, and convective flow, with flowing water, accompanied by physical and chemical binding, depending on the physical environmental conditions. In order to determine the ionic transport, these complications are usually neglected, and pure diffusion, sometimes with binding capacity, is adopted. Pure diffusion of ions in the pore solution of a concrete occurs due to differences in the concentration of the ions. Therefore, concrete should be matured and saturated and there should be no movement of water or carbonation of concrete during the test. The diffusion of chloride ions is very thoroughly discussed in a state-of-the-art published by the Swedish Road Directorate.[30]

@Seismicisolation

The chloride diffusion coefficient can be determined from several types of tests and, on the basis of the methodology used, these tests can be classified as:

1. Steady state diffusion tests
2. Non-steady state diffusion tests
3. Electric field migration tests

Another type which can be included under ionic diffusion test is the use of resistivity methods; however, these do not measure ionic transport directly.

Steady State Diffusion Tests. In this test, a thin slice of the test specimen forms a barrier between an ion source solution and another suitable solution free of the ion (sink solution). This allows ions to diffuse in a concentration gradient. The rate of diffusion is obtained by periodically determining the ion content in the sink solution. When steady state conditions are achieved, the diffusion coefficient is calculated by using Fick's first law of diffusion (Eq. 5).

If the ion source solution contains chloride ions or any negatively charged species the movement of the ions is not a pure diffusion process. The movement of the negative ions must be balanced by a movement of some positive ions, however, the diffusion rates of these ions may be different. Furthermore, some ions from the pore solution in concrete may leach out into either the ion source solution or the sink solution by diffusion. These ionic interactions are usually neglected while applying Fick's first law of diffusion; therefore, the ion in the source solution is considered to be an inert substance. Consequently, the diffusion coefficient from Eq. (5) is not a pure material property, but depends on the testing conditions.

Procedure of Steady State Diffusion Test. The most commonly used procedure to measure ion diffusion coefficient is the diffusion cell test method.[30][32] A typical diffusion cell set-up (Fig. 7) consists of a sample holder between two cells, one containing the ion source solution and the other containing the sink solution. The concentration of ions in the sink solution is kept close to zero by replacing the solution during the test. Also, the concentration of the ion source solution is maintained throughout the test. If these are not done, the concentration gradient will decrease with time and the steady state of flow will not be reached. With time the transport of ions through the test specimen will increase, as depicted in Fig. 8. The steady state region of the graph is used in Eq. (5) to calculate the diffusion coefficient.

@Seismicisolation

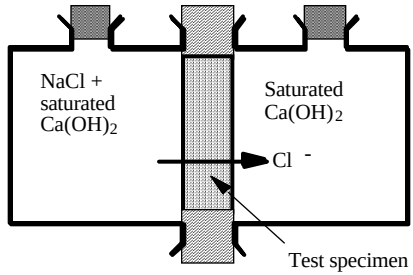


Figure 7. A typical ion diffusion cell.

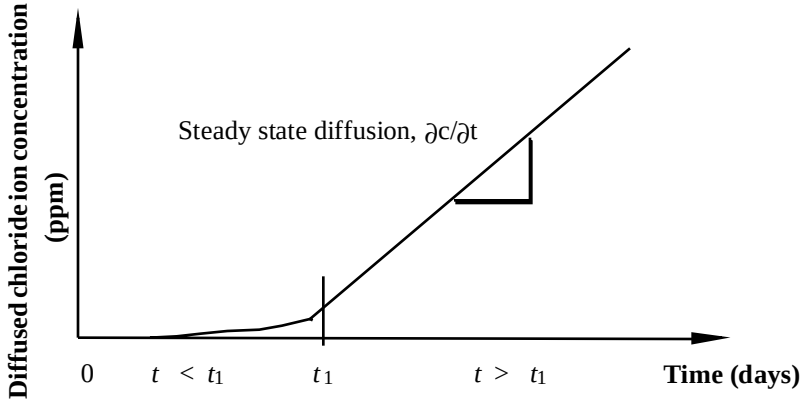


Figure 8. Data from a typical ion diffusion test.

Modifications to the test set-up and the procedure can be found in literature,[37]–[42] however, the basic principle of the test procedure is the same. Variations in sample thickness, concentration of the ion source solution and the method used to precondition the specimen prior to the test make the results difficult to compare between different procedures.

Although the diffusion cell method is widely used to determine the ion transport by diffusion, long test durations are required to achieve the steady state condition. Therefore, the test is best suited to measure the ion diffusion coefficient of hardened cement paste where thin disks, typically of 3–4 mm thickness, can be tested. In the case of cement mortar disks, with the thickness of sample between 4 mm and 10 mm, typical tests may last for months rather than weeks. The time required to achieve the steady state may

@Seismicisolation

be longer than 30 weeks for relatively impermeable concrete and for reasonably thick concrete disks (above 20 mm thickness) it may take years. The very long test duration means that hydroxides and alkalies may leach out from test specimens during the test. In order to limit this effect, the source solution and the sink solution in the diffusion cell with a saturated solution of calcium hydroxide and a concentration of potassium hydroxide that corresponds to what the binder may produce are used. Typical values of chloride diffusion coefficients reported by the Concrete Society[3] are:

High permeability concrete:	$> 5 \times 10^{-12}$ m^2/s
Average permeability concrete:	1 to 5×10^{-12} m^2/s
Low permeability concrete:	$< 1 \times 10^{-12}$ m^2/s

Non-Steady State Diffusion Test. In non-steady state diffusion tests the penetration of ions is achieved either by *immersing* the specimen in a solution containing specific ions for a certain time or by *ponding* the solution containing specific ions on the test specimen for a certain time. The penetration is maintained unidirectional by sealing all except one surface of the specimen. Either the penetration depth or the penetration profile of the specific ions in the specimen is determined and Fick's second law of diffusion is applied to determine the diffusion coefficient. Where the penetration depth is measured, the diffusion coefficient is calculated from:

Eq. (10) $$X_d = 4\sqrt{Dt}$$

where: x_d = penetration depth (m)

t = duration of exposure (s)

However, if the penetration profile is determined, Eq. (8) can be used. In the context of the test method, the various parameters in Eq. (8) can be redefined:

Eq. (11) $$c = c_0\left[1 - \text{erf}\left(\frac{x}{2\sqrt{Dt}}\right)\right]$$

where: c = ion concentration at the distance x (kg/m^3)

c_0 = ion concentration at the exposed surface (kg/m^3)

erf = error function.

x = distance from the exposed surface (m)

@Seismicisolation

As stated earlier, the diffusion coefficient varies with the concentration of solution on the exposed surface and the duration of exposure due to the variation in binding capacity of concrete at different environmental conditions. Therefore, the diffusion coefficient, by assuming that it remains constant for the material, has to be treated as an *apparent diffusion coefficient.* As a consequence, the prediction of diffusion based on a simple solution of Fick's second law of diffusion overestimates the penetration of ions.

The constant *apparent diffusion coefficient* can be derived from both non-steady state experiments, as listed above, or field measurements, by curve-fitting the measured penetration profile to the error-function solution of Fick's second law with a constant diffusion coefficient and a constant surface concentration. Such a curve fitting at an exposure time, t, will yield two regression parameters, an *achieved transport coefficient,* D_a, and an *achieved concrete surface content,* C_s. There are other procedures to determine the apparent diffusion coefficient.[43][44] If two or more profiles for different times of exposure are used, the regression parameters will not be constant and the most obvious finding will be that the transport coefficient decreases with increase in duration of exposure. Therefore, the apparent diffusion coefficient will have to be used with caution for predicting the penetration of ions in the non-steady state diffusion. The diffusion coefficient from this method will also be in the range listed for the steady state diffusion coefficient.

Immersion Test. The immersion test[30] usually involves the use of either cast cylinders or cores drilled from a structure. In order to reduce the effect of large aggregate particles on the penetration of ions, usually 100 mm diameter specimens are tested. If segregation of aggregate is suspected, the outermost 10 mm thick concrete is removed. To ensure a one-dimensional ingress of ions, all faces other than the one to be exposed are sealed. It is essential that the tests are carried out on well cured concrete so that the effect of hydration during testing can be minimized.

The test specimen is first immersed in saturated calcium hydroxide solution until constant mass is achieved, in order to prevent capillary suction of exposure liquid during the test. The specimen is then immersed in the exposure liquid for a period of at least 30 days at a constant temperature. At the end of the exposure period, either the depth of penetration or the penetration profile is determined and the diffusion coefficient is calculated by applying either Eq. (10) or (11), respectively.

The penetration profile can be obtained by cutting or drilling samples successively from the exposed surface and then analyzing the samples for

@Seismicisolation

the specific ion content. A special grinding rig (profile grinder) is commercially available which can be used to collect samples at 0.5 mm increments.

When the apparent diffusion coefficient is determined from penetration profiles of concrete on site, it may be necessary to avoid some data points closer to the surface so that a curve-fitting can be carried out and the regression parameters determined. This is because carbonation, wetting, and drying of the near surface, and other environmental conditions, alter the penetration profiles.[30]

Ponding Test. The American Association of State Highway and Transportation Officials (AASHTO) test method T259-80 (Resistance of Concrete to Chloride Ion Penetration)[45] is the only standardized test procedure for ponding test. Test specimens are of size 300 × 300 × 75 mm with a dyke at the top to pond a 3% (0.5 M) sodium chloride solution continuously for a period of 90 days. At the end of this exposure period, the solution is removed and the concrete is sampled at various depths by using a 25 mm diameter rotary hammer drill. The total chloride ion content of each sample is analyzed and plotted against the depth of sampling. The area under the chloride profile is calculated and reported as the total chloride content.

Variations to the test regime and conditioning of test specimens can be found in literature.[41][46]–[49] Also, the method used to express results of the test differed. The chloride concentration profile from this test also can be used to calculate an apparent diffusion coefficient by using Eq. (11). However, test specimens should be saturated before exposing to chlorides and the test regime should not allow evaporation of solution from the surface. If the sample is not saturated prior to testing and/or the solution evaporates during the test, the transfer of chlorides will be due to the combined transport (absorption and diffusion).

Electric Field Migration Tests. Due to very long test periods required for both steady state and non-steady state diffusion tests, methods where the transport of ions can be accelerated by the application of electrical potential gradients have become very popular recently. These tests can be collectively called *electrical migration tests.* Early developments[50] of this category of tests did not consider the complex phenomena of ion transfer satisfactorily;[30] however, recent developments considered the similarity between diffusion and migration by introducing the concept of ion mobility.[51]–[53] This has enabled the determination of an ion diffusion coefficient from the migration tests.

@Seismicisolation

Principle of the Test. When an electrical field is applied across the specimen in a diffusion cell the transfer of ions is accelerated and the process is called *ionic migration.* Furthermore, the electrical field affects the direction of movement of the ions in such a way that they move towards the electrode of opposite sign. The various processes that occur when an electrical field is applied in a diffusion cell are described by Andrade[54] (Fig. 9).

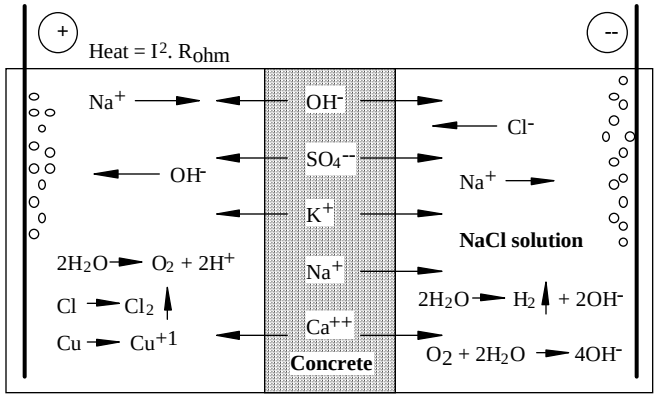


Figure 9. Processes in a diffusion cell due to an electric voltage.[54]

Here, each type of ion carries a part of the total current, i, that is proportional to the concentration, c_j, of that ion, its electrical charge, z_j, and its ionic conductivity, λ_j. This proportion of the current, i_j, in a particular electrolyte is called the *transference number*, t_j, of the ion:

Eq. (12)
$$t_j = \frac{i_j}{i} = \frac{z_j c_j \lambda_j}{\sum zc\lambda}$$

Therefore, if the current corresponding to the ion of interest is measured, it will provide information on the mobility of that ion.

The general law governing the ionic movements in electrolytes is the *Nernst-Plank equation* in which the total flow is considered to be due to diffusion, migration, and convection, i.e.,

Flux = diffusion + migration + convection

This can be written as:

@Seismicisolation

Eq. (13) $$J_j = D_j = \frac{\partial c_j}{\partial x} + \frac{z_j F}{RT} D_j c_j \frac{\partial E}{\partial x} + c_j V_j$$

where:

J_j	=	flux of species, j (g/m^{2}s)
D_j	=	diffusion coefficient of species, j (m^2/s)
∂c_j	=	variation of concentration of species, j (g/m^3)
∂x	=	variation of distance (m)
z_j	=	electrical charge of species, j
F	=	Faraday constant (J/V.mol)
R	=	gas constant (J/mol·K)
T	=	absolute temperature (K)
$\partial E/\partial x$	=	electrical potential gradient (V/m)
V_j	=	velocity of solution (m/s)

This equation indicates that the movement of charged particles in an electrolyte is the sum of the diffusion components from concentration gradients, the migration component arising from potential gradients and the flow of the electrolyte itself (capillary suction, permeability, etc.). The diffusion term is insignificant if the potential gradient is higher than about 10–20 V/m.[30] Similarly, if stationary flow conditions are assumed and there is no flow of the electrolyte the convection term can be eliminated. The pure electrical migration is then given by:

Eq (14) $$J_j = \frac{z_j F}{RT} D_j c_j \frac{\partial E}{\partial x}$$

From this, the diffusion coefficient D can be calculated if stationary conditions are established in a traditional diffusion cell.

Another form of Eq. (14) was developed by Zhang and Gjorv[55] based on Einstein's theoretical relationship between diffusion and migration. However, the main difference between the two is in the constant terms used in the expressions and the experimental observations required to calculate the diffusion coefficient are the same in both cases. Following from Eq. (14), in a steady state migration test, the diffusion coefficient can be determined from:

Eq. (15) $$D_j = \frac{J_j}{c_j} \frac{RT}{Z_j F} \frac{x}{\Delta E}$$

@Seismicisolation

In an experiment, the thickness of sample, x, the applied potential difference, ΔE, the concentration of ion in the solution, C_j and all constants will be known. Therefore, in order to calculate the diffusion coefficient, D_j, the only parameter to be determined is the value of J_j which can be obtained from the experiment.

The depth of ion penetration in migration test also can be used to calculate the diffusion coefficient. This is generally referred to as the *non-steady state* migration test. If binding is not considered, the ion profile during penetration by electrical migration follows the mass balance equation with the flow description according to Eq. (14). Therefore, following from Eq. (7):

Eq. (16) $$\frac{\partial c_f}{\partial t} = \frac{\partial}{\partial x}\left(\frac{z_j J}{RT} D_j c_j \frac{\partial E}{\partial x} \right)$$

Tang and Nilson[52] provided the following equation for calculating the diffusion coefficient from a numerical solution of the mathematical model:

Eq. (17) $$D = \frac{RT}{zFE} \frac{x_d - \alpha x_d^b}{t}$$

where:

R = gas constant (J/mol·K)

T = temperature (K)

z = ion valency

F = Faraday constant (J/V·mol)

E = electric field (V/m)

x_d = penetration depth (m)

t = testing time (s)

a and b = constants

For the chloride ion, $z = -1$ and when $E = -600$ V/m and $T = 298$ K, $a = 0.0622$ and $b = 0.589$.[56]

Test Methods. Based on the principle involved, migration tests can be classified as steady state and non-steady state tests. The non-steady state tests generally involve shorter test periods than the steady state tests as the former category is not continued until steady state conditions are established. The first non-steady state test was introduced by Whiting in 1981[57] and was referred to as *rapid chloride permeability test.*[50] This was later

@Seismicisolation

adopted as both AASHTO T277[58] and ASTM C 1202-94.[59] Another non-steady state test is the CTH method by Tang and Nilson[52] presented first in 1991. The test, set-up in either the rapid chloride permeability test or the CTH method can be used for the steady state migration tests. The procedure used in each type is described below.

The Rapid Chloride Permeability Test. The rapid chloride permeability test is carried out with a migration cell shown in Fig. 10. The test uses a 50 mm thick and 95 mm diameter specimen. This is vacuum saturated for 18 hours and enclosed between two chambers, one containing a solution of 3% by weight sodium chloride and the other with 0.3 M NaOH solution. An electric field of 60V dc is applied between the electrodes in each chamber. The test is run for 6 hours and during that time the amount of charge passing the specimen is measured by recording the current as a function of time. The total charge passed through the specimen, in coulombs, is determined by calculating the area under the current-time plot during the 6 hour test period. For this reason this test is sometimes called the *Coulomb Test.* Typical values reported by the Concrete Society[3] are:

High permeability concrete:	> 4000 coulombs
Average permeability concrete:	2000–4000 coulombs
Low permeability concrete:	< 2000 coulombs

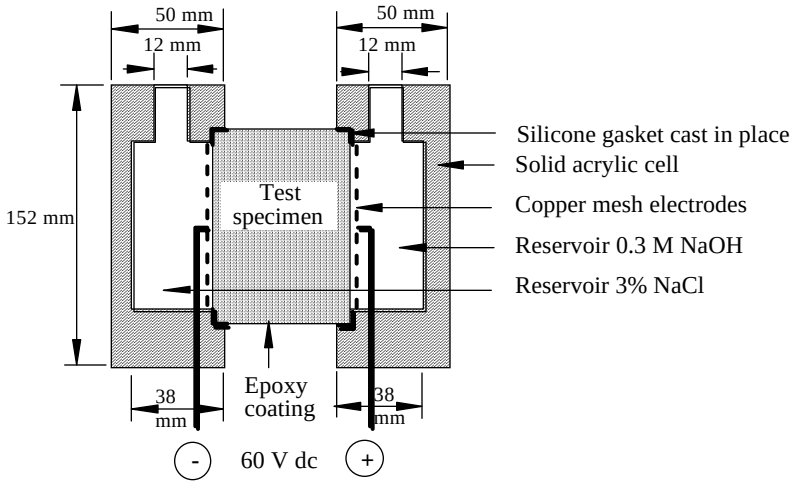


Figure 10. The rapid chloride permeability test.

@Seismicisolation

This is an indirect measurement of the chloride ion diffusion and both experience and comparison with results from other methods, such as the immersion test, are used to evaluate the test results.[60] There are severe criticisms of the usefulness of this test to determine the chloride ion diffusion.[30] Since the total charge refers to the movement of all ions present in the pore solution rather than the flux of chlorides, different binders may not provide the same classification criteria. Another objection has been that when integrating the total current from the beginning of the experiment it does not distinguish between chloride flow plus reaction or simple flow. The information from this test could be obtained by measuring the initial resistivity within a test period of a few seconds[61][62] and, hence, a test lasting for six hours cannot be justified. Finally, the very high voltage of 60 V induces heat, which in turn changes the flow speed.

An in-situ version of the rapid chloride permeability test was proposed by Whiting.[50] Here, the test surface is vacuum saturated with limewater and an acrylic dyke is attached to the concrete surface with silicone caulking compound and allowed to cure overnight; 1.5 liters of a 3% (0.5 M) sodium chloride solution is then poured into the dyke the following morning. A voltage of 80 V is applied between a copper mesh electrode in the dyke and the reinforcement and the current flow is measured for a period of 6 hours. The interpretation of the data is the same as that used in the migration cell test; therefore, all criticisms of the migration cell test are applicable to the in-situ test as well.

The CTH Method. Tang and Nilson[52] presented the CTH method in 1991 and provided the mathematical basis to calculate the chloride transport coefficient. The test set-up for the standard CTH method is presented in Fig. 11. The test specimen is 50 mm thick and is sealed with a sealing tape on all surfaces except two opposite parallel surfaces. The sealing tape is extended from the specimen to create a chamber and this is filled with a solution of saturated lime water. This is then placed in a large container with a solution of 3% NaCl in saturated lime water. Stainless steel electrodes are placed on each side of the specimen. The specimen is tilted to make it easy for gas bubbles at the cathodic plate to escape. A voltage of 30 V is applied across the specimen and the initial current is measured to estimate the required test duration. The test may last up to 48 hours depending on the quality of the concrete. After the test, the specimen is split and the two fractured surfaces are sprayed with a $AgNO_3$ solution. The depth of chloride penetration is determined from the change in color obtained due to the formation of silver chloride where chlorides are present. From the depth of chloride penetration, the diffusion coefficient is calculated by using Eq. (17).

@Seismicisolation

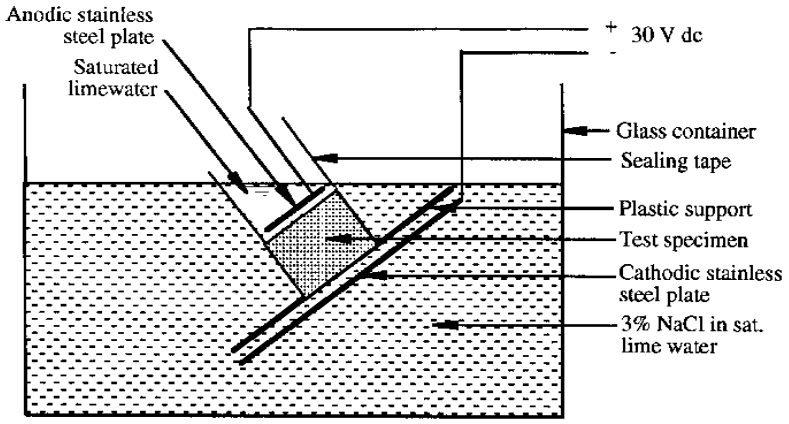


Figure 11. The CTH method.

This test has the advantage that the test duration is short compared to the steady state migration tests and still it provides the opportunity to calculate the diffusion coefficient. However, the distribution of chlorides within concrete and, hence, the depth of penetration is influenced by the chloride binding capacity. This has been addressed recently by Tang and Nilson[63] by introducing a binding capacity term to correct the diffusion coefficient from the CTH method. However, further experimental data are required to validate this approach.

Steady State Migration Tests. The basic principle of operation of the steady state migration test is the same as that of the standard diffusion cell method, the primary difference being the acceleration voltage applied in the former case. Therefore, an arrangement similar to the diffusion cell (Fig. 7) can be used for the steady state migration test, with two electrodes on either side of the test specimen to apply a potential difference across the specimen, as in the case of the rapid chloride permeability test. The test specimen, cylindrical disk of suitable dimensions, is placed in the migration cell and a voltage is applied between electrodes kept on both sides of the specimen. The catholyte in the migration cell is an ion source solution and the anolyte is a sink solution. Therefore, negative ions move towards the anode (Fig. 9) and by monitoring the increase in concentration of ions in the anolyte, a graph similar to that obtained for the steady state diffusion test (Fig. 8) can be drawn. Also, in common with the steady state diffusion test, the straight line portion of this graph can be used to determine the value of

@Seismicisolation

J in Eq. (15) from which the diffusion coefficient can be calculated. Typical values of the diffusion coefficient from the steady state migration test are presented in Table 1.

Table 1. Diffusion Coefficients from Steady State Migration Test[30]

W/C	0.35	0.40	0.50	0.75
$D \times 10^{-12}$ m^2/s	11.4	15.2	16.3	23.0

The test set-up, conditioning of samples prior to the test, intensity of voltage applied, solutions in the two compartments, type of electrodes, and the method of determining the concentration of ions in the anolyte, can be found to vary between various published data.[57]–[67] In the absence of a standard test procedure, the following aspects may be given consideration.

1. The migration cell may be of any suitable size similar to that described in ASTM C1202-94.[59]
2. The anode may be of any corrodible metal, preferably steel, and the cathode may be of stainless steel. A non-corrodible anode will produce a water electrolysis or chlorine gas evolution which is too high.
3. The electrodes may be kept as close as possible to the surface of test specimens in order to avoid any voltage drop in the electrolyte.
4. The voltage across test specimens has to be sufficiently high to accelerate the migration of ions, but not too high to prevent the generation of heat. A relatively high voltage is desirable in order to minimize the effect of polarization during long test periods.[68] The applied voltage may be between 10 and 30 V.
5. The specimen thickness should be 2–3 times the maximum aggregate size in order to avoid preferential movement of ions through the transition zone in concrete. However, it may be remembered that thicker samples would require long test durations to establish the steady state conditions.

@Seismicisolation

6. The concentration of ions in the catholyte may not be a significant parameter influencing the diffusion coefficient. For the determination of chloride diffusion coefficient, a 0.5 M (3%) NaCl solution has been suggested to be suitable.[56] The use of alkaline solution as anolyte is not desirable due to the possibility of chlorine gas evolution and the precipitation of calcium hydroxide in concrete pores. A suitable anolyte is distilled water.

4.0 ABSORPTION TESTS

The penetration of liquids in concrete as a result of capillary forces which allow a wetting fluid to be drawn along the solid-pore surface is *absorption.* On the basis of the methodology used, the measurement of absorption characteristic of concrete can be classified into three categories:

1. Tests for water absorption capacity.
2. Sorptivity tests.
3. Absorptivity tests.

Although the underlying principle of all these tests is the same (the capillary suction), there are differences in the property being measured. This can be better explained by considering the principle of water absorption in concrete.

4.1 Principle of Absorption Tests

In the absence of any external force the basic mechanism that drives water in capillary pores in concrete is capillary suction (capillarity). Surface tensional forces acting at a solid-liquid-gas interface cause a wetting liquid, such as water, to spread along the solid surface and results in capillary rise of the liquid in the capillary pore. For an ideal capillary, the Washburn's equation (Eq. 2) can be used to determine the water absorption. Therefore, the capillary transport is theoretically dependent on the viscosity, density, and surface tension, of the liquid, the angle of contact between the solid and the liquid, the length of the pore already filled with the liquid, and the radius of the capillary pore. However, in reality, other factors can be expected to influence the height of capillary rise:

@Seismicisolation

1. The roughness of the solid surface influences the angle of contact between the solid and the liquid.
2. Capillary pores in concrete are not circular or of regular cross section.
3. Capillary pores may be lined with adsorbed water.

Furthermore, various assumptions made for the postulation of Washburn's equation may not be strictly applicable in the case of concrete. For instance, Washburn assumed that the capillary is of a circular cross section and is straight,[4] however, in the capillary network in concrete, capillary pores are of variable cross section, tortuous, non-circular, and join and diverge with neighboring pores in a random manner.

The pressure difference across the interface in a capillary pore of radius, *r,* is given by Jouren equation:

Eq. (18) $$P = \frac{2\gamma\cos\phi}{r}$$

where: γ = surface tension (N/m)

ϕ = angle of contact (degrees)

r = radius of capillary pore (m)

For air/water interface, ϕ, approaching 0 degrees and the surface tension of water at 20°C is 70×10^{-3} N/m, the capillary pressure for a pore of size 1 μm is 0.14 MPa (the equivalent water head will be 14.3 m). However, the radius of the capillary pores in concrete would be much smaller than 1 μm, so that the capillary drive is likely to be much higher than that normally found with hydrostatic forces. For the same reason, the gravitational effect on capillary rise is also negligible.

In reality, the passage of water in a liquid state through dry capillaries (absorption of water) consists of two basic parameters:[69]

1. The mass of water required to saturate the concrete (a measure of the effective porosity).
2. The rate of penetration or the capillary rise (a measure of the sorptivity).

During the absorption, the capillary channels and voids begin to fill with water, meanwhile the waterfront advances. Therefore, an absorption test should measure either one or both of the above two parameters. As theoretical relationships cannot be strictly applied in the case of concrete,

@Seismicisolation

empirical relations are established to describe the rate of flow and these are used to determine the absorption characteristics in test methods.[70]

4.2 Tests for Water Absorption Capacity

The water absorption capacity tests determine the effective porosity of concrete and are not intended to measure the rate of capillary suction. Therefore, the increase in weight of a dry specimen when immersed in a shallow depth of water is generally referred to as the water absorption capacity. In this method, the absorption takes place from all surfaces, therefore, the quantity of water absorbed depends on both the ratio of surface area to volume of the specimen and the duration of immersion. Generally, the water absorption capacity is determined by drying a specimen to constant weight, immersing it in water for a specified duration of time, and measuring its increase in weight as a percentage of the dry weight.

Variations exist in the size of test specimen[32][71] and methods employed for both drying and saturating the specimen.[72]–[77] The Concrete Society[3] reported inconsistencies in the water absorption capacity due to the variations in both drying and saturation of the specimens, which is reproduced in Table 2. Details of the water absorption tests given in both the British[74] and the American[72] Standards are summarized in Table 3. It could be observed in Table 2, by comparing results of samples immersed in water for 48 hours and those boiled for 5 hours, that it is unlikely to fill all the capillary cavities in concrete by immersing the specimen for long periods.

Lawrence[32] indicated that water absorption capacity holds a good correlation with other standard material properties. Typical values of 30 minutes water absorption reported by the Concrete Society[3] are:

Low absorption concrete:	< 3%
Average absorption concrete:	3–4%
High absorption concrete:	> 4%

4.3 Sorptivity Tests

Sorptivity defines the ability of concrete to absorb water. Therefore, either the rate of inflow or the depth of water penetration is measured in sorptivity tests when water is allowed to be absorbed unidirectionally by a dry concrete under a negligible applied pressure.

@Seismicisolation

Table 2. Effect of Drying on Water Absorption Capacity[3]

Details of Drying (Degree Celsius)	Method of saturation	Concrete A	B	C	D
100	Immersed in water for half hour	4.7	3.2	8.9	12.3
100	Immersed in water for 24 hours	7.4	6.9	9.1	12.9
100	Immersed in water for 48 hours	7.5	7.0	9.2	13.1
100	Boiled for 5 hours	8.1	7.3	14.1	18.2
65	Boiled for 5 hours	6.4	6.4	13.2	17.2

Table 3. Details of Water Absorption Tests in British and American Codes

Features under consideration	BS 1881: Part 122: 1983[74]	ASTM C642: 1982[72]
Details of test sample	75 mm diameter x 32-150 mm long	Individual pieces larger than 350 cu.cm.
Details of drying	At 105°C for 72 ± 2 hours	At 100-110°C until successive weights do not differ by more than 0.5% of lesser weight.
Details of saturation	Immerse in water at 20°C for 30 minutes	(a) Immerse in water at 21°C until successive weights do not differ by more than 0.5% of lesser weight. (b) Boil for 5 hours.
Reporting results	Percentage absorption after 30 minutes immersion	(a) Percentage absorption after immersion. (b) Percentage volume of permeable pores.

Sorptivity from Volume of Water Absorbed. The first appearance of sorptivity tests in the literature of testing building materials was in 1977,[70] in which Hall described that the cumulative absorbed volume per unit area of the inflow surface (m^3/m^2), denoted by i, increases as the square root of the elapsed time, t; that is:

Eq. (19) $$i = St^{0.5}$$

@Seismicisolation

where S = sorptivity of the material ($m^3/m^2/s^{0.5}$; sometimes the unit $m/s^{0.5}$ is used). One could consider that this equation is an empirical relationship to specify a material property which governs the intake of water by capillary suction. In practice, the cumulative absorbed volume of water and square root of time follows Eq. (20), below, with a small intercept on the square root time axis.[69] That is:

Eq. (20) $$i = A + S t^{0.5}$$

where A = a positive intercept. This intercept is considered to be due to the type of surface finish influencing the open porosity of the inflow surface and, hence, filling of these pores with water in the beginning of the test.

The procedure used by Hall[70] is the basis of determining the sorptivity of concrete by using either Eq. (19) or (20). The sorptivity is determined generally by a set-up shown in Fig. 12. The test specimen of uniform cross section is placed with one surface just in contact with water and the weight of water absorbed by capillary rise is measured at fixed intervals. After obtaining at least five data points, a graph is plotted between the volume of water absorbed per unit area of inflow surface, i, and square root of time. The slope of this plot is reported to be the sorptivity, S, of the material.

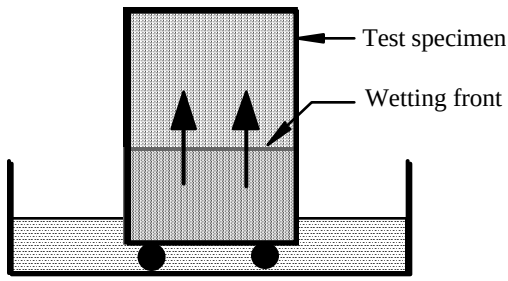


Figure 12. Set-up for sorptivity test.

Test specimens are usually coated with an epoxy emulsion on their sides to prevent any water movement through the sides during the test. The specimen should rest on rods or pins to allow free access of water to the inflow surface. The water level should not be more than 5 mm above the base of the specimen. Before weighing the specimens they should be

@Seismicisolation

removed from the container and the surfaces mopped off with a damp tissue. They should be returned to the container within 30 seconds each time they are taken out for weighing. During this time the clock should not be stopped.

Care is required in conditioning specimens before the test to remove the internal moisture content. Too severe drying may result in microcracking of concrete and this may influence the sorptivity values. At the same time, if capillary pores are not free from moisture the rate of absorption will be reduced. Other factors affecting the sorptivity measurement are the ambient conditions (both the ambient temperature and relative humidity) and the temperature of the specimen and water. Therefore, it is desirable to standardize the conditioning of the specimen, temperature of water, and the ambient test conditions, in order to obtain reliable results. Table 4 indicates sorptivity values obtained by Hall.[69]

Table 4. Typical Sorptivity Values for Concrete[69]

W/C	0.40	0.50	0.60
Sorptivity ($mm/min^{0.5}$)	0.094	0.120	0.170

Note: Mix ratio 1:2:4

It is reported[56] that the capillary suction test, according to Hall,[70] has been adopted in the Swiss Guidelines for Testing, SIA 162/1, Test No. 5: Water Conductivity[78] and the method Absorption of Water by Capillarity[79] is a tentative RILEM recommendation (No. 11.2).

Depth of Penetration of Water to Measure Sorptivity. The depth of water penetration, d, at a given time, t, could be represented by an equation similar to Eq. (20).[80]

Eq. (21) $$d = d_0 + S\, t^{0.5}$$

where: d_0 = a small intercept obtained in the beginning which would depend on the type of surface finish

S = sorptivity ($mm/min^{0.5}$)

However, the sorptivity from the volume measurement will not be the same as that obtained from the depth of penetration measurement (Table 5), although they both represent the same pore structure characteristic of concrete, viz., the rate of water penetration by capillary suction.

@Seismicisolation

Table 5. Sorptivity from Both Depth and Volume Measurements[81]

Cement content (kg/m^3)	Water content (kg/m^3)	Depth of penetration 4-hour sorptivity $mmh^{-0.5}$	Cumulative volume gain per unit area, 4-hour sorptivity, $mmh^{-0.5}$
340	136	4.50	0.17
318	191	3.00	0.25
419	168	0.70	0.06
402	201	3.30	0.23

The test set-up for the determination of sorptivity by measuring the depth of penetration of water can be the same as that used for the cumulative volume flow test. Therefore, the sample preparation and conditioning and the ambient conditions at the time of test can be the same as well. The main difference in this case is that the depth of water penetration has to be determined. There are two ways of determining the depth of penetration of water. In the first method, the test specimens are split opened at different intervals from the start of the test and the depth of water penetration is recorded by visual inspection.[82] The other method involves embedding pairs of electrodes at different depths from the inflow surface and the resistance change between them is monitored from the start of the test.[19][81] When water reaches the electrodes, the resistance changes and from this the depth of penetration is determined.

When samples are broken to determine the depth of penetration, data may be collected at 1/2, 2, 4, 8, 16, and 24 hours. It has been reported that data for prolonged exposure tests, days rather than hours, do not follow Eq. (21).[19] In such instances, Eq. (22) was found to be applicable:

Eq. (22) $d = B \ln (t)$

where: d = depth of water penetration

B = a coefficient of water penetration

t = time (days)

The Concrete Society's Report No. 31[3] indicates that it is possible to obtain information about both the porosity and pore size from the sorptivity tests. For instance, the porosity could be estimated from a plot of the height of capillary rise against the increased weight gain of the sample

@Seismicisolation

per unit area, as in Fig. 13. The main limitation of the sorptivity test is that air voids larger than a certain diameter (about 10 μm)[32] are not filled with water during the capillary absorption tests; in other words, air voids cause a reduction in sorptivity; therefore, poorly compacted concrete will tend to show lower values of sorptivity than those normally expected.

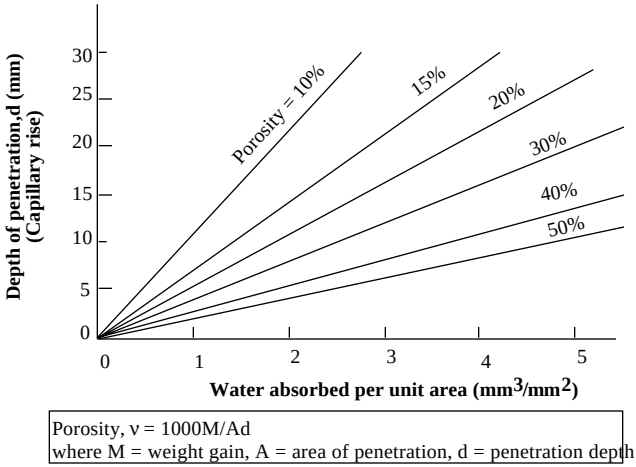


Figure 13. Method of estimating porosity from sorptivity data.[3]

4.4 Absorptivity Tests

Due to the nature of the sorptivity tests, i.e., establishment of a one-dimensional flow, the tests can only be carried out in the laboratory. However, another category of tests in which the flow does not have to be one-dimensional, meanwhile providing the absorption characteristic of concrete, can be used to test concrete both in the laboratory and on site. These are termed *absorptivity tests* in this chapter.

Absorptivity tests involve the application of low pressure so that water movement into concrete is mainly achieved by capillary suction. However, there is no control over the direction of the flow and, hence, the sorptivity, as described in Sec. 4.3, cannot be obtained. Tests in this category can be classified as:

1. Surface absorptivity tests.
2. Drill hole absorptivity tests.

@Seismicisolation

The primary difference between these two categories is in the source of water for absorption by the test specimen. In surface absorptivity tests the source of water is from a reservoir mounted on the surface of the test specimen, whereas in drill hole absorptivity tests, water is allowed to be absorbed from a hole drilled in the near surface region of concrete. The test procedure of these two categories is explained below. Different types of equipment are commercially available to measure the absorptivity on site, however, their basic principle of operation is the same.

Surface Absorptivity Tests. A low pressure test developed by Glanville[83] at the Building Research Station in the United Kingdom forms the basis of the surface absorptivity tests. Successive refinement of this test[84]–[86] led to the development of the *Initial Surface Absorption Test (ISAT),* which has later become a standard test in British Standards, BS 1881: Part 5[87] and Part 208.[88] Other tests based broadly on the principle of the ISAT can be found in literature. These include the Autoclam sorptivity test[89] and the standpipe absorptivity test.[90]–[92]

The Initial Surface Absorption Test. The rate of flow of water into concrete per unit area after a stated interval from the start of the test and at a constant applied head and temperature is defined as *initial surface absorption*. Therefore the test that measures this property is designated as the *Initial Surface Absorption Test (ISAT).* While the procedure of the test is almost the same as that proposed by Glanville in 1931,[83] there are now specifications for the initial moisture condition, surface area to be in contact with water, and the time at which measurements have to be taken. Figure 14 illustrates the test set-up and the procedure to be used to determine the initial surface absorption. The cap provides a water contact area of 5000 mm^2 and the test is carried out at a water head of 200 mm. British Standards, BS 1881: Part 5,[87] specifies the measurement of the initial surface absorption at 10, 30, 60, and 120 minutes from the start of the test. However, the 120 minutes rate of absorption measurement has been dropped in the new BS Standards, BS 1881: Part 208.[88] The rate of absorption is noted on the calibrated capillary tube over a period of 2 minutes and the results are reported in units of $mL/m^2/s$. Specimens have to be oven dried at 105°C for the laboratory test and, for in-situ testing, a drying period of at least 48 hours at ambient temperature and humidity is stipulated. Typical ISAT values for a well cured concrete reported by the Concrete Society[3] are reproduced in Table 6. The apparatus is commercially available, however, it is relatively easy to assemble it from parts illustrated in Fig. 14.

@Seismicisolation

Table 6. Typical ISAT Results on Well Cured and Oven Dried Concrete[3]

Comment on concrete absorption	ISAT results: mL/m^2/s Time after starting test			
	10 min	30 min	1 h	2 h
High	> 0.50	> 0.35	> 0.20	>0.15
Average	0.25–0.50	0.17–0.35	0.10–0.20	0.07–0.15
Low	< 0.25	< 0.17	< 0.10	< 0.07

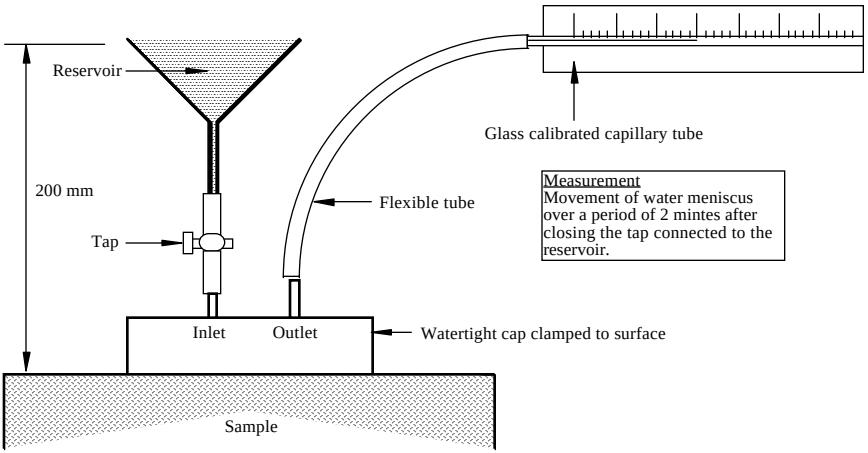


Figure 14. The initial surface absorption test.

It has been proposed[69] that the ISAT could be used to determine the sorptivity of concrete if the cumulative absorption data for the first 10 minutes, rather than the single point absorption rate, are measured. If measurements are not limited to the first 10 minutes or so, the cumulative water absorption versus square root time graph may deviate from the one-dimensional sorptivity graph because of the three-dimensional absorption in the ISAT. In order to achieve a one-dimensional penetration of water, the lateral spreading of water from the source has to be elimnated, for which one of the following methods may be used:

@Seismicisolation

1. Use a circular source of standard radius, and drill into the test surface with a core bit of the same diameter in order to isolate a cylindrical prism of material, but without detaching it.
2. The second method is to use a guard ring on the source, so that the lateral spreading from the source could be eliminated, while measuring the water absorption only from the central circular compartment.

The use of the guard ring has been found to be successful to establish a one-dimensional penetration of water[93][94] and a modified ISAT cap (Fig. 15) can now be used to measure the sorptivity of concrete on site. However, the cap should be protected from direct sunlight and any source of heat because temperature during the interval of observation has a great influence on the measurement.[84][85] Both the viscosity and surface tension of water changes significantly with temperature[95] and, hence, appropriate corrections should be applied to normalize the data to 20°C if measurements are made on site at other temperatures.[96][97]

One of the main problems of the ISAT is associated with the seal between its cap and the concrete surface.[98] The modified ISAT cap is supposed to have addressed this issue. Another limitation as an in-situ test, is often associated with the requirement of a dry surface. Dhir, et al.,[98] carried out measurements with the ISAT for a number of drying conditions and found that 48 hours drying at ambient conditions is not sufficient to obtain reliable values, instead they recommended 7 or even 14 days drying.

Autoclam Sorptivity Test. The Autoclam sorptivity test[89][99] allows the measurement of the cumulative inflow of water in the first 15 minutes from a water source of 50 mm diameter (i.e., from a base ring of internal diameter 50 mm) at an applied pressure of 0.02 bars (nearly 200 mm water head). This test pressure is the same as that used in the ISAT. In order to determine the sorptivity of concrete, the flow of water is plotted against square root of time, which gives a linear variation, and the slope of this graph is reported as a sorptivity index in $m^3/\sqrt{min}$. When the rate of flow of water is very small, relatively larger contact area can be used to obtain measurable flow rates, however, the data should be normalized to the 50 mm diameter area. Also, the guard ring arrangement can be used to achieve a one-dimensional penetration of water. Table 7 provides classification criteria based on the Autoclam sorptivity test on oven dried concretes with the standard 50 mm diameter base ring.

@Seismicisolation

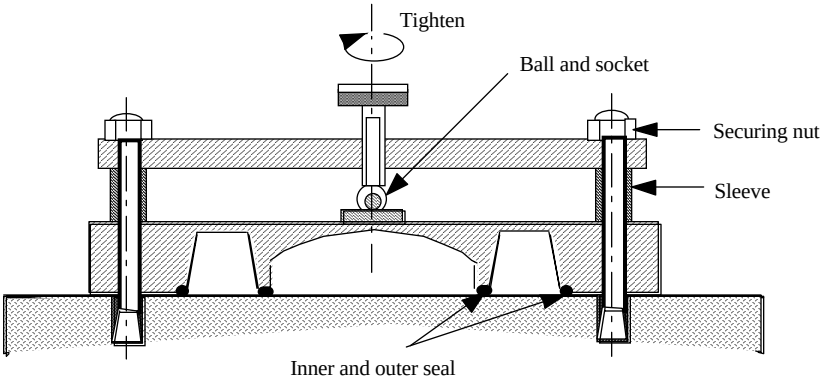


Figure 15. Modified ISAT cap.[93]

Table 7. Protective Quality of Concrete Based on Autoclam Sorptivity Index[100]

Protective Quality	Autoclam Sorptivity Index $m^3 \times 10^{-7}/\sqrt{min}$
Very good	≤ 1.30
Good	> 1.30 ≤ 2.60
Poor	> 2.60 ≤ 3.40
Very poor	> 3.40

Extensive testing by Nolan[95] indicated that if the Autoclam sorptivity test is carried out on concrete with an internal relative humidity at 10 mm depth of less than 80%, the test is capable of distinguishing the quality of concrete. Also, a linear relationship was found between the sorptivity index and the internal relative humidity at 10 mm depth when the latter was less than 80%. However, when the internal relative humidity was greater than 80% the sorptivity measurement was found to have no real benefit to distinguish the quality of concrete.

A commercially available apparatus, called the Autoclam Permeability System, can be used to carry out the Autoclam sorptivity test. This apparatus has the advantage that it is completely portable for site use and the

@Seismicisolation

measurement of the inflow of water into concrete is performed automatically every minute for the full duration of the test. These data can be displayed for manual analysis at the end of each test or transferred to a personal computer for further analysis at the end of 20 tests. Two additional tests, viz., water permeability and air permeability tests, can be carried out with the same apparatus (see later sections).

Standpipe Absorptivity Test. Another type of test, similar in principle to the ISAT, is the *standpipe absorptivity test.* In this method, a vertical tube of suitable diameter is connected to either another vertical piece or an horizontal piece, and glued onto the surface of the specimen to be tested. Water is filled up to a certain level and allowed to be absorbed by the surface. The amount of water absorbed in a certain unit of time is reported as an index of water absorptivity.

Three different types of this test could be seen in technical literature, which were called the *chimney method*,[91] the *Karsten's Pipe Test*,[90] and the *Australian Water Permeability Test*.[92] The various features of these three tests are summarized in Table 8. Although all of these tests are very simple to carry out on site, they do not have the sensitivity that the ISAT and the Autoclam sorptivity test possess.

Table 8. Details of Standpipe Tests

Type of Test	Diameter of Standpipe (mm)	Head of Water (mm)	Observation Parameter
Chimney method[91]	67	100 (constant)	Total water absorbed in 6 days with measurements at every 24 hours
Karsten's pipe test[90]	60	100 (falling)	Volume of water absorbed between 5 and 15 minutes from the start of the test
Australian Water permeability test[92]	100	200 (falling)	A graph between head and time by observing either head for 2 hours or until the head has fallen by 100 mm

@Seismicisolation

Drill Hole Absorptivity Test. This type of test involves first drilling a hole of a suitable diameter in the near surface layer of concrete to a certain depth. After thorough cleaning, the hole is plugged, either at the surface[98] or at part depth[101] by a suitable sealing material, leaving a certain cavity inside for carrying out the test. Water is admitted to this cavity at a low pressure and allowed to be absorbed by capillarity. A measure of the water absorption is obtained in terms of either the time needed for a specific volume of water to be absorbed or the quantity of water absorbed in a specific duration of the test.

Although the first test of this kind was developed by Mercer[25] in 1945, the test became more popular after the introduction of the Figg Water Permeability Test in 1973.[101] Since then, several modifications have been made[3][98][102][103] to the dimensions of the cavity, method used to seal the hole, the water head applied, and the method of monitoring the water absorption. These variations are summarized in Table 9 by giving emphasis to the most commonly adopted test procedures, viz., the *Figg Water Permeability Test* and one of its popular derivations, the *Covercrete Absorption Test*. It may be noted that the Figg water permeability test measures the absorption characteristic of concrete, as against what the name implies.

In the beginning, the lack of sensitivity with this method was criticized[98] because a very small test area was used (5.5 mm diameter hole with 10 mm deep cavity). The present dimensions of the hole may have improved the sensitivity. However, the main drawback of the drill hole absorptivity tests, compared with the surface absorptivity test, is that the test does not allow the determination of the sorptivity of concrete as water penetrates from a cylindrical source. Hall[69] indicated that the time dependence of the sorptivity (i.e., $i = S\sqrt{t}$) would deviate within 1 minute in the case of Figg water permeability test. In addition to this, it is likely that the drilling, even at slow speed, may introduce microcracks which may defeat the purpose of the test by altering the flow mechanism. Despite these possible limitations the Figg water permeability apparatus is produced commercially with the trade name *The Poroscope*, which also can be used to carry out the Figg air permeability test (see later sections). Table 10 presents a five scale tentative criteria to classify concrete on the basis of Figg water permeability values.

@Seismicisolation

Table 9. Variations of the Most Commonly Used Drill Hole Tests

Test Method	Diameter of Hole (mm)	Depth of Hole (mm)	Depth of Plug/Seal (mm)	Test Pressure (mm of Water Head)	Method of Measurement
Figg Test[104]	10	40	20	100	Time in seconds for a certain volume of flow
Covercrete Absorption Test[98]	13	50	0	200	Inflow between 10 and 11 minutes after starting the test

Table 10. Relationship Between Concrete Protective Quality and Figg Water Permeability Index

Concrete Category	Protective Quality	Measured Time, s
0	Poor	< 20
1	Not very good	2–50
2	Fair	50–100
3	Good	100–500
4	Excellent	> 500

5.0 PERMEABILITY TESTS

These tests provide a means for measuring the true permeability, as defined in Sec. 1.3. The basic requirement is that a specimen, usually a core, should be sealed on its curved face so that between its two opposite parallel faces the flow of a liquid or a gas can be promoted by an applied pressure. Under steady state conditions the coefficient of permeability is calculated from a knowledge of sample geometry and fluid characteristics, and the measurement of flow rate and applied pressure. However, if a steady state condition cannot be established due to either low permeability of the test specimen or limitations of the test conditions, a non-steady state of flow can be used to obtain a permeability index. In certain cases of non-steady liquid

@Seismicisolation

flow tests, the depth of liquid penetration can be used to obtain the coefficient of permeability (e.g., water penetration tests). Some of the tests can be used both in the laboratory and on site to measure the permeability of concrete, however, such tests are limited in number. The permeability tests are broadly classified as *liquid permeability tests* and *gas permeability tests.*

5.1 Liquid Permeability Tests

The liquid permeability of concrete can be measured by tests in which either a steady state or a non-steady state of flow of the liquid is established. Where the density of the materials is too high to establish any flow through the specimen, the depth of water penetration under a hydraulic pressure is sometimes used to determine the coefficient of permeability. Therefore, the liquid permeability tests, with water as the permeating liquid, can be classified as:

1. Steady state water flow tests
2. Non-steady water flow tests
3. Water penetration tests

Steady State Water Flow Test. The test determines the rate of flow of water at the steady state condition for a given test pressure and sample geometry. Using this data, the coefficient of water permeability or the intrinsic permeability is calculated from Eq. (3) or (4), respectively. In terms of the test parameters, Eq. (4) can be written as:

Eq. (23) $$k = \frac{Q\mu L}{A(P_1 - P_2)}$$

where: k = the intrinsic permeability (m^2)
Q = rate of flow (m^3/s)
μ = viscosity of the water (Ns/m^2)
L = length of the specimen (m)
A = area of flow perpendicular to the direction of flow (m^2)
P_1 = inlet pressure (N/m^2)
P_2 = outlet pressure (N/m^2)

@Seismicisolation

If the test specimen is fully saturated with water and there are no chemical or physical interactions between concrete and water during the test, then the permeability obtained from Eq. (23) is the *intrinsic permeability* of the concrete. Therefore, this value can be used to determine the coefficient of permeability for any other fluid by using the relationship:

$$k = \frac{K\mu}{pg}$$

where: k = the intrinsic permeability (m^2)
K = coefficient of permeability for a given fluid (m/s)
μ = viscosity of the fluid ($N \cdot s/m^2$)
ρ = density of the fluid (kg/m^3)
g = acceleration due to gravity (m/s^2)

Therefore, for water at 20°C, the relationship between coefficient of water permeability K_w, and the intrinsic permeability k is:

$$K_w = 9.75 \times 10^6 \, k$$

and for typical gases (e.g., nitrogen, oxygen, air) at normal pressures and at 20°C, a sufficiently accurate conversion is given by:

$$K_g = 6.5 \times 10^5 \, k$$

where K_g is the coefficient of gas permeability (m/s).

Test Procedure. The test essentially consists of saturating a test specimen and measuring the rate of flow of water through it due to a pressure gradient. The most commonly used test set-up (Fig. 16) consists of a permeability cell to hold the sample, a set of inlet controls to admit water at the specified test pressure while measuring the inflow, and a set of outlet controls to allow the discharge from the test specimen to be monitored along with the outlet pressure. The permeability cell itself is specially made to seal the sides of the specimen and allow the permeating liquid, water, to go through the sample without any leakage. Permeability cells of various specifications and dimensions exist in order to apply water under pressure to one side of the specimen and measure the rate of flow either at the inlet or at the outlet or sometimes at both ends. The type of test specimen, test pressure, duration of the test, and the method used to seal the specimen in the cell, are some of

@Seismicisolation

the parameters varied in the past.[11]–[13][20][32][105]–[110] The test is essentially a laboratory method and has to be carried out under controlled ambient and test conditions. Difficulties have been pointed out in establishing a steady state condition[13][36][111][112] even after subjecting the specimens to a vacuum saturation method.[98] Test durations of weeks rather than days are common with concrete, however, the use of permeability cell remains one of the most commonly used methods to determine either the coefficient of permeability or the intrinsic permeability of concrete. The range of permeability of concrete measured by this method varied from 10^{-16} to 10^{-11} m/s. Although there are no widely accepted test parameters and procedure of testing, the test is incorporated as a standard method in the American Petroleum Institute's recommendation: API designation RP 27, Recommended Practice for Determining Permeability of Porous Media[113] and in Indian Standard IS 2645, Specification for Integral Cement Water Proofing Compounds.[114]

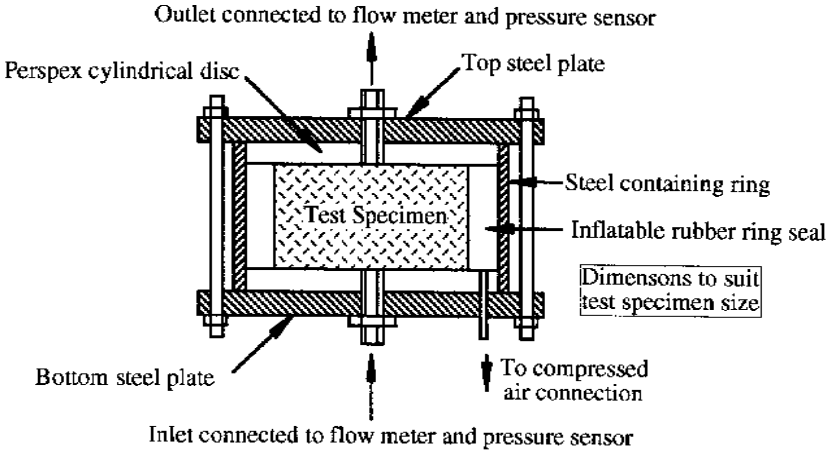


Figure 16. A typical permeability cell.

@Seismicisolation

In the absence of a widely used test procedure, the following aspects may be given consideration while deciding on a steady state water permeability test.

1. *Design of the permeability cell.* The cell should withstand the test pressure without any deformation. As high driving pressures are common with low permeability materials special attention must be given to the seal on the side of the specimen. Where confining pressures are used to seal the side of the specimen, the ratio of the confining pressure to the driving pressure must be suitably chosen. This ratio is known to have an effect on the rate of flow at low confining pressures.[115]
2. *Test specimen.* The test requires fully saturated specimens. If unsaturated specimens are used, the time taken to establish the steady state will be longer than normal and, hence, the duration of the test will increase. This is not advisable for incompletely hydrated samples. The size of the test specimen may pose another problem. If thin specimens are used in order to improve the degree of saturation, it may adversely affect the reliability of the permeability test. The height of sample may be taken as three times the maximum aggregate size in order to reduce the scatter of results.[115] The diameter of test specimens also depends on the maximum aggregate size and here a minimum size of 50 mm is preferable[32]
3. *Age of test specimens.* As unhydrated cement will react with the water during the test and, hence, reduce the permeability, it is preferable to test matured concretes.
4. *The driving pressure.* Although high test pressures may accelerate the test and establish the steady state rapidly they may result in the modification of the pore structure.[115] Leaching, associated with high pressures used in the water permeability test, may result in an increase in permeability.

Due to the interaction between water and cement hydrates, it may be expected that some pore structure modifications are unavoidable in a steady state water flow test, however, this effect can be minimized by a careful selection of the above variables. Table 11 gives typical permeability values which can be found for concrete.

@Seismicisolation

Table 11. Steady State Water Permeability Coefficients for Concrete[116]

W/C	Air Content (%)	Compressive Strength (MPa)	k (m/s) × 10^{-13}
0.35	4.0	33.1	0.37
0.45	5.8	26.1	1.26
0.55	7.3	20.0	4.68
0.65	6.8	16.6	8.14
0.75	6.5	10.6	10.90

Non-Steady Water Flow Test. Due to the difficulty of establishing the steady state of flow for most concretes, either the inflow or the outflow measurements are sometimes used to express the permeability of concrete. The test set-up for this type is the same as that used for the steady state flow measurements, i.e., a suitable permeability cell is employed in order to admit water under pressure and to measure either the inflow or the outflow, or sometimes, both inflow and outflow. The main difference is that the test is not continued until a steady state of flow is achieved. Different test pressures, duration of the test, and test procedure, can be found in literature, which make the test difficult to be standardized. However, the test is capable of identifying the variation of the quality of concrete. Two in-situ tests which make use of the non-steady water flow to characterize concrete are the *Steinart Guard Ring Test*[3] and the *Autoclam Water Permeability Test.*[99][100]

Laboratory Test. Figure 17 illustrates the cell proposed in ISO/DIS 7032,[117] RILEM recommended method for measuring water penetration as water inflow. Test specimens can be either cylinders of 150, 200, or 300 mm diameter and height to diameter ratio of unity, or cubes of sides 150, 200, or 300 mm. Usually tests are carried out at 28 days of age. However, other ages can be chosen according to any special requirements. The specimen is kept in the cell and sealed. Water is admitted through the inlet and the outflow is measured. The recommended pressures for testing are $P/3$, $2P/3$, and $4P/3$, each pressure applied for successive periods of 24 hours where P is the maximum pressure likely to be encountered by the concrete in-situ. The time and pressure at which water first penetrates the specimen and the volume of water collected during a given period at each pressure are recorded. The volume of water that has passed through the specimen in unit time for each test pressure is then calculated and expressed

@Seismicisolation

as *water penetrability*. If steady state conditions have been achieved at any of the test pressures the outflow corresponding to this could be used to calculate the coefficient of permeability, in m/s. This draft International Standards has been rejected by the British Standards Institution as the details of the method are not considered to be sufficiently well developed, in particular, with respect to the lack of standard values for applied pressure.

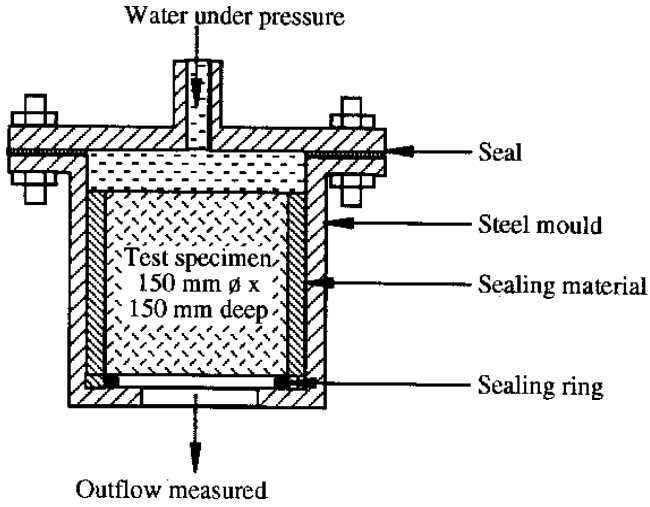


Figure 17. Test arrangement for ISO/DIS 7032.[117]

In-Situ Test. The viscous flow through a fine capillary tube under a pressure head can be expressed by Poiseuille equation:

Eq. (27) $$Q = \frac{\pi r^4}{8\eta}\frac{H}{l}$$

where: Q = rate of flow (m^3/s)
H = head of pressure (m)
r = radius of the capillary (m)
l = length of the capillary pore filled with water (m)
η = viscosity (Ns/m^2)

@Seismicisolation

Here, the head of pressure, H, comprises two components, the capillary attraction pressure and the applied head and, hence, the flow of water is due to the combined effect of applied head and the capillary suction. This is the principle of both the Steinart Guard Ring Test and the Autoclam Water Permeability Test.

Steinart Guard Ring Test. The guard ring principle is used in this test to achieve a unidirectional penetration of water. Two concentric rubber seals are glued and clamped to a concrete surface, creating two ring shaped chambers. These are filled with water and pressurized with compressed air at 7 bar (101.5 psi). The volume of water penetrating the concrete through the inner chamber is recorded.

Autoclam Water Permeability Test. This test[89][100] follows the Clam permeability test which was developed originally to determine the coefficient of permeability of concrete on site.[118] In the Clam permeability test, a 50 mm internal diameter metal base ring is glued onto the surface of concrete and after saturating the test area by ponding water in the ring for 24 hours, the rate of penetration of water through the test area at a constant pressure head of 25 psi (1.72 bar) is measured. The measurements are taken for 15 minutes and from a linear plot of the flow against time the coefficient of permeability as defined in Darcy's equation (Eq. 3) is determined. However, there are fundamental limitations as far as the determination of the coefficient of permeability based on the rate of water penetration from this test is concerned. Capillary pores filled with water require relatively high pressures to cause flow through them and, hence, the pressure used in the test may cause flow through only relatively big pores. This would mean that the test is not capable of determining the coefficient of permeability of saturated concretes. However, if the ponding is eliminated from the test procedure it would provide the rate of water penetration from a pressurized source of water, i.e., a parameter which can be used to assess the permeability characteristic of concrete can be obtained. Although an apparatus to carry out the Clam permeability test was commercially available it was discontinued when the Autoclam Permeability System[87] was introduced into the market; however, an apparatus similar to the Clam permeability test is commercially available at present with the trade name the Germann Water Permeability Test.

The Autoclam water permeability involves a procedure similar to that used for the Autoclam sorptivity test (Sec. 4.4). The main difference is in the test pressure used, i.e., a pressure of 1.5 bar is used for the Autoclam water permeability test. The inflow of water through a test area of 50 mm diameter through a surface mounted ring is measured at this pressure for a

@Seismicisolation

period of 15 minutes. From a linear plot of the cumulative inflow and square root of time, the slope is determined and reported as the Autoclam water permeability index in $m^3/\sqrt{min}$. As the inflow is measured in this test, the test location has to be dry to obtain meaningful data. Typical data to classify concrete are presented in Table 12.

Table 12. Protective Quality Based on Autoclam Water Permeability Index[100]

Protective Quality	Autoclam Water Permeability Index: $m^3 \times 10^{-7}/\sqrt{min}$
Very good	≤ 3.70
Good	$> 3.70 \leq 9.40$
Poor	$> 9.40 \leq 13.80$
Very poor	> 13.80

Water Penetration Tests. While the outflow method with a permeability cell is generally used for testing the permeability of concrete, in the case of concrete with comparatively high density it not only requires a long period of time to perform the tests, but also it is often impossible to obtain any measurable quantity of outflow water. Therefore, water penetration methods are most useful for testing relatively dense (i.e., low permeability) concrete.[6][14][19][39][91][119]–[122] Here, water under a specified hydrostatic pressure is admitted into a permeability cell for a specified duration. At the end of the test the specimens are removed and split along the diameter in order to determine an average depth of penetration of water. Two different methods can be used to estimate the permeation property of concrete based on the depth of penetration:

1. Water penetration as an index.
2. Coefficient of permeability from penetration depth.

Although the first method has been subjected to standardization,[123] the second method has become more popular[6] as it provides the coefficient of permeability. There was an attempt to calculate the diffusion coefficient from the penetration depth.[120] However, as different transport mechanisms are involved in diffusion and water penetration under applied hydrostatic head, one can question the basis of this procedure. Therefore, it is not included in this chapter.

@Seismicisolation

Depth of Water Penetration as an Index. This test is included in the German Standard DIN 1048[123] on test methods for concrete and is also covered in a draft International Standards ISO/DIS 7031.[124] The DIN 1048 water penetration test has been used in several investigations to classify concrete.[19][39][119] In this test (Fig. 18), the concrete sample, at the age of 28 days, is initially subjected to a water pressure of 100 kPa (1 atmosphere) for 2 days and then for one day each to a water pressure of 300 kPa and 700 kPa, respectively. At the end of this period, the test sample is removed from the cell, surface, dried, and split in half perpendicular to the injected face. The average depth of penetration is noted and is used as an indication of the permeability of concrete. While DIN 1048 suggests the use of slab or cube shaped specimens, ISO/DIS 7031 proposes cylindrical cores of 150, 200, or 300 mm diameter with a height ratio of at least 0.5, but not less than 100 mm height in any case. When this test was introduced in the early 70s,[91] the specimens were subjected to a water pressure of only 1 atmosphere for a period of 24 hours. It may be noted that the British Standards Institution has expressed doubts about the accuracy with which the water penetration front can be located on the face of the split specimen,[3] therefore, it is not yet a British Standard Test.

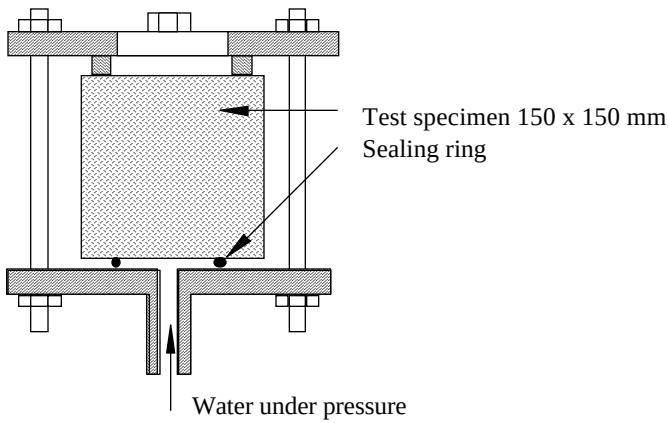


Figure 18. Test arrangement for ISO/DIS 7031.[124]

@Seismicisolation

Typical results for various forms of concrete, reported by the Concrete Society[3] are as follows:

- Dense (50 MPa) concrete with slag and superplasticizer: 5 mm
- Specification for good quality concrete to resist aggressive environment: < 30 mm
- Specification for concrete in water retaining structures: < 50 mm

Coefficient of Permeability from Penetration Depth. Valenta[14][121] developed an equation to relate the depth of penetration x (m/s) to the coefficient of permeability for non-steady state k' (m/s) by using the theory of kinetics of unsteady percolation of water into the concrete based on Darcy's formula. This equation is given by:

Eq. (28) $$x = \sqrt{2k'ht}$$

where: x = depth of penetration of water (m) at a time, t (s)
h = hydrostatic head causing the water percolation (m) (equals applied water head h_p plus capillary elevation h_o)

The value of k' from the non-steady state would be different from the coefficient of permeability, K, obtained by the steady state condition because in the case of non-steady state of flow, some time is needed for water to fill the capillary pores with no participation in effective flow through the concrete. However, it is possible to obtain the coefficient of permeability as defined by Darcy's equation for the steady state of flow[3][122] by incorporating the volume of pores filled by the advancing water front, v, as given by:

Eq. (29) $$x = \sqrt{\frac{2Kth}{v}}$$

with all the parameters as defined earlier. This is generally known as the *modified Valenta equation*. The increase in weight of the test specimen can be used to determine the volume of voids filled with water during the test and the substitution of all parameters observed in the experiment would provide the coefficient of permeability in m/s. One of the requirements of this test is that the penetration of water should be uniaxial. However, if the

@Seismicisolation

concrete is very dense and the depth of penetration is small compared to the diameter of the test area, a uniaxial penetration can be assumed. The permeability measured with this test varied from 5 to 3900 × 10^{-12} m/s for a range of concrete tested by Browne and Domone.[125]

5.2 Gas Permeability Tests

The method of measuring the gas permeability of concrete has the following advantages over parameters such as diffusion coefficient, initial surface absorption, etc.

1. It is relatively quick to measure and, hence, it enables specimens conditioned at any age to be tested without any time delay.
2. The conditions of the specimen does not change during the testing.

For these reasons and as the gas permeability of concrete is important for the *gas tightness* of concrete storage vessels[3] and mechanisms such as carbonation,[82] these tests have become quite common in order to measure the permeability of concrete. Testing concrete for gas permeability can be carried out by either keeping the head constant and measuring the flow or by monitoring the pressure decay over a specified time interval.

Constant Head Gas Permeability Tests. The constant head gas permeability tests are carried out with a permeability cell similar to that used for the water permeability tests. Air,[9][126] nitrogen,[6][108] or oxygen,[8][71][73][127][128] can be used as the permeating gas. The steady state of flow can be established within a few minutes from the start of the test.[6][9] Therefore, the rate of outflow of gas is monitored and the value corresponding to the steady state is used to calculate the intrinsic permeability of concrete by using Darcy's equation. However, in the case of gases, the compressibility of gases should be taken into account, for which the average pressure within the specimen is used in Darcy's equation.[6][8][9][126] Therefore, for the gas permeability test, Eq. (23) to calculate the intrinsic permeability becomes:

Eq. (30)
$$k_g = \frac{Q_2 \mu L}{A(P_1 - P_2)} \frac{2P_2}{(P_1 + P_2)} = \frac{2\mu L P_2 Q_2}{A(P_1^2 - P_2^2)}$$

@Seismicisolation

where: k_g = the intrinsic permeability (m^2)
μ = viscosity of the fluid (Ns/m^2)
L = length of the specimen (m)
P_2 = outlet pressure (N/m^2), usually the atmospheric pressure
P_1 = inlet pressure (N/m^2)
Q_2 = rate of flow at the outlet (m^3/s)
A = area of specimen perpendicular to the direction of flow (m^2)

In theory, the intrinsic permeability from this expression should be the same as that obtained by the use of a similar expression for the liquid (Eq. 23). However, the value of k obtained from gas permeability tests would be higher than that obtained from liquid permeability tests[6][9] due to a phenomenon known as *gas slippage*, i.e., gases have a definite velocity near the walls of the capillary pores irrespective of the applied pressure. Therefore, the rate of flow of gases depends on both the intensity of the test pressure and the type of the gas used, the extent of which was determined by Klinkenberg[129] in 1941 as:

Eq. (31) $$k_g = k(1+b/P_m)$$

where: k_g = permeability coefficient at some finite mean pressure
k = permeability coefficient corresponding to infinite mean pressure
b = constant = M/k (depends on the gas and the porous medium)
M = slope of k verses $1/P_m$ plot
P_m = mean pressure = $(P_1+P_2)/2$
P_1 = inlet pressure
P_2 = outlet pressure

Therefore, by conducting a gas permeability test at different pressures and plotting k_g versus $1/P_m$, an equivalent permeability of liquids can be obtained. Based on this theory, Klinkenberg determined the intrinsic permeability with nitrogen, hydrogen, and carbon dioxide, and found that there exists a common permeability value for these gases. For a range of concrete tested, Bamforth found that the constant, b, can be estimated by using:

Eq. (32) $$b = 1.635 \times 10^{-8} k_l^{-0.5227}$$

@Seismicisolation

where k_l is the same as k_g in Eq. (31). The value of k_l can be obtained from liquid permeability tests. Bamforth[6] found that the gas slippage effect increases as the test pressure decreases and a plot of Eq. (31) could be used to normalize the permeability coefficients for different test pressures used in gas permeability tests.

Test Methods. Although there are no British Standards for gas permeability tests, a method by which the flow of air is used to determine the intrinsic permeability of rock is available in ASTM Standard D 4525-85.[126] A permeameter similar to that shown in Fig. 16 can be used to carry out the steady state gas permeability test. Figure 19 shows one of the permeameters described in the ASTM Standard. After keeping the specimen in the holder, an air pressure of 700 kPa (7 bar) is applied to the sleeve on the circumferential face of the specimen in order to eliminate the leakage through its side. The test is performed by admitting air through the inlet valve such that a measurable flow occurs at the outlet, with very high pressures being avoided to eliminate turbulent flow. The flow rate is measured when steady state is reached, and the various parameters needed for calculating the intrinsic permeability are noted. The test is repeated with a number of test pressures, each time reducing the pressure by half of its previous value. These are used to obtain the coefficient of permeability corresponding to an infinite mean pressure, as explained earlier. The tests are continued until a set of data which gives a linear relationship between inverse of the mean pressure and the calculated permeability coefficient is obtained.

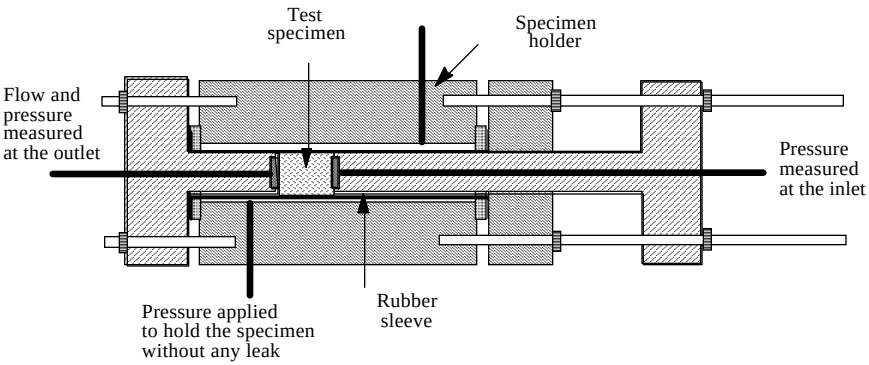


Figure 19. A typical gas permeameter.

@Seismicisolation

Several forms of gas permeameters could be found in the literature. The main difference between them is in the way specimens are sealed in the permeameter cell and the measurements are taken. The flow depends on the pressure difference, testing area, thickness and open porosity of the specimen, and the viscosity of the test gas. However, the basic procedure remains the same as that described above. Both nitrogen and oxygen are the preferred gases to carry out gas permeability measurements. Other gases may be used, however, one of the criteria for selecting a gas should be that it should not change the pore structure of concrete during the test. The test specimen should be preconditioned in a standard manner in order to eliminate the influence of moisture on the test results.

Falling Head Gas Permeability Tests. The difficulties of performing the constant head gas permeability tests on site have resulted in the development of methods which do not require the measurement of the flow at a constant pressure. The various methods which can be used to measure the gas permeability under this category fall in one of the following four distinct types:

1. Drill hole suction tests
2. Drill hole overpressure tests
3. Surface suction tests
4. Surface overpressure tests

In general, a small cavity is made in concrete by drilling into the surface in drill hole tests (both suction and overpressure tests) whereas a chamber mounted on the surface of the test specimen is used in surface tests. The pressure is reduced below atmospheric to a certain level in suction tests whereas it is increased to a specified level in overpressure tests. A measure of the change in pressure is used to derive a permeability index in both the categories, details of which are summarized in Table 13. Further relevant details of these tests are given below.

Drill Hole Suction and Overpressure Tests. In these tests it is assumed that the air flow will be through the near surface concrete either into the cavity (in suction tests) or from the cavity (in overpressure tests) and, hence, a permeability index of the cover concrete can be obtained. Table 14 gives the criteria to classify concrete on the basis of the Figg air permeability results and, as stated earlier, both the Figg water permeability test and the Figg air permeability test can be carried out with a commercially available instrument, *the Poroscope*.[130]

@Seismicisolation

Table 13. Details of Falling Head Gas Permeability Tests

Test Method	Test Area	Method of Measurement
Drill Hole Suction		
Figg Air permeability[104]	A cavity of 10 mm diameter and 20 mm deep at 20 mm below the surface	Time in seconds for a change in pressure below atmospheric from 55 to 50 kPa.
Drill Hole Over Pressure		
Hong and Parrott[128}	A cavity of 20 mm diameter and 15 mm deep at 20 mm below the surface	Time for a known drop in pressure in the cavity (no specific value stated).
Reinhardt, et al.[131]	A cavity of 14 mm diameter and 20 mm deep at 20 mm below the surface.	The time taken for a decrease in pressure from 1000 to 950 kPa.
Surface Suction		
Hilsdorf[132]	50 mm diameter area on the surface.	Time required for the pressure to increase from 20 to 50 mbar below atmospheric.
SHRP Method[133]	100 mm diameter area on the surface.	Air flow under a vacuum of 635 mm of mercury.
Torrent.[134]	60 mm diameter area on the surface	Increase in pressure from a near vacuum stage.
Surface Over Pressure		
Hansen, et al.[135]	Not specified.	Time for a specified increase in pressure near a sensor kept at a shallow depth below a pressure head on the surface.
Lydon, et al.[136]	35 mm diameter area on the surface.	Pressure decay curve for an applied pressure of 10 bar.
Autoclam air permeability[100]	50 mm diameter area on the surface.	Pressure decay from 0.5 over a period of 15 minutes.

@Seismicisolation

Table 14. Relationship Between Concrete Protective Quality and Figg Air Permeability Index

Concrete Category	Protective Quality	Measured Time, s
0	Poor	< 30
1	Not Very Good	30–100
2	Fair	100–300
3	Good	300–1000
4	Excellent	> 1000

As noted in Table 13, Hong and Parrott's method enables the determination of the intrinsic permeability of concrete from the measurement of the time taken for the air pressure in the cavity to drop over a specific range by using the following equation.

Eq. (33)
$$k = \frac{2\mu L[V_c(P_1 - P_2)]}{P_a A(t_2 - t_1)(P_1 + P_2)}$$

where:
k = intrinsic permeability
μ = viscosity of gas
L = length of the flow path
V_c = volume of the cavity
P_1 = starting pressure
P_2 = finishing pressure
P_a = atmospheric pressure
A = area of flow
$(t_2 - t_1)$ = duration of pressure measurement

The value of A/L is estimated from the geometry of the cavity and the near vicinity through which gas escapes to the atmosphere. This is monitored with liquid soap applied by brushing around the test hole.

Two possible criticisms of Hong and Parrott's test are in relation to the reliability of the value of A/L and $0.5(P_1 + P_2)(t_1 - t_2)$. Even if the assumed value of A/L in the above equation is correct it is possible that the use of different pressure ranges may result in different values of k because

@Seismicisolation

the rate of pressure decay is not linear. However, this test provides the opportunity to monitor the internal relative humidity in the test cavity and, hence, to interpret the air permeability coefficient in terms of the internal moisture content of concrete.

Surface Suction and Overpressure Tests. As listed in Table 13, either a vacuum chamber or a pressure chamber is mounted on the surface of the test specimen and either the change in pressure over a specified duration or the time required for a specified change in pressure is noted in these tests. In some cases, these observations are used as a measure of the air permeability of concrete. However, some tests involve the calculation of a permeability index.

In the Hilsdorf method[132] the time required for the pressure to increase from 20 mbar to 50 mbar below atmospheric is used to calculate a permeability index by using the equation:

Eq. (34)
$$M = \frac{(P_1 - P_0)V_s}{(t_1 - t_0)P_a\left[P_a - \frac{P_1 + P_0}{2}\right]}$$

where: M = permeability index (m^2/s)

t_0 = time at the beginning of the test (s)

t_1 = time at the end of the test (s)

P_0 = pressure inside the vacuum chamber at time t_0 (mbar)

P_1 = pressure inside the vacuum chamber at time t_1 (mbar)

P_a = atmospheric pressure

V_s = volume of vacuum chamber (m^3)

Usually the tests are performed until a constant rate of flow has been reached. This is identified by repeating the test a number of times at the same test location until consecutive tests give the same result. The concrete surface is dried with hot air for five minutes and allowed to cool for two minutes in order to eliminate the influence of the moisture content in the test area on the measured permeability index. However, it is unlikely that satisfactory drying can be achieved with this procedure. Also, if the concrete is wet, it is likely that the application of a pressure below atmospheric may cause water to migrate to the dried area from beneath, thereby reducing the volume flow path.

@Seismicisolation

One of the criticisms of the above method is that if the concrete skin is very porous air may enter easily into the test chamber through this layer of concrete. Therefore, high permeability values may be recorded even where the concrete is relatively good. This has been avoided in the method developed by Torrent[134] by using a guard ring arrangement to direct the flow uniaxially within the test zone in concrete. Also, it has been possible to calculate the coefficient of permeability with this method. Although the apparatus for carrying out the Torrent air permeability test is commercially available, it requires some explanation as to the origin of the air which degrades the vacuum in the instrument when concrete on site is not dry beyond a certain depth.

The Autoclam permeability system,[99] which enables the Autoclam sorptivity and water permeability test to be carried out, is used to determine the Autoclam air permeability index of concrete.[100] In this test the natural logarithm of the pressure monitored (Table 13) is plotted against time and the slope of the graph is reported as the Autoclam air permeability index. Although moisture influences the test results, Nolan[95] has shown that the quality of concrete can be classified in terms of the Autoclam air permeability index if measurements are taken when the internal relative humidity in a cavity in concrete at a depth of 10 mm from the surface is less than 80%. At relative humidity values above this value the air permeability measurements are reported to be of no benefit. Table 15 provides criteria which can be used to classify concrete on the basis of the Autoclam air permeability index when tests are carried out on oven dried concrete.

Table 15. Protective Quality Based on Autoclam Air Permeability Index[100]

Protective Quality	Autoclam Air Permeability Index: Ln (Pressure)/min
Very Good	≤ 0.10
Good	$> 0.10 \leq 0.50$
Poor	$> 0.50 \leq 0.90$
Very Poor	> 0.90

@Seismicisolation

6.0 FACTORS INFLUENCING PERMEATION TESTS

Both the characteristics of concrete and environmental conditions influence permeation properties. Some of the parameters which might influence the permeation tests have been mentioned while discussing test methods. As the specific influence of these factors on each of the test techniques is beyond the scope of this chapter, their general effect is included in this section. The effect of concrete on permeation properties can be found in any good book on concrete technology.

The following factors should be given adequate attention while planning a permeability test program:

1. Driving force and duration of test.
2. Ambient conditions at the time of test (temperature and humidity).
3. Moisture content of the test specimen.

One way or the other the effect of these factors have to be taken into account in any permeation test.

6.1 Test Pressure and Duration of Test

In steady state permeability tests, it is generally believed that a constant rate of flow is established, however, the flow need not be constant for the entire duration of the test and there may not be a linear relationship between the applied pressure and the flow being measured. Due to the following reasons, the permeability may change with an increase in test pressure and duration:

1. Impurities in the permeating water causing silting up and chemical action with the materials in concrete.
2. Silting up due to particles carried from one part of the concrete and deposited in the pores lower down.
3. Swelling of the cement.
4. Further hydration.
5. Calcium hydroxide washed to the bottom surface and carbonated by the atmosphere, thus forming an impermeable layer.

Among these, the silting, swelling, and further hydration, are the main reasons for the decrease in flow.

@Seismicisolation

It has been indicated earlier that if permeability tests are carried out with gas a correction for the effect of gas slippage has to be applied to the measured permeability value. The correction for the gas slippage also depends on the applied pressure, however, for sorptivity and absorptivity tests, small changes in pressure head, up to 200 mm, do not change the result to any significant extent, therefore, there is no need to apply any correction to the measured values.

Finally, in the case of ionic migration tests, the intensity of voltage applied does not necessarily result in a proportional increase in the flow of ions. The reason for this has already been discussed under ion diffusion tests.

6.2 Ambient Conditions at the Time of Test

Temperature influences the viscosity and surface tension of the fluid and both temperature and humidity affect the flow mechanism. It is possible to take account of the effect of temperature on the viscosity and surface tension of the fluid, and, hence, apply appropriate corrections for various test techniques. In some cases, empirical relationships have been derived and they can be used.

The humidity is significant in permeability measurements, however, it is difficult to account for its effect without a knowledge of the moisture content of concrete; therefore, the effect of moisture content is generally given importance in relation to the humidity effect on the permeation tests on concrete.

6.3 Moisture Content of Concrete

The moisture content reduces the flow path in the case of gas flow tests. It also influences other permeation mechanisms such as sorptivity, diffusivity, etc. The effect of moisture has been reported in various published works. Whereas the influence of moisture in laboratory studies is usually eliminated by drying the samples, the following methods can be resorted to in order to remove its effect on site.

1. Precondition the surface by forced drying
2. Independent measurement of moisture content prior to testing

The effectiveness of these techniques needs to be investigated thoroughly before either of them can be used as a standard procedure. At present only isolated data exist.

@Seismicisolation

7.0 RELATIONSHIP BETWEEN PERMEATION PROPERTIES AND DURABILITY OF CONCRETE

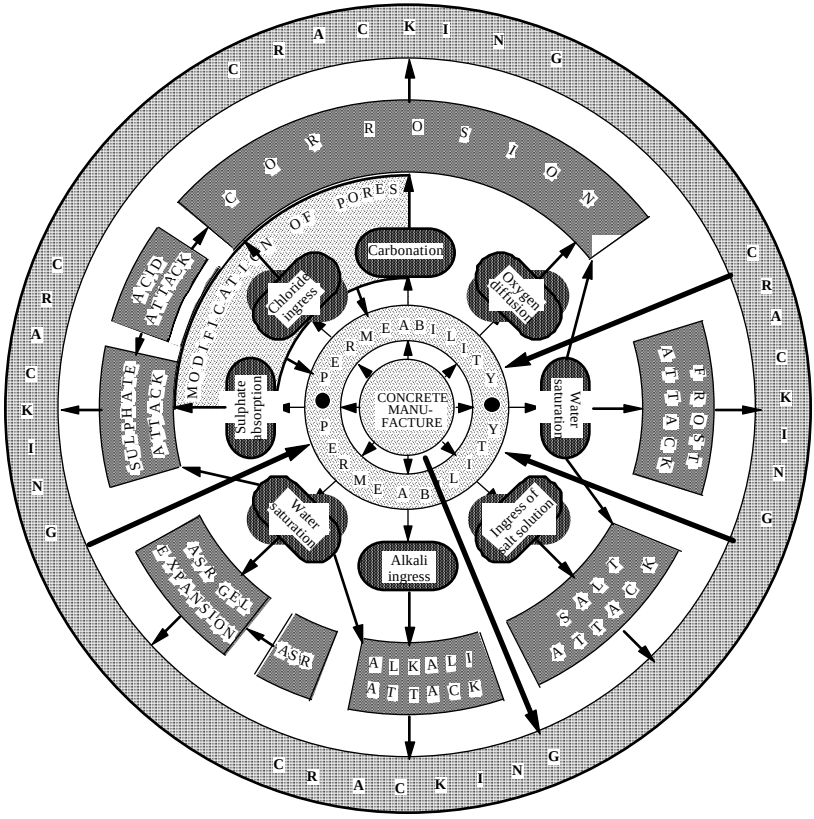
The various mechanisms of deterioration of concrete are corrosion of reinforcement, freezing and thawing damage, salt attack, alkali attack, alkali-aggregate reaction, sulfate attack, and acid attack.[137] These mechanisms are described in Ch. 1 of this book. The ingress of various ions, liquids and/or gases from the environment is responsible for either the deterioration and/or the damage due to expansive reactions as a result of these mechanisms.[138] For instance, the ingress of chlorides and/or carbonation would depassivate steel in concrete and in the presence of oxygen and water steel may start corroding. Similarly, the ingress of chemicals such as acids, alkalis and sulfates is responsible for the chemical deterioration of concrete. The overall effect of the pore structure and permeability influencing the penetration of these aggressive substances and, thereby, their effect on the durability of concrete, can be visualized in Fig. 20.[138] Further explanation of this diagram is given below.

Properties of concrete at the inception of a structure are controlled by constituent materials of concrete, method of manufacturing, and subsequent treatment given to hardened concrete. These factors govern the pore structure and permeability characteristics of the hardened concrete and also various forms of cracks in concrete. At the center of Fig. 20, therefore, the manufacture of concrete and permeability, used in a collective sense, are presented.

The next set of outer blocks in Fig. 20 represent the penetration of various aggressive substances which govern the different mechanisms of deterioration. The mechanisms of deterioration are shown next in a set of blocks outside the aggressive substances. The arrowhead lines between these two sets of blocks indicate the dependence between the penetration of aggressive substances and the deterioration mechanisms. The influence of permeation properties on the penetration of aggressive substances shown by arrowhead lines can be elaborated further.

Carbonation is the result of carbon dioxide diffusion and, hence, gas diffusion is the relevant transport property. Same is the case with the diffusion of oxygen. The ingress of chlorides is by ionic diffusion and/or by absorption of chlorides in solution form. The penetration of sulfate also is governed by both ionic diffusion and absorption in solution form. In the case of water, alkalis and salt solution, both absorption and liquid permeability are important. Finally, exposure conditions where a hydrostatic pressure exists or gas tightness is important, the liquid permeability and gas permeability, respectively, are important.

@Seismicisolation



NOTE:
Influence of concrete manufacture means the effect of the constituents, method of preparation and the subsequent treatments

A direction arrow line in this diagram means that the parameter at the tail end influences that at the arrow head

Figure 20. Interdependence of permeation properties and durability of concrete.[138]

@Seismicisolation

As a result of all the mechanisms presented in Fig. 20, concrete cracks and this in turn increases the permeation properties. In sulfate attack, chloride attack, and carbonation, slight modification of the pore structure may occur, which in turn may decrease the permeation properties. However, under prolonged action of the mechanisms, concrete will eventually crack.

The test methods discussed in this chapter can be used to measure the transport properties relevant to the various mechanisms of deterioration. Experimental evidence exists illustrating the correlation between the relevant transport properties and either the penetration of different aggressive substances or the mechanisms of deterioration. Typical correlations are presented in Figs. 21 to 24.

The dependence of carbonation on gas permeability of concrete is illustrated in Figs. 21[110] and 22.[139] In Fig. 21 the depth of carbonation after 20 weeks in an accelerated carbonation test is presented against the intrinsic permeability in a logarithmic scale. Figure 22 illustrates the variation of the depth of carbonation of 27 different mixes after 14 days in an accelerated test with the Autoclam air permeability results. In both sets of data, good correlation can be found between the depth of carbonation and the gas permeability of concrete. The variation between the two sets of data is considered to be due to the difference in sample preparation, testing conditions, and different types of cementitous materials used in the concrete. The relationship between depth of carbonation and gas permeability of concrete reported in Ref. 56, based on the work carried out in Germany, is similar to that presented in Figs. 21 and 22.

Long, et al.,[140] reported the relationship between Autoclam water permeability results and the weight loss (expressed as a percent of the initial saturated weight) due to 300 cycles of ASTM C 666 Procedure A freezing and thawing test (Fig. 23). The data presented in Fig. 23 are based on tests carried out on 27 different concrete mixtures. As can be seen, there exists a good correlation between the two. Reference 56 reports a similar relationship between the weight loss due to freezing and thawing test and the intrinsic permeability of concrete.

The dependence of chloride penetration on sorptivity of concrete can be seen in Fig. 24.[141] The data in this figure is based on ponding tests carried out on both surface treated and untreated concrete specimens. The three untreated concrete specimens showed in a linear correlation between the chloride ingress and the sorptivity values and the reduction in sorptivity due to surface treatments correspondingly resulted in a decrease in the chloride content. Basheer and Cleland[142] reported that the reduction in both the sorptivity and the chloride ingress was accompanied by a corresponding reduction in the rate of corrosion of steel bars embedded in the test specimens.

@Seismicisolation

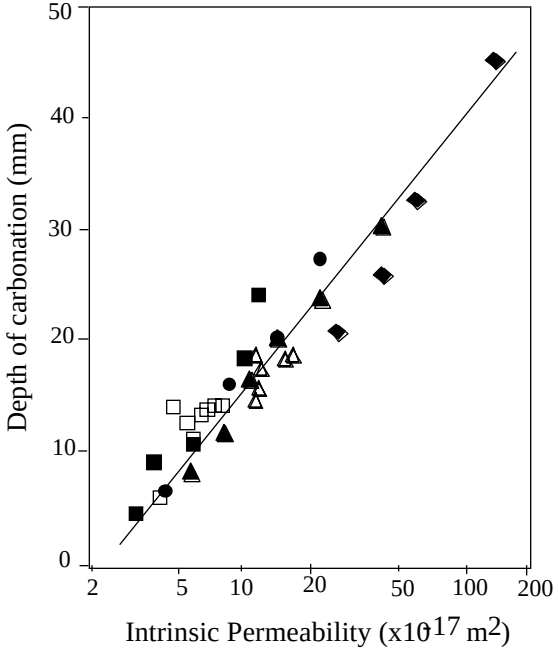


Figure 21. Relationship between permeability and depth of carbonation.[110]

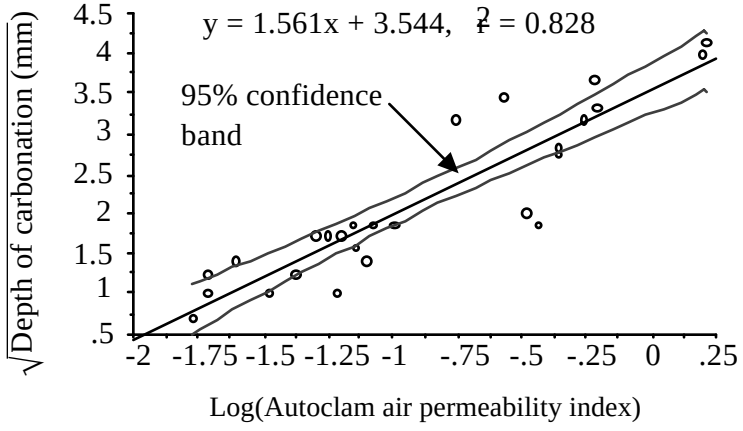


Figure 22. Relationship between autoclam air permeability index and depth of carbonation.[139]

@Seismicisolation

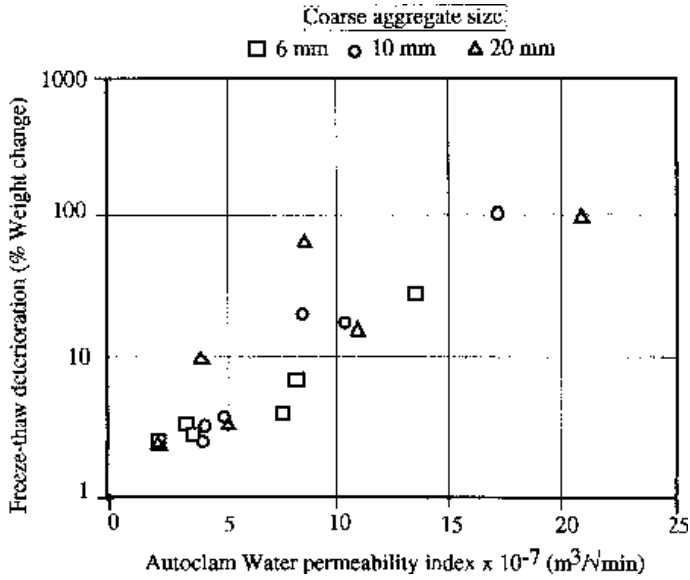


Figure 23. Relationship between autoclam water permeability index and freezing and thawing deterioration.[140]

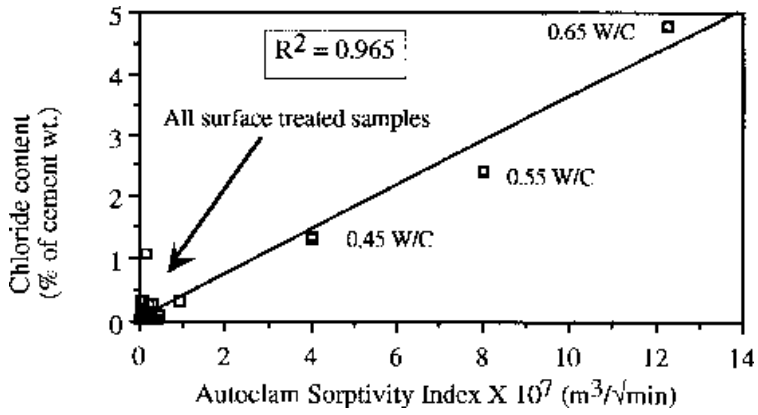


Figure 24. Relationship between autoclam sorptivity index and chloride ingress.[141]

@Seismicisolation

Whereas the dependence of various mechanisms of deterioration on permeation properties is well documented for laboratory investigations, not much data exist for in-situ investigations. Two graphs are presented below (Figs. 25 and 26) which report the dependence of both carbonation and chloride ingress on air permeability of concrete based on tests carried out with the Autoclam Permeability System on eleven concrete motorway bridges in Northern Ireland.[140][143] Although the effect of moisture was not completely accounted for in the air permeability results, large variations in both the depth of carbonation and chloride ingress corresponded with a similarly large variation in the air permeability of concrete.

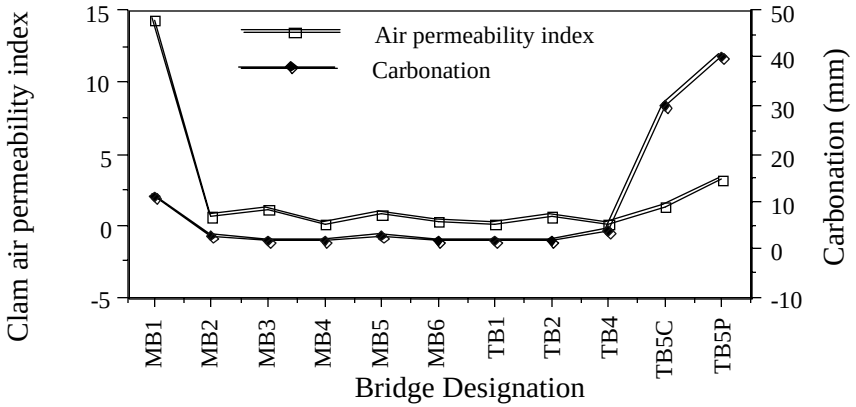


Figure 25. Dependence of carbonation on air permeability of concrete bridges.[140]

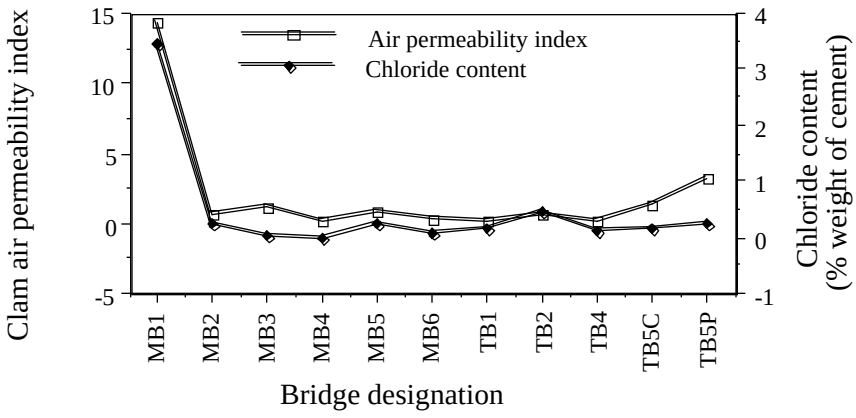


Figure 26. Dependence of chloride ingress on permeability of concrete bridges.[140]

@Seismicisolation

It may be remembered that the conceptual model relating permeation properties to both the penetration of aggressive substances and the deterioration mechanisms (Fig. 20) can be validated with data in so far as the mechanisms of deterioration involve the transport of aggressive substances and these initiate the deterioration. Also, it is relatively easy to show that there exists a good correlation between a specific mechanism of deterioration and a related transport property, however, in reality one mechanism may act as the catalyst for a number of other mechanisms and the permeation properties alone may not be sufficient to estimate both the rate and the extent of deterioration. Therefore, permeation properties allied to a knowledge of both the physical and chemical characteristics of concrete should be made use of in assessing the durability of concrete.

8.0 REMARKS ABOUT PERMEATION TESTS

On the basis of test techniques described in this chapter, the following general observations can be made.

1. Among the four parameters of the transport processes in a porous system, viz., adsorption, diffusion, absorption, and permeability, both adsorption and diffusion measurements are not suitable for testing concrete on site. An exception to this is the determination of ionic diffusivity, for which the ion migration tests can be used.
2. Both absorption and permeability methods can be used for testing concrete from structures, however, most methods involve testing cores rather than conducting tests on site. Nevertheless, both the absorptivity tests and the falling head gas permeability tests could be used in order to obtain the sorptivity and the permeability of concrete on site.
3. Among the various absorption tests, the determination of the sorptivity from absorptivity tests, such as the modified ISAT and the Autoclam sorptivity test, is useful to study the effect of both curing and other surface treatments to improve the quality of the near surface concrete.

@Seismicisolation

4. Finally, tests involving sample drilling and/or coring may alter the microstructure of concrete. Surface mounted tests have the advantage that tests are carried out on an undisturbed concrete.

REFERENCES

1. Bear, J., and Braester, C., *Fundamentals of Transport Phenomena in Porous Media,* Elsevier, Amsterdam (1972)
2. Rose, D. A., Water Movement in Unsaturated Porous Materials, *RILEM Bulletin,* 29:119–124 (1965)
3. The Concrete Society, Permeability Testing of Site Concrete—A Review of Methods and Experience, *Report of a Concrete Society Working Party*, Concrete Society Technical Report No. 31, p. 95, London (Aug., 1988)
4. Washburn, The Dynamics of Capillary Flow, *The Physics Review*, XVII(3):273–283 (March, 1921)
5. Bear, J., et al., Physical Properties of Water Percolation and Seepage, *Arid Zone Research - XXIX*, UNESCO, pp. 465, Place de Fontenoy, Paris (1968)
6. Bamforth, P. B., The Relationship Between Permeability Coefficients for Concrete Obtained Using Liquid and Gas, *Magazine of Concrete Research,* 39(138):3–11, London (March, 1987)
7. Brakel, J. Van, and Heertjes, P. M., Anomalies in Capillary Rise in Porous Media, *Proceedings, Second International CIB/RILEM Symposium on Moisture Problems in Buildings,* 10:10–12, Netherlands (Sept., 1974)
8. Cabrera, J. G., and Lynsdale, C. J., A New Gas Permeability for Measuring the Permeability of Mortar and Concrete, *Magazine of Concrete Research,* 40(144):177–182, London (Sept., 1988)
9. Dhir, R. K., et al., Near Surface Characteristics of Concrete: Intrinsic Permeability, *Magazine of Concrete Research,* 41(147):87–97, London (June, 1989)
10. Kelham, S., A Water Absorption Test for Concrete, *Magazine of Concrete Research,* 40(143):106–110 (June, 1988)
11. van der Meulen, G. J. R., and van Dijk, J., A Permeability Testing Apparatus for Concrete, *Magazine of Concrete Research,* 21(67):121–123 (June, 1969)
12. Nyame, B. K., Permeability of Normal and Lightweight Mortars, *Magazine of Concrete Research,* 37(130):44–48 (March, 1985)
13. Tylor, I. L., and Erlin, Bernard, A Proposed Simple Test Method for Determining the Permeability of Concrete, *Journal of the PCA,* Research and Development Laboratories, pp. 2–7 (Sept., 1961)

@Seismicisolation

14. Valenta, Oldrich, *Kinetics of Water Penetration into Concrete as an Important Factor of its Deterioration and of Reinforcement Corrosion—Basic Questions, Principles and Methods of Testing and Determination of Concrete Durability Under the Action of Frost, Sulfates and Acids,* (O. Valenta, ed.), pp. A177–A193, Prague (1969)

15. Neville, A. M., *Properties of Concrete,* p. 779, Pitman Books Ltd., London (1981)

16. Powers, T. C., Structure and Physical Properties of Hydrated Portland Cement Paste, *Journal of the American Ceramic Society,* 41(1):1–6 (Jan., 1958)

17. Mehta, P. Kumar, *Concrete: Structures, Properties and Materials,* p. 450, Prentice-Hall, Inc., Englewood Cliff, New Jersey, (Jan., 1986)

18. Feldman, R. F., and Sereda, P. J., A Model for Hydrated Portland Cement Paste as Deduced from Sorption—Length Change and Mechanical Properties, *RILEM Bulletin,* 1(6):509–520, Paris (Nov.–Dec., 1968)

19. Diem, Paul, Determination of Capillary Absorptiveness of Very Dense Concrete, *Betonwerk und Fertigteil-Technik,* 52(11):719–724 (Nov., 1986)

20. Mehta, P. K., and Manmohan, D., Pore Size Distribution and Permeability of Hardened Cement Pastes, *Chemistry of Cement,* 7th International Congress, p. 5 (1980)

21. Midgley, H. G., and Illuston, J. M., Some Comments on the Microstructure of Hardened Cement Pastes, *Cement and Concrete Research,* 13:197–206 (1983)

22. Nieminen, Pertti, and Romu, Martti, Porosity and Frost Resistance of Clay Bricks, *Proceedings, 8th International Brick/Block Masonry Conference,* pp. 103–109, Ireland (1988)

23. Parrott, L. J., and Killoh, D. C., Prediction of Cement Hydration, The Chemistry and Chemically Related Properties of Cement, *British Ceramic Proceedings,* 35:41–53 (Sept., 1984)

24. Parrott, L. J., Effect of Changes in U.K. Cements upon Strength and Recommended Curing Times, *Concrete, Journal of the Concrete Society,* pp. 22–24 (Sept., 1985)

25. Mercer, L. Boyd, Permeability of Concrete 1, Theoretical Considerations, Laboratory Test Methods, Details of Experimental Work with New Apparatus, *The Commonwealth Engineer,* pp. 349–357 (2 July, 1945)

26. Permeability of Concrete, *ACI SP-108,* American Concrete Institute, p. 226, Detroit (1989)

27. Lawrence, C. D., Hydrated Cement Paste Pore Structures from Nitrogen and Butane Adsorption Isotherms, *Principles and Applications of Pore Structural Characterization,* pp. 339–363, J. W. Arrowsmith, Ltd., Bristol (1985)

@Seismicisolation

28. Hansen, Torben C., Physical Structure of Hardened Cement Paste: A Classical Approach, *Materials and Constructions,* 19(114):423–436 (1986)

29. Crank, J., *The Mathematics of Diffusion,* Clarendon Press, Oxford (1975)

30. Nilsson, L. O., et al., HETEK, Chloride Penetration into Concrete, State-of-the-Art, Transport Processes, Corrosion Initiation, Test Methods and Prediction Models, The Report No. 53, Road Directorate, Copenhagen (1996)

31. Lawrence, C. D., Transport of Oxygen through Concrete, *British Ceramic Proceedings,* No. 35, pp. 277–293 (Sept., 1984)

32. Lawrence, C. D., Laboratory Testing of Cores, Papers for a One Day Conference, The Concrete Society, *Permeability of Concrete and its Control,* pp. 69–76 (12 Dec., 1985)

33. Richardson, Mark, G., The Carbonation of Concrete in the Context of Irish Materials and Environments, *Proceedings, 4th Conference of the Irish Durability and Fracture Committee,* IDFC4-1986, pp. 45–57 (Sept., 1986)

34. Tveit, A., Moisture and Moisture Transfer in Porous Materials, *RILEM Bulletin,* 29:145–150 (Dec., 1965)

35. Hedenblad, G., Moisture Permeability of Mature Concrete, *Cement Mortar and Cement Paste,* Lund Institute of Technology (1993)

36. Collins, J. F., Jr., et al., Permeability of Concrete Mixtures, Part 1: Literature Review, *Civil Engineering for Practising and Design Engineers,* 5:579–638 (1986)

37. Buenfeld, N. R., and Newman, J. B., The Permeability of Concrete in a Marine Environment, *Magazine of Concrete Research,* 36(127):67–80, London (June, 1984)

38. Kumar, A., et al., Diffusion Through Concrete, *Concrete, Journal of the Concrete Society,* pp. 31–32, London (Jan., 1987)

39. McCurrich, L. H., Reduction in Permeability and Chloride Diffusion with Superplasticiser, *Concrete, Journal of the Concrete Society,* pp. 9–10 (Aug., 1986)

40. Lambert, P., Page, C. L., and Short, N. R., Diffusion of Chloride Ions in Hardened Cement Pastes Containing Pure Cement Minerals, The Chemistry and Chemistry Related Properties of Cement, (F. P. Glasser, ed.), *British Ceramic Proceedings,* 25:267–276 (1984)

41. Buenfeld, N. R., and Newman, G. B., Examination of Three Methods for Studying Ion Diffusion in Cement Pastes, Mortars and Concretes, *Materials and Structures,* 20:3–10 (1987)

42. Page, C. L., Short, N. R., and El Tarras, A., Diffusion of Chloride Ions in Hardened Cement Pastes, *Cement and Concrete Research,* 2(3):395–406 (1981)

@Seismicisolation

43. Poulsen, E., The Chloride Diffusion Characteristics of Concrete: Approximative Determination by Linear Regression Analysis, *Nordic Concrete Research, Publication No. 9,* pp. 124–133 (1990)

44. Feldman, R. F., Pore Structure, Permeability and Diffusivity as Related to Durability, Proceedings, Eighth International Congress on Chemistry of Cement, 1:336–356, Rio De Janiero, Brazil (1986)

45. AASHTO: Standard Method of Test for Resistance of Concrete to Chloride Ion Penetration, *AASHTO Designation T259-80,* American Association of State Highway and Transportation Officials, Washington, D.C. (1980)

46. Torrent, R. J., Ebensperger, L. and Gebauer, J., On Site Evaluation of the Permeability of the Covercrete—Possibilities and Limitations, *Third CANMET/ACI International Conference on Durability of Concrete,* (V. M. Malhotra, ed.), Supplementary Papers, pp. 697–714, Nice (1994)

47. Lamond, J. F., Chloride Induced Corrosion in Existing Concrete Bridges: a 5 year SHRP Research Program, *Third CANMET/ACI International Conference on Durability of Concrete,* (V. M. Malhotra, ed.), Supplementary papers, pp. 1–16, Nice (1994)

48. Page, C. L, Lambert, P., and Vassie, P. R. W., Investigation of Reinforcement Corrosion, I: The Pore Electrolyte Phase in Chloride Contaminated Concrete, *Materials and Structures,* 24:243–252 (1991)

49. Swamy, R. N., et al., Chloride Penetration into Concrete Incorporating Mineral Admixtures or Protected with Surface Coating Material under Chloride Environments, *Concrete under Severe Conditions, Environment and Loading,* CONSEC-95, (K. Sakai, N. Banthia, and O. E. Gjorv, eds.), 2:935–944, E. & F. N. Spon, Sapporo, Japan (1995)

50. Whiting, D., In-Situ Measurement of the Permeability of Concrete to Chloride Ions, *SP 82, In-Situ/Non-Destructive Testing of Concrete,* CANMET, ACI, pp. 501–524 (1984)

51. Andrade, C., Calculation of Chloride Diffusion Coefficients in Concrete from Ionic Migration Measurements, *Cement and Concrete Research,* 23:724–742 (1993)

52. Tang, L., and Nilsson, L.O., Rapid Determination of the Chloride Diffusivity in Concrete by Applying an Electric Field, *ACI Materials Journal,* 89(1):49–53 (Jan.–Feb., 1992)

53. Gjorv, O. E. and Sakai, K., Testing of Chloride Diffusivity for Concrete, Concrete under Severe Conditions, Environment and Loading, *CONSEC-95,* (K. Sakai, N. Banthia, and O. E. Gjorv, eds.), Vol. 2, E. and F. N. Spon., Sapporo, Japan (1995)

54. Andrade, C., San Juan, M. A., and Alonso, C., Measurement of Chloride Diffusion Coefficient from Migration Tests, Paper 319, Corrosion 93, The NACE Annual Conference and Corrosion Show (1993)

@Seismicisolation

55. Zhang, T., and Gjorv, O. E., An Electrochemical Method for Accelerated Testing of Chloride Diffusivity in Concrete, *International RILEM Workshop, Chloride Penetration into Concrete*, October 15–18, Saint-Remy-les-Chevreuse, France (1995)

56. *RILEM Report 12, Performance Criteria for Concrete Durability,* (J. Kropp, and H. K. Hilsdorf, eds.), E. and F. N. SPON, 325 pp. (1995)

57. Whiting, D., Rapid Measurement of the Chloride Permeability of Concrete, *Public Roads*, 45(3):101–112 (1981)

58. *AASHTO Designation T277-83, Standard Method of Test for Rapid Determination of the Chloride Permeability of Concrete,* American Association of State Highway and Transportation Officials, Washington, D.C. (1983)

59. ASTM: Standard Test Method for Electrical Indication of Concrete's Ability to Resist Chloride Ion Penetration, ASTM C 1202-94, American Society for Testing and Materials, *1994 Book of ASTM Standards*, 04(02):620–625, Concrete and Aggregates, Philadelphia (1994)

60. Andrade, C., and Whiting, D., Comparison of AASHTO T-277 (Electrical) and AASHTO T-259 (90 day ponding) Results, Paper Presented at the RILEM International Workshop on Chloride Penetration into Concrete, October 15–18, Saint-Remy-les-Chevreuse, France (1995)

61. Streicher, P. E., and Alexander, M. G., A Chloride Conduction Test for Concrete, *Cement and Concrete Research*, 25(6):1284–1294 (1995)

62. Streicher, P. E., and Alexander, M. G., A Critical Evaluation of Chloride Diffusion Test Methods for Concrete, *Third ACI/CANMET International Conference on Durability of Concrete*, (V. M. Malhotra, ed.), Supplementary Papers, pp. 517–530, Nice (1994)

63. Tang, L., and Nilsson, L. O., Chloride Binding Isotherms—An Approach by Applying Modified BET Equation, Paper Presented at the RILEM International Workshop on Chloride Penetration into Concrete, October 15–18, Saint-Remy-les-Chevreuse, France (1995)

64. El-Belbol, S. M., and Buenfeld, N. R., Accelerated Chloride Ion Diffusion Test, Materials Research Society, *Symposium on Pore Structure and Permeability of Cementitious Materials*, 137:203–308, Boston (Nov., 1988)

65. Andrade, C., Alonso, C., and Acha, M., Chloride Diffusion Coefficient of Fly Ash Containing Concrete Calculated from Migration Tests, *Corrosion and Corrosion Protection of Steel in Concrete*, 1:783–793, (R. N. Swamy, ed.), Sheffield Academic Press (1994)

66. Arup, H., The Study of Transportation Mechanisms Using Migration Experiments, Some Caveats and Ideas for Future Research, *Chloride Penetration into Concrete Structures*, Nordic Mini-seminar, (L. O. Nilsson, ed.), pp. 36–42 (Jan., 1993)

@Seismicisolation

67. Dhir, R. K., et al., Rapid Estimation of Chloride Diffusion Coefficient in Concrete, *Magazine of Concrete Research,* 42(152):177–185 (Sept., 1990)
68. Oldham, K. B., and Myland, J. C., *Fundamentals of Electrochemical Science,* Academic Press, Inc. (1994)
69. Hall, C., Water Sorptivity of Mortars and Concretes: A Review, *Magazine of Concrete Research,* 41(147):51–61, London (June, 1989)
70. Hall, C., Water Movement in Porous Building Materials I: Unsaturated Flow Theory and its Application, *Building Environment,* 12:177–125 (1977)
71. Gowripalan, N., et al., Effect of Curing on Durability, *Concrete International,* ACI, pp. 47–54, Detroit (Feb., 1990)
72. ASTM, Standard Test Method for Specific Gravity, Absorption and Voids in Hardened Concrete, ASTM C 642-82, *Annual Book of ASTM Standards,* pp. 310–311, Philadelphia (1989)
73. Ben-Bassat, M, et al., The Effect of Differences in the Composition of Portland Cement on the Properties of Hardened Concrete, *Magazine of Concrete Research,* 42(151):59–66, London (June, 1990)
74. British Standards Institution, Testing Concrete, BS 188, Part 122: Method for Determination of Water Absorption, London (1983)
75. Cooke, R. U., Laboratory Simulation of Salt Weathering Processes in Arid Environment, *Earth Surface Processes,* John Wiley & Sons Ltd., 4:347–359 (1979)
76. Hudec, Peter P., Durability of Rock as a Function of Grain Size, Pore Size, and Rate of Capillary Absorption of Water, *Journal of Materials in Civil Engineering,* ASCE, 1(1):3–9 (Feb., 1989)
77. Keene, P. W., Some Tests on the Durability of Concrete Mixes of Similar Compressive Strength, *Magazine of Concrete Research,* 13(37):3–12 (March, 1961)
78. Swiss Federal Laboratories for Materials Testing and Research, SIA 162/1, Test No. 5, Water Conductivity, Guidelines for Testing, (1989)
79. RILEM Tentative Recommendation No. 112, Absorption of Water by Capillarity, *Materials and Structures,* 7:295–297 (1974)
80. Potter, R., and Ho, D., Quality of Cover Concrete and its Influence on Durability, SP 100, *Katharine and Bryant Mather International Conference, Concrete Durability,* ACI, 1:423–445, Detroit (1987)
81. McCarter, W. J., Ezirim, H., and Emerson, M., Absorption of Water and Chloride into Concrete, *Magazine of Concrete Research,* 44(158):31–27 (March, 1992)
82. Ho, D. W. S., and Lewis, R. K., Water Penetration into Concrete—A Measure of Quality as Affected by Material Composition and Environment, *Symposium on Concrete, The Materials for Tomorrow's Demand,* pp. 37–40 (1983)

@Seismicisolation

83. Glanville, W. H., The Permeability of Portland Cement Concrete, Building Research Establishment, Technical Paper, No. 3 (1931)

84. Levy, M., The Permeability and Absorption of Precast Concrete Products Part 1, Concrete, *Journal of the Concrete Society*, 55:88–90, London (Jan., 1960)

85. Levy, M., The Permeability and Absorption of Precast Concrete Products Part 2, Concrete, *Journal of the Concrete Society*, 55:248–251, London (Feb., 1960)

86. Levitt, M., In-Situ Permeability of Concrete, Developments in Testing Concrete for Durability, Tara Hotel, *Proceedings, The Concrete Society*, London (26 Sept., 1984)

87. British Standards Institution, Methods of Testing Concrete, BS 1881: Part 5: *Methods of Testing Hardened Concrete for Other than Strength*, London (1970)

88. British Standards Institution, Methods of Testing Concrete, BS188: Part 208 (1996)

89. Basheer, P. A. M., Long, A. E., and Montgomery, F. R.; "Clam" Tests for Measuring In-Situ Permeation Properties of Concrete, *Non-Destructive Testing and Evaluation International*, 12:53–73 (1995)

90. Meyer, A., The Importance of the Surface Layer for the Durability of Concrete Structures, SP 100, *Katharine and Bryant Mather International Conference, Concrete Durability*, ACI, pp. 48–61 (1987)

91. Soroka, I., et al., Permeability of Lightweight-Aggregate Concrete, Proceedings, *Second International CIB/RILEM Symposium on Moisture Problems in Buildings*, 11, pp. 10–12, Bouwcentrum, Rotterdam, Netherlands (Sept., 1974)

92. Farahbakhsh, Behnam, *Permeability Studies of Concrete*, M.Sc. Thesis, Department of Civil & Structural Eng., UMIST, Manchester (Feb., 1989)

93. Bamforth, P. B., et al., *Nondestructive Testing on a New and In-Place Concrete*, Conference Organized by the Institution of Civil Engineers in Cooperation with US Strategic Highway Research Program, Tara Hotel, London, pp. 29–31 (Oct., 1990)

94. Price, W. F., and Bamforth, P. B., Initial Surface Absorption of Concrete: Examination of Modified Test Apparatus for Obtaining Uniaxial Absorption, *Magazine of Concrete Research*, 45(162):17–24 (March, 1993)

95. Nolan, E. A., *Influence of Near Surface Moisture Gradients in Concrete on 'Autoclam' Permeation Measurements*, PhD. Thesis, The Queen's University of Belfast, U.K. (Oct., 1996)

96. Bungey, J. H., Millard, S. G., and Ghassemi, M. H., Environmental Effects on Surface Measurements, Proceedings, *Third International Conference on Deterioration and Repair of Reinforced Concrete Structures in the Arabian Gulf*, 1:443–457 (1989)

@Seismicisolation

97. Gummerson, R. J., Hall, C., and Hoff, W. D., Capillary Water Transport in Masonry Structures, *Building Applications of Darcy's Law*, *Construction Papers,* 1(1):17–27 (1980)

98. Dhir. R. K., et al., Near Surface Characteristics of Concrete: Assessment and Development of In-Situ Test Methods, *Magazine of Concrete Research,* 39(141):183–195, London (Dec., 1987)

99. Basheer, P. A. M., Long, A. E., and Montgomery, F. R.; The Autoclam—A New Test for Permeability, Concrete, *Journal of the Concrete Society,* pp 27–29 (July/Aug., 1994)

100. Basheer, P. A. M., A Brief Review of Methods for Measuring the Permeation Properties of Concrete In-Situ, Buildings and Structures, *Institution of Civil Engineers,* 99(1):74-83 (Feb., 1993)

101. Figg, J. W., Methods of Measuring the Air and Water Permeability of Concrete, *Magazine of Concrete Research,* 25(85):213–219, London (Dec., 1973)

102. Cather, R., et al., Improvements to the Figg Method for Determining the Air Permeability of Concrete, *Magazine of Concrete Research,* 36(129):241–245, London (Dec., 1984)

103. Pihlajavaara, S. E., and Paroll, H., On the Correlation Between Permeability Properties and Strength of Concrete, *Cement and Concrete Research,* 5:321–328 (1975)

104. Arup Research and Development, Figg Method for Measuring the Air Permeability of Hardened Concrete, *Test Kit Operation Manual,* 14086/JF13/CW, Arup Research and Development, London (Feb., 1987)

105. Nyame, B. K., and Illston, J. M., Relationship Between Permeability and Pore Structure of Hardened Cement Paste, *Magazine of Concrete Research,* 33(116):139–146 (Sept., 1981)

106. Goto, Seishi, and Roy, Della M., The Effect of W/C Ratio and Curing Temperature on the Permeability of Hardened Cement Paste, *Cement & Concrete Research,* 11:575–579 (1981)

107. Hanaor, Ariel, Testing of Concrete Specimens for Permeability at Cryogenic Temperatures, *Magazine of Concrete Research,* 34(120):155–161 (Sept., 1982)

108. Mills, R., Mass Transfer of Gas and Water Through Concrete, SP 100, *Katharine and Bryant Mather International Conference,* Concrete Durability, ACI, pp. 621–644 (1987)

109. Perraton, D., et al., Permeabilities of Silica Fume Concrete, *Permeability of Concrete, ACI SP-108,* pp 63–84, Detroit (1988)

110. Dhir, R. K., et al., Near-Surface Characteristics of Concrete: Prediction of Carbonation Resistance, *Magazine of Concrete Research,* 41(148):137–143, London (Sept., 1989)

@Seismicisolation

111. Arnold, S. R., and Littleton, I., Investigation into the Relationship Between Aggregate Absorption and the Permeability of Concrete, Dept. of Civil Engineering, RMCS, Shrivenham, Technical Note, *Materials and Structures/12*, (May, 1983)

112. Lawrence, C. D., Permeability and Protection of Reinforced Concrete, Cement and Concrete Association, Reprint 6/86, *Paper Presented at the Symposium 'Concrete Structures—The Need for Protection*, Wakefield (5 Dec., 1984)

113. American Petroleum Institute, *Recommended Practice for Determining Permeability of Porous Media*,, RP 27, 3rd Edition, API, Dallas (1952)

114. Indian Standards Institution, *Indian Standard IS 2645: 1975*, Specification of Integral Cement Water Proofing Compounds, New Delhi (1975)

115. Hooton, D., and Wakeley, L. D., Influence of Test Conditions on Water Permeability of Concrete in a Triaxial Cell, *Materials Research Society Symposium Proceedings*, Vol. 137, (L. R. Roberts, and J. P. Skanly, eds.), pp. 157–164 (1988)

116. Hope, Brian B., and Malhotra, V. Mohan, The Measurement of Concrete Permeability, *Canadian Journal of Civil Engineering*, 11:287–292 (1984)

117. *International Standards Organization, ISO/DIS 7032*, Concrete Hardened—Determination of Permeability, Draft International Standard (Based on RILEM Tentative Recommendation CPC 13.2), Geneva (1983)

118. Montgomery, F. R., and Adams, Alison, Early Experience with a New Concrete Permeability Apparatus, *Proceedings, Second International Conference of Structural Faults and Repair*, Engineering Technic Press, pp. 359–363, Edinburgh (1985)

119. Baluch, M. H., et al., Concrete Deterioration Due to Thermal Incompatibility of its Components, *Journal of Materials in Civil Engineering*, American Society of Civil Engineers, 1(3):105–119, (Aug., 1989)

120. Murata, J., Studies on the Permeability of Concrete, *RILEM Bulletin, No. 29*, pp. 47–54, (Dec., 1965)

121. Valenta, Oldrich, The Permeability and the Durability of Concrete in Aggressive Conditions, Proceedings, *10th International Congress on Large Dams*, pp. 103–117, Montreal (1970)

122. Valenta, O., Durability of Concrete—in Prague, 2nd RILEM Symposium, *RILEM Bulletin, Materiauz et Constructions*, 3(17):333–345 (1970)

123. Deutsches Institut Fur Normung ev. (DIN), *Test Methods for Concrete*, DIN 1048 (1978)

@Seismicisolation

124. International Standards Organization, ISO/DIS 7031, *Concrete Hardened—Determination of the Depth of Penetration of Water Under Pressure,* (Based on RILEM Tentative Recommendation 13.1), p.5, Geneva (1983)

125. Browne, R. D., and Domone, P. L., Permeability and Fatigue Properties of Structural Marine Concrete at Continental Shelf Depths, *Proceedings of International Conference on Underwater Construction Technology,* University College, Cardiff, p. 39 (April, 1975)

126. ASTM, Standard Test Method for Permeability of Rocks by Flowing Air, ASTM D 4525-85, *Annual Book of ASTM Standards,* Philadelphia, p. 7 (1989)

127. Cabrera, J. G., et al., Porosity and Permeability as Indicators of Concrete Performance, Durability of Concrete, *IABSE Symposium,* 57(1):249–254, Lisbon (Sept., 1989)

128. Hong, Chen Zhang, and Parrott, L. J., Air Permeability of Cover Concrete and the Effect of Curing, *Report, Cement and Concrete Association,* London (Oct., 1989)

129. Klinkenberg, L. J., The Permeability of Porous Media to Liquids and Gases, *Drilling and Production Practice, American Petroleum Institute,* pp. 200–214, New York (1941)

130. Concrete International, *Concrete Testing, Advertisement,* p. 98, Detroit (Dec., 1989)

131. Reinhardt, H. W., and Mijnsbergen, J. P. G., In-Situ Measurement of Permeability of Concrete Cover by Overpressure, T*he Life of Structures, Physical Testing,* pp. 243–250, Butterworths, London (1989)

132. Hilsdorf, Hubert K., Durability of Concrete—A Measurable Quantity, *Durability of Structures, IABSE Symposium,* 57(1):111–123, Lisbon (Sept., 1989)

133. National Research Council, Surface Air Flow Permeability Indicator, *Strategic Highway Research Programme (SHRP), Project C-101,* NRC, Information Leaflet (1991)

134. Torrent, R. J., A Two-Chamber Vacuum Cell for Measuring the Coefficient of Permeability to Air of the Concrete Cover on Site, *Materials and Structures,* 25:358–365 (1992)

135. Hansen, Anker Jon, et al., Gas Permeability of Concrete In-Situ: Theory and Practice, In-Situ/Non-Destructive Testing of Concrete, *ACI SP-82, Proceedings of International Conference,* pp. 543–556 (1984)

136. Lydon, F. D., and Al Odaallah, M., On-Surface Relative Permeability Test for Concrete, *Construction and Building Materials,* 2(2):102–105 (1988)

@Seismicisolation

137. ACI Committee 201, Guide to Durable Concrete, *American Concrete Institute, Report of ACI Committee 201,* ACI 201.2R-77, Detroit (1982)

138. Basheer, P. A. M., Long, A. E., and Montgomery, F. R., An Interaction Model for Causes of Deterioration of Concrete,*Malhotra Symposium on Concrete Technology,* American Concrete Institute, SP 144, pp. 213–233, San Francisco (21–25 March, 1994)

139. Basheer, P. A. M., 'Clam' Permeability Tests for Assessing the Durability of Concrete *PhD. Thesis, The Queen's University of Belfast,* U.K., (May, 1991)

140. Long, A. E., Basheer, P. A. M.,, and Montgomery, F. R., In-Situ Permeability Testing—A Basis for Service Life Prediction,*Advances in Concrete Technology, Proceedings,* CANMET/ACI International Conference, SP 171, pp. 651–670, New Zeland (1997)

141. Basheer, L., Assessment of the Durability Characteristics of Surface Treated Concrete, *PhD Thesis, The Queen's University of Belfast,* U.K. (Dec., 1994)

142. Basheer, L., and Cleland, D. J., Surface Treatments for Concrete Quantifying the Improvement, *Proceedings IABSE Symposium,* pp. 275–280, San Francisco (1995)

143. Basheer, P. A. M., Montgomery, F. R., and Long, A. E., In-Situ Assessment of Durability of Concrete Motorway Bridges,*G. M. Idorn International Symposium, Durability of Concrete,* American Concrete Institute, SP 131, pp. 305–311, Toronto (1990)

@Seismicisolation

17

NDT Techniques

V. M. Malhotra

1.0 INTRODUCTION

In the inspection and testing of concrete, the use of nondestructive testing (NDT) is relatively new. The slow development of these testing methods for concrete is due to the fact that, unlike steel, concrete is a highly non-homogenous composite material and most concrete is produced in ready-mixed plants and delivered to the construction site. The in-place concrete is, by its very nature and construction methods, highly variable and does not lend itself to testing by traditional NDT methods as easily as steel products.

Notwithstanding the above, there has been considerable progress in the development of NDT methods for testing concrete in recent years. A number of these methods have been standardized by the American Society for Testing and Materials (ASTM), the International Standards Organization (ISO), and the British Standards Institute (BSI).

The nondestructive tests may be subdivided into two main types. The first type includes those identified as sonic and pulse velocity tests, which involve the determination of the resonant frequency and the measurement of the velocity of a compressional pulse travelling through the concrete. Also included in this category are stress wave tests for locating the flaws or discontinuities that may be present or measuring thickness of concrete. The second type includes those tests which are used to estimate strength properties and include the surface hardness, penetration, pullout, break off,

@Seismicisolation

maturity, pull-off, and combined methods. Some of these methods are not truly nondestructive because they cause some surface damage which is generally insignificant.

2.0 RESONANT AND PULSE VELOCITY METHODS

2.1 Resonant Frequency Methods

Natural frequency of vibration is a dynamic property of an elastic system and is primarily related to the dynamic modulus of elasticity and density in the case of a vibrating beam; therefore, the natural frequency of vibration of a beam can be used to determine its dynamic modulus of elasticity. Although the relationship between the above two is valid for homogenous solid media which are isotropic and perfectly elastic, they may be applied to concrete when the size of a specimen is large in relation to the size of its constituent materials.

For flexural vibrations of a long, thin unrestrained rod, the following equation or its equivalent may be found in any complete textbook on sound:[1]

Eq. (1) $$N = \frac{m^2 k}{2\pi L^2}\sqrt{\frac{E}{\rho}}$$

and solving for E:

Eq. (2) $$E = \frac{4\pi^2 L^4 N^2 \rho}{m^4 k^2}$$

where: E = dynamic modulus of elasticity
ρ = density of the material
L = length of the specimen
N = fundamental flexural frequency
k = radius of gyration of the section about an axis perpendicular to the plane of bending ($k = t/\sqrt{12}$ for rectangular cross section where t = thickness)
m = a constant (4.73 for the fundamental mode of vibration)

@Seismicisolation

The dynamic modulus of elasticity can also be computed from the fundamental longitudinal frequency of vibration of an unrestrained specimen, according to the following equation:[2]

Eq. (3) $$E = 4L^2\rho N^2$$

Equations (1) and (3) were obtained by solving the respective differential equations for the motion of a bar vibrating: *(i)* in flexure in the free-free mode, and *(ii)* in the longitudinal mode.

Thus, the resonant frequency of vibration of a concrete specimen directly relates to its dynamic modulus of elasticity. If the concrete undergoes degradation, the modulus of elasticity will be altered and so will the resonant frequency of the specimen, therefore, monitoring the change in resonant frequency allows one to infer changes in the integrity of concrete.

The resonant frequency method was first developed by Powers[3] in the U.S. in 1938. He determined the resonant frequency by matching the musical tone created by concrete specimens, usually 51 × 51 × 241 mm prisms, when tapped by a hammer, with the tone created by one of a set of orchestra bells calibrated according to frequency. The error likely to occur in matching the frequency of the concrete specimens to the calibrated bells was of the order of 3%. The shortcomings of this approach, such as the subjective nature of the test, are obvious, but this method laid the groundwork for the subsequent development of more sophisticated methods.

In 1939 Hornibrook[4] refined the method by using electronic equipment to measure resonant frequency. Other early investigations on the development of this method included those by Thomson[5] in 1940, by Obert and Duvall[2] in 1941, and by Stanton[6] in 1944. In all the tests that followed the work of Hornibrook, the specimens were excited by a vibrating force. Resonance was indicated by the attainment of vibrations having maximum amplitude as the driving frequency was changed. The resonant frequency was read accurately from the graduated scale of the variable driving audio oscillator. The equipment is usually known as a *sonometer* and the technique is known as *forced resonance*.

The forced resonance testing apparatus as described in ASTM C 215, *Standard Test Method for Fundamental, Transverse, Longitudinal, and Torsional Frequencies of Concrete Specimens* consists primarily of two sections, one generates mechanical vibrations and the other senses these vibrations.[7]–[9] The principal part of the vibration generation section is an electronic audio-frequency oscillator which generates audio-frequency voltages. The oscillator output is amplified and fed to the driver unit for conversion into mechanical vibrations.

@Seismicisolation

In performing resonant frequency tests it is helpful to have an estimate of the expected fundamental frequency. Approximate ranges of fundamental longitudinal and flexural resonant frequencies of standard concrete specimens have been given by Jones.[10]

Calculation of Dynamic Moduli of Elasticity and Rigidity and Poisson's Ratio. The dynamic moduli of elasticity and rigidity (or shear modulus of elasticity) and the Poisson's ratio of the concrete can be calculated by equations given in ASTM C 215. These are modifications of theoretical equations applicable to specimens that are very long in relation to their cross section and were developed and verified by Pickett,[11] and Spinner and Tefft.[12] The corrections to the theoretical equations involve Poisson's ratio and are considerably greater for transverse resonant frequency than for longitudinal resonant frequency. For example, a standard 102 × 102 × 241 mm prism requires a correction factor of about 27% at fundamental transverse resonance as compared with less than 0.5% at fundamental longitudinal resonance.[13] The longitudinal and flexural modes of vibration give nearly the same value for the dynamic modulus of elasticity. The dynamic modulus of elasticity may range from 14.0 GPa for low quality concretes at early ages, to 48.0 GPa for good quality concrete at later ages.[14] The dynamic modulus of rigidity is about 40% of the modulus of elasticity.[15] It should be mentioned that more input energy is needed for longitudinal resonance and, therefore, transverse resonance made is used more often in laboratory investigations. Gaidis and Rosenberg[16] have published a new method for determining the fundamental frequencies.

Damping Properties of Concrete. *Damping* is the property of a material causing free vibrations in a specimen to decrease in amplitude as a function of time. Several investigators, particularly Thomson,[5] Obert and Duvall,[2] Kesler and Higuchi,[17] Shrivastava and Sen,[18] and Swamy and Rigby,[15] have shown that certain properties of concrete can be related to its damping ability.

Factors Affecting Resonant Frequency and Dynamic Modulus of Elasticity. Several factors influence the resonant frequency measurements, the dynamic modulus of elasticity, or both. These include the influence of mixture proportions and properties of aggregates, specimen size effect, and the influence of curing conditions. These have been discussed in detail elsewhere.[19]

Limitations and Usefulness of Resonant Frequency Methods. Although the basic equipment and testing procedures associated with the resonant frequency techniques have been standardized in various countries,

@Seismicisolation

and commercial testing equipment is easily available, the usefulness of the tests is seriously limited because:

1. Generally, these tests are carried out on small-sized specimens in a laboratory rather than on structural members in the field, because resonant frequency is affected considerably by boundary conditions and the properties of concrete. The size of specimens in these tests is usually 152 × 241 mm cylinders or 76 × 76 x 241 mm prisms.
2. The equations for the calculation of dynamic elastic modulus involve *shape factor corrections.* This necessarily limits the shape of the specimens to cylinders or prisms. Any deviation from the standard shapes can render the application of shape factor corrections rather complex.

Notwithstanding the above limitations, the resonance tests provide an excellent means for studying the deterioration of concrete specimens subjected to repeated cycles of freezing and thawing and to deterioration due to aggressive media. The use of resonance tests in the determination of damage by fire and the deterioration due to alkali-aggregate reaction have also been reported by Chefdeville,[20] and Swamy and Al-Asali.[21]

The resonant frequency test results are often used to calculate the dynamic modulus of elasticity of concrete, but the values obtained are somewhat higher than those obtained with standard static tests carried out at lower rates of loading and to higher strain levels. The use of dynamic modulus of elasticity of concrete in design calculations is not recommended.

2.2 Pulse Velocity Method

The application of pulse transmission techniques to the testing of concrete is believed to have had its origin with Obert.[22] Tests were made on concrete replacement pillars in mines and involved the use of two geophones, two high-gain amplifiers, and a camera with a moving film strip. Two holes, approximately 6.09 m (20 ft.) apart vertically, were drilled into the pillars. The geophones were placed in the backs of the holes and the holes filled with cotton waste. A hammer blow was struck at the base of the pillar and at the same time the camera lens was opened and the moving film strip exposed. After the film was developed, the transit time of the impulse in travelling from one geophone to the other was determined by measuring the distance between

@Seismicisolation

the two signals on the film, the speed of motion of the film having been controlled carefully. The velocity of the stress pulse could then be calculated.

Long and Kurtz[23] reported performing somewhat similar experiments with a seismograph in which the longitudinal velocity of the stress pulse created by a single impact was measured between arbitrarily placed geophones. They stated that only very limited experiments of this nature had been conducted, but the method appeared to hold great promise providing the apparatus could be adapted to measure much shorter time intervals than could be measured with the seismograph.

Long, et al.,[24] undertook further investigations along these lines and in 1945 reported on the instrument and technique that resulted from their work.

Subsequent investigations in North America and Europe have resulted in the development of a number of other devices quite similar in most respects. These include the Micro-timer developed by the U.S. Bureau of Reclamation, and the Condenser Chronograph developed by the Danish National Institute of Building Research.

In 1946 the Hydro-Electric Power Commission of Ontario, Canada, in an effort to develop a technique for examining cracks in monolithic concrete structures, began a series of studies which resulted in the construction of an instrument known as the Soniscope. The device, developed by Leslie and Cheesman,[25] consists basically of a stress transmitter using piezoelectric crystals, a similar pulse receiver, and electronic circuits which actuate the pulse transmitter, provide visual presentation of transmitted and received signals on a cathode-ray tube, and accurately measure the time interval between the two.

The instrument was used extensively in Canada[25][26] and the United States.[27]

During approximately the same time that the Soniscope was being developed in Canada and the United States, work of a similar nature was being conducted in England. These investigations resulted in the development of an instrument known as the Ultrasonic Concrete Tester. This instrument and its applications have been described at length by Jones.[28][29]

In recent years, portable, battery powered ultrasonic testing units have become available worldwide. One of the units available in the U.S. is called the V-Meter.[12]*

*This is the same unit which is manufactured in England and is known as PUNDIT.

@Seismicisolation

Whereas the use of the resonant frequency tests has been restricted primarily to the evaluation of specimens undergoing natural or artificial weathering, pulse velocity techniques have been applied to concrete for many purposes and, in most areas of investigation, only limited agreement has been reached concerning the significance of test results. The quantity measured by all of these instruments is the travel time of stress pulses passing through the concrete under test. If the path length between transmitter and receiver is known, or can be determined, the velocity of the pulse can be computed. It is in the interpretation of the meaning of this velocity and in its use for determining various properties of concrete that agreement is incomplete. The technique is as applicable to in-place concrete as to laboratory-type specimens and results appear to be unaffected by the size and shape of the concrete tested, within the limits of transmission of the instrument employed, provided care is taken when testing very small specimens. This, of course, is a highly desirable attribute and, in many respects, makes the pulse velocity techniques more useful than those involved in resonant frequency testing.

The use of pulse velocity techniques has been suggested for evaluating the strength of concrete, its uniformity, its setting characteristics, its modulus of elasticity, and the presence or absence of cracks within the concrete.[30] There appears to be little question of the suitability of such techniques to determine the presence, and to some extent the magnitude, of cracks in concrete although it has been suggested that if the cracks are fully water-filled, their locations may be more difficult to ascertain. In all of the other fields of investigation, independent investigators have reported widely different degrees of success through the use of these techniques.[26]

Recently Sturrup, et al.,[31] have published data dealing with the experiences of Ontario Hydro, Toronto, in the use of pulse velocity for strength evaluation.

It is generally agreed that very high velocities (> 4570 m/s) are indicative of very good concrete and that very low velocities (< 3050 m/s) are indicative of poor concrete. It is further agreed that periodic, systematic changes in velocity are indicative of similar changes in the quality of the concrete. Beyond these areas of agreement, however, it appears that the investigator must have a rather intimate knowledge of the concrete involved before attempting to interpret velocities as measures of strength or other properties of the concrete. This is particularly true if the aggregate involved is a lightweight aggregate.

@Seismicisolation

2.3 Stress Wave Propagation Methods

In recent years, considerable research has been undertaken in Canada[32] by CANMET and in the U.S.A.[33][34] by NIST to develop methods to determine flaws and discontinuities in concrete. These methods are classified as *stress wave propagation* methods and the common feature of the various methods under development is that stress waves are introduced into concrete and their surface response is monitored using a receiving transducer connected to a digital data acquisition system capable of performing frequency analysis. One of the most attractive features of the stress wave propagation methods is that access to only one surface of concrete is required.

3.0 SURFACE HARDNESS METHODS

The increase in the hardness of concrete with age and strength has led to the development of test methods to measure this property. These methods consist of the indentation type and those based on the rebound principle. The indentation methods consist principally of impacting the surface of concrete by means of a given mass having a given kinetic energy and measuring the width and/or depth of the resulting indentation. The methods based on the rebound principle consist of measuring the rebound of a spring-driven hammer mass after its impact with concrete.

3.1 Rebound Method

In 1948 a Swiss engineer, Ernst Schmidt,[35]–[37] developed a test hammer for measuring the hardness of concrete by the rebound principle. The Schmidt rebound hammer is principally a surface hardness tester with little apparent theoretical relationship between the strength of concrete and the rebound number of the hammer. However, within limits, empirical correlations have been established between strength properties and the rebound number. Further, Kolek[38] has attempted to establish a correlation between the hammer rebound number and the hardness as measured by the Brinell method.

Description. The Schmidt rebound hammer weighs about 1.8 kg and is suitable for use both in a laboratory and in the field. The main components include the outer body, the plunger, the hammer mass, and the main spring.

@Seismicisolation

Other features include a latching mechanism that locks the hammer mass to the plunger rod and a sliding rider to measure the rebound of the hammer mass. The rebound distance is measured on an arbitrary scale marked from 10 to 100. The rebound distance is recorded as a *rebound number* corresponding to the position of the rider on the scale.

Method of Testing. To prepare the instrument for a test, the plunger is released from its locked position by pushing the plunger against the concrete and slowly moving the body away from the concrete. This causes the plunger to extend from the body and the latch engages the hammer mass to the plunger rod. The plunger is then held perpendicular to the concrete surface and slowly the body is pushed towards the test object. As the body is pushed, the main spring connecting the hammer mass to the body is stretched. When the body is pushed to the limit, the latch is automatically released and the energy stored in the spring propels the hammer mass toward the plunger tip. The mass impacts the shoulder of the plunger rod and rebounds. During rebound, the slide indicator travels with the hammer mass and records the rebound distance. A button on the side of the body is pushed to lock the plunger in the retracted position, and the rebound number is read from the scale.

The test can be conducted horizontally, vertically, upward or downward, or at any intermediate angle. Due to different effects of gravity on the rebound as the test angle is changed, the rebound number will be different for the same concrete and require separate calibration or correlation charts.[39]–[41]

Correlation with Strength. Although the rebound hammer provides a quick, inexpensive means of checking the uniformity of concrete, it has serious limitations and these must be recognized. The results of the Schmidt rebound hammer test are affected by:

1. Smoothness of test surface.
2. Size, shape, and rigidity of the specimens.
3. Age of test specimen.
4. Surface and internal moisture conditions of the concrete.
5. Type of coarse aggregate.
6. Type of cement (portland, high alumina, super sulfated).
7. Type of mold.
8. Carbonation of the concrete surface.

@Seismicisolation

These limitations are discussed in detail elsewhere (see Ref. 19).

To gain a basic understanding of the complex phenomena involved in the rebound test, Akashi and Amasaki[42] have studied the stress waves in the plunger of a rebound hammer at the time of impact.

According to many researchers[38]–[40][43] there is a general correlation between compressive strength of concrete and the hammer rebound number; however, there is a wide degree of disagreement among various researchers concerning the accuracy of the estimation of strength from the rebound readings and the empirical relationship. Coefficients of variation for estimated compressive strength for a wide variety of specimens averaged 18.8% and exceeded 30% for some groups of specimens. The large deviations in strength can be narrowed down considerably by developing a proper correlation curve for the hammer, which allows for various variables discussed earlier. By consensus, the accuracy of estimation of compressive strength of test specimens cast, cured, and tested under laboratory conditions by a properly calibrated hammer, lies between ±15 and ±20%; however, the probably accuracy of estimation of concrete strength in a structure is ±25%.

Greene[44] and Klieger, et al.,[45] have established correlation relationships between the flexural strength of concrete and the hammer rebound number.

Limitations. The limitations of the Schmidt hammer should be recognized and taken into account when using the hammer. It cannot be over stressed that the hammer must not be regarded as a substitute for standard compression tests, but as a method for determining the uniformity of concrete in the structures and comparing one concrete against another.

The rebound method has won considerable acceptance and standards have been issued both by the ASTM and ISO and by several other countries for determining the rebound number of concrete.

3.2 Probe Penetration Test

Penetration resistance methods are based on the determination of the depth of penetration of probes (steel rods or pins) into concrete. This provides a measure of the hardness or penetration resistance of the material that can be related to its strength.[19]

The measurement of concrete hardness by probing techniques was reported by Voellmy[46] in 1954. Apart from the data reported by Voellmy, there is little other published work available on these tests and they appear to have received little acceptance in Europe or elsewhere. Perhaps the

@Seismicisolation

introduction of the rebound method around 1950 was one of the reasons for the failure of the above tests to achieve general acceptance.[19]

In the 1960s the Windsor probe test system was introduced in North America and this was followed by a pin penetration test in the 1980s.

The Windsor probe test system was advanced for penetration testing of concrete in the laboratory as well as in-situ. The device was meant to estimate the quality and compressive strength of in-situ concrete by measuring the depth of penetration of probes driven into the concrete by means of a powder-actuated driver. The development of this technique was closely related to studies reported by Kopf.[47] Results of the investigations carried out by the Port of New York Authority were presented by Cantor* in 1970. Meanwhile, a number of other organizations had initiated exploratory studies of this technique[48–50] and a few years later Arni[51][52] reported the results of a detailed investigation on the evaluation of the Windsor probe, while Malhotra[53]–[55] reported the results of his investigations on both 150 × 241 mm cylinders and 610 × 610 × 241 mm concrete slabs.

In 1972 Klotz[56] stated that extensive application of the Windsor probe test system had been made in investigations of in-place compressive strength of concrete and in determinations of concrete quality. The Windsor probe had been used to test reinforced concrete pipes, highway bridge piers, abutments, pavements, and concrete damaged by fire. In the 1970s, several U.S. federal agencies and state highway departments reported investigations on the assessment of the Windsor probe for in-situ testing of hardened concrete.[57]–[61] In 1984 Swamy and Al-Hamed,[62] in the U.K., published results of a study on the use of the Windsor probe system to estimate the in-situ strength of both lightweight and normal weight concretes.

Description of Test. The Windsor probe consists of a powder-actuated gun or driver, hardened alloy-steel probes, loaded cartridges, a depth gauge for measuring the penetration of probes, and other related equipment. The probes have a tip diameter of 6.3 mm, a length of 79.5 mm, and a conical point. Probes of 7.9 mm diameter are also available for the testing of lightweight aggregate concrete. The rear of the probe is threaded and screws into a probe-driving head, which is 12.7 mm in diameter and fits snugly into the bore of the driver. The probe is driven into the concrete by the firing of a precision powder charge.[8][19] For testing of relatively low-strength concrete, the power level can be reduced by pushing the driver head further into the barrel.

---

*Cantor, T. R., Status Report on Windsor Probe Test System presented at Highway Research Board Committee A2-03, Mechanical Properties of Concrete, 1970 Annual Meeting, Washington, D.C.

@SeismicIsolation

The method of testing is relatively simple and is given in ASTM C 803, Penetration Resistance of Hardened Concrete.

The manufacturer of the Windsor probe test system has published tables relating exposed length of the probe with compressive strength of concrete. For each exposed length value, different values for compressive strength are given, depending on the hardness of the aggregate as measured by the Mohs' scale of hardness. The tables are based on empirical relationships established in his laboratory; however, investigations carried out by Gaynor,[49] Arni,[51] Malhotra,[53]–[55] and several others,[50][58][64]–[66] indicate that the manufacturer's tables do not always give satisfactory results. Sometimes they considerably overestimate the actual strength and in other instances they underestimate the strength. It is, therefore, imperative for each user of the probe to correlate probe test results with the type of concrete being used. A practical procedure for developing such a relationship is described elsewhere.[63]

The probe penetrations relate to some strength parameter of the concrete below the surface which makes it possible to establish useful empirical relationships between the depth of penetration and compressive strength.

There appears to have been no systematic attempts to determine the relative influences of these factors that could affect the probe penetration tests results; however, it is generally agreed that the largest influence comes from the coarse aggregate. Apart from its hardness, the type and size of coarse aggregate used have been reported to have a significant effect on probe penetration.[51][62][65] The considerable differences shown in data tend to support the important influence of the aggregate type, however, other parameters, such as mixture proportions, moisture content, curing regime, and surface conditions, are likely to have affected these correlations to some extent and could explain some of the observed differences.

Variability is reported in terms of standard deviations and coefficients of variation with values in the latter case being calculated from the exposed length of the probe readings although more correctly they should be based on the embedded lengths of the probe. These data show that for concrete with a maximum aggregate size of 19 mm a typical value for the within-test coefficient of variation (based on depth of penetration) is about 5%.[67]

Probe Penetration Test vs. Core Testing. The determination of the strength of concrete in a structure may become necessary when standard cylinder strength test results fail to comply with specified values or the quality of the concrete is being questioned because of inadequate placing or curing procedures. It may also be required in the case of older structures where

@Seismicisolation

changes in the quality of the concrete must be investigated. In these instances the most direct and common method of determining the strength of concrete is through drilled core testing; however, some nondestructive techniques such as the probe penetration test have been gaining acceptance as a means to estimate the in-situ strength of concrete.[60][68][69]

It has been claimed that the probe penetration test is superior to core testing and should be considered as an alternative to the latter for estimating the compressive strength of concrete. It is true that the probe test can be carried out in a matter of minutes, whereas cores, if from exposed areas and if they have to be tested in accordance with ASTM C 42-87, must be soaked for 40 hours,[70] also, the cores may have to be transported to a testing laboratory, causing further delay in getting the results.

Advantages and Disadvantages of the Probe Penetration Test. The probe penetration test system is simple to operate, rugged, and needs little maintenance except for occasional cleaning of the gun barrel. The system has a number of built-in safety features that prevent accidental discharge of the probe from the gun, however, wearing of safety glasses is required. In the field, the probe penetration test offers the main advantages of speed and simplicity, and that of requiring only one surface for the test. Its correlation with concrete strength is affected by a relatively small number of variables which is an advantage over some other methods for in-situ strength testing; however, the probe test has limitations which must be recognized. These include minimum size requirements for the concrete member to be tested. The minimum acceptable distance from a test location to any edges of the concrete member or between two given test locations is of the order of 150 to 200 mm, while the minimum thickness of the members is about three times the expected depth of penetration. Distance from reinforcement can also have an effect on depth of probe penetration, especially when the distance is less than about 100 mm; the importance of aggregate type and aggregate content on the correlation is emphasized.[69]–[71]

3.3 Pin Penetration Test

In the late 1980s Nasser and Al-Manaseer[72][73] reported the development of a simple pin penetration test for the determination of early-age strength of concrete for removal of concrete form work. Briefly, this apparatus consists of a device which grips a pin having a length of 30.5 mm, a diameter of 3.56 mm and a tip machined at an angle of 22.5 degrees. The pin is held within a shaft which is encased within the main body of the tester.

@Seismicisolation

The pin is driven into the concrete by a spring which is mechanically compressed when the device is prepared for a test. The spring is reported to have a stiffness of 49.7 N/mm and stores about 10.3 Joules of energy when compressed.

When ready for testing, the apparatus is held against the surface of concrete to be tested, and a triggering device is used to release the spring, forcing the pin into the concrete. Following this, the apparatus is removed, and the small hole created in the concrete is cleared by means of an air blower. A depth gage is used to measure the penetration depth.[74]

4.0 PULLOUT TEST

A pullout test, by using a dynamometer and a reaction bearing ring, measures the force required to pullout from concrete a specially shaped insert whose enlarged end has been cast into the concrete. Because of its shape, the insert is pulled out with a cone of the concrete. The concrete is simultaneously in tension and in shear, the generating lines of the cone are defined by the key dimensions of the insert and bearing ring (Fig. 1). The pullout force is then related to compressive strength by means of a previously established relationship.

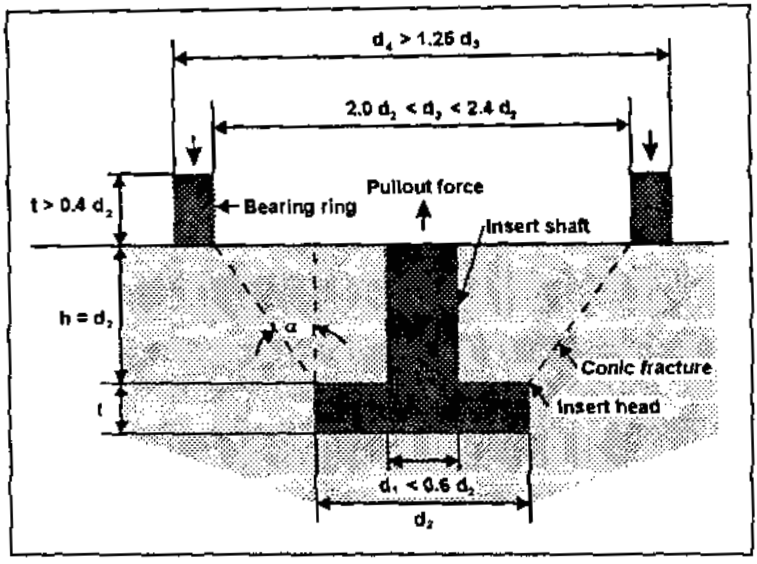


Figure 1. Schematic cross section of pullout test. *(From ASTM Standard C 900.)*

@Seismicisolation

The pullout techniques, though in use in the Union of Soviet Socialist Republics[75] since 1935, are relatively new elsewhere.[79][81] In 1944, Tremper,[76] in the United States, reported results of laboratory studies dealing with pullout tests covering strengths up to 35.2 MPa. In 1968, Tassios,[77] in Greece, reported the development of a nail pullout test.

In the 1970s Kierkegaard-Hansen,[78] in Denmark, and Richards,* in the U.S.A., have advocated the use of pullout tests on structural concrete members. A number of researchers including Malhotra,[79] Carino,[80] and others,[81] have published data dealing with laboratory studies and field testing. A pullout system, known as *LOK-Test*, based on Kierkegaard-Hansen's work is now available commercially.

The main advantage of the pullout test is it provides a direct measure of the in-situ strength of concrete. The method is relatively simple and testing can be done in the field in a matter of minutes.

A major disadvantage of the pullout test is that minor damage to the concrete surface must be repaired; however, if a pullout force corresponding to a given minimum strength is applied without failure, it may be assumed that a minimum strength has been reached in the concrete and the pullout insert need not be stressed to failure. Another disadvantage is that the standard pullout tests have to be planned in advance and, unlike other in-situ tests, cannot be performed at random after the concrete has hardened.

In order to overcome the second disadvantage mentioned, new techniques have been proposed. These include the CAPO test and the drilled-in pullout tests.[19] In the CAPO test, a hole is drilled into concrete and a special milling tool is used to undercut a 25 mm diameter slot at a depth of 25 mm. An expandable steel ring is placed into the hole and the ring is expanded into the slot using a special device. The entire assembly used to expand the ring is then pulled out of the concrete using the LOK test loading system; however, the test has found very limited acceptance because of the high variability associated with the test data in the field tests.[80] Variability may be reduced assuring a flat surface beneath the bearing ring.

The development of drilled-in pullout tests have been reported by the Building Research Establishment (BRE), U.K.,[82] and by Mailhot, et al.[83] In the BRE tests, an anchor bolt is placed in a hole drilled in hardened concrete and a pullout force is applied to cause failure in concrete. As with the CAPO test, there is a high degree of variability in the test results.

---

*Richards Owen, "Pull-Out Strength of Concrete," paper presented at the Research Session, annual meeting American Concrete Institute, Dallas, Texas, 1972.

@Seismicisolation

Another pullout method studied by Mailhot, et al.,[83] involved epoxy grouting a 16 mm long threaded rod to a depth of 38 mm in a 16 mm diameter hole. After the epoxy had cured, the rod was pulled out using a tension jack reacting against a bearing ring. Once again, the within-test variability was reported to be high.

5.0 BREAK-OFF METHOD

In 1979 Johansen[84] reported the development of a method to determine the in-situ strength of concrete. The method known as *break-off* has found some acceptance in the Scandinavian countries and has been standardized by ASTM as C 1150. Briefly, the test consists of breaking-off an in-situ cylindrical concrete specimen at a failure plane parallel to the finished surface of the concrete element. The break-off stress at failure is then related to the strength of concrete.

The principle of the break-off test is illustrated in Fig. 2. A plastic sleeve with an annular seating ring is inserted in fresh concrete to form a cylindrical test specimen and a counter bore. After the concrete has hardened, the sleeve is removed and a special loading mechanism is placed in the counter bore. A hand operated pump is used to generate a force at the uppermost section of the cylinder so as to break from the concrete mass. The test result is reported as a break-off number, which is the maximum pressure recorded by the gauge measuring the hydraulic pressure in the loading mechanism. In hardened concrete, in cases where the plastic sleeve has not been installed, a concrete coring machine with a specially shaped coring drill bit may be used to drill similarly shaped test specimens.

Carlsson, et al.,[85] Dahl-Jorgenson and Johansen,[86] and Naik,[87] investigated the use of the break-off test, and have published correlations between the break-off number and the compressive and flexural strength. Earlier investigations performed at CANMET had indicated that the test results obtained by this method had a high degree of variability, but according to Naik,[87] and others, the changes in the design of the equipment had overcome this problem.

@Seismicisolation

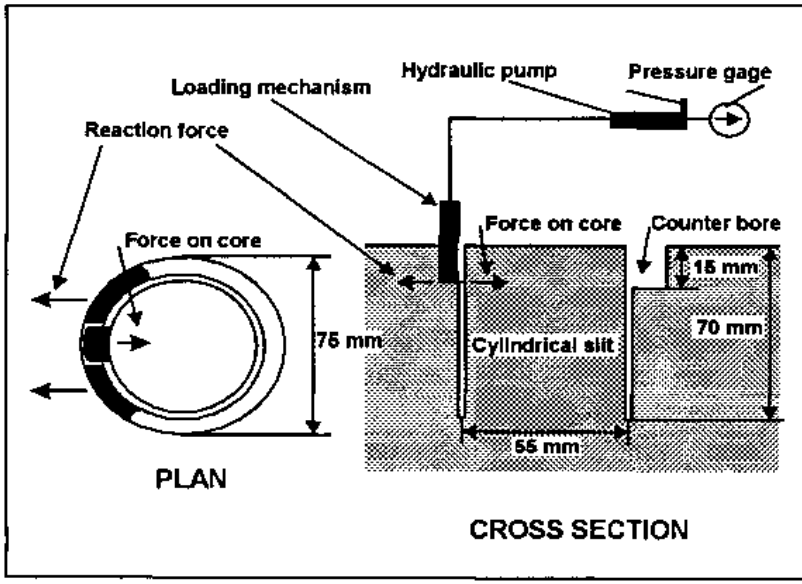


Figure 2. A schematic of the break-off method. *(From ASTM C 1150.)*

6.0 MATURITY METHOD

It is well known that the compressive strength of well-cured concrete increases with time, however, the increase in strength is governed by many factors other than curing time, the most important being the concrete temperature and the availability of moisture. The combined effect of time and temperature has been studied by several investigators since 1904, but no hypothesis was formulated in early years. Then, in the 1950s, the concept of maturity was advanced by McIntosh,[88] Nurse,[89] Saul,[90] and others,[91]–[94] and strength-maturity relationships were published. Maturity was defined as the product of time and temperature above a datum temperature of -10°C (14°F).

In 1956, Plowman[93] examined relationships between concrete strength and maturity and attempted to establish a rational basis for the datum temperature used for maturity to calculate the maturity index. He defined the datum temperature for maturity as the temperature at which the strength gain of hardened concrete ceases. From his investigations, Plowman concluded that the datum temperature was -12.2°C (10°F). These earlier studies have been extensively reviewed by Malhotra.[94]

@Seismicisolation

Maturity Functions. Maturity functions are mathematical expressions to convert the temperature history of concrete to an index indicative of its strength development.

The Nurse-Saul maturity function is as follows:

Eq. (4) $$M(t) = \sum (T_a - T_o)\Delta t$$

where: $M(t)$ = the temperature-time factor at age, t, degree-days or degree-hours

Δt = a time interval, days or hours

T_a = average concrete temperature during time interval, Δt, °C

T_o = datum temperature, °C.

It has been shown that the Nurse-Saul function does not accurately represent time-temperature effects because it is based on the assumption that the rate of strength development is a linear function of temperature.

In order to overcome some of the limitations of the Nurse-Saul maturity function, the maturity function proposed by Freiesleben Hansen and Pederson[95] can be used to compute equivalent-age at a specified temperature as follows:

Eq. (5) $$t_e = \sum e^{-\{Q\left[(1/T_a)-(1/T_s)\right]\}}\Delta t$$

where: t = equivalent age at a specified temperature, T_s, days or hours

Q = activation energy divided by the gas constant, °K

T_a = average temperature of concrete during time interval Δt, °K

T_s = specified temperature, °K

Δt = time interval, days or hours

This equation[7] is based on the Arrhenius equation which describes the influence of temperature on the rate of chemical reaction.

Byfors,[96] Naik,[97] and Carino,[98] have shown that the equivalent age maturity function based on the Arrhenius equation accounts better for the effects of temperature on strength gain and is applicable over a wider temperature range than the Nurse-Saul maturity function.

@Seismicisolation

One of the first engineering applications of the maturity method was by Swenson[99] in Canada who used it in forensic investigations to estimate the strength gain of concrete in structures.

The maturity method has been used to estimate the in-situ strength of concrete during construction. In the U.S.A. Hudson and Steele[100] used the maturity approach to predict potential strength of concrete based upon early-age tests. Their results have been incorporated into an ASTM Standard C 918, "Standard Test Method for Developing Early-Age Compression Test Values and Projecting Later-age Strengths." Malhotra[101] attempted to relate compressive strengths using accelerated-strength tests with the maturities for these tests.

The maturity of in-situ concrete can be monitored by thermocouples or by instruments called maturity meters. Basically, these maturity meters monitor and record the concrete temperature as a function of time using thermocouples or thermistors embedded in the fresh concrete and connected to strip-chart recorders or digital data recorders. The temperature-time factor or equivalent age is automatically computed and displayed. Also, disposable mini-maturity meters based on the Arrhenius equation have also become available.[98] These primarily consist of a glass tube containing a liquid which has an activation energy for evaporation that is similar to the activation energy for strength gain in concrete; the amount of evaporation from the capillary tube at a given time is indicative of strength development in the concrete.

7.0 PULL-OFF TESTS

In the mid 1970s, researchers in the U.K. developed a surface pull-off test to estimate the in-situ strength of concrete.[102] Although some test data have been published the test has found little acceptance outside the U.K.

Briefly, the pull-off test involves bonding a circular steel disc to the surface of the concrete under test by means of any epoxy resin. Prior to this bonding, sandpaper is used to abrade the surface of the concrete to remove laitance, followed by degreasing the surface using a suitable solvent. After the epoxy has cured, a tensile force is then applied to the steel disc. Because the tensile strength of the bond is greater than that of concrete, the latter fails in tension. From the area of the disc and the force applied at failure it is possible to obtain a measure of the tensile strength of concrete. The pull-off test is still in its infancy compared with other in-situ tests and as of 1992 has been standardized only in the U.K.

@Seismicisolation

8.0 COMBINED METHODS

In Europe, in general, and in Romania, in particular, the use of more than one in-situ/nondestructive testing technique to improve the accuracy of prediction of strength parameters of concrete has gained some credibility.[103][104] Some researchers have suggested the use of rebound hammer and pulse velocity techniques, while others have suggested the use of other combined methods. The proponents of this approach claim that the use of two methods, each measuring a different property, can overcome the limitation associated with the use of one method. Some case histories have been published supporting this claim; data disputing this claim are available also.

9.0 CONCLUDING REMARKS

Considerable progress has been made over the past two decades in the development and use of nondestructive methods for estimating strength of concrete. A number of these methods have been standardized by the ASTM, ISO, and other organizations, and several new methods are in the process of being standardized; however, research is needed to standardize those tests which determine properties other than strength. Radar scanning and impact/pulse echo techniques appear to be the most promising of these type of tests.

Unless comprehensive correlations have been established between the strength parameters to be predicted and the results of in-situ/nondestructive tests, the use of the latter to predict strength properties of concrete is not recommended.

ACKNOWLEDGMENT

This paper is based on a paper entitled *Nondestructive Tests*, by V. M. Malhotra, and published in the ASTM SP 169C, 1994.

@Seismicisolation

REFERENCES

1. Rayleigh, J. W., *Theory of Sound*, 2nd ed., Dover Press, New York (1945)
2. Obert, L., and Duvall, W. I., Discussion of Dynamic Methods of Testing Concrete with Suggestions for Standardization, *Proc. ASTM*, 41:1053 (1941)
3. Powers, T. C., Measuring Young's Modulus of Elasticity by Means of Sonic Vibrations, *Proc. ASTM*, 38, Part II, p. 460 (1938)
4. Hornibrook, F. B., Application of Sonic Method to Freezing and Thawing Studies of Concrete, ASTM Bull. No. 101, p. 5 (1939)
5. Thomson, W. T., Measuring Changes in Physical Properties of Concrete by the Dynamic Method, *Proc. ASTM*, 40:113, (1940). Also, discussion by T. F. Willis and M. E. de Reus, pp. 1123–1129
6. Stanton, T. E., Tests Comparing the Modulus of Elasticity of Portland Cement Concrete as Determined by the Dynamic (Sonic) and Compression (Secant at 1000 psi) Methods, ASTM Bull, No. 131, p. 17, (1944). Also, discussion by L. P. Witte and W. H. Price, pp. 20–22
7. Standard Test Method for Fundamental Transverse, Longitudinal, and Torsional Frequencies of Concrete Specimens, (ASTM C 215-91), *1992 Annual Book of ASTM Standards*, Vol. 04.02, American Society for Testing and Materials, Philadelphia
8. Malhotra, V. M., "Testing of Hardened Concrete: Nondestructive Methods," Monogr. No. 9, p. 52, American Concrete Institute, Detroit (1976)
9. Kesler, C. E. and Higuchi, Y., Problems in the Sonic Testing of Plain Concrete, Proc. Int. Symp. on Nondestructive Testing of Material and Structures, *RILEM*, 1:45, Paris (1954)
10. Jones, R., *Non-Destructive Testing of Concrete*, Cambridge University Press, London (1962)
11. Pickett, G., Equations for Computing Elastic Constants from Flexural and Torsional Resonant Frequencies of Vibration of Prisms and Cylinders, *Proc. ASTM*, 45:846 (1945)
12. Spinner, S. and Teftt, W. E., A Method of Determining Mechanical Resonance Frequencies and for Calculating Elastic Moduli from these Frequencies, *Proc. ASTM*, 61:1221 (1961)
13. Jones, R., The Effect of Frequency on the Dynamic Modulus and Damping Coefficient of Concrete, *Mag. Concr. Res.*, 9(26):69, London (1957)
14. Orchard, D. F., *Concrete Technology*, 2:181, *Practice*, John Wiley & Sons, New York (1962)

@Seismicisolation

15. Swamy, N. and Rigby, G., Dynamic Properties of Hardened Paste, Mortar, and Concrete, *Materials and Structures/Research and Testing*, 4(19):13 (1971)

16. Gaidis, J. M. and Rosenberg, M., New Test for Determining Fundamental Frequencies of Concrete,*Cement Concr. Aggregates*, CCAGDP, 8(2):117 (1986)

17. Kesler, C. E. and Higuchi, Y., Determination of Compressive Strength of Concrete by using its Sonic Properties, *Proc. ASTM*, 53:1044 (1953)

18. Shrivastava, J. P. and Sen, B., Factors Affecting Resonant Frequency and Compressive Strength of Concrete,*Indian Concr. J.*,37(1):27 (1963) and 37(3):105, Bombay (1963)

19. *Handbook of Nondestructive Testing of Concrete*, (V. M. Malhotra and N. J. Carino, eds.), CRC Press, Boca Raton, Florida (1991)

20. Chefdeville, J., Application of the Method toward Estimating the Quality of Concrete, RILEM Bull. No. 15, Special Issue—Vibrating Testing of Concrete, 2nd part, 61, Paris (1953)

21. Swamy, R. N. and Al-Asali, M. M., Engineering Properties of Concrete Affected by Alkali-Silica Reaction, *ACI Mater. J.*, 85(5):367 (1988)

22. Obert, L., Measurement of Pressures on Rock Pillars in Underground Mines, R.I. 3521, U.S. Bureau of Mines (1940)

23. Long, B. G. and Kurtz, H. J., Effect of Curing Methods Upon the Durability of Concrete as Measured by Changes in the Dynamic Modulus of Elasticity, *Proc. ASTM*, 43:1051 (1943)

24. Long, B. G., Kurtz, H. J., and Sandenaw, T. A., An Instrument and a Technique for Field Determination of the Modulus of Elasticity of Concrete (Pavements), *ACI Proceedings*, 41:11 (1945)

25. Leslie, J. R., and Cheesman, W. J., An Ultrasonic Method of Studying Deterioration and Cracking in Concrete Structures, *Journal*, American Concrete Institute, 1949; *ACI Proceedings*, 53:1043 (1953)

26. Whitehurst, E. A., A Review of Pulse Velocity Techniques and Equipment for Testing Concrete,*Proceedings*, Highway Research Board, 33:226 (1954)

27. Whitehurst, E. A., Soniscope Tests Concrete Structures, *ACI Proceedings*, 47:433 (1951)

28. Jones, R., The Non-Destructive Testing of Concrete,*Mag. of Concr. Res.*, No. 2 (June, 1949)

29. Jones, R., The Testing of Concrete by an Ultrasonic Pulse Technique, *Proceedings Highway Research Board*, 32:258 (1953)

30. Cheesman, W. J., Dynamic Testing of Concrete with the Soniscope Apparatus, *Proceedings Highway Research Board*, 29:176 (1949)

@Seismicisolation

31. Sturrup, V. R., Vecchio, F. J., and Caratin, H., Pulse Velocity as a Measure of Concrete Compressive Strengths, ACI SP 82, (V. M. Malhotra, ed.), pp. 201–228, (1984)
32. Cummings, N. A., Seabrook, P. T., and Malhotra, V. M., Evaluation of Several Nondestructive Testing Techniques for Locating Voids in Grouted Tendon Ducts, ACI, SP-128, (V.M. Malhotra, ed.), pp. 47–68 (1991)
33. Sansalone, Mary, and Carino, Nicholas J., Stress Wave Propagation Methods, *Handbook on Nondestructive Testing of Concrete*, pp. 275–304, CRC Press, Boca Raton, Florida (1991)
34. Carino, Nicholas J., Recent Developments in Nondestructive Testing of Concrete, Published in *Advances in Concrete Technology*, CANMET, (V. M. Malhotra., ed.), pp. 281–328 Ottawa (1992)
35. Schmidt, E., The Concrete Test Hammer (Der Beton-Prufhammer), *Schweiz. Bauz.*, 68(28):378, Zurich (1950)
36. Schmidt, E., Investigations with the New Concrete Test Hammer for Estimating the Quality of Concrete (Versuche mit den neuen Beton-Prufhammer zur Qualitatsbestimmung des Beton), Schweiz. Archiv. angerwandte Wissenschaft Technik (Solothurn), 17(5):139 (1951)
37. Schmidt, E., The Concrete Sclerometer, *Proc. Int. Symp. Nondestructive Testing on Materials and Structures*, Vol. 2, RILEM, p. 310, Paris (1954)
38. Kolek, J., An Appreciation of the Schmidt Rebound Hammer, *Mag. Concr. Res.*, 10(28, 27) London (1958)
39. Malhotra, V. M., Nondestructive Methods for Testing Concrete, *Mines Branch Monogr. No. 875*, Department of Energy, Mines and Resources, Ottawa (1968)
40. Malhotra, V. M., Testing of Hardened Concrete: Nondestructive Methods, ACI Monogr. No. 9, p. 188 (1976)
41. Zoldners, N. G., Calibration and Use of Impact Test Hammer, *ACI Proc.*, 54(2):161 (1957)
42. Akashi, T., and Amasak, S., Study of the Stress Waves in the Plunger of a Rebound Hammer at the Time of Impact, ACI SP-82, 17, (V. M. Malhotra, ed.) (1984)
43. Carette, G. G., and Malhotra, V. M., In-Situ Tests: Variability and Strength Prediction of Concrete at Early Ages, ACI SP-82, (V. M. Malhotra, ed.), 111 (1984)
44. Greene, G. W., Test Hammer Provides New Method of Evaluating Hardened Concrete, *ACI Proc.*, 51(3):249 (1954)
45. Klieger, P., Anderson, A. R., Bloem, D. L., Howard, E. L., and Schlintz, H., Discussion of Test Hammer Provides New Method of Evaluating Hardened Concrete, by Gordon W. Greene, *ACI Proc.*, 51(3):256-1 (1954)

@Seismicisolation

46. Voellmy, A., Examination of Concrete by Measurements of Superficial Hardness, *Proc. Int. Symp. on Nondestructive Testing of Materials and Structures*, RILEM, 2:323, Paris (1954)

47. Kopf, R. J., Powder Actuated Fastening Tools for Use in the Concrete Industry, *Mechanical Fasteners for Concrete*, SP-22, American Concrete Institute, p. 55, Detroit (1969)

48. Freedman, S., Field Testing of Concrete Strength, *Modern Concr.*, 14(2):31 (1969)

49. Gaynor, R. D., In-Place *Strength of Concrete—A Comparison of Two Test Systems*, Presented at 39th Annual Convention of the National Ready Mixed Concrete Association, New York, (1969). Published with NRMCA Tech. Information Letter No. 272 (1969)

50. Law, S. M. and Burt, W. T., III, Concrete Probe Strength Study, *Research Report No. 44*, Research Project No. 68-2C(b), Louisiana HPR (7), Louisiana Department of Highways (1969)

51. Arni, H. T., Impact and Penetration Tests of Portland Cement Concrete, *Highw. Res. Rec.*, 378:55 (1972)

52. Arni, H. T., Impact and Penetration Tests of Portland Cement Concrete, *Federal Highway Administration Rep. No. FHWA-RD-73-5* (1973)

53. Malhotra, V. M., Preliminary Evaluation of Windsor Probe Equipment for Estimating the Compressive Strength of Concrete, *Mines Branch Investigation Rep. IR 71-1*, Department of Energy, Mines and Resources, Ottawa, Canada (1970)

54. Malhotra, V. M., and Painter, K. P., Evaluation of the Windsor Probe Test for Estimating Compressive Strength of Concrete, *Mines Branch Investigation Rep. IR 71-50*, Department of Energy, Mines and Resources, Ottawa, Canada (1971)

55. Malhotra, V. M., Evaluation of the Windsor Probe Test for Estimating Compressive Strength of Concrete, *RILEM Materials and Structures*, 7:37:3–15, Paris (1974)

56. Klotz, R. C., Field Investigation of Concrete Quality Using the Windsor Probe Test System, *Highw. Res. Rec.*, 378:50 (1972)

57. Keeton, J. R., and Hernadez, V., Calibration of Windsor Probe Test System for Evaluation of Concrete in Naval Structures, *Technical Note N-1233*, Naval Civil Engineering Laboratory, Port Hueneme, CA (1972)

58. Clifton, J. R., Nondestructive Tests to Determine Concrete Strength—A Status Report, *NBSIR 75-729*, Natl. Bur. of Stand., Washington, D.C.

59. Bowers, D. G. G., Assessment of Various Methods of Test for Concrete Strength, *Connecticut Department of Transportation/Federal Highway Administration*, (Available Through National Technical Information Service, NTIS No. PB 296317, Springfield, VA) (1978)

@Seismicisolation

60. Bartos, M. J., Testing Concrete in Place, *Civil Engineering*, Am. Soc. Civ. Engrs., p. 66 (1979)

61. Strong, H., In-Place Testing of Hardened Concrete with the Use of the Windsor Probe, *New Idaho Test Method T-128-79*, Division of Highways, State of Idaho (Jan., 1979)

62. Swamy, R. N., and Al-Hamed, A. H. M. S., Evaluation of the Windsor Probe Test to Assess In-Situ Concrete Strength, *Proc. Inst. Civ. Eng.*, Part 2, June 1984 (1967)

63. Malhotra, V. M., and Carette, G. G., Penetration Resistance Methods, *Handbook on Nondestructive Testing of Concrete*, pp. 19–39, CRC Press, Boca Raton, Florida (1991)

64. Keiller, A. P., A Preliminary Investigation of Test Methods for the Assessment of Strength of In-Situ Concrete, *Tech. Rep. No. 551*, Cement and Concrete Association, Wexham Springs (1982)

65. Bungey, J. H., *The Testing of Concrete in Structures*, Chapman and Hall, New York (1982)

66. Keiller, A. P., Assessing the Strength of In-Situ Concrete, *ACI Concr. Int.*, p. 15 (1985)

67. ACI Committee 228 Report on: In-Place Methods for Determination of Strength of Concrete, *ACI Journal of Materials*, 85(5):446 (1988)

68. Malhotra, V. M., and Carette, G. G., In-Situ Testing for Concrete Strength, *CANMET Report 79–30*, Energy, Mines and Resources Canada, Ottawa, p. 20 (1979)

69. Kopf, R. J., Cooper, C. G., and Williams, F. W., In-Situ Strength Evaluation of Concrete Case Histories and Laboratory Investigations, *ACI Concr. Int.*, p. 66 (1981)

70. ASTM C 42-87, Standard Test Method for Obtaining and Testing Drilled Cores and Sawed Beams of Concrete, *Annual Book of ASTM Standards*, American Society for Testing and Materials, Philadelphia (1988)

71. Lee, S. L., Tam, C. T., Paramasivam, P., Ong., K .C. G., Swaddiwudhipong, S., and Tan, K. H., *Structural Assessment in In-Situ Testing and Interpretation of Concrete Strength*, Department of Civil Engineering, National University of Singapore (1988)

72. Nasser, K. W., and Al-Manaseer, A., New Non-Destructive Test for Removal of Concrete Forms, *ACI Concr. Int.*, 9(1):41 (1987)

73. Nasser, K. W., and Al-Manaseer, A., Comparison of Non-Destructive Testers of Hardened Concrete, *ACI Journal of Materials*, 84(5):374 (1987)

74. ASTM C 803-82, Standard Test Method for Penetration Resistance of Hardened Concrete, *Annual Book of ASTM Standards*, American Society for Testing and Materials, Philadelphia (1988)

@Seismicisolation

75. Skramtajew (sic) (also Skramtaev), B. G., *ACI Proceedings*, 34(3):285–303, Jan.–Feb., Discussion, pp. 304–305 (1938)

76. Tremper, Bailey, The Measurement of Concrete Strength by Embedded Pull-Out Bars, *ASTM Proceedings*, 44:880–887 (1944)

77. Tassios, T. P., A New Nondestructive Method of Concrete Strength Determination, *Publication No. 21*, National Technical University, Athens (1968)

78. Kierkegaard-Hansen, P., Lok-Strength, *Nordisk Betong No.* 3, p. 19 (1975)

79. Malhotra, V. M., Evaluation of the Pullout Test to Determine Strength of In-Situ Concrete, *Materials and Structures*, Vol. 8, No. 43, RILEM Jan.–Feb. 1975, pp. 19–31 (1975)

80. Carino, Nicholas, J., Pullout Tests, *Handbook on Nondestructive Testing of Concrete*, (V. M. Mahotra, and N. J. Carino, eds.), pp. 39-82, CRC Press, Boca Raton, Florida (1991)

81. Bickley, J. A., Evaluation and Acceptance of Concrete Quality by In-place Testing, *ACI SP-82*, (V. M. Malhotra, ed.), pp. 95–110 (1984)

82. Chabowski, A. J., and Bryden-Smith, D. W., Assessing the Strength of Concrete of In-Situ Portland Cement Concrete by Internal Fracture Tests, *Mag. Concr. Res.*, 32(112):164 (1980)

83. Mailhot, G., Bisaillon, A., Malhotra, V. M., and Carette, G., Investigations into the Development of New Pullout Techniques for In-Situ Strength of Determination of Concrete, *ACI Journal*, 76(2):1267 (1979)

84. Johansen, R. In-Situ Strength of Concrete, the Breakoff Method, *ACI Concr. Int.*, p. 45 (1979)

85. Carlsson, M., Eeg, I. R., and Janer, P., Field Experience in the Use of the Breakoff Tester, ACI SP82-14, *In Situ/Nondestructive Testing of Concrete*, (V. M. Malhotra, ed.), pp. 277–292 (1984)

86. Dahl-Jorgenson, E., and Johansen, R., General and Specialized Use of the Breakoff Concrete Strength Test Method, ACI SP82-15, *In Situ/ Nondestructive Testing of Concrete*,, (V. M. Malhotra, ed.), pp. 293–308, American Concrete Institute, Detroit, MI (1984)

87. Naik, T., The Breakoff Test Method, *Handbook on Nondestructive Testing of Concrete*, (V. M. Malhotra, and N. J. Carino, eds.), pp. 83–100, CRC Press, Boca Raton, Florida (1991)

88. McIntosh, J. D., Electrical Curing of Concrete, *Mag. Concr. Res.*, 1(1):21–28 (1949)

89. Nurse, R. W., Steam Curing of Concrete, *Mag. Concr. Res.*, 1(2):79–88 (1949)

90. Saul, A. G. A., Principles Underlying the Steam Curing of Concrete of Atmospheric Pressure, *Mag. Concr. Res.*, 2(6):127–140 (1951)

@Seismicisolation

91. Bergstrom, S. G., Curing Temperature, Age, and Strength of Concrete, *Mag. Concr. Res.*, 5(14):61–66 (1953)
92. Rastrup, E., Heat of Hydration in Concrete, *Mag. Concr. Res.*, 6(17):79–92 (1954)
93. Plowman, J. M., Maturity and the Strength of Concrete, *Mag. Concr. Res.*, 8(22):13–22 (1956)
94. Malhotra, V. M., Maturity Concept and the Estimation of Concrete Strength, *Information Circular IC 277*, Department of Energy, Mines and Resources, Canada (1971)
95. Freiesleben Hansen, P., and Pedersen, E. J., Maturity Computer for Controlled Curing and Hardening of Concrete, *Nordisk Beton*, 1(19), (1977)
96. Byfors, J., Plain Concrete at Early Ages, *Swedish Cement and Concrete Research Institute Rep.*, 3:80 (1980)
97. Naik, T. R., Maturity Functions, Concrete Cured During Winter Conditions, Temperature Effects on Concrete, *ASTM STP 858*, (T. R. Naik, ed.), p. 107 (1985)
98. Carino, Nicholas J., The Maturity Method, *Handbook on Nondestructive Testing of Concrete*, (V. M. Malhotra, and J. J. Carino, eds.), pp. 101–146, CRC Press, Boca Raton, Florida (1991)
99. Swenson, E. G., Estimation of Strength of Concrete, *Engineering Journal*, 50(9):27–32, Canada (1967)
100. Hudson, S. B., and Steele, G. W., Developments in the Prediction of Potential Strength of Concrete from Results of Early Tests, *Transp. Research Record*, No. 558, p. 1 (1975)
101. Malhotra, V. M., Maturity Strength Relations and Accelerated Strength Testing, *Canada Mines Branch Internal Report*, MPI (P) pp. 70–29, Department of Energy, Mines and Resources Ottawa, Canada (1970)
102. Long, A. E., and McMurray, A., The Pull-off Partially Destructive Test, *ACI SP82*, (V. M. Malhotra, ed.), pp. 327–350 (1984)
103. Samarin, A., Combined Methods *Handbook on Nondestructive Testing of Concrete*), V. M. Malhotra, and N. J. Carino, eds.), pp. 189–202, CRC Press, Boca Raton, Florida (1991)
104. Malhotra, V. M., In-Situ Nondestructive Testing of Concrete—A Global Review, *ACI SP82*, (V. M. Malhotra, ed.), pp. 1–16, (1984)

@Seismicisolation

18

Applications of Computers and Information Technology

James R. Clifton and Geoffrey Frohnsdorff*

1.0 INTRODUCTION

The science and technology of concrete are undergoing revolutionary change due to developments in computer and information technologies that are enabling concrete researchers, engineers, and practitioners to develop, store and retrieve, integrate, and disseminate knowledge on all aspects of concrete including formulation, processing, testing, and inspection, prediction of performance, repair, and recycling. The rapid growth of computer-based systems such as simulation models, databases, and artificial intelligence decision-support systems, is evidence of the impact of computer and information technologies on concrete science and technology. The purpose of this chapter is to draw attention to recent developments in computers and information technology that are having enormous influences on the direction of the material science and technology of concrete. Development in the material science of concrete in conjunction with computer and information technology will undoubtedly contribute to great improvements in the performance of concrete in the 21st century. A major advance in concrete science and technology has already resulted from the development, application, and integration of computer-based simulation

*Deceased January 1999.

@Seismicisolation

models, databases, and artificial intelligence decision-support systems. In reviewing the application of computers and information technologies to the material science of concrete a brief review of their general application to material science and engineering is presented first. Then, developments in computerized knowledge bases for concrete are reviewed and their integration to form computer-integrated knowledge systems discussed.

1.1 Computer Applications in Material Science and Engineering

Since the development of the ENIAC (Electronic Numerical Integrator and Computer), the first fully electronic computer, in 1946,[1] computers have become ubiquitous in the scientific and engineering fields. At first they were primarily used for rapid, but straightforward, numerical calculations with early applications being in the design of atomic weapons at Los Alamos and improving methods of cryptography during World War II. Then, in the 1950s, their applications were extended to data storage and retrieval beginning with the design of the EDVAC (Electronic Discrete Variable Automatic Computer) built at the University of Pennsylvania for the U.S. Army Ballistic Research Laboratory.[1] Early, and still important, applications to engineering were in "number crunching" including structural analysis using finite element modeling, computer-aided design (CAD), and relational modeling involving the fitting of data. In the early 1970s, pioneering work by Feigenbaum[2] in the development of the chemical identification expert system, Dendral, was an early introduction to the concept of AI (Artificial Intelligence) and was instrumental in demonstrating the use of computerized scientific and engineering knowledge in the solving of complex problems. A further revolution is now taking place in the computerized dissemination of data, information, and knowledge, by the development of the Internet, fostered in the U.S. Congress by the High Performance Computing Act of 1991[3] which was soon extended to define the National Information Infrastructure. Innovations in computer and communication technologies coupled with this legislative initiative have stimulated the worldwide explosive growth of the Internet.

These advances in computers and communications have enormous implications in concrete science and technology in such areas as *(i)* prediction of concrete performance through fundamental computational models resulting in more reliable service life designs of concrete; *(ii)* collaboration in research and in problem-solving efforts in the concrete field, through sharing of data, information, and knowledge among geographically-dispersed colleagues, research organizations, manufacturing

@Seismicisolation

companies, and contractors; *(iii)* development of computer-integrated knowledge systems which have the potential for representing virtually all scientific and engineering knowledge of concrete and making the knowledge readily available to those needing it. Although, at present, most knowledge of concrete is still stored in printed form and in the brains of concrete technologists, its electronic representation is growing rapidly, e.g., the ACI Manual of Concrete Practice[4] is available on CD-ROM disks and simulation models of the microstructure of cements and the transport properties of concrete can now be downloaded from the Internet.[5] Civil engineering World Wide Web sites dealing with concrete are also located on the Internet.[6]

One of the most exciting recent developments in the application of computers to the design of materials is the simulation modeling which is being extensively used by chemists in the development of new complex molecules for medical purposes.[7] In the future, we anticipate that significant advances in knowledge of concrete and other cement-based materials will result from simulation modeling.

2.0 COMPUTER MODELS

Material science involves the development and application of knowledge concerning relationships among microstructure, processing, and properties of materials. Modeling has become an integral component of material science and now drives many advances in the fundamental knowledge of materials, including cement-based materials. A model of a material can be defined as "a theoretical construct, which is made using valid scientific principles expressed in mathematical language, that can be used to make quantitative predictions about a material's structure or properties."[8] In another definition, models are considered to be theoretical and mathematical representations that predict experimental observations.[9]

2.1 Types of Models

Several types of models can be identified, including physical, conceptual, logical, statistical, constitutive, and simulation models.[10] A miniature version of a concrete dam or building can be labeled as a *physical model*. It constitutes a material representation of an object with real-world features. *Logical models* deal with axioms and rules of deductive inference that

@Seismicisolation

permit the creation of logically-correct statements by applying the rules of formal logic. Regarding applications of computers to concrete, we are interested in statistical, constitutive, and simulation models. *Statistical models* are often derived by data fitting using regression relations; however, some models, such as those developed by Parrot[12] and Powers,[11] while involving data fitting, also incorporate knowledge of physical reality. *Constitutive models* deal with observed patterns in properties[9] with mathematical relations being derived to represent the observed patterns; however, the basis for the model cannot be determined directly and cause and effect are linked by assumed mechanisms. A *simulation model* includes some sort of stored or analytical representation of a system, which is operated by prescribed algorithms that give numerical information on desired physical or other properties.[8] In the case of cement-based materials, simulation models deal directly with microstructure at the level of individual cement particles and their hydration products and the resulting microstructure. They may also cover a wide range of scales, from nanometers to meters. Such multi-scale models may be used to simulate the microstructure development in a hydrating cement paste or to predict properties of concrete in a structure. An example is a model for predicting chloride ion diffusivity of portland cement concrete.[13][14] In the future, the authors believe that simulation modeling will be an essential tool in all branches of science and engineering and it will make practical the material design of concretes optimized for their applications.

2.2 Mathematical Language of Models

The mathematical language of a model may take several forms, such as a set of deterministic empirical equations that have been fitted to experimental data, or a set of physically-appropriate differential equations whose coefficients have been determined from experimental data, or a set of differential equations or computer algorithms that do not depend on any special experimental input, only a comprehensive knowledge of physics and chemistry. Examples of models based on different mathematical languages are described by Garboczi and Bentz,[8] and Jennings, et al.[9]

2.3 Material Science Models of Cement-Based Materials

During the past three decades many computational models based on material science have been developed for cement-based materials. Prior to

@Seismicisolation

the advent of computer simulation most models of cement-based materials were of the constitutive type. In the future, simulation modeling will likely predominate. Too many models have been developed to give more than a brief review which is the intent of this section. The models are somewhat arbitrarily grouped into cement hydration models, microstructure models, and simulation models.

Cement Hydration Models. An early review of mathematical models of cement hydration was prepared by Pommersheim and Clifton.[15] They found, at the time of their review in 1979, that most models of cement systems addressed one or the other of tricalcium silicate and dicalcium silicate. The models were composed of rate equations, constitutive relations, and conservation equations. Probably the first comprehensive model for the hydration of tricalcium silicate was developed by Kondo and Ueda in the 1960s.[16] Frohnsdorff, et al.,[17] also developed an early (1968) general mathematical model which was applied to the hydration of tricalcium silicate (C_3S). The kinetics of tricalcium silicate hydration was modelled by Pommersheim and Clifton.[18][19] In their model, a hydrating C_3S particle had three product layers: inner, middle, and outer (Fig. 1), with the middle layer (or barrier layer) forming almost instantaneously and then gradually disappearing. The rate of hydration was controlled by diffusion through these product layers. This approach was further advanced by van Breugel in the HYMOSTRUC model, which incorporated particle size distribution, concentration gradients, heats of hydration, rates of diffusion, temperature, and relative humidity.[20] While not a model, the research by Nonat[21] on factors affecting the hydration of C_3S, is mentioned as it provides data needed for model development. Data was presented on kinetics of hydration of tricalcium silicate, the thermodynamics, morphological and structural characteristics of calcium silicate hydrate (C-S-H), and particle interactions during setting. It was found that the concentration of lime in the pore solution was the most important parameter affecting the hydration kinetics and the morphological and structural features of the C-S-H formed.

A major effort aimed at developing a conceptual basis for the mathematical modeling of the hydration of portland cement was performed by RILEM Technical Committee 68-MMH on Mathematical Modeling of Cement Hydration, resulting in several reports in the 1980s. A task group chaired by Taylor[22] summarized conceptual models for the hydration of tricalcium silicate (at room temperature and a water/cement ratio of 0.5 by mass), with the objective of providing an introduction to the more difficult problem of developing scientifically sound mathematical models for

@Seismicisolation

portland cement hydration. Their conceptual model considered phase equilibria, morphology and nature of the reaction products, and pore solution composition. Also, they discussed the mechanisms thought to control hydration during the three major phases of C_3S hydration: the induction, acceleratory, and deceleratory periods. In a companion study, a task group chaired by Young[23] examined the conceptual basis for the hydration of dicalcium silicate (C_2S). They concluded that C_2S hydrates slower than C_3S because, unlike C_3S, the anhydrous silicate lattice in C_2S contains no oxide ions. As part of the same general study, a task group chaired by Brown[24] examined the hydration of tricalcium aluminate (C_3A) and tetracalcium aluminoferrite. They reported that the reactions of C_3A with water and calcium sulfate produced ettringite and monosulfate, depending on the relative proportions of the reactants, and metastable calcium aluminate hydrates which converted into the cubic hydrate, C_3AH_6.

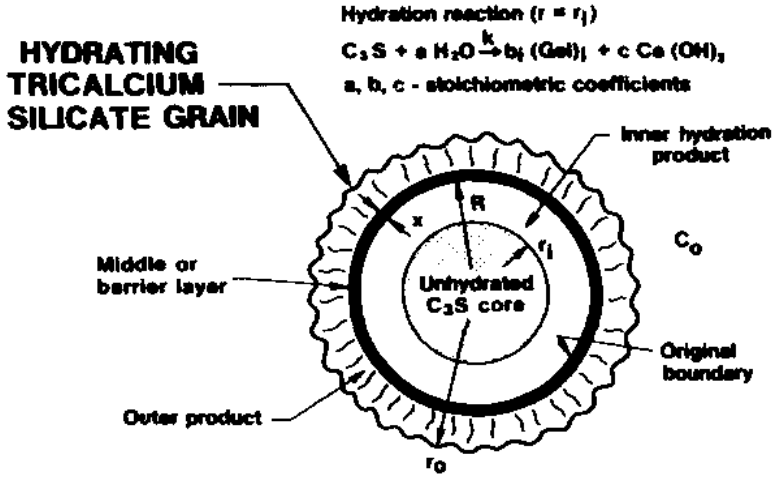


Figure 1. Schematic of hydrating C_3S grain.[18]

Few models of the hydration of typical portland cements have been reported. One of the most significant early studies was that by Brunauer, et al.,[25] who investigated the hydration of portland cement pastes at low porosities (w/c ratios of 0.2 and 0.3, by mass) and mathematically analyzed the data. In developing their model, they assumed that the hydration rate was directly proportional to the product of the rate constant, a function depending on the w/c ratio and the amount of unhydrated cement, and

@Seismicisolation

inversely proportional to the mass of hydration products raised to a positive power. Model constants were obtained using a differential method of data analysis. The model predicted that the hydration rate decreased as the hydration product volume increased and as the w/c ratio decreased. Probably the most advanced model of the hydration of a portland cement yet developed is that by Bentz.[26] It is a three-dimensional computer model for the simulation of portland cement hydration and microstructure development. This model will be further described in the section on simulation modeling.

Microstructural Models. The microstructure of cement-based materials is controlled by their constituents, the mixture proportions, processing (e.g., mixing, consolidation, and curing), and degree of hydration. The properties of the hardened cement-based materials are dependent on their microstructure; the capillary pore structure, which includes the transition zone between the cement paste and aggregates, usually governs the transport properties of concrete, while larger voids reduce the strength of concrete. Therefore, microstructure characterization and modeling have come to make a major contribution to understanding the performance of cement-based materials. The progress of microstructure modeling has been comprehensively reviewed in two parts by Jennings, et al.[9][27] Part 1 deals with historical developments and provides a general overview, while Part 2 addresses recent developments. In Part 1, models of the microstructure of cement-based materials and of shrinkage and creep are described, while Part 2 describes models linking microstructure with flow properties, moisture capacity, and shrinkage and creep. Garboczi and Bentz reported on the state-of-the-art of fundamental computer simulation models for cement-based materials[8] and with Martys, reviewed[28] relationships between transport properties and the microstructure of cement-based materials. Van Breugel[29] used simulation models to link microstructural development with hydration kinetics of cement-based materials.

The reviews by Jennings, et al., were contributions to the proceedings of a NATO Advanced Research Workshop on the Modeling of Microstructure and Its Potential for Studying Transport Properties and Durability, held in 1994.[30] The contents of the proceedings are:

Part I: Modeling Pore Structure

- Scale and resolution of models
- Spatial distributions
- Data bases and expert systems

@Seismicisolation

Part II: Transport Mechanisms and Durability

- Transport mechanisms
- Major parameters affecting transport properties
- Corrosion mechanisms and parameters

Simulation Models. The first application of simulation modeling to cement-based materials appears to be that described in 1985 by Roelfstra, Sadouki, and Wittman.[31][32] They used a two-dimensional (2-D) finite element modeling approach to simulate the elastic properties of concrete. The cement paste microstructure was treated as a continuum, but they used simulation techniques to generate realistic 2-D shapes of certain classes of aggregates. Random elastic moduli information was stored in finite elements from which they were able to make 2-D computations of elastic moduli, diffusion coefficients, and thermal expansion coefficients of the concrete. The next major development was the computer simulation model of Jennings and Johnson in 1986[33] which was later revised and improved by Struble, et al.[34] This model simulated the development of the microstructure in 3-D of a tricalcium silicate paste, starting with a numerical representation of the initial cement particle/water mixture and then, in successive iterations, operating on this stored information and calculating the progress of the changes in small increments using an algorithm for consuming the tricalcium silicate and generating hydration products. The tricalcium silicate particles were modeled as spheres with a size distribution typical of portland cement.

A continuum model developed to produce computer representations of cement microstructures is based on the mosaic method.[35] In this approach, a 2-D space is divided by a set of intersecting lines and the resulting polygonal shapes taken to represent unhydrated and hydrated cement particles and hydration products (an analogous approach was used in 3-D). Although multiple discrete phases can be modeled using this method, simultaneously modeling multiple continuous or percolated phases, such as C-S-H gel, capillary porosity, and calcium hydroxide (CH), presents a computational challenge.

An alternative approach to continuum-based models has been the development of "digital-image-based models."[28] In these models, each particle of cement or hydration product is represented as a collection of elements (pixels). Hydration can then be simulated by operating on the entire collection of pixels using a set of cellular-automaton-like rules. This allows for the direct representation of multi-size, multi-phase, non-spherical, cement particles. The model has evolved from one based simply on the

@Seismicisolation

hydration of C_3S to one that considers all of the major phases present in portland cement.[26] In addition, due to the underlying pixel representation of the microstructure, mapping the microstructure onto a finite difference or finite element grid becomes trivial. Thus, properties such as percolation, diffusivity, complex impedance, and setting behavior, are easily computed. To adequately model the hydration behavior of a cement by this approach, it is necessary to accurately characterize the starting material, the cement powder. Using a combination of scanning electron microscopy (SEM) and x-ray powder diffraction, along with imaging processing techniques, Bentz and Stutzman[36] have developed a method for obtaining 2-D images of unhydrated cements, which are converted into realistic 3-D representations for use in simulations of cement hydration.

The processes involved in the simulation model of cement hydration and the application of the model in predicting the properties of the hydrated cement paste were described by Bentz.[26] The reactions given in Fig. 2 are implemented as a series of cellular automaton-like rules which operate on the original 3-D representation of cement particles in water. Simple rules are provided for the dissolution of solid material, the diffusion of the generated diffusing species, and the reactions of diffusing species with each other and with solid phases. These rules are summarized in the state transition diagram in Fig. 3. The simulated microstructure is scanned, the rules applied to pixels exposed on the particles surfaces and, when all the possible events have occurred for these pixels, defined as one cycle (or scan), another cycle is implemented. The cycles are repeated until the reactions are complete or the desired degree of hydration has been achieved. Then, the properties of the "virtual" cement may be calculated and compared to experimental data. An example of the level of agreement between a measured cement property and the results from the model is given in Fig. 4 for chemical shrinkage. Similarly, good agreements have been obtained for degree of hydration and heat of hydration. By incorporating a maturity relationship, the model gave reasonable predictions of the compressive strengths of mortar specimens.

By a multi-scale approach, many of the material properties of concrete can be predicted starting with the hydration of C_3S to form C-S-H gel and CH at the nanometer level. Then, using the nanometer-scale model to form a continuum structure, the cement paste structure is modeled on the micrometer scale. The microstructure of the cement paste is then used to calculate appropriate properties of a continuum in which the aggregates are embedded to form a mortar/concrete model on

@Seismicisolation

the meter scale. This approach has been demonstrated for predicting the chloride ion diffusivity of portland cement mortar and concrete.[13][14]

On the nanometer scale, the connectivity of the gel pores is considered to control diffusivity, while the percolation of capillary pores is treated at the micrometer scale. Then the contributions of gel pores and capillary pores, including those from the transition zone between the cement paste and aggregates, are combined in calculating the diffusivity of mortars and concretes.

The above simulation modeling of cement-based materials is included in a 1200 page "electronic monograph" prepared by Garboczi, Bentz, and Snyder based on the simulation modeling of cement-based materials carried out at NIST (available on the Internet at http://ciks.cbt.nist.gov/garboczi). This monograph provides comprehensive insights into many aspects of the computational material science of concrete.

Silicate Reactions

$$C_3S + 5.3H \rightarrow C_{1.7}SH_4 + 1.3CH$$
1 1.34 1.521 0.61

$$C_2S + 4.3H \rightarrow C_{1.7}SH_4 + 0.3CH$$
1 1.49 2.077 0.191

Aluminate and Ferrite Reactions

$$C_3A + 6H \rightarrow C_3AH_6$$
1 1.21 1.69

$$C_3A + 3C\bar{S}H_2 + 26H \rightarrow C_6A\bar{S}_3H_{32}$$
0.4 1 2.1 3.3

$$2C_3A + C_6A\bar{S}_3H_{32} + 4H \rightarrow 3C_4A\bar{S}H_{12}$$
0.2424 1 0.098 1.278

$$C_4AF + 3C\bar{S}H_2 + 30H \rightarrow C_6A\bar{S}_3H_{32} + CH + FH_3$$
0.575 1 2.426 3.3 0.15 0.31

$$2C_4AF + C_6A\bar{S}_3H_{32} + 12H \rightarrow 3C_4A\bar{S}H_{12} + 2CH + 2FH_3$$
0.348 1 0.294 1.278 0.09 0.19

$$C_4AF + 10H \rightarrow C_3AH_6 + CH + FH_3$$
1 1.41 1.17 0.26 0.545

Figure 2. Cement model reactions (numbers below reactions indicate volume stoichiometry).[26]

@Seismicisolation

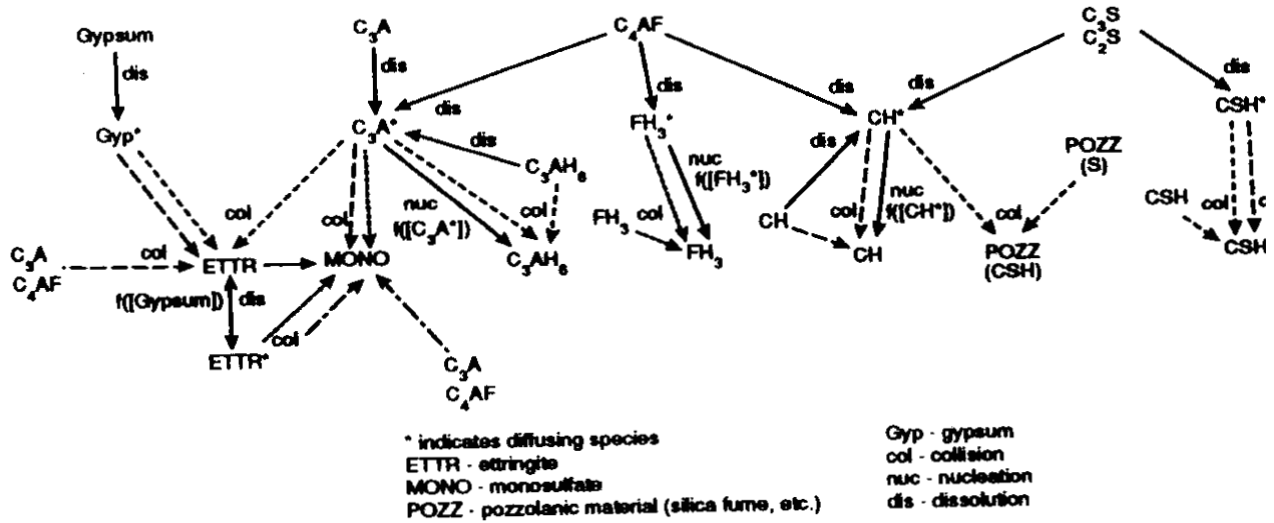


Figure 3. State transition diagram for three-dimensional cement hydration model.[26] Arrows denote reaction to form hydration product; F[X] denotes that nucleation or dissolution probability is a function of the concentration of X.

@Seismicisolation

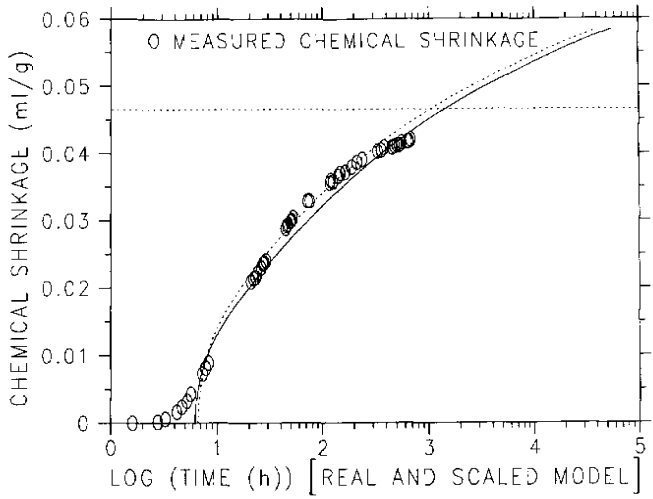


Figure 4. Measured and model chemical shrinkage vs. time for CCRL Portland cement 115 with w/c of 0.40.[26]

3.0 DATABASE SYSTEMS

A database system is defined by Date[37] as a computerized record-keeping system, while a database is a collection of computerized data files with persistent data. A database system contains a description of its structure in the form of a data dictionary and data schema, where the data dictionary[38][39] is a guide to the information in a database and the database schema provides a perspective—a way of seeing—the information in the database. In other words, a database system is a self-describing collection of files containing within itself a description of its structure.

3.1 Applications of Databases in Concrete Technology

The process of developing scientific and engineering databases in science and engineering and their application has been described by Rumble and Smith.[38] Some examples of data to be represented in concrete databases are:

- Composition and physical properties of concrete-making materials

@Seismicisolation

- Properties of concrete such as transport properties, mechanical properties, fire performance, and durability vs. mixture design
- Rheological properties and consolidation characteristics of concrete mixtures
- Performance data from research, laboratory and field studies
- Pictures of distresses in concrete materials and structures
- Representational images such as graphs of relationships and the results of models
- Standards and guidelines
- Bibliographic information

Design and development of databases which are intended to be of lasting value can require considerable effort, be expensive, and require specialized skills.[40] Nevertheless, database development should be an inherent part of any significant project related to research, design, performance testing and prediction, and evaluation of the field performance of concrete. The justification for investing in creating databases for scientific and engineering data necessitates comment. From a business standpoint, several benefits are apparent[37] which are also applicable to scientific and engineering databases; they include reduction of voluminous paper files, persistence and rapid retrieval of data, organization of data to facilitate analysis, and availability of up-to-date data. From a societal point-of-view, scientific and engineering databases can prevent "reinventing the wheel" research and also, by data-sharing, provide data to other researchers for input to models and for model validation. The integration of large amounts of data in a single database, known as "data banking,"[37] makes it practical to gain more knowledge from the processing of the data (data mining).[41] Frohnsdorff[42] has suggested that the development and maintenance of national databases for concrete and concrete materials should be supported by both the private sector and the government.

3.2 Existing Databases for Concrete and Concrete Materials

The number of numeric databases for concrete and concrete materials is far fewer than those for other materials, such as metals and plastics.

@Seismicisolation

Westbrook, Kaufman, and Cverna, recently reviewed[43] the state-of-the-art of electronic access to numeric scientific and engineering databases—of some 100 available, none of them addressed concrete. Restricting coverage to electronically-distributed (e.g., by computer disk, CD-ROM, or over the Internet) and nonproprietary databases, our search disclosed only a few dealing with concrete and concrete materials. While there must be an enormous number of printed records of data on the properties and performance of concrete, e.g., in handbooks and in the records of organizations such as Federal and State construction agencies, cement and concrete trade associations and their members, and large construction companies, few appear to be in computerized form. Examples of three numeric databases available on computer discs are *(i)* a database developed at the Oak Ridge National Laboratory for the Nuclear Regulatory Commission containing age-related material data for concrete and concrete-related materials used to construct nuclear power plants;[44] *(ii)* a database developed by North Carolina State University under the Strategic Highway Research Program[45] on the properties of high-performance concrete; and *(iii)* a research-oriented database on creep and shrinkage of concrete prepared under the auspices of a RILEM technical committee.[46] An example of a bibliographical database for technical literature is ICONDA (CIB's International CONstruction DAtabase),[46][47] which covers international literature on construction technology including concrete. It has over 25,000 citations and this listing is rapidly increasing.

An important activity pursued by both the government and private sectors has been aimed at making databases accessible through the Internet.[5] Recently, two databases for concrete have become accessible over the Internet. A database on the properties of concrete aggregates developed by the Bureau of Reclamation,[48] which can be downloaded from the Internet using FTP (File Transfer Protocol), and transferred to Microsoft Access for searching. A database based on virtually all—more than 300—portland cements manufactured in North America in 1995, prepared by Gebhardt for ASTM Committee C-1 on Cement,[49] is also accessible through the Internet.[5] In this case, the database can be searched on-line, and the search is platform-and software-independent, i.e., it is an open system. This is possible through the use of the Remote Data Access [RDA] standard, which is a standard for accessing data from distributed SQL-compliant relational databases.[50] The RDA standard provides protocols for establishing remote connections between a database client and a database server. In addition to making the concept of open, distributed databases a reality, RDA will facilitate electronic commerce in which distributed database developers

@Seismicisolation

can be compensated. The attributes of distributed databases are discussed in detail by Burleson[51] and Date.[37] We predict that by the Year 2000, distributed databases on concrete and concrete materials properties will be commonplace. By 1998, the data sets on compositions and ASTM test data of portland cements in the proficiency sample program of the ASTM Cement and Concrete Reference Laboratory[52] will be accessible from the Internet through RDA.

3.3 Standards for Databases, Database Formats, Quality of Data

An important consideration in developing databases for concrete is the standardization of formats and the quality and reliability of the data. ASTM Committee E49 on Material and Chemical Property Data pioneered the development of material database formats and guidelines for materials.[5] The committee's goal is "to promote and develop standard classifications, guides, practices, and terminology, for building, processing, and exchanging information among computerized material and chemical property databases." Because knowledge of the quality of data values will often be critical to the use of a database, databases should incorporate quality indicators such as those prepared by ASTM E 1484[53] and given in Table 1. Building on the work of ASTM E49, ACI Committee 126, Database Formats for Concrete Materials Property Data, has developed formats to be used in reporting and storing data on the composition and properties of cements, aggregates, chemical admixtures, mineral admixtures; on the processing of concrete; and on the properties and performance of concrete. Recommended database formats for chemical admixtures have the following four data segments for recording the identity of a chemical admixture and its properties and performance in concrete.[39]

- Constituent identification
- Chemical and physical characteristics
- Manufacturer's recommendations
- Performance in concrete

The recommended data elements for identification of a chemical admixture are presented in Table 2; they are typical of those for the other data segments as well as those for other concrete materials property data sets. Chemical and physical data segments for chemical admixtures are presented in Table 3, which shows the hierarchical format of the database.

@Seismicisolation

Table 1. Data Quality Standards[1]

Limited Use Data

- Data are traceable to an individual, organization, or reference
- After an independent review, an identifiable authority approved the digitized version for inclusion in the database
- Basis of data is identified
    a. Experimental measurements
    b. Derived Data
    c. Estimated Data
- Type of data is indicated
    a. Original point values
    b. Analyzed data
        1. Standard fit - specify fit and data
        2. Fit unknown

Qualified Data

- Number of measurements and data sets stated
- Nominal confidence limited estimated
- Traceable materials specification assures reproducibility
- Testing methods are specified and conform to a standard
- Data are traceable to a testing data—generating organization or individual

Highly Qualified Data

- High confidence limits determined (i.e., 0.99, 0.95, *n*)
- Perform minimum number of individual measurements
    a. From minimum number of sample lots
    b. From multiple suppliers (if appropriate)
- Data determined for each variable that significantly affects property
- Independent testing performed (other than from the producer and preferably by several leading laboratories)
- A second, independent evaluation (evaluator identified)
- Producer(s) identified

[1]From Reference 53

@Seismicisolation

Table 2. Data Elements for the Identification of Chemical Admixtures for Concrete[1]

Constituent Designation Data Segment Number	Name	Type	Format
3001.xx	Constituent Class	Essential	Alphanumeric String
3002.xx	Constituent Common Name	Essential	Alphanumeric String
3003.xx	Constituent Producer Name	Essential	Alphanumeric String
3004.xx	Constituent Producer Plant Location	Essential	Alphanumeric String
3005.xx	Constituent Producer's Identification Number	Essential	Alphanumeric String
3006.xx	Constituent Standards Organization	Desirable	Alphanumeric String
3007.xx	Constituent Specification Number	Desirable	Alphanumeric String
3008.xx	Constituent Specification Version	Desirable	Alphanumeric String
3009.xx	Constituent Specification Designation	Desirable	Alphanumeric String
3010.xx	Constituent Notes	Desirable	Alphanumeric String

[1]From Reference 39.

Table 3. Chemical and Physical Data Elements forAdmixtures for Concrete[1]

Number	Name	Type	Format
3011.xx	Chemical Name	Essential	Alphanumeric String
3012.xx	Percent by Mass	Essential	Floating Point
3013	Total Solid	Essential	Floating Point
3014	Total Solid Units (customary units)	Desirable	Alphanumeric String
3015	Total Solid Units (SI units)	Essential	Alphanumeric String
3016	Customary to SI Conversion Factor	Desirable	Floating Point
3017	pH	Desirable	Floating Point
3018	Density	Desirable	Floating Point
3019	Density (customary units)	Desirable	Alphanumeric String
3020	Density (SI units)	Essential	Alphanumeric String
3021	Customary to SI Units Conversion Factor	Desirable	Floating Point
3022	Comments	Desirable	Alphanumeric String

[1]From Reference 39

@Seismicisolation

3.4 Future Advances in Databases

Advances continue to be made in database technology in such areas as improved database languages, management systems with more efficient search capabilities, and overall ease of database development. It is to be expected that the advances will benefit concrete technology.

In the near future, the most important advances in database technology are likely to be in distributed open systems. Looking further ahead, Brodie[54] predicted that information systems of the future will go beyond distributed database technology to provide intelligent interoperability incorporating artificial intelligence and natural language processing. Ways in which artificial intelligence and databases can be integrated and how distributed artificial intelligence can be realized have been further discussed by Bell and Grimson.[55] They propose that the integration can be achieved in three ways:

1. Enhanced expert systems
2. Intelligent databases
3. Intersystem communications

In an enhanced expert system approach, the expert system (expert systems are defined in the following chapter) would be augmented with data management functions or interfaced to a dedicated general-purpose database management system; an intelligent database would have a deductive database management system embedded in it and in intersystem communication, both an expert system and a database would coexist and communicate with each other. In this case control might reside with either system or in an independent system. If the control resided with the expert system, it would have the capability of selecting databases germane to a specific problem from a matrix of distributed databases. In addition, it would control the retrieval, flow, and interpretation of data and knowledge, and transform them into conclusions and recommendations for presentation to the user. The importance to concrete technology is that the problem-solving ability of an integrated system controlled by an expert system would be limited only by the limits of our level of fundamental knowledge of concrete and our ability to represent that knowledge in an appropriate form; thus, it would have virtually unlimited potential for growth.

@Seismicisolation

4.0 ARTIFICIAL INTELLIGENCE AND KNOWLEDGE-BASED SYSTEMS

A recognized success of the artificial intelligence (AI) field has been the development of intelligent knowledge-based systems.[56] Three types, each of which can be used to solve problems in the concrete domain are expert systems, neural networks, and case-based reasoning systems. Expert systems and neural networks are well-established problem solvers while case-based reasoning is likely to become a competing technology.

4.1 Expert Systems

Expert systems are regarded as the first success of artificial intelligence (AI) technology. Their function is to capture the knowledge and heuristic reasoning of human experts and apply it to the solution of problems which are sufficiently difficult to normally require the service of domain experts.[56] Early expert systems were authentic expert systems in that they captured the knowledge, largely in the form of heuristics, of a single domain expert, e.g., an expert in a specific domain such as causes of human illness. Today's expert systems often include heuristic and factual knowledge from several experts and from other sources such as models, guides, and standards; for this reason they are sometimes termed *knowledge-based systems*. Expert systems consist of two essential elements—knowledge bases and inference (logic) systems (Fig. 5).

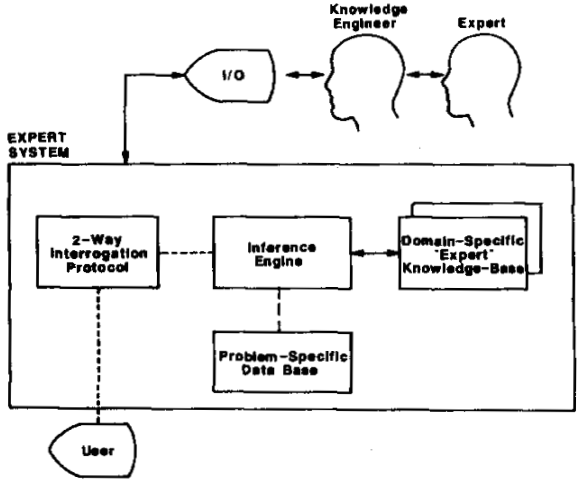


Figure 5. Architecture of an expert system.[58]

@Seismicisolation

The *knowledge base* contains concepts and knowledge the system needs about relationships among the concepts. The *inference system*, often in the form of rules, simulates the way an expert makes inferences about the subject. In their simplest and most-often-used form, expert systems are analogs of expert opinion and are often termed "shallow systems." When combined with databases or mathematical models to support expert opinion they may be termed "deep systems." In general, expert systems are most effective in limited domains in which well-defined solutions exist. Also, they are best developed for domains in which the knowledge base is relatively stable, otherwise they may be obsolete before being completed. The development, principles, and applications of expert systems to concrete have been discussed by Clifton and Oltikar,[57] and Clifton and Kaetzel.[58]

4.2 Application Domains

The value of expert systems as aids to decision making has been demonstrated in a range of technical fields. Well-known examples are in medical diagnosis,[58] identification of chemical compounds,[2] and guiding the overhaul of diesel engines.[60] Expert systems are also applicable to many types of problems which occur in concrete technology, including the following categories:[5]

1. *Diagnosis*—Diagnostic systems were among the first expert systems developed. An example from the concrete field is HWYCON[61] which was developed to assist highway inspectors in identifying the causes of distress in concrete highway pavements and bridges and recommending remedial action; it has also found use in graduate courses in engineering materials.
2. *Selection*—Selection systems can form a basis for selecting the most cost-effective durable concrete for specific applications. A prototype expert system, DURCON (from DURable CONcrete)[57] was developed in the 1980s to represent the knowledge contained in the American Concrete Institute's "Guide to Durable Concrete."
3. *Scheduling/processing planning*—Scheduling systems may have application in strategic planning or simulation in construction. In this case, the expert system is likely to contain a model of the construction process.

@Seismicisolation

4. *Monitoring/control system*—Expert systems that continuously monitor and in some cases control complex processes, can handle large amounts of input data and respond to routine situations. For example, an expert system could be used to monitor the structural condition of concrete structures.
5. *Computer-aided design*—Computer-aided design (CAD) systems based on expert system technology have enabled engineers and architects to develop customized models of plants, factories, and concrete structures.

The state-of-the-art of expert systems for construction materials, with the emphasis on concrete, was recently reviewed by Kaetzel and Clifton.[62] They found that the most successful applications of expert systems have been in the design of structures and structural components, distress identification and failure diagnostics, repair and rehabilitation, and project planning. In the area of concrete, fifteen expert systems were identified of which seven were operational.

In a recent workshop on standards for cement and concrete[63] it was recommended that standard practices and other standard documents should be expressed in the form of expert systems; one of the benefits would be that key provisions could be retrieved much more quickly than by reference to text and the interpretation of standards in an expert format would be more straightforward.

Future Trends in Expert Systems. In the 1970s and early 80s, expert systems were promoted as the solution to many of mankind's problems; eventually, the excessive optimism dissipated and many expert system development efforts were terminated. The major problem was that expectations were not being met rapidly enough. Conclusions from a recent survey were that the greatest barriers to growth in expert systems were difficulties in system integration (which relies on standards), the knowledge bottleneck (effective transfer of human knowledge into an expert system), and management inertia (the memory of artificial intelligence failures in the 1980s).[56] Automated knowledge-acquisition tools now present the potential of reducing and possibly eliminating the knowledge-acquisition barrier with domain experts being able to enter knowledge directly into an expert system without the intervention of knowledge engineers. This will simplify both the development and maintenance of expert systems. The impact of automated knowledge-acquisition on concrete knowledge will be substantial,

@Seismicisolation

e.g., the benefit of being able to capture and preserve the knowledge of the few true concrete experts would be immeasurable.

Expert systems will be increasingly interfaced with databases, neural networks, and various types of mathematical models, to form integrated systems. Visual information (graphical information and images of all sorts) will be an increasingly important component of expert systems (e.g., images of pavement distresses in HWYCON[61]), to aid in the decision-making process. Also, as suggested by the increasing attention by academic and corporate researchers,[64][65] expert systems will be distributed under the umbrella of distributed artificial intelligence. While traditional AI emulates some forms of human intelligence with single, unified systems, distributed artificial intelligence systems (DAIS) brings a decentralized approach to intelligence.[56] Applications that are especially suited to DAIS are those in which an important aspect of a problem is itself distributed. An example in concrete technology is the consolidation and curing of concrete pavements in which several processes affect the quality of the hardened concrete.

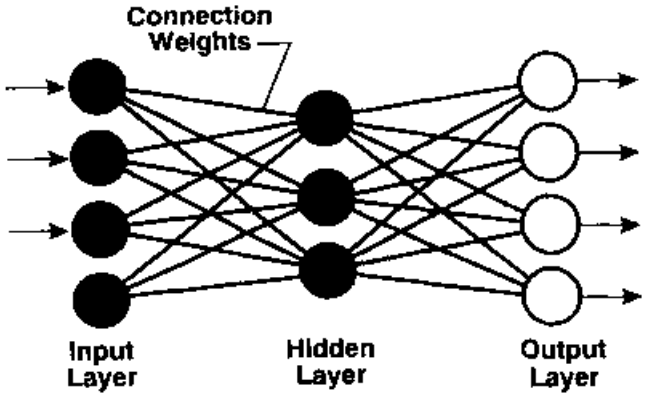
4.3 Neural Networks

As the name implies, neural networks were developed as an attempt to model the functioning of neurons in the human brain;[66] however, since, at best, they are simplistic models of human intelligence, other names have been introduced for neural networks; they include adaptive systems, parallel distributed processing models, and self-organizing systems.

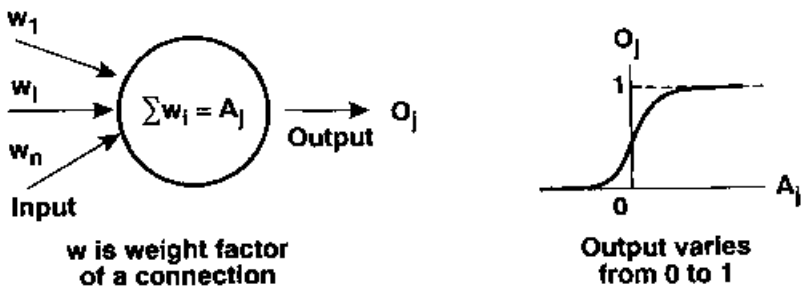
Description of Neural Networks. A brief description of neural networks is given here; detailed information may be obtained from such books as Ref. 66 and 67. Neural networks use networks of simple but highly-connected "neurons" which process input data to give the desired outputs. The connected elements can consist of one or more layers. A 3-layer network is presented in Fig. 6. Similar to regression equations, the connections between the elements have adjustable weights. Several approaches havebeen developed for adjusting the weighted connections by training with actual data. Neural networks are able to work with incomplete or unreliable sets of data. They excel at relatively low-level, data-rich tasks such as image processing.[56] With expert system technology's focus on high-level reasoning, a natural synergy should exist between neural-net (NN) and expert systems (ES). Coupled ES-NN systems could use a neural net for initial filtering and processing of data, followed by use of an expert system for specific reasoning functions.[56] For example, while neural

@Seismicisolation

networks appear to have great potential for empirically determining the effects of different variables on the performance of concrete they do not provide information on the reasons for the observed effects. In a coupled ES-NN system the expert system part could assist in determining reasons for the observed effects. Coupled ES-NN systems have been applied by the Bechtel AI Institute to inspect for defects in manufactured items and to give recommendations on corrective actions.[56]



(a)



(b)

Figure 6. Artificial neural network.[5] *(a)* A 3-layer neural network with connections. *(b)* Connection weights, W_n, and output, O_j.

@Seismicisolation

Application of Neural Networks. Some applications of neural networks to concrete and related materials have included prediction of thickening times of oil-well cements,[68] prediction of shear strength of concrete beams,[69] evaluation of the condition of deteriorating concrete structures,[70] interpretation of impact-echo test results,[71] and prediction of the depth of carbonation of concrete.[72] An example of the possible application of neural networks is the design of concrete mixtures. This is because, at present, much of the vast body of data on mixture design is incomplete and fuzzy—just the type of data for which neural networks are best suited.

4.4 Case-Based Reasoning

Case-based reasoning is based on the paradigm of human thought in cognitive psychology that contends that human experts derive their knowledge from solving numerous cases in their problem domain. Although humans may generalize patterns of cases into rules, the principle unit of knowledge is "the case."[73] Thus, the reasoning is by analogy or association with the solutions for previous similar cases. Case-based reasoning can be particularly useful in areas where traditional rule-based reasoning is relatively weak, such as knowledge acquisition, machine learning, and reasoning with incomplete information. At present, prototype computer programs are being tested for their effectiveness in problem-solving tasks using the case-based reasoning approach. Manual systems have been successfully used in medicine, law, and in design and failure analysis. Such systems have dealt with conceptual design of office buildings and building failure analysis.[74] A possible application of case-based reasoning to concrete problems is the identification of causes of concrete deterioration where the records are incomplete and traditional methods of analysis are inconclusive.

5.0 COMPUTER-INTEGRATED KNOWLEDGE SYSTEMS (CIKS) FOR CONCRETE

5.1 Features and Development of a CIKS

A computer-integrated knowledge system (CIKS) is a computerized intelligent system of integrated knowledge bases providing the knowledge needed for solving complex problems.[75] The term *knowledge base* denotes

@Seismicisolation

any entity that contains knowledge, including models, databases, images, handbooks, guides, and standards and codes. Integration means that knowledge and data flow seamlessly (automatically) across interfaces, i.e., from one knowledge base to another.[5] A CIKS can be developed to solve problems which may require the use of databases or a wide spectrum of knowledge ranging from the experience of experts in the form of heuristics to fundamental knowledge and factual data that is contained in either locally or globally distributed databases.

The development of a CIKS involves the following major steps:[5] *(i)* defining the purpose of the system and the intended users; *(ii)* identifying and developing the appropriate architecture for the system; *(iii)* developing an information model; *(iv)* developing a prototype system; and *(v)* establishing methods for determining the reliability of, and for maintaining, the CIKS. The reliability of a CIKS will depend on the quality of the knowledge it contains.

5.2 Application of CIKS to Concrete Technology

Two examples of different applications of CIKS technology to construction materials and systems are presented, followed by a description of a prototype system for reinforced concrete.

Service Life Design. The conceptual CIKS shown in Fig. 7 incorporates an expert system along with models and databases. It maps a methodology for designing a concrete mixture design to obtain a specific service life.[5] First, an expert system and mathematical models are used to define the necessary material properties required by the concrete to give the desired service life. Then, distributed databases are searched to determine if existing mixture designs can be found which will give the necessary material properties at an acceptable cost. If such a mixture design is found it is specified; if not, a new mixture must be formulated. Several methods can be used, possibly in combination, to formulate a new mixture that is more likely to give the required properties. The new mixture can be tested, either by models or standard test methods, or a combination. If the new mixture gives the required properties, it is specified; if not the process is repeated. Note that data on each new mixture designed are "banked" into the database for further reference by those who have access to the system. An operational, prototype CIKS that can provide an estimate of the service life of reinforced concrete in which the most probable mode of degradation is chloride-induced corrosion is described in a following section.

@Seismicisolation

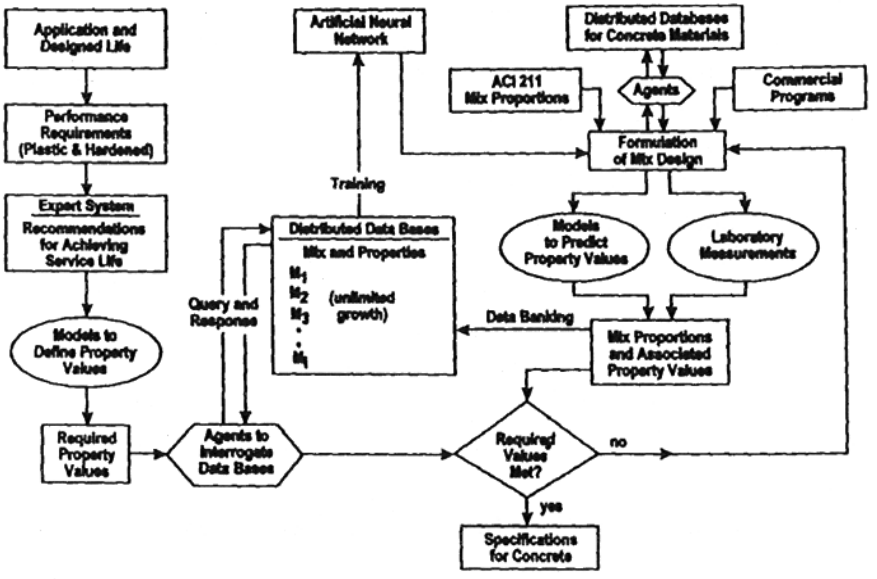


Figure 7. Conceptual CIKS for designing mixtures for HPC, based on service life requirements.[5]

Electronic Handbooks. In a recent workshop on CIKS for high-performance construction materials and systems (HPCMS),[75] a prevailing opinion was that, in the near future, a likely application of CIKS to HPCMS will be the dissemination of databases on the types, properties, and sources of commercially-available construction materials. Such databases, which could be considered to be electronic handbooks, would be of great value to designers and material specifiers. The integrating of databases with models giving reliable predictions of performance and life-cycle costs[81] should help to make apparent the technical and economical benefits of high-performance concrete and other high-performance construction materials. The integrated system should be more effective than stand-alone databases in stimulating the use of high-performance construction materials.

A Prototype CIKS for Concrete. A prototype CIKS for predicting the service life of chloride-exposed steel-reinforced concrete has recently been developed[76] (also, available on the Internet at *http://ciks.cbt.nist.gov/~bentz/welcome.html)*. The system consists of a series of hypertext markup

@Seismicisolation

language (HTML) pages and forms which can be accessed over the World Wide Web. It includes numeric and literature databases, ACI guidelines for proportioning concrete mixtures for ordinary and high-strength concretes, simulation and service life models, and guidance on analyzing experimental results. Forms for use in submitting input to the computer program are for:

1. Mixture proportioning of ordinary and high-strength concrete.
2. Estimating the chloride ion diffusion coefficient of a concrete as a function of mixture proportions.
3. Simulating the chloride concentration profile in a concrete exposed to an external source of chloride ions.
4. Predicting the service life of reinforced concrete exposed to an external source of chloride ions.

The steps in designing a concrete and predicting its service life are as follows: The main menu viewed upon accessing the system is shown in Fig. 8. The first step in obtaining a concrete with a desired service life is selecting the concrete materials and the mixture proportions. The current ACI guidelines for ordinary concrete[77] and for high-strength concrete[78] are computerized and they form the basis for designing the concrete mix proportions. The user fills in the form shown in Fig. 9 for proportioning an ordinary-strength concrete; then, a trial mixture design is proposed to the user along with the predicted chloride ion diffusivity *(D)*. The prediction of chloride ion diffusivity is based on a model developed at NIST.[13][14] The next step is to predict the service life of the reinforced concrete based on the assumption that the service life is the same as the initiation period (the time for the corrosion-threshold concentration of chloride ions to accumulate at the depth of reinforcement). The time for the threshold of chloride ions to reach the reinforcement is modeled using Fick's second law of diffusion.[79] In addition to knowing the value of *D*, the depth of concrete cover over the reinforcement, the concentration of chloride ions at the concrete surface must be known or assumed. Using the values given in "Example 1, Bridge Deck," from the report by Weyers and Cady,[80] the service life predictions for an ordinary concrete and a higher strength concrete are given in Table 4.

@Seismicisolation

1) Ordinary strength concrete mixture proportioning (ACI 211.1-91)
2) High strength concrete mixture proportioning (with/without a water reducer) (ACI 211.4R-93 Guide)
3) Predict the chloride ion diffusivity of a concrete based on mixture parameters
4) Predict the service life of a reinforced concrete structure exposed to chloride
5) Predict the chloride ion penetration profile of a concrete after a specific time
6) Advice on analyzing chloride ion penetration profile data
7) View the literature database on chloride ion diffusivity in concrete

Figure 8. Main Menu of model CIKS for concrete.[76]

Ordinary Strength Concrete Mixture Proportioning
Based on ACI 211.1-91 Standard Practice

Compressive Strength **3500** psi (Permitted range of 2000-6000 psi)
Max. Agg. Size **1.5** in. Guidance
Dry Rodded Unit Weight of Agg. 100 lbs per cubic ft.
You may specify slump by changing value below and
turning "Specific Slump" to **On** or
you may have slump selected based on construction type
selected further down (by leaving "Specify Slump" at it **Off** value).
Slump **2.0** in.
Specify Slump On
Fineness modulus of fine ***aggregate 2.8***

Figure 9. Data entry form for the model CIKS for concrete.[(7] Showing example inputs in bold characters; SI units can be selected if desired.

@Seismicisolation

Table 4. Mixture Proportions and Properties for Concrete Calculated Using the Prototype CIKS for Concrete[76]

Compressive Strength	24.1 MPa (3500 psi)	48.2 MPa (7000 psi)
w/c	0.62	0.31
Air Content	1.0%	1.5%
Cement	272 kg/m^3	597 kg/m^3
Water	167 kg/m^3	185 kg/m^3
Fine Aggregate	874 kg/m^3	470kg/m^3
Coarse Aggregate	1172 kg/m^3	1201 kg/m^3
$d \times 10^{-12}$ m^2/s	7.0	0.9
Estimated Service Life	3.8 years	29.2 years

6.0 SUMMARY

The purpose of this chapter is to draw attention to recent advances in computers and information technology that are contributing to major advances in the material science and technology of concrete. For example, these advances in computer technology have enormous implications in concrete science and technology in such areas as prediction of concrete performance, including service lives; sharing of data, information, and knowledge among geographically-dispersed concrete researchers and practitioners; and development of knowledge-based systems such as computer models and artificial intelligence decision-support systems. Also, integrating these knowledge-based systems can form systems (computer-integrated knowledge systems) that have the potential for representing virtually all scientific and engineering knowledge of concrete and making the knowledge readily available to those needing it.

In this chapter the development and application of knowledge-based systems were reviewed in the sequence: computer models; databases; artificial intelligence knowledge-based systems; and concluding with computer-integrated systems. The history of mathematical modeling of cement-based materials was reviewed from a material science perspective with an emphasis on simulation modeling as the authors believe that it will soon become the basis for the material design of concrete optimized for its application. Only a few databases were found which addressed concrete and its constituents. The development of distributed databases which are platform-independent is now possible by the use of a Remote Data Access

@Seismicisolation

(RDA) standard, which is a standard for accessing data from distributed SQL-compliant relational databases. In the future it is likely that distributed databases will be linked with expert systems, with the expert system controlling the search and retrieval of data. Three types of artificial intelligence (AI) knowledge-based systems, each of which can be used to solve problems in the concrete field, were reviewed: expert systems; neural networks; and case-based reasoning systems. Expert systems and neural networks are well-established problem solvers, while case-based reasoning will likely become a competing technology. Two examples of different applications of CIKS technology to construction materials and systems were presented, followed by a demonstration of a prototype system for predicting the service life of reinforced concrete exposed to an external source of chloride ions.

ACKNOWLEDGEMENTS

The authors appreciate the support for this review by the NIST High-Performance Materials and Systems Program. Also, we wish to acknowledge discussions with NIST's Dale Bentz and Edward Garbozci which were of great value in our coverage of computer models.

REFERENCES

1. Brenner, A. E., The Computing Revolution and the Physics Community, *Physics Today*, 49(10):24–30 (1996)
2. Buchanan, B. G., and Feigenbaum, E. A., DENDRAL and MetaDENDRAL: Their Applications Dimensions, *Artificial Intelligence*, 11:5–24 (1978)
3. *High-Performance Computing and Communications: Toward a National Information Infrastructure*, Committee on Physical, Mathematical and Engineering Sciences; Federal Coordinating Council for Science, Engineering, and Technology; Office of Science and Technology Policy, Washington, DC (1994)
4. *ACI Manual of Concrete Practice*, Available on CD-ROM from the American Concrete Institute, P.O. 9094, Farmington Hills, MI 48333-9094.
5. Clifton, J. R., Bentz, D. P., and Kaetzel, L. J., Computerized Integrated Knowledge Based Systems for High Performance Concrete: An Overview, *Report NISTIR 5947*, National Institute of Standards and Technology (1997)

@Seismicisolation

6. Shilstone, J. M., Concrete on the Internet, *Concr. Intern.*, 17(12):25–27 (1995)
7. Krieger, J. H., Chemical Research Faces Opportunities, Challenges from Information Tools, *Chem. & Eng. News*, 26–41 (1995)
8. Garboczi, E. J., and Bentz, D. P., Fundamental Computer Simulation Models for Cement-Based Materials, *Materials Science of Concrete*, (J. Skalny, ed.), American Ceramic Society, II:249–273 (1991)
9. Jennings, H. M., Hsich, J., Srinivasan, R., Haiswal, S., Garci, S., Sohn, D., Hinners, C., Heppner, S., and Neubauer, C., Modelling and Materials Science of Cement-Based Materials, Part I: An Overview, *The Modeling of Microstructure and Its Potential for Studying Transport Properties and Durability*, (H. Jennings, J. Kropp, and K. Scrivener, eds.), NATO, Series E: Applied Sciences, 304:29–62 (1994)
10. Casti, J. L., *Would-Be Worlds: How Simulation is Changing the Frontiers of Science*, John Wiley & Sons, New York (1997)
11. Powers, T. C., Physical Properties of Cement Paste, *Proceedings of the Fourth International Conference on the Chemistry of Cement, Washington, DC , 1960*, 2:577–613, National Bureau of Standards Monograph 43 (1960)
12. Parrott, L. J., Modelling the Development of Microstructure, *Proceedings of Engineering Foundation Conference on Manufacturing and Use of Cements*, Henniker, NY, pp. 43–73 (1986)
13. Bentz, D. P., Garboczi, E. J., and Lagergren, E. S., Multi-Scale Microstructural Modelling of Concrete Diffusivity: Identification of Significant Variables, *Cem. Concr. Agg.*, 20:129–139 (1998)
14. Garboczi, E. J., and Bentz, D. P., Modelling of the Microstructure and Transport Properties of Concrete, *Constrn. Build. Mats.*, 10(5):291–300 (1996)
15. Pommersheim, J., and Clifton, J. R., Mathematical Models of Cement Hydration, C*ements Research Progress 1979*, pp. 281–304, American Ceramic Society (1979)
16. Kondo, R., and Ueda, S., Kinetics and Mechanisms of the Hydration of Cements, *Proceedings of Fifth International Conference on the Chemistry of Cement, Tokyo, 1968*, 11:321–327, Cement Assoc. Japan, Tokyo (1969)
17. Frohnsdorff, G., Fryer, W., and Johnson, P., *The Mathematical Simulation of Mechanical Changes Accompanying the Hydration of Cement*, in: Ref. 16
18. Pommersheim, J. M., and Clifton, J. R., Mathematical Modelling of Tricalcium Silicate Hydration, *Cem. Concr. Res.*, 9(6):765–770 (1979)
19. Pommersheim, J. M., and Clifton, J. R., Mathematical Modelling of Tricalcium Silicate Hydration II. Sub-Models and the Effect of Model Parameters, *Cem. Concr. Res.*, 12(6):765–772 (1982)

@Seismicisolation

20. van Breugel, K., *Simulation and Formation of Structure in Hardening Cement-Based Materials*, Delft University, Delft, The Netherlands (1991)

21. Nonat, A., Interactions between Chemical Evolution (Hydration) and Physical Evolution (Setting) in the Case of Tricalcium Silicate, *Mater. Struct*, 27:187–195 (1994)

22. The Hydration of Tricalcium Silicate, RILEM Committee 68-MMH, Task Group 3 (H. Taylor, Chairman), *Mater. Struct*, 17(102):457–468 (1984)

23. Mathematical Modelling of Hydration of Cement: Hydration of Dicalcium Silicate, RILEM Committee 68-MMH, Task Group 3 (J. F. Young, Chairman), *Mater. Struct*, 20(119):377–382 (1987)

24. The Hydration of Tricalcium Aluminate and Tetracalcium Aluminate, RILEM Committee 68-MMH, Task Group 3 (P. Brown, Chairman), *Mater. Struct*, 19(110):137–147 (1986)

25. Brunauer, S., Yudenfreund, M., Odler, I., and Skalny, J., Hardened Cement Pastes of Low Porosity. VI. Mechanism of the Hydration Process, *Cem. Concr. Res*., 3(2):129–147 (1973)

26. Bentz, D. P., Three-Dimensional Computer Simulation of Portland Cement Hydration and Microstructure Development, *J. Am. Ceram. Soc*., 80(1):3–21 (1997)

27. Jennings, H. M., Xi, Y., Bazant, Z. P., Yang, M., and Neubauer, C., *Modelling and Materials Science of Cement-Based Materials, Part II Recent Developments*, in Ref. 8, pp. 197–226.

28. Bentz, D. P., Garboczi, E. J., and Martys, N. S.,*Application of Digital-Image-Based Models to Microstructure, Transport Properties, and Degradation of Cement-Based Materials*, in Ref. 8, pp. 167–185.

29. Van Breugel, K., *Models for Prediction of Microstructural Developments in Cement-Based Materials*, in Ref. 8, pp. 91–106.

30. *The Modeling of Microstructure and Its Potential for Studying Transport Properties and Durability*, (H. Jennings, J. Kropp, and K. Scrivener, eds.), NATO, Series E: Applied Sciences, 304 (1994)

31. Roelfstra, P. E., Sadouki, H., and Wittmann, F. H., le beton numerique, *Mater. Struct*., 18:327–335 (1985)

32. Wittmann, F. H., Roelfstra, P. E., and Sadouki, H., Simulation and Analysis of Composite Structures, *Mater. Sci. Eng.*, 68:239–248 (1984)

33. Jennings, H. M., and Johnson, S. K., Simulation of Microstructure Development During the Hydration of a Cement Compound, *J. Am. Ceram. Soc.*, 69:790–795 (1986)

34. Struble, L., Johnson, S., Hartmann, M., Kaetzel, L., and Jennings, H., Manual for the Cement Hydration Simulation Model, *NIST Technical Note 1269* (1989)

@Seismicisolation

35. Xi, Y., Tennis, P. D., and Jennings, H. M., Mathematical Modelling of Cement Paste Microstructure by Mosaic Pattern: Part 1. Formulation, *J. Mater. Rev*., 11(8):1943–1952 (1996)

36. Bentz, D. P., and Stutzman, P. E., SEM Analysis and Computer Modelling of Hydration of Portland Cement Particles, *Petrography of Cementitious Materials*, (S. M. DeHayes, and D. Stark, eds.), pp. 60–73, American Society for Testing and Materials (1994)

37. Date, C. J., *An Introduction to Database Systems*, 6th Edition, Addison-Wesley Publishing Co., Reading, MA (1995)

38. Rumble, R. J., and Smith, F. J., *Database Systems in Science and Engineering*, Adam Hilger, Bristol, England (1990)

39. Ferraris, C. F., Guide to a Format for Data on Chemical Admixtures in a Materials Property Database, *NISTIR 5796*, National Institute of Standards and Technology (1996)

40. Pielert, J. H., and Kaetzel, L. J., Cement and Concrete Materials Databases and the Need for Quality Testing, *Materials Science of Concrete*, (J. Skalny ed.), American Ceramic Society, III:337–358 (1992)

41. Teveris, E., A Perspective on Data Mining in the Year 2001: What Can We Expect? *TechMonitoring, SRI Consulting* (May, 1996)

42. Frohnsdorff, G., Integrated Knowledge Systems for Concrete Science and Technology, *Materials Science of Concrete*, (J. Skalny, ed.), American Ceramic Society, I:315–332 (1989)

43. Westbrook, J. H., Kaufman, J. G., and Cverna, F., Electronic Access to Factual Materials Information: The State of the Art, *MRS Bulletin*, pp. 40–48 (1995)

44. Oland, B., Marchbanks, M., and Naus, D., *Plan for Use in Development of the Structural Information Center*, Report ORNL/NRC/LTR-89/8, Oak Ridge National Laboratory, Oak Ridge, TN (1989)

45. Chi, W. K., NCSU Concrete Materials Database, *Strategic Highway Research Program*, Report SHRP/C/FR-91-103, Washington, DC (1991)

46. Reinhardt, H. W., and Funk, G. B., *Expert Systems and Database Systems*, in Ref. 8, pp. 271–285

47. *ICONDA-Agency*, Information Center for Regional Planning and Building Construction of the Fraunhofer Society, Stuttgart, Germany.

48. Morris, J. K., *An Investigative Study and Evaluation of the Database*, Thesis, Masters of Science in Engineering, The University of Texas at Austin (May 1997)

49. Gebhardt, R. F., Survey of North American Portland Cements: 1994, *Cem. Concr. Agg.*, 17(2):145–189 (1995)

50. Brady, K., and Sullivan, J., Remote Database Access, Computer Systems Laboratory, *National Institute of Standards and Technology* (1996)

@Seismicisolation

51. Burleson, D. K., *Managing Distributed Databases*, John Wiley & Sons, Inc., New York (1994)
52. Kaetzel, L. J., and Galler, M. A., Proposed Format for Data on Cements in a Material Properties Database, *Report NISTIR 6034*, National Institute of Standards and Technology (1997)
53. *Formatting and Use of Material and Chemical Property Database Quality Indicators*, ASTM E1484.
54. Brodie, M. L., Future Intelligent Information Systems: A.I. and Database Technologies Working Together, in *Readings in Artificial Intelligence and Databases*, (J. Mylopoulos, and M. L. Brodie, eds.), pp. 623–673, Morgan Kaufman (1989)
55. Bell, D., and Grimson, J., *Distributed Database Systems*, Addison-Wesley Publishing Co., New York (1994)
56. Krause, S., Knowledge-Based Systems, *Techmonitoring*, SRI International (Dec., 1995)
57. Clifton, J. R., and Oltikar, B. C., Expert System for Selecting Concrete Constituents, in *Computer Applications in Concrete Technology*, pp. 1–24, ACI SP-96, American Concrete Institute (1987)
58. Clifton, J. R., and Kaetzel, L. J., Expert Systems for Concrete Construction, *Concrete International*, 10(11):19–24 (1988)
59. Buchanan, B. G., and Shortliffe, E. H., *Rule-Based Expert Systems: The MYCIN Experiments of the Stanford Heuristic Programming Project*, Addison-Wesley Publishing Co., Reading, MA (1984)
60. Waterman, D. A., *A Guide to Expert Systems*, Addison-Wesley Publishing Co., Reading, MA (1986)
61. Kaetzel, L. J., Clifton, J. R., Klieger, P., and Snyder, K., Highway Concrete (HWYCON) Expert System User Reference and Enhancement Guide, *Report NISTIR 5184*, National Institute of Standards and Technology (1993)
62. Kaetzel, L. J., and Clifton, J. R., Expert/Knowledge Based Systems for Materials in the Construction Industry: State-of-the-Art Report, *Mater. Struct*, 28:160–174 (1993)
63. Frohnsdorff, G., and Clifton, J. R., Cement and Concrete Standards of the Future: Report from the Workshop on Cement and Concrete Standards of the Future 1995, *Report NISTIR 5933*, National Institute of Standards and Technology (1997)
64. Simon, E., *Distributed Information Systems*, McGraw-Hill Companies, London (1996)
65. Rauch, W. B., *Distributed Open Systems Engineering*, Wiley Computer Publishing, New York (1996)
66. Nelson, M. M., and Illingworth, W. T., *A Practical Guide to Neural Nets*, Addison-Wesley Publishing Co., Reading, MA (1991)

@Seismicisolation

67. Caudill, M., and Butler, C., *Understanding Neural Networks*, Volume 1: Basic Networks, Massachusetts Institute of Technology (1993)

68. Fletcher, P., and Coveney, P., Prediction of Thickening Times of Oil Field Cements using Artificial Neural Networks and Fourier Transform Infrared Spectroscopy, *Adv. Cem-Based Mat*., 2(1):21–29 (1995)

69. Goh, A. T., Prediction of Ultimate Shear Strength of Deep Beams Using Neural Networks, *ACI Struct. J*., 91(1):28–32 (1995)

70. Yasuda, N., Evaluation of Deteriorating Concrete Structures Using NeuralNetworks,*J. Mater., Conc. Struct. and Pavements,* (Japan Society of Civil Engineers), 24(496):41–49 (1994)

71. Pratt, D., and Sansalone, M., Impact-Echo Signal Interpretation Using Artificial Intelligence, *ACI Mater. J*., 89(2):178–187 (1992)

72. Buenfield, N. R., and Hassanein, *N. M., Neural Networks for Predicting the Deterioration of Concrete Structures,* in Ref. 8, pp. 415–431.

73. Kolodner, J., *Case-Based Reasoning,* Morgan Kaufman Publishers, San Mateo, CA (1993)

74. Sturrock, C., *Matching Information Technology with the Objectives of Materials Data Users*, in A Partnership for a National Computer-Integrated Knowledge System Network for High-Performance Construction Materials and Systems, pp. 10–11, NISTIR 6003, National Institute of Standards and Technology (1997)

75. Clifton, J. R., and Sunder, S. S., *A Partnership for a National Computer-Integrated Knowledge System Network for High-Performance Construction Materials and Systems*, NISTIR 6003, National Institute of Standards and Technology (1997)

76. Bentz, D. P., Clifton, J. R., and Snyder, K. A., Prediction of the Service Life of Chloride-Exposed Steel-Reinforced Concrete, *Concr. Int*., 18(12):42–47 (1996)

77. *Standard Practice for Selecting Proportions for Normal, Heavy Weight, and Mass Concrete (ACI 211.1)*, ACI Committee 211, American Concrete Institute (1991)

78. *Guide for Selecting Proportions for High-Strength Concrete with Portland Cement and Fly Ash, (ACI 211.4R-93)*, ACI Committee 211, American Concrete Institute (1993)

79. Holman, J. P., Heat Transfer, McGraw-Hill Publishing Co., New York (1981)

80. Weyers, R. E., Fitch, M. P., Larsen, E. P., Al-Qadi, I. L., Chamberlain, W. P., and Hoffman, P. C., Service Life Estimates, *SHRP S-688, Strategic Highway Research Program*, National Research Council (1992)

81. Ehlen, M A., and Marshall, H. E., The Economics of New-Technology Materials: A Case Study of FRP Bridge Decking, NISTIR 5864, National Institute of Standards and Technology (1996)

@Seismicisolation

19

Image Analysis

David Darwin

1.0 INTRODUCTION

This chapter discusses the steps needed to identify features of interest and extract quantitative information from digital images. The processes involved in image analysis include image acquisition, image processing, feature recognition, and data analysis. To be successful, image analysis requires an understanding of both the nature of the signal used to form the image and the properties of the specimen. For materials being investigated for the first time this may necessitate use of an iterative process in which the imaging and analysis parameters are refined as information is gathered. One of the key goals of this chapter is to assist in the formulation of a strategy aimed at assuring objectivity in the analysis process.

By its very nature, image analysis differs from the hunt-and-record approach, which tends to emphasize features that are of interest to the analyst without providing a statistical understanding of the occurrence of the features. This is not to say that image analysis cannot be applied to a single image—it can. Typically, when used on a single image the goal is to identify specific features; however, when a broader understanding of the material is desired multiple images must be acquired and analyzed. The balance of this chapter describes each of the principle steps required for image analysis of cementitious materials.

@Seismicisolation

2.0 IMAGE ACQUISITION

The first step in image analysis is image acquisition. This step must not be considered in isolation, since objective analysis requires an understanding of how the steps involved in acquiring and processing the data are mutually dependent. Understanding the nature of the signal and of the specimen itself is of principal importance. Although images can be generated from a number of sources for the study of cementitious materials, scanning electron and light microscopes are the principal tools. As described in Ch. 7, when using the scanning electron microscope (SEM) and associated instrumentation, signal sources typically consist of secondary electrons, backscattered electrons, and characteristic x-rays. Of these, backscattered electrons (BSE) normally provide the greatest utility, although in recent years BSE imaging and x-ray microanalysis have been combined to identify features within concrete and its constituent materials.[2] Secondary electrons (SE) primarily carry topographic information and are, therefore, not as useful as BSE for applying image analysis to bulk specimens.

The actual process of image acquisition consists of recording the signal intensity for each picture element (pixel) within a digital image. The source of the signal is typically a digital camera mounted on a light microscope or a detector mounted in an SEM. The raster (image on the digital monitor) shape is dependent on the number and spacing of the pixels. Ideally, the pixels are spaced equally in the horizontal and vertical directions, but this is not universally true. A case in point being the standard television image in which pixels are spaced farther apart in the horizontal than in the vertical direction.

Available pixel densities include 512 × 480 (television image in the Western Hemisphere) and square images with pixel densities of 2^x (typically x = 6 to 12; 64 × 64 to 4096 × 4096). Pixel densities of 512 × 512 and 1024 × 1024 are the most popular.

The information within an image is carried by the intensities of the individual pixels. In a typical image acquisition system, each pixel can have one of 2^8 = 256 discrete values or gray levels, from 0 to 255. (Note: With some systems, images can be acquired with 2^{12} = 4096 or 2^{16} = 65536 gray levels, but such "depth" is hardly justified for cementitious materials.)[2]

In the balance of the chapter, application of the scanning electron microscope is emphasized. Applications to light microscopy will be addressed as appropriate.

@Seismicisolation

2.1 Nature of the Signal and Contrast Mechanisms

In an SEM, backscattered electrons and x-rays are generated from a volume within the specimen. That volume depends upon the energy of the primary electrons, the properties of the material, and the signal itself. When a primary electron strikes a specimen it undergoes a series of interactions throughout what is described as the interaction volume. Each signal is generated from a portion of the interaction volume known as the sampling or information volume. Image resolution depends, in part, upon the size of the sampling volume, which, in turn, depends upon the size of the interaction volume. As illustrated in Fig. 1 for silicon, the interaction volume typically takes on a pear shape; secondary electrons are generated from a narrow region near the surface (typically 10 nm); backscattered electrons are generated from approximately the outer 30 percent of the interaction volume; while the x-ray generation range occupies a major portion of the interaction volume. The depth of the interaction volume, or electron range, is closely approximated by an expression developed by Kanaya and Okayama.[4]

Eq. (1) $$R_{KO} = \frac{0.0276 A E_o^{1.67}}{Z^{0.889}\rho}\ \mu m$$

in which A is the atomic weight, Z is the atomic number, E_o is the energy of the beam (or primary) electrons in keV, and ρ is the density of the material in g/cm^3. For example, R_{KO} for silicon ($A = 28.09, Z = 14, \rho = 2.34$ g/cm^3) is 6.85 µm for $E_o = 25$ keV.

The example shown in Fig. 1 demonstrates that the size of the sampling volume depends on the nature of the signal and the properties of both the primary electrons and the material being imaged. Thus, as magnification increases and the points at which the signal is obtained become closer together, ultimate resolution depends on the sampling volume. For SE, the lateral dimensions of the sampling volume closely match the size of the electron probe. For BSE and x-rays the lateral dimensions of the sampling volume are considerably greater than the size of the electron probe. At low accelerating voltages, however, the lateral dimensions of the two approach each other. (Note: imaging strategy becomes progressively more important as acceleration voltage is decreased.)[5] Under any circumstances, resolution depends upon both the surface projection of the information volume and the spacing of the pixels on the surface of the specimen.

@Seismicisolation

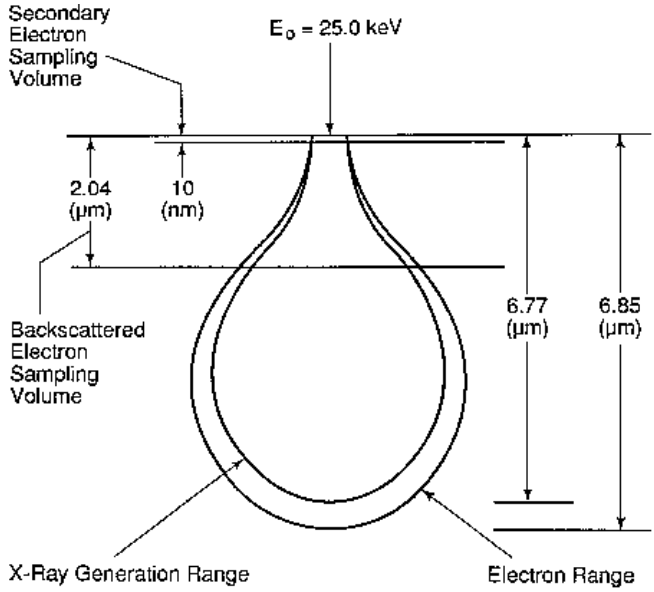


Figure 1. Interaction volumes and sampling volumes for Si, E_o = 25 keV.[3]

As a general rule, the diameter of the surface projection of the sampling volume should not be greater than two times the pixel spacing on the specimen.[5] Otherwise, the image becomes progressively less distinct as overlapping signals are assigned to the pixels. It is clear, based on Fig. 1, that the resolution obtainable with x-rays will always be poorer than that obtainable with backscattered electrons, which will, in turn, be lower than that obtainable with secondary electrons, unless special techniques or transmission electron microscopy are used.[5]

The analyst must be aware of the contrast mechanisms that are available within a signal. In backscattered electron imaging, the principle contrast mechanism is the backscattered electron coefficient, η, which is a function of atomic number. In light microscopy, contrast mechanisms are provided by the number and wave length of the photons.

For a BSE image, the contrast, C, or relative difference between signals, is

@Seismicisolation

Eq. (2) $$C = \frac{\eta_1 - \eta_2}{\eta_1}$$

in which η_1 and η_2 are, respectively, the backscattering coefficients for high and low density materials. The lower the contrast, the more difficult it is to distinguish features from each other.

The threshold equation,[5] which is based on the Rose criterion for identifying the contrast between two points,[6] defines the minimum beam current, i_B, required to see a given contrast for a given pixel dwell time, t_{pp}.

Eq. (3) $$i_B = \frac{4.0 \times 10^{-18}}{\left(\varepsilon C^2 t_{pp}\right)} A$$

in which ε is the efficiency of signal collection (signal current/primary beam current). The pixel dwell time, t_{pp}, is the time during which the signal is acquired from each pixel on the surface of the specimen.

Solving Eq. (3) for C provides guidance in developing a strategy to improve, that is lower, the detectable level of contrast.

Eq. (4) $$C = \frac{2.0 \times 10^{-9}}{\left(\varepsilon\, i_B\, t_{pp}\right)^{1/2}}$$

Choices include increasing the beam current, i_B, or increasing the pixel dwell time, t_{pp}, or a combination of the two. Any step that will increase the *total signal collected* can be used to improve the contrast available in an image or, alternatively, improve the ability of the imaging process to distinguish between signals of different but similar intensity. For a scanning electron microscope, increasing the beam current, i_B, also involves increasing the probe diameter and/or increasing the accelerating voltage. At relatively high accelerating voltages, an increase in the probe diameter will have little effect on the information volume for BSE. At low accelerating voltages, however, an increase in the probe diameter can have a significant effect on the size of the sampling volume.

@Seismicisolation

It is worth repeating that when using x-ray microanalysis the ultimate level of resolution will always be poorer than is available with BSE imaging.

For both scanning electron and light microscopy, the magnification, or more accurately the pixel size on the specimen, along with the lateral dimensions of sampling volume affect the ability to distinguish the edges of features. The reason is that the intensity of pixels at a boundary lies between the intensity of the features of either side of the boundary. Therefore, the smaller the pixel size on the specimen (usually corresponding to a higher magnification), the more accurately the boundaries can be distinguished. Boundary or *edge detection* plays an important role in image processing and data analysis.

2.2 Sample Preparation, Standards, and Imaging

Images should be acquired in as consistent a manner as possible, and techniques for preparing specimens for imaging and for establishing instrumentation settings need to be selected with this goal in mind. For both BSE imaging and light microscopy, specimens should be prepared so that features and boundaries between features are not damaged or altered. Procedures such as epoxy impregnation and polishing need to be evaluated to insure that the techniques do not damage the surface of the specimen. For example, one technique that is used with light microscopy for automated analysis of air void content involves grinding and then polishing the surface of the concrete, application of a surface stabilizer to prevent damage at the edges of the air voids, additional polishing, painting, and then filling the air voids with a gypsum powder.[7][8] The surface is carefully cleaned to insure that the gypsum powder remains only in the air voids. Carelessness in the operation can enlarge air voids and/or cause deposition of the gypsum powder in a manner that would indicate higher than actual air contents.[7][8]

Standards have played an important role in establishing reproducible intensities for both scanning electron and light microscopy.[9] It is not unusual for intensities to be set by the operator without the use of standards. This, unfortunately, adds another level of uncertainty to the process. If many images must be analyzed, the level of uncertainty increases. A standard for use with the SEM consisting of polished magnesium, a portion of which is overlaid with a thin layer of silicon, has been used successfully.[3][10] Typical application of the standard is shown in Fig. 2. A scale is added to the videoscope of an SEM, and the contrast and brightness settings are adjusted to obtain reproducible intensities for the two materials on the standard. In

@Seismicisolation

this case, the signal at the left is silicon and the signal at the right is magnesium. For light microscopy two different colored resins have been used successfully for establishing consistent brightness and contrast settings.[8]

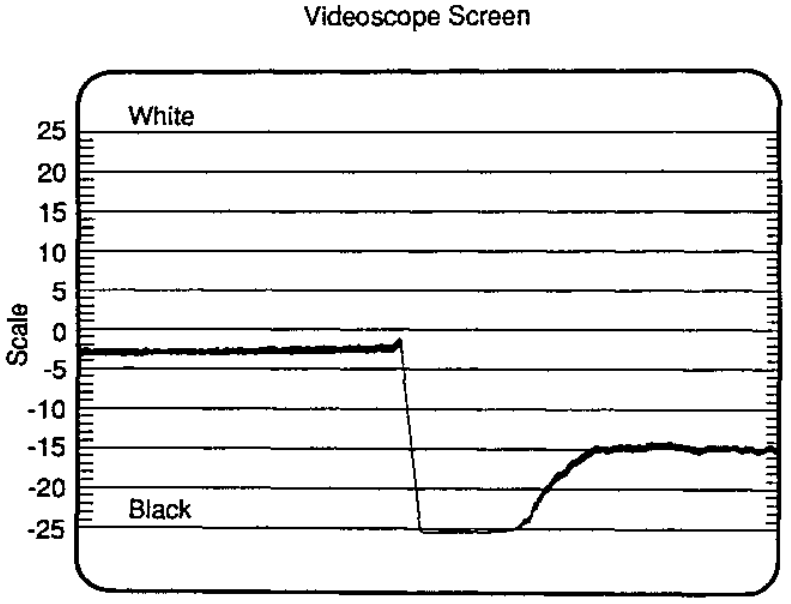


Figure 2. SEM videoscope with scale and signal produced by Si-Mg standard.[10]

It is also important to insure that both the illumination and the signal collection parameters are consistent within and between images. For a scanning electron microscope this may mean allowing the filament to reach a stable temperature prior to imaging, along with regular measurements of the beam current. It also means using a consistent working distance between the microscope pole piece and the specimen and reproducible takeoff and collection angles. For light microscopy it means uniform and reproducible illumination of the surface and a consistent magnification.

@Seismicisolation

2.3 Statistical Considerations

Whether using a scanning electron or a light microscope, any imaging strategy must include the consideration of the number of images and the area of investigation needed to achieve the desired level of statistical certainty in the analysis results. The number of frames, n, required to obtain an estimate of the area occupied by a selected phase with an acceptable error can be expressed as

Eq. (5) $$n = \frac{ZS}{\delta}$$

where Z represents the degree of statistical confidence that the area percent of the phase is within δ of the true average, S is the preliminary estimate of the population standard deviation of the area percent of a phase, and δ is the acceptable error or one-half the maximum acceptable confidence interval.[11] For 95 percent confidence that the area percent of a phase is within δ of the true average, $Z = 1.96$. If phases are analyzed during the image acquisition process, the analyst has the ability to select the number of images, n, as initial estimates of the standard deviation, S, are determined.

It is worth noting that the total sampling area obtained using Eq. (5) is generally a function of the magnification as well as the resolution. Generally speaking, as the magnification decreases, the number of images, n, decreases, but the total area that is imaged increases. This so-called scale effect is due to the tendency to less accurately define the edges of features as the effective pixel size increases. The result is an increase in the standard deviation, S, and, therefore, an increase in the required number of images. For automated analysis of air content, it has been observed that the standard deviation, S, increases with the air content, resulting in a higher required survey area as the air content increases.[8][12]

@Seismicisolation

3.0 IMAGE PROCESSING

Once an image has been acquired, features and their distinguishing characteristics must be identified prior to analyzing the data carried by the image. Image processing cannot add information to an image, but the step is critical to insuring that the analysis yields the greatest information possible.

Many image processing techniques are used because of a lack of clarity in the signal. Therefore, prior to placing major dependence on image processing procedures, it is wise to obtain the clearest possible signal. Steps include selecting the magnification, illumination (electron or light), pixel density, and signal acquisition time, as discussed in Sec. 2.0.

3.1 Contrast and Brightness

Contrast and brightness are, respectively, the difference between and the absolute value of pixel intensities. The goal of image processing should be to modify the pixel intensities so that the maximum information can be extracted.

The range of the intensities within an image can be represented using a histogram, such as shown in Fig, 3. The intensities represented by the histogram can be modified by multiplying and/or adding a constant to the initial values. Doing so can result in compression or stretching of the original histogram. It may also be desirable to normalize the histogram in cases where a large percentage of the pixels have nearly the same intensity. This is accomplished using a transfer function, $H(k)$, such as

Eq. (6) $$H(k) = \frac{1}{T} \sum_{i=0}^{k} n_i \qquad (\text{for } k = 0,...,255)$$

where T is the number of pixels, k is the original pixel value, and n_i is the number of pixels with intensity i.[13]

Applying the transfer function results in a new image in which the pixel intensities are as evenly distributed as possible.[13]

The process of histogram and, thus, image modification is normally used to aid the human eye in distinguishing individual features. The sensitivity of the human eye, however, is limited to far less than 256 gray

@Seismicisolation

levels. The response of the eye is logarithmic and humans are able to distinguish only about 20 discrete gray levels in the full range of black to white.[2][13]

Histogram compression (Fig. 4) is often used by operators to establish settings to get a good-looking image. The procedure, however, is generally a poor choice for image analysis since it tends to limit the information that can be extracted. Histogram stretching is far more advantageous since, while it adds no new information, it provides for the maximum contrast or difference in gray levels available in the image. Using histogram stretching, the clarity of selected features is enhanced. The process can involve "saturation," which forces the gray levels of some features to full black (0) or full white (255).[10][14]

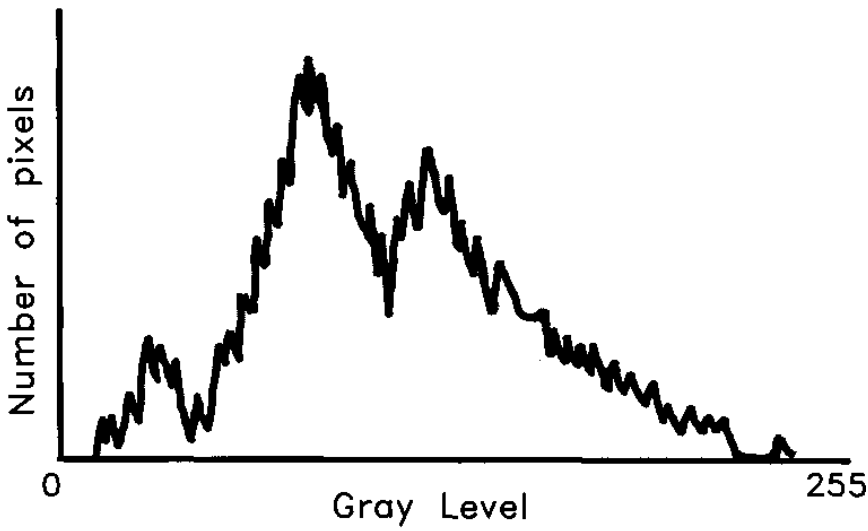


Figure 3. Intensity histogram exhibiting good usage of the available display range (after Ref. 13).

@Seismicisolation

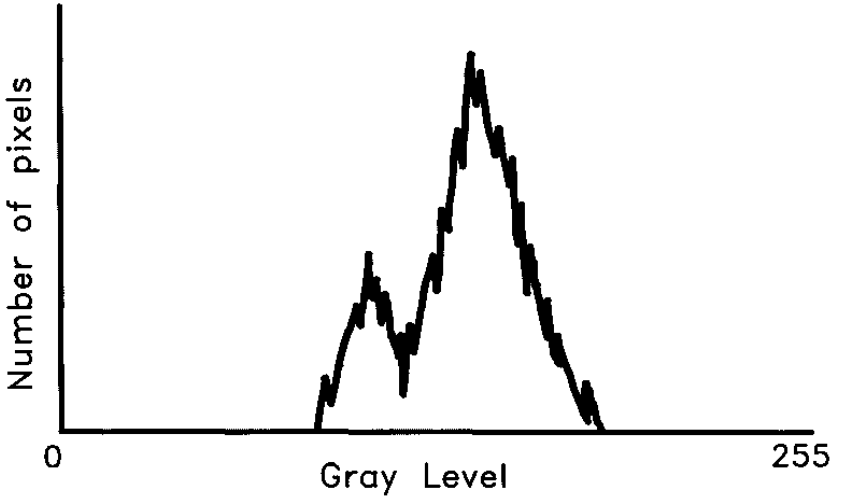


Figure 4. Example of image histogram indicating inadequate usage of available display range (after Ref. 13).

3.2 Thresholding

The process of identifying features by distinguishing discrete ranges of gray level associated with the features can involve thresholding, density slicing, or binary segmentation.[13] Each term has a somewhat different meaning. The general process of thresholding includes the other two procedures and involves the establishment of specific gray levels, or thresholds, so that features exhibiting intensities between two thresholds are assigned to the same class. The procedure works well for materials in which multiple feature classes can be identified using distinct gray level ranges. Density slicing is a similar process in which limits on gray level are selected. The gray levels of features outside of those limits are set to black.[13] Binary segmentation involves the selection of two categories of features lying on either side of a single threshold. Binary segmentation works well for a two-phase image, such as obtained with a light microscope of the surface of air-entrained concrete in which the air voids have been filled with a gypsum powder, as described earlier.[7][8]

Two strategies are usually used to establish thresholds. One involves the use of histograms for images in which the individual features have rather

@Seismicisolation

distinct gray levels. In such a case, the histogram exhibits a series of peaks separated by deep valleys. The low point in each valley is used to establish the threshold between feature classes. Figure 5 illustrates the process for a two-phase image obtained in a study of air void content using a light microscope. This procedure, however, is not always best for backscattered electron images of cementitious materials because of overlap in gray levels,[10][15] the contribution of multiple features to the gray level of individual pixels,[3][10] and the effect of porosity on modifying the signal intensity.[16]

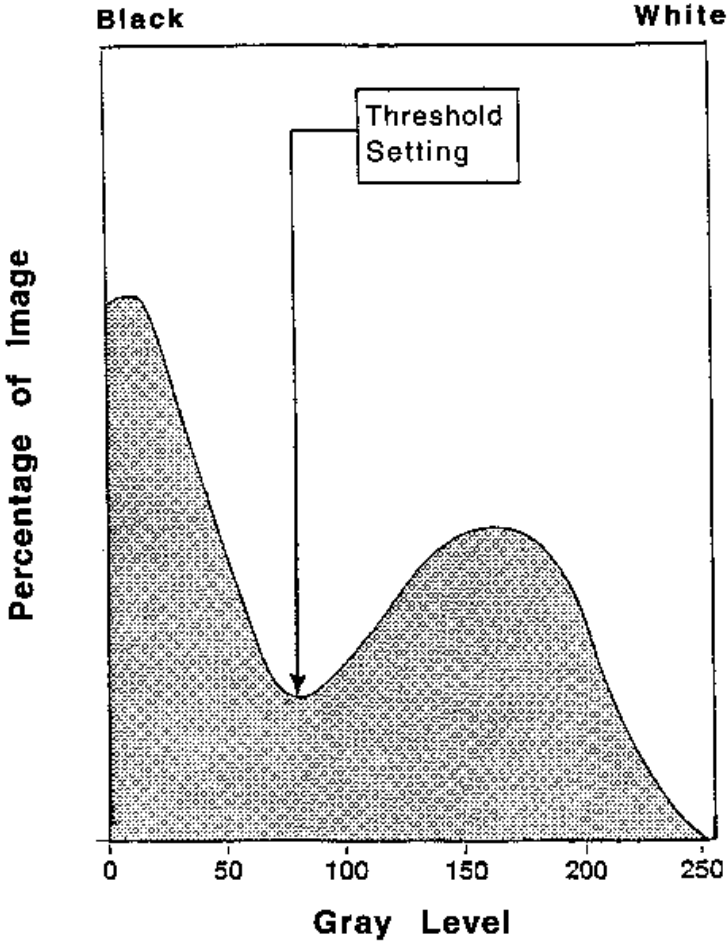


Figure 5. Gray level histogram of an air-entrained concrete image showing the threshold value distinguishing air voids from background.[8]

@Seismicisolation

The second approach involves interactive modification of the individual thresholds (perhaps using the histogram as a starting point) for use in automatic identification of features.[10][14] Using this process, the operator modifies the thresholds until the features of interest are accurately delineated on the image. This procedure works well for cementitious materials because the gray level ranges of some features are very close and often overlap.

It is highly advantageous to have reproducible gray levels when setting thresholds. The standards used for setting imaging parameters, as described in Sec. 2.2, serve this purpose well.[10][14]

3.3 Image Modification

When an image carries random information (noise) that cannot be corrected or removed by improving the collected signal, it may be necessary to modify the image to aid in feature identification and analysis. This can be done by applying a smoothing kernel to reduce local variations in gray level.[2][13] One such kernel applies an equal weight to the pixel of interest and each of the eight surrounding pixels.

Eq. (7)
$$\frac{1}{9}\begin{bmatrix} 1 & 1 & 1 \\ 1 & 1 & 1 \\ 1 & 1 & 1 \end{bmatrix}$$

In most cases, however, it will be more advantageous to weight the intensity of the pixel of interest using a kernel, such as

Eq. (8)
$$\frac{1}{10}\begin{bmatrix} 1 & 1 & 1 \\ 1 & 2 & 1 \\ 1 & 1 & 1 \end{bmatrix}$$

In each case, the gray level of the center pixel is replaced by the weighted average of the pixels within the kernel. A kernel can consist of any odd number of rows and columns. The kernel size is best chosen to be equal or slightly smaller than the size of the image structure of interest.[13] References 2 and 13 provides useful introductions to the subject.

@Seismicisolation

The process of modifying images using kernels is often referred to as filtering. Other image modifications include identifying regions of rapidly changing intensity using kernels that represent discrete approximations of derivative operators,[13] such as

Eq. (9)
$$\frac{\delta F(x,y)}{\delta x} = \begin{bmatrix} -1 & 0 & 1 \\ -1 & 0 & 1 \\ -1 & 0 & 1 \end{bmatrix}$$

Other operations, such as entropy maximization[2][17] and the local Hurst operator,[2] can be useful in extracting information from an image.

4.0 FEATURE RECOGNITION AND DATA ANALYSIS

The final steps in image analysis involve the identification of individual features and the extraction of quantitative information. The latter step often includes analyses that provide estimates of the three-dimensional properties of the material. Most commercial image analysis programs have the ability to identify and catalog the properties of surface features once the thresholding has been completed.

4.1 Feature Recognition

The purpose of image acquisition and image processing is to delineate the features of interest for use in the analysis. The thresholding process establishes regions with specific ranges of gray level. Features within specific ranges are assigned to the same class.

There are some cases, however, in which gray level alone is not adequate to distinguish between features. For example, in cement clinker, C_2S and C_3A have backscattered electron coefficients, η, that overlap. Therefore, it is impossible to distinguish these phases based on gray level alone. However, if BSE image analysis is combined with x-ray microanalysis, the two materials can be separated.[1][15] Once this is done, the features are identified as belonging to different classes and the analysis can proceed.

Another example of feature recognition that depends on more than gray level is that of identifying cracks in cementitious materials.[14][18] With

@Seismicisolation

a BSE image of a polished epoxy-impregnated specimen, cracks and voids exhibit a lower gray level than surrounding features. However, because of the overlap of information volumes (laterally and vertically), cracks and voids exhibit significantly different gray levels as they pass through or over regions of different density. For example, the absolute gray level of a crack through unhydrated cement is higher than the gray level of a crack through undesignated product. This identification problem has been solved by looking at local differences rather than absolute values of gray level.[14][18]

In the case of automatic identification of entrained air voids in concrete described earlier,[8] absolute difference in gray level, as identified through binary segmentation, has proved to be satisfactory for feature identification (Fig. 5).

Once individual features have been identified, additional steps may be required for feature recognition. For example, in the process of identifying cracks and voids, these features have similar gray levels, but they also possess distinguishing geometric properties that aid in identification. In addition, there may be regions of a feature that are not correctly assigned because of artifacts in the image or variations in the signal due to noise or even the basic nature of the imaging process. The analyst may then use steps such as erosion (removal of pixels on the perimeter of a feature) or dilation (addition of pixels) to obtain better feature definition[2] or apply other techniques to join portions of features that should be treated as contiguous.[2][14]

Once the features have been identified, additional geometric properties are measured to further characterize the features.

4.2 Data Analysis

Perhaps the most basic concept in image analysis is the stereological relationship that relates the percentage of points corresponding to each constituent, P_P, with the fraction of linear intercepts for that constituent, L_L, the constituent's area fraction, A_A, and the constituent's volume fraction, V_V.

Eq. (10) $$P_P = L_L = A_A = V_V$$

This relationship simply means that individual sampling techniques for a grid of points, a line scan, or an area analysis, can be used interchangeably

@Seismicisolation

to determine properties on a surface or volume basis. The point count and linear traverse techniques used for manual determination of air void properties in hardened concrete[19] are based on the relationship given in Eq. (10). The relationships in the equation can be used to develop strategies for analysis.[20]–[22]

Analyzing digital images rarely involves the use of a grid to develop a point count. Rather, for computer analysis the point count and area analysis become identical since every pixel can be assigned to a feature type. Individual features are identified based on contiguous pixels belonging to the same feature type. Data obtained from the areal (surface) analysis can then be used to develop an estimate of the three-dimensional properties of the features of interest.

A simpler technique, involving the use of a linear traverse or line scan in which the pixels on a horizontal line are assigned to specific feature classes, can also be used to estimate areal and volume percentages and geometric properties.

Edge detection plays a role in analysis. As discussed in Sec. 3.0, the problem of edge detection arises from the intermediate values of gray level that are measured for the pixels on a feature boundary. The ability to accurately identify an edge can significantly improve the accuracy of an analysis. As the size of the pixel relative to the size of the feature increases, the ability to detect edges is degraded. Thus, for a fixed image pixel density, edge detection improves with increased magnification and degrades with decreased magnification. Careful detection during the image processing stage is critical to developing a consistent representation for feature edges.

In cases where the geometric properties of features are of interest, the intersection of features with the boundary of the image or frame becomes important. The apparent alteration of geometric properties due to truncation by a boundary, as shown in Fig. 6, is known as the *frame edge effect*.

A number of techniques can be used to correct for the frame edge effect, including the use of a guard ring within the image,[22] as shown in Fig. 7. Any features with centers of gravity outside of the guard ring are disregarded in the analysis. Guard rings can be selected based on the maximum feature size or can be variable for features of different sizes.[23] When features occupy a significant portion of the frame area the use of a guard ring can be cumbersome.

@Seismicisolation

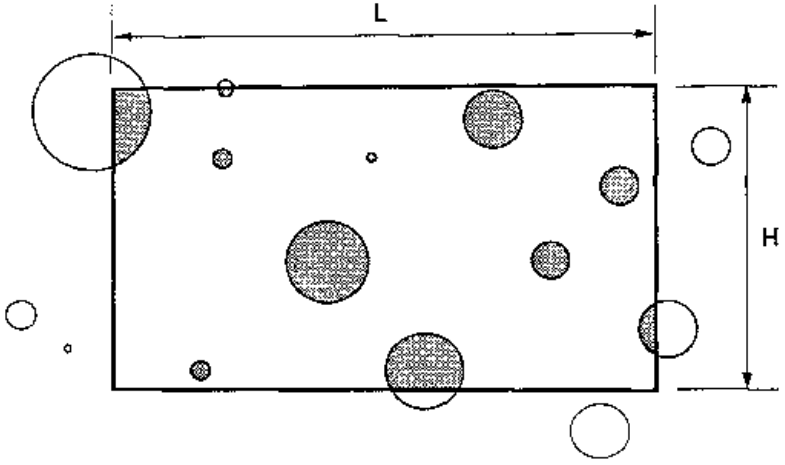


Figure 6. Field of view showing the intersection of areal features by the frame edges.[8]

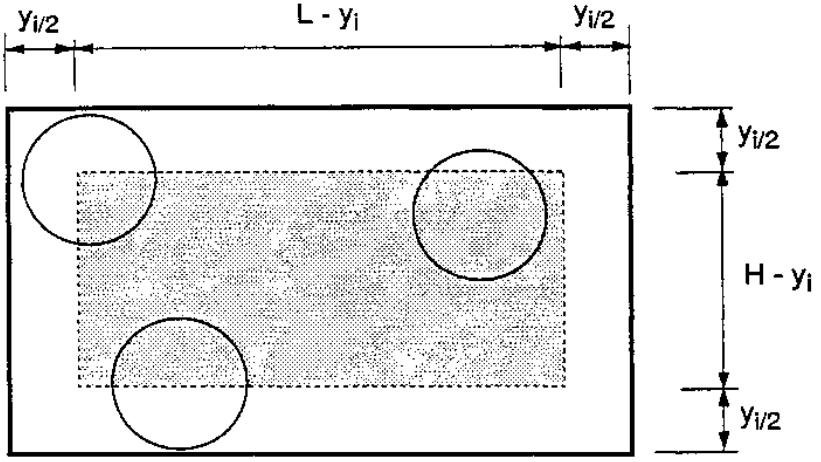


Figure 7. Application of a guard ring within the boundaries of an image for which the center of circular features of diameter y_i can be located and not be intersected by a frame edge.[8]

@Seismicisolation

An alternative procedure for correcting for the frame edge effect uses techniques of geometric probability to determine the distribution of feature properties (usually length or area). The process involves developing a matrix that describes the apparent length and area distributions of features of a specific shape as they would be measured in an image of specific size as a function of the actual distribution. An estimate of the actual geometric distribution of the features is obtained by solving the inverse problem, that is inverting the matrix for use as an operator to apply to the measured feature length or area distribution as obtained from the images.[8]

This procedure is illustrated for horizontal line segments in a frame of length L with the relation[8]

Eq. (11) $$\{N_L(i)^*\} = [K_{ij}]\{N_L(j)\}$$

Eq. (11) relates the apparent length distribution, $\{N_L(i)^*\}$, in which some of the line segments are intersected by the left or right edge of the frame, to the true length distribution $\{N_L(j)\}$. The dimensionless coefficients, K_{ij}, form an upper triangular matrix with the following values:

Eq. (12) $$K_{ij} = \begin{cases} \dfrac{L - l_i + \Delta l_i}{L} & (i=1,..,s;\ j=i) \\ \dfrac{2\Delta l_i}{L} & (i=1,..,s-1;\ j=i+1,..,s) \\ 0 & (i=2,..,s;\ j=1,..,i-1) \end{cases}$$

where, $N_L(i)^*$ and $N_L(j)$ are, respectively, the number of lines with apparent or true lengths in classes i or j; and l_i is the length corresponding to class i which contains line segments of length $l_i \pm \Delta l_i/2$.

Since $\{N_L(i)^*\}$ is actually measured in the field of view, the estimate of the true length distribution, $\{N_L(j)\}$, is calculated from this relationship as

Eq. (13) $$\{N_L(j)\} = [K_{ij}]^{-1}\ \{N_L(i)^*\}$$

@Seismicisolation

Similar procedures based on stereology can be used to develop operators that use line scan and areal data to provide estimates of three-dimensional geometric properties. Excellent summaries of stereological techniques are presented in references.[20]–[22]

REFERENCES

1. Diamond, S., and Bonen, D., A Re-Evaluation of Hardened Cement Paste Microstructure Based on Backscatter SEM Investigations, *Microstructureof Cement-Based Systems/Bonding and Interfaces in Cementitious Materials*, (S. Diamond, et al., eds.), Matl. Res. Soc. Sym. Proc., 370:13–20 (1995)
2. Russ, J. C., *The Image Processing Handbook*, CRC Press, Boca Raton, FL (1992)
3. Zhao, H., and Darwin, D., Quantitative Backscattered Electron Analysis Techniques for Cement-Based Materials, *SM Report*, No. 24, Univ. of Kansas Ctr. for Res., Lawrence, KS (1990)
4. Kanaya, K., and Okayama, S., Penetration and Energy-Loss Theory of Electrons in Solid Targets, *J. of Physics. D: Appl. Physics*, 5(1):43–58 (1972)
5. Goldstein, J. I., Newbury, D. E., Echlin, P., Joy, D. C., Romig, A. D., Lyman, C. E., Fiori, C., and Lifshin, E., *Scanning Electron Microscopy and X-Ray Microanalysis*, 2nd Ed., Plenum Press, New York (1992)
6. Rose, A., Television Pickup Tubes and the Problem with Vision, *Advances in Electronics*, (A. Marton, ed.), I:131–166, Academic Press, New York (1948)
7. Roberts, L. R., and Scali, M. J., Factors Affecting Image Analysis for Measurement of Air Content in Hardened Concrete, *Proc. Sixth Intl. Conf. on Cem. Micro.*, Albuquerque, NM, pp. 402–419 (1984)
8. Dewey, G. R., and Darwin, D., Image Analysis of Air Voids in Air-Entrained Concrete, *SM Report*, No. 29, Univ. of Kansas Ctr. for Res., Lawrence, KS (1991)
9. Joyce Loebl, *Image Analysis: Principles and Practice*, Joyce Loebl, London (1981)
10. Zhao, H., and Darwin, D., Quantitative Backscattered Electron Analysis of Cement Paste, *Cem. Concr. Res.*, 22:695–706 (1992)
11. Ostle, B., and Malone, L. C., *Statistics in Research*, 4th Ed., Iowa State Univ. Press, Ames, IA (1988)

@Seismicisolation

12. Houde, J., and Meilleur, S., Adaptation des Procédé Stéréologiques à la Mesure des Bulles d'air et des Fissures dan le Béton, *Canadian J. Civil Engrg.*, 10(3):415–428 (1983)

13. Newbury, D. E., Joy, D. C., Echlin, P., Fiori, C. E., and Goldstein, J. I., *Advanced Scanning Electron Microscopy and X-Ray Microanalysis*, Plenum Press, New York (1986)

14. Darwin, D., Abou-Zeid, M. N., and Ketcham, K. W., Automated Crack Identification for Cement Paste, *Cem. Concr. Res.*, 25:605–616 (1995)

15. Bonen, D., Discussion of the Paper Quantitative Backscattered Electron Analysis of Cement Paste by H. Zhao and D. Darwin, *Cem. Concr. Res.*, 23:749–753 (1993)

16. Diamond, S., Interactive Digital Image Feature Analysis as Applied to Cement and Concrete Microstructural Investigations, *Digital Image Processing: Tech. and Appl. in Civil Engrg.*, (J. D. Frost, and J. R. Wright, eds.), Amer. Soc. Civil Engr., New York, pp. 158–164 (1993)

17. Mouret, M., Bascoul, A., and Escadeillas, G., Study of the Degree of Hydration of Concrete by Means of Image Analysis and Chemically Bound Water, *Adv. Cem. Based Matls.*, 6:109–115 (1997)

18. Darwin, D., Abou-Zeid, M. N., and Ketcham, K. W., Application of Automated Image Analysis to the Study of Cement Paste Microstructure, *Microstructure of Cement-Based Systems/Bonding and Interfaces in Cementitious Materials*, (S. Diamond, et al., eds.), Matl. Res. Soc. Sym. Proc., 370:1–12 (1995)

19. Standard Practice for Microscopical Determination of Air-Void System in Hardened Concrete (ASTM C 457-90), *1998 Annual Book of ASTM Standards* 04.02, Amer. Soc. Test. Matls., pp. 227–239

20. Underwood, E. E., *Quantitative Stereology*, Addison-Wesley Publ. Co., Reading, MA (1970)

21. Weibel, E. R., *Stereological Methods, Vol. II Theoretical Foundations*, Academic Press, London (1979)

22. Russ, J. C., *Practical Stereology*, Plenum Press, New York (1986)

23. Hougardy, H. P., and Stienen, H., Edge Error Correction in Digital Image Analysis, *Quantitative Analysis of Microstructures in Materials Science, Biology and Medicine*, (T. L. Chermant, ed.), Practical Metallography, Special Issue 8, pp. 25–35 (1978)

@Seismicisolation

20

Specialized Techniques

Hiroshi Uchikawa

INTRODUCTION

Many techniques are used alone or in combination with others in concrete science and technology to investigate the physical, chemical, and mechanical phenomena. In spite of extensive research applying these techniques, there are still many unresolved problems. Some of the common techniques that have been used are described in previous chapters. There has been continued activity to explore the applicability of new techniques. Some are in their infancy as far as their application to concrete is concerned and some others have shown definite promise. Where appropriate, some techniques described in this chapter are also mentioned in other chapters.

In this chapter some details of fourteen types of techniques that may have application in concrete studies have been discussed. As many of them have not found widespread use in concrete some examples of their applicability to other compounds have been emphasized, thus the potentiality of these techniques can be appreciated.

@Seismicisolation

1.0 AUGER ELECTRON SPECTROSCOPY

Principle and Special Features. When an electron beam irradiates the sample, an electron on the L_2(2P)-shell is emitted through an intermediate process, called the Auger process, in such a way that an electron on the L_1(2s)-shell transfers to a vacancy on the K(1s)-shell and energy corresponding to the difference is given to the electron on the L_2(2p)-shell, as shown in Fig. 1. The method that specifies the elements in the sample by measuring the kinetic energy (E_k-2E_L) of the emitted electrons and quantitatively analyzes their content is called Auger electron spectroscopy and the apparatus used for this purpose is called Auger Electron Spectroscope (AES). The energy level of the auger electron is so low that it is measured under a vacuum as high as 10^{-8} torr using an electron energy analyzer (EEA).

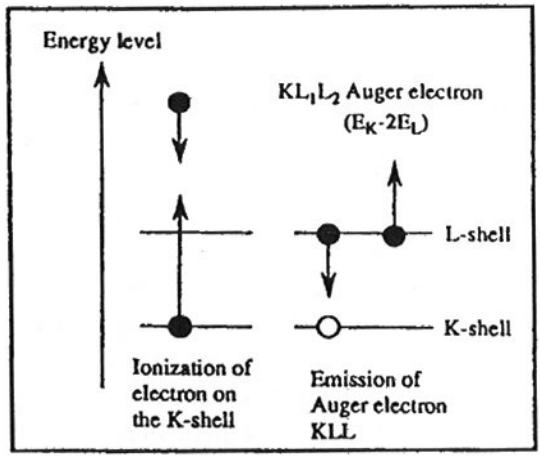


Figure 1. Emission process of Auger electron.

Since emitted energy is as low as 40 to 2,000 eV, as shown in Fig. 2,[1] the depth from which energy can be released is nanometers or less, or 1/1,000 that for the characteristic x-rays. AES is characterized by having the potential to analyze the elements contained in a microscopic region of the surface. The S/N ratio of an Auger electron is so small that energy of the electron is often expressed by the differential coefficient of energy.

@Seismicisolation

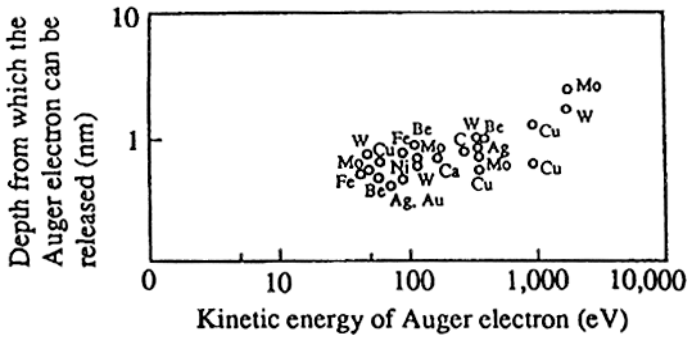


Figure 2. Kinetic energy of Auger electron and the depth from which the Auger electron can be released. (Uchikawa.)[1]

The sample for AES is generally limited to a conductive material. Recently, however, even an insulator providing no correct Auger electron spectrum due to charge-up has been used for AES by a newly developed sample inclination method. Current of primary electron beams, I_p, is the sum total of back scattered electron, I_b, secondary electron, I_s, Auger electron, I_a, and absorbed current, I_{ab}. The absorbed current is nearly equal to zero in an insulating material, the $I_p > I_b + I_s + I_a$. Electrons corresponding to I_{ab} are, therefore, charged up and released, whereupon a noise produced by them interferes with the measurements. The currents I_b and I_a, the sum total of I_s, I_b, and I_a, can be equalized to I_p by increasing I_s. The measurement can be freed from noise interference by improving the emission efficiency of secondary electron, δ. Meanwhile, δ depends upon the accelerating voltage of primary electron beam, E_p, the angle of incident electron beam, θ, and the type of sample material. The emission efficiency of the secondary electron, $\delta_{(\theta)}$, for the angle of incidence, θ, of sample is expressed by Eq. (1)[1]

Eq. (1) $$\delta_{(\theta)} = (1/\cos\theta) \times \delta(0)$$

where $\delta(0)$ is emission efficiency of secondary electron at θ of zero. Near an accelerating voltage of 5 kV of the primary electron beam at the measurement of Auger electron spectrum $\delta(0)$ is 0.3 to 0.5. Substituting 0.3 for $\delta(0)$ and 1 for $\delta_{(\theta)}$ in Eq. (1), θ is given as 72.5°. The resolving power decreased with the increase of θ. The angle of inclination of sample was, therefore, fixed to 75°.

@Seismicisolation

Apparatus. A photograph and block diagram of the Auger Electron Spectroscope are illustrated in Fig. 3. Recently, apparatus obtaining a secondary electron image and an Auger image having a two-dimensional resolving power of 50 nm or better has been developed by scanning the electron beam converged to the order of several nanometers.

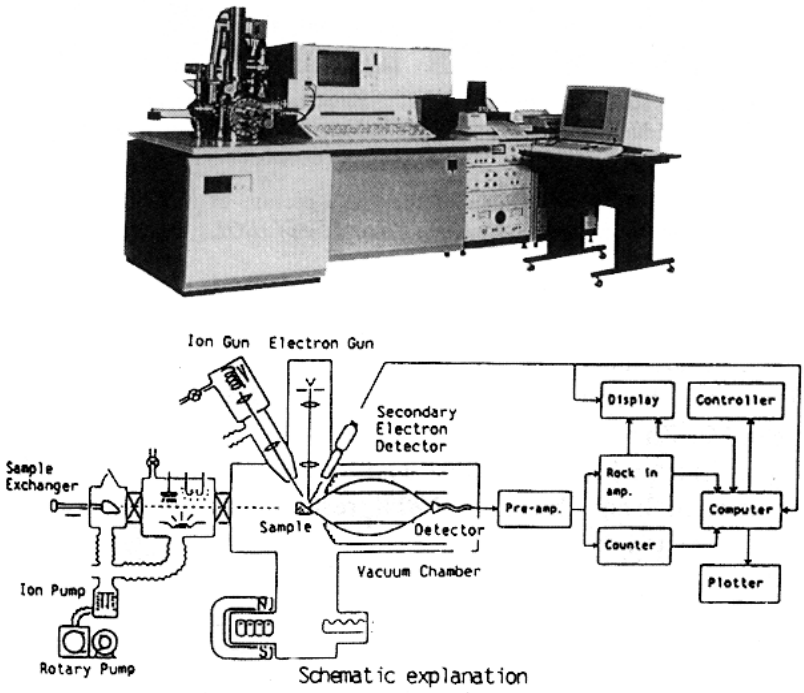
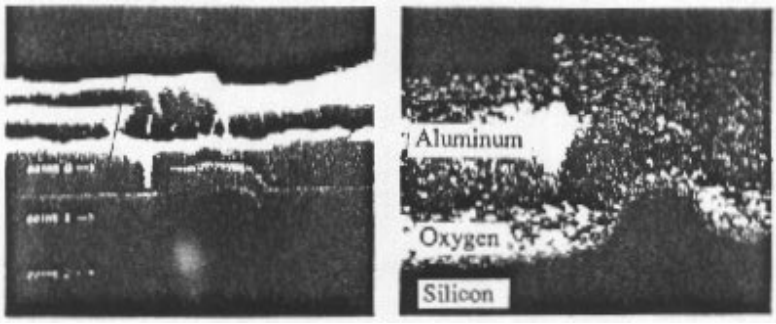


Figure 3. The photograph and block diagram of Auger electron spectroscope (JEOL JAMP-7100E).

Applications. Auger electron spectroscopy is mainly used for analyzing the surface composition of a microscopic region as small as 1μm in diameter and nanometers deep. The two-dimensional distribution of an element in the direction of depth can be determined by combining the sample inclination method with the ion-sputtering method. The two-dimensional concentration distribution can be determined at a resolving power of 50 nm, though the resolving power of EPMA is 500 to 1,000 nm, by incorporating the data processing and system control function in the same way as for CMA/EPMA. An analytical mapping is illustrated in Fig. 4.

@Seismicisolation



Secondary electron image of semiconductor device

Element distribution map determined by Auger electron spectroscope

Figure 4. Electron distribution map of the cross section of semiconductor device determined by Auger electron spectroscope. *(Courtesy of JEOL.)*

AES is widely used for the surface and depthwise analyses of ceramic and metallic materials. An Auger spectrum of the rupture cross-section of particle-particle boundaries of a sintered body prepared by sintering a mixture of Mn-Zn ferrite with 0.1 wt. percent of CaO and 0.02 wt. percent of SiO_2 is illustrated in Fig. 5.[2] The figure reveals that the atomic concentration of Si and Ca are 8 and 22%, respectively, and both atoms are unevenly deposited on the particle-particle boundaries.

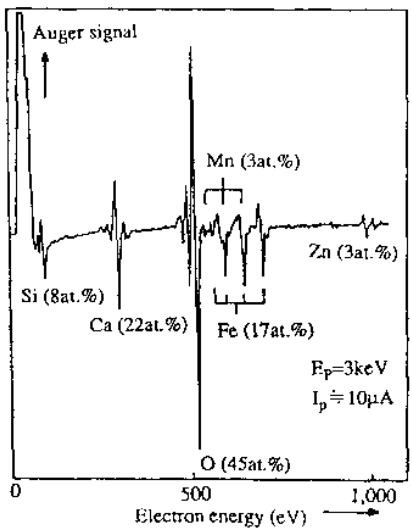


Figure 5. Auger spectra at the cross-section of grain boundary of Mn-Zn ferrite. *(Franken, et al.)*[2]

@Seismicisolation

The wettability of solder is affected by impurities. Figure 6[3] illustrates that large quantities of oxygen and aluminum are distributed on the surface of poor wettable solder *(a)*. An enlarged spectrum reveals that aluminum distributed on the surface of wettable solder is metallic while that distributed on the surface of a poor wettable one is aluminum oxide. From these results, the poor wettability of solder is attributed to aluminum oxide produced on the surface of it.

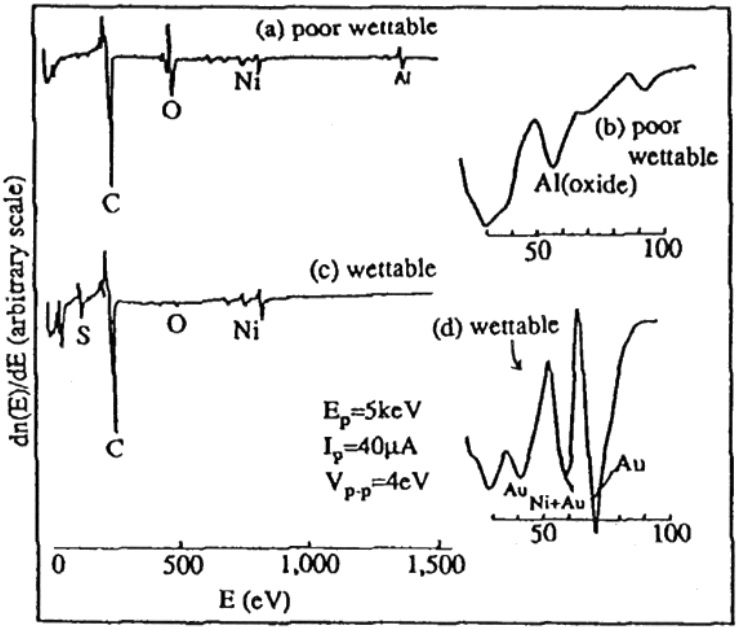


Figure 6. Auger spectrum on Au surface of four metal layer electrode (Au/Ni/Mo/Al/Si). *(Fujiwara, et al.)*[3]

The electric properties of a multilayered film used for IC depend upon the manufacturing method. The analytical result by AES of the difference of the depthwise chemical composition of a multilayered film composed of four layers of Au/Pb/Ni-Cr/TaN for IC is illustrated in Fig. 7.[4] The figure reveals that the layers are manufactured regularly, as designed by the sputtering method, while the Ni-Cr layer is thin and a large quantity of C is mixed in the TaN layer and a large quantity of O is brought onto the

@Seismicisolation

boundary of CR and TaN layers by the vapor deposition method. Moreover, the layer structure formed by the vapor deposition method is irregular, it is inferred that the difference in the electric properties of the multilayered film between the sputtering and vapor deposition methods is caused by the contamination of impurities and the irregular form of layers.

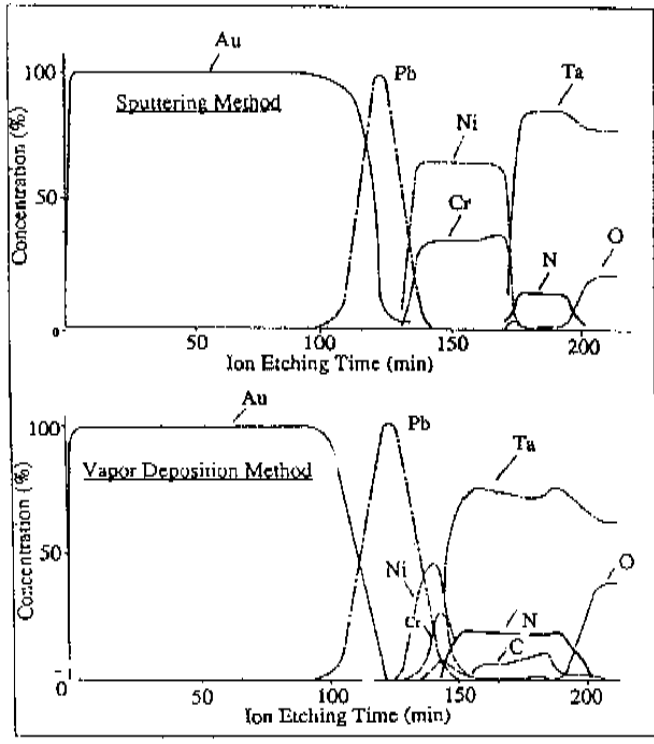
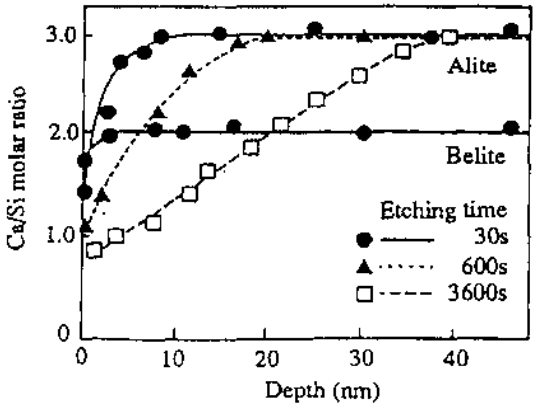


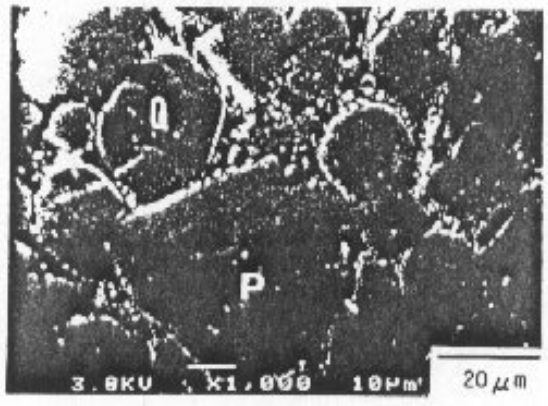
Figure 7. The depth profile of IC multi-layer film measured by AES. *(Hayashi, et al.)*[4]

Applications of AES to the cement and concrete reset are few so far. Papers on the applications of AES include one[5] presenting that the bonding state of C_3S, $C_{12}A_7$, CA and CA_2, can be estimated from the symmetry of Auger spectra of Ca, O, and Al, and another paper[6] suggesting (from the analytical result in the direction of depth of the passive layer on the reinforcement in concrete) that Ca^{2+} penetrates the passive layer when pore solution is the saturated solution of $Ca(OH)_2$, while it stays on the surface of the passive layer when Na is contained in the pore solution.

@Seismicisolation

An attempt has been made to measure the change of surface composition of clinker minerals toward the depth with time in the initial stage of hydration by AES.[1][7] The change of composition in the direction of depth from the surface of alite and belite crystals according to the dipping time in water is shown in Fig. 8.[1]





Secondary electron image
of clinker

Measuring condition of AES:

Accelerating voltage: 3.0 kV, Probe Current: 1.98×10^{-7} A
Pressure: 4.4×10^{-2} Pa, Time constant: 0.1 sec.
Ion gun voltage: 3.00 kV, Sputtering rate: 2.5 nm/min.

Figure 8. Change of Ca/Si molar ratio toward the direction perpendicular to surface after water etching determined by AES. *(Uchikawa.)*[1]

@Seismicisolation

The analytical positions are the center of alite and belite shown in the secondary electron image. The C/S molar ratios on the surface layer and at depths of 3 and 8 nm from the alite surface etched for thirty seconds are approximately 1.3, 2.1, and 3.0, respectively. Calcium ions in alite are selectively dissolved at the beginning of hydration. The position showing the theoretical value of C/S ratio of alite is 8 nm deep which depth coincides with the distance between the peak and the trough on the surface of approximately 11 nm by AFM described later. The C/S ratios on the surface layer of belite and at a depth of 3 nm from it are 1.6 and 2, respectively. The result indicates that the hydration reactivity of belite is lower than that of alite because Ca ions are dissolved at the beginning of hydration less from the shallower part in belite than in alite,

The next example is the result of studies on the adsorptive behavior of organic admixtures on each cement mineral at the initial stage of cement hydration. Carbon and sulfur, main components of organic admixture, and calcium, one of the main components of clinker minerals, were analyzed by AES in the direction of the depth from the surface of the adsorbed layer. The sample was prepared in such a way that the polished surface of clinker was dipped in a practical concentration of aqueous solution of admixture for thirty seconds.

Analytical points by AES are shown on the secondary electron image photographs of Fig. 9[8] and the changes of the concentrations of carbon, sulfur, and calcium, in adsorbed layer on alite and on the interstitial phase are shown in Fig. 10.[8]

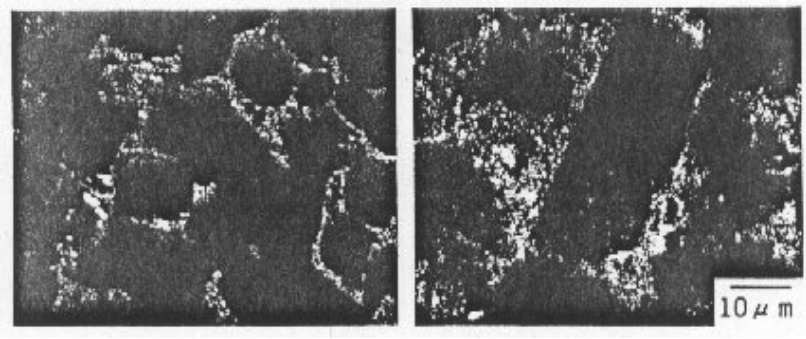


Figure 9. Secondary electron image and analyzing point by AES of polished surface of clinker dipped in aqueous solution of organic admixture. *(Uchikawa, et al.)*[8]

@Seismicisolation

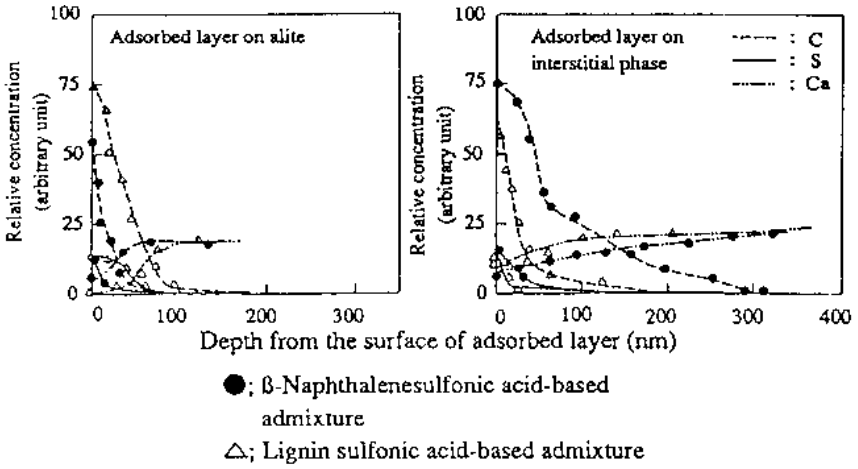


Figure 10. Secondary electron image and analysing point by AES of polished surface of clinker dipped in aqueous solution of organic admixture. *(Uchikawa, et al.)*[8]

From these results it is concluded that the organic admixtures are adsorbed preferably more on interstitial phase than on alite and the preferred adsorption is remarkable in β-naphtalenesulfonic acid-based admixture. The thickness of the adsorbed layer on alite is larger in lignin sulfonic acid-based admixture and that on interstitial phase is thicker when β-napthalenesulfonic acid-based admixture is used.

2.0 SCANNING TUNNEL MICROSCOPY AND ATOMIC FORCE MICROSCOPY

2.1 Principle and Special Features

Observation of Surface Structure. When a voltage is applied to a gap of approximately 1 nm between a needle and a conductive sample, electric current passes through the gap by the tunnel effect in the inverse proportion to the gap distance. An image showing the roughness of the surface of sample at the atomic level can be obtained by scanning the surface with the needle keeping the tunnel current constant.[9] A microscope utilizing this theory is called a scanning tunnel microscope (STM). A microscope

@Seismicisolation

substituting the atomic force between the probe and the sample for the tunnel current is called an atomic force microscope (AFM), shown in Fig. 11.[1] A method for identifying an element from the relationship between the tunnel current and the voltage is called scanning tunnel electron spectroscopy. A combined instrument of STM with SIMS or XPS is being developed for determining the structure and composition of the surface layer at the same time. It is expected to be a useful tool for characterizing a material.

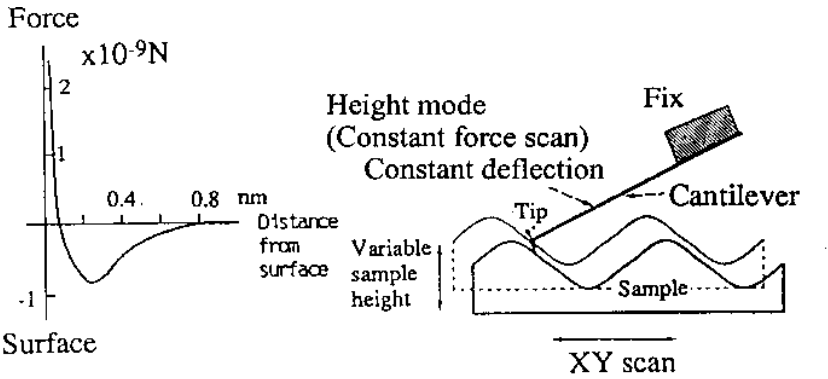


Figure 11. Diagram explaining the principle of the atomic force microscope. *(Uchikawa.)*[1]

Various improvements have been made on STM developed at Zurich Research Laboratories of IBM in 1982, for practical use. Tungsten, platinum, and/or platinum iridium alloys are used for the needle probe. It is most important, for obtaining accurate data to keep the probe clean by removing impurities deposited on it during measurement and to improve reliability. STM is characterized by having enough resolving power, as high as 0.1 nm in the vertical direction and 0.01 nm is attained for the vacuum type STM, for obtaining a real image of each atom.

Attention has been paid to STM as a tool for the final fine processing (atomic manipulation) of a material as well as for its characterization. STM is, therefore, developed to fine machining of a material at the level from the magnitude of an atom to an order of nanometer using phenomena such as electric field evaporation, movement of atom by adsorption, surface reaction of gas, and mechanical cutting.

STM and AFM require no evacuated environment, unlike electron microscopes, and they can be operated even in an ambient atmosphere, gas and water. STM and AFM are, therefore, expected to find wider application in the future.

@Seismicisolation

Measurement of Surface Force. Since the 1950s the direct measurement of the force acting between the solid surfaces has been investigated in such a way that the distance, which is controlled within a range of an order of magnitude of nm, between the surface of a solid suspended with a spring and that of another fixed solid is varied and the interactive force (F) is determined from the displacement of the spring according to the following equation:

Eq. (2) $$|F| = k\,|\Delta H|$$

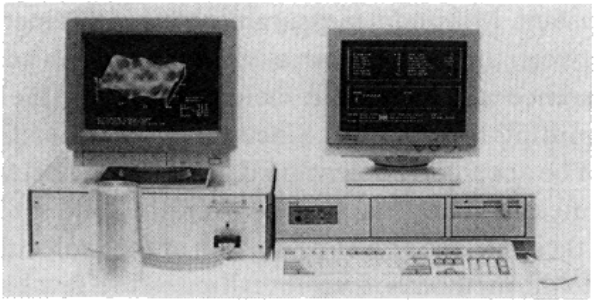
where k is a spring constant and ΔH is the displacement of spring.[10] A surface force apparatus[11] representative of that method is operated in such a way that two solid samples fixed to respective springs are brought close to a distance of 0.1 nm or less and the interactive force is obtained by multiplying the displacement of the samples caused by the interactive force by the spring constant. Minimum measurable value in this method is 10 nN. The distance between the solid surfaces is measured at an accuracy of 0.2 nm by the interference caused by white incident light from the bottom of the apparatus transmitting those solids. Since the contact position of a solid with another can be accurately determined, the distance between the solid surfaces can be measured accurately. However, the solid samples must be transparent and their surfaces must be smooth at the molecular level. The sample applied to the method is, therefore, limited to a few kinds of solids, such as a plane of cleavage of mica. The measurements by the surface force apparatus (SFA) are only a few examples, including hydration force acting between two pieces of mica in an aqueous solution of KC1,[12] force of hydrophobic mutual action of a cationic surface active agent,[13] and interactive force between surfaces covered with macromolecular adsorption film.[14]

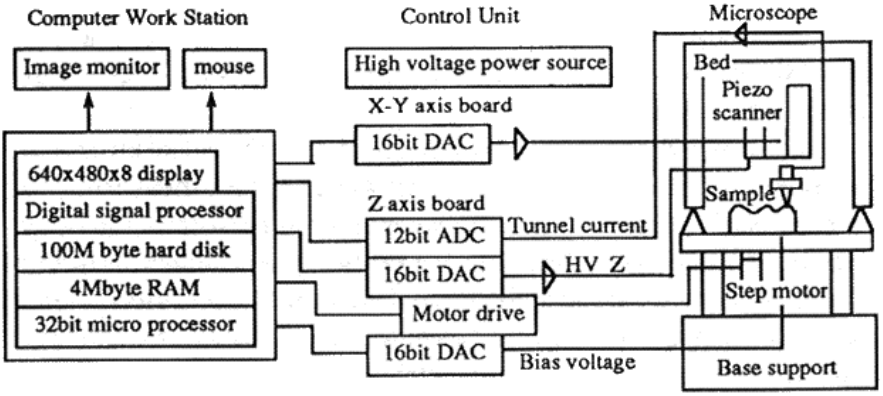
Recently, AFM has begun to be used as a tool for measuring simply and precisely the forces acting between the solid surfaces having the distance of nanometers by bringing the probe close to it to approximately 1 nm without being influenced by the surface state of the solid sample. The distance between the probe and the sample can be controlled with an accuracy of 0.05 nm using a piezoelectric element. The displacement of a cantilever caused by the force acting between the surfaces is determined at an accuracy of 0.1 nm at least, by measuring the intensity of laser beams reflected from the back side of the lever with a position-sensitive photodetector. The force acting between the surfaces *(F)* is calculated by multiplying the displacement of cantilever *(ΔH)* by the spring constant of the lever *(k)* and the lower limit of the measurement is 10^{-3} nN. Since the atomic force

@Seismicisolation

microscope cannot so accurately determine the contact position of the probe with the sample as the surface force apparatus, the measurements of the distance in the curve of the distance between the surfaces versus the force acting between the surfaces (F-D curve) with the AFM are not so accurate as those with the SFA. The AFM is, however, more easily operated than the SFA and does not require as much smooth surface of the sample as the SFA because the measuring region is small (order of μm^2) and an opaque sample can be examined.

Apparatus. Since most commercial apparatuses have both functions of STM and AFM they can be used as either STM or AFM by exchanging the needle probe. The photograph and block diagram of STM and AFM are shown in Fig. 12.





DAC: Digital analog converter; ADC: Analog-digital converter
RAM: Random access memory; HV: High voltage

Figure 12. Block diagram and photograph of STM and AFM. *(Digital Instruments Co., Nano Scope AFM.)*

@Seismicisolation

AFM is operated in such a way that the surface of a sample is scanned with the probe controlling a piezoelectric element so as to keep the repulsive force between the atoms at the tip of probe and those in the sample constant. An image of the surface structure of the sample can be obtained by the signal sent from the piezoelectric element.

2.2 Application

Observation of Surface Structure. STM and AFM are useful for observing the surface structure of insulating materials. In the field of cement and concrete research, they are used for observing the crystal structure and surface structure of clinker minerals, hydrates, and adsorbed layer of organic admixture, on the surface of cement particle.

The AFM images of the surfaces of alite before and after dipping in water for thirty seconds are shown in Fig. 13.[1][7] The smooth surface, before dipping, has a roughness of as much as approximately 1 to 2 nm and fine scratches at intervals of approximately 50 nm regarded to be abraded with abrasion grains of 0.05 μm in average diameter. The roughness of surface, after etching, is enlarged by the dissolution of elements and the distance between peaks is approximately 100 nm. The smoothness of the surface determined in an accuracy of 0.1 nm in the direction of depth is shown in Fig. 14.[1][7] The distance between the peak and the trough on the surface of alite is 10.3 to 11.5 nm. Assuming that the distance corresponds to the size of an alite crystal dissolved, four unit cells with the c-axis 2.5 nm long are leached out from the surface in the direction of c-axis. The distance is increased to 18.5 and 39.4 nm by increasing the dipping time to 600 to 3,600 seconds, respectively. The distance is proportional to 1/4 power of the dipping time, as shown in Fig. 15.[7]

The adsorptive behavior of organic admixtures on clinker minerals at the initial stage of hydration of cement was investigated by AFM. The roughness of a small region (0 to 2,000 nm) on the surface of clinker alite and a large region (0 to 50 μm) covering alite, belite, and interstitial materials surface of polished clinker dipped in water and aqueous solution of admixture was determined by AFM. The surface of clinker dipped in the aqueous solutions of admixture is rougher and the distance between peaks and the distance between the peak and the trough is larger than that dipped in water, as shown in Figs. 16[8] and 17.[15] The results shown in Fig. 17 indicate that the differences in the height of the surface adsorbing

@Seismicisolation

polycarboxylic acid-based admixture (PC), aminosulfonic acid-based admixture (AS), naphthalene sulfonic acid-based admixture (NS), and lignin sulfonic acid-based admixture (LS), between interstitial materials and alite in the cement clinker are approximately 130 nm (1%), 140 nm (2%); 190 nm (2%); 290 nm (1%), 300 nm (2%), and 110 nm (0.25%), 100 nm (0.5%), on an average, respectively. The difference of 20 nm between the height of interstitial material surface and alite surface after dipping 30 seconds in water (Fig. 17) indicates that the organic admixtures are unevenly adsorbed more to the interstitial materials than to the alite and the degree of the uneven adsorption depends on the type of admixtures.

Measurement of Surface Force. Researches on the measurements of the force acting between the surfaces with AFM include verification of the DLVO theory from the measurements of the F-D curve of aqueous solutions with various concentrations of NaC1,[16] estimation of adsorption state of a nonionic surface active agent,[17] determination of isoelectric points of the probe from the measurements of force of action in aqueous solutions with various pH values,[18] measurement of very little force of action between biomolecules,[19] and proof of the existence of steric repulsive force and estimation of its rate of contribution in the dispersion of cement particles by the addition of organic admixture by measuring the interactive force and zeta potential with the Electrokinetic Sonic Amplitude Method.[20]

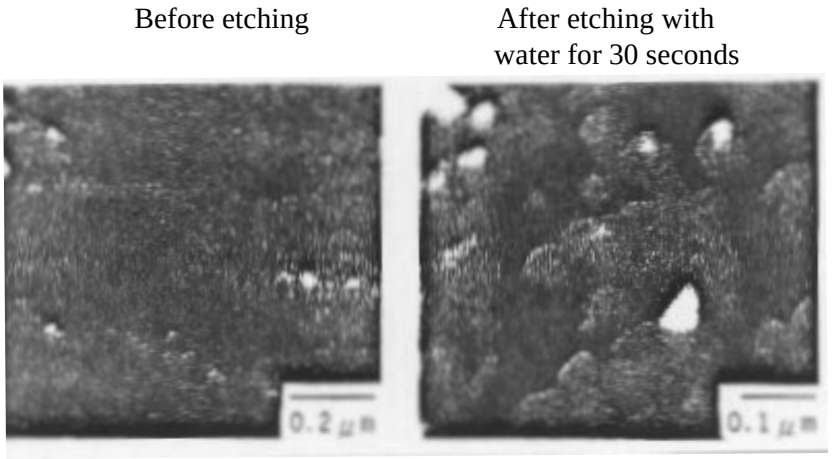
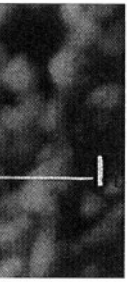
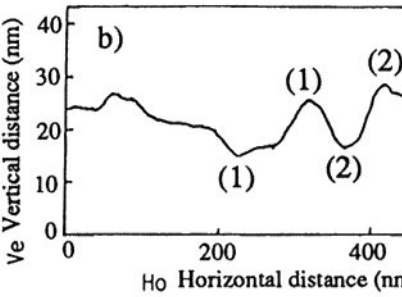


Figure 13. AFM image of clinker alite surface before and after etching with water. *(Uchikawa, et al.)*[1][7]

@Seismicisolation

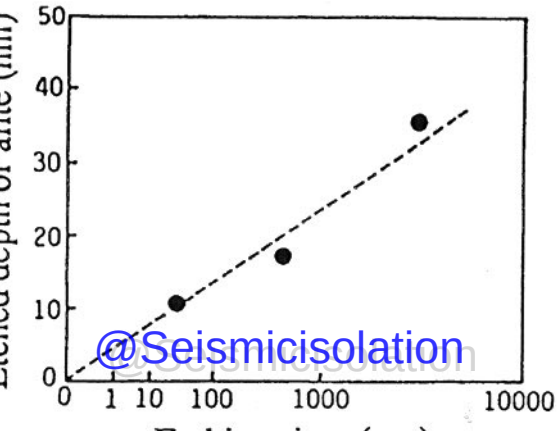




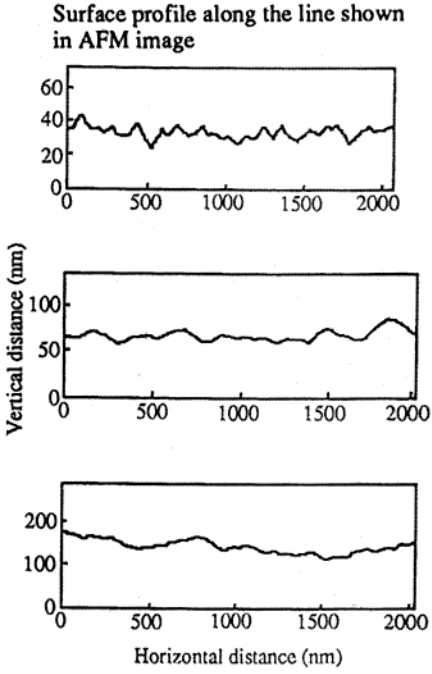
age
profile
shown

	(1)	(2)	
Horizontal distance [nm]	93.00	57.00	3
Vertical distance [nm]	10.34	11.55	1
Angle [deg]	6.35	11.45	1

ghness of the surface of clinker alite etched with water
FM. *(Uchikawa, et al.)*[1][7]



@Seismicisolation



Solution	Distance between the peak and trough (Horizontal)	Distance betwee the peak and trou (Vertical)
Water	100nm	10nm
NS	250nm	20nm
LS	250nm	30nm

@Seismicisolation

oughness of polished surface of clinker dipped in water and aqu
mixtures (range: 0–2,000 nm). *(Uchikawa, et al.)*[8]

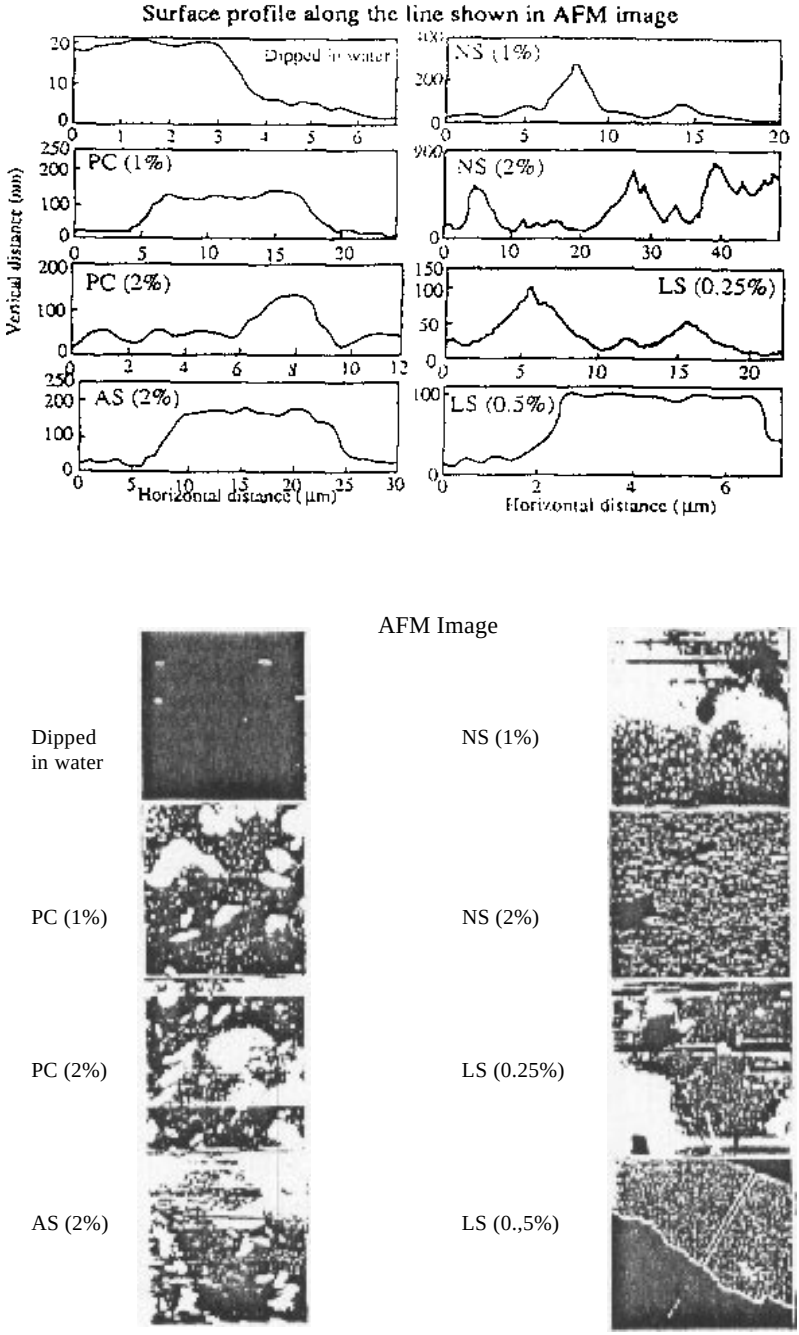


Figure 17. Roughness of polished surface of clinker dipped in water and aqueous solution of organic admixtures (range: 0–50 μm). *(Uchikawa.)*[15]

@Seismicisolation

An example of the Force Distance (F-D) curve of silicon wafer surface adsorbing naphthalene sulfonic acid-based admixture (surfactant, NS) is shown in Fig. 18.[20] The F-D curve expresses the repulsive force acting between a solid surface and needle probe as a function of distance when making the needle probe approach to the solid sample. The moving distance of the probe from the starting point and the interactive force calculated from the deflection of the cantilever are put on the X and Y-axes, respectively. The point, *S*, at which the interactive force begins linearly increasing indicates the point where the probe is brought into contact with the surface of sample. The force acting between the solid surfaces is determined as the difference of the interactive force between points *S* and *P*, and the range of the interactive force acting is determined from the moving time of the probe. There is a small difference between the F-D curve of the probe approaching the sample and that of the probe withdrawn from it.

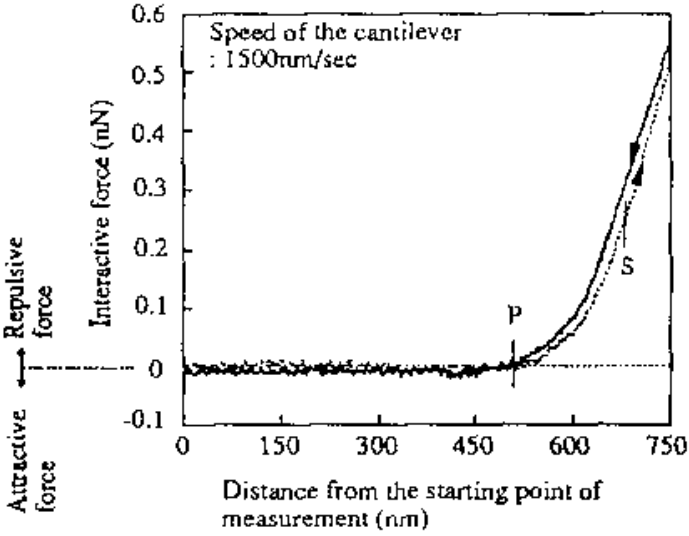


Figure 18. An example of F-D curve. *(Uchikawa, et al.)*[20]

@Seismicisolation

An example of measuring the interactive force between organic admixture and cement particles is shown in Fig. 19.[20] The polished surface of cement clinker immersed in a 10% aqueous solution of admixture was used as the sample and the interactive force was measured as the function of the distance between the needle probe and surface of admixture adsorbed clinker. The F-D curve varied according to the passage of time from the immersion in the aqueous solution of admixture. Maybe this is because the distance between the probe and the polished surface of clinker varied with time by the dissolution of component elements and the deposition of hydrates on the surface. It is, therefore, important to choose the measuring time in the study of a material such as cement which reacts during the measurement. Comparing this with the experimental results of silicon wafer, measurement was started five minutes after immersing the clinker in the admixture solution.

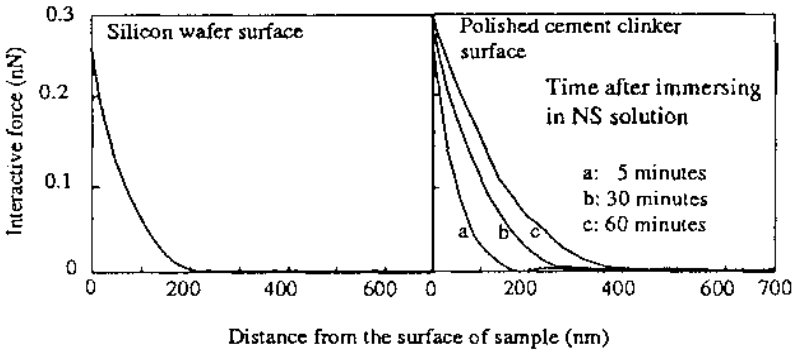


Figure 19. Relationship between interactive force and the distance from the surface of sample. *(Uchikawa, et al.)*[20]

The relationships between the distances from the surfaces of the adsorption layer of admixtures determined from the F-D curves obtained five minutes after immersing the polished surface of cement clinker in various organic admixtures and the interactive force are illustrated in Fig. 20.[20] The repulsive force, measured by the probe of 100 nm in diameter, on the polished surface of cement clinker immersed in pure water was 0.004 nN, while the maximum repulsive forces on the polished surface of cement clinker immersed in such aqueous solutions of admixtures as NS (condensate of β-naphthalene sulfonate with formalin), PC-A (copolymer of acrylic acid with acrylic ester) and PC-B (copolymer of olefin with maleic acid) were 0.24, 0.60, and 0.19 nN, respectively. It was clarified that the distance

@Seismicisolation

of the initiation of repulsive force increased with increasing the repulsive force generated from the admixture. The interactive force logarithmically fell off in inverse proportion to the distance from the surface of the adsorption layer of admixture.

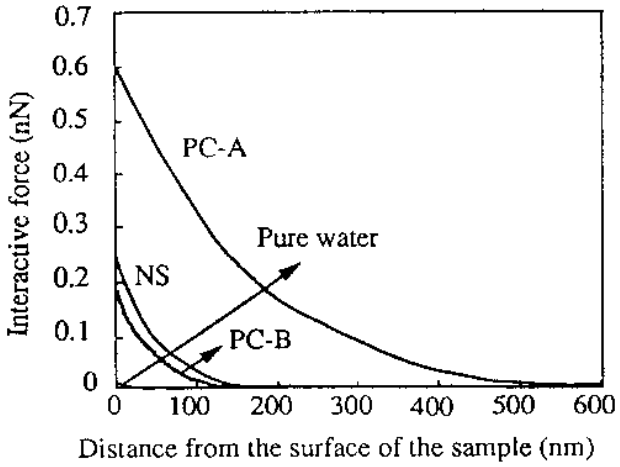


Figure 20. Relationship between the interactive force and distance from the surface of the clinker immersed in solutions of various organic admixtures. *(Uchikawa, et al.)*[20]

3.0 CHROMATOGRAPHY

3.1 Principle and Special Feature

Chromatography is a method for separating the components contained in the sample from each other by mixing the sample with the moving phase comprising liquid or gas, passing the mixture through the stationary phase comprising solid or liquid with some affinities with the components to be separated and utilizing the difference of the affinities of the components. Each component is portioned out to both phases at a specified ratio according to the affinities with both phases and hence is separated.

Chromatography is classified into Gas Chromatography (GC), High Performance Liquid Chromatography (HPLC) and Supercritical Fluid Chromatography (SFC), according to whether the mobile phase is gas, liquid or a super critical fluid.

@Seismicisolation

Gas Chromatography (GC). Gas Chromatography (GC) uses gas as the moving phase and is classified into gas-solid chromatography, using a solid adsorbent as the stationary phase, and gas-liquid chromatography, using a nonvolatile liquid. The former is appropriate for separating inorganic gas and hydrocarbons with low boiling points, while the latter is appropriate for separating general organic compounds. The components to be separated by GC are limited to gas or liquids vaporizable at a temperature of approximately 450°C. GC is, however, characterized by smaller pressure differences for mobilization because low-viscosity gas is used as the moving phase, thereby, larger theoretical plate numbers than liquid chromatography can be attained by using a longer column.

High Performance Liquid Chromatography (HPLC). High Performance Liquid Chromatography (HPLC) uses the liquid moving phase.

The classical liquid chromatography (LG), including thin-layer chromatography, paper chromatography, and column chromatography, has a low transport speed of the moving phase because it transports through the stationary phase by gravity and diffusion so that a long time is required for the analysis. HPLC uses a high-pressure-resistant filler as the stationary phase to force the moving phase to move with a pump. The transport speed of the moving phase is as high as milliliters per minute, therefore, analysis is carried out more rapidly than conventional LC.

HPLC is roughly classified into partition chromatography, ion exchange chromatography, and size exclusion chromatography, by the separation mechanism. Partition chromatography separates the components by the dipole interaction and hydrophobic interaction with the stationary phase. Ion exchange chromatography separates the components by Coulomb force acting on the electric charges between the stationary phase and the components. Size exclusion chromatography uses porous particles with a series of pores similar to the size of the molecules of the components concerned as the stationary phase to separate the components by the difference of molecular size utilizing a phenomenon that the finer the molecule, the deeper the invasion of the pore is. A typical size exclusion chromatography is gel permeation chromatography (GPC) using porous gel as the stationary phase.

Supercritical Fluid Chromatography (SFC). Supercritical Fluid Chromatography (SFC) uses a supercritical fluid produced by compressing gas to high density at a temperature and pressure exceeding the critical points as the eluent.[1] Although CO_2 containing a small quantity of an organic solvent as the modifier is generally used, hexane and some sort of gas such as Xe and N_2O can also be used, depending upon the purpose. SFC

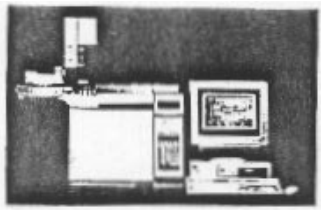
@Seismicisolation

combines the performances of gas chromatography (GC) and high performance liquid chromatography (HPLC). Thermally unstable materials and nonvolatile materials which cannot be analyzed by GC can be analyzed by SFC because the effluent containing a modifier has high solubility at a low temperature. High-resolving power separation and analysis can be made in a short time with a longer column with larger theoretical plate number, using a lower viscosity fluid than in HPLC, because the viscosity of the eluent is approximately one-tenth that of liquid with the same density and its diffusion coefficient is ten-times that of the liquid.

3.2 Apparatus

Gas Chromatography. Figure 21 shows a photograph and block diagram of GC.

GC has steadily progressed into capillary GC. The determination accuracy of the split injection of a sample is improved by using an autosampler injecting the sample for a period as short as 0.1 seconds. The loss of a component in the sample can be decreased and microanalysis can be made by applying the injection method of cold-on-column. The sensitivity of GC is enhanced by injecting the sample as much as ten microliters into a capillary column. In the thermal cracking capillary GC useful for the characterization of polymers, quantitative microanalysis of a low boiling substance can be made by a newly developed thermal desorption apparatus based on the dynamic head space method.



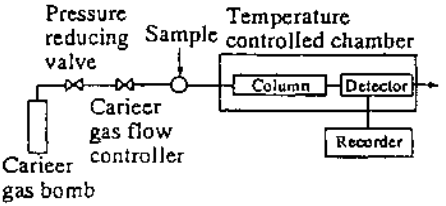


Figure 21. Photograph and block diagram of gas chromatograph. *(Hewlett Packard, HP 6890.)*

@Seismicisolation

A thick film wide pore capillary column is suitable for GC/MS and GC/FT-IR to determine trace and volatile components. High molecular weight components can be analyzed by the development of high-temperature resistant capillary columns.[21]

An ultraviolet ray absorbing detector with long light path, a non-radiative electron capture detector utilizing energy generated by microwave induced discharge in helium, and a detector combining a microwave induced plasma emission spectrometer with a photodiode array monitor,[22] have been developed to improve the sensitivity and selectivity of the detector. A combination of GC with other analytical methods, including the GC/FT-IR/MS[23] and LC/GC[24] systems, enable high-separation, high-sensitivity capillary columns to be put to practical use.

High Performance Liquid Chromatography. Figure 22 shows a photograph and block diagram of HPLC.

A high-pressure, infinite feeding, constant flow rate, nonpulsating feed pump, is required for HPLC. Various types of pumps are commercially available. Although a septum sample injector has been used for HPLC so far, a bubble injector is more widely used at present. An injector weighing the sample with a perforated disk and injecting it by rotating the disk has been developed for micro-HPLC, using a small-diameter column to prevent the peak width from widening. In the computer-based HPLC system the stable base line is obtained by the temperature gradient analysis programming the temperature of the column oven.

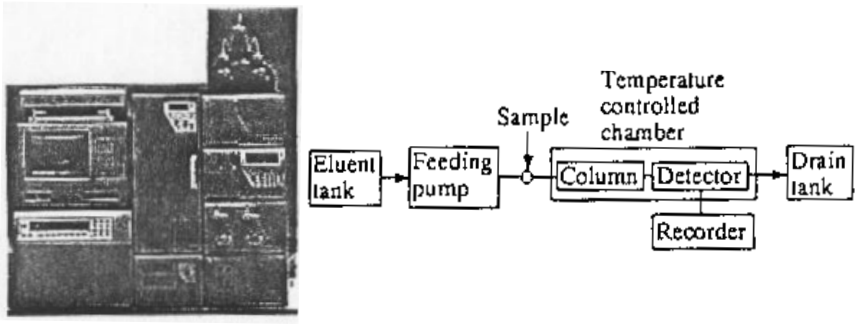


Figure 22. Photograph and block diagram of high-performance liquid chromatograph. *(TOSOH, CCP and 8020.)*

@Seismicisolation

An ultraviolet-visible detector, differential refractive index detector, and fluorescence detector, are usually used for HPLC. In order to obtain the qualitative information on the peak and improve the sensitivity, selectivity, and flexibility of detection, MS, NMR, FT-IR, ultraviolet detector, Raman spectrophotometer, ESR, electrochemical detector, detectors utilizing radioactivity, chemical emission and laser, ZGP, rotary power detector, dielectric gas detector, flame detector, and flow potential detector, are being evaluated.

Computerization is tried, not only on the application to the data processing, but also to the data transmission to a host computer as a part of laboratory automation regarding HPLC with integrator as a terminal analytical system. Fast-HPLC has recently been developed to shorten the analyzing time maintaining the separating power constant by reducing the particle size of filler as small as 3 to 5 μm and cutting down the column length.

Highly sensitive ion exchange chromatography has recently been developed and widely used by connecting a background eliminating column to the outlet of the separating column in series in the ion exchange chromatograph to remove acidic or basic material used as the eluting agent in the form of water or exchange it into lower-conductivity material, thereby feeding only target ion specimens to the conductometric cell.

Super Critical Fluid Chromatography. Figure 23 shows a photograph and block diagram of SFC. Unlike GC and HPLC, supercritical chromatograph is equipped with a control system for keeping the temperature and pressure at the critical points or higher.

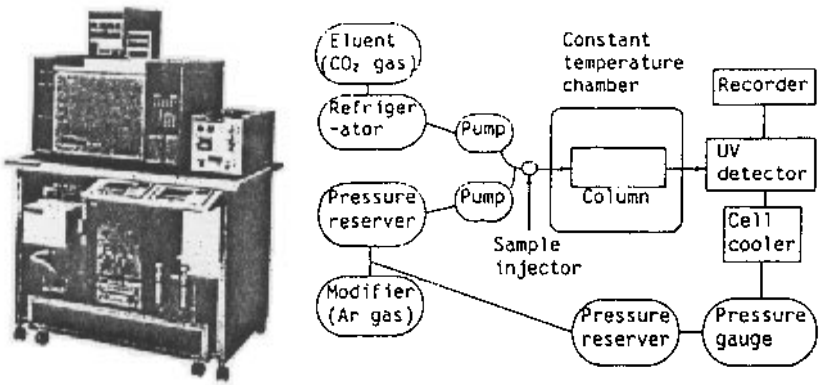


Figure 23. Photograph and block diagram of supercritical fluid chromatograph. *(JEOL, JSF-8800.)*

@Seismicisolation

3.3 Applications

Gas Chromatography. The applications in the field of cement and concrete research include an example of the measurement of the polymerization degree of silicate anions in the C-S-H by GC after trimethylsilylation of a hydrate of silica-fume-blended portland cement[25] and examples of the identification and determination of organic compounds contained in hydrated cement by analyzing gas produced by decomposing hydrated cement in a pyrolysis unit.[26]

High Performance Liquid Chromatography. Various HPLCs have recently been applied to the characterization of organic admixtures for concrete. Since the anionic organic surface active agents used as the admixture for concrete are generally nonvolatile they have been often analyzed by GC after eliminating a hydrophilic group, including a sulfonate group, mainly causing non-volatility to improve the volatility. The pretreatment is, however, complicated and poorly reproducible. Since those problems have been solved with the progress of hardware and data-processing software, HPLC is replacing GC as the tool for characterization of organic admixtures.[27] The analytical results by GPC of the molecular weight distributions and mean molecular weights of high-performance water-reducing agents mainly composed of sodium and calcium β-naphthalene sulfonates and mainly composed of sodium melamine sulfonate are shown in Fig. 24.[28] A differential refractometer is used for detecting the eluted matter and pullulan is used as the standard sample for the calculation of molecular weight. The figure reveals that even the same series of admixtures mainly composed of the same type of compounds have different molecular weight distributions and mean molecular weights in accordance with the brand.

In addition, several papers report changes in the molecular weight of a melamine sulfonic acid-based admixture by the adsorption to the cement particles by GPC,[29] molecular weight of a naphthalene sulfonic acid-based admixture determined by GPC to diffusion properties,[30] the determination of the molecular weight of lignosulfonic acid-based admixture by GPC to investigate the relationship with the adsorption to cement particles,[31] determination of a naphthalene sulfonic acid-based admixture extracted from hardened cement paste with water or potassium carbonate by HPLC,[32] the determination by HPLC of a naphthalene sulfonic acid-based admixture extracted from hardened cement paste by the hydrochloric acid dissolution-calcium hydroxide addition method,[33] the determination of the polymerization degree of trimethylsylylated silicate hydrate by GPC.[34]

@Seismicisolation

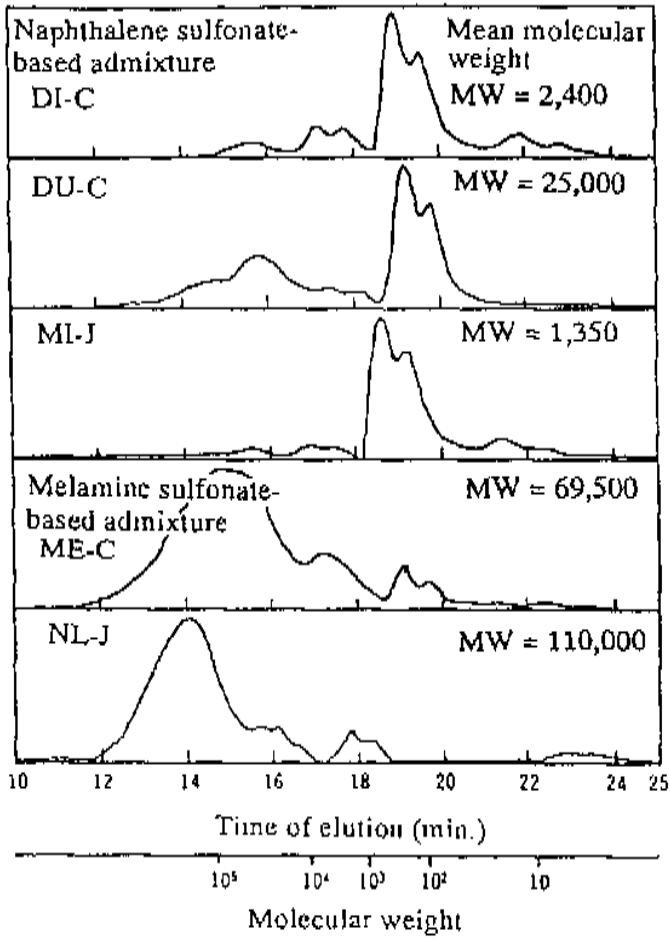


Figure 24. Chromatogram of organic admixtures measured by gel permeation chromatography. *(Uchikawa, et al.)*[28]

Super Critical Fluid Chromatography. An application example of measuring the condensation degree of silicate anion in C-S H produced in the ternary component blended cement composed of portland cement, blast furnace slag, and fly ash hardened paste, is shown in Fig. 25.[35] Since the trimethylsylylated silicate polymer derivative composed of tetramer or higher polymers is nonvolatile it cannot be analyzed by conventional gas chromatography. Although the molecular weight distribution in the sample can be obtained by high performance liquid chromatography it cannot be eluted into fractions by condensation degrees.[34] Since silicate polymer derivatives

@Seismicisolation

up to a heptamer can be clearly eluted by SFC, the change of the condensation degree of silicate anion in C-S-H according to the progress of hydration can be traced in detail. SFC is, therefore, expected to be a useful technique to relate the structural change of silicate polymer derivatives to the physical properties of mortar and concrete.

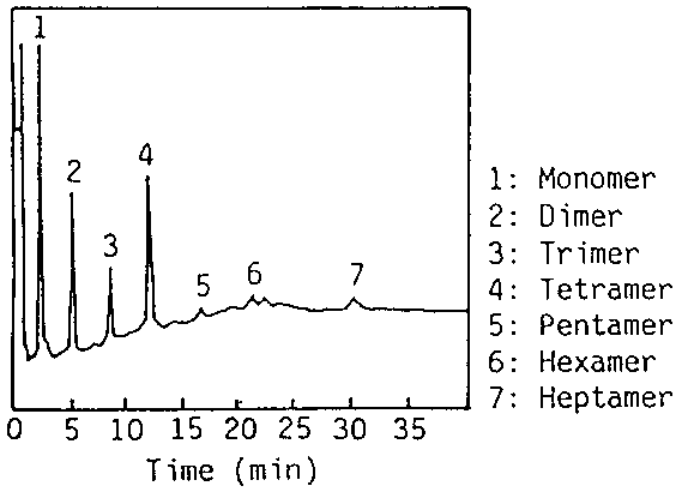


Figure 25. Supercritical fluid chromatogram of hydrated ternary components blended cement composed of slag, fly ash, and portland cement treated by TMS. *(Uchikawa, et al.)*[35]

4.0 MASS SPECTROMETRY

4.1 Principle and Special Features

Mass spectrometry is a method for ionizing the sample, separating the ionized ions by the mass difference, and estimating them. It is able to identify and determine elements and isomers, molecular weights, and molecular structures.

Mass spectrometry can detect molecular ions at a detection sensitivity of an order of magnitude of picogram (10^{-12} g). This is accomplished by supplying energy to the molecules in the sample by various methods, separating electrons from or adding them to the sample, and producing molecular ions (parent ions) with the same mass as the molecules, and separating the molecular ions with different mass numbers from each

@Seismicisolation

other by various methods. The analytical data are derived by plotting *m/z* (mass number of ion/charge of ion) (the axis of abscissa) versus the detection intensity (the axis of ordinate).

Since the ionized molecular ions have high internal energy, a part of the parent ions is divided into molecular ions with smaller mass numbers. Thus produced, a molecular ion is called a *fragment*. The molecular structure of the parent ion can be estimated from the type of the fragment.

In mass spectrometry, the sample is ionized by atomic bombardment of fast accelerated thermoelectrons, vaporization in an electric field, and irradiation with a laser beam. The ionization method is selected depending upon the polarity, volatility, thermal stability, and molecular weight, of the compound concerned.

The electron ionization, chemical ionization, atmospheric pressure chemical ionization, and thermospray ionization, are used for ionizing a molecule with molecular weight up to approximately 1,000.

The electron ionization (EI) of the gaseous sample by exposing to thermoelectrons is a method most widely used. The accelerating voltage of thermoelectrons is 70 eV and the degree of vacuum in the ionization chamber is 10^{-4} to 10^{-5} Pa. Since large internal energy is supplied to the sample by thermoelectrons, the fragments are easily produced.

The chemical ionization (CI) is a method for producing molecular ions of the sample by sending the reactant gas, including methane and ammonia, and the sample to the ion source and reacting the ions produced from the reactant gas with the molecules of the sample. Fragments are hardly produced because energy supplied to the molecular ions of the sample is lower than in EI.

The atmospheric pressure chemical ionization (APCI) is a method for producing the molecular ions for the sample by ionizing a solvent by corona discharge under atmospheric pressure and then reacting it with the molecules of the sample. The method is used for the ionization for LC/MS because the liquid sample can be used without any treatment.

The thermospray ionization (TSI) is a method for ionizing the sample molecules with ions of a solvent produced by spraying the heated sample solution. This method is useful for ionizing a solution type sample in the same manner as LC/MS.

A "soft" ionization method is used for determining compounds with the molecular weight of tens of thousands to hundreds of thousands, including protein, in such a way as to produce the parent ions alone by inhibiting the production of fragments. Such a method is applied to the determination of difficult to volatilize or thermally unstable compounds by combining with a special preparation method of sample.

@Seismicisolation

The fast atom bombardment (FAB) is a method of bombarding the sample with neutral particles of xenon, argon, and cesium, fast accelerated up to several keV of energy. The fast neutral particles produced by exchanging an electric charge with a fast ion beam shot from an ion gun in the gas chamber are bombarded onto the sample target prepared by coating the sample and an ionization promoter including glycerol. It is able to ionize difficultly volatile and thermally unstable compounds and polymers with molecular weight of 1,000 or more and obtain a stable mass spectrum because of a long ionization time.

The electrospray ionization (ESI) is a method of producing molecular ions of a solute by passing a sample solution dissolved in water through a capillary at the tip of which a voltage of 5 to 6 kV is applied at a flow rate of 50 to 200 μl/min to charge it electrically, spraying charged droplets on the electrospray ionization source under atmospheric pressure and vaporizing the solution from the droplets. The method is used not only for the same purposes as FAB, but also for producing small *m/z* ions also from high-molecular weight compounds. It can produce multivalent ions and the detection range of the method is wide.

The matrix-assisted laser desorption ionization (MALDI) is a method of ionizing the sample by mixing the sample with such a matrix as synaptic acid, for accelerating the absorption of laser, and irradiating the mixture with a N_2-laser. This method is not only used for the same purposes as for FAB and ESI, but widely used as the ionization method for the time of flight mass spectrometry (TOFMS) because the ionization time is very short.

The measuring methods for mass number of ions are classified into the magnetic field type, quadrupole type, and time of flight type, according to the detection type of molecular ion.

4.2 Apparatus

An example of the mass spectrometer is illustrated in Fig. 26. The apparatus generally comprises an ion source for ionizing and accelerating the sample, a mass analysis part for separating ions according to the difference of mass number/charge (*m/z*), and an ion detector for detecting the separated ions.

@Seismicisolation

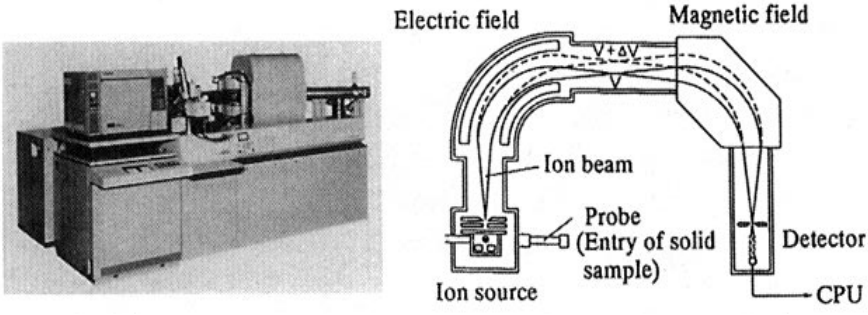


Figure 26. Photograph and block diagram of double converging magnetic field type mass spectrometer. *(JEOL, JMS-HX110A.)*

The double converging magnetic field type mass spectrometer utilizes a phenomenon that the orbit of an ion is bent by force of action from the magnetic field according to the mass of ion at the time when the ion passes through the magnetic field. Assuming that the mass number, charge, elementary charge, strength of magnetic field, curvature radius of orbit, and accelerating voltage of the ion, are m, z, e, B, R, and V, respectively, m/z will be

Eq. (3) $$m/z = ½(eB^2R^2/V)$$

Assuming that R and V are constant, m/z corresponding to the strength of magnetic field (B) can be detected by changing B. The accelerating voltage in the magnetic field type apparatus is generally several kV to 10 kV.

Even ions with the same m/z are not given constant energy by acceleration. The larger the width of the distribution the lower the resolving power of detection. It is, therefore, important to equalize the energy of an ion by using the electric field for improving the resolving power. The orbit of an ion is bent by force of action from the electric field at the time when the ion passes through the electric field. The following equation applies to the relationship between the curvature radius (R) of the orbit of ion, accelerating voltage (V) and strength of electric field (E):

Eq. (4) $$R = 2V/E$$

Only the ions with energy corresponding to V can be passed through the electric field and sent to the measuring part by keeping R and E constant.

@Seismicisolation

The unit for equalizing the energy of ions by installing an electric field before the measuring part is called a double conversing magnetic field type device.

The quadrupole type mass spectrometer has four columnar electrodes (quadrupole) arranged as shown in Fig. 27. An electric field is developed by applying dc voltage and high-frequency ac voltage to two electrodes facing each other and ions accelerated by the voltage of 10 to 20 V are passed through the electric field. The ions are vibrationally moved keeping the amplitude corresponding to *m/z* by the electric field. Since the ions with too large an amplitude collide with the electrodes, the ions with a certain value of *m/z* pass through the electric field undetected. Since the quadrupole type can be operated at lower voltage than other types it is characterized by the simple structure of spectrometer and the easy operation. It has, however, shortcomings in that the resolving power is lower and the sensitivity of *m/z* of 1,000 or more is poorer than that of the double converging magnetic field type. The block diagram of the quadrupole mass spectrometer is illustrated in Fig. 28.

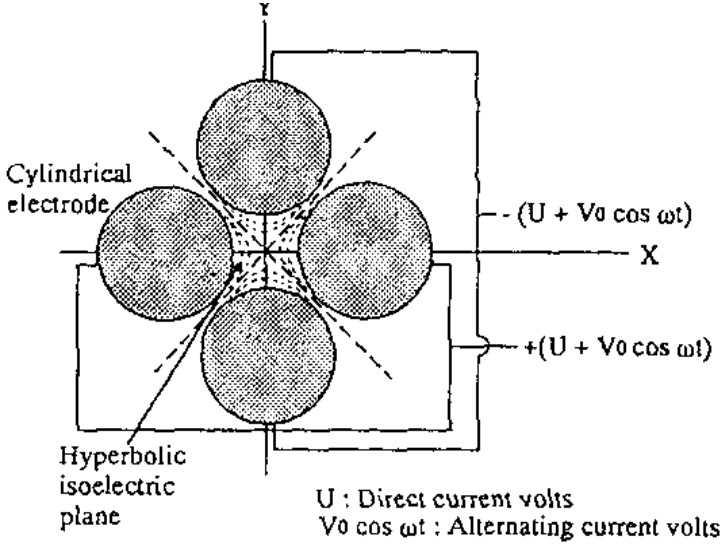


Figure 27. Schematic explanation of quadrupole electrode.

@Seismicisolation

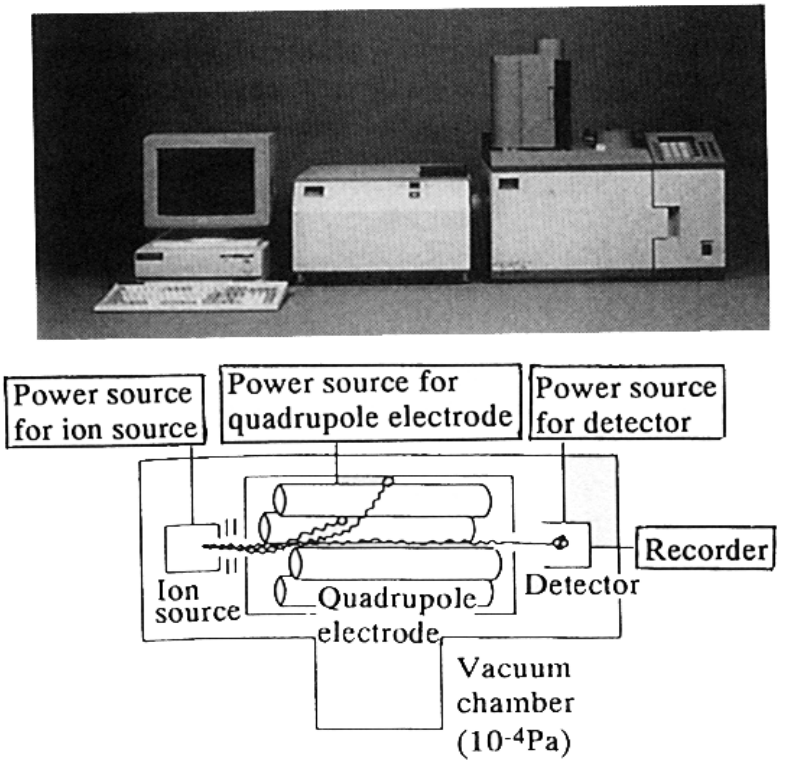


Figure 28. Photograph and block diagram of quadrupole mass spectrometer. *(Perkin Elmer, Q-MASS 910.)*

The time of flight type mass spectrometer utilizes the different flying velocity of ions in the electric field according to *m/z*. Assuming the applied voltage, the length of analytical tube, and the time of flight of ion in the analytical tube are to be *V*, *L*, and *t*, *m/z* is expressed by

Eq. (5) $$m/z = 2eVt^2/L^2$$

Assuming that *V* and *L* are constant, *m/z* can be determined by measuring the time of flight *(t)*. The time of flight method is useful for measuring the molecular weight of a substance such as protein with the molecular weight exceeding hundreds-of thousands because the measurement can be made independent of the mass number. The photograph and a block diagram of the time of flight type mass spectrometer are illustrated in Fig. 29. The time of flight mass spectrometer includes the linear type of one-way flight and the reflector type of shuttle flight of ions reflected by voltage. Since the

@Seismicisolation

reflector type has longer flight distance than the linear type, the resolving power of the former is higher than the latter.

The mass spectrometry of a mixture produces so much of parent ions and fragments that the mass spectrum is complicated and the analysis is often difficult. A tandem mass spectrometer (MS/MS) has been developed for solving those problems by detecting a specified ion using two spectrometers connected in series. The block diagram of MS/MS is illustrated in Fig. 30. The tandem-in-space type mass spectrometer is characterized by selecting only an ion (precursor ion) with specified *m/z* from various parent ions and fragments in the first MS and introducing the ion to the ionization chamber to produce another ion (product ion) and analyze in the second MS. The bombardment activation method is used for ionizing the sample by colliding it with neutral molecules including argon.

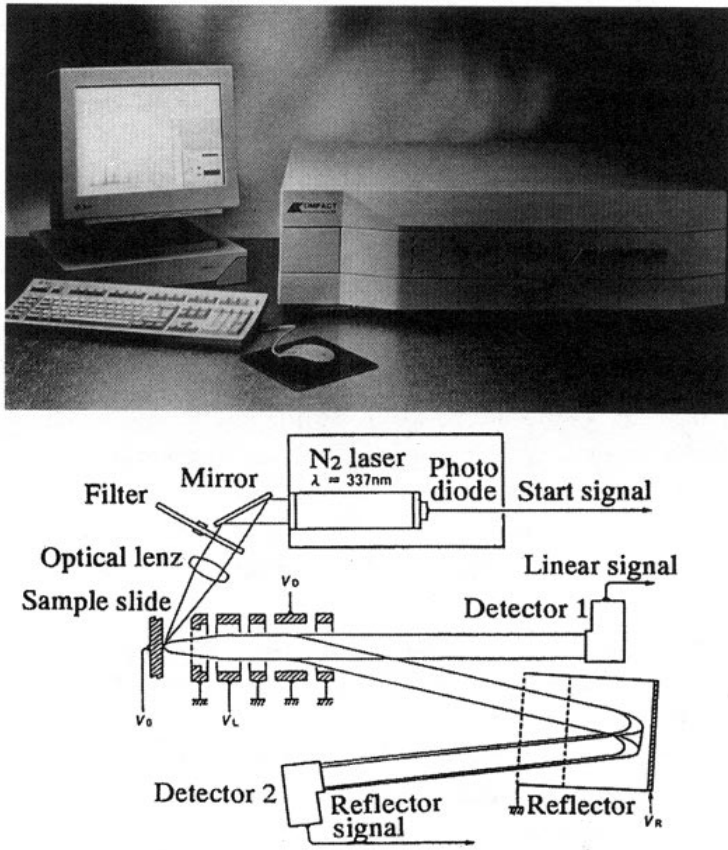


Figure 29. Photograph and block diagram of time-of-flight type mass spectrometer. *(Shimazu/Kratos, Kompact Maldi IV.)*

@Seismicisolation

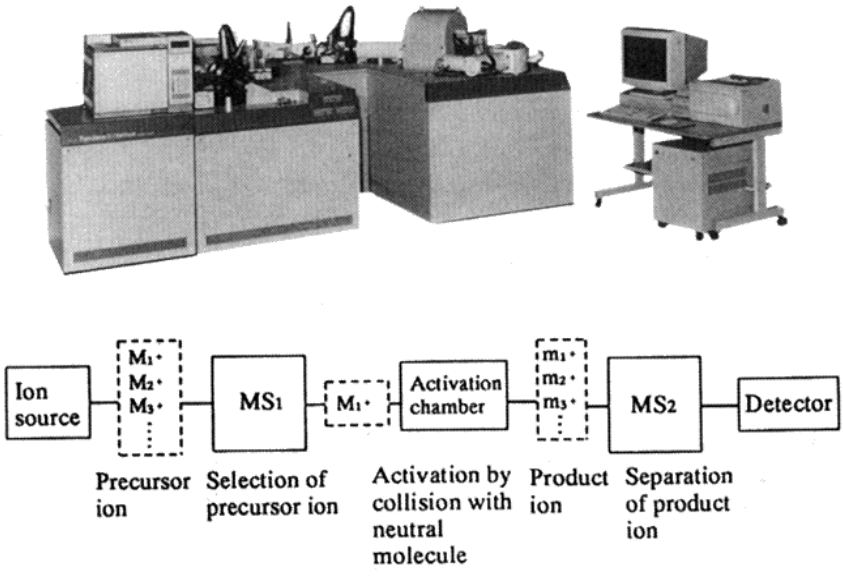


Figure 30. Photograph and block diagram of tandem-in-space type mass spectrometer (MS/MS). *(JEOL, JMS-700T.)*

4.3 Applications

Mass spectrometry (MS) has been used so far for identifying and determining trace components in the solid, liquid, and gaseous samples, estimating the molecular structures of organic compounds, and measuring the ratio of the isomer contents. Since the range of the measurable molecular weight has recently been rapidly widened MS is used for the composition analysis of biological materials and the structural analysis of protein.

An example of the identification with MS of polychlorinated aromatic compounds and a mass spectrum of a sex pheromone illustrate the utility of this technique.[36][37]

Mass spectrometry has been used for analyzing organic compounds for the high-performance water-reducing agents and for the raw materials of macro defect-free cement and polymer concrete in the fields of cement and concrete research.

@Seismicisolation

In order to estimate the origin of the carbonate compounds in hydrated cement, the permillage of the contents of carbon and oxygen isomers (^{13}C and ^{18}O), namely, $\delta_{18} = [(^{18}O/^{16}O)_s, - (^{18}O/^{16}O)_R]/(^{18}O/^{16}O)_R \times 1{,}000$ (%) and $\delta_{13} = [(^{13}C/^{12}C)_s - (^{13}C/^{12}C)_R]/(^{13}C/^{12}C)_R \times 1{,}000$ (%) are determined.[38] In those equations, $(^{18}O/^{16}O)_s$ and $(^{13}C/^{12}C)_s$ are the ratios of the isomers in the sample and $(^{18}O/^{16}O)_R$ and $(^{13}C/^{12}C)_R$ are the ratios of the isomers in the standard samples. The standard samples of carbon is Pee Dee Belemnite of the ocean-originated calcium carbonate and that of oxygen is the Standard Mean Ocean Water produced by the International Atomic Energy Agency in Austria.

The ranges of δ_{18} and δ_{13} measured using carbonates from various origins are illustrated in Fig. 31. Domain I, II, III, IV, V, VI, VII, VIII, and IX, are marine sedimentary limestone, laid from continental water, carbonate precipitated from cement in open air and fresh water, carbonate precipitated from cement in water of Paris region (no gas phase carbon comes from dissolved mineral species), carbonate in the archeological cement sample from Mycenes, mortar obtained from Knossos, an ancient shrine in Greece, carbonate produced in Champlieu, in France, carbonates in current cement with and without limestone filler, and carbonate in a mixture of cement and limestone without containing CO_2 from the atmosphere or carbon dissolved in water, respectively. In the figure, *D*, *E*, *F*, *G*, and *H* are the sample taken from a concrete bridge in Nanteuli in a suburb of Paris, the sample taken from a concrete bridge in Gargenville in a suburb of Paris, the sample containing 3% of carbonate taken from a concrete bridge built 50 years ago from gneiss and granite produced in Brest, the sample taken from a runway built from a coral reef-originated limestone and seawater of the Indian Ocean, and the low porosity sample taken from an inner wall of a block house built in Normandy in 1943, respectively. It is inferred from Fig. 31 that a half of the carbonate of *D* is limestone used as the filler, the carbonate of *E* is oceanic limestone, the carbonate of *F* is mainly produced from carbon dioxide contained in rainwater, most of the carbonate of *G* is produced from carbonate ions dissolved in the seawater and limestone, and most of the carbonate of *H* is produced from carbon dioxide contained in rainwater.[38]

@Seismicisolation

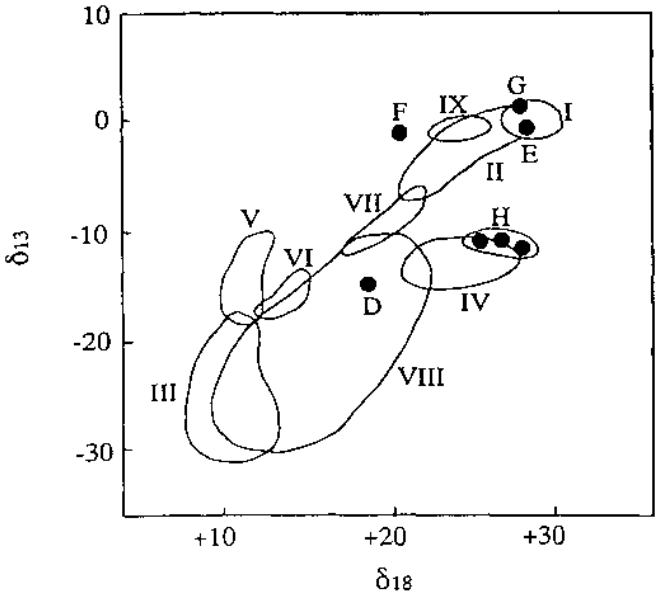


Figure 31. ^{13}C - ^{18}O diagram of various carbonates. *(Letolle, et al.)*[38]

5.0 SECONDARY ION MASS SPECTROSCOPY

5.1 Principle and Special Features

A low-penetrability ionic beam with sputtering function is used for determining the element distribution on the surface and in the direction of depth of a solid. Neutral atoms and molecules, x-rays, secondary ions, and secondary electrons, are emitted from the surface of a solid sample irradiated with high-energy ions. Secondary ion mass spectroscopy (SIMS) is a method for analyzing the composition of a sample using the secondary ions among them. An ion microprobe mass analyzer (IMMA) is an instrument for analyzing the microscopic region of the surface and has the function of observing the two-dimensional element distribution of the surface of the sample by irradiating with the ionic beam converged into hundreds of nanometers.

@Seismicisolation

When a sample is irradiated with an ionic beam such as O^{2}+, Ar+, and Cs+ of 10 to 20 keV, the atoms in the sample are given kinetic energy by the collision of ions. When the kinetic energy is sufficiently larger than a potential barrier in the material of the sample, the atoms move in the sample colliding with other atoms and, finally, the atoms in the surface layer are driven out as the secondary ions as shown in Fig. 32.[1]

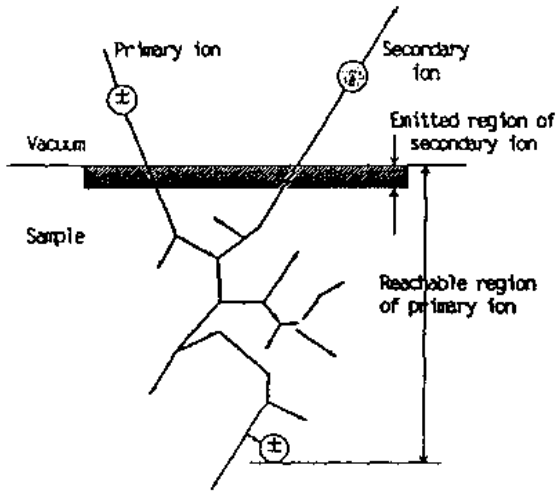


Figure 32. Interaction between incident ion and solid sample. *(Uchikawa.)*[1]

The secondary ions driven out are separated and detected with mass spectrometer and the elements contained in the sample are both qualitatively and quantitatively analyzed by SIMS as shown in Fig. 33.[39] The area of the measuring region for SIMS is hundreds of nanometers to hundreds of microns lying between those for AES and ESCA. The two-dimensional information of the surface layer of one to tens of nanometers in depth can be obtained. Even a small quantity of 100 ppm to 0.l ppb of any element can be analyzed. The sample is inclined to the direction of incident ionic beam at 45°. The secondary ions emitted from the sample by sputtering are detected. Since the sample is eroded conically, the secondary ions emitted from the rim of the hollow eroded conically make the measurement inaccurate. The area masking[40] or electronic aperture[41] method combining a restricted field lens and a restricted field slit is used for analyzing a sample in the direction of depth so that only the secondary ion emitted from the center of sputtered area are detected. An ion gun is selected considering

@Seismicisolation

the elements to be analyzed and the measuring region. Since the mass analysis has a small background and a large dynamic range, it is suitable for the microanalysis.

Charging-up during the analysis of an insulating material is prevented by covering the surface with an electron conductive layer except for the measuring region and blowing the vapor of indium only upon the measuring region to form an electron bombardment-induced conductive layer[42] or neutralizing the charge by the thermionic irradiation method or the negative ionic beam.[43]

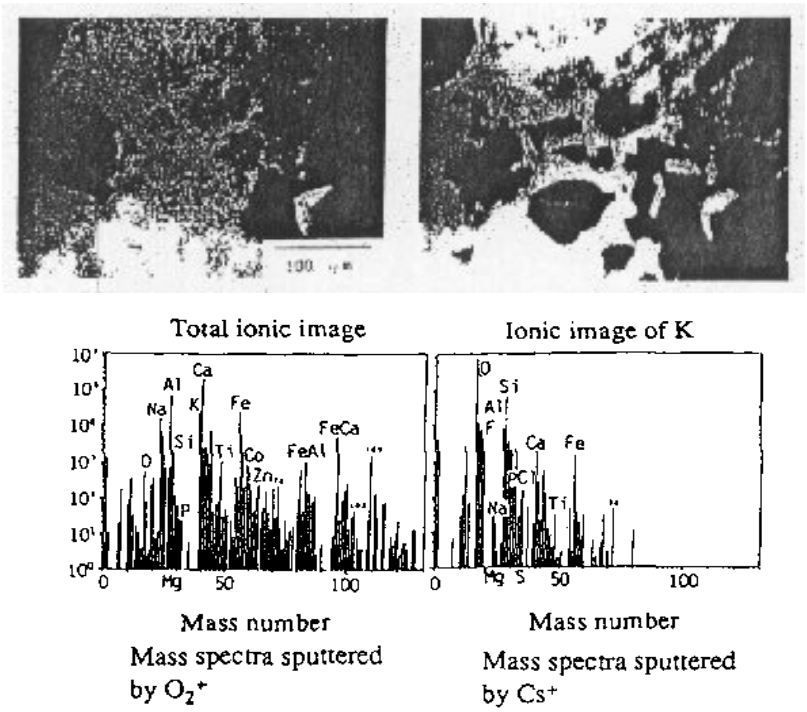


Figure 33. Ionic image and mass spectra of cement clinker determined by SIMS. *(Uchikawa, et al.)*[39]

Apparatus. A photograph and a block diagram of the secondary ion mass spectrometer are illustrated in Fig. 34. The spectrometer comprises the primary ion (Xe^+, Ar^+ and Ca^+ etc.) generating unit composed of an ion gun, an ion accelerator, and an iris for the ion beam, and the secondary ion analyzing unit.

@Seismicisolation

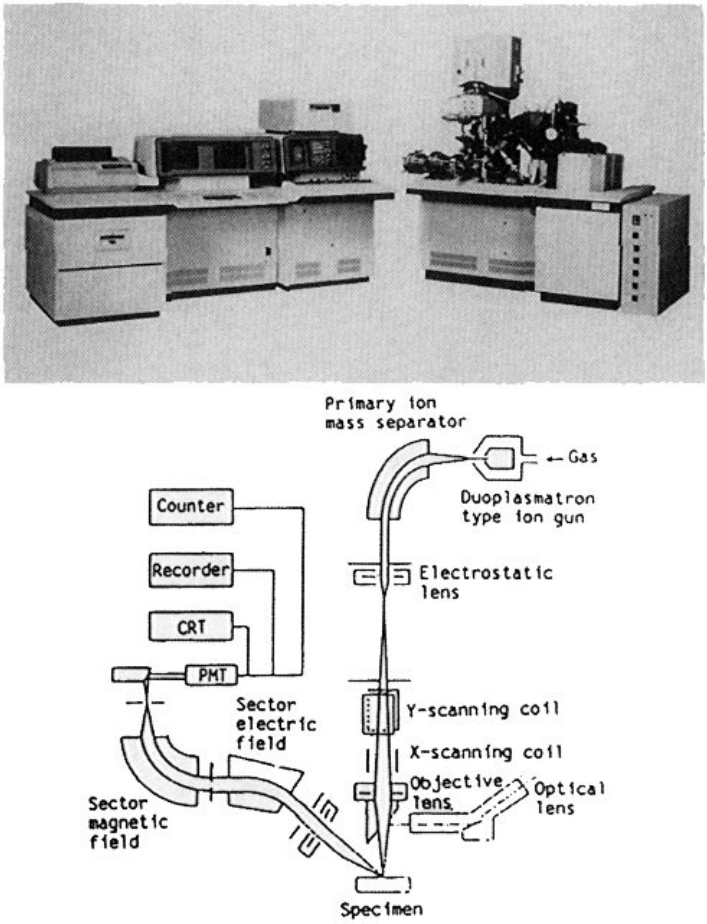


Figure 34. Photograph and block diagram of secondary ion mass spectroscope. *(Hitachi IMA-3000.)*

Application. The application of SIMS to the cement and concrete research field began to be reported in the first half of the 1980s. Papers published since then include a paper [44] inferring from the comparison of the average composition in bulk with the surface composition determined by SIMS that Fe, K and alkali are concentrated on the surface of high-early-strength portland cement, blast furnace cement and hydrated high-early-strength portland cement respectively, a paper[45] presenting the determination of the capability of normal portland cement to fix Co, Ce and Sr by SIMStogether with other analyses and the existing state of those atoms in hydrated cement, respectively, a paper[46] describing the limit of qualitative analysis of admixtures due to the structural factors and the possibility of quantitative analysis, and a paper[47] presenting by analyzing the interface between

@Seismicisolation

quartz and cement paste in mortar prepared by using quartz as aggregate left to stand in So_2 gas of the concentration of 5% that in the paste at a depth of submicrons from the interface and so Na is decreased.

The analytical result of alite in clinker by SIMS using Cs+ and O_2+ as the primary ion source is shown in Fig. 33.[39] The result indicates that alite contains trace elements including F, Ti, P, Co, and Zn, as well as minor elements including Mg, S, Na, and K. The location and name of: the cement manufacturing plant can be identified from the kind and contents of those trace elements contained in each clinker mineral.

6.0 CHROMATOGRAPHY-MASS SPECTROMETRY

6.1 Principle and Special Features

An apparatus for accurately separating a specified component from the sample and identifying it by combining a component-separating function of chromatograph with a component identifying function of mass spectrometer is called a *chromatograph-mass spectrometer*.

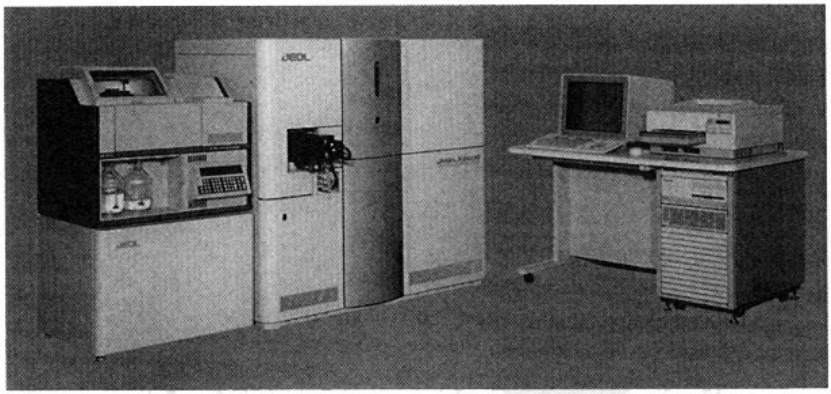
Although a volatile mixture sample is analyzed by Gas Chromatography-Mass Spectroscopy (CC/MS), a non-volatile compound is analyzed by Liquid Chromatography-Mass Spectroscopy (LC/MS), and instruments based on the thermospray, electrospray, and Frit-FAB methods, have recently been used.

6.2 Apparatus

Figure 35 shows a photograph and block diagram of LC-MS. Liquid chromatography-mass spectrometry is made by separating the components in the sample from each other with a liquid chromatograph (LC), removing the eluent at the interface, sending it to a mass spectrometer (MS), ionizing the components under high vacuum, and measuring the mass numbers of them.[28] A liquid chromatogram showing the time of elution and the intensity of eluted product on the axes of abscissas and ordinates, respectively, is obtained by LC and a mass spectrum through mass number/electric charge of ion (*m/z*) and the intensity on the axes of abscissas and coordinates, respectively. A diagram drawn by plotting the mass-spectral intensity against the time of elution at a specified *m/z* is called the mass

@Seismicisolation

chromatogram. Since the measurement is continuous, a mass spectrum at any time of elution can be obtained. The type of eluted product at a specified time in LC can be estimated by comparing the mass chromatogram with the liquid chromatogram.



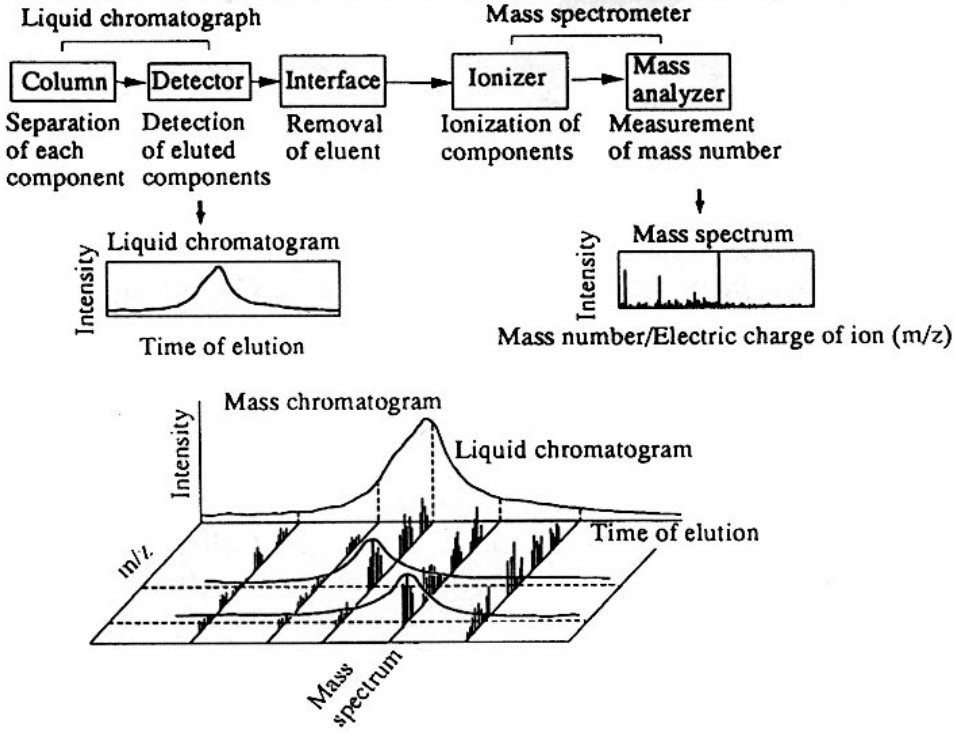


Figure 35. Photograph and block diagram of apparatus of LC-MS (JEOL, JMS-LX2000) and schematic explanation of liquid chromatography-mass spectrometry. (Uchikawa, et al.[28])

@Seismicisolation

6.3 Applications

An example of the determination of the monomer/polymer ratio of a main component, disulfonic acid/monosulfonic acid ratio, the content of low-condensates, and the poly-condensates, by separating and identifying the components of naphthalene sulfonic acid-based and melamine sulfonic acid-based admixtures by LC/MS[28] is described below.

A liquid chromatogram of an organic admixture obtained by LC/MS is illustrated in Fig. 36. Since the admixture contains various components with different hydrophilicities, hydrophobic particles including octadodecyl silica gel and aqueous solution, are used as the stationary phase (column) and moving phase (eluting solution), respectively, and a column for reversed phase partition chromatography separating the components by the difference of the hydrophobicity and hydrophilicity balance is used in this particular case. The mixture of an aqueous solution of dibutyl amine-acetic acid and CH_3CN is used as the eluting solution. The stronger the hydrophilicity of a component, the earlier the component is eluted and the stronger the hydrophobicity of a component, the later the component is eluted. Considering that disulfonic acid is more hydrophilic than monosulfonic acid and low-condensate is more hydrophilic than polycondensate when the number of sulfonate groups per monomer are the same as each other, the type of an organic sulfonic acid corresponding to each peak can be identified. Since even the same type of admixtures exhibit different sizes of peaks, the contents of the components vary according to the brands.

An example of mass spectra of naphthalene-based organic admixture and melamine-based admixture is illustrated in Fig. 37 and liquid chromatogram-mass spectrograms (mass chromatogram) of them are illustrated together with their molecular structure formulas in Fig. 38. Sulfur trioxide, naphthalene sulfonic acid monomer, naphthalene disulfonic acid monomer, dimer, trimer, tetramer, pentamer, and hexamer of naphthlene sulfonic acid, are identified by the peaks at *m/z* of 80, 207, 287, 427, 647, 867, 1088, and 1308, respectively, in mass spectra of a naphthalene-based admixture. Sulfur trioxide, condensate of melamine sulfonic acid and monomer, dimer, and trimer of melamine sulfonic acid are identified by the peaks at *m/z* of 80, 222, 247, 407 and 639, respectively, in the mass spectra of a melamine-based admixture. The main components of the naphthalene-based admixture include monosulfonate monomer and its condensate, disulfonate monomer and its condensate and sulfonic acid not forming metallic salt, while those of melamine based admixture include

@Seismicisolation

melaminesulfonic acid monomer and its condensate. Besides such information, the monomer/polymer ratio, the content of low condensates and polycondensates listed in Table 1 can also be obtained by LC/MS.

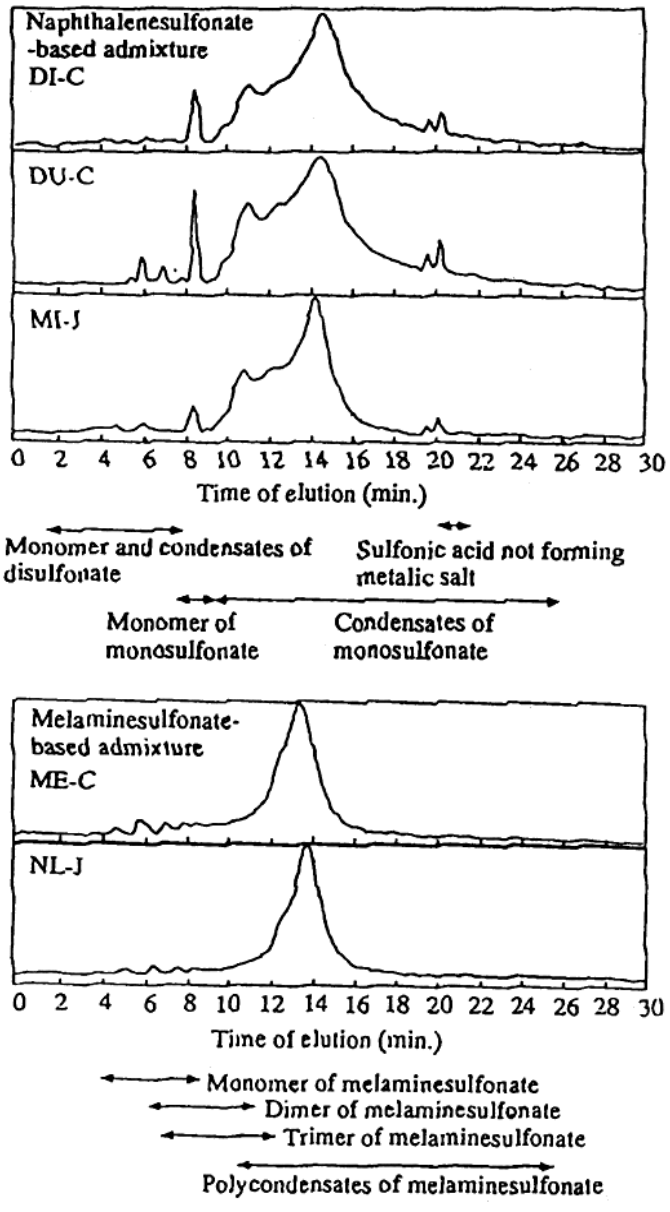


Figure 36. Liquid chromatogram of organic admixtures. *(Uchikawa, et al.)*[28]

@Seismicisolation

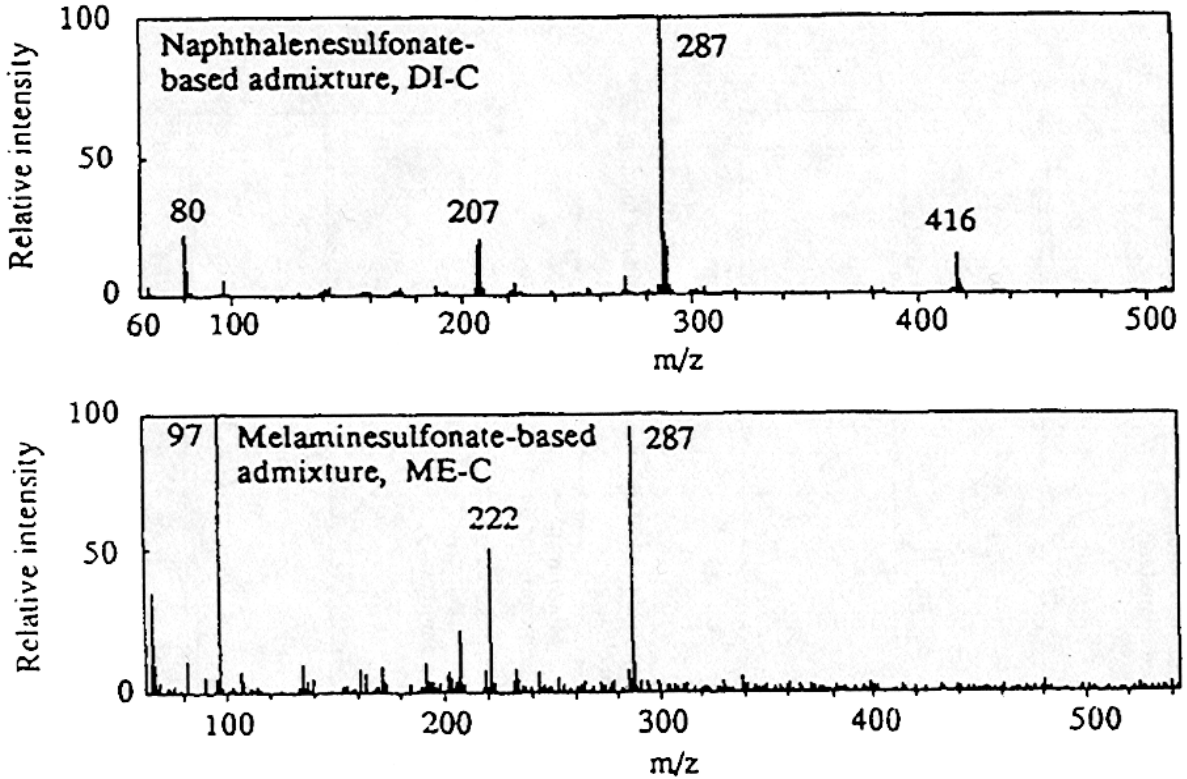


Figure 37. Mass spectra of organic admixtures. *(Uchikawa, et al.)*[28]

@Seismicisolation

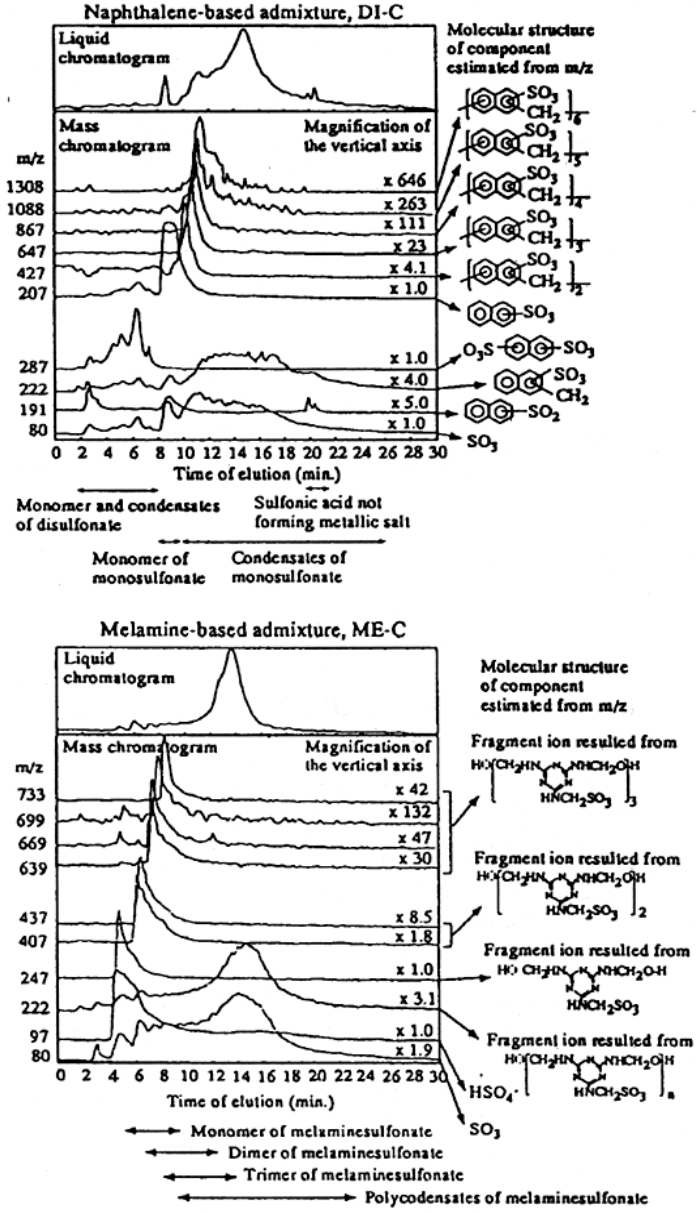


Figure 38. An example of liquid chromatogram-mass spectrogram of organic admixtures. *(Uchikawa, et al.)*[28]

@Seismicisolation

Table 1. An Example of the Composition of Various Organic Admixtures *(Uchikawa, et al.)*[34]

Admixture		Monomer/ Condensates	Disulfonate/ Monosulfonate	Content of Low Poly-Condensates	Content of High Poly-Condensates
Naphthalene sulfonate-based admixture	DI-C	Medium	Low	Medium	Much
	DU-C	High	High	Much	Much
	MI-J	Low	Low	Less	Less
Melamine sulfonate-based admixture	ME-C	Low	—	Much	Medium
	NL-J	Low	—	Less	Medium

7.0 NUCLEAR QUADRUPOLE RESONANCE ANALYSIS

7.1 Principle and Special Features

An atomic nucleus with the nuclear spin quantum number (I) of $\pm \geq ½$ has the nuclear magnetic moment and that with the nuclear spin quantum number of ≥1 has the nuclear quadrupole moment as well as the nuclear magnetic moment. The nuclear quadrupole moment is a state forming two + and - pairs in the spatial distribution of the quantity of electricity in a nucleus. Figure 39 reveals that it has two types: (*a*) uniaxial arrangement and (*b*) planar arrangement. The nuclear quadrupole moment is called also the *electric quadrupole moment*.

A substance (nucleus) placed in a static magnetic field causes the Zeeman splitting of spin energy to quantize to the nuclear magnetic quantum number (*m*) in the direction of the magnetic field. The resonance absorption is caused by irradiating with an electromagnetic wave with energy corresponding to the splitting width (energy equal to that between the levels adjoining each other at the splitting, several MHz to hundreds of MHz) as illustrated in Fig. 40*(a)*.

The nuclear magnetic resonance (NMR) method is based on the magnetic resonance adsorption by irradiating an atomic nucleus having nuclear magnetic moment with radio waves. The electron spin resonance (ESR) method is also based on the principle similar to NMR by irradiating lone pair electrons with microwaves. Another technique measures the resonance

@Seismicisolation

absorption caused by irradiating the nuclear quadrupole moment ($I \geq 1$) existing in the nucleus in advance and is called the nuclear quadrupole resonance absorption method, as illustrated in Fig. 40*(b)*.

NMR determines the molecular structure, including the state of electrons in the vicinity of the nucleus, types of bonding atomic group, state of bonding, distance between spins, and direction of spin, by the chemical shift depending upon the variation of the electron densities in the vicinity of nucleus according to the properties of the atom and the molecule and by the spin-spin interaction (J-coupling) caused by being shielded from the external magnetic field by the adjacent nuclei with magnetic moment.

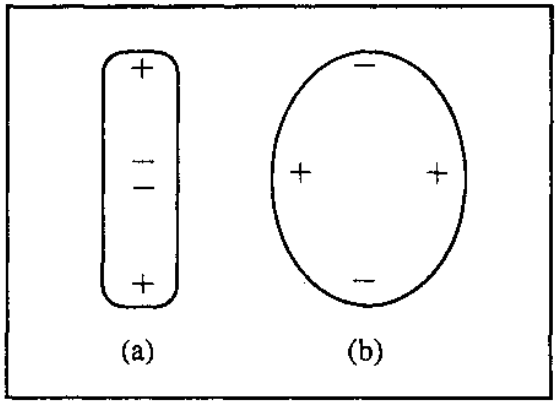


Figure 39. Schematic explanation of electric distribution on nuclear quadrupole moment.

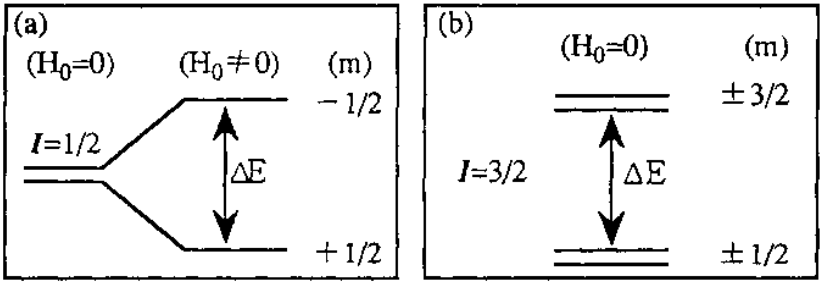


Figure 40. Split of spin energy in *(a)* NMR and in *(b)* NQR.

@Seismicisolation

The nucleus causing the resonance absorption by the radio wave turns back to the original thermal equilibrium state with the lapse of time. The process is called a *relaxation* process. The relaxation process includes the process of emitting energy and that of turning the spin directed to one direction toward random directions. The former and the latter are called the longitudinal or spin-lattice relaxation time (T_1) and the transverse or spin-spin relaxation time (T_2), respectively.

Information on rotation, vibration, and translation of molecule, can be acquired by determining the relaxation mechanism by the inversion recovery technique and by the spin echo technique. A study on the temperature dependence of T_1 is important for studying the state of electrons.

The observation of the nuclear quadrupole resonance absorption of a nucleus alone is called the pure quadrupole resonance (PQR), while the observation of two resonance absorptions of the radio wave of a nucleus caused by the Zeeman splitting (NMR) by applying the magnetic field from the outside and the nuclear quadrupole (PQR) is collectively called NQR. The resonance conditions of NMR, NQR, and ESR, are expressed by the following formulas:

Eq. (6) $$\Delta E = h\nu = h\ \gamma H_o/2\pi$$

Eq. (7) $$\Delta E = h\nu = (eQ/2) \cdot (\partial Ez/\partial Z)$$

Eq. (8) $$\Delta E = h\nu = g\beta H_o/2\pi$$

where ΔE is difference of energy between the levels, h is Planck's constant, ν is resonance frequency, γ is magnetic rotation ratio (depending upon nuclides), H_o is strength of outside magnetic field, g is spectroscopical splitting factor, and β is Bohr magnetron.

$KClO_3$ which is a typical molecule causing the electric field gradient, $\partial Ez/\partial Z$, is illustrated in Fig. 41.

By NQR the kind of nuclide can be identified because the nuclear quadrupole peculiar to the nucleus is formed and the chemical bonding state and symmetry can be determined because the electric field gradient of the nuclear quadrupole is affected by the state of surrounding electrons.

In short, NQR is characterized by:

1. The resonance frequency that largely depends upon the nuclides.
2. The resonance frequency of inorganic compounds is different from that of organic compounds though the nuclide is the same.

@Seismicisolation

3. The resonance frequency is surely changed even by slightly changing the substituent group.
4. Each transformation of a polymorphous substance has its own resonance positions and resonance frequencies.

Accordingly, NQR is an effective means for the identification of crystalline substances and phases. The NQR frequencies of various organic and inorganic compounds are listed in Table 2.[48]

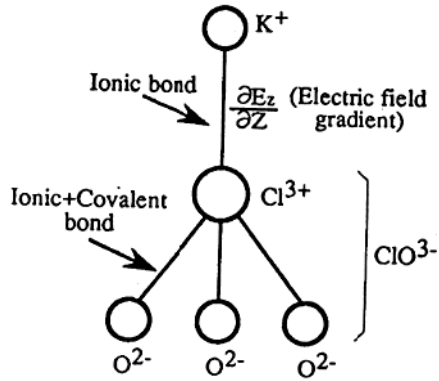


Figure 41. Electric field gradient in the $KClO_3$ crystal.

Table 2. NQR Frequency in Various Compounds *(Chihara, et al.)*[48]

Substance	Resonancing Nucleus	Temperature (K)	Frequency of Resonance (MHz)	e^2Qq/h (MHz)	η
N_2	^{14}N	4.2	3.4955	4.650	0
Cl_2	^{35}Cl	21.0	54.4850		
	^{37}Cl	21.8	42.9427		
Br_2	^{79}Br	83	382.43		
	^{81}Br	83	319.46		
I_2	^{127}I	77	643.298, 333.941	2157.12	0.1727
$NaNO_2$	^{14}N	77	4.929, 3.757	5.792	0.405
$NaNO_3$	^{14}N	298	0.5587	0.720	0
$NaClO_3$	^{35}Cl	273.2	30.032373		
	^{37}Cl	273.6	23.66998		
$SbCl_3$	^{35}Cl	21.5	20.9763, 19.3056		
	^{121}Sb	20.4	114.3493, 59.8569	383.956	0.1916
	^{123}Sb	20.4	104.4995, 68.6251, 39.3252	489.474	36
$SnCl_4$	^{35}Cl	77	24.294, 24.2226, 24.140, 23.719		0.1915
CCl_4	^{35}Cl	77	15 lines in 40.82~40.46		3
$CHCl_3$	^{35}Cl	20	38.490, 38.486		

@Seismicisolation

7.2 Apparatus

Since few instruments for measuring NQR for exclusive use are commercially available, the remodeled instruments for NMR are used in many cases.

NMR includes the continuous wave (CW) NMR and Fourier transformation (FT) NMR or pulse-NMR. CW-NMR determines the resonance absorption sweeping the external magnetic field of the frequency of the radio wave used for irradiation. FT-NMR produces the spectrum of the frequency region by the Fourier transformation of the free induction decay signal generated by the irradiation with a short, but high-power radio wave. Although the sensitivity of NMR is much lower than that of infrared and ultraviolet spectrophotometries, the FT-NMR method has such a high sensitivity by integration that the NMR signal of trace and low isotopic abundance elements can be easily obtained. The market share of the apparatus based on FT-NMR is, therefore, high.

A uniform, strong magnetic field is required for improving the resolving power of NMR. The resonance frequency of ^{1}H of the initial apparatus was approximately 40 MHz. At the end of the 1960s, it was increased up to 100 MHz. The intensity of the magnetic field has been remarkably increased by the development of superconducting magnets up to 500 to 600 MHz. The increased strength of the magnetic field, improved probe, and progress of computer, have recently made the determination of ^{27}Al and ^{29}Si as well as ^{1}H and ^{13}C in solid possible. ^{43}Ca may be determined by NMR in the near future.

Figure 42 illustrates the schematic diagram of the measuring system of NQR using NMR. The system comprises a magnet, a sample chamber, a data processor, a spectroscope, a wide band power amplifier, a Dewar (1.2 ~ 1,000 K) and a NQR probe. A magnetic field-sweeping magnet may be required. Since the width of the peak at resonance frequency of NQR is as broad as hundreds of Hertzes to MHz, which is broader than 10 to 100 Hz of that of solid NMR as well as that of liquid, the frequency generator is required to generate broad frequencies of 1 to 1,000 MHz and 10 to 200 MHz for NQR and NMR, respectively.

@Seismicisolation

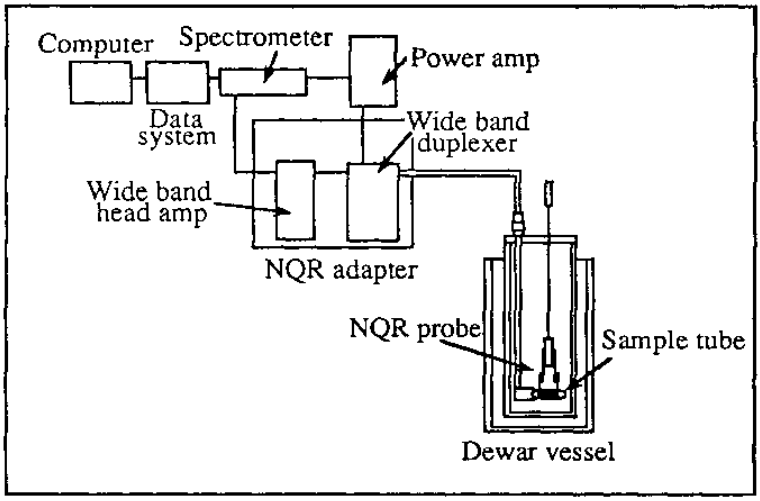


Figure 42. Block diagram of JNM-NQR220 (JEOL) system.

7.3 Applications

NQR is not popular at present. This is because the resonance absorption of a nucleus is not caused in the case when symmetry in the molecule is high though the nucleus has $I \geq 1$. For example, NaCl does not cause resonance absorption because the symmetry in the Na nucleus ($I = 3/2$) in NaCl is high though Na has the conditions causing the resonance absorption. Also, the application of NQR is limited to specific crystalline substances composed of regularly arranged atoms and molecules while it is not applied to liquids in which the interaction of atoms and molecules randomly arranged are equalized though the nuclear quadrupole is formed.

As mentioned before, NQR is a supplemental analytical means to NMR and has been applied so far to the studies mainly on Na ($I = 1$) and C1 ($I = 3/2$) in organic substances. At present, however, the study on Cu ($I = 3/2$) in high-temperature superconductors is actively carried out. In the high-temperature superconductors, the superconductive state is broken by applying a stronger external magnetic field than critical strength of magnetic field (J_c). NQR, which can measure the resonance absorption in a zero magnetic field is, therefore, effective. A temperature-measuring device is being developed because the resonance frequency of NQR is a function of the temperature.[49][50]

Examples of the application of NQR to high-temperature superconductors are provided by Asayama[51] and Imai, et al.[52]

@Seismicisolation

The measurement of NMR of solid ^{29}Si has finally been established and that of solid ^{27}Al has just started in the fields of cement and concrete research. No research on the application of NQR to these fields has been reported. This is because Si of $I = 1/2$ cannot be measured by NQR and the nuclei such as Ca and Al are relatively low sensitive though these nuclei meet the requirement of $I \geq 1$. It is expected that trace or small amounts of elements contained in cement or concrete could be measured by sharply improving the sensitivity of the instrument to obtain various new knowledge in the near future.

8.0 X-RAY ABSORPTION FINE STRUCTURE ANALYSIS

8.1 Principle and Special Features

A part of x-rays irradiating a substance is transmitted and scattered and the rest is absorbed. The relationship between the intensity of incident x-rays (I_0) and that of transmitted x-rays (I) is expressed by the following equation:

Eq. (9) $$I_0/I = \exp(-\mu t)$$

where t is thickness of sample and μ is the total linear absorption coefficient.

The linear absorption coefficient is proportional to the density (ρ) of the substance. When a uniform sample is used, μ/ρ, called mass absorption coefficient, is a value peculiar to each element independent of the state of the substance. Plotting the mass absorption coefficient versus the wavelength of x-rays, a curve in which the mass absorption coefficient is sharply changed at a wavelength is drawn, as illustrated in Fig. 43. The sharp change of mass absorption coefficient is called K-absorption edge, L_1-absorption edge, etc., by the orbits of electrons concerned. In the region where the mass absorption coefficient increases with the increase of the wavelength of x-rays, the following Victreen equation applies:

Eq. (10) $$\mu/\rho = C\lambda^3 - D\lambda^4$$

where C and D are constants.

@Seismicisolation

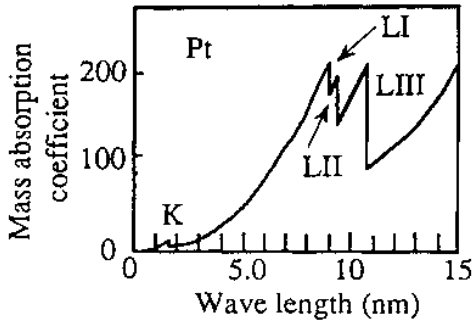


Figure 43. Wave length dependence on mass absorption coefficient by Platinum. *(Klug, et al.)*[53]

The result of detailed observation near the absorption edge indicates that there is a microstructure with different x-ray absorptivity, as illustrated in Fig. 44, in the region from x-ray absorption edge to 1,000 eV on the high-energy side. The regions from the absorption edge to approximately 50 eV and that from 50 to 1,000 eV are called the x-ray absorption near edge structures (XANES) and extended x-ray absorption fine structures (EXAFS), respectively, and both structures are collectively called the x -ray absorption fine structure. The structure is formed in such a way that photoelectrons flying out of the inner shell are scattered by the surrounding atoms during the propagation of them in the solid as spherical waves and the spherical waves are modulated to form the microstructure on the absorption spectrum. Since XAFS is a local physical phenomenon around the atom concerned, the x-ray absorption fine structure analysis is used for the analyses of ultra-fine particle, amorphous material, liquid and solid, as well as single crystal and powdered crystal.

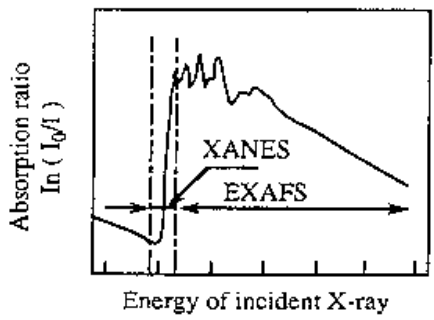


Figure 44. X-ray energy and x-ray absorpiton near absorption edge.

@Seismicisolation

The transmission method measuring the intensity of x-rays before and after transmitting the sample is widely used for determining the microstructure. Meanwhile, the fluorescent x-ray spectrometry measuring the intensity (yield) of fluorescent x-ray reflected from the sample surfaces is used for the thick and membrane samples which cannot transmit x-rays. The angle of incident x-rays in the fluorescent x-ray spectrometry is usually fixed to 45 degrees to measure the surface alone and it is applied only to heavy elements which generate a high-intensity of fluorescence x-rays. Meanwhile, Auger electron spectroscopy is used for light elements.

Although the steric configuration of atoms and the state density of conducting material can be determined by the analysis of XANES, the analysis is so complicated because XANES appears as the result of the interference effect caused by the multiple scattering between the x-ray absorbing atoms and the surrounding atoms that a structural model is required. It is inferred from the resolving power of monochromator and the absorption of x-ray in air that only the atoms having the adsorption edge in a range from 5 to 25 ev, such as titanium or higher atoms, can be measured in XANES. The information obtained by EXAFS is the radius distribution around a specified element and, accordingly, the distance between the atom absorbing x-rays, the atoms around it and the coordination number and kind can be determined by analyzing EXAFS.

8.2 Apparatus

It is desirable that the x-ray used for XAFS is uniformly strong and continuous throughout all the wavelength region. Synchrotron orbital radiation (SOR) continuously generating high-strength and high-directivity x-rays has gained attention as the radiation source, as described in Sec. 9. The equipment of SOR is, however, so large-scaled and expensive that its application is limited. Accordingly, the rotating anode type high-power x-ray generator and various devices using a thermoelectron radiating electron gun with filament composed of W and LaB_6 for generating x-rays, using an x-ray path evacuated or filled with He gas for preventing the atmosphere from absorbing x-rays and using a high diffraction intensity analyzing crystal or curved analyzing crystal for preventing the fluorescent x-rays from lowering its intensity, are generally used for determining the microstructures. The commercially available equipment can determine XAFS ranging from Al to Ra.

@Seismicisolation

Auger electron spectroscopy is mainly used for measuring the K-absorption edge of light elements including C, N, O, and F, in an ultra-soft x-ray region. Fluorescent x-ray spectroscopy and Auger electron spectroscopy are used for measuring the K-absorption edge of Na to Cl in a soft x-ray region and the L-absorption edge of Ni to Rh.

Figure 45 illustrates photographs of a general view and the spectroscopic and detection parts of commercially available equipment.

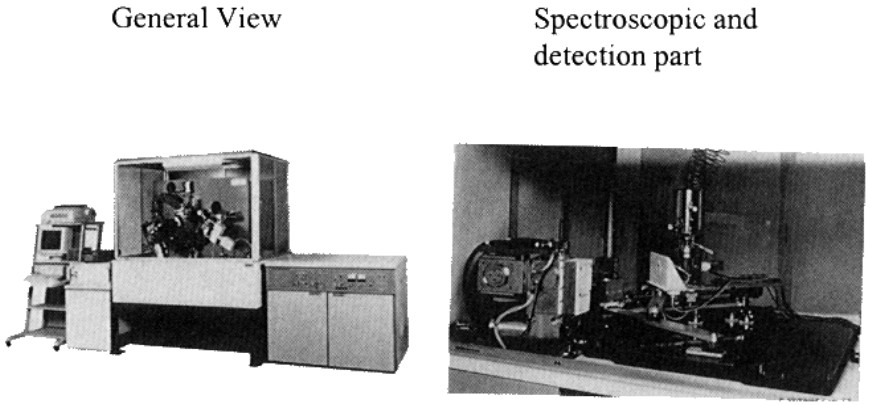


Figure 45. Extended x-ray absorption fine structure analyzer. *(Rigaku Co.)*

8.3 Applications

Examples of XANES of Pt, Au, Ta, Ta_2O_5 and PtO_2 are illustrated in Ref. 54.

The change of the coordination number and intra-atomic distance of a Ru crystal of catalyst by using alumina as carrier is traced in Ref. 55.

In the field of cement and concrete research, a paper presents that the stabilizing mechanism of a Cr compound in hardened cement is investigated by determining XAFS at the K-absorption edge of Cr in the samples prepared by adding 2,500 ppm each of Na_2CrO_4 to blast-furnace slag (Mix #l), portland cement (Mix #3), and a mixture of portland cement, blast-furnace slag, and fIy ash (Mix #2), and hydrating them for nine days.[56] The radiation source used for the experiment was NSLS (2.5 GeV and 250 mA) of Brookheaven in the U.S. The result of measurement of XAFS and the

@Seismicisolation

wave form after Fourier transform of the spectrum are illustrated in Fig. 46 and Fig. 47, respectively. The calculated results of the coordination number and the interatomic distance are listed in Table 3. Those figures reveal that the wave forms of Cr added to portland cement and in blast-furnace slag are similar to those of K_2CrO_4 and CrOOH, respectively. Table 3 reveals the similar trend in coordination number and interatomic distance. These results indicate that Cr^{6+} added to the slag is converted to harmless, immobile Cr^{3+} in it and Cr^{6+} remains unchanged in portland cement. In addition, there are studies measuring XAFS at the K-absorption edges of Ca and investigating the structures of CAH_{l0}, C_2AH_8 and C_3AH_6 in refractory cement by combining the results of NMR and XRD.[57]

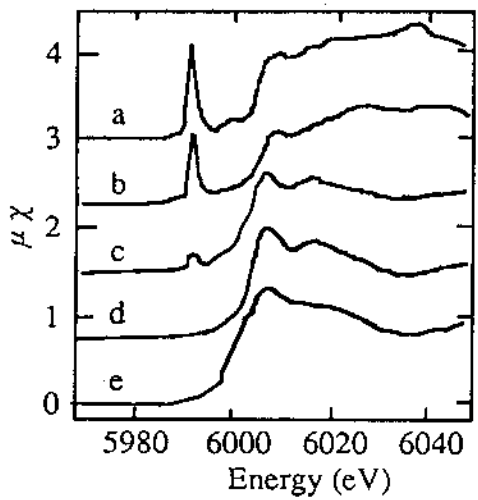


Figure 46. Near edge spectra from Cr K-edge of *(a)* K_2CrO_4, *(b)* Mix #3, *(c)* Mix #2, *(d)* Mix #1, and *(e)* CrOOH. *(Lee, et al.)*[56]

@Seismicisolation

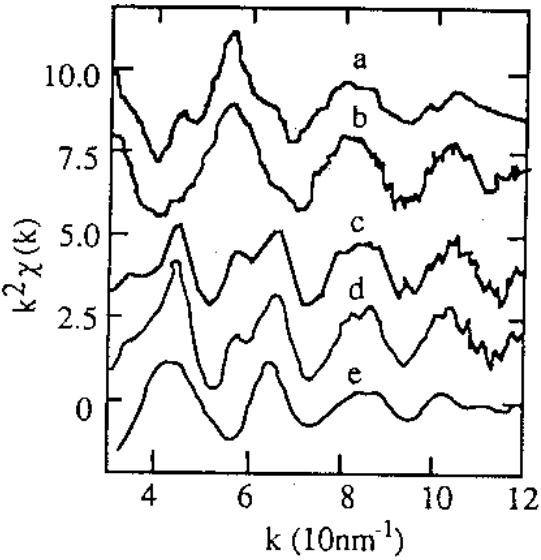


Figure 47. Patterns after Fourier transform for the sample of Fig. 46. *(Lee, et al.)*[56]

Table 3. Cr-O Interatomic Distance and Coordination Numbers of Various Na_2CrO_4 Added Samples After Nine Days Hydration *(Lee, et al.)*[56]

Sample	N (±25)	R (0.02) (Å)
K_2CrO_4	4.90	1.65
Mix # 3	5.40	1.66
Mix # 2	1.31, 4.93	1.65, 1.98
Mix # 1	6.46	1.98
CrOOH	6.21	1.98

@Seismicisolation

9.0 SYNCHROTRON ORBITAL RADIATION ANALYSIS

9.1 Principle and Special Features

The equipment for repeatedly moving electrically charged particles, including electrons and positrons, around an orbit with a constant radius in the alternative current electric field to accelerate up to the relativistic energy is called a synchrotron. When the orbit is bent, intensive light (electromagnetic wave) emitted in the tangential direction of the orbit is called synchrotron orbital radiation (SOR).

SOR is a continuous spectrum widely distributed from the infrared region to the x-ray region as illustrated in Fig. 48.[58] The peak energy (ε_p) and the number of photon (N_p) at the peak position in the continuous spectrum are expressed by the following equations:

Eq. (11) $\varepsilon_p \propto E^3/R$

Eq. (12) $N_p \propto E^4/R$

where E is kinetic energy of electron and R is radius of orbit. The smaller the radius of orbit and the larger the kinetic energy of accelerated electron, the larger the peak energy is, namely, electromagnetic waves with shorter wavelengths are emitted.

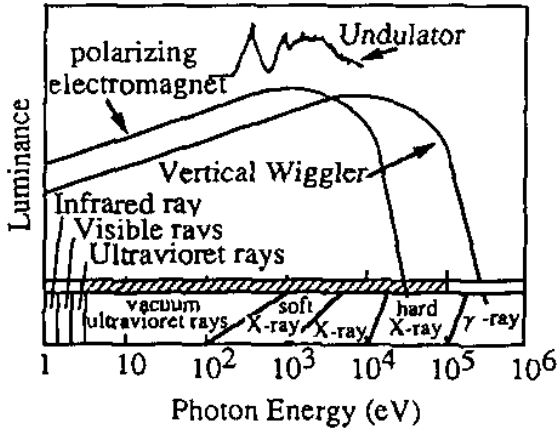


Figure 48. Energy distribution of synchrotoron orbital radiation. *(Kai.)*[58]

@Seismicisolation

The kinetic energy of accelerated electrons is expressed by the following equation:

Eq. (13) $$B \cdot R = Z(E^2 + 2EE_0)^{1/2}/2.8$$

where B is strength of magnetic field, Z is electric charge and E_0 (static energy) $= m_0c^2$. It is necessary to increase the strength of the magnetic field and radius of orbit for increasing the kinetic energy of the electrons.

The intensity of SOR is 100 to 1,000 times as high as that of a conventional light source for analysis in the far ultraviolet region and 100 to 10,000 times as high as that in the x-ray region. It has, therefore, become possible to determine a substance which is not detected and the sensitivities of EXAFS, photoelectron spectroscopy and fluorescent x-ray spectrometry and the S/N (signal to noise ratio) have been improved.

SOR is so directional that the crystal structure in a microscopic region with an order of magnitude of micrometers can be analyzed using an optical system appropriate for converging x-rays. The method of characterization by which the sensitivity and accuracy are expected to be improved by using SOR is shown in Table 4.[59]

Table 4. Research Fields Utilizing SOR *(Iida)*[59]

A. X-ray diffraction and scattering measurement
1. Small angle scattering
2. Powder diffraction
3. Interferometer
4. Topography
5. Anomalous scattering
B. EXAFS and adsorption measurement
1. Absorption measurement (bulk)
2. Surface EXAFS
3. Fluorescence EXAFS
4. Energy dispersive EXAFS
5. XANES
C. X-ray fluorescence analysis
D. Radiography
E. Photoelectron spectroscopy
1. Energy resolving
2. Angle resolving
F. Lithography
G. Microscopy

@Seismicisolation

9.2 Apparatus

A ring generating SOR is called a storage ring, which comprises a deflecting magnet forming an orbit by deflecting electron, quadrupole electromagnet for converging it, and a microwave-accelerating cavity supplying energy to the electron. Electrons in lumps move around inside the storage ring and emit pulsating light every time they pass through the deflecting electromagnet.

As illustrated in Fig. 49, electromagnetic waves with shorter wave lengths than conventional SOR can be generated by locally undulating the orbit of an electron providing it with a strong magnetic field using a superconducting magnet (wiggler) and phased radiation can be generated by periodically undulating the orbit of the electron with the magnets placed in a row (undulator) because the radiation interferes with each other.

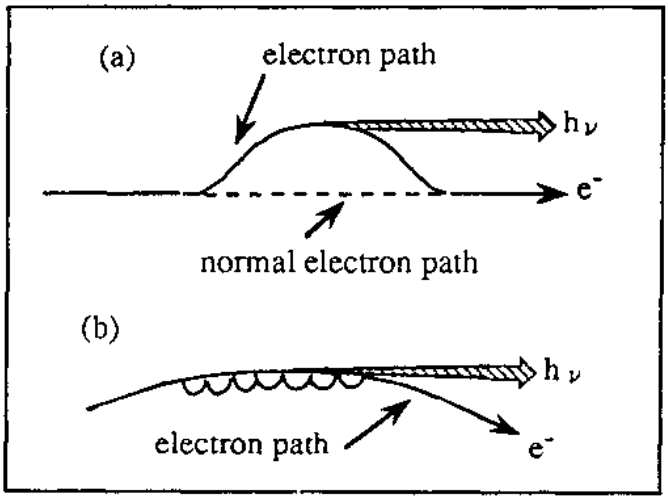


Figure 49. Schematic drawing explaining the concept of *(a)* wiggler and *(b)* undulator. *(Iida.)*[59]

@Seismicisolation

Electrons entering into the storage ring of a synchrotron are generated by the high-temperature external cathode unit and accelerated up to tens of MeV by a linear accelerator (LINAC) before entering into it. The storage ring is evacuated to 10^{-6} mm Hg for preventing the scattering caused by colliding of electrons with molecules of air. The diameters of the existing synchrotrons range from tens of meters to 2,000 m.

SOR began to be used in the 1960s and the application researches of SOR increased in the 1980s because the facilities of SOR for exclusive use were operated in various countries. Table 5 lists the main radiation facilities in various countries and Fig. 50 illustrates an example of the arrangement of the experimental radiation facilities.

Table 5. List of Major SOR Rings (Iida)[60]

Place (Laboratory)	Name of Ring	Energy (GeV)
Japan		
Tukuba (KEK)	PF	2.5
	AR	2.5-8
(ETL)	TERAS	0.8
Okazaki(IMS)	UVSOR	0.75
Tokyo(ISSP)	SOR-Ring	0.38
USA		
Stanford(SSRL)	SPEAR	3.8
	PEP	7-14.5
Upton(BNL)	NSLS(VUV)	0.75
	NSLS(X)	2.5
Ithaca(CHESS)	CESR	5.44
Stoughton(SRC)	Aladdin	1.0
France		
Orsay(LURE)	DCI	1.85
	Super ACO	0.8
Germany		
Hamburg(DESY)	DORIS II	3.7-5.3
Berlin(BESSY)	BESSY I	0.805
Italy		
Frascati(INFN)	ADONE	1.5
UK		
Daresbury	SRS	2.0
USSR		
Novosibirsk(INP)	VEPP-3	2.2
	VEPP-4	7
Under constructing or planning Rings		
France		
Grenoble	ESRF	6
USA		
Argonne(ANL)	APS	7
Berkeley(LBL)	ALS	1.5
Japan		
Nishiharima	Spring-8	8
Italy		
Trieste	ELETTRA	2

@Seismicisolation

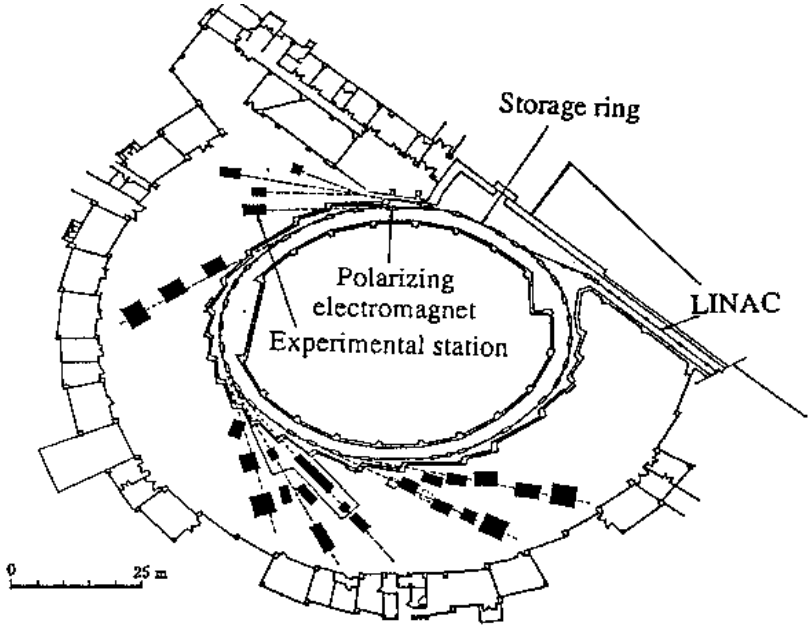


Figure 50. A plan of the arrangement of the SOR experimental facilities. *(Iida.)*[59]

9.3 Applications

Measurement using synchrotron orbital radiation has not been popularly applied to research because the light source is limited, as mentioned above. The application of it is limited to the XAFS field for the present. Several examples among the applications given in Table 4 will bedescribed herein together with the feasibilities of them.

Fluorescent X-Ray Analysis. The x-ray spectrometry using high-luminance SOR as the light source is called synchrotron radiation excited x-ray fluorescence analysis (SRXRF). The detection limit can be extended to an order of magnitude of ppb or pg. Since the wave length used for SOR can be easily changed to adjust the excitation energy to the absorption edge wave length of a specified element, the detection sensitivity of the element can be selectively raised. Since a microscopic region can be analyzed, owing to the sharp directivity, the scattering from the sample is reduced, hence the S/N ratio is improved.

@Seismicisolation

Accordingly, high-sensitivity and high-accuracy analyses of light elements using the undulator and special measurements of K-series x-rays of heavy elements using the wiggler will become feasible in the future.

Photoelectron Spectroscopy. The strength of photoelectrons of SOR per unit radiation area is 1,000 to 10,000 times that of x-rays emitted from a normal tube. Accordingly, SOR can have so strong a luminance, even by diffracting the light with a monochromator the resolving power can be improved up to 1/100 or under as much as the natural width (an order of 0.1 eV) of the characteristic x-rays. A fine chemical shift of photoelectrons can, therefore, be observed and the accuracy of the state analysis, including the analysis of the bonding state of the element, is sharply improved. Since the penetration depth of photoelectrons in the sample can be adjusted by changing the kinetic energy of photoelectrons emitted, the composition in the direction of depth can be nondestructively analyzed though the surface of the sample has been etched by irradiating it with the ion source so far, and the thickness of the sample can be measured by it. The resolving power of position 0.3μm or under can be obtained by utilizing the directivity of SOR combining a converging mirror with an undulator. That value is much smaller than the tens of microns obtained with the current microfocus x-ray diffraction. The distribution of photoelectrons can be imaged by two-dimensionally scanning SOR on the surface of the sample. It is, therefore, able to determine the three dimensional distribution of chemical bonds as well as the distribution of elements.

X-ray Diffraction Analysis and X-ray Topography. Since SOR is pallalelistic, the high-angle resolving power can be measured with the monochrome SOR. Accordingly, the precision of crystal structure analysis by such as the Rietveld method is improved.

X-ray topography is a method for projecting and photographing an image of the defect of crystal on a real space unit. It is able to be more precisely photographed for a shorter time by using higher-luminance, more highly pallalelistic SOR than a conventional light source. Examples of the direct on-time observation of TV image of the state of the interface between the crystal and the melted liquid in the crystal growing process of GaAs[61] and the observation of microdefect and strain field in the synthesis of a single crystal of silicon by the CZ method[62]–[64] have been reported.

The following applications have been reported in the field of cement and concrete research.

$CaO{\cdot}Al_2O_3$(CA), which is one of the main constitute minerals of calcium alumina cement, produces CAH_{10} and C_2AH_5 by hydration and these reaction products are converted to a stable phase C_3AH_6 with the elapse of

@Seismicisolation

time and rise of temperature. The phase transition at 50°C with time is determined by synchrotron orbital radiation-energy dispersive diffraction (SOR-EDD) and the results are illustrated in Figs. 51 and 52.[65] The results indicate that a broad peak, near 26 keV, corresponding to C_2AH_8 disappears in approximately 150 minutes, the peak corresponding to CAH_{l0} is reduced with the elapse of time and the peaks corresponding to C_3AH_6 and AH_3 are newly developed thereby by progressive transition. Detailed analysis of the broad peak near 26 keV indicates thatα phase-C_2AH_8 is produced followed by β phase one, and the α phase disappears and the β phase remains with the elapse of time. Thus, high-speed and high precision x-ray diffraction analysis can be made using the high luminance and high-wave length resolving power of SOR to understand the phase transition process in more detail.

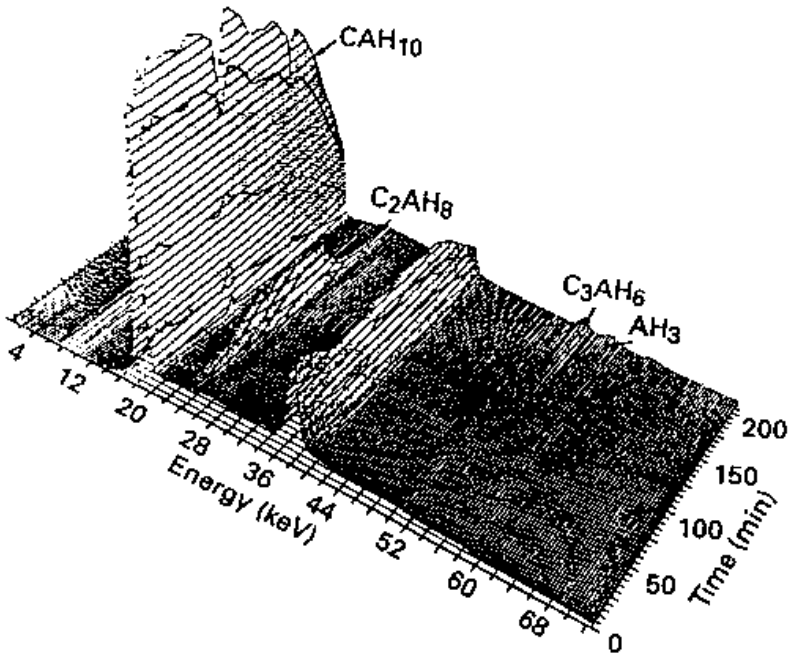


Figure 51. Time-resolved SOR-EDD patterns following the conversion of CAH_{10} to C_3AH_6 and AH_3 at 50°C. *(Rashid.)*[65]

@Seismicisolation

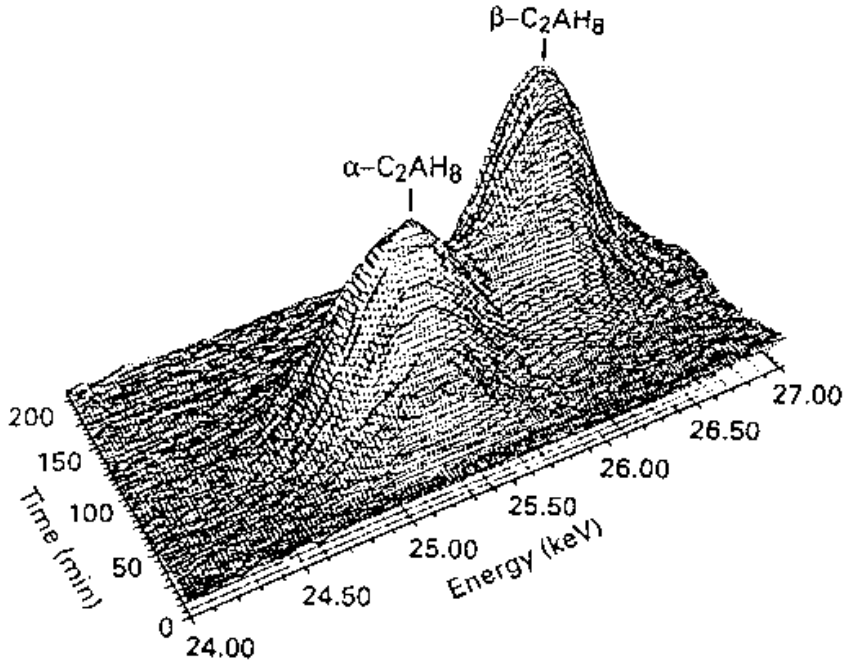


Figure 52. A blow-up of the 24–28 KeV region of Fig. 51. *(Rashid.)*[65]

10.0 MÖSSBAUER SPECTROMETRY

10.1 Principle and Special Features

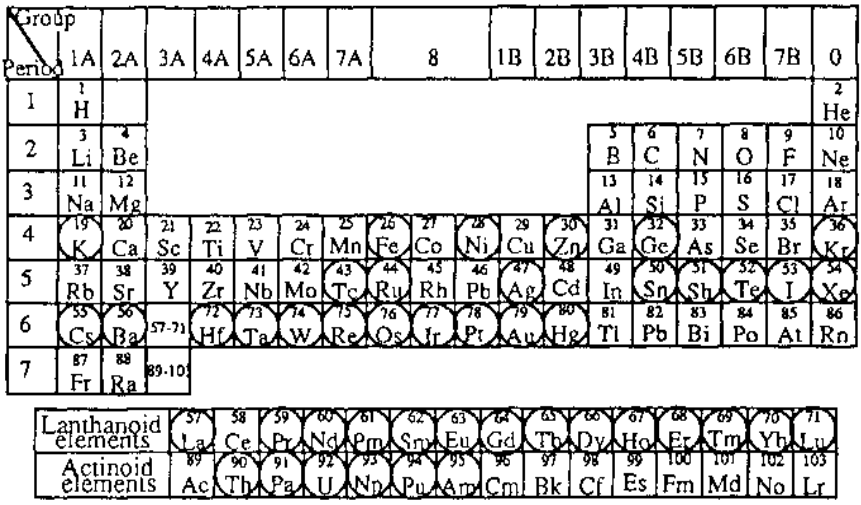
The reaction which an atomic nucleus receives by the momentum of electromagnetic waves when the atomic nucleus absorbs or emits the electromagnetic waves is called recoil. Gamma (γ)-rays have much larger recoil than other electromagnetic waves, including infrared, visible, and ultraviolet rays, because γ-rays have higher energy than these electromagnetic waves. The energy width of the excitation level of γ-rays is remarkably narrow. Since the effect of recoil in emitting γ–rays is not negligible in the gas and as the liquid phase samples consist of isolated atoms, it has generally been considered that the resonance absorption by the atomic nucleus hardly results. Mössbauer discovered in 1958 that if the atomic nuclei are firmly restricted in a solid the atoms surrounding them have charge of the recoil energy at the emission of γ-rays, hence the atomic

@Seismicisolation

nuclei lose the recoil whereupon the resonance absorption of γ-rays is observed. It is, therefore, possible to determine the physical and chemical properties of a substance by examining the resonance absorption spectrum of γ-rays emitted from the non-recoil nucleus. This method is called Mössbauer spectrometry after the name of discoverer of the resonance absorption phenomenon of γ-rays.

The elements showing the Mössbauer effect are listed in Table 6. The elements applicable to Mössbauer spectrometry among them are limited to the elements emitting low-energy (generally 150 keV or under) γ-rays and having a large mass number, namely, ^{57}Fe and ^{119}Sn.

Table 6. Elements (Enclosed with a Circle) Showing the Mössbauer Effect *(Tominaga)*[66]



The mechanism of the development of spectrum will be described using ^{57}Fe as an example.

Gamma-ray of ^{57}Co (half-life: 270 days) with low recoil, at room temperature, showing a narrow singlet peak, is used as the radiation source for exciting iron contained in the sample. For applying the spectrometry to tin, ^{119m}Sn (half-life: 245 days) is used as the radiation source. As illustrated in Fig. 53, ^{57}Co develops the second excitation level of ^{57}Fe by the orbital electron capture decay. After 91% of the second excitation level

@Seismicisolation

once moves to the first excitation level it transforms to ^{57}Fe on the normal level, emitting γ-rays of 14.4 keV after the mean life of approximately 10^{-7} seconds and the remaining 9% of that transits directly to the normal level emitting γ-rays of 136.4 keV.

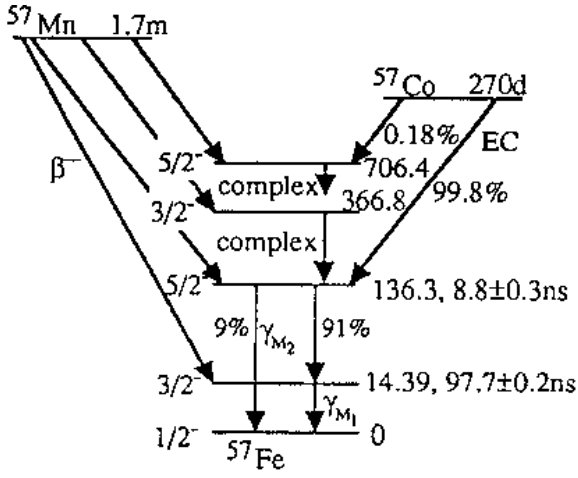


Figure 53. Decay process of ^{57}Fe. *(Tominaga.)*[66]

If the chemical state of the radiation source is the same as that of Fe in the sample, ^{57}Fe in the sample causes the resonance absorption and excites the atomic nucleus of Fe in the sample and it returns to the normal level emitting γ-rays in all directions for a short time, when γ-rays of 14.4 keV emitted by the decay of ^{57}Co transmit the sample containing iron. In this process, the strength of the transmitted γ-rays is decreased on the backside of the sample todevelop an absorption spectrum. Theγ-rays cause the resonance scattering also in directions other than the direction of transmission (Fig. 54).

If the chemical state of the radiation source is different from that of Fe in the sample, no resonance absorption occurs because the difference between the energy levels of the atomic nuclei is different. Due to the relative velocity between the radiation source and the Fe in the sample (absorber) by vibrating the radiation source the energy of incident γ-rays is converted to E_2 by the Doppler effect to cause the resonance absorption as illustrated in Fig. 54 according to the following equation:

@Seismicisolation

Eq. (14) $E_2 = E_1(1 + v/c)$

where E_1 is the energy of incident γ-rays, v is the relative velocity and c is the velocity of light.

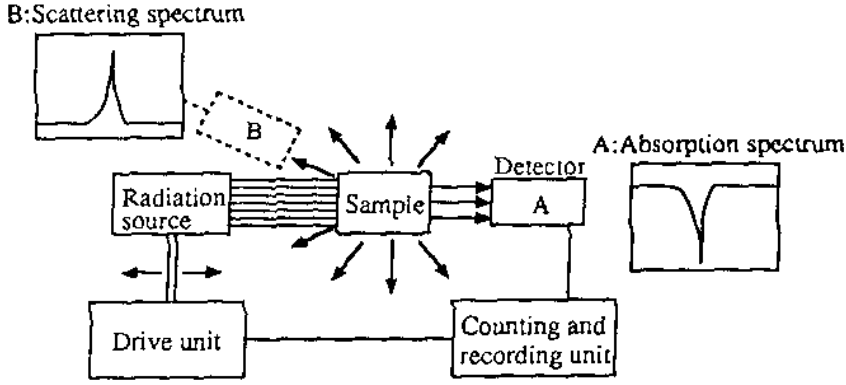


Figure 54. Process of Mössbauer Spectrum measurement. *(Tominaga.)*[66]

The energy levels of the normal and excited states of the atomic nucleus are slightly changed according to the neighboring electron state (such as valency number and steric symmetry of ligand) and the neighboring magnetic state (such as inner magnetic field of ferromagnetic or antiferromagnetic body and superparamagnetism) of the atomic nucleus. The Mössbauer spectroscopy detecting the changes provides information listed in Table 7.[67]

Isomer Shift (δ). The effective radius of the atomic nucleus in the excited state is slightly different from that in the normal state. When the electron state of the radiation source differs from that of the atomic nucleus of the elements to be analyzed in the sample, the position of the center of resonance absorption deviates from the origin on the Mössbauer spectrum as shown in Fig. 55*(a)*.[68] The phenomenon is called the *isomer shift* and the magnitude of it *(δ)* is expressed by the following equation:

Eq. (15) $$\delta = \frac{4}{5}\pi Ze^2R^2\left(\frac{\Delta R}{R}\right)\left(|\Psi(O)|a^2 - |\Psi(O)|s^2\right)$$

@Seismicisolation

where Z is atomic number, R is effective radius of atomic nucleus, ΔR is the increase in effective radius of atomic nucleus on excitation level compared to that on normal level, and $|\psi(O)|a^2$ and $|\psi(O)|s^2$ are electron density at nuclear sites in elements to be analyzed and radiation source, respectively.

Table 7. Major Information Obtained from Mössbauer Spectrum *(Sano, et al.)*[67]

Character of peak	Parameter	Direct information	Indirect information
Shift of spectrum	Isomer shift	Density of s-electron	Electric charge
	Secondary Doppler shift	Mean square displacement of nucleus	Specific heat
Splitting of spectrum	Quadruple splitting	Electric field gradient at the atomic nuclear site	Steric symmetry of ligand
	Magnetic splitting	Magnetic field at the atomic nuclear site	Internal magnetic field of ferromagnetic antiferromagnetic body
Intensity and width of spectrum	Rate of recoil		Intermolecular (intra molecular)bond (Debye temperature, etc.)

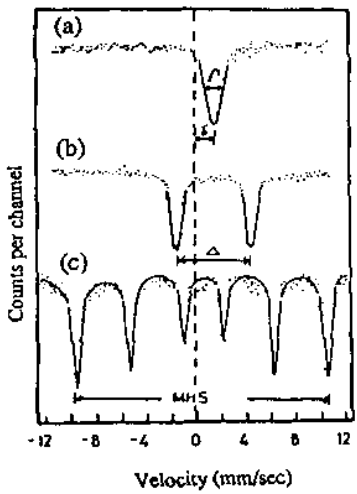


Figure 55. Isomer shift and *(a)* the line width, *(b)* quadrupole splitting, and *(c)* magnetic splitting, observed in Mössbauer spectrum. *(Hassaan, et al.)*[68]

@Seismicisolation

The electron density at the nuclear site of the radiation source can be compared with that of the element to be analyzed when the sign of ($\Delta R/R$) of nuclide is known. The value of the isomer shift is a relative indicator of electron density based on that of the element in the substance used as the radiation source from which the information on the state of oxidation and the properties of bonding can be obtained.

Quadrupole Splitting **(ΔE_Q).** When the nuclear spin at the normal or excited state is one or more the nucleus has electric quadrupole moment ($Q \neq 0$). The electric field gradient is caused in the nuclear site if there is the deviation in the extranuclear electron, atoms surrounding the nucleus, and arrangement of ions from the steric symmetry. The nucleus interacts, therefore, with the extranuclear electron, atoms surrounding the nucleus and ions to split the nuclear energy levels into two or more peaks in the Mössbauer spectrum. The distance between a pair of peaks caused by splitting (energy difference) is called the quadrupole splitting (see Fig. 55*b*).

The nuclear energy level is expressed by the following equation:

Eq. (16) $$E_{I \cdot m} = \frac{e^2 qQ}{4I(2I-1)}\left[3m^2 - I\,(I+1)\left(1+\eta^{\frac{2}{3}}\right)\right]^{\frac{1}{2}}$$

The quadrupole splitting of the elements such as ^{57}Fe and ^{119}Sn causing the transition between the levels of I = 1/2 and I = 3/2 is expressed by the following equation:

Eq. (17) $$\Delta E_Q = \tfrac{1}{2}\, e^2 qQ\left(1+\eta^{\frac{2}{3}}\right)^{\frac{1}{2}}$$

where eq is electric field gradient ($\partial^2 V/\partial z^2$) and η is asymmetric constant ($\partial^2 V/\partial y^2$)-($\partial^2 V/\partial x^2$) /($\partial^2 V/\partial z^2$).

Since the degree of the electric field gradient at the atomic nuclear site can be estimated from Eq. (17), the information on the molecular structure and the symmetry of ligand can be obtained.

Magnetic Hyperfine Splitting (MHS). When the nuclear spin is not zero, the energy level of atomic nucleus causes the Zeeman splitting by the interaction with the effective magnetic field at the nuclear site. The absorption peaks corresponding to the transitions of the split levels of Δm = 0 and ± 1

@Seismicisolation

are developed as illustrated in Fig. 55*(c)*. Since the nuclear magnetic moment at the excitation level can be found by measuring the magnetic splitting and the inner magnetic field can be found by the position of peak, magnetic substances can be identified.

Non-Recoil Rate (f). The intensity of a peak in a Mössbauer spectrum depends upon the non-recoil rates of the radiation source elements to be analyzed and the concentration of the nucleus of the element to be analyzed in the sample. The width of peak depends on the non-recoil rate of the sample and the effective thickness represented as the product of the concentration of nucleus of the sample and its sectional area. The non-recoil rate (f) is expressed by the following equation:

Eq. (18) $$f = \exp(-4\pi^2 \langle u^2 \rangle / \lambda^2)$$

where λ is wavelength of γ-rays and $\langle u^2 \rangle$ is mean square deviation of Mössbauer atom.

Equation (18) reveals that the f-value is decreased with increasing temperature and the Mössbauer effect is more easily heightened the lower the temperature. Also, it provides information on the mobility of the Mössbauer atom and, accordingly, the molecular motion and intermolecular bond strength. Some research on the phase transition, including glass transition and crystallization, is being made.

Thus, the structural changes of iron and tin compounds which cannot be detected by x-ray diffractometry can be determined by examining a spectrum obtained by Mössbauer spectrometry.

10.2 Apparatus

Photograph and block diagrams of a transmission Mössbauer spectrometer are illustrated in Fig. 56. The radiation source is vibrated by a driving unit. The γ-rays transmitting the sample are detected with a proportional counter and amplified and then a Mössbauer spectrum is obtained from the relative velocity of the radiation source and the histogram of the intensity of detected γ-rays. The amount of sample required is approximately a few milligrams to tens of milligrams (the amount of Fe).

@Seismicisolation

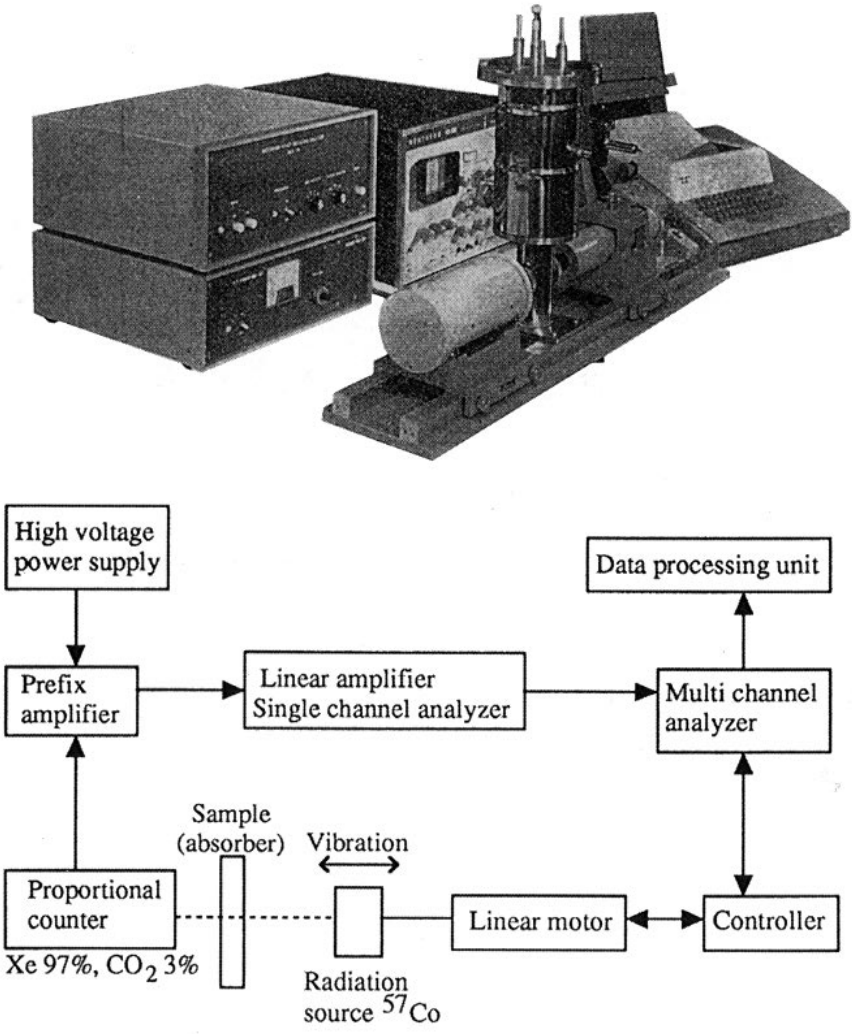


Figure 56. Photograph and block diagram of transmission Mössbauer spectrometer. *(Shimazu Co.)*

@Seismicisolation

10.3 Applications

The application of Mössbauer spectrometry is practically limited to ^{57}Fe and ^{119}Sn because it has shortcomings including low energy of γ-rays, applicability only to solid samples, inapplicability to lighter elements than potassium, and uses only the emitted number of radioisotopes with the adequate half-life as the radiation source. It is, however, applied to the study on the properties of iron compounds, including the state of electron and structural analysis, the magnetism tracing the solid reaction and phase transition, and the study on relaxation. It has recently been applied to environmental samples such as dust and deposits and the state of analysis of biomaterials.

An example of the variation of a Mössbauer spectrum with temperature is provided by Sano and Kanno.[69]

In the field of cement and concrete research, studies include the application of Mössbauer spectrometry to the state analysis of iron contained in the clinker minerals and the determination of the hydration rate by the state analysis of iron in cement paste.

An example of a Mössbauer spectrum obtained by burning various cement raw mixtures is illustrated in Fig. 57.[68] The states of iron produced by heating the raw mixture at low temperatures include Fe^{2+}, Fe^{3+} existing at the tetrahedral site *(T)* and octahedral site *(O)*. Figure 58 reveals that the ratio of Fe^{3+} *(O)* is increased by burning it at 600°C, the states of all of those three types of iron are increased by burning it at 1300°C and most of them are converted to Fe^{3+} *(T)* by burning it at 1500°C. It is, therefore, able to evaluate the degree of burning of clinker by knowing the state of iron contained in the cement raw mixture and clinker from the Mössbauer spectrum.

The Mössbauer spectrum of portland cement illustrated in Fig. 59 consists of two peaks, *(a)*. They are reduced and two peaks, *(b)*, are developed between them with the progress of hydration, and the peaks *(b)* are enlarged with further hydration. This method, therefore, is able to trace the degree of the hydration reaction and estimate the rate of hydration of cement by determining the intensity ratio of the peak *(a)* to peak *(b)*.[68]

@Seismicisolation

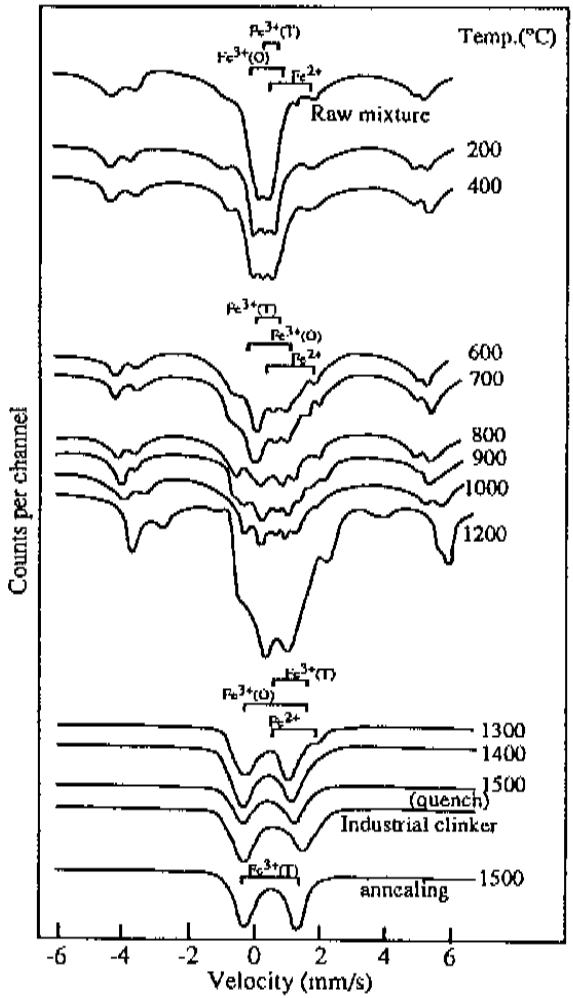


Figure 57. Mössbauer spectrum of the clinker raw mixture at different burning temperatures. *(Hassaan, et al.)*[68]

@Seismicisolation

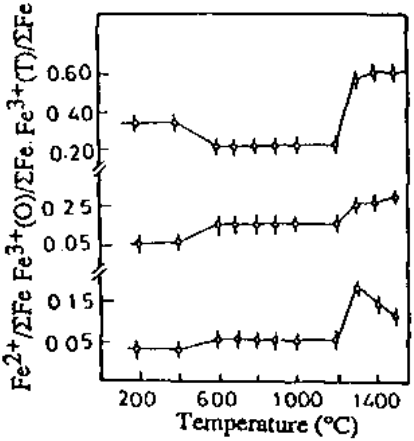


Figure 58. The ratio of Fe^{2}+, Fe^{3}+ *(T)*,and Fe^{3}+ *(O)* to the total iron as a function of burning temperature. *(Hassaan, et al.)*[68]

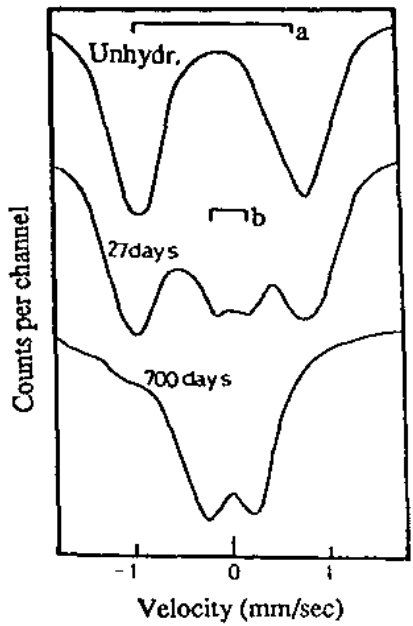


Figure 59. Mössbauer spectrum of Portland cement hydrated at different times. *(Hassaan, et al.)*[68]

@Seismicisolation

11.0 QUASI-ELASTIC NEUTRON SCATTERING ANALYSIS

11.1 Principle and Special Features

A neutron is a particle without electric charge and with the mass *(m)* of 1.0087 atomic mass unit, spin quantum number of 1/2 and magnetic moment (μ_n) of -1.9132 nuclear magnetism unit. It is produced by nuclear reaction. Energy of neutron generated from a nucleus is several MeV or more. In order to utilize the scattering and diffraction due to a crystal (for analyzing the structure of a substance), decelerated neutrons are used. A neutron beam has properties of waves and its wavelength (λ) and energy*(E)* are expressed by the following equations:

Eq. (19) $$\lambda = h/\sqrt{2mE} = h/2\sqrt{2mk_BT}$$

Eq. (20) $$E = mv^2/2$$

where T is temperature, h is Planck constant, k_B is Boltzmann constant and v is velocity of neutron. Neutron is classified by the kinetic energy or velocity as listed in Table 8. The kinetic energy of a neutron is classified by temperature into thermal neutron (near normal temperature), epithermal neutron (higher than room temperature), cold neutron (lower than room temperature), and super cold neutron (further lower than it). The classification is, however, not so rigid.

Table 8. The Classification of Neutron

	unit	Epithermal neutron	Thermal neutron	Cold neutron	Super cold neutron
Wave length λ	Å	0.29	1.8	9.0	570
Energy E	meV	1,000	25	1	0.00025
Temperature T	K	12,000	290	12	0.0029
Velocity V	m/s	14,000	2,200	440	6.9

@Seismicisolation

The scattering caused by colliding neutrons with a substance which does not change the kinetic and internal energies of the neutron, even after the collision, is called elastic scattering, while that changing those energies of the incident neutrons by letting the substance absorb a part of those energies or release neutron energy is called inelastic scattering. Thus, when a substance (scatterer) irradiated with a neutron beam changes the position with the lapse of time, the scattered neutrons develop a slightly broad energy distribution spectrum centering around the energy of the incident neutron beam except for the scattering in the forward direction at zero degrees of the scattering angle. Since such scattering as this is different from either the elastic or inelastic scatterings it is called quasi-elastic scattering. An example of elastic scattering caused by irradiating a cyclically moving crystal with a monochrome neutron beam *(a)* and examples of the quasi-elastic scattering caused by irradiating diffusing molecular liquids *(c)* and rotational diffusion in solid with a neutron beam *(d)* are illustrated in Fig. 60,[73] respectively. The spectrum shown in Fig. 60*(d)* is composed from a broad spectrum of the quasi-elastic scattering and a sharp spectrum of the elastic scattering.

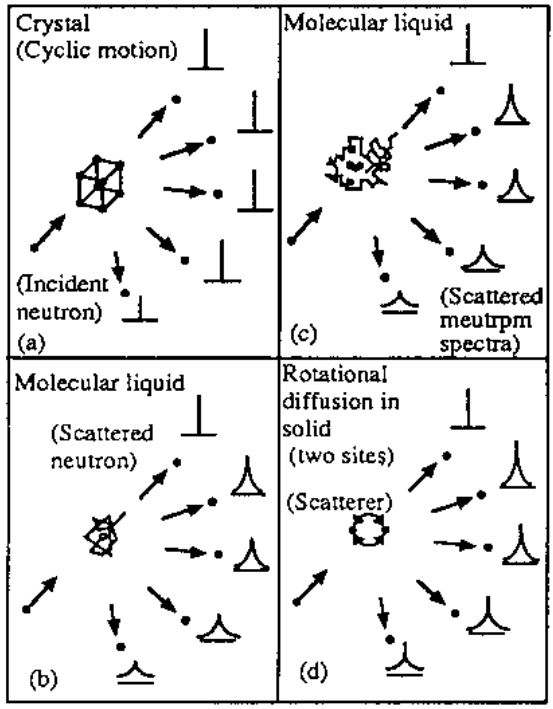


Figure 60. Various spectra of cold neutron scattering. *(Inoue, et al.)*[73]

@Seismicisolation

The probability of the scattering of the incident particles by a substance (number of particles scattered/number of incident particles) is called a scattering cross section. The scattering cross section *(s)* of a neutron composed of *N* pieces of molecules with the total scattering cross-section *(s_{inc})* in incoherent scattering is expressed by Eq. (21).[74] A wave vector of neutron by scattering is changed from k to k' and a scattering vector *(Q)* is expressed by Eq. (22).

Eq. (21) $$\frac{d^2\sigma}{d\Omega d\omega} = N\frac{k'\sigma_{inc}}{k4\pi}S_{inc}(Q,\omega)$$

where Ω is steric angle and ω is frequency.

Eq. (22) $$Q = k - k'$$

A scattering function [$S_{inc}(Q,\omega)$] of the incoherent scattering is expressed by the Fourier transform of a space-time auto-correlation function [$G(r,t)$] giving the probability of the transfer of a molecule occupying a position of $R'(0)$ at a time of zero to a position of $R(t)$ at a time of t as follows:

Eq. (23) $$S_{inc}(Q,\omega) = \frac{1}{2\pi}\iint drdt\exp(iQ\cdot r-\omega t)\cdot G(r,t)$$

Eq. (24) $$G(r,t) = \frac{1}{N}\left\langle\delta\left[r+R'(O)-R(t)\right]\right\rangle$$

The scattering function for a liquid is expressed by the following equation, using a scattering model of Fick's law:[75]

Eq. (25) $$S_{inc}(Q,\omega) = \frac{1}{\pi}\frac{DQ^2}{\left(DQ^2\right)^2+\omega^2}$$

The frequency spectrum is represented as a Lorenzian curve and its half-width ($\Delta\omega$) is expressed by Eq. (26).

Eq. (26) $$\Delta\omega = 2DQ^2$$

where D is diffusion constant.

@Seismicisolation

As mentioned above, the scattering spectrum indicates the characteristics of the dynamic structure of the scatterer. The neutron diffraction method is used for studying the static structure of a coagulated body, while the quasi-elastic scattering of neutrons is used for studying the dynamic structure. Particularly, the quasi-elastic scattering of cold neutrons is able to be used for examining the rocking motion of atoms and molecules in a coagulated body because the energy of a cold neutron is appropriately decelerated to 0.005 keV or less and the rate of change of momentum of neutrons in the scattering is large. The quasi-elastic scattering of cold neutrons is used for elucidating the dynamic properties of microstructures on the atomic level of substances, including liquid and some solids, with a large atomic diffusion coefficient, substances with fluctuating atoms and molecules such as amorphous substances, alloys and polymers, and magnetic materials with randomly mixed two types or more magnetic moments.

11.2 Apparatus

Neutrons used as the radiation source are generally produced in an atomic reaction. Relatively inexpensive neutron-generators using an accelerator are installed these days. Neutrons produced in the moderator of a reactor are mostly thermal neutrons and a few cold neutrons. A large number of cold neutrons must, therefore, be produced using a cold moderator for measuring the quasi-elastic scanning. A cold neutron source was installed for a BEPO reactor at the Howell Atomic Energy Research Institute in 1956, for the first time in the world. Most of the spectroscopes operated for measuring the quasi-elastic scattering use, at present, the cold neutron source together with a neutron spectroscope with energy resolving-power of hundreds of meV for high accuracy determination.

The cold moderator used for generating the cold neutrons is a material with the mode of motion of energy of approximately several meV at a temperature of 20 K or under and a large number of light elements per unit volume, includes solid methane, hydrogen, propane, and heavy water. A schematic drawing of JRR-3 at the Japan Atomic Energy Research Institute is illustrated in Fig. 61[72] as an example of a reactor with the cold neutron source. The type of reactor is an enriched uranium, light water decelerated, cooling pool type, and the degree of enrichment of ^{235}U of the fuel is approximately 20%, the rated thermal output is 20 MW and the maximum thermal neutron beam is approximately 2×10^{14} $cm^{-2}s^{-1}$. The cold neutron

@Seismicisolation

generator decelerates thermal neutrons with liquid hydrogen of 20 K and the cold neutrons are introduced to the beam facilities in an experimental building through a neutron duct, as shown in Fig. 62.[72]

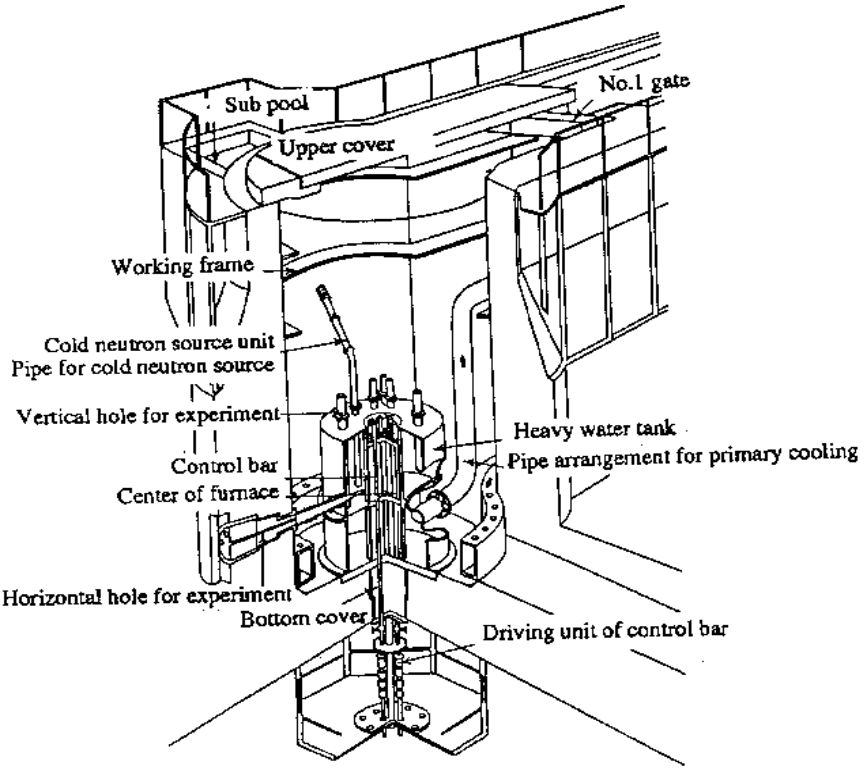


Figure 61. Schematic diagram of JRR-3. *(Kudo.)*[72]

@Seismicisolation

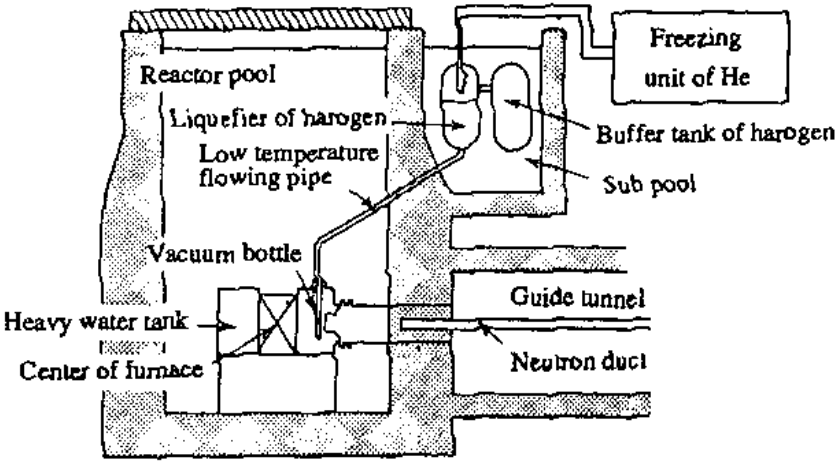


Figure 62. Diagram of cold neutron source in JRR-3. *(Kudo.)*[72]

11.3 Applications

The scattering cross section of the atomic nucleus of hydrogen to a cold neutron is approximately ten times or more as large as that of other atomic nuclei. The quasi-elastic scattering of cold neutrons is, therefore, very effective for observing the vibrating and rotating behavior of the hydrogen atom. Since the scattering cross section of atomic nucleus of heavy water is one-tenth as small as that of hydrogen, the behavior of hydrogen at a specified position can be observed by substituting heavy hydrogen for hydrogen. Accordingly, the quasi-elastic scattering of cold neutrons is used for the basic studies of liquid, including water, plastic crystal, liquid crystal, hydrogen diffusion in metal, aqueous solution of electrolyte and polymer.

The quasi-elastic scattering of neutrons is used for examining various vibrating and rotating motions of each segment in the polymer research. The vibration and rotation of each segment composing a polymer becomes active at a temperature of the glass transition point (T_g) or higher. Figure 63 illustrates a scattering spectrum of chloroprene rubber at temperatures near T_g.[76] A broad small peak which has never been observed at low temperature is observed at the foot of a peak in a spectrum at higher temperature than T_g. Maybe this is because a broad small peak caused by the quasi-elastic scattering as well as the sharp peak caused by the elastic scattering is developed by the change of the local motion of each segment controlling the motion of the whole polymer at a temperature near T_g.

@Seismicisolation

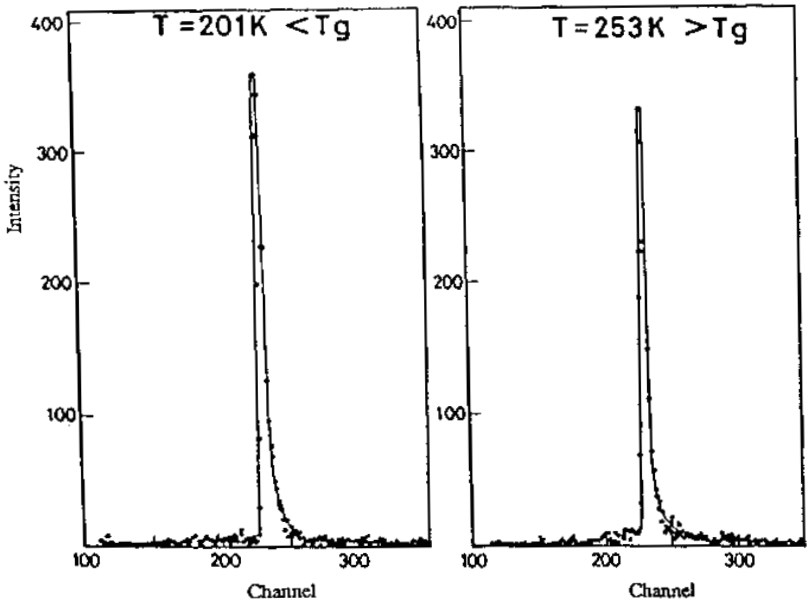


Figure 63. Change of scattering spectrum of chloroprene rubber at temperatures near T_g. *(Inoue, et al.)*[76]

The applications in the field of cement and concrete research include the determination of the change of the state of water in hardened portland cement paste with time[77] and the quantitative analysis of frozen water in hardened portland cement paste.[78]

Quasi-elastic scattering spectra of cement paste obtained by drying free water in a vacuum or by removing most of the water by igniting it have narrow energy distribution similar to that of elastic scattering, as illustrated in Fig. 64*(b)*, while a spectrum of pure water alone has broad energy distribution similar to that of quasi-elastic scattering as illustrated in Fig. 64*(c)*. A spectrum of hydrated cement shown in Fig. 64*(a)* shows a shape formed by combining the spectra for the combined water shown in Fig. 64*(b)* with that for free water shown in Fig. 64*(c)*. Accordingly, the quasi-elastic scattering spectrum for hardened cement paste can be expressed by the sun of the Lorenzian function approximating the spectrum for free water and the Gaussian function approximating the spectrum for combined water as follows:[77][79]

Eq. (27) $$S_{inc}(Q,\omega) = \frac{A}{\sigma_G\sqrt{2\pi}} e^{-\frac{1}{2}\left(\frac{\omega}{\sigma_G}\right)^2} + \frac{B}{\pi}\frac{\Gamma}{\Gamma^2+\omega^2}$$

@Seismicisolation

where A is the number of combined water molecule, B is the number of free water molecule, Γ is half-width of Lorenzian curve, σ is Gaussian standard deviation. The quasi-elastic scattering spectrum for cement paste is analyzed by finding the values of those four parameters fitted for the measurements. Since σ_G depends upon a known constant of the mechanical error independent of the sample, the parameters are easily determined in most cases. The combined water index *(I)* represented in Eq. (28) can be determined by finding the parameters.[79]

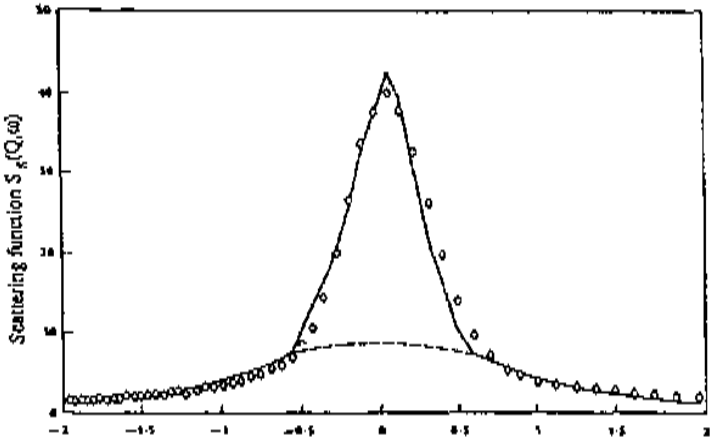
Eq. (28) $$I = A/(A + B)$$

The ratio of the combined water to water content in cement paste is measured according to the above-mentioned procedure based on the quasi-elastic scattering and the result is illustrated in Fig. 65.[77] The figure reveals that the ratio of the combined water to the water content at the ages of one day and 16 days is approximately 20 and 52%, respectively. Since the ratio is kept at approximately 75% at the age of 90 days and after, this suggests that the hydration reaction is practically terminated. The results agree with the measurements of the rate of hydration obtained by conventional methods.

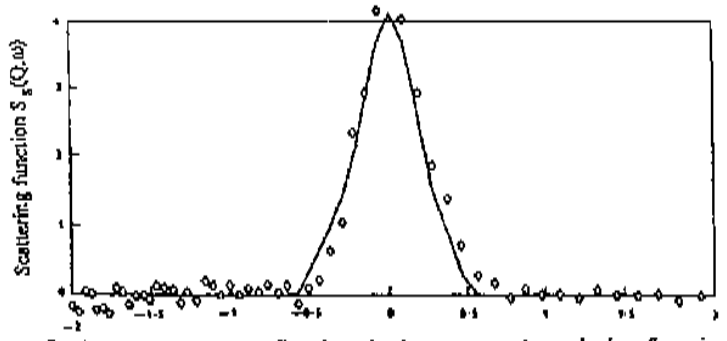
It is inferred from the analysis of the quasi-elastic scattering spectra and the investigation of the vibration and rotation behavior of hydrogen atoms that the free water, the combined water, and the hydroxyl group contained in hardened portland cement paste have translation, vibration and rotation energies, vibration and rotation energies and vibration energy, respectively.[77]

The relationship in hardened cement paste between the freezing-thawing resistance and the pore concerned is investigated by measuring the quasi-elastic scattering spectra and the following results are obtained.[94] The changes of the free water and combined water in the quasi-elastic scattering spectrum according to changing the temperature of cement paste of w/c of 0.5 are approximated by the Lorenzian function and the Gaussian function, respectively, and the results are illustrated in Fig. 66.[78] The regions above and below the Lorenzian curve represent the ratio of the combined water and that of the free water, respectively. The figure reveals that the ratio of the free water is reduced, namely, the quasi-elastic scattering is reduced with decreasing the temperature. It is inferred from this that the ratio of free water is reduced. The ratio of the region above the Lorenzian curve to the whole region corresponds to the before-mentioned combined water index (CWI) and it represents the ratio of the combined water to the water frozen by cooling in this particular case.

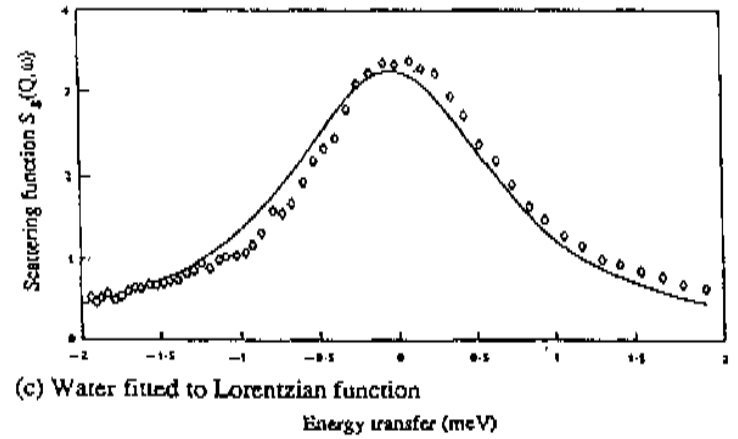
@Seismicisolation



(a) Saturated cement paste fitted to a sum of instrumental resolution and Lorentzian function



(b) Ignited cement paste fitted to the instrumental resolution function



(c) Water fitted to Lorentzian function

Energy transfer (meV)

Figure 64. Relationship between quasi-elastic scattering function and energy transfer for saturated and ignited paste and for water. *(Harris, et al.)*[79]

@Seismicisolation

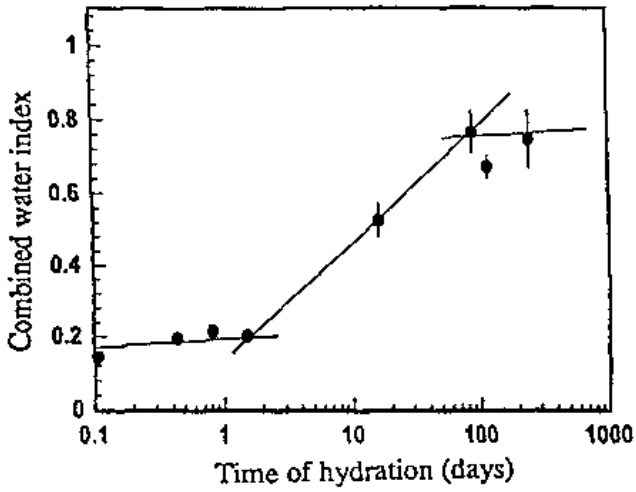


Figure 65. Progress of hydration reaction measured by quasi-elastic neutron scattering on 2.0 w/c cement paste. *(Livingston, et al.)*[77]

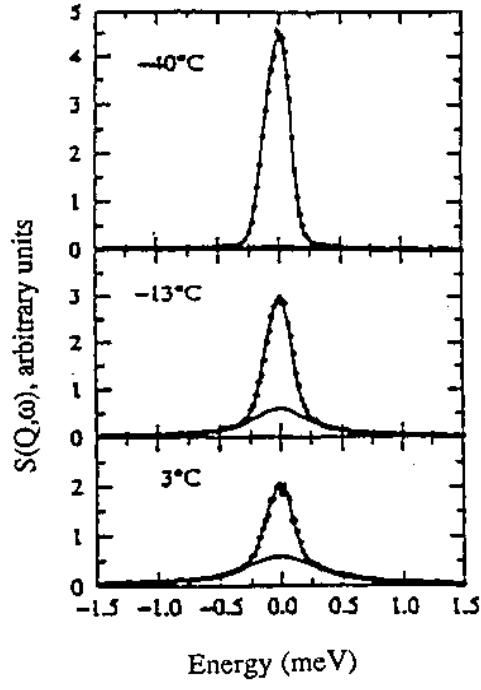


Figure 66. Quasi-elastic neutron scattering spectra for w/c = 0.5. *(Gress, et al.)*[78]

@Seismicisolation

Figure 67[78] illustrating the relationship between CWI and temperature reveals that the frozen water is increased in a temperature range from zero to -20°C and CWI is largely increased with increasing the w/c ratio in hardened cement paste. The freezing process of water is independent of the w/c ratio at a temperature of -20°C or under.

The relationship between the theoretical pore size and CWI is illustrated in Fig. 68.[78] It is concluded from the result that in hardened cement paste the ratio of frozen water is independent of the w/c ratio in the pore 15 nm in diameter or under, CWI is hardly changed in the pores 100 nm in diameter or over, and the ratio of pore 15 to 100 nm in diameter must be optimized for improving the freezing-thawing resistance.

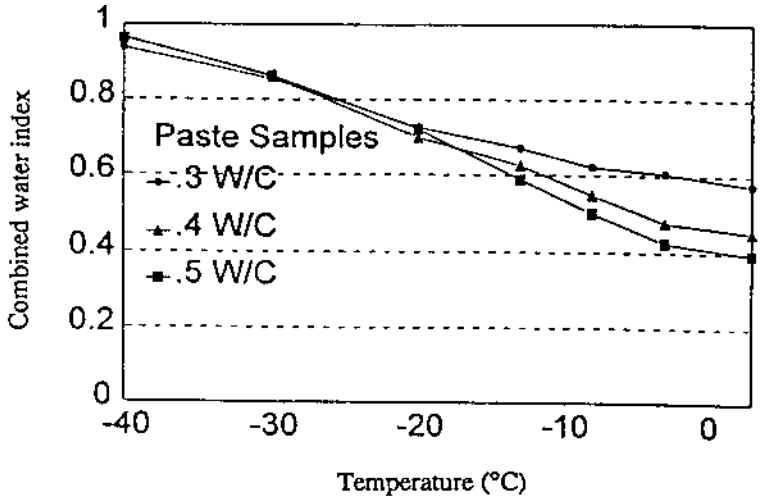


Figure 67. Combined water index versus temperature. *(Gress, et al.)*[78]

@Seismicisolation

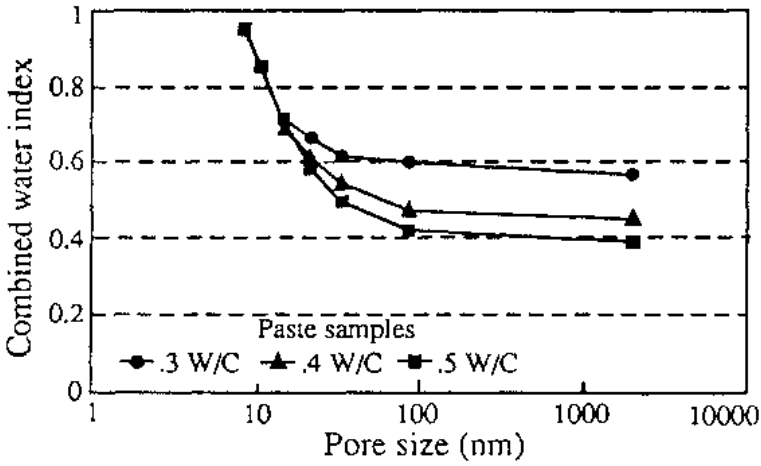


Figure 68. Combined water index versus theoretical pore size. *(Gress, et al.)*[78]

12.0 THERMOLUMINESCENCE ANALYSIS

12.1 Principle and Special Features

Irradiating crystalline substances with light or radioactive rays from the outside, the electrons in the substance are excited to various states. Although the excited electrons return to the normal state emitting light energy with the lapse of time, the electrons in certain substances are trapped by an energy level near the conduction band or valence band remaining quasi-stability unchanged even with the lapse of enough time. Gradually heating the substances at a temperature of the incandescent temperature or under at a constant rate, these quasi-stable electrons jump to the conduction band by absorbing the lattice vibration energy caused by heat, move around in the crystal as the free electrons, bond with trapped positive holes, and return to the normal state emitting light energy as illustrated in Fig. 69.[80]

@Seismicisolation

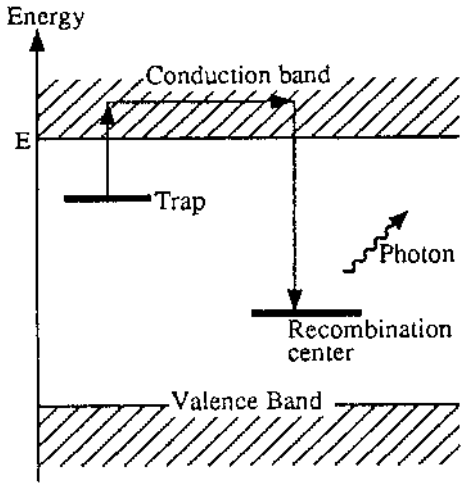


Figure 69. Energy band diagram illustrating thermo-luminescence processes. *(Chew.)*[80]

The light energy emission by heating is called thermoluminescence. When the trapped positive holes are more unstable and their energy levels are higher than the electrons, the relationship between the electrons and the positive holes is reversed. Accordingly, the positive holes act as the center of luminescence and light is emitted by bonding the trapped electrons again. The temperature at which the electrons are emitted or positive holes are formed and cause the thermoluminescence depends upon their energy levels. A curve drawn by representing the radiant light energy as a function of temperature is called a glow curve. The trapped electrons or positive holes with a single energy level develop single glow peak, while a thermoluminescent, fluorescent substance contains, generally, the trapped electron and positive holes with several energy levels, hence it generally gives a glow curve showing combined several glow peaks. Since the luminous energy is generated at a low temperature when the thermal energy barrier of electrons moving from the quasi-stable state to the luminous state is low and at high temperature when the thermal energy barrier is high, the composition and thermal and physical histories of the sample can be determined and the impurities and geological age can be identified by analyzing the temperature and intensity for generating the luminous energy.

@Seismicisolation

12.2 Apparatus

Apparatus to measure thermoluminescence is composed of a sample chamber, a temperature controller of sample, a photomultiplier, and a recording part, as illustrated in Fig. 70.[81] Light radiated from the sample with increasing temperature is detected and measured with the photomultiplier. At the same time the relationship between the intensity of radiant light and the sample temperature is recorded as a function of time by measuring the sample temperature with a thermocouple to draw a glow curve. The temperature for measurement ranges from room temperature to 500°C. The minimum amount of sample required is tens of milligrams.

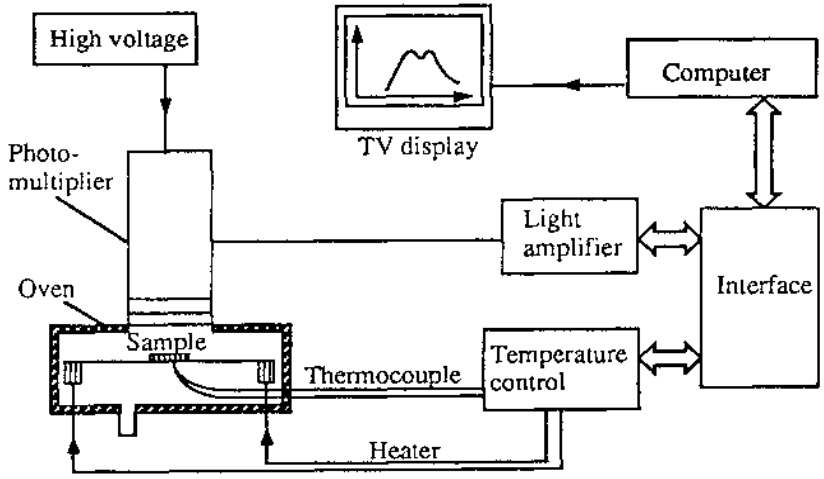


Figure 70. Schematic diagram of apparatus to measure thermo-luminescense. *(Placido.)*[81]

12.3 Applications

An example of the estimation of geological age by thermoluminescence will be described. The thermoluminescence method has recently gained attention because determination of age from twenty to thirty thousand years ago to hundreds of thousands years ago has become possible. Age can be estimated according to the following equation by determining the cumulative absorbed dose (D_N) of the natural radioactive rays to a mineral until now:

@Seismicisolation

Eq. (29) $T = D_N/D_A$

where D_A is a dose of radioactivity absorbed for a year and T is irradiation period (age). A dose of radioactivity absorbed for a year is determined by correcting the contributions of contents of ^{238}U, ^{232}Th, and ^{40}K, moisture content, and cosmic rays.

Quartz is widely used for estimating age. Quartz separated from the sample, is irradiated with several doses of γ–rays emitted from ^{60}Co and the red thermoluminescence at each dose is measured. The glow curves are illustrated in Fig. 71.[82] Although natural quartz shows a broad peak at approximately 340°C, another peak at approximately 180°C, as well as that at 340°C, are observed in a curve of that irradiated with γ-rays. The relationship between the cumulative value of thermoluminescence (TL) and the dose of γ-rays added (Gy) in a temperature region in which an artificially added dose is proportional to the amount of *TL* is illustrated in Fig. 72. The absolute value of the intersecting point of the straight line with the X-axis is the naturally cumulative absorbed dose (D_N). The geological age can be determined by Eq. (30) using thus obtained D_N.

In the field of cement and concrete research the thermoluminescence method is used for analyzing the impurities contained in cement and estimating the heat history and the remaining strength of concrete heated by a fire or other treatments.

Glow curves drawn by irradiating white portland cement with γ-rays emitted from the radiation source of ^{60}Co are illustrated in Fig. 73.[83] Figure 73 reveals that red, blue, and green lights are from monochrome thermoluminescence, especially the red, being bright. Although the red light is emitted by the radiation from Mg and Mn it is mainly caused by the radiation from Mn. The impurity of Mn causing the coloring of white portland cement can be determined using those results. This is, therefore, able to be employed as the indicator for sorting the raw materials.

A lot of thermoluminescent minerals are contained in aggregates in concrete. The thermoluminescence is, however, reduced by exposing concrete to high temperatures such as a fire. Figure 74[84] illustrates the glow curves of concrete heated for various periods of time at various temperatures. In the topmost figure, the results are represented by a series of curves. The upper curve (natural, not preheated) forms the boundary on which the other six curves (heated for different times) join at different temperatures. Generally, as the time of preheating increases, the glow intensity increases and tapers off at longer times. The trends of the changes of the intensity of thermoluminescence in the heating of concrete at 200 and

@Seismicisolation

300°C are the same as that in the heating of it at 100°C while the signal of thermoluminescence disappears by heating it at 400°C for 30 minutes. These results indicate that the change of the thermoluminescence of hardened concrete according to the changes of the heating time and heating temperature can be determined, and the exposure temperature and exposure time of concrete exposed to heat such as a fire can be estimated.

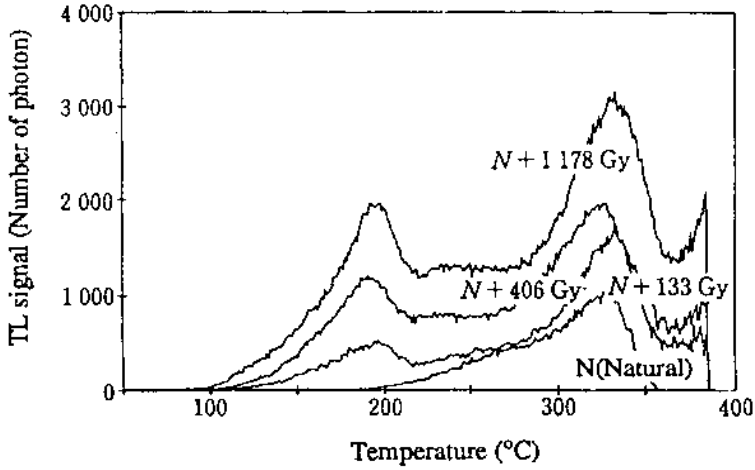


Figure 71. Change of glow curve of quartz in sample by various artifically added dose of γ-rays. *(Sakamoto, et al.)*[82]

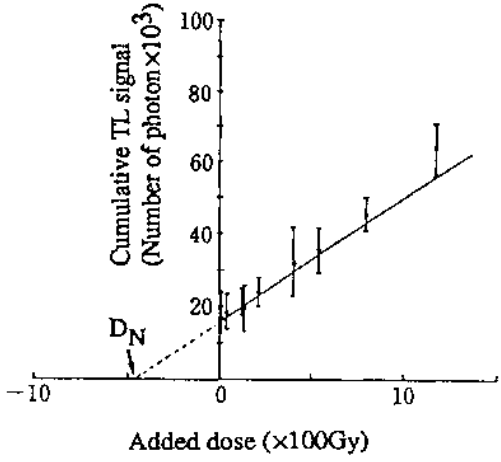


Figure 72. Relationship between cumulated thermoluminescence signal of quartz and artifically added dose of γ-rays. *(Sakamoto, et al.)*[82]

@Seismicisolation

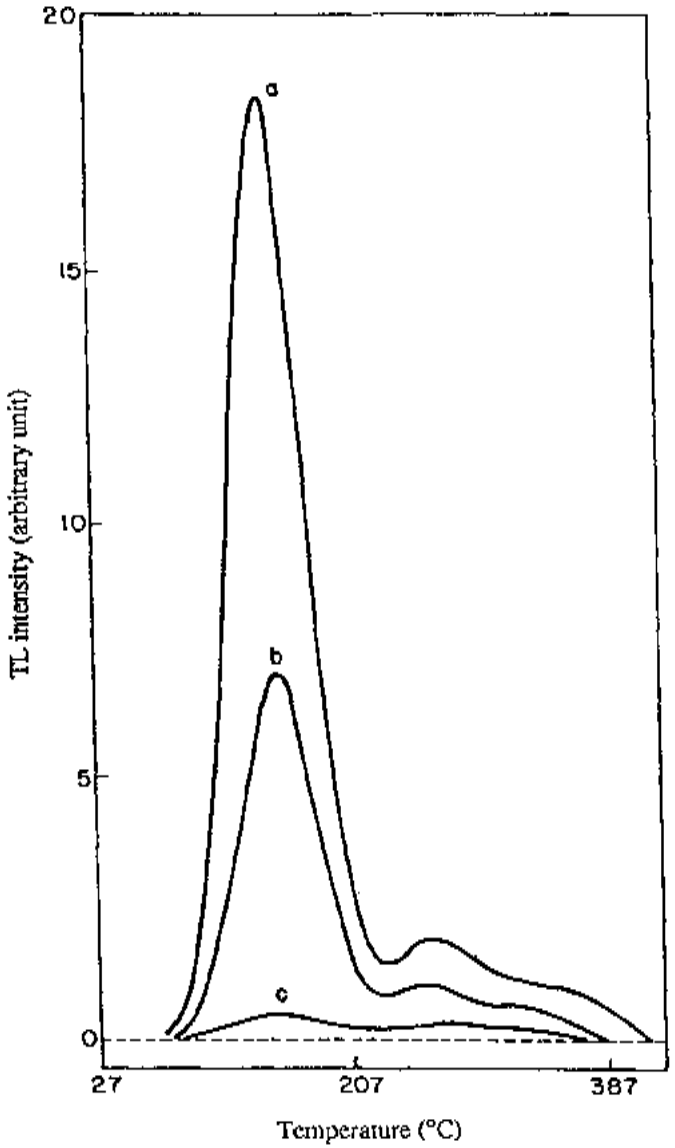


Figure 73. Monochromatic *TL* curves of white cement ($\beta = 180$°C/min). Curves *a*, *b*, and *c* correspond to *TL* recorded using red, green, and blue filters, respectively. *(Gartia.)*[83]

@Seismicisolation

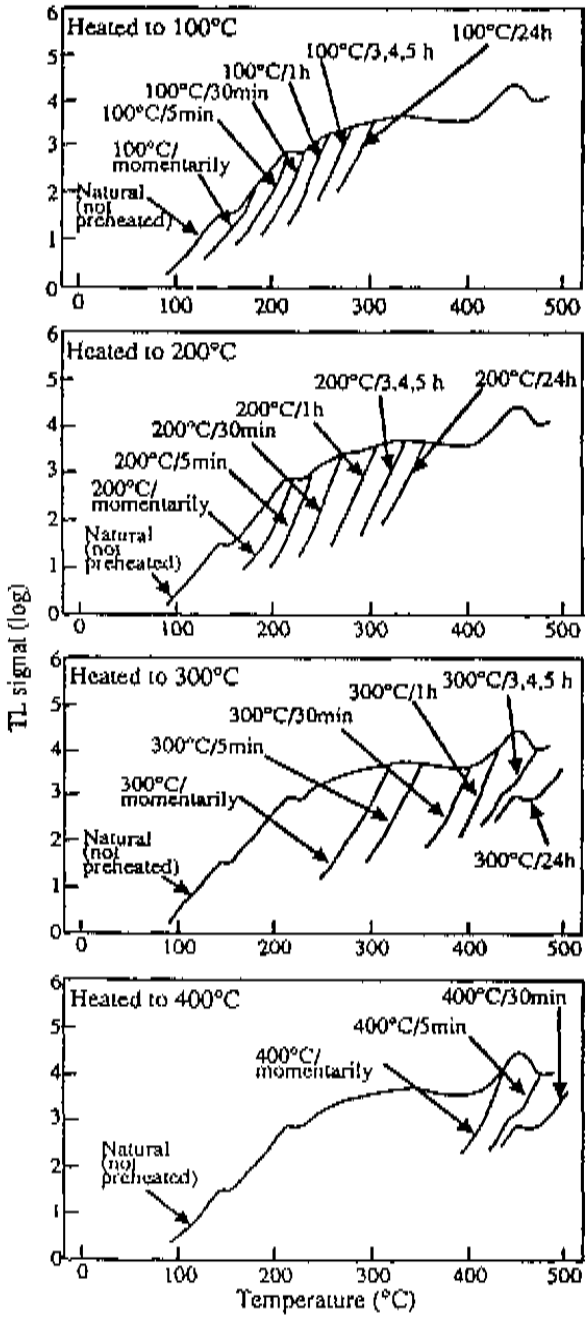


Figure 74. Glow curve of hardened cement heated for various periods of time at various temperatures. *(Chew.)*[84]

@Seismicisolation

13.0 PHOTO-ACOUSTIC SPECTROSCOPY

13.1 Principle and Special Features

The photo-acoustic effect is a phenomenon discovered by A. G. Bell in 1880. It is a phenomenon in which sound waves are generated in a vessel by intermittently irradiating a sample placed in a hermetically sealed vessel in sunlight. Viengreov used the photo-acoustic effect to measure the gas concentration in a mixed gas in 1939 and after that it has been applied to the measurement of gaseous samples. Since Robin and Rosencwaig, et al., proved in 1973 that it is remarkably effective for the spectroscopy of solid samples, photo-acoustic spectroscopy attracted the researchers' attention. The photo-acoustic spectroscopy (PAS) is a technique based on the photo-acoustic effect and it has become possible to analyze the sample as it is and solid scattering strong light, gel, and sol samples, powder and biological samples by the development of high-sensitivity microphone, light source of stable, high luminance xenon lamp and laser, and the renovation of instrumentation technology.

Although electrons composing a substance are temporarily excited by light energy absorbed in the substance irradiated with light, electrons return to the normal state emitting the energy after a while. In this process, most of emitted energy is converted to thermal energy through nonradio-active transition without radiating light though a part of it contributes to the emission of light and photochemical reactions. PAS can provide information concerning the optical and thermal properties of a substance by measuring the temperature change caused by the heat as the sound waves generated from solid, liquid, and gas coming into contact with the sample.

For instance, irradiating the sample with monochrome modulated light in a gas-enclosed vessel, the light is converted to thermal energy which raises the temperature and pressure of the ambient gas. Intermittently irradiating the sample with light at a constant frequency, the amount of heat generated from it is periodically changed, thereby changing the gas pressure according to the irradiation frequency of light, or the modulated frequency, to cause waves of condensation and rarefaction. A light absorption spectrum of a solid can be obtained from the relationship between the sound wave output and the wavelength by detecting the waves of condensation and rarefaction as sound waves with a high-sensitivity microphone.

@Seismicisolation

The temperature distribution in the sample caused by irradiating the optically uniform plate sample with light depends upon the linear absorption coefficient [β (cm^{-1})] of light of the sample.

Assuming that the depth of penetration of light is μ_β (cm^{-1}) = $1/\beta$ (cm), μ_β of a transparent sample being much larger than the thickness (l) of the sample the heat is diffused to every part of the sample. The relationship of the thermal diffusivity [α_s(cm^2)] of the sample with thermal conductivity [K_s(cal/s·cm·℃)], density [ρ_s (g/cm^3)], and the specific heat [C_s(cal/g°C)] of the sample leads to the following equation:

Eq. (30) $$\alpha_s = K_s/\rho_s C_s$$

The relationship between the thermal diffusion length (the distance from the surface of sample to the heat-generative region contributing to the thermal diffusion to the ambient gas) [μ_s(cm)] and the modulated frequency *(f)*, is expressed by the following equation:

Eq. (31) $$\mu_s = (\alpha_s/\pi f)^{1/2}$$

The magnitude of the pressure change measured by microphone depends upon μ_s. When the depth of penetration of light(μ_β) is smaller than the thickness of the thermally active layer in the sample, namely, $\mu_s > \mu_\beta$, as shown in Fig. 75,[85][86] the photo-acoustic signal is unproportional to β, saturating the signal. The photo-acoustic signal is proportional to β in the optical transparent sample ($1 < \mu_\beta$) and the sample with such a property as $\mu_s < \mu_\beta$. It is theoretically proved that the photo-acoustic signal is proportional to $f^{-3/2}$ in the sample showing $\mu_s < \mu_\beta$, while that is proportional to f^{-1} in the sample showing $\mu_s > \mu_\beta$. Also, μ_s can be reduced to be $\mu_s < \mu_\beta$ by changing the modulated frequency because μ_s is a function of $f^{-1/2}$, as shown in Eq. (31). This operation is called the photo-acoustic transparentization of a photo-acoustic opaque sample. Since the photo-acoustic signal can be proportionated to the linear absorption coefficient, (β), by the transparentization of a photo-acoustic opaque sample, it is applicable to the identification and analysis of a substance. It is necessary to correct the measurements for an optically uneven powdered sample.

@Seismicisolation

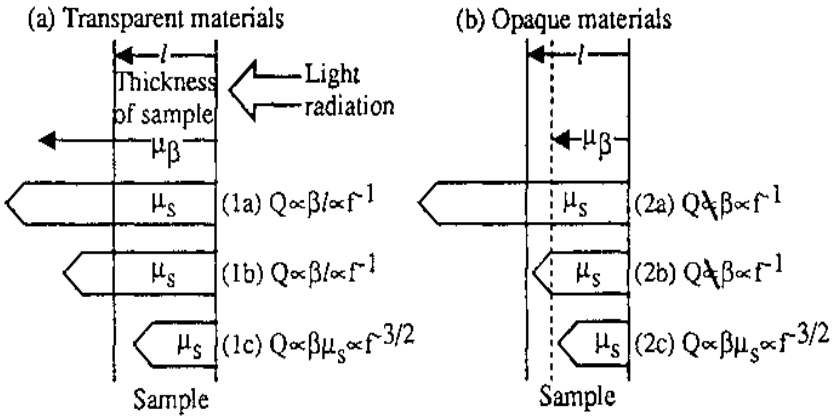


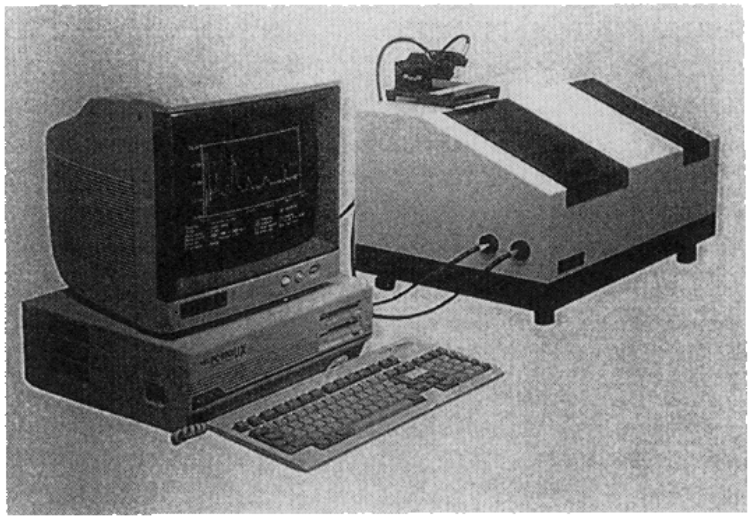
Figure 75. The relationship between PAS signal, *(Q)*, and thickness of sample, *(l)*, optical character, *(β)*, and thermal character, *(μ_s)*. *(Rosencwaig, et al. and Sawada.)*[85][86]

Since PAS measures the heat generated from the absorption of light by the sample as sound waves, it is applicable even to a low-light absorptivity substance by increasing the intensity of the light source. It is also effective for spectroscopy of a strong light-scattering substance, including powder, amorphous solid, gel, and colloid, because PAS is hardly affected by transmitted and scattered lights. PAS has the advantage in that even a sample which is hardly measured by conventional methods can be analyzed nondestructively regardless of the shape and state of the sample using the amount of as little as milligrams without pretreatment. It has a shortcoming in that the background by coexisting substances is increased because a photo-acoustic signal is emitted from almost all the substances.

13.2 Apparatus

The photograph and block diagram of a photo-acoustic spectrometer are illustrated in Fig. 76. It mainly comprises a light source, a chopper, a photo-acoustic cell, a sound sensor, an amplifier, and signal-processing system. Light or laser emitted from the high-luminance light source (300 W ~ 1 kW-xenon lamp) is modulated with the chopper (rotating chopper) and introduced to the hermetically sealed sample chamber in which the microphone is provided. The sample is irradiated with the intermittent modulated

@Seismicisolation



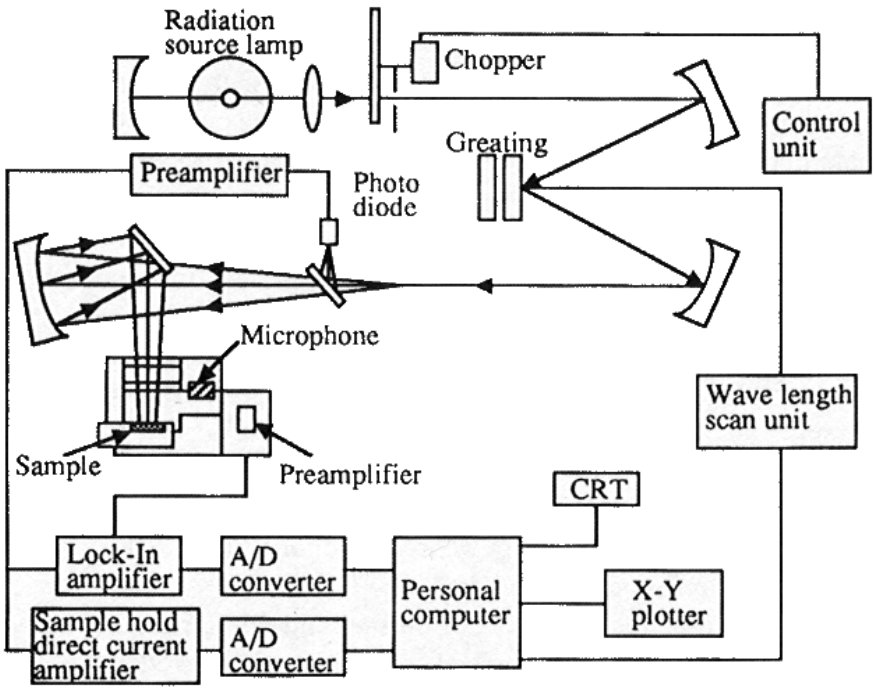


Figure 76. Photograph and block diagram of photo-acoustic spectrometer. (PASTEC, Model PAS 580.)

@Seismicisolation

light coming in the sample chamber through the incident window. The photo-acoustic signal detected with the microphone is amplified with the locked-in amplifier and the data are processed with a computer. An electron and ion beam as well as ordinary lights are used as the light source, and a piezoelectric element and a probe laser beam instead of microphone are also used as the detector to measure the elastic waves propagated through solid and liquid and apply to noncontact measurement.

13.3 Applications

Since the thickness of the sample is related to the photo-acoustic signal in PAS it is used for the measurement of the thicknesses of membrane and sample with lamellar structure, the depthwise spectroanalysis, and the thermal, acoustic, and elastic properties of a substance. PAS is widely applied to chemistry[87], biology, medical science, and environmental chemistry, as well as solid state physics.

A Fourier transform photo-acoustic spectrometer which is able to simultaneously measure all waves emitted from a light source and effectively use the light has recently begun to be used instead of the conventional dispersion type spectrometer. Since a photo-acoustic microscope has been developed to obtain the information of defects and concentration inside the samples, which are impossible to be measured with a conventional microscope, attempts have been made to apply research and quality control in the semiconductor industry and medical diagnosis.

The newly developed photo-acoustic microscope can detect defects and impurities in the sample as the change of phase and time lag of thermal and elastic waves.[88]

PAS is used for mainly measuring the surface composition of the cement minerals together with other surface analysis methods in the field of cement and concrete research. Some papers have dealt with analytical results of the surface compositions of normal and white portland cements, synthesized $Ca_3Al_2O_6$ (C_3A) and Ca_2AlFeO_5, CS, C_3S_2, C_2S, and C_3S minerals obtained by electron spectroscopy for chemical analysis (ESCA) and electron microscopy as well as PAS.[89]–[91]

The photo-acoustic spectra of normal and white portland cements are illustrated in Fig. 77.[89] Strong absorptions are observed in the spectra at a wavelength of 2.8 to 3.2 μm corresponding to Si-OH (silica gel) in white portland cement and at a wave length of 2.3 to 3.8 μm corresponding

@Seismicisolation

to M-OH [$Ca(OH)_2$] in normal portland Cement. It is, therefore, inferred from this that the hydroxyl groups on the surface of cement are slightly different from each other, according to the type of cement.

The analytical result by EACA indicates that the surface of synthesized $Ca_3Al_2O_6$ contains less Ca and more Al than the bulk part, and that the surface of Ca_2AlFeO_5 contains more Al and less Ca than that. Meanwhile, an absorption is observed at a wave length of 0.8 to l.6 μm corresponding to Al-OH in the photo-acoustic spectra and the absorbance of $Ca_3Al_2O_6$ is ten times as much as that of Ca_2AlFeO_5 as illustrated in Fig. 78.[90] It is, therefore, confirmed that much more OH groups exist on the surface of $Ca_3Al_2O_6$ than on the surface of Ca_2AlFeO_5.

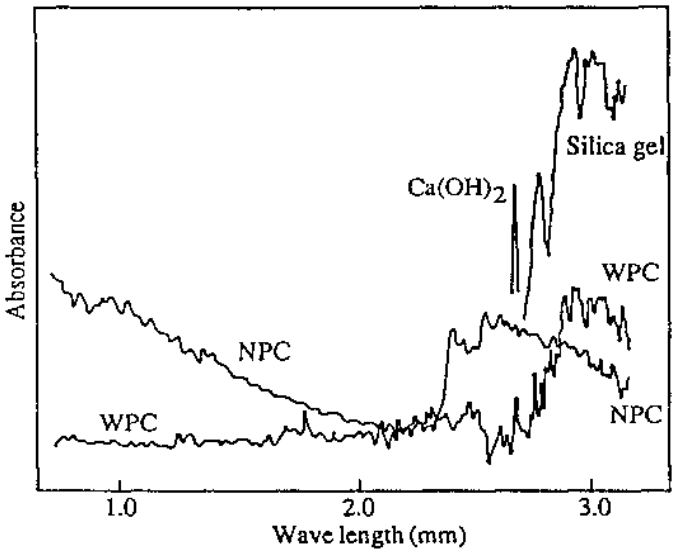


Figure 77. Photo-acoustic spectrum for commercial cements. *(Ball, et al.)*[89]

@Seismicisolation

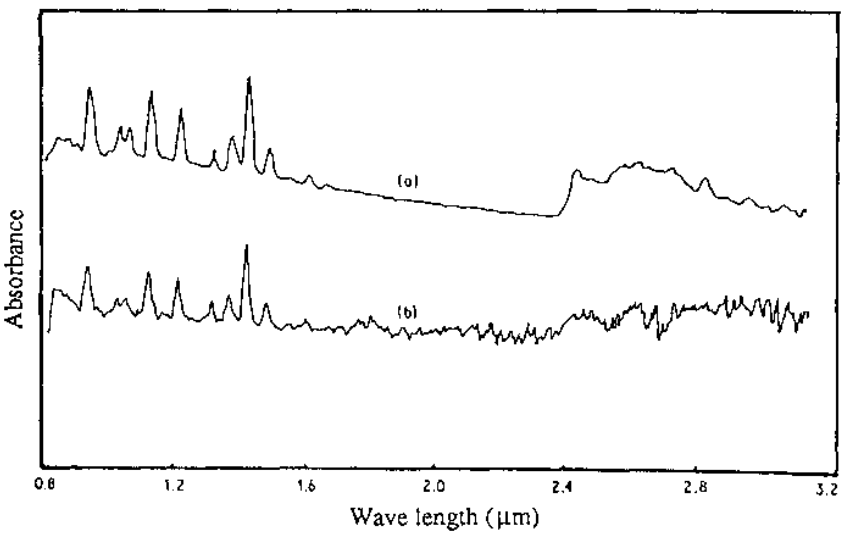


Figure 78. Photo-acoustic spectra of *(a)* C_3A (sensitivity 1 mV) and *(b)* C_4AF (sensitivity 0.1 mV). *(Ball, et al.)*[90]

The result of ESCA of the surface compositions of synthesized Cs, C_3S_2, C_2S , and C_3S, indicates that the surface compositions are different from those of bulk compositions and the anion/cation ratio in the surface compositions of C_2S is almost constant, while that of C_3S is less than l.0. Figure 79[91] reveals that a small absorption at a wavelength of 2.5 to 3.2 μm corresponding to Si-OH and M-OH is observed in C_2S, while a large absorption is observed in C_3S. This indicates that relatively stable OH groups exist on the surface of C_3S, and it may cause the reduction of the anion/cation ratio in the surface composition of C_3S.

14.0 RADIO TRACER TECHNIQUE

14.1 Principle and Special Features

The radio tracer technique is an analytical method using a radioactive isotope as the tracer and used in wide fields, including science,

@Seismicisolation

medicine, and industry. In the medical field, for instance, the state of accumulation of ^{131}I to the thyroid gland of a patient is searched by prescribing it for a patient using γ-rays from the outside of the human body, and the metabolism of glycine in the human body is studied by prescribing a ^{16}N-labeled amino acid for the patient and tracing it in the blood or urine. The radio tracer technique is conducted by measuring the radioactive energy emitted from a radioactive isotope added to the sample. The detecting sensitivity of the technique is, generally, high. The advantage of the radio tracer technique is that it is a simple system comprising the instruments, including Geiger counter, scintillation counter, proportional counter, and semiconductor detector, and a counting circuit, and it is relatively simple to determine the sample because the number of radioactive nuclides are large. Table 9 and Table 10 list the main β and γ radioactive substances.[92]

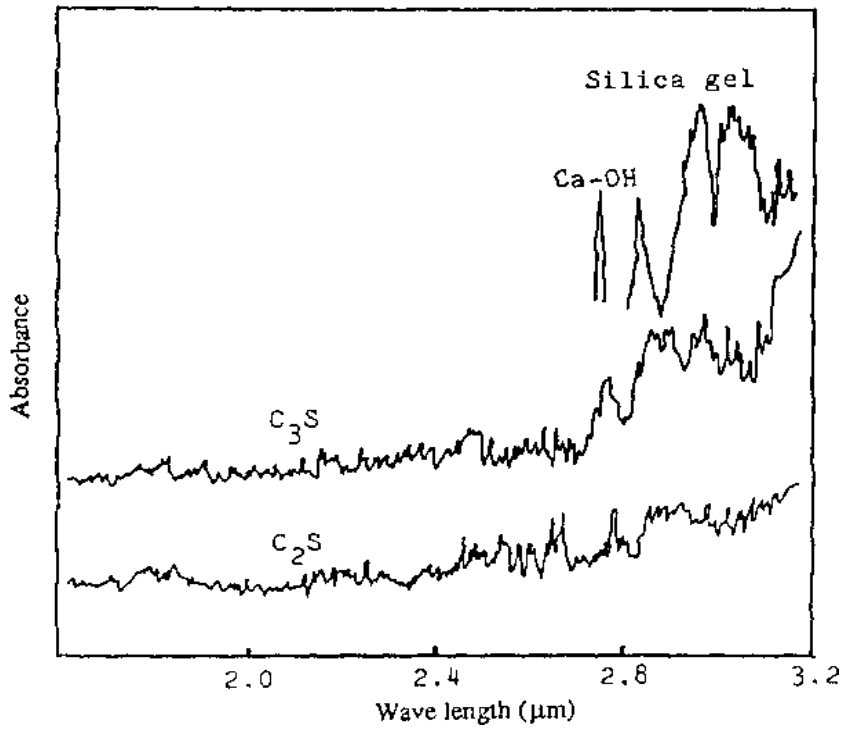


Figure 79. Photo-acoustic spectra of C_3S and C_2S. *(Ball, et al.)*[91]

@Seismicisolation

Table 9. Half Life and Energy of Major β-Ray Radiator (*Okuno, et al.*)[92]

Energy / Half life	<0.1Mev	0.1-0.3	0.3-0.5	0.5-0.7	0.7-1.0	1.0-1.5	1.5-3.0	>3.0
< 6hr				^{80}Ba ^{97}Nb ^{132}I	^{56}Mn ^{105}Ru ^{132}I	^{139}Ba	^{38}Cl ^{56}Mn ^{132}I	
6～12hr			^{152}Eu ^{212}Pb					
12～24hr	^{28}Mg ^{187}W	^{187}W ^{197m}Hg	^{69m}Hg ^{194}Ir	^{72}Ga	^{72}Ga	^{24}Na ^{28}Mg	^{24}Na ^{42}K ^{72}Ga	
1～5day	^{140}La ^{153}Sm	^{97}Ru ^{132}Te ^{153}Sm ^{199}Au	^{105}Rh ^{115}Cd ^{140}La ^{198}Au	^{76}As ^{82}Br ^{122}Sb	^{99}Mo	^{76}As ^{82}Br	^{140}La	
5～30day	^{103}Pd ^{140}Ba ^{147}Nd ^{181}Os	^{133m}Xe ^{131}Ba ^{190}Ir	^{51}Cr ^{126}I ^{131}I ^{131}Ba	^{140}Ba ^{126}I ^{147}Nd ^{190}Ir	^{48}V	^{48}V ^{86}Rb		
30d～1yr	^{127m}Te ^{170}Tm ^{182}Ta ^{185}W	^{57}Co ^{110m}Ag ^{114m}In ^{141}Ce ^{144}Ce ^{181}Hf	^{7}Ba ^{103}Ru ^{113}Sn ^{175}Hf ^{192}Ir	^{124}Sb	^{46}Sc ^{54}Mn ^{58}Co ^{95}Zr ^{95}Nb ^{110m}Ag	^{46}Sc ^{54}Mn ^{56}Fe ^{65}Zr ^{124}Sb ^{182}Ta	^{102}Rh ^{124}Sb	
1～10yr		^{134}Cs ^{155}Eu	^{125}Sb	^{125}Sb ^{134}Cs	^{134}Cs	^{22}Na ^{60}Co ^{134}Cs		
10～100yr	^{151}Sm ^{210}Pb	^{44}Ti ^{154}Eu		^{137}Cs		^{154}Eu		
> 100yr						^{26}Al ^{40}K	^{26}Al	

@Seismicisolation

Table 10. Half Life and Energy of Major γ-Ray Radiator *(Okuno, et al.)*[92]

Energy / Half life	<0.1Mev	0.1-0.3	0.3-0.5	0.5-0.7	0.7-1.0	1.0-1.5	1.5-3.0	>3.0
< 6hr				^{18}F ^{56}Mn ^{65}Ni	^{69}Zn ^{132}I ^{139}Ba	^{31}Si ^{41}K ^{56}Mn ^{65}Ni	^{56}Mn ^{65}Ni ^{132}I ^{139}Ba	^{38}Cl
6～12hr			^{212}Pb	^{212}Pb		^{135}I ^{171}Er	^{152}Eu ^{212}Bi	
12～24hr			^{28}Mg	^{64}Cu ^{72}Ga ^{187}W	^{72}Ga ^{109}Pd ^{107}Ir	^{24}Na ^{187}W	^{42}K ^{142}Pr ^{194}Ir	^{42}K ^{72}Ga
1～5day		^{105}Rh ^{132}Te ^{199}Au	^{82}Br ^{99}Mo ^{121}Sn ^{175}Yb	^{77}As ^{105}Rh ^{121}Sn ^{153}Sm	^{153}Sm ^{186}Re ^{198}Au	^{99}Mo ^{115}Cd ^{122}Sb ^{210}Bi	^{76}As ^{90}Y ^{122}Sb ^{166}Ho	
5～30day		^{33}P ^{191}Os	^{133}Xe ^{147}Nd ^{169}Er ^{177}Lu	^{48}V ^{52}Mn ^{131}I ^{140}Ba ^{147}Nd	^{86}Rb ^{126}I ^{147}Nd ^{148}Pr	^{111}Ag ^{126}I ^{140}Ba	^{32}P ^{86}Rb ^{125}Sn	
30d～1yr	^{106}Rh ^{110m}Ag	^{35}S ^{45}Ca ^{59}Fe ^{95}Nb ^{103}Ru ^{124}Sb ^{144}Ce	^{58}Co ^{59}Fe ^{95}Zr ^{110m}Ag ^{144}Ce ^{181}Hf ^{185}W	^{110m}Ag ^{124}Sb ^{141}Ce ^{174}Lu ^{182}Ta ^{192}Ir	^{102}Rh ^{170}Tm	^{56}Co ^{89}Sr ^{102}Rh	^{91}Y ^{115m}Cd ^{124}Sb	
1～10yr	^{134}Cs	^{125}Sb ^{147}Pm ^{155}Eu	^{60}Co	^{22}Na ^{113m}Cd ^{125}Sb ^{134}Cs	^{204}Tl			
10～100yr	^{3}H ^{63}Ni ^{210}Pb			^{85}Kr ^{90}Sr ^{137}Cs				
> 100yr	^{107}Pd	^{14}C ^{87}Rb		^{10}Be	^{36}Cl	^{26}Al ^{40}K		

@Seismicisolation

Radioactivation analysis as a microanalysis technique is nondestructive and with multi-element analysis is made by proceeding with a nuclear reaction by irradiating nonradioactive elements with protons and neutrons and determining the spectra of radioactive rays emitted from the newly produced radioactive elements. Since operators handle the radioactive elements it is indispensable to protect the operator from exposure to radioactive rays. It is also important for the measurement to select the measuring conditions and analyze the data by taking statistical errors in the counts into consideration.

Radioactivation analysis is widely used as an elemental analysis characterized by both radiochemical activation analysis and instrumental activation analysis. This technique is superior in the detection sensitivity and analytical accuracy to other microanalytic methods and has the advantage that the concentrations of various elements can be determined by only a simple procedure measuring γ-rays with a Ge semiconductor detector and a multichannel pulse height analyzer after the radioactivation of the elements.

Solvent extraction, ion-exchange and precipitation methods, and a method of vaporizing the hydrogenated sample and collecting it are used for preconcentration before activation to determine an element by separating chemical species of the element with different valences from each other and separating an inorganic compound from an organic compound.[93] Derivative activation analysis[94] is being studied to produce a measurable activated compound when a radioactive nuclide and a γ-ray emitting nuclide are produced from the target element or compound.

Since a high-resolving power germanium semiconductor detector has been developed, the instrumental neutron activated analysis (INAA) for detecting and determining many elements without chemical separation is mainly used at present as the activation analysis.[95] A correction method of counting the loss of γ-rays at a high counting rate and an elimination method of piled up pulse have been proposed for INNA. Programs for more accurately determining the peak area from the γ-ray spectrum have been developed. A program coping with special measurements, including the analysis, considering the self-absorption affecting the γ-ray measurement in a low-energy region and the spectral difference method for reducing the Compton background effect in the analysis of very short life nuclide, have been developed.

Attention has recently been paid to the prompt gamma neutron activation analysis (PGNAA) which is an analytical method using prompt gamma-rays generated within 10^{-14}s[96] after the collision of a neutron with an atom followed by the capture reaction. PGNAA is a unique method

@Seismicisolation

noticing some excited states of a radioactive isotope produced by irradiating the sample with neutron and measuring γ-rays emitted from the excited states. INAA requires a strong neutron radiation source generated in a nuclear reactor for high sensitivity analysis of trace elements. In PGNAA, however, the emitted γ-ray energy is approximately ten times as large as that generated by the disintegration of a radioactive nuclide used for INAA. No nuclear reactor is, therefore, required and a compact apparatus utilizing neutron radiation source using a small sized ^{252}Cf is used instead. PGNAA is, therefore, expected to be applied to an on-line analytical method for controlling the components in a manufacturing plant[97] though the analytical sensitivity of trace elements of PGNAA is inferior to that of INAA.

14.2 Apparatus

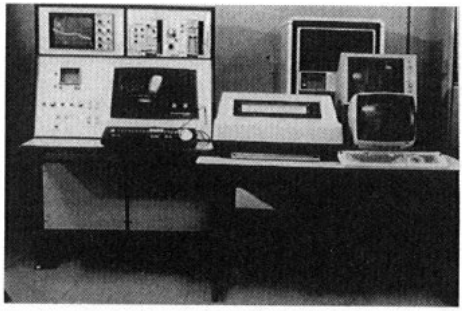
Photograph and block diagram of radioactivation analysis are illustrated in Fig. 80.[98] The radioactivated sample is automatically sent to the sample chamber with a sample changer and continuously determined. The radiation is measured with the Ge semiconductor detector built in the bottom of the equipment. Two personal computers are used for collecting and analyzing the data, respectively.

14.3 Applications

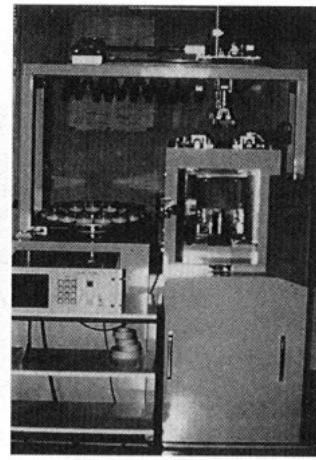
The radio tracer technique is mainly applied to check the uniformity of the mixed raw material in the field of cement and concrete. Applications including the tracing of the state of blending using ^{197}Au radioactive isotope aiming at judging the homogenizing effect in a silo when the raw material, particle diameter, blending time, volume of air blown, and amount of raw material in a silo, are changed.[99][100] Investigation of the mixing effect of the raw materials and required mixing time in a concrete mixer using experimentally manufactured ^{24}Na containing cement[101] and the determination of the diffusion coefficient and diffusion gradient of the elements in concrete using cesium, strontium, and cobalt, as the tracer[102] has also been reported.

The radioactivation analysis is put to practical use for collecting the basic data for protecting air pollution in a plant. Analyses of As, Pb, Ni, and Cr, contained in the suspended dust in the atmosphere in the vicinity of a plant by INAA together with x-ray fluorescence analysis[103]–[105] and the on-line analysis of the raw materials in a cement manufacturing plant by PGNAA have been reported.

@Seismicisolation



Data aquisition and analysis part



γ -ray detection

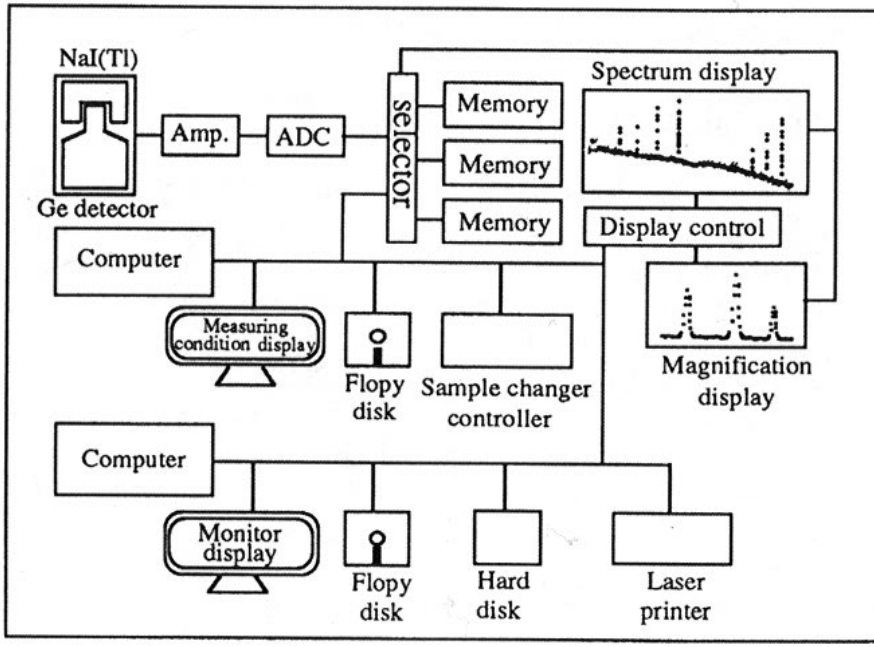


Figure 80. Photograph and block diagram of the apparatus for activation analysis. *(Suzuki, et al.)*[98]

@Seismicisolation

REFERENCES

1. Uchikawa, H., Advances in Physico-Chemical Characterization and Quality Control Techniques for Cement and Concrete,*9th Int. Congr. on the Chem. of Cement*, New Delhi, India, 1:797–883 (1992)
2. Franken, P. E. C., and Stacy, W. T., Examination of Grain Boundaries of Mn-Zn Ferrites by AES and TEM, *J. Amer. Ceram. Soc.*, 63:315–319 (1980)
3. Fujiwara, K., Ohtani, M., Kanayama, K., and Ogata, H., Application of Auger Electron Spectroscopy to Semiconductor Element, *Mitsubishi Electronics Giho* (in Japanese), 51:559–563 (1977)
4. Hayashi, Y., and Shiokawa, Y., Depthwise Analysis from Surface, in: *Advanced Analysis of Solid Surface*, p. 559, Management and Development Center (in Japanese) (1986)
5. Ivanov, B. S., Kozyrekva, N. A., and Seleva, I. I., Ozh Spektralvnyi Ainliz Mineradov Tsemontogo Klinkera (in Russian), *Zh. Prikl. Khim.*, 61(6):1295–1300 (1986)
6. Gancedo, J. R., Alonso, C., Andrade, C., and Gracia, M., AES Study of the Passive Layer Formed on Iron in Saturated $Ca(OH)_2$ Solution, *Corrosion*, 45(12):976–977 (1989)
7. Uchikawa, W., Hanehara, S., and Sawaki, D., Observation of the Change of Composition and Surface Structure of Alite and Estimation of Hydration Reactivity of Etching, *9th Int. Congr. on the Chem. of Cement*, New Delhi, India, 4:202–207 (1992)
8. Uchikawa, H., Hanehara, S., Shirasaka, T., and Sawaki, D., Effect of Admixture on Hydration of Cement, Adsorptive Behavior of Admixture and Fluidity and Setting of Fresh Cement Paste, *Cem. Conc. Res.*, 22:1115–1129 (1992)
9. Binning, G., Rohrer, H., Grassbaur, M., and Weibel, E., Vacuum Tunneling, *Physica*, 109 & 110B:2075–2077 (1982)
10. Israelachvili, J. N.,*Intermolecular and Surface Forces*, p. 135, Academic Press, London (1985)
11. Adams, G. E., and Israelachvili, J. N., Measurement of Forces between Two Mica Surfaces in Aqueous Potassium Nitrate Solutions,*Modif. Soil. Struct.*, pp. 27–33 (1978)
12. Pashley, R. M., and Israelachvili, J. N., Molecular Layering of Water in Thin Films between Mica Surfaces and its Relation to Hydration Forces, *J. Col. lnt. Sci.*, 101:511–523 (1984)
13. Israelachvili, J. N., and Pashley, R. M., Measurement of the Hydrophobic Interaction between Two Hydrophobic Surfaces in Aqueous Electrolyte Solutions, *J. Col. lnt. Sci.*, 98:500–514 (1984)

@Seismicisolation

14. Hadziioannou, G., Patel, S., Granick, S., and Tirrell, M., Forces between Surfaces of Block Copolymers Adsorbed on Mica, *J. Am. Chem. Soc.*, 108:2869–2876 (1986)

15. Uchikawa, H., Hydration of Cement and Structure Formation and Properties of Cement Paste in the Presence of Organic Admixture, Conference in Tribute to Micheline Moranville Regourd, "Importance of Recent Microstructural Developments in Cement and Concrete," Sherbrooke, pp. 63–117, *Concrete*, Sherbrooke, Canada (1994)

16. Senden, T. J., Kekicheff, P., and Drummond, C. J., Atomic Force Microscopy: Imaging with Electrical Double Layer Interactions, *Langmuir*, 10:358–362 (1994)

17. Rutland, M. W., and Senden, T. J., Adsorption of the Poly (Oxyacetylene) Nonionic Surfactant C12E15 to Silica: A Study Using Atomic Force Microscopy, *Langmuir*, 9:412–418 (1993)

18. Ishino, T., Hieda, H., Tanaka, K., and Gemma, N., Measurements of Electrostatic Double-Layer Forces Due to Charged Functional Groups on Langmuir-Blodgett Films with an Atomic Force Microscope, *Jpn. J. Appl. Phys*, 33:4718–4722 (1994)

19. Thomas, R. C., Houston, J. E., Crooks, R. M., Kim, T., and Michalske, T. A., Probing Adhesion Forces at the Molecular Scale, *J. Am. Chem. Soc.*, 117:3830–3834 (1995)

20. Uchikawa, H., Hanehara, S., and Sawaki, D., The Role of Steric Repulsive Force in the Dispersion of Cement Particles in Fresh Paste Prepared with Organic Admixture, *Cem. Conc. Res.*, Under Print.

21. Lipsky, S. R., and Duffy, M. L., High Temperature Gas Chromatography: The Development of New Aluminum Clad Flexible Fused Silica Glass Capillary Columns Coated with Thermostable Nonpolar Phases: Part I, *J. High, Resolution Chromatography and Chromatography Communications*, 9:376–382 (1986)

22. Takigawa, Y., Hanai, T., and Hubert, J., Microwave-Induced Plasma Emission Spectrophotometer Combined with Photodiode Array Monitor for Capillary Column Gas Chromatography, *J. High. Resolution Chromatography and Chromatography Communications*, 9:698–702 (1986)

23. Olson, E. S., and Diehl, J. W., Serially Interfaced Gas Chromatography/Fourier Transform Infrared Spectrometer/lon Trap Mass Spectrometer System, *Anal. Chem.*, 59: 443–448 (1987)

24. Davies, I. L., Markides, K. E., Lee, M. L., Raynor, M. W., and Bartle, K. D., Applications of Coupled LC-GC-A Review, *J. High Resolution Chromatography*, 12:193–207 (1989)

25. Durekovic, A., and Popovic, K., The Influence of Silicafume on the Mono/Disilicate Anion Ratio During the Hydration of CSF-Containing Cement Paste, *Cem. Conc. Res.*, 17:108–114 (1987)

@Seismicisolation

26. Inokawa, H., Kozakai, N., and Uchida, K., Quantitative Analysis of Organic Admixture in Cement and Hydrated Cement, *CAJ Proceedings of Cement and Concrete* (in Japanese), No. 43, pp. 162–167 (1989)
27. Horie, S., and Nakazawa, H., An Overview of LC/MS in Food Analysis (in Japanese), *Bunseki*, 1:62–69 (1996)
28. Uchikawa, H., Sone, T., and Sawaki, D., A Comparative Study of the Characters and Performance of Chemical Admixtures of Japanese and Canadian Origin, *World Cement*, 28(2):1–7 (1997)
29. Cunningham, J. C., Dury, B. L., and Gregory, T., Adsorption Characteristics of Sulfonates Melamine Formaldehyde Condensates by High Performance Size Exclusion Chromatography,*Cem. Conc. Res.*,19:919–926 (1989)
30. Ferrari, G., Basile, F., DalBo, A. S., and Mantoni, A., The Influence of the Molecular Weight of Beta-Naphthalene Sulfonate to Based Polymers on the Rheological Properties of Cement Mixes, *Il Cemento*, 4:445–454 (1986)
31. Sestauber, K., Stranel, O., and Sebok, T., Molecular Distribution on Lignin Sulfonate System, *Rap. Celul.*, 42:29–32 (1987)
32. Uchikawa, H., and Furuta, R., Application of High Speed Liquid Chromatography to Analysis of Organic Additives in Hardened Cement Paste (in Japanese), *J. Ceram. Soc. Japan*, 87(2):115–118 (1979)
33. Funato, M., Nakajima, Y., and Nakajima, K., Determination of β-Naphthalene Sulfonate Formaldehyde Condensates (β–NSF) Water Reducing Admixture in Hardened Cement Mortar by High Performance Liquid Chromatography (in Japanese), *Sement-Gijutsu-Nenpo*, 35:94–97 (1981)
34. Uchikawa, H., and Furuta, R., Hydration of C_3A-Pozzolane Paste Estimated by Trimethylsilylation, *Cem. Conc. Res.*, 11:65–78 (1981)
35. Uchikawa, H., Uchida, S., and Okamura, T., *Role of Fly Ash on the Hydration and Structure Formation of Ternary Components Blended Cement Composed of Blast Furnace Slag, Fly and Portland Cement*, Shanghai, 1991 Ash Utilization Conference, 2:65:1–14 (1991)
36. Dougherty, R. C., Negative Chemical Ionization Mass Spectrometry, *Anal. Chem.*, 53:625A–636A (1981)
37. Nishida, R., Fukami, H., and Ishii, S., Sex Pheromone of the German Cockroach Responsible for Male Wing-Raising 3, 11-Dimethyl-2-Nonacosanone, *Experientia*, 30:978–979 (1974)
38. Letolle, R., Gegout, P., Regourd, M. M., and Gaveau, B., Carbon-13 and Oxygen-18 Mass Spectrometry as a Potential Tool for the Study of Carbonate Phases in Concretes, *J. Am. Ceram. Soc.*, 73:3617–3625 (1990)
39. Uchikawa, H., and Hanehara, S., *Advances in the Characterization of Cement Clinker, Advances in the Production and Utilization of Cement-based Materials*, Eng. Found. Conf. at Fount Lodge, Potosi, MO (1991)

@SeismicIsolation

40. Tamura, H., Ikebe, Y., Sumiya, H., Toita, H., Iwamoto, H., Hirose, H., and Shichi, H., Development of New Field Limiting Method for SIMS, *Hitachi Scientific Instrument News,* 33(1):3073–3077 (1990)

41. Gooshi, Y., Maeda, H., and Sate, K., *Spectroscopy by Ion Excitation and its Application* (in Japanese), Gakkai-Shuppan Center, Japan (1986)

42. Ikebe, Y., Iwamoto, H., Toita, H., and Tamura, H., SIMS Analysis of Insulating Materials Using EBIC (in Japanese),*Surface Science,*10:345–351 (1989)

43. Tamura, H., Analysis of Insulating Materials by Negative Ion Microprobe, *J. Vacuum Soc. Japan,* 26:179–188 (1983)

44. Gerhard, W., and Nagele, E., The Hydration of Cement Studied by Secondary Ion Mass Spectrometry (SIMS), *Cem. Conc. Res.,* 13:849–859 (1983)

45. Lameille, J. M., Goutiere, G., Petit, J. C., and Regourd, M., Retention of Cobalt, Cesium, and Strontium in the Hydrates of C_3S, C_3A and Gypsum, *J. Am. Ceram. Soc.,* 70(8):604–614 (1987)

46. Nagele, E., and Schneider, U., Analysis of Surfactants Adsorbed on Cement Using Secondary Ion Mass Spectrometry (SIMS), *Cem. Conc. Res.,* 15:1022–1026 (1985)

47. Hoke, E., Eder, G., and Grassbaur, M., Analytical Electron Microscopy for Interface Characterization—Corrosion of Concrete,*Microchim. Acta,* 1:307–313 (1983)

48. Chihara, H., and Nakamura, N., Nuclear Quadrupole Resonance Spectroscopy Data, in Encyclopedia *of Experimental Chemistry,* 4th Ed. (in Japanese), Maruzen, Tokyo, 5:412 (1992)

49. Yamada, Y., High Precise Temperature Measurement by NQR Thermometer (in Japanese), *Instrumentation,* 25:35–38, Kogyou Gijyutusha (1982)

50. Shibuya, H., Recent Temperature Sensor and its Applications (in Japanese), *Instrumentation and Automation,* 9:106–110 (1981)

51. Asayama, Y., and Kitaoka, Y.,*Solid Physics*(in Japanese), 23:353 (1988)

52. Imai, T., Yasuoka, H., Shimizu, T., Ueda, Y., Yoshimura, K., and Koauge, K., Cu Spin Dynamics in High Tc and Related Oxides Investigation by Nuclear Spin-Lattice Relaxation,*Physica,* C162–164:169–170 (1989)

53. Klug, H. P., and Alexander, L. E., *X-Ray Diffraction Procedures for Polycrystalline and Amorphous Materials,* 2nd. Ed., p. 95, John Wiley & Sons (1974)

54. Ohnishi, T., Ohnishi, Y., and Yoshihara, K., Solid Surface Analysis I (in Japanese), *Kodansha Scientific, Ltd.,* p. 95, (1995)

55. Udagawa, Y., Introduction to EXAFS II (in Japanese),*The Rigaku-Denki Journal,* 26(1):27–34 (1995)

@Seismicisolation

56. Lee, J. F., Bajt, S., Clark, S. B., Lamble, G. M., Langton, C. A., and Oji, L., Chromium Speciation in Hazardous, Cement-Based Waved Forms, *Physica B,* 208/209:577–578 (1995)

57. Richard, N., Lequeux, N., and Boch, P., EXAFS Study of Refractory Cement Phase: $CaAl_2O_{14}H_2O$, $Ca_2Al_2O_{13}H_{16}$ and $Ca_3Al_2O_{12}H_{12}$, *J. Phys III,* 5:1849–1864 (1995)

58. Kai, Y.,*Encyclopedia of Experimental Chemistry,* 4th Ed., (in Japanese), Maruzen, Tokyo, 10:6 (1992)

59. Iida, A., Synchrotron Radiation Research in Analytical Chemistry (in Japanese), *Bunseki,* 6:392–398 (1984)

60. Iida, A., The Application of Synchrotron Radiation to Analytical Chemistry (in Japanese), *Bunseki,* 9:692–698 (1990)

61. Chikawa, J., Growth and Melting Processes of Semi-Conductor Crystals Observed by Live X-Ray Topography, *Prog. Cryst. Growth Charact. Mater.,* 26:255–265 (1993)

62. Kudo, Y., Kojima, S., Liuk, Y., Kawado, S., and Ishikawa, T., Novel Analysis System of Imaging-Plate Plane-Wave X-Ray Topography for Characterizing Lattice Distortion in Silicon, *Jpn. Appl. Phys.,* Part 2, 33:L823–L825 (1994)

63. Imura, K., Ishikawa, T., and Matui, J., Studies on Minute Strain Fields Around Microdefects in Silicon Single Crystals, *Journal of the Japanese Association of Crystal Growth,* 21:7687 (1994)

64. Iida, T., Sugita, Y., Takeno, H., and Abe, T., Observation of Microdefects in Silicon Crystals by Synchrotron Radiation Topography, *J. Appl. Phys.,* Japan, 62:818–821 (1993)

65. Rashid, S., Rarnes, P., Bensted, J., and Turrillas, X., Conversion of Calcium Aluminate Cement Hydrate Re-Examined with Synchrotron Energy-Dispersive Diffraction, *J. Mater. Sci. Lett.,* 13:1232–1234 (1994)

66. Tominaga, T., Mössbauer Spectroscopy, *Bunseki,* (in Japanese), 5:308–315 (1988)

67. Sane, H., and Katada, M., Mössbauer Spectroscopy (in Japanese), *Kagaku Sousetu,* 29:63–79 (1980)

68. Hassaan, M. Y., and Eissa, N. A., Application of Mössbauer Spectroscopy in Cement Studies, *Am. Ceram. Soc. Bull.,* 66:1747–1754 (1987)

69. Sane, H., and Kanno, M., Mössbauer Spectroscopic Studies on Crystallographic Phase Transition in $Fe(py)_2Cl_2$ and α-$Co(py)_2Cl_2$, *Chemistry Letters,* pp. 127–132 (1973)

70. Eissa, N. A., Hassaan, M. Y., Sallam, H. A., Salah, S. H., and Abo-Elenein, S. A., Mössbauer Spectroscopy in Cement Manufacture, *J. Mater. Sci. Lett.,* 3:88–93 (1984)

@Seismicisolation

71. Wittmann, F., Pobell, F., and Wiedemann, W., Study of the Hydration of Iron Contained in Clinker Products by Mössbauer Effect, *Z. Angew. Physik,* 19:281 (1965)

72. Kudo, H., Encyclopedia of Experimental Chemistry 4th Ed., (in Japanese), *Maruzen,* Tokyo, 14:1–19 (1992)

73. Inoue, K., Oniyanagi, Y., Iwasa, H., and Jinguji, K., Accelerator-Based Cold Neutron Sources, Quasi-Elastic Scattering Spectrometers and Investigation Using These Apparatuses, *Bulletin of the Faculty of Engin.*, Hokkaido University, 106:57–68 (1981)

74. Egelstaff, P. A., *An Introduction to the Liquid State,* London Academic Press, p. 236 (1967)

75. Windsor, C. G., Basic Theory of Thermal Neutron Scattering by Condensed Matter (B. T. M. Willis, Ed.), *Chemical Applications of Thermal Neutron Scattering,* London, Oxford University Press, pp. 1–30 (1973)

76. Inoue, K., Kaji, K., Oniyanagi, K, and Iwasa, H., Motion of Individual Polymeric Chains and Quasi-Elastic Scattering, *Bull. of the Faculty of Engineering,* Hokkaido University, 109:29–34 (1982)

77. Livingston, R. A., Neumann, D. A., Allen, A., and Rush, J. J., Application of Neutron Scattering Methods to Cementitious Materials, *Mat. Res. Soc. Sympo. Proc.,* 376:459–469 (1995)

78. Gress, D. L., Ei-Korchi, T., Livingston, R. A., Neumann, D. A., and Rush, J. J., Using Quasi-Elastic Neutron Scattering Techniques to Quantify Freezable Water in Portland Cement Paste, *Mat. Res. Soc. Sympo. Proc.,* 376:493–498 (1995)

79. Harris, D. H. C., Windsor, C. G., and Lawrence, C. D., Free and Bound Water in Cement Pastes, *Magazine of Concrete Research,* 26:65–72 (1974)

80. Chew, M. Y. L., Assessing Heated Concrete and Masonry with Thermoluminescence, *ACI Materials Journal,* 85:537–543 (1988)

81. Placido, F., Research Explores New Test Method for Fire Damaged Concrete, *Concrete,* 46:23–27 (1982)

82. Sakamoto, H., Nomura, K., Nakanishi, T., and Hashimoto, T., Encyclopedia of Experimental Chemistry 4th Ed. (in Japanese), *Maruzen,* Tokyo, 14:326–330 (1992)

83. Gartia, R. K., Ingotombi, S., and Dorendrajit Singh, S., Thermoluminescence of Cement, *Bull. Mater. Sci.,* 18:107–113 (1995)

84. Chew, M. Y. L., Effect of Heat Exposure Duration on the Thermoluminescence of Concrete, *ACI Material Journal,* 90:319–322 (1993)

85. Rosencwaig, A., and Gersho, A., Theory of the Photo-Acoustic Effect with Solids, *J. Appl. Phys.,* 47:64–69 (1976)

86. Sawada, T., Photo-Acoustic Spectroscopy (in Japanese), *Bunseki,* 9:598–604 (1987)

@Seismicisolation

87. Kreuzer, L. B., Kenyon, N. D., and Patel, C. K. N., Air Pollution. Sensitive Detection of Ten Pollutant Gases by Carbon Monoxide and Carbon Dioxide Lasers, *Science,* 177:347–349 (1972)

88. Nakata, T., Kembo, Y., Kitamori. T., and Sawada, T., Detection and Imaging of Subsurface Microcracks in Silicon Wafers Using Photo-Acoustic Microscope, *Jpn. J. Appl. Phys.,* 31:146–148 (1992)

89. Ball, M. C., Simmons, R. E., and Sutherland, I., Surface Composition of Anhydrous Portland Cements, *Cem. Concr. Res.,* 18:29–34 (1988)

90. Ball, M. C., Simmons, R. E., and Sutherland, I., Surface Composition of Anhydrous Tricalcium Aluminate and Calcium Aluminoferrite,*J. Mater. Sci.,* 22:1975–1979 (1987)

91. Ball, M. C., Simmons, R. E., and Sutherland, I., Surface Composition of Anhydrous Calcium Silicates, *Br. Ceram. Proc.,* 35:1–9 (1984)

92. Okuno, H., Murakami, Y., Araki, S., and Yoshikawa, H., Encyclopedia of Experimental Chemistry (in Japanese),*Maruzen,*Tokyo, 13:12 (1957)

93. Mon, W. M., Shah, N. K., and Wai, C. M., Extraction of Arsenic (III) and Arsenic (V) from Natural Waters for Neutron Activation Analysis, *Anal.Chem.,* 58:110–113 (1986)

94. Ehmann, W. D., Young, R. C., Koppenaal, D. W., Jones, W. C., and Rasad, M. N., Derivative Techniques in Activation Analysis,*J. Radional. Nucl. Chem.,* 112:71–87 (1987)

95. Hirai, S., Instrumental Neutron Activation Analysis (in Japanese),*Bunseki,* 9:636–641 (1987)

96. Yonezawa, N., and Ito, Y., Neutron-Induced Prompt Gamma Ray Analysis (in Japanese), *Radioisotopes,* 43:52–55 (1994)

97. Woodward, R. C., On Line Elemental Analysis, *World Cement,* 20:272–274 (1989)

98. Suzuki, S., Okada, Y., and Hirai, S., Trend of NAA, Automatization and Generalization of Activation Analysis (in Japanese), *Radioisotopes,* 43:49–52 (1994)

99. Baranyai, L., Radiotracer Investigation of Cement Raw Meal Homogenizers Part II, *ZKG,* 36:668–670 (1983)

100. Baranyai, L., Radiotracer Investigation of Cement Raw Meal Homogenizers Part I, *ZKG,* 35:175–177 (1982)

101. Breda, M., Contactless Following of Concrete Mix Homogenization, *CIB,* 86:1992–1997 (1986)

102. Idemitu, K., Furuya, H., Tsutsumi, S. R., Yonezawa, S., Inagaki, Y., and Sate, S., Migration of Cesium, Strontium, and Cobalt in Water-Saturated Concretes, *Sic Basis Nucl. Waste Manag.,* 14:427–432 (1991)

@Seismicisolation

103. Adejumo, J. A., Obioh, I., and Ogunsola, O. J., The Atmospheric Deposition of Major, Minor and Trace Elements Within and Around Three Cement Factories,*J. Radioanal. Nucl. Chem.*, 179:195–304 (1994)

104. Ambulkar, M. N., Chutke, K. L., and Garg, A. N., Multi-Elemental Analysis of Ambient Air Dust Particulates from a Cement Factory by Neutron Activation, *Sci. Total Environ.*, 141:93–101 (1994)

105. Weginwar, R. G., and Garg, A. N., Multi-Elemental Neutron Activation Analysis of Fugitive Dust Particulates from Cement Factories in Central India, *J. Radioanal. Nucl. Chem.*, 162:381–390 (1992)

106. Baron, J. P., and Alexander, J., On-Line Bulk Analysis of Raw Material in Cement Plant by Neutron Irradiation and Capture Gamma Ray, *9th Int. Congr. on the Chemistry of Cement*, New Delhi, India, 6:162–167 (1992)

107. Baron, J. P., Barnavon, T., and Alexandre, J., On-Line Bulk Analysis of Raw Material in a Cement Plant Using the Neutron Irradiation and Capture Gamma Ray Technique, *International Symposium on Nuclear Techniques in the Exploration and Exploitation of Energy and Mineral Resources*, Vienna, pp. 569–583 (1991)

108. Gibbons, T. E., An Operator's Experience with an On-Line Analyzer at Phoenix Cement, *Proc. Int. Cem. Semin.*, 29:39–63 (1993)

@Seismicisolation

Index

A

AAR gel 265
AASTHO T 227 231
Ab initio structure determination 288
Abram's law 41
Absorbed current 821
Absorption 662, 685, 693
  bands 185, 195
  limit 77
  tests 725
  water 75
Absorptivity tests 691
Ac impedance behavior 563
Ac impedance spectroscopy 467
AC1 211 39
Accelerated electron
  kinetic energy 877
Accelerating admixtures 32
Accelerating period 6
Accelerating voltage 803
Accelerators 17, 109
Acceleratory period 138
ACI 222.1-96 114
Acid attack 167
Acid-chloroform extraction method 119
Acid-soluble chloride 113
ACIS 554, 557
Activation energy 145, 644
  control 452
Additives
  organic 105
Admixtures 1, 32, 109, 139, 248, 644
  effects on hydration 143, 155
Adsorbate 24, 588
Adsorbed film thickness 550
Adsorbed water 660
Adsorption 548, 661, 662, 725
  energetics 368
  process 374, 375
  tests 667
  theory 464
Adsorption-desorption processes 541
AES 823
  analytical points 827
  applications 825
  hydration 826
AFM
  alite surface images 832
  tool for measuring 830
AFm phase 14, 16, 313
AFt phase 14, 15
AFt phases 313
Afwillite 637
Aggregates 37, 43, 63, 70, 108
  reactive and non-reactive 70
  shape and texture 93
  water absorption 75
Aging 30
  effect 37

@Seismicisolation

AI. *See* Artificial intelligence
Air
  bubbles 45
  entraining agents 32, 48, 109, 660
  entrainment 42
  permeability 724
  permeability index 716
  voids 659, 660
Akermanite 33
Albite
  spectrum 185
Alite 3, 132, 133, 135, 136, 192, 292, 293, 300, 306
  absorption bands 189
  analytical result 856
Alite/belite ratios 217
Alkali
  content determination 73
  expansivity 385
  in clinker 147
  leaching 75
  reactivity 86
  silica reaction gels 224
  sulfates 292
Alkali-aggregate reaction 43, 265
Alkali-carbonate 43
Alkali-carbonate reactions 323
Alkali-silica 43
Alkali-silica reaction 63, 65, 319
Alkali-silica reactive 73
Alkali-silicate 43
Alkaline solution 63
Alkalinity 51, 53, 456, 460
Alternating current impedance spectroscopy 487, 554
Alumina content 193
Aluminate 217, 292, 300
Aluminate phases 146, 295, 313
Aluminate-based cement 223
Aluminoferrite 292, 300
Aluminosilicate glasses 217
Aluminosilicates 647
Aluminum oxide 824
  source 2
American society for testing and materials 109
Aminosulfonic acid-based admixture 833
Amorphous phases 14
Amorphous silica 63
Analysis 127
  mortars, grouts and plasters 124
  quantitative 633
Analysis strategies 814
Analysis techniques 18, 64, 138
Analytical instruments 106
Analytical techniques 629
Anglometer 597
Anionic organic surface active agent 844
Annihilation
  positron 86
Anodic control corrosion system 452
Anodic reaction 446
  curves 461
  equation 459
Anorthite
  spectrum 185
Antifreezing admixtures 156
Apatite rock
  spectrum 187
Apparent diffusion coefficient 676
Applications
  SEM 247
  surface area measurements 522
  XRD 318
Apthitalite 256
Aqueous solution mixture 860
Aragonite 49, 167, 178, 266
Arc diameter 563
Area masking method 856
Areal analysis 814
Argillaceous limestone 184
Argillites 43
Artificial intelligence 765, 778, 781
  expert systems 781
Artificial intelligence systems 784
ASTM 737
ASTM 191 17
ASTM 294 38
ASTM C 918 755
ASTM C 1012 389
ASTM C 1038 388
ASTM C 1084 112, 113
ASTM C 109 429
ASTM C 114 112, 113, 115
ASTM C 115 509, 516
ASTM C 1152 114
ASTM C 1218 114

@Seismicisolation

ASTM C 125 93
ASTM C 1260-94 65, 78
ASTM C 1324 124
ASTM C 133 231
ASTM C 143 39, 436, 437
ASTM C 150 2, 3
ASTM C 151 430
ASTM C 187 39
ASTM C 192 437
ASTM C 204 509
ASTM C 215 739, 740
ASTM C 227 65, 385
ASTM C 232 40
ASTM C 266 17
ASTM C 289 65, 69, 71, 385
ASTM C 295 64
ASTM C 311 108
ASTM C 33 38
ASTM C 360 39
ASTM C 39 231
ASTM C 42-87 749
ASTM C 452 429
ASTM C 457 117
ASTM C 586 385, 435
ASTM C 595 3
ASTM C 618 108
ASTM C 666 48
ASTM C 803 748
ASTM C 856 231
ASTM C 876 52, 468
ASTM D 4525-85 711
ASTM G 109 466, 493
ASTM G 59 466
Atmospheric pressure chemical ionization method 847
Atom steric configuration 873
Atomic force microscope 829, 831
Atomic manipulation 829
Atomic nucleus 864
  effective radius 887
  nuclear spin quantum number 864
  reaction 884
  scattering cross section 900
Atomic-scale behavior 210
^{197}Au radioactive isotope
  application 924
Auger electron 821
  S/N ratio 820
Auger electron spectroscope 820, 822
Auger electron spectroscopy 820, 873, 874
  application 822
Auger electron spectrum 821
Auger process 820
Auger spectra symmetry 825
Auger spectrum 823
Australian water permeability test 696
Autoclam permeability system 716
Autoclam sorptivity test 692, 696
Autoclam water permeability test 703, 705
Autoclave expansion test 87
Autoclave expansion values 430
Autoclaved mixtures 28
Autoclaving 158
Automated knowledge-acquisition 784
Avogadro's number 543
Axis 837

B

Backscattered electrons 800, 801, 821
  coefficients 812
  images 810
  imaging 802
Balance equation 668, 669
Ball penetration test 39
Bangham effect 36
Bangham relation 408
Basal spacings 82
Basalts 74
  spectrum 185
Basic creep 30
Basic microstructure 241
Bauxite 132
Beam current 803
Belite 132, 292, 294, 300
  hydration reactivity 827
  IR bands 190
Bentonite
  spectrum 185
BET
  equation 541
  method 510, 514
  surface 552
  theory 511, 543, 666
Binary segmentation 809
Binders 392

@Seismicisolation

Binding agent 20
Bingham behavior 334
Bingham effect 382
Bingham flow 359, 362
Bingham model 339, 341, 361
Biological materials
  composition analysis 853
Biotite
  spectrum 187
Blaine method 509, 518
Blast furnace
  slag 33, 108, 252
  slag cement 3
  slag spectrum 188
Bleeding 40
Blended cements 308
  binders 392
Blended hydraulic cements 3
BML viscometer 360, 362, 363
Bode plots 488, 557
Boehmite 320
Bogue equation 306
Bogue-Lerch 415, 418
Bogue's calculation 299
Bohr's frequency condition 175
Boiling water extraction method 120
Boltzmann distribution 206
Bombardment activation method 852
Bonding oxygens 629
Bonds 36
  formation 19
Bottle hydrated C-S-H gel 143
Bottle hydrated portland cement
    paste 409
Bound water 23
Boundary truncation 814
Bragg angle 290
Bragg's law 276
Break-off test 752
Breakdown 343
  structural 342
Bridge deck corrosion 468
Brine 164
Brookfield rheometer 358
Brownstein and Tarr model 604
Brucite 266
BS12 17
BS1881 39
BSE image 813
BSE image analysis 812
BSE imaging 804
BSI 737
BTRHEOM 351, 353, 360, 363
Bubble spacings 45
Burnability 131
Burning zone 2
t-Butanol 637
Butler-Volmer equation 446, 447, 451

C

C bridging 630
C-axis 832
C-S-H 4, 19, 28, 218, 220,
    418, 456, 507, 523, 768
  decalcification 258
  lime-free 164
  nucleation 8
  phase 14, 19, 142, 221, 242
  spectra 195
  types 19
C-S-H silicate anion
  condensation degree 845
C/S ratios 144
C_2F solid solution 193
C_2F-C2Cr system 194
β-C_2S 650
C_2S 3, 8
  polymorphs 191
γ-C_2S 650
C_3A 11, 304
  spectra 191
C_3AH_6 146
C_3S 4, 5, 6, 8, 134, 306
C_3S paste
  hydration 316
C_4AF 3, 13, 14
  thermal peaks 149
C_4AF-C_2Cr system 194
C_4AMn hydration 196
C_6A_2F
  hot-pressed 612
Ca isotope 215
$Ca(OH)_2$ 5, 8, 15, 163
Ca-silicates 216, 218, 219
β-Ca_2SiO_4 647
Ca_2SiO_4 652

@Seismicisolation

Ca_3SiO_5 652
Ca_3SiO_5-Ca_3GeO_5 194
$CaA_{12}O_4$ melt samples 217
Cab-O-Sil 405
CaC_{l2} 159
$CaCO_3$ 266
$CaCO_3$ crystals 258
$CaCO_3$-$A_{l2}O_3$ 135
CaF_2
  as internal standard 318
CAH_{10}
  conversion 168
Calcareous minerals 130
Calcining zone 2
Calcite 88, 164, 168, 178, 266
  decomposition 160
  estimation of 184
Calcium bicarbonate 167
Calcium carbonate 132, 135, 148, 390
Calcium cations 380
Calcium chloride 155, 157, 462, 617
Calcium chloroaluminate 50
Calcium hydroxide 243
  content 140
  extraction 146
Calcium hydroxysilicate 195
Calcium lignosulfonate 427
Calcium monosulfate hydrate 167
Calcium nitrite 146
Calcium oxide
  determination 112
Calcium silicate 138
  hydration 138
Calcium silicate hydrate 316, 507, 523, 629, 768
  phase 19
Calcium sulfate 199
Calcium sulfohydroxy aluminate hydrate 16
Calcium-silica 36
Calorimetry 348
$CaMg(CO_3)_2$ 178
Canadian Standards 64
Cantilever 830
Cantilever deflection 837
CaO 134, 158, 430
  dead burnt 162
Capacitance
  interfacial double layer 466
Capillary 606
Capillary attraction pressure 705
Capillary column 842
Capillary condensation 548
  theory 541
Capillary depression 585, 586
Capillary GC 841
Capillary pores 606, 659, 660
  percolation 773
  radius 686
  structure 567
Capillary porosity 25
Capillary pressure 588
Capillary space 34
Capillary suction 685
  test 690
Capillary water 661
CAPO test 751
Carbo-aluminate 148
Carbon dioxide 49, 53, 160
Carbon relaxation times 649
Carbon tetrachloride saturation 24
Carbonate aggregates 70
Carbonate bands 196
Carbonate rocks 178, 435
Carbonate-like materials 571
Carbonates
  absence of 391
  various origins 854
Carbonation 53, 54, 111, 164, 199, 256, 258, 266, 400, 456, 460, 719, 721, 724
  diffusion process 461
  front 461
Carbonation of ettringite 261
Carbonic acid 266
Cathodic reaction 446, 461
  equation 459
Cement
  analysis 290
  compositions 107
Cement and concrete
  applications 882
  research 874
  standards 784
Cement and concrete research field
  applications 844, 901
  thermoluminescence method 909

@Seismicisolation

Cement carbonate compounds
origin estimation 853
Cement clinker surface
maximum repulsive forces 838
Cement hydration 313
models 768, 772
Cement particle surface
crystal structure 832
surface structure 832
Cement paste 1, 41, 314
microstructure 771
quasi-elastic scattering spectra 901
Cement paste-aggregate interface 318
Cement raw mixture
state of iron 892
Cement-based materials 767
microstructure 770
simulation modeling 773
Cementitious materials 19, 810
identifying cracks 812
study 800
Cenospheres 250
Ceramics 609
CH
leaching 462
precipitation 7
Chain length 652
Change
dimensional 368
Charge polarization resistance 466
Chemical admixture
identification 778
Chemical admixtures
recommended database formats 778
Chemical analysis 66
test method 231
Chemical attack 256
Chemical identification expert system 765
Chemical ionization method 847
Chemical resistance 387
Chemical shift 216, 217, 646
Chemical shift anisotropy 208
Chemical shrinkage 772
Chemical tests 65
Chemically combined water 660
Chemisorbed water 152
Chemisorption 510
Chert 80
Chimney method 696
Chloride analysis 113
Chloride attack 463, 464
Chloride diffusion coefficients 673, 675
Chloride interactions 391
Chloride ion diffusion 456, 681
Chloride ion diffusivity 767, 773
prediction 790
Chloride ion permeability 231
Chloride ion threshold 790
Chloride ions 51, 264, 459, 463, 464
diffusion 672
Chloride penetration 682, 721
Chloride procedures 114
Chloride sources 462
Chlorides 432, 724
Chloroaluminate 52, 263
Chloroform extraction method 119
Chloroprene rubber scattering spectrum 900
Chromatograph-mass spectrometer 858
Chromatography 639, 839
Chrysotile
spectrum 186
CIKS 787
applications 788, 792
development 787
Clam permeability test 705
Class C 250
Class F 250
Classical liquid chromatography 840
Clay minerals 82, 130
Clinker 2, 107, 130, 133, 292
analysis 290
composition 29
high magnesia 178
microstructure 308
minerals 832
quality 276
Clinkering temperature 161
^{57}Co
γ-ray 885
CO_2 164
Coarse aggregates 37, 108
Coating
for SEM analysis 240
Coaxial cylinder rheometer 360

@Seismicisolation

Cold compaction 20
Cold neutron generator 899
Cold neutron source reactor
  JRR-3 898
Cold neutrons 895
  applications 900
  cold moderator 898
  quasi-elastic scattering 898
Cold weather 156
Cole-Cole plot 488
Colloidal particles 335
Colorimetric method 632
Column chromatography 840
Communication advances 765
Compacting Factor Test 39
Compaction 612
Compacts 404, 405, 406, 409, 412, 413, 421
Complex plane plot 487
Complexation 631
Compliance 345
Composite material 41
Compositions of cements 107
Compression
  mercury 589
Compression pressure 405
Compressive strength 157, 418, 612, 746, 749
Compton background effect 923
Computer advances 765
Computer models
  constitutive 767
  logical 766
  physical 766
  simulation 766, 767, 768, 771
  statistical 767
Computer technology advances 790
Computer-based HPLC system 842
Computer-integrated knowledge system 787
Computer-integrated knowledge systems
  development 766
Computerization 843
Concrete 764
  analysis 109
  damage 322
  designing steps 790
  formulation 764
  inspection 764
  microanalysis 232
  microstructure 242
  organic characterization 844
  performance prediction 764, 765
  processing 764
  recycling 764
  repair 764
Concrete prism test 385
Concrete science and technology
  advance 764
  chemical phenomena 819
  mechanical phenomena 819
  physical phenomena 819
Concrete surface content 676
Concrete technology problems 783
Concrete testing 764
Condensation effects 543
Conduction 456
Conduction calorimeter 152, 154
Conduction calorimetry 130, 139, 156, 158
  C_3S 138
Conductivity 567, 662
Conductivity versus porosity 568
Cone
  slump 436
Confocal microscopy 97
Consistency 38
Constant head gas permeability tests 709
Constant phase element 488, 559
Constitutive relationship
  plastic behavior 339
Contact angle 515, 588, 595, 596, 597
  mercury 599
Contact time 649
Content analysis 110
Continuous phases 771
Continuous wave NMR 868
Continuum model 771
Continuum-based models
  alternative approach 771
Contraction 45, 380
Cooling cycles 164
Cooling rates 45
Cooling zone 2
Coordination number
  calculated results 875

@Seismicisolation

Copper nitrate staining 89
Coral limestone 184
Core 111
Core area 548
Core surface area 550
Core testing 749
Correction terms 550
Corrosion 444, 455, 456, 458, 468, 470, 721
  assessment 487
  cell 459
  current 449
  damage 441
  evaluation 476
  inhibiting admixtures 255
  inhibitors 109
  onset 457
  resistance 480
Corrosion of reinforcing steel 256, 263
Corrosion of steel 50, 52, 264
Corrosion polarization resistance 493
Corrosion potential 466, 481, 486, 493
Corrosion prevention 52
Corrosion process 489
Corrosion rate 452, 467, 472, 495
  determination 490
  measurement 442
Coulomb Test 681
Coulostatic method 467, 483
Counter electrodes 480
Counter-ions 563
Coupled ES-NN systems 785
Covercrete Absorption Test 697
CP 649
CPMAS 213, 214, 647, 649
Cr compound
  stabilizing mechanism 874
Cracking 43, 44, 52, 54, 163, 256, 456, 465
Cranston and Inkley curves 551
Creep 30, 31, 34, 37, 345, 397, 422, 664
  compliance 347
  measurements 426
  rate 399
  rig 424
Creep/recovery 344, 358
  behavior 346, 347
  technique 345
Cristobalite 63, 78, 79
Critical length 478, 480
Critical pore radius 614
Cross equation 340
Cross polarization 649
  with MAS 213
Crystal lattice defects 86
Crystalline phase 318
Crystallinity index 319
Crystallinity of quartz 79, 81
Crystallite size 291
Crystallites 28
Crystallized hydrosilicate 610
Crystallized material 28
CSA 23.2-14A 435
CSA A23.1-94 64, 82
CSA A23.2-14A 64, 71
CSA CAN 3-A5 17, 39
CTH method 682
Cubic phase 146
Curing
  high temperature 55, 389
Cyanide 197
Cyclic polarization 442
Cyclic voltammetry 485, 486
Cyclosilicate 185
Cylindrical pores 587

D

D-cracking 64
D-dried gel 36
D-dried hydrated cement 23
D-dried solid volume 537
D-dried state 22, 36
D-dry 5
D-dry condition 537, 597
DAIS 784
Damages 322
Damping 740
Darcy's equation 705, 709
Darcy's formula 708
Darcy's law 517, 664
Data analysis 799
Data banking 776
Data dictionary 775
Data mining 776
Data schema 775

@Seismicisolation

Database
advances 778
design and development 775
development 775
integrating models 789
integration 778
justification for investing 776
quality 777
reliability 777
system 775
Dataplot 304
Dead burnt CaO 162
Dead burnt MgO 161
Debye equation 488
Debye-Scherrer ring 284
Decalcification 462
Decoupling 213, 214
Defects 43, 86
Degeneracy 206
Degree of hydration 772
Deicing 46
Deicing agents 396
Deicing salt 263
Delamination 459
Delay
recycle 648
Delayed ettringite formation 265, 389
Deleterious constituents 247
Dendral 765
Density 20
organic solvents 570
ratio 39
slicing 809
values 22
Depassivation 51
Derivatization 645
Desorption 510, 662
Deterioration 42, 256, 429, 432, 508, 523, 741
cause 168
mechanisms 719
Deuterium 224
Devitrification peak 159
Diabase 78
Diatomic molecule 176
Dicalcium silicate 3, 4, 8, 146, 768
Differential refractometer 844
Differential scanning calorimetry 128
Differential thermal analysis 123
Diffraction analysis 279
Diffraction function map 284
Diffraction peaks 279
Diffraction traces 289
Diffractometer 276, 282
Diffractometry 286
Diffuse layer 563, 564
Diffusing species reactions 772
Diffusion 456
Diffusion cell 682
Diffusion cell method 674
test 673
Diffusion coefficient 578, 667, 668, 669, 671, 675, 676, 679
Diffusion control 453
Diffusion measurements 725
Diffusion processes
transient 668
Diffusion properties 576
Diffusion tests 667
Diffusivity 584, 613, 615
Digital image
pixel 800
Digital image analyzing 814
Digital image-based models 771
Dilation 813
effects 48
Dilatometer 588
Dilatometry 130
Dimensional change 368, 386, 389, 407
Dimethylformamide 638
DIN 1048 707
Dipolar interaction 213
Disjoining pressure 380, 399
Dissolution 380
of phases 298
Distillation 593, 595
DMF 645
Dolomite 43, 88, 89
content 181, 184
decomposition 160
spectrum 178
Dormant
period 6, 138
Double-counter 480

@Seismicisolation

Dreierketten 630
  chains 647
Dried condition 30
Drill hole absorptivity tests 691, 692, 697, 698
Drill hole tests 712
Drilled core testing 749
Drilled-in pullout tests 751
Dry cup method 671
Drying 316, 597
  creep 30
  procedures 599
  shrinkage 77, 427
  treatment 575, 598
  zone 2
Drying-induced alterations 583
DSC 149
DTA 128, 133, 144, 158, 167
DTG method 143
Dubinin-Radushkevich equation 545
Duplex film 247
Durability 29, 42, 44, 49, 50, 159, 256, 433, 613
Durability and permeability 719
Durability testing 429
Dynamic flow behavior 344
Dynamic modulus of elasticity 740
Dynamic-angle spinning 214

E

EACA
  analytical result 918
Early strength 158
Edge detection 804
  problem 814
Edge-sharing 630
EDTA 74
EDTA-TEA dissolution method 74
EDVAC 765
EDX analyzer 265
EDX system 238
EDXA 231, 237
  caution 239
Effective ionic diffusivity 615
Effective radius 578
Efflorescence 256
Einstein's relationship 679
Elastic behavior 345
Elastic modulus 372, 408
Elastic properties of concrete
  simulation 771
Elastic scattering 896
Elastic solid 346
Elasticity 20, 610, 740
  dynamic modulus 740
  modulus 418, 739
Elecrospray method 859
Electric field gradient 210
Electric field migration tests 673
Electric quadrupole moment 889
Electrical migration 679
  tests 677
Electrical resistivity 456
Electrically charged particles 877
Electrochemical method 493
Electrochemical noise monitoring 467
Electrochemical techniques 466, 470
Electrokinetic sonic amplitude method 837
Electromagnetic wave 864, 877
Electromagnetic waves 879
Electron 917
Electron energy analyzer 820
Electron ionization 847
Electron microscopy 917
Electron spectroscopy for chemical analysis 917
Electron spin resonance method 864
Electronic aperture method 856
Electronic discrete variable automatic computer 765
Electronic numerical integrator and computer 765
Electrons 880, 913
Electrospray ionization method 848
Element distribution 822
Element identification 237
Elemental concentrations 121
Ellis and Meter model 340
Emanation analysis 130
Endothermal effect 137, 149
Endothermal reaction 128
Energy-dispersive x-ray diffractometry 286
ENIAC 765
Entrained air voids
  automatic identification 813

@Seismicisolation

Entrainment 42
Epithermal neutron 895
Epoxy impregnated specimen 813
Epoxy impregnation 804
Equivalent circuit model 558, 559
Equivalent circuits 489
Erosion 813
ESCA result 919
Ethylene vinyl acetate 197
Ettringite 12, 14, 50, 149, 158, 167, 198, 261, 304, 320
  analysis 240
  delayed formation 54
  formation 153, 389
  needles 265
  phase 243
  recrystallization 17
  secondary formation 55
Evans diagram 447, 449, 454, 461, 463
EXAFS 872
Exchange current density 446
Expansion 43, 162, 380, 382, 387, 435
  mortar bar 320
  unexpected 73
  values 430
Expansive potential 386
Expert systems 785
  approach 781
  barriers to growth 784
  function 781
  interfaces 784
  most successful application 783
Extended x-ray absorption fine structures 872
Extensometers
  Tuckerman 369
Extinction 91
Extraction methods 119
Extranuclear electron 889
Eyring model 340, 341

F

F-D curve 838
F-H procedure 375
F-H theory 373
Failure of concrete 160
False set 17
Faraday's Law 467, 472
Fast atom bombardment method 848
Fe sample
  radiation source 886
Feature recognition 799
Feldman-Sereda model 36
Feldspar 74, 77, 79, 88
  spectrum 184
Feret's window 97
Ferrite phase 3, 12, 313
Ferrous hydroxide 51
Ferrous oxide 51
Fibrous morphology 240
Fick's first law 615, 662, 665, 667, 671
Fick's second law 463, 663, 668
Figg air permeability 712
Figg water permeability test 697, 698, 712
Film of hydration 247
Final set 6, 16
Fine aggregates 37
Fire damage 162, 256
First drying shrinkage 30
Fixed water 415
Fixed-pore model 534
Flash set 11, 12, 17, 40
  oil cement slurry 162
Flaws 506
Flight type mass spectrometer 851
Flint 195
  Thames Valley 72
Flip angle 647
Flocculated microstructure 342
Flocculated suspension 345, 349
Flocculation 335, 337, 352
Flocs 245
Flow behavior 333, 334, 352, 357, 361
Flow curve 344, 351, 360
Fluidity 38
Fluorescent x-ray spectrometry 873, 878
Fluorescent x-ray spectroscopy 874
Fluorspar 132
Fly ash 33, 50, 54, 105, 106, 108, 597
  content 354
  spectrum 188

@Seismicisolation

Force
direct measurement 830
Force distance curve example 837
Force measurement research 837
Forced resonance 739
Fourier transformation NMR 868
Fracture mechanism 26, 420
Fracture strength 413
Fragment 847
Frame edge effect 814
correction techniques 814
Free electrons 906
Free energy 372, 380
Free energy of quartz 78
Free induction decay 210
Free lime in clinkers 305
Free water 23, 117
Freeze-thaw 163, 256
Freezing 43
Freezing-thawing resistance 392
French Standard P18-589 72
Friedels salt 463
Frit-FAB method 859
Frost 43
damage 44
Full trace diffraction 288
Full-trace databases 289
Furnace slag 3

G

γ-Fe_2O_3 51
γ-rays 884, 923
correction method 923
resonance absorption spectrum 885
GaAs process 882
Galvanized steel 53
Garnet 16
Gas adsorption techniques 540
Gas chromatography 839, 841
Gas chromatography spectra 575
Gas chromatography-mass spectroscopy 859
Gas diffusion cells 669
Gas diffusion tests 667
Gas moving phase 840
Gas permeability 709, 721
tests 699
Gas slippage 710
Gas sorption techniques 510
Gas tightness 709
Gas-liquid chromatography 639, 840
Gas-solid chromatography 840
Gaussian function 901, 904
Ge semiconductor detector 924
Gehlenite 33, 132, 133, 199
Gel 659
particles 19
pores 34
Gel permeation chromatography 639, 840
Gel pores connectivity 773
Generated diffusing species diffusion 772
Geological investigation 64
Geometric probability techniques 816
German flow table 39
German standard DIN 1048 707
Germann water permeability test 705
GGBS 252
Gibbs adsorption equation 408
Gibbsite 168
Gillmore 17
Glass
PMMA impregnated 383
Glass content 33, 252, 318
estimation 159
Glass transition point 900
Glasses 217
Glassy phase 33
Glassy spheres 250
Glassy volcanic rocks 66
Glow curves 909
Glycolation 83
Göbel mirrors 284
GPC 642, 645
analytical results 844
Granite 77
spectrum 185
Granulated blast furnace slag 33
Graywackes 43
Griffith equation 421
Grinding aids 3
Gross shape coefficient 94
Grouts
analysis 124
Guard ring 474, 476, 491

@Seismicisolation

Guard ring principle 705
Gypsum 12, 13, 107, 149, 159, 195, 256, 304, 320
  ancient mortars 201
  spectrum 187

H

H_2O
  determination 5
Hagen-Poiseville law 613
Half-cell
    potential 52, 444, 445, 457, 467
  measurement 468, 469, 470
Half-cell reactions 448
Half-integer spin 206
Halsey equation 544
Hardness 13, 744
  testing 748
Harmonic oscillation 176
Hartmann-Hahn condition 214, 649
Hazardous waste 197, 224
HCl
  methanolic 633
He pycnometry 24
Head pressure 705
Heat evolution 155
Heat of hydration 772
Heat-drying 389
Helium comparison pycnometer 529
Helium inflow 533
Helium inflow technique 529, 536, 537
Helium pycnometry, 22
Hemimorphite 636
Herschel-Bulkley model 339, 341
Heterocoagulation 343
Heuristics form 781
Hexagonal phases 146
Hexamethyldisiloxane 636
Hg porosimetry 24
High frequency arc diameter 563
High performance liquid
    chromatography 839, 841
High pressure liquid
    chromatography 639
High temperature curing 55, 389
High-frequency arc 566
High-luminance SOR 881
High-performance concrete 248
High-performance construction materials
    and system 789
Hilsdorf method 714
Histogram compression 808
Histogram process 807
Histogram use 809
HMDSO 636, 645
Honeycombing 40
Hong and Parrott's method 713
Hong and Parrott's test 714
Hookean behavior 334
Hot water extraction method 73
Hot-pressed C_6A_2F 612
Hot-pressing 610
Hot-pressing techniques 612
HPC 248
HPCMS 789
HPLC 842
HPLC detectors 843
HPLC requirements 842
Humidity 26, 53, 397, 412, 420, 460
Humus 160
Hydrated cement paste 245, 509, 659
Hydrated silicates
  microstructure 540
Hydration 4, 342, 568, 641, 771
  C_3S and C_2S 8
  mechanism 5, 559
  Portland cement 218
  process 6, 14, 138
  products 19, 314, 319, 343, 508
  rate 13, 14, 152
  reactions 130, 652
  studies 194
  times 356
  tricalcium silicate 139
Hydraulic cements
  blended 3
Hydraulic radius 25, 29, 536, 537, 538, 548, 550
Hydrochloric acid 121
  extract 112
Hydrogarnet 16
  phases 14
Hydrogen evolution curve 449
Hydrogen evolution reaction 448, 459
Hydroglauberite 256
Hydrostatic head 706
Hydroxyl ion 52

@Seismicisolation

Hydroxyl stretch 199
Hydroxyl stretching band 185
HYMOSTRUC model 768
Hysteresis 341, 342, 343, 511
  loop 550
  secondary 384

I

Ice crystals 45
Ideal solids and liquids 346
IHCP 245
Illite 131
Illitic clay 130
Image
  random information 811
Image acquisition 799
  process 800, 806
  purpose 812
  system 800
Image analysis 521, 799, 808
  basic concept 813
  final steps 812
  single image goal 799
Image illumination parameters 805
Image intensity range 807
Image modification 807
Image modifying process
  kernel 812
Image processing 785, 799, 807, 812
  differences 807
  techniques 807
Image resolution 801
Image signal collection parameters 805
Imaging parameters 811
Imaging processing techniques 772
Imaging strategy 806
Immersion test 676
Impedance 487, 559
  behavior 563, 567
  spectra 490, 558
  spectroscopy 555
  technique 493
Impregnants 382, 383
Impurities 107, 181, 217
  paramagnetic and ferromagnetic 603
Incoherent scattering
  scattering function 897
Indentation methods 744
Individual feature identification 812
Induction period 6, 7, 138, 154
Inference system 782
Infrared spectrometer 86
Infrared spectroscopic method 184
Infrared spectroscopy 84, 119, 175
Initial set 6, 16
Initial setting time 40
Initial surface absorption test 692, 693
Initiation period 790
Ink-bottle pores 514
Inorganic silicates 636
Instrumental neutron activated
    analysis 923
Insulating materials
  analysis 856
  surface structure 832
Integer spin 206
Intelligent knowledge-based systems
  three types 781
Inter-layer space 25
Interaction volume 801
Interactions
  nuclear 211
Interactive force
  measuring example 838
Intercalation of the adsorbate 541
Interface characteristics 319
Interfacial double layer capacitance 466
Interfacial effect 466
Interfacial region 659
Interlayer characteristics 316
Interlayer model 535, 536
Interlayer space 539, 659
Interlayer water 317, 660
Internal standards 280, 282, 300, 301
Internal structure 539
Internet accessible databases 777
Interparticle forces 337, 345
Intrinsic diffusivity 615
Intrinsic strength 416
Intrinsic viscosity 335
Intrusion
  liquid 585
  porosimetry 587
Inversion recovery technique 866
Ion beam 917
Ion concentration 566
Ion diffusion 681
  coefficient 673

@Seismicisolation

Ion exchange
chromatography 840, 843
method 923
Ion microprobe mass analyzer 855
Ion penetration 679
Ion transport 674
Ionic beam 856
Ionic diffusion 662, 665
Ionic diffusion test 672, 673
Ionic diffusivity 615, 725
Ionic migration 677
tests 718
Ionization method 847
Ionized molecular ions
high internal energy 847
Ions
concentrations 564
power of detection 849
IR spectroscopy 195, 199
Iron
dissolution 449
half-cell 446
oxides 465
passivation behavior 458
pH-potential diagram 457
source 2
state analysis 892
Iron ore 107
Irreversible creep 31
Irreversible shrinkage 30
Irreversible structural breakdown 342
ISAT cap 694
ISO 737
ISO/DIS 7031 707
Isomer shift 887
Isopropanol 571, 572, 575
replacement curves 580
Isotherm
length change 375
reversible 374
Isotropic chemical shift 208
Isotropic shielding 208

J

J-coupling 212
Jaspar spectrum 184
Jennite 218, 220, 630
Jouren equation 686

K

K 373, 377
K-absorption edge 871
K-series x-rays 882
Kankar 178
Kaolin spectrum 185
Kaolinite 77, 130
Karsten's pipe test 696
KBr/Nujol mull technique 177
Kelvin equation 541, 543, 545
Kernel 811
Kiln dust 133
Kiln operation 306
Kiln system 307
Kilns 133
Kinetic energy 176, 856
Kinetic test 72
Kinetics theory 708
Kiselev equation 548
Knowledge
principle unit 787
Knowledge base 782
Knowledge-acquisition barrier 784
Knowledge-based systems 782
development and application 792
KOSH solution 298
Krieger and Dougherty relationship 335
Kyanite
spectrum 185

L

L_1-absorption edge 871
Laitance 40
Langmuir theory 510
Laplace equation 477
Larmor frequency 209, 210
Laser beam intensity 830
Laterite
spectrum 185
Lea and Nurse method 509, 518
Leaching mechanism for CH 462
Least squares fit 304
Length change 45, 163, 369, 375
isosteres 394
measurements 48, 572
theory 373
Length change-weight change 397
Light absorption spectrum 913

@Seismicisolation

Light microscopy 804
  reproducible intensities 804
Lignin sulfonic acid-based
    admixture 833
Lignite 160
Lignosulfonate 143, 162
Lignosulfonic acid-based admixture 844
Lime 152, 292, 305
  source 2
  unsoundness of 429
Limestone 89, 107
  analysis 181
  dolomite content 178
  dolomite-containing 184
  sorption 383
  Spratt 72
Line broadening 279
Line scan technique 814
Line shape simulation 649
Linear absorption coefficient 871, 914
Linear polarization 467
  measurement 442, 473
  technique 477
  theory 476
Linear traverse technique 813
LiOH 43
Liquid
  adsorbate 588
  scattering function 897
Liquid assisted vapor transfer 664
Liquid chromatogram 860
Liquid chromatogram-mass
    spectrogram 862
Liquid chromatography-mass
    spectrometry 860
Liquid chromatography-mass
    spectroscopy 859
Liquid moving phase 840
Liquid permeability tests 699
Liquids
  non-wetting 585
Literature databases 789
Lithium carbonate 135
LOK-Test 751
Lorenzian curve 897, 904
Lorenzian function 901, 904
Loss modulus 349, 350
Lost porosity 592
Low-porosity cement 612

M

Macro-cell corrosion current 466
Macro-cell corrosion monitoring 467
Macro-cell monitoring 493
Magic angle spinning 211, 212, 630
Magnesite 178
Magnesium carbonate
  decomposition 160
Magnesium oxide 161
Magnetic equilibrium 602
Magnetic field intensity 868
Magnetization 649
Magnets
  superconducting 215
Maleic acid 298
  dissolution 111
Marcasite 160
Marine atmosphere 49
Marine environment 256, 266
MAS 647, 649, 651
  cross polarization 213
  experiments 212
Mass absorption coefficient 871
Mass balance equation 578, 679
Mass chromatogram 860
Mass loss 467, 531, 534
  technique 467
Mass numbers 206
Mass spectra
  melamine-based admixture 862
  naphthalene-based organic
    admixture 862
Mass spectrometer 848
  flight type 851
  four columnar electrodes 850
  phenomenon 849
Mass spectrometry 846, 847, 853
Mass spectrum 860
  analysis 852
Mass transfer 668
Mass transport control 453
Mass transport processes 456
Material database formats 777
Material properties
  multi-scale approach 772
Material science
  computational models 767
  integral component 766

@Seismicisolation

Materials
substitute 317
Materials science 766
Matrix model 41
Matrix-assisted laser desorption ionization method 848
Maturity functions 754
Maturity index 753
Maturity meters 755
Maturity method
application 755
Maximum continuous pore radius 614
Maximum continuous pore size 29
Meal 131
Mechanical properties 41, 414
Median pore radius 614
Melamine based admixture
main components 862
Melamine sulfonic acid-based admixture 844
Melilite 33, 197, 318
Melt structure 217
Membrane envelope 343
Menisci forces 37
Mercury 516
compression 589
Mercury intrusion 595, 600
curve 615
porosimetry 509, 515, 584, 587, 589, 591
Mercury porosimetry 23, 75, 415, 586
Mercury purity 599
Mesopores 513
Mesoscale regions 221
MET solution 74
Metals databases 776
Methanol 23, 36, 571, 572, 579
Methylene blue test 89, 90, 91
$Mg(OH)_2$ 162, 266
MgO 430
contamination 162
in clinker 178
Mica
phlogopite 73
Mica schist
spectrum 187
Microanalysis technique
radioactivation analysis 923
Microcrack formation 389
Microcrystalline quartz 81
Microfocus x-ray diffractometer 284
Micrographs 18
Microhardness 13, 415, 417, 420
Microhardness-porosity data 416
Micromorphological studies 18
Micropore analysis 541, 552
Micropore volume distribution 553
Micropores 551
Microscope
optical 232
scanning electron 233
Microspheres 49
Microstructure 17, 256
characterization and modeling 770
models 768
Microtechniques 414
Migration
electrical 677, 679
Migration cell 680
Migration test 680, 682
set-up 684
Mineral admixtures 249
Mineralizers 135
Minerals 63
Mini-cylinders 415
Miniature rock prism test 435
Miniature samples 403
Miniature slump test 436
Miniature specimens 414, 418, 426, 429
Miniature techniques 404
Miniature testing 411
Minimum beam current 803
Mirabelite 256
Mixed internal standard method 300
Mixed potential theory 448, 449, 450
Mixing 343
Mixture components 522
Mode of degradation 789
Model
mathematical language 767
Modeling pore structure 770
Modelless
pore structure analysis 541
Modelless method 548, 552

@Seismicisolation

Models 34, 36
  computer-based 37
  constitutive 767
  logical 766
  matrix 41
  physical 766
  simulation 767
  statistical 767
Modulus of elasticity 418, 739
Moisture content 456, 531
Moisture diffusion 404
Moisture distribution 422
Molecular ions 846
Molecular mobility 603
Molecular motion 603
Molecular structure 175
Molecular weight 639
  calculation 844
  distribution 844, 845
Molecule rotation 866
Molecule translation 866
Molecule vibration 866
Molecules
  size and shape 383
Monoclinic forms 136
Monomer structures 637
Monomer/polymer ratio 860
Monosulfate 14, 16, 198, 243
  hydrate 16
Montmorillonite 82
Montmorillonitic clay 130, 159
Morphology 18
Mortar bar expansion 320
Mortar bar test 65, 385, 387
Mortar/concrete model 772
Mortars
  analysis 124
  ancient 201
Mössbauer atom mobility 890
Mössbauer effect 885, 890
Mössbauer spectrometry 885, 890
  application 892
  shortcomings 892
Mössbauer spectrum 887, 889, 890
  clinker 892
  example 892
  variation 892
Moving phase 860
MP method 541, 552
MS identification
  polychlorinated aromatic compounds 853
Mull techniques 177
Mullite
  spectrum 188
Multilayer adsorption theory 541
Multilayered film
  electric properties 824
Multimolecular adsorption 666
Multiphase material 41
Multiphase mixtures
  analysis 288
Multiple phases 318
Multiple quantum method 214
Muscovite
  spectrum 187

N

NaCl 48, 164
Nanometer phenomena 829
Nanometer-scale model 772
Nanometers 820
Naphthalene sulfonic acid-based admixture 833, 844
Naphthalene-based admixture
  main components 862
Nasser's K-probe 39
Natrolite 636
NDT techniques 737
Nearest neighbor coordination 217
Needle structure 261
Needlelike crystals 243
Needles
  ettringite 12
Nepheline 74
Nernst equation 445
Nernst-Plank equation 678
Nesosilicate 185
Neural networks 785
  applications 785
  description 785
Neural-net - NN 785

@Seismicisolation

Neutron 895
beam 895
classification 895
diffraction method 898
energy 895
kinetic energy 895
quasi-elastic scattering 900
radiation source 898
scattering 23, 896
scattering cross section 897
spectroscope 898
Newtonian behavior 334, 337, 338
Nitrate analyses 118
Nitrate attack 167
Nitrite analysis 118
Nitrobenzoic acids 139
Nitrogen
as adsorbate 24
Nitrogen adsorption 509, 537
Nitrogen isotherm 548
NMR 205, 600, 601, 603, 606, 645, 647, 649, 651
(2-D) 214
^{29}Si 222
experiment 210
measurement 870
molecular structure 866
quantum description 206
resolution 215
resolving power 868
sensitivity 868
solid state 630
spectrometer 215
spectroscopy 220
supplemental analytical means 870
^{29}Si NMR chemical shifts 216
^{29}Si MAS NMR 218
spectra 217
studies 219
NO
in kiln exhaust gases 306
Noise monitoring technique 496
Non-bridging oxygens 221
Non-recoil rate 890
Non-solid phase 18
Non-steady state diffusion tests 673
Non-steady state migration test 679
Non-steady water flow test 703
Nondestructive testing 737
Nontronitic clay 130
Normal bleeding 40
Novaculite 80
NQR
application 870
measuring system 869
popularity 869
research 870
Nuclear energy level 889
Nuclear hazardous waste 224
Nuclear interactions 211
Nuclear magnetic moment 890
Nuclear magnetic quantum number
resonance absorption 864
Nuclear magnetic resonance 205, 520, 600
Nuclear quadrupole 866, 867
Nuclear quadrupole moment
planar arrangement 864
uniaxial arrangement 864
Nuclear quadrupole resonance absorption
observation 866
Nucleation
C-S-H 8
Nucleus 864
Numeric databases 776, 789
Nurse-Saul maturity function 754

O

Obsidian 78
Octahedral site 892
Ohmic resistance control 453
Oil cement slurry
flash set 162
Old concrete 168
Olivine 636
One pulse experiment 647
Opal 43, 63, 160
OPC 583
Open-gel pores 606
Organic additives 105
Organic admixture
adsorptive behavior 827
characterization tool 844
interstitial phase 828
liquid chromatogram 860
Organic components 118
Organic compounds 139

@Seismicisolation

Organic solvents 569
interaction 571
Orthoclase
spectrum 184
Orthosilicate 636
Oscillation 176
Oscillatory shear 344, 348, 358
Osmotic pressure 380
Oven drying 597, 615
Overestimations 110
Overlapping peaks 649
Overlapping reflections 290
Overpotential 446
Overpressure tests 712
Oxidation 446, 449
Oxide Film Theory 464
Oxides 133
Oxygen concentration 471
Oxygen diffusion 52, 456
coefficient 670
Oxygens
bonding 629

P

P-dry condition 597
Paper chromatography 840
Paramagnetic interactions 217
Paramagnetic ions 649
Paramagnetic liquids 602
Partial least square regression 308
Particle shape classes 93
Particle size 505
distribution 415
Particle-particle boundaries 823
Partition chromatography 840
PAS 913, 915, 917
advantage 915
applications 917
photo-acoustic signal 917
shortcoming 915
Passivation 51, 458
Paste
hydrated cement 245
Paste-aggregate interface 247
Pattern fitting 303, 304
Penetration depth 708
Penetration measurement 690
Penetration mechanisms 583
Penetration profile 676
Penetration resistance 746
Penetration test 747, 748, 749
Penetrometer 39, 588, 589
Percolated phases 771
Periclase 161, 292
Permeability 29, 54, 247, 517, 613, 614, 665, 675, 681, 706, 708, 709, 724
index 715
intrinsic 699, 710, 713
Permeability and durability 719
Permeability cell 703
design 702
Permeability methods 518
Permeability
test 680, 696, 699, 705, 712
Permeability vs porosity 662
Permeating gas 709
Permeation characteristics 662
Permeation properties 659
Pessimum effect 70, 73
Petrographic analysis 231
Petrographic estimate 117
Petrographic examination 113
Petrographic techniques 124
Petrography 64, 124
PGNAA
emitted γ–ray energy 924
pH 7, 51, 53, 63, 264, 456, 459, 461
potential diagram 457
Phase analysis 305
software 288
Phenolphthalein 69
Phlogophite
spectrum 187
Phlogopite mica 73
Phospho-gypsum 159
Phosphoric acid extraction 67
Photo-acoustic effect 913
Photo-acoustic microscope 917
Photo-acoustic signal 914, 917
Photo-acoustic spectrometer 915
Fourier transform 917
Photo-acoustic spectroscopy 913

@Seismicisolation

Photo-acoustic transparentization 914
Photoelectron spectroscopy 878
Photoelectrons
  penetration depth 882
Phyllites 43
Physical deteriorations 256
Physicochemical phenomena 127
Picric acid 317
Piezoelectric element 830
Pin penetration test 747, 749
Pixel
  available densities 800
  dwell time 803
Plagioclase 88
Planck's constant 206, 866
Plaster 168, 430
  analysis 124
Plaster of Paris 405, 406
Plastic behavior 337, 338, 339, 351
Plastic shrinkage 40
Plastic viscosity 334, 354, 356, 359
Plasticity 38
Plasticizing substances 124
Plastics databases 776
Platinum alloys 829
Platinum iridium alloys 829
Plerospheres 250
Plombierite
  spectra 195
Plug flow 359, 360, 363
PMMA impregnant 382, 383
Point count technique 813
Poison 7
Poisson's ratio 376, 740
Polarization
  anodic and cathodic 480
  linear 472, 477
Polarization current density 472
Polarization curves 454
Polarization
    resistance 442, 478, 485, 491
Polarizers 96
Polishing 804
Poly-condensates 860
Polycarboxylic acid-based
    admixture 833
Polymer concrete 200
Polymer modified cement 197
Polymerization 196, 216, 641
  analysis 629
Polymorphs 136
Polysilicate 642
Ponding 675, 705
  test 677
Porcelain 133
Pore 514, 587
  diameters 24
  distribution 516
  filling mechanisms 547
  radius 614
  types 659
  volume 29
  water 48
Pore size distribution 22, 544, 584,
    589, 595, 606, 610
  measurement 75
Pore solution resistivity 563
Pore structure 25, 45, 205,
    528, 529, 536
  alterations 573, 583
  analysis 548
  capillary 567
  characterization 583
  modelless method 541
  models 534
Pore surface relaxivity 604
Pore-crack model 609
Porod's theory 519
Poroscope 698, 712
Porosimeters 587
Porosimetry 23, 584, 586, 589, 591
Porosity 25, 28, 97, 406,
    418, 506, 612, 691
  intrinsic 417
  measurement 76
  of aggregates 75
  values 23
Porosity vs porosity 662
Porous solids 378
Portland cement 2, 16, 105, 107, 583
  hydration 151, 218, 221, 768, 769
  IR spectra 188
  Mössbauer spectrum 892
  phases 3
  photo-acoustic spectra 917
  types 3

@Seismicisolation

Position-sensitive photodetector 830
Position-sensitive proportional counter 284
Positron annihilation 78, 86
Potash mine 392
Potassium content
  determination 74
Potassium feldspars 88
Potential-logarithmic current density curves 447
Potsdam sandstone 72
Pourbaix diagrams 457
Pourbaix plots 51
Powder compaction 404
Powder diffraction 276, 288
Powder diffractometry 291
Power-law equation 339
Power-law model 340
Powers-Brunauer model 34, 36
Pozzolan 3, 33, 108
Precipitation method 923
Precipitation of CH 7
Preheating zone 2
Preinduction period 6, 138
Pressure 593
  buildup 599
  change magnitude 914
  compression 405
Primary beam current 803
Primary electron beams 821
Primary electrons 234, 801
Prism test 71, 435
Probe diameter 803
Probe penetration 746, 747, 748, 749
Profile grinder 676
Prompt gamma neutron activation analysis 923
Protective film 51
Protein
  structural analysis 853
Proton relaxation times 649
Prototype CIKS 789
Pseudoplastic behavior 334, 336, 339
Pseudowollastonite 647
Pull-off test 755
Pullout test 750, 751
Pulse transmission techniques 741
Pulse velocity techniques 743
Pulse-NMR 868
Pure quadrupole resonance 866
Pycnometer
  helium comparison 529
Pycnometric measurements 20
Pyrite 159
Pyrosilicate 636

Q

Q peaks 647, 651
Q_1 tetrahedra 218
Q_1/Q_2 ratio 220, 222
Q_2 tetrahedra 218
Q_3 tetrahedra 218
QC system 307
QCI 79
Quadrupole coupling constant 211
Quadrupole electromagnet 879
Quadrupole interaction 210
Quadrupole mass spectrometer 850
Quadrupole splitting 889
Quality control 522
Quantitative information extraction 812
Quantitative methods 279
Quantitative phase analysis 289, 305, 322
Quantitative XRD 312
Quantum description
  NMR 206
Quartz 63, 66, 78, 80, 108
  crystallinity 79, 81
  free energy 78
  spectrum 184
Quasi-elastic scattering 902, 904
Quasi-stable electrons 906
Quick chemical test 385
Quinoline salt 631

R

Radiation source
  electron density 889
Radiation source elements
  non-recoil rates 890
Radiation targets 282
Radio frequency 205, 208, 215

@Seismicisolation

Radio tracer technique 924
advantage 920
analytical method 919
detecting sensitivity 920
Radio-frequency pulses 602
Radioactivation analysis 923, 924
application 924
Radius
hydraulic 537
Raman spectra 193
Randles equivalent circuit 466
Rapid chloride permeability test 680, 682
Rapid molecular tumbling 212
Rare species signal intensity 649
Raster shape 800
Raw materials 177
Raw meal 131, 522
Reaction products 313
Reactivity 92, 505
determination of 78
Rebar 264, 464, 469, 480, 493
Rebar corrosion 442, 472, 487, 491
Rebound hammer test 745
Rebound number 745
Rebound tests 744
Recoil 884
Recompaction 20
Recovery technique 345
Recovery of organic matter 119
Recycle delay 648
Recycle rate 649
Recycle time 648
Redox potential 51
Reduced mass 176
Reduction reaction 446, 449
Reference compound 637, 646
Reference intensity ratio 303
Reflections
overlapping 290
Reflocculation 343
Reinforced concrete 264
Reinforcing steel 52, 456
corrosion 455
Relative humidity 30, 48, 53, 376, 397, 412, 420, 460, 513, 604
conditions 536
Relaxation 520, 602
effects 556
techniques 601
Relaxation rate 222, 605
Relaxation time 488, 559, 603
proton 649
Relaxivity
pore surface 604
Remolding test 39
Remote data access 777, 792
Research collaboration 765
Resins 121
Resistivity values
electrical 456
Resonance tests 741
Resonant frequency 739, 740
tests 743
Retarders 6, 12, 17, 32, 109, 143, 154, 200
Retarding agents 109
Rheological behavior 38, 333
Rheological constants 360
Rheological equation 362
Rheology 334
Rheometers 353, 357, 358, 360
automated 362
coaxial cylinder 360
Rheometry 333
Rhombohedral form 136
Rhyolite
spectrum 185
Rice husk ash 33, 135
Rietveld method 289, 304, 882
Rigidity 740
Ring generating SOR 879
Rock analysis 65, 66
Rock cylinder test 385
Rock prism test 385, 386, 435
Rocks
composition and formation 64
fine grained 67
Roëntgen 275
Rose criterion 803
Rotary kilns 133
operating conditions 306
Roughness
measurement 93
Rust 52
Ryshkewitch equation 26

@Seismicisolation

S

Saddle effect 380
Salicylic acid 298
Salification 256
Saline solution 48
Salt 49
Salt crystallization 256
Salt resistance 392
Salt scaling 46, 163, 263
Salt solution 432
Salt weathering 256
Salt-related deterioration 263
Sample chamber 587
Sample container 215
Sample drying 597
Sample preparation 177, 306, 509
Sampling volume
  lateral dimensions 801
  size 801
Sand ratio 353
Sandstone
  Potsdam 72
Scaling 43
Scanning electron
    microscope 255, 800, 803
Scanning electron
    microscopy 124, 231, 772
  reproducible intensities 804
Scanning tunnel electron
    spectroscopy 829
Scanning tunnel microscope 828
Scawtite 197
Scherrer equation 279
Schiller equation 26
Schmidt rebound hammer 744, 745
Schrodinger wave equation 176
Scientific and engineering databases
  application 775
  process of developing 775
Scintillation counter 284
Seawater 266
  attack 49
Secondary electron 800
  emission efficiency 821
  image 827
Secondary ettringite formation 55, 389
Secondary ion mass spectroscopy 855
Secondary ions 856
Segregation 40, 358, 359
Self-decoupling 213
SEM 772
  coating analysis 240
  principle 234
  videoscope 804
SEM/EDXA 232, 236
  applications 241
Service life 788
Set accelerators 109, 118
Set retarders 109, 200
Set-retarding agents 118
Set-retarding chemical admixture 255
Setting 39, 153
Setting times 16
SFA 830
Shape and surface texture
  measurement 95
Shape coefficient 94
Shape factor corrections 741
Shear 334, 342
Shear modulus of elasticity 740
Shear rheometers 357
Shear thinning 334, 336
Shielding
  isotropic 208
Shorthand system 107
Shrinkage 30, 54, 75, 397, 427
  irreversible 397
  limit 77
Signal to noise ratio 878
Silica 49
  gel 553
  minerals 86
  reactive 67
  soluble 110, 112
  source 2
Silica fume 34, 42, 106,
    108, 158, 254, 354
Silicate
  hydrates 167
  inorganic 636
  octameric 646
Silicate paste
  hydrated 146
Silicate phases 216

@Seismicisolation

Silicate polymer derivatives 845
Siliceous carbonate aggregates 70
Siliceous clay 130
Siliceous limestone 184
Silicic acids 635
β-Silicomolybdic acid 634
Silicomolybdic acid complex 631
Silicon wafer
  experimental results 838
Siloxane 36
  bonds 629
  groups 26, 420
Simulation modeling
  constitutive 767
  logical 766
  physical 766
  simulation 767
  statistical 767
Sink solution 673
SiO_2 63
Size exclusion
    chromatography 639, 840
Slag 33, 50, 252
  activation 158
  cement 3
  content estimation 310
Slip 359, 360, 362, 363
Slump 333, 437
  test 39, 436
Small angle scattering
  neutron 519
  x-ray 316, 519
Smectites 82
SMF 154
Sodium content
  determination 74
Sodium cyanide 197
Sodium gluconate 436
Soft ionization method 847
Software 288
Solder wettability 824
Solid material dissolution 772
Solid phase 18
Solid volume 534, 537
  change 536
Solid-liquid interface 567
Solids
  volume fraction 334
Soluble silica 112
Solvent extraction 923
Solvent replacement 599
Solvent replacement
    technique 24, 569, 575, 576, 581
Solvents 298
Soniscope 742
Sonometer 739
SOR
  continuous spectrum 877
  directivity 882
  equipment 873
  intensity 878
  photoelectrons 882
  radiation facilities 880
SOR-EDD
  phase transition 883
Sorbates 510, 514
Sorption 406, 510
  isotherm 511
Sorptivity 688, 721, 725
  test set-up 690
  values 689
Soxhlet extraction 114
Spalling 43, 465
Specific surface area 505, 517, 608
Specimen pixel size 804
Specimen pre-conditioning 241
Specimen preparation 240
Spectra of C-S-H 220
Spectroanlaysis
  depthwise 917
Spectrophotometry 630
Spectroscopy
  IR 84, 175
Spectrum development mechanism 885
Sphericity 93
Spin 206
Spin energy levels 210
Spin system 209, 210, 214
Spin-echo signal 602
Spin-echo technique 866
Spin-echo time 602
Spin-lattice relaxation 602, 866
Spin-locking 649
Spin-spin relaxation 520
Spin-spin relaxation time 604, 606, 866
Spinel 159
Spratt siliceous limestone 72
Spurrite decomposition 133

@Seismicisolation

Sputtering method 824
Square root of time equation 461
SRXRF
  detection limit 881
Staining procedures 89
Staining techniques 88
Standardized test methods 737
Standpipe absorptivity test 692, 696
Static flow technique 338
Stationary phase 860
  high-pressure-resistant filler 840
Steady state conditions 680
Steady state diffusion tests 673
Steady state migration test 682
Steady state techniques 466
Steady state water flow tests 699
Stearate salts 118
Stearic acid 118
Steel 456, 464
Steel corrosion 50, 264, 462, 463
Steel oxidation 461
Steel rebar 468
Steel/concrete corrosion process 489
Steinart guard ring test 703, 705
Stereological techniques 817
Stern layer 563, 564
Stern-Geary equation 472, 491
Stiffening 16
Stiffness 419
Stoke's law 516
Storage modulus 349, 351
Storage modulus and yield stress 350
Storage ring 879
Strain
  instantaneous 346
  values 350
Strain rate 334, 338, 352
Strength 28, 29, 41, 42
  accelerators 109
  intrinsic 416
  prediction 307
  testing 231
Strength development 156, 415, 418, 612
  rate 388
Strength testing 748, 755
Strength vs. porosity 415
Strength-forming phase 220
Strength-porosity 608, 609
Strength-time curves 418
Stress 334
Stress conditions 26, 420
Stress pulse 742, 743
Stress wave propagation methods 744
Structural breakdown 342, 343
Structural studies 218
Structure analysis 288
Structure determination
  ab initio 288
Substance
  acoustic properties 917
  elastic properties 917
  thermal properties 917
Substitute materials 317
Suction tests 712
Sugars 143
Sulfate analysis 111, 113, 115
Sulfate attack 256, 261
  analysis 240
Sulfate determinations 117
Sulfate ions 263, 265
Sulfate procedure 115
Sulfate resistance 386, 388
Sulfates 133, 256
Sulfide procedure 115
Sulfo-aluminate
  production 132
Sulfonated melamine formaldehyde 32
  superplasticizer 154
Sulfonated naphthalene formaldehyde 32
Sulfonic acid
  di- /mono- ratio 860
Sulfur analyses 115
Sulfur impregnant 382
Sulfur impregnated porous glass 380
Sulphate minerals 320
Super cold neutron 895
Superconducting magnet 215, 879
Supercritical chromatograph 843
Supercritical fluid
    chromatography 839, 840
Superplasticizer 143, 154, 196, 354
Superplasticizing admixtures 32
Supplementary cementing materials 33
Surface absorption 693
Surface absorptivity tests 691, 692

@Seismicisolation

Surface adsorbed water 317
Surface adsorption
  energetics 368
Surface area 24, 507, 514, 521, 522, 536, 537, 546
  measurement 508, 516
  portland cement paste 523
Surface area-to-volume ratio 506
Surface creep 664
Surface force apparatus 830
Surface free energy 372
Surface imperfections 506
Surface layer
  C/S molar ratios 827
  two-dimensional information 856
Surface porosity 97
Surface projection diameter 802
Surface pull-off test 755
Surface quality 505, 507
Surface roughness 97
  measurement 93
Surface structure
  sample image 832
Surface tension
  mercury 585, 595, 599
Surface-to-volume ratio 605
Suspensions 334
  flocculated 345
Swelling 30, 34, 36
  clay mineral 82, 90
  stresses 382
Synchrotron 877
Synchrotron orbital radiation 873, 877
  dispersive 883
  measurement 881
Synchrotron radiation excited x-ray fluorescence 881
Synchrotron storage ring 880
Syngenite 17
System integration
  difficulties 784

T

Tafel equation 447
Tafel extrapolation 467, 480
Tafel plot 480
Tafel relationship 481
Tafel slope extrapolation 442
Talc
  spectrum 185
Tandem mass spectrometer 852
Tattersall's apparatus 353, 360, 361, 363
Tattersall's two point test 39
TEA 74
Techaranite
  spectra 195
TEM observation 221
Tensile stress 599
Terminology 344
Test specimens 702
TET solution 74
Tetracalcium aluminate hydrate 196
Tetrahedral coordination 218
Tetrahedral site 892
Tetrahydrofuran 639
Tetrakis 646
Tetramethylsilane 646
TG 144, 156
Thames Valley flint 72
Thaumasite 167, 261, 320
Thawing 43
Thenardite 256
  crystals 263
Thermal analysis 127, 167
Thermal diffusion length 914
Thermal effects 128
Thermal energy 913
Thermal equilibrium state 866
Thermal expansion 162
Thermal neutron 895
Thermal techniques 138, 158, 159
Thermochemical analysis 130
Thermodilatometry 131
Thermodynamically distinct C-S-H phases 221
Thermoelectrons 847
Thermograms 136
Thermogravimetric analysis 130
Thermoluminescence 907
  estimation of geological age 908
  measuring apparatus 908
Thermoluminescence intensity change results 909
Thermoluminescent minerals 909
Thermospray ionization method 847
Thermospray method 859

@Seismicisolation

Theta filter 283, 291
Thin-layer chromatography 840
Thiocyanates 156
Thixotropic 359
Thixotropy 336, 342, 343
Threshold radius 614
Thresholding 809
  process 809
Thresholds
  interactive modification 811
Tidal zone 49
Time domain 210
Time-resolved x-ray diffraction 285
Titrating 69
TMA 74
TMS 638, 646
  method 635, 641
Tobermorite 28, 158, 164, 218, 220, 221, 316
  spectra 195
  structure 630
Toluene 639
Topaz
  spectrum 185
Torrent air permeability test 715
Tourmaline 185
Trace impurities 289
Transference number 677
Transient diffusion processes 668
Transition zone 38, 42, 659, 660
Transitory Complex Theory 465
Transmission electron microscopy 232, 802
Transmission line model 477, 480
Transmission Mössbauer spectrometer 890
Transpiration test 671
Transport coefficient 676
Transport mechanisms 662, 771
Transport processes 658, 665, 725
Trapped electrons
  positive holes 907
Tremolite
  spectrum 186
Tricalcium aluminate 3
  hydration 146
Tricalcium silicate 3, 4, 136, 768
  hydration 147
  size distribution 771
Triclinic forms 136
Tridymite 63
Triethanolamine 17, 146, 200
  admixture 149
Trimethylsilyl ester 646
Trimethylsilylated silicate hydrate 844
Trimethylsilylation 630, 636
  analysis 635
Trisilicate 636
Tuckerman extensometers 369
Tuckermann extensometers 427
Tungsten alloys 829
Turbidimetry 516
Tuutti's model 461
Two-arc behavior 567

U

UBC rheometer 360
UE angles 92
Ultrasonic concrete tester 742
Underestimations 110
Undulatory extinction 91
Unmixed internal standard 301

V

V-t plots 546
Vacuum type STM 829
Valenta equation 708
van der Waals' forces 34, 242, 405
Vapor deposition method
  layer structure 825
Vapor diffusion 664
Vapor flux 662
Vaterite 164
Vebe consistometer 39
Vebe Test 39
Vermiculites 43
Vertical kilns 133
Vibration
  modes 177
Vibrational transition 177
Vibrations
  frequency of 738
  of molecules 176
Vicat 17
  apparatus 39
Virtual cement properties 772

@Seismicisolation

Viscoelastic behavior 345
Viscoelastic material 346
Viscoelastic properties 349
Viscoelasticity 38
Viscometer 362
Viscosity 334
  intrinsic 335
VMR 630
Void fraction 406
Volcanic rocks 66
Voltammetry 486
Voltammetry techniques 485
Volume change 536
Volume expansion 379
Volume instability 378

W

W/c 115, 353
W/c ratio 41
W/s ratios 418
Wagner turbidimeter 509
Wagner turbidimetry 516
Wall effect 359
Warming cycles 164
Washburn's equation 664, 685
Waste and by-products 133
Water 419
  adsorption 604
  analysis 115
  as adsorbate 24
  cement ratio 41
  fixed 415
  free and bound 23
  interlayer 317
  role of 36
  structural 36
Water absorption 75, 76, 694
  capacity tests 686
  tests 687
Water content 115, 117
Water flow test
  non-steady 703
Water gain 40
Water in concrete 660
Water mobility 521
Water penetrability 703
Water penetration 690, 703, 707
  tests 706
Water permeability 699
Water reducing admixtures 32
Water removal 597
Water sorption 514
Water to cement ratio 75
Water vapor transmission test 671
Water vapor transpiration test 671
Water-cement ratio 115, 242
Water-repellents 118
Water-repelling agents 109
Wave equation 176
Wavelengths
  x-ray 275
Weathering
  of rocks 77
Weight changes 130
Wetting 36
  angles 585
White coat plasters 430
Whole-powder-pattern 289
  decomposition method 289
  fitting 289
Windsor probe test 747, 748
Wollastonite 164
Workability 38, 39, 436, 437
  aids 109, 118

X

X-axis 837
X-ray absorption
  edge 871
  fine structure 872
  near edge structures 872
X-ray absorptivity 871
X-ray analysis
  computers 286
  software 286
X-ray analyzer 231
X-ray diffraction 78, 122, 276, 285, 312, 882
  analysis 883
X-ray diffractometer 282
X-ray diffractometry 286, 290, 890
X-ray microanalysis 804, 812
X-ray powder diffraction 772
  patterns 304
X-ray scattering
  small angle 316

@Seismicisolation

X-ray spectrometry 881
X-ray topography 882
X-rays 801, 870
  diffraction 276
X-rays intensity measurement
  transmission method 873
XAFS
  local physical phenomenon 873
  measurement result 874
XANES 872
  analysis 873
  examples 874
Xonotlite 647
  spectra 195
XRD
  applications 318
  hydration products studies 314
  use in blended cements 308
XRD-XRF 285
Xylose 162

Y

Yield stress 334, 337, 345, 347, 353, 356, 359
Young's modulus 20, 408, 412, 413, 414, 421

Z

Zeeman splitting 889
Zeolite 74, 647
Zingg shape classification 93

@Seismicisolation